

German Microwave Conference - GeMiC 2006 -

Universität Karlsruhe (TH)

March 28 - 30, 2006

www.gemic2006.de

Conference Guide

Prime Sponsors



VDE



ITG INFORMATIONSTECHNISCHE
GESELLSCHAFT IM VDE

Antennas
Microwave Techniques



IEEE

German IEEE
MTT/AP Chapter



MTT-S



IMA

Institut für Mikrowellen-
und Antennentechnik e.V.



GEROTRON

www.gerotron.de



Universität Karlsruhe (TH)
Research University · founded 1825



Forschungszentrum
Karlsruhe

About the Conference

Welcome to the **German Microwave Conference - GeMiC 2006** - which will be held from March 28 to 30, 2006 in Karlsruhe, Germany.

The conference site, the Auditorium Maximum of the Universität Karlsruhe (TH), is located near the Baroque Palace in the center of Karlsruhe, Germany. Founded in 1825 as the first Polytechnical School in Germany, the areas that the University has traditionally focused on are engineering, the natural sciences and economics. Heinrich Hertz conceived and performed his brilliant fundamental experiments confirming Maxwell's theory at the University of Karlsruhe (1886-1888). The University of Karlsruhe has close scientific and academic relations to the Karlsruhe Research Center (Forschungszentrum Karlsruhe); this is one of the largest national science and engineering research institutions in Europe.

We would like to thank the many scientists and engineers who are attending the **GeMiC 2006**. A very strong program has been assembled with 1 plenary and 21 normal sessions, including 7 invited and 108 contributed papers from both international and German authors. It will provide ample room for scientific exchange of information about latest achievements in the field of technologies, circuits and systems. In order to come together and to know each other, there will be a conference dinner on Wednesday, March 29, 2006.

Parallel to the conference, an exhibition will take place, where major suppliers and representatives of RF & microwave equipment will present their products. The exhibition is organized by **GEROTRON**.

We also thank the institutional sponsors of the **GeMiC 2006**, the Universität Karlsruhe (TH), and the Forschungszentrum Karlsruhe (Karlsruhe Research Center), the IEEE as co-sponsor through the IEEE MTT Society, and the German IEEE MTT/AP Chapter, as well as the Expert Groups "Microwave Techniques" and "Antennas" of the German VDE/ITG. It is organized by the German Institute for Microwave and Antenna Technology, IMA, a scientific, non-profit organization with the intention to promote R&D activities at universities, research centers and companies in the fields of microwaves, antennas and optoelectronics.

Werner Wiesbeck and Manfred Thumm
Conference Chairmen

Conference Committees

Conference Chairmen:

Prof. Dr.-Ing. Dr. h.c. Dr.-Ing. E.h. Werner Wiesbeck

Institut für Höchstfrequenztechnik und Elektronik, Universität Karlsruhe (TH)

Prof. Dr. rer. nat. Dr. h.c. Manfred Thumm

Institut für Höchstfrequenztechnik und Elektronik, Universität Karlsruhe (TH)
and Karlsruhe Research Center (Forschungszentrum Karlsruhe, FZK)

Local Organizing Committee:

Dipl.-Ing. Thomas Fügen

Institut für Höchstfrequenztechnik und Elektronik, Universität Karlsruhe (TH)

Simone Gorré

Institut für Höchstfrequenztechnik und Elektronik, Universität Karlsruhe (TH)

Bernhard Holstein

Institut für Höchstfrequenztechnik und Elektronik, Universität Karlsruhe (TH)

Dipl.-Ing. Thorsten Kayser

Institut für Höchstfrequenztechnik und Elektronik, Universität Karlsruhe (TH)

Karin Richter

Institut für Höchstfrequenztechnik und Elektronik, Universität Karlsruhe (TH)

Technical Chair:

Dr.-Ing. habil. Jürgen von Hagen

DaimlerChrysler AG, Sindelfingen

Technical Program Committee

Prof. Dr.-Ing. Fritz Arndt, University of Bremen

Dr.-Ing. Klaus Beilenhoff, United Monolithic Semiconductors GmbH, Ulm

Dr.-Ing. Christian Bornkessel, IMST GmbH, Kamp Lintfort

Dr.-Ing. Jochen Christ, Marconi Communications GmbH, Backnang

Prof. Dr.-Ing. Jürgen Detlefsen, Technical University of Munich

Dr.-Ing. Achim Dreher, Deutsches Zentrum für Luft- und Raumfahrt e. V., Oberpfaffenhofen

Prof. Dr.-Ing. Thomas Eibert, Universität Stuttgart

Prof. Dr.-Ing. Joachim Ender, FGAN, Wachtberg-Werthhoven

Prof. Dr.-Ing. Dietmar Fasold, Fachhochschule München
Dr.-Ing. Heinz-Peter Feldle, EADS Deutschland GmbH, Ulm
Dr.-Ing. Georg Fischer, Bell Labs Europe, Lucent, Nürnberg
Prof. Dr.-Ing. Roland Gabriel, KATHREIN-Werke, Rosenheim
Dr.-Ing. Gerd Gottwald, Robert Bosch GmbH, Abstatt
Dipl.-Ing. Thomas Greiner, Tyco Electronics/Electronic Modules, München
Prof. Dr.-Ing. Volkert Hansen, Bergische Universität, Wuppertal
Dr.-Ing. Dirk Heberling, IMST GmbH, Kamp Lintfort
Dr.-Ing. Patric Heide, EPCOS AG, München
Prof. Dr. rer.nat. habil. Matthias A. Hein, TU Ilmenau
Dr.-Ing. Wolfgang Heinrich, Ferdinand-Braun-Institut für Höchstfrequenztechnik, Berlin
Prof. Dr.-Ing. Rolf H. Jakoby, Technische Universität Darmstadt
Prof. Dr.-Ing. Rolf H. Jansen, RWTH Aachen
Prof. Dr.-Ing. Reinhard Knöchel, Universität Kiel
Prof. Dr.-Ing. Viktor Krozer, Technical University of Denmark, Lyngby
Prof. Dr.-Ing. Heinz Lindenmeier, Universität der Bundeswehr, Neubiberg
Dr.-Ing. Johann-Friedrich Luy, DaimlerChrysler AG, Ulm
Dr.-Ing. Siegbert Martin, Marconi Communications GmbH, Backnang
Prof. Dr.-Ing. Wolfgang Menzel, Universität Ulm
Prof. Dr.-Ing. habil. Alberto Moreira, Deutsches Zentrum für Luft- und Raumfahrt e. V., Weßling
Dipl.-Ing. Bruno Plehn, EADS Deutschland, Ulm
Dr.-Ing. Christof Rohner, Rohde & Schwarz, München
Prof. Dr.-Ing. Christian Schäffer, Technische Universität Dresden
Prof. Dr.-Ing. Lorenz-Peter Schmidt, Universität Erlangen-Nürnberg
Dr.-Ing. Martin Schneider, Universität Bremen
Prof. Dr.-Ing. Klaus Solbach, Universität Duisburg-Essen
Prof. Dr.-Ing. Martin Vossiek, Technische Universität Clausthal
Dr.-Ing. Josef Wenger, DaimlerChrysler AG, Ulm
Dr.-Ing. Leif Wiebking, Siemens AG, München
Chief Eng. Antennas Helmut Wolf, EADS Astrium, München

Sponsors

Thanks are due to:

- **Universität Karlsruhe (TH)**
- **Karlsruhe Research Center (Forschungszentrum Karlsruhe, FZK)**
- **IEEE Microwave Theory and Techniques Society (MTT-S) and the German IEEE MTT/AP Chapter**
- **German VDE/ITG, Expert Groups "Microwave Techniques" and "Antennas"**
- **GEROTRON, Gräfelfing**
- **EADS Deutschland, Ulm**
- **KATHREIN-Werke, Rosenheim**
- **DaimlerChrysler AG, Stuttgart**
- **Ericsson, Backnang**
- **Elcoteq Communications Technology GmbH, Offenburg**

for their sponsoring and support.

Information for Oral and Poster Presenters

Oral presentations

All conference rooms for oral presentations will have a computerized LCD projector (data projector) and an overhead projector. Be present at least 10 minutes before the start of your underlinesession and inform the session chairman of your arrival.

Time schedules for talks are as follows:

Plenary talks:	35 minutes (30 min. for presentation plus 5 min. for discussion)
Contributed talks:	20 minutes (17 min. for presentation plus 3 min. for discussion)

For the speakers who want to use the data projector:

1. Strongly recommended:

Speakers should bring only a compact disk or a USB-Memory-Stick with the presentation files in "ppt" (power point) format. Of course "pdf" is also possible. In each conference room an assistant and a notebook computer will be available for the presentations. Speakers should preview their presentation on the computers in the "Prescreening Room" up to 20 minutes before the session is scheduled to start. After prescreening the presentation will be transmitted via LAN to the notebook computer in the conference room.

2. In case that 1. is not feasible:

Speakers should bring their own notebook computers. The computer settings should be as follows:

Screen resolution:	1024 x 768
Refresh rate:	60 - 85 Hz
Output port for display:	VGA monitor 15 pins standard output.

Speakers should be present in the conference room 20 minutes before the session starts to preview their presentation.

3. "Prescreening Room":

Location: Wardrobe Room of AUDIMAX, ground floor, near the main entrance.

Available time for prescreening:

Tuesday, March 28:	10:30 - 18:00
Wednesday, March 29:	08:00 - 18:00
Thursday, March 30:	08:00 - 11:00

Poster presentations

Posters should have a height of 118.9 cm and a width of 84.1 cm (A0 size). On Tuesday, March 28, posters should be set up at 10:30 and taken down at 18:00. On Wednesday, March 29, posters should be set up at 8:30 and taken down at 18:00.

The presenter is expected to remain at the poster during the hours of the poster sessions.

Tuesday, March 28:	10:30 - 11:00	15:20 - 15:50	17:30 - 18:00
Wednesday, March 29:	10:30 - 11:00	15:20 - 15:50	17:30 - 18:00

Official Language

The official language of the conference is English, which should be used in all printed materials, presentations, and discussions.

Registration Desk

Conference materials will be distributed at the registration desk in the foyer of the AUDIMAX. The opening hours of the desk are as follows:

Tuesday, March 28:	09:00 - 18:00
Wednesday, March 29:	08:00 - 18:00
Thursday, March 30:	08:00 - 13:30

Conference Digest

The accepted papers are published on the GeMiC 2006 Conference CD-Rom. A copy will be made available to each participant on arrival at the conference.

Coffee Breaks

Coffee, tea and refreshments will be available in the Foyer of the AUDIMAX during the coffee break.

Conference Dinner

A conference dinner (buffet) will be held on the evening of Wednesday, March 29, 2006. All participants are requested to wear the conference badge provided at the time of registration.

Date and Time: Wednesday, March 29, 2006 at 18:00 o'clock
Location: Conference venue, Foyer AUDIMAX

GeMiC 2006 Secretariat

Institut für Höchstfrequenztechnik und Elektronik (IHE)
Universität Karlsruhe (TH)
Kaiserstr. 12
76131 Karlsruhe, Germany

and

Conference Venue AUDIMAX

Phone: +49-(0)-721-608-7729

Fax: +49-(0)-721-608-2917

e-mail: gemic2006@ihe.uka.de

Internet Room

Several PCs for internet access, LAN ports and Wireless LAN will be provided in the internet room at the AUDIMAX. Please bring your own PC if you wish to use the LAN ports. Internet access will be free for everyone attending the conference. The room will be open during the following dates and times:

Tuesday, March 28:	10:00 - 18:00
Wednesday, March 29:	08:00 - 20:00
Thursday, March 30:	08:00 - 13:00

Wireless Access

In order to get access to the wireless network of the Universität Karlsruhe (TH) (called DUKATH), you need a radio adapter card, which supports the 802.11b or 802.11g standard.

You can make a wireless connection to one of the available networks by choosing the network name (SSID server set Identifier) of your wireless adapter to "ANY" or by selecting the strongest signal from the offered SSIDs. The SSID must begin with "dukath...". For further details refer to the instructions for your wireless adapter.

Activate DHCP (dynamic host configuration protocol) on your computer. Check out whether you have got a correct IP address (for example with the "ipconfig" command in a DOS window). It must begin with "129.13...".

When you open a browser window you will automatically be redirected to the DUKATH authentication website (https://dukath-www.rz.uni-karlsruhe.de/index_en.html). Here you have two possibilities to get access to the internet:

1. If you only want to surf in the internet, type in the conference slogan "**microwave**" on the bottom of the authentication website and select the conference "**GEMIC2006**". Then press the apply button. As long as the browser window is open you will have access to HTTP and/or HTTPS applications.
2. With your individual guest account that was issued with the conference documents, you can get full access to the internet. You can start mail, SSH, HTTP applications or establish a VPN tunnel to your home network. Type in your individual user name and your password and press the apply button. Keeping the following window open you will have full access to the internet (open a new window with "ctrl n"). For further questions or problems please contact the responsible person of the internet room.

Exhibition

From Tuesday, March 28, until Wednesday, March 29, the exhibition in parallel to the Conference is open in the Foyer of the AUDIMAX. The exhibition is organized by GEROTRON. The Exhibitors are:

Alfred Tronser GmbH

Engelsbrand

Anritsu GmbH

München

Ansoft Corporation

München

CST

Darmstadt

Elcoteq Communications Technology GmbH

Offenburg

EMC-Technik & Consulting GmbH

Stuttgart

EMCO Elektronik GmbH

Planegg

Globes Elektronik GmbH & Co. KG

Heilbronn

Roland Häfele Leiterplattentechnik e.K.

Schriesheim

Mauritz GmbH & Co. KG

Hamburg

Mician GmbH

Bremen

OPTOcon GmbH

Dresden

Panasonic Electronic Devices Europe GmbH

Lueneburg

Tactron Elektronik Schmidt-Fürst oHG

Martinsried

(status February 5, 2007)

GeMiC 2006 Program

Tuesday, March 28, 2006

Time	Audimax A	Audimax B	Seminar-Room
11:00 - 12:40	1a Passive Circuits & Components	1b EM Field Theory	—
12:40 - 13:40	Lunch		
13:40 - 15:20	2a Filters & Multiplexers	2b Antennas I	—
15:20 - 15:50	Coffee Break		
15:50 - 17:30	3a Active Circuits & Systems I	3b Antennas II	—
10:30 - 18:00	4	Poster Session I	

Wednesday, March 29, 2006

Time	Audimax A	Audimax B	Seminar-Room
08:30 - 10:30	5 Opening & Plenary Session		—
10:30 - 11:00	Coffee Break		
11:00 - 12:40	6a Active Circuits & Systems II	6b Ultra Wideband	6c Gyrotrons & High Power mm-Waves
12:45 - 13:40	Lunch		
13:40 - 15:20	7a Active Components & Devices	7b Antennas III	7c Special Session on EM Exposure
15:20 - 15:50	Coffee Break		
15:50 - 17:30	8a MEMS & Tunable Circuits	8b Radars, Sensors & Imaging Systems I	—
08:30 - 18:00	9 Poster Session II		
18:00 - 22:00	Conference Dinner (Buffet)		

Thursday, March 30, 2006

Time	Audimax A	Audimax B	Seminar-Room
08:30 - 10:30	10a Measurements & mm-Wave Techniques	10b Radars, Sensors, and Imaging Systems II	10c Special Session on μ - & mm-Wave Mat. Processing
10:30 - 11:00	Coffee Break		
11:00 - 12:40	11a mm- & Sub-mm Wave Components, Circuits & Systems	11b Radars, Sensors, and Imaging Systems III	—
12:40 - 13:00	Closing Session		—

Sessions

Session 1a - Passive Circuits and Components

Tuesday, March 28, 2006

11:00 - 12:40

Room: Audimax A

Session Chairs: Werner Wiesbeck (University of Karlsruhe (TH))

Rainer Lenz (University of Karlsruhe (TH))

1a-1: **Evaluation of Potting Possibilities for RF Circuits up to 24 GHz**

M.O. Olbrich, W. Kiermeier, E. Biebl

Technische Universität Muenchen, Fachgebiet Hoehstfrequenztechnik, Munich, Germany

1a-2: **Broadband Wilkinson Divider**

A. Wentzel, D. Pienkowski

Technische Universität Berlin, Microwave Engineering Group, Berlin, Germany

1a-3: **A Lumped Element Circulator with Semi-Additive Metallized Conductors**

R. Stonies, D. Teufer, D. Schulz

University of Dortmund, Lehrstuhl für Hochfrequenztechnik, Dortmund, Germany

1a-4: **Impedance Matching of a Loaded Microstrip Transmission Line by Parasitic Elements**

H. Matzner, S. Ouzan, H. Moalem, I. Arie

Holon Institute of Technology, Department of Communication Engineering, Holon, Israel

1a-5: **The Bifurcated E-Plane T-Junction and Its Application to Waveguide Diplexer Design**

J. Bornemann, M. Mokhtaari

Department of Electrical and Computer Engineering, University of Victoria, BC, Canada

Session 1b - EM Field Theory

Tuesday, March 28, 2006

11:00 - 12:40

Room: Audimax B

Session Chairs: Thomas Eibert (University of Stuttgart)
Florian Berbl (Technical University of Munich)

1b-1: **A Fast Spectral Domain Approach for Analyzing Larger Structures Embedded in Multilayered Media**

T. Vaupel (1), T.F. Eibert (2)

(1) FGAN-FHR, Wachtberg, Germany

(2) University of Stuttgart, Germany

1b-2: **Coupling Structures for Terahertz Near-field Microspectroscopy**

G. Staats (1), L.M. Fernandez Ortega (1), U. Schade (2), D. Schondelmaier (2), K. Holldack (2)

(1) Technische Universität Dresden, Germany

(2) Berliner Elektronenspeicherring-Gesellschaft für Synchrotronstrahlung m.b.H. (BESSY), Berlin, Germany

1b-3: **Numerical Computation of Field and Temperature Distribution for a Device Aiming at Local Brain Exposure of Rodents in Vivo at 2 GHz**

A. El Ouardi (1), A. Bitz (1), J. Streckert (1), T. Reinhardt (1), V. Hansen (1), D. Krause-Finkeldey (2), K. Ladage (2)

(1) University of Wuppertal, Electromagnetic Theory, Wuppertal, Germany

(2) Ruhr-Universität Bochum, Institute of Anatomy, Bochum, Germany

1b-4: **On the Calculation of the Radiation Properties of Dipole Antennas in Cylindrical Boreholes Considering Large Scatterers**

A. Becker, Y. Zhou, V. Hansen

University of Wuppertal, Faculty of Electrical, Information and Media Engineering

1b-5: **Numerically Efficient MPIE-MoM Technique for Analysis of Microstrip Structures in Layered Media**

Z. Genc (1), H.H. Balik (2)

(1) University of Firat, Department of Informatics, Turkey,

(2) University of Firat, Department of Electrical and Electronics Eng., Turkey

Session 2a - Filters and Multiplexers

Tuesday, March 28, 2006

13:40 - 15:20

Room: Audimax A

Session Chairs: Arne Jacob (University of Hamburg-Harburg)
Jürgen Detlefsen (Technical University of Munich)

2a-1: **Suspended Stripline Bandpass Filters with Inductive and Mixed Coupling**

W. Menzel (1), A. Balalem (2)

(1) Microwave Techniques, University of Ulm, Germany

(2) Microwave and Communication Engineering Chair, University of Magdeburg, Germany

2a-2: **Compact Broadband Filters for Hybrid Circuits using Flip-Chip-Technology**

T. Baras, F. Muhammad, A.F. Jacob

Tech. Univ. Hamburg-Harburg, Hochfrequenztechnik, Hamburg, Germany

2a-3: **Ka-Band Diplexer Design Using Filter Characteristics with Transmission Zeros - Realised Without Implementation of Cross Couplings**

U. Rosenberg (1), J. Ebinger (1), S. Amari (2)

(1) Ericsson GmbH, Microwave Technology Center, Backnang, Germany

(2) Royal Military College, Department of Electrical and Computer Engineering, Kingston, ON, Canada

2a-4: **Dielectric Rod Waveguide Couplers as Harmonic Filters for Millimeter and Sub-Millimeter Wave Frequencies**

A. Hofmann, M. Manglberger, S. Biber, J. Weinzierl, L.P. Schmidt, H. Brand

University of Erlangen-Nuremberg (UEN), Institute for Microwave Engineering (LHFT), Erlangen, Germany

2a-5: **A Novel 2-GHz Tunable Differential Three-Branch Channelized Bandpass Filter Integrated on Silicon**

S. Darfeuille (1), R. Gomez-Garcia (2), B. Barelaud (1), L. Billonnet (1), B. Jarry (1), H. Marie (3), P. Gamand (3)

(1) XLIM, UMR CNRS 6172, Université de Limoges, Limoges, France

(2) Dpto. SSR, ETSI Telecomunicación, Universidad Politécnica de Madrid, Spain

(3) Innovation centre RF, Philips Semiconductors, Caen, France

Session 2b - Antennas I

Tuesday, March 28, 2006

13:40 - 15:20

Room: Audimax B

Session Chairs: Dirk Heberling (IMST GmbH, Kamp Lintfort)
Marc Rüttschlin (University of Karlsruhe (TH))

2b-1: **Improved Patch Antenna Network Model**

K. Solbach, D. Trung Tran

University Duisburg-Essen, Hochfrequenztechnik, Duisburg, Germany

2b-2: **A K-band Biconical Antennas System for Wireless Wideband Communication Equipments**

V. Stornelli (1), M. Caramanico (2), M. Di Fabrizio (2), A. Brigante (2)

(1) Dept. of Electrical Engineering, University of L'Aquila, Italy

(2) R&D Dept. Thales Italia, Chieti Scalo, Italy

2b-3: **Design of an Airborne Dual-Polarized Triple Stacked Patch Antenna for Broadband SAR Applications in P-Band**

M. Limbach, B. Gabler, R. Scheiber, R. Horn

Deutsches Zentrum für Luft- und Raumfahrt e.V. (DLR), Oberpfaffenhofen, Germany

2b-4: **Unidirectional Slot Subarray-Antenna with High Efficiency for X-Band Application**

C. Löcker (1), T. Vaupel (1), T.F. Eibert (2)

(1) FGAN-Research Inst. for High Frequency Physics and Radar Techniques, Wachtberg-Werthhoven, Germany

(2) University of Stuttgart, Institute of Radio Frequency Technology, Stuttgart, Germany

2b-5: **A Novel 24 GHz 4-Quadrant Slot Antenna**

P.K. Talukder, F.J. Schmückle, W. Heinrich

Ferdinand-Braun-Institut für Höchstfrequenztechnik (FBH), Berlin, Germany

Session 3a - Active Circuits and Systems I

Tuesday, March 28, 2006

15:50 - 17:30

Room: Audimax A

Session Chairs: Ingmar Kallfass (Fraunhofer Institute for Applied Solid-State Physics, Freiburg)
Viktor Krozer (Technical University of Denmark, Lyngby)

3a-1: **Systematic Measurements for Testing the Influence of an Internal Noise Source on the Phase Noise of an Oscillator**

M.H.W. Hoffmann, H. Weiß

University of Ulm, Dept. of Microwave Techniques, Ulm, Germany

3a-2: **A Wideband Amplifier with 2.4mm Connectors Operating up to 48GHz**

M. Häfele (1,3), C. Schick (1), F. Hernandez-Guillen (1), A. Trasser (1), P. Abele (1,2), H. Schumacher (1)

(1) Dept. of Electron Devices and Circuits, University of Ulm, Germany

(2) United Monolithic Semiconductors (UMS) GmbH, Ulm, Germany

(3) DaimlerChrysler AG, Research and Technology, Ulm, Germany

3a-3: **Load Variation Tolerant Balanced Amplifier with Two Element LC-Coupler**

I. Ibrahim, N. Peters, H. Heuermann

Department of High Frequency Technologies, University of Applied Science Aachen, Germany

3a-4: **A Low Power, Variable Gain Common-Gate LNA**

T. Stücker, N. Christoffers, R. Kokozinski, S. Kolnsberg, B.J. Hosticka

Fraunhofer Institute of Microelectronic Circuits and Systems (IMS)

3a-5: **Cost-Effective, Power-Efficient and Configurable YIG Replacement Signal Source**

U.L. Rohde (1,2), A.K. Poddar (2)

(1) University of Cottbus, Germany

(2) Synergy Microwave Corp., NJ, USA

Session 3b - Antennas II

Tuesday, March 28, 2006

15:50 - 17:30

Room: Audimax B

Session Chairs: Klaus Solbach (University of Duisburg-Essen)
Matthias Geissler (IMST GmbH, Kamp Lintfort)

3b-1: A New TEM Double-ridged Horn Antenna for Ground Penetrating Radar Applications

A. Teggatz, A. Jöstingmeier, A.S. Omar

Inst. for Electronics, Signal Processing and Communications, FEIT, University of Magdeburg, Magdeburg, Germany

3b-2: Multipath Mitigation Through Cylindrical Microstrip Phased Array Antenna

D. Mastela (1), L. Reindl (1), T. Zander (1), L. Wiebking (2), M. Kawalkiewicz (3)

(1) University of Freiburg, Institute of Microsystems Technology, Freiburg, Germany

(2) Siemens AG, CT PS7, Munich, Germany

(3) Warsaw University of Technology, Warsaw, Poland

3b-3: A Low Cost Low Profile 19 GHz Scanning Receiver Array with a Nonradiative Dielectric Waveguide Feeding Network

U. Schmid, W. Menzel

University of Ulm, Microwave Techniques, Ulm, Germany

3b-4: Development on Ku-Band Feed Chains for Satellite Antennas

C. Hartwanger, R. Gehring, U.P. Hong, H. Wolf

EADS Astrium GmbH, Munich, Germany

3b-5: Characterization of 35 GHz Tunable Reflectarray Unit-Cells Using Highly Anisotropic Liquid Crystal

R. Marin, A. Mössinger, J. Freese, R. Jakobý

Technische Universität Darmstadt, Institut für Hochfrequenztechnik, Darmstadt, Germany

Session 4 - Poster Session I

Tuesday, March 28, 2006

10:30 - 18:00

Room: Foyer

Session Chair: Christiane Kuhnert (University of Karlsruhe (TH))

4-1: **Measurement and Modelling of a High Power Amplifier for the Integration in MIMO-OFDM System Simulations**

C. Kuhnert, A. Ossowska, W. Wiesbeck

Universität Karlsruhe (TH), Institut für Höchstfrequenztechnik und Elektronik, Karlsruhe, Germany

4-2: **IEEE 802.15.4/ ZigBee™ Compliant Intermediate Frequency Limiter and Received Signal Strength Indicator for RF Transceivers**

R. Vaijinath, S.M. Deokar

E&TC Dept, Sihgad College of Engineering, India

4-3: **Analysis of Modes in Rectangular-Waveguide Noncontacting Shorting Plunger**

V. Bilik, J. Bezek

Slovak University of Technology, Faculty of Electrical Engineering and Information Technology, Bratislava, Slovakia

4-4: **Constraints for Radio based Quality Testing in Industrial Environments**

G. Saala (1,3), S. Schulteis (2,3), J.F. Luy (1,3), W. Wiesbeck (2,3)

(1) DaimlerChrysler AG, RMI/DI, Ulm, Germany

(2) Universität Karlsruhe (TH), Institut für Höchstfrequenztechnik und Elektronik, Karlsruhe, Germany

(3) Universität Karlsruhe (TH), Joint Research-Center on Reliability of Automotive Systems (ZAS), Germany

4-5: **Design and Performance of an UWB Antenna for a Mono-static Microwave Radar System**

A. Ruengwaree, A. Ghose, G. Kompa

University of Kassel, Department of High Frequency Engineering, Kassel, Germany

4-6: **Determination of Dielectric Material Parameters using a Flexible Waveguide Setup**

T. Kayser, M. Pauli, W. Wiesbeck

Universität Karlsruhe (TH), Institut für Höchstfrequenztechnik und Elektronik, Karlsruhe, Germany

4-7: Compact Planar Filters for Wireless Communications Systems

M.G. Banciu (1), N. Militaru (2), A. Ioachim (1), G. Lojewski (2)

(1) National Institute of Materials Physics, Microwave Group, Bucharest-Magurele, Romania

(2) "Politehnica" University of Bucharest, Faculty of Electronics, Telecom. and Inf. Tech., Bucharest, Romania

4-8: Wideband Single Patch E-shaped Compact Microstrip Antenna for High Speed Wireless Local Area Networks

G.P. Rao (1), K. Agarwal (1), M.V. Kartikeyan (1), M.K. Thumm (2,3)

(1) Department of Electronics & Computer Engineering, Indian Institute of Technology, Roorkee, Uttranchal, India

(2) Forschungszentrum Karlsruhe, Institut für Hochleistungsimpuls und Mikrowellentechnik, Karlsruhe, Germany

(3) Universität Karlsruhe (TH), Institut für Höchstfrequenztechnik und Elektronik, Karlsruhe, Germany

Session 5 - Plenary Session

Wednesday, March 29, 2006

08:30 - 10:30

Room: Audimax A and B

Session Chair: Jürgen von Hagen (DaimlerChrysler AG, Sindelfingen)

Welcome Address

Prorektor Prof. Dr.-Ing. Jürgen Becker
Universität Karlsruhe (TH), Karlsruhe

Welcome, Introduction to the Conference

Prof. Dr.-Ing. Dr. h.c. Dr.-Ing. E.h. Werner Wiesbeck
Universität Karlsruhe (TH), Karlsruhe

5-1: The European Satellite Navigation System Galileo - Technical Implementation (Invited)

H.L. Trautenberg, T. Weber
EADS Astrium GmbH, Munich, Germany

5-2: System and Technology Aspects for Advanced Phased Array Radar Frontends (Invited)

H.-P. Feldle
EADS Deutschland GmbH, Ulm, Germany

5-3: Trends in Basestation RF Technology (Invited)

G. Fischer
Bell Labs Europe, Lucent, Nürnberg, Germany

Session 6a - Active Circuits and Systems II

Wednesday, March 29, 2006

11:00 - 12:20

Room: Audimax A

Session Chairs: Martin Vossiek (Clausthal University of Technology)
Viktor Krozer (Technical University of Denmark, Lyngby)

6a-1: **A 2.14 GHz Inverse Class F Si-LDMOS Power Amplifier with Voltage Second Harmonic Peaking**

W. Gerhard, R. Knöchel

Christian-Albrechts University of Kiel, Department of Electrical Engineering, Microwave Laboratory, Kiel, Germany

6a-2: **Linearisation of High Power Amplifier with Optimised Zone 0 Terminations**

B. Bunz, A.Z. Markos , A. Ahmed, G. Kompa

University of Kassel, Fachgebiet Hochfrequenztechnik, Kassel, Germany

6a-3: **Experimental Study of Time-Domain to Frequency-Domain Correlation for GaAs-HBT Based TWAs for 20 Gbps and 40 Gbps**

C. Meliani, M. Rudolph

Ferdinand-Braun-Institut für Hoehstfrequenztechnik (FBH), Berlin, Germany

6a-4: **An Oscillator with Reduced Phase Noise and Improved Harmonic Characteristics Based on a Corrugated CPW EBG Structure**

C.G. Hwang, N.H. Myung

Dep. of Elec. Engineering and Computer Sc., Korea Advanced Inst. of Sc. and Technology, Daejeon, Korea

Session 6b - Ultra Wideband

Wednesday, March 29, 2006

11:00 - 12:40

Room: Audimax B

Session Chairs: Werner Wiesbeck (University of Karlsruhe (TH))
Werner Sörgel (University of Karlsruhe (TH))

6b-1: **Periodical Protrusions for UWB Slot Antennas**

J.N. Hwang (1), W. Sörgel (2), W. Wiesbeck (2)

(1) Department of Communication Engineering, National Chiao Tung University, Taiwan

(2) Universität Karlsruhe (TH), Institut für Höchstfrequenztechnik und Elektronik, Karlsruhe, Germany

6b-2: **Pulse-Length Modulator for Analogue-to-Digital Conversion of Radio Frequency Signals**

C. Hartmann, K. Blau, M. Hein

Technische Universität Ilmenau, Department for RF and Microwave Techniques, Ilmenau, Germany

6b-3: **A SiGe Monocycle Impulse Generator for Impulse Radio Ultra-Wideband Applications**

J. Dederer, A. Trasser, H. Schumacher

University of Ulm, Dept. of Electron Devices and Circuits, Ulm, Germany

6b-4: **Modified M-Sequence UWB-Radar**

J. Sachs (1), R. Herrmann (1), M. Kmec (1), P. Peyerl (2)

(1) Technische Universität Ilmenau, Institut für Informationstechnik, Ilmenau

(2) MEODAT GmbH, Ilmenau, Germany

6b-5: **Design of a 10GSps 5 bit flash A/D converter**

P. Monsurrò (1), A. Thiede (2), A. Trifiletti (1)

(1) University of Rome "La Sapienza", Rome, Italy

(2) University of Paderborn, Paderborn, Germany

Session 6c - Gyrotrons and High Power Millimeter-Waves

Wednesday, March 29, 2006

11:00 - 12:40

Room: Seminar-Room

Session Chair: Manfred Thumm (Karlsruhe Research Center)

6c-1: Gyrotron Research at Forschungszentrum Karlsruhe

G. Dammertz (1), A. Arnold (2), D. Bariou (3), E. Giguet (3), R. Heidinger (4), S. Illy (1), J. Jin (1), F. Legrand (3), W. Leonhardt (1), C. Lievin (3), G. Neffe (1), B. Piosczyk (1), T. Rzesnicki (1), M. Schmid (1), M. Thumm (1,2)

(1) Forschungszentrum Karlsruhe, Ass. EURATOM-FZK, IHM, Eggenstein-Leopoldshafen, Germany

(2) Universität Karlsruhe (TH), Institut für Höchstfrequenztechnik und Elektronik, Karlsruhe, Germany

(3) Thales Electron Devices, Vélizy-Villacoublay, France

(4) Forschungszentrum Karlsruhe, Ass. EURATOM-FZK, IMF, Eggenstein-Leopoldshafen, Germany

6c-2: An 84 GHz, 500 kW, CW Gyrotron

M.V. Kartikeyan (1), E. Borie (2), B. Piosczyk (2), M.K. Thumm (3)

(1) Department of Electronics & Computer Engineering, Indian Institute of Technology Roorkee, Uttaranchal, India

(2) Forschungszentrum Karlsruhe, Institut für Hochleistungsimpuls und Mikrowellentechnik, Karlsruhe, Germany

(3) Universität Karlsruhe (TH), Institut für Höchstfrequenztechnik und Elektronik, Karlsruhe, Germany

6c-3: Studies on a 250 GHz, 50 W, CW Second Harmonic Gyrotron for Spectroscopy

M.V. Kartikeyan (1), E. Borie (2), M.K. Thumm (2,3)

(1) Department of Electronics & Computer Engineering, Indian Institute of Technology Roorkee, Uttaranchal, India

(2) Forschungszentrum Karlsruhe, Institut für Hochleistungsimpuls und Mikrowellentechnik, Karlsruhe, Germany

(3) Universität Karlsruhe (TH), Institut für Höchstfrequenztechnik und Elektronik, Karlsruhe, Germany

6c-4: Low Power Verification of a new RF Output System for a 170 GHz, 2 MW Coaxial Cavity Gyrotron

T. Rzesnicki (1), J. Jin (1), B. Piosczyk (1), M. Thumm (1,2), G. Michel (3), D. Wagner (4)

(1) Forschungszentrum Karlsruhe, Institut für Hochleistungsimpuls- und Mikrowellentechnik, Karlsruhe, Germany

(2) Universität Karlsruhe (TH), Institut für Höchstfrequenztechnik und Elektronik, Karlsruhe, Germany

(3) Max-Planck-Institut für Plasmaphysik, Greifswald, Germany

(4) Max-Planck-Institut für Plasmaphysik, Garching, Germany

6c-5: **Internal Quasi-Optical Mode Converter for a Coaxial Gyrotron**

J.B. Jin (1), M. Thumm (1,2), T. Rzesnicki (1), B. Piosczyk (1)

(1) Forschungszentrum Karlsruhe, Ass. EURATOM-FZK, IHM, Karlsruhe, Germany

(2) Universität Karlsruhe (TH), Institut für Höchstfrequenztechnik und Elektronik, Karlsruhe, Germany



Session 7a - Active Components and Devices

Wednesday, March 29, 2006

13:40 - 15:20

Room: Audimax A

Session Chairs: Wolfgang Heinrich (Ferdinand-Braun-Institut für Höchstfrequenztechnik, Berlin)
Klaus Beilenhoff (United Monolithic Semiconductors GmbH, Ulm)

7a-1: **Modeling HBT Low-Frequency Noise for Circuit Simulation**

M. Rudolph (1), F. Lenk (1), S. Gribaldo (2,3), O. Llopis (2,3), W. Heinrich (1)

(1) Ferdinand-Braun-Institut für Höchstfrequenztechnik (FBH), Berlin, Germany

(2) Lab. d'Analyse et d'Architecture des Syst. du Centre National de la Rech. Scientifique, Toulouse, France

(3) University Paul Sabatier, Toulouse, France

7a-2: **Avalanche Breakdown in GaInP/GaAs HBTs**

P. Baureis

University of Applied Sciences Würzburg, Germany

7a-3: **Design and W-CDMA Characterization of a Wideband AlGaIn/GaN HEMT Power Amplifier for Future 3G Multiband Base Station Applications**

D. Wiegner (1), U. Seyfried (1), W. Templ (1), T. Naß (1), S. Weber (1), S. Wörner (1), I. Dettmann (2), R. Quay (3), F. van Raay (3), H. Walcher (3), H. Massler (3), M. Seelmann-Eggebert (3), R. Reiner (3), R. Moritz (3), R. Kiefer (3)

(1) Alcatel-SEL AG, Research Centre Stuttgart, Germany

(2) Institute of Electrical and Optical Communication Engineering at University of Stuttgart, Germany

(3) Fraunhofer Institute of Applied Solid State Physics, Freiburg, Germany

7a-4: **Large-Signal Modeling of AlGaIn/GaN HEMTs with Analytically Calculated Thermal Resistance**

E. Chigaeva (1), I. Dettmann (1), M. Berroth (1), H. Roll (2), H. Schweizer (2)

(1) Institute for Electrical and Optical Communications Engineering, Universität Stuttgart, Germany

(2) 4th Physical Department, Universitaet Stuttgart, Germany

7a-5: **Bias Dependent, Compact Low-Frequency Noise Model of GaInP/GaAs HBT: Experimental Identification and CAD Implementation**

M. Borgarino (1), N. Corciulo (1), C. Florian (2), P.A. Traverso (2), F. Fantini (1), F. Filicori (2)

(1) University of Modena and Reggio Emilia, Information Engineering Department, Modena, Italy

(2) University of Bologna, DEIS Department, Bologna, Italy

Session 7b - Antennas III

Wednesday, March 29, 2006

13:40 - 15:20

Room: Audimax B

Session Chairs: Heinz Chaloupka (University of Wuppertal)
Stephan Schulteis (University of Karlsruhe (TH))

7b-1: Low-order Models for Spatial Diversity Systems Including Real Antenna Characteristics

O. Klemp, G. Armbrecht, H. Eul

Universität Hannover, Institut für Hochfrequenztechnik und Funksysteme, Hannover, Germany

7b-2: Improved Antenna Isolation in Transmit/Receive Applications

D. Esser, B. Solan, H. Chaloupka

University of Wuppertal, Department of Electrical, Information and Media Engineering, Wuppertal, Germany

7b-3: Miniaturization of Mobile Phone Antennas by Utilization of Chassis Mode Resonances

W.L. Schroeder, P. Schmitz, C. Thome

BenQ Mobile GmbH & Co. OHG, Product Innovation Center, Bocholt, Germany

7b-4: Integration of Inverted F-antennas in Small Mobile Devices with Respect to Diversity and MIMO Systems

S. Schulteis, C. Kuhnert, J. Pontes, W. Wiesbeck

Universität Karlsruhe (TH), Institut für Höchstfrequenztechnik und Elektronik, Karlsruhe, Germany

7b-5: Evaluation and Optimization of CDMA System Performance in Macrocell Environments Based on Antenna Radiation Pattern

J.A. Pontes, S. Schulteis, M.A. Baldauf, W. Wiesbeck

Universität Karlsruhe (TH), Institut für Höchstfrequenztechnik und Elektronik, Karlsruhe, Germany

Session 7c - Special Session on EM Exposure

Wednesday, March 29, 2006

13:40 - 15:20

Room: Seminar-Room

Session Chairs: Christian Bornkessel (IMST GmbH, Kamp Lintfort)
Michael Baldauf (University of Karlsruhe (TH))

7c-1: **Minimising the Electromagnetic Exposure at Hot-Spot Areas Using Hybrid (DVB-H/UMTS) Networks**

P. Unger, M. Schack, T. Kürner

Dep. of Mobile Radio Systems, Inst. for Com. Tech., Braunschweig Tech. University, Braunschweig, Germany

7c-2: **Exposure Reduction in GSM Networks by Cell Splitting**

M.A. Baldauf, S. Knörzer, W. Sörgel, W. Wiesbeck

Universität Karlsruhe (TH), Institut für Höchsthfrequenztechnik und Elektronik, Karlsruhe, Germany

7c-3: **Exposure Measurements of Modern Digital Broadband Radio Services**

C. Bornkessel (1), M. Wuschek (2)

(1) IMST GmbH, Test Centre EMC, Kamp-Lintfort, Germany

(2) University of Applied Sciences Deggendorf, Deggendorf, Germany

7c-4: **Compact Setup for an Homogeneous Plane-Wave Exposure for In-Vivo Experiments**

S. Tejero, S. Schelkshorn, J. Detlefsen

Technische Universität München, Institute for Highfrequency Engineering, Munich, Germany

7c-5: **A Survey Study on Some Symptoms and Sensations Occurred in Eyes Caused by Daily Talking Durations of Mobile Phones**

H.H. Balik (1), K. Balikci (2), A. Akbal (1), I.C. Ozcan (3), D. Turgut-Balik (4), Z. Genc (2)

(1) University of Firat, Dept. of Electrical and Electronics Eng. Elazig, Turkey

(2) University of Firat, Dept. of Informatics, Elazig, Turkey

(3) University of Firat, University Health Center, Elazig, Turkey

(4) University of Firat, Dept. Biology, Elazig, Turkey

Session 8a - MEMS and Tunable Circuits

Wednesday, March 29, 2006

15:50 - 17:50

Room: Audimax A

Session Chairs: Erwin Biebl (Technical University of Munich)
Georg Fischer (Bell Labs Europe, Lucent, Nürnberg)

8a-1: **RF-MEMS as the Bridge Between Digital Control and High Performance Analog RF (Invited)**

G. Fischer

Bell Labs Europe, Lucent, Nürnberg, Germany

8a-2: **Accurate Design and Yield Analysis of Tunable Distributed MEMS Bandpass Filter**

S. Simion (1), G. Bartolucci (2), R. Marcelli (3)

(1) MTA, Dept. of Communications and Computer Science, Bucharest, Romania

(2) University of Roma "Tor Vergata", Dept. of Electronics Engineering, Rome, Italy

(3) CNR, Institute for Microelectronics and Microsystems, Microwave Microsystems Group, Rome, Italy

8a-3: **Switching Speed Analysis of Low Complexity RF-MEMS Switches**

C. Siegel (1), V. Ziegler (1), C. von Wächter (1), B. Schönlinner (1), U. Prechtel (1), H. Schumacher (2)

(1) EADS Deutschland GmbH, Corporate Research Centre, LG-ME, Munich, Germany

(2) University of Ulm, Dept. of Electron Devices and Circuits, Ulm, Germany

8a-4: **RF MEMS Market**

J. Bouchaud, B. Knoblich, H. Wicht

Wicht Technologie Consulting, Munich, Germany

8a-5: **Using Metamaterial Structures with Frequency Agile Basestations**

G. Dehm-Andone, G. Fischer

Bell Labs Europe, Lucent, Nürnberg, Germany

8a-6: **Tunable Transmission Lines on Silicon Based upon Periodic Photonic Bandgap Structures**

S. El Rai (1), R. Tempel (1), D. Jäger (2)

(1) ATMEL Duisburg GmbH, Duisburg, Germany

(2) Universität Duisburg-Essen, Zentrum für Halbleitertechnik und Optoelektronik, Duisburg, Germany

Session 8b - Radars, Sensors and Imaging Systems I

Wednesday, March 29, 2006

15:50 - 17:30

Room: Audimax B

Session Chairs: Alberto Moreira (Deutsches Zentrum für Luft- und Raumfahrt e. V., Weßling)
Josef Wenger (DaimlerChrysler AG, Ulm)

8b-1: **A Multi-Frequency Microwave Aperture Synthesis Radiometer for High-Resolution Imaging**

M. Jirousek, M. Peichl, H. Suess

DLR (German Aerospace Center) Oberpfaffenhofen, Microwaves and Radar Institute, Wessling, Germany

8b-2: **An Optical Design for Real-Time Terahertz Imaging**

C. Jördens (1), G. Thorwirth (2), M. Koch (1)

(1) Technische Universität Braunschweig, Institut für Hochfrequenztechnik, Braunschweig, Germany

(2) Jena-Optronik GmbH, Jena, Germany

8b-3: **Broadband Millimeter-wave FMCW Radar for Imaging of Humans**

A. Dallinger, S. Schelkshorn, J. Detlefsen

Technische Universität München, Lehrstuhl für Hochfrequenztechnik, Munich, Germany

8b-4: **Spatial Resolution of Millimeter Wave Imaging at 75-100 GHz and 600 GHz**

H. Phat Tran, F. Gumbmann, J. Weinzierl, L.P. Schmidt

University of Erlangen-Nuremberg, Institute for Microwave Technology, (LHFT), Erlangen, Germany

8b-5: **The ALMA Front End**

H. Rudolf

European Southern Observatory, ALMA, Garching, Germany

Session 9 - Poster Session II

Wednesday, March 29, 2006

8:30 - 18:00

Room: Foyer

Session Chair: Thomas Fügen (University of Karlsruhe (TH))

9-1: **Recent Progress in Optimizing Phase-Correcting Mirrors for a Multi-Frequency Gyrotron**

X. Yang (1), A. Arnold (1,2), G. Dammertz (1), K. Koppenburg (1), M. Thumm (1,2)

(1) Forschungszentrum Karlsruhe, Association EURATOM-FZK, IHM, Karlsruhe, Germany

(2) Universität Karlsruhe (TH), Institut für Höchstfrequenztechnik und Elektronik, Karlsruhe, Germany

9-2: **Compact Base-Station Filters Using TM-Mode Dielectric Resonators**

M. Höft, T. Magath

Communications Lab. of European Tech. Center, Panasonic Electronic Devices Europe GmbH, Lueneburg, Germany

9-3: **A High Gain Gap Coupled Fed Microstrip Array Antenna**

E. Gelbart, H. Matzner

Department of Communication Engineering, Holon Academic, Institute of Technology, Holon, Israel

9-4: **Concept and Development of a New MOBILE-Gate with All Optical Input**

A. Poloczek, W. Wang, J. Driesen, I. Regolin, W. Prost, F.J. Tegude

University of Duisburg-Essen, Center for Semiconductor and Optoelectronics, Duisburg, Germany

9-5: **A New Design of Lumped Element Bandpass Filter in L-Band**

P. Mapar, G.R. Askari, S. Pourjafari

Information and Communication Technology Institute, Isfahan University of Technology, Isfahan, Iran

9-6: **Active Microwave Filters based on the Combined Dynamic Negatrons**

N.A. Filinyuk, A.M. Kuzemko, L.B. Lischinskaya, M.M. Salech, S.M.M. Jourban, E.V. Vojtsehovska

Vinnitca National Technical University, Vinnitca, Ukraine

9-7: A Proximity Fed Circularly Polarized Microstrip Patch Antenna with a Cross Slot in the Ground Plane

K. Agarwal (1), G.P. Rao (1), M.V. Kartikeyan (1), M.K. Thumm (2,3)

(1) Department of Electronics & Computer Engineering, Indian Institute of Technology, Roorkee, Uttaranchal, India

(2) Forschungszentrum Karlsruhe, Institut für Hochleistungsimpuls und Mikrowellentechnik, Karlsruhe, Germany

(3) Universität Karlsruhe (TH), Institut für Höchstfrequenztechnik und Elektronik, Karlsruhe, Germany

9-8: Phase Sensitivity To Soil Moisture In Controlled Anechoic Chamber: Measurements and First Results

K. Ben Khadhra (1), M. Nolan (2), T. Börner (1), D. Hounam (1), M. Chandra (3)

(1) German Aerospace Center (DLR), Microwaves and Radar Institute, Oberpfaffenhofen, Wessling, Germany

(2) Institute of Northern Engineering, University of Alaska, Fairbanks, USA

(3) TU Chemnitz, Elektrotechnik und Informationstechnik, Chemnitz, Germany

Session 10a - Measurements and Millimeter Wave Techniques

Thursday, March 30, 2006

08:30 - 10:30

Room: Audimax A

Session Chairs: Jürgen Detlefsen (Technical University of Munich)
Martin Schneider (University of Bremen)

10a-1: **Cavity Perturbation Method for Temperature Controlled Characterization of Liquid Crystals up to 38 GHz**

A. Penirschke (1), S. Mueller (1), F. Goelden (1), A. Lapanik (2), V. Lapanik (3), V. Bezborodov (3), W. Haase (2), R. Jakoby (1)

(1) Technische Universität Darmstadt, Institut für Hochfrequenztechnik, Darmstadt, Germany

(2) Technische Universität Darmstadt, Institut für Physikalische Chemie, Darmstadt, Germany

(3) Belarusian State University, Institute of Applied Physics, Minsk, Belarus

10a-2: **Concealed Weapon Detection with active and passive Millimeterwave Sensors, two Approaches**

H. Essen (1), H.H. Fuchs (1), M. Hägelen (1), S. Stanko (1), D. Nötel (1), S. Erukulla (1), J. Huck (1), M. Schlechtweg (2), A. Tessmann (2)

(1) Research Institute for High Frequency Physics and Radar Techniques (FGAN-FHR), Wachtberg, Germany

(2) Fraunhofer Institut für Angewandte Festkörperphysik (IAF), Freiburg, Germany

10a-3: **Microwave and Millimeterwave Propagation within the Marine Boundary Layer**

H. Essen, H.H. Fuchs

Research Institute for High Frequency Physics and Radar Techniques (FGAN-FHR), Wachtberg (Germany)

10a-4: **An Investigation into the Feasibility of S-Parameter Measurements at X-Band Frequencies with Gaussian Beam Techniques**

M. Sabielny

EADS - Defence Electronics, OPEE11, Ulm, Germany

10a-5: **Near-Field Planar Characterization Applied to the Design of Digital and Radiofrequency Systems**

E. Marzolf (1), M. Drissi (1), A. Ziyat (2)

(1) INSA de Rennes, IETR, Rennes, France

(2) Mohammed First University, Laboratory of Electronics & Systems, Oujda, Morocco

Session 10b - Radars, Sensors and Imaging Systems II

Thursday, March 30, 2006

08:30 - 10:30

Room: Audimax B

Session Chairs: Jörg Schöbel (University of Braunschweig)
Karin Schuler (University of Karlsruhe (TH))

10b-1: **Effects of Water and Ice Layer on Automotive Radar**

A. Arage (1), W.M. Steffens (1), G. Kuehnle (1), R. Jakoby (2)

(1) Robert Bosch GmbH, Automotive Electronics, Leonberg, Germany

(2) Technische Universität of Darmstadt, Institute of Microwave Engineering, Darmstadt, Germany

10b-2: **Microwave Remote Sensing of Stratospheric Trace Gases Using Digital Fast Fourier Transform Spectrometers**

S.C. Müller (1), A. Murk (1), C. Monstein (2), N. Kämpfer (1), H. Meyer (2)

(1) University of Berne, Institute of Applied Physics, Berne, Switzerland

(2) ETH Zürich, Institute of Astronomy, Zürich, Switzerland

10b-3: **A 76 GHz Folded Reflector Antenna for True Ground Speed Measurement**

A. Hantsch (1), W. Menzel (2)

(1) Robert Bosch GmbH, Department CR/ARE1, Gerlingen, Germany

(2) University of Ulm, Department of Microwave Techniques, Ulm, Germany

10b-4: **Observation of a Walking Pedestrian with a 24GHz Automotive Radar Sensor**

F. Fölster, H. Rohling, H. Ritter

Hamburg University of Technology, Department of Telecommunications, Hamburg, Germany

10b-5: **Vehicle Occupant Monitoring with Capacitive Arrays**

M. Fritzsche (1), C. Prestele (1), T. Schwarz (1), S. Prutyanyy (2)

(1) DaimlerChrysler AG, Research & Technology, Active Safety & Driver Assistance Lab, Ulm, Germany

(2) University of Stuttgart, Dep. of Electrical Engineering, Stuttgart, Germany

Session 10c - Special Session on Microwave and Millimeter-Wave Material Processing

Thursday, March 30, 2006

08:30 - 10:30

Room: Seminar-Room

Session Chairs: Jürgen von Hagen (DaimlerChrysler AG, Sindelfingen)
Mario Pauli (University of Karlsruhe (TH))

10c-1: **Prospects of Electromagnetic Materials Processing by Use of cm-, mm- and μm -Waves (Invited)**

M. Willert-Porada

University of Bayreuth, Faculty of Applied Natural Sciences, Materials Processing, Germany

10c-2: **Optimisation of the Microwave Assisted SHS of Intermetallics in Single Mode Applicators (Invited)**

C. Leonelli, G. Poli, P. Veronesi

University of Modena and Reggio Emilia, Department of Materials and Environmental Engineering, Modena, Italy

10c-3: **Accelerated Curing of Adhesive with Microwave (Invited)**

R. Emmerich (1), M. Graf (1), W. Krause (1), F. Henning (1), P. Kölzer (2)

(1) Fraunhofer Institut für Chemische Technologie, Pfinztal, Germany

(2) Fraunhofer Institut Produktionstechnologie, Aachen, Germany

10c-4: **Highly Efficient Slotted Waveguide Feeding Systems for 2.45 GHz Industrial Applicators**

S. Stanculovic (1), L. Feher (1), M. Thumm (1,2)

(1) Research Center Karlsruhe, Institute for Pulsed Power and Microwave Technology, IHM, Karlsruhe, Germany

(2) Universität Karlsruhe (TH), Institut für Höchstfrequenztechnik und Elektronik, Karlsruhe, Germany

10c-5: **MW Disinfestations of Pallets**

B. Bisceglia (1), R. De Leo (2), N. Diaferia (3)

(1) University of Salerno, Department of Electrical and Information Engineering, Fisciano, Italy

(2) University of Sannio at Benevento, Engineering Faculty, Benevento, Italy

(3) Università Politecnica delle Marche, Dipartimento di Elettromagnetismo e Bioingegneria, Ancona, Italy

10c-6: **A Novel Antenna Design for Soil Decontamination with Microwaves**

M. Pauli, T. Kayser, W. Wiesbeck

Universität Karlsruhe (TH), Institut für Höchstfrequenztechnik und Elektronik, Karlsruhe, Germany



Session 11a - mm- and Sub-mm-Wave Components, Circuits and Systems

Thursday, March 30, 2006

11:00 - 12:40

Room: Audimax A

Session Chairs: Lorenz-Peter Schmidt (University Erlangen-Nuremberg)
Hans Rudolf (E.S.O., Garching)

11a-1: **Application of Silicon Micromachining Techniques for the Manufacturing of New Passive THz-Components**

S. Biber, J. Schür, L.P. Schmidt

University of Erlangen-Nuremberg, Institute for Microwave Technology, (LHFT), Erlangen, Germany

11a-2: **Influence of Metallic Primers on the Attenuation of CPW in the Millimeter- and Submillimeter Range**

V. Müllerwiebus, K. Schünemann

Hamburg University of Technology, Microwave Engineering Department, Hamburg, Germany

11a-3: **A Collector-Up SiGe-HBT for High Frequency Applications**

M. Joodaki (1), H. Hillmer (2)

(1) Infineon Technologies AG, Munich, Germany

(2) Univ. of Kassel, Dept. of Tech. Electronics, Institute of Nanostructure Tech. and Analytics (INA), Kassel, Germany

11a-4: **Tunable Microwave Transmission through a Periodically Corrugated Waveguide**

V. Pogrebnyak, E. Akray, N. Küçükaltun

Dep. of Electrical and Electronics Eng., Faculty of Eng. and Architecture, Çukurova University, Adana, Turkey

11a-5: **FDTD Analysis of a Microwave/mm-wave FET Based on the Fully Distributed Model**

A. Taeb, A. Abdipour, A. Mohammadi

Amirkabir Univ. of Tech., E.E. Department, Microwave/mm-wave & Wireless Com. Research Lab., Tehran, Iran

Session 11b - Radars, Sensors and Imaging Systems III

Thursday, March 30, 2006

11:00 - 12:40

Room: Audimax B

Session Chairs: Wolfgang Menzel (University of Ulm)
Klaus Solbach (University of Duisburg-Essen)

11b-1: **Improving FMCW-based Object Tracking Using Phased Array Antennas Combined With Sigma-Point Kalman Filters**

D. Mastela (1), L. Reindl (1), L. Wiebking (2), T. Zander (1)

(1) University of Freiburg, Department of Microsystems Engineering, Freiburg, Germany

(2) Siemens AG, CT PS7, Munich, Germany

11b-2: **Detection, Localisation and Tracking of Foreign Objects Using UWB-Pulses**

A. Gülck, O. Schimmer, R. Knöchel

Microwave Laboratory, Faculty of Engineering, University of Kiel, Germany

11b-3: **SNR Considerations for Widebeam, Short-Range Synthetic Aperture Radar Processing**

F. Gerbl, E.M. Biebl

Technische Universität München, Fachgebiet Höchsthfrequenztechnik, Munich, Germany

11b-4: **Factor and Principle Component Analysis for Automatic Landmine Detection Based on Ground Penetrating Radar**

F. Abujarad, A.S. Omar

University of Magdeburg, Microwave and Communications Engineering, Magdeburg, Germany

11b-5: **Spatial Time Domain Reflectometry for Monitoring Transient Soil Moisture Profiles - Applications of the Soil Moisture Group, Univ. of Karlsruhe**

R. Becker (1,2), S. Schlaeger (1,3), C. Hübner (1,4), A. Scheuermann (1,5), W. Schädel (1,6)

(1) Universität Karlsruhe (TH), Soil Moisture Group, Karlsruhe, Germany

(2) IMKO, Mikromodultechnik GmbH, Ettlingen, Germany

(3) SCHLAEGER - mathematical solutions & engineering, Karlsruhe, Germany

(4) University of applied sciences, Department of electrical engineering, Mannheim, Germany

(5) Universität Karlsruhe (TH), Institute of Rock Mechanics and Soil Mechanics, Karlsruhe, Germany

(6) Universität Karlsruhe (TH), Institute for Water and River Basin Management, Karlsruhe, Germany

Additional Meetings

(only for the respective members)

General Meeting IMA

Date: Tuesday, March 28, 2006

Time: 18:00 - 20:00

Location: Gastdozentenhaus (Kamin Zimmer)

MTT Board Meeting

Date: Tuesday, March 28, 2006

Time: to be announced

Location: to be announced

Meeting ITG Fachausschuss 7.3

Date: Wednesday, March 29, 2006

Time: 12:40

Location: Gastdozentenhaus (Dürer Raum)

Author Index

Abdipour A.	11a (PDF)	Biebl E.M.	11b (PDF)	Driesen J.	9 (PDF)
Abele P.	3a (PDF)	Bilik V.	4 (PDF)	Drissi M.	10a (PDF)
Abujarad F.	11b (PDF)	Billonnet L.	2a (PDF)	Ebinger J.	2a (PDF)
Agarwal K.	4 (PDF)	Bisceglia B.	10c (PDF)	Eibert T.F.	1b (PDF)
	9 (PDF)	Bitz A.	1b (PDF)		2b (PDF)
Ahmed A.	6a (PDF)	Blau K.	6b (PDF)	Emmerich R.	10c (PDF)
Akbal A.	7c (PDF)	Borgarino M.	7a (PDF)	Erukulla S.	10a (PDF)
Akray E.	11a (PDF)	Borie E.	6c (PDF)	Essen H.	10a (PDF)
Amari S.	2a (PDF)		6c (PDF)		10a (PDF)
Arage A.	10b (PDF)	Bornemann J.	1a (PDF)	Esser D.	7b (PDF)
Arie I.	1a (PDF)	Borngraeber J.	6a (PDF)	Eul H.	7b (PDF)
Armbrecht G.	7b (PDF)	Bornkessel C.	7c (PDF)	Fabrizio M. Di	2b (PDF)
Arnold A.	6c (PDF)	Bouchaud J.	8a (PDF)	Fantini F.	7a (PDF)
	9 (PDF)	Brand H.	2a (PDF)	Feher L.	10c (PDF)
Askari G.R.	9	Brigante A.	2b (PDF)	Feldle H.-P.	5
Balalem A.	2a (PDF)	Bunz B.	6a (PDF)	Fernandez L.	1b (PDF)
Baldauf M.A.	7b (PDF)	Börner T.	9 (PDF)	Filicori F.	7a (PDF)
	7c (PDF)	Caramanico M.	2b (PDF)	Filinyuk N.A.	9 (PDF)
Balik H.H.	1b (PDF)	Chaloupka H.	7b (PDF)	Fischer G.	5
	7c (PDF)	Chandra M.	9 (PDF)		8a (PDF)
Balikci K.	7c (PDF)	Chigaeva E.	7a (PDF)		8a
Banciu M.G.	4 (PDF)	Christoffers N.	3a (PDF)	Florian C.	7a (PDF)
Baras T.	2a (PDF)	Corciulo N.	7a (PDF)	Freese J.	3b (PDF)
Barelaud B.	2a (PDF)	Dallinger A.	8b (PDF)	Fritzsche M.	10b (PDF)
Bariou D.	6c (PDF)	Dammertz G.	6c (PDF)	Fuchs H.H.	10a (PDF)
Bartolucci G.	8a (PDF)		9 (PDF)		10a (PDF)
Baureis P.	7a (PDF)	Darfeuille S.	2a (PDF)	Fölster F.	10b (PDF)
Becker A.	1b (PDF)	Dederer J.	6b (PDF)	Gabler B.	2b (PDF)
Becker R.	11b (PDF)	Dehm-Andone G.	8a (PDF)	Gamand P.	2a (PDF)
Berroth M.	7a (PDF)	Deokar S.M.	4 (PDF)	Gehring R.	3b (PDF)
Bezborodov V.	10a (PDF)	Detlefsen J.	7c (PDF)	Gelbart E.	9
Bezek J.	4 (PDF)		8b (PDF)	Genc Z.	1b (PDF)
Biber S.	2a (PDF)	Dettmann I.	7a (PDF)		7c (PDF)
	11a (PDF)		7a (PDF)	Gerbl F.	11b (PDF)
Biebl E.	1a (PDF)	Diaferia N.	10c (PDF)	Gerhard W.	6a (PDF)

Ghose A.	4 (PDF)	Ioachim A.	4 (PDF)	Kuehnle G.	10b (PDF)
Giguet E.	6c (PDF)	Jacob A.F.	2a (PDF)	Kuhnert C.	4 (PDF)
Goelden F.	10a (PDF)	Jakoby R.	3b (PDF)		7b (PDF)
Gomez-Garcia R.	2a (PDF)		10a (PDF)	Kuzemko A.M.	9 (PDF)
Graf M.	10c (PDF)		10b (PDF)	Kämpfer N.	10b (PDF)
Gribaldo S.	7a (PDF)	Jarry B.	2a (PDF)	Kölzer P.	10c (PDF)
Gumbmann F.	8b (PDF)	Jin J.	6c (PDF)	Kürner T.	7c (PDF)
Gülck A.	11b (PDF)		6c (PDF)	Küçükaltun N.	11a (PDF)
Haase W.	10a (PDF)	Jin J.B.	6c (PDF)	Ladage K.	1b (PDF)
Hansen V.	1b (PDF)	Jirousek M.	8b (PDF)	Lapanik A.	10a (PDF)
	1b (PDF)	Joodaki M.	11a (PDF)	Lapanik V.	10a (PDF)
Hantsch A.	10b (PDF)	Jourban S.M.M.	9 (PDF)	Legrand F.	6c (PDF)
Hartmann C.	6b (PDF)	Jäger D.	8a (PDF)	Lenk F.	7a (PDF)
Hartwanger C.	3b (PDF)	Jördens C.	8b (PDF)	Leo R. De	10c (PDF)
Heidinger R.	6c (PDF)	Jöstingmeier A.	3b (PDF)	Leonelli C.	10c (PDF)
Hein M.	6b (PDF)	Kartikayan M.V.	4 (PDF)	Leonhardt W.	6c (PDF)
Heinrich W.	2b (PDF)		6c (PDF)	Lievin C.	6c (PDF)
	7a (PDF)		6c (PDF)	Limbach M.	2b (PDF)
Henning F.	10c (PDF)		9 (PDF)	Lischinskaya L.B.	9 (PDF)
Hernandez-Guillen F.	3a (PDF)	Kawalkiewicz M.	3b (PDF)	Llopis O.	7a (PDF)
Herrmann R.	6b (PDF)	Kayser T.	4 (PDF)	Lojewski G.	4 (PDF)
Heuermann H.	3a (PDF)		10c (PDF)	Luy J.F.	4 (PDF)
Hillmer H.	11a (PDF)	Khadhra K. Ben	9 (PDF)	Löcker C.	2b (PDF)
Hoffmann M.H.W.	3a (PDF)	Kiefer R.	7a (PDF)	Magath T.	9 (PDF)
Hofmann A.	2a (PDF)	Kiermeier W.	1a (PDF)	Manglberger M.	2a (PDF)
Hollmack K.	1b (PDF)	Klemp O.	7b (PDF)	Mapar P.	9
Hong U.P.	3b (PDF)	Kmec M.	6b (PDF)	Marcelli R.	8a (PDF)
Horn R.	2b (PDF)	Knoblich B.	8a (PDF)	Marie H.	2a (PDF)
Hosticka B.J.	3a (PDF)	Knöchel R.	6a (PDF)	Marin R.	3b (PDF)
Hounam D.	9 (PDF)		11b (PDF)	Markos A.Z.	6a (PDF)
Huck J.	10a (PDF)	Knörzer S.	7c (PDF)	Marzolf E.	10a (PDF)
Hwang C.G.	6a (PDF)	Koch M.	8b (PDF)	Massler H.	7a (PDF)
Hwang J.N.	6b (PDF)	Kokozinski R.	3a (PDF)	Mastela D.	3b (PDF)
Häfele M.	3a (PDF)	Kolnsberg S.	3a (PDF)		11b (PDF)
Hägelen M.	10a (PDF)	Kompa G.	4 (PDF)	Matzner H.	1a (PDF)
Höft M.	9 (PDF)		6a (PDF)		9
Hübner C.	11b (PDF)	Koppenburg K.	9 (PDF)	Meliani C.	6a (PDF)
Ibrahim I.	3a (PDF)	Krause W.	10c (PDF)	Menzel W.	2a (PDF)
Illy S.	6c (PDF)	Krause-Finkeldey D.	1b (PDF)		3b (PDF)

	10b (PDF)	Poddar A.K.	3a (PDF)	Scheiber R.	2b (PDF)
Meyer H.	10b (PDF)	Pogrebnyak V.	11a (PDF)	Schelkshorn S.	7c (PDF)
Michel G.	6c (PDF)	Poli G.	10c (PDF)		8b (PDF)
Militaru N.	4 (PDF)	Poloczek A.	9 (PDF)	Scheuermann A.	11b (PDF)
Moalem H.	1a (PDF)	Pontes J.	7b (PDF)	Schick C.	3a (PDF)
Mohammadi A.	11a (PDF)	Pontes J.A.	7b (PDF)	Schimmer O.	11b (PDF)
Mokhtaari M.	1a (PDF)	Pourjafari S.	9	Schlaeger S.	11b (PDF)
Monstein C.	10b (PDF)	Prechtel U.	8a (PDF)	Schlechtweg M.	10a (PDF)
Monsurrò P.	6b (PDF)	Prestele C.	10b (PDF)	Schmid M.	6c (PDF)
Moritz R.	7a (PDF)	Prost W.	9 (PDF)	Schmid U.	3b (PDF)
Mueller S.	10a (PDF)	Prutyanyy S.	10b (PDF)	Schmidt L.P.	2a (PDF)
Muhammad F.	2a (PDF)	Quay R.	7a (PDF)		8b (PDF)
Murk A.	10b (PDF)	Raay F. van	7a (PDF)		11a (PDF)
Myung N.H.	6a (PDF)	Rai S. El	8a (PDF)	Schmitz P.	7b (PDF)
Mössinger A.	3b (PDF)	Rao G.P.	4 (PDF)	Schmückle F.J.	2b (PDF)
Müller S.C.	10b (PDF)		9 (PDF)	Schondelmaier D.	1b (PDF)
Müllerwiebus V.	11a (PDF)	Regolin I.	9 (PDF)	Schroeder W.L.	7b (PDF)
Naß T.	7a (PDF)	Reindl L.	3b (PDF)	Schulteis S.	4 (PDF)
Neffe G.	6c (PDF)		11b (PDF)		7b (PDF)
Nolan M.	9 (PDF)	Reiner R.	7a (PDF)		7b (PDF)
Nötel D.	10a (PDF)	Reinhardt T.	1b (PDF)	Schulz D.	1a (PDF)
Olbrich M.O.	1a (PDF)	Ritter H.	10b (PDF)	Schumacher H.	3a (PDF)
Omar A.S.	3b (PDF)	Rohde U.L.	3a (PDF)		6b (PDF)
	11b (PDF)	Rohling H.	10b (PDF)		8a (PDF)
Ossowska A.	4 (PDF)	Roll H.	7a (PDF)	Schwarz T.	10b (PDF)
Ouardi A. El	1b (PDF)	Rosenberg U.	2a (PDF)	Schweizer H.	7a (PDF)
Ouzan S.	1a (PDF)	Rudolf H.	8b (PDF)	Schädel W.	11b (PDF)
Ozcan I.C.	7c (PDF)	Rudolph M.	6a (PDF)	Schönlinner B.	8a (PDF)
Pauli M.	4 (PDF)		7a (PDF)	Schünemann K.	11a (PDF)
	10c (PDF)	Ruengwaree A.	4 (PDF)	Schür J.	11a (PDF)
Peichl M.	8b (PDF)	Rzesnicki T.	6c (PDF)	Seelmann-Eggebert M.	7a (PDF)
Penirschke A.	10a (PDF)		6c (PDF)	Seyfried U.	7a (PDF)
Peters N.	3a (PDF)		6c (PDF)	Siegel C.	8a (PDF)
Peyerl P.	6b (PDF)	Saala G.	4 (PDF)	Simion S.	8a (PDF)
Pienkowski D.	1a (PDF)	Sabiely M.	10a (PDF)	Solan B.	7b (PDF)
Piosczyk B.	6c (PDF)	Sachs J.	6b (PDF)	Solbach K.	2b (PDF)
	6c (PDF)	Salech M.M.	9 (PDF)	Staats G.	1b (PDF)
	6c (PDF)	Schack M.	7c (PDF)	Stanculovic S.	10c (PDF)
	6c (PDF)	Schade U.	1b (PDF)	Stanko S.	10a (PDF)

Steffens W.M.	10b (PDF)		9 (PDF)	Wentzel A.	1a (PDF)
Stonies R.	1a (PDF)		9 (PDF)	Wicht H.	8a (PDF)
Stornelli V.	2b (PDF)		10c (PDF)	Wiebking L.	11b (PDF)
Streckert J.	1b (PDF)	Tran D. Trung	2b (PDF)		3b (PDF)
Stücke T.	3a (PDF)	Tran H. Phat	8b (PDF)	Wiegner D.	7a (PDF)
Suess H.	8b (PDF)	Trasser A.	3a (PDF)	Wiesbeck W.	4 (PDF)
Sörgel W.	6b (PDF)		6b (PDF)		4 (PDF)
	7c (PDF)	Trautenberg H.L.	5		4 (PDF)
Taeb A.	11a (PDF)	Traverso P.A.	7a (PDF)		6b (PDF)
Talukder P.K.	2b (PDF)	Trifiletti A.	6b (PDF)		7b (PDF)
Teggatz A.	3b (PDF)	Turgut-Balik D.	7c (PDF)		7b (PDF)
Tegude F.J.	9 (PDF)	Unger P.	7c (PDF)		7c (PDF)
Tejero S.	7c (PDF)	Vaijinath R.	4 (PDF)		10c (PDF)
Tempel R.	8a (PDF)	Vaupel T.	1b (PDF)	Willert-Porada M.	10c (PDF)
Templ W.	7a (PDF)		2b (PDF)	Winkler W.	6a (PDF)
Tessmann A.	10a (PDF)	Veronesi P.	10c (PDF)	Wolf H.	3b (PDF)
Teufer D.	1a (PDF)	Vojtsehovska E.V.	9 (PDF)	Wuschek M.	7c (PDF)
Thiede A.	6b (PDF)	Wagner D.	6c (PDF)	Wächter C. von	8a (PDF)
Thome C.	7b (PDF)	Walcher H.	7a (PDF)	Wörner S.	7a (PDF)
Thorwirth G.	8b (PDF)	Wang L.	6a (PDF)	Yang X.	9 (PDF)
Thumm M.	4 (PDF)	Wang W.	9 (PDF)	Zander T.	3b (PDF)
	6c (PDF)	Weber S.	7a (PDF)		11b (PDF)
	6c (PDF)	Weber T.	5	Zhou Y.	1b (PDF)
	6c (PDF)	Weinzierl J.	2a (PDF)	Ziegler V.	8a (PDF)
	6c (PDF)	Weiß H.	8b (PDF)	Ziyyat A.	10a (PDF)
	6c (PDF)		3a (PDF)		

Microwave and Millimeterwave Propagation within the Marine Boundary Layer

Helmut Essen, Hans-Hellmuth Fuchs

Research Institute for High Frequency Physics and Radar Techniques (FGAN-FHR),
Neuenahrer Str. 20, D-53343 Wachtberg (Germany)
Email: h.h.fuchs@fgan.de

Short Abstract—A series of measurement campaigns were initiated at the Baltic Sea to validate existing radar propagation models under various atmospheric conditions in the marine environment. To assess the radar propagation within different layers simultaneously at X-, Ka- and W-band measurements were performed, using the experimental three frequency radar MEMPHIS operating against point targets at different heights above sea, carried on a naval vessel, which moved on outbound and inbound courses. The paper describes the experimental approach and gives representative results.

Keywords- millimeterwave radar, propagation, refraction, duct, model)

I. INTRODUCTION

Within the marine boundary layer radar propagation is influenced by the atmospheric conditions, the sea surface and the transmission geometry. At classical radar bands up to 18 GHz multipath propagation at low sensor level above the sea imposes severe problems. Therefore it is of considerable interest to investigate the propagation characteristics at alternative frequency bands. Millimeterwave radar sensors are much less influenced by multipath effects, as the sea surface is much rougher in comparison to the radar wavelength than at lower frequencies; however refraction and turbulence are also of importance at millimeterwave frequencies. Measurements have been conducted during recent years to validate existing radar propagation models under various atmospheric conditions. To assess the radar propagation within different layers simultaneously at X-, Ka- and W-band measurements were performed, using the experimental three frequency radar MEMPHIS operating against point targets at different heights above sea, carried on a ship, which moved on outbound and inbound courses.

For the time being, only little data exist with the full information content needed for a thorough validation of radar propagation models, that means that radar data exist for

different frequency bands, to validate the modelling of the frequency characteristics, that data exist for different geometries at equal environmental conditions, to validate the influence of geometry and that input data for all relevant environmental parameters exist for the set of radar data. During the measurements discussed in the following a complete environmental characterization was performed [1] by the FWG, Kiel.

II. EXPERIMENTAL CONDITIONS

The experiments were mainly conducted at the Baltic Sea, but at different seasons of the year. Some data were gathered over sea close to Singapore. The radar MEMPHIS [2], operating simultaneously at X-Band, Ka-Band and W-Band, was located at a height of about 20 m, thus representing a geometry with possibly strong influences of multipath and ducting. During the experiments a vessel was moving on outbound and successively on inbound courses. For the radar measurements trihedral reflectors acting as point targets were mounted at different heights and displaced by range, two looking to the bow and two looking to the stern of the ship. All reflectors had the same size and a nominal RCS of 48.5 dBsm at 94 GHz. The vessel was additionally equipped with a GPS unit to determine its location which was transferred via a data link to the data acquisition of MEMPHIS where it was recorded together with the radar data. The GPS information transferred by radio link was also used for tracking of the target.

The environmental characterization during the trials covered a description of the sea and sea/air interface using sensors mounted on free drifting buoys, on a research vessel and using radio probes on balloons, which were launched on a regular schedule.

During the measurement period different meteorological conditions could be covered. Fig. 1 compares the refractivity conditions of the atmosphere for RF and electro-optical (EO) propagation by means of a plot of air/sea temperature

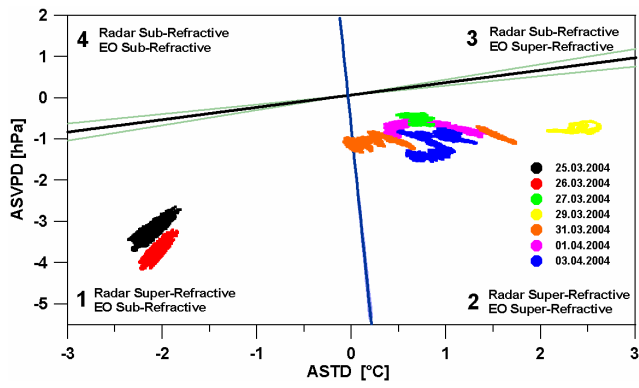


Figure 1. ASVPD versus ASTD as extracted from the FWG data for one measurement period

difference (ASTD) versus air/sea vapour pressure difference (ASVPD). The example exhibits solely superrefractive conditions. The varying ASTD and the negative ASVPD changes the layer structure above the sea surface, particularly the height of the evaporation duct.

III. MEASUREMENTS

The boat runs were conducted over ranges close the horizon, which means over more than 25 km. The time series of calibrated range profiles showing the two reference reflectors on board the ships was plotted in pseudo-color representation. Fig. 2 shows an example for an inbound run at 35 GHz.

The traces for both reflectors, separated by range, can clearly be distinguished. Using the profiles range diagrams for each reflector were deduced by tracking of the respective trace. In order to evaluate and study the propagation effects the range dependant free space attenuation and the nominal RCS of the corner reflectors were subtracted resulting in two-way propagation factors for each corner reflector. Fig 3a, b, c gives the respective example of an inbound run.

All diagrams show a pronounced signal fading due to multipath propagation with fade depths up to 30 dB for 9.4 GHz and 35 GHz.

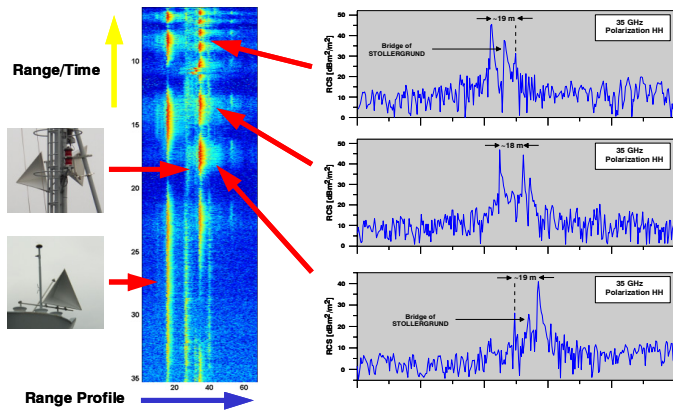


Figure 2. Series of range profiles and single range profiles for 35 GHz at an inbound run

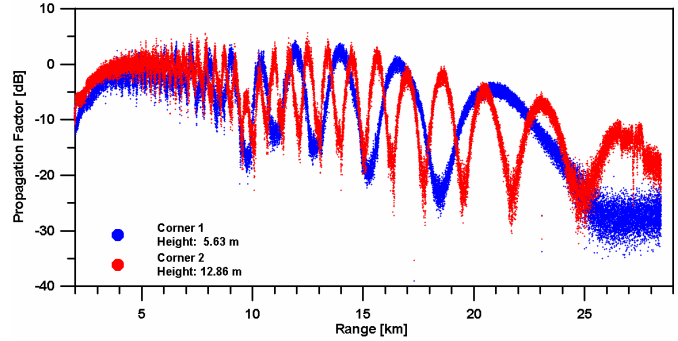
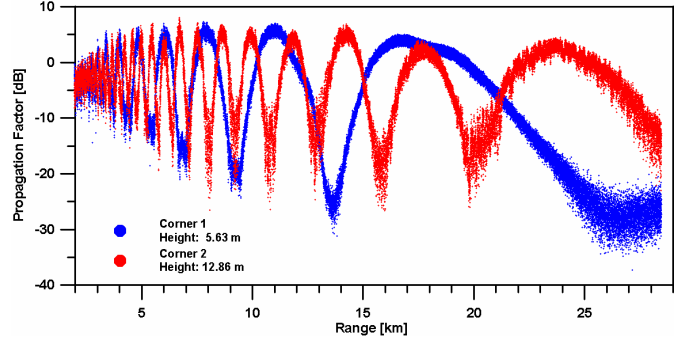
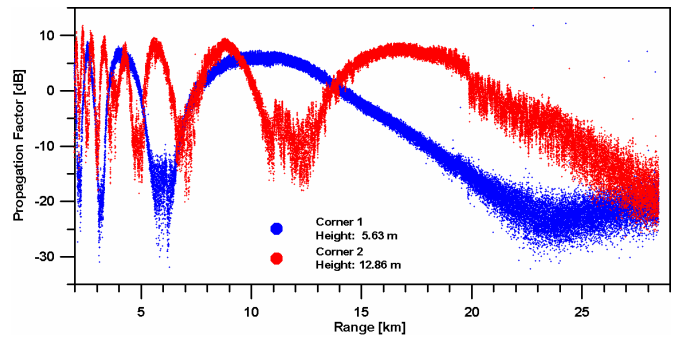


Figure 3. Range diagrams for inbound run 9.4 GHz (a), 35 GHz (b) and 94 GHz (c)

The resulting fading characteristic by the interference pattern depends on the transmission geometry, namely the sensor and target height, and on the used wavelength. Increasing roughness of the reflecting sea surface diminish the depth of the fading minima due to an enhanced diffuse incoherent scattering process. This effect is more pronounced at the shorter millimeter waves than at X-band, e.g. at 94 GHz.

The amplitude in the maxima of the interference pattern of the X-band and Ka-band signal does not vary much with range confirming superrefractive conditions. At 94 GHz additional atmospheric attenuation effects degrade the signal up to 12 dB with range but the maximum amplitude of the propagation factor does not fall below -10 dB near the geometrical horizon.

Varying refractive conditions in the atmosphere change the periodicity of the multipath interference pattern. Notable is the degree of displacement associated with shorter wavelength. Different refractive conditions can replace a minimum by a maximum. As an example Fig. 4 compares the propagation

IV. MODELLING OF PROPAGATION CHARACTERISTICS

For the prediction of the range characteristics of radar cross section two programs, PIRAM [5] and TERPEM [3] had been used. To calculate the propagation factors for a given transmission geometry it is necessary to know the environmental parameters, namely the profiles of temperature, humidity and wind speed. Appropriate measurements were accomplished by the free drifting buoys [2]. Based on this data sets PIRAM computed profiles of the modified refractivity $M(h)$ and duct heights applying standard solution methods (Charnock-Smith). These profiles and the radar transmission geometry have been used in TERPEM to calculate coverage diagrams and 2-way propagation factor vs. range characteristics based on a hybrid model using parabolic equation techniques and ray optics. Fig. 5 shows the simulation at 35 GHz for two cases. Both sample cases represent superrefractive conditions but with different impact on the propagation. The first one on 27 March looks like the coverage diagram of a standard atmosphere with no layer structure. At that time high humidity, low ASTD and upcoming fog removed the existing evaporation duct. The maxima of the propagation factor vary less than 5 dB with range up to the horizon and fall off beyond this limit with about 2 dB/km.

Fig. 6 and 7 shows the comparison between measured and calculated propagation characteristics of both runs. The curves fit the experimental results very well independent on frequency and height.

It may, however, be noted that the calculated multipath minima especially at 94 GHz are considerably overemphasized. The latter is due to a lack in precision for the description of the roughness of the sea surface at millimeterwaves. Surface roughness is modeled by modifying the Fresnel reflection coefficients by a roughness reduction factor and correlating the

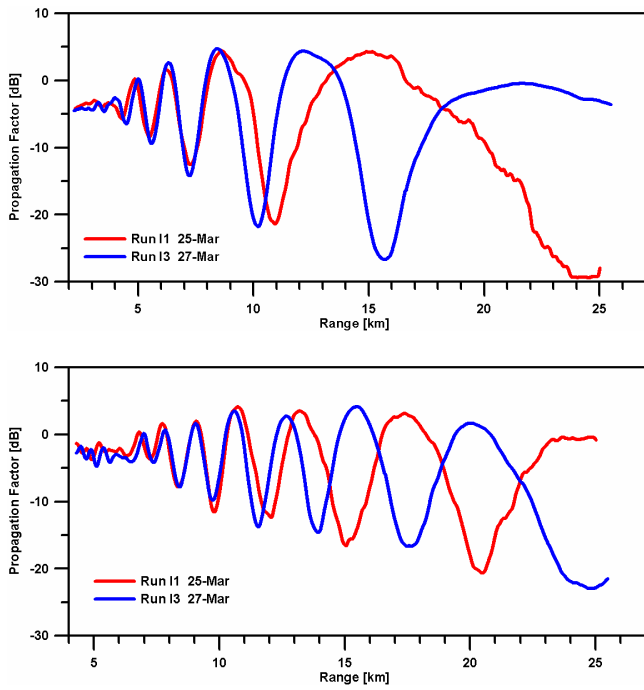


Figure 4. Comparison of propagation factor for run I1 and I3 at 35 GHz
a: corner reflector height 5.6 m, b: corner reflector height 12.9 m

factors of two runs measured at 35 GHz on two different days. In order to ease the comparison the measured data were averaged over 1.5 min. The meteorological situation on the first day (March 25) was characterized by an onshore air-flow with a characteristic height of the evaporation duct of about 6 m while on the second day (March 27) during off-shore air-flow the duct height dropped down to < 1 m till an upcoming fog in the night removed any layered structure. As shown clearly in the diagrams this has an impact on the range performance of radar systems. Depending on the path geometry a multipath maximum can shift the maximum range of the radar system beyond the visible horizon.

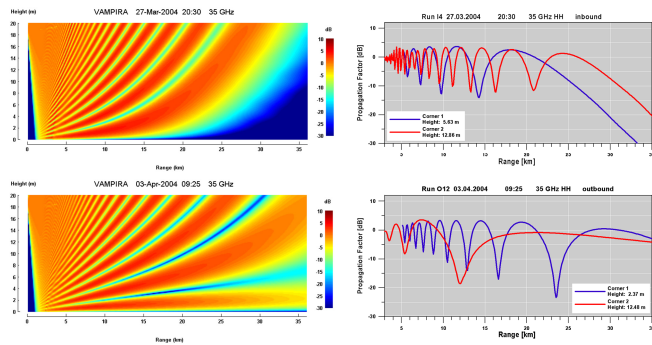


Figure 5. Coverage diagram and extracted 2-way path loss diagrams at 35 GHz for two corner reflector heights. Input buoy data from 27 March (a) and 03 April (b)

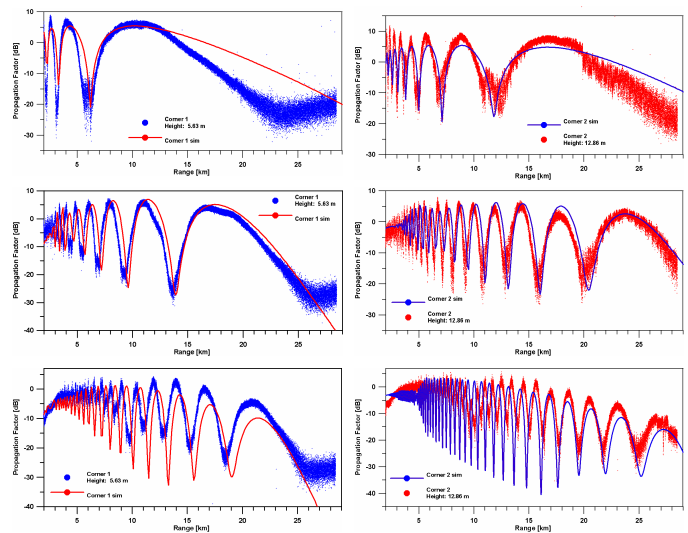


Figure 6. Comparison of propagation factor at 9.4 GHz, 35 GHz and 94 GHz between simulation and measurement, run on 27 March.

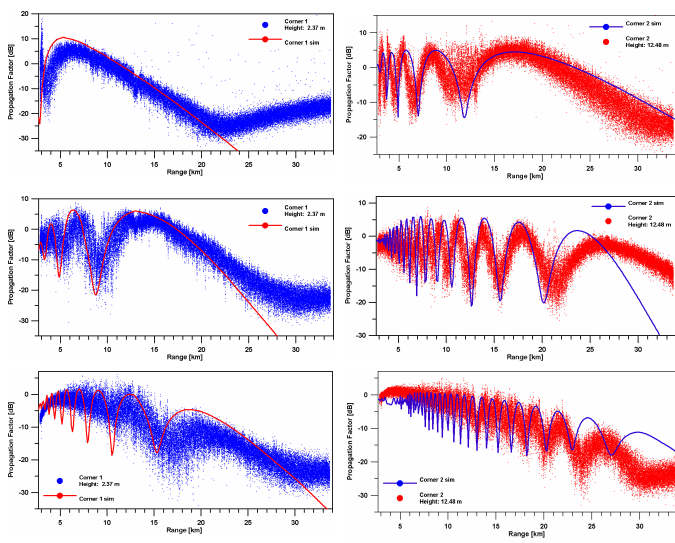


Figure 7. Comparison of propagation factor at 9.4 GHz, 35 GHz and 94 GHz between simulation and measurement, run on 1 April.

rms wave height with wind speed. For 35 GHz the depth of the minima is modeled best, which may lead to the assumption that the roughness model used here is most appropriate for this frequency.

V. RESULTS

The comparison of experimental results and simulations at millimeterwaves show that the parabolic equation model TERPEM gives a good estimation for the propagation factor over a wide range of frequencies, ranging from 10 GHz to 94 GHz. This was already found during earlier experiments [4]. A general result of the radar experiments is, that for

maximum range also millimeterwave radar should be taken into account. Detection of ships is possible for ranges up to and over the horizon in the majority of environmental conditions in the Atlantic and Mediterranean and specifically in the Baltic Sea. Using the 35 GHz frequency band, rain is less important, which at 94 GHz is a major concern, if the extend of the rain cell is big enough. The 94 GHz band exhibits another advantage: For an object like a naval vessel, where scatterers are distributed over different heights, the related interference patterns could be so dense that the resulting overall signal fading is very low. The proof of this effect especially at 94 GHz is due to current research. The experiments in tropical environment, namely in Singapore, however, showed, that the propagation conditions in that type of environment can differ considerably.

REFERENCES

- [1] S. Boehmsdorff and H. Essen, "MEMPHIS, an experimental platform for mm-wave radar," DGON Intl. Conf. On Radar, 1998, Munich, pp. 405 – 411.
- [2] T.K. Scholz and J. Förster, "Environmental characterization of the marine boundary layer for electromagnetic wave propagation", SPIE 11th Intl. Symposium on remote sensing, RS 06 Optics in Atmospheric Propagation and adaptive systems VII, Maspalomas, 2004.
- [3] TERPEM, Version 5.1, Signal Science Ltd, 1994 – 98.
- [4] H. Essen, H.-H. Fuchs, "Millimeterwave propagation within Boundary Layers over Sea, Comparison of Modelling and Experimental Data", SPIE 9th Intl. Symposium on Remote Sensing, Conf. 4884-12, Agia Pelagia, 2002.
- [5] J. Claverie and Y. Hurtaud, "Propagation transhorizon en atmosphère marine - Modélisation et nouveaux résultats expérimentaux", 49th AGARG EPP Symposium, Télé-détection du milieu de propagation, 19, Izmir, 1991..

Impedance Matching of a Loaded Microstrip Transmission Line by Parasitic Elements

H. Matzner¹, S. Ouzan¹, H. Moalem¹, and I. Arie¹

¹HIT – Holon Institute of Technology, Department of Communication Engineering, 52 Golomb St., Holon 58102, Israel, haim@hait.ac.il, 03-5026730

An impedance matching of a loaded microstrip transmission line by parasitic elements is presented. A 1:2 microstrip splitter is taken as a test case, and a comparison is made between a standard $\lambda/4$ matching to our $\lambda/4$ parasitic matching. Simulation and measurement show that the quality of the standard $\lambda/4$ matching is better, while the impedance bandwidth is almost the same. The advantages of the parasitic matching technique are shortly discussed.

Keywords-component; impedance matching; parasitic matching elements.

I. INTRODUCTION

Impedance matching is needed in most RF and microwave systems. Generally, in the various matching techniques the conductors of the matching subsystem must be physically connected to the conductors of the transmission lines or waveguides of the matched system. In the present work we propose an easier impedance matching technique for a loaded microstrip transmission line, by using only parasitic elements. That is, in our case there is no physical connection between the conductors of the matching subsystem and the conductors of the main system. A 1:2 microstrip splitter is chosen as test case to check the quality of the proposed parasitic matching technique. The return loss of the splitter is checked, by a simulation and a measurement, in three cases: without matching, with a standard $\lambda/4$ microstrip transformer, and with a parasitic $\lambda/4$ transformer.

The structure of the paper is as follows: in chapter II we present the configurations of the unmatched splitter, the splitter matched by standard $\lambda/4$ microstrip transformer, and the splitter matched by the parasitic $\lambda/4$ transformer. In chapter III the simulated return loss of the 3 configurations is displayed, and in chapter IV measurement results are shown. Chapter V is devoted to conclusions and discussion.

II. CONFIGURATIONS OF THE UNMATCHED AND THE MATCHED SPLITTER

A. The 1:2 Microstrip Splitter.

A simple microstrip splitter is presented in figure 1. The microstrip transmission lines are printed on a FR4 substrate having $\epsilon_r \approx 4.7$, 1.6 mm thickness and having width of 2.95 mm. The characteristic impedance of the microstrip transmission lines is 50 Ω .

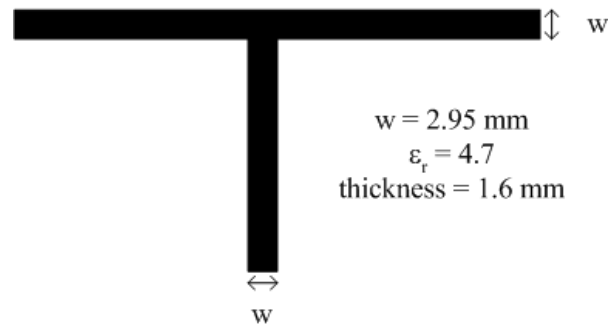


Figure 1. A 1:2 microstrip splitter. The 50 Ω transmission line are printed on a 1.6 mm thick FR4 substrate having $\epsilon_r \approx 4.7$. The widths of the lines are 2.95 mm.

The splitter is unmatched. The load seen by the main line equals to $Z_L = 50 \parallel 50 = 25 \Omega$, hence the reflection coefficient at the load is given by

$$\Gamma = (25 - 50) / (25 + 50) \quad (1)$$

$$|\Gamma| = 1/3 \text{ and}$$

$$\text{SWR} = (1 + 1/3) / (1 - 1/3) = 2 \quad (2)$$

B. A Standard $\lambda/4$ transformer matching.

As shown in [1], in order to perform the $\lambda/4$ transformer matching, we have to find a distance d measured from the load to the right edge of the transformer, which is a transmission line having a characteristic impedance Z_0 , with length $\lambda/4$. The solutions are

$$Z_{q1} = Z_0 [(1 - |\Gamma|) / (1 + |\Gamma|)]^{1/2} ; d_1 = \lambda (\theta + \pi) / 4 \pi \quad (3)$$

$$Z_{q2} = Z_0 [(1 + |\Gamma|) / (1 - |\Gamma|)]^{1/2} ; d_2 = d_1 \pm \lambda / 4 \quad (4)$$

Where $\Gamma = |\Gamma| \exp(j\theta)$. For a real load the standard solution is the first one, for which $d = 0$ and

$$Z_q = (Z_0 \cdot Z_L)^{1/2} = 35.35 \Omega \quad (5)$$

The width of the transformer is 5 mm and its length is 40 mm at $f = 1$ GHz. The splitter containing the $\lambda/4$ microstrip transformer is shown in figure 2.

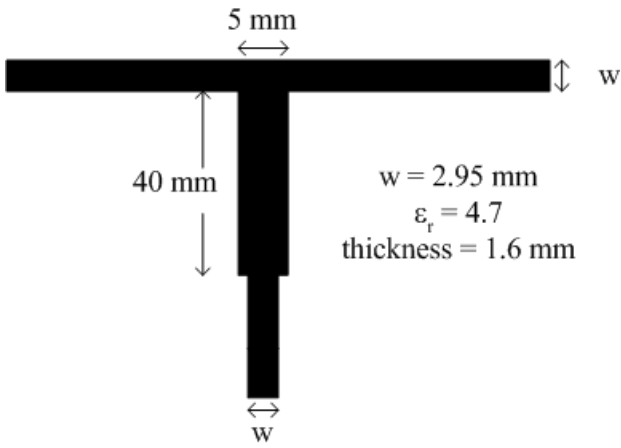


Figure 2. A 1:2 microstrip splitter containing a $\lambda/4$ standard microstrip transformer. The length of the transformer is 40 mm at $f = 1$ GHz, its width is 5 mm and its characteristic impedance is 35.35Ω .

C. $\lambda/4$ Parasitic Matching Configuration

In order to perform the parasitic matching we first produce a new transmission line, by adding another dielectric layer and another parasitic conductor above the added dielectric layer.

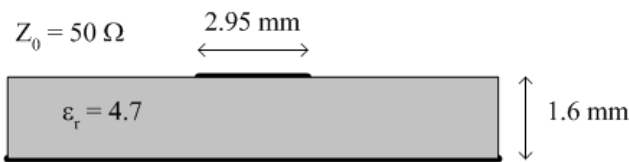
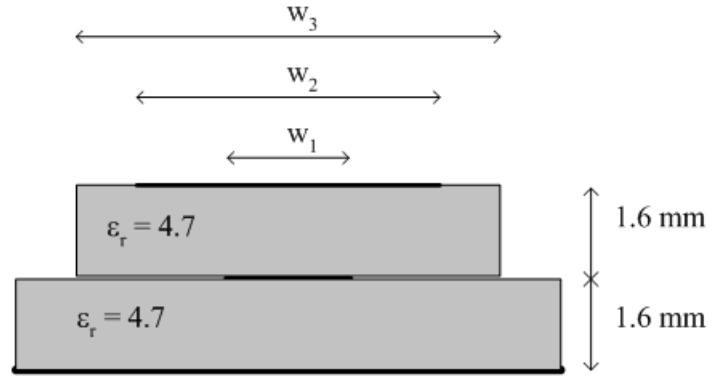


Figure 3. A standard microstrip transmission line, having characteristic impedance equals to 50Ω , used in the microstrip splitter.

Side views of the microstrip line and the new line are shown in figures 3 and 4. The new transmission line has been designed and simulated by the CST – Microwave Studio in order to have a characteristic impedance 35.35Ω . Its wavelength at $f = 1$ GHz was found by the CST software as well.



$$w_1 = 2.95, w_2 = 17 \text{ mm}, w_3 = 37 \text{ mm}, Z_0 = 35.35 \Omega$$

Figure 4. A new transmission line, based on the standard microstrip transmission line shown in figure 3. The characteristic impedance of this transmission line is 35.35Ω . A piece of length $\lambda/4$ of this line is used for the parasitic matching.

In order to perform the parasitic matching, we simply take a piece having the same structure as the structure of the upper part of the transmission line shown in figure 4, and place it on the microstrip line at the calculated matching position. One can check the optimal position of the piece by let it slide a little bit around the matching position. When the desired matching quality is achieved, the matching piece can optionally be fixed to the line by dielectric screws. An upper view of the parasitic matching is shown in figure 5.

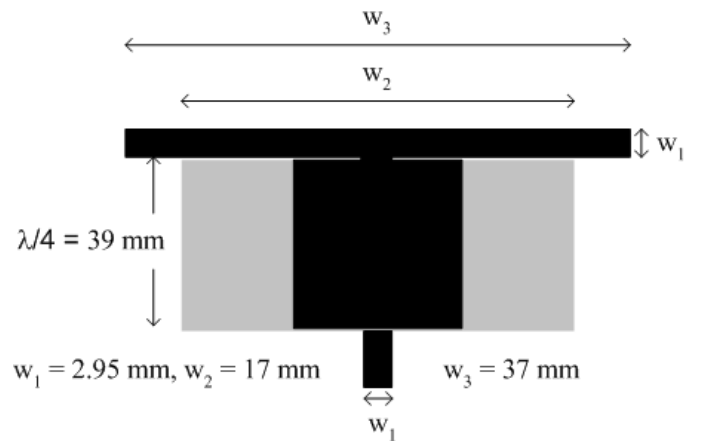


Figure 5. The parasitic $\lambda/4$ technique. The characteristic impedance of the microstrip line having on it the parasitic piece is 35.35Ω . The length of the $\lambda/4$ piece is 39 mm at $f = 1$ GHz.

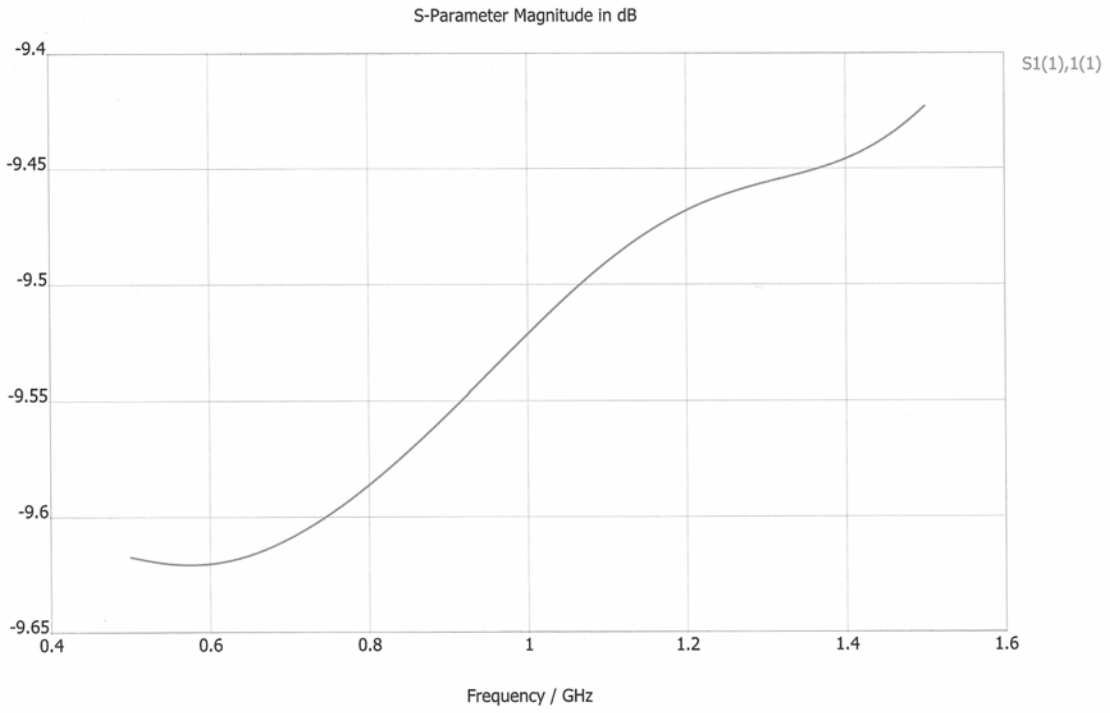


Figure 6: S_{11} simulation of the unmatched splitter.

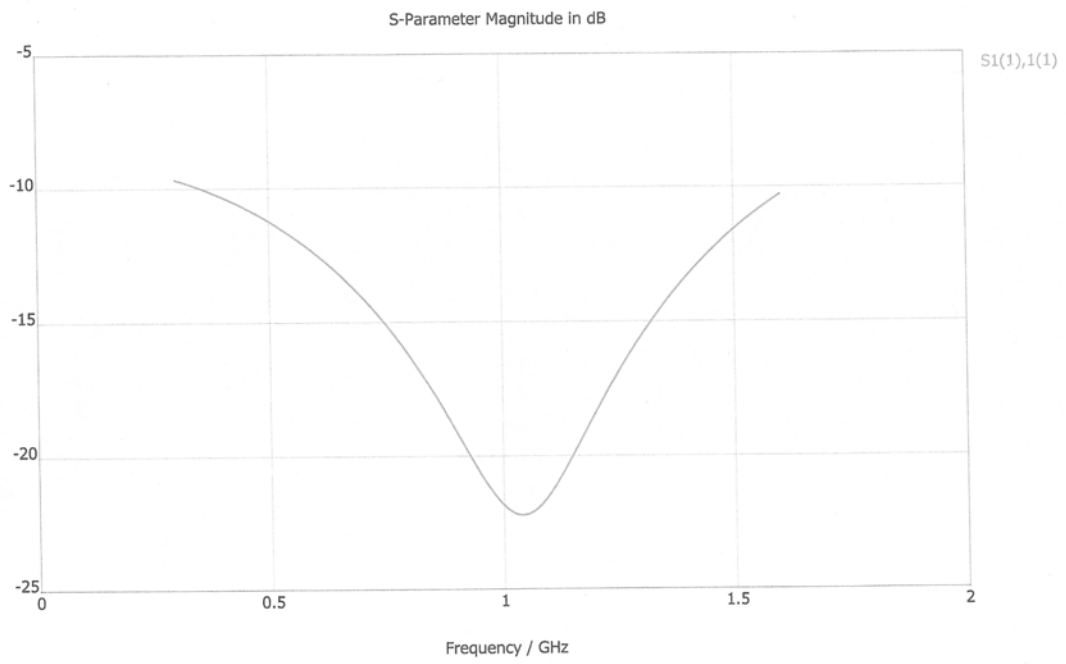


Figure 7: S_{11} simulation of the splitter, matched by the standard 1/4 microstrip transformer.

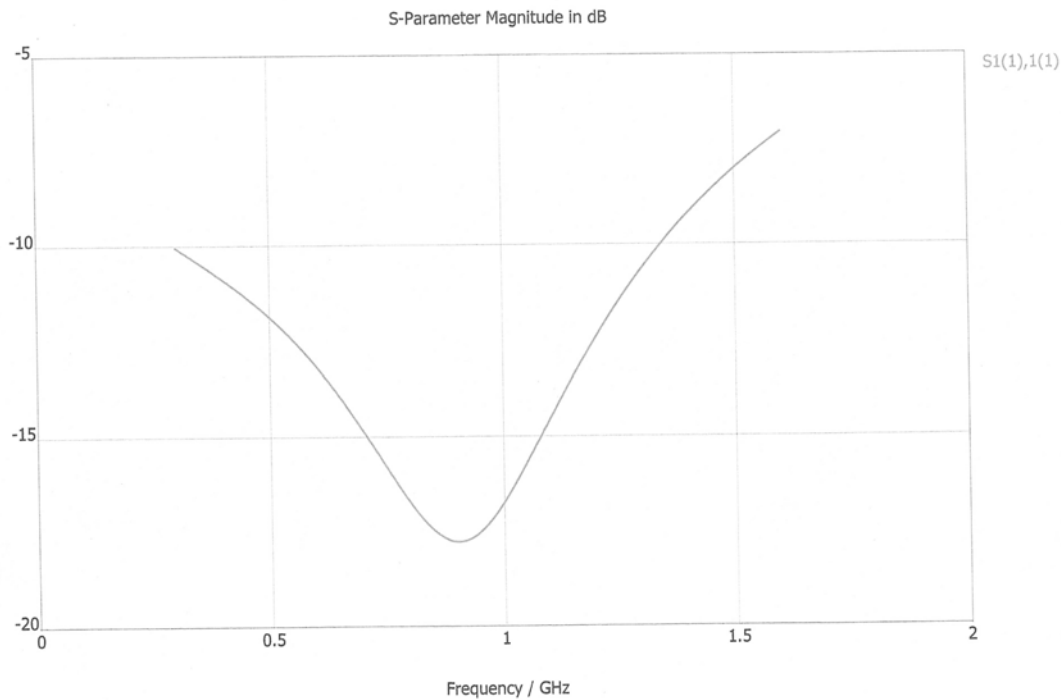


Figure 8: S_{11} simulation of the splitter matched by the $\lambda/4$ parasitic transformer.

III. SIMULATIONS OF THE SPLITTER

Simulations of the unmatched splitter, the splitter matched by the standard $\lambda/4$ microstrip transformer and a simulation of the splitter matched by the parasitic $\lambda/4$ transformer are presented in figures 6, 7, 8 respectively. It is shown that the quality of the matching by the standard $\lambda/4$ microstrip transformer technique is quite better: the bandwidth for return loss less than -10 dB is between 0.3 and 1.6 GHz, and the minimal value of the return loss is -22 dB. In the case of the $\lambda/4$ parasitic transformer the bandwidth for return loss less than -10 dB is between 0.3 and 1.35 GHz, and the minimal value of the return loss is -18 dB.

IV. MEASUREMENTS OF THE SPLITTER

Similar results are obtained by measurements. S_{11} measurement of the unmatched splitter, the splitter matched by the standard $\lambda/4$ microstrip transformer technique and the splitter matched by the $\lambda/4$ parasitic transformer is shown in figures 9, 10 and 11 respectively. It is seen that the bandwidths of the splitters are quite the same, while the average value of the return loss in the case of the standard $\lambda/4$ microstrip transformer matching is lower than that obtained by the $\lambda/4$ parasitic transformer.

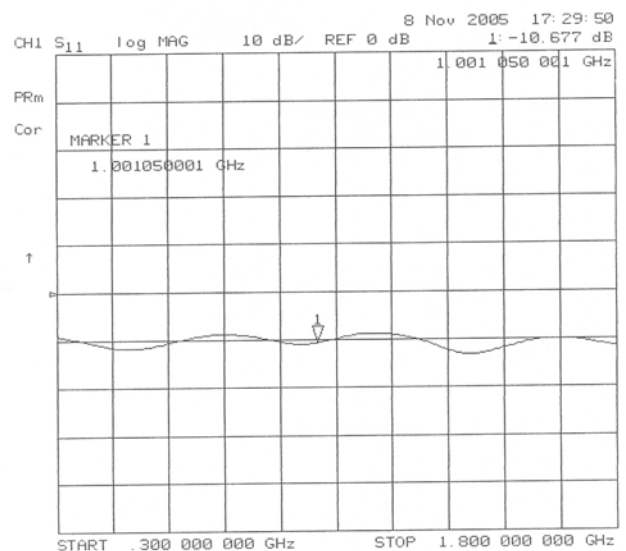


Figure 9: S_{11} measurement of the unmatched splitter.

IV. CONCLUSIONS

A kind of a parasitic $\lambda/4$ transformer matching technique, suitable for microstrip and similar transmission lines has been presented. It is shown that a very good matching level has been obtained, with the present method, albeit with a little bit lower quality than the matching quality achieved by the standard $\lambda/4$ microstrip transformer matching technique. The advantage of the present method is that one can check, after the simulation, the matching level of the *real* circuit, without yet fixing the parasitic matching element to the circuit. One can try to find the optimal position of the matching element, or try other parasitic matching elements. When the matching level is obtained, the matching piece can be fixed to the main circuit

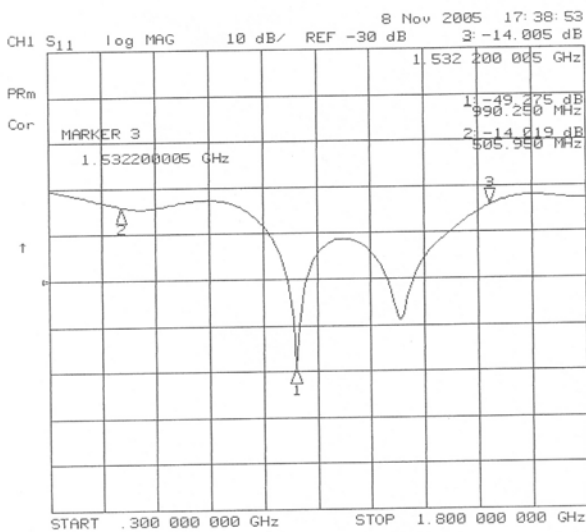


Figure 10: S_{11} measurement of the splitter matched by the standard $\lambda/4$ microstrip transformer.

by dielectric screws. This method is appropriate for emergency cases, to improve the matching level, or for fine tuning, after the circuit has been produced. It is also interesting to investigate the efficiency of other parasitic matching elements like stubs, tapers etc.

[1] P. M. Pozar, Microwave Engineering, John Wiley & Sons, 3rd Ed., 2005, chapter 5.

[2] N.N. Rao, Elements of Engineering Electromagnetics, 5th Ed., PrenticeHall, 2000, chapter 7.

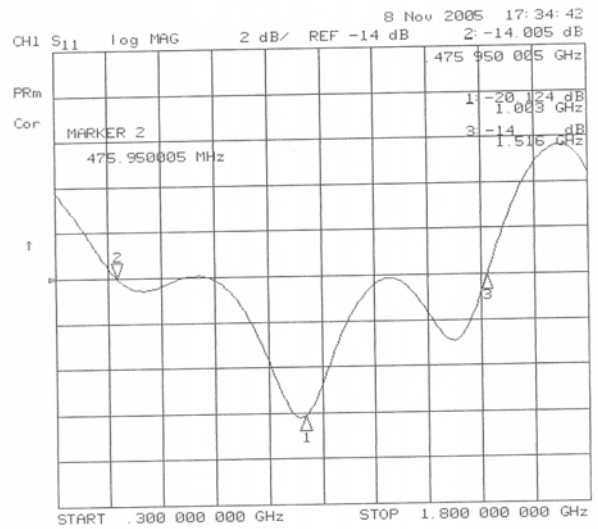


Figure 11: S_{11} measurement of the splitter matched by the parasitic $\lambda/4$ transformer.

The ALMA Front End

Hans Rudolf

European Southern Observatory, ALMA,
Karl-Schwarzschild-Straße 2, 85748 Garching, Germany, +49-89-3200 6397, hrudolf@eso.org

Abstract—The Atacama Large Millimeter Array (ALMA) is a 50 antenna array of radio telescopes that is currently being built in Northern Chile. In order to devide the efforts it is based on equal partnership between Europe and North America. The Front End is the analogue part of the receiver. It converts two orthogonally polarised 30 to 960 GHz signals into an IF of 4 to 12 GHz. All Front Ends are fed with a coherent Local Oscillator that is optically transmitted over the distance from the centre of the array to the antennae. This distance can reach 14 km.

The RF band is split into 10 receiving bands. For each band a receiver, called a cartridge, is designed. The cartridges are housed in a common vacuum chamber and cooled to 4 K. The specifications of the Front End are extremely challenging, for instance the sensitivity is specified between 6 and 10 photons, according to the RF frequency. The first cartridges are finished and not only meet, but exceed these specifications.

I. INTRODUCTION

The Atacama Large Millimeter Array (ALMA) is a revolutionary instrument in its scientific concept and its engineering design [1]. ALMA will provide scientists with precise images of galaxies in formation seen as they were twelve billion years ago; it will reveal the chemical composition of heretofore unknown stars and planets still in their formative process; and it will provide an accurate census of the size and motion of the icy fragments left over from the formation of our own solar system that are now orbiting beyond the planet Neptune [2]. These science objectives, and many hundreds more, are made possible owing to the design concept of ALMA that combines the imaging clarity of detail provided by a 50-antenna interferometric array together with the brightness sensitivity of a single dish antenna.

The challenges of engineering the unique ALMA telescope begin with the need for the telescope to operate in the thin, dry air found only at elevations high in the Earth's atmosphere where the light at millimetre and sub-millimetre wavelengths from cosmic sources penetrates to the ground. ALMA will be sited in the Altiplano of northern Chile at an elevation of 5000 metres (16,500 feet) above sea level. The ALMA site is the highest, permanent, astronomical observing site in the world. On this remote site the 50 12-meter diameter ALMA antennas will each operate superconducting receivers that are cryogenically cooled to less than 4 degrees above absolute zero. The signals from these receivers are digitized and transmitted to a central processing facility where they are combined and processed at a rate of 1.6×10^{16} operations per second. As an engineering project, ALMA is a concert of 50 precisely-tuned mechanical structures each weighing more than 50 tons,

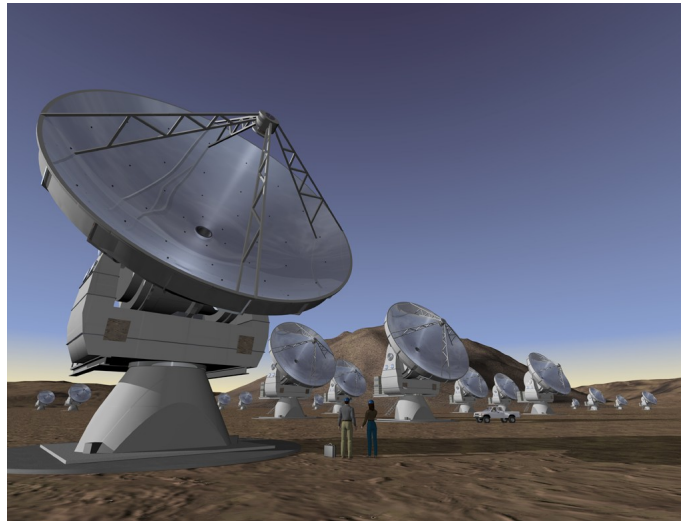


Fig. 1. An artist view of ALMA

superconducting electronics cryogenically cooled, and optical transmission of terabit data rates – all operating together, continuously, on a site more than 5 kilometres high in the Andes mountains [3].

ALMA is an international astronomy facility based on an equal partnership between Europe and North America, in cooperation with the Republic of Chile, and is funded in North America by the U.S. National Science Foundation (NSF) in cooperation with the National Research Council of Canada (NRC), and in Europe by the European Southern Observatory (ESO) and Spain. ALMA construction and operations are led on behalf of North America by the National Radio Astronomy Observatory (NRAO), which is managed by Associated Universities, Inc. (AUI), and on behalf of Europe by ESO [1]. In addition, Japan has also entered the ALMA project. A preliminary agreement has been signed by all partners. The Japanese activities are led on behalf of the National Astronomical Observatory of Japan (NAOJ) [4].

II. THE ALMA FRONT END ASSEMBLY

A. The Scientific Specifications

The required frequency coverage (all atmospheric windows from 31.3 to 950 GHz) is achieved in 10 separate bands. The band edge frequencies were chosen to provide good coverage of the windows while limiting the edge frequency ratio for each band to < 1.35 , considered the largest feasible value.

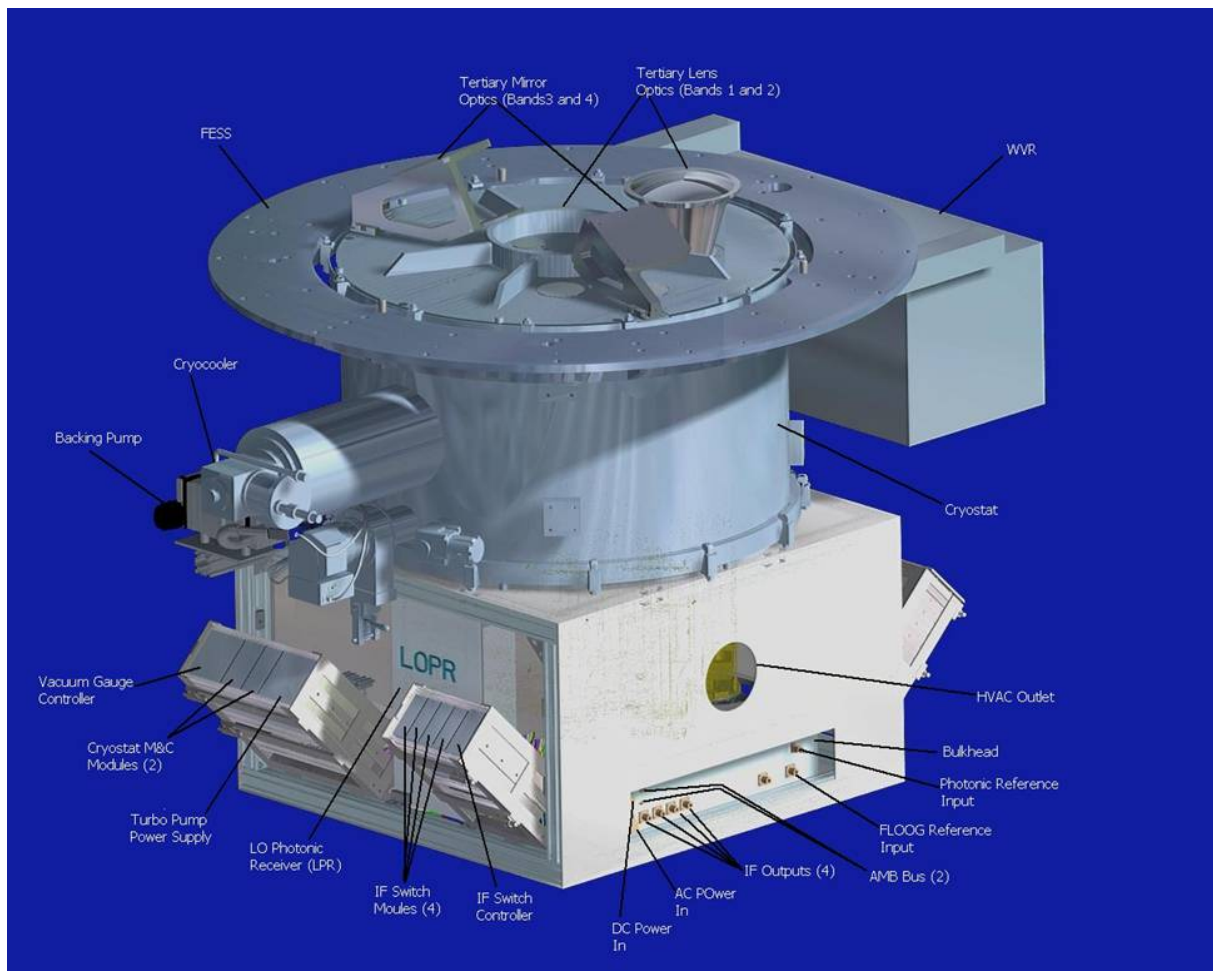


Fig. 2. A 3D drawing of the Front End Assembly

The exact frequencies follow closely the recommendations of a scientific working group [5].

specifications call for a band specific noise temperature of

$$T_{SSB} = A(f) \frac{hf}{k} + 4K \quad (1)$$

TABLE I
THE ALMA FREQUENCY BANDS

Band	Manufacturer	Frequency	Noise Temperature
1	–	31.3 - 45 GHz	26 K (SSB)
2	–	67 - 90 GHz	47 K (SSB)
3	HIA	84 - 116 GHz	60 K (SSB)
4	NAOJ	125 - 163 GHz	82 K (SSB)
5	Chalmers	163 - 211 GHz	105 K (SSB)
6	NRAO	211 - 275 GHz	136 K (SSB)
7	IRAM	275 - 373 GHz	219 K (SSB)
8	NAOJ	385 - 500 GHz	292 K (SSB)
9	SRON/NOVA	602 - 720 GHz	261 K (DSB)
10	(NAOJ)	787 - 950 GHz	344 K (DSB)

The requirements on the noise temperature of these receivers are extremely challenging and range from 6 to 15 photons. The

over the full frequency range. The frequency specific value $A(f)$ follows the following values:

$$\begin{aligned} \text{below 275 GHz} & \quad A(f) = 10 \\ 275 \text{ GHz} - 500 \text{ GHz} & \quad A(f) = 12 \\ \text{above 602 GHz} & \quad A(f) = 15 \end{aligned}$$

A value of $\frac{2}{3}$ of the indicated value must be met over 80 % of the frequency range.

In order to synthesise an image in the correlator, it is extremely important to maintain the coherence between antennas. This coherence must be preserved in both amplitude and phase noise. The amplitude noise, expressed in terms of Allan variance (σ^2) must exceed $5.0 \cdot 10^{-7}$ for timescales between 0.1 seconds and 10 seconds. The phase jitter (1 second) must be better than $38fs$ and the phase drift better (300 seconds) than $12.5fs$ (corresponding to 4.3° at 950 GHz).

B. The Technical Implementation

All of the components described in this section are parts of the Front End Assembly, which includes the vacuum chamber with cryocooler and an attached frame that houses the room temperature electronics.

1) *The Cartridges:* Cryogenically cooled components of the front end (FE) that are specific to one band are in separate assemblies known as *cartridges*, but these are housed in a common vacuum chamber and cooled by a common cryocooler. Only four of the bands will be implemented initially, band 3, band 6, band 7, and band 9. Two bands will be provided as contribution from NAOJ, band 4 and band 8. These bands will follow shortly after the four initially implemented bands. For band 5 funding is available for the development and production of eight pre-production cartridges from the sixth framework programme of the European Union.



Fig. 3. A picture of the band 7 cartridge

For the two lowest-frequency bands, the initial active el-

ement is an HFET amplifier. The HFET amplifiers, along with the filters and mixers that follow them, are cooled to a nominal temperature of 15K. All other cartridges employ Superconductor-Insulator-Superconductor (SIS) mixers for frequency translation. The SIS mixers, along with the InP amplifiers and isolators are cooled to a nominal temperature of 4.0K.

Each band has its own tertiary optics, consisting of a lens or a pair of ellipsoidal mirrors, to match the wave that arrives at the secondary focus to a corrugated feed horn. The signal is separated into the two polarisations, nominally linear and orthogonal, and delivered in waveguide to the amplifier or mixer. For bands 1 through 6 (to 275 GHz), polarisation splitting is achieved in an orthomode waveguide junction just after the feed horn. For higher frequencies, it is achieved with a wire grid within the tertiary optics, and in these cases each channel has a separate feed horn.

In all cases, the signal is converted to an IF band between 4 and 12 GHz, either by the SIS mixer or by a Schottky diode mixer. The mixers for both polarisation channels are driven at the same LO frequency. For the HFET bands, a filter ahead of the mixer produces a single-sideband response (upper sideband for band 1 and lower sideband for band 2). The SIS bands are of two different types: sideband separating (2SB) and double sideband (DSB). The 2SB case supplies two IF outputs simultaneously, carrying opposite sidebands of the LO. The DSB case supplies a single IF output carrying a linear combination (nominally equal) of responses from both sidebands. Bands 3 through 8 use 2SB mixers, and bands 9 and 10 use DSB mixers. In order to utilize fully the signal transmission system and correlator, each polarisation channel delivers 8 GHz of instantaneous bandwidth at IF.

Each IF output from a mixer is amplified in a cooled pre-amplifier closely associated with that mixer. The cooled amplifiers and mixers are supported by active bias circuits. Gains are near 35 dB in most cases, allowing the subsequent cable loss (especially the transition to room temperature) to have negligible effect on the receiver noise temperature. Currently the pre-production of eight Front End assemblies is under way. The amplified IF signals are brought out of the vacuum chamber on coaxial cables amplified with room temperature LNAs and delivered to IF Processing assemblies.

2) *The IF Processing Assembly:* Each IF Processing assembly accepts one signal from each band and contains additional amplification, switching to select one band's signal for further processing, gain equalization, and variable attenuation to adjust the power to a specified level. There are 4 IF processing assemblies. Two for each polarisation and for each side-band.

3) *The 1st Local Oscillator:* Nearly all time-dependent functions in the array must be coherent with a single master oscillator from which reference signals are derived and distributed. This is a hydrogen maser. A mm-wavelength reference is then synthesized for the first LO. This is the only variable-frequency signal that is distributed to the antennas. The process uses a microwave synthesizer to produce 8.62-11.08 GHz in 5 MHz steps, followed by synthesis of 27-142

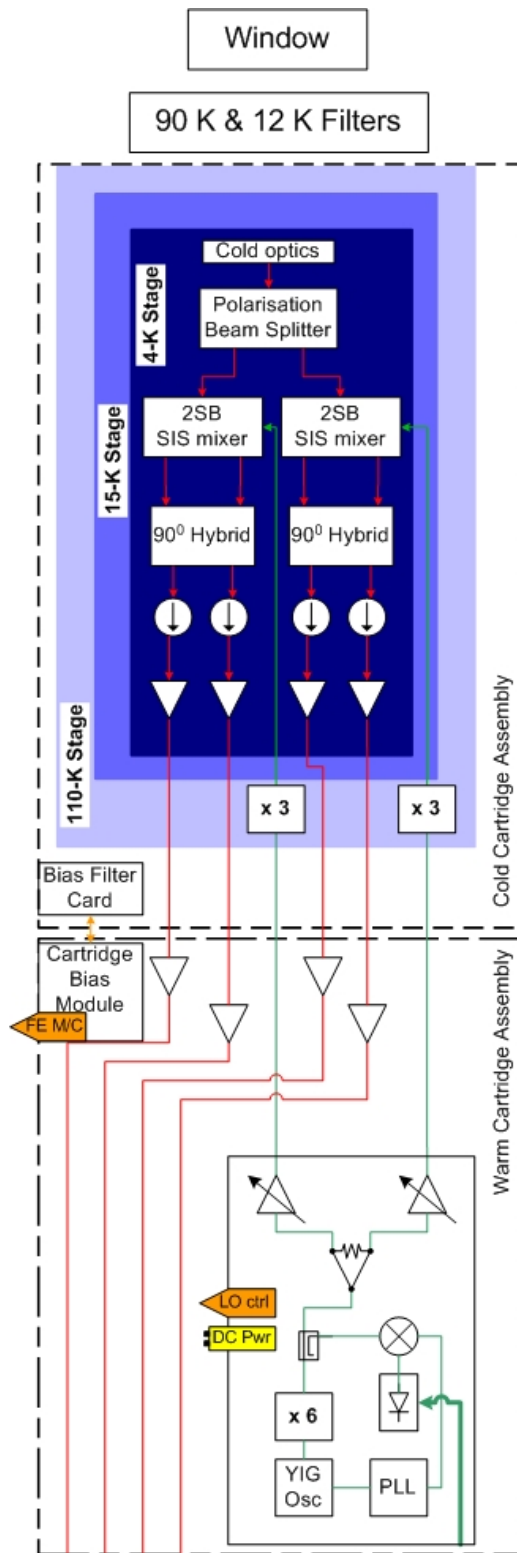


Fig. 4. A block diagram of the band 7 cartridge

GHz as the difference between two laser-generated optical frequencies.

Generation of the mm/sub-mm wavelength first LO is based on phase-locking a local VCO to the highest-feasible reference

frequency that can be distributed from the center. The two-laser reference signal is recovered by photomixing. The phase-locked signal is then amplified with GaAs and InP amplifiers and multiplied to higher frequencies, as needed, in diode multiplier assemblies; these multipliers are operated at cryogenic temperatures (110K) to maximize efficiency. Reference frequencies in the range 68.5 to 141.3 GHz are needed to cover bands 2 through 10 with cold multiplication factors of 1 (no multiplier), 2, 3, 5, or 9. The band 1 reference and VCO are at 27.3 to 33 GHz. The local VCO is implemented as a YIG-tuned microwave oscillator and amplifier/multiplier chain. The YTO frequencies and hence the required multiplication factor are chosen for engineering reasons, but the minimum oscillator frequency is kept above 12 GHz to avoid the possibility of spurious sidetones of the LO falling in the RF band that extends +/- 12 GHz from the LO. The locked VCO is offset from the reference by 20 - 40 MHz from a direct digital synthesizer through which phase tracking (fringe rotation) and phase switching are implemented.

4) *The Cooler & Vacuum System:* The vacuum chamber with cryocooler and cartridges is part of the overall FE Assembly, located in the centre of the antenna's receiver cabin, a room behind the focal plane that moves with both axes of antenna pointing. To maintain good optical alignment, the FE Assembly is rigidly attached to the antenna structure very near the focal plane. The overall weight of the front assembly is in the order of one metric ton.

A single 3-stage Gifford-McMahon cryocooler is used; the stages are nominally at 110K, 15K, and 4K. The cryocooler is supported by a single-stage helium compressor that is mounted outdoors on a platform that rotates with the antenna in azimuth but not in elevation.

5) *The Calibration Device:* In general, calibration of the ALMA instrument will rely on observations of known astronomical sources. To supplement this and to compensate for the shortage of appropriate natural sources, a calibration device will be built into each antenna for the purpose of generating calibration signals.

The calibration device consists of a robot arm that places a load of a known temperature in front of the observing cartridge. Two loads are available, one at ambient temperature and one at 60° C. The absolute error of the gain after calibration will be less than 3 % and less than 5 % for frequencies higher than 373 GHz.

This procedure will be repeated every 5 minutes.

6) *The Water Vapour Radiometer:* The water vapour column density is measured by special radiometers (WVRs) built into each antenna. These measure the brightness temperature of the sky at several frequencies around the 183 GHz water line. Assuming that the sky brightness at these frequencies is dominated by emission from the water vapour, the spectral shape helps determine the altitude, temperature, and degree of saturation of the line. In principle, this allows the column density of water vapour to be deduced, and from it the signal delay at the observing frequency.

III. RESULTS

ALMA is currently in the pre-production phase. On the Chajnantor site antenna foundations and buildings are being built. The first four cryostats are at the Front End integration Centres. The first cartridges have been completed and are currently integrated in the cryostat to form the first Front End.

Though the specifications have been beyond the state of the art when they were postulated, not only most of them are met, but some are exceeded with a considerable margin. In figure 5 a plot of the receiver noise performance for the first band 7 cartridge is shown.

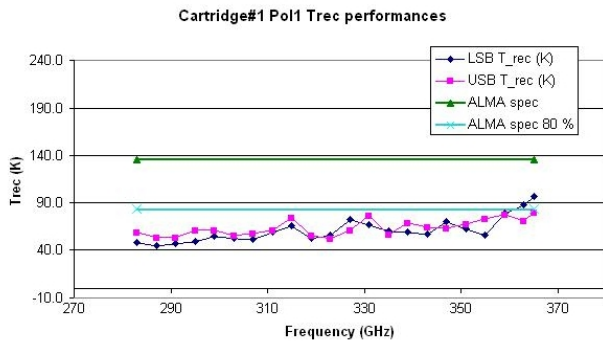


Fig. 5. A noise figure plot of the band 7 cartridge

It can be seen, that the specification is clearly met. Also the other specifications that are important for system sensitivity, such as image rejection as shown in figure 6 or compression ratio are met and exceed the expectations. The other cartridges meet and exceed the specifications in a similar way.

IV. CONCLUSION

The ALMA Front End is a milestone in development of radio astronomy receivers. Compared to all existing systems, not only it brings the frequency limit for ground based radio astronomy to the threshold of 1 THz, but also has it pushed the sensitivity to new frontiers. The specifications that were set beyond the -then- state of the art [5] are not only met but in many cases even exceeded.

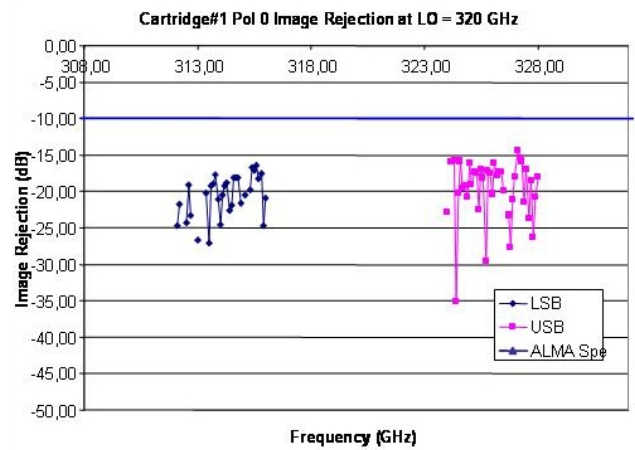


Fig. 6. The image rejection for the band 7 cartridge

Currently the pre-production of eight Front End assemblies is under way. The first ALMA Front End is being integrated in the North American Front End Integration Centre in Charlottesville, VA.

REFERENCES

- [1] Atacama Large Millimeter Array. Homepage. <http://www.eso.org/projects/alma/>, 2005.
- [2] Science with ALMA. Paper. <http://www.eso.org/projects/alma/publications/papers/alma-science.pdf>, 2002.
- [3] ALMA Construction Project Book. Homepage. <http://www.alma.nrao.edu/projectbk/construction/>, 2002.
- [4] Status of the Atacama Large Millimeter Array. Paper. <http://www.eso.org/projects/alma/publications/papers/AlmaStatus2004.pdf>, 2004.
- [5] ALMA Scientific Specifications and Requirements. Alma-90.00.00.00-001-a- spe. <http://www.eso.org/projects/alma/publications/papers/2005-05-26ALMA-90.00.00.00-001-A-SPE.pdf>, 2004.

Concealed Weapon Detection with Active and Passive Millimeterwave Sensors, Two Approaches

Helmut Essen¹, Hans-Hellmuth Fuchs¹, Manfred Högelen¹, Stephan Stanko¹, Denis Nötel¹,
Sreenivas Erukulla¹, Johann Huck¹, Michael Schlechtweg², Axel Tessmann²

¹Research Institute for High Frequency Physics and Radar Techniques (FGAN-FHR),
Neuenahrer Str. 20, D-53343 Wachtberg, Email: Essen@fgan.de

²Fraunhofer Institut für Angewandte Festkörperphysik (IAF)
Tullastr. 72, D-79108 Freiburg, Email: Michael.Schlechtweg@iaf.fraunhofer.de

Abstract—The increasing interest in the security of public spaces leads to a demand for sensor technology beyond metal detectors. Two different approaches of concealed weapon detection using millimeter wave systems are presented in this paper. The design of a passive radiometric sensor in the W-band is presented. On the active side, an FMCW radar system at 94 GHz is introduced for the scanning of persons. The resulting images are shown which enable a first comparison of both approaches.

I. INTRODUCTION

Sensors used for security purposes have to cover the non-invasive control of humans, baggage and letters with the aim to detect weapons, explosives and chemical or biological threat material. Those sensors have to cope with different environmental conditions. Preferably, the control of people has to be done over a longer distance. In times of increasing threat by terrorist attacks the control of passengers at airports and stations is one of the major items. People carrying concealed weapons or explosives or those, who have other terroristic attacks in mind, have to be detected under all circumstances. Very similar requirements have to be met for all aspects of homeland security. Currently, emphasis is placed on system concepts and technology for this type of applications employing millimeterwave, submillimeterwave and terahertz sensors. This is based on the capability of these frequency bands to look through textile material and the possibility to achieve a geometric resolution, which is sufficient to resolve critical items within the necessary range.

II. MILLIMETERWAVE TECHNOLOGY FOR SECURITY APPLICATIONS

Due to other applications, civilian and military, the frequency region around 94 GHz is best developed. Both, devices and components, have been designed and manufactured by Fraunhofer IAF, who have been involved with the demonstrators discussed below. Key components are low noise and medium power HEMT amplifiers [1] and a miniaturized single chip FMCW radar at 94 GHz [2].

Demonstrators have been set up using active and passive sensors. A single channel Dicke type radiometer was designed using three stacked LNAs and a PIN SPDT to switch between

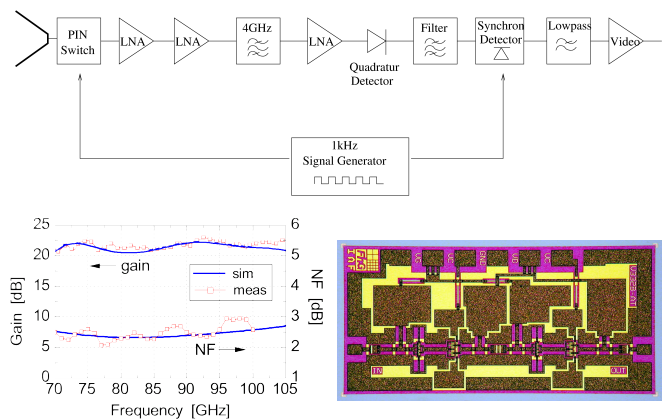


Fig. 1. Radiometric channel of the Dicke type (top), layout of an LNA (right) and LNA performance (left) [1].

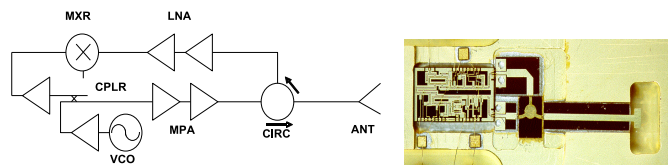


Fig. 2. Functional diagram of single chip FMCW radar (left) and layout at 94 GHz (right)[2].

receiver and the matched second port, which serves as a reference. While the bandwidth of the amplifier chain is 20 GHz, the total bandwidth is limited by the PIN switch to 4 GHz. The overall gain, in this case, is 60 dB. The general set-up and a photo of the LNA layout as well as typical performance curves are shown in Figure 1. To show the rapid improvements in LNA development, the system was then modified to work as a total power sensor. By definition, a total power setup is twice as sensitive as a Dicke type system and offers a lower system noise temperature as no PIN switch is necessary at its input. The second demonstrator, which was involved in the comparative test, is based on the single chip FMCW radar at 94 GHz sketched in Figure 2. It was combined with a linear scanning antenna [3] for the azimuth scan and mounted on a



Fig. 3. Scanning beam antenna for the FMCW radar at 94 GHz

single axis positioner for the elevation scan. Figure 3 shows a photo of the scanning beam antenna.

III. SHORT RANGE IMAGING FOR CONCEALED WEAPON DETECTION AT 94 GHz

A. Passive Sensing

Passive mm-wave imaging with or without artificial illumination by an incoherent noise source is optimal for detecting concealed weapons, which are worn under any kind of clothes. Because of the incoherent illumination, no polarizing effects on the surface or in the clothing material itself occur.

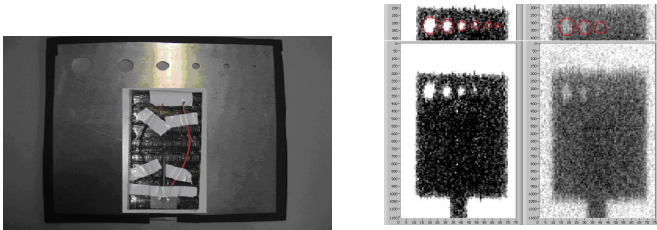


Fig. 4. Photo of sample array of holes and its radiometric raw image

The measurements were done with natural illumination through a window and to be more representative for indoor applications with an incoherent noise source illuminating the scene. First results were achieved at relatively slow scanning speed using a dummy instead of a human being. During these experiments the scanning scheme was optimized. Figure 4 shows the measurement result for a sample consisting of a linear array of holes in a metal plate without any image processing applied. The radiometric image demonstrates the distortions due to scanning and also the limits of resolution with respect to reproduction of the true geometry and due to noise.

To test the possibility of detecting concealed objects, either metallic or not, like a gun, in a first step measurements were conducted with a dummy wearing a coat with a hidden gun and two other metallic objects. To enhance the contrast of the metallic items the radiometric image was processed using a threshold algorithm. Using different sample objects made up of metal, ceramic and plastic material, it was shown that it

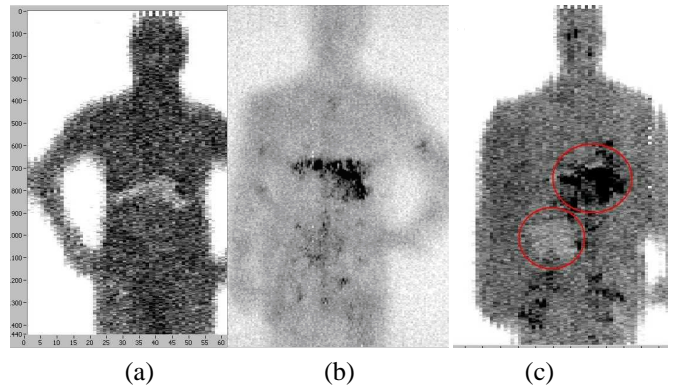


Fig. 5. Indoor images at 94 GHz (Dicke radiometer) for a human with a concealed gun without illumination (a), a dummy with illumination (b) and an illuminated human carrying chocolate and a gun (c).

is possible not only to detect suspicious materials but also to get a significant image showing the outline of the object. Due to limitations in the scanning algorithm the scanning time for these first experiments was unacceptably low at approximately 20 minutes.

With the advent of LNAs with an improved noise figure, as described in Section 1, effort was put into an optimisation of the scanning process. The scanning time was reduced to 2.5 minutes using only a single channel receiver. This enabled measurements of sample objects under the clothing of real humans even in indoor environments [4]. Fig. 5a shows a radiometric image of a man with a gun hidden under his jacket. Fig. 5b shows a dummy in a similar arrangement in a closed room but with artificial illumination. As the detection of plastics and explosives is an important issue, measurements using chocolate as a replacement for explosives were conducted. Fig. 5c shows the result of a human carrying a gun and a block of chocolate under the clothes, illuminated by a noise source.

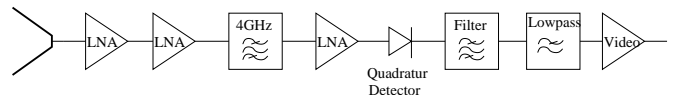


Fig. 6. Radiometric sensor in total power setup avoiding the Dicke type switch. The overall gain of the LNAs is around 60 dB. This system is twice as sensitive as a Dicke type sensor.

Using radiometers with LNAs so stable that a Dicke type system can be replaced by a total power sensor (see also Fig. 6) leads to reduced noise temperature and therefore increased dynamic range of the system.

Figure 7 shows an example of a radiometric outdoor measurement using a total power radiometer at 94 GHz. Weapons and other devices can be detected although hidden inside a coat. It must be emphasized that the ceramic knife is detected, which is not possible with a conventional metal detector. This measurement shows well the high spatial resolution of the scanning system, especially when looking at the cell phone and the PDA, where you can see many details of the objects. The

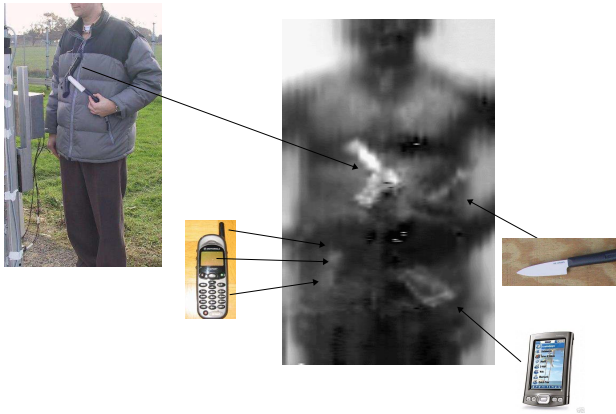


Fig. 7. Photo (left) and radiometric image (right) of a person scanned with a total power sensor under outdoor conditions. In the left picture the weapons (gun and ceramic knife) were put in front of the coat for clarification reasons. While producing the radiometric image (left) they were hidden inside the coat. The high spacial resolution of the system using 94 GHz, is noticed from the image, which is why so many details of the scene are clearly visible. For example, the darker display and the brighter housing of the PDA are clearly distinguishable. A cell phone is visible on the other hanging upright. Details like the display as well as the keyboard and the small external antenna are detected.

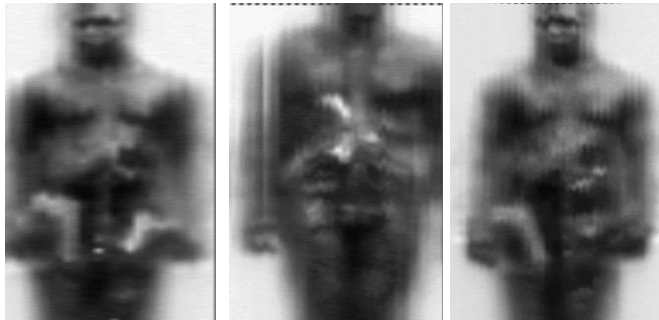


Fig. 8. Radiometric outdoor images of persons concealing weapons under leather jackets using a Dicke radiometer [5].

pictures in Figure 8 show measurements of humans wearing concealed weapons under leather jackets.

B. Active Imaging

For a direct comparison between an active and a passive scanning system a demonstrator based on a FMCW radar module at 94 GHz was developed und assembled (Fig. 9). Due to the scanning beam antenna a 2-dimensional scan of a person can be performed much faster than by using a two axis positioner. The duration of a complete measurement is typically in order of a few minutes. Because the antenna's field of view is limited to $\pm 10^\circ$ the optimum distance to the target is about 3 to 4 meters. This range combined with the width of the antenna beam provides a spacial resolution, which is much worse than the resolution of the passive system described above. The resonant structure of the antenna (Fig. 3) limits the useful bandwidth to 400 MHz, which makes this type of antenna inapplicaple for passive radiometric systems, where high bandwidth is a crucial factor. In a radar based system



Fig. 9. Image of the FMCW radar scanner mounted on a positioner.

this bandwidth allows to discriminate the scene in range with a resolution of approximately 37 cm. In combination with a scanning system a 3-dimensional image of the target can be created.

Figure 10 shows the radar images of two men and a dummy created using the radar based security scanner. The comparison of these results with images generated using a passive scanner demonstrates, that both systems point out different properties of the measured target. It is planned to combine the passive and active approaches in order to detect more details about the test object in order to increase the reliability of security applications.

However, investigations of the detectability of metallic objects by means of the active radar scanner revealed that this system in stand-alone mode does not match the requirements of concealed weapon detection. The first reason for this is that the surface of most weapons, like knives and guns, consist of a small set of flat metal facets. The dominant type of scattering on flat surfaces is specular reflexion, therefore these objects can only be detected, if one of the illuminated surfaces is perpendicular to the radar line of sight. Certainly, under convenient conditions the radar will see a flash of the metal object, but this is not enough for a reliable detection. This shortcoming can be fixed by application of several radar sensors in a bi- or multistatic configuration, which would significantly increase the probability of detection. Figure 11 shows images of an unarmed man and a man with a gun on his chest. The position of the gun is marked with a red circle. Although the weapon was not covered by clothing, the radar image gives no clue about it, while the passive scanner usually shows even the shape of the gun.

Moreover, the detection of concealed weapons by means of a radar scanner is complicated because of the different scattering and absorption properties of fabric. While woolen clothes are nearly transparent in the millimeterwave range, heavy cotton can cause strong specular scattering itself, which

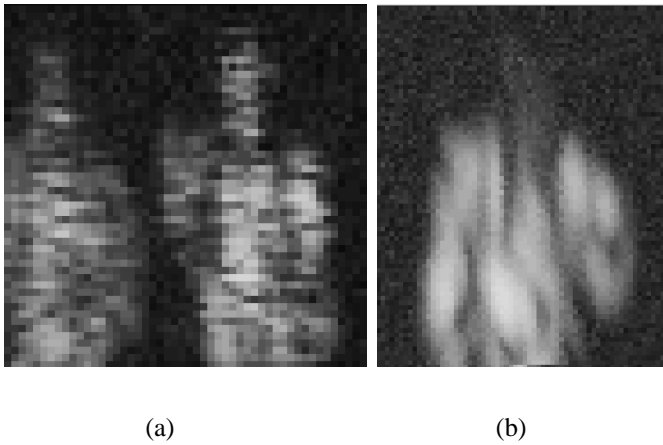


Fig. 10. Images of two men (a) and a dummy (b) generated using a 94 GHz FMCW radar scanner.

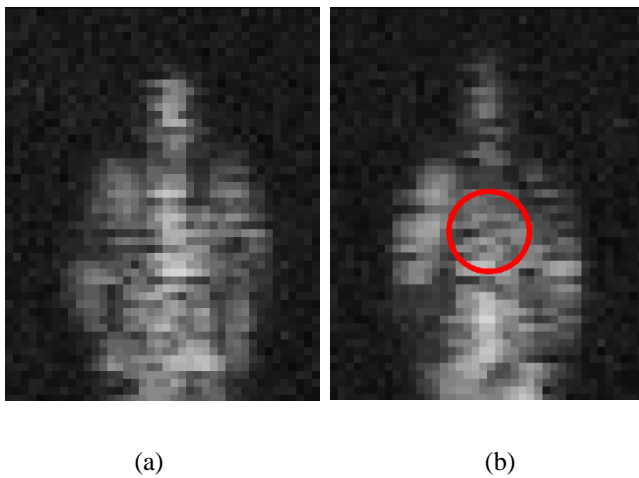


Fig. 11. Images of an unarmed man (a) and a man with gun (b). The position of the gun is marked with a red circle.

disturbs the image and leads to a masking of reflections from metallic objects. Under certain conditions even the wrinkles of the clothing can act as small scattering centers. In order to understand all these phenomena further investigations on this field are necessary.

IV. RESULTS

Two approaches for concealed weapon detection were tested, one using a radiometer, the other employing a miniature FMCW radar. The passive system delivers encouraging results with good image quality, at rather long scanning times. It was shown that indoor use is feasible passively and can be enhanced by artificial illumination sources. The active sensor offers higher scanning speed and works independent of the ambient temperature.

Due to the monostatic geometry, which is in favour of specular reflections even from fabric, depending on its type, it is much more difficult to detect and image concealed metallic objects using an active scanning system. The probability of detection can be improved using several radar sensors in a

multistatic configuration. For the future it is also planned to introduce fully polarimetric methods, which are likely to allow a discrimination between different types of scattering and acting as a polarimetric filter for reflections from the surface of the fabric and from underneath.

REFERENCES

- [1] M. Schlechtweg, A. Tessmann, A. Leuther, C. Schwörer, H. Massler, M. Mikulla, M. Walther, R. Lösch, *Advanced Millimeter-Wave ICs Using Metamorphic HEMT Technology*, 32nd International Symposium on Compound Semiconductors (ISCS05), September 2005.
- [2] A. Tessmann, S. Kudzus, T. Feltgen, M. Riessle, C. Sklarczyk, W.H. Haydl, *Compact Single-Chip W-Band FMCW Radar Modules for Commercial High-Resolution Sensor Applications*, IEEE Transactions on Microwave Theory and Techniques 50 (2002), 2995.
- [3] Waveband Corporation, Van Ness Ave, Suite 1105, Torrance, CA 90501, info@waveband.com
- [4] J. Huck, *Personenscanner*, Diploma Thesis, Fachhochschule Koblenz, Koblenz, June 2005.
- [5] S. Erukulla, *Design and Optimisation of Millimetrewave Sensors for Security Imaging*, Master's Thesis, Chalmers University of Technology, Göteborg, February 2006.

A multi-frequency microwave aperture synthesis radiometer for high-resolution imaging

Matthias Jirousek, Markus Peichl, Helmut Suess

DLR (German Aerospace Center) Oberpfaffenhofen, Microwaves and Radar Institute,
P.O. Box 1116, 82230 Wessling, Germany
E-mail: matthias.jirousek@dlr.de, markus.peichl@dlr.de, helmut.suess@dlr.de

Abstract—Many geophysical parameters can be determined with the aid of a passive microwave sensor. To achieve a high spatial resolution in passive microwave imaging the method of aperture synthesis can be applied. Narrowband radiometric measurements within a wide frequency range allow extracting more surface information on observed objects or materials and it is possible to obtain depth information on layered structures. Furthermore the advantages of using a range of different centre frequencies, i.e. a higher spatial resolution with increasing frequency and a higher penetrating capability at lower frequencies, can be combined in many cases to enhance the overall imaging capabilities. Thus our recent interest is focused on the development of an experimental system offering those features but keeping the costs affordable. In this paper the basic system concept and some reconstruction algorithms are outlined and illustrated by an imaging simulation.

Keywords— aperture synthesis; radiometry; multi-frequency

I. INTRODUCTION

One of the main focuses in the development of imaging radiometers is improving the spatial resolution. This means that for a line scanner or push broom system the size of the required real aperture antenna has to be increased. In the case of the line scanner the mechanical inertia sets an upper limit on the size of the moved antenna. Push broom systems become rapidly bulky devices, if high-resolution two-dimensional imaging is demanded. An alternative imaging system without any rotating or mechanical scanning devices is the aperture synthesis radiometer (ASR). Hereby the signals of many small real aperture antennas arranged in a thinned array are complex correlated in pairs. Hence the measured values depend on the antenna distances, i.e. the baselines or spatial frequencies, and their adequate combination is a truncated measure of the spatial frequency spectrum of a scene. Thus the maximum spatial resolution is given by the maximum baseline. For an ideal system imaging an arbitrary brightness temperature scene T_B under far-field conditions, the spatial frequency spectrum, which is also called the visibility function \underline{V} , can be determined as follows [1, 2]:

$$\underline{V}(u_\lambda, v_\lambda) = \int_{-1}^1 \int_{-1}^1 \frac{T_B(l, m) P_{nm}(l, m)}{\sqrt{1-l^2-m^2}} \times \exp(-j2\pi(u_\lambda l + v_\lambda m)) dl dm \quad (1)$$

Hereby the baseline is given by its coordinates u_λ and v_λ , which are normalized to the wavelength. The spatial coordinates $l = \sin\Theta \cos\Phi$ and $m = \sin\Theta \sin\Phi$ are given in direction cosines of a spherical coordinate system, in whose center the array is located. $P_{nm}(l, m)$ describes a normalized average of the antenna power patterns, which are assumed to be quite similar for a first approximation. As can be seen, (1) constitutes a two-dimensional Fourier-transformation between the visibility function $\underline{V}(u_\lambda, v_\lambda)$ and the brightness temperature distribution $T_B(l, m)$. In a real system the visibility function is recorded discretised in steps of Δu_λ and Δv_λ and is limited to a maximum baseline of $u_{\lambda, \max}$ and $v_{\lambda, \max}$. The discrete sampling leads to a limitation of the maximum unique area of l and m given by

$$|l_{\max}| < \frac{1}{2\Delta u_\lambda} \quad \text{and} \quad |m_{\max}| < \frac{1}{2\Delta v_\lambda}, \quad (2)$$

for a rectangular sampling grid. The limitation of the measurement domain to $u_{\lambda, \max}$ and $v_{\lambda, \max}$ determines the theoretical maximum spatial resolution Δl and Δm to be

$$\Delta l > \frac{1}{u_{\lambda, \max}} \quad \text{and} \quad \Delta m > \frac{1}{v_{\lambda, \max}}. \quad (3)$$

These four conditions are a main driver for the design of a system. Since the visibility values are only a function of the antenna distance, a thinned array is feasible, which allows an enormous reduction of the required antenna elements compared to a push broom system, where a filled array has to be realized. As investigated earlier in literature and by ourselves [2, 3], array geometries like 'T', 'U', 'Y' or 'O' are suitable structures to cover the u - v or spatial-frequency domain properly.

An additional benefit of an ASR system is the flexible focusing capability [1]. It can be achieved purely mathematically during the data processing, which has to be done by hardware using a push broom or a line scanner system. Hence, with an ASR it is also possible to measure in the near field of the synthetic aperture. This will be one major application area of the experimental system presented here.

In order to penetrate dielectric materials properly, frequencies in the lower microwave region have to be used.

Since a narrowband measurement at a single frequency will deliver only information for a specific constellation of the wavelength, the dielectric constant, and the physical structure of an object, the use of multiple narrowband frequency channels is preferable. In this case a multitude of different images can be analyzed individually or in combination, which is superior to the investigation of only one broadband image. A suitable application of this approach can be found in the detection and analysis of hidden objects as in the case of buried landmine retrieval [4].

II. OUTLINE OF THE SYSTEM CONCEPT

A major advantage of an ASR compared to a line scanner imaging system is the simultaneous observation capability of all pixels of a two-dimensional area. In this case a two-dimensional array is necessary for an operational use that produces for all possible baselines the correlation values within a snapshot period. For a high-resolution system this leads inevitably to an enormous hardware expense. For instance, a regularly assigned array with a maximum baseline of $N=79$ times the minimum antenna spacing $\Delta=\Delta u_\lambda=\Delta v_\lambda$ along the u and v axis following a ‘T’ or a ‘U’ structure would require a minimum number of $n_{\text{receiver}}=3N+1=238$ receivers. Hence the total number of baselines would be

$$n_{\text{baseline}} = \frac{n_{\text{receiver}}(n_{\text{receiver}} - 1)}{2} = 28203, \quad (6)$$

and therefore 28203 correlators would be required. Note, that for such an array geometry some baselines are redundantly measured, so that the number of required correlators can be reduced somewhat. However, as this number is still in the same order, the demand on the hardware expense and the costs will still be high. Additionally it should be mentioned, that the maximum baseline for a ‘U’ or ‘T’ array is oriented in the diagonal direction and has a length of $2^{1/2}N\Delta$.

As a simplest solution to reduce the expense for an experimental system, a two-elements interferometer can provide all the correlation data [1]. In this case the correlation values for each baseline have to be measured successively. This requires an almost static scene, where the brightness temperature distribution does not change significantly during the measurement period. The major disadvantage of this extremely flexible sampling method is the long measurement duration, which increases about quadratically with the length of the maximum baseline, i.e. the maximum spatial resolution.

Following the previous considerations a hybrid solution between the fully two-dimensional system and the simple two-elements interferometer was deemed to be the most practicable way, which is given by a rotatable one-dimensional array. Thus the spatial-frequency domain is sampled along concentric rings in the u - v plane. As a compromise this approach combines to some extent the advantages of both system concepts. On the one hand only a few receivers and correlators are required due to the one-dimensional array configuration. On the other hand the measurement time is reduced considerably, because it is just a function of the total number of the angle increments, for

which the array arm has to be rotated. A conceptual drawing of the intended system configuration is shown in Fig. 1.

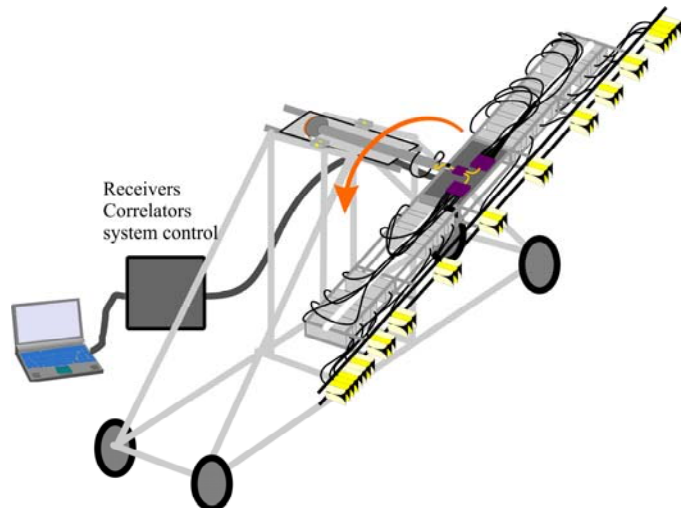


Figure 1. Conceptual drawing of the experimental aperture synthesis radiometer using a rotating linear thinned array.

The linear array is rotatable by 360° and also the tilt angle of the rotation plane is adjustable to some extent. The whole system is mounted on a mobile base frame for a flexible adjustment to the scenes of interest. Another option could be to mount the arm in a horizontal frame so that the antennas' main lobes point to the ground in order to apply for landmine detection. To minimize the number of receivers and thus the complexity and costs, the intention is to find a linear array with lowest redundancy and an adequate two-dimensional sampling performance for a given maximum baseline.

A constraint of the sampling theorem for a linear array is that all the required baselines are a multiple of the minimum spacing without any gap in the sampled spatial frequency domain. In the literature many attempts have been reported to solve this problem. Most of them optimize to a minimum redundancy criteria, but do not provide a zero gap of baselines. The array optimization is a very time and computer-power consuming task, which increases non-linearly with the number of single antenna elements. In [6] low redundancy array configurations with zero gaps to a maximum of 30 elements are computed. We choose an array with 15 elements and a maximum spacing of 79 times the minimum spacing. The solution has the following form for the position in spacing with respect to the first element at 0,

$$d_{55} = [0,1,2,5,10,15,26,37,48,59,65,71,77,78,79]. \quad (7)$$

The array was selected in accordance to a pretended maximum length L of about 2.8m for the linear array using the equation $L=n_{\text{spacing}}\lambda\Delta$ and $\Delta=1/(2l_{\text{max}})=1/(2m_{\text{max}})$ from (2). The wavelength was computed for a desired highest frequency of about 6.5GHz to be 46mm, and the maximum field of view was estimated to be about $\Theta_{\text{FOV}}=80^\circ$, $l_{\text{max}}=m_{\text{max}}=\sin(40^\circ)$, for the type of broadband antennas to be used. Hence a maximum

spacing of $n_{\text{spacing}} = 79$ can be computed from previous considerations.

In order to allow a multiple frequency measurement and a sufficient penetration depth within a broad frequency range, the minimum and maximum frequency has been chosen to be $f_{\text{min}} = 1.4\text{GHz}$ and $f_{\text{max}} = 6.5\text{GHz}$. The array length of about 2.8m allows a theoretical spatial resolution of $\Delta l = 0.016$ ($f = f_{\text{max}}$) according to an angular resolution of 0.9° at boresight, and $\Delta l = 0.071$ ($f = f_{\text{min}}$) according to 4° for the lowest frequency. Due to our present fixing of $\Delta u_\lambda = 0.75$ ($f = f_{\text{max}}$) the field of view of the experimentally ASR is limited to $l_{\text{max}} = 0.67$ ($f = f_{\text{max}}$) or 82.5° , which is still in accordance with the broadband antenna beamwidth.

The computed baseline distribution in the u - v domain is shown as an example for three centre frequencies in Fig. 2. In this example the one-dimensional array has only four elements leading to a total of five baselines and no sampling gaps for the highest frequency. The rotation angle dependence is shown for increments of 10° and for the frequencies of 1.5GHz , 4GHz and 6.5GHz . The minimum spacing is 35mm and the array dimension is 175mm .

It can be seen that with the lowest frequency only lower range of spatial frequencies can be sampled, whereby with the highest frequency also higher spatial frequencies are recorded. In addition, the spatial frequency samples from different centre frequencies have a different radial location. In order to perform an image reconstruction from the sampled visibility values, a variety of strategies to process the single data sets can be performed:

- Each brightness temperature map is reconstructed separately for each centre frequency. Thus one obtains as many images as centre frequencies, each one showing the specific frequency characteristics that can be used in combination with further image processing tools.
- The visibility values of several centre frequencies are combined adequately and used together for the image reconstruction. This can be useful to enhance the alias-free field of view given by the sampling grids in the u - v plane. In addition, many parameters like the type of interpolation to achieve an admissible tiling or the choice of an adequate weighting function encourage the reconstruction in different ways. As mentioned before, with different centre frequencies different spatial frequencies are measured.
- An alternative method is the combination of the reconstructed images in the spatial domain, whereas equivalent parameters are tunable as in the frequency domain.

All variants are common in the sense that the sampled visibility function has to be interpolated to a rectangular, hexagonal, or another admissible tiling to fulfill the sampling theorem. A basic requirement to perform this is that the polar sampling grid of the original measurements has a sufficient density. Once the right grid in the spatial frequency domain is established, the intrinsic image reconstruction using a simple

Fourier transform or more advanced procedures [3, 7] can be applied as required.

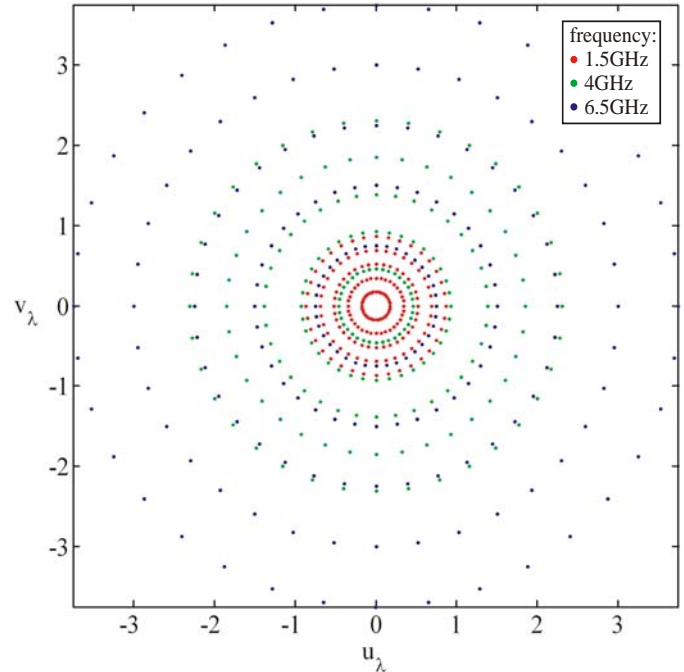


Figure 2. Distribution of samples in the u - v plane for a four elements array with positions at $d_s = [0, 2, 4, 5]$, a 10° rotational step size, and three center frequencies.

In order to allow the required broadband operation, Vivaldi type antennas are used as a suitable solution. They cover the frequency range from 1.4GHz to 6.5GHz , and they are thin enough in one dimension that two antennas can be located in a distance of $\Delta u_\lambda = 0.75$ ($f = f_{\text{max}}$) or 35mm , respectively. This small antenna distance leads inevitably to mutual coupling effects, which can significantly affect the amplitude and the phase behaviour of the antenna patterns. The influence of this distortions and the impact on the image reconstruction performance was not investigated yet. Measurements in the anechoic chamber and computer simulations of the imaging process shall identify the requirements to cope with that in the image reconstruction process. A disadvantage of the Vivaldi antennas as used in our rotating linear array configuration is that during the rotation the linear polarization of the antennas is varying with respect to the observed scene. The related impact to a reconstructed image depends on many parameters like the material, the incidence angle, the frequency and the specific polarization characteristics of the antennas. In our first system concept these impacts are neglected, but the system is extendable to cope with this issue in future.

In order to perform the required complex correlations at a frequency range of 1.4GHz to 6.5GHz a heterodyne receiver concept was chosen. In this configuration a sideband separation or rejection has to be implemented due to the fact that the real or imaginary part of the correlation result is eliminated as a consequence of a double sideband conversion and correlation. In principal there are three ways of realization. First a two stage frequency conversion can be used to mask out the second sideband using a suitable filter bank. In our case four high pass

filters are necessary having an intermediate (IF) centre frequency of 800MHz and a maximum bandwidth of 100MHz. Another method is the use of a tunable YIG-filter. Both principals are very cost and weight intensive for a multi-receiver system so that we selected a third method, using an image rejection mixer. The second sideband is attenuated with this concept up to 25dB depending on the accuracy of the hybrids for the given specifications.

For the intrinsic correlation process a digital correlator concept is selected because of the following advantages compared to an analogue solution: less required space to accommodate the required 105 correlators, no distinct drift and aging behaviour, and the requirement of considerably less receiver output power due to no analogue distribution network. The 105 correlators were implemented almost completely in a FPGA device supplemented with the required auxiliary electronics. The input signals are first 1-bit quantized, then sampled and finally complex digitally correlated. The quantization loss can be almost corrected for by applying the Van Vleck theorem [2]. For the quadrature component of the Visibility samples the 90° phase shifter is implemented as a finite impulse response (FIR) filter. The output correlation values are finally passed to a computer via an USB device which is also used to control the correlator.

The system is realised in a modular concept. Each receiver path is separated into two building blocks. The first mainly containing the RF components as a switch to select between the antenna and a calibration load, a low noise amplifier, an image rejection mixer, and also a high-gain IF amplifier are built in one housing. All these building blocks are mounted on the rotating arm as shown in Fig. 1. The second building block contains a bandpass filter, a second IF amplifier and a power divider in order to separate the total power measurement from the correlation. Additionally an analogue 90° hybrid for verification and backup of the digital quadrature is included. A block diagram of all 15 receiver paths is illustrated in Fig. 3. The total gain of each path is approximately 100dB to achieve an output power range of -4dBm to 0dBm with respect to the receivers' frequency responses. Additionally various attenuators are included in order to allow also measurements of an active illumination of a scene for high-contrast indoor measurements.

The LO signal is generated by a synthesizer and amplified to adjust for the required mixer LO power level. The LO signal is divided into 15 channels in order to feed each receiver path. The power dividers are also located on the rotating arm as close as possible to the receivers. The phase difference between the single receiver paths due to different cable lengths or differences in the circuits are measured and mathematically corrected for.

The IF frequency range was chosen to 20MHz - 40MHz. The main reason for this selection was determined by the digital quadrature circuit and the maximum possible sample frequency of the FPGA that turned out to be 120MHz for the implemented digital circuit. Simulations showed that the bit error rate (BER) of the FIR filter implementation is a minimum for a signal frequency being a quarter of the sample frequency.

The 20MHz bandwidth limits the range of acceptable BER, which is less than 15% for a single frequency at the bandlimits.

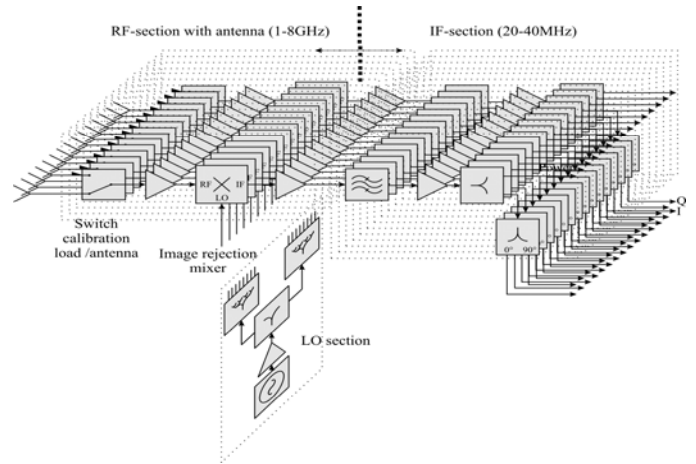


Figure 3. Block diagram of the 15 elements receiver system.

The average receiver noise temperature of the whole receiver chain was measured using a hot-cold method. It is located in the range of $T_E = 300\text{-}500\text{K}$ depending on the centre frequency. Using this the radiometric resolution of the aperture synthesis system is estimated using the following equation [1]:

$$\Delta T = \frac{T_A + T_E}{\sqrt{2\Delta f \tau}} \frac{A_{\text{syn}}}{\sqrt{N} A_{\text{real}}} \quad (8)$$

It is determined to be 0.25K-3.3K for an assumed antenna temperature of $T_A = 300\text{K}$, an integration time $\tau = 140\text{ms}$, an assumed aperture size A_{real} of the Vivaldi antennas of $0.005\text{m}^2\text{-}0.04\text{m}^2$ (for the frequencies between 1.5GHz-6.5GHz), an estimated synthetic aperture A_{syn} of about 17m^2 , and the number of samples to be $N = 180^\circ/0.5^\circ \times 79 = 28440$ measured Visibility values for a two-dimensional Nyquist sampling.

III. IMAGE RECONSTRUCTION

The rotational sampling character of the system and its spatial geometry leads to a grid forming concentric rings as in a cylindrical coordinate system. On such a grid no direct Fast Fourier Transform algorithm (FFT) without any interpolation is known in the literature. Several approaches are proposed and applied to the given problem, e.g. an interpolation to a pseudo-polar grid with a fast back-projection transformation [8], an up-sampling algorithm [9], and a tomographical algorithm [10] used mainly for computer tomography. The latter one shows the best results and allows a fast implementation. The basic rule of this algorithm is given by the Fourier-slice theorem, which makes use of the superposition principle of the Fourier transform. The slices, which in our case are the visibility values $V_\Theta(w)$ given for the radial baseline component w of the same axial baseline component Θ , are separately inverse Fourier transformed to a function $Q_\Theta(t)$ for each Θ using $t = l \cos\Theta + m \sin\Theta$. The inverse Fourier transformed slices $Q_\Theta(t)$ are then integrated over Θ to generate the reconstructed brightness temperature $\text{Trec}_B(l,m)$ as outlined in (9). In the

discrete case, finally an interpolation of the $Q_{\Theta}(t)$ values in the t direction to a given l - m grid is performed [10].

$$\begin{aligned} \text{Trec}_B(l,m) &= k(l,m) \int \int_{-\infty-\infty}^{\infty} V(u_{\lambda}, v_{\lambda}) e^{2\pi j(u_{\lambda}l+v_{\lambda}m)} du dv \\ \text{Trec}_B(l,m) &= k(l,m) \int \int_0^{2\pi} V(w, \Theta) e^{2\pi jw(l \cos \Theta + m \sin \Theta)} w dw d\Theta \quad (9) \\ \text{Trec}_B(l,m) &= k(l,m) \int_0^{\pi} Q_{\Theta}(t) d\Theta, \quad Q_{\Theta}(t) = \int_{-\infty}^{\infty} V_{\Theta}(w) w |e^{2\pi jw t} dw \end{aligned}$$

The one-dimensional inverse Fourier transform is implemented using a FFT algorithm and zero padding in order to simplify the interpolation.

This approach shall be demonstrated next in a simulation example. Here a dish function with several rectangular areas of different brightness temperatures as shown in Fig. 4a-d was used as the original input scene. This function was sampled in the spatial frequency domain following the cylindrical grid and then some noise of a realistic level was added to the Visibility values. Finally the image reconstruction was performed using the tomographical method.

The key simulation parameters were: a minimum baseline increment in radial direction of 0.5 times the wavelength λ , a maximum baseline of 79 times the increment, i.e. 39.5λ ; an axial increment Θ of 0.5° , a standard deviation for the noise level of 0.5K, a Hamming window applied to the visibility data, and an increase in the visibility pixel number by a factor of 10 for zero padding. It can be clearly recognized, that this method for the image reconstruction can deliver results showing the demanded and expected image quality.

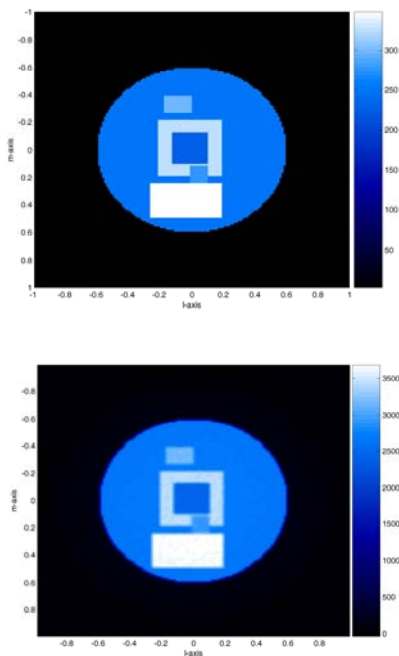


Figure 4. Image reconstruction example for a simulated scenario: a) original brightness temperature distribution, b) reconstructed result, and a profile of b) for c) $l=0$ and d) $m=0$.

IV. CONCLUSION

The main parameters and the concept of an experimental ASR system were briefly outlined. A multi-frequency ASR in the lower microwave region can offer many potentials for hidden object detection and security screening, for instance. However, the system is more complicated than a single-frequency-band ASR, but the benefits are deemed to be worthwhile for further investigation and development.

V. REFERENCE

- [1] M.Peichl, H.Suess, M.Suess and S.Kern, "Microwave imaging of brightness temperature distribution of extended areas in near and farfield using two-dimensional aperture synthesis with high spatial resolution," *Radio Science*, vol. 33, pp. 781-801, May/June 1998.
- [2] A.R.Thompson, J.Morgan and G.Swenson Jr., "Interferometry and synthesis in radio astronomy," John Wiley & sons, New York, 1986.
- [3] M.Peichl, M.Greiner, H.Süß, "DLR activities on aperture synthesis radiometry," *IGARSS 2000*, Honolulu, Hawaii, USA, 24-28 July 2000.
- [4] M. Peichl, S. Schulteis, S. Dill, H. Süß, "Application of microwave radiometry for buried landmine detection," *GRS 2002*, Bonn, Germany, 3-5 September 2002.
- [5] R.Mersereau, "The processing of hexagonally sampled two-dimensional signals," *Proc. of the IEEE*, Vol. 67, June 1979.
- [6] C.S.Ruf, "Numerical Annealing of Low-Redundancy Liner arrays," *IEEE Trans. on Ant. and Prop.*, Vol. 41, p. 85ff, January 1993.
- [7] M.Peichl, M.Greiner, V.Wittmann, E.Anterrieu, B.Picard, N.Skou, S.Sobjaerg, "Midterm Report: Scientific Inputs for the SMOS Level 1 Processor Development," ESA cont.No. 17312/03/NL/FF, March 2004.
- [8] A.Averbuch, R.R.Coifman, D.L.Donoho M.Elad, M.Israeli, "Fast and accurate polar Fourier transform," *IEEE Asilomar conference on signals systems and computers*, 2003, Vol. 2, p 1933ff
- [9] W.G. Carrara, R.S.Goodman, R.M.Majewski, "Spotlight synthetic aperture radar," Artech House, Boston London 1995
- [10] A.C.Kak, M.Slaney, "Principles of Computerized Tomographic Imaging," SIAM Press, 2001

Suspended Stripline Bandpass Filters with Inductive and Mixed Coupling

Wolfgang Menzel, Atallah Balalem¹

Microwave Techniques, University of Ulm, PO Box, D89069 Ulm, Germany,

E-Mail: wolfgang.menzel@ieee.org

¹ Now with the Microwave and Communication Engineering Chair, University of Magdeburg, Germany,

E-Mail: balalem@iesk.et.uni-magdeburg.de

Short Abstract—As previous work has shown, the performance of capacitively coupled suspended stripline filters is asymmetric with higher out-of-band attenuation at low frequencies. As is demonstrated in this paper, this relation is inverted using inductively coupled filters. A symmetric behavior can be achieved using a mixed coupling. Based on the inductive coupling, together with modified shunt resonators, dual band filters (lowpass and bandpass) can be realized, too. A number of filter designs with simulated and experimental results are shown using different coupling elements.

Keywords — *suspended stripline, lumped-element filters, planar filters, bandpass filters, dual-band filters*

I. INTRODUCTION

Suspended stripline (SSL) is an excellent transmission line medium for the realization of compact low-loss filters [1-4]. While previously mainly transmission line type filters were investigated, a wide variety of very compact, quasi-lumped filters have been demonstrated within the last years; a summary of this work is given in [5]. In this presentation, new results with respect to filters with inductive and mixed coupling are reported.

The ideal cross section of the SSL as considered throughout this work is shown in Fig. 1. RT Duroid 5880 is used as substrate material. Transmission line structures may be placed both on the top as well as on the bottom side of the substrate. The channel dimensions are selected wide enough to realize the necessary circuit elements, but small enough to suppress waveguide modes up to about 20 GHz. For the experimental realization, small grooves are added to the sides of the mount to clamp the substrate. As long as no metallization is connected to the side of the mount, such grooves have hardly any effect. With most of the filters presented in this contribution, however, narrow inductive strips to ground (at the side of the mount) are included. In such cases, the grooves result in an increased inductance which may shift the filter response slightly. For the test filters shown here, a mount of 30 mm length

with coaxial connectors is used, and measurements are performed with a coaxial calibration.

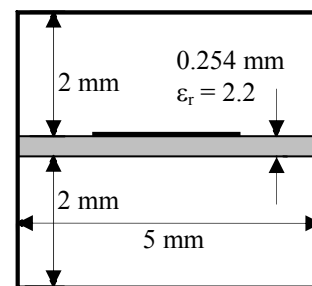


Fig. 1: Cross section of suspended stripline as used within this contribution.

A typical section of the equivalent circuit and the respective principal layout of a SSL bandpass filter as reported in [5] is displayed in Fig. 2. The SSL shunt resonators are formed by patches as capacitances and thin inductive strips to ground (at the edge of the substrate). An inset may increase the inductance. The inverter between the shunt resonators basically is formed by three capacitances in a Π -circuit with negative shunt capacitances (Fig. 3, [6]). In this configuration, the negative capacitances easily can be "realized" decreasing the values of the shunt resonator capacitances. At frequencies below the passband, both the shunt inductances and the series capacitances contribute to a high attenuation, while the reduced shunt capacitances result in a reduced high frequency attenuation. This asymmetric behavior of such a filter can be seen in the simulated [7] example given in Fig. 4.

By further increasing the coupling capacitors (with overlapping resonators on opposite substrate sides) and a suitable design of the resonators, even broadband highpass filter results can be achieved with such structure [5].

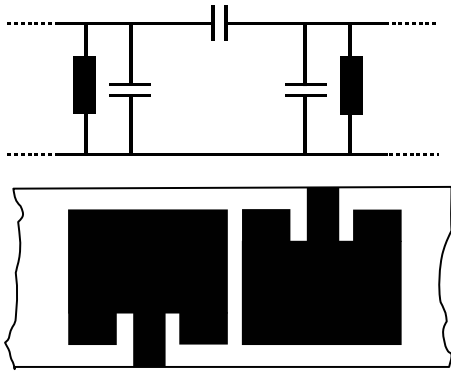


Fig. 2: Typical section of the equivalent circuit and the respective part of the layout of a SSL bandpass filter.

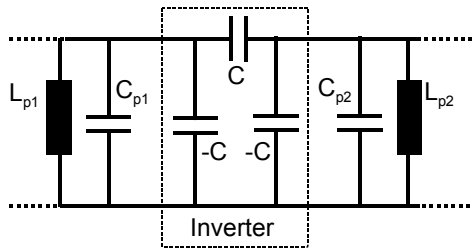


Fig. 3: Detail of the equivalent circuit pointing out the inverter structure of capacitive coupling.

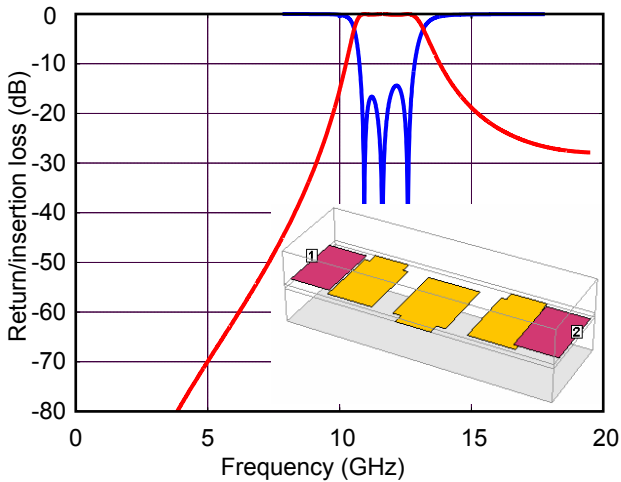


Fig. 4: Filter structure (inset figure) and simulated return and insertion loss of a capacitively coupled bandpass filter. Filter length is 10.6 mm.

II. INDUCTIVELY COUPLED FILTERS

An alternative to capacitive coupling is inductive coupling which can be realized in SSL using thin strips to connect the resonators. The equivalent circuit of such coupling is indicated in Fig. 5. The negative inductances associated with this type of inverter can be combined with the resonator inductances. Thus, in this case, the values of the resonator inductances are reduced. With respect to an inductively coupled bandpass filter as depicted in the inset of Fig. 7, the decrease of the shunt

inductances results in an increased attenuation above the filter passband, while below the passband, due to the inductive coupling, attenuation is reduced. Once again, an asymmetric filter performance results, but in an inverse way as compared to the capacitively coupled filter.

A photograph of such an inductively coupled test filter is shown in Fig. 6. Simulated as well as measured performance of this filter are demonstrated in Fig. 7, showing the asymmetric behavior. Agreement between simulation and experiment is excellent; passband insertion loss is less than 0.5 dB including 14 mm excess transmission line length and the transitions to the coaxial measurement system.

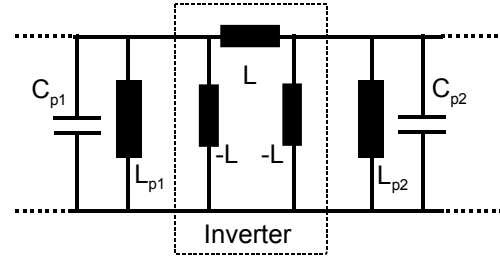


Fig. 5: Detail of the equivalent circuit pointing out the inverter structure of inductive coupling.

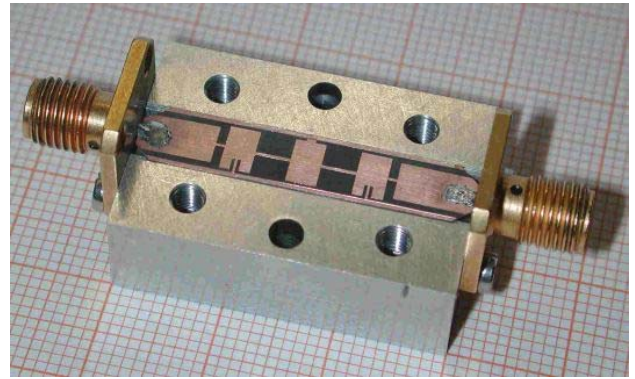


Fig. 6: Photograph of the opened bandpass filter with inductive coupling.

III. FILTER WITH MIXED COUPLING

As has been shown in the previous sections, the selection of the type of coupling results in different asymmetric behavior of SSL bandpass filters. This may be advantageous in some cases, but one might also want to achieve a more symmetric filter performance. To this end, a mixed coupling of the shunt resonators in a SSL filter is proposed. For example, input and output lines can be connected to the external resonators by thin strips, while the inner resonator is coupled capacitively. Such a filter is shown in Fig. 8, and Fig. 9 gives its return and insertion loss. The response of this filter is much more symmetric than that of the two filters presented before. As the shunt inductive strips of the filter were quite

narrow (0.2 mm), insertion loss is slightly higher, and some tolerance problems occurred, leading to a lower attenuation at higher frequencies. The resonance slightly below 20 GHz is due to higher order mode excitation in the mount.

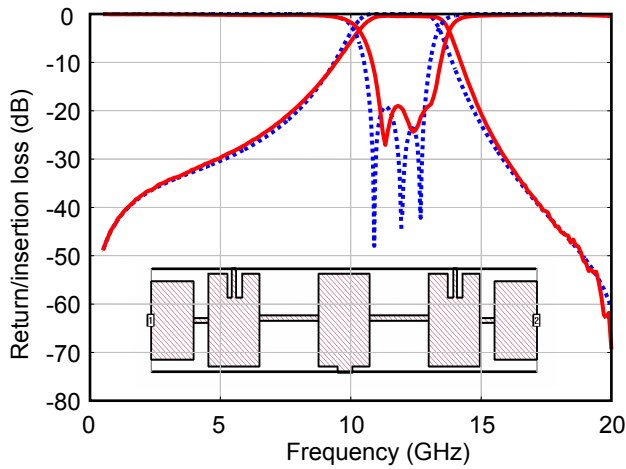


Fig. 7: Filter layout (inset figure) and simulated return and insertion loss of an inductively coupled bandpass filter. Filter length is 16 mm. Dotted lines: simulation, solid lines: experiment.

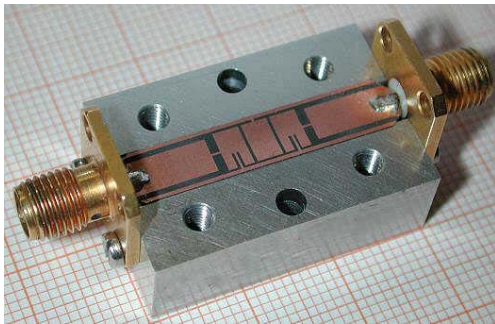


Fig. 8: Photograph of the bandpass filter with mixed coupling.

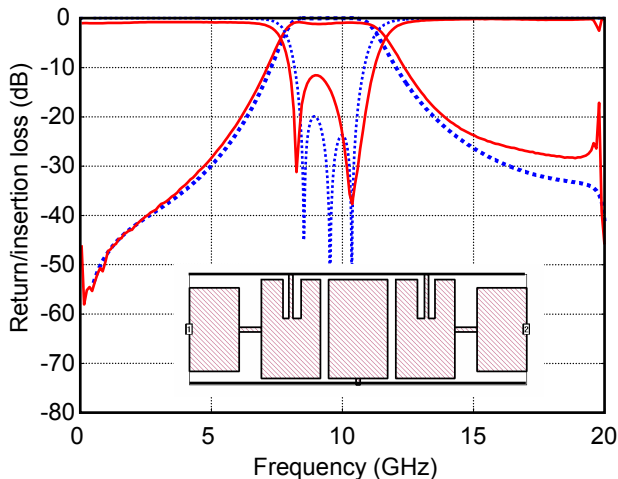


Fig. 9: Filter layout (inset figure) and simulated (dotted lines) and measured (solid lines) return and insertion loss of a bandpass filter with mixed coupling. Filter length is 10.8 mm.

IV. DUAL BAND FILTER

Regarding the filter layout of the inductively coupled filter in the inset of Fig. 7, except for the thin strips forming the shunt inductances, it looks very similar to a SSL lowpass filter with patches as shunt capacitances and narrow line elements as series inductances. If the shunt inductances of the inductively coupled bandpass filter now are replaced by a series resonator connected to ground (Fig. 10), such a structure exhibits both a lowpass as well as a bandpass performance. In a SSL configuration, this can be realized by removing the shunt strip of each resonator from the top layer and adding another patch to the opposite side together with an inductance to ground (Fig. 11), resulting in the detailed equivalent circuit of Fig. 10. By properly adjusting the circuit elements, a dual band filter results, e.g. [8, 9], here the combination of a lowpass and a bandpass filter. From a different point of view and with a wider bandwidth of the bandpass response, such a structure could equally be considered as a bandstop filter.

A photograph of the combined lowpass/bandpass filter and its results are plotted in Fig. 12 and 13, respectively. The cut-off frequency of the lowpass response is 4 GHz, the bandpass response is centered at 12.3 GHz. Bandwidth is 1.7 GHz. Lowpass and bandpass insertion loss are below 0.4 dB and 0.8 dB, respectively. Attenuation between 5.5 GHz and 8.5 GHz is higher than 50 dB resulting from three transmission zeroes generated by the specific form of the three resonators. Simulation and experiment agree well with some slight deviations in the return loss which partly is due to the transitions to the coaxial measurement system.

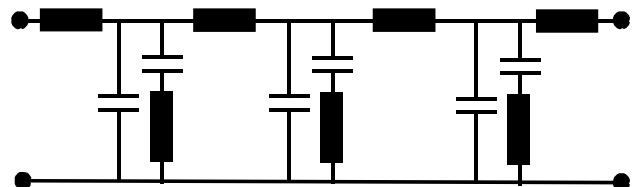


Fig. 10: Equivalent circuit of the dual SSL filter.

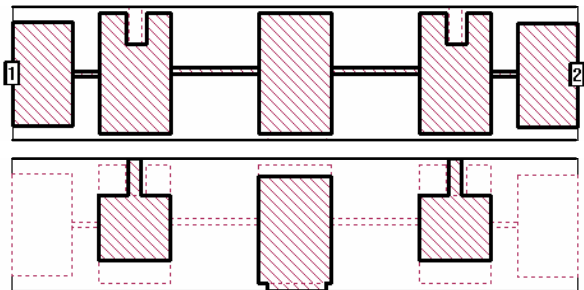


Fig. 11: Top and bottom layout of a dual band (lowpass and highpass) SSL filter.

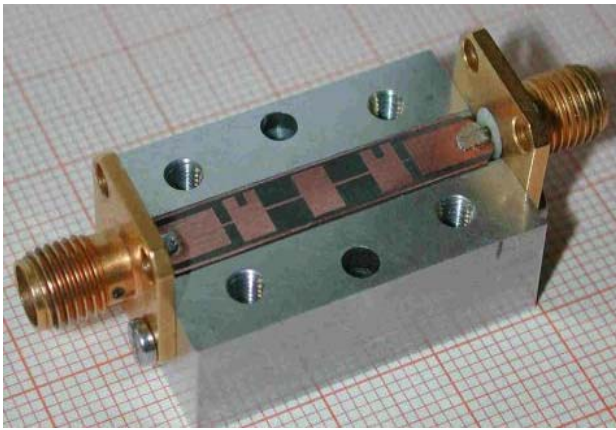


Fig. 12: Photograph of the opened dual-band filter with inductive coupling.

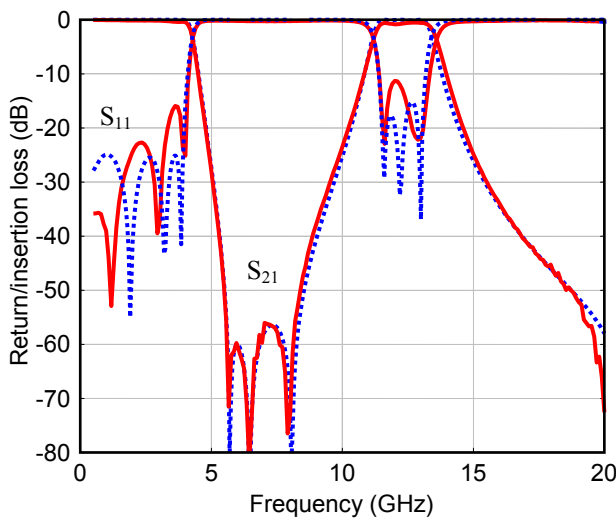


Fig. 13: Simulated (dotted lines) and experimental (solid lines) insertion and return loss of the dual SSL filter.

V. CONCLUSION

Quasi-lumped suspended stripline filters with different types of inverter or coupling, respectively, have been demonstrated. While both pure capacitive and inductive coupling lead to asymmetric bandpass responses, a mixed coupling allows to achieve a much more symmetric performance. In addition, by extending the principle of inductive coupling, the combination of lowpass and bandpass response in a single filter has been demonstrated. The realized and tested filters show an excellent agreement with the simulated response.

REFERENCES

- [1] J. D. Rhodes: Suspended Substrates provide alternatives to coax. *Microwave Syst. News*, vol. 9, pp. 134-143, Aug. 1979.
- [2] J. D. Rhodes and J. E. Dean: MIC broadband filters and contiguous duplexers. *9th Europ. Microwave Conf. Dig.*, 1979, pp. 407- 411.
- [3] C. I. Mobbs and J. D. Rhodes: A generalized Chebyshev suspended substrate stripline bandpass filter. *IEEE Trans. Microwave Theory Tech.*, vol. MTT-35, pp. 397- 402, May 1983.
- [4] J. E. Dean: Suspended substrate stripline filters for ESM applications. *IEE Proc.*, Vol. 132, Pt. F, July 1985, pp. 257 - 266.
- [5] W. Menzel, A. Balalem: Quasi-Lumped Suspended Stripline Filters and Duplexers. *IEEE Trans. on MTT*, vol. MTT-53, Oct. 2005, pp. 3230 - 3237.
- [6] G. Matthaei, L. Young, E.M.T. Jones, "Microwave filters, impedance matching networks, and coupling structures," Reprint by Artech House, 1980.
- [7] SONNET, Version 10, Sonnet Software Inc.
- [8] S. Sun, L. Zhu: Compact dual-band microstrip bandpass filter without external feeds. *IEEE Microwave and Wireless Components Letters*, Vol.15, Oct. 2005, pp. 644 - 646.
- [9] C. Quendo, E. Rius, C. Person: An original topology of dual-band filter with transmission zeros. *2003 IEEE MTT-S International Microwave Symposium*, June 2003, Volume 2, pp. 1093 - 1096.

Internal Quasi-Optical Mode Converter for a Coaxial Gyrotron

J.B. Jin (1), M. Thumm (1,2), T. Rzesnicki (1), and B. Piosczyk (1)

(1) Forschungszentrum Karlsruhe, Ass. EURATOM-FZK, IHM, Postfach 3640, D-76021 Karlsruhe, Germany

(2) Universitaet Karlsruhe, IHE, D-76128 Karlsruhe, Germany

Jianbo.Jin@ihm.fzk.de

Abstract: A quasi-optical mode converter is investigated for a 170GHz, $TE_{34,19}$ mode coaxial-cavity gyrotron, where the ratio of caustic to cavity radius is 0.323. The dimpled-wall launcher is numerically analysed and optimised to provide a wave beam with scalar Gaussian contents of 94.8% and well-focused field at its aperture. The mirror system is adapted to transform the complicated fields radiated from the launcher into a fundamental Gaussian structure. The tolerance conditions of the mirror system to fabrication errors are also investigated. The achieved conversion efficiency is 97% including amplitude and phase.

Keywords-Gyrotron;quasi-optical mode converter;mode conversion; phase-correction

I. INTRODUCTION

A 2MW, 170GHz, $TE_{34,19}$ coaxial cavity gyrotron is under development in cooperation between European research institutes (FZK Karlsruhe, CRPP Lausanne, HUT Helsinki) and European tube industry (TED, Velizy, France), which is expected to be used for electron cyclotron resonance heating (ECRH) of magnetically confined plasmas in the International Thermonuclear Experimental Reactor (ITER). The internal quasi-optical (q.o.) mode converter of the gyrotron consists of a waveguide so called dimpled-wall launcher and a beam-forming mirror system [1]. High power measurements showed that the RF stray radiation inside the tube is about 9%, which does not satisfy the requirement of more than 95% power transmission inside the gyrotron, so the q.o. mode converter should be improved. The analysis shows that for the coaxial-cavity gyrotron operating at a very high order cavity mode like $TE_{34,19}$, due to the ratio of the caustic to the cavity radius of 0.323 as shown in Fig.1, it is very difficult to design a dimpled-wall launcher by conventional methods [2] both to provide a well-focused wave beam and to achieve high Gaussian contents at the aperture of the launcher. The fields on the cuts are relatively strong and produce relatively large diffracted power. In this paper the launcher is numerically optimized to provide low fields on the launcher cuts with relatively good Gaussian contents at the aperture. The fields radiated from the launcher are quite complicated, so the mirror system should be adapted to obtain high Gaussian contents in the outgoing wave beam and to avoid stray radiation.

II. DIMPLED-WALL LAUNCHER

The launcher used in the converter is similar to a Denisov-type launcher [2], where wall distortions (scattering surface) transform the input eigenwave to an eigenwave of the weakly perturbed transmission line. The perturbations of the launcher wall can be described as

$$R(\varphi, z) = R_0 + \alpha z + \sum_{i=1}^N \delta_i \cos[\Delta\beta_i z - l_i(\varphi + \varphi_{i0})] \quad (1)$$

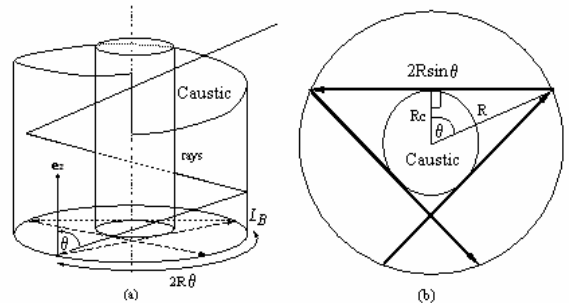


Fig.1 Geometrical optical description of ray propagation of the $TE_{34,19}$ mode in a cylindrical waveguide: (a) side view; (b) top view.

The first launcher was designed at FZK for the $TE_{34,19}$ mode coaxial-cavity gyrotron with the selection rules $l_1=1, l_2=2$ and $l_3=3$. The field contours on the launcher wall are shown in Fig.2(a), the schematic contour of the launcher wall is shown in Fig.2(b). The average and peak values of power densities on the cuts are 87.3W/cm^2 and 18.4W/cm^2 , respectively, where the power density at the input of the launcher is 57W/cm^2 . The scalar Gaussian content is 90.8% at the aperture of the launcher, which is defined as the amplitude correlation coefficient of the field to an ideal fundamental Gaussian distribution. The radiated fields are numerically analyzed using a commercial code based on the Fast Multipole Method (FMM) [3], the field strength contours are shown in Fig.3. From Fig.2 and Fig.3 we can see that due to the relatively high fields on the cuts there is some diffraction from the cuts of the launcher.

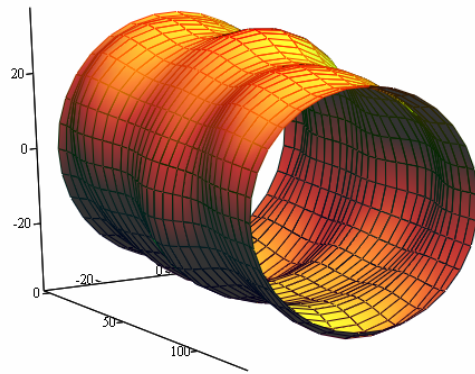
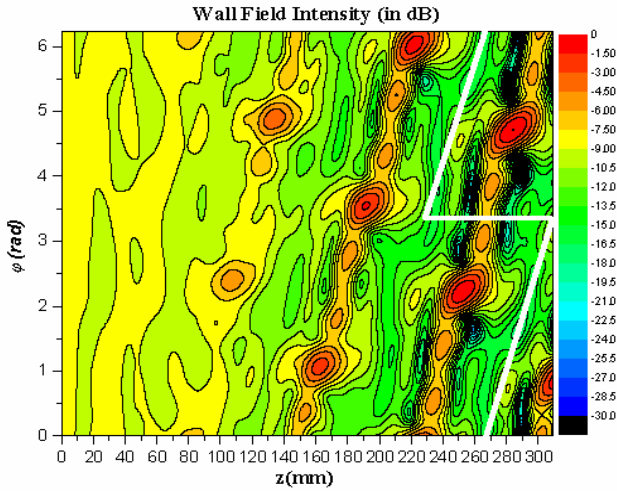


Fig.2 (a) Contours of the field on the unrolled waveguide-wall of launcher; (b) schematic contour of the launcher wall.

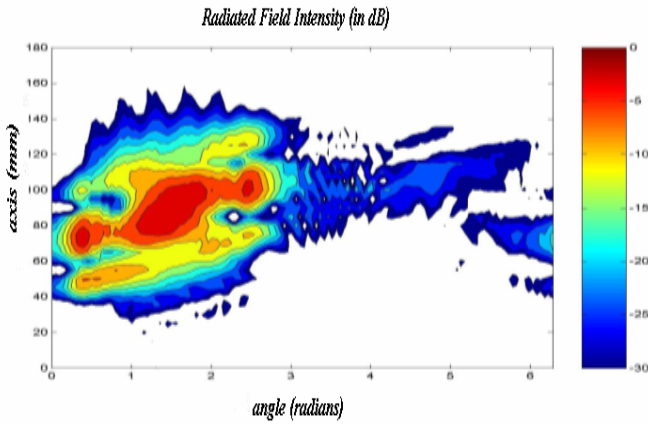


Fig.3 Contours of the strength of the radiated field.

In order to depress the fields on the cuts, the launcher has been redesigned with the selection rules $l_1=1, l_2=2, l_3=3, l_4=5$ and

$l_5=6$ and optimised [4]. The contours of the fields on the optimised launcher wall are shown in Fig.4(a), the schematic contour of the wall is shown in Fig.4(b). The surface of the launcher wall can be described as

$$R(\phi, z) = R_0 + \alpha z + \sum_{i=1}^N [a_i(z) \cos(l_i \phi) + b_i(z) \sin(l_i \phi)] \quad (2)$$

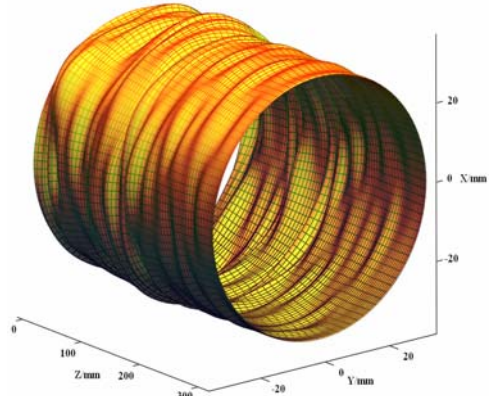
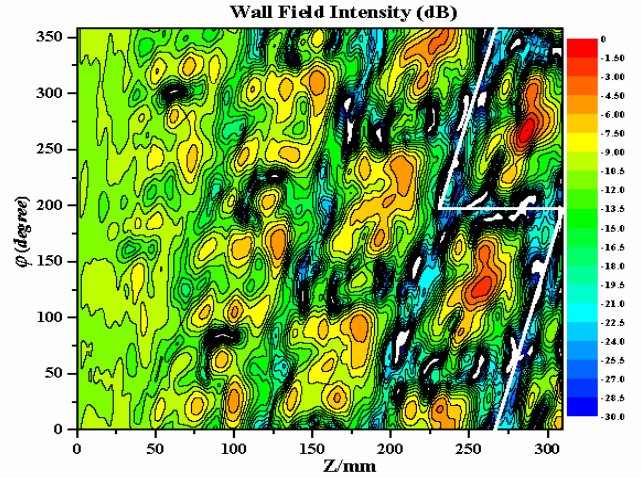
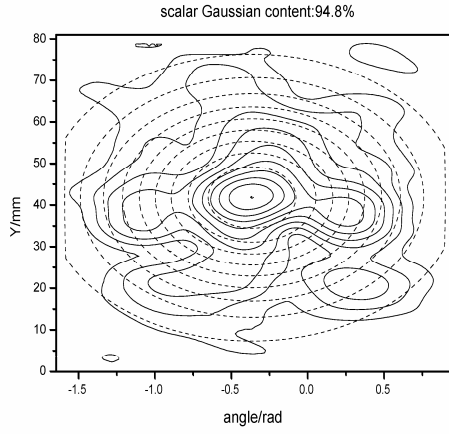


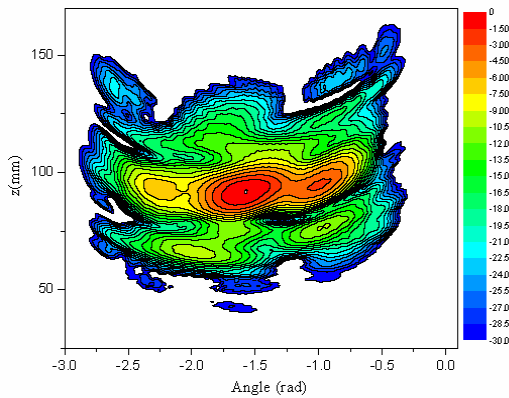
Fig.4 (a) Contours of the field on the wall of the optimized launcher; (b) Schematic contour of the wall of the optimized launcher.

The field contour at the aperture of the launcher is shown in Fig.5(a), where the scalar Gaussain content is 94.8%. Average and peak value of the normalized fields of -25.3dB and -20.7dB on the cuts are achieved, the corresponding power densities are 1.9W/cm^2 and 5.4W/cm^2 , respectively. The maximum of the power density on the launcher wall is 400.8W/cm^2 , which satisfies the requirement of the cooling system for the launcher that power densities on the wall should be smaller than

500W/cm². In principle, the act of cutting open the waveguide perturbs the field from the closed waveguide solution and the modes are no longer exact TE or TM ones in the waveguide launcher. In the case that the field intensities on the cuts are very low, the power diffraction losses are small and very low power is reflected from the cuts, so that the fields in the waveguide can be well approximated by modes of the unperturbed waveguide. The radiated fields can be calculated from the scalar diffraction integral, and the results are shown in Fig.5(b).



(a)



(b)

Fig.5 Field contours: (a) at the aperture of the optimized launcher; (b) on the quasi-elliptic mirror.

III. DESIGN OF THE MIRROR SYSTEM

As shown in Fig.5(b), the radiated fields are quite complicated, toroidal mirrors are insufficient to transform the outgoing wave beam into a nearly fundamental Gaussian wave beam with high Gaussian contents. So the internal mirror system consists of a quasi-elliptic and two phase correcting mirrors with non-quadratic surface functions which are adapted to provide

high conversion efficiency which is defined as the correlation coefficient of the outgoing wave beam to an ideal fundamental Gaussian distribution including amplitude and phase. The investigation shows that there is a great influence of the focal lengths of the quasi-elliptic mirror on the conversion efficiency [5]. This can be found from Fig.6. Focal lengths of 100mm and 5000mm of the quasi-elliptic mirror are chosen for the TE_{34,19} mode gyrotron. The beam waist is 25mm set at 350mm after the window along the path of propagation.

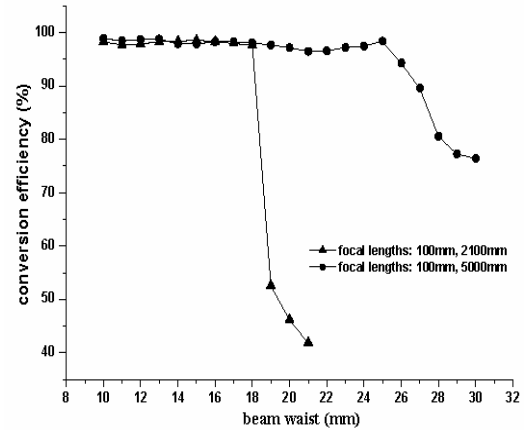


Fig.6 Conversion efficiencies.

IV. TOLERANCE CONSIDERATIONS FOR THE MIRROR SYSTEM

The tolerance conditions of the mirror system to fabrication errors are also investigated. In the iterative optimisation of the phase correcting mirror, by taking the fabrication errors into account, a realizable mirror system is obtained. The calculation results show that the smaller the curvature radius of the milling tools is, the higher the conversion efficiency is. With the curvature radius of the milling tools of 0.5mm, the realizable mirror system would provide a conversion efficiency of 97% in the window plane including amplitude and phase as shown in Fig.7. The power transmission is shown in Fig.8, the relative power in the window plane is 96.8%, namely the stray radiation inside the tube is 3.2%. Fig.9 shows the amplitude contour and phase pattern of the outgoing wave beam in the window plane.

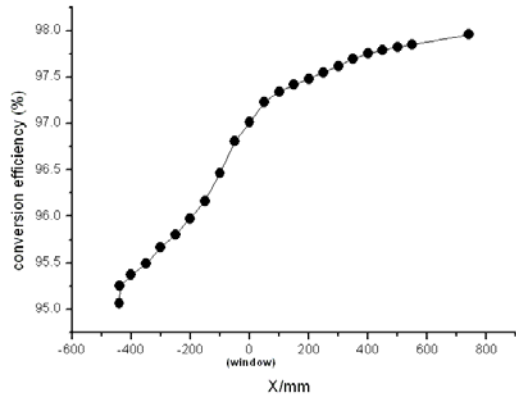


Fig.7 Conversion efficiencies along the path of propagation

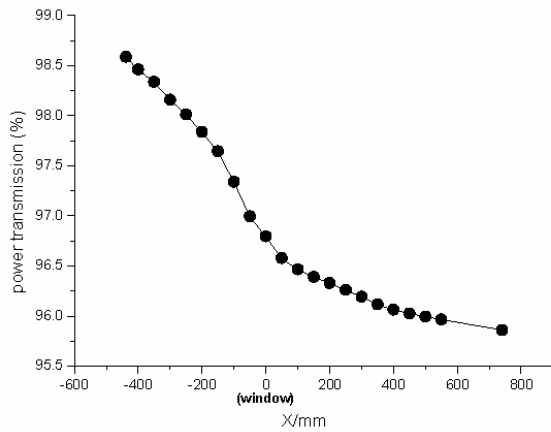


Fig.8 Power transmission along the path of propagation.

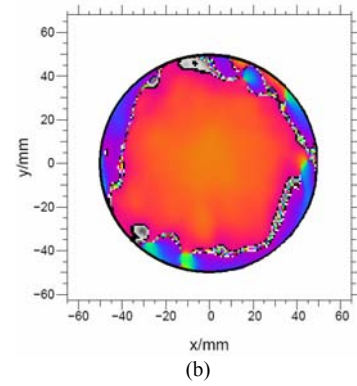
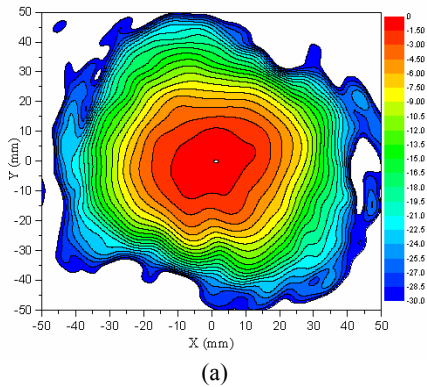


Fig.9 Field distributions in the window plane: (a) amplitude contour, (b) phase pattern.

ACKNOWLEDGEMENTS

This work was partly supported by the virtual HGF Research Center VH-FZ-24 and a PhD fellowship of FZK.

REFERENCES

- [1] J. Jin, B.Piosczyk, G. Michel, M. Thumm, O. Drumm, T. Rzesnicki, and S. Zhang, *The Design of a quasi-optical mode converter for a coaxial-cavity gyrotron*, Joint 29th Int. Conf. on IRMMW & 12th Int. Conf. on Terahertz Elect., Karlsruhe, Germany, 2004, pp.669-670.
- [2] A.A.Bogdashov and G.G.Denisov, Radiophys, *Asymptotic theory of high-efficiency converters of higher-order waveguide modes into eigenwaves of open mirror lines*, Quantum Electronics, Vol. 47, pp. 283-295, 2004.
- [3] J. Neilson, *Surf3d and TOL: Computer codes for design and analysis of high-performance QO launchers in gyrotrons*, Joint 29th Int. Conf. on IRMMW & 12th Int. Conf. on Terahertz Elect., Karlsruhe, Germany, 2004, pp. 667-668.
- [4] J. Jin, M. Thumm, B. Piosczyk, and T. Rzesnicki, *Theoretical investigation of an advanced launcher for a 2MW, 170GHz, TE_{34,19} coaxial cavity gyrotron*, accepted by IEEE Trans. Microwave Theory Tech..
- [5] J. Jin, B. Piosczyk, M. Thumm, T. Rzesnicki, and S. Zhang, *Quasi-optical mode converter/mirror system for a high power coaxial-cavity gyrotron*, submitted to IEEE Trans. on Plasma Science.

An Oscillator with Reduced Phase Noise and Improved Harmonic Characteristics Based on a Corrugated CPW EBG Structure

Cheol Gyu Hwang, and Noh Hoon Myung

Department of Electrical Engineering and Computer Science
Korea Advanced Institute of Science and Technology (KAIST),
373-1 Guseong-dong, Yuseong-gu, Daejeon, Republic of Korea
Phone: +82-42-869-5443
Fax: +82-42-869-8557
E-mail: ckck2@kaist.ac.kr

Short Abstract— This paper presents a novel microwave oscillator circuit incorporating a corrugated coplanar waveguide (CCPW) electromagnetic bandgap (EBG) structure as its resonator component. The fully planar oscillator showed a reduced phase noise characteristic of -90.2 dBc/Hz at 100 kHz offset and a superior second harmonic suppression of -42.67 dBc.

Keywords-corrugated CPW; EBG; harmonic suppression; oscillator; phase noise

I. INTRODUCTION

In the last several years, the EBG structure, which has its origin in optics, has been successfully applied to various microwave components such as power amplifiers [1], filters [2], and antennas [3]. There has also been strong interest in application of this structure in microwave oscillator applications. In this regard, several novel oscillator circuits utilizing the advantages of the EBG structure have been proposed, where planar integration of the chip is the primary concern. H.W. Liu *et al.* reported an efficiency improved VCO using a defected ground structure (DGS) as a harmonic tuner of the oscillator circuit at the expense of additional chip area [4]. Y.T. Lee *et al.* showed the phase noise enhancement of an oscillator using a DGS structure as a resonator component of a conventional oscillator circuit [5]. They used a DGS as a harmonic suppressor or a novel phase noise reduction component of a conventional oscillator circuit.

However, DGS based oscillators inherently have the disadvantages of requiring an additional air gap between the perforated backside metal plane and a metallic shielding enclosure package [6],[7]. These problems in turn lead to reliability problems and difficulty in miniaturization of the chip. Also, the inherently required five or six periods of the unit cell in the implementation of such a structure may lead to a size problem. Additionally, the extra processing of the backside metal plane increases the complexity in a fully

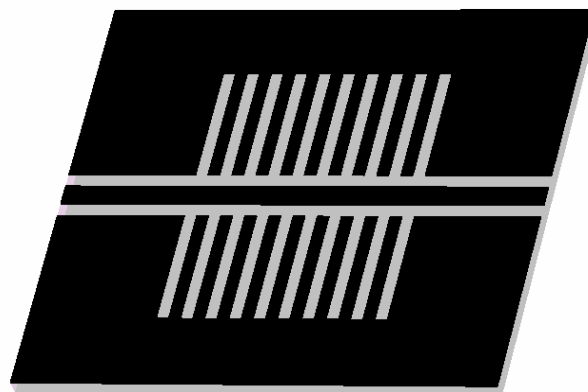


Fig. 1. Corrugated CPW EBG structure.

monolithic application of the chip. In this paper, a novel compact EBG based oscillator based on CCPW technology is presented for the first time. The CCPW structure, originally suggested as a low pass filter, is modified to the microwave resonator component of the oscillator circuit maintaining its advantages of uniplanar structure and compactness. The higher quality factor of the structure relative to that of the conventional CPW resonator plays a role of phase noise reduction of the oscillator circuit. In addition, the unique harmonic characteristic of the CCPW plays a role of harmonic suppression of the oscillator circuit, which leads to enhancement in dc-ac power efficiency of the circuit.

II. DESIGN OF A CCPW RESONANT CELL

Recently, a one-quarter wavelength deep high impedance CCPW structure [8] was proposed as a planar version of Sievenpiper's high-impedance surface originally proposed in [9]. As can be seen in Fig. 1, the CCPW structure consists of a center strip separated by a narrow gap from two ground planes

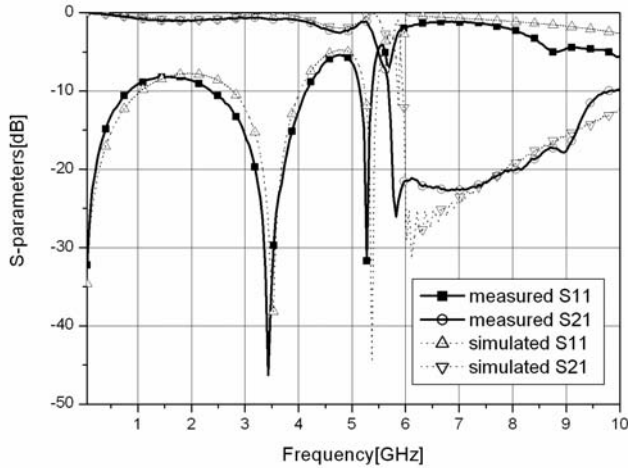


Fig. 2. Simulated and measured S-parameter of the CCPW EBG resonant cell.

and a numerous high impedance slots running down into the ground planes of the structure. The width of the slot is much shorter than the wavelength and the depth of the slot is one-quarter wavelength. This one-quarter wavelength of each slot transforms the zero impedance of the ground plane to infinite, and forbids the propagation of transverse magnetic surface waves along the CPW line. Consequently, a deep stopband corresponding to the bandgap of any other EBG structure is generated. Its inherent uniplanar characteristic and compactness in size solve the aforementioned problems of conventional DGS based oscillators and affords greater possibility of monolithic application of EBG structures.

Fig. 2 shows the simulated and measured S-parameter of the CCPW structure fabricated on a RT/Duroid 6010 substrate having a dielectric constant of 10.2 and thickness of 25mil. The widths of the line and the gap of the 50 ohm CPW transmission line were calculated as 0.9 mm and 0.55 mm, respectively. The depth of the slot was set to 5 mm, which corresponds to one quarter wavelength at the offset frequency of 6 GHz.

The cutoff frequency of 6 GHz near the resonator application frequency of 5.5 GHz causes the input impedance of the CCPW structure to vary rapidly from 50 ohm as the frequency deviates from the resonant frequency. This characteristic contributes to a higher input phase slope at the gate circuit. From this, a higher quality factor than that of a circuit without the CCPW structure is achieved [5],[10]. Therefore, an oscillator with reduced phase noise could be achieved utilizing the deep attenuation in $S(1,1)$ at 5.5 GHz as the resonance frequency of the circuit. The resonance frequency and subsequent oscillation frequency can be easily tuned by changing the depth of the CCPW structure.

Another advantage of the CCPW resonator is its harmonic tuning characteristic. The harmonics of the circuit can be suppressed by controlling the reflection phase of terminating resonance, as suggested in [11]. The length between the CCP-

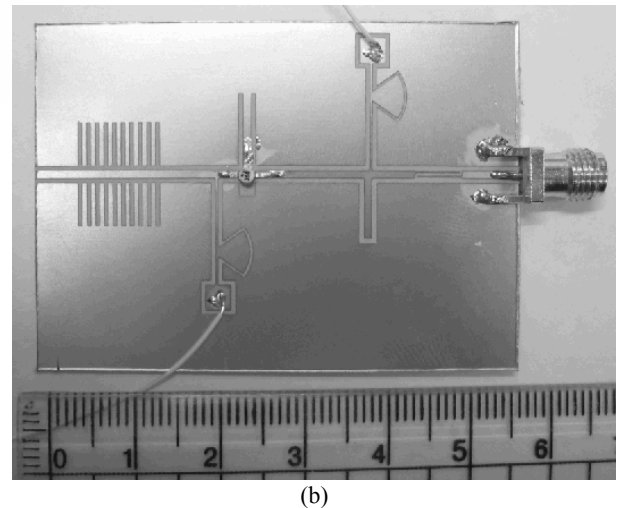
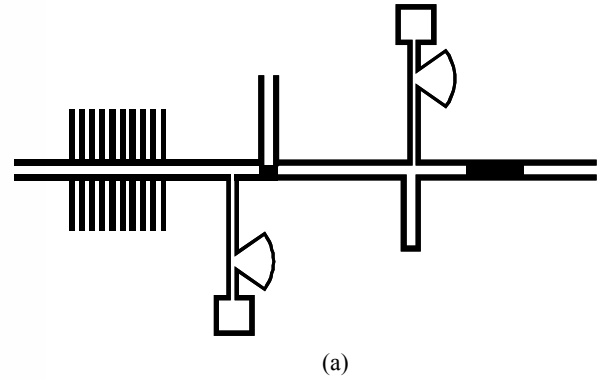


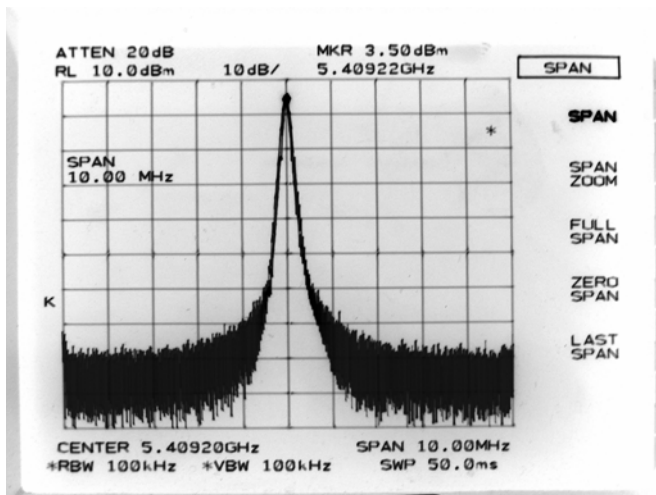
Fig. 3. (a) Layout and (b) photograph of the oscillator with CCPW resonant cell.

W structure and the transistor was tuned to 9.09 mm in order to negatively feedback the second harmonic component signal of the oscillator circuit. In addition to this methodology, we utilized the inherent absence of any n th-harmonic in the $S11$ characteristic of the 5.5GHz CCPW resonator so as to reduce the harmonics of the final oscillator circuit. From this suppression of harmonics, an increase in the fundamental output power and dc-ac power efficiency could be achieved.

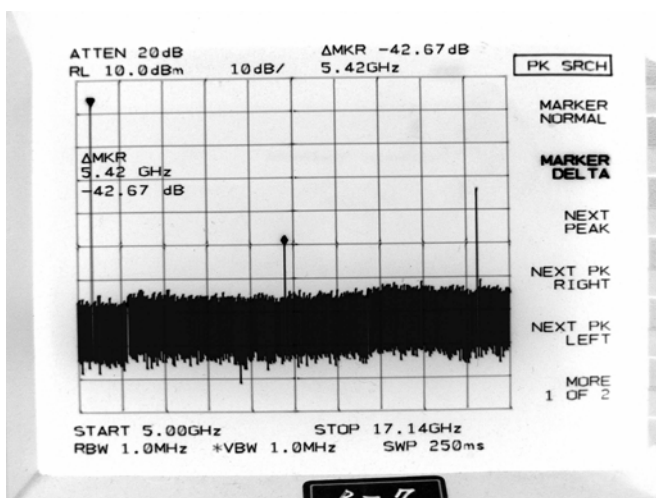
The total size of the CCPW EBG resonator structure was only $12 \text{ mm} \times 9.5 \text{ mm}$, which corresponds to $0.57 \lambda_g \times 0.45 \lambda_g$, where λ_g is the wavelength of resonance frequency.

III. DESIGN OF OSCILLATORS

Fig. 3 shows the layout and fabricated result of a 5.5 GHz oscillator circuit. Negative resistance to compensate for the loss in the resonator was generated using a short stub in the source terminal of the transistor, which can be easily fabricated in CPW technology. Output matching stubs were tuned to meet the small signal oscillation condition, and the designed CCPW cell was implemented as a fundamental frequency selection component of an oscillator circuit. For co-



(a)



(b)

Fig. 4. Measured output spectrums. (a) Fundamental output power spectrum. (b) Harmonic characteristic.

mparison, a conventional CPW oscillator without the CCPW resonator structure was also designed and fabricated. The other components, i.e. except the CCPW structure, were set to be identical including the transistor, an Agilent ATF- 36077 pHEMT. The fabrication processes of the oscillators were extremely simple without any via-hole process, pattern on the backside metal layer, or any lumped element soldering process.

IV. MEASUREMENT RESULTS

Fig. 4 shows the photograph of the measured fundamental output spectrum and harmonic performance of the fabricated CCPW oscillator. The oscillator exhibits a measured oscillation frequency of 5.41 GHz with a measured peak output of 3.50 dBm at a bias condition of $V_{ds} = 1.5$ V and $V_{gs} = -0.2$ V. Phase noise is measured as -90.2 dBc/Hz and -115.3 dBc/Hz at offsets of 100 kHz and 1 MHz, respectively.

The second and third harmonic suppressions were measured as -42.67 dBc, and -27.00 dBc, respectively. Even more harmonic suppression is expected if we add another CCPW harmonic tuner at the output stage of the circuit.

These results constitute a greater than 10dB improvement in phase noise performance and more than 20 dB improvement in second harmonic suppression when compared to those of a conventional CPW oscillator without the CCPW structure.

V. CONCLUSION

In this paper, a novel oscillator that incorporates a uniplanar CCPW EBG structure as a resonator component of the conventional CPW oscillator circuit was presented. The introduction of the CCPW EBG structure was verified to be effective in reducing the phase noise and enhancing the harmonic performance and dc-ac power efficiency of the oscillator circuit in a very small chip size increment. The small size and uniplanar structure characteristic of the circuit can be easily applied to MMIC applications of the circuit while avoiding the drawbacks of the conventional DGS based EBG oscillators.

ACKNOWLEDGMENT

This research was supported by KOSEF through MICROS and ADD through RDRC at KAIST.

REFERENCES

- [1] C. Y. Hang, V. Radisic, Y. Qian, and T. Itoh, "High efficiency power amplifier with novel PBG ground plane for harmonic tuning," 1999 IEEE MTT-S International Microwave Symposium Digest, vol. 2, pp. 807-810, 1999.
- [2] A. Griol, D. Mira, A. Martinez, J. Marti, and J.L. Corral, "Microstrip multistage coupled ring bandpass filters using photonic bandgap structures for harmonic suppression," Electronics Letters, vol. 39, pp. 68-70, 2003.
- [3] Y.J. Sung and Y. S. Kim, "An improved design of microstrip patch antennas using photonic bandgap structure," IEEE Transactions on Antenna and Propagation, vol. 53, pp. 1799-1804, May 2005.
- [4] H. W. Liu, X.W. Sun, and Z. F. Li, "A VCO with harmonic suppressed and output power improved using defected ground structure," Proceeding of SBMO/IEEE MTT-S IMOC 2003, pp. 163-167, 2003.
- [5] Y. T. Lee, J. S. Lim, J. S. Park, D. Ahn, and S.W. Nam, "A novel phase noise reduction technique in oscillators using defected ground structure," IEEE Microwave and Wireless Components Letters, vol. 12, No. 2, pp. 39-41, February 2002.
- [6] Zhengwei Du, Ke Gong, Jeffrey S. Fu, Baoxin Gao, and Zhenghe Feng, "Influence of a metallic enclosure on the S-parameters of microstrip photonic bandgap structures," IEEE Transaction on Electromagnetic Compatibility, vol. 44, No. 2, pp. 324-328, May 2002.
- [7] J. Z. Gu, W. Y. Yin, R. Qian, C. Wang, and X. W. Sun, "A wideband EBG structure with 1D compact microstrip resonant cell," Microwave and Optical Technology Letters, vol. 45, No. 5, pp. 386-387, June 2005.
- [8] S. J. Kim, and N. H. Myung, "A new PBG structure: Corrugated CPW," Microwave and Optical Technology Letters, vol. 39, No. 5, pp. 412-414, December 2003.
- [9] D. Sievenpiper, L. Zhang, R. F. J. Broas, N. G. Alexopoulos, and E. Yablonovitch, "High-impedance electromagnetic surfaces with a forbidden frequency band," IEEE Transaction on Microwave Theory and Tech., vol. 47, pp. 2059-2074, 1999.

- [10] K. Kurokawa, "Some basic characteristics of broadband negative resistance oscillator circuits," *Bell Syst. Tech. J.*, vol. 48, pp. 1937-1955, July 1969.
- [11] Q. Xue, K. M. Shum, and C. H. Chan, "Novel oscillator incorporating a compact microstrip resonant cell," *IEEE Microwave and Wireless Components Letters*, vol. 11, No. 5, pp. 202-204, May 2001.

Recent Progress in Optimizing Phase-Correcting Mirrors for a Multi-Frequency Gyrotron

X. Yang¹, A. Arnold^{1,2}, G. Dammertz¹, K. Koppenburg¹, M. Thumm^{1,2}

¹Forschungszentrum Karlsruhe, Association EURATOM-FZK, IHM, D-76021 Karlsruhe, Germany

²also Universitaet Karlsruhe, IHE, Kaiserstr. 12, D-76128 Karlsruhe, Germany

e-mail: xiaokang.yang@ihm.fzk.de . Tel: (49) 07247-822455

Abstract — For a multi-frequency 1 MW short pulse gyrotron at Forschungszentrum Karlsruhe (FZK), the existing adapted phase-correcting mirrors (on the basis of plane mirror surfaces) of an internal beam-shaping mirror system have been modified in order to reduce potential diffraction losses, which may be introduced during the procedure of mirror fabrication, due to the requirement of very strong perturbations on the mirror surfaces in order to obtain a small beam radius at the gyrotron Brewster output window. This paper describes the steps to design two adapted phase-correcting mirrors on the basis of smooth elliptical mirrors with quadratic surface contour function. Simulation results show for these newly improved phase-correcting mirrors, that the perturbations on the surfaces of the elliptical mirrors are obviously reduced. For all nine operating modes from TE_{17,6} at 105 GHz to TE_{23,8} at 143.3 GHz, a nearly fundamental Gaussian distribution at the gyrotron output window is predicted.

I. INTRODUCTION

In nuclear fusion devices, the availability of MW gyrotrons with fast frequency step tunability permits the use of a simple fixed, non-steerable mirror antennas for local electron cyclotron resonance heating and current drive at different magnetic fields, as well as gives more flexibility for the stabilization of neo-classical tearing modes (NTM) through the possibility of current drive without changing the magnetic field. For plasma stabilization in the ASDEX-Upgrade tokamak, there is great interest in step-tunable gyrotrons operating at frequencies between 105 GHz and 140 GHz [1]. For this purpose a multi-frequency test gyrotron is under construction at FZK in a cooperative parallel development with the Institute of Applied Physics in Nizhny Novgorod, Russia [2-4]. The complementary key tasks for FZK are the development of: a cavity operating in a wide range of magnetic fields and with proper choice of a set of operating modes with the same direction of rotation; a broadband quasi-optical mode converter transforming all operating modes into a fundamental Gaussian beam with low diffraction losses; an ultra-broadband CVD-diamond Brewster window and a low power cold test measurement set-up.

Due to the large Brewster angle of 67.2°, the maximum effective window diameter for currently available CVD-diamond disks (140 mm diameter) is about 50 mm, and the length of the waveguide to house the disk is 149 mm [5]. This window configuration adds a strict requirement for the gyrotron output beams with different frequencies.

At the GeMic-2005 conference [6], we reported about how to design two adapted phase-correcting mirrors on the basis of plane mirror surfaces to match the requirement of the small effective diameter (50 mm) at the Brewster window. The surfaces of these adapted phase-correcting mirrors are shown in Fig.1. From theoretical view, this design is reasonable; a very good fundamental Gaussian output beam has been predicted. However, the adapted phase-correcting mirrors require accurate mirror fabrication and alignment. But in practice, diffraction losses may be introduced due to the procedure of mirror fabrication by a numerically controlled milling machine because of the tolerances of the very strong perturbations on the mirror surfaces. Preliminary cold measurements have shown higher sensitivity of the output beams on the alignment of the mirror system, and relatively high diffraction losses. In order to increase the tolerance of the adapted phase-correcting mirrors during the procedure of fabrication and alignment, it is necessary to re-design new phase-correcting mirrors on the basis of smooth mirrors with curved surfaces for our 1MW multi-frequency gyrotron.

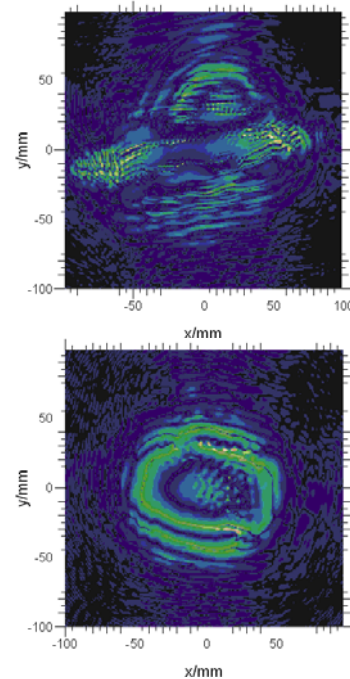


Fig. 1. Mirror surface of existing adapted phase-correcting mirror2 (upper) and phase-correcting mirror3 (lower).

II. BEAM-FORMING MIRROR SYSTEM WITH SMOOTH CURVED SURFACES

Same as in the case of [6], we keep the launcher and the first quasi-elliptical mirror unchanged while modifying the last two mirrors in order to fit the requirements of the new CVD-diamond Brewster window. Conventional smooth mirrors with curved surfaces, such as toroidal or elliptical mirrors are widely used as beam-forming mirrors to obtain the desired fundamental Gaussian distribution at the gyrotron output window. These mirrors are inexpensive, easy to manufacture, and also relatively easy to align. In the case of toroidal mirrors, the positions and the orientations of the mirrors are found by evaluating the moments of the first and second order of the power distribution. This design technique requires knowledge of both the amplitude and the phase distribution of the input beam and the desired output beam. The design procedure is: (1) back propagate the desired beam onto the last mirror; (2) generate the resulting amplitude distribution with the first and second mirrors; (3) generate the resulting phase distribution with the last mirror. This design procedure incorporates a fast scalar diffraction code for nonparallel apertures, which allows a rapid synthesis of the mirror profiles. In the case of the $TE_{28,8}$ mode 140 GHz prototype gyrotron of FZK, two toroidal mirrors have been used as the beam-forming mirror system [7]. Both simulations and cold measurements have shown that an efficiency of more than 98% has been achieved to convert the $TE_{28,8}$ cavity mode at 140 GHz into a fundamental Gaussian beam.

Extensive calculations have been done to optimize the two elliptical mirrors. Results show that the optimized mirror surface contours depend strongly on frequency, beam radius at the window, distance between window and the last mirror, angle of incidence and quality of the RF beam from the launcher and the first quasi-elliptical mirror. Fig. 2 shows the surface contours of the two optimized elliptical mirrors.

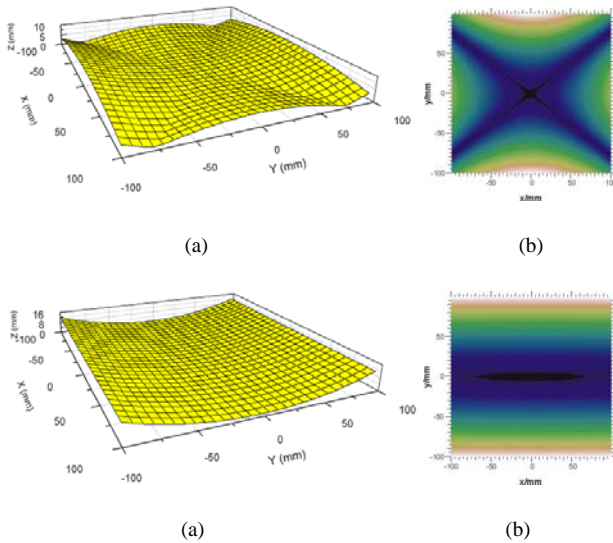


Fig. 2. Calculated mirror surface (a) and surface contour (b) of elliptical mirror 2 (upper) and elliptical mirror 3 (lower).

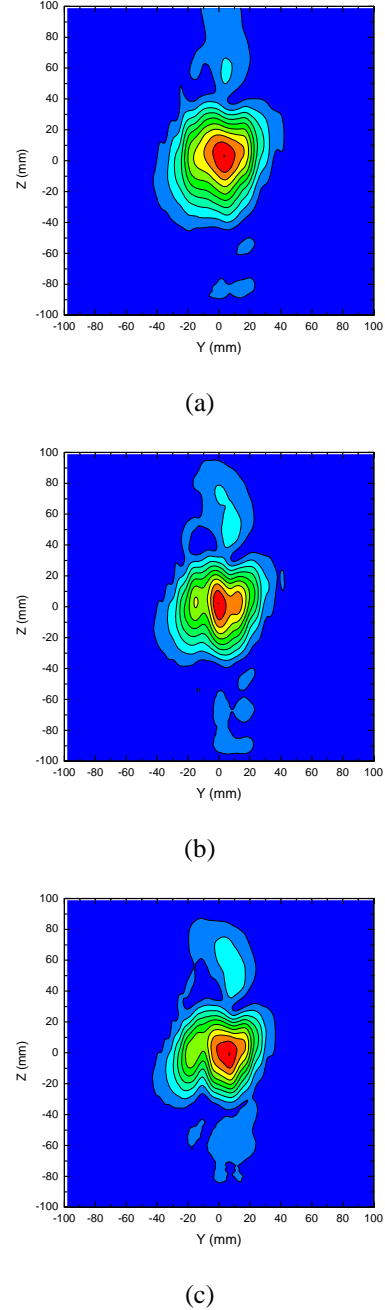


Fig. 3. Calculated field distribution on the last mirror. Normalized field contours are shown in linear scale with 0.1 increments from the peak: (a) $TE_{17,6}$ mode, (b) $TE_{20,7}$ mode, (c) $TE_{22,8}$ mode.

On the basis of the two smooth surface elliptical mirrors shown in Fig.2, we can calculate the field and power distributions on the last mirror and at the middle position of the Brewster window. Fig. 3 shows some examples of field distributions on the last mirror for the modes $TE_{17,6}$ at 105 GHz, $TE_{20,7}$ at 124.1 GHz and $TE_{22,8}$ at 140 GHz respectively. All other operating modes present nearly same beam patterns as shown in Fig.3.

From Fig. 3 one can see that all beams have a near Gaussian-like distribution; but due to the non-optimized launcher the beam quality is not good and there are sidelobes around the main beam. Thus diffraction losses would be introduced. In order to reduce diffraction losses, the launcher should be redesigned (with lower

overmode factor of 1.07 instead of 1.17). Highly efficient quasi-optical mode converters should have both an optimized launcher and an optimized beam-forming mirror system.

The third elliptical mirror adjusts the beam patterns to the output window. Fig. 4 shows power distributions at the middle position of the CVD-diamond Brewster window. The beams shift by ± 5 mm in horizontal direction around the center of the window plane. Unfortunately this beam-forming mirror system has no broadband characteristics; it can not match the requirement of small effective window diameter for all nine operating modes.

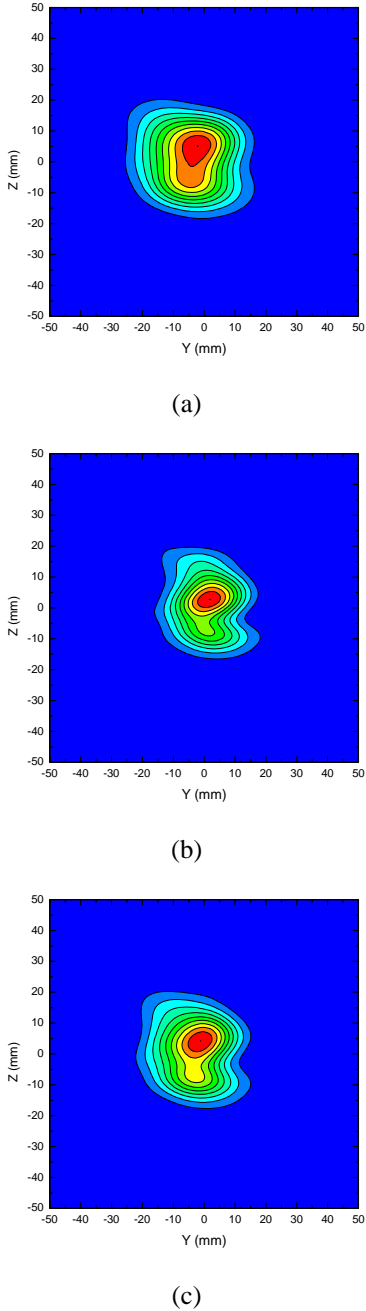


Fig. 4. Calculated power distribution at the middle position of the Brewster window. Normalized power contours are shown in linear scale with 0.1 increments from the peak: (a) $TE_{17,6}$ mode, (b) $TE_{20,7}$ mode, (c) $TE_{22,8}$ mode.

III. BEAM-FORMING MIRROR SYSTEM WITH ADAPTED PHASE-CORRECTING SURFACES

On the basis of the mirror system with two smooth elliptical mirrors described in section II, we can further optimize this system employing a numerical procedure such as the extended Katsenelenbaum-Semenov algorithm [8] to obtain adapted phase-correcting mirrors which have broadband characteristics. The optimization process is nearly in the same way as what we used in [6], the only difference is that we set conventional elliptical mirrors as the initial mirror surfaces for the optimization rather than plane mirror surfaces.

Fig.5 shows the surface contours of the two optimized adapted phase-correcting mirrors. A comparison with Fig.2 shows clearly that there are only small perturbations on the mirror surfaces. This may reduce the diffraction losses introduced by tolerances in mirror fabrication, and also reduce the sensitivity of mirror alignment.

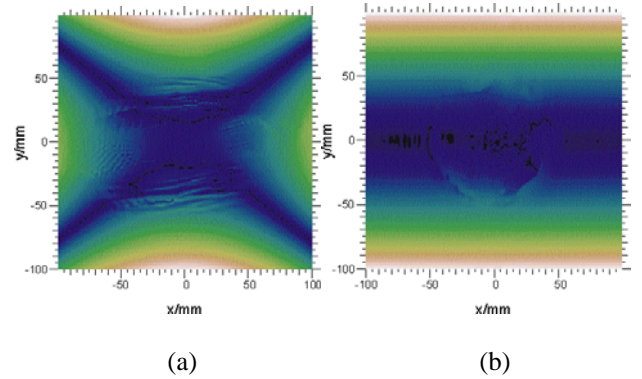


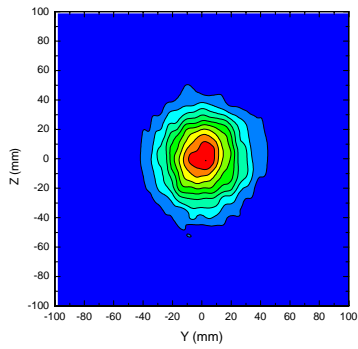
Fig. 5. Calculated surface contour of adapted phase-correcting mirror 2 (upper) and phase-correcting mirror 3 (lower).

Fig. 6 shows field distributions on the surface of the last phase-correcting mirror. It is very clear that after the adjustment of the second phase-correcting mirror, all the beams present near fundamental Gaussian distribution.

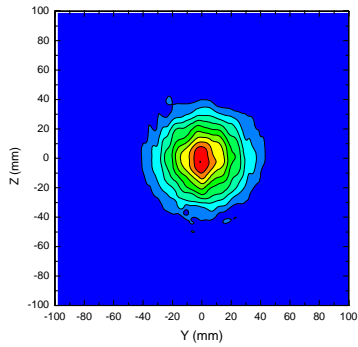
The third phase-correcting mirror adjusts the beam patterns to the gyrotron output window. Fig. 7 shows the power distributions. In comparison to the beam patterns in Fig.4, adapted phase-correcting mirrors can be used for gyrotron broadband operation and give much better fundamental Gaussian pattern than elliptical mirrors do.

IV. CONCLUSIONS

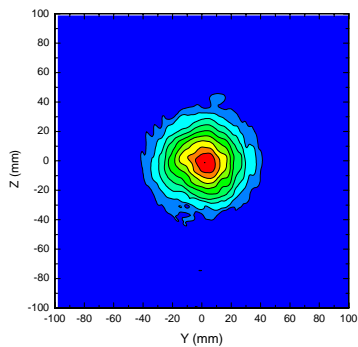
Two adapted phase-correcting mirrors have been redesigned on the basis of two elliptical mirrors with smooth surfaces. There are only small perturbations on the mirror surfaces, and near fundamental Gaussian distribution for all nine operating gyrotron modes is predicted by the simulations. This design may reduce the diffraction losses introduced during mirror fabrication and make the alignment of mirror system less sensitive.



(a)



(b)

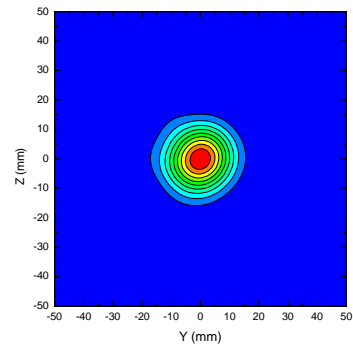


(c)

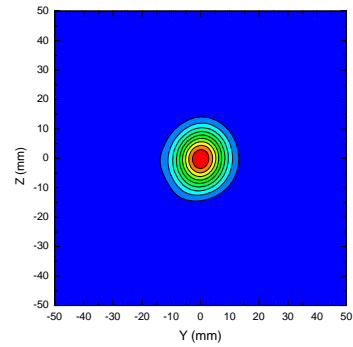
Fig. 6. Calculated field distribution on last mirror. Normalized field contours are shown in linear scale with 0.1 increments from the peak: (a) TE_{17,6} mode (105 GHz), (b) TE_{20,7} mode (124.1 GHz), (c) TE_{22,8} mode (140 GHz).

REFERENCES

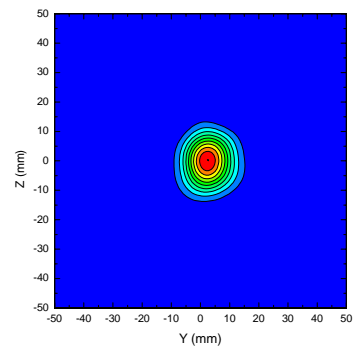
- [1] F. Leuterer, et al., "Plans for a new ECRH system at ASDEX-Upgrade", *Fusion Engineering and Design*, vol. 66-68, pp.537-542, 2003.
- [2] V. Zapevalov, et al., "Development of a Prototype of a 1 MW 105-156 GHz Multifrequency gyrotron," *Radiophysics and Quantum Electronics*, vol. 47, pp.396-404, 2004.
- [3] E. Borie, et al., "Possibilities for Multifrequency Operation of a Gyrotron at FZK," *IEEE Trans. Plasma Science*, vol. 30, pp.828-835, 2002.
- [4] K. Koppenburg, et al., "Fast Frequency-Step-Tunable High-Power Gyrotron with Hybrid-Magnet-System", *IEEE Trans. Electron Devices*, vol. 48, pp.101-107, 2001.



(a)



(b)



(c)

Fig. 7. Calculated power distribution at middle position of the Brewster window. Normalized power contours are shown in linear scale with 0.1 increments from the peak: (a) TE_{17,6} mode, (b) TE_{20,7} mode, (c) TE_{22,8} mode.

- [5] X. Yang, et al., "Design of an Ultra-Broadband Single-Disk Output Window for a Frequency Step-tunable 1 MW Gyrotron," *23th Symposium on Fusion Technology (SOFT)*, Venice, Italy, September 20-24, 2004, B25.
- [6] X. Yang, et al., "New Internal Beam-Forming Mirror System for a Multi-Frequency 1 MW F-Band Gyrotron," *GeMic-2005*, April 5-7, 2005, Ulm, Germany.
- [7] M. Thumm, X. Yang, et al., "An High Efficiency Quasi-Optical Mode Converter for a 140 GHz, 1 MW CW Gyrotron" *IEEE Trans on Electronics Devices*, Vol.52 (2005), pp.818-824.
- [8] B. Z. Katsenelenbaum, V.V. Semenov, "Synthesis of Phase Correctors Shaping a Specified Field," *Radio engineering and electronic physics*, vol.12, pp.223-231, 1967.

The Bifurcated E-Plane T-Junction and Its Application to Waveguide Diplexer Design

Jens Bornemann and Marjan Mokhtaari

Department of Electrical and Computer Engineering, University of Victoria, Victoria, BC, V8W 3P6, Canada

Abstract—The bifurcated E-plane T-junction is presented. Its advantages with respect to waveguide diplexer design are: It allows full E-plane height operation, thus permitting good power handling capability, is simple to model, and provides additional tuning parameters for the computer-aided design. The performance of the junction is compared to those of other junctions and its advantages are demonstrated in a full diplexer design. The combined mode-matching and coupled-integral-equations code used for the design is verified by measurements and comparison with results obtained by commercially available software packages.

Keywords – waveguide junctions; T-junctions; bifurcations; diplexers; computer-aided design.

I. INTRODUCTION

The computer-aided design of waveguide diplexers has been a research topic for more than two decades, and a very large number of papers have been published. The synthesis and design of applicable channel filter structures is well understood. However, the overall diplexer design, which includes the waveguide junction joining filters and the common port, is not always a straightforward process.

Waveguide T-junctions are often used in diplexer configurations, and it was always felt that the T-junction required certain dimensional parameters to achieve an acceptable match within the relevant frequency ranges. Therefore, T-junctions with compensating elements are frequently employed either within the volume of the junction, e.g. [1] – [6], or just outside of it, e.g. [7], [8]. Other options include Y-shaped junctions in both H- and E-planes, e.g. [9] – [11] and E-plane bifurcations, e.g. [11], [12].

More recently, it was demonstrated that diplexers and multiplexers involving H-plane T-junctions can be designed without compensating elements - either as manifold designs, [13], [14], or even when the branching arm acts as the common port [15]. H-plane technology, however, is prone to passive intermodulation phenomena and, therefore, has limited applications in satellite systems where the E-plane manufacturing process is preferred, e.g. [16]. Possible leakage between transmit and receive channels also prohibits the use of standard E-plane bifurcations.

Thus the common E-plane T-junction (Fig. 1, left) is often used in front-end diplexer designs. Acceptable diplexer performance, however, seems possible only with reduced-

height T-junctions that require matching waveguide transformers to full-height technology at all ports, e.g. [17]. Full-height E-plane junctions, i.e., without transformers, have only been used in manifold-type configurations, but they suffer from poor common-port return loss [18] or spurious resonances [19].

Therefore, this paper presents the bifurcated E-plane T-junction (Fig. 1, right) as an alternative to previous diplexers with the branching arm as common port. This junction not only allows full-height, high-power handling operation but also is much simpler to model than those containing elements within the junction volume and provides additional compensation elements for the computer-aided design. Leakage between transmit and receive channels, as known from classical bifurcated configurations ([11], [12]), is eliminated since the bifurcation is confined, thus excluding the channel filters.

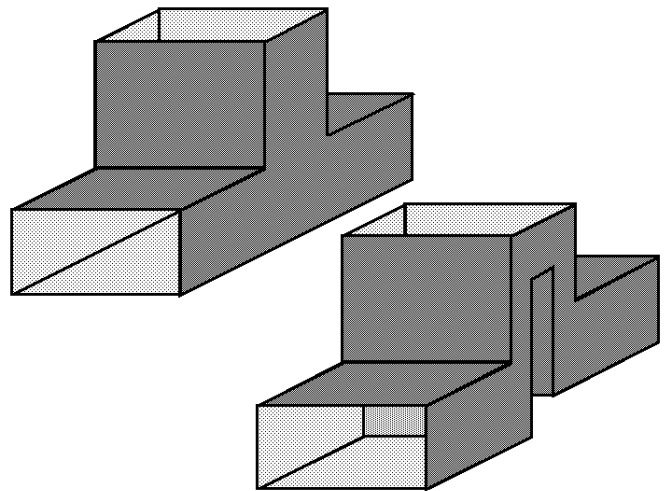


Figure 1. E-plane T-junctions: regular (left), bifurcated (right).

II. BIFURCATED E-PLANE T-JUNCTION

The bifurcated E-plane T-junction is shown in Fig. 1 (right) and, as far as computer analysis is concerned, consists of an E-plane bifurcation and two connected E-plane corners. In order to highlight some of the advantages of this junction, Fig. 2 compares its performance with those of the standard E-plane T-junction and a ridged junction. Shown is the input reflection coefficient in dB seen into the branching port (usually the common port in a diplexer design).

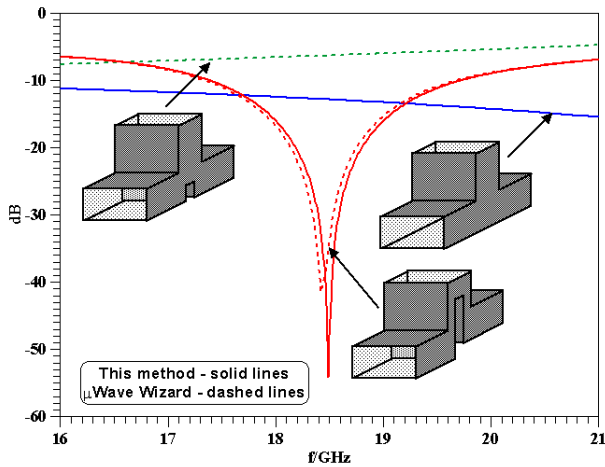


Figure 2. Reflection coefficient in dB of the branching (upward) port of ridged, standard and bifurcated E-plane T-junctions.

Both standard and ridged junctions show nearly constant reflection coefficients over the frequency range. Whereas the standard T-junction is simply modeled using a Mode-Matching Technique (MMT) or Coupled-Integral-Equations Technique (CIET), the ridged junction either requires a complex modal analysis [20] or more general numerical schemes such as the Finite-Element Method (FEM) used in the μ Wave Wizard[®]. In contrast, the bifurcated T-junction is not only easily modeled using modal techniques; it also creates a very acceptable return loss over a bandwidth usually wide enough for diplexer applications. This is achieved by offsetting the left and right arm for a given thickness of the bifurcation. The excellent agreement between the results obtained with our MMT-CIET code and those from the μ Wave Wizard[®] verifies the basic performance of the bifurcated E-plane T-junction.

III. DIPLEXER DESIGN

The basic steps in a computer-aided design of a diplexer are well known. In the first step, individual channel filters are separately synthesized and/or optimized employing either singly or doubly terminated filter theory. In the second step, the filters are combined at the respective ports of a three-port junction, and junction and filter dimensions are iteratively optimized according to given diplexer specifications.

A conventional E-plane T-junction diplexer with inductive-iris filters in reduced-height waveguide technology and matching transformers to WR75 waveguide at all three ports is shown in the inset of Fig. 3. The performance computed with this method is in good agreement with measurements within a dynamic range of approximately 70 dB. Thus Fig. 3 verifies the MMT-CIET code in a diplexer arrangement. Note that a loss analysis based on perturbation theory and Q-efficiency is included but shows little effect, as the inside of the entire component is silver-plated.

Various diplexer designs are now presented for 18/19 GHz using WR51 waveguides. Specifications call for 24 dB in-band return loss and 60 dB attenuation in the respective bands. Based on the channel bandwidths of 17.9GHz – 18.4GHz and

18.8GHz – 19.2GHz, seven- and six-resonator inductive-iris filters, respectively, are employed.

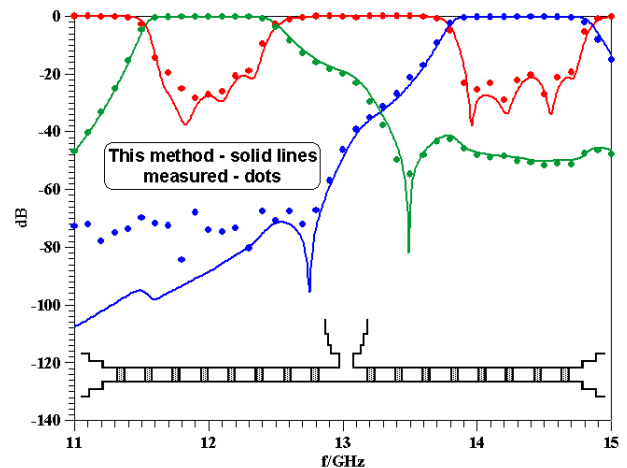


Figure 3. Computed and measured [17] performance of a traditional E-plane T-junction diplexer in reduced-height waveguide technology with matching transformers to WR75 waveguide.

Fig. 4 presents the conventional design similar to that in Fig. 3. All design specifications, as depicted by the thin solid lines, are met, but the design is complicated by E-plane waveguide transforms and a relatively low power handling capability due to the reduced waveguide height in the channel filters.

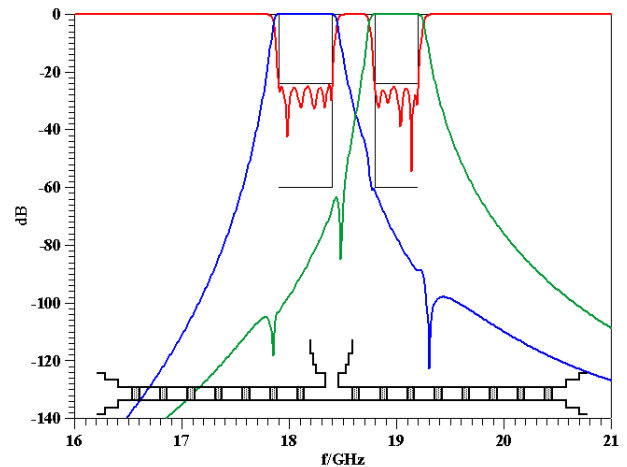


Figure 4. Performance of traditional E-plane T-junction 18/19 GHz diplexer.

In order to eliminate the disadvantages of this component, a straightforward design without transformers and full-height filter channels is attempted in Fig. 5. After extensive optimization, which includes the entire parameter sets of both filters, the specifications are still not quite met. Further optimization might improve the return loss behavior but only at the expense of further detuning the filters and, consequently, failing to meet the isolation specifications. Additional filter components (cavities) will have to be incorporated for this design to satisfy specifications without additional matching elements.

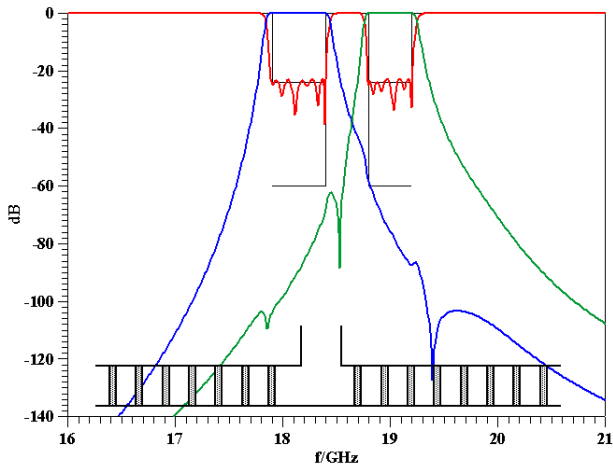
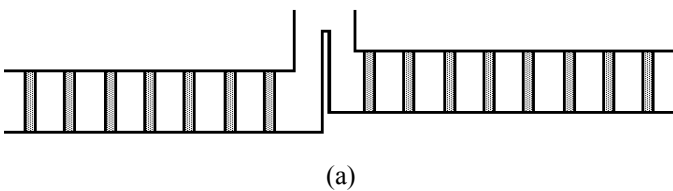
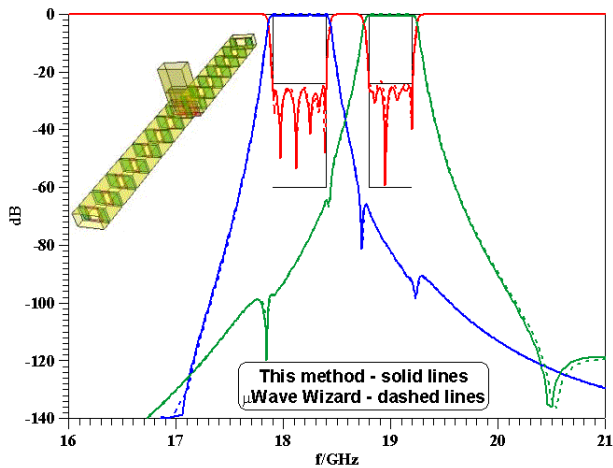


Figure 5. Performance of full-height E-plane T-junction 18/19 GHz diplexer.

A diplexer design involving the bifurcated E-plane T-junction is presented in Fig. 6. For comparison with the insets of Fig. 4 and Fig. 5, Fig. 6a depicts the side view of this design; the inset of Fig. 6b shows a 3D view. Due to the advantages of the bifurcated T-junction, all ports have regular-height waveguide dimensions, thus avoiding the use of impedance transformers. Moreover, the filters are designed in full waveguide height, which reduces losses and increases power handling capability.



(a)



(b)

Figure 6. Sideview (a), performance (b) of a diplexer employing the bifurcated E-plane T-junction in WR51 waveguide technology and comparison with results obtained with the μ Wave Wizard[®].

The performance of this diplexer is shown in Fig. 4b and satisfies specifications. A comparison with the professional

software package μ Wave Wizard[®] shows excellent agreement, thus validating the principal design approach.

As shown in Fig. 2, the bandwidth of the bifurcated E-plane T-junction is narrow but acceptable for many diplexer applications. While the bifurcation is fairly wideband, the narrowband characteristic is mainly introduced by the two waveguide corners. In order to alleviate this restriction, mitered corners can be used. Such a diplexer design employing the bifurcated E-plane T-junction with mitered corners is shown in Fig. 7. This configuration has the potential of diplexing frequency bands which are further apart than the ones shown in this paper.

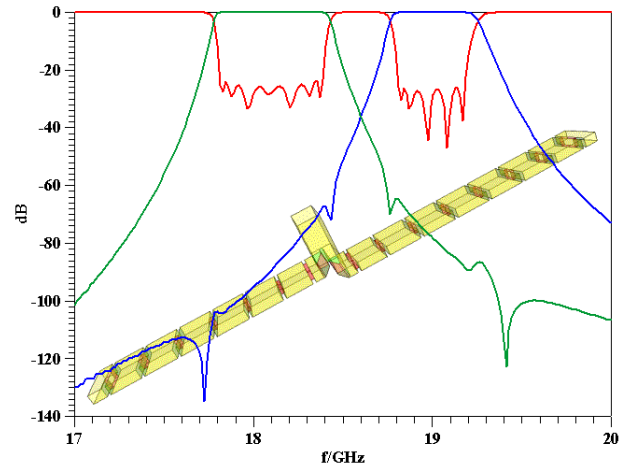


Figure 7. Diplexer design employing the bifurcated E-plane T-junction with mitered corners (μ Wave Wizard[®]).

IV. CONCLUSIONS

The bifurcated E-plane T-junction presents a viable option for diplexer designs in E-plane waveguide technology. Through its full-height operation, it has the potential to accommodate a large variety of different channel filters. Compared to conventional designs, the bifurcated T-junction is easy to model, allows for better power handling capability and permits the offsets in side-arm locations to be used as additional optimization parameter. The simulation code is based on an efficient MMT-CIET combination and is verified by comparison with measurements and commercially available software. Mitered corners may be introduced for wide-band separation of individual frequency bands.

ACKNOWLEDGMENT

The authors are greatly indebted to Dr. Jaroslaw Uher of MDA Space (formerly EMS Technologies), Ste-Anne-de-Bellevue, PQ, Canada for valuable discussions and helpful suggestions.

REFERENCES

- [1] T. Shen, K.A. Zaki and T.G. Dolan, "Rectangular waveguide diplexers with a circular waveguide common port", IEEE Trans. Microwave Theory Tech., Vol.51, pp. 578 – 582, Feb. 2003.

- [2] Y. Rong, H. Yao, K.A. Zaki and T.G. Dolan, "Millimeter-wave Ka-band diplexers and multiplexers", *IEEE Trans. Microwave Theory Tech.*, Vol. 47, pp. 2325-2330, Dec. 1999.
- [3] E. Ofli, R. Vahldieck and S. Amari, "Novel E-plane filters and diplexers with elliptic response for millimeter-wave applications", *IEEE Trans. Microwave Theory Tech.*, Vol. 53, pp. 843-851, Mar. 2005.
- [4] D.A. Cargill, T. Dolan and P. Pramanick, "Optimization of waveguide diplexers using shadow specification", *IEEE MTT-S Int. Microwave Symp. Dig.*, pp. 2107-2110, June 2001.
- [5] K.-L. Wu and H. Wang, "Rigorous modal analysis of H-plane waveguide T-junction loaded with a partial-height post for wide-band applications", *IEEE Trans. Microwave Theory Tech.*, Vol. 49, pp. 893-901, May 2001.
- [6] H.-W. Yao, A.E. Abdelmonem, J.-F. Liang; X.-P. Liang; K.A. Zaki, and A. Martin, "Wide-band waveguide and ridge waveguide T-junctions for diplexer applications", *IEEE Trans. Microwave Theory Tech.*, Vol. 41, pp. 2166 – 2173, Dec. 1993.
- [7] J.M. Rebollar and J.R. Montejo-Garai, "Asymmetric H-plane T-junction for broadband diplexer applications", *IEEE AP-S Int. Symp. Dig.*, pp. 2032-2035, July 2000.
- [8] T. Sieverding and F. Arndt, "Field theoretical CAD of open or aperture matched T-junction coupled rectangular waveguide structures", *IEEE Trans. Microwave Theory Tech.*, Vol. 40, pp. 353 - 362, Feb. 1992.
- [9] F.M. Vanin, D. Schmitt and R. Levy, "Dimensional synthesis of wide-band waveguide filters and diplexers", *IEEE Trans. Microwave Theory Tech.*, Vol. 52, pp. 2488-2495, Nov. 2004.
- [10] I.V. Bragin, S.E. Chadov, V.I. Gusevskii and E. Lavretski, "Waveguide diplexer using E-plane tee of improved symmetry", *Proc. 13th Int. Conf. Microwaves, Radar, Wireless Communications*, Vol. 2, pp. 513-516, May 2000.
- [11] A. Morini and T. Rozzi, "Constraints to the optimum performance and bandwidth limitations of diplexers employing symmetric three-port junctions", *IEEE Trans. Microwave Theory Tech.*, Vol. 44, pp. 242-248, Feb. 1996.
- [12] J. Dittloff and F. Arndt, "Rigorous field theory design of millimeter-wave E-plane integrated circuit multiplexers", *IEEE Trans. Microwave Theory Tech.*, Vol. 37, pp. 340 – 350, Feb. 1989.
- [13] L. Accatino and M. Mongiardo, "Hybrid circuit-full-wave computer-aided design of a manifold multiplexers without tuning elements", *IEEE Trans. Microwave Theory Tech.*, Vol. 50, pp. 2044-2047, Sep. 2002.
- [14] J.R. Montejo-Garai, J.A. Ruiz-Cruz and J.M. Rebollar, "Full-wave design of H-plane contiguous manifold output multiplexers using the fictitious reactive load concept", *IEEE Trans. Microwave Theory Tech.*, Vol. 53, pp. 2628-2632, Aug. 2005.
- [15] A. García-Lampérez, S. Llorente-Romano, M. Salazar-Palma and T.K. Sarkar, "Efficient electromagnetic optimization of microwave filters and multiplexers using rational models", *IEEE Trans. Microwave Theory Tech.*, Vol. 52, pp. 508-521, Feb. 2004.
- [16] J. Bornemann and J. Uher, "Design of waveguide filters without tuning elements for production-efficient fabrication by milling", in *Proc. 2001 Asia-Pacific Microwave Conf.*, pp.759-762, Dec. 2001.
- [17] J. Bornemann, J. Uher and K. Patel, "Efficient full-wave CAD of waveguide diplexers", *Proc. ANTEM 96 Symp. Antenna Technology and Applied Electromagnetics*, pp. 591-594, Aug. 1996.
- [18] F. Arndt, J. Bornemann, D. Grauerholz, D. Fasold and N. Schroeder, "Waveguide E-plane integrated circuit diplexer", *IEE Electronics Letters*, Vol. 21, pp. 615-617, July 1985.
- [19] M. Guglielmi, "Simple CAD procedure for microwave filters and multiplexers", *IEEE Trans. Microwave Theory Tech.*, Vol. 42, pp. 1347-1352, July 1994.
- [20] V.A. Labay and J. Bornemann, "Generalized modal scattering matrix of discontinuity-distorted waveguide multiport junctions", *Int. J. Numer. Model.*, Vol. 10, pp.153-167, May-June 1997.

A Collector-Up SiGe-HBT for High Frequency Applications

Mojtaba Joodaki¹, Hartmut Hillmer²

¹Infineon Technologies AG, Campeon 1-12, 81726 Munich, Germany

²University of Kassel, Dept. of Technological Electronics, Institute of Nanostructure Technologies and Analytics (INA), Heinrich-Plett Street 40, D-34132 Kassel, Germany, Tel: +49 89 234 45912, E-Mail: mojtaba.joodaki@infineon.com

Short Abstract— A new method for realization of a collector-up SiGe-HBT on SOI substrate for high frequency applications is introduced and its dc and ac characteristics are predicted using a two dimensional device simulator. The simulation results show considerable improvements in all aspects of dc current gain, f_T , f_{max} and maximum available gain/maximum stable gain (MSG/MAG) in comparison with a state of the art emitter-up SiGe-HBT with similar doping profile and germanium content. Another advantage of common-emitter collector-up transistor is that the emitter is connected to the ground and the substrate capacitor is shorted. This provides a higher frequency performance for circuit designs.

Keywords— SiGe HBTs; RF Applications; collector-up bipolar transistor; RF integrated circuits.

I. INTRODUCTION

Improvement of the SiGe-HBTs performance for high frequency applications has a very high priority in semiconductor business. Everyday we face new high frequency designs which require low-cost devices with higher frequency performance. For such applications the device of the choice is SiGe-HBT. Since in a bipolar transistor a very low emitter resistance is needed, conventionally it is realized in emitter-up configuration. In this way emitter is highly doped and collector is realized through an arsenic doped n-buried layer, which results in an acceptable collector resistance. These are all achieved at the cost of high collector-base and collector-substrate capacitance. Recently, device engineers are interested to implement a low-resistance silicide layer instead of the arsenic n-buried layer, which could provide a much lower resistance [1]. In this case, collector-up transistor can be realized with a low emitter-resistance.

On the other hand, in the last decade several genuine approaches for fabrication of emitter-up SiGe-HBT are introduced, which extremely enhanced the performances [2]. Although the methods of realization are different but most of them aimed at achieving two main goals; low-base resistance and a structure free from parasitic homo-junction bipolar transistor at the emitter-base junction. In the proposed fabrication process lateral solid-phase epitaxy of amorphous silicon [3] with a thick in-situ p-doped polysilicon base are used to achieve the above mentioned goals in the collector-up SiGe-HBT.

In the next section the new fabrication process is described. Section III covers the simulation results and section IV is the conclusion.

II. THE FABRICATION PROCESS

At the first step a SOI substrate with silicide strips for the low-resistance emitter contacts should be prepared (Fig. 1a). This is explained in reference [1]. Then an n⁺ layer for emitter is provided using a phosphor or arsenic implantation. The phosphor implantation gives a lower resistance but a higher diffusion constant of doping, which requires a thicker emitter to have a low doping concentration emitter at the emitter-base junction. This implantation could also be done later in the process, the same as selectively implanted collector (SIC) in the emitter-up structure. But this might induce some defects in the base and collector. In this work the silicon thickness is 250 nm, which is adequate to achieve a thick external base layer and a low doping concentration emitter at the base-emitter junction. In the next step a thin layer of silicon dioxide is thermally formed and patterned and silicon is etched and a 50 to 100 nm thick thermal oxide is made (Fig. 1b). Then at both sides of the transistor two windows are opened to be used as seed for lateral epitaxial overgrowth over oxide process [3] and covered by silicon nitride. Using the lateral epitaxial overgrowth and a CMP the highly p-doped crystalline external base areas are made. After CMP the structure in Fig. 1d is achieved. In this part to have a crystalline silicon layer over the active area of the device for the following epitaxial SiGe base and silicon collector, a 10 to 20 nm thick silicon layer with low doping is deposited. Since the oxide between base and emitter is thinner than 100 nm the silicon layer over it will also be crystalline. After that a 5 nm SiGe emitter-base spacer, 10 nm high concentration boron doped SiGe, and 10 nm SiGe base-collector spacer are epitaxially deposited. A low percentage of carbon concentration should be used with the highly boron doped SiGe to reduce the boron out-diffusion to the emitter. In this part collector epitaxy is made and the structure is etched as shown in Fig. 1e. To hinder any undesired direct contact of base and emitter outside of active area of the transistor and reach the n⁺-doping for emitter contact, the silicon at the both sides of the structure is etched. A thin silicon dioxide is thermally formed and followed with a thicker low temperature oxide deposition. The openings for emitter and collector contacts are created and using the same phosphor implantation, the n⁺ areas for emitter and collector are achieved. Fig. 1f shows the final structure.

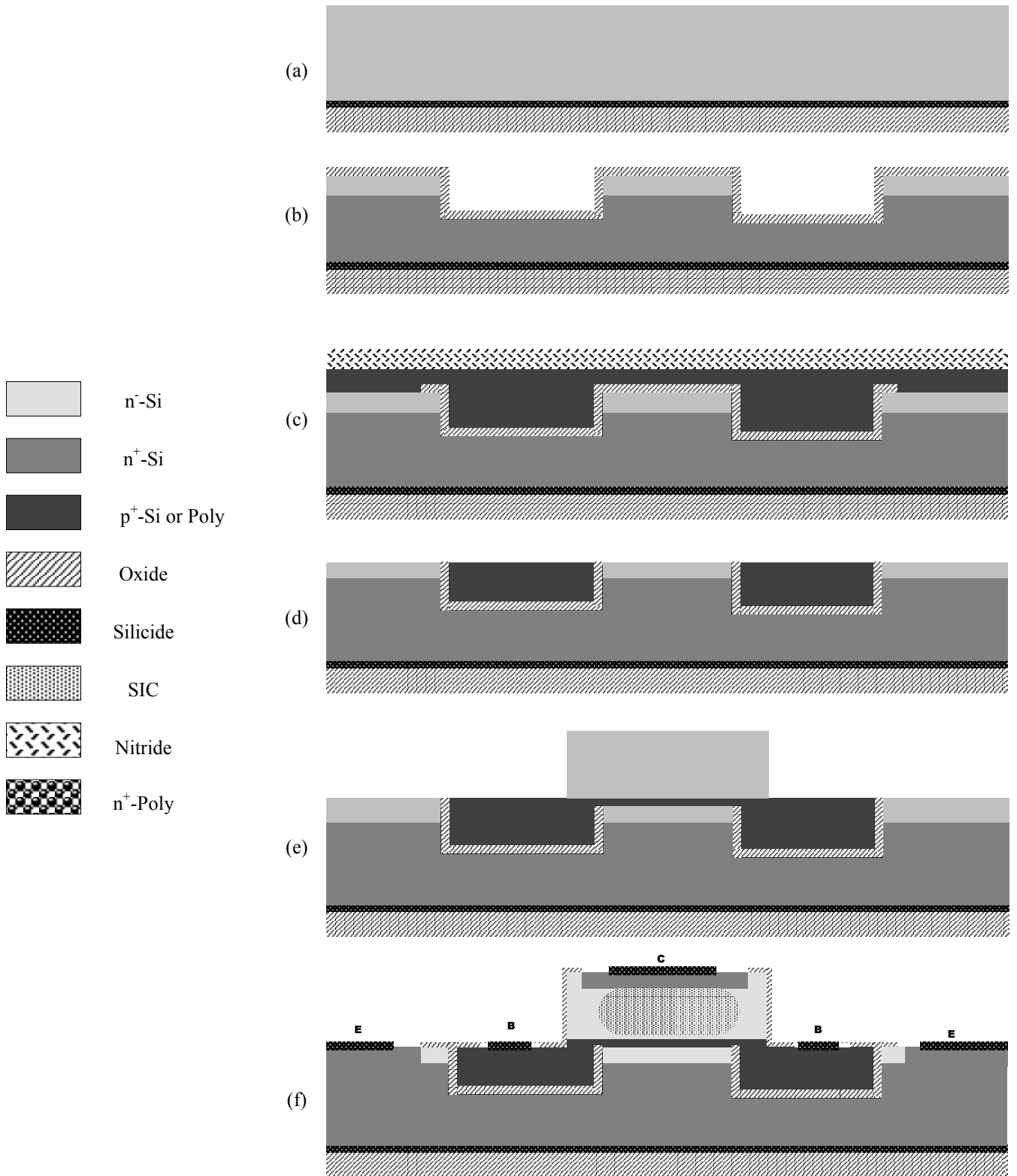


Figure 1. The proposed fabrication process for the collector-up SiGe-HBT.

III. SIMULATION RESULTS

To present the advantages of the collector-up configuration over the emitter-up SiGe-HBT, the 2D device simulator of ATLAS from Silvaco Inc is implemented. The dc and ac simulations are performed for both emitter-up and collector-up transistors with similar material properties and model parameters. The model parameters are adjusted using measured data of a fabricated emitter-up SiGe-HBT (SiGe2RF). For a reasonable comparison all the doping profiles, germanium contents, and geometrical dimensions for both devices are the same. The only differences are that in the collector-up transistor the collector is 75 nm thinner and the SIC is not used and a uniform phosphor doping of $1e17 \text{ cm}^{-3}$ is used instead. It is known that SIC will improve high frequency performance but may degrade the collector-emitter breakdown voltage. Fig. 2 shows the standard emitter-up structure of SiGe-HBT. Both devices have an emitter area of $0.5\mu\text{m}\times 1\mu\text{m}$.

Figs. 3 and 4 show the Gummel-plots and dc current gains for both structures, respectively. Since the parasitic pn-junction between mono-emitter and implanted external base has a considerable effect on the base current of emitter-up configuration, the current gain of the collector-up transistor is improved. All the simulations are performed at collector voltage of 1.5 V.

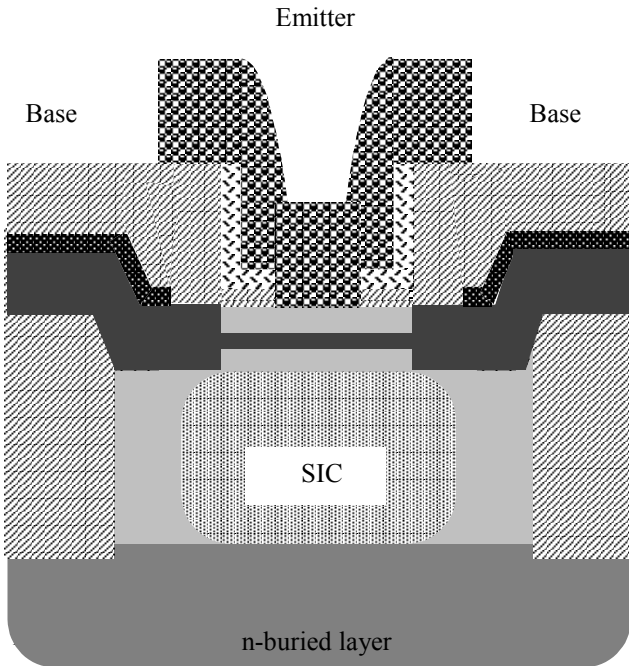


Figure 2. The emitter-up SiGe-HBT structure used in the simulations.

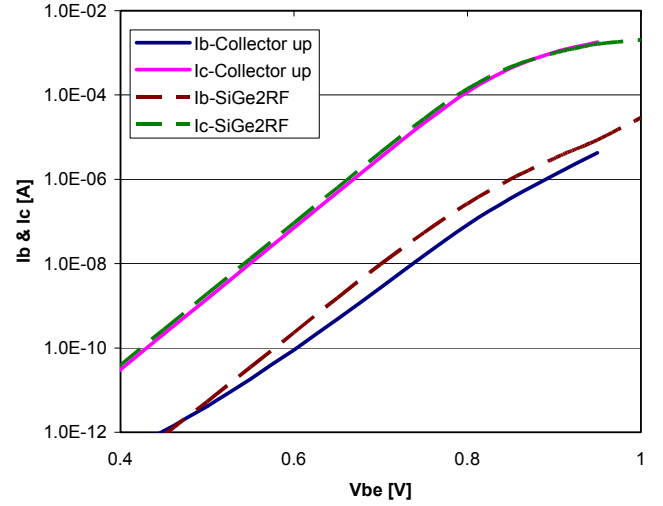


Figure 3. Gummel-plots for the collector-up and SiGe2RF (emitter-up) transistors.

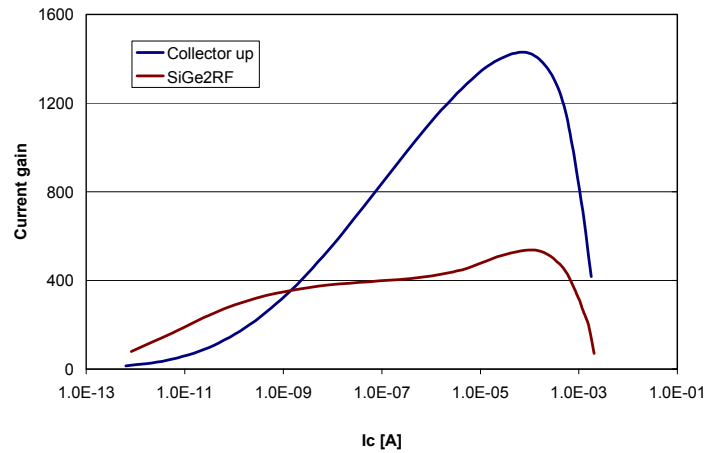


Figure 4. Dc common-emitter current gain for the collector-up and SiGe2RF (emitter-up) transistors.

Since SIC is not used in the collector-up configuration a collector-base breakdown voltage of 11.5 V is achieved while 9 V for the emitter-up configuration. But as the corresponding current gain is higher in collector-up configuration the emitter-base breakdown voltages of both structure are equal to 2.5 V. A higher collector-base breakdown voltage is desired in many RF applications. Figs. 5, 6, and 7 depict the MSG at 2 GHz, f_T , and f_{max} for both emitter-up and collector-up variants, respectively. Collector-base capacitor for the both variants is extracted from S-parameters and is $1.55E-14 \text{ F}$ for the emitter-up transistor and $6.9E-15 \text{ F}$ for the collector-up transistor. This means a reduction of more than 55%. Since collector capacitor is effectively reduced and the effect of the parasitic pn-junction in low doped emitter is reduced in the collector-up structure, the MSG, f_T , and f_{max} all are improved by 36%, 23%, and 84%, respectively. Large improvement of f_{max} results from improvement of f_T and reduction of collector-base capacitor and base resistance.

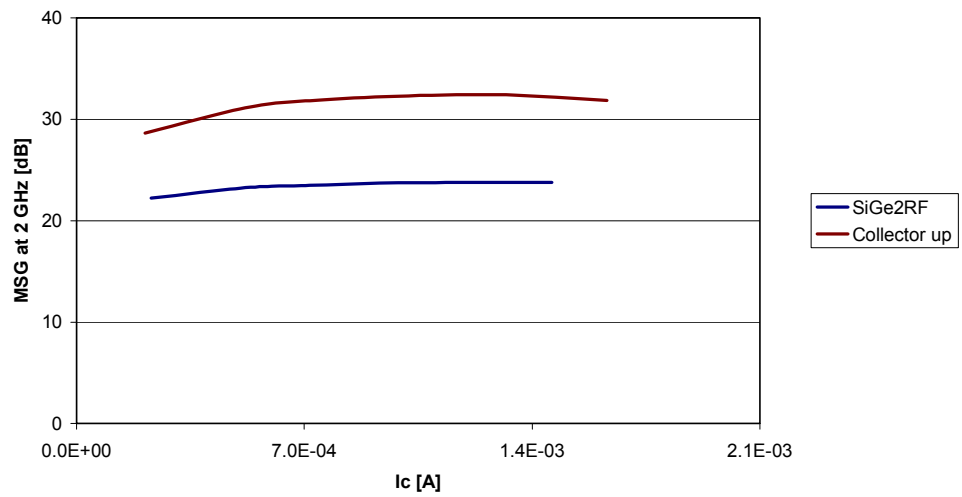


Figure 5. MSG at 2 GHz for the collector-up and SiGe2RF (emitter-up) transistors.

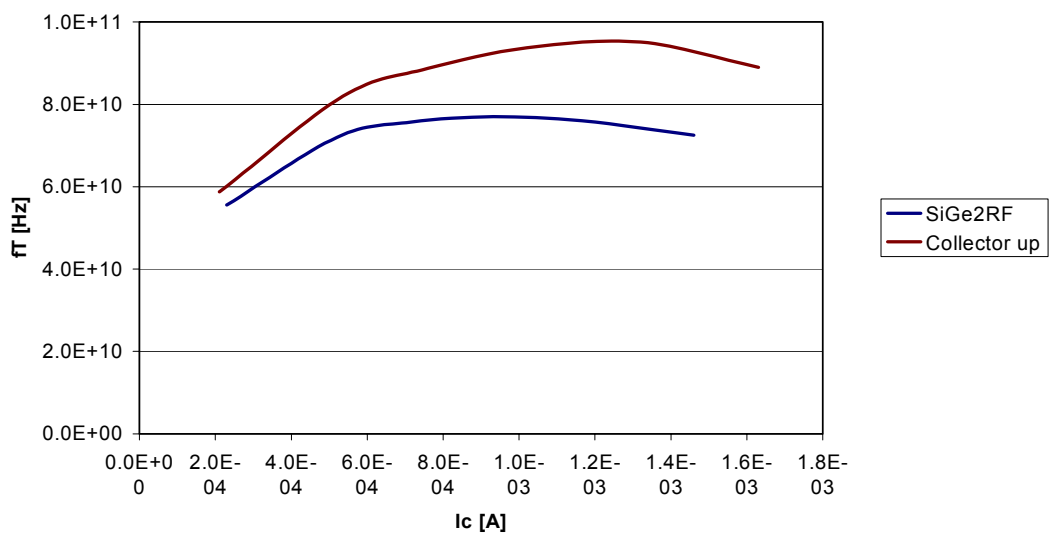


Figure 6. Transit frequency (f_T) for the collector-up and SiGe2RF(emitter-up) transistors.

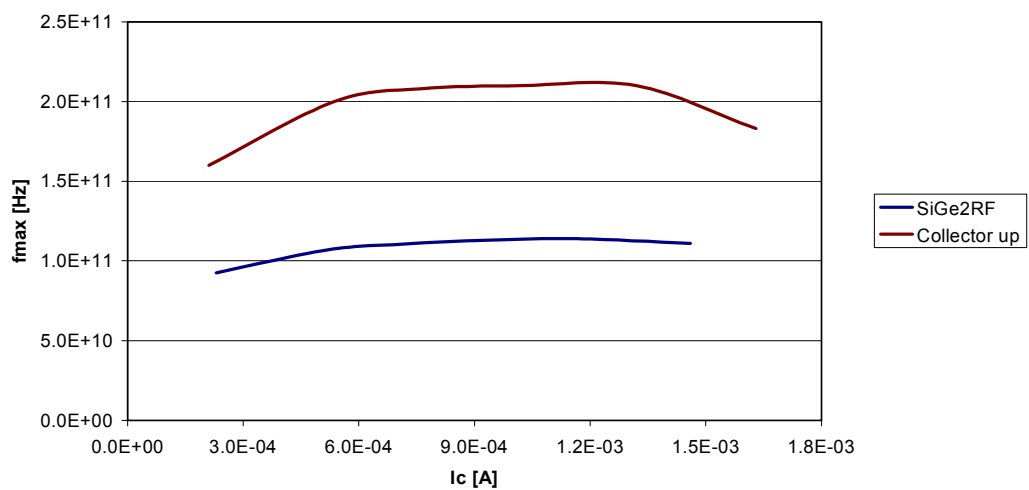


Figure 7. Maximum oscillation frequency (f_{max}) for the collector-up and SiGe2RF(emitter-up) transistors.

IV. CONCLUSION

In this paper a new fabrication process is introduced for realisation of the collector-up SiGe-HBT. Using a two dimensional device simulator the dc and ac characteristics of the transistor are predicted and compared to those of a standard emitter-up SiGe-HBT (SiGe2RF) with similar doping, emitter size, and Ge concentration in the base. In the collector-up structure by shorting the substrate and emitter to the ground the effect of the substrate capacitor is cancelled out and the collector-base junction has a lower capacitance. In addition the effect of the parasitic bipolar transistor is minimised and collector-base breakdown voltage is improved. The simulation results show great improvements in f_T , f_{max} , and MSG for the collector-up structure while the collector-emitter breakdown voltage is almost the same for both variant.

REFERENCES

- [1] R. Wilson, C. Quinn, B. McDonnell, S. Blackstone, and K. Yallup, "Bonded and trench SOI with buried silicide layer," ESC Symp. on Semicond. Wafer Bonding, Reno, May 1995.
- [2] J.-S. Rieh, B. Jagannathan, H. Chen, K. T. Schonenberg, D. Angell, A. Chinthakindi, J. Florkey, F. Golan, D. Greenberg, S. J. Jeng, M. Khater, F. Pagette, C. Schnabel, P. Smith, A. Stricker, K. Vaed, R. Volant, D. Ahlgren, G. Freeman, K. Stein, and S. Subbanna, "SiGe HBTs with cut-off frequency of 350 GHz," IEEE IEDM, pp. 771-774, 2002.
- [3] Y. Morimoto, S. Nakanishi, N. Oda, T. Yamaji, H. Matuda, H. Ogata, and K. Yoneda, "Influence of the existence of an underlying SiO₂ layer on the lateral solid-phase epitaxy of amorphous silicon", J. Electrochem. Soc. vol 141, No. 1, January 1994.

Compact Base-Station Filters Using TM-Mode Dielectric Resonators

Michael Höft and Thore Magath

Communications Laboratory of European Technology Center, (www.panasonic-eutc.com),
Panasonic Electronic Devices Europe GmbH, Zeppelinstr. 19, D-21337 Lueneburg, Germany,
phone: +49 (0) 4131 899-228, fax: +49 (0) 4131 899-262, e-mail: Michael.Hoefl@eu.panasonic.com

Abstract – A compact base-station filter using TM-mode dielectric resonators is presented. The TM-mode operation is chosen because of its capability of realizing compact resonator cavities at convenient quality factors. Fundamental properties of those dielectric resonators are discussed. Furthermore, results of a realized filter panel are shown. To improve the insertion loss performance of the TX-RX-duplexer, the lowpass filter is included in the phasing section.

I. INTRODUCTION

In Fig. 1 the basic setup of a cylindrical TM-mode dielectric resonator is shown. A dielectric rod with diameter dc and height H is placed coaxially in a cylindrical, metallic cavity with diameter do and the same height as the dielectric rod. A hole with diameter di might be included into the ceramic to allow the intrusion of a tuning screw for the adjustment of the resonance frequency.

Bandpass filters with TM_{010} -mode dielectric resonators have first been reported 1978 by Kobayashi and Yoshida [1]. In comparison to other dielectric resonators, they show relatively wide spurious-free stopband performance. The drawback is the requirement of having a proper electric contact between the ceramic material and the top and bottom of the metallic cavity. Due to different coefficients of thermal expansion, mechanical stress might be harmful to this contact. On the other hand, an air-gap at the bottom or top would lead to an undesired frequency shift.

Different solutions to overcome this problem were presented. In [1] the mechanical stress was avoided by letting the ceramic rod expand into holes at the top and bottom of the housing to reduce the frequency shifting due to thermal changes of the air-gap. However, the essential problem of the frequency stability was not solved. In [2] the problem was solved by using a dielectric shielding cavity of the same material as the inner dielectric rod. This technique was improved in [3] by fabricating a dielectric shielding cavity and the inner rod out of a single block. Furthermore, dual mode operation was achieved by integrating two perpendicular in-

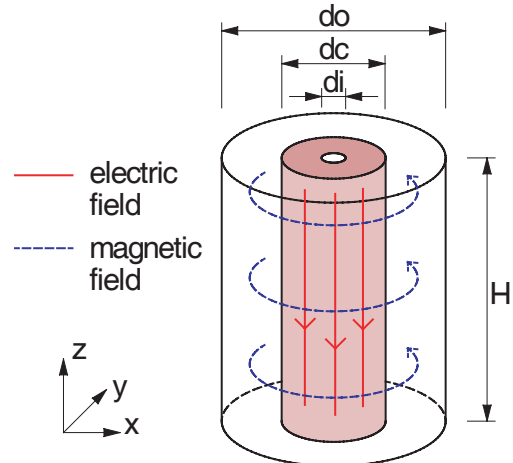


Fig. 1: Basic setup of a circular TM-mode dielectric resonator.

ner rods into the ceramic block, although multi-mode operation of TM-mode resonators for a channel dropping filter using triple mode resonance was already reported in [4] before.

In [5] different coupling and tuning mechanisms were discussed. Moreover, cross-coupling was introduced to realize elliptic bandpass filters. In [6, 7] a similar cross coupling technique was applied to realize a bandpass filter at 1.9 GHz for a micro-cell base-station. In [8] further miniaturization technologies of dielectric resonator filters for mobile communications are reviewed.

Our solution to overcome the mechanical stress between the dielectric rod and the enclosing cavity is the application of a flexible cover as published in [9]. Furthermore, the top and bottom of the cavity are silver-plated to avoid any air-gaps and resulting frequency shifts.

Our design was realized at 2 GHz, since our objective is the application in base-stations for third generation mobile communication systems [10].

II. BASIC ANALYSIS

Field simulations have been performed to characterize the basic behavior of a single TM-mode resonator (as depicted in Fig. 1) with respect to its fundamental and first spurious mode frequency as well as the expected unloaded quality factor. The dielectric material consists mainly of the compounds ZrO_2 and TiO_2 . It has a relative dielectric constant of approx. $\epsilon_r \approx 42$ and an unloaded quality factor of 20.000 at 2 GHz. The housing is silver-plated ($\sigma = 60 \cdot 10^6$ S/m).

The TM_{ij0} -modes are independent of the height H of the resonator, which is $H = 27$ mm for the realized filter panel. The dependency of the fundamental and first spurious mode of a single resonator on its outer cavity diameter do is shown in Fig. 2. The inner diameter di is fixed to $di = 3$ mm. The ceramic radius $rc = dc/2$ is varied to keep the fundamental mode at a constant frequency of $f_1 = 1.95$ GHz. How the ceramic radius rc depends on outer diameter do is presented in Fig. 3. Also, the simulated quality factor is shown in Fig. 3. Note, that the real quality factor is lower due to (1) non-ideal contacts between the ceramic and the cover and (2) to lower conductivity of the housing because of its surface roughness. Moreover, the outer diameter should be chosen slightly smaller for reasons of tunability of the resonator, since the tuning screw can only lower the frequency. This and the losses due to the tuning screw itself will further lower the quality factor measured.

The first spurious mode and the quality factor both increase with growing outer cavity diameter do . However, the space in the realized filter panel and correspondingly the size of the diameters were limited. To save costs, the ceramics for the receive channel (RX) bandpass filter with center frequency of $f_c = 1.95$ GHz and the transmit channel (TX)

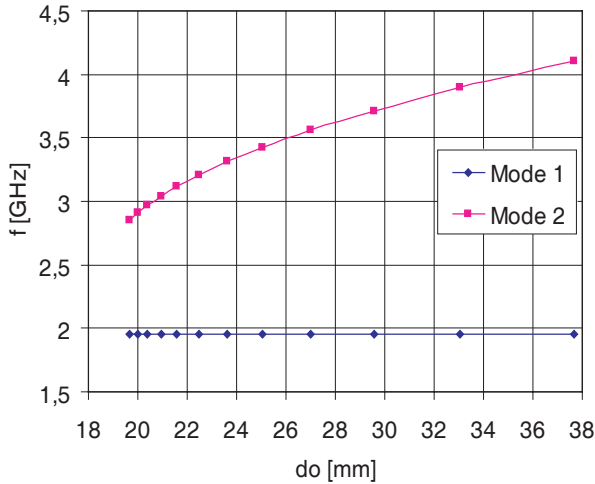


Fig. 2: Fundamental and first spurious mode of TM-mode resonators in dependence of outer diameter do .

bandpass filter with $f_c = 2.14$ GHz were chosen to have the same diameter of $dc = 12$ mm, while the outer diameter of the cavities were chosen differently to achieve the desired center frequencies. The resulting outer diameter of the RX-resonators was set to $do = 21.6$ mm, while the outer diameter of the TX-resonators was set to $dc = 18.7$ mm. Consequently, the first spurious modes were expected to be at $f_2 = 3.1$ GHz and $f_2 = 3.2$ GHz, respectively, whereas the simulated quality factors were $Q = 5200$ and $Q = 4800$, respectively. The measured values were approx. 30 % lower than the simulated ones.

III. REALIZED FILTER PANEL

In Fig. 4 a block diagram of the designed filter panel is shown. The filter panel consists of a TX-RX-duplexer and a single receive unit. Isolators are included to achieve a matching which is virtually independent of units connected. Besides the bandpass filters, lowpass filters are added to suppress spurious response up to 12.75 GHz. Since the requirements for the receiving filters are not so strict as for the transmitting path, a three section stepped-impedance lowpass filter instead of a seven section one was included for the single RX path.

In Fig. 5 a photograph of the realized filter panel is depicted, which has a size of $169 \times 76 \times 39$ mm³. In Fig. 6 the corresponding concept drawing of the setup is sketched. The bandpass filters are to support the 20 MHz center band of the UMTS-spectrum. Due to this, simple three and four pole Chebychev bandpass filters are sufficient, which facilitates the compact design of the overall unit. The RX resonator cavities have a rectangular base shape of approx. 20×20 mm² instead of a circular shape to achieve a more

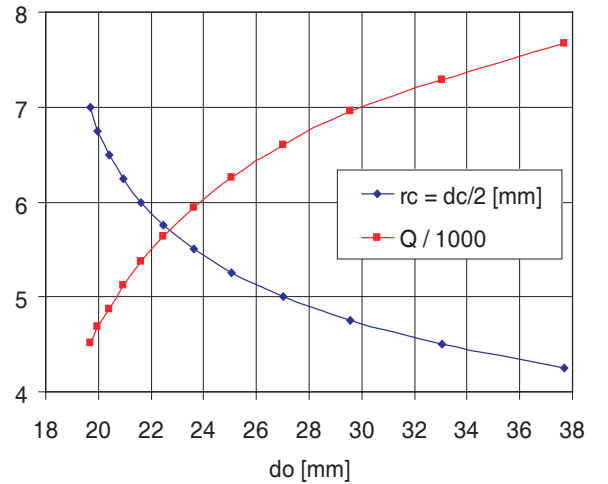


Fig. 3: Quality factor and ceramic radius rc of a TM-mode resonator for $f_0 = 1.95$ GHz.

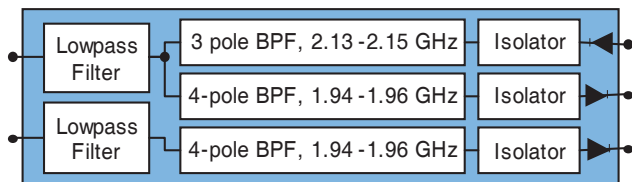


Fig. 4: Block diagram of the designed base station filter.

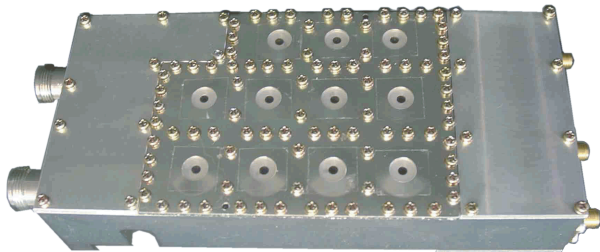


Fig. 5: Photograph of the compact base station filter with TM-mode dielectric resonator.

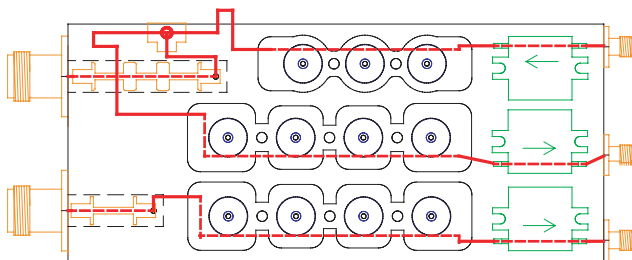


Fig. 6: Concept drawing of the filter.

compact layout. Note, that the coupling apertures have to be considered for the exact determination of the cavity size, since the resonance frequency strongly depends on the outer dimensions of the cavity as can be inferred from Fig. 3.

A brief summary of the measured performance of the filter panel is given in Table 1. Exemplary, in Fig. 7 the insertion loss S_{21} of the single RX filter is shown within a frequency range of 1.6 GHz to 3.8 GHz. The bars indicate the blocking specification required. The first spurious response lies in the range of 2.8 GHz to 3.0 GHz. In Fig. 8 the measured temperature performance of the return loss of an RX filter is shown for a temperature range of -10°C to 70°C . In Fig. 9 the measured temperature performance of the insertion loss is depicted. The frequency shift of the

Table 1: Summary of the measured performance.

	Insertion Loss	Return Loss	Isolation	Signal Rejection
Duplexer TX	0.75 dB	-30 dB	-32 dB	> 70 dB @RX
Duplexer RX	0.80 dB	-27 dB	-26 dB	> 70 dB @TX
Single RX	0.65 dB	-28 dB	-29 dB	> 70 dB @TX

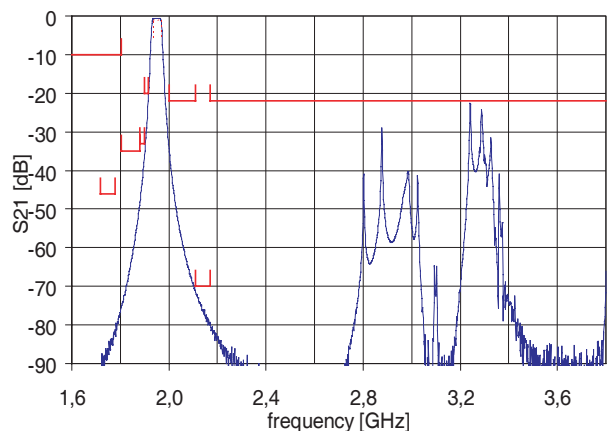


Fig. 7: Measured spurious performance of the filter.

-20 dB blocking value at the lower stopband side amounts to 0.43 MHz, i.e., 5 kHz/K, while the corresponding blocking value at the upper stopband has a shift of 1.04 MHz, i.e., 13 kHz/K. By adjusting proportions of the compounds of the ceramic material, the temperature compensation can further be improved. Note, that the the expansion of the metallic body also needs to be considered for the compensation.

IV. IMPROVEMENT

In Fig. 10 the concept drawing of an improved design of the filter panel is depicted. The insertion loss performance of the realized TX-RX-duplexer is reduced by including the lowpass filter into the phasing section. In doing so, the lowpass filter for the RX path could be realized as a three section stepped-impedance lowpass filter. This lowpass filter is placed at the output of the RX path, since the phasing section for the RX path was quite short. Furthermore, in the first version there was a minor interference between the closely placed isolators, which slightly deteriorated the insertion loss performance. As a result, the insertion loss has become lower than 0.65 dB for all paths: the bandpass filters are contributing ≈ 0.35 dB, the isolator ≈ 0.2 dB and the lowpass filter and coaxial lines for connection and phasing section ≈ 0.1 dB. I.e., the bandpass contributes only roughly half of the losses.

V. CONCLUSIONS

A compact base-station filter using TM-mode dielectric resonators was presented. Fundamental properties of the dielectric resonators were discussed. To improve the insertion loss performance of the realized TX-RX-duplexer, the lowpass filter is included into the phasing section. As a result, the bandpass only contributes roughly half of the insertion losses of the filter panel.

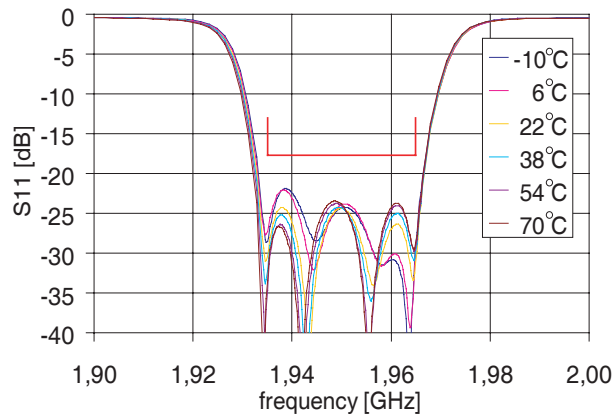


Fig. 8: Measured temperature performance of the return loss.

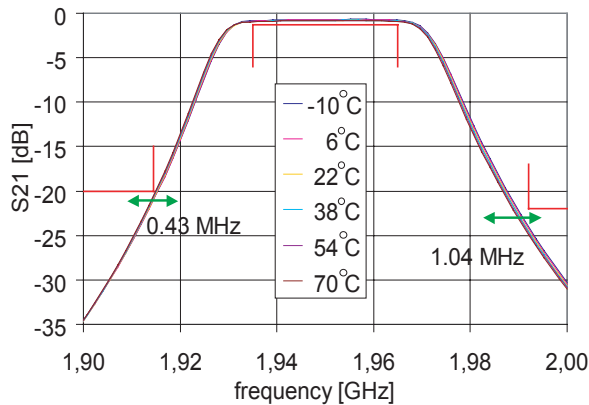


Fig. 9: Measured temperature performance of the insertion loss.

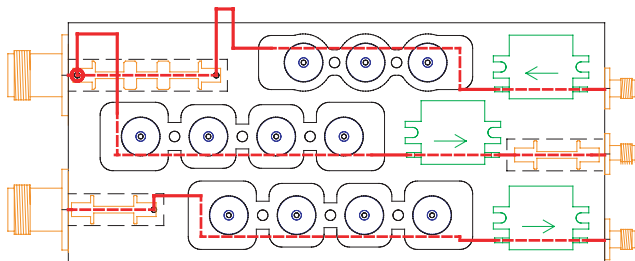


Fig. 10: Concept drawing of improved design for lower insertion loss.

REFERENCES

- [1] Y. Kobayashi, S. Yoshida, "Bandpass filters using TM_{010} dielectric rod resonators," *Proc. IEEE MTT-Symposium*, 1978, pp. 233-235.
- [2] T. Nishikawa, K. Wakino, Y. Ishikawa, "800 MHz band channel dropping filter using TM_{010} mode dielectric resonator," *Proc. IEEE MTT-Symposium*, 1984, pp. 199-201.
- [3] Y. Ishikawa, J. Hattori, M. Andoh, T. Nishikawa, "800 MHz high power duplexer using TM dual mode dielectric resonators," *Proc. IEEE MTT-Symposium*, 1992, pp. 1617-1620.
- [4] T. Nishikawa, K. Wakino, H. Wada, Y. Ishikawa, "800 MHz band dielectric channel dropping filter using TM_{110} triple mode resonance," *Proc. IEEE MTT-Symposium*, 1985, pp. 289-292.
- [5] Y. Kobayashi, H. Furukawa, "Elliptic bandpass filters using four TM_{010} dielectric rod resonators," *Proc. IEEE MTT-Symposium*, 1986, pp. 353-356.
- [6] I. C. Hunter, *Theory and design of microwave filters*, No. 48 in Electromagnetic waves series, London: IEE, 2001, p. 316.
- [7] V. Walker, I. C. Hunter, "Design of cross-coupled dielectric-loaded waveguide filters," *IEE Proc. Microw. Antennas Propag.*, vol. 148, no. 2, April 2001, pp. 91-96.
- [8] K. Wakino, T. Nishikawa, Y. Ishikawa, "Miniaturization technologies of dielectric resonator filters for mobile communications," *IEEE Trans. Microwave Theory Tech.*, vol. 42, no. 7, Jul. 1994, pp. 1295-1300.
- [9] T. Yamakawa, T. Ishizaki, "Dielectric resonator, dielectric filter, and method of supporting dielectric resonance element," *European Patent Application*, EP1505687A1, Feb. 2005.
- [10] O. Bartz, S. Burger, M. Tzortzakakis, "UMTS Filterpanel for European Market," *Matsushita Technical J.*, vol. 48, no. 6, Dec. 2002, pp. 458-463 (http://www.panasonic-eutec.com/support/pdf/MTJ12_2002.pdf).

Observation of a walking pedestrian with a 24GHz automotive radar sensor

Florian Fölster*, Hermann Rohling*, Henning Ritter*

*Hamburg University of Technology

Department of Telecommunications, Eißendorferstraße 40, 21073 Hamburg, Germany

Email: {f.foelster, rohling, henning.ritter}@tu-harburg.de

Telephone: +49 (40) 42878 3228, Fax: +49 (40) 42878 2281

Abstract— In this paper the echo signal of a moving pedestrian will be considered as an example of a velocity extended radar target. Based on measurements and simulations, target characteristics inside the radar receive signal differing from a point-target model will be analyzed and the necessity of new and alternative signal processing strategies for close-up applications will be shown.

I. INTRODUCTION

Active safety systems will be used in automotive applications to increase comfort and safety. In safety related systems mainly the protection of pedestrians, so called vulnerable road users, is considered in current research projects [1].

While radar systems are commonly used to detect positions and velocities of all objects inside the surrounding of vehicles, up to now, mainly optical systems are considered for the task of object classification and target recognition. But it has already been shown, that radar sensors can also be applied for the purpose of target classification [2]. To deliver this additional information about the type of object, the commonly used point-target model for radar detections is not sufficient any more since the information about target characteristics is covered inside the echo signal details differing from this simple model.

Considering extended targets, usually range- or angular-extended targets are addressed [3]. In addition to this, radar targets can also be velocity-extended and have to be handled in case of target tracking and recognition accordingly. Recent publications have shown that even simple radar sensors are capable to record micro-Doppler profiles of walking humans [4], [5]. In this paper we will use the example of a walking pedestrian to demonstrate the additional information inside the radar echo signal which could be achieved if the targets are handled with a non point-like target model.

II. GAIT ANALYSIS

The movement of a walking pedestrian is characterized by a non uniform motion. Even when the center of gravity is moving with a constant velocity, all parts of the person's body perform an individual technically complicated, but periodical process of acceleration and deceleration. The reason therefore is to minimize the overall energy consumption [6], [8]. To give an impression, Fig. 1 presents two video frames with a time difference of $T = 12$ ms showing a walking person and

the respective motion vectors of different body parts. All the details in the measured movement are called micro-Doppler.

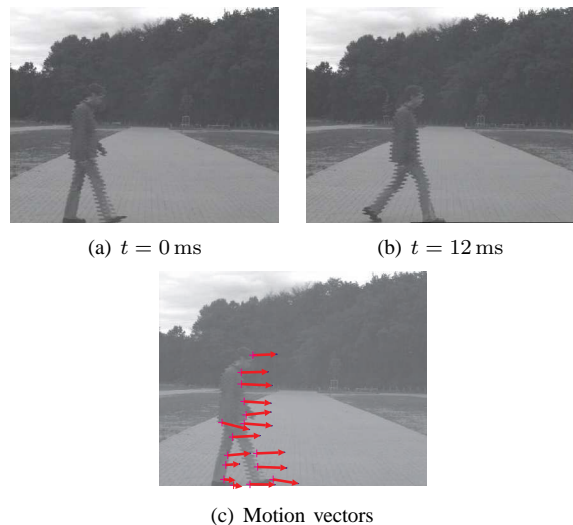


Fig. 1. Motion visualization of different body parts

The periodicity of the motion is given by the so called walk cycle, which is defined as two subsequent steps. Within this cycle one foot is always on the ground for a non running movement. Fig. 2 shows a drawing of such a walk cycle to visualize the periodic process for the trunk as well as legs and arms. The different parts of the body are separated by colors, blue color for the moving trunk and red color for left arm and leg. Right arm and leg movement is depicted in green color. On the time axis seven different events are given in percent of one cycle.

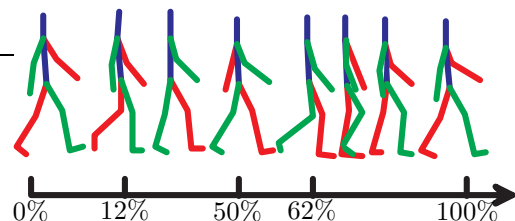


Fig. 2. Drawing of typical human walk cycle

III. SIMULATION

To simulate the radar echo signal of a walking-pedestrian the characteristics of the human's motion have to be described by an adequate object model. Since swinging arms can not be postulated for all walking persons they will be neglected inside the model. Furthermore, radar detections of arms are less relevant given by the smaller radar cross section compared to trunk and legs.

To describe the movement of body and legs, their movement will be approximated by a simple cosine oscillation in the direction of motion superimposed to the motion of the center of gravity. If the direction of motion is assumed to be the r -direction, the overall motion of one specific body part can be described by

$$r(t) = r_0 + \int_{\tau=0}^t v(\tau) d\tau \quad (1)$$

where the velocity $v(t) = \bar{v}(t) + \tilde{v}(t)$ consists of a macroscopic \bar{v} and a microscopic component \tilde{v} . We define the macroscopic velocity as the velocity of the center of gravity and the microscopic velocity as the target specific velocity of a single body part with zero-mean over a whole walk cycle T_C .

$$\int_{t=0}^{T_C} \tilde{v}(t) dt = 0 \quad (2)$$

Motion components orthogonal to the direction of gait will be neglected given by their very small deflection.

If $f_s = 2/T_C$ is the step frequency of every single step, then the movement of the outermost part of the leg can be described by the step length L and the equation

$$\tilde{v}_{\text{Legs}}(t) = \pm L \cdot f_s \cdot \cos(\pi f_s t) \quad (3)$$

This description implies an approximation of the legs as simple pendulums, which is sufficient for the desired application. The plus and the minus signs are representing the right and the left legs which have an opposite phase. Given by the normal walk cycle, the average speed of the whole body is consequently defined by:

$$\bar{v} = L \cdot f_s. \quad (4)$$

Besides the movement of the legs, also an oscillation of the trunk is described in the relevant literature [6], [7]. Fig. 3 visualizes the velocity oscillation at the thorax-abdomen segment according to [7].

The period length is thereby one per step, thus $1/f_s$, and the amplitude $v_{\%}$ is depending on the respective part of the body and has a value proportional to the average speed of motion with values up to $v_{\%} = 20\%$.

$$\tilde{v}_{\text{Trunk}}(t) = L \cdot f_s \cdot v_{\%} \cdot \cos(2\pi f_s t) \quad (5)$$

In the example given in Fig. 3 the amplitude has a value of $v_{\%} = 7\%$.

The combination of the respective movements of legs and trunk leads to a range over time plot like shown in Fig. 4.

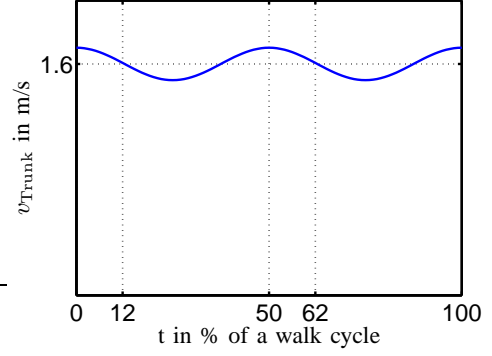


Fig. 3. Horizontal movement velocity $\tilde{v}_{\text{Trunk}}(t)$ of the thorax-abdomen segment

The step length is set to $L = 0.8$ m and the step frequency to $f_s = 2$ Hz which leads to an average speed of 1.6 m/s. Compared to the oscillation of the leg's velocities, the one from the trunk is only poorly visible. At time instance $t = 0.5$ s all three mentioned body parts have reached the same position, but do have different velocities.

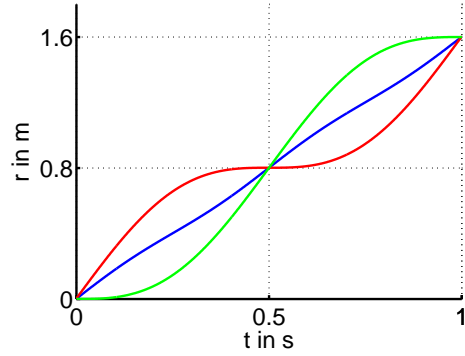


Fig. 4. Dependency of range and time for a moving person

In details these are one standing foot with $v_1 = 0$ m/s, the trunk with a velocity slightly above the average velocity $v_2 = 1.8$ m/s and the free leg with the twice the average velocity $v_3 = 3.2$ m/s. Consequently, this kind of target can be considered as a velocity extended target caused by the great difference between maximal and minimal velocity of up to twice the average velocity compared to a maximal range extension of one step length. Fig. 5 shows the range-velocity diagram (RV-diagram) of the target at time instance $t = 0.5$ s for the three mentioned points.

For the simulation program and analytical description of the radar echo signal all different points of the body have to be considered with their specific movement. For this purpose, a six-point model shown in Fig. 6 will be used to analyze the effects of the moving body within the radar echo signal.

To analyze the target type related effects, the radius and velocity measurements for each of the six points can be calculated at a certain time t . Furthermore, the range-velocity

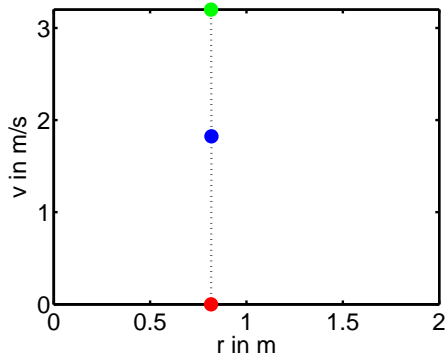


Fig. 5. Range-velocity diagram at time $t=0.5s$

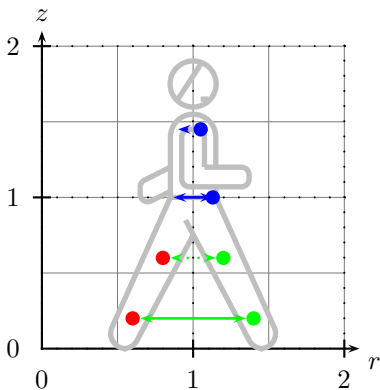


Fig. 6. Six-point model for walking pedestrian simulation

diagram will be used to interpret the target specific movements differing from point-target behavior. In Fig. 7 an example of a simulated range-velocity diagram is given for the person walking with a step frequency of $f_s = 2$ Hz and the respective step length of $L = 0.8$ m.

IV. MEASUREMENT RESULTS

After the theoretical considerations about the gait analysis and the simulated range-velocity diagram shown in Fig. 7 the same setup with a radial walking person is recorded by a 24 GHz radar sensor. For this purpose a modified automotive pulse-radar sensor is used for high resolution pulse-Doppler measurements. To detect the expected micro-Doppler signatures within the radar echo signal, the radar parameters are set to a range resolution of $\Delta r = 0.08$ m and a velocity resolution of $\Delta v = 0.09 \frac{m}{s}$.

Fig. 8 shows the results for a person walking with a walking pedestrian with average speed of $\bar{v} = 1.4$ m/s. The intensity of the grayscale depicts the intensity of the received echo strength. This recorded measurements are directly comparable with the simulated results of the previous section. Besides the mean velocity of $\bar{v} = 1.4$ m/s also reflections with higher velocity of the free leg and lower velocity components of the

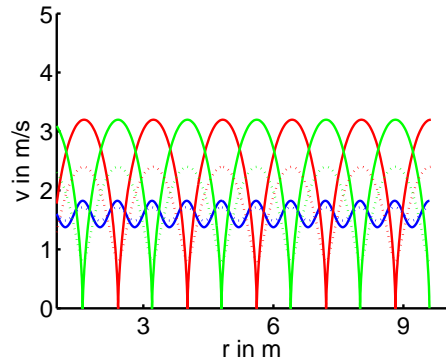


Fig. 7. Simulated overlaid range-velocity diagram for the body (blue) as well as the legs (red and green) of a pedestrian walking at radial speed of $\bar{v} = 1.6 \frac{m}{s}$. The step length is set to $L = 0.8$ m and the respective step frequency is given by $f_s = 2$ Hz

supporting leg can be clearly seen. Also the oscillation of the trunk's velocity is visible within the recorded data.

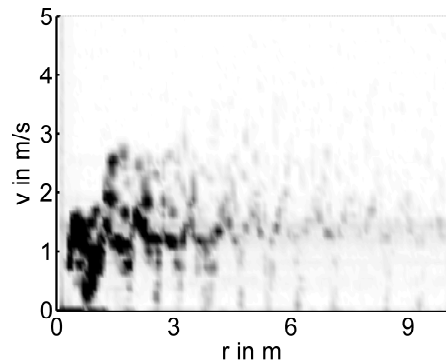


Fig. 8. Measured range-velocity plot of a pedestrian walking with a speed of $\bar{v} = 1.4 \frac{m}{s}$

Radar echo signals of arms and legs are based on much smaller radar-cross-sections and are therefore reflected with a lower intensity. For this reason, the following considerations will concentrate on the trunk's reflections to estimate the step length and frequency of the walking person.

V. SIGNAL PROCESSING FOR PEDESTRIAN TRACKING

For radar applications in realistic multi-target situations, a signal processing architecture including target detection, data association and tracking are essential for reliable target handling and the appropriate situation analysis. During this signal processing all target related parameters have to be estimated and processed over adjacent measurements.

To use the additional information about the targets it has to be extracted from the receive signal. Therefore, the signal processing structure will be adapted to the specific situation and target type, since the commonly used point-target model is not able to handle properly this kind of radar reflections.

Fig. 9 gives the respective block diagram of the used signal processing, which is in this case manly an add-on to

the classical signal-processing chain. The additional signal processing block requires the original unfiltered raw data besides the track association since the low-pass character of a tracking procedure is undesired for the given task.

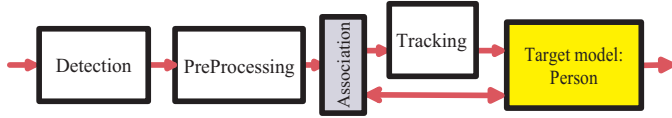


Fig. 9. Signal processing chain for step frequency estimation

A. Tracking of macroscopic target movements

The general idea of target tracking is to predict the target movements and to generate an object reference over adjacent measurements. Furthermore, some missed detections and the influence of noisy measurements can be handled and improved by the tracking and signal processing procedure. Since automotive target maneuvers are slow compared to the measurement update rate often constant velocity models are used for tracking purpose.

Considering the above mentioned person walking with a speed of 1.4m/s it is quite obvious to talk about a target moving with constant velocity. When taking the radar measurements into account the whole thing looks different. While the measured oscillation of the trunk's velocity could be mistaken for measurement errors, detections of arms and legs will lead to ghost targets with low lifetime as illustrated in Fig. 10.

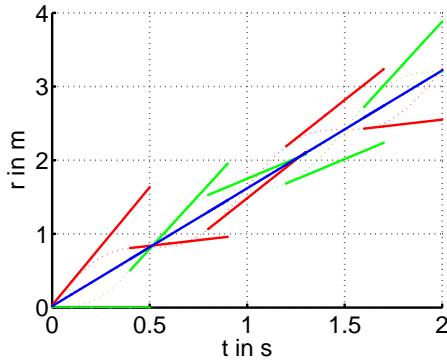


Fig. 10. Tracking of macroscopic and microscopic target movements

A proper tracking of leg reflections will only be possible, if their reliable detection can be postulated and the update rate of the tracker is high compared to the step frequency of the person in connection with a non constant velocity tracking model. Furthermore, it will be of great use, if it is known that a person is present to adapt the tracking motion model. For most automotive applications the task of the tracker is to find the macroscopic movement of the target, while any additional information about the target is hidden inside the microscopic target movement.

B. Tracking of microscopic target movements

Based on the measurements presented in section IV an ordered-statistic-based target detection scheme is used to detect all reflections of the walking person's trunk and apply a target tracker to the detected data. The detection results are shown in Fig. 11 as black dots, while the resulting target track is given by the solid line.

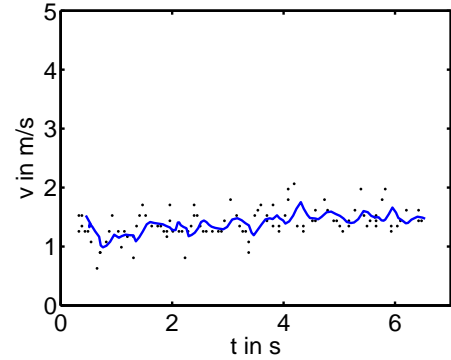


Fig. 11. Radar detections of the trunk based on the data presented in Fig. 8

Besides a reliable tracking of the target, fluctuations of the measured velocity are obvious and will be used for step frequency estimation. For this purpose, a spectral estimation of the frequency components within the original non tracked raw target detections is used. The results of this frequency estimation procedure is shown in Fig. 12.

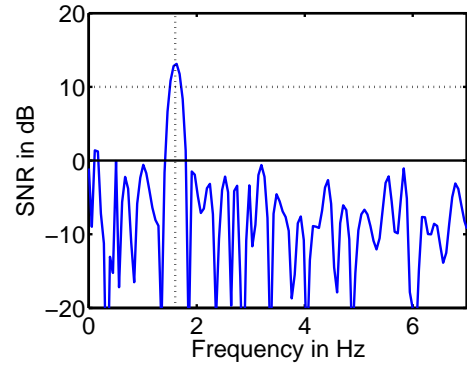


Fig. 12. Spectral estimation of trunk velocity fluctuation

Among others one main frequency with a signal-to-noise ratio of 13 dB is clearly visible and will be considered as the demanded step frequency. Using the known macroscopic velocity \bar{v} of the target track, the step length can be easily calculated.

$$L = \frac{\bar{v}}{f_s} = 87.5 \text{ cm} \quad (6)$$

The gained value of a step length close to 90 cm is a reasonable estimate of the step length of the real walking person and gives a good indicator that the measured velocity fluctuation is based on target characteristics and not on measurement noise.

VI. CONCLUSIONS

Objects to be detected by automotive radar sensors do not show up as simple point-like targets inside the radar receive signal. As an example this paper deals with the radar echo signals of pedestrians. Based on theoretical considerations of gait analysis and simulations the relevant characteristics of radial walking persons were presented and exemplified by practical measurements.

The estimation of the step frequency was used as an example to demonstrate detailed target information which can be extracted from recorded signals when the signal processing strategy is adapted to the respective target type.

REFERENCES

- [1] M.-M. Meinecke, M.-A. Obojski, M. Töns, and M. Dehesa, "SAVE-U: First experiences with a pre-crash system for enhancing pedestrian safety," in *The 5th European Congress on Intelligent Transportation Systems and Services 2005*, Hannover, Germany, June 2005.
- [2] F. Fölster, H. Rohling, and M.-M. Meinecke, "Pedestrian recognition based on automotive radar sensors," in *The 5th European Congress on Intelligent Transportation Systems and Services 2005*, Hannover, Germany, June 2005.
- [3] K. Schuler, R. Lenz, and W. Wiesbeck, "Digital Beam-Forming for Automotive SRR," in *International Radar Symposium IRS 2005*, Berlin, Germany, September 2005, pp. 613–617.
- [4] P. van Dorp and F. Groen, "Real-time human walking estimation with radar," in *Proc. International Radar Symposium 2003*, Dresden, Germany, September 2003, pp. 645–649.
- [5] M. Nalecz, R. Rytel-Andrianik, and A. Wojtkiewicz, "Micro-doppler analysis of signals received by FMCW radar," in *Proc. International Radar Symposium 2003*, Dresden, Germany, September 2003, pp. 645–649.
- [6] J. Perry, *Gait analysis : normal and pathological function*. Thorofare, NJ: Slack, 1992.
- [7] C. Lutzenberger, "Dynamik des menschlichen Ganges," Ph.D. dissertation, Technische Universität München, Düsseldorf, 2002.
- [8] K. Götz-Neumann, *Gehen verstehen - Ganganalyse in der Physiotherapie*. Stuttgart, Germany: Georg Thieme Verlag, 2003.

Accurate Design and Yield Analysis of Tunable Distributed MEMS Bandpass Filter

S. Simion¹, G. Bartolucci², R. Marcelli³

¹MTA – Dept. of Communications and Computer Science – George Cosbuc 81-83, Bucharest, 050141, Romania, phone: +40722-229-569, e-mails: stefan.simion@yahoo.com; stefan_simion@rdslink.ro

²University of Roma “Tor Vergata”, Dept. of Electronics Engineering – Via della Ricerca Scientifica 100, 00133, Roma, Italy, e-mail: bartolucci@eln.uniroma2.it

³CNR – Institute for Microelectronics and Microsystems, Microwave Microsystems Group – Via del Fosso del Cavaliere 100, 00133, Roma, Italy, phone: +39 06 4993-4536, e-mail: Romolo.Marcelli@psm.rm.cnr.it

Abstract—The paper presents the design and yield analysis of a tunable bandpass filter consisting of capacitive coupled distributed MEMS transmission lines. It is used an accurate equivalent circuit based on the electromagnetic MEMS analysis results. The yield analysis takes into account the filter parameter dispersion due to the technological resolution.

Keywords - tunable filter; MEMS; electromagnetic analysis; yield analysis

I. INTRODUCTION

Due to the very small series resistance, MEMS (Micro-Electro-Mechanical-System) devices are very attractive for the realization of low insertion loss microwave circuits, such as switches, phase shifters and BPSK modulators. [1], [2], [3]. Another recent application for MEMSs is to realize low insertion loss tunable filters. The tunable property is due to the possibility to change the MEMS equivalent capacitance versus the DC voltage applied on the MEMS bridge [4], [5], [6], [7], [8].

A possibility to realize bandpass filter is to use resonators, capacitive coupled [9]. If the resonators are based on artificial transmission lines, by using MEMSs or Schottky-varactor diodes, the filter may have tunable characteristics [7].

In this paper, the bandpass filter consisting of MEMS resonators is firstly designed and optimized. They are presented details regarding an accurate design procedure based on an electromagnetic analysis of the MEMS structure. In the second part of this paper, a yield analysis of the filter is performed in order to estimate the influence of the circuit parameters dispersion on the filter characteristics (insertion loss and return loss) due to the technological resolution.

II. FILTER DESIGN

The filter consists of capacitive coupled artificial transmission lines. Each resonator has an equivalent electrical length equals to 180° , at the central frequency of the bandpass filter. In order to change the central frequency of the filter to another value, the transmission line electrical length must be equal to 180° at this new frequency. This aim could be attained if the artificial transmission line is realized by using

voltage controlled capacitors, periodically loading a transmission line. If the capacitive MEMSs are used to model the capacitors, the artificial transmission line is a distributed MEMS transmission line (DMTL).

Fig. 1a shows the schematically representation of the bandpass filter having a symmetric structure, consisting of capacitive coupled DMTLs, while in Fig. 1b, the schematically representation of a DMTL is presented. In Fig. 1b, R_{MEMS} and C_{MEMS} are the equivalent MEMS resistance and capacitance, respectively (C_{MEMS} also includes the effect of the MEMS series inductance), $2l_{CPW}$ is the CPW length which connect two consecutive MEMSs and Δl_i is the CPW length which must be added to the both ends of the i^{th} DMTL, to assure that the DMTL electrical length is equal to 180° at the central frequency of the bandpass filter.

In this paper, a Butterworth filter having the central frequency of 20GHz, the fractional bandwidth of 4% and the attenuation of at least 20dB for frequencies at 0.5GHz outside the frequency passband edges, has been designed and analyzed. The equivalent electrical lengths of each DMTL, θ_i and the coupling capacitances, $C_{i-1,i}$ may be computed using the formulas given in [9]. For this data, the filter consists of 3 DMTLs and 4 coupling capacitors ($\theta_1=163^\circ$, $\theta_2=175^\circ$, $C_{01}=42\text{fF}$ and $C_{12}=7\text{fF}$ – see Fig. 1a). For the DMTLs, imposing the Bragg frequency, $f_B=125\text{GHz}$, as well as the characteristic impedance of the structure, $Z_c=50\Omega$, it is obtained 31fF for the MEMS equivalent capacitance.

The geometry for the capacitive MEMS used in this paper is given in Fig. 2, where W and w_{CPW} are the width of the CPW central line under the MEMS bridge and between two consecutive MEMSs, respectively, s_{CPW} is the distance between the CPW central line and the CPW grounds and w is the bridge width. Using a simple formula [8], the MEMS capacitance of 31fF may be obtained for $w=60\mu\text{m}$, $W=150\mu\text{m}$, $g=2.5\mu\text{m}$, $t_d=0.3\mu\text{m}$. The $[S]$ parameters of the structure shown in Fig. 2 have been obtained by using the

electromagnetic simulator IE3D–Zeland, for the data given in the previous section and for $l_{CPW}=110\mu\text{m}$, $w_{CPW}=50\mu\text{m}$, $s_{CPW}=125\mu\text{m}$ (CPW characteristic impedance $Z_{cl}=82\Omega$), $t=1\mu\text{m}$ (gold), $l_p=100\mu\text{m}$, $\Delta l=5\text{--}10\mu\text{m}$ and three values of g ($2.5\mu\text{m}$, $2\mu\text{m}$ and $1.5\mu\text{m}$). The substrate is silicon (0.4mm thickness and $\epsilon_r=11.7$) of resistivity equals to $6\text{K}\Omega\text{cm}$, covered by $1\mu\text{m}$ SiO_2 layer.

Using these [S] parameters, the values for the lumped components of the MEMS equivalent circuit given in Fig. 3a have been developed, obtaining: $L_{sb}=16\text{pH}$, $R_{sb}=0.055\text{--}0.07\Omega$, $R_{MEMS}=0.1\text{--}0.3\Omega$ and $C_{MEMS}=38,4\text{--}46\text{fF}$ for the bridge displacement between 0 and $1\mu\text{m}$ (practically C_{MEMS} does not depend on the frequency, for frequencies between 15GHz and 25GHz [10]). Also, it may be shown that the bridge displacement of $0.5\mu\text{m}$ and $1\mu\text{m}$ may be obtained for DC voltages of 27V and 32V, respectively (see again [10]).

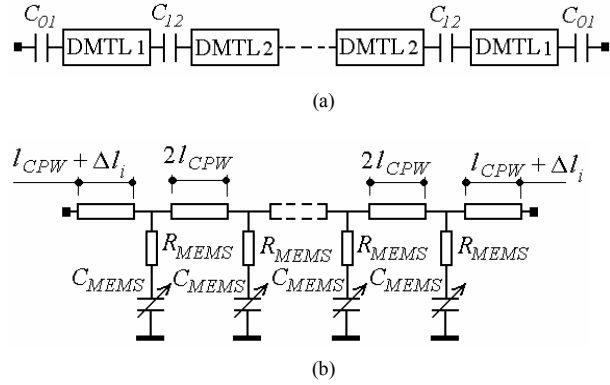


Figure 1. Schematically representation for the capacitive coupled DMTLs bandpass filter (a) and for one DMTL which is part of the filter.

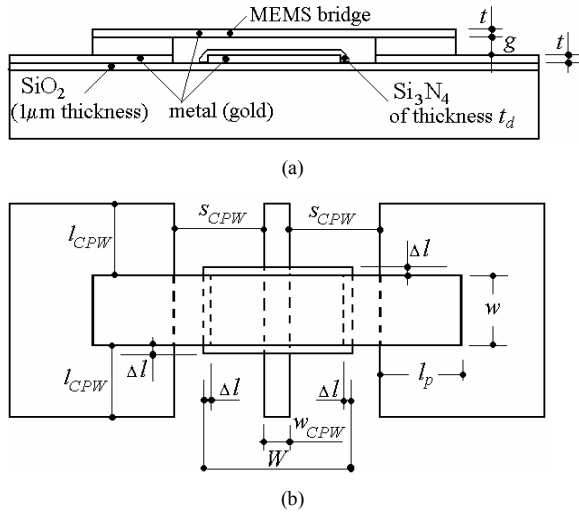


Figure 2. The cross section (a) and the top view (b) of the MEMS structure used in this paper.

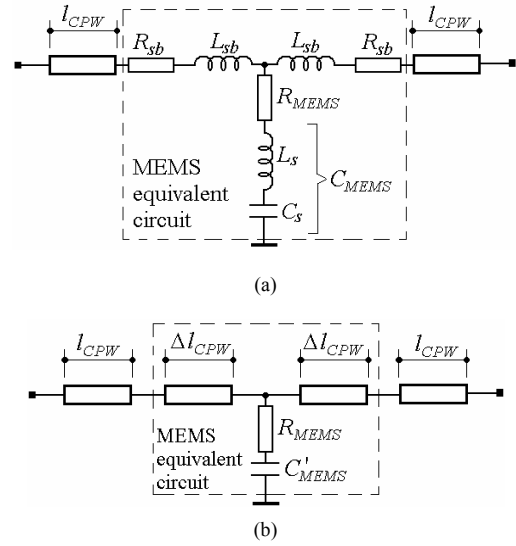


Figure 3. The MEMS equivalent circuits obtained from the [S] parameters computed by using IE3D software, for the structure shown in Fig. 2, using lumped elements only (a) and CPW transmission lines (b).

For the DMTL design, in this paper a cell equivalent circuit as in Fig. 3b was used, where the CPW transmission line of length Δl_{CPW} and characteristic impedance Z_{cl} models the inductance L_{sb} , so C_{MEMS} from Fig.3a is replaced with $C'_{MEMS} = C_{MEMS} - C_{sb}$, where $C_{sb} = \frac{L_{sb}}{Z_{cl}^2}$.

For the analyzed structure, $\Delta l_{CPW}=23\mu\text{m}$. The effect of the series resistance, R_{sb} , may be take into consideration, adjusting the metal thickness of the CPW of length Δl_{CPW} . This equivalent circuit for the DMTL cell was used to design the filter.

The filter DMTLs have been designed for a central frequency of 20GHz and $C_{MEMS}=41\text{fF}$ (bridge displacement of $0.45\mu\text{m}$), computing l_{CPW} and Δl_i , knowing the equivalent electrical length of each resonator, θ_i , given above. They were imposed the characteristic impedance of the

filter, $Z_c = \sqrt{\frac{2L'_{CPW}}{C_{MEMS} - C_{sb} + 2C'_{CPW}}} = 50\Omega$ and the CPW

characteristic impedance, $Z_{cl} = \sqrt{\frac{L'_{CPW}}{C'_{CPW}}} = 82\Omega$ (chosen to

minimize the circuit length as well as the CPW attenuation constant), where L'_{CPW} and C'_{CPW} are the equivalent inductance and capacitance for the CPW of length $l_{CPW} + \Delta l_{CPW}$ (see Fig. 1b). They are obtained $L'_{CPW}=77\text{pH}$, $C'_{CPW}=11\text{fF}$, then $l_{CPW}=88\mu\text{m}$. Therefore, the equivalent electrical length for one DMTL cell is 22° , so the three DMTLs of the filter consist of 7 cells.

The filter has been numerically analyzed and optimized, by using Microwave Office software [11], such as to fit the parameters imposed for the filter. Finally they are obtained: $C_{01}=43\text{fF}$, $C_{12}=7.5\text{fF}$, $l_{CPW}=94\mu\text{m}$, $\Delta l_1=117\mu\text{m}$ – for DMTL1 and $\Delta l_2=257\mu\text{m}$ – for DMTL2 (see Fig. 1b).

In Fig. 4a,b,c, the frequency dependence of S_{11} and S_{21} magnitudes are given, for C_{MEMS} equals to 46fF, 41fF and 38fF, respectively, corresponding to 0, 0.45 μm and 1 μm of bridge displacement. From these figures, it is observed that the central frequency is changed over ~1GHz (from ~19.4GHz to ~20.4GHz). In the filter passband, the insertion loss is ~4dB, while the return loss is higher than 20dB.

The coupling capacitances may be realized as MIM capacitors, using Si_3N_4 as dielectric.

III. YIELD ANALYSIS

The filter characteristics differ significantly before and after optimization, although the filter parameters change slightly during the optimization procedure. But, the variation of the filter parameters may be caused due to the technological resolution which leads to parameters dispersion of the elements which are part of the circuit.

In order to evaluate these technological effects on the filter characteristics, a yield analysis has been performed by using again Microwave Office software, when the central frequency is 20GHz.

For the clarity of the graphical results shown below, the yield analysis has been performed for 10 iterations only. It is easy to verify that these first iterations are very representative, because for a large number of iterations the conclusions are practically the same.

In Fig. 5a,b, the magnitude of S_{11} and S_{21} are shown, taking into account the effect of the technological resolution on the CPW geometry. In Fig. 5a, it was assumed that $w_{CPW}=50\mu\text{m}\pm 5\mu\text{m}$ and $s_{CPW}=125\mu\text{m}\pm 5\mu\text{m}$, while in Fig. 5b, $w_{CPW}=50\mu\text{m}\pm 3\mu\text{m}$ and $s_{CPW}=125\mu\text{m}\pm 3\mu\text{m}$. In the both cases, the insertion loss and the return loss are ~4dB and higher than 20dB, respectively, in the filter passband. Only the central frequency is slightly changed, but this may be fixed by changing C_{MEMS} , adjusting the DC voltage applied on the metal bridges. Therefore, for usual technological resolutions the effect of w_{CPW} and s_{CPW} dispersion is small.

The second yield analysis has been performed for $C_{01}=43\text{fF}\pm 10\%$ and $C_{12}=7.5\text{fF}\pm 10\%$ (see Fig. 6a) and also for $C_{01}=43\text{fF}\pm 5\%$ and $C_{12}=7.5\text{fF}\pm 5\%$ (see Fig. 6b). In this analysis, four independent capacitances have been assumed: two independent capacitances C_{01} and two independent capacitances C_{12} . Again the worst results have been obtained for the return loss, while the insertion loss is ~4dB for dispersion of $\pm 10\%$, as well as $\pm 5\%$. The return loss is greater than 17dB for dispersion of $\pm 5\%$, but it is possible to obtain a value smaller than 15dB for a dispersion of $\pm 10\%$. The results obtained after this yield analysis show

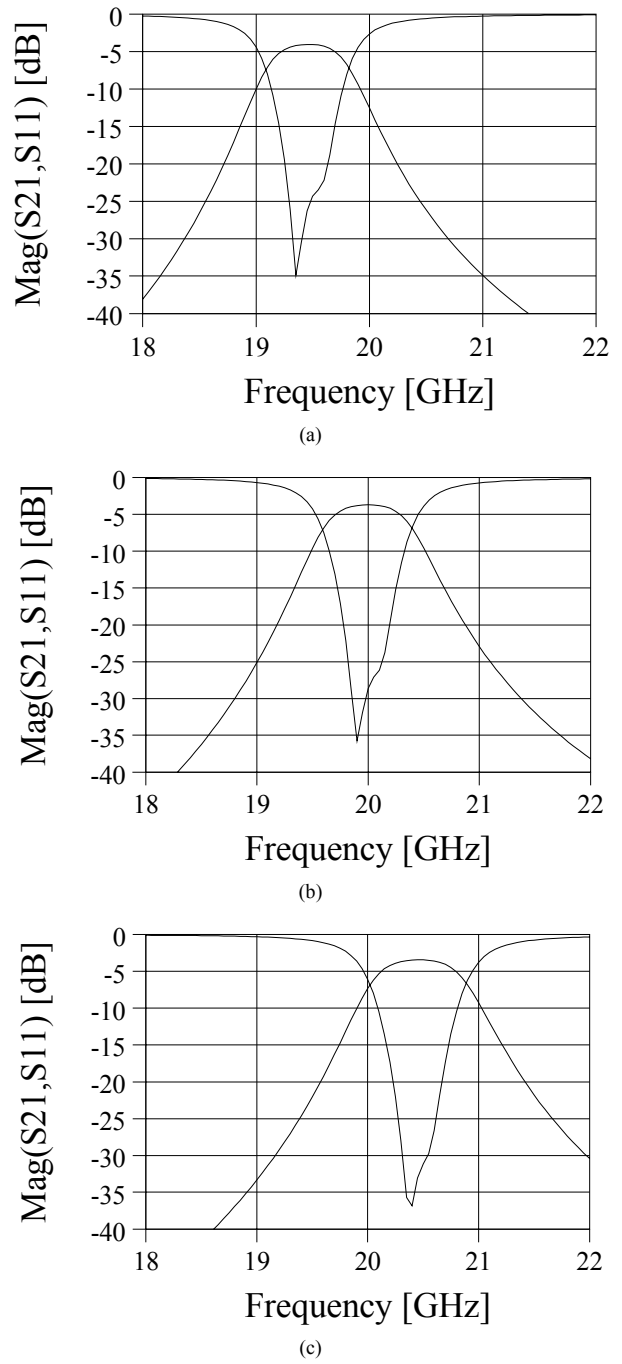
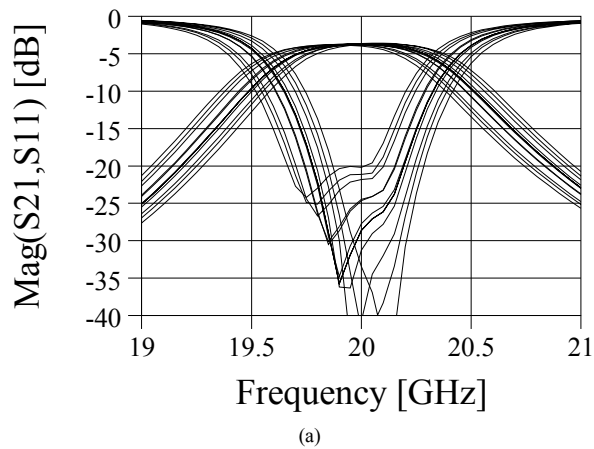
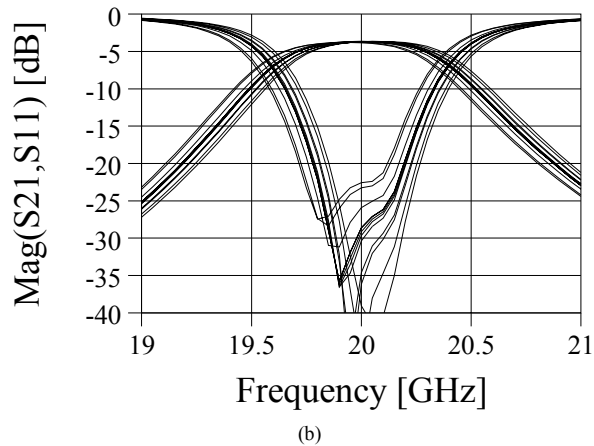


Figure 4. Magnitude of S_{21} and S_{11} in [dB] for C_{MEMS} equal to 46fF (a) 41fF (b) and 38fF (c).

that for dispersion of C_{01} and C_{12} less than $\pm 10\%$, the insertion loss is weakly affected and the return loss is good for the most application requirements. Taking into account that C_{01} and C_{12} are MIM capacitors, a maximum dispersion of $\pm 10\%$ means a technological resolution better than 5 μm .



(a)

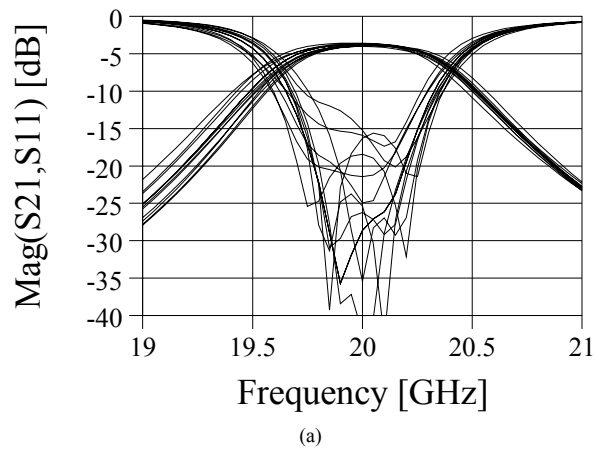


(b)

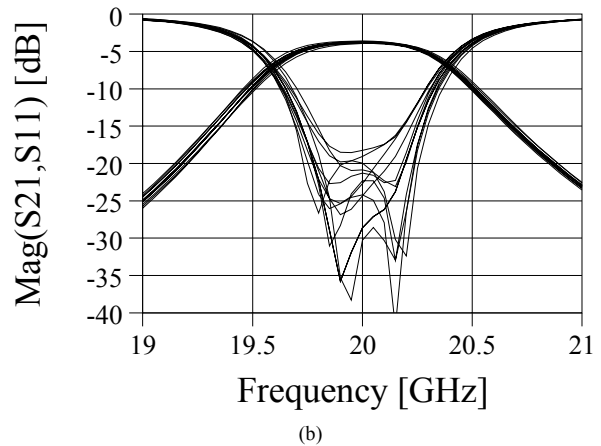
Figure 5. Magnitude of S_{21} and S_{11} in [dB] when w and s have a technological resolution of $\pm 5\mu\text{m}$ (a) and $\pm 3\mu\text{m}$ (b), around the nominal values of $50\mu\text{m}$ and $125\mu\text{m}$, respectively.

The last yield analysis has been performed assuming that the dispersion of the MEMS capacitances is $\pm 10\%$ (see Fig. 7a) and $\pm 5\%$ (see Fig. 7b), considering that the all 21 MEMS have independent values. In this case, again the insertion loss is $\sim 4\text{dB}$. The return loss has the smallest value compare to the results obtained in the previous analyses. From Fig. 7a,b, it is observed that for a dispersion of the MEMS capacitances of $\pm 10\%$, which means a technological resolution of $\sim 5\mu\text{m}$, the return loss could be less than 10dB , while for a dispersion of $\pm 5\%$, which means a technological resolution of $\sim 3\mu\text{m}$, the return loss could be less than 15dB . Therefore, a good return loss for the most practical purposes may be obtained for technological resolution better than $5\mu\text{m}$.

In the all yield analyses performed and presented above, the technological resolution referred to the wrong alignment of the successive process masks. Other important technological factor which may affect the circuit performances is the thickness of the Si_3N_4 layer. If this factor is taken into consideration, it may be shown that the technological resolution must be better with the same percentage as the



(a)



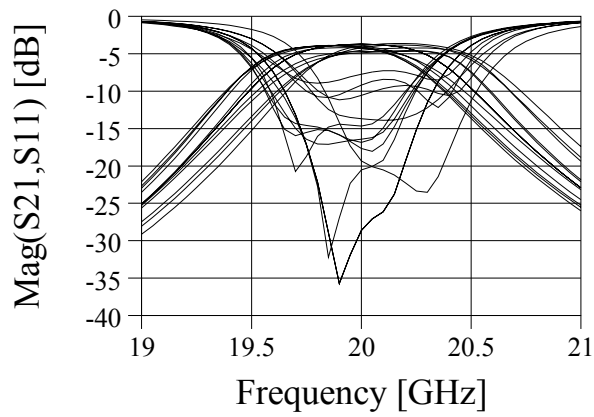
(b)

Figure 6. Magnitude of S_{21} and S_{11} in [dB] when C_{01} and C_{12} have a technological dispersion of $\pm 10\%$ (a) and $\pm 5\%$ (b), around the nominal values of 43fF and 7.5fF , respectively.

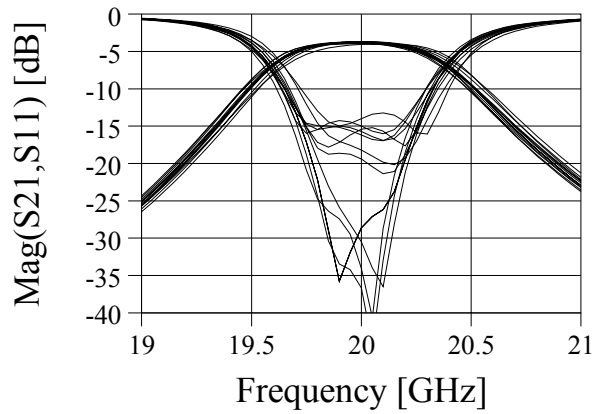
Si_3N_4 thickness is changed over the wafer, given also in percentage variation.

IV. CONCLUSION

In this paper, a filter consisting of a distributed transmission lines capacitive coupled has been designed, optimized and finally yield analyzed. The design procedure is based on an accurate equivalent circuit developed taking into account the electromagnetic analysis results, performed on the MEMS structure, by using the IE3D-Zeland software. The filter has been analyzed and optimized by using the Microwave Office software. The optimization is necessary, but the difference between the values of the filter parameters before and after optimization was small. Therefore, a filter analysis taking into account the technological resolution must be performed before the technological implementation of the filter. For this aim, a yield analysis of the filter has been performed by using again the Microwave Office software. The analysis results show that for usual parameter dispersion, the insertion loss is not changed significantly, but the return loss



(a)



(b)

Figure 7. Magnitude of S_{21} and S_{11} in [dB] when C_{MEMS} 's have a technological dispersion of $\pm 10\%$ (a) and $\pm 5\%$ (b), around the nominal values of 41fF.

shows an important changed, especially when the dispersion increases the difference between the MEMS capacitance values.

ACKNOWLEDGMENT

S. Simion thanks to Institute of Microtechnology – Bucharest, for its support in the frame of MATNANTECH national research program.

REFERENCES

- [1] J. Rizk, G. L. Tan, J. B. Muldavin, G. M. Rebeiz, "High-isolation W-band MEMS switches", IEEE Microwave and Guided Wave Letters, vol. 11, pp. 10-12, January 2001.
- [2] J. S. Hayden, G. M. Rebeiz, "Low-loss cascable MEMS distributed X-band phase shifters", IEEE Microwave and Guided Wave Letters, vol. 10, pp. 142-144, April 2000.
- [3] N. S. Barker, G. M. Rebeiz, "Distributed MEMS transmission-line BPSK modulator", IEEE Microwave and Guided Wave Letters, vol. 10, pp.198-200, May 2000.
- [4] K. Entesari, G. M. Rebeiz, "A differential 4-bit 6.5-10-GHz RF MEMS tunable filter", IEEE Transaction on Microwave Theory and Techniques, vol. 53, pp. 1103-1110, March 2005.
- [5] K. Entesari, G. M. Rebeiz, "A 12-18-GHz three pole RF MEMS tunable filter", IEEE Transaction on Microwave Theory and Techniques, vol. 53, pp. 2566-2571, August 2005.
- [6] A. A. Tamijani, L. Dusopt, G. M. Rebeiz, "Miniature and tunable filters using MEMS capacitors", IEEE Transaction on Microwave Theory and Techniques, vol. 51, pp. 1878-1885, July 2003.
- [7] Y. Liu, A. Borgioli, A. Nagra, R. York, "Distributed MEMS transmission lines for tunable filter applications", John Wiley & Sons, Inc., pp. 254-260, 2001.
- [8] G. M. Rebeiz, "RF MEMS: theory, design and technology", John Wiley & Sons Inc., 2003.
- [9] G. L. Matthaei, L. Young, E. M. T. Jones, "Microwave filters, impedance-matching networks and coupling structures", Artech House, Inc., 1980.
- [10] S. Simion, "Design and analysis of tunable bandpass filter consisting of distributed MEMS transmission lines", Proc. of the IEEE Int. Semiconductor Conf. - CAS2005, Sinaia, Romania, pp.111-114, 2005.
- [11] Microwave Office 2001 – Applied Wave Research, Inc.

A 76 GHz Folded Reflector Antenna for True Ground Speed Measurement

Andreas Hantsch¹, Wolfgang Menzel²

¹Robert Bosch GmbH, Department CR/ARE1, Robert-Bosch-Platz 1, 70839 Gerlingen, Germany, andreas.hantsch@gmx.net

²University of Ulm, Department of Microwave Techniques, Albert-Einstein-Allee 41, 89081 Ulm, Germany, wolfgang.menzel@ieee.org

Abstract—A 76 GHz multibeam folded reflector antenna for true ground speed measurement applications is presented. The antenna radiates four independent beams with 30° radiation angle. Antenna far and near field measurement results are given. 3dB-width of the antenna beams is between 3.2° and 3.9°. The antenna was used in a continuous wave doppler radar sensor. Results of the measured velocity and slip angle during a counterclockwise circular driving are presented.

I. INTRODUCTION

Radar sensors for automotive applications have become of great interest during the last years. Especially sensors in the 24 and 76 GHz bands for applications like adaptive cruise control, parking aid and lane change assistants have been investigated thoroughly. Some of them are commercially available, whereas others are still in research and development.

Another application that is of high importance is true ground speed measurement of vehicles. Driver assistance systems like the electronic stability program, the antilock braking system or the traction control system depend on the exact knowledge of the state of vehicle movement. It is characterized as shown in Fig. 1 by its speed vector v and yaw rate $\dot{\psi}$. The side slip angle β is defined as the angle between speed vector v and the longitudinal axis of the vehicle. It is very important in vehicle stability considerations. However, at the moment, only the yaw rate can be measured directly at reasonable costs in series vehicles. Longitudinal speed is measured by using wheel speed sensors. Unfortunately they suffer from uncertainties when the wheels are blocking or skidding or when the size of the wheel changes. The side slip angle is not measured at all.

Radar sensors that measure only longitudinal true ground speed have been investigated by numerous authors [1]–[7]. Such sensors are commercially available as reference measurement systems for vehicle tests or for special applications e.g. in agricultural machinery. For cost reasons they usually work in the 24 GHz frequency band.

Radar sensors that are additionally capable of measuring side slip angle are not available commercially. Some research has been done by a few authors [2], [4]–[7], but limited accuracy and high costs have prevented these sensors to be commercially successful.

In this paper we present a 76 GHz antenna arrangement for true ground speed and side slip angle measurement radar

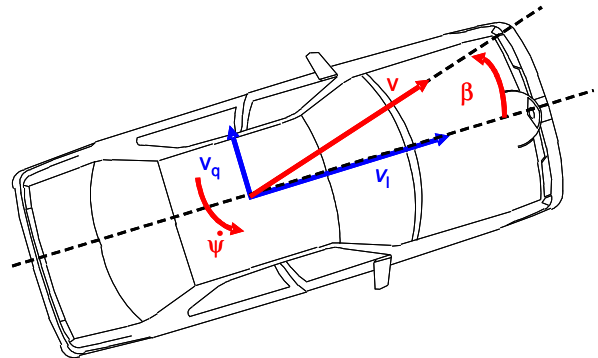


Fig. 1. Velocity and side slip angle of an automobile.

sensors. It is very compact and manufacturable at potentially low costs.

II. RADAR SENSOR TOPOLOGY

Speed measurement by means of radar is done by radiating an electromagnetic wave towards the road and measuring the doppler-shift of the backscattered wave. The basic principle is shown in Fig. 2. The doppler-shift f_d can be calculated by

$$f_d = 2 \frac{f_0}{c_0} \sin \theta (v_x \cos \varphi + v_y \sin \varphi) \quad , \quad (1)$$

where f_0 is the frequency of the radiated wave, c_0 is the speed of light, v_x and v_y are the speed vector components and θ and φ are the radiation angles in elevation and azimuth. The vertical speed v_z is assumed to be zero. In order to measure the speed vector two orthogonal beams are needed. If, in addition, one wants to compensate for nick or roll angles of the sensor, two more beams are advantageous [4]–[7]. The sensor topology with four beams is shown in Fig. 3.

Radiating four beams can be done in several ways. It is most obvious to use four independent antennas. However, this needs much space and alignment of the antennas might be difficult. Other possibilities are using bifocal lens [6], [7] or leaky wave antennas [2], [4]. In this paper we propose to use a bifocal folded reflector antenna [8]. This kind of antenna is very compact to build, has very low losses and is easy to manufacture. As we will show below, it has the ability to radiate four beams with only one physical aperture.

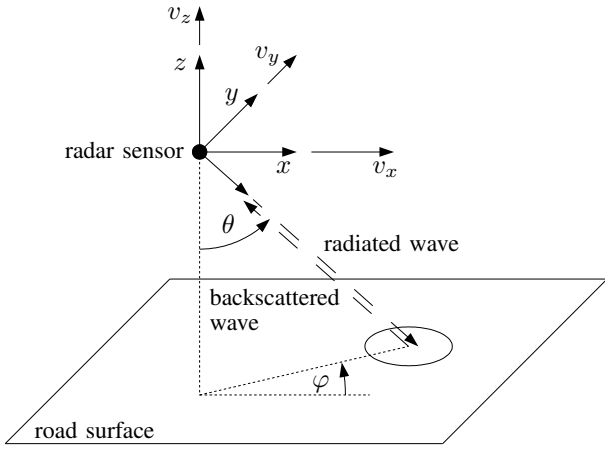


Fig. 2. Basic principle of radar ground speed measurement.

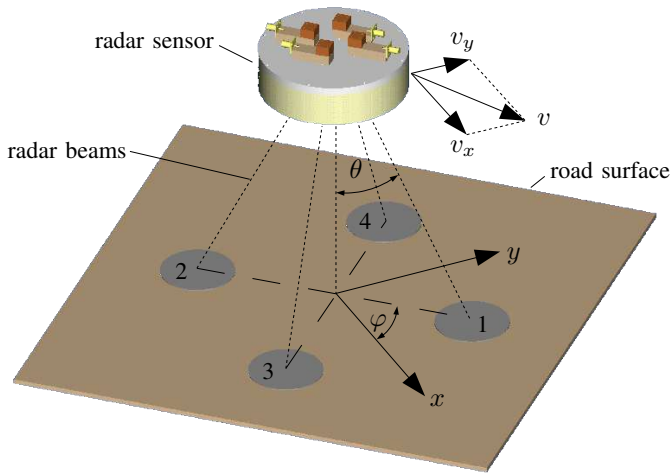


Fig. 3. Radar sensor topology.

III. ANTENNA DESIGN

The basic principle of the bifocal folded reflector antenna can be found in [8]. Fig. 4 depicts the cross section of the antenna that was realized. It mainly consists of two parallel reflect-arrays and four circular waveguide feeds. The feed waveguides with horn openings are inserted into an alloy mounting plate. The RF energy is radiated from the horn to the upper reflector. There it is reflected by the polarizing grid and phase shifted by patches printed on the reflector. The wave then propagates to the lower reflector where it is once again reflected and phase shifted. Additionally, the polarization is twisted by 90° . Finally, due to the twisted polarization, the wave can pass the polarizing grid. As outlined in [8] the phase shifting on both reflectors controls the focus points and the radiation characteristics. The phase shifting on both reflectors of the antenna is symmetric with respect to the midpoint. Thus, it is possible to radiate similar beams from all four feed points.

The realized antenna has an outer diameter of 150mm, a distance between the two reflectors of 35mm and four feed

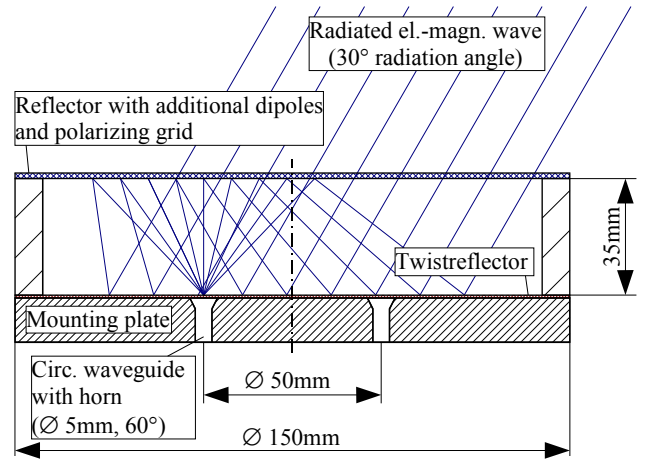


Fig. 4. Functional principle of 4-beam folded reflector antenna (antenna cross section).

points on a circle with a radius of 25mm. The reflector diameter is 120mm. However, as can be seen from Fig. 4, not the entire aperture can be used for each beam. The large tilting angle of 30° leads to shadowing effects at the wall and limitations in phase shifting properties. Thus the effective aperture is somewhat smaller than the physical aperture. A photograph of the antenna can be seen in Fig. 5.

IV. ANTENNA MEASUREMENT RESULTS

A. Far Field Measurements

Radiation diagrams have been measured at 76.5 GHz for each port in two planes (E-Plane and H-Plane). Results of Port 1 and 2 are shown in Fig. 6. Beams are radiated at an angle of 30° in one plane and 0° in the other plane. 3dB-beamwidths are between 3.2° and 3.9° and side lobe level is around -14dB. Port 3 and 4 show similar characteristics.

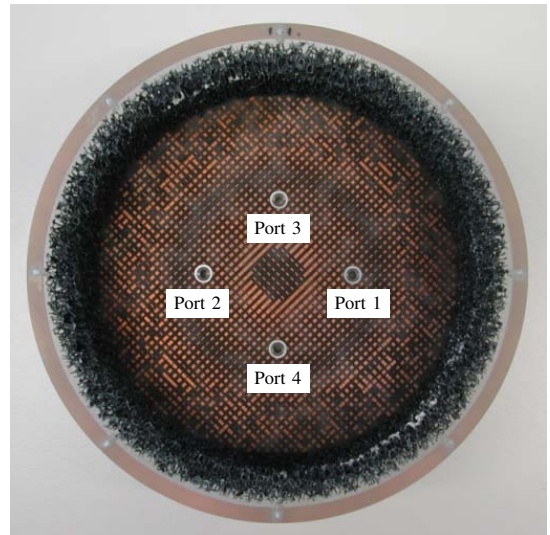


Fig. 5. Photograph of the 4-beam folded reflector antenna (upper reflector removed).

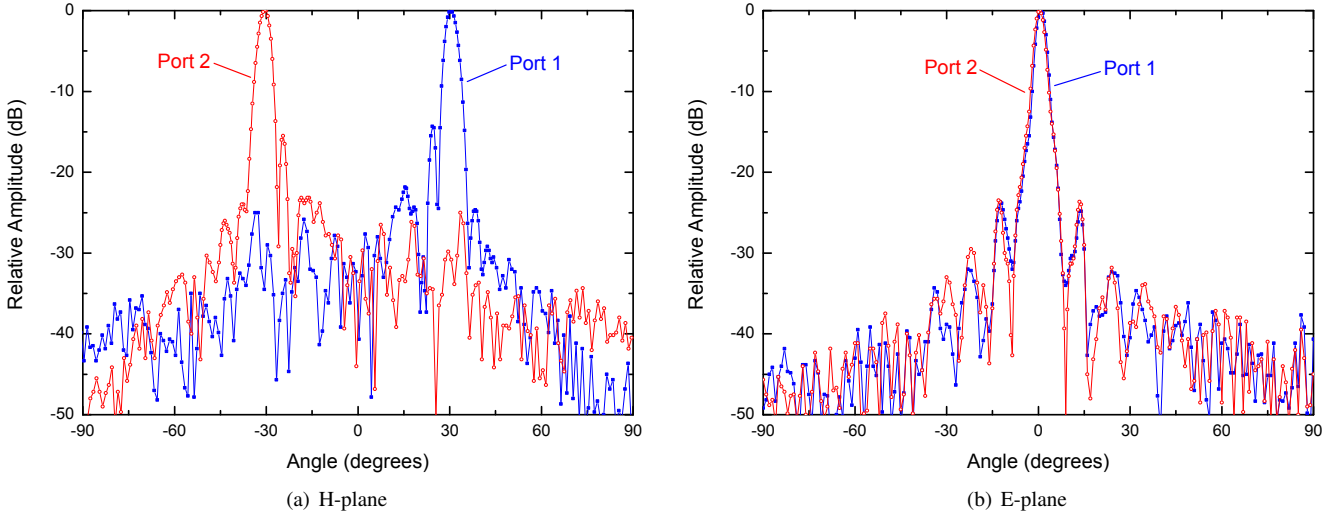


Fig. 6. Measured H- and E-plane radiation diagrams (76.5 GHz, Port 1 and 2, 3dB-beamwidths: $3.9^\circ/3.9^\circ$ resp. $3.2^\circ/3.3^\circ$)

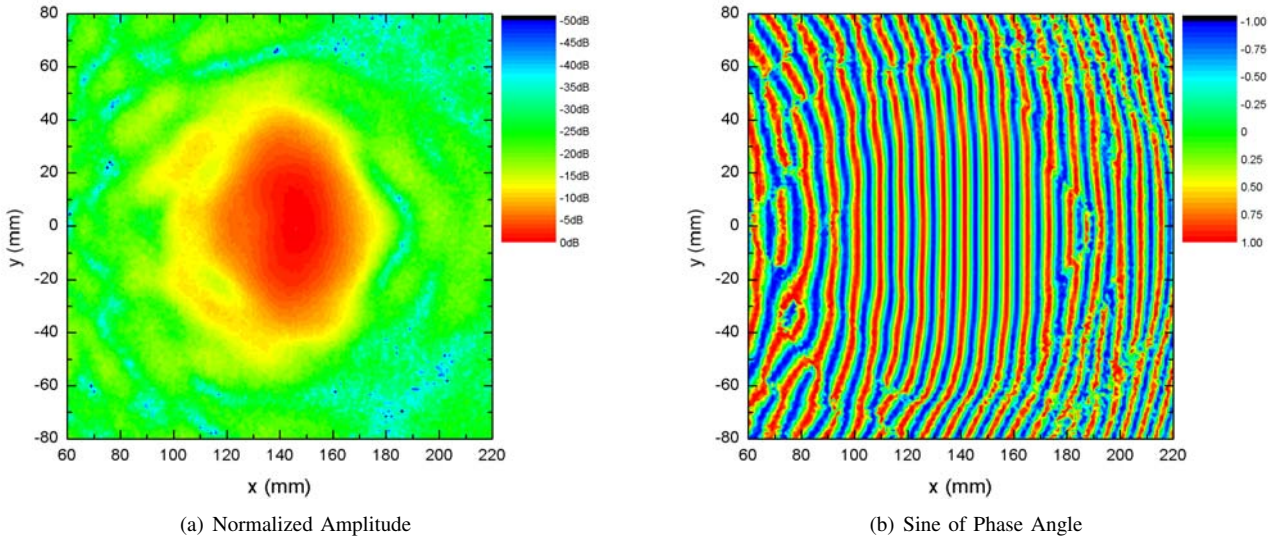


Fig. 7. Measured near field amplitude and phase characteristics (76.5GHz, RF input at port 1, other ports left open, 25cm distance between twistreflector and measurement plane, (160×160) mm² area, data points measured every 1mm in x- and 1.04mm in y-direction)

B. Near Field Measurements

Although far field measurements are rather important for antenna characterization and verification, they are not very representative for the desired application of the antenna as a ground speed sensor. More insight into the characteristics as a speed sensor is gained by measuring the field properties on a plane parallel to the antenna aperture. This plane represents the road surface where the radiated field of the antenna is incident when used as a true ground speed sensor. Both components, amplitude and phase, of the field need to be measured. Fig. 7 shows the near field characteristics of Port 1 measured at 76.5GHz on a plane in a distance of 25cm to the twist-reflector of the antenna. The antenna was moved in steps of 1mm

in x-direction and 1.04mm in y-direction using a xy-linear table. An open waveguide was used as illuminating antenna. The amplitude characteristic shows an elliptical spot on the measurement plane. Within this spot, the phase characteristic is close to a plane wave characteristic. The phase fronts consist of evenly spaced almost straight lines. This is important in order to get a small spectrum of the doppler signal for accurate speed measurements. Measurements of the other ports show similar results.

V. TRUE GROUND SPEED MEASUREMENT

The antenna was used in a continuous wave doppler radar sensor for true ground speed measurement. It was mounted at

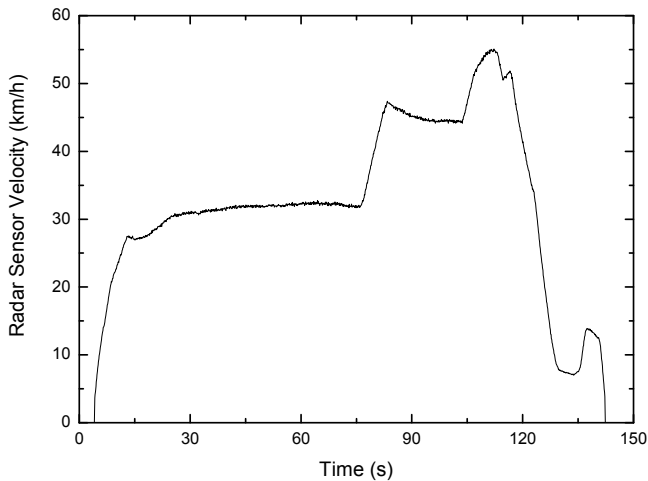


Fig. 8. Measured absolute velocity at sensor position (counterclockwise circular driving, 100ms measurement-time)

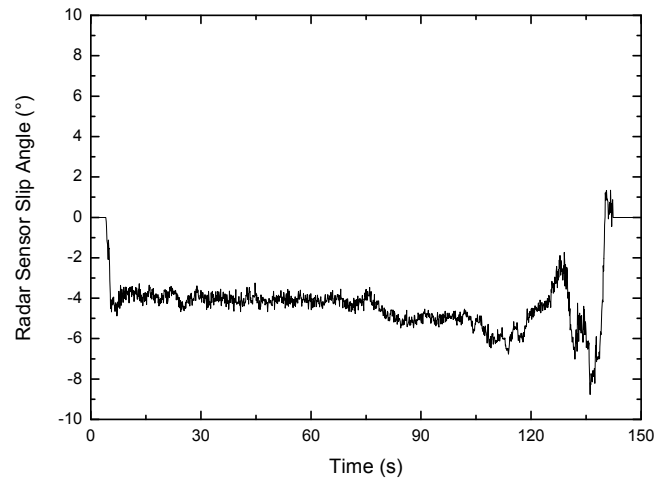


Fig. 9. Measured slip angle at sensor position (counterclockwise circular driving, 100ms measurement-time)

the rear bumper of a car and driving tests have been performed. Fig. 8 and 9 show the measured velocity and slip angle of the car at the sensor position. In order to get the side slip angle β one would need to transform those values to the center of mass by using the yaw rate $\dot{\psi}$ and the sensor position. Also, a compensation for an inaccurate mounting angle of the sensor would be needed. The measured velocity shows the variations in vehicle speed very clearly. After an acceleration to about 30km/h the speed was kept constant while driving counterclockwise on a circular course with 30m radius. The measured slip angle during this phase is about -4° . Later, the speed was increased to about 45km/h, still driving on the same circular course. The slip angle changes to about -5° . When the speed is increased even further to about 55km/h, the slip angle increases to approximately -6° . During the last phase the speed is decreased. The slip angle decreases accordingly. The following increase in slip angle is due to leaving the circular course by driving a sharp curve. It has to be noted that the measured slip angle shows very little variation due to measurement noise. Depending on the speed of the vehicle the standard deviation of the slip angle is in the range of 0.1° to 0.2° .

VI. CONCLUSION

A 76 GHz folded reflector antenna with 4 beams and 30° radiation angle has been presented. The antenna employs a bifocal principle to radiate 4 independent beams with only one physical aperture. It has a very compact size and it can be manufactured very easily. 3dB beamwidths between 3.2° and 3.9° for the four lobes have been demonstrated. Near field

measurements have shown the incident field properties on the road, when the antenna is used for true ground speed radar sensors. Road tests have shown the potential of the antenna for accurate true ground speed and slip angle measurements.

ACKNOWLEDGMENT

The authors would like to thank Dr. Frank Bögelsack of the University of Ulm, Department of Microwave Techniques for assisting with near field measurements and Hardy Haas and Dr. Martin Sackmann of Robert Bosch GmbH, Department CR/AEV2 for proving a test vehicle and performing road tests.

REFERENCES

- [1] T. M. Hyltin, T. D. Fuchser, H. B. Tyson, W. R. Regueiro, *Vehicular Radar Speedometer*, SAE International Automotive Engineering Congress and Exposition, 730125, January 1973.
- [2] N. Kees, M. Weinberger, J. Detlefsen, *Doppler measurement of lateral and longitudinal velocity for automobiles at millimeterwaves*, IEEE MTT-S International Microwave Symposium Digest, vol. 2, pp. 805-808, June 1993.
- [3] M. Weinberger, *Eigengeschwindigkeitsmessung für Kraftfahrzeuge mit dem Doppler-Effekt im Millimeterwellen-Bereich*, Ph.D. Thesis, Technische Universität München, 1993.
- [4] N. Kees, *Kraftfahrzeugsensoren zur Eigengeschwindigkeitsmessung, Navigation und Fahrbahnzustandserkennung*, Ph.D. Thesis, Technische Universität München, 1995.
- [5] H. Laqua, *Berührungslose Geschwindigkeitsmessung von Straßen- und Schienenfahrzeugen mit Mikrowellensensoren*, Ph.D. Thesis, Universität Fridericiana Karlsruhe, 1995.
- [6] R. H. Rasshofer, E. M. Biebl, *A Low Cost W-Band Multi-Beam Doppler Radar for Automotive Applications*, IEEE MTT-S International Microwave Symposium Digest, vol. 2, pp. 971-974, June 1997.
- [7] R. H. Rasshofer, *Radarsensoren mit aktiven, integrierten Millimeterwellenantennen*, Ph.D. Thesis, Technische Universität München, 1999.
- [8] W. Menzel, M. Al-Tikriti, R. Leberer, *A 76 GHz multiple-beam planar reflector antenna*, European Microwave Conference, Milan, 2002.

Accelerated Curing of Adhesive with Microwave

Rudolf Emmerich¹, Matthias Graf¹, Wenzel Krause¹, Frank Henning¹, Patrick Kölzer²

¹Fraunhofer Institut für Chemische Technologie, Joseph-von-Fraunhofer-Str.7,
D-76327 Pfinztal, Germany +49 (0) 721 4640 0, rem@ict.fraunhofer.de

²Fraunhofer Institut Produktionstechnologie, Steinbachstraße 17 D-52074 Aachen, Germany

Short Abstract—A new process for non-fusion adhesive bonding of polymers with each other is presented. The adhesive is heated with microwave, that reduce the curing time to a scale that the non-fusion adhesive bonding can integrated in a process line. (Abstract)

Microwave; non-fusion adhesive bonding; polymer; curing;

I. INTRODUCTION

The use of light weight parts in automotive industry and aerospace industry leads more and more to the combination of dissimilar materials. These parts take over supporting properties. For the joining of the materials smart technologies are demanded, which the benefits of the materials combinations ensure without destroying the properties of the individual part. Therefore joining materials is a key global technology. The article concerns the joining thermoplastic materials with each other. In particular the car industry uses more and more pre-assembled modules for front end or door panels in which dissimilar polymeric material are combined. For these modules for example an automated joining technology has to be available.

There are several joining technologies used for this task. There are mechanical based fixing systems like screws, combination of metal and polymeric in form of a hybrid part, adapting elements, inserts and so on.

Another is the non-fusion adhesive bonding of similar or varying materials. Contemporary industries, in particular aerospace, automotive and construction industry, are required to join a wide variety of dissimilar materials. As adhesives solvent based materials like Polyurethane or Epoxy solution adhesives are mostly used. The advantages of adhesive bonding are:

- Dissimilar materials may be joined.
- Large variations in work thickness are permissible.
- Work temperatures are low, thus maintaining the parent material physical properties and eliminating thermal distortion.
- Many adhesives have elastic properties allowing flexibility within the joint.

- Adhesives may have liquid and gas sealing properties.

The disadvantages are:

- Labour intensive process in respect of joint and adhesive preparation processes making automation difficult.
- Poor production cycle times making process uncompetitive.

In this paper a new technology for accelerating curing of adhesives with microwaves are presented.

II. MATERIAL ASPECTS

In the project is used a Polyurethane (PUR) solution adhesive. This adhesive is applied for thick-film adhesive bonding in combination of polymer and metal or polymer and polymer. To develop a microwave curing process the information of the dielectric function of this adhesive as a function of temperature is necessary. This data was measured in a resonant cavity at a frequency [1] of 2.45GHz [Fig.1].



Figure 1: Resonant cavity to measure the dielectric function of the adhesive

The determination of the dielectric function from the measurement data is given by the well-known equations:

$$(1) \quad \varepsilon' = 1 + \frac{V_c}{2V_s} \frac{f_c - f_s}{f_s} \quad \varepsilon'' = \frac{V_c}{4V_s} \left(\frac{1}{Q_s} - \frac{1}{Q_c} \right)$$

Resonance frequency f_c of the empty cavity, resonance frequency f_s of the filled cavity, quality Q_c of the empty cavity, quality Q_s of the filled cavity, volume V_c of the cavity, volume V_s of the sample.

The result of this measurement as a function of temperature is shown in Fig. 2.

- : Real part of the dielectric function
- ▲: Imaginary part of the dielectric function.

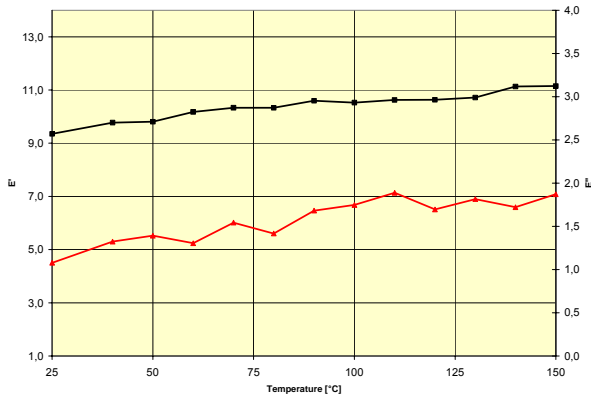


Figure 2: Dielectric function of the adhesive

The adhesive is a good microwave absorbing material. The real part and the imaginary part of the dielectric function increases with increasing temperature. The dielectric loss levels to a constant value of about 1.8 over a temperature of about 100°C that indicates that the adhesive starts cross-linking at 100°C.

The polymer substrates are made of Polypropylene (PP) and Polycarbonate (PC). Polypropylene is a non polar material and is transparent for microwave. Polycarbonate absorbs microwave only little, and the resulting temperature does not exceed for the material any critical temperature.

III. NUMERICAL SIMULATION OF THE MICROWAVE FIELD

A common and powerful tool for the determination of the electromagnetic field distribution in complex geometries with variable shapes and inhomogeneous media is numerical simulation using FEM. For the introduced calculations the software tool FEMLAB 3.0a (COMSOL AB, Sweden) was used, which is an advanced, more general software package for numerical modelling and simulation. The solution of Maxwell's equations is supported by an "Electromagnetic Module" with various application modes.

For a harmonically oscillating electric field at 2.45 GHz Maxwell's Equations can be combined to the wave equation

$$(2) \quad \nabla \times \left(\frac{1}{\mu_r} \nabla \times \vec{E}_0 \right) - \varepsilon_0 \mu_0 \omega^2 \left(\varepsilon_r - \frac{i\sigma}{\omega \varepsilon_0} \right) \vec{E}_0 = \vec{0}$$

using the relative permeability μ_r , electric field \vec{E}_0 , permeability of vacuum ε_0 , permittivity of vacuum μ_0 , frequency of the electromagnetic field f , angular frequency $\omega = 2\pi f$, relative permittivity ε_r and electric conductivity σ .

This equation was solved by FEMLAB [4] in a region of interest which is bordered by some simple boundaries. For more qualitative studies metallic surfaces can be considered as perfect electric conducting:

$$(3) \quad \vec{n} \times \vec{E} = 0$$

using the surface normal vector \vec{n} .

For the technical realization a slot antenna is selected. The design and the principle set-up are given in Figure 3. In the slot antenna two holes are drilled for the use of an IR detector, which measures the temperature of the adhesive through the slot.

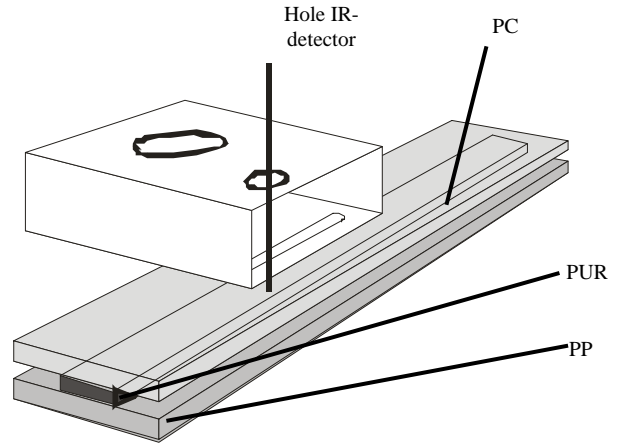


Figure 3: Design of the slot antenna

The simulation is performed for this geometry. The electrical field for the set-up is shown in Figure 4. It has its highest values at the slot of the antenna. The resulting heating occurs completely in the PUR adhesive (Fig. 5). There is a well-defined heating spot in the adhesive. The substrates Polypropylene and Polycarbonate stay cold.

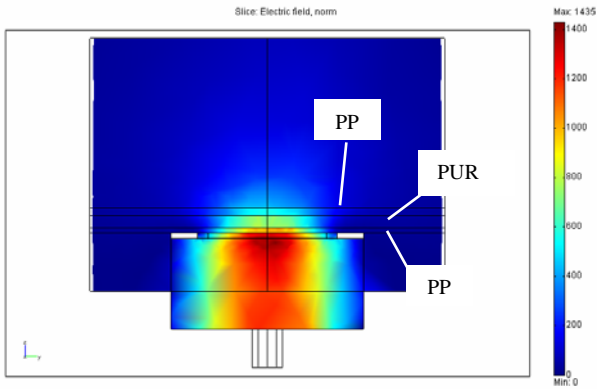


Figure 4: Electrical field

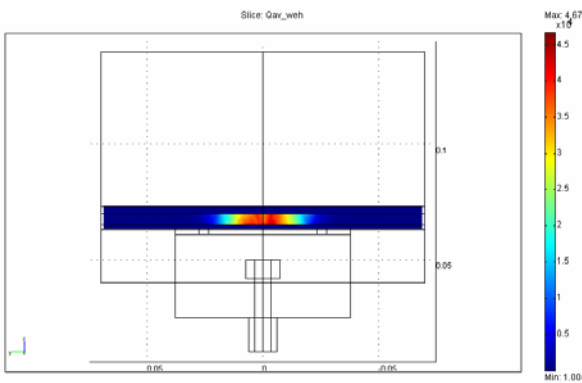


Figure 5: Resistive heating

IV. TECHNICAL REALIZATIONS

In Fig. 6 the principle set-up is given of the lab machine for accelerating curing with microwaves for a head lamp.

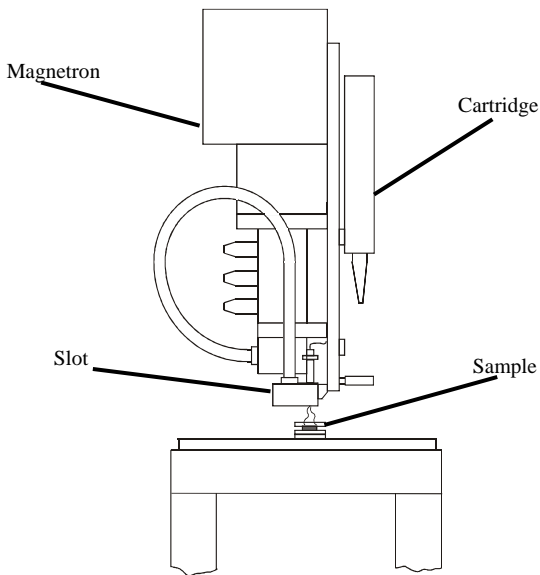


Figure 6: Principle set-up

The adhesive is applied to the sample with a cartridge. The microwave is applied with a slot antenna to the sample. The adhesive absorbs microwave and is heated up. Through the slot antenna the temperature of adhesive during microwave radiation is measured. The temperature signal is used to control the microwave power.

In Figure 7 a photo of the set-up is shown. The head-lamp housing consists of a transparent Polycarbonate pane and a black Polypropylene body. Between these two parts the Polyurethane solution adhesive is applied. Then the two parts are put together and placed in a retainer.

The microwave radiator is fixed on portal crane. The portal crane can move in three axes so it can trace the contour of the head lamp housing. After the head-lamp housing is placed in the retainer the microwave radiation starts and the portal crane begins to move. Six positions at the glue line are heated with microwave and there the curing is accelerated. The microwave radiation time cycle time is about 10s to reach a handling stability of the adhesive. Six positions are chosen at the contour of the head lamp, so that the total radiation time is 60s. Times for move of the portal crane to each position is also 10s. The total cycle time is therefore 120s.

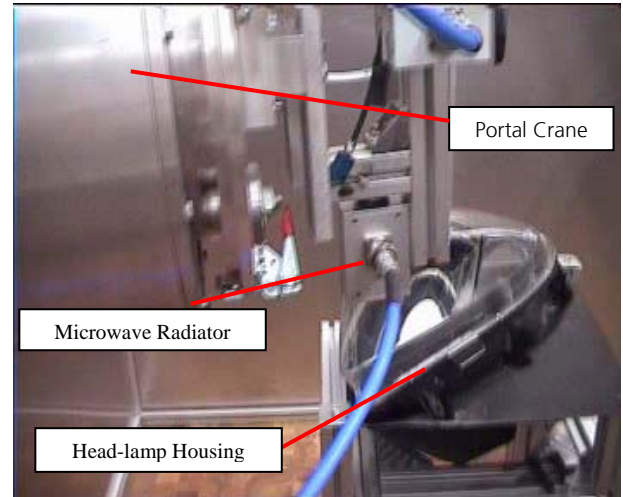


Figure 7: Lab machine for accelerating curing with microwaves.

The whole lab-machine is housed in metallic cage to protect the environment for leakage radiation.

Figure 8 shows the cured adhesive of the processed head lamp in detail. The Polycarbonate and the Polypropylene are not influenced by the microwave radiation. The adhesive is properly cured without thermal damage.



Figure 8: Processed part of the head lamp

V. CONCLUSION

In the project a new lab-machine and process for accelerated curing of adhesives is developed. It is shown, that the cycle time of Polyurethane solution adhesive can be reduced about 90%. This cycle time is short enough to put the microwave curing in the production line. The rest of the adhesive in the glue line will cure at room temperature in circa 5min. The

cycle time can easily more reduced with the help of more than one slot antenna, which is fixed on the portal crane. The head-lamp housing in particular the Polycarbonate pane is not affected by microwaves.

ACKNOWLEDGMENT

The authors wish to thank the Fraunhofer Gesellschaft for its financial support.

REFERENCES

- [1] A. C. Metaxas; R. J. Meredith, "Industrial microwave heating." Peter Peregrinus Ltd., London (1983)
- [2] FEMLAB Electromagnetics Module User's Guide, COMSOL AB, 2004
- [3] R. Emmerich, P. Kölzer, „Mikrowellenunterstütztes Verkleben dargestellt am Demonstratorbeispiel Scheinwerfergehäuse“, Workshop Simulation und Fügetechnik langfaserverstärkter Thermoplaste, March 2005, Pfinztal

Effects of Water and Ice Layer on Automotive Radar

Alebel Arage¹, Wolf M. Steffens¹, Goetz Kuehnle¹, Rolf Jakoby²

¹Robert Bosch GmbH, Automotive Electronics - Driver Assistance / Development Long Range Radar, Daimlerstrasse 6, D-71229 Leonberg, Germany, (+49)711/811-47434, alebel.arage@de.bosch.com

²Technische Universität of Darmstadt, Institute of Microwave Engineering, Merckstrasse 25, D-64283 Darmstadt, Germany, (+49)6151/16-4893, jakoby@hf.tu-darmstadt.de

Short Abstract—This experiment is carried out at the Robert Bosch GmbH, to analyse the signal degradation of millimeter wave radar Sensors in adverse weather conditions. It reveals that, the existence of water layer on the surface of antenna lens or its radome is the main cause for performance limitation of automotive radar sensors and provides information to identify such phenomena.

Keywords—Electromagnetic radiation effects; Millimeter wave radare; Road vehicle radar

I. INTRODUCTION

Automotive radar sensors, which fundamentally use millimeter wave signals, increasingly become one of the important comfort and collision mitigation products in the automotive market. Their performance may be affected by wetness due to adverse weather conditions unless proper antenna lens or radome design is used. The extension of automotive radar sensors from comfort to safety systems may further require intelligent features, such as detection of weather phenomena and performance controlling during adverse weather conditions. Hence, this work examines effects of water and ice on the millimeter radar performance and methods to identify such phenomena.

The wetness of antenna lens or radome surface generally affects electromagnetic wave propagation at higher frequencies and causes a considerable loss. Several studies of microwave propagation have already shown that this loss contributes a significant amount to the attenuation due to rain [1-3].

This paper presents the theoretical analysis and the measurement results of the losses due to water as well as ice layer on the surface of radome, to explore the possibility of developing a method for detecting partial or total degradation of automotive radar sensors by rainy and snowy weather conditions. Primarily it deals with losses due to water layer on the surface of radome and illustrates their dependency on the frequency, the water layer thickness and the polarization. To study these losses, the standard theoretical analysis “Fresnel formula for reflection and transmission” has been applied on multilayer wave propagation model [4, 6].

These theoretical results have been already compared with measurements, in particular for 76.5 GHz band, and they confirm limitations on automotive long range radar application during rainy and snowy weather conditions. On the other hand, ice layer on the surface of dielectric radome because of

its negligible absorption coefficient [10] causes no harm to the performance of automotive radar sensors.

The automatic identification of critical performance losses and system adaptability for such changes in the propagation medium make automotive radars more intelligent and robust in adverse weather conditions like rain and snow. Based on the result of this work, the detection of performance losses is implemented in the new generation of Bosch Automotive Long Range Radar (LRR2) system [9].

II. WAVE PROPAGATION MODEL

The model is based on infinitely extended four plain dielectric layers of air, radome, water film and air again. To simplify the theoretical analysis, these dielectric media are assumed to be homogeneous and isotropic, considering a plane, time-harmonic electromagnetic wave incident upon a radome medium and propagating through the water film. In this model, a radome with optical thickness equal to multiples of half wave length in medium and with low refractive index is considered, to have a reflection free medium.

Any arbitrarily polarized plane wave may be resolved into two waves, namely perpendicular and parallel components to the plane of incidence. Since the boundary conditions at a discontinuity surface for these two waves are independent to each other, they will have different expressions for reflection and transmission of electromagnetic wave at the dielectric medium. Therefore, according to “Fresnel formula for reflection and transmission” [4, 6] and after mathematical simplification, the expression for reflectivity and transmissivity of an electromagnetic wave for the above model is given as follows:

$$R_v = |r_v|^2 = \frac{\left(\frac{\Omega}{n} - \frac{n}{\Omega}\right)^2}{(2 \cot(\delta))^2 + \left(\frac{\Omega}{n} + \frac{n}{\Omega}\right)^2}, \quad (1)$$

$$R_h = |r_h|^2 = \frac{\left(\frac{1}{\Omega n} - \Omega n\right)^2}{(2 \cot(\delta))^2 + \left(\Omega n + \frac{1}{\Omega n}\right)^2}, \quad (2)$$

$$R = R_h \cos^2(\psi) + R_v \sin^2(\psi), \quad (3)$$

$$T_v = |t_v|^2 = \frac{1}{\cos^2(\delta) + \left(\frac{1}{2} \left(\frac{n}{\Omega} + \frac{\Omega}{n}\right) \sin(\delta)\right)^2}, \quad (4)$$

$$T_h = |t_h|^2 = \frac{1}{\cos^2(\delta) + \left(\frac{1}{2} \left(\Omega n + \frac{1}{\Omega n}\right) \sin(\delta)\right)^2}, \quad (5)$$

$$T = T_h \cos^2(\psi) + T_v \sin^2(\psi), \quad (6)$$

$$\Omega = \frac{\cos(\alpha)}{\sqrt{1 - \left(\frac{\sin(\alpha)}{n}\right)^2}}, \quad (7)$$

$$\delta = \frac{2\pi}{\lambda} d \sqrt{n^2 - \sin^2(\alpha)}. \quad (8)$$

Where:

- Ω is the ratio of incidence angle to refraction angle,
- α is angle of the incidence wave,
- n is the complex index of refraction of water,
- d is the water-film thickness,
- δ is the phase term of propagated wave in medium as a function of incidence angle and water-film thickness,
- λ is the wave length of the propagated electromagnetic field,
- ψ is the polarization angle of the incidence wave
- r_v, r_h are the reflection coefficients for perpendicular and parallel wave components respectively,

- t_v, t_h are the transmission coefficients for perpendicular and parallel wave components respectively,
- R, T are the total reflectivity and total transmissivity respectively,
- R_v, R_h are the reflectivities for perpendicular and parallel wave components respectively,
- T_v, T_h are the transmissivities for perpendicular and parallel wave components respectively.

For the practical interest of automotive radar, a linearly polarized electromagnetic wave ($\psi = 45$ deg), incident perpendicular to the radome i.e. $\alpha = 0$ deg, $R_v = R_h = R$ and $T_v = T_h = T$, has been considered. Due to the nature of complex refractive index of water for millimetre waves and its strong dependency on frequency and temperature [5, 7, 8] the reflectivity and the transmissivity show different characteristics. As shown in Fig. 1, at a constant temperature the reflectivity from water film raises steeply for a very small thickness and reaches its maximum by a quarter of the wave length in the medium, i.e. $d = \lambda / 4n$. The absorption of electromagnetic wave in water increases with frequency as well as with water film thickness. Consequently, the reflectivity will approach a constant value, which remains below unity and decreases with increase in frequency.

Fig. 2 shows the transmissivity of a water film as a function of its thickness for three automotive radar frequencies. The water film transmits millimetre wave signals with the longer wave length and attenuates those with shorter wave length, strongly. For a 76.5 GHz signal, for example, more than 90 % of the transmitted energy will be attenuated at the water film thickness of 0.23 mm, where its reflectivity reaches a maximum of about -3 dB. This tendency of signal attenuation increases rapidly with further rise in water film thickness and absorption of almost all transmitted energy occurs with thicknesses above 1.0 mm, 0.56 mm, 0.45 mm for signals at 24 GHz, 76.5 GHz and 140 GHz respectively. The water film with thicknesses mentioned above can be easily formed in the propagation path during rain or snow and can block automotive radar functioning.

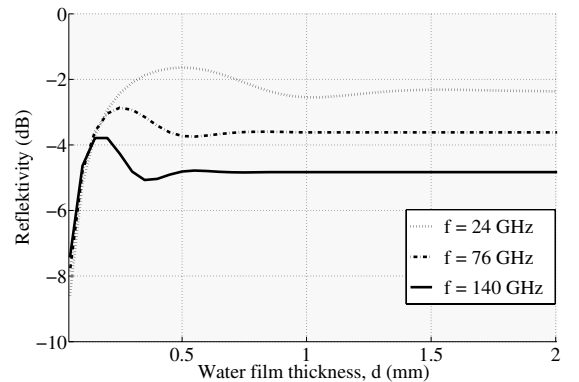


Figure 1. Reflectivity from water film at 20 °C.

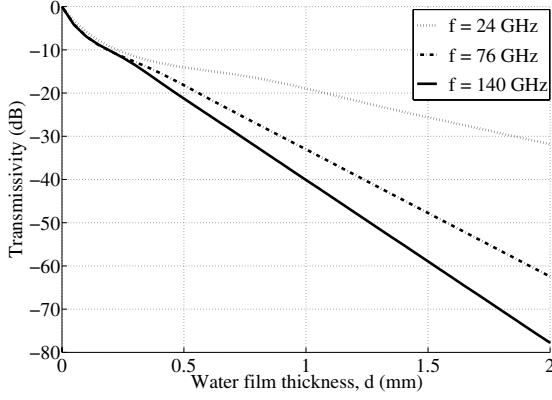


Figure 2. Transmissivity through water film at 20 °C.

A layer with complex refractive index such as water film (as polar material) causes additionally a phase and amplitude difference between components of the reflected wave as well as components of the transmitted wave. Hence, the reflected and transmitted waves in the above case may be elliptically polarized depending up on the angle of incidence. The cross-polarized components, orthogonal to the polarisation of the incidence wave, for the reflected and transmitted waves can be derived from the amplitude and phase relation of the corresponding perpendicular and the parallel wave components [4, 6]:

$$p_{rX} = \frac{1}{2} \sin(2\psi) |r_v - r_h|, \quad (9)$$

$$p_{tX} = \frac{1}{2} \sin(2\psi) |t_h - t_v|. \quad (10)$$

Where p_{rX} and p_{tX} are the cross-polarization coefficients of reflected and transmitted waves respectively. Its square gives the corresponding reflectivity and transmissivity. They will have maximum values, according to (9) and (10), for a 45 deg linear polarized incident wave. They depend on water film thickness and frequency analogous to that of the corresponding co-polarized component as discussed earlier (see Fig. 1 and Fig. 2). Fig. 3 and Fig. 4 show in addition reflectivity and transmissivity of the cross-polarized components in comparison to the measured value for a 76.5 GHz wave with angle of incidence between -10 deg and +10 deg. These cross-polarized waves are considered as polarization losses due to water film unless they are received with proper antenna arrangement.

Fig. 5 and Fig. 6 show the outcome of this theoretical analysis, how the attenuation of the transmitted energy in water film could be determined automatically for radar that is designed to detect or measure the corresponding reflectivity. This concept is used to monitor maximum detection range of a target as well as object detection capability of the automotive radar during adverse weather conditions.

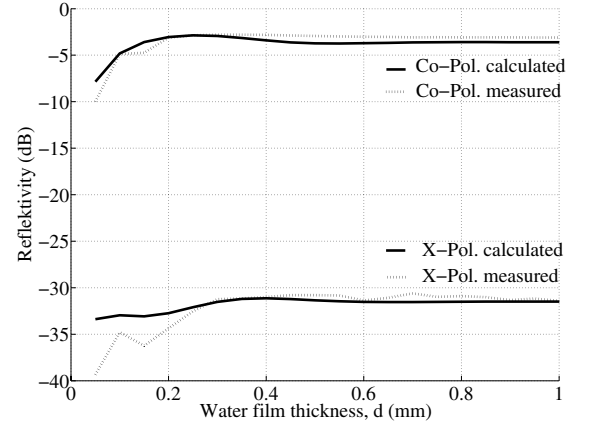


Figure 3. Reflectivity from water film at 76.5 GHz.

III. MEASUREMENT

This experiment is conducted with E-band horn antennas (beamwidth: azimuth = 13.2 deg, elevation = 20.4 deg.), connected to a Vector Network Analyser via a transmission - reflection module from Anritsu operating at 22.5 MHz to 90 GHz. The two antennas are aimed at 76.5 GHz radome with a wet tissue paper arrangement mounted on mast. The measured co-polarization and cross-polarization components of the reflectivity and transmissivity have been presented in Fig. 3 and Fig. 4 respectively.

This technique offers the advantages of building a water film with a resolution of about 0.05 mm on the radome surface easily. However, one needs careful attention to avoid possible air layer between papers as well as to keep the wetness grade constant while the measurement takes place. These may be a potential cause of measurement inaccuracy and may introduce difference between the theoretical and practical results. The thickness of water film is determined from the amount of water on the tissue paper, which has been measured with a 0.1 g resolution precision balance, divided by its surface area.

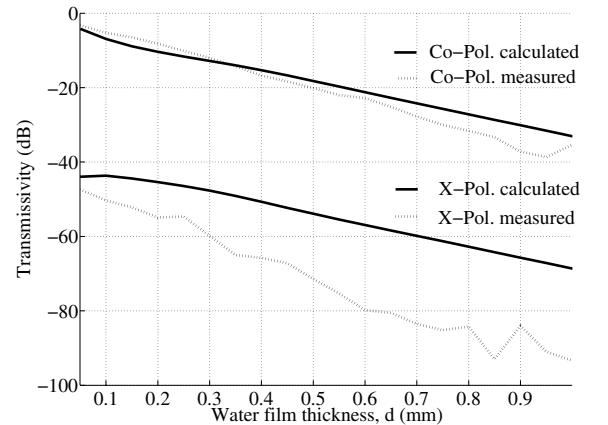


Figure 4. Transmissivity through water film at 76.5 GHz.

Furthermore, an application oriented experiment has been carried out with the new generation of Bosch Automotive long range radar sensor, which works based on Frequency Modulation Continuous Wave (FMCW) principle [9]. In the radar system a method, which measures the reflectivity from a water film on the surface of the antenna lens or its radome and assesses the degree of radar performance loss in terms of reduction in maximum detection range or object detection capability, has already been implemented. A radome with very low reflection factor has been arranged just in front of the radar sensor perpendicular to the direction of propagation. So that, in case of wet radome, reflected signals from the water film could be entirely focused on the radar antenna. It was possible to vary the degree of wetness on the radome surface by regulating the flow rate of water through a water sprayer, which has been mounted over the radar sensor. The radar vehicle is driven slowly towards a retro reflector with specified Radar Cross Section ($RCS = 3.0$ square meter). Based on relations between reflectivity and transmissivity of electromagnetic signals in water film the maximum detection range of the radar has been measured. Fig. 5 shows these measured results in terms of the maximum detection range for dry radome versus water film thickness and they are well in the range of the theoretical analysis. The relation between radar transmitted power and its maximum detection range of a target with a specified RCS is given in radar literature, for example, in [11].

In addition, a measurement is carried out in a constant traffic scenario by using spray water on the surface of automotive radar that uses plan-convex lens antenna without radome [9]. It has been observed that, exerted aerodynamic forces on the surface of the lens repress the formation of homogeneous water film. Therefore, the possibility of occurrence for total degradation or the so called absolute blindness of radar sensor could be minimized. Nevertheless, Fig. 6 shows strong reduction in the capability of radar object detection by wet antenna lens.

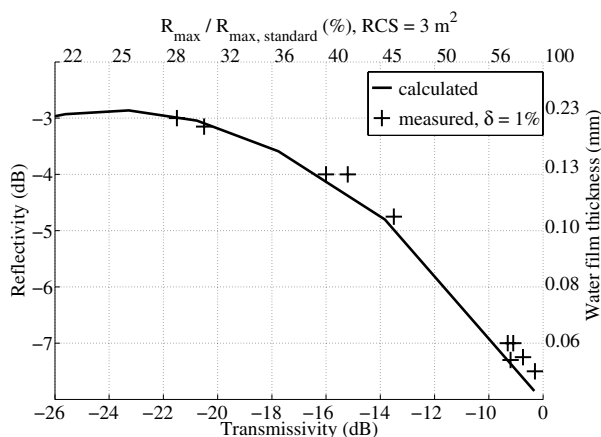


Figure 5. Maximum detection range versus reflectivity from water film on the surface of radome at 76.5 GHz.

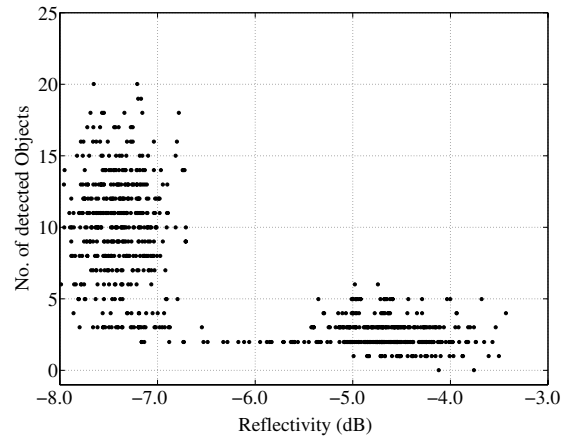


Figure 6. Correlation of radar detection capability to reflectivity from water film on the surface of antenna lens at 76.5 GHz.

IV. CONCLUSION

Water film in the propagation path of electromagnetic waves acts as signal attenuator and may lead to partial or total obstruction of radar signals in millimetre frequency range. In this paper, it has been demonstrated, in the theoretical analysis as well in the practical measurements, that the formation of water film on the surface of antenna lens or its radome causes a strong limitation on automotive long range radar performance during rainy and snowy weather conditions. Dielectric material, like ice layer with its negligible absorption coefficient, exerts generally less influence on the performance of automotive radar sensor. Therefore, the formation of water film during adverse weather conditions has to be suppressed with proper antenna lens and radome design extensively.

Further scope of this work shows that the reflected signal from the water film at the above frequencies is large enough to be recognized by any standard radar principle and so it can be utilised for the very important requirements of intelligent automotive radar, like:

- Self detection of the radar performance losses,
- System adaptability to changes of the propagation medium in adverse weather conditions like rain and snow and,
- Transfer of weather indicators to other vehicular systems.

ACKNOWLEDGMENT

The authors are very grateful to Peter Knoll, Juergen Hildebrand, Joachim Hauk and colleagues of AE-DA/ELR department of Bosch GmbH for their technical assistance to ensure the project runs smoothly.

REFERENCES

- [1] M. R. Islam, A. R. Tharek, J. Din, J. Chebil, "Measurement of wet antenna effects on microwave propagation - an analytical approach", Microwave Conference, 2000 Asia-Pacific, pp. 1547-1551, Dec. 3-6, 2000.
- [2] B. C. Blevins, "Losses due to rain and radomes and antenna reflecting surfaces", IEEE Trans. on antennas and propagation, pp. 175-176, AP-13 (1965).
- [3] M. R. Islam, A. R. Tharek, "Wet antenna effects on microwave propagation - an overview and results from sprayer tests", Proceeding of International Wireless Telecommunication Symposium (IWTS'2000), Kuala Lumpur, pp. 94-97, May 17-20, 2000.
- [4] H. Mayer, Physik Dünner Schichten, Band 4, Teil 1, Wissenschaftliche Verlagsgesellschaft M. B. H., Stuttgart, 1950, pp. 123-205.
- [5] J. A. Saxton and J. A. Lane, "Dielectric dispersion in pure polar Liquids at very high radio-frequencies", Proceed. Royal Soc., Ser. A, vol. 213, pp. 400-408 & 473-492, July 22, 1952.
- [6] M. Born und E. Wolf, Principles of Optics, 7th Edition, Cambridge University Press, Cambridge, 2003, pp. 38-70 & 735-789.
- [7] J.B. Jasted and S. H. M. El Sabeh, "The Dielectric properties of Water in Solutions", Trans. Faraday Soc., vol. 49, pp. 1003-1011, 1953.
- [8] E. Grant, T. J. Buchanan und H. F. Cook, "Dielectric behaviour of Water at Microwave Frequencies", J. Chem. Phys., vol. 26, pp. 156-161, 1957.
- [9] Götz Kühnle, Hermenn Mayer, Herbert Olbrich, Wolf Steffens and Hans-Christion Swoboda, "Low-Cost Long-Range Radar for Future Driver Assistance Systems", Auto Technology, November 2003.
- [10] Akira Ishimaru, Wave Propagation and Scattering in Random Media, volume 1, Academic Press, New York, 1978, pp. 41-68.
- [11] Jerry L. Eaves and Edward K. Reedy, Principles of Modern Radar, Van Nostrand Reinhold company Inc.: New York, 1987, pp. 1-27.

A New TEM Double-ridged Horn Antenna for Ground Penetrating Radar Applications

A. Teggatz, A. Jöstingmeier and A. S. Omar

Institute for Electronics, Signal Processing and Communications, FEIT
Otto-von-Guericke-University of Magdeburg, PF 4120, 39016 Magdeburg, Germany
alexander.teggatz@et.uni-magdeburg.de, <http://iesk.et.uni-magdeburg.de/hf/>

Abstract — Within this contribution we will present two major modifications of the standard design of the TEM double-ridged horn antenna, that increase its performance. By filling the space between the ridges partially with dielectric material it is possible to extend the frequency range to the lower end while maintaining the size of the original setup. In addition an absorber structure has been introduced in order to decrease the antennas return loss. The suggested concept has been applied to subsurface radar applications in both, 3d field simulations and various measurement experiments. The ability of this modified TEM horn antenna with respect to the detection of non-metallic objects inside the soil will be verified.

I. INTRODUCTION

The detection of buried objects such as landmines or unexploded ordnance by means of ground penetrating radar (GPR) is an intensely investigated field of research. In the past a variety of antennas has been used in GPR [1], such as Vivaldi antenna, resistively loaded dipoles, bow-tie antenna, spiral antenna and TEM double-ridged horn antenna [2]. The latter one has been used very successfully in GPR. It fulfills the basic requirements of such a system, namely, a low return loss, a wide frequency band and a reasonable gain.

In this contribution we suggest two modifications of the standard TEM double-ridged horn antenna that further improve its performance. Our design goals which are not met by the standard structure are a return loss of less than -15 dB and single main lobe operation in the frequency range from 2 GHz to 10 GHz. Fig. 1 shows the suggested structure. The design goals are achieved basically by two modifications, namely, an integrated wave absorber and a dielectric which partially fills the gap between the ridges.

Two prototypes of the new antenna design have been manufactured and the electromagnetic parameters of both structures have been measured in an anechoic chamber. The experimental results will demonstrate that the desired design parameter have been achieved successfully.

The ability of the suggested antenna structure to detect buried objects inside the soil will be proven by simulations and experiments. For the GPR simulations the same 3d field simulation tool (Microwave Studio) has been used as for the optimization of the antenna in free space. It allows for simulating the complete real world GPR environment including the antenna, the soil and different buried objects [3].

Nevertheless, real experimental data will also be presented that demonstrate the possibility to detect buried objects by means of subsurface radar with outstanding resolution.



Fig. 1. Improved TEM double-ridged horn antenna.

II. TEM HORN ANTENNA DESIGN

There are basically two major differences between the suggested design and the standard TEM double-ridged horn antenna like it has been investigated in [4] and [5]. Firstly, the space between the ridges is partially filled with dielectric. This is done in order to decrease the lower frequency limit and by doing so increasing the frequency range of the antenna. At the coaxial feeding line the dielectric homogeneously fills up the gap between the ridges, whereas it has the shape of a wedge at the aperture of the antenna as shown in Fig. 2.

Thus the dielectric filling has maximum effect where it is needed most, namely, at the feeding of the TEM horn antenna. At this place the dimensions of the housing are small leading to a quite large lower frequency limit. This constraint is then relaxed by the dielectric. At the aperture, however, a smooth transition between free space and the antenna is required in order to keep the overall return loss small. This is guaranteed by the wedge shape of the dielectric filling inside the double-ridged TEM horn antenna. The best trade-off between a

reasonable average return loss and the maximum extension of the operating frequency down to the low frequency end has been obtained for dielectric materials with a moderate permittivity like that of PTFE, which is close to 2.

Secondly, the suggested TEM horn antenna has an integrated wave absorber where standard TEM horns have a short circuit. From 3d field simulations it has turned out that it cannot be avoided that a small portion of the energy is transmitted to the waveguide in the back direction of the antenna. This effect might occur for frequencies higher than 4 GHz where this waveguide starts to support wave propagation. Although the amount of energy transmitted in this direction is quite small it really has a bad impact on the return loss of the antenna. Hence an integrated wave absorber has been suggested in order to get rid of thus unwanted reflection. The absorber consists of a double wedge of absorbing foam located in a short-circuited waveguide section as it is shown in Fig. 3.

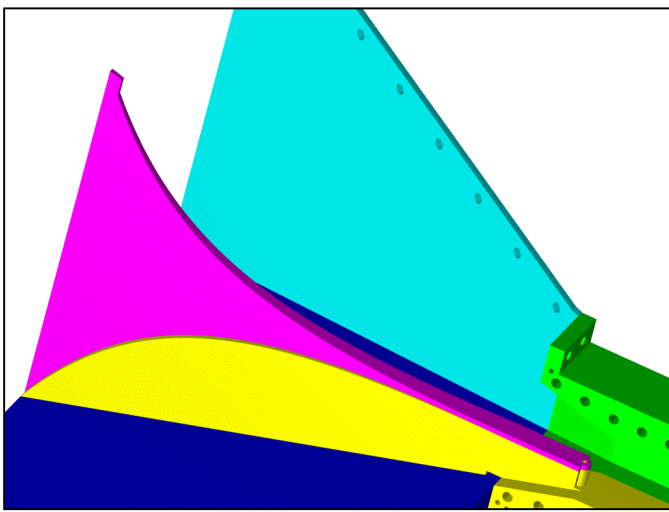


Fig. 2. Wedge shaped dielectric filling between the ridges.

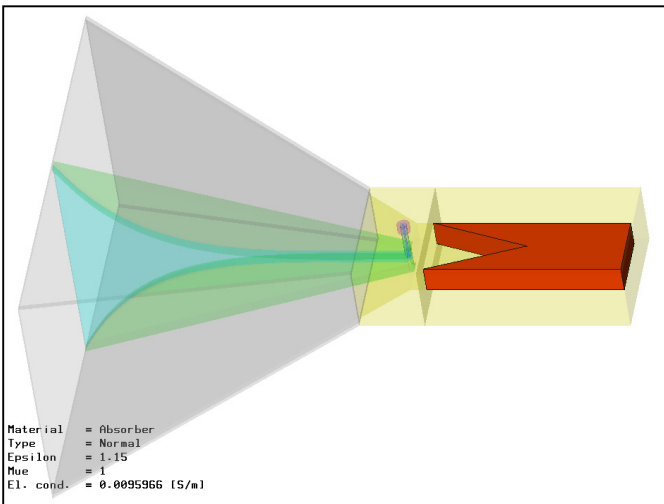


Fig. 3. Absorber with a double wedge of absorbing foam.

The suggested modifications of the usual TEM horn antenna design do not affect the radiation characteristic significantly. The single main lobe in the horn axis remains stable up to 10 GHz. At higher frequencies the it starts to split into several side lobes pointing in off-axis directions with a dip of up to 6 dB between them along the main axis, exactly like it has been predicted before by simulation in [4] and [5].

III. ANTENNA CHARACTERISTICS

The electromagnetic characteristics of the suggested TEM double-ridged horn antenna design has been verified by both, simulation techniques and different measurement experiments.

A Return Loss

The measured and simulated return loss of the TEM horn are presented in Fig. 4. There is a good agreement up to 5 GHz. For higher frequencies a discrepancy between the measured and simulated results occurs, that might result from losses, or inaccuracies in the fabrication. However, the measured return loss is even better than the simulated one.

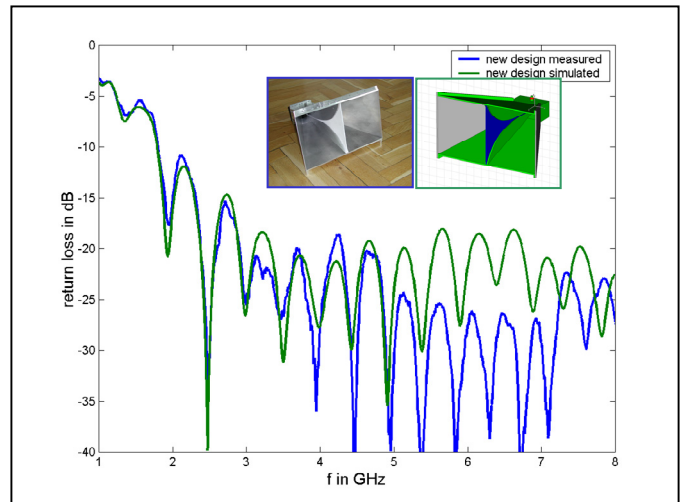


Fig. 4. Measured and simulated return loss in dB.

B Radiation Pattern

The measured E- and H-plane radiation pattern are presented in Fig. 5. For both planes a minimum beam size is observed between 3 GHz and 4 GHz as it has been predicted by the simulation of the suggested antenna design. In the H-plane the shape of the beam is almost frequency independent between 2 GHz and 5 GHz.

Furthermore the simulations show that the directivity of the simulated TEM double-ridged horn antenna is almost constant between 2 GHz and 6 GHz. However, the single main lobe starts to split up into different side lobes at higher frequencies. Thus the overall antenna performance is significantly degraded for frequencies above 10 GHz (Fig. 6).

IV. SIMULATION OF A GPR-ENVIRONMENT

The applicability of the suggested TEM horn antenna for GPR has also been investigated. Figs. 7 and 8 show the quasi-monostatic GPR simulation setup. For the simulation of the electromagnetic field the 3d field simulator Microwave Studio has been used. It is possible to automate the process of the antenna movement above the considered ground section by using an ActiveX connection which allows for changing parameter of the field simulation from another application [3].

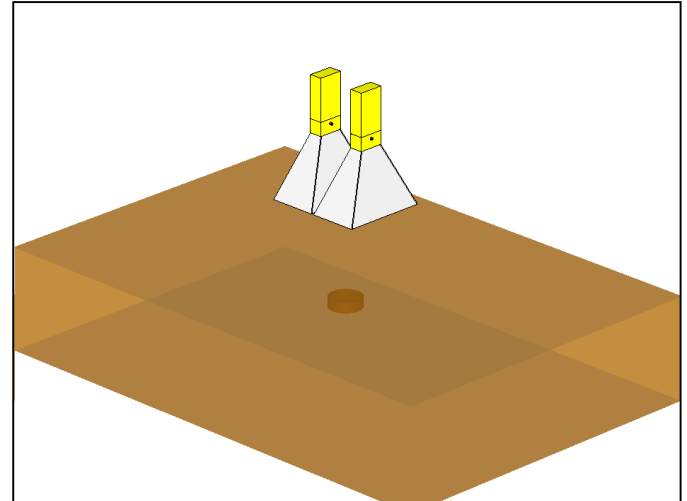


Fig. 7. Perspective view of the GPR simulation setup.

Both antennas are moved in a fixed distance, in steps of 1 cm at a height of 20 cm above the surface of the soil. The cylindrical test object with a diameter of 10 cm, a height of 3 cm and a permittivity of 1 has been placed in a depth of 7 cm below the surface of the homogeneous soil with a depth of 30 cm and a permittivity of 3. Figs. 9 and 10 show the corresponding results of such a GPR simulation setup.

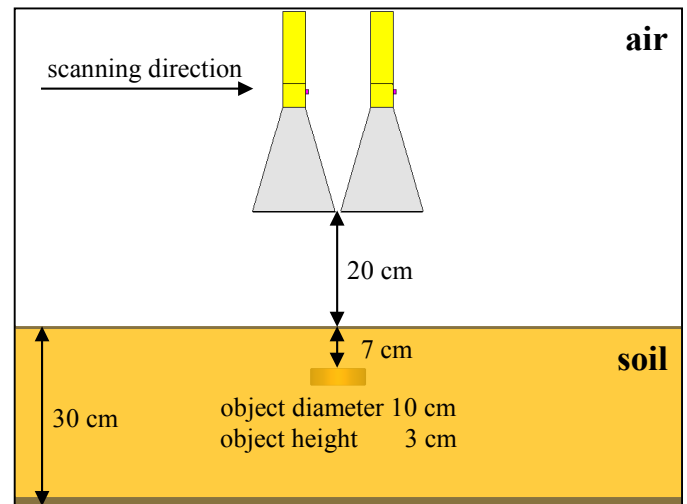


Fig. 8. Side view of the GPR simulation setup.

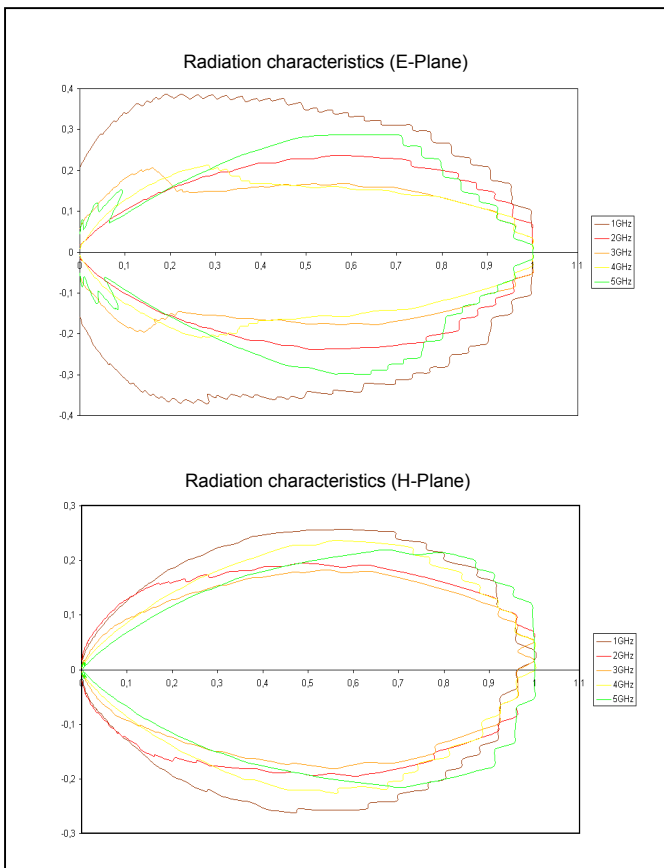


Fig. 5. Measured farfield pattern in E-plane and H-plane.

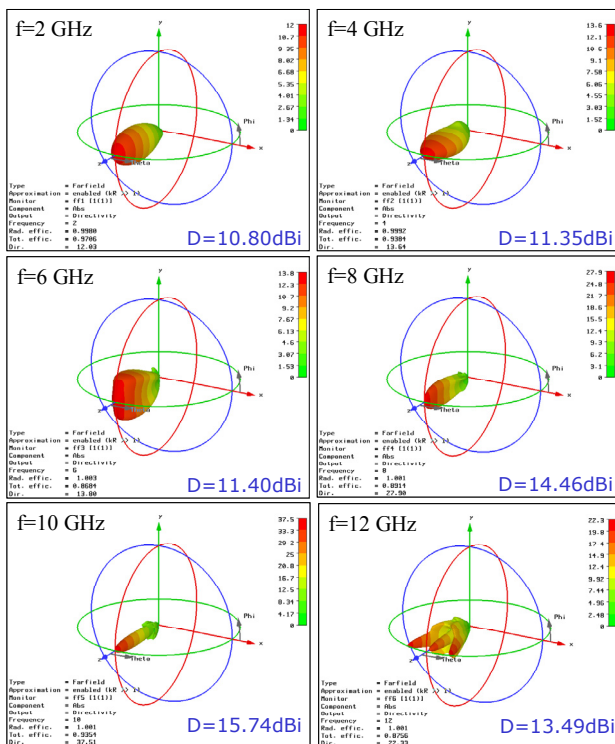


Fig. 6. Farfield patterns between 2 GHz and 12 GHz.

V. GPR MEASUREMENTS

To verify the subsurface radar ability of the modified TEM double-ridged horn antenna experimentally it has been used for measurements in a GPR environment. The reflection coefficients and the transmission coefficients have been measured by connecting the horn antennas to the two ports of a network analyzer to perform a stepped frequency continuous wave (SFCW) measurement. In this quasi-monostatic setup as it is shown in Fig. 11 the two antennas are moved together in a fixed distance of 18 cm in steps of 1 cm at a height of 30 cm above the surface of the soil. The position and orientation of the 3 test objects inside the soil is illustrated in Fig. 12.

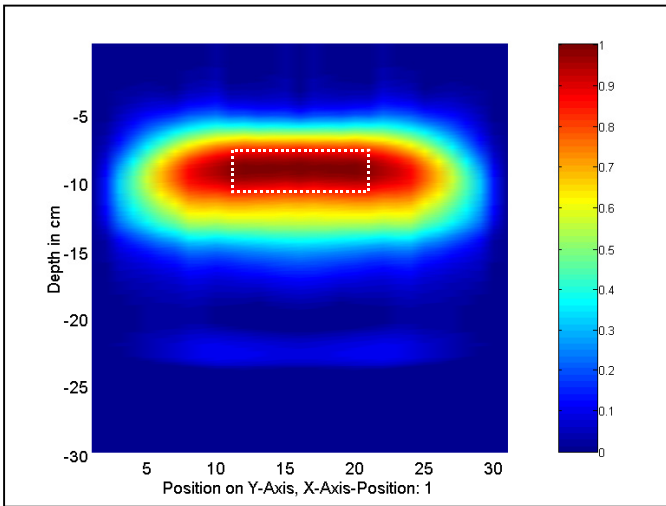


Fig. 9. B-scan simulation – transmission signal S_{21} .

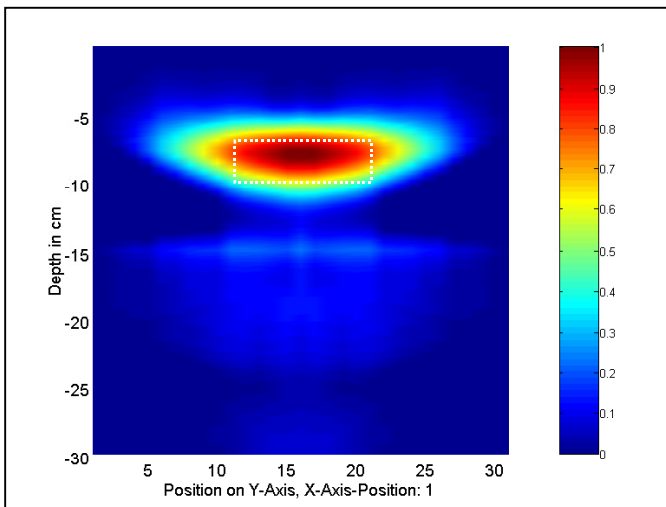


Fig. 10. B-scan simulation – reflection signal S_{22} .

The simulation has been done in the frequency range between 1 GHz and 5 GHz. For every considered antenna position either the reflection coefficient for one of the antennas namely, S_{11} or S_{22} , or the transmission coefficients S_{21} and S_{12} are taken into account to generate a cross-section image (B-scan) with the different antenna positions on the x-axis and the depth on the y-axis. As the permittivity of the soil is known the depth information is corresponding directly to the time domain results. Though no further processing has been applied to the results of the simulation the position of the cylindrical object in the soil can clearly be identified.

The buried target can clearly be identified using the transmission signal as it is shown in Fig. 9. However, the true cross section of the target can be determined with a better accuracy using the resulting reflection signal S_{22} as it is shown in Fig. 10. Obviously the reflection signal of a single antenna yields better results with respect to the actual size of the target because of the smaller footprint size of a single antenna.

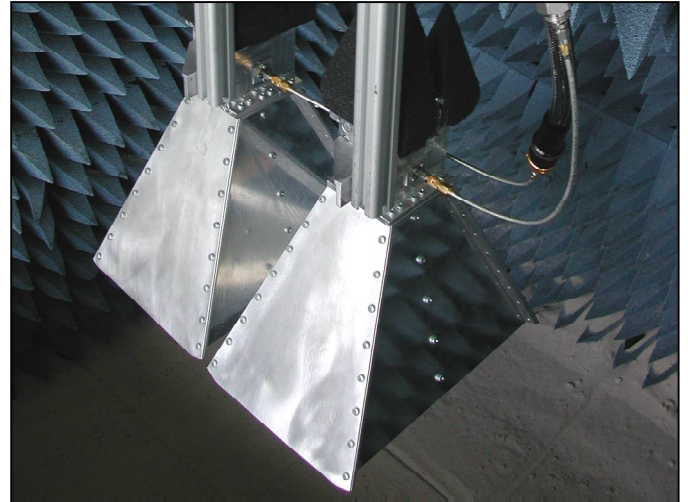


Fig. 11. GPR facility with TEM horn antenna configuration.

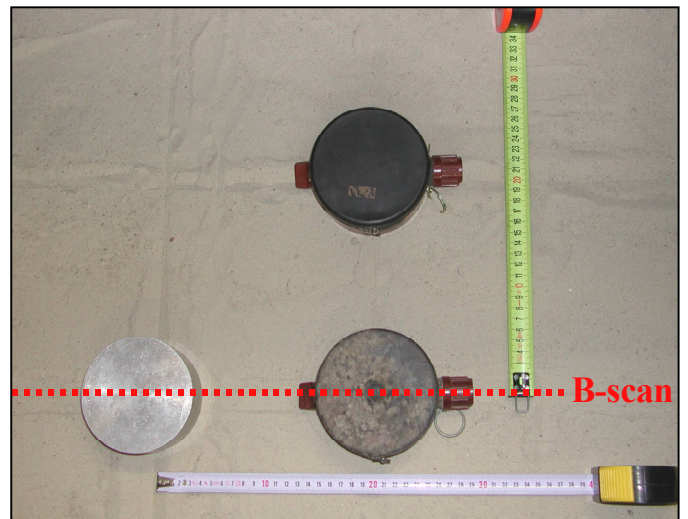


Fig. 12. Test object configuration inside the soil.

Both, the metal cylinder and the two emptied anti-personal landmines (APM) have been placed in a depth of 7 cm below the surface of the soil. The scattering parameter for 48 different antenna positions with a step width of 1 cm have

been taken into account to form the B-Scan image across the metal cylinder and one of the anti-personal mines which is shown in Fig. 13. The reflections of the metal body are much stronger than the reflections that occur due to the APM. However, a further processing could increase the contrast and reveal the correct size and position for both objects.

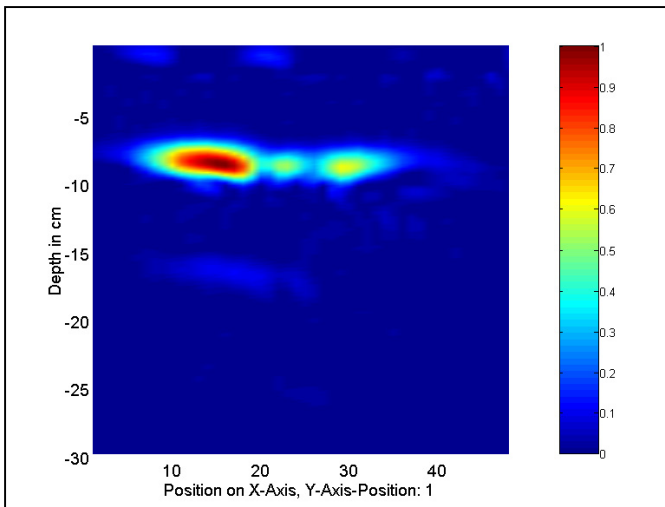


Fig. 13. B-scan measurement above two object in the soil.

VI. CONCLUSION

Within this contribution an improved design of the TEM double-ridged horn antenna has been presented. The design goals have been achieved by two modifications, namely, an integrated wave absorber and a dielectric wedge between the ridges. The characteristics of the suggested antenna have been investigated by field simulations and experiments. The GPR applicability of the suggested antenna structure and the detection of different buried metallic and non-metallic objects with an outstanding resolution have been proven successfully by various simulations and measurements.

- [1] D.J. Daniels, *Surface-Penetrating Radar*, London: The Institution of Electrical Engineers IEE, 1996.
- [2] A.G. Yarovoy, L.P. Lighthart, Ultra-wideband antennas for Ground Penetrating Radar, Proc. International Symposium on Antennas for Radar Earth Observation, Delft University, Netherlands, 8-9 June 2000, pp. 1-5.
- [3] A. Teggatz, A. Jöstingmeier, T. Meyer, and A. S. Omar, Simulation of a Ground Penetrating Radar Environment by Means of FDTD Methods Using an Automatic Control Approach, in proc. 2004 IEEE AP-S / URSI International Symposium, vol. 2, pp. 2095-2098, Monterey, June 2004.
- [4] C. Bruns, P. Leuchtman, R. Vahldieck, Analysis and Simulation of a 1-18-GHz Broadband Double-Ridged Horn Antenna, in *Transactions on Electromagnetic Compatibility*, vol. 45, no. 1, February 2003.
- [5] D. Baumann, C. Fumeaux, P. Leuchtman, R. Vahldieck, Finite-volume time-domain (FVTD) modeling of a broadband double-ridged horn antenna, *International Journal of Numerical Modeling* 2004, no. 17, pp. 285-298.

Microwave remote sensing of stratospheric trace gases using digital Fast Fourier Transform spectrometers

Stefan C. Müller¹, Axel Murk¹, Christian Monstein², Niklaus Kämpfer¹, Hansueli Meyer²

¹University of Berne, Institute of Applied Physics, Sidlerstrasse 5, 3012 Berne, Switzerland, ++41316318923, stefan.mueller@mw.iap.unibe.ch

²ETH Zürich, Institute of Astronomy, Scheuchzerstrasse 7, 8092 Zürich, Switzerland

Abstract—The Institute of Applied Physics observes middle atmospheric trace gases, such as ozone and water vapour, by microwave radiometry. We report on the comparison of measurements using a novel digital Fast Fourier Transform and acousto optical spectrometers. First tests made on ground are presented as well as first experience about the use of such spectrometers under aircraft conditions.

I. INTRODUCTION

Two key domains in atmospheric research are global warming and ozone depletion. They require detailed information about the atmospheric state and their single parameters. Thus observations are important to understand processes and to detect changes. A well established technique to measure trace gases is microwave radiometry, which detects pressure broadened emission lines of atmospheric constituents. By a suitable retrieval process it is then possible to obtain an altitude profile of the observed species from the detected spectrum. The maximum and minimum altitude of the profile depends on resolution and bandwidth of the spectrometer in use.

The radiometers built and operated at the Institute of Applied Physics for groundbased and airborne observations of ozone and water vapor use traditional low resolved filter banks or acousto optical spectrometers (AOS). With resolutions up to 24.4 kHz for the narrow band and a bandwidth of 1 GHz for broad band units the AOS are suitable for the determination of profiles from about 15 to 65 km altitude. One problem of this kind of spectrometer type is its sensitivity to temperature fluctuations and vibrations. Both situations are present during operations in an aircraft.

A new approach is the usage of digital Fast Fourier Transform (FFT) spectrometers. We dispose of a narrowband unit with a resolution of 12 kHz on 25 MHz bandwidth and also of a broadband one with 61 kHz resolution over 1 GHz. The last one was developed by ETH Zürich [1]. These novel spectrometers are employed in an aircraft instrument [2] in addition to the AOS for comparative measurements.

II. DIGITAL FAST FOURIER TRANSFORM SPECTROMETERS

A. Description

The principle of an FFT-spectrometer is well known for a long time but realizable for real-time applications only since the development of fast signal processors. As shown in figure 1 it consists of two parts. The first one is the analogue to digital converter for sampling the incoming signal. The sampling frequency f_{sampling} determines finally the bandwidth f_{max} of the spectrometer according to Nyquists theorem $f_{\text{sampling}} \geq 2 \cdot f_{\text{max}}$. The second part is the Field Programmable Gate Array (FPGA) a collection of logical gates that calculates the FFT by hardware what makes the operation very fast. The number of samples taken for one calculation determines the frequency resolution.

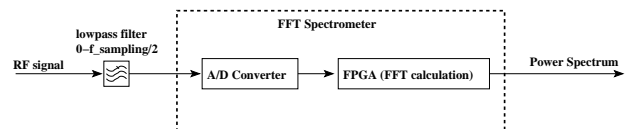


Fig. 1. Principle of an FFT spectrometer. The signal is sampled by a fast A/D converter and then processed by an FPGA that calculates the FFT in real-time.

Table I shows technical specifications of the two units in use at our institute.

parameter	broadband Acqiris	narrowband Beam
distributers	ACQIRIS	BEAM Ltd.
ADC sampling rate	2 GHz	50 MHz
bandwidth	1 GHz	25 MHz
ADC resolution	8	14
number of channels	16384	2048
resolution	61 kHz	12 kHz
integration onboard	16 μ s-70000s	40 μ s-several s

TABLE I

TECHNICAL SPECIFICATIONS OF THE USED FFT SPECTROMETERS.

B. System requirements and tests

When observing a target, e.g. the atmosphere, calibration of the signal is done according to formula (1) using an absorber

at ambient temperature as hotload and an absorber in liquid nitrogen as coldload. T_B is the brightness temperature of the radiation, V is the measured output and indices H and C correspond to the hotload and the coldload.

$$T_B(\text{target}) = \frac{T_{B_H} - T_{B_C}}{V_H - V_C} \cdot (V(\text{target}) - V_C) + T_{B_C} \quad (1)$$

Thus we assume that the spectrometer's behaviour is linear. A second point is that the whole measurement system is in a stable state during one calibration cycle. So it is desired that the time of stability of the spectrometers is much larger than the one of the whole system.

1) *System stability*: First stability tests in the laboratory have been very encouraging. Allan variance measurements [3] as seen in figure 2 have given an Allan time of about 200 seconds for the narrowband spectrometer BEAM that is one order of magnitude greater than for our AOS that is specified with 30 seconds. The broadband spectrometer shows even more. Its Allan time is greater than 1000 seconds [1].

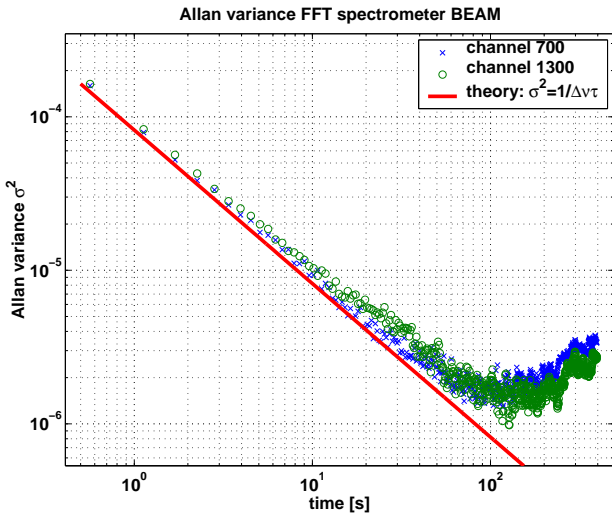


Fig. 2. Allan variance of individual channels of the narrow band FFT spectrometer BEAM.

2) *Linearity*: Another important point is the linearity of the system. For a proper calibration of the instrument we need linearity between the two reference loads and the atmospheric measurement. The test has been done using a noise source that could be attenuated in well defined steps and then observing one channel. The result shown in figure 3 with the broadband unit gives a deviation from linearity that is less than on 1 % over a range of more than 40 dB.

3) *Frequency axes*: A big advantage of the FFT spectrometers is the well known frequency axes and the good separation between the channels. This is seen in figure 4. The sidelobes are suppressed by 13 dB and originate from the Fast Fourier Transformation of a rectangular function. It can be described by the function $\sin(x)/x$. For each place on the axes where $\sin(x) = 0$ a new channel begins. Theory and measurement fit exactly.

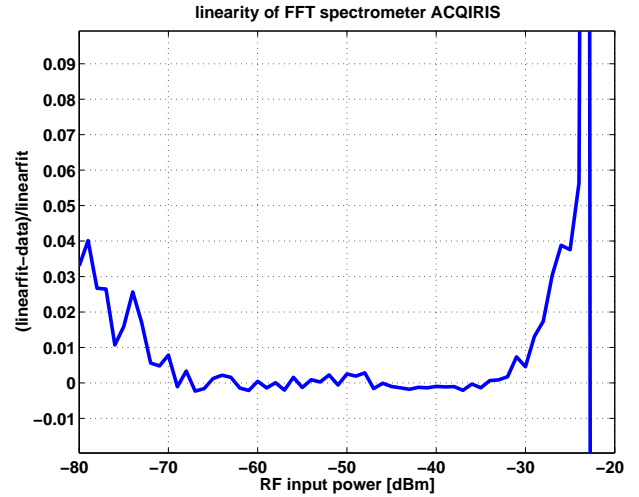


Fig. 3. Relative difference of the data and its linear fit from a linearity measurement of the broadband FFT spectrometer.

On the contrary our AOS has a nonlinear frequency axes due to geometrical reasons. In our case calibration of the axes is done using a comb generator with a signal each 100 MHz and then the channel frequencies are defined with a polynomial fit. Additionally the frequency axes is dependent on temperature what results in drift effects especially in an environment like inside an aircraft with changing temperatures. One can propose to calibrate often with the comb generator, but this will also result in a loss of measured spectra.

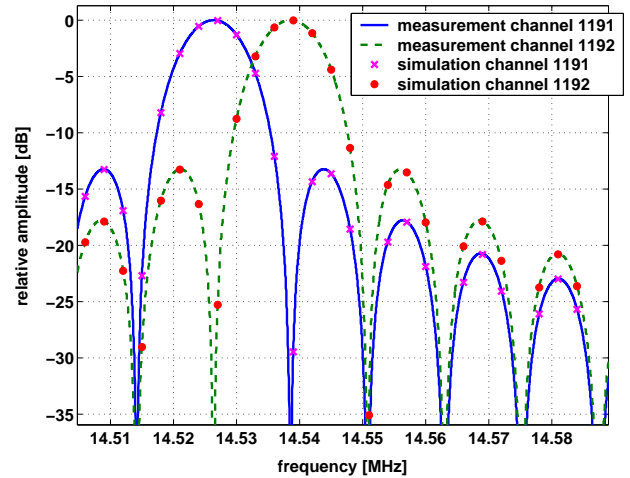


Fig. 4. Measured characteristic of a channel of the FFT spectrometer Beam compared to a simulation.

C. Radiometric tests

A first test was done looking with the heterodyne receiver AMSOS [2] at 183 GHz to a microwave absorber immersed in liquid argon. The theoretical value of the boiling temperature of argon is 86.7 K taken into account the actual pressure situation. The result in figure 5 shows a good matching of the broadband AOS and FFT spectrometers and 1 K lower for

the narrowband. But all values are too high in comparison to theory. A possible explanation is that only 99% of the antenna beam looks into the argon and 1% or less captures some of the ambient temperature. It is not yet clear where the offset between narrowband and broadband come from.

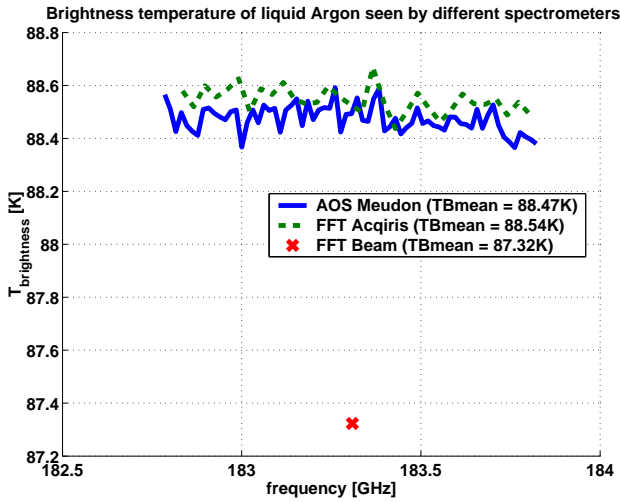


Fig. 5. Brightness Temperature of liquid argon seen by different spectrometers. Channels are binned to a bandwidth of 20 MHz for FFT Beam, 32 MHz for FFT Acqiris and 15 MHz for AOS Meudon.

III. ATMOSPHERIC MEASUREMENTS

A. Spectrometer intercomparison in summer 2005

During summer 2005 first measurements of stratospheric ozone with the ground-based radiometer GROMOS at 142 GHz have taken place during a spectrometer intercomparison campaign [4]. The scheme is shown in figure 6. In a first step the frequencyband is mixed down to an intermediate frequency (IF) of 3.7 GHz. Then is splitted up in four paths and again downconverted to the specific input band of each spectrometer. Together with the two described FFT spectrometers two AOS and a conventional filterbank were attached to the radiometer. One AOS was a broadband from Observatoire de Meudon and a narrowband from Elson Research Inc.. An offset in measured brightness temperatures between the FFT and AOS spectrometers has been detected in figure 7 but line amplitude and line form between all of them including filterbank was equal as can be seen in figure 8. The origin of the offset was caused by nonlinearities in the different IF chains.

As a consequence of that all IF chains of the airborne radiometer AMSOS [2] have been checked and adapted for the measurements from aircraft described in section III-B.

B. Measurements from aircraft during SCOUT-O3 campaign

In november 2005 the Institute of Applied Physics participated with a Learjet of the Swiss Air Force at the SCOUT-O3 campaign in Darwin, Australia. With the radiometer AMSOS [2] it is possible to measure either H_2O at 183.3 GHz in the upper sideband (figure 11) or O_3 at 175.4 GHz in the lower

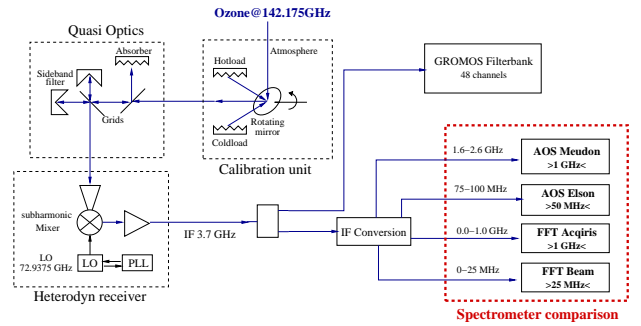


Fig. 6. Scheme of the radiometer GROMOS during intercomparison campaign in summer 2005.

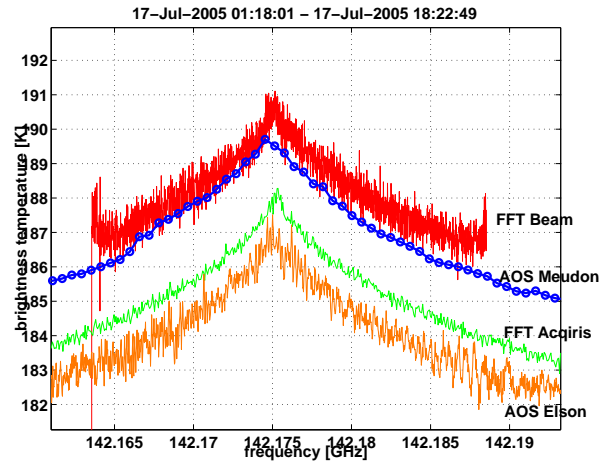


Fig. 7. Comparison of narrow and broadband AOS and FFT spectrometers at line center. An offset in brightness temperature is measured between all spectrometers.

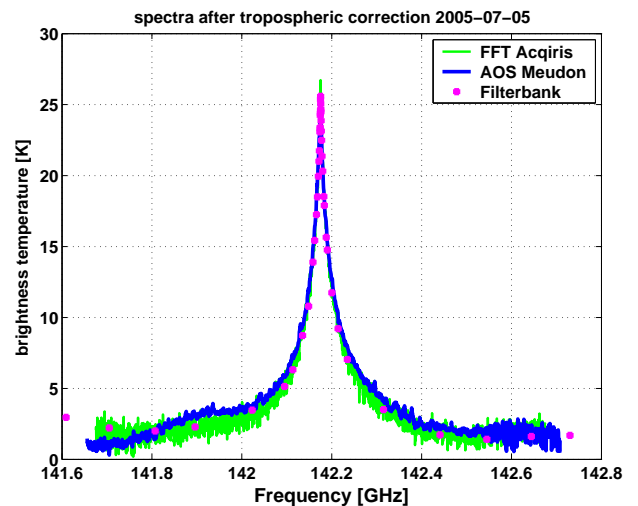


Fig. 8. Comparison of line amplitude and line form between broadband AOS, FFT and a 48 channel filter bank.

sideband (figure 9). The ripple in the ozone spectrum is due to standing waves in the input optics of the receiver. The channels in the high resolved FFT spectrometers are binned together

to around 1 MHz. Both examples show a good matching for both spectrometer types but with the AOS we see a higher brightness temperature in the ozone line as with the FFT. The differences plotted in figure 12 and 10 can give us an advice to this offset. Good matching would mean that there would be only the rest noise around 0 K. What we notice is on the left and on the right side a rise of 1-2 Kelvin. The discrepancy originates at the last downconversion. For downconversion to the input band of 0-1 GHz we need a steep roll-off filter next to the LO Frequency, in our case 3.2 GHz and also at the end of the analyze band at 4.2 GHz. Is this not the case, we get unwanted components of other frequency bands as shown in figure 14. Unfortunately this affected the ozone line in the measurement. What we see with the FFT Acqiris is a mix of brightness temperature from the ozone line of 57 Kelvin and from the part at the lower frequencies of around 48 Kelvin that reduces the ozone line. The abrupt rise in the center of figure 12 is caused by wrong calibration the of the frequency axis of the AOS, which is also visible in figure 13. We can clearly see the line shifted to the left of the theoretical center at 183.310 GHz by contrast to the FFT spectrometers. This shows the problems of frequency instability on the AOS but can be corrected afterwards.

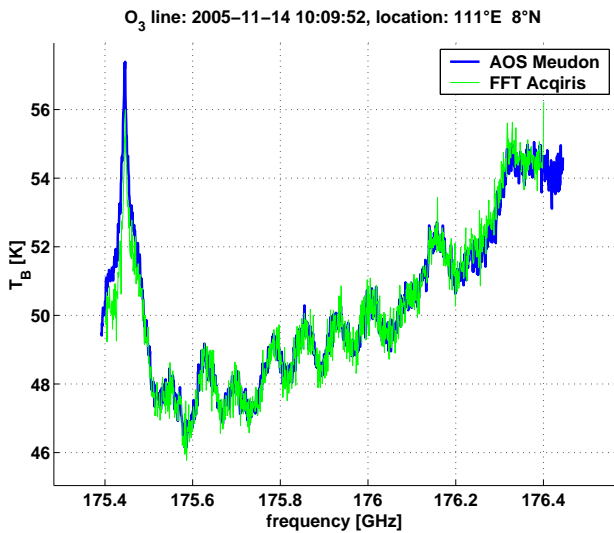


Fig. 9. O₃ line at 175 GHz. The channels of both spectrometers are binned to approximately 1 MHz.

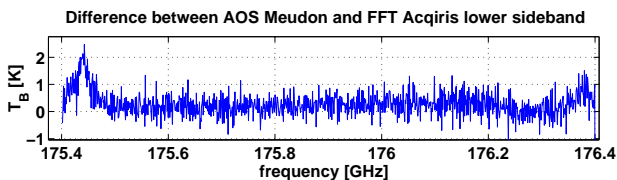


Fig. 10. Difference between broadband FFT and AOS spectrometer in the lower sideband.

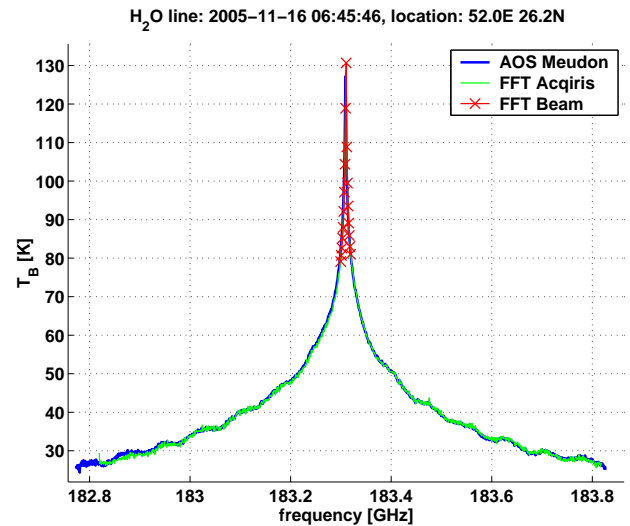


Fig. 11. H₂O line at 183 GHz. The channels of the spectrometers are binned to approximately 1 MHz.

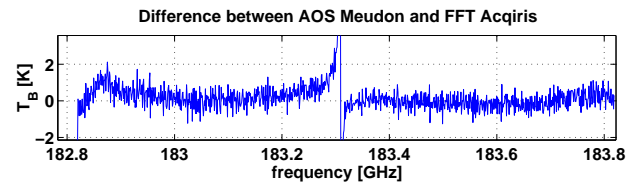


Fig. 12. Difference between broadband FFT and AOS spectrometer in the upper sideband.

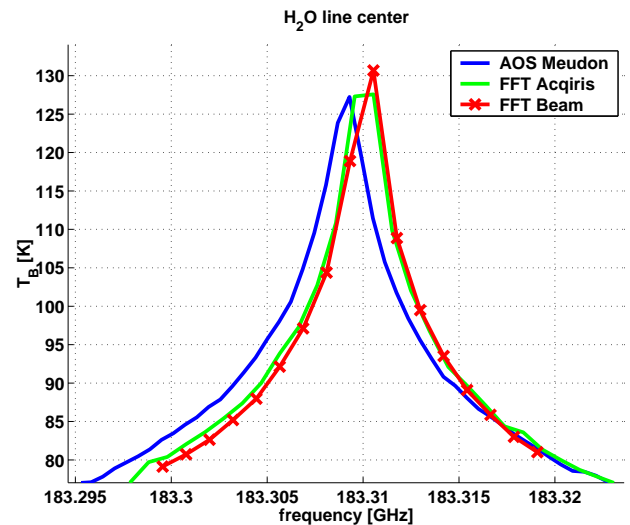


Fig. 13. H₂O line center. The channels of the spectrometers are binned to approximately 1 MHz.

IV. CONCLUSION

The novel technique of Digital Fast Fourier Transform spectrometers is a promising alternative to conventional acousto optical spectrometers. They are superior concerning resolution and stability and they proof to be linear to a high degree. First measurements of stratospheric ozone and water vapour from

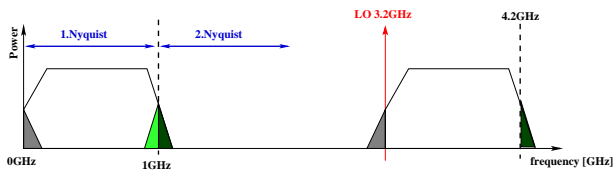


Fig. 14. Difficulties in downconversion to the first Nyquist band. If the LO frequency extend into the analyzed band, the part filled in gray color will be folded into the spectrum and will disturb it. If the bandpass filter covers more than the first Nyquist band the part from the neighbored Nyquist band (dark green) will also be folded into the spectrum (light green).

ground as well as from aircraft during SCOUT-O3 campaign in november 2005 were very successful.

ACKNOWLEDGMENT

This work has been supported through the Swiss National science foundation under grant 200020-107665. The technical development of the 1 GHz FFT was financed by the Swiss Kommission für Technologie und Innovation (KTI) grant number 6421.2 IWS-IW and by the Swiss National science foundation under grant 200020-105366.

Special thank belongs to the Swiss Air Force and their pilots for the support during the aircraft campaign.

REFERENCES

- [1] A. O. Benz, P. C. Grigis, V. Hungerbühler, H. Meyer, C. Monstein, B. Stuber, and D. Zardet. A broadband FFT spectrometer for radio and millimeter astronomy. *Astronomy & Astrophysics*, 2005.
- [2] Vladimir Vasic, Dietrich G. Feist, Stefan Müller, and Niklaus Kämpfer. An airborne radiometer for stratospheric water vapor measurements at 183 GHz. *IEEE Transactions on Geoscience and Remote Sensing*, 43(7):1563–1570, July 2005.
- [3] R. Schieder and C. Kramer. Optimization of heterodyne observations using Allan variance measurements. *Astronomy & Astrophysics*, 373(2):746, July 2001.
- [4] Stefan C. Müller, Niklaus Kämpfer, Christian Monstein, Hansueli Meyer, Axel Murk, and Vladimir Vasic. A novel spectrometer concept for microwave remote sensing of middle atmospheric trace constituents. In Klaus Schäfer, Adolfo T. Comerón, James R. Slusser, Richard H. Picard, Michel R. Carleer, and Nicolaos Sifakis, editors, *Remote Sensing of Clouds and the Atmosphere X*, volume 5979, pages 280–288, October 2005.

Large-Signal Modeling of AlGaIn/GaN HEMTs with Analytically Calculated Thermal Resistance

E. Jutzi¹, I. Dettmann¹, M. Berroth¹, H. Roll², and H. Schweizer²

¹Institute for Electrical and Optical Communications Engineering, Universität Stuttgart, 70550 Stuttgart, Germany

Email: ElenaChigaeva@int.uni-stuttgart.de

² 4th Physical Department, Universität Stuttgart, 70550 Stuttgart, Germany

Abstract—A large-signal model of AlGaIn/GaN HEMTs grown on sapphire substrate with gate width $W_g = 2 \times 150 \mu\text{m}$ and gate length $L_g = 250 \text{ nm}$ is presented. The equivalent circuit model accurately describes the sub-threshold region and takes into account the self-heating effects. The thermal resistance has been calculated analytically. The DC, small-signal and large-signal behaviour are accurately described by the model.

I. INTRODUCTION

AlGaIn/GaN High Electron Mobility Transistors (HEMTs) attract much attention due to their capability to handle high powers at high frequencies. A lot of outstanding results have been already reported showing high output powers in a wide frequency range, for example 10.7 W/mm at 10 GHz [?] or 0.5 W/mm at 60 GHz [?]. For the application of AlGaIn/GaN transistors in high-power RF-circuits precise and reliable models for circuit simulators are required. The model should reflect not only the small-signal but also the nonlinear large-signal behaviour. Several authors have already published some modeling results on AlGaIn/GaN HEMTs [?] – [?]. Most models have been designed for transistors on a substrate with good thermal conductivity such as SiC or Si, where the thermal effects are less pronounced than in devices on sapphire substrates. However, sapphire substrates are still commonly used, since they are available with larger wafer diameters and at lower cost. Thus, accurate modeling of thermal effects of sapphire-based devices is required. Moreover, analytical equations for the thermal resistance are desired to perform the device layout optimisation with respect to thermal management.

II. EFFECT OF SELF-HEATING ON TRANSISTOR PERFORMANCE

AlGaIn/GaN-HEMTs on sapphire substrates have been characterised in terms of DC-behaviour, S-parameters, output versus input power and intermodulation distortion. A microwave transition analyser has been used to determine amplitude and phase of the output harmonics. The intermodulation distortion measurement has been performed with a spectrum analyser.

Accurate thermal modeling is necessary to describe the deviation between the DC and the dynamic transfer characteristics, which are compared in Fig. ???. In DC operation the drain-source current is limited by the channel temperature, which in

turn increases by $\Delta T \propto R_{th} \cdot P_{diss}$ with dissipated power. The dynamic transfer characteristic has been derived from harmonics measurements at the bias point of $V_{ds} = 14 \text{ V}$, $V_{gs} = -2 \text{ V}$ at a frequency of $f = 1 \text{ GHz}$ and the input power of 10 dBm. At gate-source voltages smaller than the gate bias voltage the drain currents of both, the DC- and the dynamic characteristics are nearly the same. However, for higher input voltages the dynamic drain current is noticeably larger than the DC current. Since the dynamic measurements are performed at a frequency of 1 GHz, the channel temperature cannot follow the variations of the dissipated power. Consequently, the dynamic characteristic is measured under isothermal conditions determined by the bias point. This deviation between the DC- and the dynamic transfer characteristic due to self-heating effects must be accurately reflected by a large-signal model.

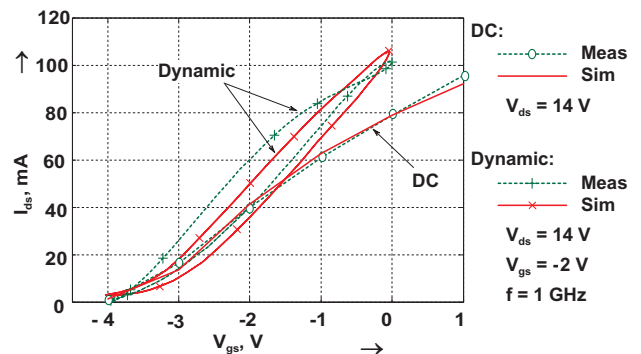


Fig. 1. Comparison of the DC and dynamic transfer characteristics.

An opening of the dynamic transfer characteristic results from the frequency-dependent impedances of the transistor.

III. NON-LINEAR EQUIVALENT CIRCUIT DEVICE MODEL

The large-signal equivalent circuit of AlGaIn/GaN HEMTs can be divided into three sub-circuits: the external circuit, the internal transistor and the thermal equivalent circuit, as shown in Fig. ???. The external bias-independent parasitic elements comprise the pad capacitances C_{pgs} , C_{pgd} and C_{pds} , the series inductances L_g , L_d and L_s and the series resistances R_g , R_d and R_s . These values are extracted with the standard "cold"-method [?]. The internal transistor circuit consists of nonlinear bias-dependent elements such as the drain-source current

source I_{ds} , the nonlinear gate capacitances C_{gs} and C_{gd} and bias-independent elements such as the channel resistances R_{gs} and R_{gd} . The gate leakage currents of the Schottky diode are modeled with current sources I_{gs} and I_{gd} governed by the Shockley equation. The thermal equivalent circuit consists of the current source I_{th} representing the dissipated power $P_{diss} = I_{ds} \cdot V_{dsi}$, the thermal resistance R_{th} and the thermal capacitance C_{th} . The voltage drop across the thermal resistance corresponds to the temperature rise ΔT in the transistor channel affecting the drain current. The thermal time delay is given by $\tau = R_{th} \cdot C_{th}$.

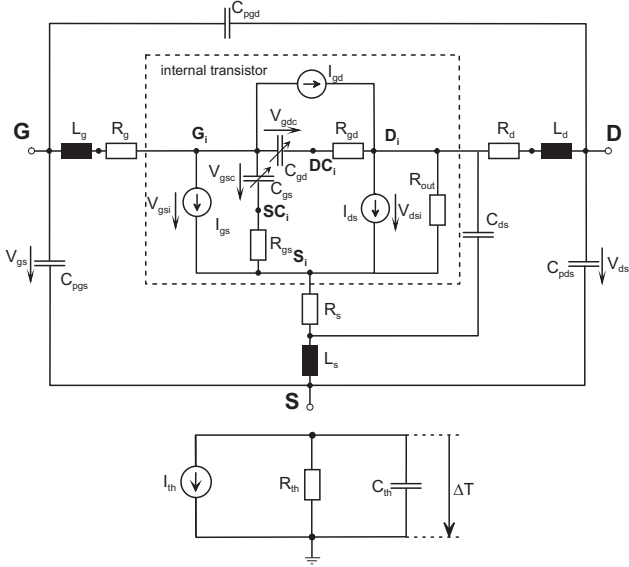


Fig. 2. Large-signal equivalent circuit of AlGaIn/GaN HEMTs

A. Thermal resistance

There are several ways to determine the thermal resistance R_{th} , which is an important model parameter. Special equipment and test structures are required to measure R_{th} , which are not easily available [?]. Therefore, R_{th} is usually determined by a numerical fit. For our model the thermal resistance is analytically calculated [?]. This method allows for geometrical parameter optimisation in order to achieve minimal power dissipation and hence a small temperature increase in the transistor.

Several aspects should be taken into account during the calculation to get a realistic value of the thermal resistance. The typical power transistor has a multifinger layout, which results in thermal coupling between the gate fingers. Furthermore, the device structure comprises layers with different temperature-dependent thermal conductivities. The calculation of the total device thermal resistance consists of the following main steps:

- calculate the heat spreading angle for each layer,
- calculate the thermal resistance of each layer,
- account for the temperature dependence of the thermal conductivity.

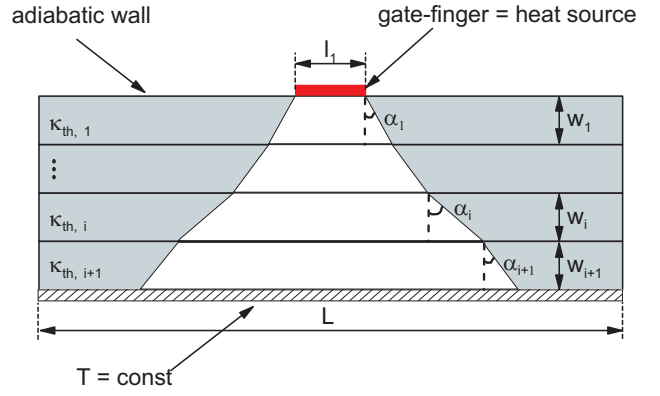


Fig. 3. Heat spreading angle

1) *Calculation of the effective heat spreading angle:* To simplify the calculations an effective heat spreading angle definition can be introduced [?]. The heat inside a layer is assumed to spread within a defined angle α_i ,

$$\tan \alpha_i = \left(1 - \frac{l_i}{L}\right) \cdot \frac{w_i + \frac{\rho_i}{1 + \rho_i} l_i}{w_i + \frac{1}{1 + \rho_i} l_i} \quad \text{with} \quad \rho_i = \frac{\kappa_i}{\kappa_{i+1}}, \quad (1)$$

that depends on the ratio of the thermal conductivities κ_i and κ_{i+1} of the adjacent layers and geometrical dimensions of the heat source and the layer, such as layer thickness w_i , layer width L and heat source width l_i . With knowledge of this angle the heat pattern on the next interface can be calculated as shown in Fig. ???. This pattern serves as a heat source for the next layer.

2) *Calculation of the thermal resistance of a single layer:* The heat flow equation takes the same form as the Poisson-equation without free charges:

$$\nabla^2 T = 0, \quad (2)$$

where T is the temperature, which is analogous to the electric potential.

Assuming the transistor is placed on an ideal heat sink, the bottom has a constant temperature. Usually the transistor is surrounded with air or a plastic packaging having a very small thermal conductivity. Therefore, the remaining boundaries can be considered as adiabatic. To simplify the analytical solution the gate is regarded as the sole heat source. These boundary conditions are equal to the boundary conditions of a multiple coupled microstrip line [?]. Therefore, calculation of the thermal resistance is analogous to the calculation of the capacitance.

3) *Temperature dependence of the thermal conductivity:* To take into account the temperature dependence of the thermal conductivity $\kappa(T)$ Kirchoff's transformation can be used [?]. The real temperature T in (??) is replaced by a linearised temperature θ to simplify the heat transport equation by

shifting the nonlinearity into the boundary condition:

$$\theta(T) = T_0 + \frac{1}{\kappa(T_0)} \int_{T_0}^T \kappa(T') dT' \quad (3)$$

The real temperature T is calculated from the reverse transformation of (??).

B. Drain current model equations

The main non-linearity appears in the drain-source current source and therefore should be accurately modeled. The current equations from [?] have been modified to achieve better convergence and accuracy in the subthreshold region [?]:

$$I_{ds} = f_1(V_{gsi}) \cdot \tanh(\alpha V_{dsi}) \cdot (1 + \lambda V_{dsi}) \cdot \left(1 - \kappa \frac{I_{ds}}{\Delta T}\right) \quad (4)$$

with

$$\begin{aligned} f_1(V_{gsi}) &= ff_1 \cdot ff_2 \\ ff_1 &= CD_{V_C} \cdot \left\{1 + \tanh\left[\beta(V_{gsi} - V_C) + \gamma(V_{gsi} - V_C)^3\right]\right\} \\ &\quad + CD_{V_{SB}} \cdot \left\{1 + \tanh\left[\delta \cdot (V_{gsi} - V_{SB})\right]\right\} \\ ff_2 &= \tanh\left\{1 + a \cdot \ln\left[1 + \exp\left(\frac{V_{gsi} - V_{th}}{a}\right)\right]\right\} \end{aligned}$$

The function $f_1(V_{gsi})$, which consists of two parts, describes the transfer properties of the transistor. Parameter CD_{V_C} represents the drain-source current at the gate voltage V_C , where the transconductance is maximum $g_m = g_{m, max}$. Parameter β is calculated by $g_{m, max}/CD_{V_C}$. Parameters $CD_{V_{SB}}$, V_{SB} and δ model the parasitic MESFET at high gate voltages. The second term ff_2 models the drain-source current in the sub-threshold region with the parameter V_{th} as the threshold voltage. The slope of the drain-source current in the linear transistor region is controlled by the parameter α . Parameter λ models the drain current in the saturation region. The resistance R_{out} , which decreases with frequency, accounts for the finite drain-source current in the pinch-off region.

The nonlinear capacitances C_{gs} and C_{gd} are described by the charge conservative model developed by R. Osorio [?].

The model has been implemented in ADS, Agilent Technologies, as a symbolically defined device (SDD).

IV. MODEL VERIFICATION

The model has been verified on sapphire based AlGaIn/GaN HEMTs with a gate width $W_g = 2 \times 150 \mu\text{m}$ and a gate length $L_g = 250 \text{ nm}$. The devices have been grown and fabricated at the 4th Physical Department, Universität Stuttgart.

In the sub-threshold region the model of this work shows closer agreement with measurement than the model of [?]. The difference between both models is clearly illustrated by the logarithmic plot of the drain-source current as a function of the gate-source-voltage in Fig. ??.

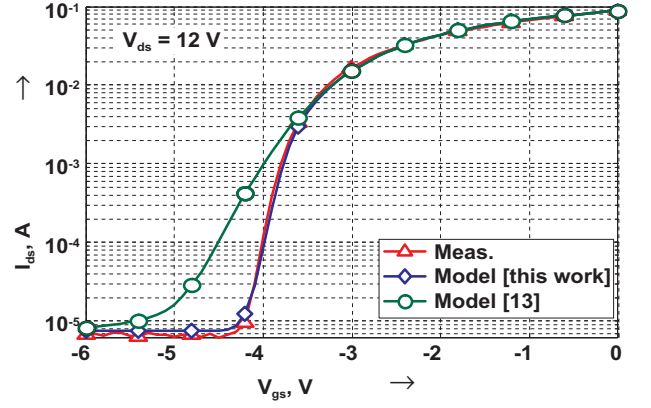


Fig. 4. Measured and simulated transfer characteristics

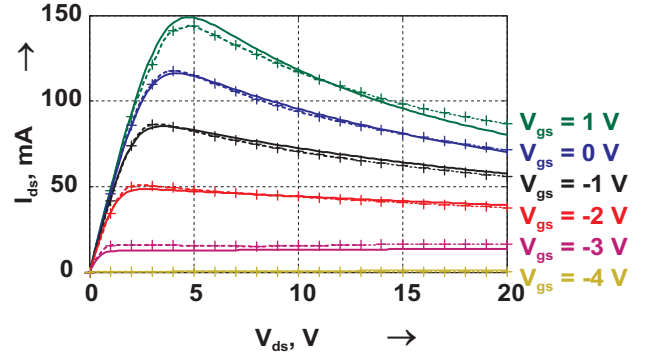


Fig. 5. Measured (line with crosses) and simulated (line) output characteristics

Comparison of the DC output characteristics presented in Fig. ?? shows a good agreement of measured and simulated data, even at high gate-source and drain-source voltages, where self-heating becomes significant and causes negative slopes. The accumulated mean relative error in the complete voltage range is smaller than 4 %.

The accuracy of the capacitance model is examined under RF small-signal excitation in the saturation region at $V_{ds} = 14 \text{ V}$ and $V_{gs} = -2 \text{ V}$. Good agreement between measured and simulated S-parameters has been achieved in the frequency range from 100 MHz to 30 GHz, as shown in Fig. ?. The mean relative error for all S-parameters except S_{12} is smaller than 6%.

The overall model behaviour is usually evaluated under large-signal conditions. At 1 GHz the input power has been swept for a transistor bias point of $V_{ds} = 14 \text{ V}$ and $V_{gs} = -2 \text{ V}$. The output power P_{out} , the gain and the power added efficiency (PAE) are accurately modeled, as can be seen from Fig. ?. Since the amplitude and phase of the input and the output signals have been measured, a reconstruction of the time-domain signals is possible. Taking into account a time delay between the input and the output signals the simulated and measured dynamic transfer characteristic can be plotted. The deviations between DC- and dynamic characteristics are also accurately reflected by the model as presented in Fig. ?.

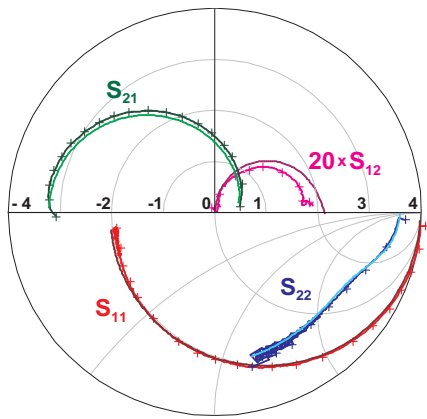


Fig. 6. Measured (line with crosses) and simulated (line) S-parameters

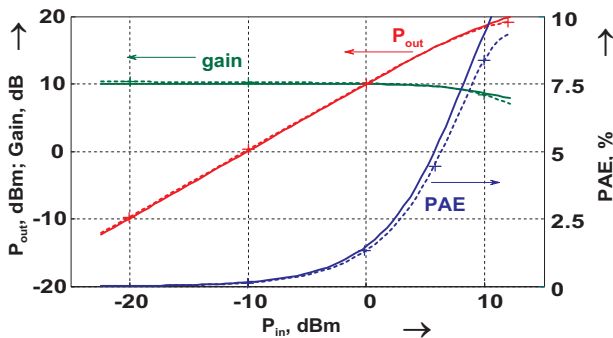


Fig. 7. Measured (line with crosses) and simulated (line) output power, gain and PAE

Two-tone intermodulation measurements reveal even small, hidden nonlinearities of the device under test. For the measurements the same bias point as above has been chosen. The center frequency and the spacing of the two tones are 2 GHz and 1 MHz, respectively. The measured and the simulated fundamental signals deviate not more than 0.6 dB as presented in Fig. ???. The third order intermodulation products (IMD3) have been simulated with a relative error of 11%. Due to the continuity of the higher order derivatives of the model equations, the simulation converges also for high powers.

V. CONCLUSION

An accurate and compact model for AlGaIn/GaN HEMTs has been presented. The analytical calculation of the thermal resistance allows for quick optimisation of the transistor geometry in respect to self-heating effects. The model is appropriate for circuit design, since the detailed large-signal behaviour such as the 3rd order intermodulation is reflected.

ACKNOWLEDGMENT

Research reported here was performed in the context of the network TARGET - "Top Amplifier Research Groups in a European Team" and supported by the Information Society Technologies Programme of the EU under contract IST-1-507893-NOE, www.target-net.org

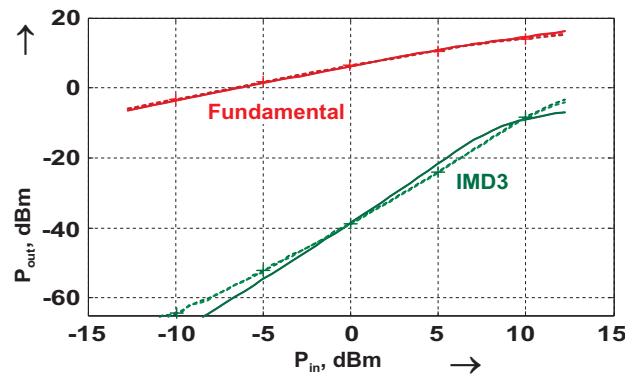


Fig. 8. Measured (line with crosses) and simulated (line) IMD

REFERENCES

- [1] V. Tilak, B. Green, V. Kaper, H. Kim, T. Prunty, J. Smart, J. Shealy, L. Eastman, *Influence of Barrier Thickness on the High-Power Performance of AlGaIn/GaN HEMTs*, IEEE Electron Device Letters, Vol. 22, No. 11, Nov. 2001, pp. 504-506.
- [2] R. Quay, A. Tessmann, R. Kiefer, R. Weber, F. van Raay, M. Kuri, M. Riessle, H. Massler, S. Müller, M. Schlechtweg, G. Weimann, *AlGaIn/GaN HEMTs on SiC: Towards Power Operation at V-Band*, IEDM 2003, Washington, USA, December, pp. 23.2.1-23.2.4.
- [3] B.M. Green, H. Kim, V. Tilak, J.R. Shealy, J.A. Smart, and L.F. Eastman, *Validation of an Analytic Large Signal Model for AlGaIn/GaN HEMTs on SiC Substrates*, in IEEE Advanced Concepts in High Performance Devices Conference, (Ithaca, NY), pp. 237-241, Aug. 2000.
- [4] J.W. Lee, K.J. Webb, *A Temperature-Dependent Nonlinear Analytical Model for AlGaIn/GaN HEMTs on SiC*, IEEE Transactions on Microwave Theory and Techniques, Vol. 52, pp. 2-9, Jan. 2004.
- [5] F. van Raay, R. Quay, R. Kiefer, M. Schlechtweg, and G. Weimann, *Large Signal Modeling of AlGaIn/GaN HEMTs with $P_{sat} > 4$ W/mm at 30 GHz Suitable for Broadband Power Applications*, IEEE MTT-S International Meeting, Microwave Symposium Digest, pp. 451-454, 2003.
- [6] P.M. Cabral, J.C. Pedro, and N.B. Carvalho, *Nonlinear Device Model of Microwave Power GaN HEMTs for High Power-Amplifier Design*, IEEE Transactions on Microwave Theory and Techniques, Vol. 52, pp. 2585-2592, Nov. 2004.
- [7] G. Dambrine, A. Cappy, F. Heliodore, and E. Playez, *A New Method for Determining the FET Small-signal Equivalent Circuit*, IEEE Transactions on Microwave Theory and Techniques, vol. 36, no. 7, pp. 1151-1159, 1988.
- [8] R. Anholt, *Electrical and Thermal Characterization of MESFET's, HEMT's, and HBT's*, Artech Haus, 1995.
- [9] J.C. Freeman, *Channel Temperature Model for Microwave AlGaIn/GaN Power HEMTs on SiC and Sapphire*, IEEE MTT-S International Meeting, Microwave Symposium Digest, pp. 2031-2034, 2004.
- [10] F.N. Masana, *Thermal Characterisation of Power Modules*, Microelectronics Reliability, vol. 40, pp. 155-161, 2000.
- [11] H.F. Cooke, *Precise Technique Finds FET Thermal Resistance*, Microwaves and RF, vol. 25, pp. 8587, Aug. 1986.
- [12] W.B. Joyce, *Thermal Resistance of Heat Sinks with Temperature-Dependent Conductivity*, Solid-State Electronics, vol. 18, pp. 321-322, 1975.
- [13] M. Bertho, E. Chigaeva, I. Dettmann, N. Wieser, W. Walthes and M. Grözing, *Nonlinear GaN-HEMT Modeling Including Thermal Effects in Second Joint Symposium on Opto- and Microelectronic Devices and Circuits*, (Stuttgart, Germany), pp. 236-239, Mar. 2002.
- [14] R. Osorio, W. Marsetz, M. Demmler, M. Schlechtweg and M. Bertho, *Large Signal Modeling and Verification for MODFETs Based on a New Analytical Gate Charge Equation in 4th International Workshop on Integrated Nonlinear Microwave and Millimeterwave Circuits*, (Duisburg, Germany), pp. 95-100, 1996.

Avalanche Breakdown in GaInP/GaAs HBTs

Peter Baureis

University of Applied Sciences Würzburg, Röntgenring 8, 97070 Würzburg, , Germany, E-Mail: baureis@faw.fh-wuerzburg.de

Abstract—Device destruction in gallium arsenide based multifinger heterojunction bipolar transistors (HBTs) mainly occurs due to thermal induced avalanche breakdown. Depending on the collector current density, different regions of avalanche breakdown in the collector are identified. A non-destructive pulsed measurement method of the collector base breakdown voltage at low and high current densities is developed. The measured breakdown voltages could be used to develop compact HBT simulation models.

Keywords — *Avalanche breakdown, electrothermal effects, heterojunction bipolar transistors, power amplifier, reliability.*

I. INTRODUCTION

The weak avalanche breakdown behavior is included in modern circuit simulation models for bipolar transistors [1], [2] to allow the circuit designer to predict the safe operating region of the transistor in power amplifier applications and to predict the transistors nonlinear distortion characteristics [3]. These models determine a collector base breakdown voltage V_{cbk} independent of collector current density j_c . A model improvement has been done by Scott and Low [4] and Kloosterman [5]. Their [4] one dimensional model – based on pulsed measurements - determined a linear increase of V_{cbk} with j_c at low collector current density followed by a linear decrease of V_{cbk} with j_c at high current density. The critical current density for the transition between low and high current densities occurs at $j_{ccrit} = N_c \cdot q \cdot v_{sat}$ (1), with N_c as averaged collector doping density, v_{sat} the electron saturation velocity in the collector and q the electron charge. This principal behavior could be explained as follows: At zero collector current density, the peak electric field occurs at the base-collector interface. Avalanche breakdown is initiated at this position when this electrical field achieves a value of E_{max} . In GaAs $E_{max} \approx 3...4 \cdot 10^5$ V/cm is the electric field at which impact ionization begins to be significant for avalanche breakdown [6]. As the current density in the collector increases, the negative space charge from the injected electrons decreases the

effective doping density $N_{eff} \approx N_c - \frac{j_c}{q \cdot v_{sat}}$ (1) and lowers

the maximum electrical field in the collector. Under this low current density operating conditions Reisch [7] predicted a linear increase of the breakdown voltage for constant doping profile in the collector:

$$V_{cbk}(j_c) = V_{cbk}(0) + \frac{W_c^2}{2 \cdot e \cdot v_{sat}} \cdot j_c \quad (2), \text{ where } W_c \text{ is the}$$

thickness and ϵ the permittivity of the collector region. At collector current densities higher than j_{ccrit} , the maximum electrical field occurs at the collector-subcollector part of the

base-collector space charge region under breakdown conditions as indicated in Fig. 1. A further increase of j_c lowers the breakdown voltage V_{cbk} considerable as the pulsed measurements on GaInP/GaAs HBTs in common emitter configuration show in Fig.2. Here a typical dc and pulsed output characteristic (collector current versus collector-base voltage with constant base current as parameter) of a single finger HBT with $2,5 \cdot 10 \mu m^2$ emitter area is shown. The critical current density $j_{ccrit} = 1.6 \cdot 10^4$ A/cm² predicted by eq. (1) fits to the measured data if the emitter area is used to calculate the collector current density. The paper is organized as follows: Section II investigates the breakdown mechanism under DC and pulsed operating conditions in single finger and multifinger HBT. Section III describes the investigated test structures and measurement results.

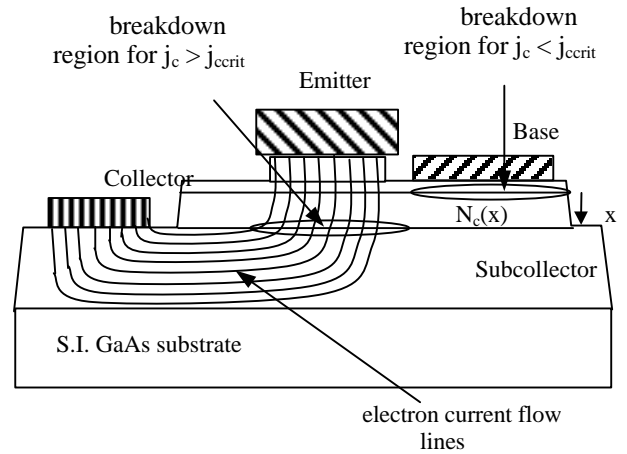


Figure 1. Schematic cross-section of mesa type HBT indicating areas of breakdown (not scaled).

II. BREAKDOWN MECHANISM

The HBT breakdown characteristics is determined by the collector doping profile $N_c(x)$. In the case of zero collector current, the electrical field is determined by $N_c(x)$ and the applied voltage. An increase in the applied collector-base Voltage V_{cb} increases the resulting electrical field up to E_{max} and breakdown occurs at $V_{cb} = V_{cbk0}$. The highest field appears at the base-collector interface as indicated in Fig.1. Under normal forward operating conditions of a npn HBT an electron current flows into the collector space charge region which itself consists of positive fixed charges from the ionized dopants. As a result the total charge level in the collector decreases, which decreases the resulting electrical field. Thus breakdown should occur at higher voltages ($V_{cbk} > V_{cbk0}$). In this mesa type transistor, the calculated increase of V_{cbk} with j_c using (2) predicts a breakdown voltage increase of

$\Delta V_{cbk} = 6.4$ V up to the critical current density j_{ccrit} . In contrast to the simple one-dimensional model, the measurements in Fig. 2 show an increase of only $\Delta V_{cbk} \approx 0.5$ V. The reason for this discrepancy is the fact that there are always areas in the collector space charge region where no electron current flow is present. This region is located under the base contact layer and is indicated in Fig. 1 with breakdown region for $j_c < j_{ccrit}$. Due to this two dimensional effect, the breakdown will occur in the transistor region where no current flow is present - at approximately V_{cbk0} . Therefore the breakdown voltage in compact bipolar models for mesa type transistors should be kept constant: $V_{cbk} = V_{cbk0}$ for $j_c < j_{ccrit}$.

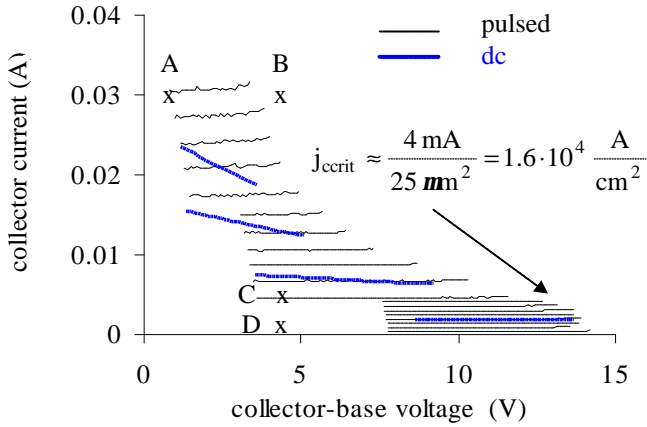


Figure 2. Measured pulsed and dc output characteristic of a $25 \mu\text{m}^2$ emitter area single finger HBT.

At higher current densities $j_c > j_{ccrit}$, the net charge in the collector changes its sign (base pushout occurs [8]). Under these conditions the highest electrical field appears at the subcollector side of the space charge region. Further increase of the collector current density at constant collector base voltage increases the resulting field at this location and thus reduces V_{cbk} . Fig. 2 shows a measured output characteristic which confirms the above description. In addition dc measurements are included in Fig. 2 to show that the breakdown voltage under pulsed conditions is always greater than the breakdown voltage at dc for $j_c > j_{ccrit}$. In contrast to the published compact models for avalanche breakdown, [1],[2],[4], the dependence of the measured breakdown voltages on the collector current density for breakdown j_{cbreak} is strongly nonlinear as shown in Fig.3. A simulation of the dependence of V_{cbk} on j_{cbreak} is included using the equations for the calculation of the collector field and the resulting avalanche current from [5]. As model parameters $W_c=1 \mu\text{m}$, $N_c=10^{16} / \text{cm}^3$, $\alpha_n=1.899 \cdot 10^7$ 1/m, and $b_n=5.75 \cdot 10^7$ V/m are used. Here α_n and b_n are the parameters to calculate the ionization coefficient of electrons in the GaAs collector layer. Their values are determined empirically by Bulman[9]. In this 1-d simulation it is also possible to calculate the electrical field in the reverse biased base-collector junction. In Fig. 4 the results are plotted at 4 different operating points which are indicated in Fig. 2. At the operating points A and B ($j_c > j_{ccrit}$) base pushout occurs and the effective basewidth is increased by the injection width $W_i(A)=0.8 \mu\text{m}$ and $W_i(B)=0.65 \mu\text{m}$. In this situation the maximum electrical field E_{max} occurs at the collector-subcollector interface. At operating point B E_{max} is

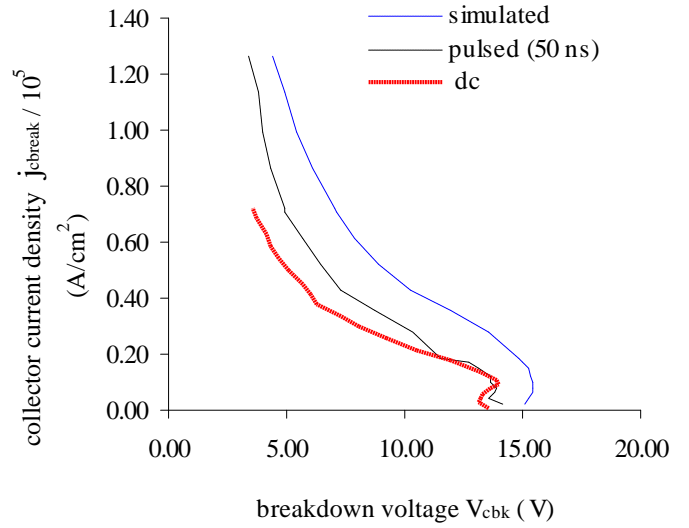


Figure 3. Comparison of the collector current density for breakdown j_{cbreak} extracted from Fig. 2 with simulated data using the Mextram weak avalanche breakdown model [5]

high enough to initiate the breakdown of the transistor. At the operating points C and D ($j_c < j_{ccrit}$) E_{max} is located at the base-collector interface. At D the collector is not fully depleted while at C a nearly constant electrical field profile is achieved.

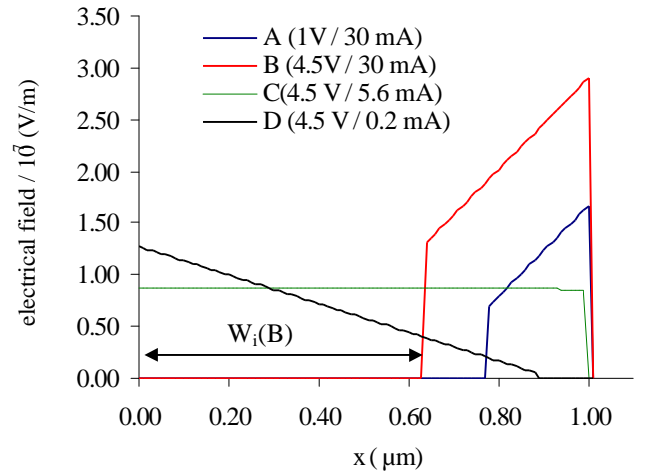


Figure 4. Calculation of the electrical field in the collector with $N_c=10^{16} / \text{cm}^3$ for the same HBT as used in Fig. 2. The 4 different operating points are indicated in Fig. 2. The vertical position x in the collector is defined in Fig. 1.

The models [1],[2],[4],[5] do not include thermal effects. In GaAs based HBTs the collector current collapse can occur in multifinger transistors [10] resulting in a current flow only through a single finger. This collapse increases j_c and therefore reduces the avalanche breakdown voltage V_{cbk} if the resulting current density after the thermal collapse is greater than j_{ccrit} . In this situation, the breakdown voltage of a multifinger transistor is lower than in a single finger device and equals the base collector voltage for the onset of the collector current collapse. Therefore avalanche breakdown is caused by a thermally triggered increase of the collector current density $j_c > j_{cbreak}$.

The thermal collapse itself is not necessarily accompanied with a destruction of the device. Thus if the current collapse occurs at low electric field in the collector, the collapse phenomenon could be observed in the transistors DC output characteristics as increased negative output conductance (e.g. DC measurement in Fig. 7). To analyze this complicated interactions, pulsed and DC measurement techniques to determine the HBTs output characteristics are developed.

III. MEASUREMENT RESULTS

The devices under test were supplied by United Monolithic Semiconductors (UMS) from their HB20D GaInP/GaAs HBT process. Capacitance voltage measurements of the base-collector junction allowed to extract the constant collector doping with $N_c=1 \cdot 10^{16} / \text{cm}^3$ and the collector thickness with $1 \mu\text{m}$. Therefore the onset of base pushout occurs at $j_{\text{crit}} \approx 1.6 \cdot 10^4 \text{ A/cm}^2$ assuming $v_{\text{sat}}=1 \cdot 10^7 \text{ cm/s}$. At this current density a change of breakdown voltage with current density is expected. As test structures we used single finger transistors with emitter area between $6 \mu\text{m}^2$ up to $200 \mu\text{m}^2$ and one multifinger transistor with four emitter fingers and a total emitter area of $100 \mu\text{m}^2$.

The common emitter measurements of the HBTs are performed under pulsed conditions where the base current is pulsed and the collector voltage is held constant. The complete measurement equipment is computer controlled over the GPIB bus. The pulsed measurements are performed with a pulse width of 300 ns and a duty cycle of 0.4 % to avoid thermally induced current collapse phenomena. Fig. 5 shows the on wafer measurements of the pulsed current waveforms using tungsten probe tips where the pulsed base current is supplied with a resistor of 3.3 kΩ in series to the base contact. The collector voltage is supplied by a DC power supply for currents up to 2A and voltages up to 20 V. Additionally a broadband (10 kHz – 18 GHz) bias tee is used to prevent low frequency oscillations. The collector current I_c is measured as voltage drop on a 10Ω series resistor with a digital oscilloscope. The triggering of the oscilloscope is performed on the falling edge of the pulse. Therefore the shown timebase during the pulse is negative. Steady state is achieved after approximately -200 ns. After this time delay reliable current measurements are possible.

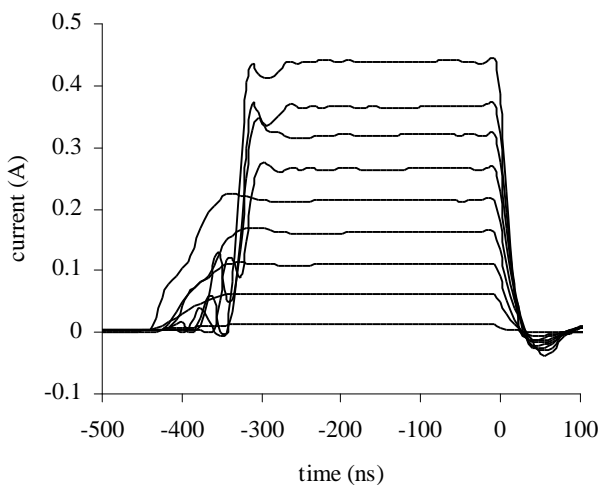


Figure 5. Measured on wafer current waveform up to 400 mA.

The transistors active collector area could not be easily obtained due to a two dimensional current flow in the collector and possible underetching of the thick collector layer. Therefore the measured currents are always related to the active emitter area to calculate the collector current density. The breakdown voltage V_{cbk} is then extracted from the type of non-destructive measurements shown in Fig. 2. There, one characteristic is measured applying a constant base current pulse and increase the applied collector-base voltage V_{cb} in 100 mV steps. To detect the onset of avalanche breakdown the history of the measurement is used to allow the measurement of the next operating point. V_{cb} is increased until I_c changes more than 1 % during this 100 mV voltage step. This 1 % current increase criterion is used to estimate the breakdown voltage V_{cbk} in a non-destructive way. Therefore the whole output characteristics is measured using only one device. Measurements shown by [4] used one device for each curve. Therefore 19 transistors would be necessary to achieve the results shown in Fig. 2. If we use e.g. 2 % current increase with a V_{cb} voltage step of 100 mV as stop criterion for the voltage sweep, a destruction of the transistor occurs.

An explanation that the 1 % criterion is sufficient to detect the breakdown voltage is given as follows: The collector current in the linear operating region of bipolar transistors at constant base current is determined by three effects: Base width modulation (Early effect), temperature dependent common emitter current gain and avalanche multiplication. The destination of all three effects at DC operating conditions is not possible. The collector current increase at the onset of considerable avalanche multiplication shown in the pulsed measurements of Fig. 2 and Fig. 7 is caused by avalanche multiplication because the Early effect could be neglected in our HBTs: The Early effect is suppressed due to the high base doping accompanied with low emitter and collector doping resulting in a collector current increase of only 0.05 % if we assume an early voltage $> 200\text{V}$. Additionally the current gain of these transistors has a negative temperature coefficient resulting in negative output conductance under DC operating conditions.

Fig.6 shows the results of the determined breakdown Voltage V_{cbk} from pulsed measurements as a function of the collector current density j_c for three different sized single finger devices. The measured current density versus breakdown voltage characteristic is scalable with the determined emitter area. For a collector current density smaller $1.6 \cdot 10^4 \text{ A/cm}^2$,

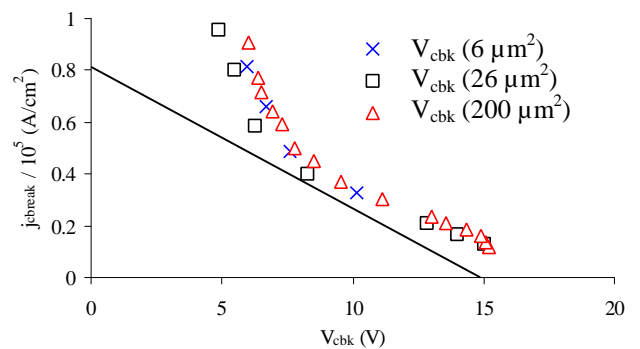


Figure 6. Dependence of the collector current density for breakdown j_{cbreak} versus breakdown voltage V_{cbk} for 3 different emitter areas ($6, 26, 200 \mu\text{m}^2$)

V_{cbk} is nearly constant at approximately 15 V. For $j_c > 1.6 \cdot 10^4$ A/cm² the characteristics is given as a nonlinear function of j_c .

The straight line included in Fig. 6 gives the save operating regime of the device and sets the maximum emitter current density for class A power amplification to achieve maximum output power: The operating point for maximum output power should therefore be at $V_{ce} \approx 8$ V with $j_c \approx 0.35 \cdot 10^5$ A/cm², which translates in a maximum power density of approximately $1.4 \cdot 10^5$ W/cm² with the assumption of 50 % power added efficiency. This means: to achieve an RF output power of 1.4 W, a transistor with an emitter area of 1000 μm^2 has to be used without consideration of self heating effects which worsens the situation.

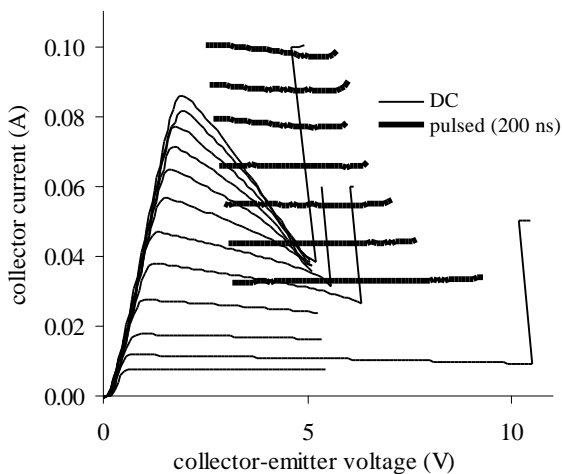


Figure 7. Comparison of the measured pulsed (200 ns) and dc output characteristics of a 4 finger HBT with a total emitter area of 100 μm^2

A comparison of DC with pulsed measurements is done in Fig. 7 on a four finger transistor with a total emitter area of 100 μm^2 . The DC measurements could not be extended to the same level of V_{cb} as shown in the pulsed measurements. The reason for the destruction is the increased junction temperature caused by self-heating, resulting in a current collapse due to the negative temperature coefficient of the current gain [10]. The collapse occurs in a way that at a certain temperature difference between the hottest and the coldest finger, the colder finger is switched off while the hotter finger has increased current density. This process repeats until only one finger carries the whole collector current at four times the current density in our four finger device. If the current density at a certain V_{cb} exceeds the value shown in Fig. 6, catastrophic destruction through avalanche breakdown occurs. This is shown in a strong increase of I_c in the DC measurement of Fig. 7.

IV. CONCLUSION

The nonlinear dependence of the avalanche breakdown voltage under different collector current densities is measured

in a non-destructive way under pulsed and DC operating conditions. Two regions of operation could be distinguished: At $j_c < j_{crit}$ the breakdown occurs in the part of the collector space charge region where no current flow is present. Therefore nearly no change of V_{cbk} with j_c is observed. At $j_c > j_{crit}$ a strong nonlinear decrease of V_{cbk} with j_c is measured. The behavior can be used to predict the maximum available power density under class A power operation. The difference between the DC and the pulsed breakdown voltages V_{cbk} is explained by a thermally triggered avalanche breakdown caused by a current collapse in multifinger HBTs which increases j_c at the hottest finger. The measurements presented could be used to build a new compact electro-thermal HBT transistor model for circuit simulation which includes a weak avalanche breakdown voltage dependence as shown in Fig. 4. This will give circuit designers the possibility to simulate the save operating region of multifinger power transistors under DC and pulsed operation.

REFERENCES

- [1] C.C. Mc Andrew, J.A. Seitchik, D.F. Bowers, M. Dunn, M. Foisy, I. Getreu, M. McSwain, S. Moinian, J. Parker, D.J. Roulston, M. Schröter, P. van Wijnen and L.F. Wagner "VBIC95, The Vertical Bipolar Inter-Company Model", IEEE J. Solid-State Circuits, Vol.31, No. 10, pp. 1476-1483, 1996.
- [2] S. Heckmann, R. Sommet, J.M. Nebus, J.-C. Jacquet, D. Flriot, P. Auxemery and R. Quere, "Characterization and Modeling of Bias Dependent Breakdown and Self-Heating in GaInP/GaAs Power HBT to Improve High Power Amplifier Design", IEEE Trans. MTT, Vol. 50, No. 12, pp. 2811- 2819, 2002.
- [3] G. Niu, J.D. Cressler, S. Zhang, U. Gogineni and D.C. Ahlgren, "Measurement of Collector-Base Junction Avalanche Multiplication Effects in Advanced UHV / CVD SiGe HBT's", IEEE Transactions on Electron Devices, Vol. 46, No5, May 1999, pp. 1007-1015.
- [4] J.Scott and T. Low, "Avalanche Breakdown in HBTs: Variation with Collector Current and Effect on Linearity", 2000 IEEE GaAs IC Symposium Technical Digest, pp. 237-240.
- [5] W.J. Kloosterman, J.C.J Paasschens and R.J. Havens, "A comprehensive Bipolar Avalanche Multiplication Compact Model for Circuit Simulation", 2000 BCTM, Sep. 2000, pp. 172-175.
- [6] B.J.Baliga, R.Ehle, J.R.Shealy, W. Garwacki "Breakdown Characteristics of Gallium Arsenide", IEEE Electron Device Letters, Vol. 2, No. 11, Nov. 1981, pp. 302-304.
- [7] M.Reisch, "On Bistable Behavior and Open-Base Breakdown of Bipolar Transistors in the Avalanche Regime – Modeling and Applications", IEEE Trans. Electron Devices, Vol. 39, No. 6, June 1992, pp. 1398-1409.
- [8] C.T. Kirk, "A Theory of Transistor Cutoff Frequency (fT) Falloff at High Current Densities", Trans. IRE, Vol ED-9, March 1962, pp. 164-174.
- [9] G.E. Bulman, V.M. Robbins and G.E.Stillman, "The determination of impact ionization coefficients in (100) gallium arsenide using avalanche noise and photocurrent multiplication measurements", IEEE Trans. Electron Devices, Vol. 32, pp. 2454-2466, 1985
- [10] W.Liu and A. Khatibzadeh, "The collapse of current gain in microwave multi-finger heterojunction bipolar transistors: Its substrate dependence, instability criteria and modeling", IEEE Trans. Electron Devices, vol. 41, pp. 1698-1707, 1994.

Unidirectional Slot Subarray-Antenna with High Efficiency for X-Band Application

Claudius Löcker*, Thomas Vaupel* and Thomas F. Eibert†

* FGAN-Research Institute for High Frequency Physics and Radar Techniques (FHR)

Neuenahrer Str. 20, 53343 Wachtberg-Werthhoven, Germany

† University of Stuttgart, Institute of Radio Frequency Technology,
Pfaffenwaldring 4770550 Stuttgart, Germany

Abstract—Slot antennas in metallic ground planes are very attractive radiation elements for conformal antenna application. For unidirectional radiation, a slot requires a back reflector close to the aperture. Unfortunately, the resulting parallel plate structure enables parasitic parallel plate mode propagation resulting in a low radiation efficiency. In this contribution we investigate unidirectional, low profile slot configurations with parallel plate mode suppression by shorting pins. Starting with a parametric study on the effects of shorting pin location and back reflector distance, we present a bow tie slot element with 85% efficiency. This element was further used in a linear, four element antenna subarray with 70% efficiency.

I. INTRODUCTION

Antennas in printed circuit technology are widely used due to their low profile, robustness, light weight and low cost. Electronic warfare, communication and automotive are only some fields where they play an important role. Traditionally, many designs are available in literature for patch antennas. The patch antenna can be seen as a cavity resonator with only narrow bandwidth. For wideband application the quality factor of the resonator can be reduced by using thick substrates. However, this structure can easily suffer from power leakage due to surface wave propagation. Moreover, the patch antenna has an inherently dielectric surrounding which is not well suited for integration in metallic surfaces.

Slot antennas are a pretty good alternative for conformal

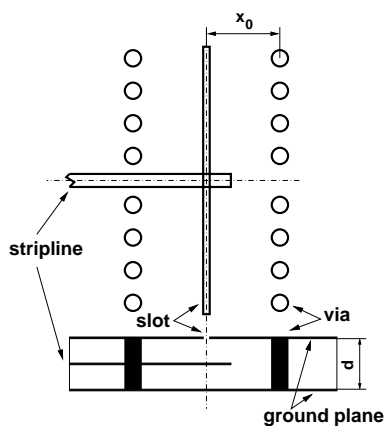


Fig. 1. Geometry of rectangular slot element.

antenna applications. Since the radiation characteristic of a

slot is bidirectional, a reflector must be placed close to the slot, yielding in a thin structure. However, this configuration

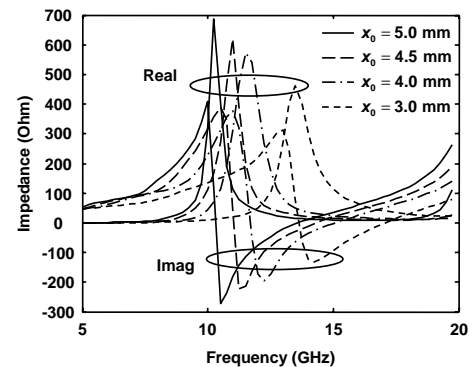


Fig. 2. Parametric study: Input impedance with respect to via distance x_0 .

provides parallel-plate mode propagation. Higher order modes can be avoided if their cut-off frequency is higher than the frequency band of operation. But suppression of the fundamental TEM mode starting at 0 Hz is a difficult task. One method to suppress these parasitic modes is the use of shorting-pins, which was first introduced by [1].

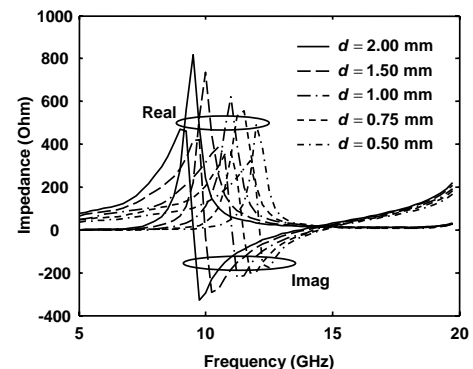


Fig. 3. Parametric study: Input impedance with respect to reflector distance d .

Shorting pins or vias have a strong influence on impedance, resonance and broadband behavior. We investigated a single slot element theoretically by a parametric study and present simulation and measured data of a fabricated slot. The slot

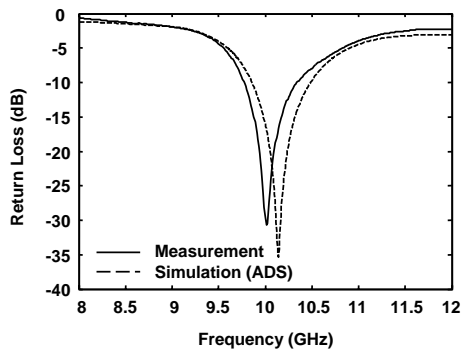


Fig. 4. Rectangular slot element, simulated and measured return loss.

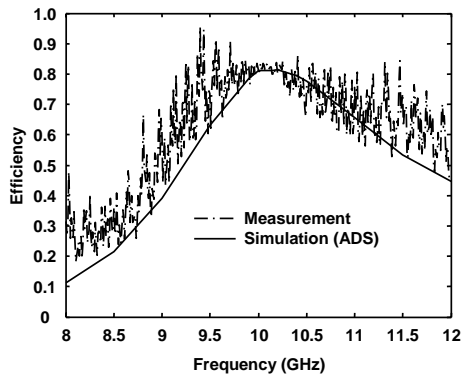


Fig. 5. Rectangular slot element, simulated and measured efficiency.

was also investigated concerning mutual coupling properties. Starting from this design, a tapered bow-tie is described as a single element and as an element in a four element linear subarray, which is intended to be the radiating element in a one dimensionally curved array antenna.

II. RECTANGULAR SLOT ELEMENT

In order to get a deeper theoretical insight, a single slot element was first investigated by a parametric study. The geometry of the rectangular slot element is depicted in Figure 1. Parameters were the via distance x_0 and the reflector distance d . The dielectric between the two metallic plates has a permittivity of 2.2. Contrary to figure 1, the slot was excited by a magnetic δ -gap voltage source. A surface/volume integral equation method for the analysis of planar circuits with additional 3-D-components embedded in a multilayered medium of infinite extent is applied to determine the terminal impedance [2]. As the layered medium environment is analytically considered by its spectral domain Green's function, only the magnetic surface currents in the slot aperture and the electric volume currents for the vias must be discretized. Figure 2 and figure 3 show the real and imaginary part of the terminal impedance with respect to the via position x_0 and reflector distance d . The curves show a typical resonator behavior. The vias and the reflector shift the imaginary part of the impedance to the inductive region. The frequency of the first resonance (corresponding to the peak input resistance) increases and the peak value decreases and broadens with

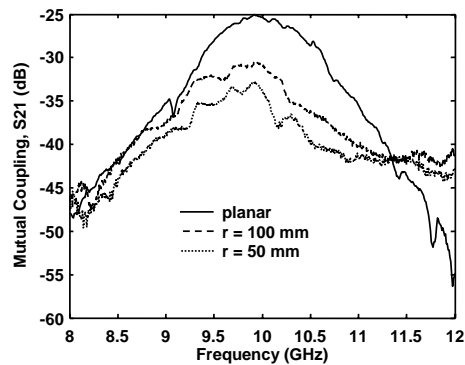


Fig. 6. Mutual coupling: Transmission Measurement, collinear slot configuration.

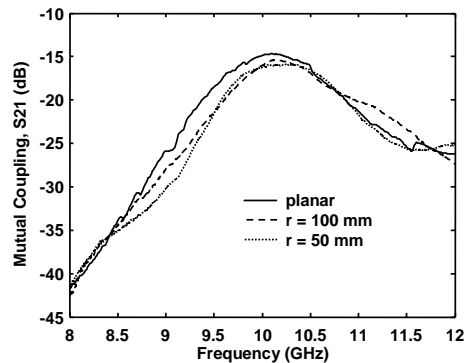


Fig. 7. Mutual coupling: Transmission Measurement, broadside slot configuration.

smaller via and reflector distances.

The slot was fabricated on a Rogers Duroid 5880 substrate. The slot is excited by an open ended stripline. The length of the stub determines the up and down shift of the imaginary part to get an optimized impedance matching. The width of the stripline was chosen for 50 Ω line impedance. Figure 4 shows measured and simulated data of the return loss of the rectangular slot element. Simulations were done by Agilent's ADS2003A Momentum. Copper and dielectric losses were included. The measured efficiency in figure 5 was determined by the gain over directivity relationship. The directivity was estimated by integration of the radiating fields over all radiation directions, whereas the gain was quantified by the gain transfer method. The bandwidth of the slot (return loss < -10 dB) is about 5% and the efficiency doesn't decrease below about 80% in the band of operation.

Mutual coupling between elements in an array antenna is also an important aspect. Two appropriate slot configurations are collinear and broadside slot arrangements. Center-center distances with respect to the first slot are 22.5 mm and 52.5 mm in the collinear configuration, whereas in the broadside slot configuration the separation between the slots could be chosen to 15 mm and 45 mm. The coupling was determined by two port transmission measurements with a network analyzer.

The remaining port of the third slot was matched with a 50 Ω load. The slots were etched on a planar substrate and

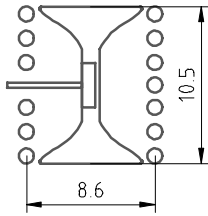


Fig. 8. Geometry of bow-tie slot element [mm].

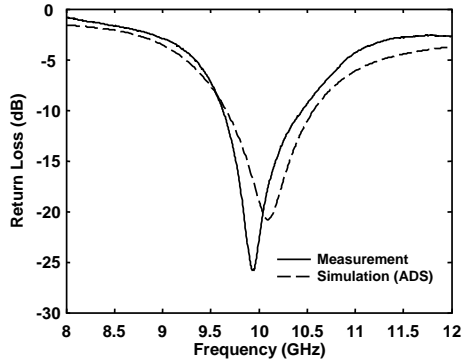


Fig. 9. Bow-tie slot element, simulated and measured return loss.

on two cylindrical structures with a radius of 50 mm and 100 mm. Figure 6 and figure 7 show measured S_{21} scattering coefficients, which describe the coupling behavior with respect to varying radii of the mounting structure. A smaller coupling was measured for the collinear arrangement compared to the broadside configuration. This is because of the radiating null in the corresponding direction. The relative large coupling in the second case is caused by the radiated space wave traveling along the slot ground plane. The curves also show that the coupling decreases with decreasing the radius of the cylinder.

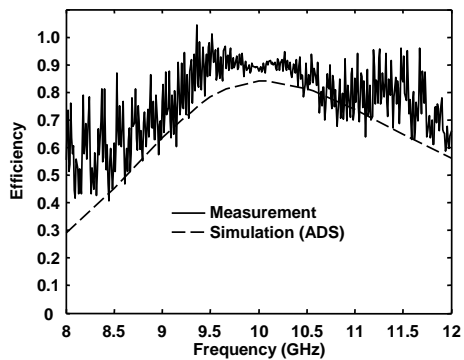


Fig. 10. Bow-tie slot element, simulated and measured efficiency.

III. BOW-TIE SLOT ELEMENT

In order to increase the bandwidth, the slot was carefully widened like a bow-tie. The length of the slot was also decreased but at the cost of an increased substrate height. The substrate thickness for the bow-tie element is 2 mm, whereas

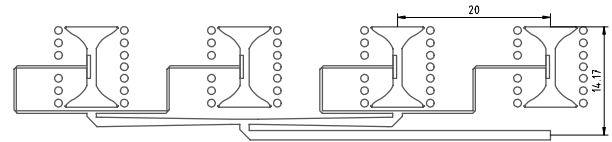


Fig. 11. Geometry of four element subarray [mm].

the permittivity remained 2.2. As shown in figure 8, the feeding stripline ends under the aperture and was widened to a rectangular shape. The feeding line is placed 0.5 mm under the aperture, so the stripline is no more symmetrical. Furthermore the line impedance has been increased to 100Ω . However, the feeding line was linearly tapered to a line impedance of 50Ω in order to get measurement results with a 50Ω network analyzer system. Figure 9 and figure 10 depict the simulated and measured return loss and efficiency respectively. The bandwidth could be increased to 0.8 GHz and is higher than for the rectangular slot element. The measured antenna efficiency is about 85-90% in the band of operation.

The bow-tie slot antenna was used as an element radiator

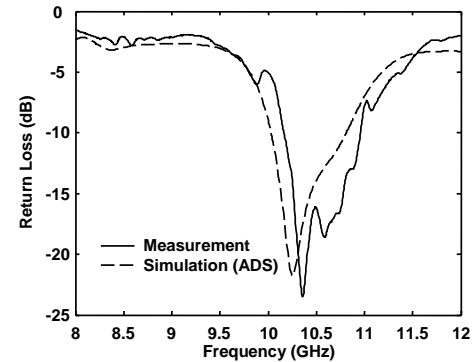


Fig. 12. Four element subarray, simulated and measured return loss.

in a four element subarray, figure 11. The element distance is 20 mm. Since the subarray separation should not exceed 16 mm, the parallel feed consists of closely spaced parallel lines. The T-type power divider has tapered branches to increase the bandwidth. The feeding line was also carefully optimized to increase the bandwidth. Figure 12 shows simulated and measured return loss results. The measured bandwidth is about 7%. The efficiency of the subarray with respect to the accepted circuit power is depicted in figure 13 and amounts to 70% in the band of operation.

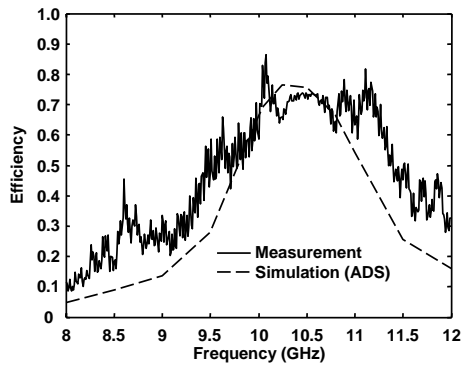


Fig. 13. Four element subarray, simulated and measured efficiency.

IV. CONCLUSION AND OUTLOOK

We investigated theoretically the impact of shorting pins location and backreflector distance on the input impedance of a rectangular slot element and showed by measurements that vias are suitable for parallel plate mode suppression and bandwidth enhancement. Mutual coupling results were also presented on mounting structures with different radii. The radiation performance of a second bow-tie like aperture was described. This element was used in a four element subarray with 7% bandwidth and 70% efficiency in the band of operation. The bandwidth of the presented array should be further increased. The subarray is intended as the radiating element in a one dimensionally curved antenna array.

REFERENCES

- [1] D. J. Sommers, *Slot Array Employing Photoetched Tri-Plate Transmission Lines*, IEEE Trans. Microwave Theory Tech., vol. 3, no. 2, pp. 157-162, Mar. 1955.
- [2] T. Vaupel, V. Hansen, F. Schäfer, *Radiation Efficiency Analysis of Submm-Wave Receivers Based on a Modified Spectral Domain Technique*, Radio Science, vol. 38, no. 4, pp. 13-1–13-12, Aug. 2003.

Numerically Efficient MPIE-MoM Technique for Analysis of Microstrip Structures in Layered Media

Zulfu GENC¹ and Hasan H. Balik²

¹University of Firat, Department of Informatics, 23119, Turkey, +904242370000/3160, zulfugenc@hotmail.com

²University of Firat, Department of Electrical and Electronics Eng., 23119, Turkey, +904242410099, hasanbalik@gmail.com

Short Abstract— In this study, full-wave space-domain approach is presented for analysis of some passive microwave circuits in planarly layered media. The Electromagnetic fields are described in terms of a mixed potential integral equation (MPIE) formulation. This formulation is based on the method of moments (MoM) in spatial domain and utilizes closed-Green's functions. We have introduced new microwave filters consists of coupled microstrip open-loop resonators and analyzed to demonstrate the efficiency and accuracy of MPIE-MoM technique.

Keywords-Method of Moments;mixed potential integral equation;microstrip;layered media;Green's functions

I. INTRODUCTION

Passive microwave devices embedded in stratified media have been extensively studied in the literature and numerous planar structures have been designed using integral equation based techniques. Integral equation can be formulated in various ways. Among these, mixed potential integral equation (MPIE) is one of the most successful methods for the analysis of microwave circuits and planar antennas [1-3]. Alternative formulations are the electric field integral equation (EFIE) and magnetic field integral equation (MFIE). For numerical modeling of small-to-medium-sized printed planar geometries used in monolithic integrated microwave and millimeter structures, the method of moments (MoM) [4] is generally accepted to be one of the most efficient and robust methods. The MoM formulation in electromagnetic problems starts with writing the integral equations (MPIE, EFIE or MFIE). Generally, EFIE or MFIE is applied in the spectral-domain, while MPIE is applied in the spatial-domain. It should be noted that EFIE and MFIE use the Green's functions of the electric and magnetic fields as their kernels, whereas the MPIE uses the Green's functions of the scalar and vector potentials, of which singularities are of the order of $1/R$, and, therefore, are less singular [5]. Hence, the use of MPIE in conjunction with the spatial-domain MoM has been preferred for the characterization of planar printed geometries in general. More recently, this formulation was improved by the introduction of suitable closed-form Green's functions in spectral and spatial domains for general media [6]. With the use of closed form Green's functions, calculation of the oscillatory and slow converging Sommerfeld integral is no more necessary. In the derivations, the main goal is to put these closed-form representations in an appropriate form for the solution of MPIE-MoM. MPIE is formulated as the governing equation of

the printed geometries in layered planar media, and the spatial-domain MoM is used to solve for the unknown current densities in the structure.

In this paper, formulation of MPIE-MoM is concisely explained from a theoretical point of view in the next section. Then, scattering parameter analysis and simulation algorithm are introduced. In numerical examples section, the MPIE-MoM formulation is applied to new filter configurations and the results are compared from commercial EM software, em Sonnet. The final section presents the conclusions.

II. FORMULATION OF MPIE-MoM

For the sake of illustration, a typical microstrip structure in layered environment is shown in Figure 1. It is assumed that conductors are lossless and infinitesimally thin and all layers extend to infinity in transverse domain (xy-plane). The thickness and permittivity of each layer are denoted as h_i and ϵ_{ri} , respectively.

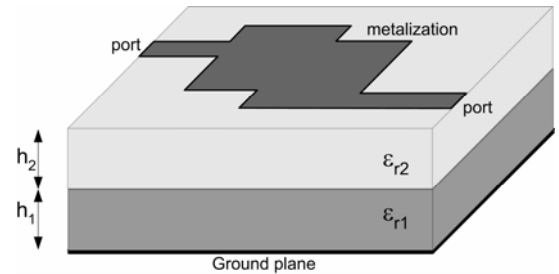


Figure 1. A general microstrip structure in layered media.

In the MPIE-MoM formulation, first the electric field is written in terms of scalar and vector potentials as

$$\mathbf{E} = -j\omega\mathbf{A} - \nabla\phi \quad (1)$$

Then, the vector and scalar potentials are expressed in terms of convolution integrals involving surface density \mathbf{J} and charge density ρ on the metallization as

$$\mathbf{A} = \overline{\mathbf{G}}^A * \mathbf{J} \quad (2)$$

$$\phi = G^q * \rho \quad (3)$$

By employing the continuity equation ($\nabla \cdot \mathbf{J} + j\omega\rho = 0$), the charge density ρ in the scalar potential equation can be written

in terms of surface current density and from (1), the tangential components of electric field on the metallization can obtain as

$$E_x = -j\omega G_{xx}^A * J_x + \frac{1}{j\omega} \frac{\partial}{\partial x} (G^q * \nabla \cdot \mathbf{J}) \quad (4)$$

$$E_y = -j\omega G_{yy}^A * J_y + \frac{1}{j\omega} \frac{\partial}{\partial y} (G^q * \nabla \cdot \mathbf{J}) \quad (5)$$

where * denotes convolution and $G_{xx}^A = G_{yy}^A$. The explicit expression for the Green's functions of the scalar potential in (4) and (5) is:

$$G^q * \nabla \cdot \mathbf{J} = G_x^q * \frac{\partial J_x}{\partial x} + G_y^q * \frac{\partial J_y}{\partial y} \quad (6)$$

Figure 2 shows the block diagram for the solution of MPIE-MoM. In the first step, the unknown current distribution on the metallization is expanded as a set of known basis functions with unknown coefficients or amplitudes as:

$$J_x(x, y) = \sum_m \sum_n I_x^{(m,n)} B_x^{(m,n)}(x, y) \quad (7)$$

$$J_y(x, y) = \sum_m \sum_n I_y^{(m,n)} B_y^{(m,n)}(x, y) \quad (8)$$

where $B_x^{(m,n)}$, $B_y^{(m,n)}$ are the known basis functions with unknown amplitudes $I_x^{(m,n)}$, $I_y^{(m,n)}$, defined at (m,n) -th position on the subdivided horizontal conductor. In this study, the basis functions used to approximate the current density on the metallization are chosen to be rooftop functions, by the use of which the unknown current distribution on metallization can be modeled very accurately.

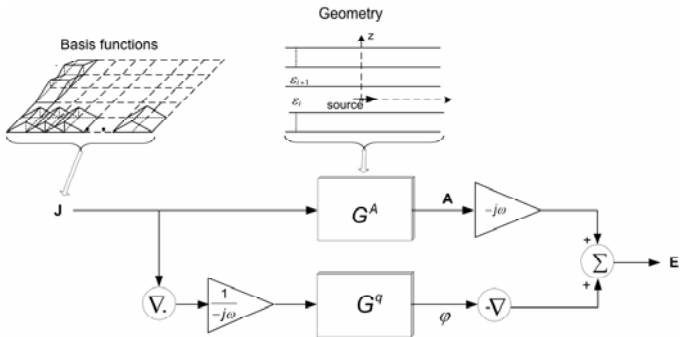


Figure 2. The block diagram for the solution of MPIE-MoM

In the second step, current densities in (7) and (8) are substituted into the electric field expressions of (4) and (5), and boundary conditions are applied. Application of the boundary conditions is performed in the integral sense through the well-known testing procedure of the MoM, where the field expressions are multiplied by testing functions $T_x^{(m',n')}$, $T_y^{(m',n')}$ and integrated on the conductors and set to zero ($\langle T_x^{(m',n')}, E_x \rangle = 0$ and $\langle T_y^{(m',n')}, E_y \rangle = 0$). The resulting matrix equation for the unknown amplitudes of the basis functions has the following form:

$$[Z][I] = [V]$$

$$\begin{bmatrix} Z_{xx} & Z_{xy} \\ Z_{yx} & Z_{yy} \end{bmatrix} \begin{bmatrix} I_x \\ I_y \end{bmatrix} = \begin{bmatrix} V_x \\ V_y \end{bmatrix} \quad (9)$$

where $[Z]$ is $N \times N$ impedance matrix and the entries Z_{ij} represent the mutual impedances between the testing and basis functions, $[V]$ is the $N \times 1$ excitation matrix and V 's represent the excitation voltages due to the current source(s), and finally $[I]$ is the $N \times 1$ current coefficient matrix. As an example, a typical matrix term involving both the scalar and vector Green's functions are given in the following form:

$$Z_{xx} = \left\langle T_x^{(m',n')}, G_{xx}^A * B_x^{(m,n)} \right\rangle + \frac{1}{w^2} \left\langle T_x^{(m',n')}, \frac{\partial}{\partial x} \left[G_x^q * \frac{\partial B_x^{(m,n)}}{\partial x} \right] \right\rangle \quad (10)$$

In the above equation, \langle, \rangle denotes inner product and * denotes convolution operator. After forming the matrix entries, two major steps are left to find the unknown coefficients of basis functions: i) evaluation of these matrix entries, ii) solution of the matrix equation for the coefficients of the basis functions. Analytical methods introduced by Alatan et. al [7] are used for the evaluation of these matrix entries. After the evaluation of inner product terms and substituting them into (9), the current densities on the conductors are obtained by solving the matrix equation. Finally, the circuit parameters such as the scattering parameters are extracted from the current distribution.

2.1. Scattering Parameter Analysis

In order to obtain the scattering parameters, a general two port transmission line is used. Having calculated the current densities on the conductor, the current on each port of the transmission line is written as a linear combination of complex exponentials by using the generalized pencil of function (GPOF) method [8] as

$$I(l) \approx \sum_{i=1}^N I_i \cdot e^{(\alpha_i + j\beta_i)l} \quad (11)$$

where l is the distance along the port transmission line, α_i is the attenuation and β_i is the propagation constants of the i^{th} mode of current waves.

2.2. Simulation Algorithm

A simplified flowchart of the algorithm according to the MPIE-MoM solution method described in the previous sections is given in Figure 3. The software starts by reading the layout file that includes the operating frequency, layer information, meshing parameters, and port definitions. According to the meshing parameters, the geometry is subdivided and the number of unknowns is determined. After calculating the coordinates of the basis and test functions, similarities among the inner product terms are tabulated in order to assist the computation in the further steps. Then MoM matrix is filled using the basis functions and Green's functions. The resulting

linear system is solved for the unknown basis amplitudes. Finally, circuit parameters are saved.

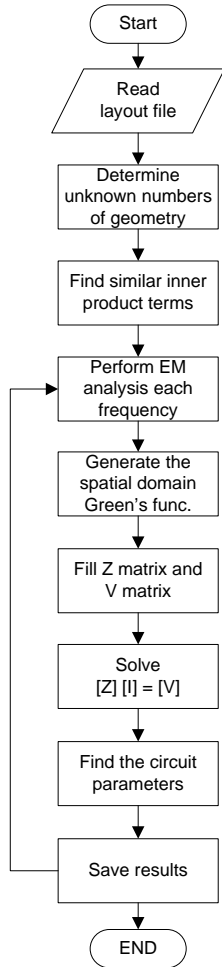


Figure 3. Simple flowchart of the algorithm

III. NUMERICAL EXAMPLES

In this section, the MPIE-MoM formulation is applied to new filter configuration consists of coupled microstrip open-loop resonators. For the examples, general microstrip geometry in a layered media is assumed where all layers and the ground plane extend to infinity in the horizontal plane, and the conductors are lossless and thin. The S-parameters provided here are normalized with respect to 50-Ω reference impedance. The method used in this work is compared with the results obtained from the well-known commercially available full-wave EM Simulator Sonnet.

First example is the dual-mode linear phase filter as shown in Figure 4. The filter consists of a set of microstrip coupled open-loop resonators with a spacing of 1.5mm and an open-gap of 0.5mm on a substrate with a thickness of 1.27mm and $\epsilon_r = 10.2$. The size of open-loop resonator is 6.5mm, the width of coupled open-loop arms is 1mm and the length of the feed line is 3mm. The geometry was analyzed by using the MPIE-MoM technique, over a frequency range of 2.0 GHz to 3.0 GHz.

Figure 5 is comparison of the S-parameters for the dual mode linear phase filter.

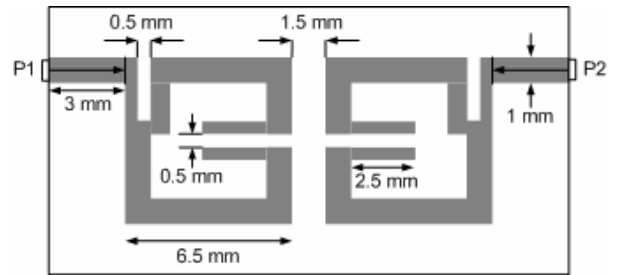


Figure 4. Geometry of the dual-mode linear phase filter.

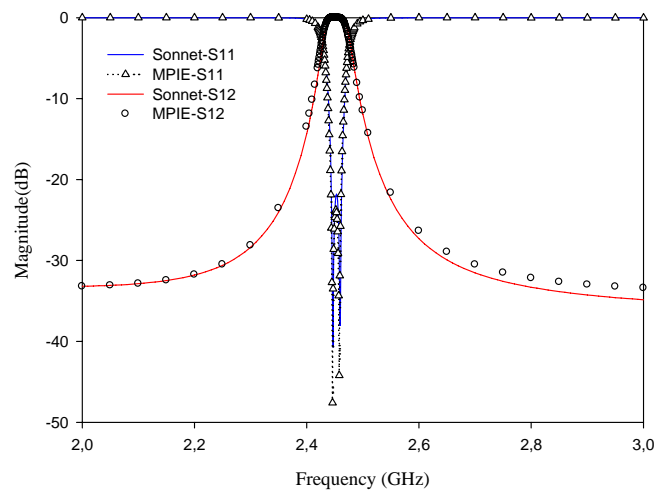


Figure 5. Magnitudes of S_{11} and S_{12} of the dual-mode linear phase filter shown in Figure 4.

Second example is the dual-mode elliptic filter as shown in Figure 6. As shown in Figure 6, the difference from dual-mode linear phase filter is diagonal placement of resonator feed lines. For the same frequency range, analysis results obtained using MPIE-MoM technique is represented in Figure 7.

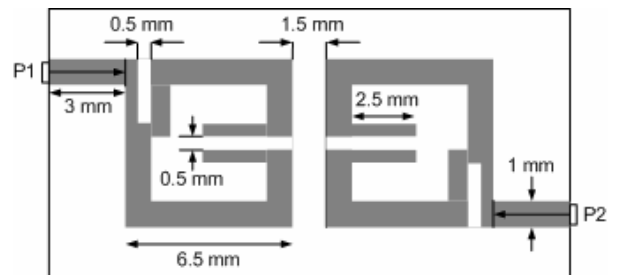


Figure 6. Geometry of dual-mode elliptic filter.

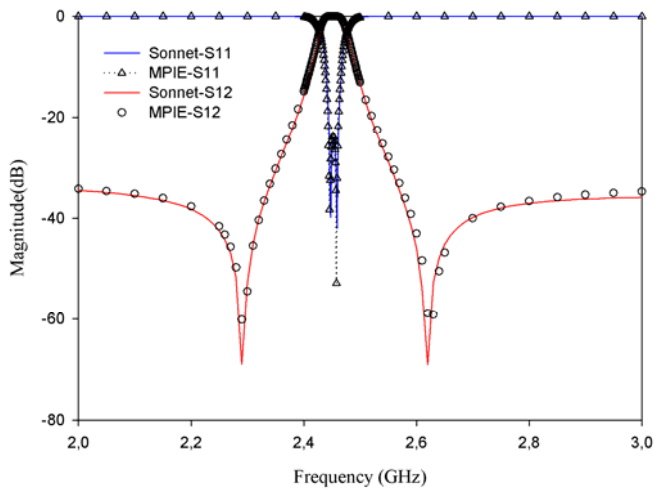


Figure 7. Magnitudes of S_{11} and S_{12} of the dual-mode elliptic filter shown in Figure 4.

When seeing frequency response of filters shown in Figure 5 and 7, both filters represent band-pass filter characteristics. The two types of filters have been constructed from same type of resonators by exchanging feed lines as cross and diagonally.

IV. CONCLUSION

This paper presents a numerically efficient MPIE-MoM solution for analysis of microstrip structures in a layered media. New microwave filters consists of coupled microstrip open-loop resonators are analyzed to demonstrate the efficiency and accuracy of MPIE-MoM technique. The results obtained are in

good agreement with the results obtained from well-known EM software SONNET. Analyzed new designed filters demonstrate linear phase and elliptic frequency characteristics with having narrow band and high selectivity features. Because of these features, these filters were found to be suitable for sensitive microwave circuits needed in mobile communication systems.

REFERENCES

- [1] M. Tsai, F.D Flaviis, O. Fordham, and N. G. Alexopoulos, "Modeling Planar Arbitrarily Shaped Microstrip Elements in Multilayered Media", *IEEE Trans. Microwave Theory and Tech.*, vol.45 no.3, March 1997.
- [2] J.R Mosig and F.E. Gardiol, "General Integral Equation Formulation for Microstrip Antennas and Scatters", *IEE Proc.*, vol.132, Pt. H, no.7, pp. 424-432, Dec. 1985.
- [3] J. R. Mosig, "Arbitrarily Shaped Microstrip Structures and Their Analysis with a Mixed Potential Integral Equation", *IEEE Trans. Microwave Theory and Tech.*, vol. 36, no.36, pp. 314-323, Feb. 1988.
- [4] R. F. Harrington, *Field Computation by Moment Methods*, Melbourne, FL: Krieger, 1983
- [5] N. V. Shuley, R. R. Boix, F. Medina, M. Horno, "On the Fast Approximation of Green's Functions in MPIE Formulations for Planar Layered Media", *IEEE Trans. Microwave Theory and Tech.*, vol. 50, no.9, pp. 2185-2192, Sep. 2002.
- [6] G. Dural and M. I. Aksun, "Closed-Form Green's Functions for General Sources And Stratified Media", *IEEE Trans. on Microwave Theory Tech.*, vol. 43, pp. 1545-1552, July 1995.
- [7] L. Alatan, M. I. Aksun, K. Mahadevan and T. Birand, "Analytical Evaluation of the MoM Matrix Elements," *IEEE Trans. on Microwave Theory Tech.*, vol. 44, pp. 519-525, Apr 1996.
- [8] Y. Hua and T. K. Sarkar, "Generalized Pencil-of-Function Method for Extracting Poles of an Em System from its Transient Response," *IEEE Trans. on Antennas and Propagation*, vol. AP-37, pp. 229-234, Feb. 1989.

Switching speed analysis of low complexity RF-MEMS switches

C. Siegel¹, V. Ziegler¹, C. von Wächter¹, B. Schönlinner¹, U. Prechtel¹, H. Schumacher²

¹EADS Deutschland GmbH, Corporate Research Centre, LG-ME, 81663 Munich, Germany, +498960724203

²University of Ulm, Dept. of Electron Devices and Circuits, Albert Einstein Allee 45, 89081 Ulm, Germany

Abstract — Tunable microstrip filters, phase shifting elements, and switches in the GHz range were previously realized in a low complexity technology. This paper now presents time dependent measurements of the RF-signal to evaluate the switching behavior of this technology.

The measured switching time for a 300 μ m long cantilever in air is below 75 μ s. It depends on the amplitude and the sign of the DC actuation due to semiconductor effects in the actuation path that lead to a delay of 60 μ s before the cantilever starts to move down. This delay can be decreased by a higher voltage peak, illumination of the switches to generate additional charges, and an additional doped area. With this doped region of minority charges, the switching time can be reduced below 30 μ s for actuation with negative and positive sign.

The opening time is between 40 μ s and 20 μ s depending on the bending radius of the switches. The movement starts immediately after turning off the actuation voltage and is limited by the mechanic resonance frequency of the switch and the damping by the atmosphere.

Index Terms — RF-MEMS, switching speed, tunable filter, phase shifter, microwave switch.

I. INTRODUCTION

For the communication between airplanes and satellites as well as for electrically steerable antennas for radar systems, highly integrated RF-front-ends with good RF performance are needed. Electrically steerable antennas in a radar application can move the antenna beam faster than mechanical systems and thus reach higher frame rates. Further on, a phased array antenna is flat or can even be conformal which is important for putting the antenna on top of an airplane.

RF-MEMS elements are good candidates for certain building blocks of these antennas. They have shown very good RF-performance in microwave applications in terms of low insertion loss and high linearity [1]-[2]. They have very low power consumption and thus allow a high element density without thermal problems. But there are still some challenges for RF-MEMS like their limitations in switching speed, their high actuation voltage for electrostatic actuation, or their complex packaging. Also their reliability has to be proven and many concepts have problems with higher RF-power handling.

Using a very simple processing technology might be an approach to overcome many of these challenges. As previously demonstrated in [3]-[4], a low complexity technology was used to realize microwave filters, phase shifting and switching devices. In this paper, the

switching time and behavior of these devices is evaluated.

II. PRINCIPLE OF OPERATION

The RF MEMS devices consist of a clamped-free aluminium silicon sandwich with an intrinsic stress gradient such that the free parts bend up (Fig. 1). The device is built on high resistivity silicon with silicon oxide as dielectric on top. Below the tip of the movable cantilever there is a second thin metallisation layer as path for the RF-signal.

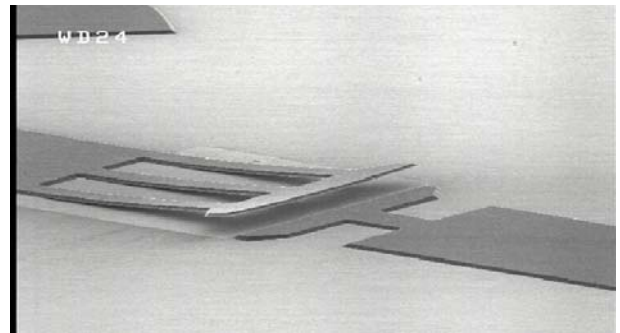


Fig. 1 REM- picture of a bended series switch

There are no additional bias electrodes necessary, because the actuation voltage is applied between the top metallisation and the backside. The high resistivity silicon acts as a dielectric in the RF regime, but can transport the charges for the DC actuation. The electric field that pulls the bended beams down to the substrate is effective entirely between the oxide and the air gap. At the anchor of the bending structure the pull-down force is highest because the air gap is smallest. During switching, the cantilever starts to roll down from this point, which leads to suitable actuation voltages of e.g. 30V. A second advantage of the rolling movement is that the air below the switch is pushed out to the tip of the cantilever and thus it is not a typical squeeze film damping situation that limits in other cases the switching speed.

Depending on the length of the bending cantilever a large actuation path can be reached. A typical tip height of a 300 μ m long beam is 17 μ m.

At last, a rather high restoring force is available, which results in a high release voltages of about 70% of the actuation voltage.

III. REALIZED DEVICES AND CIRCUITS

This technology offers the possibility to lift parts of microstrip or coplanar transmission lines into the air above the substrate. By applying the actuation voltage, the bended parts can be switched down to the substrate. This element can be used to realize a capacitive series switch with a big series capacitance in the down-state and a small parasitic capacitance in the up-state [4]. A similar device is also used for the switching speed measurements. Another effect is that a line that is lifted up in the air changes its electrical length, because the effective ϵ_r becomes smaller. This effect can be used to build switchable filters [6]. With the relatively large actuation path a large frequency shift of about 20% of the operation frequency can be reached. The left picture in Fig. 2 shows a switchable band-stop filter in microstrip configuration, where the ends of the resonant line can be switched and thus the resonance frequency is shifted. Another application is phase shifters [3]. On the right side of Fig. 2 there is a coplanar line phase shifter that changes the phase for 22° at 35GHz with a maximum insertion loss of -0.33 dB.

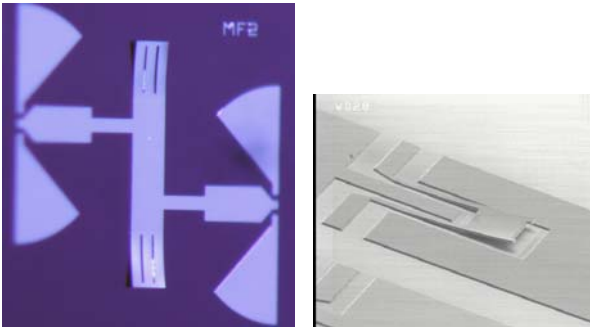


Fig. 2: left: RF-MEMS switchable band-stop filter, right: U-shaped coplanar line phase shifter

IV. SWITCHING SPEED

The switching behavior of RF-MEMS is of interest for many applications, e.g. when used as phase shifters in electrically steerable antennas whose scanning speed is limited by the switching time. Air damping and the mechanical resonance frequency of the movable parts are the main limiting factors [5]. Operated in low pressure environment the switching speed can be increased, but bouncing becomes a negative effect.

a. Measurement Setup

The time response of $300\mu\text{m}$ long and $70\mu\text{m}$ wide switches with no holes was measured with a 35GHz signal that was monitored using a Schottky diode converter and an oscilloscope. The actuation is an amplified alternating positive and negative square signal from a function generator with 1ms negative voltage square, 1ms off, 1ms positive voltage square and again 1ms off (Fig. 3, small picture). An LC-block protected the signal source from the actuation voltage. Due to the LC-block, the actuation voltage applies at the switch $13\mu\text{s}$ after the signal is set at the frequency generator.

b. Opening of the Switch

The opening speed was measured for two different series switch designs with different intrinsic stress gradients, resulting in actuation voltages of 37V (switch A) and 70V (switch B), respectively.

As high resistivity silicon is used as substrate material and no additional actuation electrodes are implemented to apply the ground signal for the actuation but the backside of the wafer, the resistance of the substrate is in series with the oxide capacitance.

The RC time constant for the $4\text{k}\Omega\text{cm}$ substrate is calculated to be $2.1\mu\text{s}$ for the capacitance of the switch in the down state across the silicon oxide.

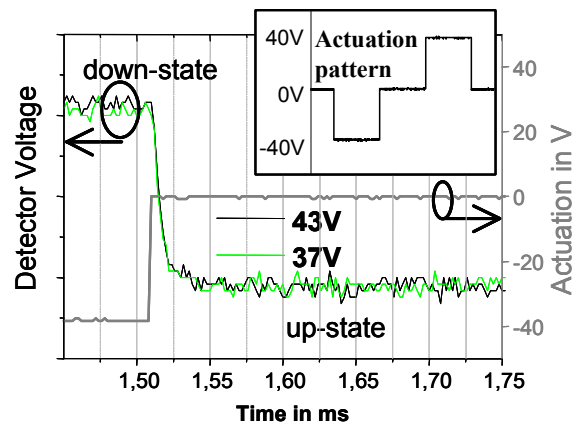


Fig. 3 Opening behavior of switch A after different applied actuation voltage amplitudes. Small picture: whole actuation pattern in 4ms.

The opening time depends mainly on the mechanical resonance frequency of the beam and the damping of the atmosphere. It is independent of the amplitude and the sign of the switching voltage that was applied before to actuate the cantilever. The movement of the switch starts immediately with turning off the actuation voltage and takes about $40\mu\text{s}$ for switch A (Fig. 3) and less than $20\mu\text{s}$ for switch B (Fig.4).

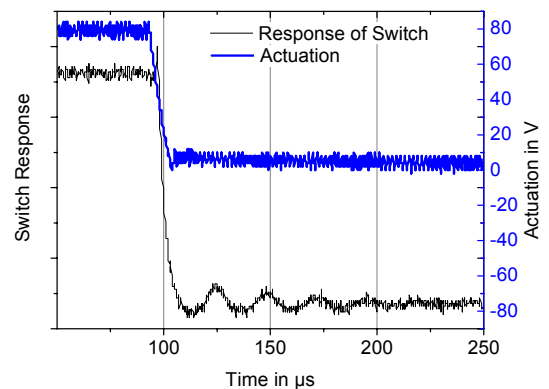


Fig. 4 Opening of switch B with smaller bending radius and more restoring force is faster but shows bouncing for $100\mu\text{s}$.

Switch B is faster in the opening movement. This can be explained with the higher restoring force, corresponding with the higher release voltage, and with a reduced air damping. The air damping occurs mainly

close to the area where the cantilever is being lifted off the substrate during the opening movement in a squeeze film like manner. The air has to fill the gap between substrate and cantilever. For switch B with the smaller bending radius this area is smaller thus, the damping is reduced. Switch B shows furthermore a weak bouncing effect in the up-state that lasts for $100\mu\text{s}$ which is another indication of reduced air damping. A bouncing frequency of 43kHz was observed.

The optimum mechanical switching behavior is achieved when the spring constant of the cantilever and the damping of the air result in a critical damping [7].

Besides the amount of bending, also the geometrical design has an influence on the bouncing behavior. The series switch of Fig. 1 that consists of three thin cantilevers with a connecting beam on the tip has a higher mechanical Q-factor and thus shows bouncing effects in the up-state even with the weak bended cantilevers. In the down-state bouncing could not be observed. To get more accuracy in terms of the damping effects, tests in reduced pressure environment can be made in the future.

The influence of the geometry of the cantilevers on the switching time has been extracted by measuring the closing time of cantilevers with widths varying from $60\mu\text{m}$ to $200\mu\text{m}$. The time for a switch to move down to the substrate increases in the measured range of widths linearly by $5\mu\text{s}$ (narrow to wide cantilever). For a switch design that is optimized for switching speed this can be taken into account with openings in wide structures.

c. Closing of the Switch

The time response of the closing is more complex and depends on the sign of the applied actuation voltage. Therefore, negative and positive switching pulses will be described separately. The backside contact is always on ground potential, the actuation voltage is applied on the RF-line.

- *Negative actuation pulse:* To build up the potential for negative switching pulses an inversion channel has to be created. The time for this is limited by the generation rate of holes in the high resistivity n-type silicon. This is confirmed by the observation that illuminating the wafer with light can decrease the switching time. A photon that is absorbed in the silicon can create an electron-hole pair, thus speeds up the generation of the minority charges. Only if there are enough holes below the oxide, the electric field drops completely across the oxide and the air gap above, and the switch starts to move downwards.

This effect leads to a delay between the application of the external switching pulse and the start of the movement of the switch. The delay depends further on the amplitude of the applied voltage (Fig. 5). It reduces from $90\mu\text{s}$ to $55\mu\text{s}$ for switch A by increasing the actuation voltage from 37V to 43V . More voltage means a larger space charge region where the minority charges can be selected and a faster separation of electrons and holes, thus less recombination.

After the delay, the switching movement takes only 17 to $13\mu\text{s}$ (37 to 43V) and is not the dominant effect for the overall switching time.

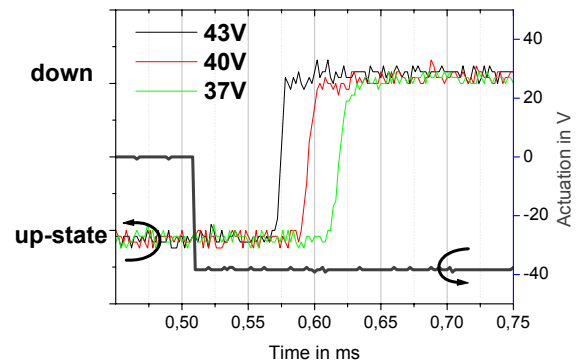


Fig. 5 Closing of the switch with negative actuation: Influence of higher actuation voltage, from -37V to -43V , the delay time decreases and the movement gets faster

For fast switching times and at the same time avoiding extra charging of the dielectric layer, high bias voltage was applied for a few $10\mu\text{s}$ to reduce the delay time and was then reduced to the necessary switching voltage.

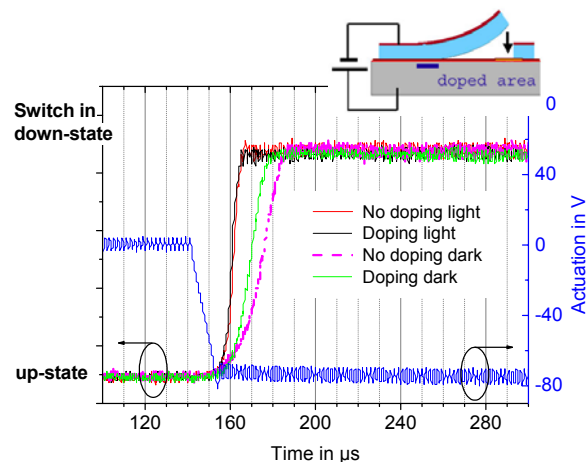


Fig. 6 Switches of type B with and without additional doped area below the anchor of the switch (small picture) and high enough voltage to avoid the delay time. No difference in switching time is observed if illuminated. If not illuminated, switches with doped area are $10\mu\text{s}$ faster than without.

To suppress this semiconductor effect, a highly doped region with minority charges was implemented in the anchor region of the switches (Fig. 6, small picture). This region is a reservoir of minority charges and also increases the area where minority charges are collected. They can be transported laterally below the oxide from the anchor region of the switch.

Fig. 6 presents the measured switching behavior for switches of type B with and without doped area with and without illumination with light. For an actuation voltage of 80V , the delay time disappears completely. If the generation rate for holes is high enough due to an illumination of the wafer, no difference can be seen whether the anchor region is doped or not. The switches are closed $20\mu\text{s}$ after the voltage is applied. For not illuminated switches, the doped ones show a $10\mu\text{s}$ shorter closing time than switches without doped area.

Also, it was found that switches with doped area show a more reproducible switching time than switches without doped area. The reason for that is not clear at the moment.

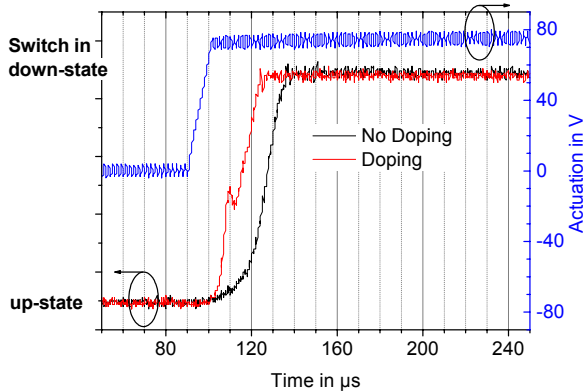


Fig. 7 Actuation with positive voltage, with and without additional doping area, titanium aluminium sandwich on the backside, identical switch as in Fig. 6

- *Positive actuation pulse:* Switching with positive actuation voltage should be faster because no minority charges have to be generated in the substrate. But there was also a delay of up to $100\mu\text{s}$ observed due to the silicon aluminium Schottky contact at the backside of the wafer. This diode behaves for positive actuation in reverse direction like an additional resistor that leads to a RC time constant of several $10\mu\text{s}$. An additional titanium layer between the silicon and the aluminium at the backside contact decreases this effect considerably. It reduces the Schottky barrier, thus the diffusion current is increased. To avoid the Schottky diode completely, a doping of phosphor on the backside can be done to get an ohmic contact.

The doped area close to the anchor of the cantilever that was introduced to decrease the switching time for negative actuation voltages also speeds up switching with positive one while the Schottky barrier is present (Fig. 7). An explanation is that without doped area, in the moment when the actuation voltage is applied, first the capacitance at the anchor region where the electric field is highest is filled with electrons before the electrons are available for the switching region. With a highly doped area of holes, the holes get pushed through the backside contact, the fixed negative charges compensate the electric field in the anchor region, and collecting electrons for the switching region can start immediately. The holes do not recombine with the electrons coming through the Schottky barrier because of their long lifetime in high resistivity silicon. So these electrons are additionally available in the switching area.

The doped region below the RF-line did not show any influence on the losses as long as the region is completely covered with the metallization. Doped regions next to RF-lines increase the line losses.

V. CONCLUSION

The switching behavior of RF-MEMS devices built in a very low complexity RF-MEMS technology and using a bended clamped-free aluminium silicon cantilever was investigated.

Air damping and the mechanical properties of the cantilevers mainly dominate the time, which is necessary to open the switch. Smaller bending radius not only results in higher restoring force but also in reduced air damping, also causing bouncing due to the increased mechanical Q-factor. The opening time in ambient atmosphere is below $40\mu\text{s}$ for $300\mu\text{m}$ long switches with 37V actuation voltage and $20\mu\text{s}$ for switches with 70V .

The observed closing time of $70\mu\text{s}$ is mainly dominated by an electrical delay time due to semiconductor effects. It was shown that this delay can be reduced by applying a high voltage peak. Another solution is to implement an additional doped area of minority charges below the anchor region of the bended cantilevers. This reduces the switching time to below $50\mu\text{s}$ without additional voltage peaks. A closing time of $20\mu\text{s}$ was demonstrated, with additional voltage, doping, and illumination with light. The actual mechanical closing time from 10% to 90% of the output signal is below $10\mu\text{s}$.

These results compare favorably to switching times of conventional clamped-clamped beam designs.

VI. ACKNOWLEDGMENTS

This work is supported by the European Union in the framework of FP6 2003 AERO1 #516121 project Retina.

REFERENCES

- [1] G. M. Rebeiz, J. B. Muldavin, "RF MEMS switches and switch circuits," *IEEE Microwave Mag.*, pp 59-71, December 2001.
- [2] A. Abbaspour-Tamijani, L. Dussopt, G. M. Rebeiz, "Miniatur and Tunable Filters Using MEMS Capacitors," *IEEE Transaction on Microwave Theorie and Techniques*, Vol. 51, No.7, pp 1878-1885, July 2003.
- [3] C. Siegel, V. Ziegler, U. Prechtel, H. Schumacher, "Low-complexity RF-MEMS technology for microwave phase shifting applications," *German Microwave Conf.*, pp.13-16, Ulm, Germany, 5.-7. April 2005.
- [4] V. Ziegler, C. Siegel, B. Schönlinner, U. Prechtel, H. Schumacher, "RF-MEMS switches based on a low-complexity technology and related aspects of MMIC integration," *European Microwave Week*, Paris, France, October 2005.
- [5] P. G. Steeneken, *et al.*, "Dynamics and squeeze film gas dumping of capacitive RF MEMS switch," *J. Micromech. Microeng.* 15, pp 176 - 184, UK, 2005.
- [6] C. Siegel, V. Ziegler, B. Schönlinner, U. Prechtel, H. Schumacher, "Very low complexity RF-MEMS technology for wide range tunable microwave filters," *European Microwave Week*, Paris, France, October 2005.
- [7] W. van Spengen, P. Czamecki, R. Puers, J. van Beek, I. De Wolf, "The influence of the package environment on the functioning and reliability of RF-MES switches", *IRPS*, pp 337 - 341, 2005

Multipath mitigation through cylindrical microstrip phased array antenna

D. Mastela¹, L. Reindl¹, T. Zander¹, L. Wiebking², M. Kawalkiewicz³

¹University of Freiburg, Institute of Microsystems Technology, Freiburg, Germany, reindl@imtek.de, dariusz.mastela.ext@siemens.com, thomas.zander.ext@siemens.com

²Siemens AG, CT PS7, Munich, Germany, leif.wiebking@siemens.com

³Warsaw University of Technology, Warsaw, Poland, mkwalki@mion.elak.pw.edu.pl

Abstract— Generally, microwave tracking systems prove to be very vulnerable to multipath distortions. Multipath distorted range measurements can hardly be processed and thus lead to heavy distortions of position estimates. To improve time-of-flight measurements in severe multipath environments extension of the tracking system architecture with a phased array antenna is proposed. The prototype of the antenna has been built and successfully implemented in the existing tracking system

I. SYSTEM CONCEPT

Multipath propagation is a real challenge for microwave tracking systems. The multipath effects that occur under severe propagation conditions (many metal objects) can become crucial for performance of such a system. The transmitted signal and its replicas reach the base station at slightly different times as a result of reflections. These short multi-path reflections can overlap with the line-of-sight signal causing a significant deterioration of range measurement. The use of omni-directional antennas creates many opportunities for this kind of signal degradation (Figure 1). The multipath-induced ranging errors are transferred into the localization errors. To improve the performance of a system three solutions are usually taken into consideration. The first one assumes increasing the bandwidth of the system. This change, however, would hurt ISM standards [3]. This suggests a necessity of using other technologies e.g. UWB technology. The second solution considers deploying of time-domain estimation method. This technique is based on a state-space model of a discrete-time linear oscillator generating samples of the radar output signal. The transition and observation matrices can be derived from a singular value decomposition of the data covariance matrix.

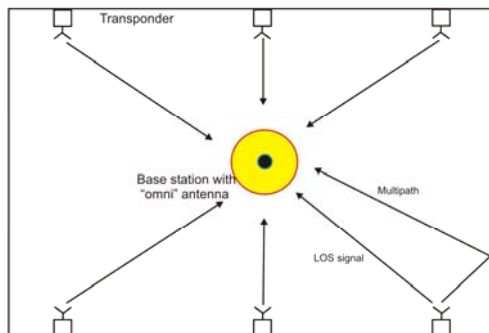


Figure 1. Tracking with omnidirectional antenna

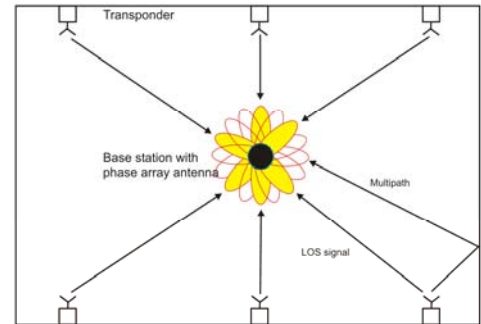


Figure 2. Tracking with phased array antenna

The desired frequency estimates are then contained in the complex angles of the state matrix [5]. The time-domain methods are very promising but also time consuming which makes them unsuited for real-time application yet. The third approach involves increasing an attenuation factor of multipath signals. The attenuation can be additionally increased by use of directional antennas. Such antennas will heavily attenuate reflected signals that typically arrive at angles well off the active beam lobe. Desired directivity and 360° azimuth coverage can be achieved deploying a phased array antenna (Figure 2). Such an antenna detects the presence of a signal and switches the beam that gives the best performance in terms of e.g. signal strength. It can be implemented as an add-on technology to intelligently address the needs of already existing radio tracking systems.

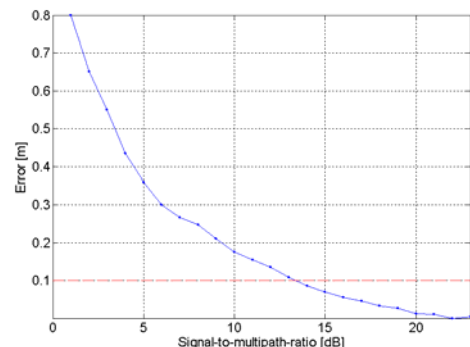


Figure 3. Performance improvement through attenuation of multipath signal

The question is how strong the multipath should be attenuated to achieve a desired performance. Measurements made with two coaxial cables representing a line-of-sight signal and a multipath signal, indicate that acceptable performance is found at attenuations of 15 dB that guarantee errors bounded by 10 cm (Figure 3).

II. ANTENNA CONCEPT

The developed concept of a phased array antenna utilizes patch elements placed on a metal cylinder. The element patterns are oriented radially outward. Only a few of the elements of the array are used to form a single beam, so the array can be approximated by a small linear array [4].

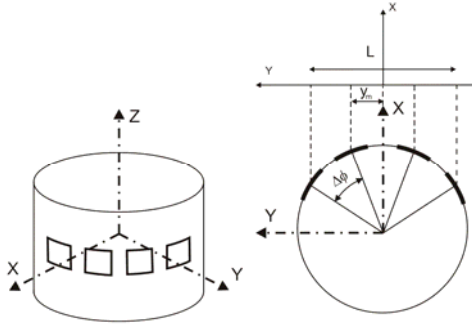


Figure 4. Antenna concept

The locations of patch elements can be projected onto linear axis as shown in Figure 4. One has to take into account that the elements are not equally spaced over the linear array. The amplitudes of the current of each element can be calculated according to e.g. Taylor distribution [1].

$$i(y_m) = \frac{\lambda}{L} \left[1 + 2 \sum_{n=1}^{\bar{n}-1} f(n, A, \bar{n}) \cos\left(\frac{2\pi n y_m}{L}\right) \right] \quad (1)$$

The side lobe level determines A and $f(n, A, \bar{n})$. These can be found in [1]. Here they are omitted for brevity. As a radiating element a microstrip patch antenna with coaxial feed has been chosen.

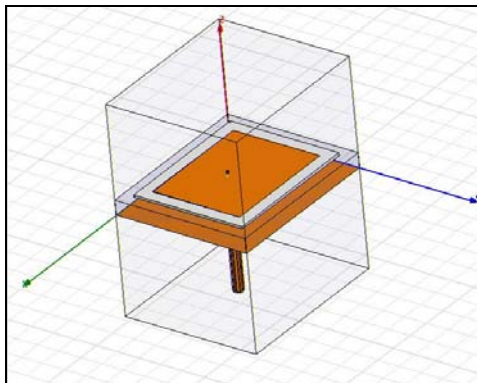


Figure 5. Simulation model of coaxial fed microstrip patch

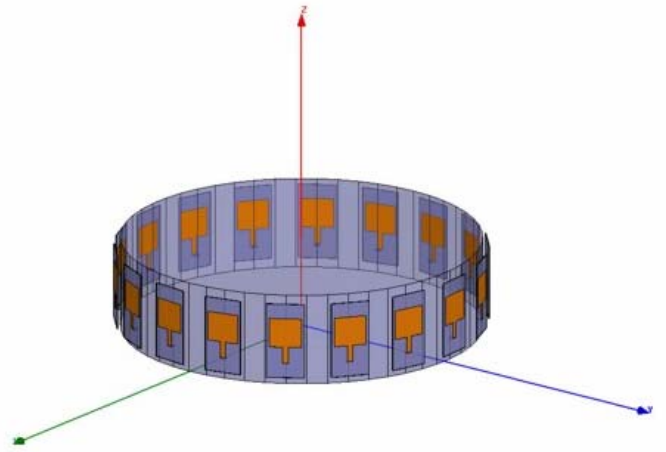


Figure 6. Simulation model of the antenna

The air-gap has been added in order to decrease the effective permittivity and therefore to improve the bandwidth [2]. A number of sixteen patches was specified to obtain a capability to switch the beam at 22.5 degree step. Four elements form a single beam, and therefore the diameter of the cylinder was chosen to be equal 0.6λ . The simulation model of a single patch and of the complete antenna configuration generated with Ansoft's HFSS software are shown in Figure 5 and Figure 6, respectively

III. FEEDING NETWORK

The feeding network consists of four identical segments containing a two-state phase shifter, an attenuator and the 1-to-4 switch (Figure 7). The phases are determined to excite the radiating elements in co-phase. Attenuators are set to achieve a good compromise between side lobe level (SLL) and half-power beam width (HPBW). Due to the 1-to-4 switches the number of required phase shifters and attenuators could be minimized from sixteen to four elements. The fabricated prototype of the antenna is shown in Figure 8. In contrast to the simulation model we decided to additionally extend the antenna in vertical direction. Sixteen vertical microstrip arrays were etched and mounted on the metal cylinder. Every vertical patch array contains a LED diode which shows the direction the phased array antenna radiates at the moment.

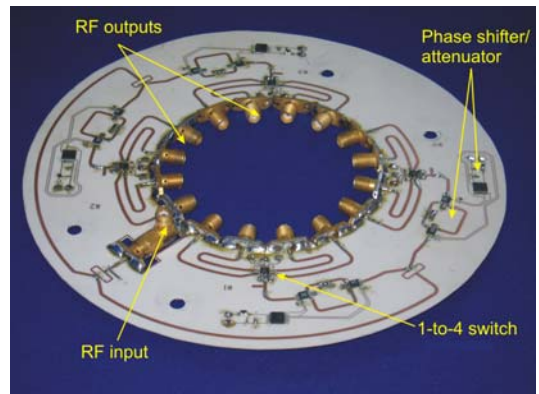


Figure 7. Feeding network



Figure 8. Photo of the antenna prototype

IV. PATTERN MEASUREMENTS

Figure 9 shows the radiation pattern of a measured beam compared with the simulated one. There is a good coincidence between both characteristics. The measured HPBW and SLL are almost the same as obtained during simulations. Figure 10 shows sixteen partially overlapping patterns, which all can be excited in the antenna. The adjacent patterns are shifted 22.5 degrees which exactly meets our demands.

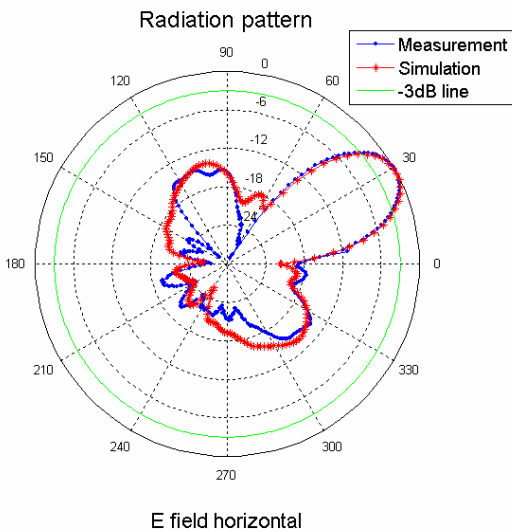


Figure 9. Single beam

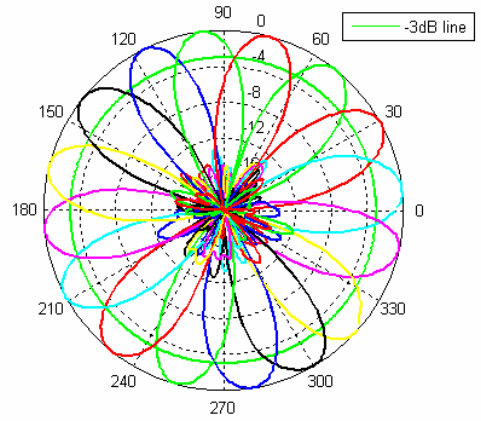


Figure 10. Measured switched beams

V. PERFORMANCE COMPARISON

The focus of this section is a performance comparison of a FMCW radar system deploying an omnidirectional and our new phased array antenna. The measurements described in this section were conducted in the old computer center of Siemens Research Center in Munich (Germany), which represented a typical example of an open plan office area. To evaluate the impact of the antenna directivity on the system performance, we were particularly interested in the distance measurements (Figure 11). Before we started with the ranging tests, signal strength measurements were accomplished to characterize channel properties. The experiments were performed using a base station mounted on a small trolley. The vehicle was moved along a specified path within the test area. The experiments were conducted with the base station and transponder remaining within line of sight to each other. Both antennas the omni-directional and the phased array (one at a time) were applied in the base station. Results of this measurement are presented hereafter.

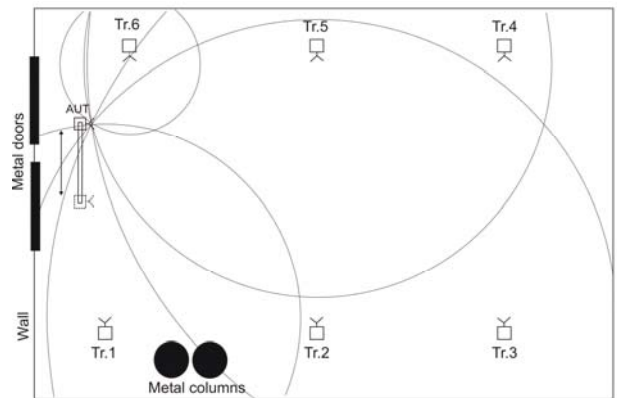


Figure 11. Measurement concept

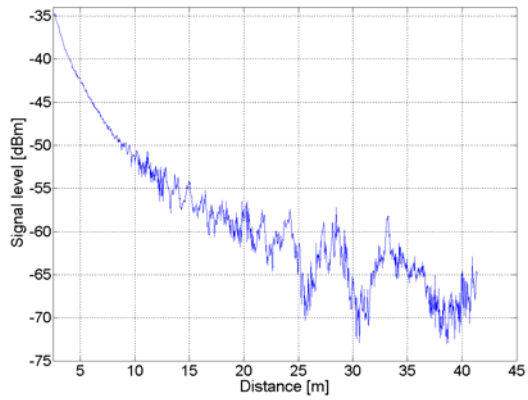


Figure 12. Measured signal strength with omnidirectional antenna

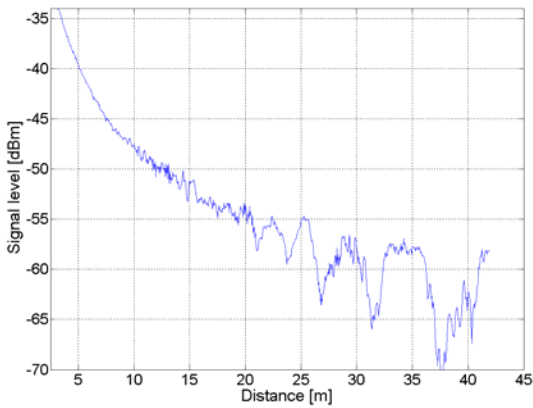


Figure 13. Measured signal strength with phased array

There are three main components in the received signal: path loss, slow fading and fast fading. By comparing figures 12 and 13 we can note that the path loss measured using both antennae are nearly the same. This is plausible, since the path loss depends on the environment, which remains the same in both cases. The long-term fading components are also similar in appearance. This equivalence is plausible, considering that the vertical patterns of the antennae are very similar. Both the omnidirectional antenna and the phased array are in the same manner vulnerable to the ground and ceiling reflections. There is, however one significant difference which is that the signal measured with the omni-directional antenna has higher amplitude of short-term oscillations than the phased array. This can be explained by the horizontal patterns of the antennae. The standard antenna receives signals from all directions. The phased array antenna, however, covers only a small fraction of that. This makes the phased array antenna more immune to the short-term fading. By ranging experiments a set of two subspaces were chosen that are likely to be representative of harsh propagation conditions. First measurements were taken near to metal doors (Figure 11), where a strong impact of mirror-like reflection was expected. The precision of range measurement using the omnidirectional antenna is remarkably bad. On the other hand only a very slight degradation of the accuracy of the measurement with the phased array antenna can be observed. The metal door serving as specular reflector

deteriorates the performance of the ranging system with omnidirectional antenna. A presence of strong oscillations can be noted (Figure 14). These are related to constructive and destructive interferences that affect the line-of-sight peaks.

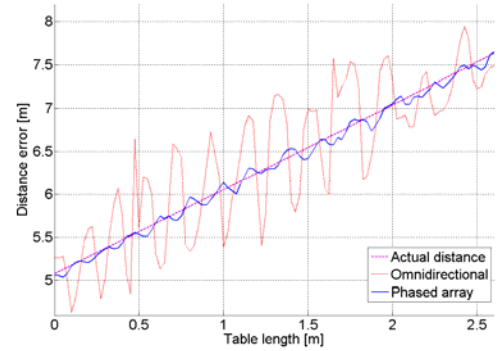


Figure 14. Distance measured in presence of specular reflector

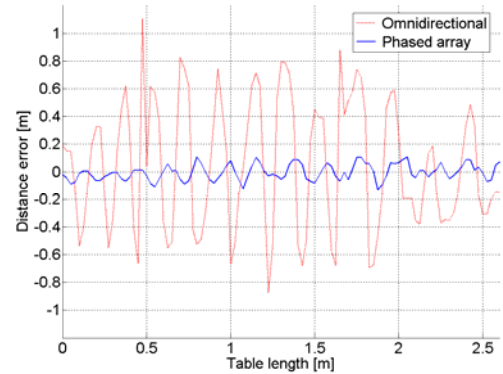


Figure 15. Error in measured distance

The measurements were also taken in the lower subspace of the test area, where pipe scatters are present. In this case metal columns acting as scattering center degrade the system performance.

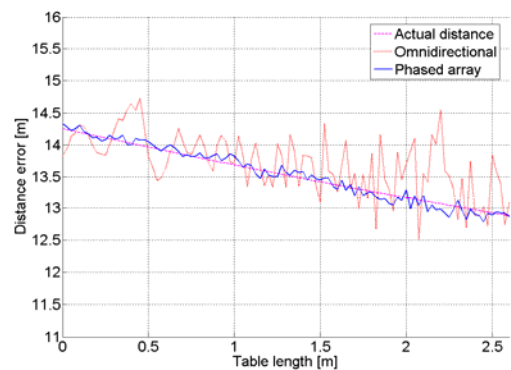


Figure 16. Distance measured in presence of scattering object

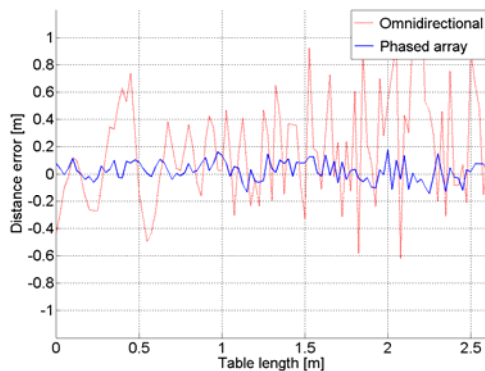


Figure 17. Error in measured distance

The conformal structure of the pipe can lead to creeping waves. These waves are tangential to a smooth surface and follow the back region of the body. The creeping wave can interfere with mirrored reflected wave in both constructively and destructively manner. In comparison with second zone the obtained results have more random character (Figure 16). Analyzing pictures above it becomes obvious that in both cases the phased array antenna tends to remarkably reduce the severity of multipath distortions. The errors in the range measurements using the omnidirectional antenna exceed the acceptable accuracy limits of twenty centimeters by many decimeters. At the same time the errors in the range measurements using the phased array antenna are bounded by ten centimeters.

VI. CONCLUSIONS

A microstrip cylindrical phased array for localization applications was designed, built and benchmarked. The model of microstrip cylindrical antenna was simulated using HFFS. The radiation properties of microstrip patches mounted on a copper cylinder have been investigated. Measured patterns match the simulation results very well. The circular geometry of the array provides 360° coverage in the azimuth plane. At the same time switched beams will attenuate reflected signals that typically arrive at angles well off the active beam and improve measurement accuracy. The solution presents a cost-effective and easily implementable way to mitigate multipath effects in microwave tracking systems. Utilization of the phased array radar in Local Positioning Radar [3] did an impressive contribution to enhance the accuracy of estimated distance. The phased array antenna has been implemented in add-on technology that intelligently addresses the needs of already existing radio tracking system.

REFERENCES

- [1] Stutzman W. L. and Thiele G. A., *Antenna Theory and Design*, John Wiley and Sons, NY, USA, 1981.
- [2] Dahele J.S. and Lee K. F., *Theory and experiment on microstrip antennas with airgaps*, IEE Proceedings, Vol. 132, Pt. H, No. 7
- [3] Wiebking, L.; "Entwicklung eines zentimeter-genauen, mehrdimensionalen Nahbereichs- Navigationssystems", Dissertation, TU-Clausthal, 2003
- [4] Chatterjee D. and Plumb R. G., *Numerical Modeling of Antenna Arrays for Rapidly Deployable Radio Networks TISL Technical Report TISL-10920-14*
- [5] Gulden P., Vossiek M., Storck E., Heide P., *Application of state space frequency estimation techniques to Radar Systems*. Salt Lake City, Utah, 2001 (pp.2099-2104)

Bias Dependent, Compact Low-Frequency Noise Model of GaInP/GaAs HBT: Experimental Identification and CAD Implementation

M.Borgarino¹, N.Corciulo¹, C.Florian², P.A.Traverso², F.Fantini¹, F.Filicori²

¹University of Modena and Reggio Emilia, Information Engineering Department,
Via Vignolese 905, 41100 Modena, Italy, +39 059 2056168, borgarino.mattia@unimo.it

²University of Bologna, DEIS Department,
Viale Risorgimento 2, 40136 Bologna, Italy, +39 059 2056168, cflorian@deis.unibo.it

Abstract—In the present paper, the experimental identification of a compact low-frequency noise model of GaInP/GaAs Heterojunction Bipolar Transistors and its implementation in a widely employed RF CAD software is described. The model is analytical so that its CAD implementation does not require look-up tables. In addition to the usual control of the noise sources through the DC or the mean value of the base current, the model reported in the present work is flexible enough to allow for the control of the noise sources through the instantaneous value of the base current.

Low frequency noise; modelling; CAD; characterization; simulation; HBT.

I. INTRODUCTION

The application of compact low-frequency noise models of heterojunction bipolar transistors, both on silicon and GaAs substrates, to simulate the phase noise of microwave oscillators has recently received large interest in the international technical literature [1-2]. In particular, in these circuits the low-frequency noise encounters large signal conditions leading to the problem of correctly accounting for the noise sources modulation, whose theory is still today in progress [2-4].

The noise source modulation topic can be approached in several ways spanning from a system level interpretation [4] to a physics level [3]. A very interesting approach consists in the use of compact low-frequency noise model [1-2], which stays in the middle between a pure physics based and a system-level approach. The development of compact low-frequency noise model typically faces the great difficulties of localizing the intrinsic noise sources inside the transistor small signal schematic. The number of intrinsic noise sources are indeed larger than the typically available experimental data, that are two auto-spectra and one cross-spectrum: the base current fluctuations spectrum (S_{IB}), the collector current fluctuations spectrum (S_{IC}), and their cross-spectrum (S_{IBIC^*}), respectively, when the noisy device is described through noise short-currents and the voltage spectrum (S_V) and the current spectrum (S_I), and their cross-spectrum (S_{IV^*}), respectively, when the noisy device is described through input referred equivalent noise generators.

In the praxis, the models are therefore developed forcing the noise sources to be an as small as possible subset of the intrinsic noise sources usually recognized to be present in a small signal model (see for instance [2,5]). This task can be done by exploiting additional measurements performed under different experimental conditions (e.g. by changing the value of an emitter degeneration resistor or the transistor configuration) with the aim of gaining a larger amount of experimental data [2,6]. These praxis lead to identify approximated models at the cost of large experimental time and of “ad-hoc” characterization set-up.

Aim of the present work is the identification of compact low-frequency noise model without the application of approximation and/or “ad-hoc” experimental set-up. The proposed method is based on the so-called correlation resistance (R_{CORR}), which is defined when the noisy bipolar transistor is described in terms of S_I , S_V , and S_{IV^*} . The idea of using R_{CORR} to identify compact low frequency noise models stems from its property of being a useful indicator of the relative weights of each intrinsic noise source [7].

Even if at a first glance it may appear trivial, a very important passage for the model release is to get a clear and effective implementation of the identified low frequency noise compact model in an EDA tool.

The paper is organized as follows. First the experimental set-up employed to carry out the characterization is presented. Then how the correlation resistance can be used to extract a low-frequency noise compact model will be reminded and some results will be presented. The obtained model will be then presented and its implementation in the Agilent ADS simulator described. A conclusion section closes the paper.

II. EXPERIMENTAL SET-UP

When one desires to perform a low-frequency noise characterization of a bipolar transistor accounting also for the correlation properties, two approaches are possible: the multi-impedance technique or the short currents method [2,8]. The former replicates the noise characterization methodology typically employed in the microwave

frequency range; it is a highly time consuming experimental approach, that makes sense when one only or at least few bias points should be addressed. On the other hand, the identification of the compact noise model required for large signal applications needs the characterization of the devices on a large number of bias points. This leaves the multi-impedance approach still possible but scarcely advisable. On the other hand, the short currents method is very well suited to address a large numbers of bias points, because it allows for a large reduction of the characterization time [8]. The operation principle of the experimental set-up is based on the noise short-current description of a noisy devices as depicted in Figure 1. The base and collector current fluctuations of the bipolar transistor are drained and amplified in voltage fluctuations by two low noise transimpedance amplifiers (EG&G5182). In order to make the characterization more comfortable and less time consuming, the experimental set-up has been automated as described in [9,10].

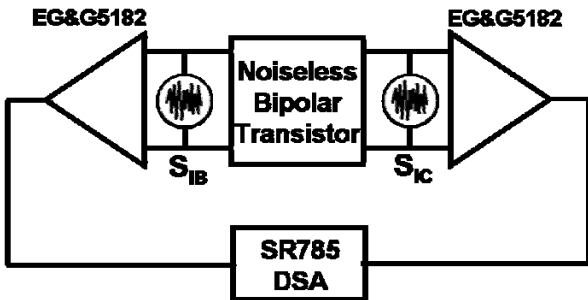


Figure 1. Experimental set-up operation principle sketch.

These voltage signals at the output of the two low noise transimpedances are acquired by a Dynamic Signal Analyzer (Stanford Research RS785), which is controlled by a home written LabView code running on a PC. Further duties of the control software are to report at the transistor base and collector planes the measured noise signals by taking into account the gain of the transimpedance amplifiers and by de-embedding from the brutal experimental data the noise contributions of the transimpedances as well as of the bias networks. These networks are home fabricated circuits automatically controlled through electromechanical actuators implemented using stepper micro-motors driven by a specific driver (National Instrument MID7602) [9]. In particular, it is worth here pointing out that in the base channel, between the transimpedance amplifier and the base terminal of the transistor under investigation, an analog conditioning stage (not indicated in Figure 1), essentially constituted by a common-base and an audio transformer connected in cascade, is inserted. When high noise, low dynamic input impedance bipolar transistors have to be measured, this precaution is mandatory, in order to avoid that the S_{IC} and S_{IBIC^*} spectra are corrupted by the transimpedance noise and by a fraction of the base current fluctuations, as better detailed in [11]. This countermeasure do not apply to silicon-based bipolar transistors, that exhibits indeed lower low frequency noise magnitudes and higher dynamic input impedances. Of course, the bias networks as well as the transimpedance amplifiers are battery powered, to minimize the impact of the 50Hz interferences on the final measurements.

III. MODELING STRATEGY

The home written LabView code, equipping the experimental set-up, does not only make automated the characterization step, along with the related control and data acquisition and elaboration, but it does also offer a modeling environment, which allows a direct access to the de-embedded experimental data, in order to make quicker and comfortable the extraction of low-frequency noise models. The modeling environment supports all the three most employed low-frequency noise models, that is the input referred equivalent noise sources model (S_V, S_I, S_{IV^*}), the short current noise sources model ($S_{IB}, S_{IC}, S_{IBIC^*}$), and the compact noise model, depicted in the following Figure 2. In this way it is provided guarantee that the three extracted models are all equivalent, leaving therefore to the final user the freedom to choice one among them on the basis of the specific needs. The extraction procedure is based on the R_{Corr} , whose expression in terms of the compact model noise sources reveals that it is the weighted mean of four resistances where the weights are the intensity of each noise source as pointed out by the following expression:

$$R_{Corr} = \frac{(r_{bb1} + R_{ce})S_{ibe1} + (R_{bb} + R_{ce})S_{ibe2} + (R_{bb} + R_{ce} + r_{\Pi})\frac{S_{ice}}{\beta^2} + (Z_{in} + r_{bb1} + r_{bb2})S_{ibc}}{S_{ibe1} + S_{ibe2} + S_{ibc} + \frac{S_{ice}}{\beta^2}} \quad (1)$$

The R_{Corr} spectrum acts thus as an useful indicator of the relative importance of each source at each frequency, effectively guiding thus towards the model identification without *a priori* neglecting any source and without invoking additional measurements carried out under several experimental conditions.

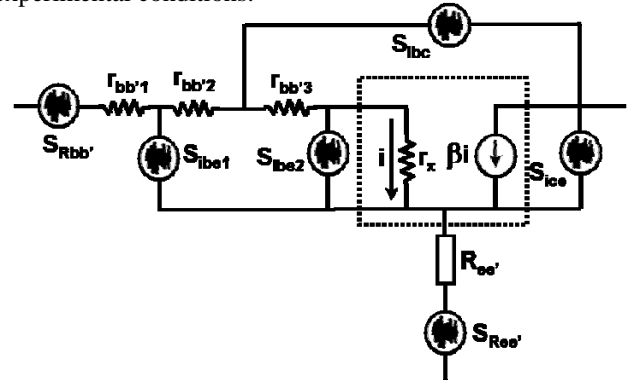


Figure 2. Compact low frequency noise model.

IV. EXPERIMENTAL DATA

The experimental set-up briefly described in the previous section has been applied to GaInP/GaAs Heterojunction Bipolar Transistors (HBT's). The characterization was carried out at wafer level, contacting the device under test through microwave coplanar microprobes. Since the low-frequency noise properties of a bipolar transistor are practically independent of the collector-emitter voltage (V_{CE}), the bias base current (I_B) was spanned from 20 μA to 40 μA while V_{CE} was kept fixed at 1 V.

Figure 3 compares the measured and simulated spectra of $R_{C_{orr}}$ at $I_B=30 \mu A$ as obtained in the modeling environment. A good agreement was obtained by suitably tuning the contribution provided by each source. In particular, for each source is possible to act on one white noise component, one flicker noise component, and two lorentzian noise components:

$$S_I = white + \frac{K_{1/f}}{f} + \frac{K_{GR1}}{1 + \left(\frac{f}{f_{c1}}\right)^2} + \frac{K_{GR2}}{1 + \left(\frac{f}{f_{c2}}\right)^2} \quad (2)$$

The white noise components account for the theoretical values of shot and thermal noise. The procedure has been repeated on all the investigated bias points obtaining similar good agreements. Then an analytical expression reproducing the coefficient ($K_{1/f}$, K_{GR1} , K_{GR2}) of each noise component for each noise source was identified. Table I reports, as an example, the coefficients for the S_{ibe1} noise source. Similar tables were obtained for the other noise sources

TABLE I. ANALYTICAL MODEL OF SIBE1 SOURCE

Noise Component	Analytical Equation
White	$2qI_B$
Flicker ($K_{1/f}$)	$5 \cdot 10^{-11} (I_B - 12 \cdot 10^{-6})^2 + 4.5 \cdot 10^{-16} I_B - 8.84 \cdot 10^{-21}$
Lorentzian (K_{GR1})	$3 \cdot 10^{-23}$
Lorentzian (K_{GR2})	$6.10^{-19} I_B - 1.1 \cdot 10^{-23}$

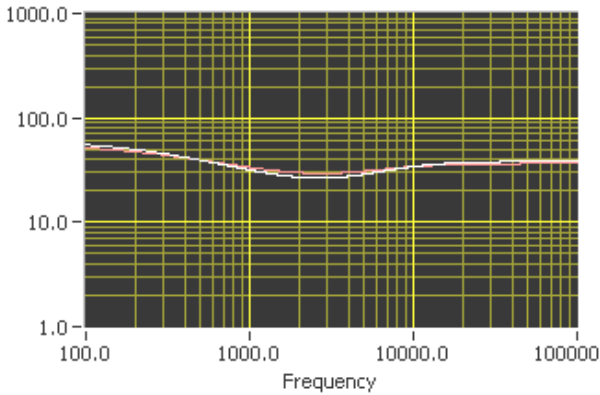


Figure 3. Correlation resistance modeling for $I_B=30 \mu A$.

The value of the correlation resistance in Figure 3 is well below the value of the dynamic base-emitter resistance indicating that the noise sources associated with surface recombination mechanisms occurring in the extrinsic region of the devices (S_{ibe1} and S_{ibc} in Figure 2) are important. These sources indeed weights low value resistances in the analytical expression of the correlation resistance. It is here worth reminding that in the past the decrease in the correlation resistance value was employed to detect the hot carrier induced damage of the extrinsic surface in the base-emitter junction of SiGe bipolar transistor [12].

V. MODEL IMPLEMENTATION

Figure 4 depicts the implementation of the model in the Agilent ADS software. One can note that the schematic in Figure 4 reproduces as close as possible the compact low-frequency noise model in Figure 2 where the sub-network identified by the dashed rectangle has been replaced by the non-linear noiseless HBT model in Figure 4. It is here worth noticing that the low-frequency noise implementation proposed in Figure 3 does not access the transistor non-linear model, which is often provided by the foundry in a form non accessible to the final user.

Each of the four controlled current generators implements the corresponding noise source of the compact noise model. Concerning the noise contributions due to the $S_{Ree'}$ and $S_{Rbb'}$, the extraction revealed that their contributions were negligible. The analytical dependences on I_B of the different noise components of each source (see Table I for the S_{ibe1} source) is introduced through Symbolically Defined Devices (SDD). In this way, the noise sources can be made controlled by any form of the base current, ranging from the mean value to the instantaneous value [2,13,14]. The model leaves therefore to the user the freedom of choosing how to modulate the noise sources. It is here worth reminding that, as already stated in the introduction, the modulation of the noise sources in cyclostationary model is still an open matter of discussion.

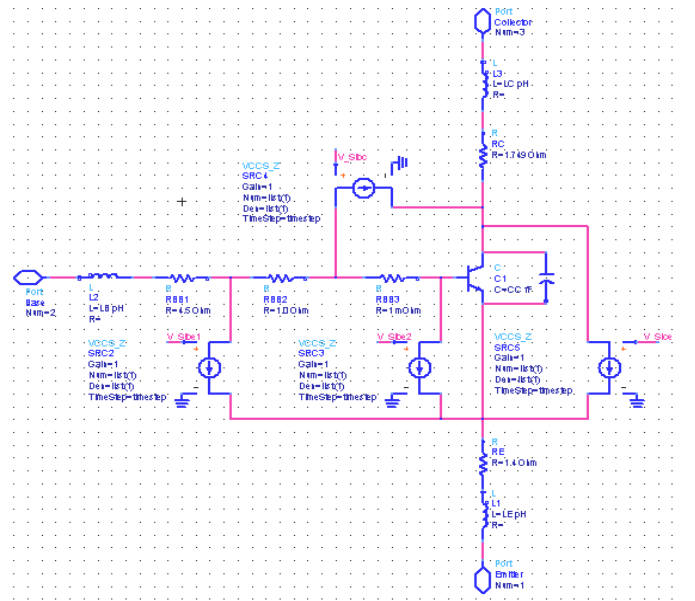


Figure 4. ADS implementation of the compact low-frequency noise model.

The low frequency noise properties of the investigated HBT has been simulated in terms of a short current description properly setting the scattering parameter simulations in the ADS software. The comparison with the experimental data reveals a good agreement between simulations and measurements as pointed out by Figures 5 and 6.

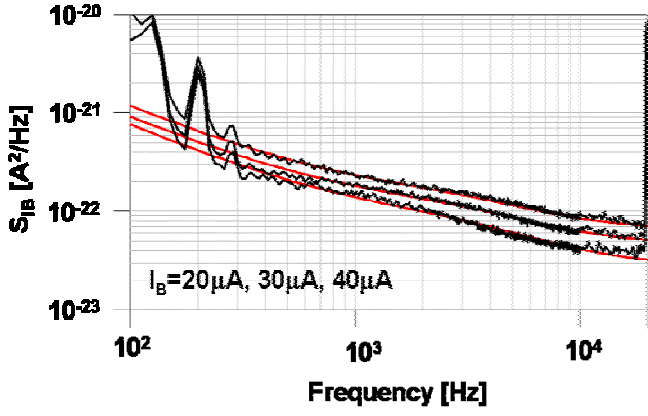


Figure 5. Measured and simulated S_{IB} .

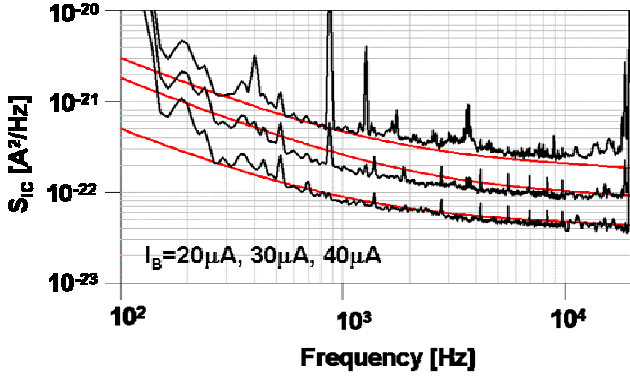


Figure 6. Measured and simulated S_{IC} .

The identified low frequency noise model has been then applied to a 4GHz Colpitts oscillator depicted in Figure 7. In this schematic, the intrinsic noise sources S_{ibe1} , S_{ibe2} , S_{ibc} , S_{ice} are modulated by the instantaneous extrinsic base current flowing in the base. In order to gain a sensibility to the impact of each source on the phase noise, the phase noise was simulated through an Harmonic Balance analysis by accounting for all the intrinsic noise sources or by enabling one intrinsic noise source at a time. Figure 8 compares the obtained phase noise spectra. The bold black line is the simulation carried out accounting for all the intrinsic noise sources. The figure points out that the S_{ibe1} source contribution is moderate on all the frequency offset while the S_{ice} source contributes always important, specially for frequency offset higher than 10kHz, where it becomes the dominant source. It is worth reminding that the S_{ice} source represents the most important contribution to the S_{IC} source, which in its turn is directly related to the S_V generator by the following equation:

$$S_V = \left(\frac{Z_{in}}{\beta} \right)^2 S_{IC} \quad (3)$$

where Z_{in} and β are the dynamic input impedance and the current gain, respectively, of the bipolar transistor.

The pushing factor approach, which evaluates the phase noise in terms of sensitivity of the phase to the voltage applied at the extrinsic base-emitter junction [15,16], forecasts that the phase noise can be reduced by placing a high-value capacitance

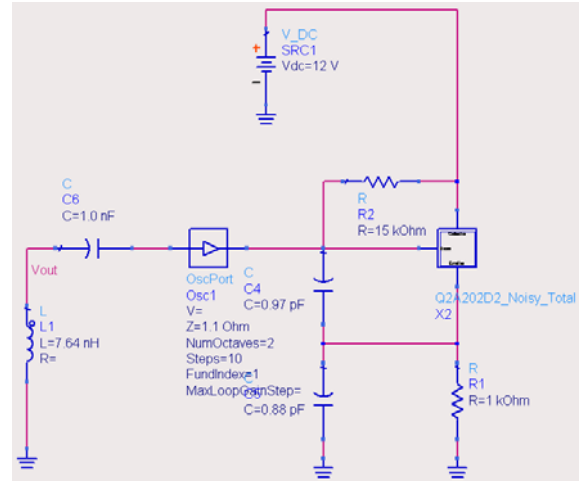


Figure 7. 4GHz Colpitts oscillator.

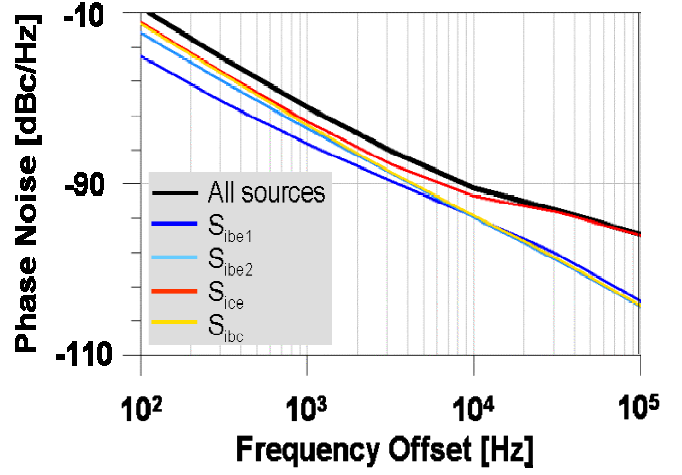


Figure 8. Simulated phase noise.

on the base-emitter junction, so that the S_V noise generator remains the only extrinsic generator of interest [1,17]. The phase noise spectra in Figure 8 suggest therefore that the phase noise of the Colpitts oscillator for frequency offset higher than 10kHz can not be reduced through this capacitor. The phase noise in this frequency offset range is critical in the applications, because the low pass filtering effect of the Phase Locked Loop may be no more effective, and the synthesizer phase noise remains established by the Voltage Controlled Oscillator phase noise [18], as a consequence.

At frequency offset lower than 1kHz the sources S_{ibc} and S_{ibe2} become important. It is worth noticing that these sources are both related to fluctuation mechanisms occurring at the extrinsic base surface of the transistor [19,20]. Figure 8 shows thus that close to the carrier the quality of the extrinsic base surface is the main factor limiting the oscillator spectral purity.

VI. CONCLUSIONS

Thanks to the use of a home-developed, automated experimental set-up the low-frequency noise model of GaInP/GaAs HBT's has been identified adopting the correlation resistance methodology. The model is released in the form of a compact model where the noise sources are embedded into the transistor equivalent circuit. Each source exhibits white, flicker and generation-recombination noise sources. The dependence on the bias base current of these components has been provided through analytical expressions allowing the implementation of the model in a RF simulator without invoking look-up tables.

The got model has then been implemented in the Agilent ADS EDA software. A good agreement has been obtained between measured and simulated low-frequency noise spectra for all the investigated bias points. The result shows that the experimental identification and the following implementation of the low-frequency noise model adopted in the present work can be a promising procedure to get models allowing reliable prediction of phase noise in oscillators and noise figure in mixers. One of the most outstanding property of the obtained intrinsic source analytical compact noise model is that it permits to choose the kind of modulation to be applied to the noise sources (DC, mean value, or instantaneous value). This flexibility turns out in an interesting tool to investigate the modulation of the noise sources, which is still today an open matter of discussion.

The identified compact low-frequency noise model has been applied to the design of a 4GHz Colpitts oscillator. The simulations revealed that for offset frequency higher than 10kHz the S_{ice} intrinsic noise source dominates the oscillator phase noise while closer to the carrier the oscillator spectral purity is limited by the quality of the extrinsic base surface of the HBT via the S_{ibe2} and S_{ibc} noise sources.

ACKNOWLEDGMENT

The present work was carried out in the frame of the national Italian university research program COFIN entitled "Non-linear noise models and design of low phase-noise oscillators for high performance communication systems".

REFERENCES

- [1] G.Cibiel, M.Regis, O.Lllopis, A.Rennane, L.Bary, R.Plana, Y.Kersalé, V.Giordano, "Optimization of an Ultra Low-Phase Noise Sapphire-SiGe HBT Oscillator Using Nonlinear CAD", IEEE Trans. Ultrasonics, Ferroelectrics, and Frequency Control, vol. 51, no. 1, pp. 33-41, January 2004.
- [2] J-C.Nallatamby, M.Prigent, M.Camiade, A.Sion, C.Gourdon, J.J.Obregon, "An Advanced Low-Frequency Noise Model of GaInP-GaAs HBT for Accurate Prediction of Phase Noise in Oscillators", IEEE Trans. Microwave Theory and Techniques, vol. 53, no. 5, pp. 1601-1612, May 2005.
- [3] A.Cappy, F.Danneville, G.Dambrine, B.Tamen, "Noise analysis in devices under nonlinear operation", Solid-State Electronics, vol. 43, pp. 21-26, 1999.

- [4] F.Bonani, S.Donati, G.Ghione, "Noise Source Modeling for Cyclostationary Noise Analysis in Large-Signal Device Operation", IEEE Trans. Electron Devices, vol. 49, no. 9, pp. 1640-1647, September 2002.
- [5] D.R.Pehlke, A.Sailer, W-J. Ho, J.A.Higgins, M.F.Chang, "Direct Parametric Extraction of 1/f Noise Source Magnitude and Physical Location from Baseband Spectra in HBTs", Proc. IEEE Trans. Microwave Theory and Techniques Symposium, pp. 1305-1308, 1996.
- [6] T.G.M.Kleinpenning, A.J.Holden, "1/f Noise in n-p-n GaAs/AlGaAs Heterojunction Bipolar Transistors: Impact of Intrinsic Transistor and Parasitic Series Resistances", IEEE Trans. Electron Devices, vol. 40, no. 6, pp. 1148-1153, June 1993.
- [7] M.Borgarino, L.Bary, D.Vescovi, R.Menzozi, A.Monroy, M.Laurens, R.Plana, F.Fantini, J.Graffeuil, "The Correlation Resistance for Low-Frequency Noise Compact Modeling of Si/SiGe HBTs", IEEE Trans. Electron Devices, vol. 49, no. 5, pp. 863-870, May 2002.
- [8] L.Bary, M.Borgarino, R.Plana, T.Parra, S.J.Kovacic, H.Lafontaine, J.Graffeuil, "Transimpedance Amplifier-Based Full Low-Frequency Noise Characterization Setup for Si/SiGe HBTs", IEEE Trans. Electron Devices, vol. 48, no. 4, pp. 767-773, April 2001.
- [9] M.Borgarino, M.Rossi, F.Fantini, "Low Noise, Low Interference Automated Bias Networks for Low Frequency Noise Characterization Set-Up's", Proc. 13th GAAS Symposium, Paris, France, 2005, pp. 473-476
- [10] M.Borgarino, A.Bogoni, F.Fantini, M.Peroni, C.A.Cetronio, "Semi-Automated Experimental Set-Up for CAD-oriented Low Frequency Noise Modeling of Bipolar Transistors", Proc. 12th GAAS Symposium, Amsterdam, The Netherlands, 2004, pp. 355-358
- [11] M.Borgarino, "Full direct low frequency noise characterization of GaAs heterojunction bipolar transistors", Solid-State Electronics, vol. 49, pp. 1361-1369, 2005.
- [12] M.Borgarino, J.Kuchenbecker, J-G.Tartarin, L.Bary, T.Kovacic, R.Plana, F.Fantini, J.Graffeuil, "Hot carrier effects in Si-SiGe HBTs", IEEE Trans. on Device and Material Reliability, vol. 1, no. 2, 2001, pp. 86-94.
- [13] F.Filicori, P.A.Traverso, C.Florian, M.Borgarino, "Identification Procedures for the Charge-Controlled Non-Linear Noise Model of Microwave Electron Devices," Proc. Second International Symposium on Fluctuations and Noise - Noise in Devices and Circuits II, Maspalomas, Spain, May 2004, pp. 337-348.
- [14] F. Filicori, P.A. Traverso, C. Florian, "Non-Linear Modeling of Low-to-High-Frequency Noise Up-Conversion in Microwave Electron Devices," Proc. First International Symposium on Fluctuations and Noise - Noise in Devices and Circuits, Santa Fe, NM, USA, Jun. 2003, pp. 192-203.
- [15] O.Llopis, J-M.Dienot, J.Verdier, R.Plana, M.Gayral, J.Graffeuil, "Analytical investigation of frequency sensitivity in microwave oscillators: application to the computation of phase noise in a dielectric resonator oscillator", Ann. Telecommun., 51, n.3-4, 1996, pp. 121-129.
- [16] J.Verdier, O.Llopis, R.Plana, J.Graffeuil, "Analysis of Noise Up-Conversion in Microwave Field-Effect Transistor Oscillators", IEEE Trans. Microwave Theory and Tech., vol. 44, no. 8, 1996, pp. 1478-1483.
- [17] M.Regis, O.Llopis, B. van Haaren, R.Plana, A.Gruhle, J.Rayssac, J.Graffeuil, "Ultra Low Phase Noise C and X Band Bipolar Transistors Dielectric Resonator Oscillators", Proc. IEEE Intern. Frequency Control Symposium, 1998, pp. 507-511.
- [18] D.Leenarts, J. van der Tang, C.Vaucher, "Circuit Design for RF Transceivers", Kluwer Academic Publishers, 2001, ISBN 0792375513.
- [19] A. van der Ziel, X.Zhang, A.H.Pawlikiewicz, "Location of 1/f Noise Sources in BJT's and HBJT's - I. Theory", IEEE Trans. Electron Devices, vol. ED-33, no. 9, september 1986, pp. 1371-1376.
- [20] M.B.Das, "On the Current Dependence of Low-frequency Noise in Bipolar Transistors", IEEE Trans. Electron Devices, vol. ED-22, no. 12, december 1975, pp. 1092-1098.

An optical design for real-time terahertz imaging

C. Jördens¹, G. Thorwirth², M. Koch¹

¹Technische Universität Braunschweig, Institut für Hochfrequenztechnik, Schleinitzstr. 22, 38106 Braunschweig, Germany, +49-531-391-2017, ch.joerdens@tu-bs.de
+49-531-391-2000, martin.koch@tu-bs.de

²Jena-Optronik GmbH, Prüssingstr. 41, 07745 Jena, Germany, +49-3641-200 140, guenter.thorwirth@jena-optronik.de

Short Abstract Terahertz (THz) imaging relies on broadband picosecond pulses (0.1 to 3 THz). Here, we propose a design for concave mirrors that pave the way to a multifocus system for real-time imaging with a line of THz foci. We present simulation results of our optical design carried out with ZEMAX.

Keywords-terahertz; imaging; mirrors; ray tracing

I. INTRODUCTION

Terahertz time-domain spectroscopy THz-TDS [1] relies on picosecond pulses in the frequency range from 100 GHz to 3 THz. This broadband radiation is ideally suited for imaging applications, having a large potential for non-destructive testing, quality control and security applications. Furthermore, THz waves will give a better spatial resolution than microwaves. Since the first THz image of Hu et al. in 1995 [2], which was obtained exactly 100 years after the first x-ray image, a lot of research was done in this field including reflection and tomography measurements. But still there are hurdles that impede THz imaging systems to be widely used in industry [3]. Besides aspects of cost and size the data acquisition speed is one of the main challenges. To obtain a THz-image the sample is typically scanned in x and y direction through the focus of the beam (cf. Fig. 1). It typically takes an hour or even longer to obtain a 200 by 200 pixel image using this scheme. An alternative scheme uses two-dimensional electro-optic sampling combined with a CCD camera. This scheme allows for higher scanning rates but has the disadvantage of a reduced signal-to-noise ratio [4].

Our idea is to use an array of THz emitters that is imaged to a line of intermediate THz foci which then are imaged onto an array of THz receiver antennas. The intermediate foci in the sample plane should have a rod-like shape and a finite overlap between two neighbouring foci to allow for an unbroken inspection of the entire sample without any gaps between neighbouring channels.

In this paper we present a design for concave metal mirrors which could be arranged in an array such that each emitter-intermediate focus-receiver path is mediated by its own set of mirrors. The mirrors are designed with the optical ray tracing software ZEMAX. A commercial THz multifocus system may employ 30 or more of such foci. Using the multi-focus scheme a 2 D THz image can be obtained by scanning the sample only in one dimension. This technique should decrease the scanning time drastically without lowering the signal-to-noise ratio.

Furthermore, it should facilitate the use of THz scanners for industrial or security applications.

II. CONVENTIONAL THZ OPTICS AND BEAM PROPERTIES

THz pulses are generated and detected with photoconductive dipole antennas which are excited with femtosecond (fs) laser pulses [1]. Some THz systems use lenses to guide the THz radiation. Yet, most use off-axis parabolic mirrors as shown in Fig. 1. In our laboratory we use off-axis parabolic mirrors with a focal length of 60 mm in a standard four mirror setup, see Fig. 1. Using standard photoconductive dipole antennas a focus beam diameter of less than 1 mm can be achieved in the sample plane [5] assuming a Gaussian beam shape. A typical spectrum for a measured THz waveform is shown in the inset of Fig 1. The ray tracing calculations are performed taking into account discrete spectral power densities to model the shown spectrum.

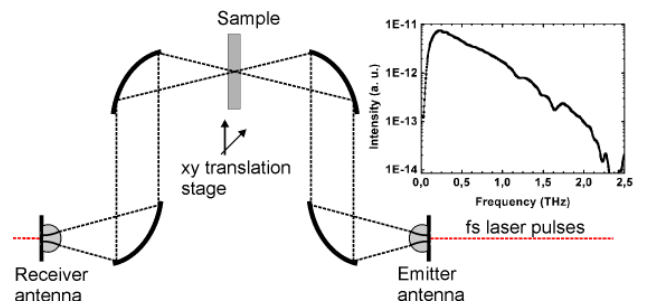


Figure 1. Quasioptical setup with four off-axis parabolic mirrors for guiding the THz radiation. Inset: Spectrum of a typical THz pulse.

III. MULTIFOCUS APPROACH

THz imaging with a standard setup as described above requires a rather a long scanning time due to the two dimensional movement of the sample. Currently we are developing a multifocus THz system with an array of emitter and receiver antennas, see Fig. 2. The goal is to reduce the scanning time by moving the sample only in one direction. Perpendicular to the moving direction there is a line of THz foci generated and detected by emitter and receiver arrays,

respectively. The scanning time of an image with n times n pixels can be reduced from n^2 to n by having emitter and receiver arrays of n antennas. Furthermore, we aim for rod shaped foci instead of circular foci. Rod-like foci which are separated by less than the long axis diameter provide redundant information. This allows for a complete inspection of the object under investigation. In a first step we target for eight channels with a channel separation 30 mm.

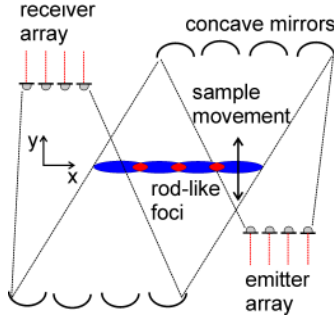


Figure 2. Schematic drawing of a multifocus setup with rod-like shaped foci in the sample plane; only four channels are shown for simplicity.

IV. SIMULATION RESULTS OF THZ MIRRORS

To know which focus diameter needs to be achieved we first perform reference calculations. We simulate the full width at half maximum beam diameter (FWHM) of a THz pulse at the receiver focus after four off-axis parabolic mirrors of a standard setup as shown in Fig. 1. We assume a pulse spectrum which resembles that shown in the inset of Fig. 1, and obtained a FWHM of 0.72 mm in both, x and y direction. This agrees well with experimental data. We regarded this calculated beam diameter as a benchmark for all further simulation steps towards our multifocus system. The full width half maximum beam diameter at the receiver plane of the multifocus system must be in the same range as that of the standard system in order to have sufficient signal intensity.

Starting point for our simulations were two elliptical mirrors for each channel. Mirrors are preferred over lenses, since lenses will lead to chromatic aberration, which is an issue when dealing with broadband radiation. We introduce biconic distortion to these mirrors to create a line focus. The mirror surface can be described by the following formula

$$z = \frac{c_x x^2 + c_y y^2}{1 + \sqrt{1 - (1 + k_x)c_x^2 x^2 - (1 + k_y)c_y^2 y^2}} \quad (1)$$

where $c_x = 1/R_x$ and $c_y = 1/R_y$ with R being the two radii of elliptic mirrors and k as the conic constant. Parameters are as follows: $R_x = 65.1$ mm, $R_y = 50.22$ mm, $k_x = -0.5$, and $k_y = -0.5$.

Fig. 2 shows the polychromatic Huygens point spread function (inset), and the corresponding cross sections in x and y direction. The full width at half maximum diameter in y -

direction, i.e. in moving direction (cf. Fig. 2) is 2.2 mm, which allows for a high scanning resolution. In x -direction the rod-like foci have a FWHM of over 40 mm. Hence neighboring foci largely overlap which guarantees an unbroken inspection. The FWHM of the beam diameter at the receiver plane is 0.82 mm and 0.73 mm in x and y direction, respectively. This matches the requirements set by the standard setup concerning signal intensity.

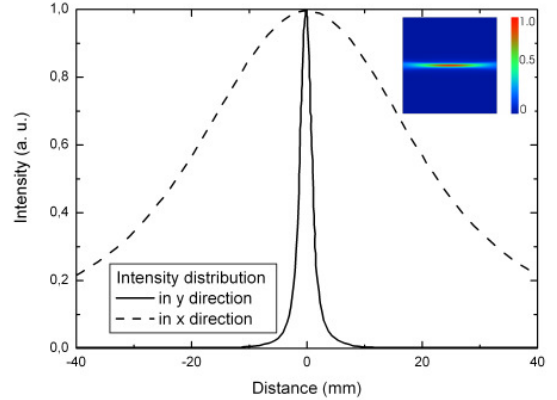


Figure 3. Point spread function of the focus inside the sample plane, x and y cross section, polychromatic plot in the inset (64 mm times 64 mm).

V. CALCULATION ACCURACY

All results are obtained with time and memory extensive (ZEMAX-) Huygens point spread function calculations, which take into account the following design properties:

- The Huygens method accounts for the evolving shape of the diffraction image as the beam propagates along the image surface. This is an important effect when the image surface is tilted with respect to the incoming beam.
- The Huygens method may provide more accurate results (compared to the FFT method) in the case of high transverse aberrations for the simulated biconic mirrors, which only focusses rays along one direction.
- The Huygens method takes into account the defined wavelength distribution (cf. inset of Fig. 1) of a polychromatic source (FFT method takes into account the defined primary wavelength only).

The calculations of the point spread functions are based on a Dirac function distribution of the THz emitter. Therefore the real illumination distributions inside the intermediate plane and inside the receiver plane can be described by the convolution integral of this point spread function and the local distribution of the THz emitter.

In order to accurately model diffraction effects the dimensions of optical elements should exceed the wavelength

by far; at least by a factor of 5 to 10. Yet, this requirement is not fulfilled here for all the discrete wavelengths of the THz source (see above). Therefore the calculations can describe the physical properties of the mirror design only to a first approximation.

VI. EXPERIMENTAL VERIFICATION WITH OPTICAL RADIATION

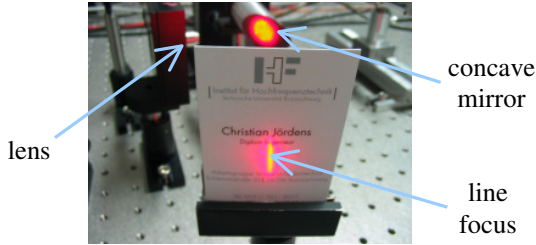


Figure 4. Illumination distribution in the visible range at the sample plane.

In order to verify the simulation results we characterize the mirrors at first in the visible range. The investigation in the THz region is planned later on, since the alignment is more complicated. In the visible we use a helium-neon laser at 632.8 nm and a lens. The illumination distribution is used to characterize the mirrors. The first mirror focuses the laser radiation x direction and collimates it in y direction. In the sample plane we achieve a rod-like shaped focus (cf. Fig. 4), as it can be seen in the illumination of the business card. The second mirror afterwards focuses the laser radiation in x and y direction again.

VII. CONCLUSION

We presented the design for concave mirrors which will be an integral part of future multifocus THz systems for real-time imaging. These mirrors will be the basis for a flexible optical design which is easily extendable to more than eight channels. It offers the same intensity distribution in each channel and a line function at the intermediate plane with a high spatial resolution in moving direction. The focus diameter at the receiver plane is comparable with that of the reference system. We showed the experimental verification in the visible range. The next steps will be the characterization in the THz frequency range as well as the design of lenses with the same features.

REFERENCES

- [1] P. R. Smith, D. H. Auston, M. C. Nuss, "Subpicosecond photoconduction dipole antennas," *IEEE J. Quantum Electron.* QE, vol. 24, pp. 255-260, February 1988.
- [2] B. B. Hu, M. C. Nuss, "Imaging with terahertz waves," *Opt. Lett.*, vol. 16, 1716-1719, August 1995.
- [3] X.-C. Zhang, "Terahertz wave imaging: horizons and hurdles," *Phys. Med. Biol.*, vol. 47, pp. 3667-3677, October 2002.
- [4] Q. Wu, T. D. Hewitt and X.-C. Zhang, "Two-dimensional electro-optic imaging of terahertz beams," *Appl. Phys. Lett.*, vol. 69, pp. 1026-1028, June 1996.
- [5] S. P. Mickan, K.-S. Lee, T.-M. Lu, E. Barnat, J. Munch, D. Abott, X.-C. Zhang, "Thin film characterization using terahertz differential time-domain spectroscopy and double modulation," *Proceedings of SPIE* vol. 4591, pp. 197-209, 2002.

Cost-Effective, Power-Efficient and Configurable YIG Replacement Signal Source

Ulrich L. Rohde¹, *Fellow, IEEE*, Ajay K. Poddar², *Senior Member, IEEE*

¹Prof., University of Cottbus, Germany and Chairman of Synergy Microwave Corp., NJ, USA, E-Mail: ulr@synergymw.com

²Senior Design Engineer, Synergy Microwave Corp., NJ, USA, Phone: 973-881-8800, E-Mail: akpoddar@synergymw.com

Abstract—YIG (Yttrium-Iron-Garnet) based signal sources (VCO) are renowned for their configurability, broadband tunability and ability to generate high spectral purity signal at microwave frequency. However, YIG based signal sources are costly, power hungry, and not suited for fabrication by current integrated circuit (IC) technology. Nor are they immune to electromagnetic interference (EMI), vibration effects, microphonics, phase hits, and frequency modulation. This paper discusses the promising alternative approach, which is cost effective, power-efficient, configurable, and easily amenable for integration in IC form. The measured phase noise is typically –140 dBc/Hz @ 1MHz offset from the carrier frequency over the tuning range (600MHz-6GHz), and to our knowledge, this is the best phase noise performance for this band using printed multi-coupled slow-wave (MCSW) resonator with so far reported.

Keywords- EMI; IC; MCSW; YIG; VCO

I. INTRODUCTION

Ultrawideband (UWB) has drawn the interest among the research and wireless communication communities due to its configurability and adaptability, which enables it to coexist with many concurrent services. There are currently various mobile communication standards in use worldwide, and the specifications placed upon such reconfigurable signal sources are stringent since they result from the worst scenarios of the various standards. The different standards operating in the frequency range of up to 6 GHz, with even higher frequencies, arises the need and gives a key role to multi-standard RF transceiver which combine several cellular and cordless phone standards as well as wireless LAN functionalities in one unit. Hence, the need to enable the “global roaming” features between a wide variety of networks operating at different frequencies call for the development of cost-effective, power-efficient, and configurable voltage controlled oscillator (VCO) that can cover wide frequency ranges. Transceiver components such as VCOs, power dividers, amplifiers, and phase shifters must also be capable of wideband performance to cover the frequency band of various systems. This place more demand on the topologies and technologies used to implement reconfigurable wideband VCO operation with low-power and low phase noise characteristics [1-9].

As the frequency band for the wireless communication shifts higher, generation of the power efficient ultra low noise wideband and thermal stable compact signal sources with low cost become more and more challenging due to the frequency limitations of the active devices. The technique of harmonic generation has been proven to be a cost-effective solution to

extend tuning range of the oscillator circuits [10]. These techniques are based on the nonlinearity of the transconductance of the active device under large signal drive conditions but it introduces distortions and has poor phase noise performances. The nonlinear diode (Gunn diode or Schottky diode) oscillators are suitable for frequencies higher than 18 GHz, but not for lower RF regime and wide tuning range, and also not suited for fabrication by current integrated circuit (IC) technology [11-13]. This limitation has made it more attractive to pursue alternative approaches such as N-Push VCOs, RF-MEMS (Micro Electro Mechanical System) VCOs, OEO (Opto Electronic Oscillator), YIG (Yttrium-Iron-Garnet) VCOs, and MCSW (Multi-Coupled Slow-Wave) VCOs topologies [14-19].

The N-Push coupled oscillator topology extends the frequency generation capabilities of the active device (bipolar/FETs) beyond the limitation caused by the cut-off frequency and minimizes the phase noise in comparison with the single individual uncoupled oscillator by the factor N, where ‘N’ is the number of uncoupled oscillator modules [1]. The drawback of N-Push approach is the complicated design and discontinuous tuning over the band due to the mismatch in phase shift between the successive oscillators circuits in N-Push configuration [2].

RF-MEMS VCO technology is on the verge of revolutionized wireless communication systems. RF-MEMS based VCO’s components such as inductors, variable capacitors, and resonators are superior in performances in term of quality factor, noise, linearity, power consumption, size, and cost, which cannot be achieved by conventional approach, thereby, makes VCO as a prime candidate for wireless connectivity. However, MEMS devices, unlike ICs, contain moving fragile parts that must be properly packaged and meet the requirements such as protection against handling, shielding against electromagnetic fields, near hermetic cavity seal, low temperature process, good heat-exchange, minimal thermal stress, and RF electrical feed through [4].

The OEO is a hybrid feedback oscillator, which converts optical energy from a laser to microwave signals. In recent year the concept of an OEO has emerged that exhibits exceptionally high spectral purity signals but the major challenge in the OEO is mode locking and circuit has to operate in a single mode from those available multi-modes. This places a limit on the frequency of oscillation and tuning range, therefore not suitable for configurable signal source for multi-mode and multi-band application [15,16,17].

This work was supported in part by the U.S. government (DARPA and U.S Army).

YIG oscillators are well known for broadband configurable signal source but at the cost of size, power and integrability in IC form. Unlike conventional signal sources (Oscillators/VCOs), a YIG based oscillator's quality factor (Q) performance increases with frequency, particularly at millimeter wave frequencies [18]. In a YIG oscillator, a YIG sphere is used as a reactive component, and it is placed in a magnetic field to set its resonant frequency. For a tunable YIG oscillator, the YIG sphere is placed in the air gap of an electromagnet, and the current applied to the windings is varied as desired in order to obtain the desired frequency of oscillation. YIG based synthesizer gives low noise performance, and broadband tunability in comparison to the standard signal sources. However, YIG require a significant amount of power (typically >20V, 200mA) to operate and generates excessive heat, which may harm the other electronic components in the transceiver modules. In addition to this, YIG is prone to vibration, lighting, electromagnetic interference (EMI), microphonics, phase hits, and frequency modulation, all of which have a detrimental effect in designing modern communication systems. The above effect may cause interruptions in the carrier signal and affects the radio's bit-error-rate (BER) [14].

In view of the limitations of known YIG resonators for integrability and power-effective operation, the present work describes a novel and innovative topology as MCSW (Multi-coupled slow-wave) VCO, which supports multi-octave-band tunability in compact size and easily amenable for integration in the integrated chip form [2,14]. MCSW VCO is planar structure and broadband in nature, and is well suited for MMIC fabrication with affordable price. Competing other alternative semiconductor technologies may not deliver the same level performance in terms of cost, size, power, linearity, tunability, adaptability, reconfigurability, and integrability. With the potential to enable wide operational bandwidths, eliminate discrete resonators (YIG sphere), and produce high Q planar resonators for ultra low noise VCOs in the context of a planar fabrication process compatible with existing IC and MMIC processes, MCSW (Multi-coupled slow-wave) VCO is widely believed to be promising technology to meet the present and future requirements [2,19].

To solve the frequency-agility issue, radio manufactures that serve the point-to-point and point-to-multi-point markets would prefer to use MCSW VCO that could emulate configurability, wideband tunability and low phase noise, yet eliminate the crude YIG based signal source; and deliver higher transmission speeds, cost and power-effective solutions for present and later generation of the communication systems.

II. THEORY

Multi-octave-band tunability and low phase noise performance have always been assumed to be opposing requirements due to the problem of controlling the loop parameters, and the optimization of the time average loaded Q of the resonator over the band simultaneously. This work relates to a method for increasing the tuning bandwidth and improving the phase noise in voltage-controlled oscillator (VCO) of the type, which employs planar-coupled slow-wave and progressive delay resonator in distributed domain,

integrated with the varactor diode as a tuning element. The novel approach (patent pending) allows for a substantial reduction in phase noise by dynamically optimizing impedance transfer function and coupling factor across the guided distributed medium of the planar multi-coupled network [2].

YIG oscillator possesses very wide tuning and good spectral purity. Unfortunately, frequency change of YIG oscillator depends on externally supplied magnetic field. An instant change of magnetic field is far from easy, as well as providing magnetic field is not easily compatible with MMIC fabrication. They consist of a YIG resonator with high-unloaded quality factor (Q), set in a resonant cavity and the resonance frequency of the cavity is tuned according to the strength of a magnetic field, applied through the main tuning coil. When modulation is required, a second coil can be added to the design but the bandwidth and phase noise are essentially limited by the circuit elements surrounding the sphere and resonant cavity, including the active device. In addition to this, heating device may be incorporated to stabilize and compensates the variation of the frequency of a YIG oscillator over wide external operating temperature range [14,16,18]. YIG oscillators are usually the preferred choice of signal source for designs requiring low phase noise, wide modulation bandwidths, and moderate tuning speed but no true advances in lowering the operating frequency (below 2000 MHz), power consumption, vibration effects, microphonics and packaging technology for integrated chip solutions.

In contrast, MCSW (Multi-coupled slow-wave) is a planar-coupled resonator technology, has several distinct advantages over YIG technology, and overcome the drawbacks of YIG based oscillator. This paper discusses a novel device called MCSW VCO, which can serve as a direct substitute for configurable low noise signal source for microwave communications, test equipments, radar, local multipoint-distribution systems (LMDS), and multi-channel multipoint-distribution systems (MMDS).

Wideband VCOs have employed either an FET or a bipolar transistor as the active device coupled to the YIG resonator. FET can operate at higher frequencies than bipolar transistor can, but bipolar transistors have significantly better $1/f$ noise characteristics. No single broadband device has been available that can be tuned to frequencies with both the bipolar and FET microwave frequency ranges. Attempts have been made to increase the high frequency limit of bipolar transistor-based YIG oscillators by increasing the high frequency limit of the transistors, but these transistors have also tended to have higher minimum frequencies of operation. YIG oscillator circuits can be designed to operate at either low or high frequencies but it is difficult to design a single circuit that can be tunable over broadband (decade). In addition, since the design of a new YIG oscillator is much like that of an integrated circuit (IC), development of an oscillator with a non standard frequency requires (non-recurring-engineering) NRE cost, in addition to the cost of the oscillators.

Thus, there is a need for broadband tuned oscillators in a single device that can be made easy replacement of the YIG oscillator. A new MCSW architecture (patent pending) has

been proposed in this paper, which can be tuned from 600 MHz to 6000 MHz and the topology is suitable for monolithic implementation. In order to facilitate a broad yet precise description of the present work, the circuit topology and layout of the resonating structure is selected in such a way that it minimizes the effect caused by temperature and mechanical stresses, and supports uniform negative resistance over fairly wide tuning range.

The investigation perform under this research includes the study of the integrated dynamically tuned MCSW resonator for minimum jitter caused due to mechanical and thermal stress, thereby less prone to phase hits over the tuning range. The additional feature of this topology is user defined frequency band by adjusting the length/spacing and optimizing the phase velocity and group delay of the MCSW resonator networks.

Fig. 1 shows the block diagram of novel oscillator topology MCSW VCO (patent pending), capable of operating over a wide tuning (600-6000MHz) and temperature range (-40°C to $+85^{\circ}\text{C}$) with minimal frequency drift due to the temperature. Unfortunately each development design of VCO using microstripline resonator has its price, since they occupy larger PCB area and for the same space exhibit much lower Qs compared to high Q, YIG resonator. For the most part, these disadvantages have been overcome by means of novel MCSW topology, which acts as a Q-multiplier, using noise filtering network, noise cancellation network, phase compensating network, and noise feedback bias circuit [2-9].

As shown in Fig.1, multi-mode coupled-resonator is connected across the base and collector of the three terminal active device (bipolar/FETs), which can be characterized as high Q mode coupling resonator that eventually improves the time average loaded Q of the MCSW resonator over the multi-octave-band operation.

As depicted in Fig.1, the active impedance created by the 3-terminal active device (bipolar/FET) has a negative real part with a real magnitude, and an imaginary part with an imaginary magnitude. The real magnitude is a function of the imaginary magnitude and the imaginary magnitude is selected such that the real magnitude compensates the loss of the MCSW resonator as well coincides with a maximum-slope inflection point of the phase characteristic curve for improved group delay. In addition to this, the mode coupling approach includes a methodology for optimum dynamic coupling to enhance the dynamic loaded Q, and to reduce or eliminate phase hits, while reducing the susceptibility to microphonics to an extremely low level, and retaining low phase noise and broadband tunability [2,3,8].

Typical phase noise of the commercial YIG resonator based wideband oscillator is -135dBc/Hz @1MHz for a frequency band of 2000-6000MHz. and moreover, it is difficult to operate YIG oscillator below 2000MHz frequency. Thus the research described herein explores the topology for the wideband oscillator (\sim decade bandwidth: 600-6000MHz) and offers cost-effective and promising alternative to the YIG based UWB signal source in the frequency range of L, S, C, X, and Ku band.

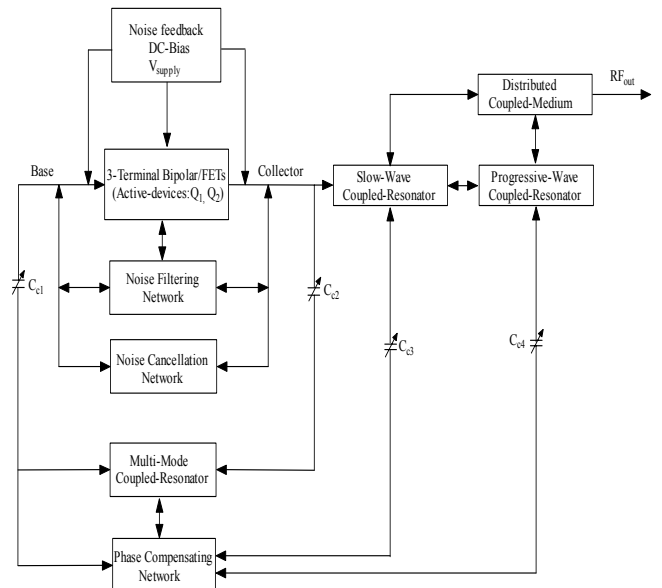


Fig. 1: Block diagram of configurable MCSW VCO (600MHz-6GHz)

III. UWB CONFIGURABLE VCOS

The scope of this research work is to replace YIG oscillator and also overcome the limitations of the known YIG resonators for integrability, vibrations, cost-effective, and power-effective operations. The design is based on innovative topology that supports the fast convergence by using dynamically tuned distributed coupled resonator for maximum group delay, thereby, improved dynamic loaded Q, and hence low noise performance over the band. The MCSW VCO circuit as shown in the Figs.1 and 2 comprise an active device (bipolar/FETs), noise-filtering network, and a noise cancellation network that are connected in parallel between the base and collector terminals (patent pending).

Fig. 2 shows the layout of MCSW VCO for the frequency band (600-6000 MHz), and can be easily extended to other frequency band. A noise feedback and DC bias circuit is coupled across the base and collector terminals of the active device as depicted in Fig.1. A multi-mode coupled resonator network as shown in Fig.1 is capacitively coupled across the base and collector terminals. A slow-wave coupled resonator and a progressive-wave-coupled resonator described in Figs.1 and 2 are coupled in distributed domain at the collector terminal. A phase compensating network is capacitively coupled between the base terminal and the slow-wave and progressive-wave coupled resonators. An RF output signal is coupled through a distributed coupled medium, which is coupled across the slow-wave and progressive-wave resonator networks. As shown in the Fig. 2, the coupled distributed resonator network is symmetrically structured to minimize the stray reactance that would otherwise limit or reduce the circuit tuning range or bandwidth. MCSW resonators, which are depicted much like a high Q planar resonator in an equivalent circuit, can achieve the phase-noise performances of a YIG oscillator but over a wide tuning range and operating temperature range at low cost.

An object of this work was to improve the Q value of the printed planar resonator by cascading a plurality of resonating network, which include a passive frequency selective circuit such as MCSW resonators having multiple asymmetric coupled line to increase the phase derivative and group delay $[\delta\phi/\delta\omega]$ of the resonator in a given cycle. Therefore, oscillators/VCOs circuit is designed such that the phase condition occurs in the steepest part of the phase characteristics curve of the planar-coupled resonators. In this way, coupled mode resonance may substantially coincide with a maximum-slope of the phase characteristic curve of the oscillator circuit, and the operation of the oscillator circuit about this point results in the circuit operating within the lowest phase noise domain of the phase characteristic curve, thereby improved effective dynamic loaded Q [2,5,6,7,8].

The layout shown in Fig. 2 is 6-layer board, fabricated on 64mil thick Roger substrate of dielectric constant 3.38 and loss tangent $2.7E-4$. The choice of substrate depends on size, higher-order modes, surface wave effects, implementations (couplings, line length, width, spacing, and spacing tolerances), dielectric loss, temperature stability, and power handling (dielectric strength and thermal conductivity). In many applications, keeping resonator structures to a minimum size and weight is very important. It would seem that planar resonator structures which can be fabricated using printed-circuit technologies would be preferred whenever they are available and are suitable because of smaller sizes and lighter weight. In this paper, we introduce a new class of planar resonators based on coupled slow-wave structure, depicted like saw-tooth/gear structure, which is not only compact size but also have a wider tuning range. Furthermore, MCSW is loaded with variable capacitor for uniform loaded Q over the tuning range. As we know that if there were no dispersion, the phase velocity would be constant but this is true only for the unloaded line. However, for the periodically loaded line the phase velocity is frequency dependent, therefore, there is trade-off between constant phase velocity and dispersion.

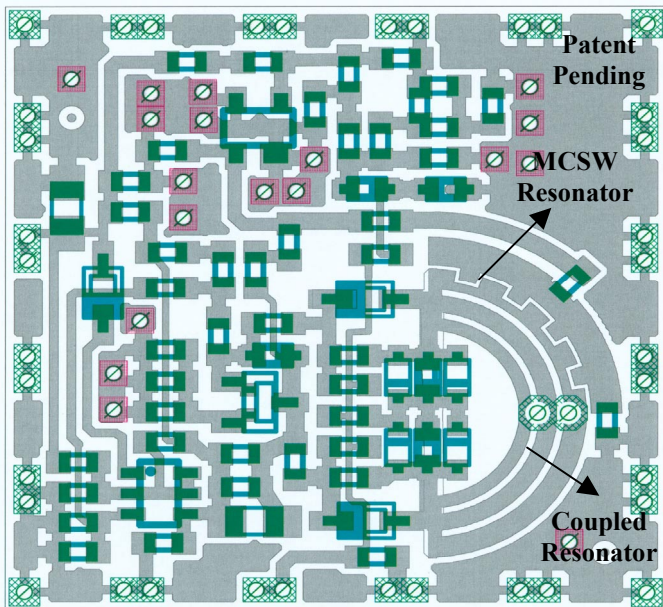


Fig. 2: Layout of the MCSW VCO (600MHz-6GHz) (Patent pending)

Fig. 3 illustrates the measured Q of the uncoupled, coupled and MCSW resonator. The quality factor (Q) is given by

$$Q = \frac{\omega_0}{2} \left[\frac{\partial \phi}{\partial \omega} \right]; \quad \omega_0 = 2\pi f_0 \quad (1)$$

where f_0 and ϕ are the resonant frequency and phase of the oscillator signal.

The dynamic time average Q factor of the resonator, as well as the tuning diode noise contribution, sets the noise performance of the VCO, and in general, the dynamic loaded Q is inversely proportional to the frequency range of the VCO [2]. The phase noise can vary dramatically over the tuning range of a multi-octave-band VCOs; therefore it is a major challenge to explore and find ways to realize uniform loaded Q over the tuning range. As shown in the Fig. 3, MCSW resonator network supports uniform loaded Q over the band within the variations of 10%, therefore uniform phase noise performance within 5dB for octave-band. For optimum phase noise performance over the tuning range, variation of the loaded Q should be minimum over the tuning range. The expression of the phase noise is given by [2] as

$$\mathcal{L}(f_m) = 10 \log \left\{ \left[1 + \frac{f_0^2}{(2f_m Q_L)^2 (1-m)^2} \right] \left[1 + \frac{f_c}{f_m} \right] \frac{FkT}{2P_0} + \frac{2kTRK_0^2}{f_m^2} \right\} \quad (2)$$

$$\mathcal{L}(f_m) = 10 \log \left\{ \left[1 + \frac{f_0^2}{(2f_m Q_0)^2 m^2 (1-m)^2} \right] \left[1 + \frac{f_c}{f_m} \right] \frac{FkT}{2P_0} + \frac{2kTRK_0^2}{f_m^2} \right\} \quad (3)$$

where m , Q_0 , Q_L , f_0 , f_c , f_m , F , K_0 , R , k and T are defined as ratio of the loaded and unloaded Q, unloaded Q, loaded Q, oscillation frequency, flicker corner frequency, offset frequency from the carrier, noise factor, oscillator voltage gain, noise resistance of the tuning diode, Boltzman's constant and temperature in degree K.

From (2) and (3), minimum phase noise can be found by differentiating (7) with respect to m , and equating to zero for maxima and minima as $\frac{\partial}{\partial m} [\mathcal{L}(f_m)]_{m=m_{opt}} = 0$

$$\frac{d}{dm} \left[10 \log \left\{ \left[1 + \frac{f_0^2}{(2f_m Q_0)^2 m^2 (1-m)^2} \right] \left[1 + \frac{f_c}{f_m} \right] \frac{FkT}{2P_0} + \frac{2kTRK_0^2}{f_m^2} \right\} \right] = 0 \Rightarrow m_{opt} = 0.5 \quad (4)$$

The variable coupling capacitors C_c (C_{c1} , C_{c2} , C_{c3} , C_{c4}), as shown in Figs. 1 and 2 are designed for the optimum loading of the coupled resonator network across the active device, and dynamically tuned for optimum loaded Q ($m_{opt}=0.5$) for minimum phase noise performance across the band.

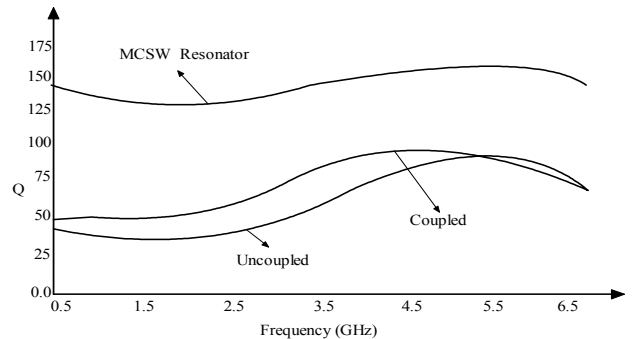


Fig. 3: Measured quality factor (Q) of the planar resonators

The values of the coupling capacitor C_c are derived from the input stability circle, and it should be within the input stability circle so that the circuit will oscillate at a particular frequency for the given lowest possible value of the C_c over the band. The noise factor F of the oscillator is minimized by noise feedback circuit [2], and dynamically controlling the conduction angle of the active device by adjusting optimum drive level corresponding to the desire oscillation frequency. By doing so, the control parameters such as negative resistance, loop gain, and phase shift can be adjusted for improving the phase noise performance over the band. Fig. 4 shows the typical phase noise plot at 10 kHz offset with respect to “m” for MCSW VCO circuit for typical frequency 1 GHz as shown in the Figs. 1 and 2. As depicted in Fig. 4, for different values of noise figure F ($F_3 > F_2 > F_1$), the phase noise is minimum at m_{opt} , and the plot is typically like ‘bath-tub’ curve, which is shifted symmetrically about m_{opt} . This implies that for low noise wideband application, the value of m should be dynamically controlled over the tuning range and should lie in the vicinity of m_{opt} for minimum noise performance [2].

IV. VALIDATION

The experimental results demonstrate the new design approach for multi-octave-band tunability. Fig. 5 shows the measured phase noise plot of the MCSW VCO, which is better than -140dBc/Hz @ 1MHz offset from the carrier for the frequency band (600-6000 MHz), and is not limited to these frequencies, can be easily extended to millimeter wave range. The circuit works at 5V and 20mA, and tuning voltage is 0-30V. The typical RF output power is 5dBm over the tuning range and second harmonic rejection is better than -20dBc .

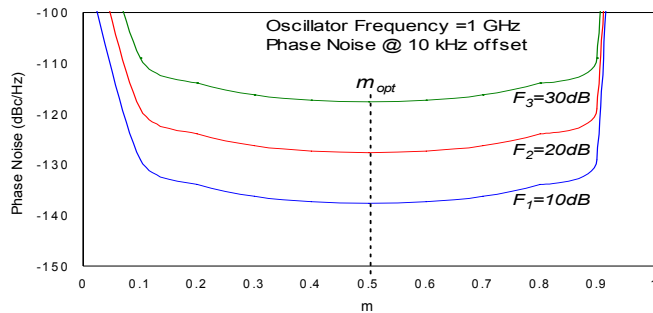


Fig. 2. Phase noise vs. m (Q_1/Q_0) of the resonator

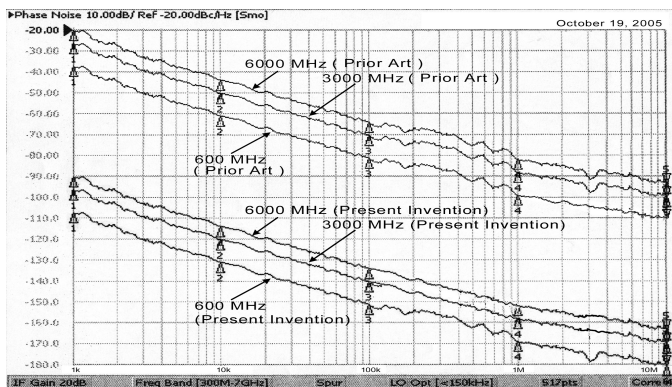


Fig. 3: Phase noise plot of UWB configurable YRO (600MHz-6GHz)

V. CONCLUSION

The freedom of selection of the frequency, low phase noise, low phase hits, low power consumption, multi-octave-band tunability, compact size, and stable over temperature will make this technology promising and attractive for next generation high frequency mobile communication systems and test and measuring instruments. Other features and advantages of the present technology include power efficiency, low phase noise, and amenability to integration in chip form

REFERENCES

- [1] U. L. Rohde, A. K. Poddar, J. Schoepf, R. Rebel, and P. Patel, "Low Noise Low Cost Ultra Wideband N-Push VCO," *IEEE MTT-S*, 2005.
- [2] U. L. Rohde, A. K. Poddar, and G. Boeck, *Modern Microwave Oscillators for Wireless Applications: Theory and Optimization*, John Wiley & Sons Inc., 2005.
- [3] U. L. Rohde and A. K. Poddar, "Reconfigurable Wideband VCOs," *IEEE, PIMRC2005*, Germany, September 11-14, 2005
- [4] U. L. Rohde and A. K. Poddar, "MEMS Enabled VCO for Wireless Connectivity," *GigaHertz2005*, Sweden, November 8-9, 2005.
- [5] U. L. Rohde and A. K. Poddar, "An Analytical Approach of Minimizing VCO Phase Noise," *APMC*, China, December 4-7, 2005.
- [6] U. L. Rohde and A. K. Poddar, "Configurable Ultra Low Ultra Wideband Power Efficient VCOs", 11th European Wireless, Conference, Cyprus, 10-13 April 2005.
- [7] U. L. Rohde, A. K. Poddar, and R. Rebel, "Ultra Low Noise Low Cost Octave-Band Hybrid-Tuned VCO," *IEEEECCE05*, May 2005, Canada.
- [8] U. L. Rohde and A. K. Poddar, "A Unified Method of Designing Low Noise Oscillator," *International Microwave and Optoelectronics Conference (IMOC'2005)*, Brazil, July 25-28, 2005
- [9] U. L. Rohde and A. K. Poddar, "Configurable Adaptive Ultra Low Noise Wideband VCOs," *IEEE, ICU05*, Sept., 2005, SFIT, Switzerland.
- [10] P. Heymann, R. Doerner, and Rudolf, "Multi harmonic Generators for Relative Phase Calibration of Nonlinear Network Analyzers," *IEEE Trans. Instr. Meas.*, pp. 129-134, vol. 50, no. 1 Feb. 2001.
- [11] A. K. Poddar, J. K. Bansal and K. N. Pandey, "Millimeter Wave Evanescent Mode Power Combiner Gunn Oscillator in Suspended Stripline Configuration," *Mathematical Methods in Electromagnetic Theory, IEEE/MMET, International Conference*, pp.384-386, June 1998.
- [12] A. K. Poddar, J. K. Bansal and K. N. Pandey, "Broad-band tunable planar active radiating elements with Evanescent mode using Notch antenna", *Mathematical Methods in Electromagnetic Theory, IEEE-MMET'98 International Conference*, pp. 550-552, June 1998.
- [13] A. K. Poddar, S. K. Koul and B. Bhat, "Millimeter Wave Evanescent Mode Gunn Diode Oscillator in Suspended Stripline Configuration", *IR & MM Wave*, pp. 265-266, July 1997, USA.
- [14] U. L. Rohde and A. K. Poddar, "Distributed Coupled Resonator (DCR)/VCO Limit Phase Noise and Phase Hits", *IEEE RWS*, San Diego, California, USA, 14 -20, January 2006.
- [15] S. Romisch, J. Kitching, E. S. Ferre-Pikal, L. Hollberg, and F. L. Walls, "Performance Evaluation of an Optoelectronic Oscillator", *IEEE Tran. Ultrason. Ferr.*, 47, Sept 2000, pp. 1159-1165.
- [16] A. Sen Gupta, D. A. Howe, C. Nelson, A. Hati, F. L. Walls, and J. F. Nawa, "High Spectral Purity Microwave Oscillators: Design Using Conventional Air-Dielectric Cavity *IEEE Tran. Ultrason. Ferr.*, 51, October 2004, pp. 1225-1231.
- [17] X. S. Yao and L. Maleki, "High frequency optical sub carrier generator", *Electron. Lett.*, vol. 30, no. 18, September 1994, pp. 1525-1526.
- [18] R. Leier, "SiGe Silences YIG Oscillator Phase Noise", *Microwave & RF*, pp. 79-82, January 2006.
- [19] Z. A. Shaik, P.N. Shastry, and S.N. Prasad, "A Novel Distributed Voltage-Controlled Oscillator for Wireless Systems", *IEEE RWS*, San Diego, California, USA, 14 -20, January 2006.

Concept and Development of a New MOBILE-Gate with All Optical Input

Artur Poloczek, Wei Wang, Jörn Driesen, Ingo Regolin, Werner Prost, F.-J. Tegude

University of Duisburg-Essen, Center for Semiconductor and Optoelectronics, D-47048 Duisburg, Germany
Phone: +49 (0)203 379 3878, E-Mail: poloczek@hlt.uni-duisburg.de

Short Abstract—We demonstrate a concept and first results of an all optical driven MOBILE-Gate. We propose the transmission of the clock at a different wavelength than the data signal, but via a single optical fiber. Therefore, a staggered wavelength selective pin-diode is developed enabling the detection of both signals within a single spot. PSpice simulations based on experimental single device data are presented, indicating a circuit performance >10 Gbit/s.

Keywords - MOBILE; RTD; HBT; RTBT; OEIC; pin-diode, wavelength selective detection

I. INTRODUCTION

The Monostable Bistable Transition Logic Element (MOBILE) [1] is an attractive approach for both robust and high speed logic circuits with a very low device count. A MOBILE is formed by two series connected Resonant Tunneling Diodes (RTD). The gate enables the execution of logic operations with an intrinsic latch function [1] provided by clocked operation. Therefore, the drive of the gate with a return-to-zero clock input is essential.

The combination of the MOBILE-Gate with optoelectronic devices such as photo-diodes forms an Opto Electronic Integrated Circuit (OEIC) with high functionality suitable for high speed fiber communication applications. On Indium Phosphide Substrate (InP) an 80 Gbit/s intrinsic operation of a MOBILE with a photo-diode as data terminal was presented in [2]. But, the monitoring of the output signal was performed by an electro-optic sampling system, only. An OEIC MOBILE with an optical data input, and electrical output has been demonstrated successfully by the authors in [3]. There, the clock signal has been supplied electrically and the optical data stream has been detected by a pin photo-diode. This concept is not practical for front end fiber communication systems, because the MOBILE gate needs a phase locked clocking and data stream.

In this paper an extended concept with an additional optical clock input terminal is presented. A heterostructure bipolar transistor (HBT) is used to switch between the high and low clock level. To offer high functionality, the intended optical receiver detects the optical clock control and data signal modulated on two different wavelengths selectively, but using a single spot of illumination. Thus, the phase locked clock

control and data stream can be transmitted through a single fiber.

II. CONCEPT

The MOBILE requires a phase locked transmission of the data signal, detected by PD₁, and the clock signal, which will be detected by PD₂. The two RTDs are in series connected and form the classical MOBILE-Gate. The base-emitter-diode of transistor T₂ works as level shifter for the subsequent stage. The switching of the MOBILE occurs if the photo current of PD₁ exceeds the peak-current difference of RTD₁ and RTD₂.

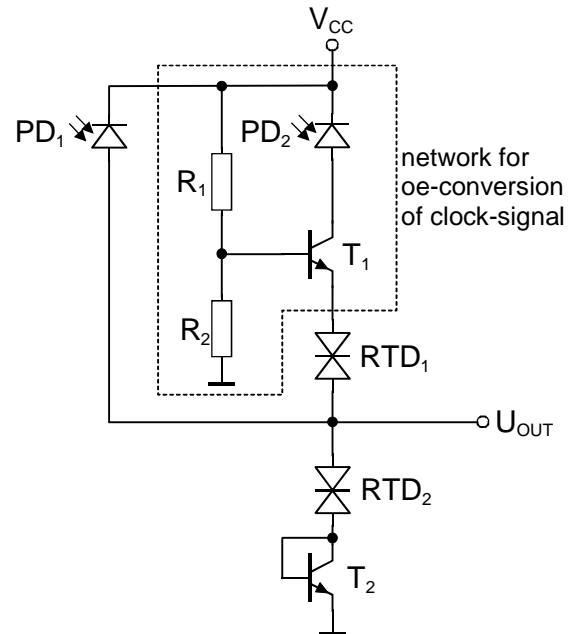


Figure 1. Circuit design for optical MOBILE-Gate clocking

The replacement of the electrical clock signal with an optical equivalent is beneficial, because the clock signal may be transported through the same fiber. It is necessary to convert the response of a photo detector into a voltage drop across the RTDs. Here, this is solved by the transistor T₁ (HBT), the resistors R₁ and R₂ and the pin-diode PD₂, bordered by the dashed line in Fig. 1. The resistors work as a biasing network

for T_1 . The photo detector PD_2 is placed in the collector branch of T_1 .

Without illumination on PD_2 , a current flow in the collector of T_1 is prevented. Thus, the current is flowing mainly through R_1 , the base-emitter-diode of T_1 , the RTDs and the base-emitter-diode of T_2 . The main voltage drop occurs on R_1 . In this case the voltage across the RTDs corresponds to a low level clock signal.

If PD_2 is illuminated, the collector branch is opened because of the generated photocurrent. Due to the current gain of T_1 , the base current decreases to approximately zero. Now, the voltage drop on R_1 is negligible. In this case, the voltage drop on the RTDs corresponds to a high level clock signal.

Due to the mentioned working behavior of T_1 , the variation of voltage drop across PD_2 during the clock conversion does not change drastically. Thus, the transshipping of charge at the capacitance of PD_2 is minimized and the high speed performance of the circuit is optimized.

III. SIMULATION

A. Device Models

The presented concept was simulated by PSpice V 14.2. The used HBTs are modeled by a fitted Gummel-Poon based model. Fig. 2 shows the equivalent device models for RTD and pin-diode simulation.

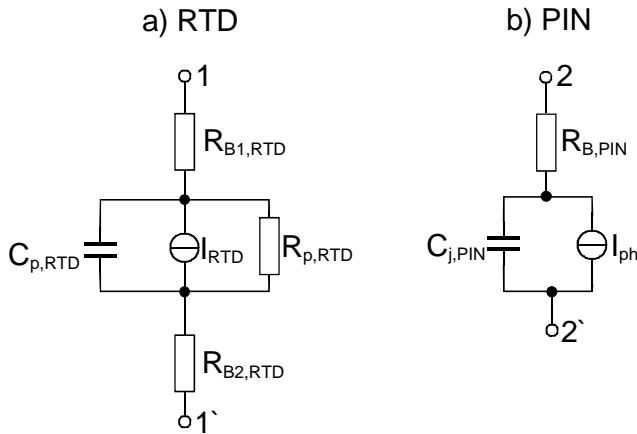


Figure 2. Device models for a) RTD and b) pin-diode

The resistors R_{Bx} represent the lead resistances of both devices. The capacitance of the RTD and the junction capacitance of the pin-diode are represented by $C_{p,RTD}$ and $C_{j,PIN}$. For improved convergence of the simulation, a high value ohmic resistor $R_{p,RTD}$ is included in parallel to $C_{p,RTD}$. I_{RTD} is a voltage controlled current source and describes the typical IV-characteristics of a RTD by a stage function. The first positive differential range (PDR1) and the negative differential range (NDR) are described separately in both directions by hyperbolic functions in the form

$$I_{range} = 1 \pm \tanh(f(\pm V_{11'} \pm V_{px})), \quad (1)$$

where “f” is a fitting factor and V_{px} is the peak voltage of each direction. The second positive differential range (PDR2) is described by a conventional diode equation. The model was fitted to measured data of RTD devices fabricated in our laboratory [3].

The model used for the pin-diode describes the behavior of the device in reverse direction only, where it works as a photo detector. This is sufficient, because the pin-diodes used are biased negatively at any time. The generated photo current is modulated by the voltage controlled current source $I_{ph,sim}$. Within the simulation, the optical input power of the pin-diodes corresponds to the applied voltage to I_{ph} . This ratio is equal to the measured responsivities on $\lambda=1.55 \mu\text{m}$ (PD_1) and $\lambda=1.3 \mu\text{m}$ (PD_2) of InGaAs single pin-diodes with 600 nm absorption layer thickness, investigated in our department [3].

$$R = \frac{I_{photo}}{P_{opt}} = \frac{I_{ph,sim}}{V_{ph,sim}} \quad (2)$$

B. Simulation Results

The function of the oe-conversion network for the clock signal branch, is shown in Fig. 3, which gives the timing diagram of the base potential and base current of T_1 .

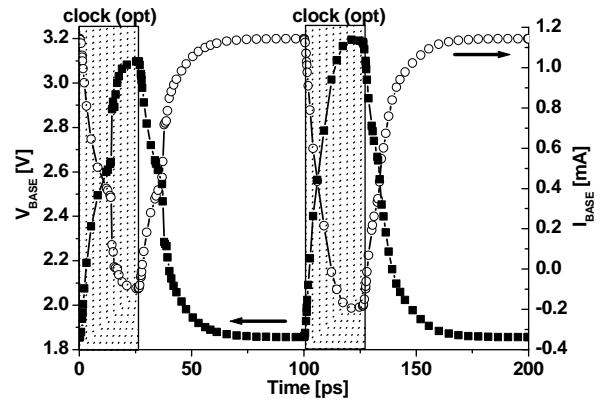


Figure 3. Simulated base potential and base current of T_1

The illumination of PD_2 provides a collector current to the transistor T_1 and enables its normal open operation in combination with the base network R_1 and R_2 . The MOBILE is connected with low losses to the electrical bias V_{CC} : the electrical clock is high. The resulting electrical clock potential over the RTDs is

$$V_{clk,high} = V_{BASE,on} - V_{BE,T1} - V_{BE,T2} \approx 1.7 \text{ V} \quad (3)$$

Without illumination, the collector from T_1 is disconnected from V_{CC} . The remaining current is the base-emitter current provided by the base network which is much higher than the previous base current during the open operation of T_1 and leads

to a voltage drop across R_1 . The resulting voltage drop over both RTDs is

$$V_{\text{clk,low}} = V_{\text{BASE,off}} - V_{\text{BE,T1}} - V_{\text{BE,T2}} \approx 0.3 \text{ V} \quad (4)$$

Fig. 4 shows the simulated output timing diagram at 10 GHz. If the data pin-diode PD_1 is illuminated, the output of the MOBILE-gate reaches the high state. If PD_1 stays dark, the MOBILE-gate remains in low state.

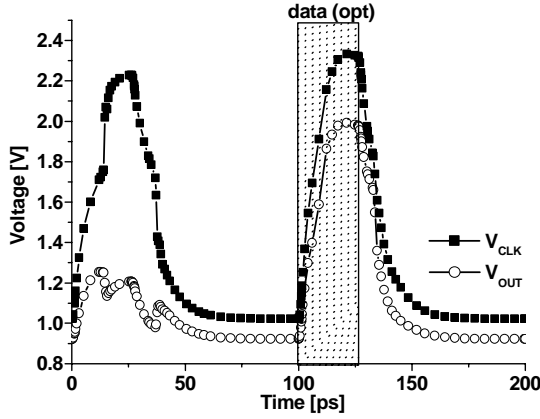


Figure 4. Simulated output timing diagram of the MOBILE-gate with all optical input

IV. DETECTOR

A. Detector Concept

The idea of driving the all optical input MOBILE-gate with a single fiber requires a phase locked transmission of the clock signal and the data signal simultaneously. This may cause further speed limitations which are not considered, here. The separation of both signals can be realized using two different wavelengths or by polarized light. Here, a wavelength selective detector optimized for the two favored wavelengths $\lambda_1=1300$ nm and $\lambda_2=1550$ nm for fiber communication is chosen.

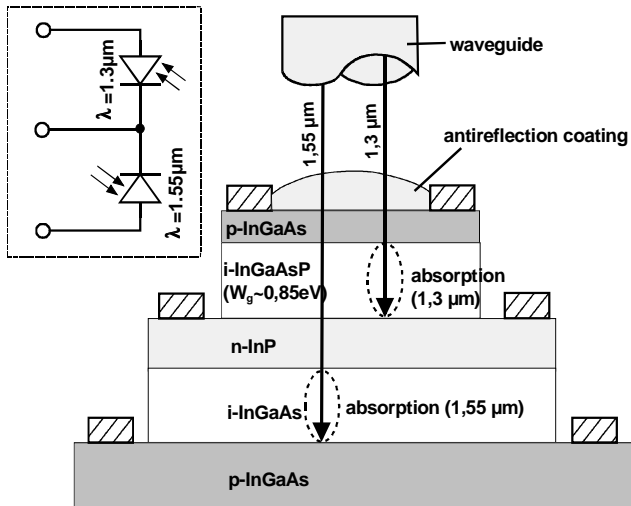


Figure 5. Cross section of the wavelength selective detector and its equivalent circuit (insert)

The idea is to stack two absorption layers with different band gaps, so that the upper layer absorbs only the low wavelength signal (λ_1) and is transparent for the other one. The high wavelength signal (λ_2) is absorbed in the lower layer [4]. Thus, both optical signals are detected and demultiplexed in parallel. The configuration shown in Fig. 5 requires an equal cathode potential for both pin-diodes. This restriction is considered by the presented circuit design.

B. Epitaxy

The layer stack of the investigated detector was grown in a low-pressure metal-organic vapour phase epitaxy (LP-MOVPE) system AIX200 with horizontal RF-heated reactor heating. The growth was carried out using nitrogen carrier gas at constant 50 mbar reactor pressure and with a V/III ratio between 5 and 40 using tertiarybutylarsin (TBAs) and tertiarybutyl-phosphine (TBP) as group-V precursor. As group-III precursor trimethylindium (TMIn) and trimethyl-gallium (TEGa) were used. The p-type doping of the InGaAs contact layers was realized using diethylzinc (DEZn), while the maximum value was limited to $8 \times 10^{18} \text{ cm}^{-3}$ to prevent the zinc diffusion into the following layers. N-type doping of the InP layer was adjusted up to $1.5 \times 10^{19} \text{ cm}^{-3}$ by ditertiary- butylsilicon (DitBuSi).

C. Process Technology

The devices were processed by optical contact lithography and conventional wet chemical etching using a triple mesa design with ring metallisation on each contact layer. The critical etching of 600 nm InGaAsP was performed by $\text{H}_2\text{SO}_4:\text{H}_2\text{O}_2:\text{H}_2\text{O}$ (1:1:10) with an etch rate of ~ 2 nm/s highly selective on InP. The underetching slope and mesa surface is acceptable but may be further optimized with a dry etching process in future. To manage the contact bridges between the measurement pads and the intrinsic device with a total height up to $1.6 \mu\text{m}$, a spin on glass (BCB) is used to support the contact line.

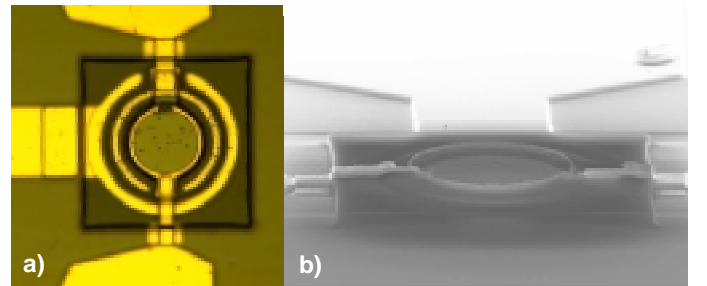


Figure 6. a) Optical - and b) SEM-micrograph of a fabricated pinip-single device with $21 \mu\text{m}$ diameter active area

D. Device Results

The processed pinip-devices are characterized concerning their DC I/V-characteristics and responsivity (see Fig. 7 and 8). The dark current of the InGaAs-diode moves in a typical range of ~ 20 nA. Looking at the upper InGaAsP-diode the dark current reaches values, which are higher by about one order of magnitude. This may be caused by poorer crystal quality of the

quaternary material and the mesa surface of the upper absorption layer.

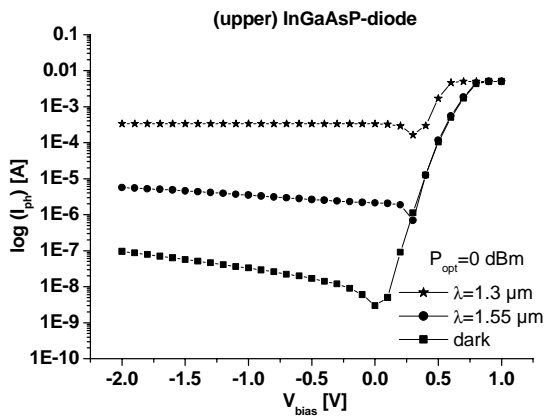


Figure 7. DC-Measurements and responsivity results of the upper InGaAsP pin-diode

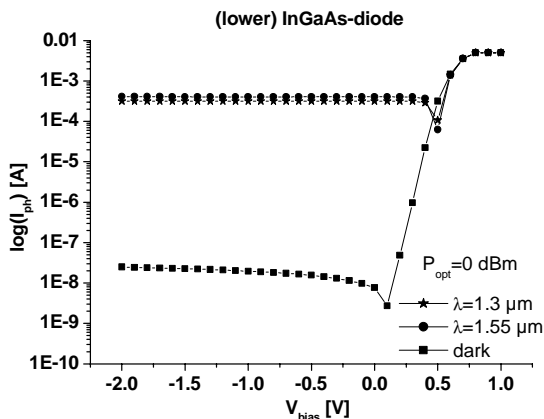


Figure 8. DC-Measurements and responsivity results of the lower InGaAs pin-diode

The responsivity measurements were accomplished with a cw-semiconductor laser providing $\lambda=1,3 \mu\text{m}$ and $\lambda=1,55 \mu\text{m}$ through a cleaved fiber. With regard to the InGaAsP-diode, the generated photocurrents differ by approximately two orders of magnitude. The lower InGaAs-diode is sensitive to both wavelengths and provides almost no selectivity. The measured responsivities are close to each other. Thus, the resulting crosstalks are $C_{1,55\mu\text{m}} = -20,6 \text{ dB}$ and $C_{1,3\mu\text{m}} = -0,19 \text{ dB}$. The optimization of crosstalk on $\lambda=1,3 \mu\text{m}$ is in progress. Here, we analyze the composition of the quaternary absorption material due to its absorption coefficient α and band gap W_g on the one hand, and we check the device design for possible diffused light sources on the other hand. The work on wavelength selective devices continues with investigation of the RF-performance.

V. INTEGRATION CONCEPT

For ease of fabrication of the OEIC, the layer stack height should be as low as possible. This is necessary to minimize the epitaxy costs and to ensure the stability of process. One possible solution is shown in Fig. 9. The thickness of the

absorption layers depend on the required responsivity and on the RF-performance of the device. They make up the main part of the layer stack thickness. The HBT is integrated with the

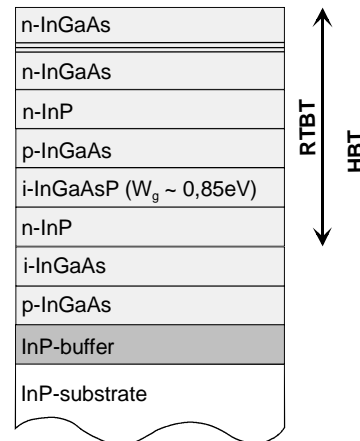


Figure 9. Layer stack for integration of the all optical input MOBILE-Gate

upper pin-diode. The p-contact, the absorption and the n-contact layers are suited for the base, collector and subcollector layers of a DHBT. The RTD quantum well is positioned in the emitter cap of the HBT. Thus, the use of a resonant tunneling bipolar transistor (RTBT) is possible. By removing the quantum well from the top, a conventional HBT is provided. With this integration concept, the total height of the layer stack is kept lower than $3 \mu\text{m}$ and is suited for processing with optical lithography.

VI. CONCLUSION

A concept for a MOBILE-gate with all optical input is presented and verified by simulation. Epitaxy parameters, technology details and first measurement results of photo detectors with improved functionality are presented in this paper. Furthermore, a technology concept for integration of the complete circuit is given. The proposed concept makes the MOBILE suitable for high speed fiber communication systems, because the optical clock control and the data stream can be transmitted phase locked through one fiber.

- [1] K. Meazawa, T. Mizutani, "A New Resonant Tunneling Logic gate Employing Monostable-Bistable Transition," Jpn. J. Appl. Phys., Vol. 32, pp. L 42-L 44, 15 January 1993
- [2] K. Sano, K. Murata, T. Otsuji, T. Akeyoshi, N. Shimitzu, E. Sano, "80 Gbit/s optoelectronic delayed flip-flop circuit using resonant tunneling diodes and uni-traveling-carrier photodiode," Electronics Letters, Vol. 35, No. 16, 5 August 1999
- [3] W. Prost, P. Kelly, A. Gutzzeit, V. Khorenko, A. Matiss, J. Driesen, A.-C. Mofor, A. Bakin, A. Poloczek, S. Neumann, A. Stöhr, D. Jäger, M. McGinnity, A. Schlachetzki, F.-J. Tegude, "Design and Modelling of a III/V Mobile-Gate with Optical Input on a Silicon Substrate," 17th Indium Phosphide and Related Materials Conference, Glasgow, UK, 8-12 May 2005
- [4] J.C. Campbell, A.G. Dental, T.P. Lee, C.A. Burrus, "Improved Two-Wavelength Demultiplexing InGaAsP Photodetector," IEEE Journal of Quantum Electronics, Vol. QE-16, No.6, June 1980

Numerical computation of field and temperature distribution for a device aiming at local brain exposure of rodents in vivo at 2 GHz

A. El Ouardi¹, A. Bitz¹, J. Streckert¹, T. Reinhardt¹, V. Hansen¹,
D. Krause-Finkeldey², K. Ladage²

¹University of Wuppertal, Chair of Electromagnetic Theory,
Rainer-Gruenter-Str. 21, 42119 Wuppertal, Germany,
+49 202 439 1949, hansen@uni-wuppertal.de

²Ruhr-Universitaet Bochum, Institute of Anatomy, Bochum, Germany

Abstract—A device for the 2 GHz (UMTS) local exposure of six rats in vivo based on a double-cone waveguide is presented. Further numerical computations of field and temperature distribution in the rats' head for investigations of possible influences of mobile communication signals on the brain are shown.

I. INTRODUCTION

One of the biological systems that is often suspected to be sensitive to electromagnetic exposure is the blood-brain barrier (BBB). There are controversially discussed results from several in vitro and in vivo investigations. In this project effects of microwave exposure (UMTS modulation) on the pattern of mRNA / protein expression in rats is studied. To do so partial brain exposure in vivo is necessary, since the blood compartment and the components of the BBB vessel wall are a functional entity and should be maintained during experiments, whereas none of the in vitro models used so far acquires the complex interaction of structural BBB components. The contribution describes the exposure concept for the running experiments. A number of 6 restrained rats shall be exposed simultaneously for at least 2 hours, whereby in sequentially performed tests a blinded scrambling of different applied specific absorption rates (0 W/kg, 2 W/kg, and 10 W/kg) shall be provided. The exposure of the rats' brains shall be as localized and as uniform as possible, but with SAR_{max} not exceeding the thermal limit which was recently acquired in a pilot study. The stability of the exposure field and therefore also the rf shielding of the set-up is another point of importance.

II. RF EXPOSURE SYSTEM

For the rf exposure of a number of animals an approved concept is to arrange the subjects on a circle around a common source, e.g. to use a carousel [1] or a radial waveguide [2] arrangement, and to align the snouts towards the feed. For the case of investigations of BBB, however, such a concept has been criticized by experts [3], arguing that the sensitive sensors around the rodents' snouts could be overexposed thus masking the expected small effects from the brain. Another concept which avoids the latter is to place a loop antenna

directly onto the head of a restrained rat [4]. The use of such an open structure, yet, is disadvantageous if multiple animals must be exposed, because of electromagnetic coupling between adjacent antennas and due to the rising complexity of the feeding network. In order to overcome these problems we modified the concept of the flat radial waveguide and constructed a spherical TEM waveguide [5] with a coaxial feed at the tip and the exposure field leaking from the rim (Fig. 1).

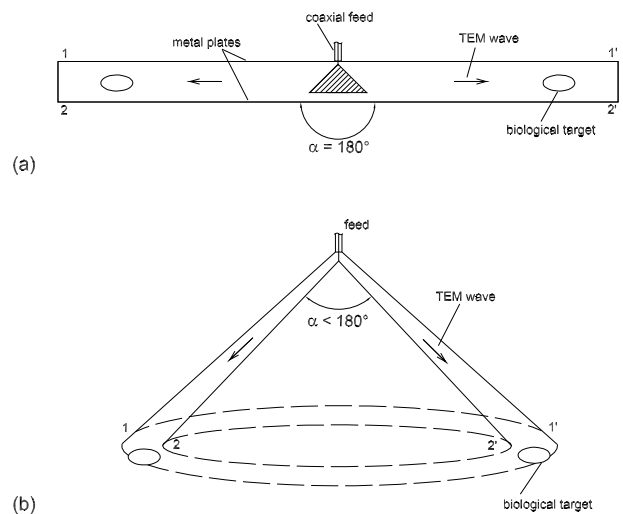


Fig. 1. Evolution from a flat cylindrical radial waveguide (a) to a spherical waveguide (b)

The spherical waveguide has been approached by a double-cone with a hexagonal basis for reasons of fabrication (Fig 2a). In the feed element at the top the input power is uniformly distributed over the six compartments of the waveguide. Since the exposure field should be concentrated to a rather small area at the lower aperture of the double-cone a pair of metal bars with a gap of 6 mm in between was built into each

compartment (Fig 2b).

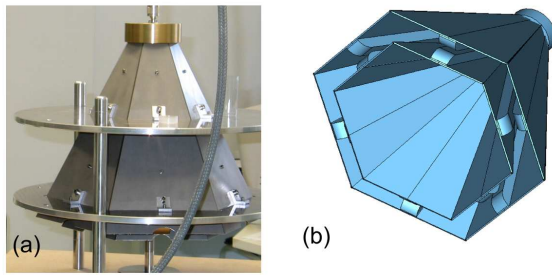


Fig. 2. Double-cone waveguide (a) with inner bar structure (b)

The 6 rocket restrainers for the immobilisation of the rats are fixed in such a way that the rats' brains are always positioned immediately below the gap between the bars (Fig. 3). Thereby, a very localized exposure is achieved.



Fig. 3. Positioning of the restrainers below the bar structure of the waveguide

In order to avoid electromagnetic coupling between the exposure fields of adjacent animals the restrainers are placed into compartments (Fig. 4) which are shielded against each other and against the environment by using metal walls and hinged flaps covered with finely woven metal grids.

The size of the ground plane is 1.1m x 1.1m, the height from the ground plane to the tip is 40 cm. Figure 5 shows the scheme of the experimental apparatus. The signal source consists of a UMTS generator and a booster amplifier whereby the applied power is controlled by the computerized experimental protocol. The actual input power level is also monitored via a coupler/detector combination.

III. RESULTS

As a consequence of the unavoidable reflection from the rats the ratio between the field strengths in the waveguide and in the rats' head is rather high. Still, due to the very strong magnitude of the field in the bar structure an electrical exposure field within the rats' brain of more than 385 V/m is achieved for a total feed power of 1 W. Fig. 6 shows a typical

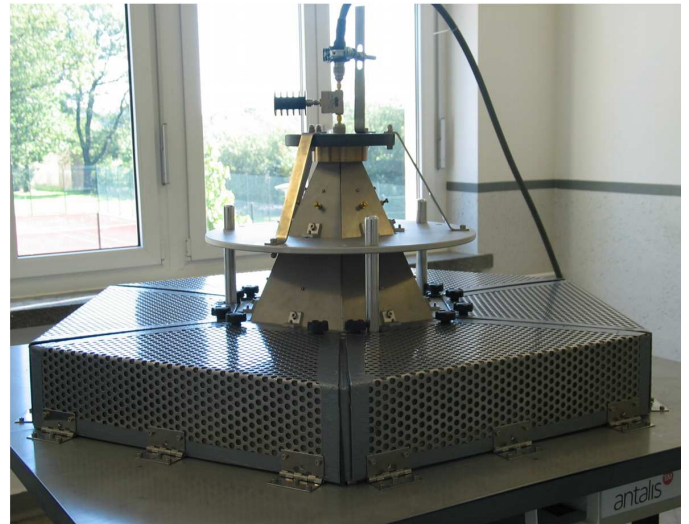


Fig. 4. Implemented local exposure system for 6 rats

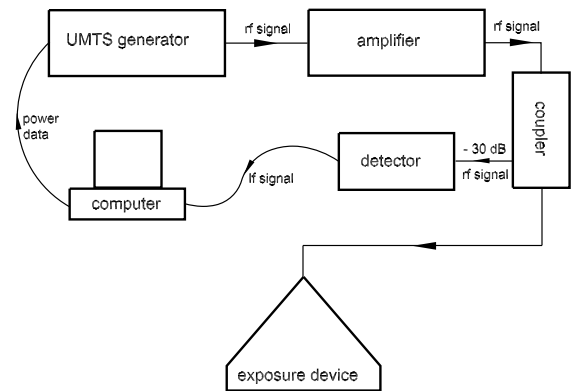


Fig. 5. Scheme of the experiment for local brain exposure at 2 GHz

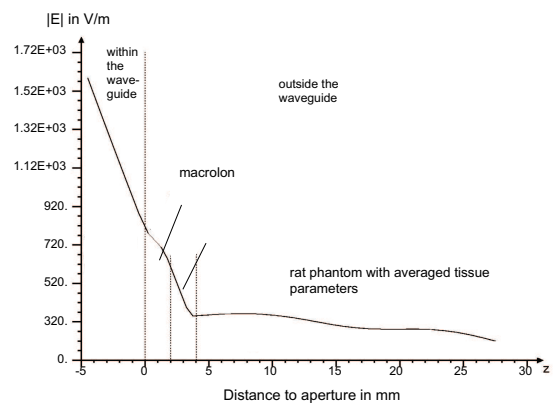


Fig. 6. Decay of the electrical field for the transition from waveguide to the rat's body

line plot of the electric field for the present sequence of layers.

The cut of the normalized electrical field distribution shown in fig. 7 demonstrates that the field concentrates mainly in the rat's head and that the field radiated from the rat's body is very small. Thus, the measures for shielding the outer space from the exposure field can be kept rather simple. For the field strength at the location of the rats' heads within the six rocket restrainers the max/min-ratio is only 1.09.

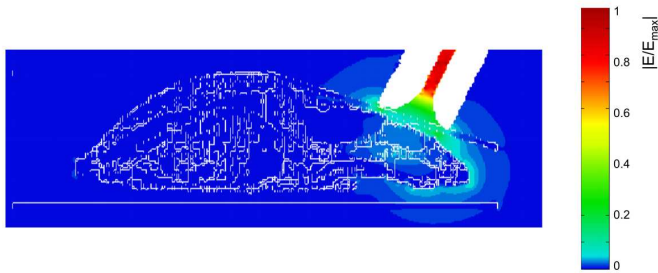


Fig. 7. Numerically calculated field distribution on the basis of an anatomical Wistar rat model

Fig. 8 gives the SAR distribution across the anatomical rat model in a logarithmic (a) and in a linear (b) scale. Obviously, the electromagnetic field energy is mainly dissipated within the central region of the head, as desired. The evaluation of the computations yields an SAR, averaged over the total volume of the brain (mass 2 g), of 8.2 W/kg per 100 mW input power at the tip of the waveguide.

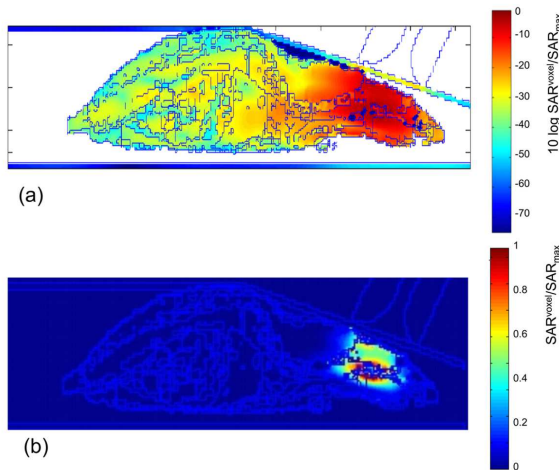


Fig. 8. Numerically calculated SAR distribution (a) logarithmic plot (b) linear plot

The calculation of the temperature distribution by numerical solution of the bio-heat equation also reflects the localized exposure of the animals (Fig. 9) and gives additional hints on the local heat-flow due to the thermal isolation and transition properties of the different kinds of tissue.

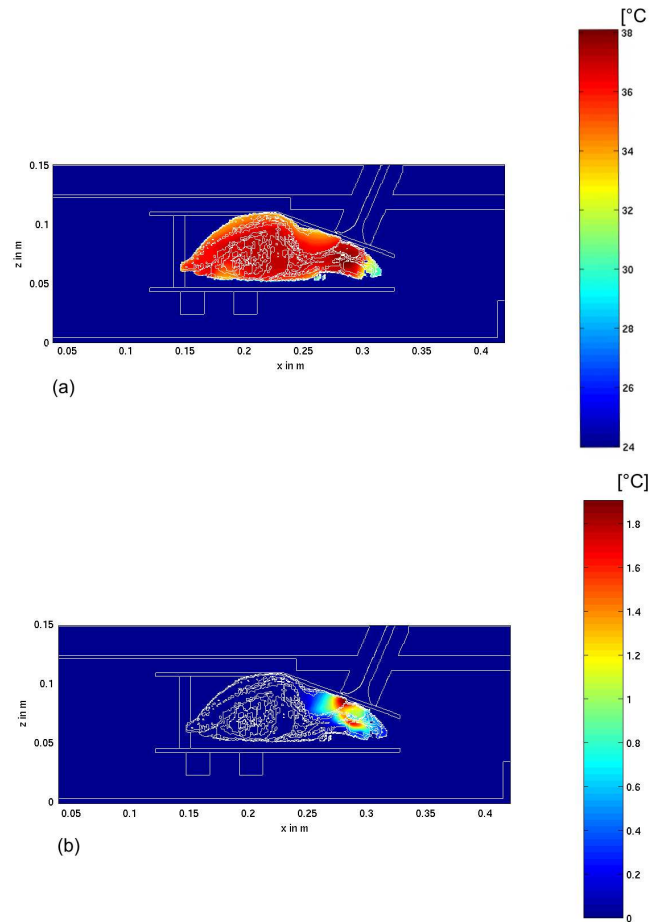


Fig. 9. Numerically calculated temperature distribution (a) absolute steady-state temperature for 357 mW input power (b) temperature difference between rf exposed case and unexposed case assuming a constant ambient temperature of $24^{\circ}C$ and a blood temperature of $37^{\circ}C$

Furthermore, measurements of the local brain temperature in rf exposed cadavers of rats were performed. To do so, a fibre optic temperature probe was contacted to the brain of the subjects via a tiny bore through the cranial bone and temperature change was recorded during application of the rf field at 2 GHz. A typical time course of the temperature development between onset and switch-off of the rf signal for an input power of 100 mW is shown in fig. 10.

From the slope of the temperature curve one can also derive the SAR exhibiting an average value of 7.75 W/kg @ 100 mW. Applying the standard deviation of $\pm 18\%$ this measured value fits well with the SAR calculated from the electrical field distribution.

In order to adjust the power for the final experiments in such a way that no thermal effect occurs (i.e. $\Delta T < 0.1^{\circ}C$) one has to consider that - in contrast to the temperature development

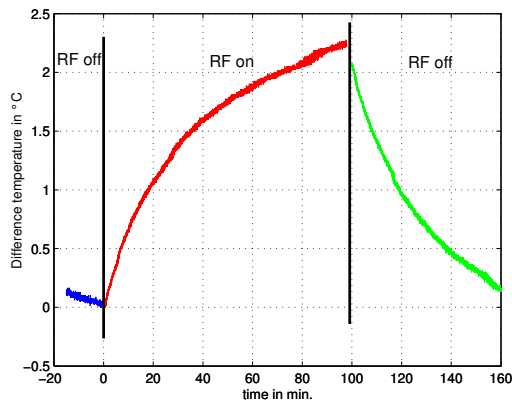


Fig. 10. Measured difference temperature in the brain of a rat cadaver versus time for rf power of 100 mW switched on and off

in cadavers - the temperature change in living animals is much smaller due to the blood flow and due to the thermal regulatory system. From fig. 10, for instance, a temperature rise in the cadaver of more than 2°C can be read. The calculation of the temperature in fig. 9 already considers the influence of the blood flow. Therefore, re-calculated for the standard input power of 100 mW, a temperature rise of only 0.3°C is found. This corresponds famously to results that were achieved by temperature measurements with narcotised rats for the same exposure field. The temperature rise in vital rats is expected to be even smaller due to the active thermal regulation. Thus, the calculations from the thermal rat model and the measurements with narcotised animals, respectively, are judged to give worst case results for the temperature increase enabling an rf power adjustment with a sufficient safety distance for an experiment with healthy living rats.

IV. CONCLUSION

An exposure device for the local application of 2 GHz-fields to the brain of rats was described and characterised by field and SAR calculations and measurements. Moreover, numerical and experimental determinations of the brain temperature were shown and a procedure was presented for the adjustment of the power that excludes a thermal overload of the animals.

ACKNOWLEDGMENT

The authors would like to thank Drs. G. Friedrich and F. Gollnick from Forschungsgemeinschaft Funk, Germany, for initialising and scientifically supporting this project.

REFERENCES

- [1] Burkhardt, M., Spinelli, Y., Kuster, N.: Exposure setup to test effects of wireless communications systems on the CNS. *Health Physics*, vol. 73, pp. 770-778, 1997.
- [2] Hansen, V. W., Bitz, A. K., Streckert, J. R.: RF exposure of biological systems in radial waveguides. *IEEE Trans. EMC*, vol. 41, no. 4, pp. 487-493, 1999.
- [3] Workshop "The Blood-Brain-Barrier - Can it be influenced by RF field interactions?", Forschungsgemeinschaft Funk/COST 281, Reisenburg, Germany, November 2003.

- [4] Leveque, P., Dale, C., Veyret, B., Wiart, J.: Dosimetric analysis of a 900-MHz rat head exposure system. *IEEE Trans. MTT*, vol. 52, no. 8, pp. 2076-2083, 2004.
- [5] Hansen, V., Streckert, J.: Waves in GTEM cells - A combined analytical - numerical approach. 17th Int. Wroclaw Symp. and Exhibition on Electromagnetic Compatibility, Wroclaw, 29.6. - 1.7.2004, 435-439.

Linearisation of high power amplifier with optimised zone 0 terminations

B. Bunz, A.Z. Markos, A. Ahmed and G. Kompa

University of Kassel, Fachgebiet Hochfrequenztechnik
 Wilhelmshöher Allee 73, D-34121 Kassel, Germany, Tel: +49-561-804-6535, Fax: -6529
 E-mail: bunz@hfm.e-technik.uni-kassel.de, <http://www.uni-kassel.de/fb16/hft/bunz.html>

Abstract – This paper presents an investigation of optimum zone 0 source and load terminations for high power amplifiers. Measurements with an error-corrected two-tone measurement system have been performed to determine optimised terminations, which are then implemented into the matching networks via an optimised bias circuitry. Measurements with a 4 W Filtronic GaAs HEMT resulted in a 1.2 dB variation of the output power and 10 dB the IMD 3 products by 10 dB.

Index terms - power transistors, memory effects, source- / load pull, amplifier

I. INTRODUCTION

GaAs offers a mature technology towards high linear power amplifier applications. To establish high data transfer rates, high modulation bandwidths as well as complex modulation schemes using non-constant envelope (e.g. QPSK) have been established.

When driven under two-tone and multi-tone stimulus, terminations in different zones influence the RF behaviour [1-4]. The frequency conversions for a two-tone stimulus are demonstrated in fig. 1.

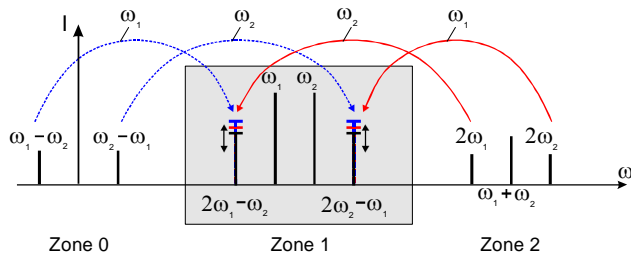


Fig. 1: Frequency conversions in a transistor for a two-tone stimulus.

Sevic et al. [6] have proposed an envelope load-pull system, using a combination of a semi-automatic impedance network and a bias tee. Williams et al. [2] have proposed a two-tone time domain measurement system and investigated envelope termination effects on efficiency with a HBT device.

In this paper, an envelope (zone 0) source- and load-pull measurement system is presented, being an extension of an inhouse realised active RF load- / and source-pull system [1]. It comprises active load modules to avoid extensive use of different electronic signal generators. The zone 0 terminations have been realised with passive terminations.

The results of the measurements are then implemented in an high power amplifier design.

II. MEASUREMENT SETUP

A schematic diagram of the measurement setup is shown in fig.2.

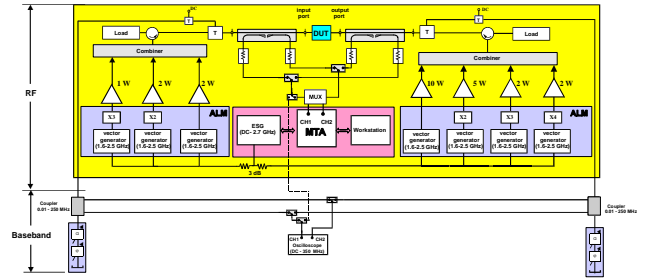


Fig. 2: Schematic diagram of the measurement system.

The measurement system concept consists of one signal source to avoid problems with synchronisation between multiple signal sources. For controlling harmonic RF source and load reflection coefficients, frequency multipliers are introduced to establish a frequency conversion to the desired harmonic. Via an active load- and source-pull, arbitrary passive and active load configurations can be adjusted. The different signal paths are fed via combining networks and isolators to the DUT. Via bi-directional couplers, impinging and reflected waves are coupled out and fed via a multiplexer to the MTA. To establish an envelope source- and load pull, the RF load-pull concept is transferred to the envelope frequency region. A combination of high- and low frequency bias tees is used to separate the low frequency signal from the DC and RF signal. The envelope source- / and load pull has preliminary been realised with passive components. Couplers are used to feed the signals via a multiplexer to an oscilloscope.

Controlling software has been developed for the analysis of the present tones. Power levelling for both tones has been introduced to ensure a constant impinging wave.

III. ENVELOPE LOAD- / SOURCE PULL

For an investigation of the envelope impedance terminations, first on a GaAs pHEMT (Filtronic FPD 400 AF), two tone measurements were performed. Fundamental center frequency was 900 MHz with a tone

spacing of 100 kHz. While zone 0 source pull resulted in negligible RF variations, only zone 0 load pull results are presented. In figure 3, the output power of the lower main tone is displayed. While a maximum of output power with an envelope short termination is given, a minimum of the output power with an open can be observed. In figure 4 the intermodulation products are displayed. Concerning the intermodulation products of third order, a maximum with an open termination is given, while a minimum is apparent with a short termination. Only one half of the Smith chart is displayed because of the variation of the envelope termination showing an axial symmetry with the $\text{Im } \Gamma = 0$ axis [2]. Thus for amplifier design, a broadband envelope termination approximating a short should be designed.

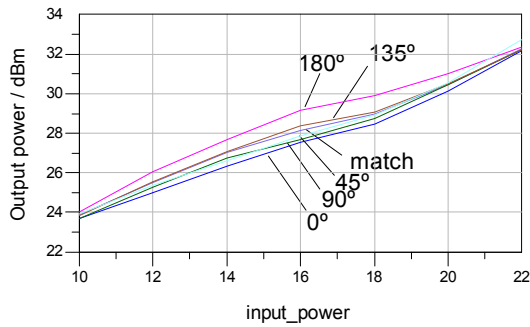


Fig. 3: Lower output tone as function of input power for different envelope load terminations.

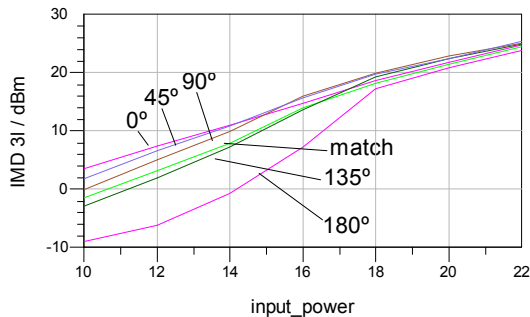


Fig. 4: Lower third intermodulation product as function of input power for different envelope load terminations.

IV. BIAS CIRCUIT DESIGN

Bias circuits in amplifiers are required to deliver the supply voltages and currents to the DUT and keep them constant without disturbing the RF path. In classical PA design the bias circuit is usually designed to provide high impedances as compared to the impedances of the input/output of the device and the matching circuits. This is to prevent RF power loss, which degrades the efficiency of amplifiers. In this approach the zone 0 terminations are undetermined.

Thus, in the bias circuit, lumped capacitors have been added to realize a low broadband impedance. The length of a $\lambda/4$ line bias network is optimized in such a way that to create a parallel resonance at the design frequency

(900MHz) of the amplifier using a shunt capacitor at the drain side of the network as shown in figure 5.

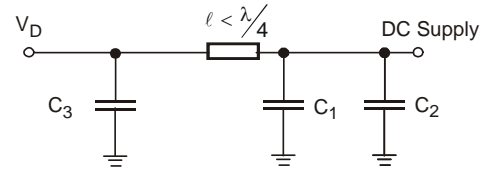


Fig. 5: Optimized bias network.

In that way a high electric resistivity is given at the design frequency while maintaining low impedances at envelope frequencies.

V. HIGH POWER AMPLIFIER DESIGN

Two realisations of the amplifier were compared to each other. In one realisation a classical bias network design was performed, in a second realisation, an envelope termination of a short was realised (see fig. 6). The measurement results shown in figure 7 and 8 validate the measurement results obtained with zone 0 load-pull. While the variation of output power of the main tones is limited by 1 dB, the intermodulation products of third order could be reduced by more than 10 dB. So the optimization of the bias networks offer one possibility to linearize an amplifier.

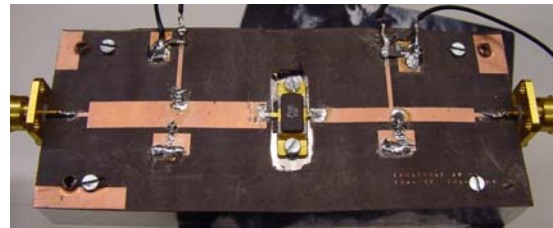


Fig. 6: Realisation of high power amplifier.

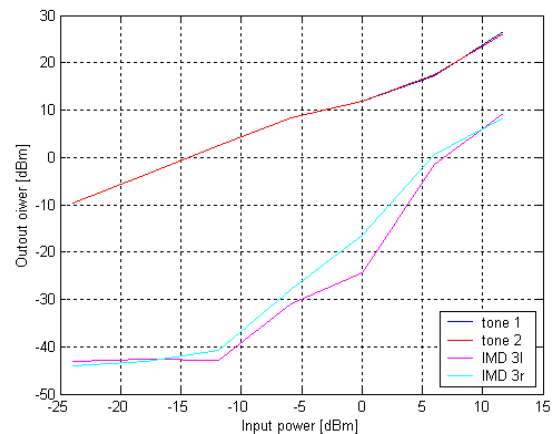


Fig. 7: Characterisation of amplifier without optimized envelope termination.

For the optimised amplifier, a single tone characterisation has been performed and resulted at the 1 dB compression point in 34.5 dBm output power and 47 % PAE.

VI. CONCLUSION

A investigation of optimum zone 0 terminations has been performed and a short has been found to result in a maximum C/IMD ratio. The terminations have been realised in a high power class A HEMT-based amplifier design. Two realisations (without, with optimised bias circuit) have been realised and resulted in an improvement of the ratio C/ IMD by 10 dB.

ACKNOWLEDGEMENT

The authors gratefully acknowledge the support from German Ministry of Education and Research (BMBF), and from the Information Society Technologies Programme of the EU under contract IST-1-507893-NOE “Top Amplifier Research Groups in a European Team (TARGET)”.

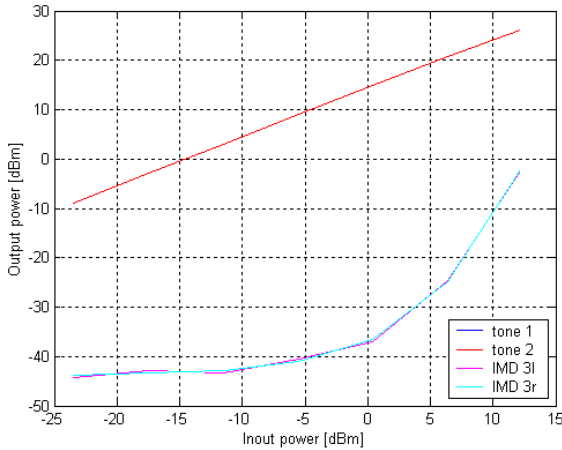


Fig. 8: Characterisation of amplifier with envelope termination being a short.

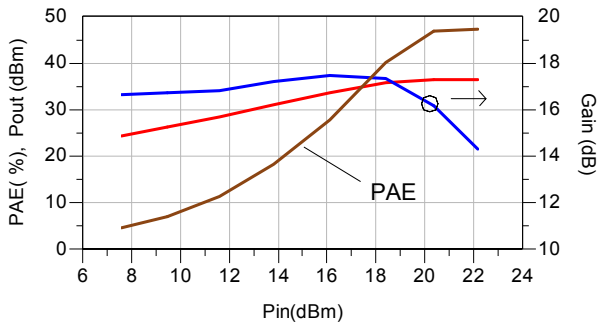


Fig. 9: Single tone characterisation of optimised amplifier

REFERENCES

- [1] B. Bunz and G. Kompa, "Investigation of Envelope impedance termination towards RF behaviour of GaN HEMT power devices", *European Microwave Conference Proceedings, Paris, 2005*, pp. 1595-1598.
- [2] D.J. Williams, J. Leckey, and P. Tasker, "A study of the effect of envelope termination on intermodulation asymmetry using a two-tone time domain measurement system," *IEEE MTT-S Int. Microwave Symp.*, 2002, pp. 1841 – 1844.
- [3] J.C. Pedro and N.B. Carvalho, "Physical sources of device level nonlinearity and circuit level linearisation techniques", *TARGET Tutorial on Linearisation*, Rome, 2004, pp. 65 -86.
- [4] A. Ahmed, B. Bunz, M. Gamal-El Din, and G. Kompa, "Measurement setups for memory effects characterisation in GaN HEMT power device", *Top Amplifier Research Groups in a European Team (TARGET) Tutorial on Device characterisation, Amsterdam, October 2004*.
- [5] A. Khanifar, N. Maslennikov and B. Vassilakis, "Bias circuit topologies for minimization of RF amplifier memory effects", *European Microwave Conference Proceedings, 2003*, pp. 1349 – 1352
- [6] J. F. Sevic, K.L. Burger, and M. B. Steer, "A novel envelope-termination load-pull method for ACPR optimisation of RF/microwave power amplifiers", *IEEE MTT-S Int. Microwave Symp.*, Phoenix, 1998, pp. 445 – 448.

LOW POWER VERIFICATION OF A NEW RF OUTPUT SYSTEM FOR A 170 GHz, 2 MW COAXIAL CAVITY GYROTRON

T. Rzesnicki¹, J. Jin¹, B. Piosczyk¹, M. Thumm^{1,2}, G. Michel³, D. Wagner⁴

¹Forschungszentrum Karlsruhe GmbH, Institut für Hochleistungsimpuls- und Mikrowellentechnik,
P.O. Box 3640, D-76021 Karlsruhe, Germany

²Universität Karlsruhe, Institut für Höchstfrequenz und Elektronik, 76128 Karlsruhe, Germany

³Max-Planck-Institut für Plasmaphysik, 17491 Greifswald, Germany

⁴Max-Planck-Institut für Plasmaphysik, 85740 Garching, Germany

The design of the quasi optical (q. o.) RF output system for the first industrial prototype of the European 170 GHz, 2 MW, CW coaxial cavity gyrotron for electron cyclotron heating and current drive in ITER has been verified at a low power level. Results of measurements with a high quality $TE_{34,19}$ -mode generator are in good agreement with the design calculations. This strengthens the confidence both to the employed design codes and to the manufacturing quality of the launcher and mirrors.

Keywords: Coaxial Cavity Gyrotron, RF Output System, Quasi Optical Converter, Low Power Measurements, Electron Cyclotron Heating

I. INTRODUCTION

The development of a prototype of a 2 MW, CW coaxial cavity gyrotron at 170GHz for ITER operating in the $TE_{34,19}$ mode is in progress within a cooperation between European research institutions and European tube industry. As part of that work the design of critical gyrotron components is verified experimentally at FZK [1]. In this paper only the design and results of experimental verification of the quasi-optical (q. o.) RF output system are presented. The task of the q. o. system is to convert the RF-power generated in the $TE_{34,19}$ -cavity mode into a free-space beam with a high content of the fundamental Gaussian mode. The schematic arrangement of the RF output system is shown in Fig. 1. To realize a better coupling of the $TE_{34,19}$ mode to the free space beam, a launcher with a dimpled wall structure has been chosen. Due to the wall perturbations the Gaussian mode content of the field radiated from the launcher cut is increased in comparison to a launcher with a smooth surface which has an output pattern with a Gaussian mode content of only 80%. In addition the decreased amplitude of the microwave field at the cut of the launcher reduces the diffraction losses and results thus in a reduction of the microwave stray losses inside the gyrotron tube as has been discussed in [2]. Theoretically a conversion of a field pattern with low Gaussian mode content into the fundamental Gaussian free space mode would require two mirrors with special adapted phase correcting surfaces. The calculated

surface contours of the phase correcting mirrors can only be realized in approximate way.

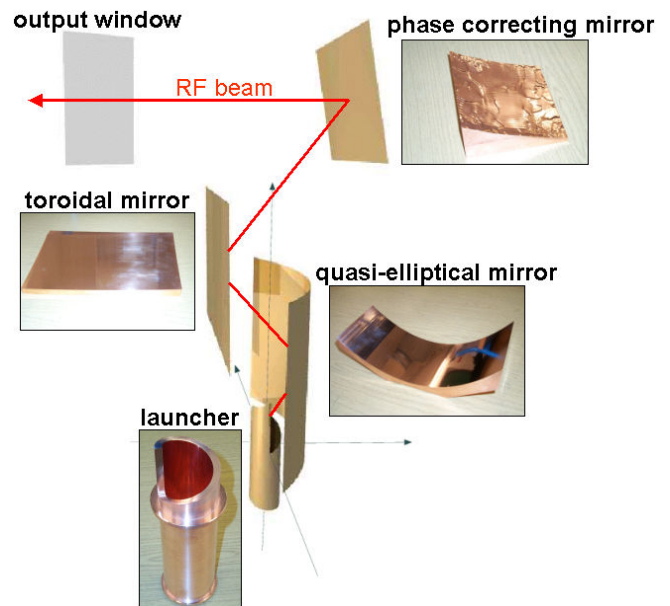


Figure 1. Arrangement of the q.o. RF-output system

This results in some microwave stray radiation losses inside the tube. Therefore, as a compromise between low stray radiation losses and large Gaussian mode content in the output beam only one phase correcting mirror (3rd) has been chosen. In that case only the amplitude distribution of the RF-beam has been optimized to be Gaussian at the position of the gyrotron output window, without considering the phase distribution. The phase front has to be corrected with an additional mirror outside of the gyrotron.

To check the performance of the RF output system before installation in the prototype tube, experimental tests at low power ("cold") have been performed. Results are reported in the following.

II. LOW POWER MODE GENERATOR

To perform cold tests a low power $TE_{34,19}$ -mode generator has been developed as reported in [2]. A photograph is shown in Fig. 2. The low power quasi-Gaussian HE_{11} mode from a horn-antenna is transformed using two cylindrical lenses to an astigmatic Gaussian beam focused onto quasi-parabolic mirror. After reflection at the mirror the phase corrected rays go through the translucent wall of a coaxial cavity and are focused onto the caustic to excite the mode. The quality of the generated mode is very sensitive to the accuracy of the mechanical fabrication.

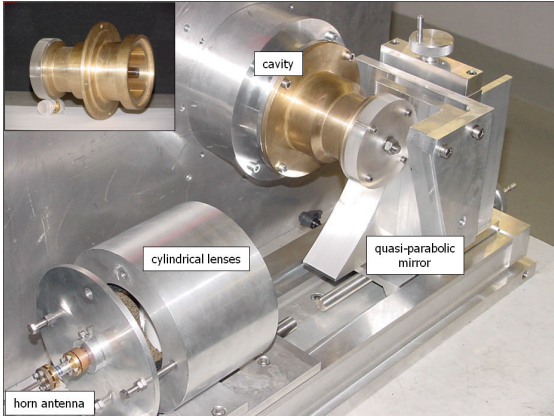


Figure 2. Low power $TE_{34,19}$ -mode generator

Three different $TE_{34,19}$ -mode generators have been manufactured and used for measurements. The field pattern of all three generators measured in both polarizations are shown in Fig. 3. In the first mode generator the quality of the $TE_{34,19}$ mode excited at 169.67 GHz was not satisfactory because of small mechanical deformations of the resonator section of the mode exciter (Fig. 3, upper row). Nevertheless the measured mode purity (using a k-spectrometer) was fairly good and also the content of the mode rotating in opposite direction was as low as $\sim 1\%$. The cavity used in the second mode generator was originally designed for excitation of the $TE_{93,2}$ mode. Here, it has been also successfully used for the excitation of the $TE_{34,19}$ mode (Fig. 3, middle row), however with a frequency of 171.92 GHz. The third mode generator was manufactured according to the design of the first mode exciter design with a small reduction of the outer cavity radius in order to shift the frequency of the generated $TE_{34,19}$ mode closer to the desired frequency of 170 GHz. Finally, with this mode generator the $TE_{34,19}$ mode has been obtained at 170.3 GHz with excellent purity (Fig.3, lower row). The content of the mode rotating in opposite direction was estimated to be as low as 0.5 to 0.7 %.

III. RESULTS OF "COLD" TEST MEASUREMENTS

Cold tests of the quasi optical RF output system have been performed with all three mode exciters: at 169.67 GHz (small mechanical profile deformation), at 171.92 GHz (designed for $TE_{93,2}$) and at 170.3 GHz (excellent quality mode). Measurements of amplitude and phase distributions have been performed in different planes. The dynamic range is around 50 dB. The experimental setup is shown in Fig. 4. The mode generator is connected to the launcher and the mirrors. The

geometrical arrangement of the q. o. system is the same as designed for the 2 MW prototype coaxial cavity gyrotron. The RF-power distribution is measured in different planes.

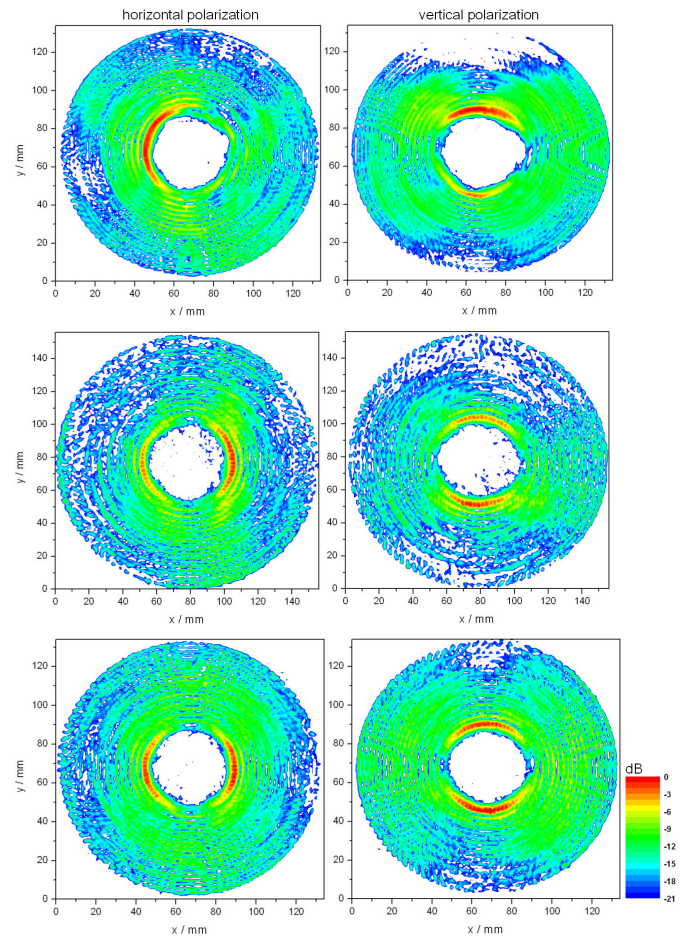


Figure 3. Results of $TE_{34,19}$ -mode excitation with three mode generators: 1st: cavity with mechanical deformation (upper row), 2nd: cavity designed for $TE_{93,2}$ mode (middle row) and 3rd: re-fabricated first cavity (bottom row)

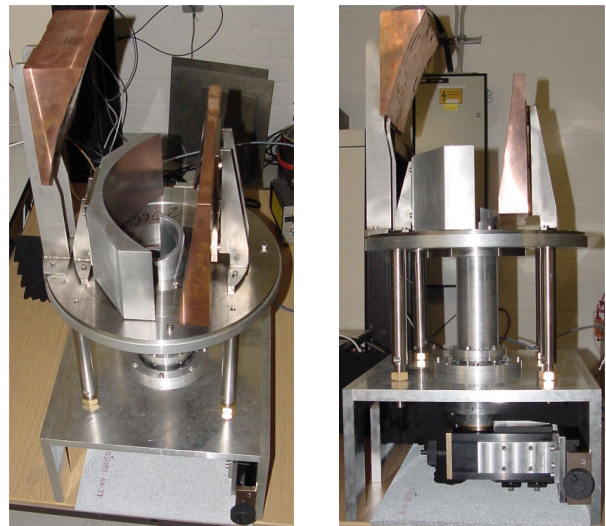


Figure 4. RF output system as assembled for the "cold" tests

As mentioned above the field distribution of the first mode generator at 169.67 GHz, shows some azimuthal asymmetry (Fig.3 upper row), although the prior measured mode purity (using a k-spectrometer) and also the right-hand rotating mode content was very high. The field pattern of the RF output system measured in different planes was found to be sensitively dependent on the azimuthal position of the mode generator. Therefore, the measurements have been performed at an "optimum" azimuthal position. As optimum that position has been taken at which the agreement of the measured distributions was best in comparison with the expected design calculations. Although the quality of the generated mode is not the best the measured distributions at different planes are in reasonable agreement with calculations (Fig. 5). The Gaussian amplitude content in the measured pattern at the gyrotron window plane was estimated to be 90%. The phase front of the beam must be corrected with an additional mirror after the gyrotron window.

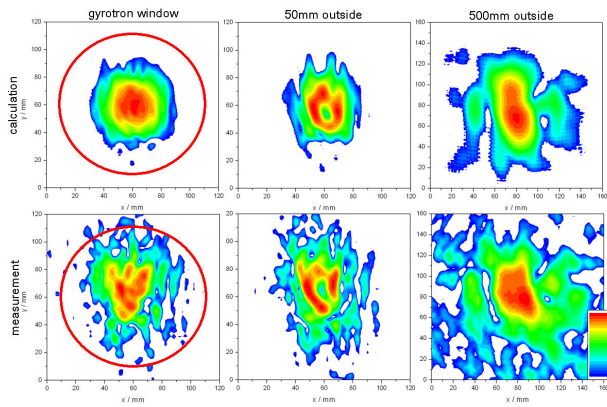


Figure 5. Results of cold tests at three planes in comparison with calculations performed with the first $TE_{34,19}$ -mode generator at 169.67 GHz. The window aperture (96 mm diameter) is indicated.

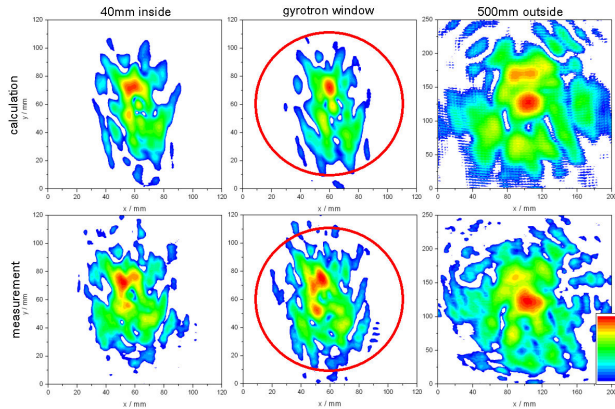


Figure 6. Results of cold tests at three planes in comparison with calculations performed with the second mode generator at 171.92 GHz. The window aperture (96 mm diameter) is indicated.

The quality of the second mode generator is good, however the frequency of 171.92 GHz is slightly to high. Due to the frequency difference the Brillouin angle is decreased by approximately 1 degree. This results in a significant shift of the position of the microwave beam at each mirror. Consequently the beam pattern is modified mainly because the correct beam

phase modification at the 3rd mirror is not feasible anymore. The properties of the microwave beam have been calculated for these conditions (Fig. 6, upper row). Although the field patterns, especially near the plane of the gyrotron window, are not anymore similar to a Gaussian distribution there is a good agreement between measurements and calculations (Fig.6). This confirms the confidence in the design code and in the accuracy of mechanical fabrication of all parts of the q. o. RF output system.

In the measurements using the second and third mode generator, first the field patterns radiated from the launcher have been measured after the quasi-elliptical mirror at the position of the second mirror. The results have been compared with the calculated values using the FZK scalar diffraction interpret code. In addition they have been taken to design the second and third mirrors. The results are shown in the Fig. 7.

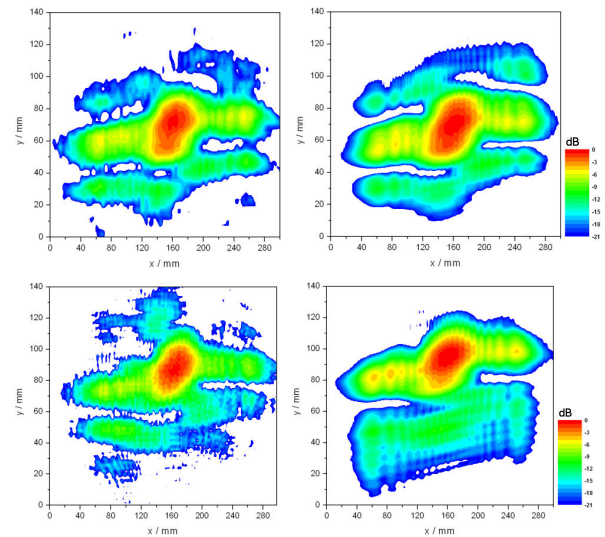


Figure 7. The field radiated from the launcher at the position of the second mirror: measurement (left) and calculation (right) at 170.3 GHz (upper row) and 171.92 GHz (bottom row)

Fig. 8 shows measured and calculated field distributions of the RF output beam in different planes. The gyrotron window is placed 350 mm from the gyrotron axis. The agreement between experimental results and calculations is good. The reason for the small differences is seen both in the approximation of the mathematical modeling of the launcher and mirrors and in experimental errors. The conversion of such a complex cavity mode requires an accurate modeling of the diffraction effect at the launcher cut. In addition, the precise fabrication of the components with the complicated surface structure is a great challenge. The main goal of the design of the quasi optical system was to obtain a field distribution with high Gaussian amplitude content on the gyrotron window plane. The results have shown that such an amplitude condition without the flat phase can be realized only in single planes. The field patterns are changing very quickly depending on the position. For example at 50mm behind the window the amplitude distribution has a power minimum of -12 dB in the middle (Fig.8). The general reason for this is the fact that the gyrotron window is located near the beam waist in the near field area of the system. Therefore all results can be extremely

sensitive to any variation of the beam features, e.g. due to insufficient accuracy of components fabrication.

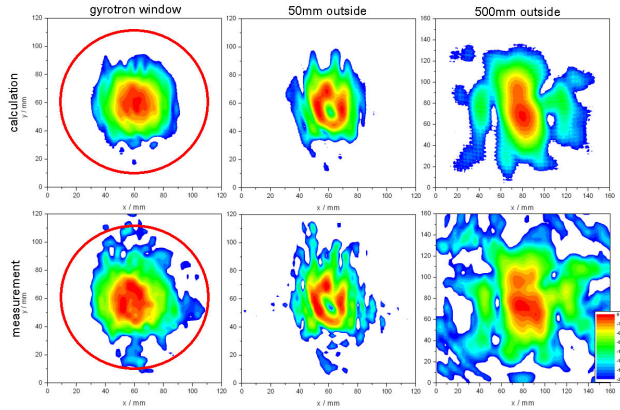


Figure 8. Distribution of the RF output beam at three planes outside the gyrotron. Upper row: results of calculations; lower row: results of measurements performed with the third $TE_{34,19}$ -mode generator at 170.3 GHz. The window aperture (96 mm diameter) is indicated

IV. OUTLOOK AND CONCLUSIONS

The design of the q. o. RF output system for the first prototype of the European 2 MW, CW coaxial gyrotron for ITER has been successfully validated in low power measurements. Three different mode generator cavities have been manufactured and used for performing the cold tests. With the third mode cavity the $TE_{34,19}$ mode has been excited

with excellent mode purity. Using this mode generator very good agreement between experiment and design calculations has been obtained. This confirms both the design calculations and the manufacturing quality of the launcher and mirrors.

A further improvement of the quality of the RF output beam requires a better launcher and a better modeling of the launcher which allows to increase the Gaussian mode content radiated from the launcher cut and which take diffraction effects into account. Due to this an increase in the Gaussian mode content of the RF output beam as well a significant reduction of the stray radiation losses in the mirror box is expected [3].

V. REFERENCES

- [1] B. Piosczyk, et al., "170 GHz, 2 MW Coaxial Cavity Gyrotron – experimental verification of the design", Proc. The Joint 30th Int. Conf. on Infrared and Millimeter Waves and 13th Int. Conf. On Terahertz Electronics, Williamsburg, USA, 2005, pp. 289-290.
- [2] T. Rzesnicki, et. al., "170 GHz, 2 MW Coaxial Cavity Gyrotron – design and experimental verification of the RF output system", Proc. 6th Int. Vacuum Electronics Conf., Noordwijk, The Netherlands, 2005, pp. 303-306.
- [3] J. Jin, et. al. "Investigation of an Advanced Quasi-Optical Mode Converter for a Coaxial Gyrotron", Proc. The Joint 30th Int. Conf. on Infrared and Millimeter Waves and 13th Int. Conf. On Terahertz Electronics", Williamsburg, USA, 2005, pp. 299-300.

Improving FMCW-based Object Tracking Using Phased Array Antennas Combined With Sigma-Point Kalman Filters

D. Mastela[†], L. Reindl^{*}, L. Wiebking[‡], T. Zander[†]

^{*}University of Freiburg, Department of Microsystems Engineering, Freiburg, Germany, reindl@imtek.de

[†]University of Freiburg, Department of Microsystems Engineering, Freiburg, Germany,
{[dariusz.mastela](mailto:dariusz.mastela@imtek.de)|[thomas.zander](mailto:thomas.zander@imtek.de)}.ext@siemens.com

[‡]Siemens AG, CT PS7, Munich, Germany, leif.wiebking@siemens.com

Abstract—Frequency modulated continuous wave (FMCW) radar techniques are methods of choice when it comes to localization-based applications in harsh (e.g. dusty, smoky) environments. In this paper, we propose a significant improvement to the current industry standard by replacing hardware and software components with advanced counterparts.

I. INTRODUCTION

An industry standard high-precision localization system is given by local positioning radar (LPR) [7]. This is the baseline setup we use for comparing purposes in this paper. LPR is designed to work based on a 5.8 GHz FMCW-radar in environments for which the following problems apply:

- combined outdoor/indoor tracking (e.g. fork lifters), so often no GPS signal available
- uncomfortable environment, especially dusty, dirty or foggy which makes usage of optical systems like lasers impossible
- high precision demands which can not be fulfilled by civil GPS receivers

Like GPS, it uses the exactly known information about the position of its beacons (transponders) to generate the position estimation. An object under observation is equipped with a “base station”, in fact an entire embedded system containing an antenna, an FMCW signal generator module and a signal processing hardware/software system. The base station broadcasts an FMCW signal and all available transponders respond to this signal via an own transmit channel to allow distinct identification of the transponder ID.

An omni-directional antenna, mounted onto the tracked object, emits upsweep and downsweep microwave chirps. The echoes of all contributing transponders are processed within the frequency domain (FFT) and the radar Doppler equations,

$$\begin{aligned}\Delta f_{up} &= \frac{8Bd}{cT} - f_0 \cdot \frac{v}{c} \\ \Delta f_{down} &= \frac{8Bd}{cT} + f_0 \cdot \frac{v}{c}\end{aligned}\quad (1)$$

where B = denotes the bandwidth, T = sample period, d = object to transponder distance, v = object to transponder speed and c = speed of light. A special derivative of

a sequential extended Kalman filter (EKF) in round-robin scheduling calculates an estimation of the object’s location. This setup uses kinematic and observation models within the EKF algorithm which combines observations (measurements) with prior state estimations to aim towards best-guess overall system state estimation. The initial position setup is obtained by multilateration numerics. In a perfect environment with no reflections and distortions, LPR’s resolution is within ten centimeter range.

This paper will give a detailed theoretical explanation why this setup is not sufficiently suitable to fulfill high-accuracy requirements and present an approach to overcome some of the limitations. This is done by applying two changes to the system. We will use a custom-design antenna array to reduce common multi-path errors which leads to a more stable signal availability. Furthermore, we will demonstrate situations of significant improvement of system state estimation by replacing the original sequential EKF algorithm by a generic sigma-point Kalman-filter SPKF engine. This paper focuses on a two-dimensional coordinate plane, however there is no doubt that these improvements would be found in a three-dimensional test setup as well.

II. IMPROVING THE ANTENNA

For localization based on the outlined concept it is essential that the antenna is able to receive the transponder signal from any direction. If its characteristics violently prefers a certain direction, chances are high that position calculation accuracy degrades because many measurements from a certain direction can not be incorporated into the filter algorithm, thus reducing the absolute number of usable samples per cycle. Because of this, usually omni-directional antennas are used which aim towards minimization of direction preference. These antennas are common industry standard and well-understood developments. But in fact the transponder echo concept raises another problem when it comes to localization, especially in indoor setups. It is necessary to have a direct line-of-sight configuration for as many transponders as possible in order to get an accurate position estimation.

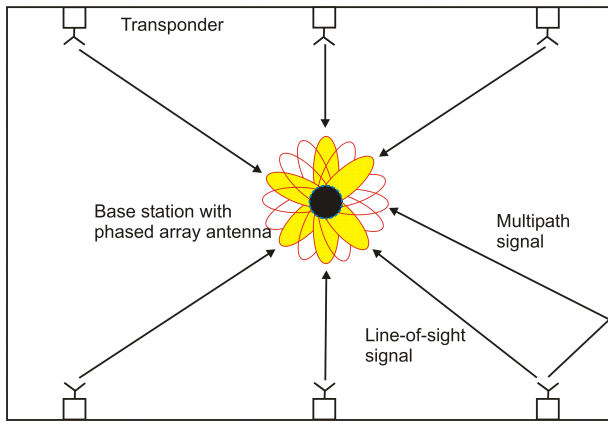


Fig. 1. Typical indoor scenario for localization. The base station can not distinguish between a multi-path signal's pathways.

In figure 1 this situation is illustrated. In case the walls don't absorb too much of the signal power, it's practically impossible to tell the difference between the line-of-sight signal and its reflected twins. As the result, reflected signals might erroneously be taken for the direct line-of-sight signal which would lead to a wrong position estimation.

To solve this dilemma, we present in [1] a solution based on an array of 16 patch antennas in a cylindrical topology (figure 2). Suitable control mechanisms allow to form 16 beams of which each one covers about 22.5 degrees in the (x, y) -plane and can uniquely be enabled or disabled. This antenna has proven to perform significantly better in experimental one-dimensional multi-path scenarios and is therefore our method of choice for the achieved improvement to FMCW-based two-dimensional tracking. Please refer to [1] for details about the antenna design.

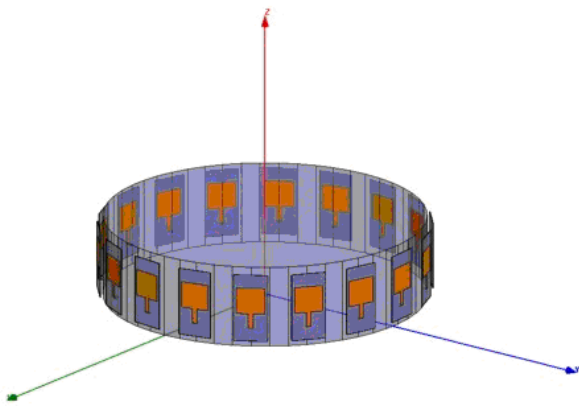


Fig. 2. Array of 16 uni-directional antennas, mounted on a cylindrical surface

III. REPLACING THE EKF BY SPKF

The EKF is an extension to the Kalman filter which uses Taylor approximation to overcome the classic limitation of acting as optimum minimum mean square error estimator (MMSEE) in the unlikely case that the entire state-space is purely linear. It uses exactly the same numerical framework as the Kalman filter, however for the calculation of the state covariance matrix, precision is mangled by first order linearisation.

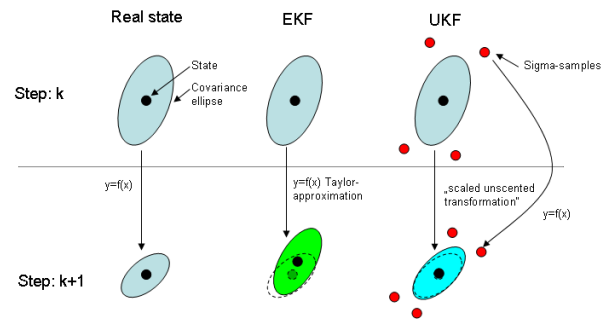


Fig. 3. Generation of prior state estimation and state covariance for EKF (approximation) and UKF (sigma point transformation)

Especially the state covariance estimation is known to degrade because of linearisation especially in highly non-linear processes. To improve tracking filter accuracy with non-linear state transfer functions $f(\cdot)$ and observation propagation functions $h(\cdot)$, a new approach of MMSEE has been under academic research for some time. This improvement, the class of *sigma-point Kalman filters* (SPKF) represents today's cutting edge MMSEE. The most significant difference is that it does no longer perform updates to the state covariance matrix based on a Taylor approximated state model, instead it applies a non-linear state transfer function to all distribution density-representative *sigma-points* and samples the state covariance from scratch. This scheme is known to model most processes perfectly to second order, for a pure spatial Gauss-Markov-process even to third order. The theoretical explanation is given in [3]. The sigma-point Kalman filter has already proven to perform more accurate than the industry's standard EKF in several research projects, for example in [4] and [5]. For the tracking filter toolkit *libtf*, which is in active development right now, a numerically efficient SPKF implementation, the *square root unscented Kalman filter* (SR-UKF) has been chosen. Probably the most interesting property of this filter is that it comes with no extra computational costs compared to the EKF. Usually we can expect a slightly larger memory footprint in real-world applications but today's computers shouldn't have a problem with that. However, still the industry is hesitating in replacing their EKF implementations by UKF derivatives, for the main reason that the actual implementation of an efficient SR-UKF is very complex if it needs to be done from scratch. With *libtf*, we will provide a toolkit which allows rapid deployment of native C/C++-applications, thus enabling relatively easy replacement of existing EKF algorithms by the superior SR-UKF. This is exactly what we have done for this experimental setup.

IV. EXPERIMENTAL SETUP AND MODELING

To verify the theoretical approach that the phased array antenna combined with the SPKF outperforms the standard omni-dimensional antenna, a difficult physical setup has been chosen. This tracking method has specific problems with metallic surfaces as they practically replicate identical "virtual" transponders. This introduces a significant difficulty to extract all necessary information from the spectrum to evaluate

the Doppler equations (1). The LPR system relies on an edge detection algorithm to browse the spectrum for valid transponders. The more multi-path artifacts are present, the lower the likelihood to locate the correct edges will be. The phased array antenna can efficiently eliminate nearly everything which is outside a beam's 22.5 degree lobe. Especially for object tracking close to corners this is a tremendous advantage.

Our setup consists of six transponders, two pairs of three in an almost equally spaced orientation. Within the covered area between these beacons, the object under observation with its base station is located and meant to describe an almost rectangular movement with one intermediate when switching from x-only-movement to y-only-movement and back. The room itself is highly contaminated with metallic objects such as columns, doors and partially the ground itself. For reliable results we slightly modified the origin LPR measurement principle. The base station with the antenna probe is moved to the next location manually and precisely before taking a measurement snapshot. Because of this, tracking is based on transponder-distance estimation entirely. The main reason for this is that LPR is already a mature and tightly integrated embedded system and applying all necessary changes to make it take control of the phased array antenna independently would have been far over the top for a proof-of-concept survey. Instead just the experiment is performed and the data processing can be done offline.

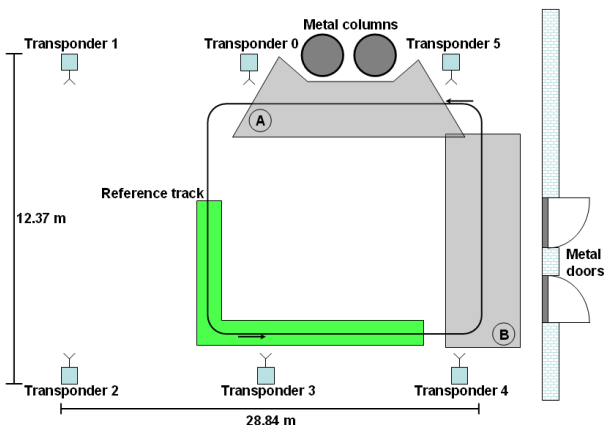


Fig. 4. Overview of the experimental scenario

The experiment is illustrated in figure 4. The transponder setup is shown as well as the reference track and the major obstacles. In the gray marked sector B we can expect multi-path distortion caused by the metal doors whereas in the gray range A the dominant error source is most likely the two large metal columns. In the green highlighted area a relatively clean signal from at least five transponders can be expected. The two filters are set up as follows:

- The genuine sequential LPR EKF which is stable, mature and has constantly been improved over the last years with all its additional features is used. It is a highly specialized derivative of standard EKF methods to address this specific application. It iterates over all non-gated transponders sequentially for the entire algorithm. The observation

noise covariance R in only a 2-by-2 matrix containing the variances for a transponder's distance and velocity measurements. This means it does not compute a minimum mean square error estimation among all available transponders, instead a least square solution to the error of a single transponder's distance/velocity observation vector is calculated. This may result in a better overall estimation if a small number of transponders is available after gating but can also decrease accuracy if many transponders contribute. We will recognize both effects later. It also includes a particularly smart observation distance pre-gating algorithm which calculates an "ellipse of trust" for any subsequent transponder measurement and omits distance estimations which reside outside this ellipse. A post-gating algorithm which ensures that the velocity resides in a reasonable range is applied as well. This gating scheme is also an adaptive algorithm which performs surprisingly well for most situations. Significant parts of this filter have been developed in [2].

- The SR-UKF is used "as is" with a very simple observation gating which simply drops a transponder distance value if its deviation from the observation estimation exceeds a certain threshold. This algorithm is not adaptive. Post-gating is not performed.

The gating criteria are necessary because signal multi-path is not a noise component. It is an annoying, destructive measurement influence which is more or less deterministic if it is possible to identify its sources. Unfortunately LPR is not able to do that and their peaks are far beyond measurement error modeling. Consequently, because MMSEE methods do not exclude parts of the observation vector completely because of an unexpected variance level, instead they *will* render the estimation useless if not gated, for both the EKF and the SPKF observation gating is a must.

The process model is quite simple and not bound to specific properties of this particular setup to maintain the same "general" setup as the commercial LPR version. For presented 2D-tracking based on a position/velocity vector, we use for the state transfer function $\hat{f}()$,

$$\begin{aligned} x'_k &= x_{k-1} + \dot{x}_{k-1} \cdot \Delta t \\ y'_k &= y_{k-1} + \dot{y}_{k-1} \cdot \Delta t \\ \dot{x}'_k &= \dot{x}_{k-1} \\ \dot{y}'_k &= \dot{y}_{k-1} \end{aligned}$$

where Δt is the cycle time to the next measurement, and the observation transfer function $h()$,

$$d'_{k,i} = \sqrt{(x'_k - t_{x,i})^2 + (y'_k - t_{y,i})^2 + (\Delta z_i)^2} \quad \forall i \quad (2)$$

where i denotes the set of transponders, d the measured distance, t the transponder's position with respect to the reference coordinate plane and Δz the height difference between the antenna and the transponder. The process noise is modeled as a standard piecewise white constant acceleration model. For

one coordinate, e.g. x this means,

$$Q_x = \begin{bmatrix} \frac{\Delta t^2}{2} & \Delta t \end{bmatrix}^T \cdot \begin{bmatrix} \frac{\Delta t^2}{2} & \Delta t \end{bmatrix} \cdot \sigma_{vx}^2 \quad (3)$$

where σ_{vx} reflects the acceleration-caused uncertainty of the velocity information, thus the entire process noise matrix defaults to:

$$Q = \begin{pmatrix} \frac{\Delta t^4}{4} & 0 & \frac{\Delta t^3}{2} & 0 \\ \frac{\Delta t^3}{2} & 0 & \Delta t^2 & 0 \\ 0 & \frac{\Delta t^4}{4} & 0 & \frac{\Delta t^3}{2} \\ 0 & \frac{\Delta t^3}{2} & 0 & \Delta t^2 \end{pmatrix} \quad (4)$$

This matrix is fed directly into the EKF initialization cycle whereas the UKF is initialized with the upper triangular Cholesky-factorization S_Q such that $Q = S_Q^T \cdot S_Q$.

The observation noise model for the SR-UKF is even more simple. Because in a real-world scenario it is usually not feasible to rely on coupled variances among different transponders, whereas for example in this particular experiment one might assume a strong relation between transponder number four and five, all transponders are assumed to have the same variance and no covariance to the others, hence the observation noise root is assumed to,

$$S_R = I \cdot \sigma_a \quad (5)$$

where I is the unit matrix and σ_a the absolute base station to transponder distance estimation uncertainty. Because transponder velocity measurements are not used in this experiment, they are not processed by the $h(\cdot)$ function thus not included in the S_R matrix.

V. ANALYSIS AND RESULTS

After obtaining all raw data measurements, it is interesting to benchmark the tracking filters with the omni-directional antenna because it can be expected that the SPKF shines with worse measurements. Figure 5 shows one loop of the experimental track filtered by the LPR EKF.

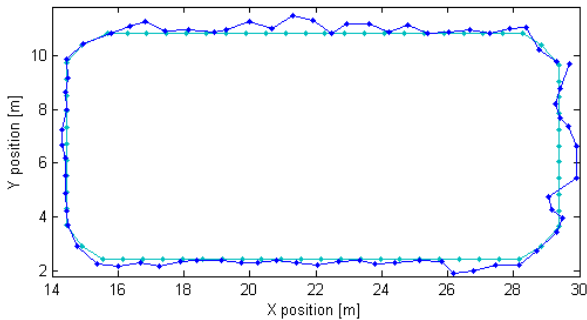


Fig. 5. The loop with the default LPR EKF

As expected, the sections A and B which are gray marked in figure 4 are critical to LPR's desired accuracy of 10cm to 20cm. Multi-path effects cause that many of these position estimations are based on only three to four transponders, and

very likely some of these measurements are not the direct line-of-sight signals. The entire region A ($y = 10.80m$, $x = 16m \dots 29m$) is over-dominated by the gating algorithm rather than the tracking filter. The UKF results (Figure 6) aren't any better; because of the simpler gating method partially even worse. The generic UKF's standard deviation is indeed 5cm higher than the LPR EKF's.

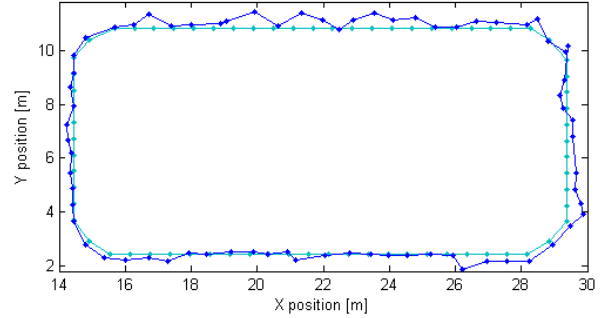


Fig. 6. The loop with the SR-UKF

Section B suffers from similar problems, but differently signed. The EKF is obviously much more susceptible to the metal doors. The reason for this effect is the aforementioned sequential method. The multi-path signals lie within the gating ellipse, so the distance values aren't dropped but they are actually no line-of-sight signals. Because the UKF calculates an error-minimal solution to the transponder distances among each other whereas the LPR EKF does not, instead it only relies on a transponder-to-next-transponder uncertainty, the generic UKF is far less sensitive to this problem. As a result, its estimated position curve matches the real position tighter, yielding a 4cm better standard deviation in this critical section.

In fact, the only part where we can truly compare the tracking filters is the green section of figure 4 because the gating allows virtually all transponder signals to pass through. So the UKF always gets a complete observation vector and the LPR EKF does not need to prematurely exit its iteration over all transponders. The result can be anticipated by visually comparing the lower left quadrant of the figures 5 and 6. There are only two situations in which the EKF is slightly more accurate; in the beginning of the green section ($x = 14.46m$, $y = 6.72m \dots 5.52m$) and one single sample at ($x = 20.96m$, $y = 2.43m$). The debug log file indicates that in all these cases no more than four transponder signal made it through gating. Consequently, UKF results are more accurate in this part of the track (table I).

The single bad sample at ($x = 20.96m$, $y = 2.43m$) is exceptionally worth mentioning. This is the only sample based on less than five transponders in the entire range ($y = 2.43m, x = 15.56m \dots 25.76m$), the only sample worse than EKF's estimation in this range and this x -position is exactly between the x -coordinates of the metal columns near the upper part of the track. At the very same x -position in section A the LPR EKF also yields its worst position estimation of the entire track. This is a very good example to demonstrate how

sensitive to multi-path effects the LPR system really is. As the result of the filter benchmarking using the omni-directional antenna it can be said that the overall performance of both filters covering the entire test track is nearly identical as the standard deviation difference is only $6mm$ as given in table I. However an important result is that as soon as the signal reception is good enough to process at least five of the six transponders, the generic SR-UKF is constantly superior to the genuine LPR EKF.

In the last setup the omni-directional antenna has been replaced by the custom phased array antenna which is described in detail in [1], combining both new developments.

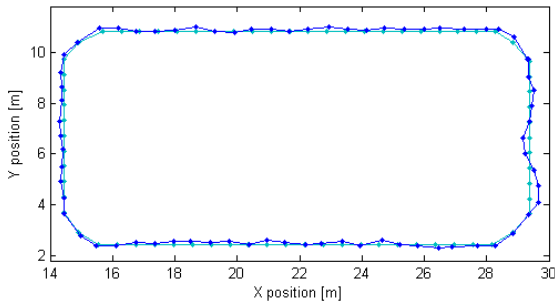


Fig. 7. The loop with the phased array, filtered by SR-UKF

The result is displayed in figure 7. It is clearly obvious that the phased array is significantly less susceptible to most multi-path effects. Although the log file shows that gating is still necessary for many samples, the antenna's narrow lobes ensure that the direct line-of-sight signals are recognized more often in the spectrum processing instead of multi-path signals which are only slightly off, so the absolute number of correct line-of-sight signals for Kalman-Filter processing is higher compared to the omni-directional antenna. The numeric result is revealed in table I. Especially in the strongly contaminated sections A and B the improvement is beyond bliss; the standard deviation is almost as good as the omni antenna's in the green section, even better than the genuine EKF's performance with the omni antenna in the green section; the overall position estimation is twice as accurate. The only significant multi-path sensitivity can be observed in close proximity to the metal doors ($x = 29.38m$, $y = 4.10m \dots 7.30m$) and even in this zone within section A the average deviation is almost $20cm$ better than with the omni-directional antenna. The visual also looks cleaner; it is less scattered and no spontaneous leaps are visible.

	LPR EKF	Generic UKF	
	Omni	Omni	Phased array
Section A	0.283	0.337	0.138
Section B	0.390	0.349	0.138
Green section	0.142	0.127	0.096
Overall	0.237	0.243	0.124

TABLE I

OMNI-DIRECTIONAL VS. PHASED ARRAY ANTENNA: POSITION ESTIMATION STANDARD DEVIATION, IN METERS

However multi-path effects are in fact still persistent and might influence the position estimation if they reside within the 22.5 degrees every patch antenna covers. So for example the aforementioned bad sample at ($x = 20.96m$, $y = 2.43m$) between the x -coordinates of the metal columns is still an issue. At this very position, again, two transponder signals are dropped by the gating because they are way off; obviously those two signals enclose a dominant multi-path signal within the 22.5 degrees lobe.

VI. CONCLUSIONS

The main error source for the FMCW-tracking system LPR is signal multi-path distortion, not a noisy signal which is the primary target for the class of MMSEE algorithms. As a result, even a less difficult but typical real-world LPR scenario involves situations in which the errors are close to deterministic but can not properly modeled and are beyond measurement variance; Because of this, there are situations like section A and B with the omni-directional antenna, in which additional helper algorithms like gating dominate the overall filter behavior so that in one situation the genuine LPR EKF performs better, in a different situation the generic UKF.

In this paper we have shown that, whenever a direct line-of-sight is given for all transponders, the generic UKF outperforms this highly specialized sequential EKF derivative developed for LPR because of its better mathematical accuracy and numerical covariance estimation. This is reflected by the constantly better filtering results in the green section. Furthermore, replacing the generic omni-directional antenna by the custom phased array antenna establishes a tremendous performance boost to the overall position estimation. In many cases, multi-path distortions are mitigated significantly in a way that in the end more direct line-of-sight signals are available for the actual position estimation. As the result, the proposed combination of the sigma-point Kalman filter with the phased array antenna outperforms the old configuration in every tested scenario.

REFERENCES

- [1] D. Mastela, L. Reindl, T. Zander, L. Wiebking, M. Kawalkiewicz: "Multipath mitigation through cylindrical microstrip phased array antenna", University of Freiburg, Department of Microsystems Engineering, 2006
- [2] D. Mastela: "Implementation of an extended Kalman filter in a local positioning radar system", Diploma thesis, Institute of Electrical Information Technology, TU Clausthal, 2003
- [3] Simon J. Julier, Jeffrey K. Uhlmann: A new extension of the Kalman Filter to nonlinear systems, Department of Engineering Science, The University of Oxford, 1997
- [4] Rudolph van der Merwe, Eric Wan: The square-root unscented Kalman filter for state and parameter estimation, OGI School of Science & Engineering, Oregon Health & Science University, 2001
- [5] Rudolph van der Merwe, Eric Wan: Sigma-Point Kalman Filters for integrated navigation, OGI School of Science & Engineering, Oregon Health & Science University, 2004
- [6] Mohinder S. Grewal, Lawrence R. Weill, Angus P. Andrews: Global Positioning Systems, Inertial Navigation and Integration, John Wiley and Sons, 2001, ISBN-0-471-20071-9
- [7] Leif Wiebking: Entwicklung eines zentimetergenauen mehrdimensionalen Nahbereichsnavigationssystems, Dissertation, Institute of Electrical Information Technology, TU Clausthal, 2003, ISBN 3-18-399408-9

Constraints for Radio based Quality Testing in Industrial Environments

Gerd Saala^{1,3}, Stephan Schulteis^{2,3}, Johann-Friedrich Luy^{1,3}, Werner Wiesbeck^{2,3}

¹DaimlerChrysler AG, RMI/DI, Wilhelm-Runge-Str. 11, 89081 Ulm, Germany, +49-731-505 2278, gerd.saala@daimlerchrysler.com

²University of Karlsruhe (TH), IHE, Engesserstr. 5, 76128 Karlsruhe, Germany, +49-721-608 7676, stephan.schulteis@ihe.uka.de

³Joint Research-Center on Reliability of Automotive Systems (ZAS), University of Karlsruhe (TH)

Abstract—Today’s cars are complex systems regarding built in electronics, especially radio based systems. Therefore it is no longer sufficient to perform only Electro Magnetic Compatibility (EMC)-testing during systems-development. Additional fast and accurate methods for quality-testing are needed in production. In this paper basic constraints of electromagnetic field distribution in non shielded areas are discussed.

I. INTRODUCTION

During the past years wireless communications and services gained great importance in all fields of everyday life. Especially in the automotive sector this enforced the number of radio based systems rising enormously. Beside e.g. radio-broadcasting-systems and GSM/UMTS-communication-systems there are comfort services like “Keyless-Go” and even security relevant systems like Adaptive-Cruise-Control (ACC). Hence today’s cars are complex systems regarding the built-in electronic components. With rising complexity testing of systems’ compatibility and functionality is not sufficient in development-phase only. Rather quality-testing has to be performed in production-phase for each manufactured car at the end of the production line. However measurement constraints in production-phase differ greatly from those of Electromagnetic-Compatibility-(EMC)-Testing during system-development.

The various wireless services implemented in today’s cars are spread over a large frequency range. Figure 1 shows some important services over frequency. Boundaries of the frequency scale are given by Long Wave (LW) radio broadcast beginning at 150 kHz at lower end and ACC-Radar at 77 GHz at the upper end. In between these boundaries some important, widespread communication services are located. Investigations in this work concentrate on MW and VHF radio broadcasting systems shown as gray columns in Fig. 1.

In contrast to EMC-testing there is no standardization available for quality-testing of radio based systems. Systems are fully integrated into the car in final production state. Many components are interconnected within the whole system, the car. These interconnections include e.g. wiring between antenna and radio tuner. Hence most of the components’ interfaces are not available directly. For testing of systems functionality it may not be sufficient to avoid dropping signal

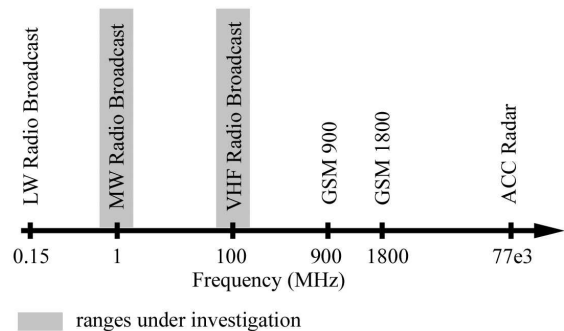


Fig. 1. Considered frequencies and services

levels due to failure of component’s interconnections like broken wires. Whereas the focus of EMC-tests is mainly on interferences between correctly working components during system development, in quality testing additionally side effects of improper assembly have to be considered. Examples of such side effects could be unwanted signal coupling between squeezed or strongly bent harnesses or interfering radiation at improper connections. This necessitates precise measurements. Due to inaccessible interfaces at built-in components, also capabilities of the tested components have to be used to measure e.g. attenuation of antenna paths or signal quality.

In this work some basic constraints for wireless testing of radio based systems are considered. The motivation and considerations about selection of the frequency ranges focused are given in section II. Simulations of the field distribution in a static testing scenario concerning influences of metal shielding walls are described in III. Based on simulation results possibilities to homogenize the field distribution are investigated in IV. These include proper selection of transmit antennas and applicability of RF-absorbers. Finally, measurements in an industrial environment are presented in section V. A conclusion of the results is given in VI.

II. BASIC CONSTRAINTS FOR TESTING OF RADIO-SYSTEMS

For wireless testing of radio based systems selection of the kind of testing area is greatly influenced by two constraints, the production flow and the behavior of the radio channel. Considering the production flow, strict timing constraints have to be fulfilled to fit in the quality tests. This leads to wireless testing of radio based components instead of contacting antennas directly e.g. using shielded couplers mounted on the antenna. In addition cost reasons induce measurements without complete shielding as in an anechoic chamber. A possible testing area with static Systems Under Test (SUT) is shown in Fig. 2. The cars 1 and 2 are the SUT, which are located at a fixed position during performed quality tests. Disturbing objects like other cars approaching from behind (e.g. cars 3 and 4), cars passing sidewise or men walking through the testing zone can appear in the proximity of the SUT. Hence field distribution in the radio link cannot be regarded as constant. Nevertheless variant influences have to be considered in measurements.

In recent years the time variant radio channel within buildings has been well investigated and characterized considering communications purposes as in [1]–[3]. In these fields also radio propagation in factory environment has been examined in measurements [4] and statistical modeling [5]. In contrast to characterization of a radio communication channel, in wireless quality testing it is not sufficient to know the statistical behavior of the radio-channel in general e.g. to calculate the link budget. For precise measurements of signal level and -quality the state of the radio-channel has to be known in time of the measurement. As basis for development of new methods for precise measurements, influences of the time variant industrial environment have to be analyzed. Investigations have to include detection and characterization of disturbances on the field distribution e.g. from moving objects. Therefore dependencies in location and time have to be considered.

For services at very low (LW radio broadcast) and very high (e.g. ACC) frequencies field distribution is expected to be less sensitive on environmental influences. This is because wireless tests of services at very low frequencies have to be based on either capacitive or inductive coupling in the close proximity of the car. At frequencies greater than 3 GHz free space propagation loss becomes large enough to reduce negative

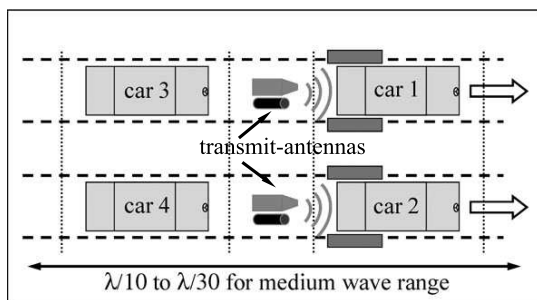


Fig. 2. Example of a testing area

influences due to reflections from moving objects close to the testing area. With short ranges and line of sight (LOS) between transmit-antennas and SUT fading due to multipath-propagation is also expected to have minor effects. In contrast propagation loss especially in MW and VHF range are low. Compared to very low frequencies working ranges in space are larger at MW and VHF. Thus moving objects like cars or even men beside the SUT are expected to have serious influences on behavior of the radio link. In this range the wavelengths are longer or in range of the dimensions of objects moving in the environment. Hence such obstacles have far greater influence on the electromagnetic field compared to ranges of higher frequencies. For GSM900 wavelength ($\lambda \approx 0.3$ m) is shorter than object's dimensions by a factor of about ten. Propagation loss may not be sufficient to suppress reflections and resulting interferences. Whereas much work is done for characterization of radio channels of wireless telephony systems, only few investigations can be found in literature in fields of radio broadcasting systems. Therefore investigations in this work concentrate on MW, VHF.

III. SIMULATIONS

To analyze influences of moving objects like other cars in the proximity of the test-area onto the field distribution a simple but typical test scenario is simulated. A main focus is also on the applicability of metal shielding walls. Simulations are done for frequency-bands of MW-radio-broadcasting-services (526.5 kHz - 1606.5 kHz, $\lambda = 186$ m to 570 m) and VHF-radio-broadcasting-services (87.5 MHz - 108 MHz, $\lambda \approx 3$ m). For electro-magnetic-field-calculations the Method of Moments (MoM) as a full wave solution is applied using the software-tool "EMSS FEKO", see [6].

Time variant scenarios have to be simulated due to moving objects within the area of consideration. Hence a parametric model of the static testing-configuration is created, see Fig. 3. The scenario contains a steady SUT ($x = -2.5$ m, ..., $+2.5$ m; $y = -0.95$ m, ..., 0.95 m; with a height of 1.5 m), a metallic cuboid as moving obstacle ($\Delta_x = 1.9$ m \times $\Delta_y = 5$ m \times $\Delta_z = 1.5$ m) and metallic shielding walls ($\Delta_y = 8$ m \times $\Delta_z = 3$ m) at $x = \pm 2$ m which can be switched on or off. The shielding walls are parallel to the SUT. In driving direction the shielding is assumed to be open to enable the car under test to leave the test stand without additional actions necessary. Realistic antennas are implemented as field source at (0 m, -2.8 m, 3 m) and receive antenna in the rear window of the car ($z = 1.2$ m). For time variant analysis multiple simulations are performed with different positions of the obstacle on each step. Hence the results do not show realistic dependencies in time but only in location.

Simulations are performed for single frequencies in MW and VHF band with an obstacle approaching from behind (distance $d = 7$ m, ..., 0.5 m) and thereafter from the side ($d = 5$ m, ..., 0.5 m to the shielding wall) of the SUT as depicted in Fig. 3 without shielding walls. Thereafter simulations are repeated with metallic shielding walls introduced into the scenario.

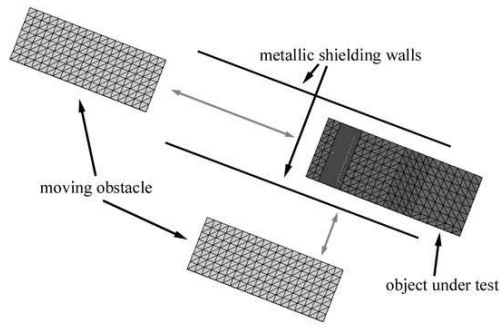


Fig. 3. FEKO simulation model

A. Simulation Results

To visualize the influence of changes in the scenario, the electric field strength is always compared to the case without any disturbing obstacles. The resulting ratio E_{Δ} of the electric field is given by

$$E_{\Delta} = 20 \log \frac{E_{\text{disturbed}}}{E_{\text{undisturbed}}} \quad (1)$$

with $E_{\text{disturbed}}$ the electric field with an obstacle present at the test area and $E_{\text{undisturbed}}$ the electric field with the SUT and no obstacle within the scenario.

Because of the long wavelength at MW-frequencies the exact position of an obstacle has minor influence on the field distribution compared to VHF. In VHF more explicit dependencies on distance and direction of the approaching obstacle occur. In Fig. 4 and 5 the resulting ratio of the electric field E_{Δ} is shown at $z = 1.2\text{m}$ for obstacles being very close to the SUT and metal shielding walls beside the test stand. In case of an approaching obstacle from the side, the metal shielding walls greatly reduce negative influences on the field distribution as shown in Fig. 4. For a car approaching from behind, see Fig. 5, a strong influence occurs. In this case the metal shielding acts like a wave guide. Due to strong interferences the disturbance is worse compared to the case without shielding walls.

The results for the obstacles further apart and those of simulations in the frequency range of MW show similar effects. Hence the benefit from reducing influences of sidewise moving objects could be canceled out by negative effects due to interferences caused by objects moving behind the SUT or in between the shielding walls. Thus statistical behavior of the field distribution cannot be reduced significantly using open metallic shielding.

IV. POSSIBILITIES TO HOMOGENIZE FIELD DISTRIBUTION

In addition to metallic shielding walls investigated in simulations, possibilities of transmit antennas and absorber materials to reduce negative influences are considered.

A. Selection of Transmit-Antennas

The pattern of transmit antennas determines the distribution of the radiated field in the testing environment. In directions of

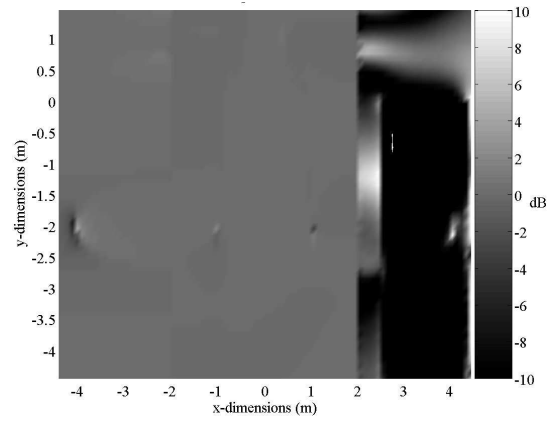


Fig. 4. Ratio of field strength (as in equation 1) at VHF range for a car approaching from the side and metallic shielding walls beside the SUT ($d = 0.5\text{ m}$ to shielding walls)

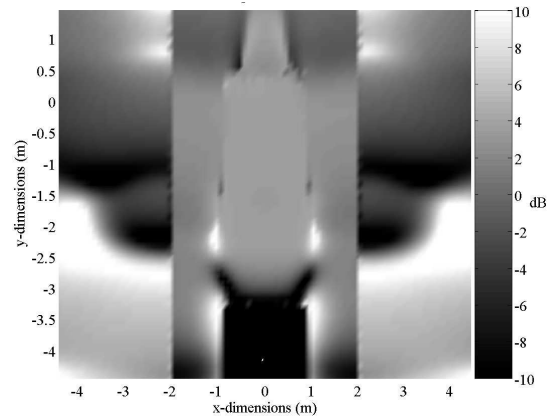


Fig. 5. Ratio of field strength (as in equation 1) at VHF range for a car approaching from behind ($d = 0.75\text{ m}$) and metallic shielding walls beside the SUT.

low field strength due to antenna characteristics no dominant reflections may be caused by obstacles. Therefore the choice of transmit antennas may also affect the dependency of field distribution on the variant test environment. Basically the electro magnetic field should be concentrated within the vicinity of the car under test. Therefore transmit antennas should have directivities as high as possible. In addition small antennas are needed because of space constraints. Due to a strong frequency dependence of antenna characteristics three basic frequency ranges have to be considered for antenna selection.

- At frequencies in the range of MW-radio-broadcast-services small antennas have low radiation efficiency and directivity can not be achieved. In most common MW-receivers the receive antenna consists of an electric field probe, which is small compared to the used wavelength, connected to a impedance transformer. Thus a small magnetic ferrite antenna would have to be applied close to the SUT or fed with high power due to its low radiation efficiency. For distances of a few meters it might be better to generate a quasi-static electric field to couple directly to the receiving field probe instead of radiating

an electromagnetic wave.

- At frequencies around 100 MHz it is possible to employ efficiently radiating antennas. However due to space limitations it is still not possible to use directive antennas to reduce environmental influences. Thus a common dipole should be used
- For GSM900 and services with higher frequencies the use of directive antennas is possible. At 900 MHz spacing constraints still have to be considered. Thus benefits of small antenna arrays and broadband antennas have to be compared. In cases where multiple frequencies have to be used broadband antennas like logarithmic periodic antennas are well suited. They have moderate directivity and a high number of different antennas is avoided.

B. Applicability of Shielding- and Absorber-Materials

For MW and VHF ranges no directive antennas are applicable. Hence capabilities of absorber materials are regarded especially for these ranges. To keep the possibility of performing tests for different services and frequencies in the same testing area, absorbers and shielding should not degrade performance on field distribution outside their working frequency range. Available absorber materials cover ferrite tiles, pyramidal absorbers and several flat broadband absorbers like graphite loaded silicone absorber.

Pyramidal absorbers have very high attenuations up to 30 dB. The height of pyramidal absorbers is a quarter wavelength in their working ranges. For VHF range the height is greater than 1 m and the weight of one pyramid reaches up to 20 kg [7]. An alternative to pyramidal absorbers are ferrite tiles. Their working range starts at about 30 MHz and attenuation is up to 30 dB and better than 10 dB over a large bandwidth (up to 2 GHz). The tails have a weight of about 30 kg/m² and have to be glued onto a metal ground [8]. This leads to serious degradation of the field distribution for lower frequencies. Other low-profile absorbers like absorber-foams have working frequency ranges starting at about 1 to 5 GHz [9]. Additionally most absorbers have far degraded attenuation for waves not impinging perpendicular to the absorbers ground plane, like reflections from a car approaching from behind the car under test. The needed metal ground plain would seriously degrade the performance of tests for frequencies outside the working range of the absorber.

Hence there are no well suited RF-absorbers available for the scenario depicted.

V. MEASUREMENTS OF FIELD DISTRIBUTION

Compared to generation of a constant field distribution by shielding, another possibility to deal with statistical behavior of the electromagnetic field is to consider fluctuations within the measurement. Therefore changes of the field distribution have to be known either deterministically or statistically. To measure field-strength at the receive antenna deterministically it is possible to reconstruct the current distribution either on or around the receive antenna. Known methods for reconstruction

of field and current distributions are tomographic back projection like in [11] and back propagation of electromagnetic fields as in [10]. In both approaches mentioned before the electromagnetic field has to be scanned precisely. Therefore measurements either take a long time or large arrays of well decoupled measurement probes are needed. These requirements cannot be reached in fast measurements in an industrial environment.

Hence the field strength at the receive antenna has to be described statistically. In recent years similar measurements for characterization of the radio channel regard general quality of reception in outdoor [17] and indoor [2] environment. Additionally man made noise is influencing the behavior of the radio channel [12]. The measurements described here focus on possibilities to analyze the current behavior of the radio channel in time and location. For this purpose a two-channel VHF measurement system [13] is used. It is based on two common car radio receivers, which are adapted to the needs of the measurements. The signal-level and coded stereo-baseband-signal (MPX-signal) is available to be sampled with high sampling rates using a data-acquisition-card [15]. In the described measurements raw signals are sampled with a rate of 200 kHz. The system is calibrated using a RF-signal generator [16]. The same signal generator is then used as source for the locally transmitted signal at 100 MHz. The standard deviation of the raw signal levels during calibration is well below 0.5 dB for the whole range of signal levels received during the measurements. As receive antennas calibrated biconical antennas [14] are used.

In Fig. 6 the fading of the signal levels of both channels are shown under different conditions. In order to suppress the fast fading the raw sampled signals are averaged (lowpass filtered) in blocks of 10000 samples ($\tau = 50$ ms). The values of the zero mean fading $Y_{zmf,i}$ at antenna i are given by

$$Y_{zmf,i}(n) = Y_i(n) - \bar{Y}_i \quad (2)$$

with the current absolute signal level $Y_i(n)$ at antenna i . There are three cases shown in Fig. 6. Whereas antenna B has a fixed position for all measurements, antenna A is moved away from antenna B to distances $d = [1 \text{ m}; 1.6 \text{ m}; 360 \text{ m}]$ in parallel to the drive way beside the antennas. All antennas are polarized horizontally. The undisturbed measurement without moving obstacles occurred, shows a flat signal level. In the second measurement a vehicle passed by the antennas with a velocity of about $10 \frac{\text{km}}{\text{h}}$. The minimum distance to the receive antennas was about 1.5 m. During the third measurement a car was shunting slowly in a distance of about 1 m to 3 m from antenna B (4.6 m to 7.6 m from antenna A).

With disturbances the signal level is seriously fading even for larger distances of the passing vehicle at the beginning and the end of the second measurement. In principal the receive level can change more than 10 dB within a few seconds. To analyze the similarities between the two receive channels in detail the block by block crosscorrelation of both signals is calculated. The values are correlated in blocks of 40 samples,

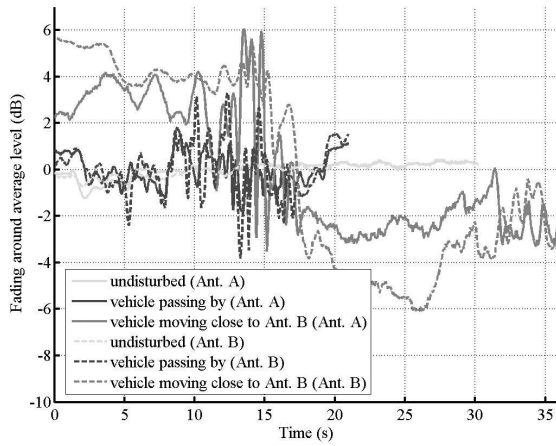


Fig. 6. Zero mean fading (see (2)) of signal-level under different conditions

see (3).

$$\rho_{AB}(n) = \frac{E \left\{ \left(\vec{S}_A - \bar{S}_A \right) \left(\vec{S}_B - \bar{S}_B \right) \right\}}{\sqrt{E \left\{ \left(\vec{S}_A - \bar{S}_A \right)^2 \right\}} \sqrt{E \left\{ \left(\vec{S}_B - \bar{S}_B \right)^2 \right\}}} \quad (3)$$

with \bar{S}_i the average of vector \vec{S}_i for the intervals

$$\vec{S}_i = \left[Y_i \left(n - \frac{BS}{2} \right), \dots, Y_i \left(n + \frac{BS}{2} \right) \right], \{n \in Z\}$$

with the absolute signal level Y_i at antenna i , the block-size $BS = 40$ and $Y_i(n) = 0$ for $n < 1$ and $n > n_{max}$.

Comparing the crosscorrelation of the three measurements in Fig. 7, it is noticeable that a switching of the correlation coefficient occurs in regular intervals for continuously moving vehicles (case 2 and at the end of case 3). Hence a detection and characterization of several disturbances of the field distribution might be possible. This may be useful to monitor changes of the field distribution or its statistic e.g. using a reference antenna close to the SUT.

VI. CONCLUSION

Basic constraints for wireless testing in production facilities have been discussed. It is shown that a variant environment has serious influence on electromagnetic field distribution. Further it is not possible to avoid statistical behavior in a testing area which is not shielded completely. Statistics are changing due to moving obstacles. Hence changes may be tracked during measurements for higher accuracy. Possibilities to identify and characterize typical disturbances of field distribution are subject of further investigations.

REFERENCES

[1] H. Hashemi, *The Indoor Radio Propagation Channel*, In Proceedings of the IEEE, Vol. 81, NO. 7, pp. 943-968, July 1993.
 [2] R. Schramm, *DVB-T Indoor Messungen in Berlin Parameter des Übertragungskanal Sender-Empfänger*, Technische Blaue Berichte Nr. 184, Institut für Rundfunktechnik GmbH, München, Okt. 2003. [Online]. Available: <http://www.irt.de/IRT/publikationen/BlaueBerichte/Blaue%20%20Bericht%20184%20Schramm-einseitig%20Okt.pdf>.

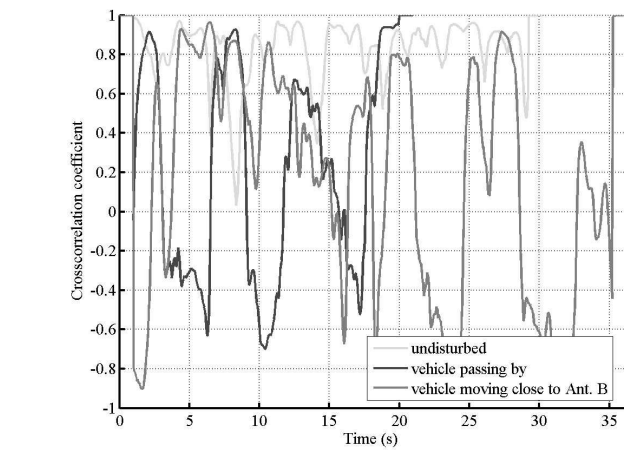


Fig. 7. Crosscorrelation of receive levels from antenna A and antenna B under different conditions

[3] P. Preiner, R. Überbacher, A. Kaczmarczyk, and G. Neubauer, *Evaluation of Elektromagnetic Field Distributions near Mobile Communication Base Stations - Creating a MATRIX of field distributions according to different scenarios*, ARC Seibersdorf Research GmbH - Information Technologies for Safety and Communications, Aug. 2003. [Online]. Available: <http://www.cost281.org/download.php?fid=409> (Jan. 2006).
 [4] T. S. Rappaport and C. D. McGillem, *UHF Fading in Factories*, IEEE Journal on Selected Areas in Communications, Vol. 7, NO. 1, pp. 40-48, Jan. 1989.
 [5] P. Yegani, and C. D. McGillem, *A Statistical Model for Factory Radio Channel*, In IEEE Transactions on Communications, Vol. 39, NO. 10, pp. 1445-1453, Oct. 1991.
 [6] FEKO <http://www.feko.info>, 2004.
 [7] *Datasheet - C-RAM SFC Pyramiden Absorber*, Emc-Technik & Consulting GmbH, Emilienstr. 35, 70563 Stuttgart, Germany, <http://www.emc-technik.de>, 2005.
 [8] *Datasheet - C-RAM FT Ferritfliesen Absorber*, Emc-Technik & Consulting GmbH, Emilienstr. 35, 70563 Stuttgart, Germany, <http://www.emc-technik.de>, 2005.
 [9] *Datasheet - ECCOSORB AN*, Emerson & Cuming Microwave Products, 28 York Avenue, Randolph, MA 02368, <http://www.eccosorb.com>, 2005.
 [10] K. Persson, and M. Gustavsson, *Reconstruction of Equivalent Currents using a Near-Field Data Transformation - with Radome Applications*, Progress In Electromagnetics Research, Pier 54, pp. 179-198, 2005.
 [11] C. Fischer, *Multistatisches Radar zur Lokalisierung von Objekten im Boden*, Chapter 6, Universität Karlsruhe, Fak. f. Elektrotechnik und Informationstechnik. Diss. v. 14.07.2003.
 [12] R. Achatz, and R. Dalke, *Man-made Noise Power Measurements at VHF and UHF Frequencies*, NTIA Report 02-290, U.S. Department of Commerce, Dec. 2001. [Online]. Available: <http://www.its.bldrdoc.gov/pub/ntia-rpt/02-390.pdf> (Feb. 2006).
 [13] S. Schulteis, C. Waldschmidt, W. Sörgel, and W. Wiesbeck, *Measurement Techniques for Diversity and MIMO Antenna Qualification*, Proceedings of the International Conference on Electromagnetics in Advanced Applications, pp. 167-170, Torino, Italy, Sept. 12-16 2005.
 [14] *Datasheet to Schwarzbeck Balun VHA 9103 with biconical Elements BBVK 9138*, Schwarzbeck Mess-Elektronik, An der Klinge 29, D-69250 Schönau, Tel.: +49 6228 1001, [Online]. Available: <http://www.schwarzbeck.de/Datenblatt/91039138.pdf> (Jan. 2006).
 [15] *Datasheet S Series Multifunction DAQ NI 6115 PCI*, National Instruments, 2005. [Online]. Available: http://www.ni.com/pdf/products/us/4daqsc197-198_ETC_212-213.pdf (Jan. 2006).
 [16] *Datasheet Agilent ESG-A and ESG-D Signal Generators (ESG-D E4433B)*, Agilent Technologies, Nov. 2005. [Online]. Available: <http://cp.literature.agilent.com/litweb/pdf/5989-4074EN.pdf> (Jan. 2006).
 [17] M. Nishi, A. Okinaka, K. Takata, and T. Yoshida, *Measurements of UHF Band Radio Propagation in mobile outdoor Environments by use of existent TV broadcasting Waves*, IEEE Antennas and Propagation Society International Symposium, Vol. 1, pp. 252 - 255 vol.1, 16-21 June 2002.

Tunable Microwave Transmission through a Periodically Corrugated Waveguide

Victor Pogrebnyak, Eser Akray, Neşet Küçükaltun

Department of Electrical and Electronics Engineering, Faculty of Engineering and Architecture,
Çukurova University, Adana 01130, TURKEY, 90 (322) 3386868, vpog@cu.edu.tr, e_akray@yahoo.com,
nkucukaltun@yahoo.com

Measurements show that transmission through the periodically corrugated waveguide varies from zero to a maximum value upon a shift of one periodic plate with respect to another on the half period of corrugation. The experiments demonstrate that the waveguide can be used to control transmission of microwave radiation.

Keywords - periodic waveguide; stop band; tunability.

I. INTRODUCTION

The main physical phenomenon caused by periodicity is Bragg reflection. It results in the opening of the forbidden gap in the spectrum of the periodic structure. The Bragg reflection occurs both in the case of unbounded periodic medium as well as in a case of a bounded periodic structure like a periodic waveguide. However, in the waveguide geometry dispersions become more complex due to their folding and crossing. As a result, besides Bragg reflections there arise non-Bragg reflections in the periodic waveguide. The spectrum of a planar waveguide acquires qualitatively new, and very promising from practical point of view, features if the periodicity is introduced into the waveguide by the lateral modulation. In the latter case the transmission properties become controllable due to opportunity to change the lateral modulation profile. For example, gaps can be tuned by means of shifting of periodic boundaries [1, 2].

In [2], it was shown that the relative shift of two periodic plates in the waveguide causes transformation of the band-structure spectrum to the gapless one. In the last case a wave propagates in the periodic waveguide without the Bragg reflection. Here we are reporting on the experimental observation of this phenomenon at a microwave range of wavelengths.

II. EXPERIMENTAL RESULTS

We measured the transmission properties of a planar waveguide, made of two metal plates having the identical sinusoidal profile $y(x) = \xi \cos(qx)$. Where $q = 2\pi/a$; ξ and a are the amplitude and the period of the corrugations, equal correspondingly to 0.415 cm and 3.15 cm

in our experiment. The preliminary calibration measurement showed that the number of periods for optimal observation of the Bragg reflection ranges between 18 and 25. The upper plate could slide with respect to the lower forming the phase shift θ between the plates.

A standard microwave setup with three horn antennas was used for measuring of transmission characteristics of the periodic waveguide at a frequency range 8-12 GHz. We investigated propagation of the TE wave, having the polarization vector E parallel to the grooves of the corrugation.

Location of a gap, f_g , in the waveguide frequency spectrum and its width, δf_g , could be tuned by changing a waveguide thickness d and phase shift between plates in accordance with formulas given in [1,2]. At some of waveguide thickness, f_g can coincide with one of the cutoff frequencies f_{0p} , where $f_{0p} = (c/2d)p$, c is speed of light, p is the mode index ($p = 1, 2, 3, \dots$). In this geometric resonance case the cutoff frequency splits into two values, separated by the forbidden gap δf_g . We investigated the propagation of the third mode of the waveguide. Corresponding to this mode resonant thickness can be found from the formula [3]

$$d_r = \frac{a_r}{2} \sqrt{p^2 - m^2} \quad (1)$$

For $p = 3$, the geometric resonance occurs at $d_r = 4.49$ cm and $m = 1$. The cutoff frequency splits into two values

$$f_{31}^{\pm} = \left[1 \pm \frac{\sqrt{2}}{3} \frac{\xi}{d_r} (1 - \cos \theta)^{1/2} \right] f_{03} \quad (2)$$

where f_{03} is the cutoff frequency of the third mode for the smooth waveguide; for the thickness given in Eq. (2), $f_{03} = 10.02$ GHz. A value of the gap, $\delta f_g = f_{31}^+ - f_{31}^-$,

depends on the phase shift θ between the plates. In a case of the symmetrical waveguide, $\theta = \pi$, Eq. (2) gives $f_{31}^+ = 10.63$ GHz and $f_{31}^- = 9.40$ GHz, with a gap $\delta f_{31} = 1.23$ GHz. If $\theta = 0$ (asymmetric waveguide), the gap vanishes. Fig. 1 shows the measured transmission properties of the waveguide for these two cases.

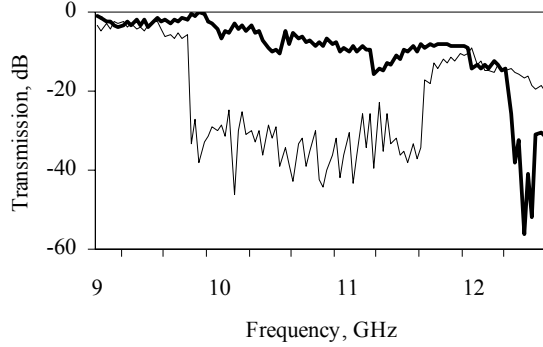


Fig.1. Measured transmission characteristics for the periodically corrugated waveguide in two cases: the thick solid line (curve 1) for the asymmetric waveguide, $\theta = 0$; and thin solid line (curve 2) for the symmetric waveguide, $\theta = \pi$.

The symmetric waveguide, $\theta = \pi$, yielded the band gap 1.24 GHz (curve2), close to the theoretical value 1.23 GHz. This band gap vanished upon a shift of the upper plate by π (curve1); a wave propagates without reflections. The dependence of the transmission on the phase shift is plotted in Fig.2 for the selected from the band gap frequency of 10.42 GHz.

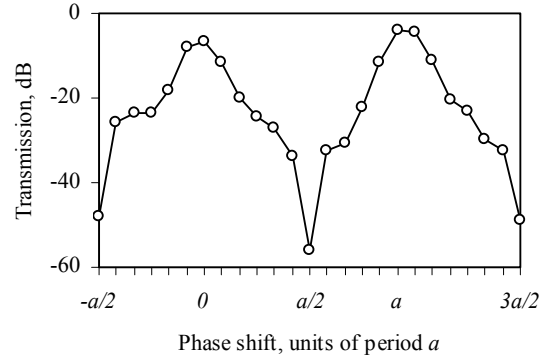


Fig. 2. The measured transmission through the corrugated waveguide at a fixed frequency of 10.42 GHz is plotted as a function of the phase shift θ between the plates.

These results are in a good agreement with Eq. (2) describing the controllable stop band in the spectrum for the periodically corrugated waveguide.

III. CONCLUSION

The wave transmission through a planar periodically corrugated waveguide was investigated theoretically and experimentally. The 1.24 GHz stop band was observed at the X-band of frequency. The width of the stop band could be controlled by changing the on the relative position of two corrugated plates. The transmission varies from zero to a maximum value upon shifting of one periodic plate with respect to another on the half period of the corrugation.

REFERENCES

- [1] V. A. Pogrebyak, "Geometric Resonance in a Periodic Waveguide", *Journal of Applied Physics*, vol. 94, no. 10, pp. 6979-6981, 2003.
- [2] V. A. Pogrebyak, "The Controllable Band Structure for a Periodic Quantum Well", *Physical Review B*, vol. 69, no. 24307, 2004.
- [3] V. A. Pogrebyak, "Non-Bragg Reflections in a Periodic Waveguide", *Optics Communication*, vol. 231, pp. 201-207, 2004.

A Novel 24 GHz 4-Quadrant Slot Antenna

Prodyut K. Talukder, F. J. Schmückle, and W. Heinrich

Ferdinand-Braun-Institut für Höchstfrequenztechnik (FBH), Gustav-Kirchhoff-Str. 4,
12489 Berlin, Germany, +49-30-6392-2628

Abstract—A slot antenna developed for near-range communications in the 24 GHz frequency range is presented. It is compatible with the common planar flip-chip type of integration and radiates laterally providing 90-degree coverage. The antenna consists of a resonant structure thus acting as a filter as well. Basic antenna design is explained and tolerances in practical realization are studied.

Keywords – Slot antenna, flip-chip, sector antenna, planar integration, resonant antenna.

I. INTRODUCTION

The concept of integrating the antenna with the RF front-end is attractive for various applications, particularly if miniaturization and low assembly cost are desirable. The classical solution is the patch antenna [1,2], but using a planar packaging approach it is always located at the top and lateral radiation is a problem. This is complemented by the slot antenna presented in this paper, which shows truly lateral radiation with about 90 degree of coverage, small form-factor, and is fully compatible with flip-chip packaging.

The primary idea is to combine a slot antenna with a parallel-plate cavity in order to build a resonant antenna [3,4]. The size is a bit more than half a wavelength. Using 4 sectors allows easy beam steering in the entire lateral plane. Employing bump and via fences facilitate cost-effective fabrication. The antenna cavity is excited by a current-driven bump. The design has to consider all necessary technological constraints as well as the electrical requirements. In the following, the development of this antenna is described, followed by simulation results obtained by means of em simulation (FDTD).

II. ANTENNA DESIGN

A. The Structure

The basic structure of the antenna is shown in Fig. 1. The antenna is built as a sandwich structure. It consists of two metalized planar substrates, flip-chip mounted face-to-face thus forming a parallel-plate resonator. This resonator is partitioned into 4 quadrants by bump fences. Below and above this sandwich structure arbitrary blocks with proper shielding (electric walls) are required to ensure appropriate beam forming. In reality, these blocks may contain other electronic modules or the battery, for instance. This allows to integrate an RF front-end together with a complete transceiver function into a cube of compact size.

A more detailed picture is given in Fig. 2, where one can see the lower half of the antenna with its layers in a hierarchical view. For the antenna substrates, backside-metalized Rogers 4003 material ($\epsilon_r = 3.38$) of 508 μm thickness is used. The slot metalization is 35 μm thick and the aperture height, i.e., the distance between the two metalizations of the parallel-plate wave guide, is 300 μm . The excitation bump is short-circuited on the top metalization and the current flows back over the bump fences.

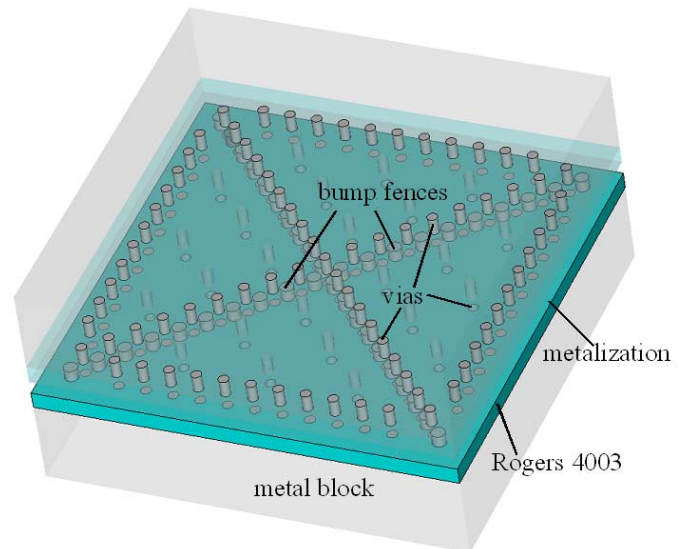


Fig. 1 : Basic structure of the antenna

The bump fences reflect the electromagnetic waves generated by the excitation bump in a way similar to a horn antenna and form an electrical separation between the 4 quadrants. They also have the function of mechanically connecting the upper and lower half of the resulting set-up. Within the upper and the lower substrate, via fences at the edges form an artificial shielding and prevent resonances in the substrate. For this purpose, some vias are distributed over each quadruple section (see Figs. 1 and 2).

B. Design Issues

The design was performed by means of electromagnetic simulation using CST MWS. The most essential specification for the antenna is that its resonant frequency should meet the center frequency of the ISM band at 24.1 GHz. The shape of the antenna lobe is not an equally important issue because the antenna is to be applied in near-range communications with comparatively low constraints on radiation pattern.

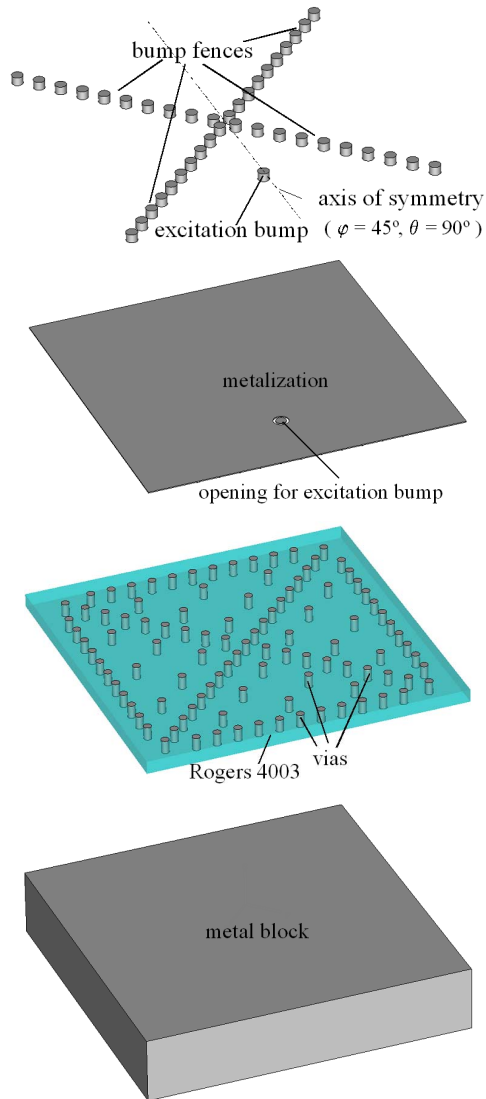


Fig. 2 : Detailed view of the lower symmetrical half of the antenna.

Moreover, the bump and via fences must have a certain density to make sure that there is only low coupling between the sections and that no resonances occur in the substrates, respectively. On the other hand, the distance between the bumps cannot be chosen arbitrarily small because picking and placing needs some space between the bumps. Similar restrictions hold for the minimum via pitch in the substrate.

The diameter of the excitation bump also affects the resulting center frequency of the antenna. Electromagnetic simula-

tion is necessary to check the structure for parasitic resonances and to optimize the layout.

III. RESULTS

In order to obtain comprehensive information on the antenna and to ensure optimum yield, not only the optimum dimensions were determined but also the influence of tolerances was studied.

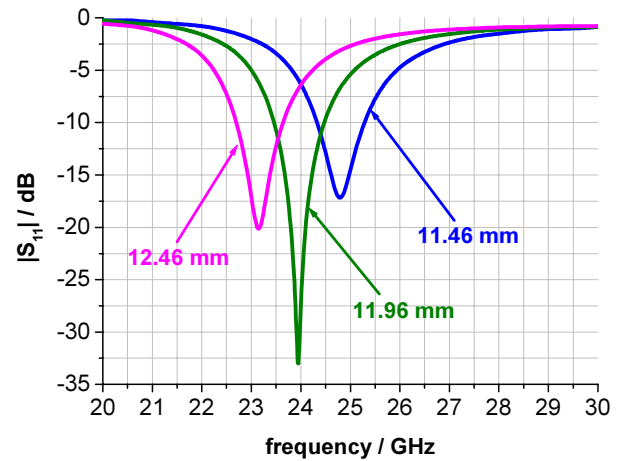


Fig. 3 : Influence of the outer dimensions on the resonant frequency: input reflection at the excitation port against frequency with the lateral substrate dimension as a parameter.

A first investigation dealt with the number of vias and bumps in the fences necessary to keep crosstalk sufficiently low. For very coarse fences, additional resonances occur due to the relatively strong coupling. Increasing the bump density, the desired single-resonance behavior is found but the value of the resonant frequency still changes because the resulting inductance of the bump fences varies. For our purposes, we find that 9..10 vias or bumps at each arm yield good results.

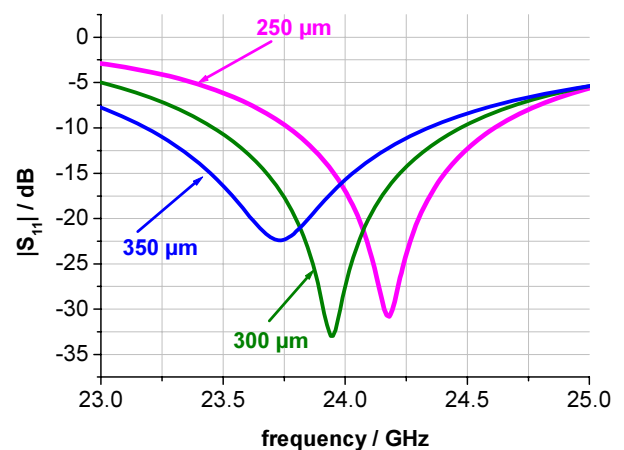


Fig. 4 : Effect of the aperture height (250...350 micrometers).

In the first step of antenna design itself, the outer dimensions of the antenna structure are to be defined to set the resonant frequency to the desired value. Fig. 3 shows the reflection at the excitation port of the antenna. For a center frequency of 24.1 GHz, an outside length of approximately 11.88 mm must be chosen.

The next important parameter to be checked is the height of the aperture, i.e., the distance between the two metal plates. The corresponding results are plotted in Fig. 4. As one can see this is a critical parameter, because a variation of 50 μm in either direction results in a 0.5 GHz shift.

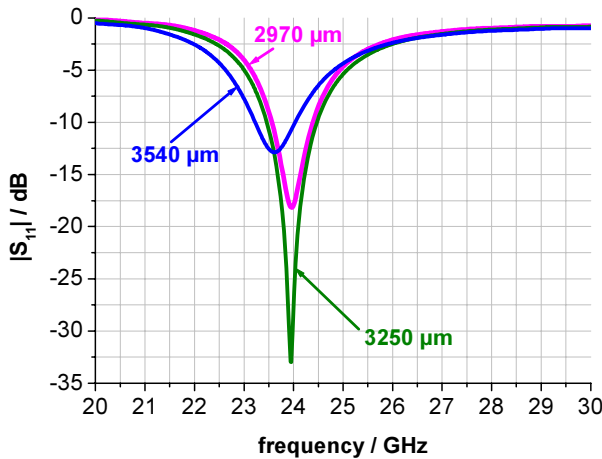


Fig. 5 : Influence of the excitation bump distance from antenna center on matching and resonant frequency.

The position of the excitation bump is important in order to achieve a good matching. Therefore, the bump was moved along the symmetry axis (Fig. 2) with various distances to the center point of the antenna as shown in Fig. 5. Two conclusions can be drawn from that figure. First, best matching occurs for a distance around 3250 μm . Second, shifting the bump causes also a shift in resonant frequency, with a strength depending on the actual position. Thus, the outer side length has to be adapted in order to fix the resonant frequency to the specified value.

A further parameter is the diameter of the excitation bump. The bonding process allows relatively large tolerances here (as for the other bumps). So, the ball with an initial diameter of 400 μm will vary its diameter after melting and bonding. The height, which is nominally 300 μm , can then vary between 250 μm and 350 μm . Considering that the volume is preserved during bonding and assuming a cylindrical shape after bonding this means that the diameter of the excitation bump may vary between some 340 μm and 420 μm . The curves in Fig. 6 indicate that this results in about 0.1 GHz shift. A diameter variation of the other bumps, i.e., those in the fences, shows an even less important influence.

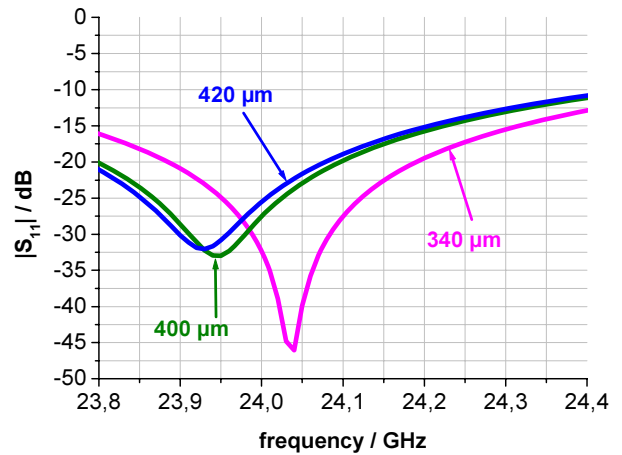


Fig. 6 : Influence of the diameter of the excitation bump on matching and resonant frequency.

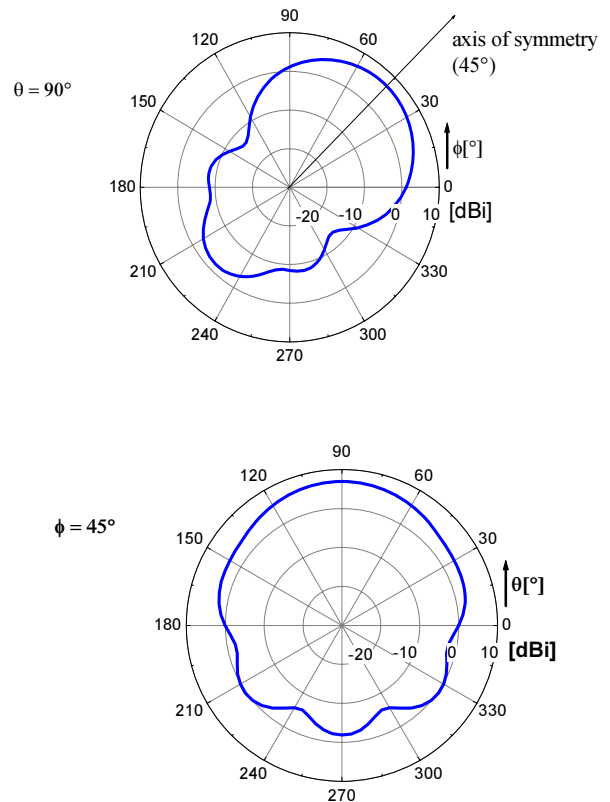


Fig. 7 : Radiation pattern of the slot antenna (antenna structure is rotated by 45°, for the axis of symmetry see Fig. 2).

The antenna is not optimized for a sharp main lobe with low side lobes as necessary in other cases. Because of the small outer dimensions of the antenna, its gain potential is limited. So the radiation pattern shows a comparatively wide main lobe.

However, the goal of having beam focusing in a 90 degree quadrant is fulfilled. Fig. 7 shows the radiation pattern. We find the main beam in the $\varphi = 45^\circ$ and $\theta = 90^\circ$ -direction along the symmetry axis (see Fig. 2). Fig. 8 adds a 3-D picture for the radiation pattern. The gain of the antenna is 6.8 dBi (in a loss-free system).

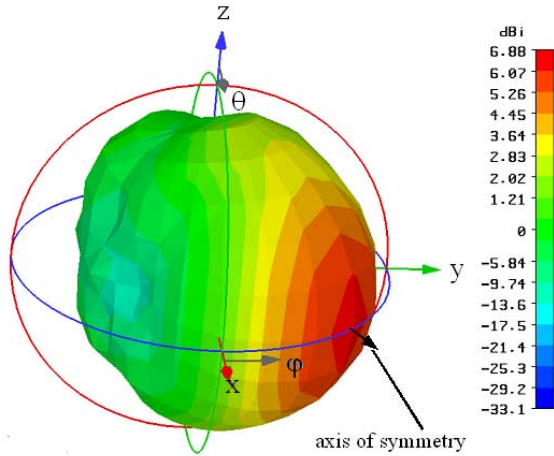


Fig. 8 : 3-D radiation pattern of the slot antenna.

IV. REALIZATION AND MEASUREMENTS

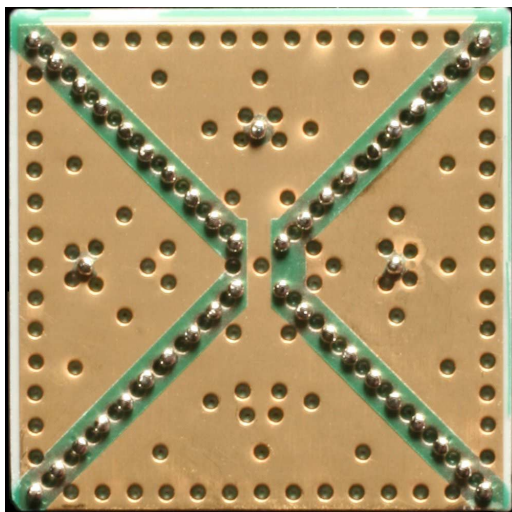


Fig. 9 : Photograph of the lower half of the antenna showing the via and bump fences as well as the excitation bumps (surrounded by additional fences of vias for lower coupling).

Various type of antennas have been realized and measured so far. An example of a realized antenna is shown in Fig. 9. The top photograph shows the lower half of a mounted antenna

with the via and bump fences and the excitation bumps. In this example, additional vias were placed around the excitation bumps in order to keep coupling effects into the substrate as low as possible.

Fig. 10 provides measurement data of the first realized antennas. Generally, the characteristics are in good agreement with the predicted ones (see Figs. 3,5). There is still a 1.5 GHz shift in resonant frequency, which needs to be removed by optimizing the mounting technology and adjusting the design.

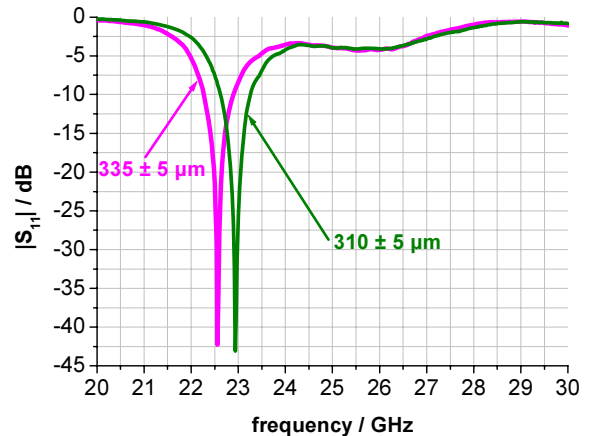


Fig. 10 : Measurements of the antenna for two different realized heights of the aperture.

V. CONCLUSION

A novel 24 GHz slot antenna is presented which radiates into 4 quadrants. It is compatible with planar integration technology. Due to the cavity-like effects of the structure the antenna acts as a filter as well. A patent was granted [4].

Acknowledgements

This work is funded by the German BMBF under contract 16SV1657. The authors gratefully thank Mr. Marko Neuner for fabricating the antenna samples and Mr. Steffen Schulz for performing the measurements.

REFERENCES

- [1] C.G. Christodoulou, P.F. Wahid, "Fundamentals of Antennas," SPIE Press, P.O.Box 10, Bellingham, Washington, USA.
- [2] C.A.Balanis, "Antenna Theory: Analysis and Design," New York, Wiley 1982, 1996.
- [3] C.Meliani, P. Talukder, J. Hilsenbeck, M. Huber, G. Böck and W. Heinrich, "Integrated Circuits and 3-D-Packaging for Low-Power 24 GHz Front End," Frequenz 3-4, 2004, Band 58, pp. 74-79.
- [4] German patent No. 10 2004 014 018 Mikrowellenantenne für in Flip-Chip-Technologie hergestellte Halbleiterbaugruppen.

Gyrotron Research at Forschungszentrum Karlsruhe

G. Dammert^{1a}, A. Arnold², D. Bariou³, E. Giguet³, R. Heidinger^{1b}, S. Illy^{1a}, J. Jin^{1a}, F. Legrand³, W. Leonhardt^{1a}, C. Lievin³, G. Neffe^{1a}, B. Piosczyk^{1a}, T. Rzesnicki^{1a}, M. Schmid^{1a,2}, M. Thumm^{1a,2}

¹Forschungszentrum Karlsruhe, Ass. EURATOM-FZK, ^aIHM, ^bIMF I, Hermann-von-Helmholtz-Platz 1, D-76344 Eggenstein-Leopoldshafen, Germany, +49 7247 82 4160, guenter.dammert@ihm.fzk.de

²Universität Karlsruhe, IHE, D-76128 Karlsruhe, Germany

³Thales Electron Devices, 2 Rue Latécoère, F-78141 Vélizy-Villacoublay, France

Short Abstract— One of the important heating schemes for fusion plasma devices is given by the electron-cyclotron-resonance-heating. This application, however, is limited to the lack of powerful sources operated at the appropriate frequency. At the Forschungszentrum Karlsruhe, a 1 MW, 140 GHz gyrotron for continuous wave operation has been developed for the ECRH system built up at the new stellarator facility in Greifswald / Germany. Due to the successful results with the prototype, seven 140 GHz CW gyrotrons were ordered. The first series tube was operated at the Forschungszentrum Karlsruhe. A power of 920 kW at an efficiency of 45 % (with energy recovery) could be obtained for pulse lengths of 180 s (limited by the available high-voltage power supply). A 30 minute pulse was performed with an output power of 570 kW. For the next fusion plasma device ITER, gyrotrons with higher output power of about 2 MW are desirable. In short-pulse experiments, the feasibility of coaxial-cavity gyrotrons with an output power up to 2 MW in continuous wave operation has been demonstrated and the information for a technical design has been obtained.

Keywords-components; gyrotron, coaxial cavity, quasi-optical system, diamond window, mode converter, depressed collector

I. INTRODUCTION

In next step thermonuclear fusion experiments, electron cyclotron wave (ECW) systems will be used for plasma heating and current drive. This strategy relies on millimeter-wave sources, that generate output powers in the Megawatt level in continuous wave (CW) operation.

For the stellarator W7-X now under construction at the Max-Planck-Institute for Plasma Physics in Greifswald (IPP), a power of 10 MW is needed for the electron-cyclotron-resonance-heating (ECRH) in CW operation. In a European collaboration between European research laboratories and European industry Thales Electron Device (TED) in France, conventional gyrotrons designed for an output power of 1 MW at 140 GHz have been developed. They are equipped with a single-stage depressed collector for increasing the efficiency and reducing the power loading, an advanced quasi-optical mode converter with minimized stray radiation inside the gyrotron, and a single-disk diamond window made by chemical vapor deposition (CVD-diamond) [1].

For the next fusion plasma device ITER, about 24 MW of ECRH (and electron-cyclotron-current-drive) at 170 GHz CW will be needed. Units with higher output power of about 2 MW will considerably reduce the cost for the ECRH.

An output power of 1-1.5 MW seems to be the limit for stable operation of conventional gyrotrons. Whereas those with coaxial cavities have the potential to fulfill the requirements for 2 MW output power. At the Forschungszentrum Karlsruhe, investigations on a short-pulse gyrotron with a coaxial cavity have been performed with the goal to demonstrate the feasibility and to provide all necessary information for a technical realization of a 2 MW, CW gyrotron at 170 GHz. Based on these results, an industrial prototype of a 2 MW, CW coaxial cavity gyrotron is under fabrication and a suitable test facility is under construction at CRPP Lausanne, Switzerland.

Fig. 1 shows a scheme of the 170 GHz pre-prototype gyrotron.

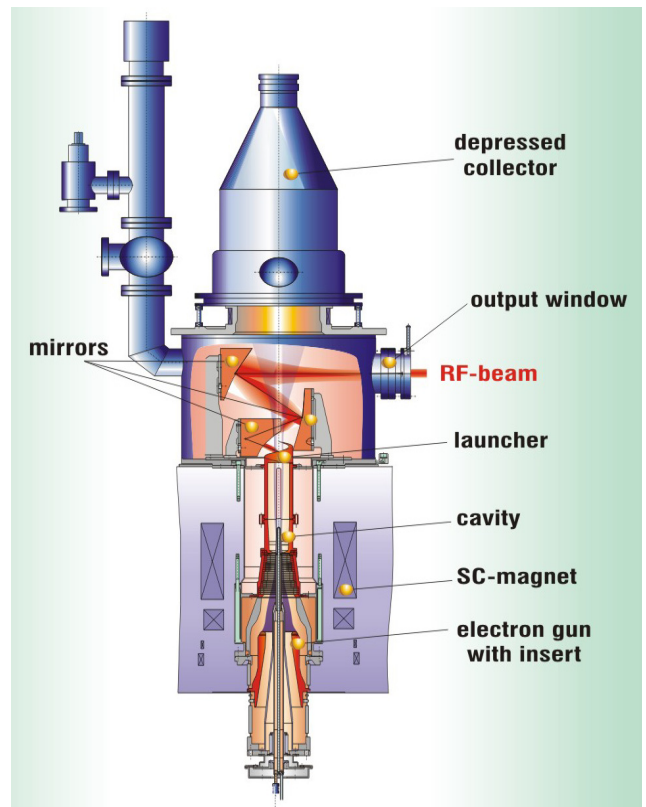


Figure 1. View of the 170 GHz pre-prototype gyrotron.

II. CONVENTIONAL GYROTRON

A. Design

The RF-cavity operates in the $TE_{28,8}$ mode. It is a standard cylindrical cavity with a linear input taper and a non-linear output taper. Special care has been taken for the design of the quasi-optical mode converter [2] to have very little amount of stray radiation. The radius of the antenna waveguide launcher is slightly uptapered towards the output by an angle of 4 mrad in order to avoid parasitic oscillation in this region. Due to the low fields along the edge of the helical cut, this advanced dimpled-wall launcher generates a well focused Gaussian-like field pattern with low diffraction. In combination with a three mirror system the desired Gaussian output beam pattern can be obtained.

TABLE I. PARAMETERS OF THE CONVENTIONAL GYROTRON

RF output power	1 MW
Accelerating voltage	81 kV
Beam current	40 A
Cavity mode	$TE_{28,8}$
Efficiency	45 %
Cavity radius	20.48 mm
Self consistent quality factor	1100
Cavity magnetic field	5.56 T
Launcher taper	0.004 rad
Launcher efficiency	98 %
Window aperture	88 mm

B. Experimental results: short pulse operation

The long-pulse results of the measurements on the pre-prototype and the prototype tube were reported in earlier publications [3]. With the prototype, two problems were faced. The specified output power of 1 MW has not completely achieved and the pulse length was limited to about 15 minutes even at reduced power of 534 kW. The reason for the limit in power is seen in a poor electron emitter quality (cathode) which leads to an inhomogeneous electron emission and thus to a poor beam quality. The limitation in pulse length was due to a pressure increase during the pulse which was caused by a temperature increase of the internal ion getter pumps. This temperature increase was proven by an infrared measurement after a long pulse [4].

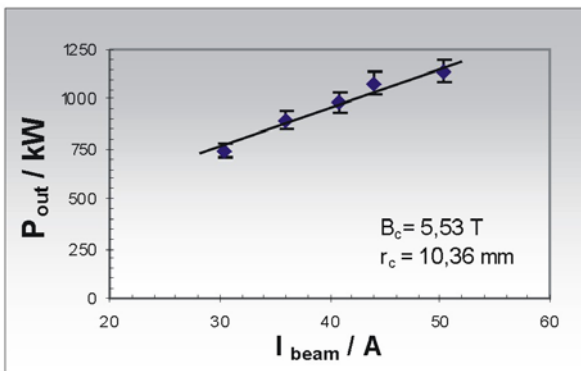


Figure 2. Dependence of output power on electron.

To eliminate the limitation in output power for the series tubes, a better quality assurance of the emitter ring has to be performed before installing it into the gyrotron. To avoid the pulse length limitation it was decided to use external ion getter pumps with better shielding against RF stray radiation.

Knowing the reasons for the limitation in power and pulse length, the development phase for the gyrotrons was finished and seven series tubes were ordered. The first series tube had been delivered to FZK and tested in short and long pulse operation.

Fig. 2 shows the output power of the series tube versus beam current at constant magnetic field. The saturation in power as seen in the prototype could not be found indicating the good emission of the cathode. An output power of 1 MW at 40 A and 1.15 MW at 50 A was measured in short pulse operation (ms). The corresponding efficiencies without depressed collector were 31 % and 30%, respectively.

RF-field distribution measurements (perpendicular to the output RF-beam direction) were performed at different positions with respect to the window. The Gaussian content was calculated to be 97.5 %.

C. Experimental results: long pulse operation

The optimisation procedure for finding the operating parameters at high output power in long pulse operation was performed in 1s-pulses assuming that the instantaneous power is well described by the frequency difference between the initial frequency and the instantaneous frequency (after one second). In a range between 5.52 – 5.56 T of the magnetic field at the cavity, no maximum for the output power was found. The power increased slightly with increasing magnetic field. In order to achieve the maximum output power, the accelerating voltage (this corresponds to the energy of the electrons inside the cavity) was adjusted and followed nicely the law that the ratio between magnetic field and the relativistic factor γ has to be constant. Increasing the voltage beyond this value leads to an excitation of neighbouring modes. The measurements were performed at a constant beam current of 40 A, but with optimising the electron beam radius inside the cavity.

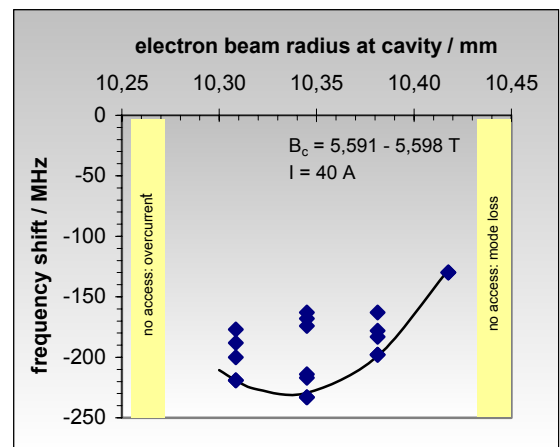


Figure 3. Dependence of output power on electron beam radius in cavity for optimum output power. The allowed range for excitation of the desired mode is only 10.27 to 10.43 mm.

A strong dependence of the output power has been found for different electron beam radii inside the cavity (Fig. 3). The desired mode can only be excited in a narrow range between 10.25 mm and 10.43 mm. At lower beam radii, arcing occurs, at higher radii a wrong mode (or the counter-rotating mode) is excited. The optimum value of the beam radius decreases slightly with decreasing cavity field and beam current.

In long pulse operation, the power was measured calorimetrically by the temperature increase of the cooling water of the RF-load. This load is placed about 6m away from the gyrotron window. The RF beam is focused and directed by two matching mirrors into the load. In order to reduce the power loading on the surface, a set of polarizers are installed to produce a circularly polarized beam. The first matching mirror owns a corrugated surface. A small amount of the RF beam is focused on a horn antenna with a diode detector to get a signal proportional to the output power. This signal, however, is not used for power measurements as the calibration is complicated and can vary easily.

In long pulse operation, the gyrotron was operated with depressed collector. The electrons are decelerated after the RF interaction by a negative voltage U_{body} which usually is chosen to a value between 25 and 30 kV.

Fig. 4 (top) shows the gyrotron operating parameters for a pulse length of three minutes. Shown are the beam current I_{beam} , the body voltage U_{body} , the accelerating voltage U_{acc} , the diode signal U_{diode} and the pressure inside the tube measured as the current of the ion getter pumps. It is increasing very smoothly and stays well in the allowed operating range. The increase of pressure is less than a factor of two.

The highest output power inside the load for a three minute pulse was measured to 922 kW. Including the external stray radiation determined by the calorimetric measurement performed inside the microwave chamber, the total power was 920 kW with an efficiency of 45%. The directed power was measured to 906 kW and thus the specified value of 900 kW for the Gaussian content has been achieved.

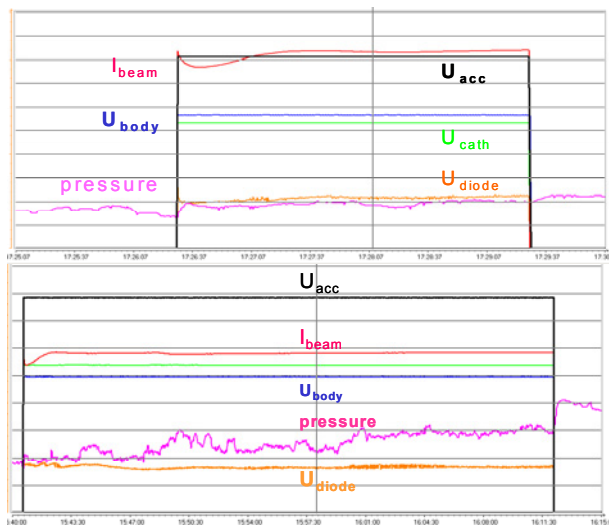


Figure 4. Operation parameters for the 180 s, 950 kW. (top) and the 1893 s, 540 kW pulse (bottom).

At Forschungszentrum Karlsruhe, the available HV power supply is only able to operate up to three minutes at full power, but at reduced electron beam current at less than 30 A longer pulses can be achieved. Fig. 4 (bottom) shows the operating parameters for a pulse of about 31 minutes (1893 s) with an output power of 540 kW. It can be seen by the diode signal that the output power is very stable. The scale for the pressure is logarithmic with a factor of 1.8 per division. The pressure increase is lower than a factor of 2 ending up at about $6 \cdot 10^{-9}$ mbar.

After the successful tests at the Forschungszentrum Karlsruhe, the tube was delivered to IPP Greifswald for tests at highest output power and a pulse length of 30 minutes. A directed output power of 865 kW was measured inside the load, and a total output power of about 910 kW was estimated taking the losses in the transmission line into account (world record in energy content).

III. COAXIAL CAVITY 170 GHz GYROTRON

A. Design of the pre-prototype tube

Table II summarizes the parameters of the pre-prototype gyrotron. It operates in the $TE_{34,19}$ -mode [5]. It is in most respect identical to the long-pulse prototype [6,7] which is under construction. However, the field of the superconducting magnet available at Forschungszentrum Karlsruhe is limited to 6.7 T. Thus the accelerating voltage has to be reduced to values below 80 kV in order to enable operation at 170 GHz. (The industrial prototype will be operated at 90 kV with a cavity magnetic field of 6.87 T). The reduction in accelerating voltage for the short-pulse tube also reduces the available output power to 1.5 MW. The electron gun is a coaxial magnetron injection gun. Special care has been taken to avoid regions of trapped electrons which may cause a Penning discharge. The water cooled coaxial insert can be aligned with high accuracy with respect to the electron beam in the cavity under operating conditions. The geometry of the cavity is shown in Fig. 5.

TABLE II. PARAMETERS OF COAXIAL CAVITY GYROTRON (PRE-PROTOTYPE)

RF output power	1.5 MW
Accelerating voltage	80 kV
Beam current	75 A
Cavity mode	$TE_{34,19}$
Cavity radius	29.55 mm
Launcher taper	0.002 rad
Window aperture	100 mm

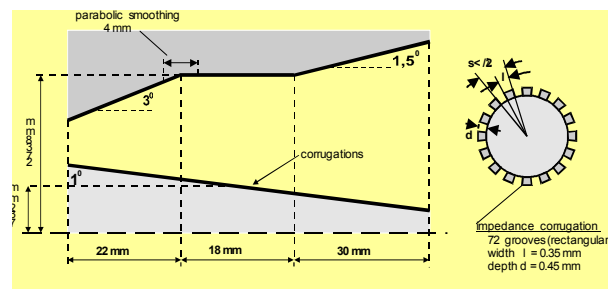


Figure 5. Geometry of the $TE_{34,19}$ coaxial cavity.

The built-in quasi-optical (q.o.) mode converter transforms the cavity mode into a free space beam. It consists of a launcher with smooth wall dimpling and a helical cut and three mirrors, a quasi-elliptical one and a toroidal one followed by a phase correcting mirror. The mirrors were optimized as a compromise between low stray radiation inside the tube and maximum Gaussian content of the RF output beam.

The window unit contains a single quartz-disk with a thickness of 15 half wavelengths at 170 GHz (the long-pulse gyrotron uses a single-disk CVD-diamond window with a thickness of 5 half wavelengths.) The collector can be operated as a single-stage depressed collector for reducing the power density and for increasing the overall efficiency.

B. Experimental Results

During the first measurements parasitic oscillations at low frequency of about 259 and 328 MHz occurred. They could be suppressed successfully by external RF-absorbing material. The LF resonances have also been found in numerical simulations using the code "CST Microwave Studio". The simulations now will be applied to the geometry of the industrial prototype tube.

The performance of the electron gun and electron beam has been found to be in agreement with the design objective as far as the properties have been observable during the gyrotron operation. Stable operation up to $I_b \approx 80$ A and $U_{acc} \approx 80$ kV has been obtained without any observable beam instabilities.

The nominal co-rotating TE_{-34,19} mode at 170 GHz has been excited stably in single-mode operation over a wide parameter range. However, the experimental results are not fully in agreement with calculations. In particular, the observed mode sequence is more dense than predicted by simulations limiting the excitation range of the nominal mode to lower voltages than expected. At an accelerating voltage of 73 kV a microwave output power of 1.15 MW was obtained with 20 % efficiency (without depressed collector). The reasons for the discrepancy need further investigations.

The performance of the q.o. RF output system has been studied both at low power levels ("cold") and at high power ("hot") with the gyrotron. A good agreement has been found between the "cold" and "hot" measurements and calculations. A mistake in the optimization of the mirrors has been discovered. The q.o. RF output system with the redesigned mirrors has been tested at low power. The experimental results are in good agreement with the design calculations confirming the reliability of calculations and the accuracy of fabrication. With the incorrect q.o. system which is installed in the pre-prototype the amount of stray microwave losses has been measured to be 8 % of the output power. It has been found that the internal microwave losses are efficiently absorbed by an array of water cooled Al₂O₃ tubes. Based on these results internal absorbers will be installed in the industrial prototype tube for absorbing of at least 50 % of the stray radiation.

IV. CONCLUSIONS AND PERSPECTIVES

The first of seven series gyrotrons for the stellarator W7-X has been tested up to three minutes at full power at FZK and up to 30 minutes at IPP Greifswald. It yielded an output power of 1 MW in short pulse operation with an efficiency of 30% (without depression) and about 950 kW in long pulse operation (180 s) with an efficiency of 45% (with depression). The output power in almost CW operation (30 minutes) was measured to 910 kW.

The second tube will arrive at Forschungszentrum Karlsruhe end of November 2005.

As a next step for the coaxial-cavity gyrotron, the operation with a new redesigned quasi-optical mode converter will be performed. To clarify the different behaviour of the tube with respect to theoretical predictions, a careful investigation of mode competition has to be performed.

REFERENCES

- [1] R. Heidinger et al., IEEE Trans. Plasma Science **30** (2002) 800-807.
- [2] M. Thumm et al., IEEE Trans Plasma Science **52** (2005) 818-824.
- [3] G. Dammertz et al., IEEE Trans Plasma Science **30** (2002) 808-818.
- [4] G. Dammertz et al., IEEE Trans Plasma Science **52** (2005) 808-817.
- [5] O. Dumbrajs et al., 26th Int. Conf. on Infrared and Millimeter Waves, Toulouse (2001) 10-14.
- [6] B. Piosczyk et al., IEEE Trans. Plasma Science **32.2** (2004) 413-417.
- [7] J. P. Hogge et al., Proc. 13th Joint Workshop on Electron Cyclotron Emission and Electron Cyclotron Heating, Nizhny Novgorod, Russia, (2004) 393-397.

An Investigation into the Feasibility of S-Parameter Measurements at X-Band Frequencies with Gaussian Beam Techniques

Michael Sabielny

EADS - Defence Electronics, OPEE11, Woerthstr. 85, D-89077 Ulm, Germany
Telephone: +49-(0)731-392-4213
Email: michael.sabielny@eads.com

Abstract—Theoretical design and analysis of Frequency Selective Surfaces (FSS) often attracts the attention of the electromagnetics community as FSS are complex but also instructive passive electronic devices for filtering applications. Unlike conventional RF filters FSS usually do not operate on guided waves but on freely propagating waves. This makes the design even more challenging as frequency, polarization, incident angle, and possible onset of grating lobes have to be considered carefully during the design process. In the past years a lot of work has been published on different theoretical design methods whereas contributions on suitable measurement methods of FSS are still quite rare. This contribution therefore aims to fill up this gap by the investigation of the feasibility of an FSS measurement setup at X-band frequencies using low-cost Components-Of-The-Shelf (COTS) materials. In contrast to other publications the whole measurement process including necessary calibration procedures will be studied completely by means of numerical simulation techniques.

I. INTRODUCTION

Contemporary FSS simulators usually make the assumption of periodic boundary conditions in one or two dimensions to limit the problem under investigation to just one unit cell of the FSS. It is a common procedure to assume a totally plane FSS even if the actual FSS will be curved. This is allowed as long as the radii of curvature are electrically large compared to the operating wavelength. Usually after all theoretical analysis and design steps have been accomplished a test sample of the FSS will be produced for subsequent measurements.

Usually the design process is based on the periodic boundary assumption which is equivalent to a structurally unlimited FSS whereas the test sample is limited somewhere for reasons of cost and producibility. The first idea that most engineers develop is simply to put the test sample between two horn antennas connected to a network analyzer and to see what happens. This at least may give a rough estimate of the FSS properties, for instance if the FSS is transmissive in one polarization and reflective in the other polarization. When measurements have to be more accurate one realizes that this free space approach has some serious disadvantages:

- 1) If the test sample is too small a notable portion of the transmitted electromagnetic energy spills over into the surrounding medium and will be lost.
- 2) Unavoidable diffraction effects at the edges of the test sample lead to an increase of electromagnetic energy behind the FSS which would not be there if the FSS was an unlimited device.
- 3) If X-band standard gain horn antennas are used as exciter and receiver then the relation $d_{ff} = 2D^2/\lambda$ for the minimum far-field distance leads to values of $d_{ff} = 2.7m$ which make the fulfillment of the first mentioned aspects even more complicated.

The next step usually is the introduction of large absorbing walls surrounding the FSS test sample, thus minimizing diffraction effects. A corresponding measurement setup has been described in [1] and promises to give acceptable, but still noisy results in FSS measurements. But these results only refer to the magnitude of the finally requested S-parameter set, results on phase information have not been reported.

The waveguide simulator technique [2] is an approach which offers much more accuracy in magnitude as well as in phase though it is a destructive method since specially shaped waveguide inlets have to be cut or manufactured. Furthermore this method is only capable of spot-checking the FSS performance because one waveguide inlet under excitation of a specific waveguide mode corresponds to only one possible direction of incidence and frequency point. This is obviously too few information for a complete assessment of the FSS.

Another short summary of possible FSS measurement techniques can be found in [3] which ultimately points to a suitable means of FSS non-destructive measurements - the Gaussian beam approach.

II. THE GAUSSIAN BEAM MEASUREMENT SETUP

The theory of Gaussian beams applied to quasi-optical applications has been described extensively elsewhere [4] and will not be repeated here. The main idea is to introduce dielectric focussing lenses in front of the horn antenna in order to bundle electromagnetic energy at a certain region on the test sample and make this energy decay very rapidly towards the edges of the test sample, thus avoiding diffraction and spill-over effects.

Recently Gagnon and Shaker reported such a measurement system, first for the measurement of the dielectric constant of pure dielectric test samples [5], [6] and later for the measurement of FSS test pieces as well [7]. The ideas and results presented by the authors are very promising, although the frequency of operation was located in Ka-band. For application in X-band several aspects of the FSS measurement setup have to be reviewed and modified.

A. Proposed X-Band Measurement Configuration

The measurement setup by Gagnon and Shaker is shown in Fig. 1. As can be seen the lenses have been designed with a certain distance between itself and the corresponding horn antenna. The device under test (DUT) is located within the focal region of the Gaussian beam.

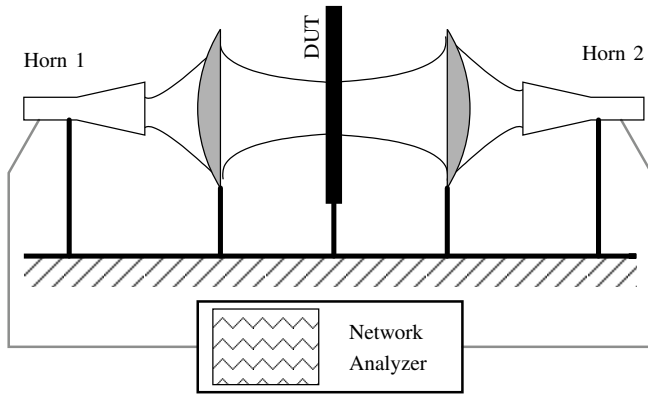


Fig. 1. FSS measurement setup as shown in [7] for Ka-band application

The novel aspect of the X-band measurement setup will now be explained. While common X-band horn antennas exhibit much larger dimensions in their aperture and flare length it is worthwhile to design the dielectric lenses in such a way that they can be plugged directly into the aperture of the horn antenna. This configuration has the advantage that spill-over losses now are completely eliminated and all electromagnetic energy, excepting that portion being reflected at the curved surface of the lens inside the horn antenna, will be focused within the Gaussian beam. Mechanically the new setup removes 2 of 5 supporting structures, thus reducing cost and error-proneness.

B. Design Procedure of the Dielectric Lens

The first step in the design procedure is to calculate the shape of the Gaussian beam which is launched by the X-band horn directly and without any other focussing devices. As explained in [4] rectangular horn antennas produce a symmetrical Gaussian beam as long as the aperture ratio fullfills $b/a = 0.7$. An available X-band horn antenna with aperture dimensions $a = 192.5\text{mm}$ and $b = 143.8\text{mm}$ with a ratio of $b/a = 0.737$ has been considered to match this requirement sufficiently. The necessary steps to calculate the beam waist w_0 as well as its location inside the horn antenna are displayed in Fig. 3. Following [4] the beam radius $w(z)$ at

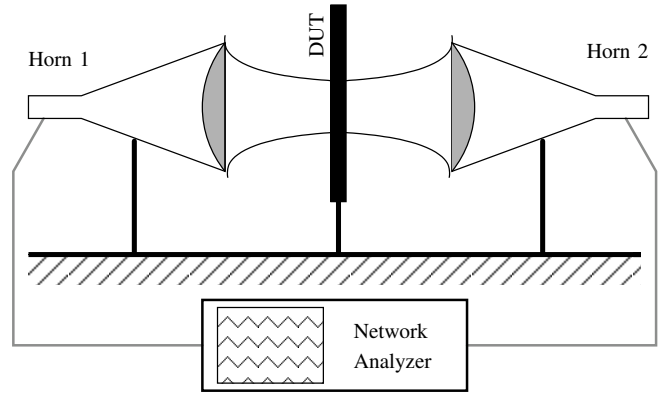


Fig. 2. Novel measurement setup for FSS at X-band

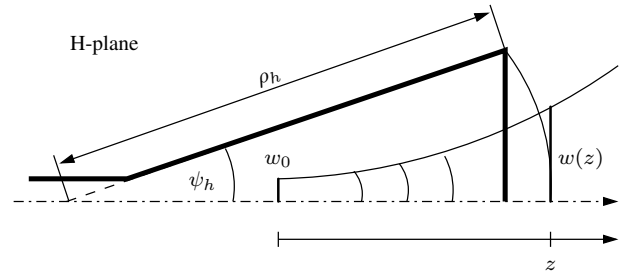


Fig. 3. Calculation of the beam waist and its location applied to the dimensions of a given horn antenna

the aperture of the horn antenna can safely be approximated with $w(z) = 0.35a$ for rectangular horn antennas. Then it is easy to compute the beam waist w_0 with:

$$w_0 = \frac{w}{\sqrt{1 + \left(\frac{\pi w^2}{\lambda R}\right)^2}}, \quad (1)$$

where Gaussian beam radius of curvature equals the horn parameter ρ_h . The location of the beam waist is then found with:

$$z = \frac{\pi w_0}{\lambda} \sqrt{w^2 - w_0^2}. \quad (2)$$

Generally the beam waist w_0 has to comply with

$$w_0 \geq \lambda \quad (3)$$

which is required by the paraxial wave equation. Here all calculations are presented only for the H-plane of the horn antenna. Since in the E-plane the horn parameters ρ_e and ψ_e are slightly different from their H-plane counterparts the beam waist and its location should be calculated for the E-plane as well. As suggested in [8] the final values for w_0 and z can be derived from the average of the respective two parameters. The Gaussian beam launched by the horn antenna has to be transformed by a dielectric lens in order to focus the electromagnetic energy. For a conventional plano-convex dielectric lens the focal distance depends only on the shape and the selected material. The hyperbolic convex surface of

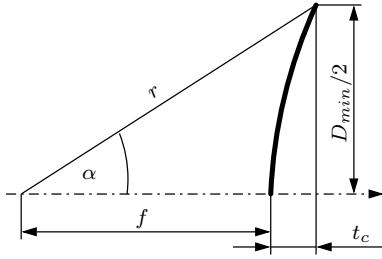


Fig. 4. Parameters of a hyperbolic lens surface as part of a plano-convex dielectric lens

the lens in Fig. 4 follows the equation:

$$r = \frac{(\sqrt{\epsilon_r} - 1) f}{\sqrt{\epsilon_r} \cos \alpha - 1}, \quad (4)$$

with f as the desired focal distance. If the following param-

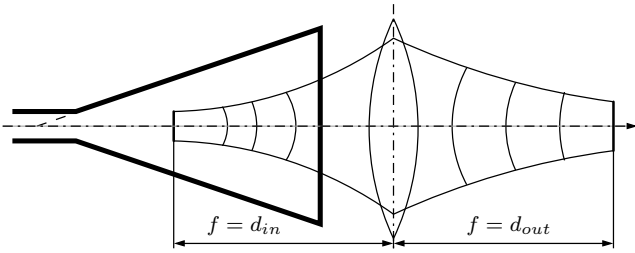


Fig. 5. Combination of a horn antenna with a suitable dielectric lens for optimum gaussian beam coupling

eters (frequency $f = 10\text{GHz}$, lens material $\epsilon_r = 2.3$, $a = 195.2\text{mm}$, $b = 143.8\text{mm}$, $\rho_h = 347.1\text{mm}$, $\rho_e = 319.6\text{mm}$, $\psi_h = 16.3\text{deg}$ and $\psi_e = 13.0\text{deg}$) are fixed then by changing the focal distance some interesting results with respect to lens diameter and lens thickness can be obtained.

TABLE I
LENS DIAMETER D AND CENTRAL THICKNESS t_c AS A FUNCTION OF FOCAL DISTANCE f

f	$D_{min} = 3w$	t_c	$D_{min} = 4w$	t_c
250	433	115	577	173
300	495	128	660	193
350	559	143	746	216

It becomes obvious that the larger the focal distance the larger the lens diameter as well as the central thickness of the lens. The mentioned minimum lens diameter results from the recommendations in [4]. Anyway, all results are completely impractical due to the huge size and the resulting weight of such lenses. Instead the lens has to be made much smaller. This can be accomplished by reducing f until in the limit the lens plugs into the horn antenna aperture. If done in this way the recommendations for D_{min} are no longer needed since there is no spill-over around the lens at all. The result of this procedure is depicted in Fig. 6, showing a plug-in lens made of Tivar1000.

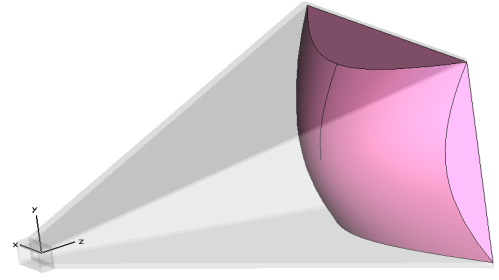


Fig. 6. Dielectric lens with $\epsilon_r = 2.3$, $t_c = 64.47\text{mm}$ and $f = 139.5\text{mm}$ plugged into an X-band standard gain horn antenna

C. Simulation Results

In order to assess the characteristics of the designed horn antenna with plug-in lens a complete numerical simulation¹ of this component has been performed. Some results are depicted in Fig. 7. The shape of the launched Gaussian beam is clearly visible as well as the location of the output beam waist w_{out} , which has been precalculated with a distance of 75mm to the aperture of the antenna.

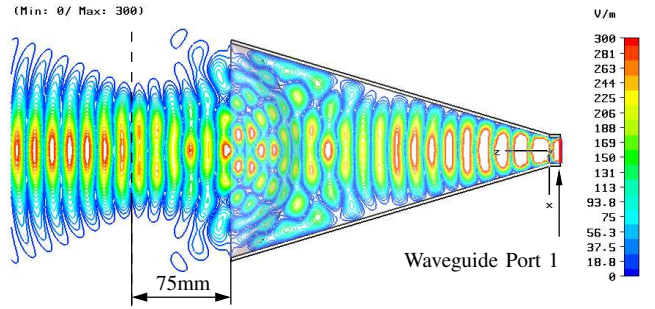


Fig. 7. Radiated electric field of the lens antenna in the H-plane at $f = 9.6\text{GHz}$, isoline representation, clamped to the range of 0 to 300 V/m

The positioning of the whole measurement system now becomes very simple. In order to measure a flat DUT, either of FSS or of dielectric type, the two lens antennas have to be separated in such a way that the distance between the respective surface of the DUT and its neighboring antenna aperture is exactly 75mm. If the DUT had a thickness of 10mm then the whole aperture-to-aperture separation had a length of 160mm.

III. CALIBRATION PROCEDURE

As any test fixture for S-parameter measurements also this free-space setup has to be equipped with a calibration procedure. In the context of conventional transmission line measurements with network analyzers 5 different calibration standards are frequently used in varying combinations: THRU, LINE, MATCH, SHORT and OPEN. THRU and LINE are quite similar to each other in their scattering matrix representation. Furthermore, in free-space applications the OPEN standard (representing a reflection coefficient of $r = +1$)

¹All simulations in this contribution have been made using CST Studio Suite 2006.

is only realizable via Artificial Magnetic Conductors (AMC) [9] which in general do not provide $r = +1$ over a large bandwidth. This is also the reason for not using the TRL calibration method here, as suggested in [10] because of the similarity of the THRU and the LINE standard. For broadband application several LINE standards have to be used which makes the calibration even more complicated. To overcome this situation the TMR calibration method has been used in [5]–[8], although in a hard-coded way using a specific type of network analyser. Indeed, for free space applications the TMR as well as the LMR methods are the only methods inherently suitable for broadband application [11], [12].

In this study the 3 calibration standards THRU, MATCH and REFLECT have been incorporated in the following way:

THRU

two lens antennas with an aperture distance of 150mm as shown in Fig. 11,

MATCH

one lens antenna radiating into free space as shown in Fig. 7 with S_{12} and S_{21} assumed to be zero,

REFLECT

two lens antennas with an aperture distance of 160mm together with a PEC-reflector of 10mm thickness exactly in the middle between both apertures.

In all mentioned calculations the S-parameters at both waveguide ports have been recorded. A suitable deembedding procedure is described in [11] and will not be repeated here.

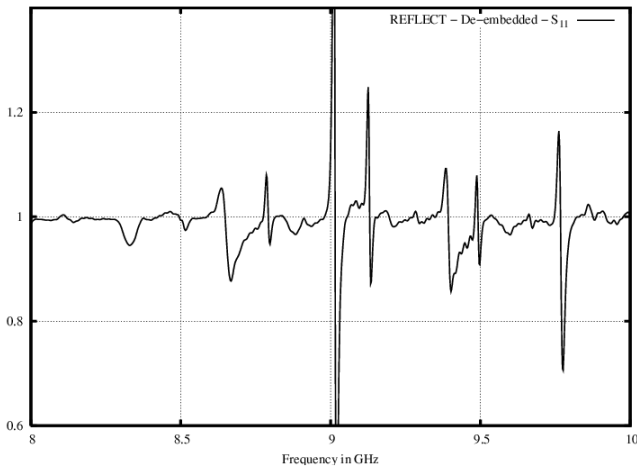


Fig. 8. De-embedded reflection coefficient S_{11} of the reflection standard, expected value is $|S_{11}| = 1$, phase not shown here

It is worthwhile to check the calibration procedure by using the three calibration standards one by one as a DUT, to de-embed the measured raw S-parameter data and to compare these results with theoretically known values, since the reflection and transmission properties of these standards are very simple. This is especially valid under the nearly ideal conditions of a numerical analysis method. As expected the standards THRU and MATCH show an excellent agreement, THRU does not have any reflection but a full transmission

with correct values in magnitude and phase. A corresponding excellent behaviour was observed with the MATCH standard serving as a DUT. Only the REFLECT standard shows notable deviations from the expected values as depicted in Fig. 8.

IV. DE-EMBEDDING OF A FLAT DIELECTRIC TEST SAMPLE

As a prerequisite for measuring frequency selective surfaces with such a Gaussian beam setup it has to be shown that the designed measurement system is capable of successfully extracting the real S-parameter data of a dielectric test piece from the raw measured data. For reasons of convenience a test sample made of Tivar1000 (the same material of the two dielectric lenses) with a thickness of 10mm has been used. The raw S-parameter data has been recorded and subsequently de-embedded. The results of this operation are depicted in Fig.9 and Fig. 10.

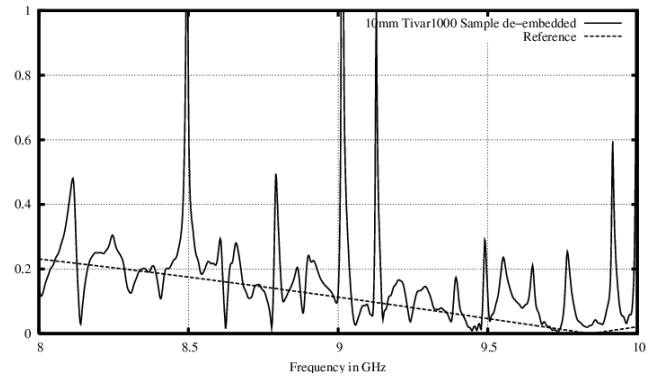


Fig. 9. De-embedded reflection coefficient S_{11} of a 10mm thick dielectric Tivar1000 test sample compared to expected values

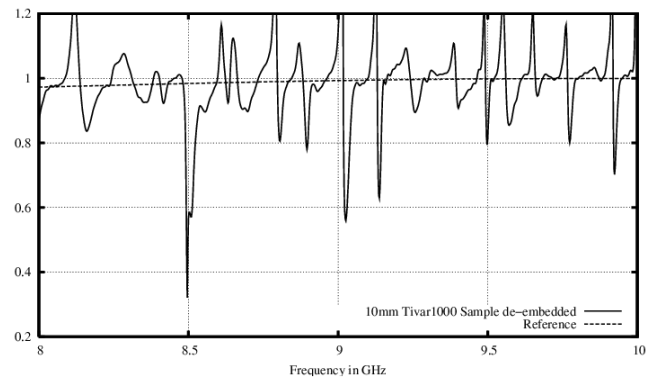


Fig. 10. De-embedded transmission coefficient S_{21} of a 10mm thick dielectric Tivar1000 test sample compared to expected values

V. REVIEW OF THE OBTAINED RESULTS

The de-embedded S-parameter data is obviously of very poor quality. While the phase data (not shown here) exhibits a slightly better behavior all de-embedded magnitude data is superpositioned with effects of standing waves. Although the general shape of the curves roughly resembles the corresponding references it has to be stressed that with only the

Clamp to range: (Min: 0/ Max: 300)

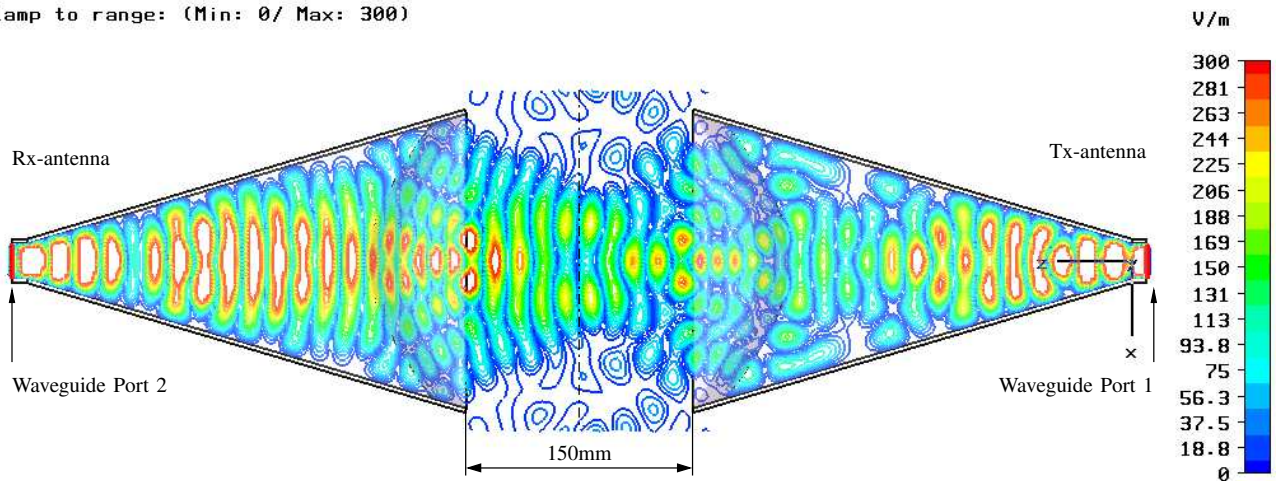


Fig. 11. Distribution of the electric field in isolines between two equal lens antennas at $f = 9.6\text{GHz}$ with an aperture distance of 150mm, excitation by waveguide port 1

knowledge of the de-embedded data the shown reference curve would never have been found.

A subsequent review of the applied Gaussian beam theory then has revealed some weaknesses of the design which should be considered carefully in future applications:

- 1) Both lenses are rather thick than thin lenses due to their f/D -ratio. This affects the rules of the Gaussian beam transformation, the foundation of the whole design process.
- 2) The beam waist of $w_0 = 40.37\text{mm}$ inside the horn is only a little bit larger than λ at X-band frequencies which affects the validity of the paraxial wave equation applied in this context.
- 3) The phase distribution at the confocal distance behind both lenses is not as plane as expected. This indicates the presence of higher-order Gauss-Hermite modes which should not be there.
- 4) Standing waves on the test sample excite a different mode spectrum in both apertures, different from that one measured during the free-space calibration. This is the reason why the de-embedding does not work properly.

Since the de-embedding procedure of the dielectric DUT has failed no further attempts with de-embedding FSS test samples have been made.

VI. CONCLUSIONS

The results of this study indicate that low-cost COTS Gaussian beam measurement systems for application at X-band frequencies are *not* feasible as far as a high level of accuracy of the measured S-parameter data in magnitude and in phase is required. Any separation of the lenses from the horn antennas in order to reduce higher order modes will result in an immense increase of lens size and weight, thus making the whole system impractical and expensive. The question for alternate solutions remains to be answered. Maybe the idea of specially designed corrugated feed horn-lens combinations as

proposed in [13] and translated into X-band compatible sizes can solve this problem. But this would be no longer a low cost measurement system.

REFERENCES

- [1] C. Mias, C. Tsakonas, and C. Oswald, "An investigation into the feasibility of designing frequency selective windows employing periodic structures (ref. ay3922)," The Nottingham Trent University - Department of Electrical and Electronic Engineering, Tech. Rep.
- [2] H. A. Wheeler, "A survey of the simulator technique for designing a radiating element," in *Phased Array Antennas*, A. Oliner and G. Knittel, Eds. Artech House, 1972, pp. 132–148.
- [3] T. K. Wu, Ed., *Frequency Selective Surface and Grid Array*. New York: John Wiley & Sons, 1995.
- [4] P. F. Goldsmith, *Quasi-optical Systems*. Piscataway: IEEE Press, 1998.
- [5] N. Gagnon, J. Shaker, P. Berini, L. Roy, and A. Petosa, "Material characterisation using a quasi-optical measurement setup," *IEEE Transactions on Instrumentation and Measurement*, vol. 52, no. 2, pp. 333–336, 2003.
- [6] N. Gagnon, J. Shaker, A. Petosa, and P. Berini, "Low-cost free-space measurement of dielectric constant at ka band," *IEE Proceedings Microwaves, Antennas & Propagation*, vol. 151, no. 3, pp. 271–276, 2004.
- [7] N. Gagnon and J. Shaker, "Accurate phase measurement of passive non-reciprocal quasi-optical components," *IEE Proceedings Microwaves, Antennas & Propagation*, vol. 152, pp. 111–116, 2005.
- [8] N. Gagnon, "Design and study of a free-space quasi-optical measurement system," Communications Research Centre Canada, Ottawa, Tech. Rep. CRC-RP-2002-002, July 2002.
- [9] D. J. Kern, D. H. Werner, A. Monorchio, L. Lanuzza, and M. J. Wilhelm, "The design synthesis of multiband artificial magnetic conductors using high impedance frequency selective surfaces," *IEEE Transactions on Antennas and Propagation*, vol. 53, no. 1, pp. 8–17, 2005.
- [10] D. K. Ghodgaonkar, V. V. Varadan, and V. K. Varadan, "A free-space method for measurement of dielectric constants and loss tangents at microwave frequencies," *IEEE Transactions on Instrumentation and Measurement*, vol. 37, no. 3, pp. 789–793, 1989.
- [11] K. J. Silvonen, "A general approach to network analyzer calibration," *IEEE Transactions on Microwave Theory and Techniques*, vol. 40, no. 2, pp. 754–759, 1992.
- [12] K. Silvonen, "LMR16 - a self-calibration procedure for a leaky network analyzer," *IEEE Transactions on Microwave Theory and Techniques*, vol. 45, no. 7, pp. 1041–1049, 1997.
- [13] M. Le Goff, J. L. Le Bras, B. Deschamps, D. Bourreau, A. Peden, and S. Toutain, "Focussing horn design for wide band quasi optical circuit measurements without time-gating," in *Proceedings of the 2nd ESA Workshop on Millimetre Wave Technology and Applications: antennas, circuits and systems*, Espoo, Finland, 27-29 May 1998, pp. 269–274.

On the calculation of the radiation properties of dipole antennas in cylindrical boreholes considering large scatterers

Andreas Becker, Yi Zhou, Volkert Hansen, University of Wuppertal

Abstract—In this paper we deal with the calculation of the radiation properties of dipole antennas in cylindrical boreholes under consideration of large scatterers in the farfield of the antennas. For this purpose, the dipole antennas are modeled with the method of moments, utilizing the Green's function for the electric field in a cylindrical stratified medium, and the large scatterers are modeled with the geometrical optics and the concept of using the radar cross sections of simple structures, respectively.

I. INTRODUCTION

Borehole radars are used for subsurface detection of geological targets like water-bearing layers or holes or similar inhomogeneities. They typically consist of mandrel-mounted transmitting and receiving dipole antennas (see Fig. 1). By making use of an array of receiving antennas the direction of arrival, and by this the location of radar targets, can be estimated.

The goal of this paper is the investigation of the influence of large scatterers on the currents on the receiving antennas. An obvious approach is to model the antennas and their cy-

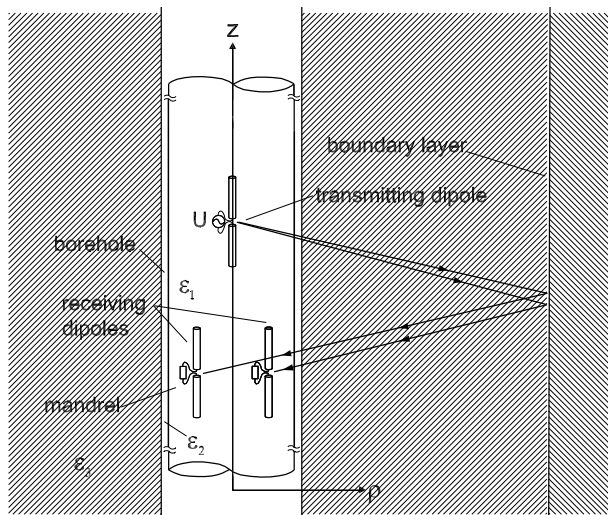


Fig. 1. Geometry of the borehole radar and two reflected rays due to a boundary layer far away from the antenna-system (not to scale).

lindrical surrounding using the Method of Moments (MoM) based on the Green's function of the cylindrical stratified medium. The influence of large scatterers might then be calculated by making use of the following procedure:

- 1) Calculation of the radiated fields at the location of the scatterers.
- 2) Calculation of the scattered fields by making use of geometrical optics or of the appropriate radar cross sections for simple structures.
- 3) Calculation of the currents on the receiving antennas, which are excited by the scattered fields and by fields propagating along the borehole.

However, for the first step the Green's function must be provided for source points in the innermost layer and for observation points in the outermost layer far away from the borehole, what is very time-consuming and prone to numerical errors. These difficulties do not occur if both source and observation points are located in the same innermost layer. Therefore, the following strategy has been adopted:

- 1) It is assumed that large scatterers far away from the antennas (e.g. the boundary layer shown in Fig. 1) do not significantly influence the current distribution of the transmitting antenna.
- 2) The directive gain of the transmitting antenna is calculated by a MoM-analysis of the transmitting antenna in the receiving mode.
- 3) The input impedance, and by this the radiated power, is calculated by a MoM-analysis of the transmitting-antenna in the transmitting mode.
- 4) The farfield of the transmitting antenna at the position of the large scatterers is calculated by using the directive gain and the radiated power.
- 5) The scattered field is calculated by making use of the geometrical optics or of the appropriate radar cross sections for simple structures.
- 6) The induced current at the receiving antenna is calculated by a MoM-analysis, using the scattered field as excitation.

This paper is organized as follows: Section II starts with a short general description of the method of moments applied to dipoles in cylindrical stratified media (scatterers neglected). Then it is described how the strategy to calculate the radiated fields is realised efficiently within the MoM-solution procedure. In section III it is presented how large scatterers can be considered in the solution procedure. In section IV numerical examples are presented and in section V a short summary and an outlook are given.

II. METHOD OF MOMENTS

In the context of this paper we consider linear e_z -orientated dipoles in a cylindrically layered medium (see Fig. 2). The current density on the surface of these dipoles is calculated with the method of moments [1], which is based on the series expansion

$$\mathbf{J}(\mathbf{r}) = e_z J(\mathbf{r}) = \sum_{n=1}^N e_z \beta_n(\mathbf{r}) I_n \quad (1)$$

of the current density, using N unknown weighting coefficients I_n , and enforcement of the boundary conditions of the electric field at the surface of the perfectly conducting dipoles. In (1) β_n is the so called basis-function. By making

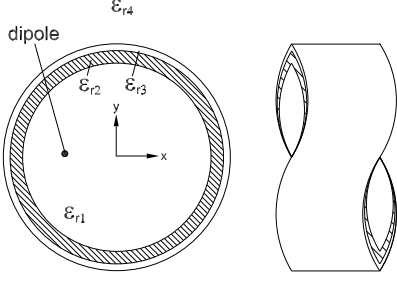


Fig. 2. Cylindrically layered medium with embedded antenna as a design model for the antenna in the borehole.

use of the Galerkin's method [6] one can derive the scalar equation

$$-\sum_{n=1}^N Z_{m,n} I_n = \int_{A_m} E_z^{inc}(\mathbf{r}) \beta_m(\mathbf{r}) dz, \quad (2)$$

with

$$Z_{m,n} = \int_{A_m} \int_{A_n} G_{J,zz}^E(\mathbf{r}, \mathbf{r}') \beta_n(\mathbf{r}') \beta_m(\mathbf{r}) dz' dz. \quad (3)$$

In (2) and (3) A_m and A_n are the areas of the test-function β_m and the basis-function β_n , respectively; $E_z^{inc}(\mathbf{r})$ is the z -component of the incoming field and is used to model both incoming plane waves (receiving mode) and voltage sources on the antennas (transmitting mode). $G_{J,zz}^E$ is the Green's function, which describes the relationship between an e_z -orientated current density and the e_z -component of the electric field. For the considered cylindrical medium $G_{J,zz}^E$ is given by ([2] and [3]):

$$\begin{aligned} [G_{J,zz}^E]^* &= \frac{-\omega\mu}{8\pi} \sum_{n=-\infty}^{\infty} \int_{-\infty}^{\infty} \frac{J_n(k_{1\rho}\rho') J_n(k_{1\rho}\rho)}{(k_1 k_{1\rho})^2} \\ &\cdot f_n(\varphi, \varphi', z, z') [k_{1\rho}^2, 0] \cdot \tilde{\mathbf{R}}_{1,2} \cdot \begin{pmatrix} k_{1,\rho}^2 \\ 0 \end{pmatrix} dk_z \\ &+ j\omega\mu \underbrace{\left(1 + \frac{1}{k_1^2} \frac{\partial}{\partial z^2}\right) \frac{e^{jk_1|r-r'|}}{4\pi|r-r'|}}_{\text{direct field}}, \quad (4) \end{aligned}$$

with

$$f_n(\varphi, \varphi', z, z') = e^{jn(\varphi-\varphi')} e^{jk_z(z-z')}. \quad (5)$$

The conjugated complex in (4) results from the fact that in [2] and [3] a time dependence of the form $\exp(-j\omega t)$ and in the context of this paper a time dependence of the form $\exp(j\omega t)$ is used. In (4) $k_{1\rho} = \sqrt{k_1^2 - k_z^2}$, k_1 is the wave number of the innermost layer and $\tilde{\mathbf{R}}_{1,2}$ is the reflection matrix for the boundary between layer 1 and layer 2, which is recursively found by starting at the outermost layer N . By combining (2) and (4), and by fulfilling (2) for all test-functions a linear equation system to calculate the coefficients I_n can be derived:

$$\mathbf{Z}\mathbf{I} = \mathbf{U}. \quad (6)$$

The vector \mathbf{U} contains the right side of (2), the matrix \mathbf{Z} contains the coefficients $Z_{m,n}$ and \mathbf{I} is a vector containing the unknown current coefficients I_n . (6) can be used for both the transmitting and the receiving case. \mathbf{U} depends on the excitation (incoming fields or voltage sources) whereas \mathbf{Z} does not depend on the excitation and thus does not need to be re-calculated, if the excitation changes. The calculation of the entries of \mathbf{Z} is, due to the integration in (4), the most

time consuming step in the computational solution procedure. As mentioned above, a direct calculation of the far-field (i.e. the field in the outermost layer) with the corresponding Green's function is time-consuming and prone to numerical errors. Consequently, the following procedure is chosen to calculate the radiated field:

- 1) The matrix \mathbf{Z} is calculated.
- 2) For the lossless case, the directive gain of the transmitting antenna can be calculated with ([5])

$$D_g(\vartheta, \varphi) = 4\pi \frac{|I_r(\vartheta, \varphi)|^2}{\int_0^{2\pi} \int_0^\pi |I_r(\vartheta, \varphi)|^2 \sin\vartheta d\vartheta d\varphi}. \quad (7)$$

$I_r(\vartheta, \varphi)$ is the current in the source point of the antenna, if a plane wave impinges onto the antenna, and it is found by solving (6), using the appropriate excitation \mathbf{U} . The incoming field in layer i , due to a homogeneous plane wave in the outermost layer N , can be calculated by [4]:

$$\begin{aligned} \begin{bmatrix} E_z^i(\rho) \\ H_z^i(\rho) \end{bmatrix} &= \sum_{n=-\infty}^{\infty} e^{-jk_z z} e^{-jn(\phi-\varphi_{inc})} \\ &\left(H_n^{(1)}(k_{i\rho}\rho) \tilde{\mathbf{R}}_{i,i-1} + J_n(k_{i\rho}\rho) \tilde{\mathbf{I}} \right) \cdot \mathbf{a}_{i,n}. \quad (8) \end{aligned}$$

The first element of $\mathbf{a}_{i,n}$ describes the z -component of the electric field and the second component the z -component of the magnetic field, both in layer i . $\mathbf{a}_{i,n}$ is found recursively from $\mathbf{a}_{N,n}$, which is given by

$$\mathbf{a}_{N,n} = (-j)^{-n} \begin{bmatrix} E_{N,z} \\ H_{N,z} \end{bmatrix}. \quad (9)$$

$E_{N,z}$ and $H_{N,z}$ are the z -components of the electric and magnetic field in the outermost layer N , respectively. For the analysis $\mathbf{H}^{inc} \cdot \mathbf{e}_z = H_{N,z} = 0$ is assumed, an assumption which is based on the fact that the antennas are orientated in e_z -direction and thus as a first approximation the farfield fulfills $\mathbf{H} \cdot \mathbf{e}_z = 0$, too. The computational cost for the calculation of (8) is very low because only the term $e^{-jk_z z}$ changes, if all observation points \mathbf{r} lie on one common axis parallel to the z -axis.

- 3) The input impedance Z_{in} of the antenna is calculated applying the method of moments using a delta-gap source U at the source point as excitation. Then the radiated power is given by:

$$P_{rad} = \frac{1}{2} \frac{|U|^2}{|Z_{in}|^2} \Re\{Z_{in}\}. \quad (10)$$

- 4) The radiated field is calculated with

$$\mathbf{E}(\mathbf{r}) \approx E_\vartheta(r, \vartheta) \mathbf{e}_\vartheta = \frac{e^{-jkr}}{r} \sqrt{Z_f \frac{P_{rad} D_g(\vartheta)}{2\pi}}. \quad (11)$$

III. ASYMPTOTIC CONSIDERATION OF THE INFLUENCE OF LARGE SCATTERERS

Once the radiated field is known, the influence of large scatterers can be considered by proceeding in the following way:

- 5a) The field reflected by a very large scatterer is calculated by means of geometrical optics [6] and for this purpose, the required field in the reflection point is calculated with (11).
- 5b) When applying subsurface detection the shape of scatterers is normally not known. Not too large scatterers

can be considered by using the concept of radar cross section (RCS) [7] applied to simple structures like plates and spheres. In a way very similar to the two-way bistatic radar equation the absolute value of the electric field at the position of the receiving antenna can then be calculated with

$$E_r = \sqrt{\frac{2Z_F P_{rad} G_s \sigma}{(4\pi)^2 r_s^2 r_r^2}} \quad (12)$$

with r_s the distance between transmitting antenna and scatterer, r_r the distance between scatterer and receiving antenna and σ the radar cross section of the scatterer.

- 6) The scattered field is substituted by an equivalent homogeneous plane wave and the field produced by this wave at the location of the receiving antenna is calculated with (8). This is valid if the scatterer is in the farfield of the antennas.
- 7) The induced current is calculated by applying the method of moments using the scattered field in the innermost layer as excitation. For this (6) is solved using the appropriate \mathbf{U} , which is calculated by using the field in the innermost layer as described above.

In this whole process, the matrix \mathbf{Z} , which comprises the coupling of antennas due to waves propagating inside the borehole, remains unchanged.

IV. NUMERICAL EXAMPLES

A. Mandrel mounted antennas in a cylindrical borehole

First of all, we consider a center-fed dipole in a three-layered cylindrical medium (see Fig. 3) with $2\rho_1 = 0.08m$, $2\rho_2 = 0.097m$, $\epsilon_{r1} = 3$, $\epsilon_{r2} = 1$ and $\epsilon_{r3} = 10$ for $f = 60$ MHz. In Fig. 4 the directive gain of this dipole

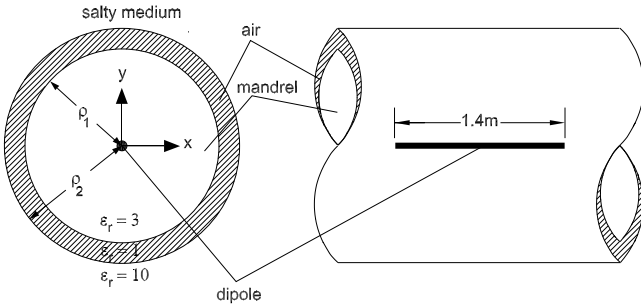


Fig. 3. Geometry of a dipole antenna in a three-layered cylindrical medium to model the case of an antenna mounted in a mandrel which is positioned into an air filled borehole (dipole not to scale).

is compared to the directive gain of the same dipole located in free space. Obviously, the directivity increases due to the larger electrical size of the dipole ($\epsilon_{r1} = 3$) and the borehole causes some kind of focus-effect towards $\vartheta = 90^\circ$.

We now consider a system consisting of two dipoles, as shown in Fig. 5. Of course, a real-life borehole radar uses broadband signals and antenna arrays for subsurface detection (see e.g. [8] and the references within) but this simple model is nevertheless very useful for theoretical analysis.

In our case, the dipole on top is fed at the center-point with $U = 1V$ ($f = 60$ MHz) and we start with a distance d between the boundary layer and the borehole, which approaches infinity. For this case, the input impedance of the transmitting dipole is compared to that of the same dipole

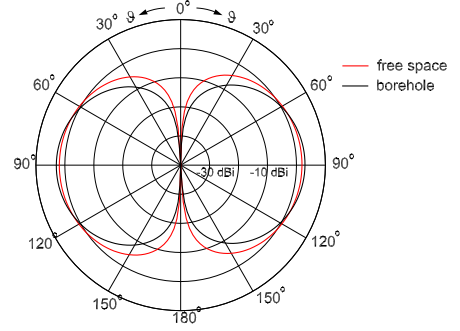


Fig. 4. Directive gain of the transmitting dipole in the borehole ($\rho_1 = 0.08m$, $\rho_2 = 0.097m$, $\epsilon_{r1} = 3$, $\epsilon_{r2} = 1$, $\epsilon_{r3} = 10$, $f = 60$ MHz) compared to the directive gain of the same dipole located in free space.

located in free space (see table 1). Obviously, mainly due to $\epsilon_{r1} = 3$, the input impedance of the mandrel mounted dipole strongly differs from the input impedance of the same dipole in free space (see table 1). As a result of the strongly decreased imaginary part of the input impedance, the radiated power increases and thus the center-point current of the second dipole increases, too (see table 1).

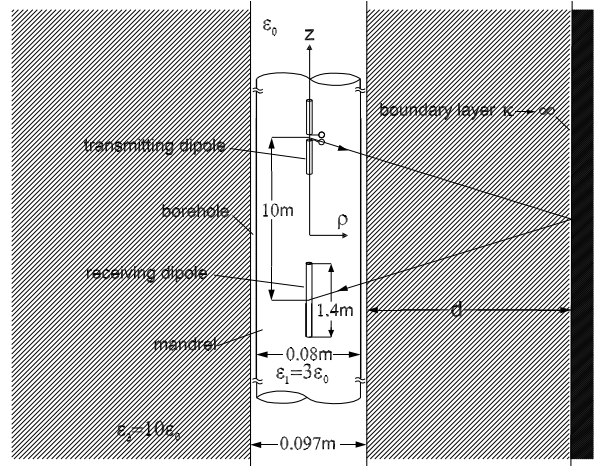


Fig. 5. Geometry consisting of two antennas and a reflected ray due to a perfectly conducting flat boundary layer far away from the antennas (not to scale).

B. Mandrel mounted antennas in a cylindrical borehole under consideration of a perfectly conduction boundary layer

Now, we consider the additional influence of the perfectly conducting flat boundary layer (see Fig. 5) to the current induced at the receiving dipole. In Fig. 6 the center-point current of the second dipole, induced by the reflected signal and by the direct signal (due to the propagation inside the borehole), is shown as a function of the distance d . In contrast to practical problems both antennas have no lateral

TABLE I

INPUT IMPEDANCE Z_{in} OF THE TRANSMITTING DIPOLE AND CENTER-POINT CURRENT I_2 OF THE RECEIVING ANTENNA IN THE BOREHOLE ($\rho_1 = 0.08m$, $\rho_2 = 0.097m$, $\epsilon_{r1} = 3$, $\epsilon_{r2} = 1$, $\epsilon_{r3} = 10$, $f = 60$ MHz) COMPARED TO THE VALUES FOR FREE SPACE.

	Z_{in}	$ I_2 $
free space	$(16.6 - j526)\Omega$	$1.01 \cdot 10^{-6}$ A
borehole	$(64.4 + j35.4)\Omega$	$7 \cdot 10^{-6}$ A

displacement and the surrounding is lossless. Additionally, the distance between both dipoles is relative large. Therefore, the direct signal is very small in comparison to the reflected signal and this results in the small oscillations which can be seen in Fig. 6.

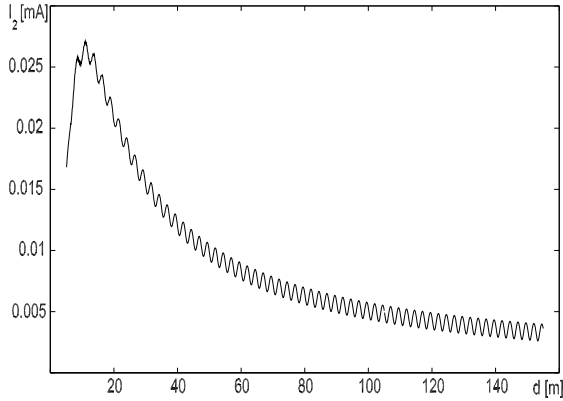


Fig. 6. Induced current at the second dipole as a function of the distance d to the perfectly conducting flat boundary layer.

C. Mandrel mounted antennas in a cylindrical borehole under consideration of perfectly conducting scatterers

Next, we remove the perfectly conducting boundary layer and consider two perfectly conducting spheres (see Fig. 7), which are modelled by using the appropriate RCSs found in the literature [7]. Due to their omnidirectional backscattering spheres are worst case geometries for subsurface detection. The wave propagation in the surrounding is modelled with a damping of $0.1\text{dB}/\text{m}$, which is a realistic value for salty ground. In Fig. 8 the induced current I_2 at the center of the second dipole is shown as a function of the position of the antennas. I_2 shows a very strong oscillation because for this configuration the scattered signal and the direct signal are of the same order of magnitude. It should be mentioned that in practical problems supply and control cables cause additional coupling between the transmitting and receiving antennas. Consequently, it is very important to suppress the direct signal by making use of time gating or other techniques. Therefore in Fig. 9 I_2 is shown in case that the direct signal has been suppressed. Obviously, the maxima appear when the center ($z' = 5$ m) of the two antennas is at the height of the scatterers.

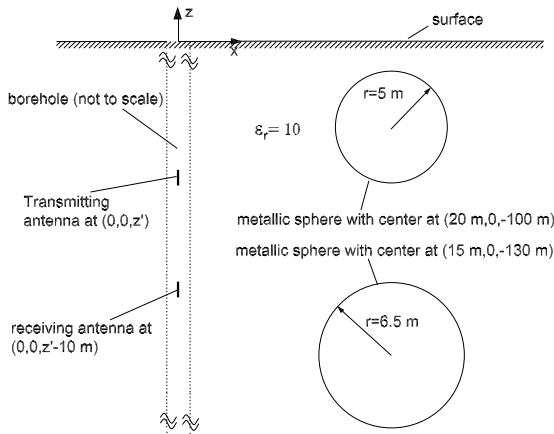


Fig. 7. Geometry consisting of two antennas and two perfectly conducting bodies far away from the antennas (borehole not to scale).

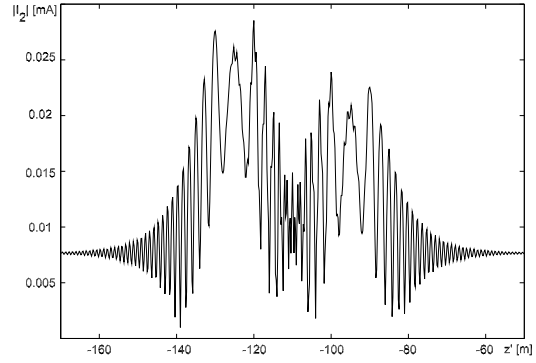


Fig. 8. Induced current at the second dipole as a function of the position z' .

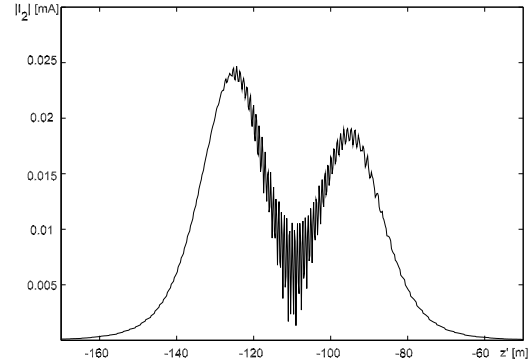


Fig. 9. Induced current at the second dipole as a function of the position z' (direct signal suppressed).

V. SUMMARY AND OUTLOOK

In this paper a tool to simulate dipole antennas in boreholes under consideration of large scatterers is proposed. This tool can be used on standard PCs, which are not suited to compute such structures with other often used numerical techniques (like the FDTD or the FEM) due to the resulting huge amount of necessary memory and CPU-time. Numerical examples are presented, which deal with the coupling of two dipole antennas in a 3-layer medium under consideration of a perfectly conducting flat boundary layer and two perfectly conducting bodies, respectively. The proposed method can easily be extended to model e.g. perfectly conducting wedges by considering diffracted rays in the solution procedure.

REFERENCES

- [1] Sadasiva M. Rao, Donald R. Wilson and Allen W. Glisson Electromagnetic Scattering by Surfaces of Arbitrary Shape, IEEE Transactions On Antennas and Propagation, VOL AP-30, NO. 3, MAY 1982
- [2] Calculation of Sommerfeld Integrals for Modeling Vertical Dipole Array Antenna for Borehole Radar, IEICE Trans. Elektron., VOL.E86-C, NO.10 OCT 2003
- [3] W. C. Chew, Waves and Field in Inhomogeneous Media, Piscataway, NJ: IEEE Press, 1995
- [4] Satoshi Ebihara, Directional Borehole Radar with Dipole Antenna Array Using Optical Modulators, IEEE Transactions On Geoscience and Remote Sensing , VOL 42, NO. 1, JAN 2004
- [5] C. A. Balanis, Antenna Theory, John Wiley & Sons, New York, 1982
- [6] C. A. Balanis, Advanced Engineering Electromagnetics, John Wiley & Sons, New York, 1989
- [7] E. F. Knott, M. T. Tuley, J. F. Shaeffer, Radar Cross Section, Artech House, 1985
- [8] Satoshi Ebihara, Masahiro Kiso, Frequency Spectrum Change of Borehole Radar Signals and Blind Separation, Proceedings of the 10th Conference on Ground Penetrating Radar, Delft, Netherlands, 2004

Compact Broadband Filters for Hybrid Circuits using Flip-Chip-Technology

Torben Baras, Faisal Muhammad and Arne F. Jacob

Arbeitsbereich Hochfrequenztechnik - Tech. Univ. Hamburg-Harburg, 21073 Hamburg, Germany

Tel: +49 40 42878 3370, Fax: +49 40 42878 2755, email: t.baras@tuhh.de

Abstract— A compact broadband filter is presented. The design is based on a microstrip substrate wherein half of the filter is located on a thinfilm chip and mounted in flip-chip fashion. Revealing a fractional bandwidth of as much as 50% and a measured insertion loss less than 1.5 dB at 20 GHz, the required real-estate remains small compared to state-of-the-art designs. Exemplarily, a hybrid K-Band doubler and buffer-amplifier were realized solely using flip-chip-technology in conjunction with the developed filters. Measured results agree very well with predictions from commercial software tools.

I. INTRODUCTION

Planar, ceramic based microwave circuits are widely used in communication systems. Especially in high end applications such as satellite communications, they are preferred for reliability reasons, facile processing and small feature sizes as little as $10\ \mu\text{m}$ by means of photolithography. Low Temperature Cofired Ceramics (LTCC) on the other hand allows the implementation of complex, though very compact RF-circuits in a multilayer substrate. While this technology is well known from mass market applications, the resolution in standard processes cannot be smaller than $100\ \mu\text{m}$.

In the presented approach, we extend a standard planar alumina substrate to a quasi multi-layer substrate by using flip-chip technology. Thus, this concept confines the advantages of both planar substrates and multilayer LTCC technology. Exemplarily, we verify this approach on vertical microwave filters. The design goals are a small size, low insertion loss, low return loss and a broadband transfer function, which inhibits DC current conduction from input to output port. This filter type can e.g. serve as a DC-block in order to separate two active stages on the bias level, where planar, interdigital capacitors [1] or coplanar quarter wave couplers [2] were utilized in the past. In the following, a detailed discussion is presented also covering the impact on manufacturing and placement tolerances.

II. FLIP-CHIP FILTER GEOMETRIES

The general concept of the developed filters is portrayed in Fig. 1: A microstrip alumina substrate contains one part of the filter structure. A second part is located on a chip without any back-metallization. Thus coupling occurs between both substrate and chip layer. The distance between chip and substrate is adjusted using appropriate gold stud bumps, which not only serve as electrical interconnects but also improve mechanical stability. The bumps in our filters were generated by means of a manual ball bonder (*Hybond*) using optical

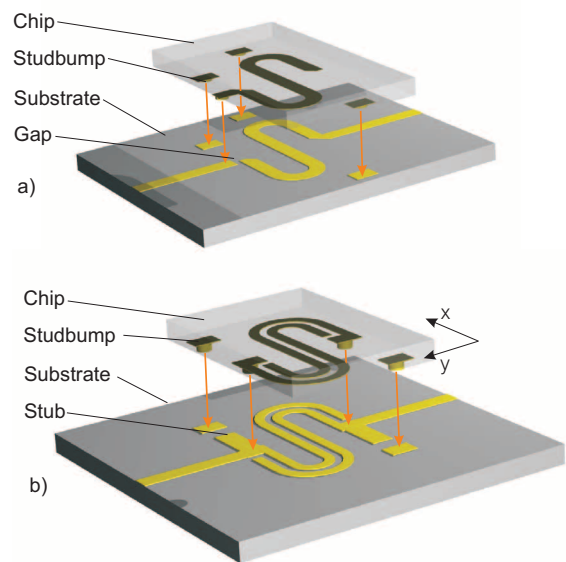


Fig. 1. Illustration of the vertically coupled line flip-chip filter (a) and broadband interdigital flip-chip filter (b): Part of the filter structure is located on the microstrip substrate, while the other part is added by mounting a small chip without backside metallization.

alignment procedures. The repeatability was determined to be approximately $10\ \mu\text{m}$ for lateral positioning. The attachment has been accomplished using thermocompression tools and a *Finetech* fineplacer with a placement accuracy of $5\ \mu\text{m}$ according to the manufacturers specification. The mounting profile of the chip was a linear temperature ramp of 7°K/s and a force of $1.0\ \text{N/bump}$.

A. Vertically Coupled Line Filter

A first investigated structure is a quarter wavelength vertically coupled line filter as illustrated in Fig. 1 (a). The line on the bottom substrate is equipped with a gap and the counterpart on the chip overlaps the meander in the same way. This quarter wavelength coupled line section is arranged in a S-shape for optimally occupying the real estate. The structure has been simulated and optimized using a 3D-software [3] and realized on alumina substrate with a nominal thickness of $127\ \mu\text{m}$ and a stud bump height of $20\ \mu\text{m}$. The realized test vehicle is shown in Fig. 2 together with measured and simulated results. The filter enables a very broad band of transmission with an upper resonance slightly above 40 GHz, which is determined by the

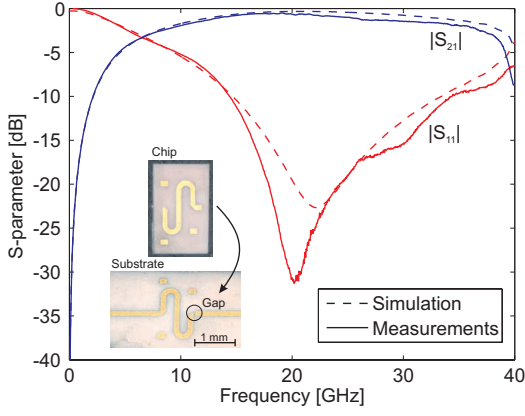


Fig. 2. Results of a 20 GHz center frequency vertically coupled line filter in flip-chip-technology. The stud bump height is approximately $30\ \mu\text{m}$. The inset shows designed test structures on alumina substrate.

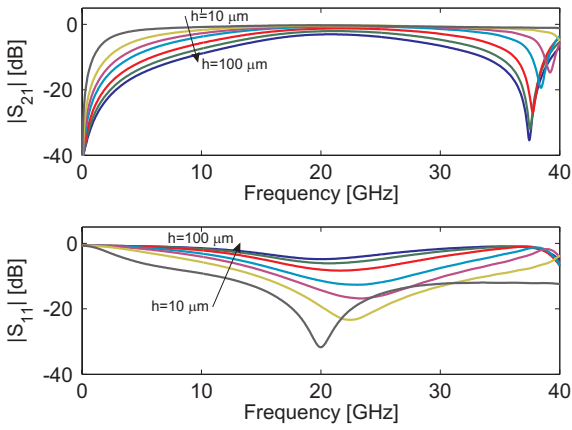


Fig. 3. Simulation results of the vertically coupled line filter for stud bump heights from $10\ \mu\text{m}$ to $100\ \mu\text{m}$.

overlap length.

The influence of the stud bump height on the filter characteristic was studied in the simulation program. Results of this analysis for a fixed coupled line width of $100\ \mu\text{m}$ are displayed in Fig. 3. Reducing the distance between chip and substrate increases the mutual capacitance between the vertically coupled lines, thus a general improvement in the transfer function is observed. In a physical structure, the final bump height is determined by its size before compression and the applied force. In our case, a height of $20\ \mu\text{m}$ could be conveniently reached. The repeatability is mainly determined by machine parameters that allow sufficiently tight control here.

B. Broadband Interdigital Filter

A second investigated structure is shown in Fig. 1 (b). The vertically coupled lines were extended by also introducing lateral coupling. A stub was added to improve the flatness in the passband region. Here, the stud bump height was chosen to $60\ \mu\text{m}$. Measured results for a 10 GHz center frequency filter

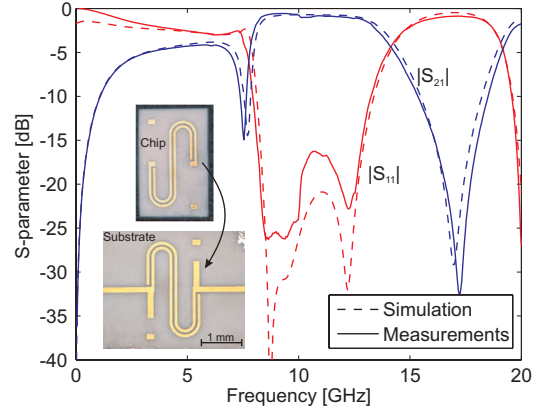


Fig. 4. Results of a 10 GHz center frequency flip-chip-filter with a stud bump height of approx. $60\ \mu\text{m}$. The inset shows designed test structures on alumina substrate.

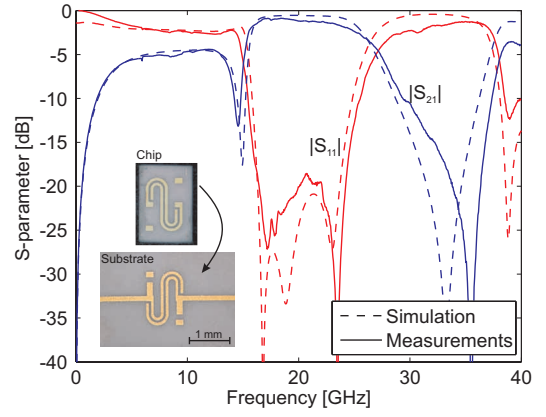


Fig. 5. Results of a 20 GHz center frequency flip-chip-filter with a stud bump height of approx. $60\ \mu\text{m}$. The inset shows designed test structures on alumina substrate.

are displayed in Fig. 4 together with the predictions of the software. Excellent agreement is revealed over the entire range with a passband from 8 to 13 GHz. The measured insertion loss is about 0.8 dB at center frequency.

Scalability of this type of filter was evaluated by a second filter, this time at a center frequency of 20 GHz, with a flat passband from 16 to 24 GHz. An insertions loss of 1.1 dB was measured showing a slight increase towards higher frequencies. While the agreement between simulations and measurements is excellent below 20 GHz, the software underestimates losses above this frequency. We attribute this effect to the surface roughness of the conductors and the ceramics as well as to the contact resistances, which can not be modeled in the software. Corresponding test vehicles are depicted in the insets in Figs. 4 and 5.

As in the previously proposed structure, a parameter study in simulations was utilized to gain knowledge of the influence of manufacturing tolerances on the filter performance. As seen in Fig. 6, an increase in height decreases the fractional bandwidth, while all deviations from $60\ \mu\text{m}$ target height

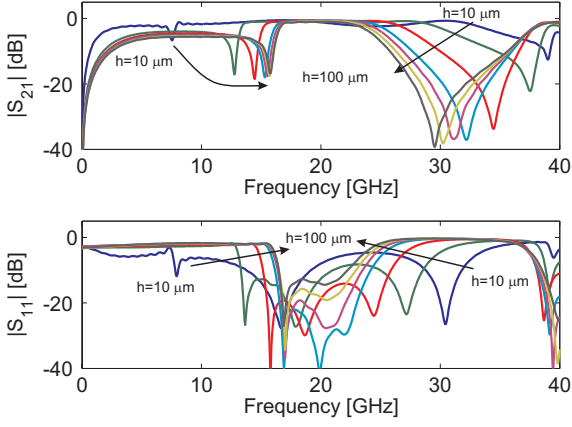


Fig. 6. Simulation results of the broadband interdigital filter for stud bump heights from $10\ \mu\text{m}$ to $100\ \mu\text{m}$.

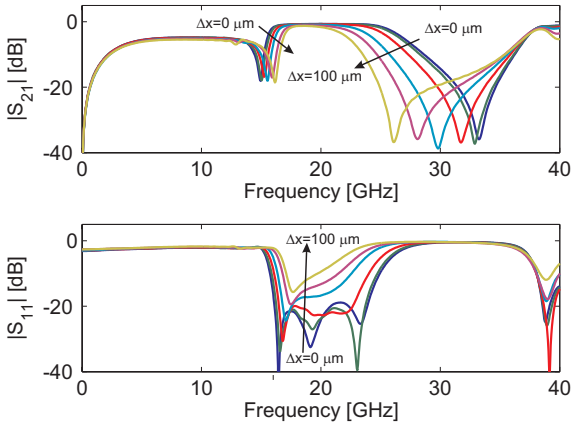


Fig. 7. Simulated placement tolerance analysis for a displaced chip by Δx from the ideal position relative to the substrate.

increase the input reflection.

Secondly, lateral placement tolerances (see Fig. 1 (b) for coordinate conventions) were investigated as shown in Figs. 7 and 8 in $20\ \mu\text{m}$ increments. For symmetry reasons, displacement in only positive directions needs to be considered. An offset in x -direction decreases the transmission bandwidth, while the input reflection increases. Up to a displacement of $\Delta x = 40\ \mu\text{m}$, the filter performance is only little affected. Similar tendencies can be seen in the results for y -displacements, which were simulated up to $\Delta y = 60\ \mu\text{m}$. Any larger value would cause the bumps to short the lateral coupled lines, which entirely changes the filter function. Yet the sensitivity to y -displacement is much lower as compared to x -displacements, since the S -shaped coupled line sections mostly take course in the same direction as the displacement. Within the simulated range no significant change is observed.

III. HYBRID CIRCUIT DESIGNS

In this work, we exclusively used flip-chip technology on a thinfilm alumina substrate ($h=127\ \mu\text{m}$), as shown in Fig. 9.

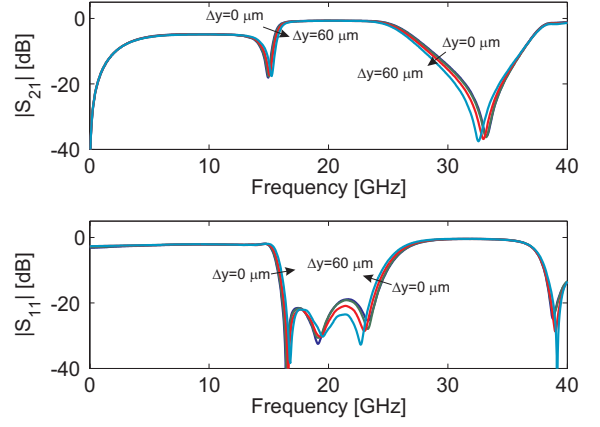


Fig. 8. Simulated placement tolerance analysis for a displaced chip by Δy from the ideal position relative to the substrate

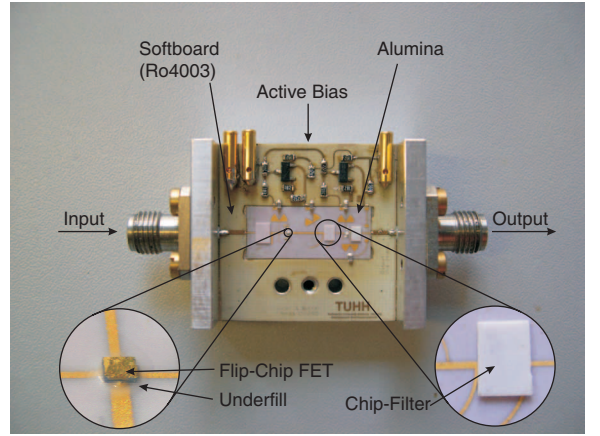


Fig. 9. Used package style for evaluating the designed hybrid circuits: A softboard (Ro4003) hosting active bias electronics and connections to the SMA-connectors is framing the hybrid circuit designed on alumina substrate. The chip components were exclusively mounted in flip-chip-technology using thermo-compression techniques.

In order to facilitate biasing of the circuits, an active biasing network was employed as proposed in [4], located on one side of the soft-substrate. The used transistor is a discrete low noise pHEMT (*EPB018A5* of *Excelics Semiconductor*) that was mounted and simulated in a flip-chip fashion by modifying bond-inductances and bond pad capacitances in the manufacturers model. The chip dimensions are $290 \times 320\ \mu\text{m}$ wherein the smallest pad is $60 \times 68\ \mu\text{m}$, thus the placed stud bumps must not exceed $50\ \mu\text{m}$ in diameter in order to provide a margin for compression. The chip was mounted in the same way as the filters, not exceeding 300°C (maximum temperature as per manufacturer).

The first here presented circuit is a frequency doubler for input signals around a center frequency of $10\ \text{GHz}$ (see Fig. 10 (a) for layout details). It is based on a single FET design operated in the vicinity of the transistors pinch-off region. For the core design, a reflector type topology was adapted [5]: Two filters are located at the gate and the drain terminals,

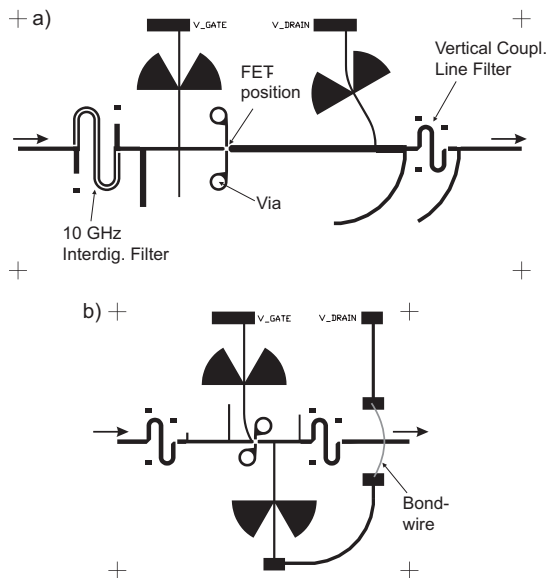


Fig. 10. Layouts of the designed circuits on Al_2O_3 substrate with thickness of $127\ \mu\text{m}$: a) X-Band/K-Band doubler and b) K-Band buffer amplifier (designs are shown without mounted chips).

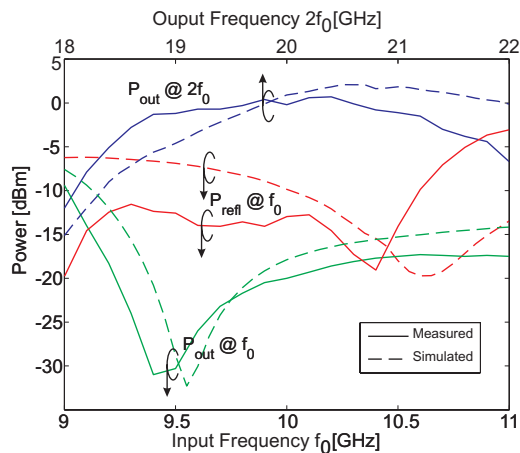


Fig. 11. Measured and simulated output power of the leaking fundamental, the desired first harmonic and the reflected power at the input terminal. The circuit was driven with a constant input power of $4\ \text{dBm}$ at f_0 .

wherein the filter at the gate contact is transparent for signals at the fundamental frequency f_0 but reflects the generated harmonic $2f_0$ and vice versa for the drain terminal. In our case, the presented vertically coupled line filter could be directly inserted in the output reflection network (see layout), thus improving miniaturization of the circuit. Both measured and simulated results for the developed circuit are shown in Fig. 11. The frequency sweep shows some inconsistency in the reflected power, which in turn impacts the conversion efficiency. We attribute this observation to uncertainties in the transistor model, which are known to occur especially at bias points close to pinch-off. The second herein presented circuit is a single FET amplifier (for layout see Fig. 10 (b)), which was designed for buffering signals of the proposed doubler or Ka-Band VCOs in general. The FET is biased at a drain

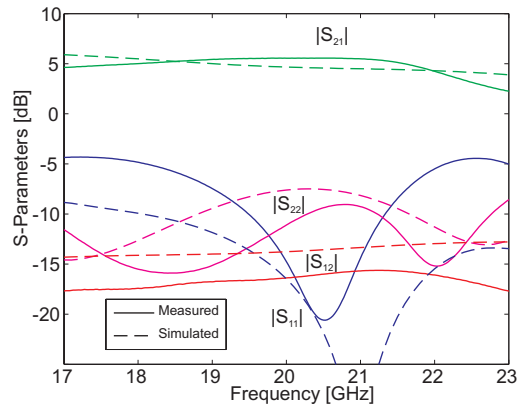


Fig. 12. Measured and simulated scattering parameters of the designed buffer K-band amplifier.

current of $I_{DS}=25\ \text{mA}$. This circuit solely uses the coupled line filters as DC-blocks, which especially at the gate side help to achieve stable operation. According to the results shown in Fig. 12, the forward gain of approximately $5\ \text{dB}$, the reverse isolation and output matching perform equal or even better than simulated. Again the input reflection is increased as in the application of the doubler before.

IV. CONCLUSIONS

Multilayer filters utilizing planar substrate technology were realized by means of flip-chip interconnects. Measured results and simulations of the presented prototypes agree very well, revealing a low insertion loss between 0.7 and $1.1\ \text{dB}$ at center frequency. A placement tolerance analysis showed, that uncertainties associated with the manufacturing equipment has only a minor impact on the performance. The functionality of the filters could be successfully demonstrated in two active circuits. The proposed method appears to be a useful alternative to realize multilayer circuits on planar substrates, where true multilayer technology cannot be applied.

ACKNOWLEDGMENT

The authors wish to acknowledge funding and support of this work by the German Aerospace Center (DLR) on behalf of the German Ministry of Education and Research (BMBF) under research contract 50 YB 0314.

REFERENCES

- [1] W. Dressel, T. Mangold, L. Vietzorreck, and P. Russer, "Time domain characterization of multichip module elements," *Microwave Symposium Digest, 2001 IEEE MTT-S International*, vol. 2, pp. 1033–1036, 2001.
- [2] I. Huynen and G. Dambrine, "A novel CPW DC-blocking topology with improved matching at W-band," *IEEE Microwave and Guided Wave Letters*, vol. 8, no. 4, pp. 149–151, 1998.
- [3] Computer Simulation Technologies GmbH, "Microwave Studio, version 5.1.2," www.cst.de.
- [4] Agilent Technologies, "Direct broadcast satellite systems, application note A009," www.semiconductor.agilent.com, 1999.
- [5] Y. Iyama, A. Iida, T. Takagi, and S. Urasaki, "Second-harmonic reflector type high-gain FET frequency doubler operating in K-band," *Microwave Symposium Digest, 1989, IEEE MTT-S International*, vol. 3, pp. 1291–1294, 1989.

A lumped element circulator with semi-additive metallized conductors

Robert Stonies, Daniel Teufer and Dirk Schulz
High Frequency Institute
University of Dortmund
Germany
Email: robert.stonies@udo.edu

Abstract—A symmetrical 3-port lumped element circulator built by the use of thin film technology including electroplating is presented allowing very compact devices.

A semi-additive metallization process yields high accuracy in reproduction of the structure with small features while allowing the implementation of via-holes. Two technological procedures are presented and compared.

The lumped element circulator performance is numerically calculated and optimized to some extent, providing valuable information about important device performances. A comparison with measured scattering parameters shows good agreement with the calculation.

I. INTRODUCTION

Circulators and isolators are the most important non-reciprocal passive devices in microwave engineering. They have been discussed in detail concerning their design, principles of operation and their performance.

Among the regarding publications, many kinds of circulators, in particular waveguide and stripline circulators, have been examined with numerical methods to characterize them. However, to the knowledge of the authors, lumped elements have not been treated this way so far. The reason may be that high aspect ratios and complex gyromagnetic media cause some difficulties in the numerical simulation.

This paper demonstrates the power of a numerical approach for the design and optimization of compact lumped element circulators that among others yields inner quantities such as field distributions and measurable outer quantities such as scattering parameters.

Further investigations and new designs that are reasonable for industrial production processes are of great interest due to the rising demand for mobile r.f. and microwave systems.

This work presents a small, fully symmetrical 3-port circulator designed for a popular ISM-frequency. A hybrid setup is chosen due to the advantage of using standard industrial processes for the production of printed circuit boards to realize the coupling network and additional reactive lumped elements. Even though the isolation-bandwidth is about 70 MHz only for the presented sample device, broadband types may be developed through further design optimizations including additional matching elements and a careful selection of the ferrite material.

Starting with a basic structure taken from [1], numerical simulations are performed. Geometric parameters are modified

until the circulator works at the desired frequency and shows an acceptable performance.

Finally, a circulator is built and the simulations are compared with measurements to proof the results.

II. DESIGN CONSIDERATIONS

The most frequently used passive non-reciprocal device is a 3-port circulator or an isolator, respectively. The latter one is typically obtained from the circulator by the termination of one port.

In contrast to distributed devices such as the stripline-junction-circulator inter alia discussed by Bosma [2] and Fay [3], circulators built from lumped elements are comparably small. There is no need to satisfy the well known condition $kR = 1.84$ [2], [4] for the normal mode excitation of a ferrite disc where R denotes the radius of the thin disc and

$$k^2 = \omega^2 \epsilon_r \epsilon_0 \mu_0 \left[\frac{\mu^2 - \kappa^2}{\mu} \right]. \quad (1)$$

Herein k is the wavenumber and μ as well as κ are elements of the Polder tensor appropriate to a normally magnetized ferrite disc.

$$\overleftrightarrow{\boldsymbol{\mu}} = \begin{bmatrix} \mu & -j\kappa & 0 \\ j\kappa & \mu & 0 \\ 0 & 0 & 1 \end{bmatrix} \quad (2)$$

For a lumped element circulator a size-reduction of 5-10 [5] referring to distributed circulators can be achieved with adequate performance. Without loss of generality a 2.45 GHz (center frequency) device is exemplarily dealt with in the following.

The most interesting part of a lumped element circulator is the magnetic circuit, sometimes named isoductor. It consists of a coupling network that is at least partly embedded into gyromagnetic media invoking the non-reciprocity. A simple equivalent circuit for a circulator therefore shows three coupled inductors and an additional capacitor at each port for tuning (figure 1a). Performance is - amongst others - influenced by the coupling between the inductors L , which depends upon ferrite properties and the geometry of the coupling network.

Details about general theory of lumped element circulators are discussed in some detail in [1], [4], [6]–[11].

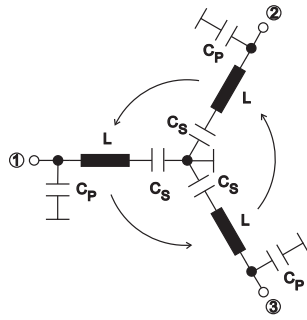


Fig. 1. Equivalent circuit with additional capacitors for tuning and matching

The addition of series and parallel capacitors allows to tune and match the circulator (figure 1 b). By adding more reactive parts including inductors, the matching can be converted from narrow band to broadband. The elements of the matching network are to be placed carefully not to invoke unwanted influence to the non-reciprocal magnetic circuit.

In case of our small 2.45 GHz lumped element circulator RG4 ferrite material from AFT company (Backnang, Germany) is used. The saturation magnetization of this material is $80 \text{ kA}\cdot\text{m}^{-1}$ and the dielectric constant is 14.3 with a loss tangent of $0.94\cdot 10^{-4}$. A magnetic dc bias field is used to saturate the ferrite and results in *above resonance* condition.

Having started with some analytical calculations such as an estimation about the capacitance needed to resonate at the desired frequency for a given inductor length, numerical simulations are made now to include parasitics and obtain detailed information about field quantities on the one hand and performance on the other hand.

Two different technological concepts are investigated and compared with respect to their suitability. The first one is a double-sided standard printed circuit board process with drilled via-holes, typically used in modern fabrication. The second one is a sequential layer build-up process facilitating a very thin insulation layer between the conductor layers as well as very fine structure features with high accuracy. Both processes have in common that a semi-additive metallization process is used to form the lumped elements.

III. SIMULATION AND OPTIMIZATION

Nowadays, high frequency circuits are most often designed using numerical computations. Running the programs on usual personal computers is fast enough for almost any common problem to be solved. A computer program that suits to calculate the characteristics of a lumped element circulator is *Microwave Studio*© (CST company, Germany), because the necessary algorithms for gyromagnetic media are included. Furthermore, non-uniform meshing is implemented enabling to handle the high aspect ratios of these devices.

Based on the finite integration technique, the integral counterpart of the finite differences in time domain approach, the lumped element circulator is solved full three-dimensionally. The physical model is completely generated out of basic

shapes using a visual basic script. This gives the possibility for parametric sweeps of all model parameters that may become of interest.

As an important result of the calculation scattering parameters are obtained. Assuming only linear behavior, they characterize the the 3-port completely.

Moreover, the numerical treatment of the lumped element circulator with the finite integration scheme gives valuable insight into the device. Among others, critical electrical field strengths can be found and places of high losses can be detected. With the help of all this information, the structure can be improved.

Parasitic elements are included a priori and there is no restriction regarding the geometry in opposite to pure analytical approaches. An exemplary model is depicted in figure 2.

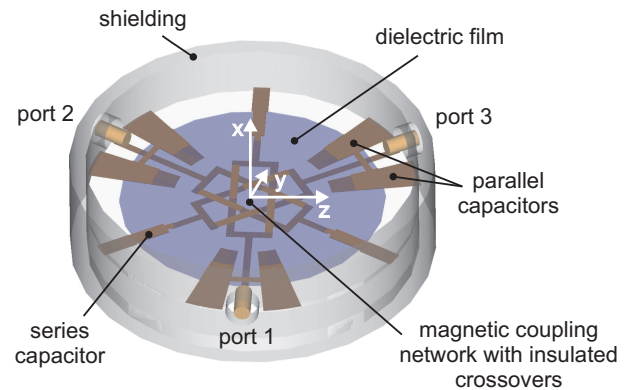


Fig. 2. Three-dimensional view of the simulation model's geometry showing the interwoven conductor structure, ports and some additional lumped capacitors

The parasitics appear to influence the characteristics in particular. Especially the crossover capacities are responsible for a significant decrease of the operating frequency.

The calculation time is within the range of several hours up to a week depending on the number of mesh cells necessary to approximate the structures. Execution time also depends on the frequency range of interest as the excitation function is correlated to it.

To speed up the calculation, the lumped capacitors may be substituted through idealized capacitors first, virtually connected between two mesh points. Once the necessary capacity is evaluated, a separate parametric simulation model including a single capacitor model can be used to obtain the exact geometries. To be more exact with that capacitors, a full three-dimensional electrodynamic calculation is performed at the design center frequency. Finally, the geometries of all simulations are combined into one CAD-file and masks are generated.

As can be concluded from figure 3 and as expected, fringing fields tend to increase the capacity to an amount that does not allow to neglect them. It is supposed that electric field quantities resulting from an excitation with 1 W input power at 2.45 GHz (figure 4) are well below the dielectric breakdown limitations of the insulation.

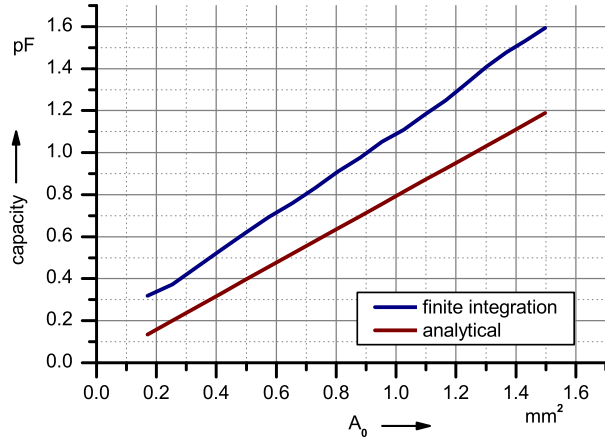


Fig. 3. Comparison between analytically calculated capacity using the formula for an ideal parallel-plate capacitor and a full three-dimensional electro-dynamically calculated capacity

Assuming linearity an estimation of the power handling capability is possible.

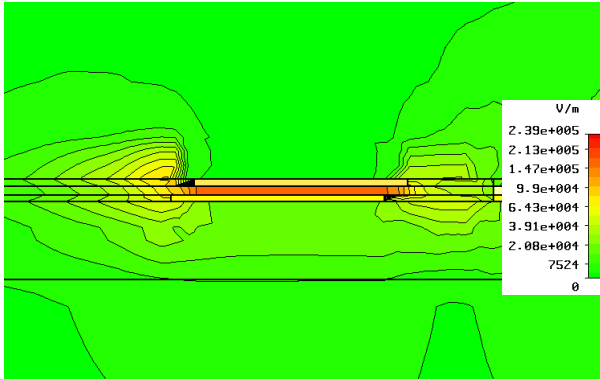


Fig. 4. Electric field (plane $y=0$ as indicated in figure 2) concentrating in the vicinity of crossing conductors, normalized to 1 W input power at 2.5 GHz

Another interesting observation, already predicted in [7], is that the r.f. magnetic field is not at all homogeneously distributed in the ferrites. It is rather clearly concentrated around the conductors (figure 5). The ferrites' bulk shows a magnetic field that is less than 10 percent of the field close to the conductor.

IV. TECHNOLOGICAL ASPECTS

At least two conductor layers with an insulation in between are a prerequisite for the interwoven coupling network. Two different processes are evaluated, both involving a *semi-additive metallization*.

A. Common double-sided printed circuit board process

This manufacturing process is common in the electronic industry for the production of two-sided microwave circuit boards based on PTFE or ceramic substrates.

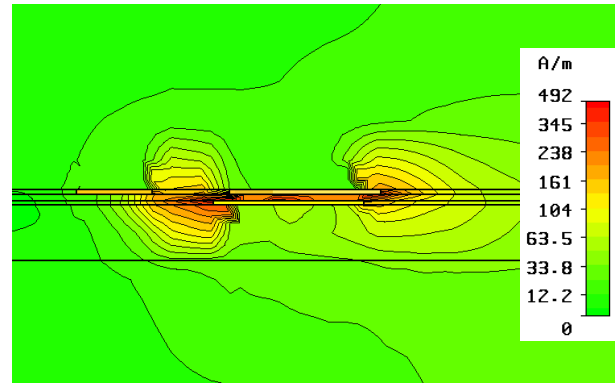


Fig. 5. Magnetic field (plane $y=0$ as indicated in figure 2) concentrating in the vicinity of conductors, normalized to 1 W input power at 2.5 GHz

The substrate materials used for in this case, FR4 glass reinforced epoxy (140 μm) and MylarTM (DuPont) polyester film (175 μm), are drilled (250 μm diameter) to form the necessary via-holes first. Sputtering thin layers of titanium and copper on both sides gives adhesion and basic conductivity. Furthermore, the vias are activated for later electroplating implicitly. A 25 μm dry film photoresist FP325 (Elga Europe) is laminated on both sides and structured with a MA56 mask aligner (Suess). Electroplating is now used to grow copper into the resist grooves and form the conductors. Because of the complicated structure with an island-like topology and the combination of very small and big feature sizes this is a difficult task. A simple acidic copper electroplating bath without special additives or widely used *high speed* electrolytes would not yield good results because of a bad thickness distribution or very rough surfaces. A newly developed acidic copper electrolyte system *CVF-1* (Enthone) is successfully applied. It is especially intended to be used in via-fill applications and produces very plane surfaces and shows a good homogeneity of thickness.

After electroplating, the resist is stripped and the seed layers are removed through chemical etching. The structures look like the one depicted in figure 6 a.

B. Sequential layer build-up

The sequential layer build-up process does not need drilling and allows very thin insulation layers. Furthermore, only single-sided processing takes place simplifying the handling of the substrates. Even materials may be used that are difficult to machine such as ceramics.

First, the substrate is coated with titanium and copper on one side through sputtering to provide a seed layer for later electroplating. Then, the FP325 dry film resist is laminated and structured. Copper is electroplated to a height of 15 μm into the grooves. The resist is stripped and the seed layers are etched. Now, a second layer of FP325 is laminated on top. It is structured with the via and feed-line pattern before the surface is completely sputter-coated with titanium and copper again. An additional electroplating process enhances the layer thickness to 15 μm . Finally, AZ-3210 (ALLRESIST), a thick

film positiv photo resist, is spin-coated onto the sample and structured to protect the later bridges and vias of the top layer from being etched in the following.

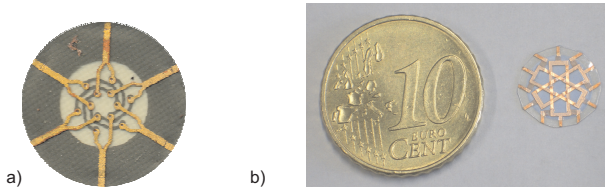


Fig. 6. Photo of two final substrates (10 mm diameter) carrying lumped element structures, a) two-sided isoductor with drilled via-holes, b) sequentially built structure with lumped capacitors and FP325 insulation layer

The layout used to structure the bottom conductors in the second process includes additional interdigital lumped capacitors for matching and tuning. SEM pictures of two different types are depicted in figure 7.

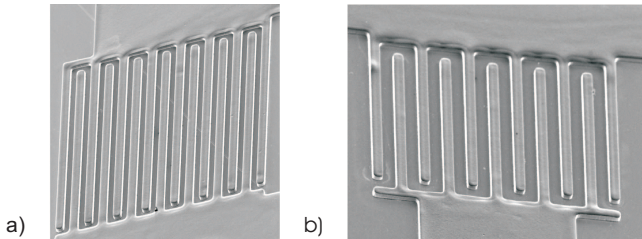


Fig. 7. Scanning electron microscope pictures of the capacitors (metallization thickness $15 \mu\text{m}$), a) parallel capacitor with $30 \mu\text{m}$ wide, $713 \mu\text{m}$ long and $17 \mu\text{m}$ spaced arms b) series capacitor with $30 \mu\text{m}$ wide, $470 \mu\text{m}$ long and $30 \mu\text{m}$ spaced arms

The process described first does not include additional capacitors. Only the coupling network is realized to compare to the results of the simulation. However, this structure is included to offer an alternative and industrial conformal process. The sequential layer build-up appears to be more reliable and is therefore preferred and extended with additional elements.

V. COMPARISON WITH MEASURED DATA

To verify the calculated performance, the structures are mounted into a jig (figure 8) containing the ferrites and providing the SMA connectors to interface to a vectorial network analyzer.

It is noticeable from figure 8 that the *active* part of the circulator is small compared to the complete jig. More compact cases are currently under construction.

A 360B vectorial network analyzer (Wiltron) is used to record scattering parameters. The dc magnetic field is generated by a current-controlled electromagnet with a slitted yoke (figure 9).

For the double-sided processed structure including drilled vias, figure 10 shows a comparison between the calculated and measured performance. It should be recalled that the layout for the structure only consists of the isoductor conductors. No capacitors are included and hence there is only the small parasitic capacity of the line-crossings that act as a tuning

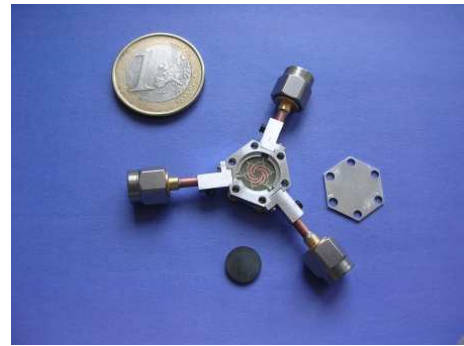


Fig. 8. Jig with SMA-connectors and mounted lumped element substrate to connect to a network analyzer

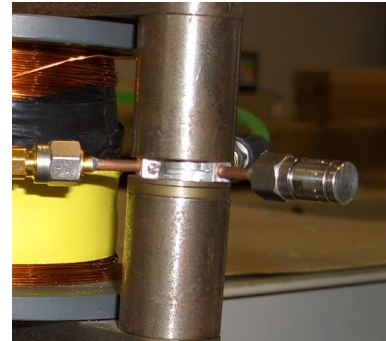


Fig. 9. Fully assembled circulator mounted into the electromagnet's yoke slit, one port is terminated with 50Ω

element for the device. This leads to a much higher resonance frequency close to the gyromagnetic resonance frequency, reduces bandwidth and implies higher insertion losses. The inclusion of explicit lumped tuning elements is no problem at all and similar to the sequential layer build-up.

A second structure, provided by the sequential layer build-up process, is also measured and the scattering parameters are compared with the calculated ones. As can be seen from figure 11, the measured data agree with the data resulting from a numerical calculation but the center frequency is slightly shifted to lower frequencies. The authors assume that the reasons for this shift are inaccuracies in the calculation and in the technological process. First, the ferrite is treated as to be magnetized completely homogeneously, which is not true in reality. Magnetostatic calculations show, as expected, that the magnetic field is much stronger close to the circumference than it is in the middle of the thin disc. Second, thin layers are represented by one mesh-cell in height only to keep the time for calculation short. This may lead to some inaccuracies, especially concerning the field distribution at edges.

Nevertheless, the comparison shows a good agreement and with some correction and modifications it will be possible to predict the behavior of a lumped element circulator with high accuracy by means of numerical calculations.

ACKNOWLEDGMENT

The authors would like to thank M. Kilouli and H. Verbunt from Enthone for an excellent support and valuable discussions about the electroplating process. They would also like to thank W. Arnold and U. Hoeppe from AFT for supplying the ferrite material.

REFERENCES

- [1] R. Knerr, C. E. Barnes, and F. Bosch, "A compact broad-band thin-film lumped-element l-band circulator," *IEEE Transactions on Microwave Theory and Techniques*, vol. 18, no. 12, pp. 1100–1108, 12 1970.
- [2] H. Bosma, "On stripline y-circulation at uhf," *IEEE Transactions on Microwave Theory and Techniques*, vol. 12, pp. 61–72, 1 1964.
- [3] C. E. Fay and R. L. Comstock, "Operation of the ferrite junction circulator," *IEEE Transactions on Microwave Theory and Techniques*, vol. 13, no. 1, pp. 15–27, Januar 1965.
- [4] J. Helszajn, *Principles of Microwave Ferrite Engineering*. Wiley-Interscience, 1969.
- [5] I. Ikushima and M. Maeda, "A temperature-stabilized broad-band lumped-element circulator," *IEEE Transactions on Microwave Theory and Techniques*, vol. 22, no. 12, pp. 1220–1225, Dezember 1974.
- [6] R. Knerr, "A lumped-element circulator without crossovers," *IEEE Transactions on Microwave Theory and Techniques*, pp. 544–548, 5 1974.
- [7] A. Schuchinsky, "Lumped element circulator (lec) with variable couplings," *IEEE MTT-S Digest*, pp. 1165–1168, 1999.
- [8] H. Katoh, "Temperature-stabilized 1.7-ghz broad-band lumped-element circulator," *IEEE Transactions on Microwave Theory and Techniques*, vol. MTT-23, no. 8, pp. 689–696, 8 1975.
- [9] J. Deutsch and B. Wieser, "Resonance isolator and y circulator with lumped elements at vhf," *IEEE Transactions on Magnetics*, vol. 2, no. 3, pp. 278–282, 9 1966.
- [10] E. Fliegler, "A 350-mhz broad-band lumped element circulator as a protective isolator," *IEEE Transactions on Microwave Theory and Techniques*, 5 1969.
- [11] I. Ikushima and M. Maeda, "A temperature-stabilized broad-band lumped-element circulator," *IEEE Transactions on Microwave Theory and Techniques*, vol. 22, no. 12, pp. 1220–1225, 12 1974.
- [12] R. H. Knerr, "A compact thin film lumped element circulator using a capacitor, common to all three arms, for broadbanding or switching," *International Microwave Symposium*, vol. G, pp. 393–396, 5 1970.

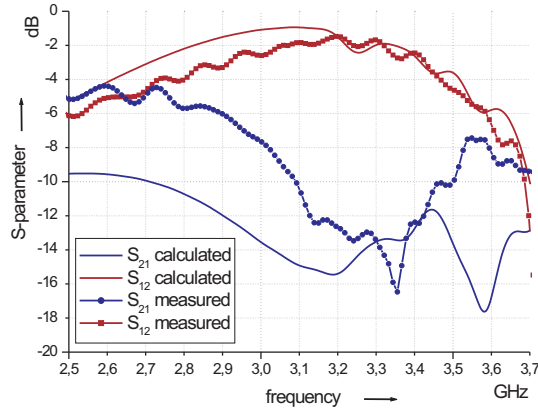


Fig. 10. Calculated and measured S-parameters of a circulator with a structure processed double sided with drilled vias

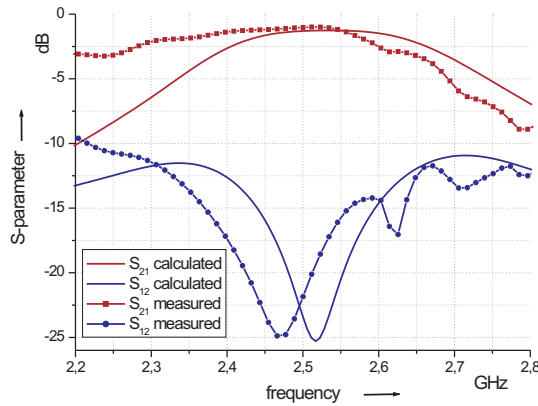


Fig. 11. Calculated and measured S-parameters of a circulator with a structure processed with a sequential layer build-up

VI. CONCLUSION AND OUTLOOK

A very compact L-band lumped element circulator is developed and built using industrial standard techniques. It is shown that a numerical computation can be used efficiently to design the device and to perform optimizations. Electroplating is used to build three-dimensional structures such as an interwoven conductor network and interdigital capacitors. The hybrid character of the devices results in high flexibility as it is possible to exchange the substrates carrying the lumped elements independently. Field distributions are examined to gain information about critical parts and to optimize the magnetic coupling circuit. Further designs will be made incorporating additional elements for broadbanding [12] and an enhanced simulation model will be setup to allow for better and faster prediction of the device characteristics. Further miniaturization and power handling capabilities will be examined as well as the temperature dependency that may be compensated by additional lumped elements [8].

Ka-Band Diplexer Design Using Filter Characteristics with Transmission Zeros - Realised *Without* Implementation of Cross Couplings

Uwe Rosenberg¹, Jürgen Ebinger¹ and Smain Amari²

¹Ericsson GmbH, Microwave Technology Center, Gerberstr. 33, 71522 Backnang, Germany,
Phone: +49 (0)7191 132744, uwe.rosenberg@ieee.org

²Royal Military College, Department of Electrical and Computer Engineering, Kingston, ON, Canada K7K 7B4,
smain.amari@rmc.ca

Short Abstract— A novel diplexer design is introduced that uses filter characteristics with transmission zeros (TZs). These TZs are realized by dedicated cavity resonances at the single filter input ports. This approach allows an overall compact design since there are no structural constraints as in conventional configurations with cross coupled cavities. All cavities are arranged in an H-plane structure. The interfacing of the respective cavities at all ports by E-plane T-junctions facilitate the compactness. They are realized at one side (below the cavity structure) for easy integration and mounting. The frequency allocations of the different channels can be easily exchanged by mounting the diplexer in a 180-degree position. This is possible due to a point symmetry for the single channel ports with respect to the common port. The approach has been verified by several diplexer designs for Ka-band applications. As an example, a 28GHz diplexer with 6th order filters is presented – good coincidence of theoretical and measured results demonstrate the validity of the approach.

Keywords-component; waveguide diplexer; asymmetric filter characteristics; extracted pole filters; symmetrical interface ports

I. INTRODUCTION

Transceiver equipment for radio or satellite transmission systems often use waveguide diplexers for the separation of the receive and transmit signals served by the antenna. These diplexers are commonly of the branching type, i.e., the two filters are directly connected to a suited 3-port waveguide junction providing the common port (e.g., [1]). In the eighties 3D electromagnetic CAD tools based on methods such as mode matching or finite element methods became available. Since then there has been a continuous effort focused on suitable 3-port junction structures for the interconnection of the filters (e.g., [2-6]). In most of these designs standard inline cavity filters are used providing a standard Chebyshev response with theoretically all transmission zeros at infinity. In recent designs [5,6] filter responses with transmission zeros at finite frequencies were used. Thus, tailored filter functions can be realized to achieve the required isolation between the frequency bands with a lower filter order compared to the standard Chebyshev designs. The main advantages are lower insertion loss and smaller size due to the lower number of

cavities. However, the introduced designs [5,6] use cross couplings in triplet or quadruplet cavity structures for the realization of the transmission zeros. Therefore, there are constraints and limitations for the overall diplexer structure including a suitable alignment/positioning of the three interface ports.

In this contribution a diplexer design is presented that uses filter characteristics with transmission zeros at finite frequencies. The transmission zeros are brought about by assigned cavity resonances directly coupled to the single filter input ports. The remaining filter resonances are sequentially coupled from the respective single port interface to the common port. Hence, this concept allows a flexible arrangement of the cavities without the restrictions of grouped cross coupled cavity configurations. This flexibility can be used for overall compact diplexer arrangements considering the single port locations symmetrical to the common port position. The latter aspect provides easy change of the lower and upper frequency band allocations at the respective interfaces by mounting the unit in a 180-degree position, since all interfaces are situated on one side. The advantages of this novel concept are demonstrated by a 28GHz diplexer with 6th order filters. Good coincidence of computed and measured results prove the overall design approach.

II. FILTER DESIGN

A diplexer design task generally starts with the evaluation of appropriate filter functions for a given specification. The main requirements of the 28GHz diplexer design are summarized in table 1. The most relevant rejection requirement for the filter characteristics results from the isolation between the served frequency band which is the closest to the passband. In addition the environmental and technological aspects have to be considered. For example, a low cost realization from aluminum at 28GHz, has to take into account the frequency change of ± 35 MHz over the operating temperature range due to the material expansion. This is, the filter passband has to be enlarged and the stopband requirements have to be considered closer to the passband.

TABLE I. SUMMARY OF SPECIFICATIONS

Passband 1:	28.05 to 28.45 GHz
Passband 2:	29.06 to 29.46 GHz
Insertion loss:	<1dB
(between common and single ports in the respective useful band)	
Return loss:	<-20dB
Rejection/Isolation:	>70dB
(between the single filter ports within the passbands)	
Rejection at ± 2.5 GHz:	>60dB
(between common and single filter ports)	
Operating temperature range:	-45 to 60°C
Interfaces:	WR34 at all ports

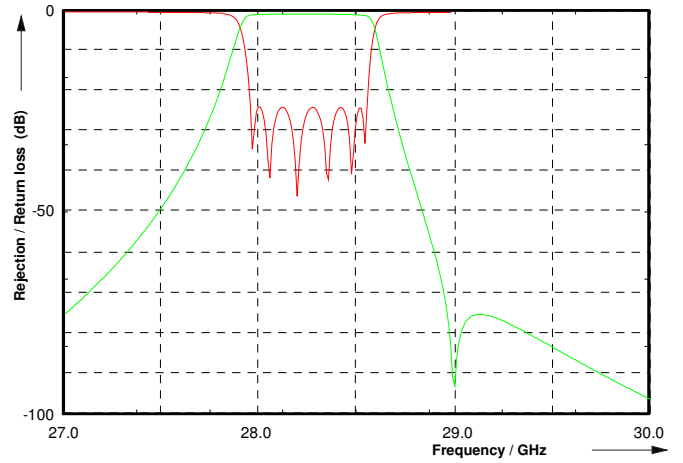


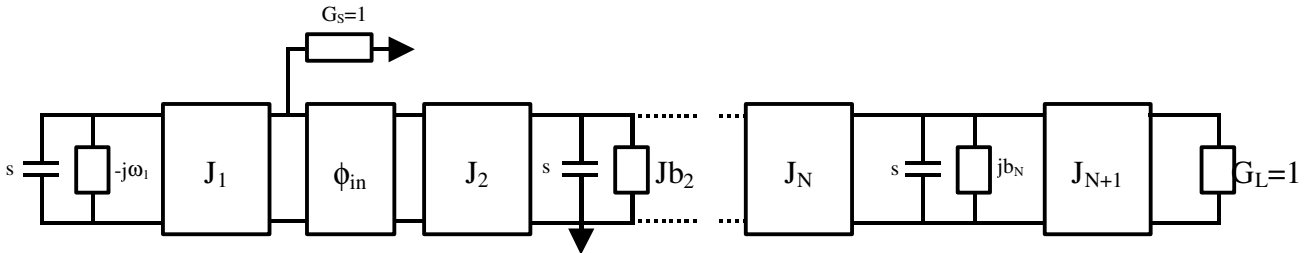
Figure 1. Synthesized characteristic of the filter for the lower passband

The investigations of all relevant aspects for a compact and low cost design yield 6th order filter functions with a 600MHz passband (return loss 23dB) and one transmission zero 800MHz above or below the passband, respectively, i.e., at the passband of the other diplexer filter. Fig. 1 shows, for example, the synthesized filter characteristic for the lower band filter of the diplexer. Each transmission zero is implemented by a cavity resonance coupled to one interface port of the filter (extracted pole, cf. [7]), while the other resonances are sequentially coupled from the input to the output port. Thus, all couplings of the filters can have the same nature since there are no particular sign conventions for the generation of transmission zeros as in cross coupled filter structures. That is, both filters have the same configuration which facilitates a symmetrical arrangement for the final diplexer interfacing.

The normalized coupling values of the single filters are obtained by following e.g. the synthesis in [7], which also provides the frequency offsets of the resonances and the required phases between the extracted pole cavity and the first

sequentially coupled resonator. Both filters exhibit very similar coupling values (cf. Fig. 2). The main difference are the frequencies of the extracted pole cavities and the phases between these cavities and the respective first sequentially coupled filter cavities.

An H-plane cavity structure has been chosen for the realization of these filter characteristics. The required phase between the input and the first sequential coupled cavity is realized by the length of a waveguide section. The cavities at the interfaces are directly coupled by E-plane junctions, that is, the interfaces are perpendicular to the cavity structure. The inline structure of the filters is folded to accommodate with an overall compact design with symmetrical interface locations (cf. next section).



Lower band filter: ($f_0 = 28.25$ GHz, $BW = 600$ MHz, TZ at 29.05 GHz, $R = 23$ dB, $n = 6$):

$$J_1 = 2.2688, J_2 = 0.3726, J_3 = 0.6443, J_4 = 0.5997, J_5 = 0.6319, J_6 = 0.8993, J_7 = 1.0633$$

$$\phi = -63.96^\circ$$

$$b_1 = -2.6299, b_2 = 0.3067, b_3 = 0.0519, b_4 = 0.0210, b_5 = 0.0126, b_6 = 0.0100$$

Upper band filter: ($f_0 = 29.26$ GHz, $BW = 600$ MHz, TZ at 28.46 GHz, $R = 23$ dB, $n = 6$):

$$\phi = 64.76^\circ$$

$$J_1 = 2.3446, J_2 = 0.3619, J_3 = 0.6436, J_4 = 0.5997, J_5 = 0.6319, J_6 = 0.8993, J_7 = 1.0633$$

$$b_1 = 2.7041, b_2 = -0.2993, b_3 = -0.0504, b_4 = -0.0204, b_5 = -0.0123, b_6 = -0.0097$$

Figure 2. Top: Low pass circuit of N^{th} order extracted pole filter with on transmission zero at $s_1 = j\omega_1$; Bottom: Normalized coupling values, phase shifts and center frequency offsets of the lower and upper band filters for the diplexer design

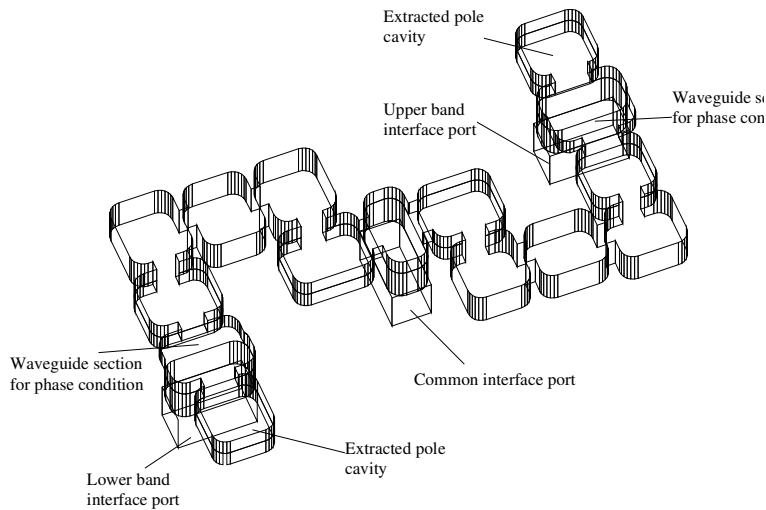


Figure 3. Outline of diplexer structure

III. DIPLEXER CONFIGURATION

Fig. 3 depicts an outline of the diplexer configuration with the H-plane cavity filter structures. All interfaces are realized by E-plane T-junctions. The five sequentially coupled cavities of each filter are folded to compose a compact U-shape. One end of each U structure is directly connected via an iris to the common port T-junction located in the center of the unit. The cavity at the other end of each U structure is coupled via an iris to a short waveguide section. The length of this section is determined according to the respective phase condition obtained from the synthesis. These waveguide sections are also connected to E-plane T-junctions. The opposite port of each of these T-junctions, couples via an iris the respective 6th cavity of the filters – which implements the transmission zero. The single channel interfaces are provided by the perpendicular ports of these T-junctions. Consequently, all interfaces are situated at one side of the diplexer perpendicular to the filter cavity structures (cf. Fig. 3). This overall configuration facilitates compactness and the final integration in an equipment.

The initial designs of the filter structures start according to the

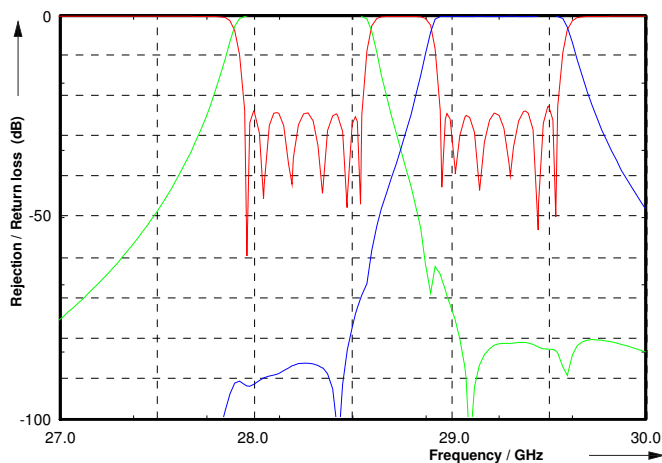


Figure 4. Computed diplexer responses

U-shapes determined for the diplexer configuration. That is, the design considers the intercavity irises at the respective side-walls to accommodate with the desired U-shape structure. In a second step, these structures are used for a first diplexer design. The little differences of the cavity sizes and the phase waveguide sections of the two filters will cause a deviation from the desired symmetry of the interface locations. Hence, a final design step is necessary considering suitable adjustments of the cavity alignments to obtain exactly symmetrical locations for the interface ports.

The design of the single filter as well as the diplexer structures has been supported by the CAD tool ‘Microwave wizard’ from MICIAN GbR. These computations also considered finite radii in the structures which are evident for a realization with state-of-the-art CNC milling techniques. The computed results of the final diplexer structure with radii – providing also the symmetry of the interface ports – are shown in Fig. 4.

IV. REALISATION AND RESULTS

The diplexer is realized in a flat sheet from aluminum containing the structural part with the cavities, irises and T-junctions (see Fig. 6). The waveguide interfaces with WR34 size are situated on the backside of the structural part. This part is completed by a simple lid containing some screws for post manufacturing fine tuning. Both, structural part and lid are silverplated and finally joined by soldering. The measured results shown in Fig. 5 exhibit good agreement with the computed responses. The insertion loss at the respective center frequencies is less than 0.6 dB which corresponds to a Q efficiency of 65% (the theoretical unloaded Q factor is app. 5000). Regarding the useful bands including the margin for the frequency drift over temperature (this is a considered bandwidth of 470MHz) the insertion loss is still below 0.9 dB. Wide spurious free bands are achieved due to the application of the fundamental mode resonances for the cavity designs. This compact and easy acting design facilitates large scale and low cost series production.

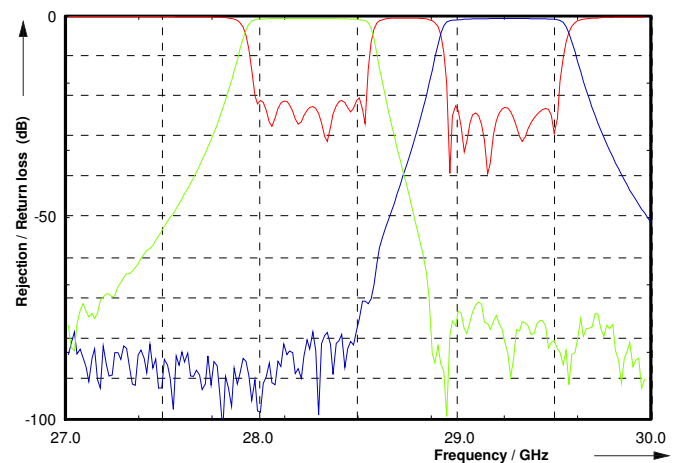


Figure 5. Measured characteristics of the realized diplexer

V. CONCLUSIONS

Filters providing an arbitrarily located transmission zero at finite frequencies with the same cavity structure were applied to a novel diplexer design. The transmission zeros are brought about by dedicated cavities at the single signal ports of the diplexer like an extracted pole. It was shown that with this approach an overall compact design with symmetrical interface port locations can be realized which also facilitates low cost production in large quantities. The concept was proven by a 28GHz diplexer design with two 6th order filters. Good agreement of computed and measured results prove the introduced design approach.

ACKNOWLEDGMENT

The authors would like to thank Mr. Rainer Weihbrecht for accurate manufacturing of the hardware.

REFERENCES

- [1] J. Uher, J. Bornemann, U. Rosenberg, *Waveguide Components for Antenna Feed Systems: Theory and CAD*, Artech House, Boston – London, 1993
- [2] J. Dittloff, F. Arndt, "Computer-Aided Design of Slit-Coupled H-Plane T-Junction Diplexers with E-Plane Metal-Insert Filters", *IEEE Transactions on Microwave Theory and Tech.*, vol. 36, no. 12, pp. 1833-1840, Dec. 1988.
- [3] A. Morini, T. Rozzi, "Analysis of Compact E-Plane Diplexers in Rectangular Waveguide", *IEEE Transactions on Microwave Theory and Tech.*, vol. 43, no. 8, pp. 1834-1839, Aug. 1995.
- [4] T. Shen, K.A. Zaki, T.G. Dolan, "Rectangular Waveguide Diplexers With a Circular Waveguide Common Port", *IEEE Transactions on Microwave Theory and Tech.*, vol. 51, no. 2, pp. 578-582, Feb. 2003
- [5] E. Ofli, R. Vahldieck, S. Amari, "Novel E-Plane Filters and Diplexers With Elliptic Response for Millimeter-Wave Applications", *IEEE Transactions on Microwave Theory and Tech.*, vol. 53, no. 3, pp. 843-851, March 2005
- [6] R. Beyer, P. Krauss, U. Rosenberg, T. Sieverding, "Compact Rx/Tx Channel Duplexer with Tuning Capability for Integration in a 26GHz High Capacity Short Haul Radio Equipment", *European Microwave Conference (EuMC2003)*, CD-ROM, Milan, Italy, Sept. 2003
- [7] S. Amari, U. Rosenberg, "Synthesis and Design of Novel In-Line Filters With One or Two Real Transmission Zeros", *IEEE Transactions on Microwave Theory and Tech.*, vol. 52, no. 5, pp. 1464-1478, May 2004

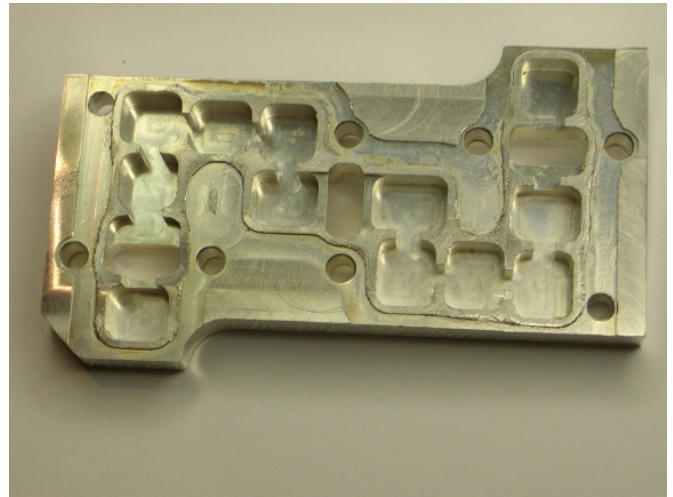


Figure 6. Photograph of the structural diplexer part

Design and W-CDMA Characterization of a Wideband AlGaIn/GaN HEMT Power Amplifier for Future 3G Multiband Base Station Applications

D. Wiegner¹, U. Seyfried¹, W. Templ¹, T. Naß¹, S. Weber¹, S. Wörner¹, I. Dettmann², R. Quay³, F. van Raay³, H. Walcher³, H. Massler³, M. Seelmann-Eggebert³, R. Reiner³, R. Moritz³, and R. Kiefer³

¹ Alcatel SEL AG, Holderaeckerstrasse 35, 70499 Stuttgart, Germany (specification, board assembly and characterization), fax: +49 711 821 32455, e-mail: Dirk.Wiegner@alcatel.de

² Institute of Electrical and Optical Communication Engineering at University of Stuttgart, Pfaffenwaldring 47, 70569 Stuttgart, Germany (board design and simulation)

³ Fraunhofer Institute of Applied Solid State Physics, Tullastrasse 72, 79108 Freiburg, Germany (GaN technology, modelling and packaging)

Abstract— A single stage wideband amplifier based on an AlGaIn/GaN HEMT power cell with a total gate-width of 16 mm matched to 50 Ohm has been successfully developed and characterized by use of a single-carrier W-CDMA signal. A very wide bandwidth of more than 1.7 GHz covering several mobile radio frequency bands within L- and S-band with peak output power levels up to 44 dBm has been demonstrated with meeting 3GPP ACLR requirement in the complete measured frequency range. The maximum measured output power level was 45.8 dBm translating into a power density of 2.4 W/mm, which is superior compared to that of established technologies like LDMOS. The presented power amplifier shows the impressive potential of AlGaIn/GaN HEMT technology regarding output power and bandwidth, supporting the development of future multiband/multistandard capable base stations.

Keywords- multiband/multistandard, AlGaIn/GaN HEMT technology, wideband amplifier, W-CDMA test signal

I. INTRODUCTION

Since the number of mobile radio standards (GSM, UMTS, WiMAX, etc.) and frequency bands (900 MHz, 2100 MHz, 2500 MHz, etc.) increased in mobile communication in recent years, the demand for multiband/multistandard capable base stations arose [1], e.g. in order to reduce system manufacturers' product diversity and to support the flexibility of mobile operators. Additionally linearity and efficiency requirements of future base stations increase, due to new modulation schemes with peak-to-average ratios (PAR) of e.g. 10.5 dB for single carrier W-CDMA signals, which are used in order to improve data rate, necessary to allow new applications like music or video download. These requirements of future mobile base stations directly translate into the power amplifier module, which is located in the transmit path of a base station and which is one of the most challenging components when realising a multiband/multistandard capable base station. Established technologies like LDMOS e.g. provide high power and good linearity but only a limited bandwidth especially for high output power levels. New wide bandgap semiconductor

device technologies like GaN HEMT promise an improved power and broadband capability, due to superior physical properties like high breakdown voltage and high carrier mobility. A high breakdown voltage allows to apply higher supply voltages, resulting in an increased power density and thus increased impedance level of the power transistor itself. An increased impedance level facilitates realisation of broadband matching circuit to the 50 Ohm in- and output of the amplifier module. First reported promising results of assembled wideband power amplifiers [2,3], covering several hundreds of MHz and providing power levels up to 100 W, show a high potential of GaN technology for future wideband/multiband amplifier applications.

II. DEVICE TECHNOLOGY

The AlGaIn/GaN HEMT technology is based on multiwafer MOCVD growth on 2-inch s.i. SiC substrates using an Aixtron 2000 multiwafer reactor. The T-gate technology is e-beam defined with a gate length of $l_g = 300$ nm. The basic sub cells with a gate-width of $W_g = 2$ and 4 mm yield a maximum drain current density of > 900 mA/mm and a transconductance of > 200 mS/mm at $V_{DS} = 35$ V. The current gain cut-off frequency f_T of the 2 mm device is beyond 30 GHz. Currently the maximum operational voltage is $V_{DS} = 35$ V with a corresponding on-state breakdown voltage of $BV_{DS} > 70$ V. The basic cell of 2 mm yields a saturated output power density of 6 W/mm and a linear gain of 23 dB at $V_{DS} = 35$ V and 2 GHz single carrier operation. Single carrier power added efficiency (PAE) can be as high as 58 % with proper second harmonic tuning. The devices are diced and soldered by Au/Sn process. They are packed in standard LDMOS packages optimised for broadband operation without internal prematching. Thus, special care is taken for the stabilisation of the devices with respect to low- and high frequency oscillations without compromising the broadband operation. The optimisation of the bond wires within the package is found useful for that purpose. Further, odd mode suppression is

achieved by various means, such as the introduction of additional losses and additional bond wires.

III. POWER AMPLIFIER DESIGN

Fig.1 shows the typical block diagram of a power amplifier module. The circuit consists of an input and output matching block and a bias circuit for the gate and drain of the transistor. While the output matching network is designed for highest output power, the input matching network is designed for flat gain and high bandwidth. The bias circuits also guarantee the stability of the amplifier. The bias point was found by power sweep simulation over different bias points. At the optimum bias point the gain is nearly constant over the power sweep.

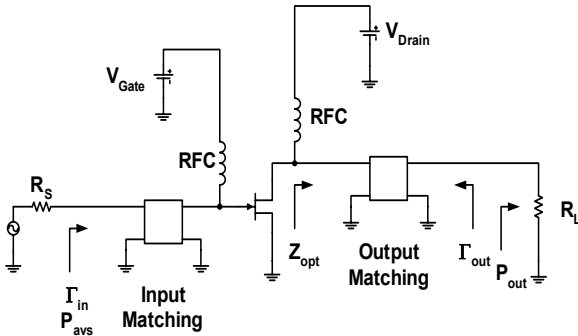


Figure 1. Power amplifier module

To obtain the maximum output power, the reference impedance Z_0 (typically 50Ω) must be transformed to the optimum output impedance Z_{out_opt} of the transistor. Z_{out_opt} can be derived from load-pull measurements, simulation or by the load line method [4]. With the load line method the optimum resistance R_{opt} inside the transistor can be approximately calculated to

$$R_{opt} = \frac{1}{8} \cdot \frac{(V_{DS} - V_K)^2}{P_{out}} \quad (1)$$

where V_K is the knee voltage, V_{DS} the drain voltage and P_{out} the output power of the transistor. For high voltage power transistors as GaN transistors, R_{opt} is closer to the reference impedance Z_0 compared to e.g. a LDMOS transistor with the same output power. However, due to the parasitic capacitances of the transistor and the housing R_{opt} is transformed to Z_{out_opt} with a value well below 50Ω . The parasitic output capacitance limits the bandwidth of the transistor. Since the output capacitance of a GaN transistor is smaller than e.g. that of an LDMOS device with comparable output power, GaN transistors are more attractive for broadband applications. At the input of the transistor a matching network is required to obtain a flat gain characteristic over the required frequency range. The input circuit of the transistor can be modelled as a series LC resonance circuit in series with the reference impedance Z_0 as shown in Fig.2.

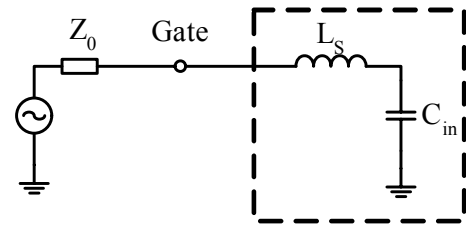


Figure 2. Simplified input circuit of the transistor

To get a high bandwidth, Z_0 must be transformed to low values. The required matching network should have a low quality factor Q in order not to limit the bandwidth performance of the transistor and to get a flat gain characteristic. In addition, matching networks should also guarantee low reflection coefficients at the input and output of the amplifier. However, both high bandwidth and low reflection can not be fulfilled at the same time for a single transistor amplifier at the input, as bandwidth and reflection coefficient are coupled by Fanos limit [5]. At the output the reflection coefficient is determined due to the necessity of matching the reference impedance Z_0 to Z_{out_opt} . Therefore input and output reflection coefficients are secondary design goals for a broadband single transistor power amplifier.

Since a large signal model has been available from FhG-IAF Freiburg, Z_{out_opt} has been found by load pull simulation. At 2000 MHz, Z_{out_opt} of the GaN power cell has a value of $(3.7 + j1.2) \Omega$. The change of Z_{out_opt} over the required frequency range is sufficiently small. The output matching network has been designed using the Smith chart. Capacitors in the output matching network for matching purposes have been avoided since they introduce losses in this network, which degrades the overall efficiency of the amplifier. The matching network consists of five line sections. The quality factor Q of the network is kept low enough in order not to affect the large signal bandwidth of the transistor over the required frequency range.

To obtain a large small signal bandwidth and a flat gain characteristic, the input matching network transforms the 50Ω reference impedance to 1.5Ω . A multisection transformer at the input has been designed using the Smith chart. The multisection transformer consists of line sections with varying line impedances. Each line section is terminated by a shunt capacitor. Using shunt capacitors instead of e.g. quarter-wave transmission lines reduces the overall size of the matching network and allows tuning the network after production. Three sections have been used to get a sufficiently low Q factor of the network.

The bias networks at the input and the output of the transistor have been designed by using quarter-wave transformers. The length of the lines are determined by the upper frequency limit. This guarantees an inductive behaviour of the bias network over the whole frequency range. The impedance of the bias network is several times higher than the impedance of the matching network over the whole frequency range and therefore the bias network has no impact on the matching network. A proper termination of the bias network for both high and low frequencies is important. The impedance of the bias network should be constant from DC to the

modulation bandwidth. This reduces nonlinearities when the amplifier is driven near the compression point [6].

Stability is an important issue for power amplifiers. Since power transistors show a very high transconductance g_m , they tend to become instable due to parasitic feedback capacitances. Inband stability is guaranteed by the design of the matching networks. However, to achieve outband stability additional loss must be included. This can be realised either in the output or in the input matching network. However, it is not recommendable to add loss in the output matching network because this will degrade the efficiency of the amplifier. In many cases stability problems occur at frequencies near the lower frequency limit of the amplifier pass band. At these frequencies the matching network is blocked by the decoupling capacitors and the transistor sees mainly the impedance of the bias network. Inductive behaviour of the gate and drain bias network at these frequencies will potentially cause oscillation. Adding a small series resistor in the gate bias network improves the stability of the amplifier. Placing a series resistor in the drain bias network is not possible, since a high current is flowing through the drain bias line. Therefore a small shunt resistor decoupled by a capacitor is placed in the bias network. The design and simulation of the wideband amplifier has been done at the Institute of Electrical and Optical Engineering at University of Stuttgart.

IV. PROTOTYPE ASSEMBLY

The designed wideband GaN amplifier has been assembled as a first amplifier demo-board by Alcatel SEL model workshop. In- and output matching has been realised by microstrip lines and lumped elements. The realised amplifier prototype is illustrated in Fig.3.

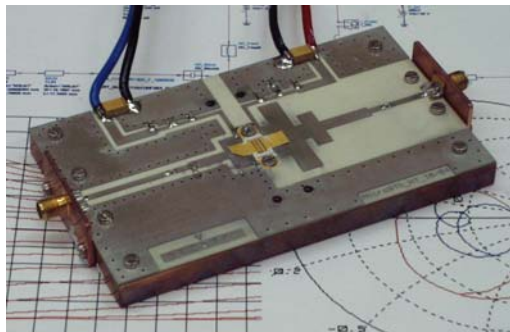


Figure 3. 16 mm GaN wideband amplifier prototype

The GaN power bar with a total gate-width (TGW) of 16 mm housed in a single standard LDMOS package is depicted in Fig.4. The power bar itself consists of eight basic GaN power cells with a TGW of 2 mm, each. Packaging and bonding was done at FhG-IAF Freiburg. The GaN HEMT power cells themselves are based on a FhG-IAF Freiburg proprietary AlGaIn/GaN HEMT technology. In order to reduce the source inductance and to support stabilisation of the power cells, bonding was done over an additional substrate. Due to the current stress on drain side, a plurality of bond wires has been used.

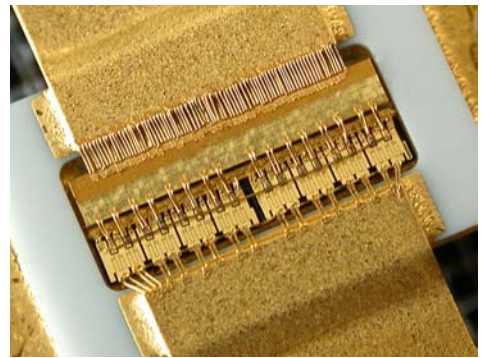


Figure 4. Packaged GaN power cell (TGW = 16 mm)

V. CHARACTERIZATION RESULTS

First characterization measurements at a supply voltage of $V_{DS} = 35$ V have been performed by using a single-carrier W-CDMA test-signal with a peak-to-average ratio (PAR) of approximately 10.5 dB which means no reduction of signal dynamic. Furthermore, no linearisation was used for the measurements. The amplifier has been characterized with respect to 3GPP Adjacent Channel Leakage Ratio (ACLR) specification, which requires a signal suppression of -45 dBc at 5 MHz frequency offset and -50 dBc at 10 MHz frequency offset. Fig.5 illustrates the frequency characteristic of the assembled amplifier within a wide measured frequency range from 1000 MHz up to 2800 MHz at a peak input power level of approximately 32.5 dBm.

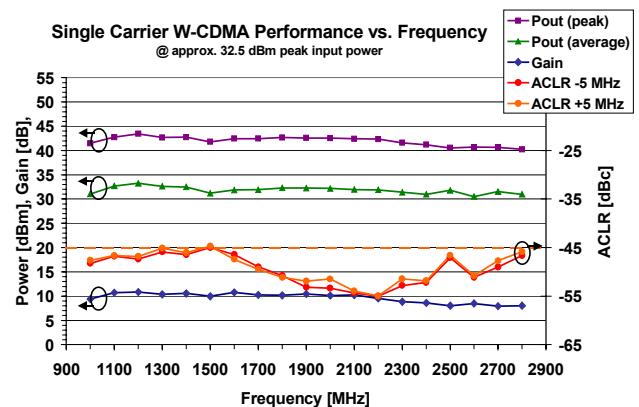


Figure 5. Frequency characteristic at nearly constant input power

The effective ripple of the presented final amplifier stage can be seen by means of the gain curve. The gain is about 10 dB over a wide frequency range. At 32.5 dBm peak input power, the amplifier achieves a maximum measured peak output power of approximately 43 dBm at 1200 MHz and is above 40 dBm within the complete frequency range. The related average output power is above 30 dBm for the used W-CDMA signal. Since measured ACLR is clearly better than the required -45 dBc for wide frequency ranges, an improved output power characteristic can be achieved by adjusting the input power level considering 3GPP ACLR conformance, as shown by Fig.6. Since the amplifier is intended to cover frequency bands within the frequency range from 1800 MHz up to 2700 MHz, comprising GSM, UMTS and WiMAX

bands, the power adaptation has been performed within this limited frequency range.

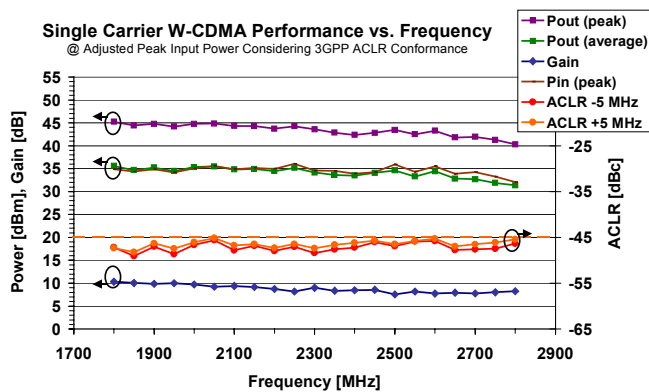


Figure 6. Improved frequency characteristic by adjusted input power level

The achieved peak output power level is now above 43 dBm, with a related average output power level of approximately 34 dBm over a very wide frequency range. Maximum achieved peak output power is 45 dBm at 1800 MHz. 3GPP ACLR specification is met within the complete measured frequency range.

Fig.7 shows the related power sweep measurement at 2000 MHz by use of a single-carrier W-CDMA test-signal. 1 dB compression point can be found approximately at a peak output power level of 44 dBm. 3GPP ACLR at 5 MHz offset will be met up to a peak output power of nearly 45 dBm, ACLR at 10 MHz is well below the required - 50 dBc and thus completely uncritical.

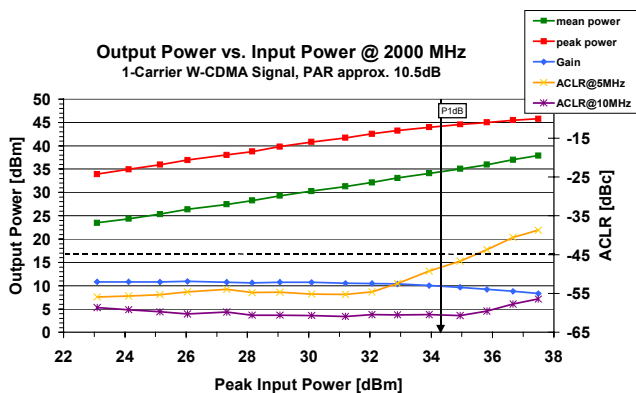


Figure 7. Power sweep measurement

The measured gain is approximately 10.8 dB for low input power levels, when the applied test-signal is not driven into compression. Fig.8 shows the spectrum of a single-carrier W-CDMA signal directly at the output of the 16 mm wideband GaN amplifier, at 2000 MHz. The shape of the spectrum at 2000 MHz suggests that 3GPP ACLR requirements at 5 MHz offset (required: - 45 dBc, measured: - 47.48 dBc, - 46.66 dBc) as well as at 10 MHz offset (req.: - 50 dBc, meas.: - 59.08 dBc, - 59.55 dBc) are clearly met at a peak output power of approx. 21.8 W (43.4 dBm). The corresponding average output power is approx. 2.2 W (33.4 dBm).



Figure 8. Single-carrier W-CDMA spectrum at 2.0 GHz and 43.4 dBm peak output power

CONCLUSION

This work presents promising results of a GaN HEMT based wideband power amplifier matched to 50 Ohm for base station applications in 3G mobile communication. The used design approach in order to achieve a wideband characteristic has been discussed and the assembled amplifier has been characterized with respect to 3GPP ACLR specification. By use of a single-carrier W-CDMA signal, the presented wideband amplifier covers a very wide frequency range from 1000 MHz up to 2800 MHz, meeting 3GPP ACLR. By input power adaptation, a peak output power level of approximately 43 dBm can be achieved over a wide frequency range. Maximum measured output power at 2000 MHz is 45.8 dBm translating into a power density of 2.4 W/mm, which exceeds power densities of established technologies like e.g. LD MOS or GaAs.

ACKNOWLEDGMENT

The authors wish to acknowledge the support of the German Ministry of Education and Research (BMBF) under contract 01BU382 and 01BU386 in the context of the ‘Leitinnovation ‘Mobile Internet’’. The continuous support of the epitaxial and technology department at Fraunhofer IAF as well as the support of the radio department and model workshop at Alcatel R&I Stuttgart is gratefully acknowledged.

REFERENCES

- [1] W. Koenig, S. Walter, U. Weiss, D. Wiegner, ‘‘A multiband frontend for a medium range base station - an important step towards SDR’’, 3rd Karlsruhe Workshop on Software Radios, WSR’04, March 17/18, 2004, Karlsruhe.
- [2] A. Maekawa, M. Nagahara, T. Yamamoto and S. Sano, ‘‘A 100W high efficiency GaN HEMT amplifier for S-band wireless system’’, European Microwave Conference, October 03.-07., 2005, Paris, France.
- [3] D. Wiegner, T. Merk, U. Seyfried, W. Templ, S. Merk, R. Quay, F. van Raay, H. Walcher, H. Massler, et al. ‘‘Multistage broadband amplifiers based on GaN HEMT technology for 3G/4G base station applications with extremely high bandwidth’’, European Microwave Conference, October 03.-07., 2005, Paris, France.
- [4] Steve C. Cripps, ‘‘RF power amplifiers for wireless communications’’, pp. 24, Artech House, 1999.
- [5] David M. Pozar, ‘‘Microwave engineering’’, John Wiley and Sons Inc., 1998.
- [6] Joel Vuolevi and Timo Rahkonen, ‘‘Distortion in RF power amplifiers’’, Artech House, 2003.

Pulse-length modulator for analogue-to-digital conversion of radio frequency signals

Christian Hartmann, Kurt Blau, Matthias Hein

Technische Universität Ilmenau, Department for RF and Microwave Techniques,
Helmholtzplatz 2, 98693 Ilmenau, Germany, +49 3677 69-1583, Christian.Hartmann@TU-Ilmenau.de

Abstract—Modern communication systems require amplifiers with excellent linearity and, at the same time, an efficiency as high as possible, especially for mobile applications. Switch-mode amplifiers seem to be suitable to meet these constraints. Such an amplifier cannot be driven by the radio frequency signal itself, but requires a 1-bit analogue-to-digital conversion. Beside the commonly used sigma delta modulation, pulse-length modulation can be applied, too. In this paper, we present an approach for an all-analogue pulse-length modulator for a working frequency of 250 MHz. Challenges of the design are identified and possibilities for further improvements proposed.

I. INTRODUCTION

Switch-mode amplifiers have commonly been used in power amplifiers at audio frequencies for many years, as they combine very high efficiency (about 90%) and excellent linearity, in contrast to conventional class-AB push-pull amplifiers. These features make the application of a switch-mode architecture very attractive for RF-power amplifiers also, where efficiency rarely exceeds some 30%. Only with class-C, class-D, or even more sophisticated architectures it has been possible to approach efficiencies around 75% at radio frequencies [1]. However, the use of these architectures is limited to RF-signals with constant envelopes, which seriously limits the choice of modulation schemes, especially if high spectral efficiency is required. A class-S-switch mode amplifier enables the amplification of signals with randomly varying envelopes without the application of complex envelope elimination and restoration (EER) techniques, necessary for the use of conventional switch-mode-amplifiers like class-E [2]. On the other hand, a drawback of a class-S-amplifier is that the RF-signal cannot be amplified directly, but has to be digitised in an appropriate way. Until now, bandpass sigma delta modulators (BDSM) have been applied for this purpose. The BDSM concept inherently suffers from stability problems and high quantisation noise levels outside the operating bandwidth. To achieve bandwidths substantially greater than 15 MHz, the loop filter becomes complex. To avoid such difficulties, we have investigated a pulse-length modulator (PLM) at radio frequencies. This concept has been used for a variety of applications at lower frequencies, for several decades. The PLM avoids the above mentioned drawbacks completely, as there are no stability problems and, particularly if implemented as an analogue modulator, no quantisation noise in the output signal. Another advantage of the pulse-length modulator is its relatively simple architecture, which also clearly distinguishes it from a bandpass sigma delta modulator.

II. REALISATION OF THE PULSE-LENGTH MODULATOR

Figure 1 sketches the principle of a classical pulse-length modulator. It consists of a comparator as a key component, driven at one input by a reference signal (e.g., a sawtooth), and at the second input by the signal of interest. At its output, the comparator provides a pulse-length modulated signal, whose polarity depends on the application of the reference signal to the inverting or non-inverting input. In principle, the pulse-length modulator converts the amplitude of the input signal to a corresponding duty cycle of its output signal.

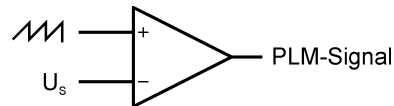


Fig. 1. Principle of a pulse-length modulator, realised with comparator and sawtooth signal.

A sawtooth signal has the disadvantage that the steep falling edges occupy a very broad bandwidth, which makes it difficult to generate and handle such signals at radio frequencies. To moderate this problem, it is possible to use a triangle signal instead, which significantly reduces the required bandwidth. The simplest way to generate a triangle signal is the use of the charge function of a RC-network. If the RC-network is driven by a rectangle signal and its time constant $\tau = RC$ is adjusted sufficiently long (typically about ten times the period of the rectangle signal), the voltage across the capacitor assumes a triangular shape. We have adapted this technique to synthesise a triangle signal. The driving rectangle signal was generated by a comparator driven by a sinusoidal signal at 1 GHz, as indicated in Fig. 2 below. It is important that the edges of the triangle signal have good linearity, because distortion of the modulator output signal would occur otherwise. Particularly, if the RC-time constant is too low, the output signal of the RC-network would assume the rounded shape typical of the charge-/ discharge function and would thus cause a phase error in the modulated signal. Therefore, special care has to be paid to the quality of the triangle signal for a good performance of the modulator.

The following figure shows the complete block diagram of the pulse-length modulator realised in this study. The comparator is operated with a triangle signal at 1 GHz and its input signal is a sinusoidal at 250 MHz. The frequency of the reference was chosen four times the signal frequency, to

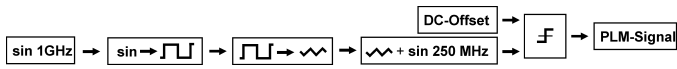


Fig. 2. Block diagram of the realised pulse-length modulator.

achieve enough spectral distance between both signals, making the separation of the signals at the amplifier output possible without too much effort in the necessary lowpass filter. In particular, the oversampling ratio has to be high enough to avoid the Bessel spectrum of the pulse-length-modulated signal to interfere with the input signal spectrum. The amplitude of the n -th harmonic of the Bessel spectrum decreases with increasing order n , as illustrated by the following equation [3].

$$c_{n,q} = \frac{1}{j2\pi n} J_q(n\Delta\Phi) \left[e^{+j(n\omega_0 + q\omega_m)\frac{\tau_0}{2}} - (-1)^q e^{-j(n\omega_0 + q\omega_m)\frac{\tau_0}{2}} \right],$$

where q is the order of the Bessel-function J_q , τ_0 is the pulse width of the unmodulated output signal, and ω_m is the modulating frequency ($\omega_m = 250$ MHz in our case). Hence, if these spectral components are sufficiently separated from the input signal, harmonic distortion can be avoided. The fourfold oversampling presents a reasonable compromise between accuracy and circuit complexity.

We found out that it is advisable not to feed the triangle signal and the input signal to separate inputs of the comparator, but to combine them by a directional coupler and feed them to a single input, to obtain lower nonlinear distortion of the comparator. The remaining input was grounded, or tied to a DC-offset voltage. The comparator used in our study was a very fast type in SiGe-technology, the ADCMP580 from Analog Devices. It exhibits output rise/fall times of typically 35 ps and a low RMS-Jitter of 200 fs. This is important in several respects. First, the rise/fall time of the output signal determines the minimum pulse width, which consists of the sum of one rise time and one fall time, and which sets the minimum output power of the amplifier driven by the PLM. Secondly, very steep pulse edges are necessary to achieve a high efficiency in a switch-mode amplifier, which is limited mainly by losses during the switching cycles. To keep these low, the amplifier output stage has to be switched as quickly as possible.

III. MEASUREMENT RESULTS

A parameter of particular interest is the linearity of the pulse-length modulator. Therefore, we have carried out a classical two-tone frequency intermodulation measurement with two test signals of identical power at 250 MHz and 251 MHz. A typical result for third-order intermodulation is shown in figure 3. An intermodulation distance of about 44 dB was observed. To check if the intermodulation follows the cubic power law expected for a memory-less nonlinearity of third order, the power of the test signals was decreased by 10 dB. Interestingly, the intermodulation distance hardly changed. Similar results were obtained for second-order intermodulation measurements, with test signals at 120 MHz and 130 MHz,

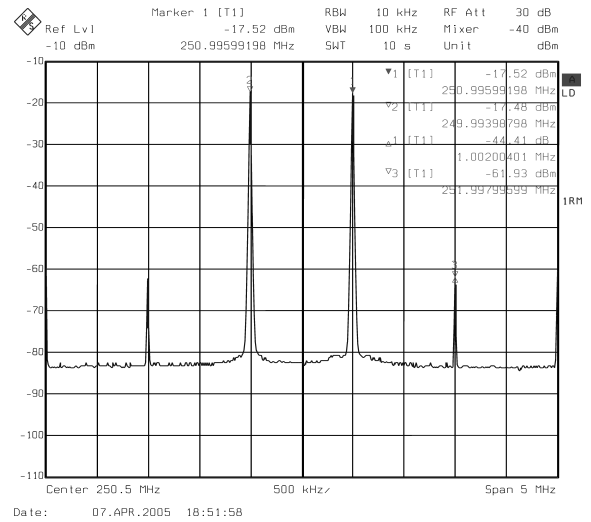


Fig. 3. Spectrum of the third-order intermodulation of the pulse-length modulator for an input power level of 5 dBm, with an intermodulation distance of 44 dB.

where the intermodulation product at 250 MHz was observed. Again, the intermodulation distance remained essentially unaffected by the power at the fundamental tones. These results indicate that the intermodulation is dominated by hysteretic processes in the comparator. Further studies are under way to understand this behavior in greater detail.

Another figure of interest is the signal-to-noise ratio (SNR) of the modulator. Within an estimated bandwidth of 25 MHz, the PLM shows a SNR of approximately 31 dB was derived from a spectral analysis of the PLM, corresponding to an average of 17 dB per MHz bandwidth. One reason for this relative small value can be associated with the quality of the triangle signal, which is depicted in figure 4.

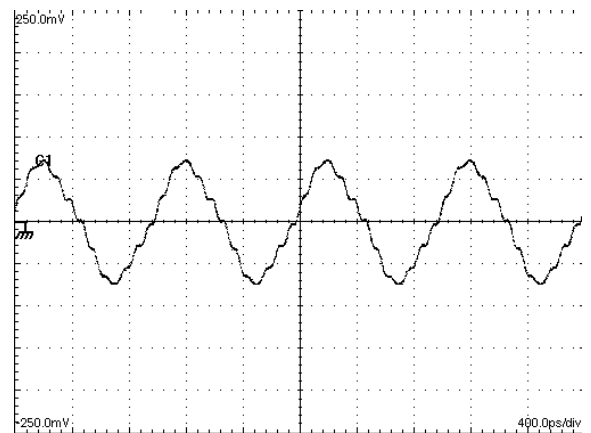


Fig. 4. 1 GHz-triangle signal for the pulse-length modulator. The edges of the signal show a significant ripple, leading to additional distortion in the output signal.

It can be observed that there is some ripple superimposed to the triangle signal, probably caused by parasitic inductances of the RC-network in conjunction with the very fast rise time of the rectangle signal driving it. The ripple leads to additional

jitter of the comparator output signal, which adds to the noise level at the output and deteriorates the SNR.

Furthermore, the noise figure of the modulator was derived from measured data to amount to about 34 dB, in fair agreement with the performance expected from numerical simulations. Although this value appears high at first glance, it has to be noted that the triangle signal and the input signal were added by means of a directional coupler, which had a coupling attenuation of 20 dB. Hence, if the directional coupler were omitted from the circuit by feeding the triangle signal and the input signal to separate comparator inputs, the noise figure would amount to 14 dB only. Nevertheless, we used the directional coupler on purpose, because we wanted to minimise distortion as mentioned above.

Figure 5 shows the output signal of the modulator achieved for 1 GHz clock frequency, as monitored by a fast sampling oscilloscope. The variation of the duty cycle over one period of the sinusoidal input signal and the fourfold oversampling can be clearly observed. Because the oscilloscope was DC-coupled, the logic levels at the comparator output with 50 Ω -termination are also visible, which are specified for 0 V for the high-level and -400 mV for the low-level (CML-levels). For a good efficiency of the entire RF-power amplifier system, the power consumption of the modulator block is also of importance, particularly at low RF-output power levels. The described modulator circuit has primarily been designed to demonstrate the principle-of-operation of pulse-length-modulation at RF-frequencies, with less attention on the power consumption. The DC power required for this modulator amounts to 500 mW, which is not yet suited for an application in a mobile device like a cell-phone, but which could be reduced in advanced designs. In addition, in a base station power amplifier, this DC power demand would be negligible, with almost no influence on the overall efficiency. More generally, reliable estimations of the efficiency (or the power-added efficiency) can be made only in terms of the complete amplifier system. In particular, the architecture of the final power stage has dominant impact on the overall efficiency.

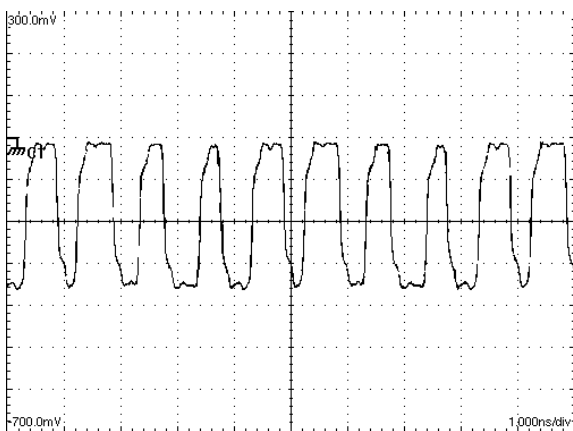


Fig. 5. 1 GHz-pulse-length-modulated signal at the comparator output.

IV. DISCUSSION AND CONCLUSION

We have investigated the possibility to use a pulse-length modulator for 1-bit analogue-to-digital conversion of a switch-mode amplification of radio frequency signals. While the principle-of-operation could be successfully demonstrated at 250 MHz with a fourfold oversampling, the performance of the realised modulator can be improved further. This holds especially for the noise level, which results from several sources. First of all, the jitter of the comparator is important, as this directly increases the noise level of the output spectrum. Another problem may arise if the input signal continues to vary after having set the comparator at the rising edge of the reference signal. In such a case, the reset of the comparator at the falling edge of the reference signal may occur at a different time than the one which corresponds to the amplitude of the input signal at the instant of setting. This effect can be called an "aperture error", as the pulse-length is not determined at one sampling instant, but within a time window depending on the input signal [4]. This contributes significantly to the noise level. A solution to this problem could be the application of a track-and-hold stage at the modulator input, which samples the input signal within a very short time interval and then holds the amplitude through the converting cycle of the modulator. Unfortunately, the realisation of an appropriate track-and-hold stage would be a challenging task, because of the demand for very high operating speeds. A more general problem is the quality of the triangle signal. In our setup, the edges of the triangle signal showed some ripple, probably caused by the parasitic inductance of the capacitor in the RC-network. This ripple leads not only to additional noise from a random shifting of the switching moments, but also degrades the linearity of the modulator. In total, we have successfully illustrated pulse-length modulation with a simple circuit architecture and with promising performance at RF frequencies. In addition, we have identified several approaches to improve the performance of the pulse-length modulator. With the availability of faster and faster comparators on the market, it seems to be possible to extend the operation of pulse-length modulation to frequencies that are of interest for mobile communication systems.

ACKNOWLEDGMENT

The authors would gratefully like to thank Georg Fischer of *Lucent Technologies* for intense and fruitful discussions.

REFERENCES

- [1] Hung, T.-P., Metzger, A. G., et al.: *Design of High-Efficiency Current-Mode Class-D Amplifiers for Wireless Handsets*, In: IEEE transactions on microwave theory and techniques, Vol. 53, No. 1, January 2005
- [2] Raab, F. H., Sigmon, B. E., Myers, R. G., Jackson, R. M.: *L-Band Transmitter Using Kahn EER Technique*, In: IEEE Transactions MTT, Volume 46, No. 12, pp. 2220, December 1998
- [3] Hölzer, E., Holzwarth, H.: *Theorie und Technik der Pulsmodulation*, Berlin: Springer Verlag, 1957
- [4] Schleifer, W.-D.: *Digital-Analog- und Analog-Digital-Wandlung mit Hilfe der Puls-Dauer-Modulation*, Munich: Dissertation TU München, 1986

Exposure Measurements of Modern Digital Broadband Radio Services

Dr. Christian Bornkessel¹, Prof. Dr. Matthias Wuschek²

¹IMST GmbH, Test Centre EMC, C.-F.-Gauss-St. 2, D-47475 Kamp-Lintfort, Germany, +49-2842-981-383, bornkessel@imst.de

²University of Applied Sciences Deggendorf, Edlmairst. 6+8, D-94469 Deggendorf, Germany, +49-991-3615-522, matthias.wuschek@fh-deggendorf.de

Short Abstract—This paper describes methodologies for exact exposure measurements in the vicinity of modern digital broadband RF transmitters like DVB-T, DAB and UMTS stations. The measurement parameters for the spectrum analyser measurements are derived from the signal characteristics of the RF signals in frequency and time domain. Study designs of present measurement campaigns are also presented.

Keywords - radiation protection, RF exposure, exposure measurements DVB-T, DAB, UMTS

I. INTRODUCTION

In the present debate about possible health risks of electromagnetic radiation, the location fixed RF transmitters like DVB-T, DAB and UMTS stations are still in the focus of the public discussion. Besides numerical field strength prediction techniques, especially exposure measurements have proven to be a practicable measure highly accepted in the public to show the compliance of transmitters with radiation protection guidelines and exposure limits.

Whereas GSM mobile phone base stations, analogue radio and TV transmitters are still operating for some years or decades with their exposure characteristics and field distribution widely studied [1-2], more and more digital broadband RF services like UMTS, DVB-T and DAB transmitters had come into operation during the last months.

These transmitters exhibit RF signal schemes completely different from narrowband, analogue RF services. Therefore, new measurement methodologies have to be developed to exactly capture all relevant components of the transmitted signal. Moreover, for time-variant signals like UMTS, techniques have to be developed to extrapolate the measured momentary value to the maximal operational state of the station, as is demanded in some exposure standards.

The correct measurement of modern digital broadband RF signals proves to be a challenge for the measurement personnel and the measurement apparatus and requires a deep understanding in the signal characteristics of the services as well as in the operational principles of modern RF measurement equipment. This is especially important due to the emotional driven exposure debate, where measurement errors may have disastrous consequences for the acceptance of these new communication services in the public.

The paper starts with an analysis of the shapes of DVB-T, DAB and UMTS signals. From their characteristics in frequency and time domain demands for appropriate measurement equipment and actual measurement parameters are derived.

II. SIGNAL CHARACTERISTICS

A. DVB-T

For DVB-T, a multi-carrier modulation with COFDM (Coded Orthogonal Frequency Division Multiplexing) is used. The data stream is divided into several thousands of partial data streams. A very broad spectrum results with a bandwidth of 7.6 MHz in the UHF (470-862 MHz) and 6.6 MHz in the VHF (174-223 MHz) TV frequency range. Fig. 1 shows a real measured UHF DVB-T spectrum.

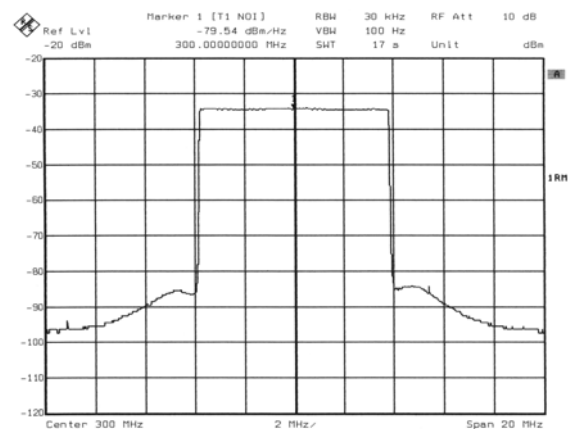


Figure 1. Spectrum of a DVB-T signal (UHF band)

In the time domain, the DVB-T signal exhibits a noise like character. Very typical for noise like signals is the large difference between short time maxima U_{Peak} and the RMS value U_{RMS} of the signal. This difference is described by the crest factor C [dB] as

$$C = 20 \cdot \log (U_{Peak}/U_{RMS}). \quad (1)$$

Crest factors at real DVB-T transmitters are in the range of 10 to 12 dB.

B. DAB

For DAB, the data stream is divided into about 1,500 different carriers. The modulation is COFDM as with DVB-T. For DAB, frequencies in the bands 174-230 MHz and 1452-1492 MHz are reserved. Presently in Germany primarily the band 223-230 MHz is used.

The DAB spectrum is very similar to DVB-T, but the signal bandwidth is only about 1.5 MHz. Fig. 2 shows a real measured DAB spectrum in VHF band.

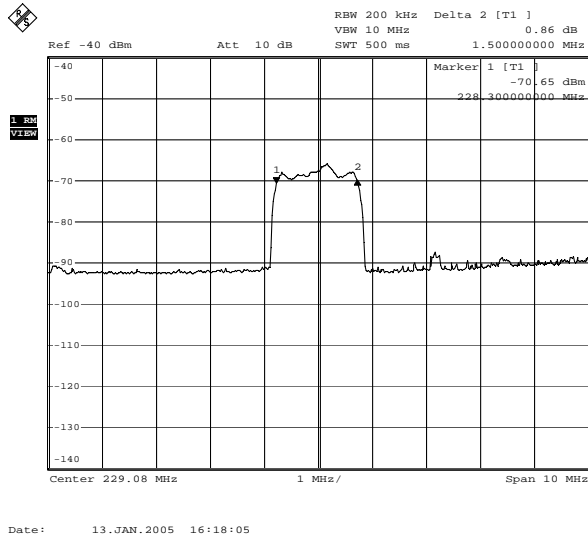


Figure 2. Spectrum of a DAB signal in VHF band

In time domain the DAB signal is also noise like with a crest factor of about 10 dB.

C. UMTS

UMTS uses a multiple access technique, where several users as well as the signalization is separated by different spreading codes (WCDMA - Wideband Code Division Multiple Access). By multiplication with the spreading code, the data signal is spread in the spectrum.

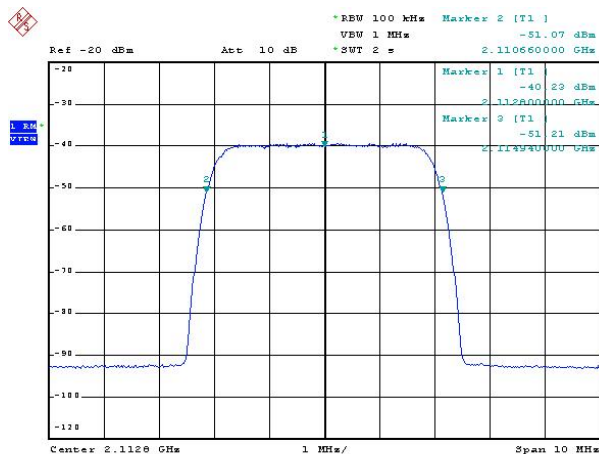


Figure 3. Spectrum of a UMTS signal

Fig. 3 shows a real measured UMTS signal in frequency domain. The 10 dB bandwidth is about 4.3 MHz, in the literature 4.6 MHz is often stated. In time domain UMTS signals are also noise like with typical crest factors in the region of 8 to 10 dB. In contrast to DVB-T and DAB, the crest factor at UMTS is not constant in time, but varies with the traffic of the station. The downlink frequency range for UMTS is 2110-2170 MHz.

Due to the power control of UMTS, the radiated power of a station is dependent on the transmitted data volume and the connection quality to the UMTS terminal. The minimal transmit power results from the permanent signalling. Presently, the stations are adjusted in that way, that 15 to 20 % of the maximal power is used by the signalling. The remaining is available in principle for the data channels, whereas a real UMTS station does not allow for transmit power more than 50 to 75 % of the maximal power.

Due to the power control a spectral measurement gives only the present exposure value, because the operational state of the station during the exposure measurement is not known.

III. CONSEQUENCES FOR THE MEASUREMENT TECHNIQUES

The investigations, reported about in this paper, deal with suited measurement techniques for the determination of the public exposure to modern digital broadband radio services. The public focus areas to be investigated exclude the “safety distance” and are located several tenth to several hundreds of meters away from the station. The available field strengths are as low, that broad band field probes can not be used due to their lack in sensitivity. Therefore, spectrum analysers or measurement receivers with appropriate receive antennas have to be used. As a method for the determination of the maximal exposure in a defined volume, the so called “sweeping method” is recommended. Here, the volume is scanned with a hand driven antenna with continuously polarization and direction changes to pick up the signal maximum. During the scan, the spectrum analyser runs in the “Max hold” mode to fix the maximum signal during the sweep.

The measurement parameters of the analyser, first of all resolution bandwidth and detector type, are important for the correctness of the measurement result. They have to be chosen in accordance to the measured signal. Here, many investigations with synthetically as well as real life signals had been carried out. The key results are described in the following.

A. DVB-T and DAB

For the exposure measurements it is of utmost importance, that the RMS power has to be determined instead of the short term maximal power. This is due to the thermal model of RF power reaction in the human body, which underlies the exposure limit concept.

A measurement of the peak power of the DVB-T signal overestimates the real exposure in the order of the crest factor. Therefore, for correct measurements the RMS detector of the analyser has to be used. Depending on the analyser type the sweep time has to be chosen large enough, because the RMS

detector needs a lot of samples per frequency step to perform a real RMS computation. As an example, for measurements with modern Rohde & Schwarz analysers (e.g. ESPI-3) minimal sweep times of 100 ms are necessary. With the resulting 10 sweeps per second, also the “sweeping method” for volume maximum detection can be used with satisfactory accuracy.

The resolution bandwidth has to be chosen in accordance to the signal bandwidth, that is 6.6 or 7.6 MHz for DVB-T VHF or UHF bands and 1.5 MHz for DAB. If these large bandwidths are not available at the analyser, the measurements can be performed with the highest bandwidth available. The results have then to be corrected with a factor, which takes into account the signal bandwidth and the used resolution bandwidth. In this case, however, a tendency towards an overestimation of the real exposure was found. Channel power measurements are possible too, but in practice time consuming, because every channel has to be measured in a separate run. An exemption represents the Selective Radiation Meter SRM-3000 by Narda, where in “Safety Evaluation” mode a channel power measurement across several DVB-T channels in one single run is possible.

In the investigations, the reproducibility had been studied in conjunction with the defined measurement parameters. To that purpose, 10 consecutive measurements were performed in several Line-of-Sight (LOS) and non-LOS scenarios at indoor and outdoor measurement sites. Reproducibility was found to be in the order of ± 1 dB. Taking into account the uncertainties of the measurement equipment, an overall measurement accuracy of ± 3 dB can be achieved (confidence interval 95 %).

B. UMTS

Basically, exposure measurements in the surrounding of UMTS stations can be performed with spectral measurement techniques in a similar manner as for DVB-T and DAB. Due to the noise like signal characteristic with high crest factor, the RMS detector remains compulsory. The resolution bandwidth has to be chosen to 5 MHz. For older types of spectrum analysers channel power measurements or a smaller bandwidth with afterwards correction can be used alternatively, although in practical measurements especially in scenarios without direct sight to the base station (NLOS) a trend for an erroneous assessment of the exposure has been found [4]. The statements concerning sweep time are the same as for DVB-T/DAB.

As mentioned before, the UMTS signal varies strongly in time because of the power control mechanisms at the base station. The relevant exposure regulations, in Germany the 26. BImSchV [5], demand for an exposure assessment at the maximal operational state of the radio station. Because in reality it is not practicable to set the UMTS station to be measured artificially in the maximal operational state during the time of the measurement, extrapolation techniques for the measured temporary values have to be used. These techniques, known for example from measurements around GSM base stations [7], base on the measurement of signalling channels emitted from the station with a time constant power. By multiplying the measured exposure from the signalling channels with a factor, relating the maximal possible power of the station to the power of the signalling channels, the exposure

at the maximal operational state of the station can be determined.

Whereas for GSM base stations these extrapolation technique can be performed in an easy way with spectrum analysers, this method does not work with UMTS. The reason is, that in UMTS signalling and transport channels are not separated in frequency as in GSM, but in different codes. Therefore an extrapolation for UMTS, based on frequency domain measurements, becomes strongly erroneous: As a worst case the measurement personnel must assume, that during the measurement only signalling, but no traffic was present. Under the assumption, that 15 % of the station power is used for signalling (this percentage can vary from station to station!) one has to multiply the measured exposure by $100/15=6.67$ in terms of power units to get the maximal exposure (another multiplication by a factor 2 has to be done to account for the second frequency channel, which is applied to the Federal Network Agency (BNetzA) by most network operators. Assuming that the station was actually in 50 % load during the measurements due to traffic, the real exposure would have been overestimated by 5.2 dB! Another argument against spectral measurement is the fact, that some network operators presently operate a three sector station only with one base station and a power splitter. This kind of station can not be detected during an ordinary frequency selective measurement which would result in an underestimation of the exposure.

These problems can be overcome with another kind of measurement technique: Instead frequency selective spectrum analysers code selective devices must be used, which offer the possibility to separate signalling and traffic channels in code domain. Among the signalling channels especially one channel is very important for an exact exposure extrapolation: The so called Primary Common Pilot Channel (P-CPICH) is permanent on air with a presently constant and well known amplitude (mostly 10 % of the maximal station power). Insofar code selective equipment, measuring the UMTS signal, decoding it and separating the P-CPICH from the other channels would resolve the problem.

Presently two types of measurement equipment are available on the market, which allows for an decoding of the UMTS signal and an extraction of the P-CPICH: Firstly spectrum analysers with a special WCDMA decoding software can be used (e.g. Rohde & Schwarz TS-EMF, i.e. spectrum analysers with decoding software RFEX, Narda SRM-3000). Secondly, separate devices, so called drive testers, can be used (e.g. Rohde & Schwarz Radio Network Analyser "TSMU"). The presented examples distinguish not only by WCDMA decoding, but also by providing a software especially adapted for exposure measurements concerning human safety in electromagnetic fields. Fig. 4 shows as an example the output of an UMTS measurement with Rohde & Schwarz RFEX software. “Scr. Code” stands for “Scrambling Code”, which distinguishes different UMTS base stations.

The devices TSMU, SRM-3000 and TS-EMF were tested extensively and found to give reproducible and accurate UMTS exposure measurement results [4]. TSMU and SRM-3000 offer in addition to a fast mode also a slow measurement mode, which has to be preferred to get the more accurate results. Slow

mode requires very slow sweeping speed in the measurement volume, because otherwise the exposure was found to be underestimated and the spread in results between consecutive measurements increased.

Scr. Code	Frequency MHz	Field strength V/m	Power density $\mu\text{W}/\text{cm}^2$
22	2112.8	0.145	5.58E-03
105	2112.8	0.0106	2.98E-05
375	2112.8	0.023	1.40E-04
175	2167.2	0.047	5.86E-04
Sum (RMS):		0.1545	V/m
Sum (Square):		0.0239	V/m
Max. Value:		0.1450	V/m

Figure 4. Example of a UMTS measurement output

The absolute sensitivity of the tested code selective measurement systems is in the area of -100 dBm (measured as P-CPICH level from a signal generator connected to the code analyser). Taking into account typical antenna factors and cable losses, field strengths in the range of the minimal necessary field strengths for UMTS coverage can be detected. When several UMTS signals are present at the same time, the dynamic decreases to typ. 20 dB, i.e. signals on the same carrier frequency, which are more than 20 dB below the strongest signal, cannot be detected.

The reproducibility of several consecutive measurements in different scenarios was measured to be ± 1.8 dB. This value is somewhat worse than with frequency selective DVB-T or DAB measurements, which may be due to the code selective algorithm in the measurement apparatus. Taking into account the uncertainties of the measurement equipment, an overall measurement accuracy of ± 3 dB can be achieved (confidence interval 95 %).

As measurement antennas for the UMTS downlink frequency range 2110-2170 MHz 3-axis isotropic antennas (as provided with the Rohde & Schwarz TS-EMF and Narda SRM-3000 devices) as well as logarithmic-periodical (log-per.), dipole or horn antennas can be used. All these types were tested to user influence, i.e. the question was investigated, to which degree the person holding the antenna during the measurement influences the results in comparison to the "free space" case. As a result it was found, that log-per. and horn antennas offer only minimal influence of about 0.1-0.2 dB compared to free space, whereas with dipole and isotropic antenna differences up to 2 dB, at direct contact of the person to antenna even more, have been measured. Taking also practicability considerations into account, log-per. antennas should be preferred for UMTS exposure measurements with the sweeping method. In comparison to the 3-axis probes, log-per. antennas provide also an increase in decoding rate, because at the 3-axis probes the axes are switched sequentially, resulting in a 3 times longer measurement time compared to 1-axis antennas.

IV. FUTURE WORK

The investigations reported about in this paper are part of two studies for the German Federal Office for Radiation Protection. The development of suited measurement techniques

serves as a base for a comprehensive measurement campaign. The study design is as follows:

Concerning DVB-T and DAB, an extensive measurement campaign at more than 200 measurement points is carried out presently in the surrounding of DVB-T transmitter locations in the Munich and Nuremberg area. By comparing the exposure results with measurements of analogue TV exposures, taken at identical measurement locations before, it is possible to detect changes in the exposure of the public due to the introduction of the DVB-T transmitters. Concerning DAB, the comparison is performed to the FM radio network.

Concerning UMTS, the field distribution around several typical Node B base station configurations will be measured to get a knowledge about the real public exposure situation in the vicinity of UMTS stations. An interesting point in the investigation is the additional measurement of GSM signals around stations, which transmit GSM and UMTS services simultaneously. In that way, differences between both exposure parts can be investigated. The UMTS measurements also cover long time measurements to study in influence of traffic in the UMTS network on the exposure situation.

The results of the measurement parts of both studies will be published in the future.

REFERENCES

- [1] Chr. Bornkessel, M. Neikes and A. Schramm, "Elektromagnetische Felder in NRW - Untersuchung der Immissionen durch Mobilfunk-Basisstationen", Study for the Ministry of Environment and Nature Conservation, Agriculture and Consumer Protection Nordrhein-Westfalia, Final Report, IMST GmbH, Kamp-Lintfort, 2002.
- [2] Chr. Bornkessel and M. Schubert, "Entwicklung von Mess- und Berechnungsverfahren zur Ermittlung der Exposition der Bevölkerung durch elektromagnetische Felder in der Umgebung von Mobilfunk Basisstationen", Study for the German Federal Office for Radiation Protection, Interim Report "Analyse der Immissionenverteilung", IMST GmbH, Kamp-Lintfort, 2004.
- [3] M. Schubert, Chr. Bornkessel and M. Wuschek, "Bestimmung der Exposition der Bevölkerung in der Umgebung von digitalen Rundfunk- und Fernsehsendern", Study for the German Federal Office for Radiation Protection, Interim Report "Entwicklung und Beschreibung eines Verfahrens zur Expositionsabschätzung", IMST GmbH, Kamp-Lintfort and EM-Institut GmbH, Regensburg, 2005.
- [4] Chr. Bornkessel, M. Schubert and M. Wuschek, "Bestimmung der realen Feldverteilung von hochfrequenten elektromagnetischen Feldern in der Umgebung von UMTS-Sendeanlagen", Study for the German Federal Office for Radiation Protection, Interim Report "Entwicklung geeigneter Verfahren", IMST GmbH, Kamp-Lintfort and EM-Institut GmbH, Regensburg, 2005.
- [5] Chr. Bornkessel, M. Schubert and M. Wuschek, "Bestimmung der realen Feldverteilung von hochfrequenten elektromagnetischen Feldern in der Umgebung von UMTS-Sendeanlagen", Study for the German Federal Office for Radiation Protection, Interim Report "Entwicklung geeigneter Verfahren", IMST GmbH, Kamp-Lintfort and EM-Institut GmbH, Regensburg, 2005.
- [6] 26. BImSchV, Sechszwanzigste Verordnung zur Durchführung des Bundes-Immissionsschutzgesetzes (Verordnung über elektromagnetische Felder - 26. BImSchV), BGBl. Jg. 1996 Teil I Nr. 66, 20.12.1996.
- [7] Messempfehlung für GSM-Basisstationen, Bundesamt für Umwelt, Wald und Landschaft (BUWAL) und Bundesamt für Metrologie und Akkreditierung (METAS), Bern, 2002.

A SiGe Monocycle Impulse Generator for Impulse Radio Ultra-Wideband Applications

Jochen Dederer, Andreas Trasser and Hermann Schumacher

University of Ulm, Dept. of Electron Devices and Circuits, Albert-Einstein-Allee 45, 89069 Ulm, Germany,
phone: +49 731 5031590, e-mail: jochen.dederer@uni-ulm.de

Abstract— A compact 0.56 mm x 0.56 mm SiGe ultra-wideband (UWB) impulse generator is presented. The realized circuit generates ultra-short, symmetrical pulses with a peak-to-peak amplitude of 260 mV. The spectrum of the generated pulses has a -10 dB bandwidth of 7.5 GHz centered around 6 GHz. The pulse shape is similar to the first derivative of the Gaussian pulse and the corresponding power spectral density fits very well into the FCC regulatory spectrum mask.

I. INTRODUCTION

There are several possibilities for generation of UWB impulses. Step recovery diodes (SRD's) are used to generate step functions with extremely small transition times. Various impulse generators using SRD's together with a pulse shaping network have been published [1], [2]. The major drawback here is that these circuits can not be fully integrated. Other approaches use an oscillator that is time-gated with an external switch. Most previous work based on a gated-oscillator method includes an integrated monocycle impulse generator and transmitter [3]. However, the spectrum of the generated pulse sequences does not meet the FCC emission restrictions. An example for an impulse generator with active pulse shaping circuits is a CMOS impulse generator that generates output impulses which are similar to the fifth derivative of a Gaussian pulse [4]. Based on simulation results, the authors conclude that this approach will meet the FCC mask without additional filtering. A common approach for an impulse generator with passive pulse shaping circuits is to use an analog differentiator in the form of a L-C network together with a resistive load. The impulse duration and the achievable amplitude is determined by the L-C pulse shaping network and the rise-time of the signal that controls the pulse shaping stage. Similar to approaches with hybrid pulse generators using SRD's, the main difficulty here is to provide a control signal with very short transition times. Previously published work on impulse generators with passive pulse shaping circuits shows simulated pulse amplitudes in the range of 30 mV_{pp} [5]. In this work we present a novel, fully integrated SiGe HBT impulse generator that exhibits pulse amplitudes of 260 mV_{pp}. The pulse shape of the generated pulses is an excellent approximation of the first derivative of the Gaussian pulse. The broadband output spectrum of the ultra-short pulses is well centered in the allocated spectrum mask and meets the emission restrictions for UWB transmission without the need of complex filter structures. The presented design is optimized with regard to a simple and compact circuit topology together with a minimum

power consumption of the actual pulse shaper circuit.

II. TECHNOLOGY

The presented circuit has been designed and fabricated using the commercially available ATMEL SiGe2 HBT technology [6] which offers both, SIC (selectively implanted collector) transistors with an f_T of 80 GHz and non-SIC transistors with a lower f_T of 50 GHz but a larger collector-emitter breakdown voltage BV_{CE0} . Both types of transistors are used in this approach. The passive and active devices are realized on low-resistivity 20 Ω cm substrate. The process offers three metallization layers.

III. MONOCYCLE PULSE SHAPE

Several possible monocycle pulse shapes for UWB are described in [7]. Most commonly used is a monocycle pulse shape that can be obtained by taking the first derivative of the Gaussian pulse. This monocycle can be represented by

$$f(t) = -\frac{At}{\sqrt{2\pi}\sigma^3} \exp\left(-\frac{t^2}{2\sigma^2}\right) \quad (1)$$

where A defines the amplitude and σ determines the pulse width. The normalized pulse shape and the corresponding power spectral density of such a Gaussian monocycle with $\sigma = 25$ ps are shown in Fig. 1 and Fig. 2, respectively. The center frequency of the pulse spectrum is about 6.8 GHz and corresponds to the center of the allocated UWB frequency band from 3.1 GHz to 10.6 GHz.

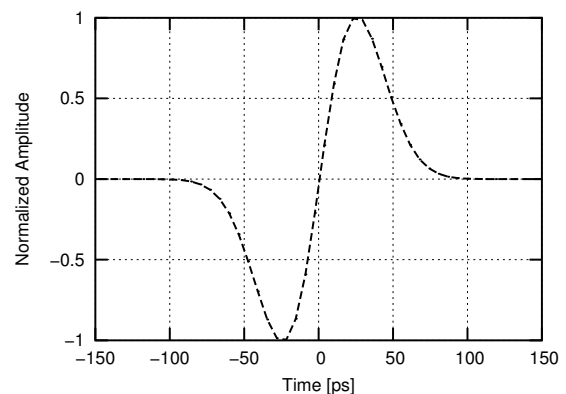


Fig. 1. Normalized pulse shape of Gaussian monocycle with $\sigma = 25$ ps

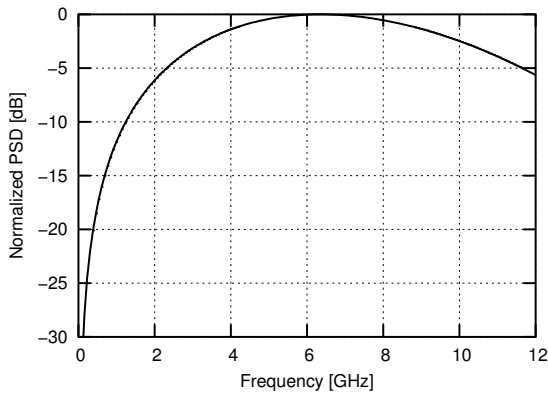


Fig. 2. Normalized power spectral density (PSD) of Gaussian monocycle with $\sigma = 25$ ps

IV. CIRCUIT DESIGN AND LAYOUT

The pulse generator circuit can be divided into three function blocks. The objective of the first function block is the generation of a squarewave signal with sufficiently short transition times for the actual pulse shaping in the succeeding function blocks. The first function block is realized as a limiting amplifier with two differential amplifier stages, each followed by a pair of emitter followers for decoupling of the stages as shown in Fig. 3.

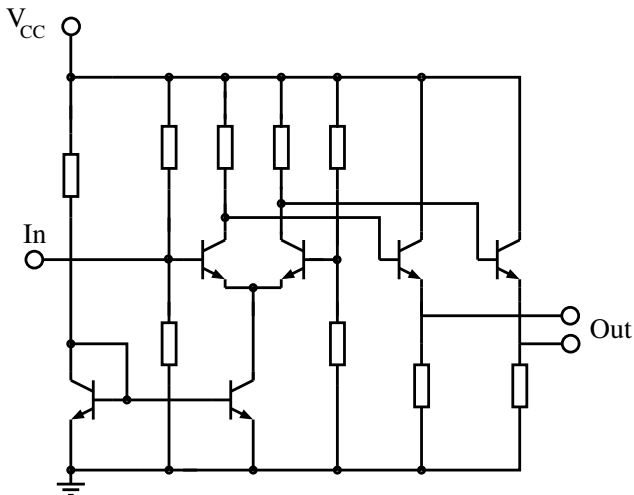


Fig. 3. Single stage of limiting amplifier

This first function block provides a control signal with very short transition times and makes the following pulse shaping almost independent of the risetime of the input signal - for the evaluation of the chip the pulse generator can even be operated with sinusoidal inputs. The two amplifier stages draw 5 mA at 3 V and 9 mA at 6.5 V, respectively. For low repetition rate input signals, this function block could be powered down in between the generated pulses. The limiting amplifier is followed by a C-R differentiating highpass network. This function block transforms the rising edge of the squarewave

signal into an output signal with a pulse shape similar to the Gaussian pulse and accordingly the falling edge of the squarewave into a pulse with negative amplitude. Only the positive pulse activates the pulse shaper, see below. The third and last function block is the actual monocycle pulse shaper. As stated earlier, the targeted pulse shape is obtained by taking the first derivative of the Gaussian pulse. The pulse shaper circuit consists of a single transistor in common emitter configuration with a resistive feedback R_E and the analog differentiator which is formed by inductor L and capacitor C together with the off-chip resistor R_L as shown in Fig. 4.

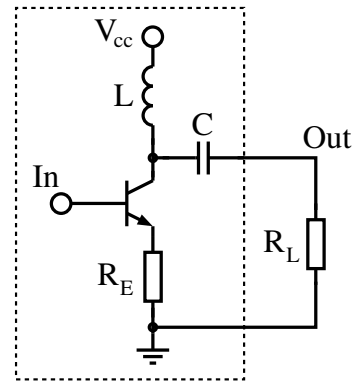


Fig. 4. Monocycle pulse shaper circuit

The sizes of the transistor, the inductor and the capacitor are chosen with regard to a maximum amplitude of the generated pulses while maintaining the targeted pulse duration together with a moderate pulse ringing due to the resulting L-C parallel resonance circuit. The transistor serves as a switch which is controlled by the output signal of the preceding differentiating network. Therefore the monocycle pulse shaper circuit only draws current in the presence of the positive, ultra short pulses at the base of the transistor. The complete chip, pads included, has a size of 0.56 mm x 0.56 mm. A microphotograph of the chip is shown in Fig. 5.

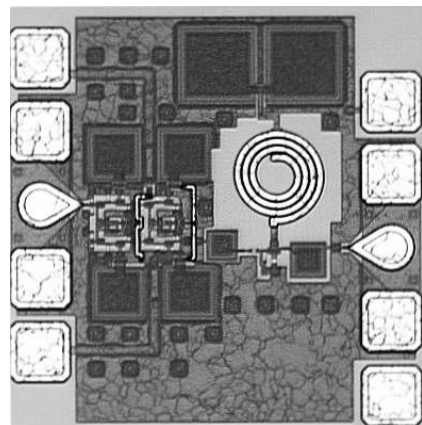


Fig. 5. Microphotograph of the monocycle impulse generator

V. MEASUREMENT RESULTS

All presented measurements were performed on-wafer in a $50\ \Omega$ test environment. Measurements in the time- and frequency domain were carried out using a digital sampling scope together with a 50 GHz sampling head and a spectrum analyzer, respectively. A conventional sinusoidal RF source generated the input signal to the circuit. Two on-wafer ground-signal-ground microwave probes were used to contact the input and output ports of the circuit.

A. Time-Domain Measurements

Fig. 6 shows the measured output pulses with a peak-to-peak amplitude of 260 mV and a pulse duration of 150 ps. The latter is defined as the time interval between the 10% points of the negative and positive peak of the monocycle.

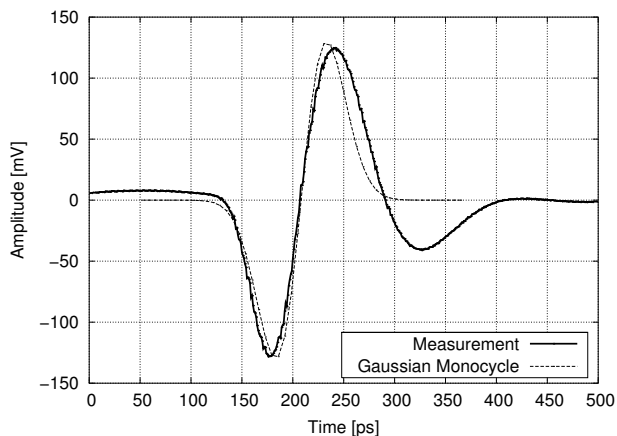


Fig. 6. Comparison of measured monocycle waveform with Gaussian monocycle ($\sigma=25$ ps, scaled to the amplitude of the measured pulse)

As shown in Fig. 6, excellent agreement between the mathematical derived, targeted monocycle pulse shape with $\sigma = 25$ ps (as described in Equation (1)) and the measured pulse shape has been achieved. The measured pulses show a good symmetry and a moderate ringing level.

B. Frequency-Domain Measurements

The spectrum of pulse sequences with regular pulse-to-pulse intervals shows discrete energy spikes corresponding to the repetitive period of consecutive pulses. The measured output spectrum of such a 50 MHz pulse train and its compliance with the FCC regulatory spectrum mask for indoor UWB devices [8] is depicted in Fig. 7.

For this pulse sequence, the monocycle pulse shaper circuit as shown in Fig. 4 draws $84\ \mu\text{A}$ at 2.5 V which equals a power consumption of only $210\ \mu\text{W}$. The signal energy of the pulse sequence is spread across the full allocated bandwidth and the corresponding output spectrum is well centered in the FCC spectrum mask. The spectral regrowth for low frequencies up to approximately 1 GHz is due to feed-through of spectral components of the squarewave signal to the output of the

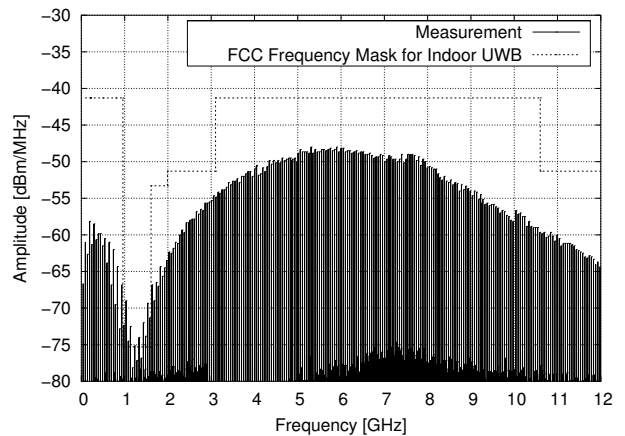


Fig. 7. Comparison of measured power spectral density with FCC regulatory mask for indoor UWB devices

circuit. Increasing the data rate leads to a concentration of the signal energy on less spectral lines while increasing the level of each spectral line. A random pulse-to-pulse interval smoothes the output spectrum as the RF energy is distributed more uniformly across the band. In the past, several papers have been published, presenting time-hopping modulation schemes with the focus on the spectral shaping of Impulse Radio UWB systems [9].

VI. CONCLUSION

We have demonstrated a novel UWB monocycle impulse generator in a commercially available SiGe HBT technology. The impulse generator exhibits pulses with a peak-to-peak amplitude of 260 mV. The corresponding spectral power density has a -10 dB bandwidth of 7.5 GHz which fits very well into the allocated spectrum mask. Good agreement between the targeted, mathematical derived pulse shape and the measured pulse shape has been achieved. The overall power consumption of the presented chip is 73.7 mW for a 50 MHz pulse repetition frequency. However, it can be reduced to a few milliwatts using a suitable power-down circuit for the limiting amplifier. The presented results qualify this circuit for operation in Impulse Radio UWB applications.

ACKNOWLEDGMENT

The authors wish to thank ATMEL GERMANY GmbH Heilbronn for the excellent support.

REFERENCES

- [1] J. Han and C. Nguyen, "Ultra-wideband electronically tunable pulse generators", *IEEE Microwave and Wireless Components Letters*, vol.14, issue 3, pp. 112-114, March 2004.
- [2] J. Han and C. Nguyen, "A new ultra-wideband, ultra-short monocycle pulse generator with reduced ringing", *IEEE Microwave and Wireless Components Letters*, vol.12, no. 6, pp. 206-208, 2002.
- [3] A. Azakkour, M. Regis, F. Pourchet, G. Alquie, "A new integrated monocycle generator and transmitter for ultra-wideband (UWB) communications", *IEEE Radio Frequency Integrated Circuits (RFIC) Symp.*, 12-14 June 2005, Long Beach, CA, USA.
- [4] H. Kim and Y. Joo, "Fifth-derivative Gaussian pulse generator for UWB system", *IEEE Radio Frequency Integrated Circuits (RFIC) Symp.*, 12-14 June 2005, Long Beach, CA, USA.

- [5] Y. Zheng, H. Dong and Y. P. Xu, "A novel CMOS/BiCMOS UWB pulse generator and modulator", *IEEE MTT-S International Microwave Symposium Digest*, vol. 2, pp. 1269-1272, 2004.
- [6] A. Schüppen, J. Berntgen, P. Maier, M. Tortschanoff, W. Kraus and M. Averweg, "An 80 GHz SiGe production technology", *III-V Review*, vol. 14, pp. 42-46, August 2001.
- [7] X. Chen and S. Kiaei, "Monocycle shapes for ultra wideband system", *IEEE Proc. of Int. Symp. Circuits and Systems (ISCAS)*, vol.1, pp. 597-600, 2002.
- [8] Federal Communications Commission: "First report and order: Revision of Part 15 of the commission's rule regarding ultra-wideband transmission systems", ET Docket 98-153, April 2002.
- [9] J. Romme and L. Piazzo, "On the power spectral density of time-hopping Impulse Radio", *IEEE Conference on Ultra Wideband Systems and Technologies (UWBST)*, Baltimore, pp. 241-244, May 2002.

A Low Cost Low Profile 19 GHz Scanning Receiver Array with a Nonradiative Dielectric Waveguide Feeding Network

Ulf Schmid¹, Wolfgang Menzel¹

¹University of Ulm, Microwave Techniques, Albert-Einstein-Allee 41, 89081 Ulm, Germany
Tel.: +49-7 31-502 63 50, E-Mail: ulf.schmid@uni-ulm.de, wolfgang.menzel@ieee.org

Abstract—A 19 GHz scanning receiver array is presented based on a frequency scan of the LO signal fed to an array of mixers. To allow a low loss, low profile setup, the LO feed is implemented in non-radiative dielectric (NRD) waveguide technique. Scan range is nearly 30° with an LO frequency variation from 22.8 GHz to 24.8 GHz. In addition a modification of the LO feed is proposed for a wider scan with a reasonably low LO frequency variation.

I. INTRODUCTION

Antennas with electronic scanning facilities are becoming increasingly important not only in the car industry. In the higher frequency range, this typically is associated with increasing loss and cost using conventional phased array techniques. A possible solution is the use of frequency scanned arrays, as it is demonstrated for automotive radar applications, e.g. in [1]. In [2] a wide scanning range was achieved with a frequency scanned antenna array using a suspended stripline negative index transmission line. A frequency sweep, on the other hand, poses other problems, e.g. it reduces range resolution for a FM/CW radar sensor. In [3], [4] alternative approaches have been presented using heterodyne principles with a frequency sweep in the LO path. Thus, RF frequency can be kept constant, and available bandwidth can be fully exploited for other purposes. In order to keep the LO and, consequently, the IF frequency variation small, long delay lines between the tapping points of the LO feed line have been selected [5], leading to a rather bulky and costly setup as rectangular waveguide was chosen for low loss behaviour. The non-radiative dielectric (NRD) waveguide on the other hand is known to be a low loss waveguide especially for increased frequencies, while allowing for low profile and low cost applications [6]. Therefore, in this contribution, a 19 GHz receiver array using an NRD-guide LO feed line is investigated. The RF signal is received by an array of 4 microstrip antenna elements. Each antenna element is connected to a mixer. The LO signal is distributed via a serial NRD-guide feeding providing the frequency dependent phase shift for beam scanning. In the mixers the RF signals are down converted to the IF band including the phase shift. The Wilkinson power combiner adds the IF signals in-phase.

An LO variation of 2.0 GHz in the 22.8 GHz to 24.8 GHz range allows for a 28° scan. In order to have a wide scanning

range while maintaining the circuit rather small, the LO signal is chosen to be higher than the RF signal (high-frequency injection). The receiver array consists of two layers. Antenna elements, mixers, filters and the IF power combination are implemented as planar structures on Ultralam 2000 ($\epsilon_r = 2.48$, thickness = 0.26 mm). The LO feeding network is made of an NRD-guide with Rogers TMM 6 ($\epsilon_r = 6$, $W_{NRD} = 6$ mm, $H_{NRD} = 3.18$ mm). The total height of the antenna is 3.5 mm only, plus the backside aluminium plate.

II. SETUP OF THE RECEIVER ARRAY

A basic block diagram of the investigated scanning array is given in figure 1. Each of four antenna elements is connected to a mixer. The LO signal is distributed via a serial NRD-guide feeding. An NRD-guide section with one of the

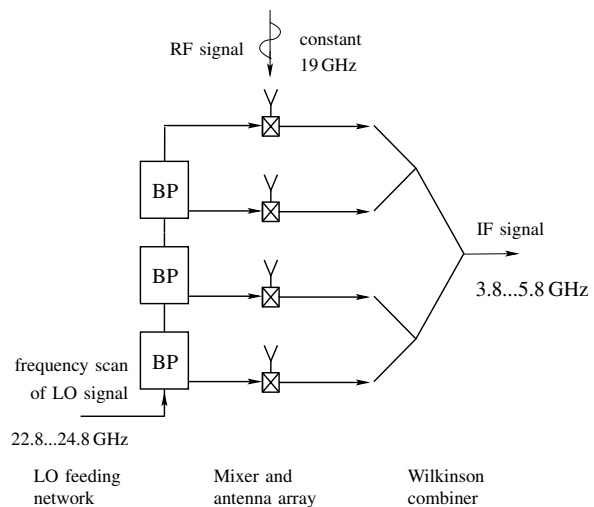


Fig. 1. Basic block diagram of the scanning array.

couplers is depicted in figure 2. First, a 3 resonator NRD-guide bandpass is designed, where the 4 impedance inverters are implemented by drill holes in the dielectric material. Then one of the smaller holes is replaced by the coupler NRD-guide to microstrip line including the coupling slot in the common ground metallization between the planar structure and the backside LO feeding network. The coupling values of the couplers are adjusted for an equal power distribution,

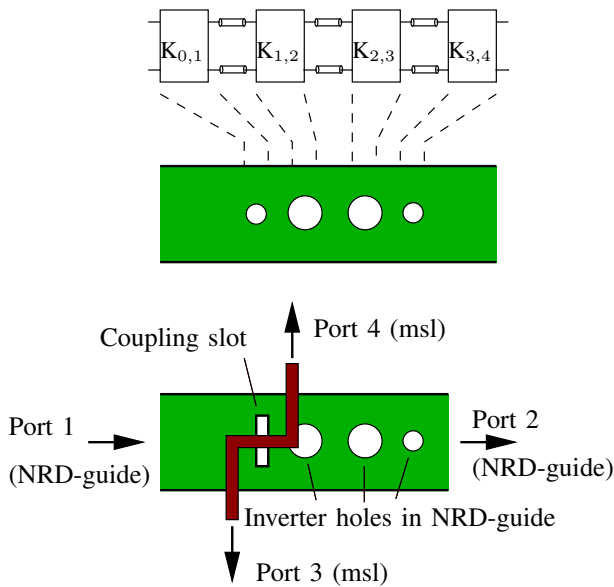


Fig. 2. Design steps of the couplers NRD-guide to microstrip line.

although some deviations occur over the operation bandwidth. Figure 3 shows the simulated S parameters of one exemplary coupler with a coupling coefficient of -10 dB. In the range from 22 GHz to 24.5 GHz a constant coupling factor of -10 dB is observed. Above 24.5 GHz the coupling factor is slowly increasing.

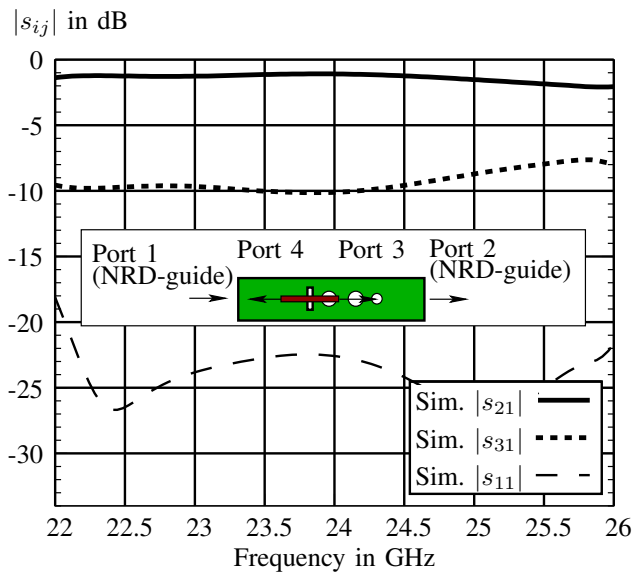


Fig. 3. Simulated S parameters of the second coupler.

The NRD-guide feeding network is operated in the longitudinal section electric (LSE) mode. This makes the delay lines shorter, as the wavelength is shorter compared to the longitudinal section magnetic (LSM) mode. The mixers are implemented as single balanced mixers, using low barrier silicon Schottky diode pairs DMF 2828(504-012) for low LO power consumption. The basic principle of the mixers

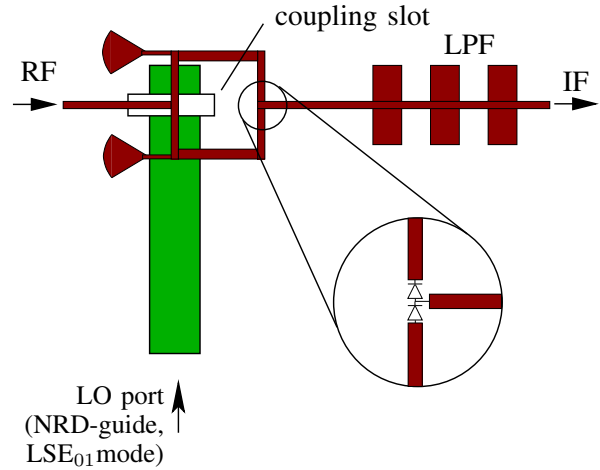


Fig. 4. Setup of the balanced mixer.

is shown in figure 4. The LO signal must be divided in two equal amplitude anti-phase signals to pump each diode. The coupling mechanism of the transition from NRD-guide to microstrip line via the slot in the common ground plane provides this 180° phase difference between the two microstrip line branches. In this way for the LO signal the connecting point between the two diodes is set virtually to ground. Radial stubs are used for a broadband IF blocking. The IF signals finally are combined in-phase by a four-to-one Wilkinson combiner network (see figure 5). A stronger weighting of the inner two channels is used for reduction of the side lobe level and in order to compensate for the deviation of the power distribution of the LO feeding network mentioned above.

III. RESULTS

The receiver array mounted for antenna measurements is shown in figure 5. Its lateral dimensions are 120 mm x 95 mm. This might be reduced by a smaller design of the planar parts. The thickness is 3.5 mm, plus the backside aluminium plate.

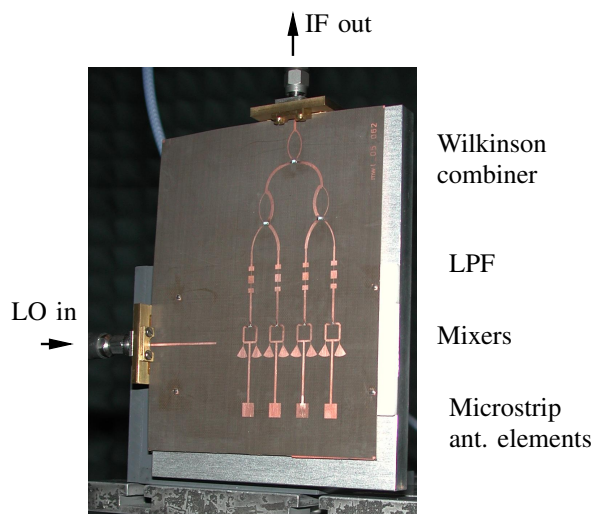


Fig. 5. Photo of the complete antenna.

A block diagram of the basic measurement setup for the radiation diagrams of the antenna is given in figure 6. Part of the transmit signal is fed to another mixer providing a reference signal. Both reference (IF) signal and receiver array output are fed to the downconverter of a network analyzer operated in a dual frequency mode. In this way, a coherent and sensitive measurement setup could be achieved [7].

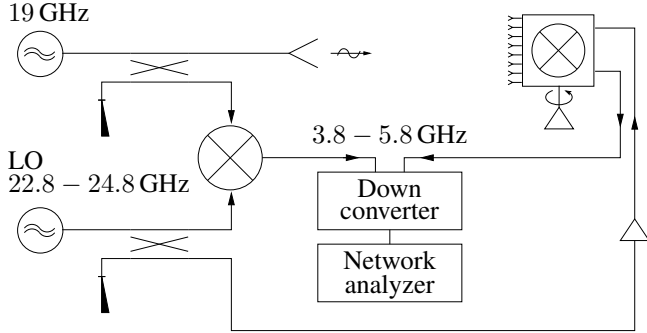


Fig. 6. Basic block diagram of the antenna measurement setup.

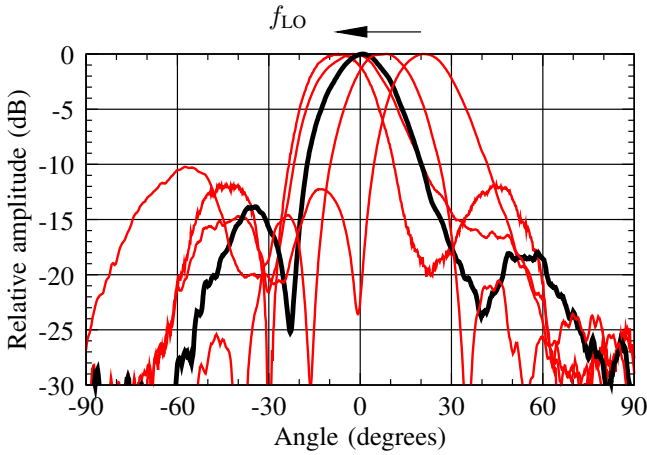


Fig. 7. H-plane radiation diagrams of the antenna array operated in the receive mode at 19 GHz (LO frequency 22.8 GHz to 24.8 GHz, IF frequency 3.8 GHz to 5.8 GHz, all diagrams normalized to 0 dB).

Figure 7 shows the H-plane radiation diagrams of the receiver arrangement at 19 GHz for LO frequencies from 22.8 GHz to 24.8 GHz, resulting in a scan range from -7° to $+21^\circ$. Figure 8 shows that in the frequency range from 22.8 GHz to 24.8 GHz the side lobe level is below -10 dB. Measurement of the radiation diagrams for a wider range of LO frequencies showed that allowing a slightly higher side lobe level of -8 dB, the scan range is extended to -11.8° to $+23.5^\circ$.

In [5] it was shown that by inserting a 3.8 GHz to 5.8 GHz signal at the IF port and a 22.8 GHz to 24.8 GHz signal at the LO input port (figure 5), the antenna can also be operated in transmit mode with a constant RF signal at 19 GHz.

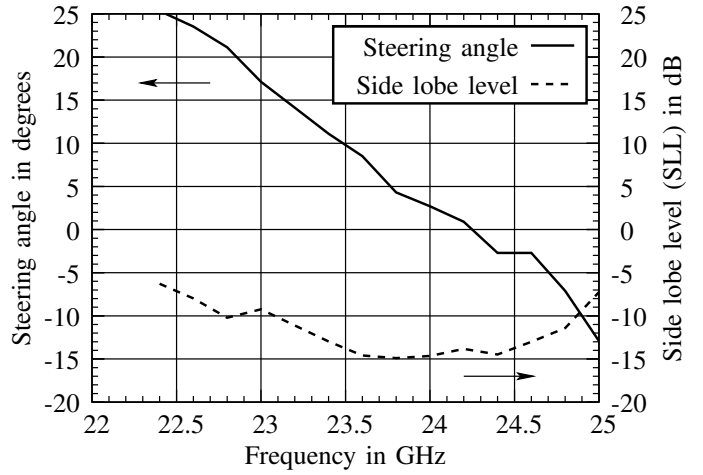


Fig. 8. Measured steering angle and side lobe level of the radiation diagram of the receiver array dependent on the LO frequency.

IV. TWO-PATH BANDPASS FILTER FOR STEEP PHASE INCREMENT

In [8] a class of two-path multimode bandpass filters using the NRD-guide (figure 9) was proposed, providing an additional pole of attenuation in the stop band close to the cut-off frequency thus offering higher rates of cut-off than one-path NRD-guide bandpass filters.

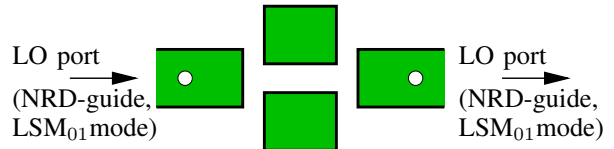


Fig. 9. Basic block diagram of the two-path NRD-guide bandpass filter.

In this contribution two-path bandpass filters are proposed to provide a steep phase increment over frequency to allow for a wide scanning range with a low LO frequency variation. The step from the one-path NRD-guide to the two-path NRD-guide excites both the LSE and the LSM mode in the two-path NRD-guide section. This increases the order of the bandpass filter by 1. The symmetry along the NRD-guide prevents the excitation of the LSE mode in the one-path NRD-guide section. So actually the two-path NRD-guide bandpass filter is a resonator of order 4 and has therefore a steeper phase increment compared to the one-path NRD-guide bandpass filter. In figure 10 only 3 zeros can be observed, this is because of improper filter design.

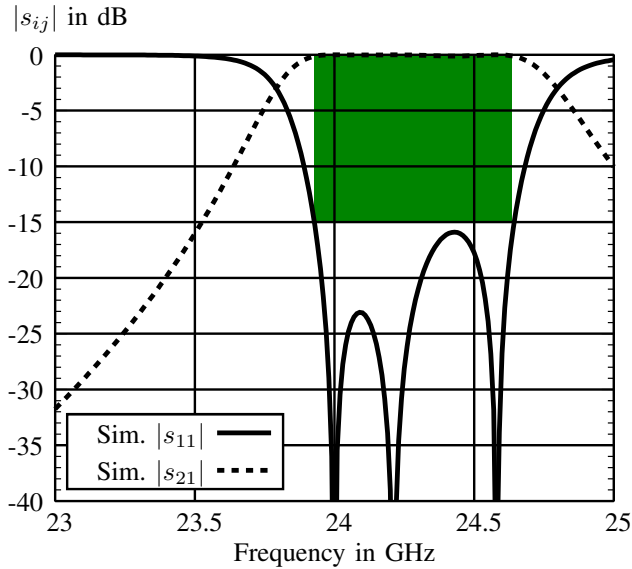


Fig. 10. Simulated S-parameters of the two-path NRDguide bandpass filter.

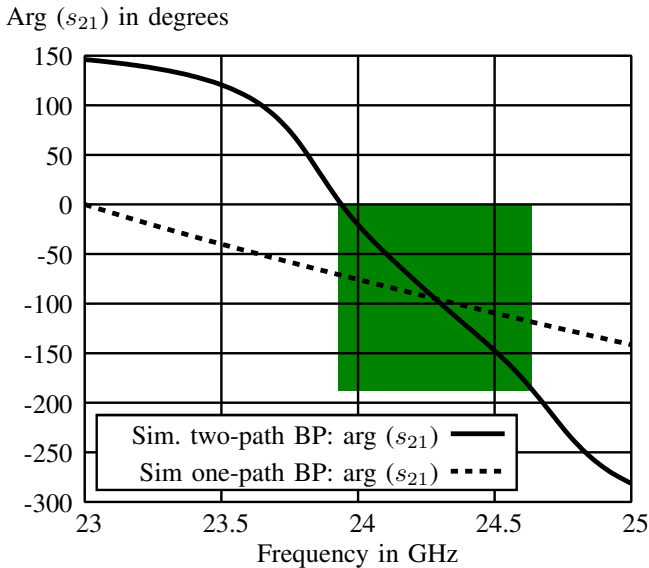


Fig. 11. Phase behavior of the two-path NRD-guide bandpass filter (figure 9) and of the one-path NRD-guide bandpass filter (figure 2, middle), showing the steeper characteristic of the first.

The comparison of the phase increments (figure 11) of a two-path NRD-guide bandpass filter and of a one-path NRD-guide bandpass filter shows the big advantage of the first. In the 0.72 GHz range from 23.92 GHz to 24.64 GHz where return loss is below -15 dB (figure 10), a variation of the phase increment by 188° is achievable, leading to a wider scanning range compared to the 2 GHz range from 23 GHz to 25 GHz where only a variation of the phase increment by 145° is achievable with the one-path NRD-guide bandpass filter.

V. CONCLUSION

A 19 GHz scannable receiver array with four antenna elements has been presented. The antenna beam scanning is achieved by a frequency scan of the LO signal. In this array, scan range was limited to -11.8° to $+23.5^\circ$ due to a phase offset of the couplers and a limited phase increment. Preliminary investigations have been presented for a scanning receiver array with reduced LO frequency variation and wider scanning range using two-path NRD-guide bandpass filters. Such an array is currently under investigation and is expected to make a scanning range of $\pm 50^\circ$ feasible. For a smaller beamwidth in the H-plane, the array can be easily extended to 8 antenna elements. In the E-plane the beam might be narrowed by using a set of serial fed patches. The lateral dimensions of the antenna (120 mm x 95 mm) could be further reduced by the use of smaller designs of the planar parts including approved and low cost MMIC mixers. The possibility to drive this type of antenna arrays in a transmit mode was shown in a previous contribution [5], where the scan range is identical to the scan range in receive mode but inverse over LO frequency.

REFERENCES

- [1] P. Relph and H. Griffiths, "An electronically scanning antenna for automotive radar systems," *IEEE Colloquium on Automotive Radar and Navigation Techniques*, pp. 535–537, 1998.
- [2] W. Menzel and M. Sathiaselvan, "Frequency scanned antenna array using a suspended stripline negative index transmission line," in *European Microwave Conference*, 2005, pp. 253–256.
- [3] T. Nishimura, N. Ishii, and K. Itho, "Beam scan using the quasi-optical antenna mixer array," *IEEE Transactions on Antennas and Propagation*, vol. 47, no. 7, pp. 1160–1165, July 1999.
- [4] M. Kim, J. Hacker, A. Sailer, and J. Hong, "A heterodyne-scan phased-array antenna," *IEEE Microwave and Guided Wave Letters*, pp. 7/1–7/7, 1999.
- [5] U. Schmid and W. Menzel, "A 24 GHz scanning receiver array," in *Symposium on Antenna Technology and Applied Electromagnetics, ANTEM 2002*, pp. 319–322.
- [6] —, "A 24 GHz microstrip antenna array with a non-radiative dielectric waveguide (nrd-guide) feeding network," in *Symposium on Antenna Technology and Applied Electromagnetics, ANTEM 2005*, pp. 266–267.
- [7] W. Menzel and R. Werner, "A high dynamic range extension for antenna measurements in the mm-wave range," in *MIOP, Stuttgart, Germany*, 2001, pp. 94–97.
- [8] J. Huang and K. Wu, "A two-path multimode bandpass filters using the nonradiative dielectric (nrd) waveguide technology," in *IEEE Transactions on Microwave Theory and Techniques Symposium*, vol. 3, 1995, pp. 1547–1550.

Broadband Wilkinson Divider

Andreas Wentzel and Dariusz Pienkowski

Technische Universität Berlin, Microwave Engineering Group, Einsteinufer 25, 10587 Berlin, Germany,
tel. 00493031426984, pienkows@mwt.ee.tu-berlin.de

Short Abstract — This paper introduces a hybrid wideband architecture of the Wilkinson divider with tapered line and compares it with two-stage architecture. Such a combiner is broadband and works from 0.5 up to 3.5 GHz. The limiting factor of this solution is the insertion loss.

Keyword: wilkinson power divider, combiner, tapering, power amplifier

I. INTRODUCTION

The Wilkinson power divider is often made in microstrip or stripline form and is in common use in RF design, since it was introduced quite a lot years ago [1]. The divider/combiner is used to combine the power of multiple transistors in an amplifier or antennas in a system, or divide the power among channels in a receiver [2]. The main disadvantage of the circuit is relatively narrow band of operation, which gains more on importance when ultra wide band solutions are required. Even with the use of new wide band gap SiC or GaN transistors achieving high output power in power amplifiers require the use of power combining and dividing. Dividing is required at the input of the power amplifier and combining is needed at its output. In ideal case, when two amplifiers are considered the output power can be doubled. However, the combiner and splitter, which are in most cases the same structure introduces losses. Therefore a low loss combiner is required what for one frequency or even narrow band operation could be realized. The problem enlarges when broadband power amplifier like this shown in [6] are combined. This two-stage 5-W wide-band RF power amplifier has been designed using a SiC MESFET power stage covering the frequency range from 10 MHz up to 2.4 GHz. Another important combiner parameter is isolation. The output power of one amplifier should not appear at the output of another amplifier's output. With high output power this issue gains on importance. Thus, power combiner has to feature with low loss and good isolation over a wide band at the same time.

One of the established methods that enable the broadband operation of the Wilkinson divider (combiner) is the use of multiple stages, as it was introduced in [3]. Generally, each stage makes the bandwidth wider, but simultaneously introduces transmission losses, which are critical for high power applications, as it is already written. This leads to the trade-off between the losses and the bandwidth. More sections require also more area. In case of system on board solutions it is not the problem, but in some cases where area constraints are important it could play an important role. Another possibility for broadband operation is the use of tapered lines as it is

described in [4]. The tapered solution requires a similar area, but shows the wider bandwidth.

An optimum solution seems to be a hybrid one that combines two-stage and tapered combiners. Therefore, in this paper we introduce two-stage Wilkinson power combiner with the second section tapered. We investigate and compare a two-stage combiner with a combiner with the second stage tapered. This paper is organized as follows: section II describes the design of the compared circuits, section III compares measured and simulated data regarding insertion loss, return loss at the input and output and isolation. Section IV completes this paper.

II. CIRCUIT REALIZATION

The simplified schematic of the two-stage Wilkinson combiner is shown in Figure 1.

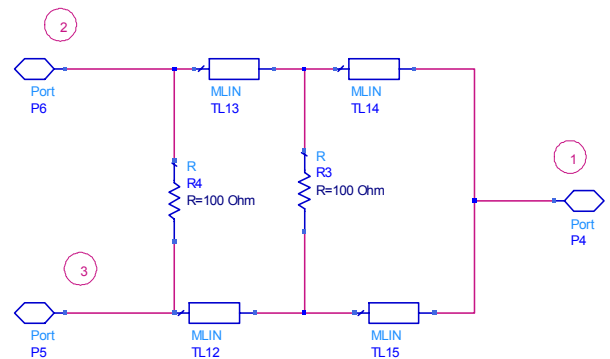


Figure 1. Two-stage Wilkinson combiner.

This combiner is called “normal” further in the scope of this text. This circuit represents a lossy three-port network which can be made having all ports matched with isolation between the output ports (port 3 and port 2) [5]. It has the useful property of being lossless when the output ports are matched; that is, only reflected power is dissipated. This normal Wilkinson combiner contains two pairs of quarter-wavelength transmission lines having a characteristic impedance of $\sqrt{2} \cdot Z_0$ (70.7Ω if we define Z_0 to be 50Ω) and two bridging resistors with a value of $2 \cdot Z_0$ (100Ω) to match the ports. The electrical length of the transmission lines is different in each stages; it is optimized for the broad band operation. The second combiner introduced in this paper is shown in Figure 2. This circuit is called “tapered” further in the text. The first stage is almost

identical with the “normal” combiner, and the second stage is tapered. In reality more complicated structures are used, because of area and feasibility constraints. Therefore, transmission lines fabricated on the laminate are not straight; they are curved this way, that small surface mounted resistor can be placed at the end of the branches. Moreover in physically realized structure which has been simulated additional microstrip components (Tee, Bends, Steps) are used. Therefore it was possibly to use the automatic layout

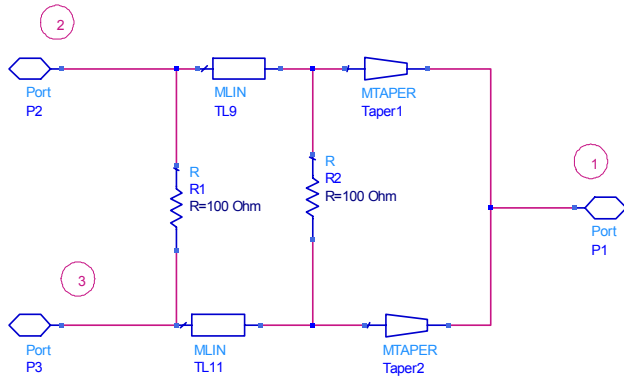


Figure 2. Two-stage Wilkinson divider with the second stage tapered.

generation tool, the feature from ADS. The photograph of these two dividers is shown in Figure 3. It is clear to see from the photograph that second tapered stage consumes less area.



Figure 3. Photograph of the realised combiners; tapered on the left, normal on the right side.

Among a possible few solutions for tapered microstrip line the triangular taper has been chosen, because of the fact that such transmission lines are available in layout design software ADS form Agilent. The impedance of the triangular tapered transmission line along its length $Z(z)$ and the reflection coefficient magnitude response $|\Gamma|$ varies like it is shown in Figure 4 and 5. The Z_0 means the impedance seen at the beginning of the line, Z_L is the load impedance connected to the line. This two figures show the possibility of broadband operation of such a transmission line. The impedance along the line length and the reflection coefficient do not change as

rapidly as in the case of normal transmission line. Thus with proper combining of transmission and tapered lines desired passband operation of the divider can be achieved.

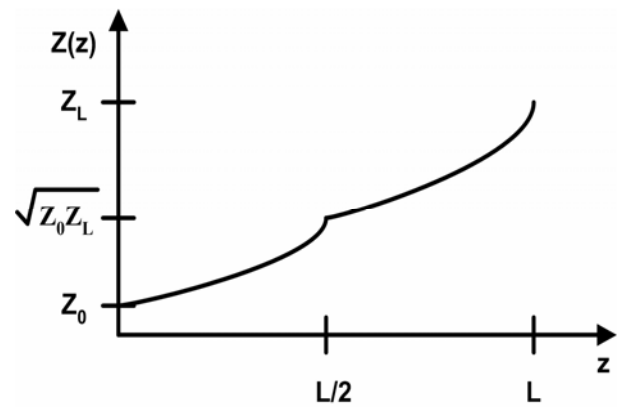


Figure 4. Variation of impedance of a tapered line

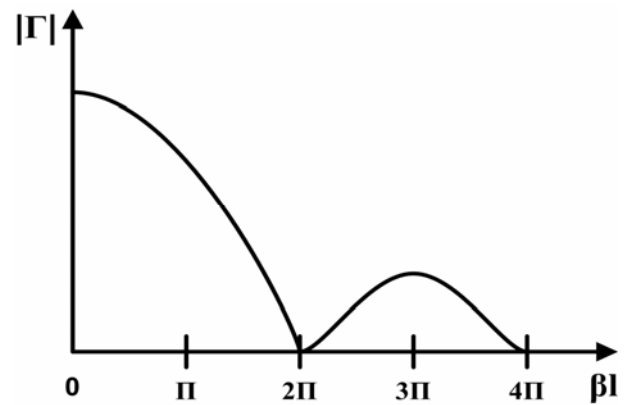


Figure 5. Reflection coefficient magnitude response of a triangular taper

III. MEASUREMENT RESULTS

In this section measurement data of the combiners are shown. Both combiners have been fabricated using the RO 4003 PCB laminate form ROGERS and measured in the frequency range form 500 up to 5000 MHz. The resistors used the circuit posses of 1 % tolerance. On the each following Figure we compare both types of combiners.

In Figure 6 the input reflection coefficient at Port 1 (common port) of both combiners is shown. If we assume that -10 dB is the highest possible value; we see that the input matching at Port 1 for “normal” combiner is not satisfactory for the frequencies higher than 2.5 GHz. In turn, the tapered combiner shows good input matching at this port in the whole, measured frequency range.

In Figure 7 the input reflection coefficient at Port 2 and Port 3 is shown. Since the circuits are symmetrical both values are the same, and for that reason only input matching at Port 3 is depicted. Taking the same criterion as an in the previous case we see that both solutions work in wide frequency range.

The transmission loss of the combiners is shown in Figure 8. This is important parameter and should be as low as possible. The “normal” combiner has lower insertion losses than “tapered” up to 2.5 GHz, but for the higher frequencies the losses are unacceptable. In turn, “tapered” combiner works in wider frequency range. With maximum 1 dB loss it works up to 3.5 GHz, when the “normal” combiner only up to 2 GHz. The insertion loss of the second branch (S_{13}) is identical and not shown here..

The last measured parameter is isolation between the ports shown in Figure 9. Once again taking as a criterion the value of 10 dB is easy to see that “tapered combiner” works at least up to 5 GHz. In turn, “normal” combiner works up to 2.5 GHz. However the lowest value of less then -35 dB shows the “normal” combiner.

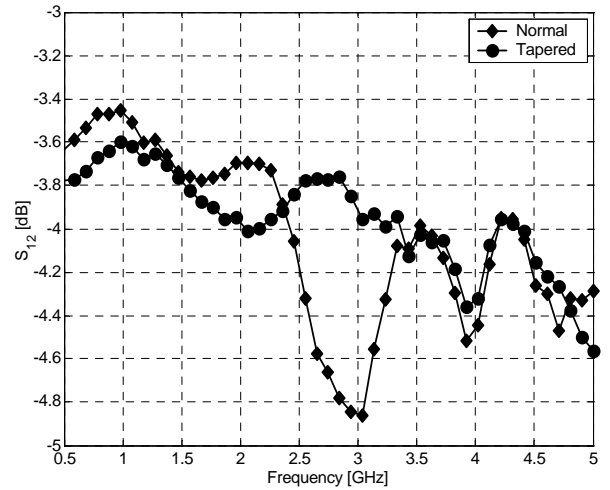


Figure 8. Measured S_{12} of the combiner.

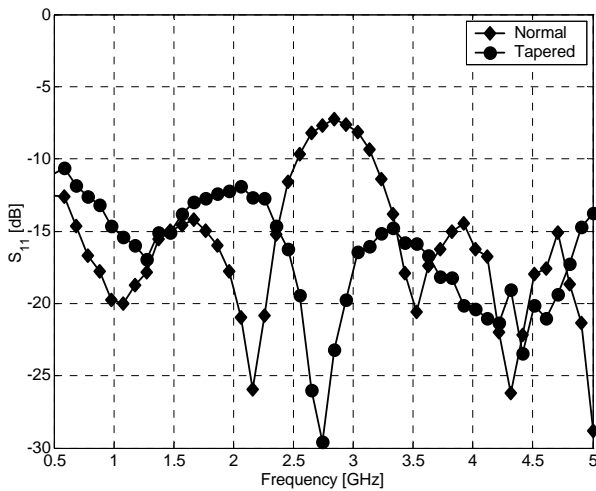


Figure 6. Measured S_{11} of the combiner.

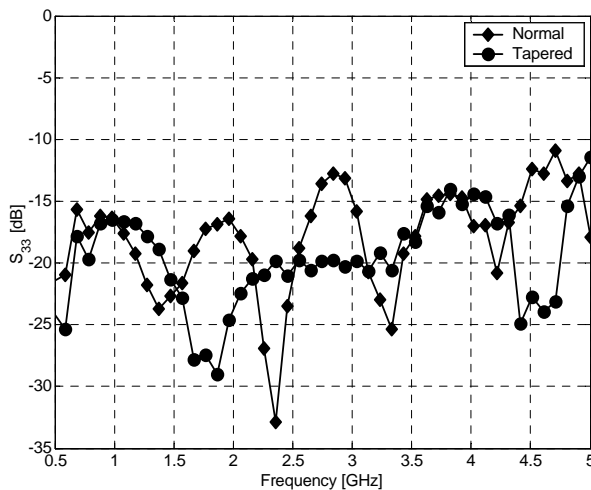


Figure 7. Measured S_{33} of the combiner.

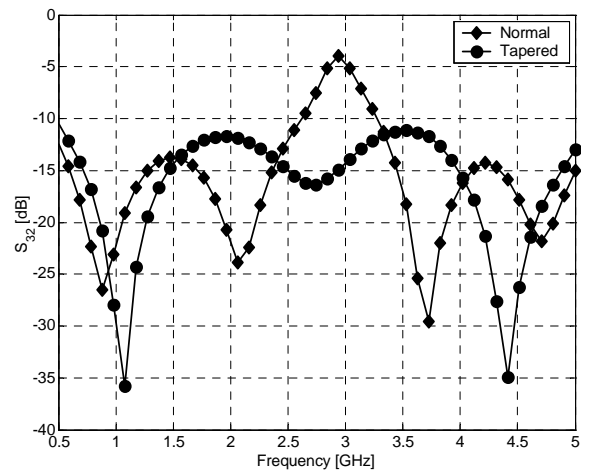


Figure 9. Measured S_{32} of the combiners.

IV. CONCLUSION

Two wideband architecture of the Wilkinson divider are shown in this paper. Two-stage transmission line architecture is compared with the architecture with the second stage tapered. The second architecture is broadband and works up to 3.5 GHz, since the architecture without tapered stage only up to 2.5 GHz. The limiting factor of the tapered solution is insertion loss, because other parameters are broadband. Two stages untapered solution is limited by insertion losses, isolation and input matching at the common port.

There are several possibilities to improve the performance of the combiner presented in this paper. The third stage would also increase the the transmission loss, but additive inductive and capacitive elements connected in the branches of existing two stages will help to decrease loss.

REFERENCES

- [1] E. Wilkinson, "An *N*-Way Hybrid Power Divider", IRE Transactions on Microwave theory and Techniques, January 1960, p. 116-119
- [2] I.D. Robertson, S. Lucyszyn, "RFIC and MMIC design and technology", IEE Circuits, Devices and Systems Series 13
- [3] S. B. Cohn, "A Class of Broadband Three-port TEM Hybrids", IEEE Transaction on Microwave Theory and Techniques, vol MTT-16, No 2, February 1968, pp 110 - 116
- [4] D.I. Stones, P. D. Chowm, "Q and V band Combiners" MTT-S Digest, 1991, pp 1049 – 1052.
- [5] D. Pozar, "Microwave Engineering", 3rd Edition, John Wiley & Sons, Inc., 2005
- [6] Sayed, A.; Boeck, G. "Two-stage ultrawide-band 5-W power amplifier using SiC MESFET", Transactions on Microwave Theory and Techniques, Volume 53, Issue 7, July 2005 Pages:2441-2449

Improved Antenna Isolation in Transmit/Receive Applications

D. Esser, B. Solan and H. Chaloupka

University of Wuppertal, Department of Electrical, Information and Media Engineering
Rainer-Gruenter-Str. 21, D-42119 Wuppertal, Germany, Phone +49 202 439 1938, E-Mail: h.chaloupka@uni-wuppertal.de

Short Abstract — This paper shows how TX-RX-isolation can be significantly improved if two-port antennas with passive cross-talk cancellation are employed. An antenna structure composed of two half-wave spaced monopole antennas serves as an example to demonstrate how the frequency response of the residual antenna cross-talk can be adjusted to meet various system demands.

Keywords — *antennas; mutual coupling; duplexing; radio-repeater*

I. INTRODUCTION

Systems with simultaneously operating transmitters and receivers require an excellent isolation between receive and transmit paths for preventing the transmit signal to cause saturation and intermodulation distortion in the sensitive receiver part. Furthermore, masking of the receive signal by spectral transmit signal components falling into the receive band has to be avoided. In case that frequency bands for transmit (TX) and receive (RX) are sufficiently wide separated in frequency, bandpass filters and/or filter duplexers are used to provide the required isolation.

On the other hand, there are applications e.g. radio repeaters where RX and TX bands have to be closely spaced (or even have to occupy the same band), where in principle the demanded isolation cannot be achieved with microwave filters or where isolation provided by filters is not sufficient. The following discussions are focused on this type of applications.

In case of a shared antenna nonreciprocal ferrite circulators are used to isolate RX and TX ports. Besides the limited isolation of circulators (< 35 dB) a very high return loss (matching) is required at the port of the shared antenna. Alternatively, two-port antennas with isolated ports can be used (self-duplexing antennas). High antenna-port isolation is well-known to be available from widely spaced antennas or – in case of narrow spacing- if they possess mutually orthogonal polarization (dual-polarized antennas, see e.g. [1]). However, in contrast to common belief high isolation between antenna ports can also be achieved for relatively closely spaced copolar antennas.

From the most general point of view a two-port antenna can be considered as an arbitrary open structure with 2 ports. Both ports are associated with radiated far fields. Their angular

dependence can (for a given frequency) be characterized by complex-valued vector radiation patterns (short port patterns)

$$\vec{C}_m(\Theta, \Phi) = \sqrt{g_m(\Theta, \Phi)} \exp(j\varphi_m(\Theta, \Phi)) \vec{p}_m(\Theta, \Phi) \quad (1)$$

with $m=1,2$ as the port number, g_m as the antenna gain function and φ_m as the phase function, both corresponding to port m . The phase functions φ_m are referenced for a common point (usually center of antenna structure). Polarization is characterized by the unit phasor \vec{p}_m with $|\vec{p}_m|=1$. For two-port antennas without dissipative losses and perfectly isolated ports the two port-patterns have to be mutually orthogonal, which means that

$$\oint \vec{C}_1^*(\Theta, \Phi) \cdot \vec{C}_2(\Theta, \Phi) d\Omega = 0 \quad (2)$$

holds. The integral in eq.(2) is carried out over the unit sphere and $d\Omega$ denotes the element of solid angle. The physical meaning of orthogonality in conjunction with a pair of port patterns can be explained by considering the totally radiated power in case of a two-port antenna where both ports are excited simultaneously. This totally radiated power can be compared with the radiated power values in case of separately excited ports. In general, the totally radiated power differs from the sum of the radiated power values for separate port excitation, but in the special case of mutually orthogonal patterns radiated power superposition holds. In case of dual-polarized antennas, eq.(2) is met due to mutually orthogonal polarization with

$$\vec{p}_1^* \cdot \vec{p}_2 = 0.$$

However, in case of port patterns with identical polarization eq.(2) is met by different angular dependence of the far field phases φ_1 and φ_2 (common reference point) and/or antenna gain functions g_1 and g_2 . Based on this fact, it was shown in previous publications [2,3] that isolated ports can even be achieved if the total size of the antenna structure is significantly smaller than half a free space wavelength (e.g. $\lambda_0/10$). In case of these very compact antennas for diversity and MIMO applications, isolation is obtained by cost of a considerably reduced frequency bandwidth and/or efficiency [2]. In contrast to these previous publications, the present paper deals with two-port antennas with an element spacing on the

order of about $\lambda_0/2$ and is focused on high antenna port isolation in a considerably wide frequency band for transmit/receive applications (self-duplexing two-port antenna).

II. COMBINATION WITH FILTER FUNCTION IN CASE OF NARROW-SPACED RX AND TX BANDS

Due to the physical origin of TX-RX-decoupling via isolated antenna ports it (of course) does not rely on the utilization of different non-overlapping frequency bands for TX and RX. Therefore, it could in principle even be used in case of simultaneous TX and RX operation in an identical frequency band (e.g. for on-frequency radio repeater). In this section a different situation is considered, namely the case where TX and RX occupy non-overlapping frequency bands, but the guard band between these bands is much too small to allow TX/RX isolation exclusively via microwave bandpass filters. By considering this special case, the combined effect of antenna port isolation and bandpass filtering can readily be discussed (see Fig. 1).

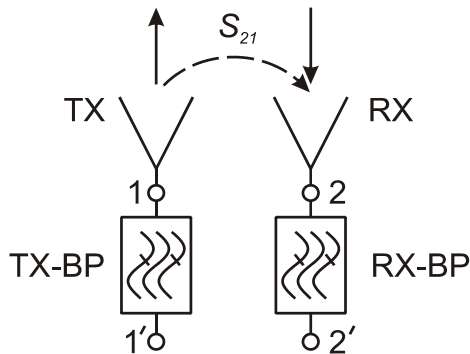


Figure 1. Transmit/receive operation in non-overlapping TX and RX frequency bands with transmitter bandpass TX-BP, receiver bandpass RX-BP and non-vanishing cross-talk (S_{21}) between the antenna ports.

Fig. 2 schematically shows the situation one has to deal with if due to system demands the width of the guard band between TX and RX bands surpasses the selectivity properties available from realistic bandpass (BP) filters. Starting with the given TX and RX bands the insertion loss response $L_{TX}(f)$ and $L_{RX}(f)$ of TX-BP and RX-BP are depicted in Fig. 2. The path from TX-port 1' to RX-port 2' is given by the chain composed of TX-BP, (unwanted) transmission link between the antennas (cross-talk) and RX-BP. In a rigorous evaluation of the overall insertion loss L of this chain, multiple reflections at these chain components had to be taken into account. However, if the cross-talk attenuation $L_A/dB = -20\log|S_{21}|$ is assumed to exceed 10 dB, multiple reflection can be neglected. Thus, the combined filter insertion loss can be estimated by the sum $L_{TX}(f) + L_{RX}(f)$. The curve for this combined filter insertion loss in Fig. 2 (solid line) clearly indicates that due to finite filter selectivity and a relatively narrow guard band, the available attenuation can drop to unacceptable low values (22 dB in the example) at frequencies close to the inner edges of the bands. If an overall insertion loss L is demanded (70 dB in the example) the

remaining attenuation $L - L_{TX} - L_{RX}$ has to be provided by the antenna isolation $L_A/dB = -20\log|S_{21}|$. The curve for this required cross-talk attenuation L_A is also shown in Fig. 2 and serves as an representative example for systems requirements.

III. BASIC PRINCIPLE OF CROSS-TALK COMPENSATION

A pair of co-polarized antennas with a spacing of about $\lambda_0/3$ to $2\lambda_0/3$ exhibits a cross-talk attenuation on the order of 10 to 20 dB. This level of isolation turns out to be not sufficient for the class of application addressed in section II.

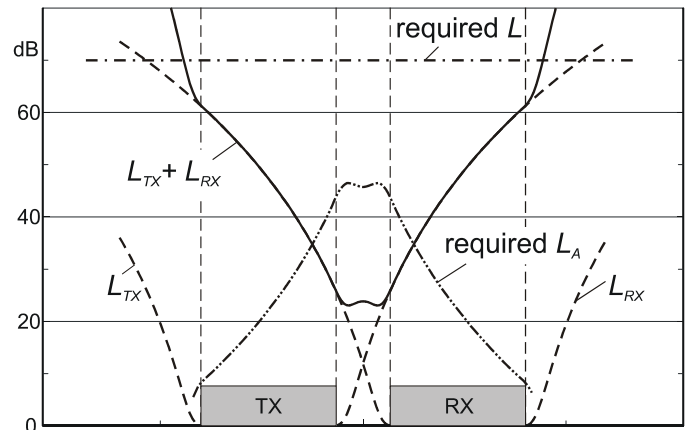


Figure 2. Determination of the required cross-talk attenuation $L_A/dB = -20\log|S_{21}|$ from TX and RX filter response L_{TX} and L_{RX} and the required overall TX-RX isolation L .

Isolation between the antenna ports can be enhanced by employing cancellation techniques. These techniques require a modification of the antenna structure such that in addition to the already existing “propagation path A” (Fig. 3, left) a second path B is created (Fig. 3, right) whose parameters can be adjusted to cancel the unwanted transmission via path A. If the paths are modeled via linear passive two-ports (lower part of Fig. 3) the perfect cancellation (perfect port isolation) requires that for shorted port 2 the two output currents are directly opposed, i.e. $I_{2,B} = -I_{2,A}$.

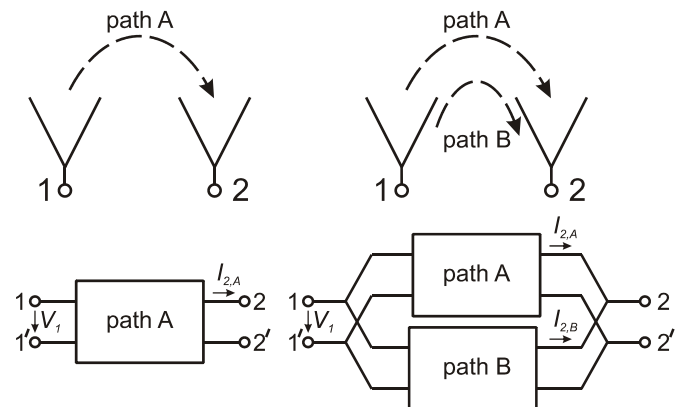


Figure 3. Left: Two-port antenna without cross-talk cancellation and corresponding model. Right: Cancellation of path A by a second path B and corresponding model.

There are different options for the realization of the second path. In [2,3] we have shown that an external passive (ideally loss-less) reciprocal and non-radiating decoupling-network can be placed between the antenna ports. However, the second path can also be created within the radiating structure [4]. It should be noted that in [5] a cancellation techniques (“feedforward isolation enhancement”) is proposed for increasing the isolation in case of dual-polarized microstrip patch antennas. In contrast to our approach the output signals of the two paths are summed up with a resistive power combiner preventing the output signal of path A to flow back into path B. Since the principle of this alternative concept relies on components with dissipative loss, the simplicity of the circuit is achieved at the expense of an increased attenuation of the received signal.

In contrast to our previous papers on this subject special emphasis will be devoted to structures which allow variations in the frequency response of the cross-talk attenuation. In particular, it will be demonstrated that with path B being itself composed of multiple paths perfect isolation can be achieved at multiple frequencies.

IV. DESIGN EXAMPLE

A. Antenna Structure

The concept of cross-talk cancellation as described in section III can in principle be applied to any two-port antenna. A structure with an element spacing of about a half free space wavelength (λ_0) was chosen in order to demonstrate that high isolation (> 40 dB) in a sufficiently wide frequency regime can be obtained even if a stringent restriction for the spacing between TX element and RX element applies and, furthermore, both elements are using identical polarization.

A configuration composed of two 2.45-GHz monopoles with about half-wave spacing was chosen as a starting structure. It possesses a crosstalk $|S_{21}|/\text{dB} = -L_A/\text{dB}$ of about 16 dB. A "second path" (see Fig. 3, right) was realized by placing a microstrip structure between the two monopole antennas (Fig. 4). The planar conductors are separated from the metallic ground plane by means of a 1 mm thick dielectric layer with $\epsilon_r = 4$. In a first step the lateral strip width w was chosen small enough to ensure that no propagating mode except the quasi-TEM mode is supported. In order to keep the transmission coefficient of this second path sufficiently small (about -16 dB) both ends of the transmission line were separated from the metallic rods of the monopoles by a gap of width s . Furthermore, another gap of width g is placed in the center (see Fig. 4). This microstrip structure acts as a second path (see Fig. 3, right) which together with the path due to mutual coupling between the two monopoles forms a two-path circuit. By a proper choice of the geometric parameters of the microstrip structure a transmission null (practically isolation > 50 dB) can be achieved at one prescribed frequency.

In a second step the width w of the microstrip sections was significantly increased in order to allow a dual-mode propagation along these line sections. For $w > \lambda_0/2\sqrt{\epsilon_r}$ a propagating quasi-TE₁₀ mode (with maximum electric field strength at the lateral edges) can be supported, but is not

excited due to symmetry properties. For $w > \lambda_0/\sqrt{\epsilon_r}$ the quasi-TE₂₀ mode begins to propagate. In this case the microstrip structure supports two different transmission paths between the monopole antennas, one path due to the quasi-TEM mode and the second path due to the quasi-TE₂₀ mode. Together with the path due to mutual coupling between the two monopoles a three-path behavior occurs. In principle, a three-path structure allows cancellation and thus perfect transmission nulls (ideal port isolation) at two different frequencies which can be chosen independently from each other. This latter case, namely a structure with dual-mode operation was studied in details by means of numerical simulations (section B), followed by some experiments (section C).

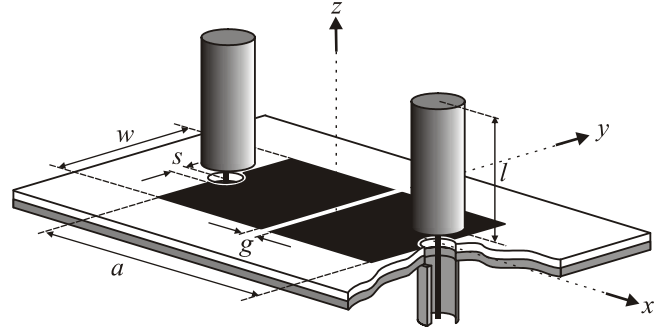


Figure 4. Antenna structure under consideration. Two coaxially fed monopole antennas with planar microstrip structure for cross-talk cancellation. Port 1 on the left side ($x < 0$) of the structure.

B. Numerical Simulations

By means of numerical simulations (CST MICROWAVE STUDIO [6]) the properties of the antenna structure according to Fig. 4 with width w large enough to allow quasi-TEM and quasi-TE₂₀ propagation were extensively studied. Fig. 5 depicts the frequency response of $|S_{21}|$ (cross-talk) for differently chosen geometric parameter of the microstrip structure (curves b, c and d) in comparison to the case without microstrip cancellation structure (curve a). Fig. 5 clearly indicates that the cross-talk level is significantly reduced in comparison to curve a) with about 16 dB isolation. Furthermore, as a novel result, it is seen that due to the 3-path structure minima occur at two different frequencies and the allocation of these frequencies can be varied to a large extend by means of changes in the geometrical parameters. This allows the frequency response of the residual cross-talk to be tailored to specific requirements. Fig. 2 can serve as an example for such a required response. Figs. 6 and 7 depict different cuts through the radiation pattern corresponding to the case that port 1 is fed and port 2 is terminated by a matched load. Additionally, the port pattern of port 2 is added to the azimuthal pattern in Fig. 6. Data were taken for case d) in Fig. 5 and frequency at the second minimum of $|S_{21}|$. Due to the symmetry of the structure the patterns for ports 1 and 2 follow from each other by mirroring at the symmetry plane between both monopoles. Figs. 6 and 7 indicate that the magnitude pattern in the plane $\Theta = \pi/2$ deviates from a circle (about 3 dB variations). This is due to the fact that - even if port 2 is isolated from port 1 - the second monopole and also the planar microstructure contribute to the pattern.

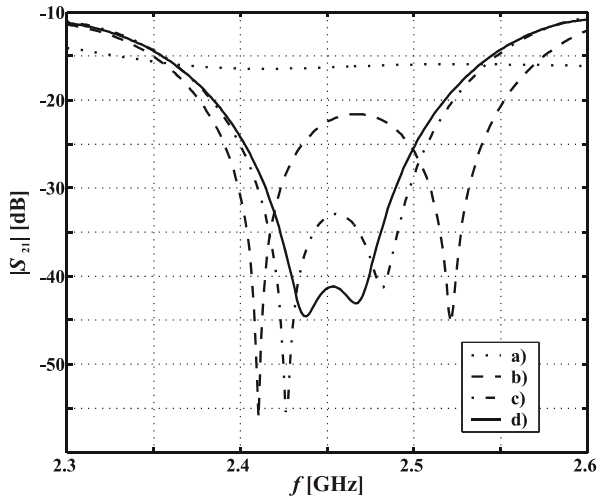


Figure 5. Frequency response of crosstalk for different choice of geometry parameter (curves b,c and d) of planar structure in Fig. 4 in comparison to the case without planar cancellation structure (curve a).

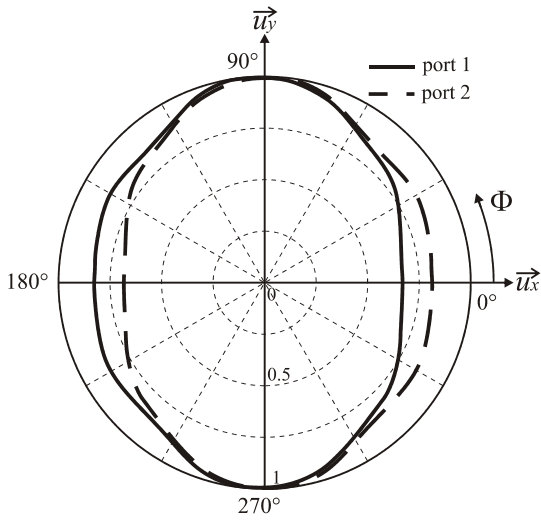


Figure 6. Azimuthal magnitude pattern for port 1 and 2 (relative field strength E_θ) at $\Theta = 90^\circ$ (xy-plane).

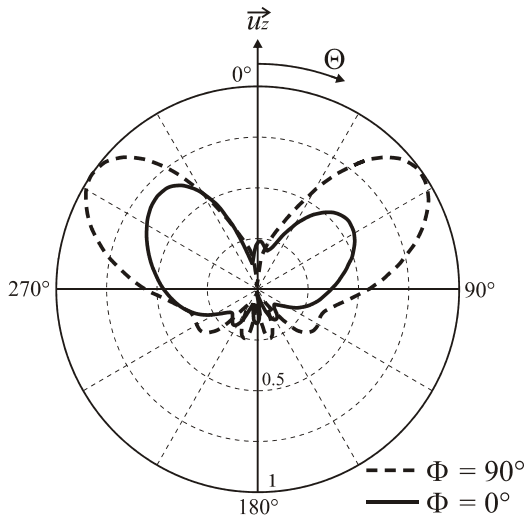


Figure 7. Elevation magnitude pattern of E_θ for port 1 at $\Phi = 0^\circ$ and $\Phi = 90^\circ$.

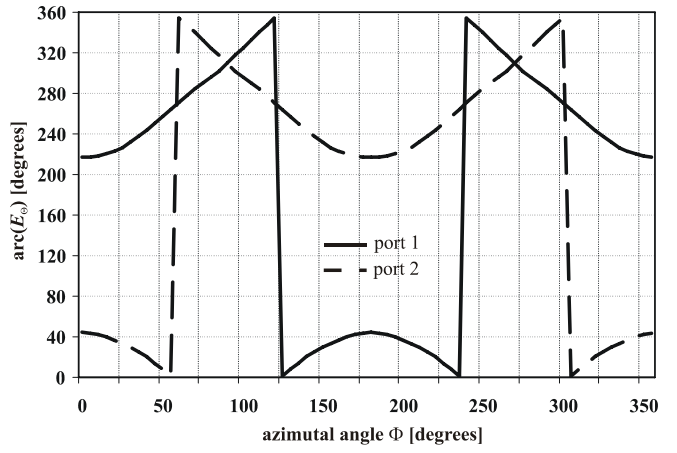


Figure 8. Azimuthal angular dependence of the phase of the electrical field strength E_θ for port 1 and 2 corresponding to Fig. 6.

Since the ports are isolated from each other the corresponding complex-valued port patterns of both ports are mutually orthogonal in the sense of (2). This is mainly due to the difference in the angular phase-variations of the far field for port 1 and 2, demonstrated with the azimuthal angular dependence of the phase angle of the electrical field (Θ -component) in Fig. 8.

C. Experimental Results

In order to verify the results from computer simulations the antenna structures with differently chosen parameters of the microstrip structure were manufactured (see Fig. 8) and experimentally analyzed by means of S-parameter measurements with a network analyzer (Agilent E 8363A).

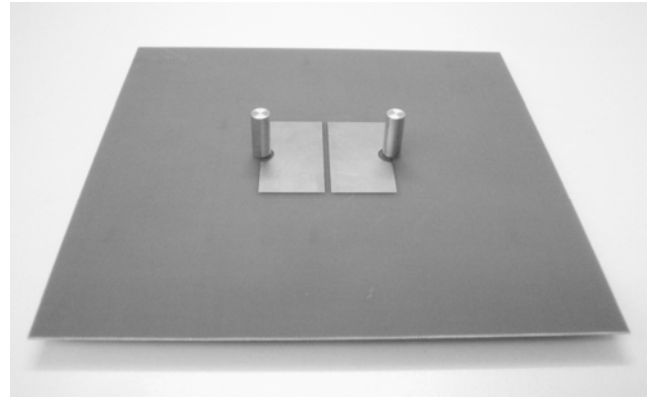


Figure 8. Photograph of the experimentally investigated antenna structure. Port 1 on the left side.

The result for one particular choice of these parameters (monopoles: diameter 9 mm, length $l = 23.2$ mm, distance $a = 63.3$ mm; microstrip structure: width $w = 58.8$ mm, gap width $g = 2.9$ mm) is shown in Fig. 9. The experimentally determined port isolation exceeds 42 dB and 30 dB at a fractional bandwidth of 1.2 % and 3.3 %, respectively.

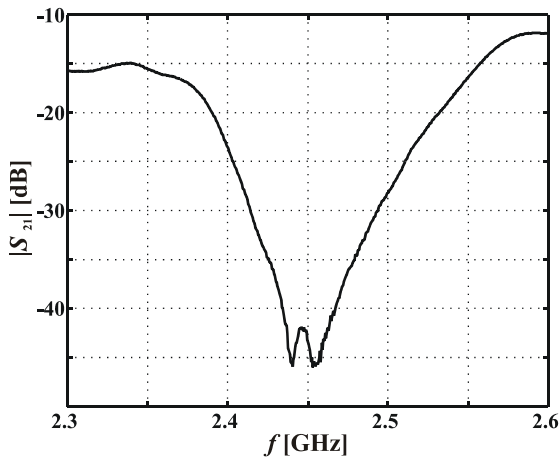


Figure 9. Experimental results for the crosstalk between ports 1 and 2 for antenna structure according to Fig. 8 (particular choice of geometric parameters). VSWR<2 for frequency range from 2.2 GHz to 2.8 GHz.

V. CONCLUSIONS

A pair of half-wave spaced monopole antennas was used as an example to demonstrate that high isolation between antenna ports can be achieved via a passive cross-talk cancellation technique. The proposed antenna structure provides multiple-path propagation (M paths) between the antenna ports which (theoretically) allows perfect isolation at $M-1$ frequency points. The presented approach can be exploited where due to a

narrow frequency spacing filter properties are not sufficient for providing the demanded TX-RX isolation.

It was experimentally shown that in spite of the narrow element spacing an isolation of more than 45 dB could be achieved.

The usefulness of an even higher isolation between the antenna ports becomes questionable if the antenna system suffers from additional indirect coupling due to time-varying scattering from nearby objects.

References

- [1] H. Wong, K.-L. Lau, K.-M. Luk, "Design of Dual-Polarized L-Probe Patch Antenna Arrays With High Isolation," IEEE Transactions on Antennas and Propagation, Vol. 52, No. 1, January 2004.
- [2] H.J. Chaloupka, X. Wang, "Novel Approach for Diversity and MIMO Antennas at Small Mobile Platforms," IEEE PIMRC-Symp. Dig., vol. 1, pp. 637-642, 2004.
- [3] H.J. Chaloupka, D. Eßer, X. Wang, "Port Decoupling for Antennas with Narrow Element Spacing," Proc. 2004 European Conference on Wireless Technology, pp. 221-224, Amsterdam, October 2004.
- [4] D. Eßer and H.J. Chaloupka, "Design Approach for a Class of Compact Multiport Antennas," IEEE 2005 International Symposium on Microwave, Antenna, Propagation and EMC Technologies for Wireless Communications (MAPE 2005) Proceedings, Volume I of II, pp. 144-147, Beijing, China, August 8-12, 2005.
- [5] S.I. Karode and V.F. Fusco, "Dual Polarised Microstrip Patch Antenna using Feedforward Isolation Enhancement for Simultaneous Transmit/Receive Applications," Nat. Conference on Antennas Propag., Conf. Publicat. No. 461, pp. 49-52, IEE.
- [6] CST GmbH, D-64289 Darmstadt, Germany, MICROWAVE STUDIO V5.

Near-Field Planar Characterisation Applied to the Design of Digital and Radiofrequency Systems

Eric Marzolf¹, Mhamed Drissi¹, Abdelhak Ziyat²

¹INSA de Rennes, IETR, 20 avenue des Buttes de Coësmes, 35043 Rennes cedex, France, e.marzolf@ieee.org

²Mohammed First University, Laboratory of Electronics & Systems, BP 524, 60000 Oujda, Morocco

Abstract—Near-field planar characterisation is a very attractive tool for the circuit designer dealing with digital and radiofrequency systems. The characterisation method is firstly introduced, and its key points are underlined. The power of near-field mapping is illustrated by the means of two examples coming from the digital as much as from the radiofrequency areas.

Keywords-characterisation; electromagnetic compatibility; mapping; near-field; radiofrequency systems.

I. NEAR-FIELD PLANAR CHARACTERISATION

The observation of the electromagnetic field on the surface of a device allows the collecting of a quantity of information relating to the complex phenomena arising within a system when operating under its normal conditions. The planar mapping of the electromagnetic field over a given surface shows to have several advantages over other more classical characterisation methods used in radiofrequency and microwaves: the vectorial network analysis is for instance based on the measurement of global entities, needing the introduction and the calibration of ports with well defined measurement planes. This procedure become rapidly cumbersome when the number of input/output pins increases as it is the case of digital circuits on a printed circuit board. Meanwhile, the proposed characterisation, as it operates without contact, by using a collecting probe sensitive to a given field component, makes it possible to analyse directly the device under its working conditions.

Moreover, the fact that the characterisation is performed in near-field zone permits the rendering of complex phenomena, as the interaction of the different modes, may they be of propagating or evanescent type, and makes it possible to model the radiating of electrical and magnetic sources. More specifically, it is also thinkable to determine with this kind of measurement method the radiated emission of the electromagnetic fields over a printed circuit board and to solve the problems dealing with electromagnetic compatibility [1-2].

The wealth of information comes from the point that it is of geographical nature, localised within a plane, thus it helps to associate the observed phenomenon with the different components or the geometry of the studied system.

This method of near-field characterisation can be based on measurements using a near-field scanner (see Fig. 1), or on 3D field simulation with the availability of modern and powerful

CAD tools, as their methodology and goals are the same: the planar mapping of the electromagnetic phenomena.



Figure 1. Measurement setup of the planar near-field scanner with positioner, spectrum analyser and controlling computer

The near-field probe is an essential element within the measurement system [3-4]. This probe can be of current loop type or of voltage monopole/dipole type, and will be sensitive to a specific component of the electromagnetic field: Fig. 2 shows some examples of realised probes at IETR. Two essential parameters which are characterising a near-field probe are the resolution and the sensitivity. If the sensitivity is proportional to the size of the probe, as the electromagnetic field is integrated along the structure, the resolution is better when the probe is smaller. When designing a near-field probe, a compromise has to be found between these two parameters, the resolution and the sensitivity. The realised probes have a length of 10mm, the width of the rectangular probe is of 6mm. The singularity introduced at the end of the triangular probe permits to increase somehow its resolution.

The measured return loss of the built probes is presented in Fig. 3 within the frequency band of 0 GHz to 8 GHz. They all show a good behavior up to 4 GHz. At higher frequencies however, there are some resonance effects which are appearing, due to the size of the probes.



Figure 2. Near-field probes of current loop type (H_{xy}) and voltage monopole type (E_z)

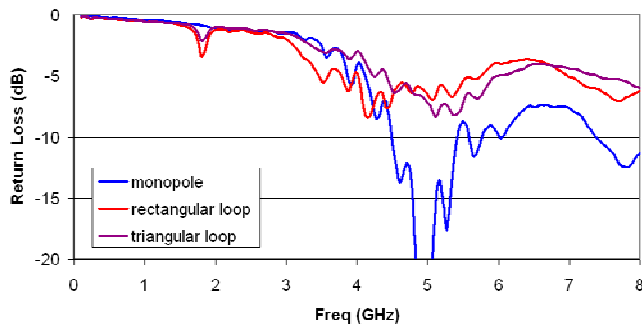


Figure 3. Return loss of the realised near-field probes

The near-field probe used for the electromagnetic field mapping is connected to the measurement device which can be, depending on the case, a spectrum analyser or a vectorial network analyser. The spectrum analyser is used for the characterisation of independent systems producing by themselves the radiating sources. The vectorial network analyser is very interesting as it is possible to normalise the amplitude and the phase of the measure, by an injection of a reference in the device under test.

II. APPLICATION TO THE DESIGN OF DIGITAL AND RADIOFREQUENCY SYSTEMS

The near-field characterisation method is illustrated by means of two examples coming from different areas: the measurement of radiated emission of the electromagnetic field over a digital printed circuit board, thus dealing with an electromagnetic compatibility problem, and the characterisation of the physical phenomena occurring in a microwave filter, in order to assess the circuit designer.

A. Digital printed circuit board

The near-field characterisation is applied to a printed circuit board (Fig. 4), built around an integrated circuit of FPGA type (ALTERA EPM7032), a voltage regulator, various decoupling capacitors for the biasing, and a RAM memory. The circuit is fed by a clock signal of 10 MHz with the help of an external signal generator.

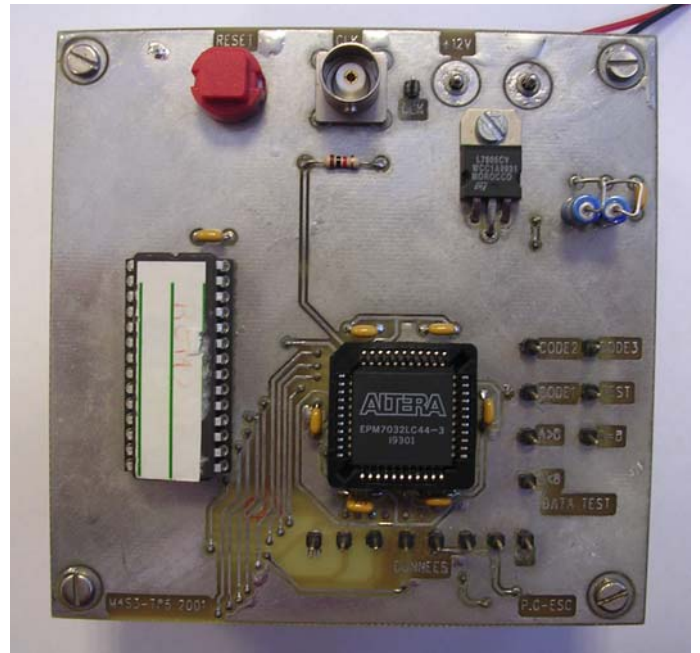


Figure 4. Digital printed circuit board built around an FPGA from ALTERA, a voltage regulator, decoupling capacitors, and a RAM memory

The measurement of the electromagnetic field is made in a plane located at a height of 5mm above the level of the board, on the side of the components, for ease of identification with the different parts; however it is also possible to perform the measurement on the side of the backplane. As the frequency is of 10 MHz and the indicated height of 5mm, the measurement is really done in the near-field reactive zone. As the components have some relief, the chosen height cannot be smaller than a certain amount. The BNC entry of the coaxial cable for the clock signal also restricts the measurement area which can be scanned by the probe.

The near-field is sampled on a surface of 60mm * 100mm with a step of 1mm in both directions. The used probe is of rectangular current loop type and is oriented in the x-direction. The measurement is made with means of a spectrum analyser, and the measured power is proportional to the H_y component of the electromagnetic field.

The field mapping is done at the fundamental frequency of the clock signal (10 MHz), as much as at the fifth harmonic (50 MHz), and their respective maps are shown in Fig. 5 and 6 for both frequencies.

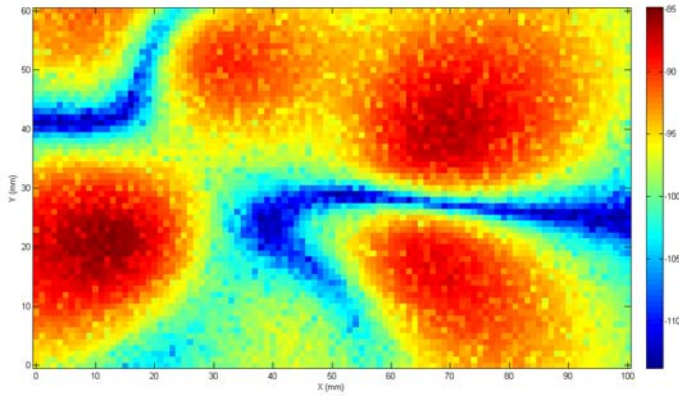


Figure 5. Near field measured on the surface of the digital printed circuit board for the fundamental frequency of the clock signal (10 MHz)

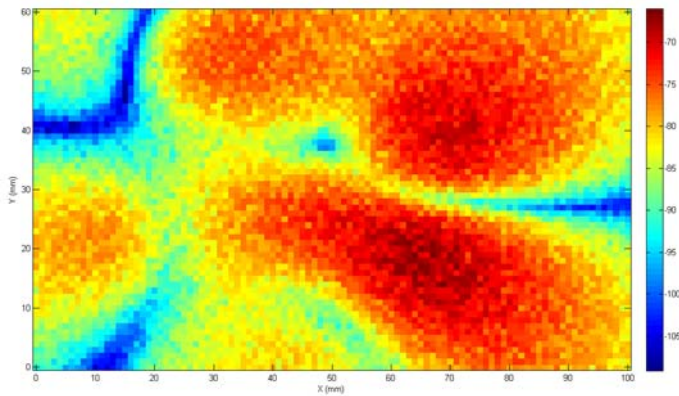


Figure 6. Near field measured on the surface of the digital printed circuit board for the fifth harmonic frequency of the clock signal (50 MHz)

For the fundamental frequency of 10 MHz, the signal dynamic is of 30 dB and the maximum of power is of -85 dBm. For the fifth harmonic, the signal dynamic is of 40 dB and the maximum of power is of -66 dBm, almost 20 dB greater than at the fundamental frequency.

The electromagnetic field concentrates over the principal devices (FPGA, voltage regulator, memory, decoupling capacitors,...), with some variations on the highest measured levels depending on the considered frequency.

The limitation of the resolution is due to the size of the probe (its width is of 6mm), however for our working frequency (10 MHz), this is largely enough for sizing all the variations of the electromagnetic field. The sampling step has voluntarily been chosen small compared to the size of the probe, thus corresponding to a spatial oversampling of the measurement.

B. Microwave filter

Another application of the near-field characterisation concerns the visualisation of physical phenomena occurring within microwave devices. The treated example deals with a microwave filter, made of three sections of quarter-wavelength (see Fig. 7).

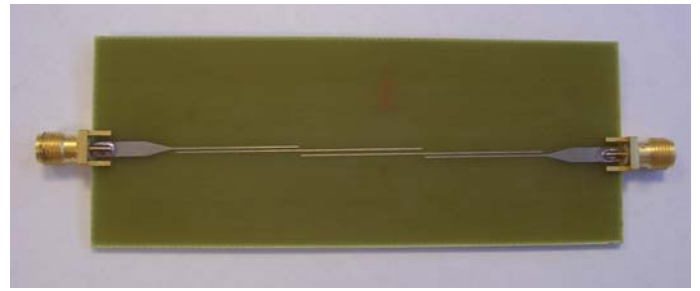


Figure 7. Photography of the microwave filter

The performances of this microwave filter are presented in Fig. 8. The working bandwidth is centered around 2 GHz, having an insertion loss of 1.4 dB and a band pass window, defined at -3 dB on the S_{21} , from 1.7 GHz to 2.3 GHz.

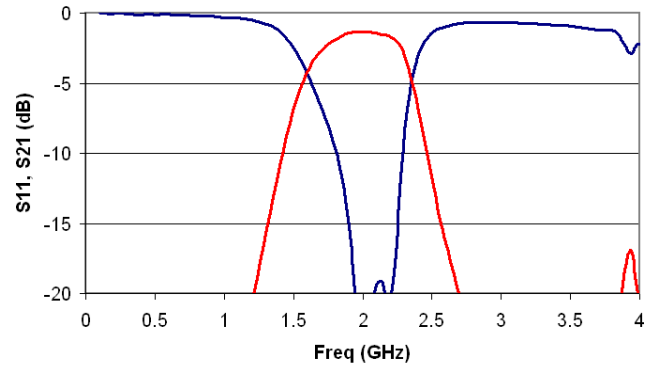


Figure 8. S-parameters of the microwave filter

The measurement of the electromagnetic field is performed by means of a vectorial network analyser and a probe of triangular loop type, the other part of the filter is closed with a 50 ohm load. The field mapping is done for three different frequencies (1 GHz, 2 GHz and 3 GHz), each frequency corresponding to a different working of the microwave filter: the frequency of 2 GHz is the centre frequency of the pass band, the frequency of 1 GHz is part of the lower stop band, and the frequency of 3 GHz corresponds to a rejection within the higher part of the stop band. The frequency mapping for each of these frequencies is performed on a surface of $100\text{mm} \times 20\text{mm}$, at a height of 2mm above the substrate, and with a sampling step of 1mm in both directions.

For the frequency of 2 GHz (see Fig. 9), the power transferring from port 1 to port 2 is well noticeable. The coupling between port 1 and the probe is of -40 dB. The minimum of signals are also well defined.

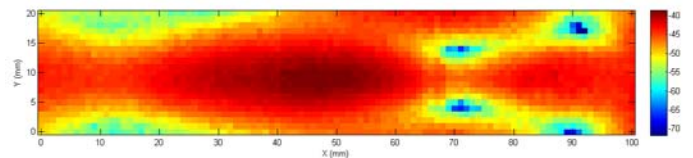


Figure 9. Near field measured at the surface of the microwave filter for the frequency of 2 GHz

For the frequency of 1 GHz (see Fig. 10), the electromagnetic energy is localised near port 1. The incident wave is simply reflected back, and no power is transferred to port 2.

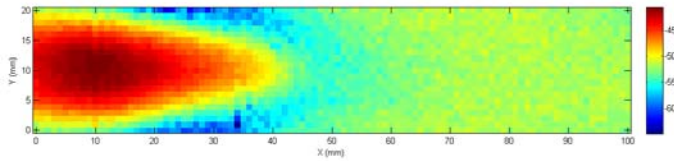


Figure 10. Near field measured at the surface of the microwave filter for the frequency of 1 GHz

For the frequency of 3 GHz (see Fig. 11), the energy is also concentrated in the area corresponding to port 1, but it is more spread than in the previous case. In fact, a wave front is visible in the map, showing the presence of a stationary wave system established over the coupled lines.

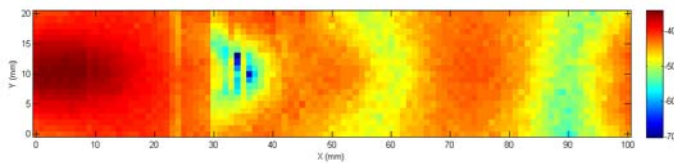


Figure 11. Near field measured at the surface of the microwave filter for the frequency of 3 GHz

III. CONCLUSION

The principles of the near-field characterisation are highlighted in this paper. This method can be applied to very different situations, especially when it is difficult to access to particular measurement points, and for the analysis of test cases working under operating conditions.

Moreover, the determination of the electromagnetic field distribution on a plane surface permits to identify the observed phenomena and to associate them clearly with components or the geometry of the device under test, and to model the equivalent radiating sources.

The advantages of this characterisation method makes it an ideal tool for the designer willing to integrate the SI/EMC constraints in the stages of the design flow, or to understand the working of a system by visualising the different coupling mechanisms appearing within it.

REFERENCES

- [1] J.-J. Laurin, Z. Ouardhiri, J. Colinas, "Near-field imaging of radiated emission sources on printed-circuit boards", IEEE Int. Symp. EMC, Montreal, 2001.
- [2] S. Ben Dhia, M. Ramdani, E. Sicard, "Electromagnetic compatibility of integrated circuits, techniques for low emission and susceptibility", Springer Verlag, 2006.
- [3] Y. Gao, I. Wolff, "A new miniature magnetic field probe for measuring three-dimensional fields in planar high-frequency circuits", IEEE Trans. MTT, vol. 44, 1996, pp. 911-918.
- [4] J.-M. Kim, W.-T. Kim, J.-G. Yook, "Resonance suppressed magnetic field probe for EM field-mapping system", IEEE Trans. MTT, 2005, vol. 53, pp. 2693-2699.

SNR Considerations for Widebeam, Short-Range Synthetic Aperture Radar Processing

Florian Gerbl, Erwin M. Biebl

Technische Universität München, Fachgebiet Höchsthfrequenztechnik
 Arcisstr. 21, 80333 München, Deutschland
 Telephone: +49-89-289-23931, Email: gerbl@tum.de

Abstract—Synthetic aperture radar (SAR) techniques were originally developed to obtain high resolution images of scenes far away from the (airborne or spaceborne) imaging system. Data is collected over a large synthetic aperture to numerically obtain a higher resolution than that achievable by using the width of the antenna’s footprint at the range of the target to distinguish between distinct targets. However, even for short ranges, where a narrow beam produces high resolution due to only small beam widening on the short path, the application of wide beams in conjunction with numerical imaging techniques can be advantageous for detecting objects with radar cross sections that vary with the aspect angle. One of the degrees of freedom in the design of an imaging radar system is the antenna’s beamwidth. Issues concerning the choice of a proper beamwidth with respect to the estimation accuracy for targets with radar cross sections varying with the aspect angle will be addressed in the following.

I. INTRODUCTION

The azimuth resolution of a real aperture radar system is determined by the width of the antenna beam at the range of the target. For a certain divergence angle of the beam, the resolution decreases as the range to the target increases. In case of short ranges, the width of the antenna beam at the target might be made sufficiently small, so that for high azimuth resolution no additional signal processing might be needed. However, real world targets exhibit radar cross sections that vary with the aspect angle, which might yield additional problems. When a very narrow beam is used, the region of aspect angles under which the target is illuminated and the scattered signals are received by the radar system is very limited. Therefore, it is possible that an existing target is not detected by the radar system due to a disadvantageous aspect angle and its corresponding potentially low radar cross section. Illuminating targets from different aspect angles and thus increasing the amount of information obtained can be achieved by increasing the beamwidth and processing the received data into a radar image. In the following investigation, thermal system noise will not be considered. Only noise contributions due to the radar cross sections varying with the aspect angle will be taken into account.

II. MODEL OF THE TARGET

The type of target investigated in the following is an idealized one exhibiting an amplitude radar cross section consisting of N statistically distributed specular reflexions, modeled by

Dirac pulses, each with equal phase and weight unity, where the probability for a reflexion to occur at a certain angle is equal for all angles. Therefore, the amplitude radar cross section $\rho_{\vartheta}(\vartheta)$ as a function of the aspect angle ϑ is

$$\rho_{\vartheta}(\vartheta) = \sum_{n=1}^N \delta(\vartheta - \vartheta_n), \quad (1)$$

where the values ϑ_n are uniformly distributed within the angle interval $[-\pi, \pi]$. Fig. 1 shows one of the possible realizations of the amplitude radar cross section for $N = 3$ randomly chosen angles.

III. IMAGING SETUP

A monostatic setup as depicted in fig. 2 will be considered in the following. A continuous signal at the frequency ω is transmitted by an antenna that is supposed to have a very small aperture. Its beamwidth is assumed to be $2\vartheta_0$. The antenna is directed into the positive z -direction. For the sake of simplicity, the antenna pattern is assumed to have a constant (non-zero) value for $-\vartheta_0 \leq \vartheta \leq \vartheta_0$ and to be 0 otherwise. The antenna is moved along the x -axis. An object at the location $(0, 0, z_t)$ is within the antenna’s beam for $-x_0 \leq x \leq x_0$, where

$$x = z_t \tan \vartheta \quad (2)$$

and especially

$$x_0 = z_t \tan \vartheta_0. \quad (3)$$

It is assumed that the motion of the system is slow as compared to the velocity of the electromagnetic wave, c , so that the

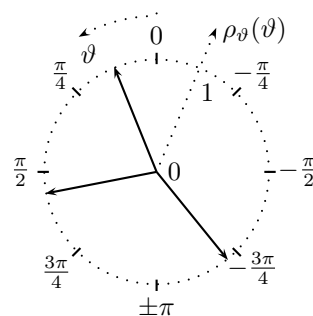


Fig. 1. A randomly generated $\rho_{\vartheta}(\vartheta)$ for $N = 3$

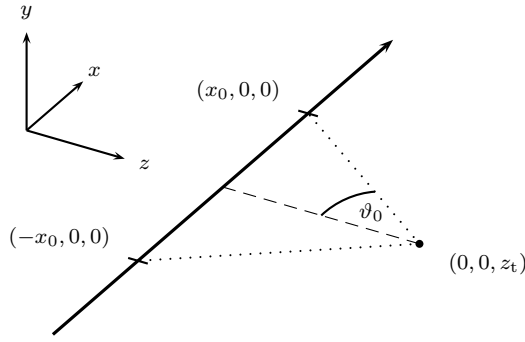


Fig. 2. Imaging setup

Doppler effect can be neglected. The received signal is I/Q-mixed with the transmitted signal and phase and magnitude of the received signal are determined, so that for a target with amplitude radar cross section $\rho_\vartheta(\vartheta)$ at the location $(0, 0, z_t)$ the result of this procedure is

$$s_x(x) = \rho_\vartheta(\vartheta(x)) \cdot \frac{1}{d_x^2(x)} \cdot \exp\left\{-j\frac{2\omega d_x(x)}{c}\right\}, \quad (4)$$

where

$$d_x(x) = \sqrt{x^2 + z_t^2} \quad (5)$$

is the distance between the antenna and the target. In terms of ϑ , the signal can be expressed as

$$s_\vartheta(\vartheta) = \rho_\vartheta(\vartheta) \cdot \frac{1}{d_\vartheta^2(\vartheta)} \cdot \exp\left\{-j\frac{2\omega d_\vartheta(\vartheta)}{c}\right\}, \quad (6)$$

with

$$d_\vartheta(\vartheta) = \frac{z_t}{\cos \vartheta}. \quad (7)$$

IV. IMAGE PROCESSING

Synthetic aperture radar techniques combine measurement results from various antenna positions to obtain a reflectivity image of the target scenery. One way to combine measurement results is to compensate the signals received at different locations for propagation effects and integrate the compensated signals over that interval of angles for which the measurements were carried out. In [1], this procedure is used for a circular path of the antenna around the scenery to be imaged. Analogously, signals obtained for measurements along a straight line can be compensated and integrated to obtain a reflectivity image. The compensation is accomplished by using a focusing operator

$$\xi_\vartheta(\vartheta) = d_\vartheta^2(\vartheta) \cdot \exp\left\{j\frac{2\omega d_\vartheta(\vartheta)}{c}\right\}. \quad (8)$$

The imaging result $\iota(\vartheta_0)$ at the location corresponding to the true target location is

$$\iota(\vartheta_0) = \int_{-\vartheta_0}^{\vartheta_0} s_\vartheta(\vartheta) \xi_\vartheta(\vartheta) d\vartheta = \int_{-\vartheta_0}^{\vartheta_0} \rho_\vartheta(\vartheta) d\vartheta. \quad (9)$$

For $\vartheta_0 = \pi$, i.e. for one complete circulation, the result is

$$\iota(\pi) = \int_{-\pi}^{\pi} \rho_\vartheta(\vartheta) d\vartheta = 2\pi \cdot \frac{1}{2\pi} \int_{-\pi}^{\pi} \rho_\vartheta(\vartheta) d\vartheta = 2\pi \overline{\rho_\vartheta}, \quad (10)$$

where $\overline{\rho_\vartheta}$ is the mean value of ρ_ϑ over all angles from $-\pi$ to π . Processing the signals received over an interval $[-\vartheta_0, \vartheta_0]$ in the proposed way and multiplying with a factor π/ϑ_0 yields an estimate of 2π times the mean value of the amplitude radar cross section. It is desirable to obtain an estimate that is close to the real value. A measure quantifying the inaccuracy Δ_{rel} of the estimation is the mean square error normalized to the power of the desired signal

$$\Delta_{\text{rel}}(\vartheta_0) = \frac{\text{E}\left\{\left(\iota(\vartheta_0) - \frac{\vartheta_0}{\pi} \iota(\pi)\right)^2\right\}}{\left(\frac{\vartheta_0}{\pi} \iota(\pi)\right)^2}. \quad (11)$$

Its reciprocal value can be interpreted as a signal-to-noise ratio (SNR), quantifying the accuracy of the estimation. The SNR can be written as

$$\text{SNR}(\vartheta_0) = \frac{1}{\Delta_{\text{rel}}(\vartheta_0)}. \quad (12)$$

Since all of the Dirac pulses forming the amplitude radar cross section exhibit weight unity, the integration of ρ_ϑ over a certain interval of angles yields the number of Dirac pulses within the respective interval. Therefore, $\iota(\vartheta_0)$ is a random variable for randomly chosen targets and can have integer values from 0 to N . For a certain value of ϑ_0 , the probability for exactly n Dirac pulses being in the interval $[-\vartheta_0, \vartheta_0]$ is

$$P(\iota(\vartheta_0) = n) = \binom{N}{n} p^n(\vartheta_0) (1 - p(\vartheta_0))^{N-n}, \quad (13)$$

where

$$p(\vartheta_0) = \frac{\vartheta_0}{\pi} \quad (14)$$

is the probability for an angle randomly chosen out of $[-\pi, \pi]$ to be in $[-\vartheta_0, \vartheta_0]$. The expected value of $\iota(\vartheta_0)$ is (according to [2])

$$\text{E}\{\iota(\vartheta_0)\} = p(\vartheta_0)N = \frac{\vartheta_0}{\pi}N = \frac{\vartheta_0}{\pi} \int_{-\pi}^{\pi} \rho_\vartheta(\vartheta) d\vartheta = \frac{\vartheta_0}{\pi} \iota(\pi). \quad (15)$$

The SNR can therefore be written as

$$\text{SNR}(\vartheta_0) = \frac{\text{E}^2\{\iota(\vartheta_0)\}}{\text{E}\left\{\left(\iota(\vartheta_0) - \text{E}\{\iota(\vartheta_0)\}\right)^2\right\}}, \quad (16)$$

where the denominator is by its definition the variance σ^2 of the random variable $\iota(\vartheta_0)$ given by (according to [2])

$$\sigma^2(\vartheta_0) = Np(\vartheta_0)(1 - p(\vartheta_0)) = N\frac{\vartheta_0}{\pi} \left(1 - \frac{\vartheta_0}{\pi}\right). \quad (17)$$

Using (15) and (17), the SNR can finally be reformulated as

$$\text{SNR}(\vartheta_0) = \frac{N}{\frac{\pi}{\vartheta_0} - 1}. \quad (18)$$

For one complete circulation, i.e. $\vartheta_0 \rightarrow \pi$, the SNR tends to ∞ , which means that the estimate is correct. In case the antenna is moved along the x -axis, the target can only be viewed at angles between $-\pi/2$ and $\pi/2$. The maximum possible value for ϑ_0 is therefore $\pi/2$. That means that the maximum achievable SNR for a straight path is

$$\text{SNR}_{\max} = \text{SNR}\left(\frac{\pi}{2}\right) = N. \quad (19)$$

Using an antenna with a half aperture angle smaller than 90° yields a suboptimal SNR. The degradation of the SNR with respect to SNR_{\max} ,

$$\Delta\text{SNR} = \frac{\text{SNR}(\vartheta_0)}{\text{SNR}_{\max}} = \frac{1}{\frac{\pi}{\vartheta_0} - 1}, \quad (20)$$

is independent of N . The antenna's beamwidth can be chosen in such a way that the degradation ΔSNR is within a certain limit. A half aperture angle $\vartheta_0 = 60^\circ$, for example, yields an SNR 3 dB below the maximum SNR achievable on a straight path.

V. SIMULATION

Simulations have been conducted for an antenna moved along the x -axis. Care has to be taken at the change of variables from the integration over the aspect angle to an integration over the x -coordinate. The integration

$$\iota_x(x_0) = \int_{-x_0}^{x_0} \rho_x(x) \cdot \frac{1}{z_t \left(1 + \frac{x^2}{z_t^2}\right)} dx \quad (21)$$

provides an unweighted estimate of $2 \cdot \overline{\rho_\vartheta} \cdot \arctan(x_0/z_t)$ for a target at $(0, 0, z_t)$. The amplitude radar cross section as a function of x instead of ϑ then is

$$\rho_x(x) = \sum_{n'} \delta(x - z_t \tan \vartheta_{n'}) \cdot z_t (1 + \tan^2 \vartheta_{n'}), \quad (22)$$

where n' are the indices of only those reflexions which are within $[-\pi/2, \pi/2]$ and therefore visible from locations on the x -axis. The simulations have been done as follows. For each number of reflexions N , 10,000 targets were generated randomly. For each of those targets, the signals received along the x -axis and the imaging algorithm for a target at a distance $z_t = 1$ m were simulated for various half aperture angles between 1° and 89° . For each of those angles, the square error divided by the square of the desired value was determined and the mean value was calculated over all targets with equal number of reflexions. The SNR is the reciprocal value of this mean value.

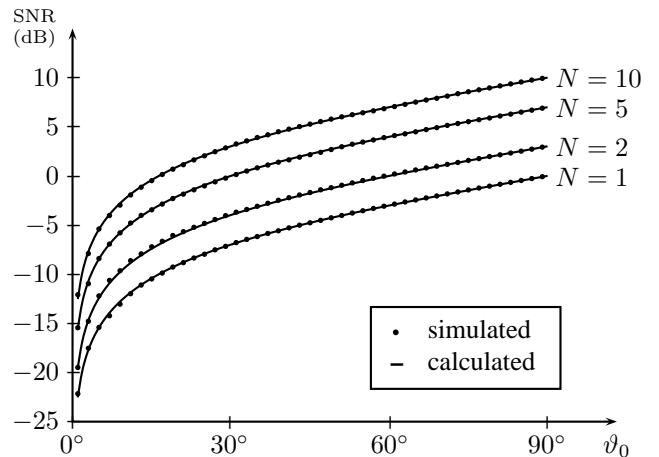


Fig. 3. Simulation and calculation results: signal-to-noise ratio over half aperture angle

Fig. 3 shows the SNR for various half aperture angles ϑ_0 for targets with 1, 2, 5, and 10 specular reflexions, both predicted by (18) and obtained by simulation, on a logarithmic scale. The agreement of both calculation and simulation lends evidence to the analytic derivation.

VI. CONCLUSION

Synthetic aperture radar imaging using very narrow antenna beams exhibits the disadvantage that estimates of the mean amplitude radar cross section might be poor for targets whose radar cross sections vary with the aspect angle. The usage of wide antenna beams and appropriate signal processing can help improve the estimation performance. It has been proven analytically and substantiated numerically that the signal-to-noise ratio as defined above increases with increasing beamwidth. For antenna movement along a straight line, the maximum interval of aspect angles is limited to 180° . Therefore, the maximum achievable signal-to-noise ratio is limited. The maximum allowable degradation of the signal-to-noise ratio as compared to the maximum achievable signal-to-noise ratio determines the necessary beamwidth, which can be calculated using the formulas derived above.

REFERENCES

- [1] A. Broquetas, J. Palau, L. Jofre, and A. Cardama, "Spherical wave near-field imaging and radar cross-section measurement," in *IEEE Transactions on Antennas and Propagation*, vol. 46, no. 5, May 1998, pp. 730 – 735.
- [2] L. Råde and B. Westergren, *Springers Mathematische Formeln*. Springer-Verlag, 1997, p. 416.

Miniaturization of Mobile Phone Antennas by Utilization of Chassis Mode Resonances

Werner L. Schroeder, Paul Schmitz, and Christian Thome

BenQ Mobile GmbH & Co. OHG, Product Innovation Center, Neutorplatz 3-4, D-46395 Bocholt, Germany,
phone +492842951768, werner.schroeder@benq.com

Abstract—The miniaturization of mobile phone antennas by means of purposeful tuning of chassis mode resonances is discussed. A simple approach to antenna independent analysis of chassis mode resonances is introduced. A novel technique for simultaneous tuning of a bar-type phone chassis in two frequency bands is presented. The optimum design and placement of capacitive coupling elements for excitation of electric dipole type resonances is considered. Experimental results for a GSM quad-band antenna mock-up featuring a record bandwidth to volume ratio confirm the usefulness of the approach.

I. INTRODUCTION

The design trend for mobile phones goes for ever smaller devices and very low profile. Antenna miniaturization is therefore a topic of high interest. The challenge is largest for the GSM850 and EGSM900 bands (824...894 MHz and 880...960 MHz), where free space wavelength exceeds maximum device dimension by a factor of 3 to 5. Contiguous coverage of both bands with a traditional PIFA (located over the main PCB) is possible only at the expense of volume and, in particular, of device thickness, which is in conflict with the above mentioned design trend. It is on the other hand well known that the volume of the antenna element itself is not the primary factor which limits bandwidth (in the sense of the Wheeler-Chu limit). At low-band frequencies (GSM850/EGSM900) radiation is rather dominated by the chassis. Attainable bandwidth as the result of the interplay between the chassis and a coupling element (antenna) was analyzed in [1] in terms of a dual-resonant lumped element equivalent circuit. It was concluded that a very small, effectively non-radiating coupling element can be used if properly designed to excite a radiating current density on the chassis. Similar considerations have earlier been presented in different context in [2] drawing on the concept of characteristic modes [3]. Application of characteristic mode theory to the analysis of the radiation properties of a handset chassis has been subject some recent papers [4]–[7]. The present paper addresses the purposeful tuning of the resonance frequency of a characteristic chassis mode as a major technique for antenna miniaturization. The model problem which is considered in this study is the design of a very small GSM quad-band antenna attached to a 100 mm by 40 mm PCB by means of (i) chassis mode tuning and (ii) optimum placement of the antenna element. An upper limit on device thickness of 10 mm is assumed. The methods presented are shown to allow for an 8 dB bandwidth of 150 MHz about the lower GSM bands (henceforth: “low-band”, 824...960 MHz) and a 10 dB

bandwidth of 300 MHz about the DCS / PCS band (henceforth: “high-band”, 1710...1990 MHz) at an antenna volume of only 2 cm³ plus roughly 1 cm³ keep-out volume over the PCB.

II. TUNING AND EXCITATION OF CHASSIS MODES

The theory of characteristic modes for conducting bodies [3] is, already in its general formulation, without actual evaluation of a specific structure’s modes, very helpful as an heuristic concept. As shown in [3], the operator $\hat{\mathbf{Z}}$ which relates the surface current density \mathbf{J}_s on a conducting body to the exciting (incident) electric field $\mathbf{E}_{\text{tan}}^{\text{ex}}$ as

$$\mathbf{E}_{\text{tan}}^{\text{ex}} - \hat{\mathbf{Z}}\mathbf{J}_s = \mathbf{E}_{\text{tan}}^{\text{ex}} - (\hat{\mathbf{R}} + j\hat{\mathbf{X}})\mathbf{J}_s = \mathbf{0}, \quad (1)$$

leads via the eigenvalue problem

$$\hat{\mathbf{X}}\mathbf{J}_{s,n} = \lambda_n \hat{\mathbf{R}}\mathbf{J}_{s,n} \quad (2)$$

to a complete, orthogonal set of real eigenfunctions $\{\mathbf{J}_{s,n} : n \in \mathbb{N}\}$ (characteristic modes) with real eigenvalues λ_n . Since

$$\langle \mathbf{J}_{s,m}, \hat{\mathbf{Z}}\mathbf{J}_{s,n} \rangle = 2P_{\text{rad},n}(1 + j\lambda_n)\delta_{mn}, \quad (3)$$

where

$$P_{\text{rad},n} = \frac{1}{2} \langle \mathbf{J}_{s,n}, \hat{\mathbf{R}}\mathbf{J}_{s,n} \rangle, \quad (4)$$

the surface current density due to the exciting electric field can be written in the form

$$\mathbf{J}_s = \sum_n \frac{\langle \mathbf{J}_{s,n}, \mathbf{E}_{\text{tan}}^{\text{ex}} \rangle}{(1 + j\lambda_n) 2P_{\text{rad},n}} \mathbf{J}_{s,n}. \quad (5)$$

By application of the complex Poynting theorem it is easily shown that the eigenvalue λ_n is related to the time averages of stored magnetic and electric energies of the n -th mode as

$$\lambda_n = 2\omega \frac{\langle W_{\text{mag},n} \rangle - \langle W_{\text{el},n} \rangle}{P_{\text{rad},n}} \quad (6)$$

and hence goes to zero as the n -th mode approaches its resonance frequency ω_n . (5) and (6) provide the theoretical guideline for utilization of a chassis mode. Effective excitation of the n -th mode requires that λ_n be small, i.e. that the mode is near resonance at the operating frequency and that the reaction $\langle \mathbf{J}_{s,n}, \mathbf{E}_{\text{tan}}^{\text{ex}} \rangle$ between the modal current density and the exciting field (due to the antenna, or coupling element in this context) be large. These concepts are applied below taking recourse to a simplified analysis method.

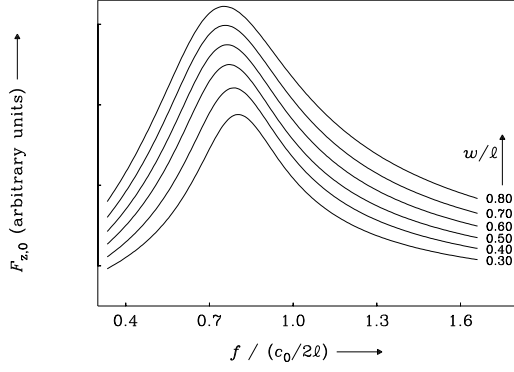


Fig. 1. Frequency dependence of the co-polarized component $F_{z,0}$ (7) for a plate of length ℓ (along z) and width $w < \ell$ under broadside z -polarized plane wave illumination near the half-wavelength resonance.

A. Low-band chassis mode tuning

In the low-band, only the dipole type chassis mode along the long axis, $\mathbf{J}_{s,1}$ is useful. Its resonance frequency ω_1 is, for typical chassis lengths, nevertheless too high and hence λ_n in (5) too far away from zero to assure effective excitation. The first and most important step towards antenna miniaturization is therefore the reduction of ω_1 . Since most commercial software packages unfortunately do not support eigenmode analysis of open structures in a useful way, a simple hands-on approach to excite independent analysis of the dipole mode was chosen. By post-processing of simulated current densities under plane wave excitation (polarized along the z -axis, the long axis of the chassis), the magnitude of the first moment of the current density on the conductor surface S

$$\mathbf{F}_0 := \iint_{r \in S} \mathbf{J}_s(\mathbf{r}) dS = j\omega \mathbf{p}, \quad (7)$$

is evaluated and recorded over frequency (Fig. 1). \mathbf{p} denotes the electric dipole moment. Resonance frequency and radiation quality factor of the dipole mode are estimated by a numerical fit of the resonator model

$$F_{z,0} \approx \frac{A}{1 + jQ_{\text{rad},1} \left(\frac{\omega}{\omega_1} - \frac{\omega_1}{\omega} \right)} \quad (8)$$

to the simulation data.¹ This model is subsequently employed to investigate options for resonance tuning of the chassis. Due to mechanical design restrictions capacitive loading is preferred. Caps as shown in Fig. 2, for instance, can in principle easily be integrated into the housing of a mobile phone. Fig. 3 shows their effect on the resonance frequency and radiation quality factor of the dipole mode for a plate of length $\ell = 100$ mm over width w taking height h as parameter. The graph for $h = 0$ mm represents the original board. The example illustrates that a sizable reduction of

¹ Note that the frequency of maximum radiation of electric the dipole mode is $\omega_{\text{max},1} = Q_{\text{rad},1} \omega_1 / \sqrt{Q_{\text{rad},1}^2 - \frac{1}{2}} > \omega_1$.

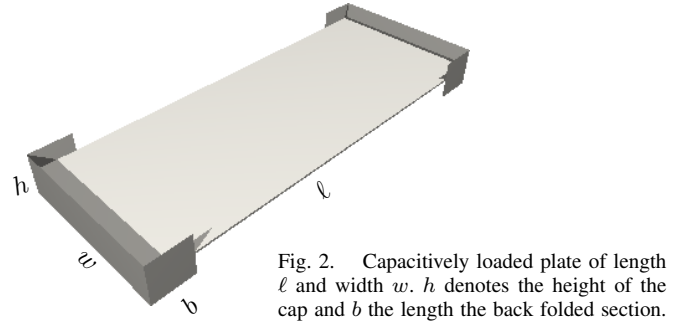


Fig. 2. Capacitively loaded plate of length ℓ and width w . h denotes the height of the cap and b the length the back folded section.

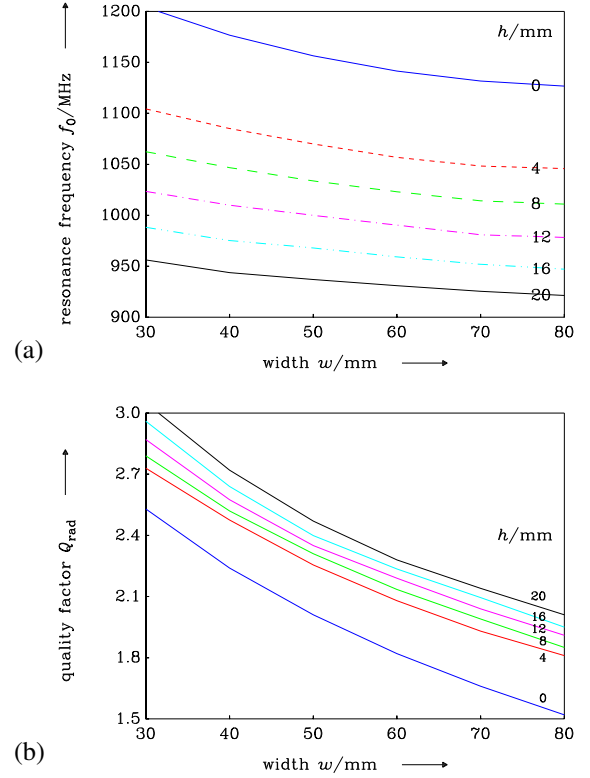


Fig. 3. Resonance frequency (a) and radiation quality factor (b) for the structure after Fig. 2 for $\ell = 100$ mm and $b = 10$ mm

resonance frequency is possible even for a moderate height of the device of, say, $h = 10$ mm.

B. High-band chassis mode tuning

At high-band the converse problem is encountered. The assumed device dimensions ($100 \text{ mm} \times 40 \text{ mm}$) are too large for an effective excitation of the electric dipole mode. Alternatively, utilization of a magnetic dipole mode or a quadrupole mode might be considered (with the proper modification and extension of the chassis structure). Since the goal is antenna miniaturization under the restriction of a very low device profile, options for realization of an electrical dipole type resonance at a higher frequency, i.e. for reduction of the electrical length of the device in high-band are considered instead. A novel solution to this problem is shown in Fig. 4a. One of the short edges of the chassis is screened by a vertical plate which is connected to the center of the short edge and

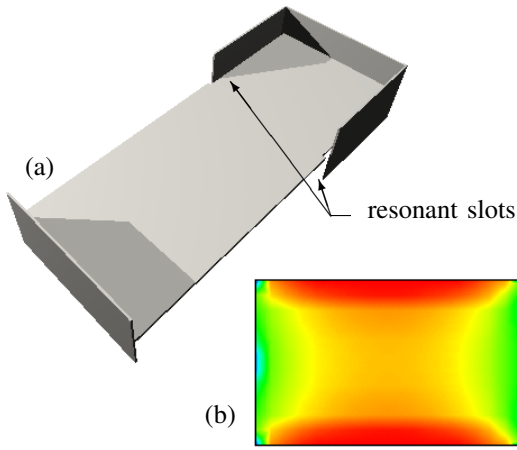


Fig. 4. Electrical length reduction by resonant screen: (a) structure ($\ell = 100$ mm, $w = 40$ mm, $h = 20$ mm, slot length 35 mm + 10 mm along long and short edges, respectively), (b) current density at 1780 MHz.

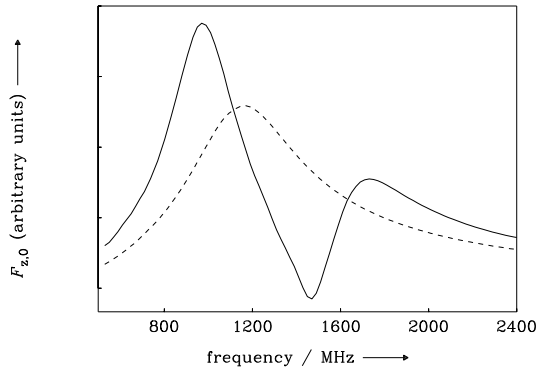


Fig. 5. Dual-resonant behaviour of $F_{z,0}$ after (7) for the structure given in Fig. 4. Dashed line corresponds to unloaded board.

folded back around the long edges to form a quarter-wave resonant slot on either side. Thereby a current density node is enforced on the board near the open ends of the slots. The length of the free (unscreened) part of the board is chosen such that it supports a half-wavelength resonance at high-band. The capacitive load at the unscreened end of the board in Fig. 4a is not substantial for the approach. The magnitude of the resultant resonant current density distribution as calculated by IE3D is depicted in false colors in Fig. 4b. A radiating half-wavelength resonance, corresponding to an electric dipole, is observed on the unscreened end of the board and a parasitic, essentially non-radiating quarter-wave resonance in the slot region. The approach is obviously fully compatible with the method selected in Subsection II-A for chassis mode tuning in low-band, i.e. it allows for simultaneous extension and reduction of the chassis' electrical length in low-band and high-band, respectively. Analysis of the first moment of the radiation vector (7) under broadside, z -polarized plane wave illumination clearly shows the dual resonant behaviour of the structure (Fig. 5).

C. Capacitive coupler

For restrictions imposed by mechanical design a capacitive coupler is desired.² To derive a heuristic design argument, it is helpful then to exploit reciprocity so as to rewrite the relevant ($n = 1$) reaction term which appears in (5) in the form

$$\langle \mathbf{J}_{s,1}, \mathbf{E}_{\tan}^{\text{ex}} \rangle = \iint_S \mathbf{J}_{s,1} \mathbf{E}_{\tan}^{\text{ex}} dS = \iiint_V \mathbf{E}_1 \mathbf{J}^{\text{ex}} dV \quad (9)$$

where \mathbf{E}_1 denotes the electric field from the (supposedly undisturbed) dipole mode and \mathbf{J}^{ex} , extending over V , is the impressed current density due to the coupler. Although a strict distinction between chassis (mode) and coupler field is not possible, some qualitative insight can be gained. Firstly, the plate of a capacitive coupler is obviously best placed in front of one of the short edges of the board, where \mathbf{E}_1 is maximum. Since V is small, one may approximate \mathbf{E}_1 in the vicinity of the edge as $\mathbf{E}_1 \approx -\mathbf{grad} \varphi_1$, arbitrarily setting $\varphi_1 = 0$ on the chassis. By application of the divergence theorem and the equation of continuity (9) can then be approximated as

$$\langle \mathbf{J}_{s,1}, \mathbf{E}_{\tan}^{\text{ex}} \rangle \approx \frac{-1}{j\omega} \iiint_V \varphi_1 \rho^{\text{ex}} dV = \frac{-1}{j\omega} \bar{\varphi}_1 q^{\text{ex}} \quad (10)$$

where ρ^{ex} and q^{ex} denote the charge density and charge, respectively, on the coupler plate and $\bar{\varphi}_1$ is a charge density weighted average of φ_1 over the coupler such that (10) holds. The counter-charge on the chassis where $\varphi_1 = 0$ drops out. If the impressed charge q^{ex} , or likewise the current, is taken as fixed, the only relevant optimization parameter is obviously $\bar{\varphi}_1$. Otherwise, if the voltage applied to the exciter is considered fixed, the parameter is $\bar{\varphi}_1 C$, where C is the coupler capacitance. For given apparent power, $\bar{\varphi}_1 \sqrt{C}$ is of interest. Since $|\bar{\varphi}_1|$ increases rapidly with lateral distance from the edge of the PCB, capacitance must be gained by area, not by reducing distance to the PCB. In practice, the distance between chassis and coupler and the area of the latter are limited by total available volume. Options to maximize $|\bar{\varphi}_1|$ under the constraint of limited coupler volume still exist. One of them is a tip like tapering of the coupler sided end of the PCB (Fig. 6). The electric field lines corresponding to the dipole mode which leave from the short edge of the PCB are thereby concentrated towards the center and diverge more rapidly away from the PCB. Furthermore, remembering that $\bar{\varphi}_1$ is an average of φ_1 , weighted with the charge density ρ^{ex} on the coupler, $|\bar{\varphi}_1|$ can be increased by shifting and confining coupler area to the outer boundary of the available volume as accomplished by the ring shaped coupler in Fig. 6.

III. EXPERIMENTAL RESULTS

To verify the concepts considered in Section II, a mock-up of a miniature quad-band GSM antenna on a 1 mm thick FR4 board of dimensions 100 mm by 40 mm was manufactured. The basic simulation model is shown in Fig. 6a and a hardware realization in Fig. 6b. For chassis mode tuning a 10 mm high combination of capacitive load for low-band and quarter-wave

²An inductive coupler would have to be placed near the maximum of the current density of the dipole mode, i.e. at the center of the chassis and be large in case of a bar-type chassis.

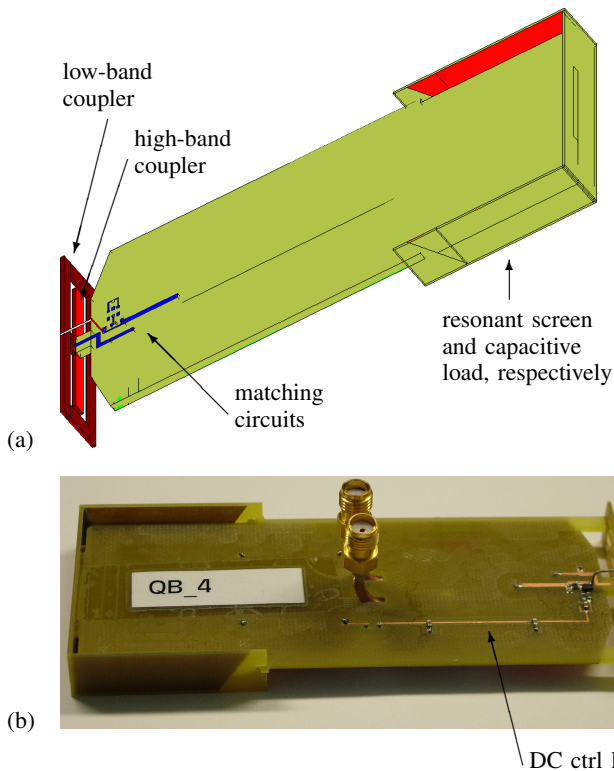


Fig. 6. Mock-up of a miniature quad-band antenna: (a) simulation model, (b) photo. (Note that the long strip line is a DC control line for an electrical tuning circuit which is not reported in this paper.)

resonant screen for high-band is placed at one of the ends of the board. The other end is equipped with a dual-feed capacitive coupler arrangement for low- and high-band. The low-band coupler is a rectangular, ring shaped strip conductor. It encloses the strip shaped high-band coupler. The dielectric (0.76 mm Ultralam 2000) between the two couplers is mostly milled away to reduce the capacitance between the two couplers. Either coupler is connected to a separate transmission line matching circuit (tapped, shorted microstrip lines). No effort was made to miniaturize the matching circuits. Their size could be significantly reduced and they might be realized using inner layers of a multilayer PCB. The coupler arrangement is 10 mm high and extends only 4 mm beyond the edge of the board. The total volume occupied is 2 cm^3 to which must be added a keep out volume of roughly 1 cm^3 below and above the tapered edge of the PCB. Fig. 7a shows the low-band input reflection coefficient. An 8 dB bandwidth of roughly 150 MHz can be observed. The high-band return loss is at least 10 dB over the whole band. The isolation between the two ports is better than 9 dB everywhere. Free space radiation efficiency (radiated over accepted power) was measured separately for port 1 and 2 using the calorimetric method [8]. Including (excluding) dissipation in the 50Ω termination which was in either case placed at the alternate port, radiation efficiencies of $0.85 \dots 0.88$ ($0.9 \dots 0.93$) were observed in low-band and $0.73 \dots 0.80$ ($0.81 \dots 0.90$) in high-band. The latter values could be improved by augmenting the sharp edges of the PCB metallization in the slot region with conductors having a smooth surface.

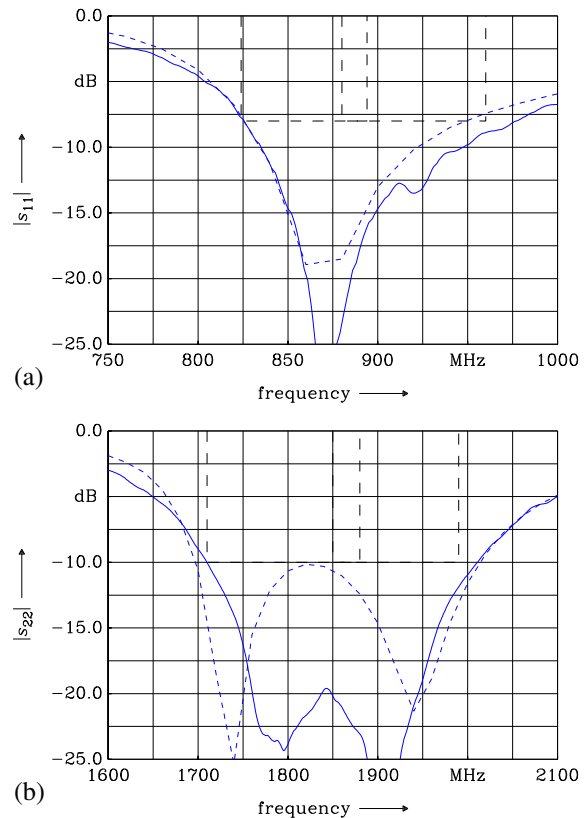


Fig. 7. Measured (solid) and simulated (short dashes) input reflection magnitude at ports 1 (low-band) and 2 (high-band) for the structure after Fig. 6. The GSM bands are indicated by long dashes.

REFERENCES

- [1] P. Vainikainen, J. Ollikainen, O. Kivekäs, and I. Kelder, "Resonator-based analysis of the combination of mobile handset antenna and chassis," *IEEE Trans. Antennas Propagat.*, vol. 50, no. 10, pp. 1433–1444, Oct. 2002.
- [2] E. H. Newman, "Small antenna location synthesis using characteristic modes," *IEEE Trans. Antennas Propagat.*, vol. 27, no. 4, pp. 530–531, July 1979.
- [3] R. F. Harrington and J. R. Mautz, "Theory of characteristic modes for conducting bodies," *IEEE Trans. Antennas Propagat.*, vol. 19, no. 5, pp. 622–628, Sept. 1971.
- [4] J. Villanen, J. Ollikainen, O. Kivekäs, and P. Vainikainen, "Compact antenna structures for mobile handsets," in *3rd COST 284 Management Committee Meeting Workshop*, Budapest, Oct. 2003. [Online]. Available: <http://www.ctsystemes.com/zeland/publi.htm>
- [5] E. Antonino-Daviu, M. Cabedo-Fabres, M. Ferrando-Bataller, and J. Herranz-Herruzo, "Analysis of the coupled chassis-antenna modes in mobile handsets," in *Proc. IEEE Antennas and Propagation Society Int. Symp. Digest*, Monterey: IEEE, June 2004.
- [6] M. Cabedo-Fabres, E. Antonino-Daviu, A. Valero-Nogueira, and M. Ferrando-Bataller, "On the use of characteristic modes to describe patch antenna performance," in *Proc. IEEE Antennas and Propagation Society Int. Symp. Digest*, Columbus, OH: IEEE, June 2003, pp. 712–715.
- [7] E. Antonino-Daviu, M. Cabedo-Fabres, M. Ferrando-Bataller, A. Valero-Nogueira, and M. Martinez-Vazquez, "Novel antenna for mobile terminals based on the chassis-antenna coupling," in *IEEE AP-S Int. Symp. and URSI National Radio Sci. Meeting*, Washington, DC: IEEE, July 2005.
- [8] W. L. Schroeder and D. Gapski, "Direct calorimetric measurement of small antenna radiation efficiency," in *Proc. IEEE Antennas and Propagation Society Int. Symp. Digest*, no. P57.3, Washington, DC: IEEE, July 2005.

Coupling Structures for Terahertz Near-field Microspectroscopy

G. Staats¹, Ll. M. Fernandez Ortega¹, U. Schade²,
D. Schondelmaier² and K. Holldack²

¹ Technische Universität Dresden, Mommsenstraße 13, 01069
Dresden, Germany

² Berliner Elektronenspeicherring-Gesellschaft für
Synchrotronstrahlung m.b.H. (BESSY), Albert-Einstein-Str.
15, 12489 Berlin, Germany

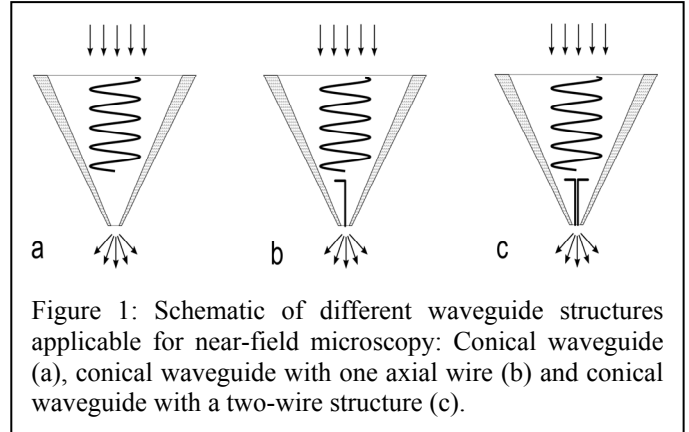
Short Abstract—Near field optical elements for free space focussing on Terahertz (THz) radiation were studied using analytical and numerical approaches for conical waveguides. One of the most promising candidates, a self-similar logarithmic periodical coupling structure (LPCS) embedded into a conical parabolic waveguide, was further experimentally studied with respect to spectral transmission losses using a scaled model at GHz frequencies. Since both studies confirmed the expected broadband and high transmission properties of LPCS structures compared to conventional conical waveguides, a prototype structure for THz frequencies realized by a x-ray lithography technique is presented.

Keywords—nearfield, coupling structures, THz-microscopy

I. INTRODUCTION

THz-Imaging has found applications in the range of quality control, semiconductor measurement, chemical analysis and biological investigations [1-4]. The main problem for imaging is the spatial resolution limit due to diffraction. Therefore only features with a dimension of the wavelength are resolvable, e.g. structures in the range of 1 mm to 100 μm . With new near-field imaging techniques [5], however, it is possible to reach spatial resolutions of up to $\lambda/1000$ [6]. Unfortunately, most methods [7-13] require extremely brilliant sources to compensate high losses by apertures used to confine the radiation field.

Using the highly brilliant and broadband coherent synchrotron radiation (CSR) it was developed at BESSY from the electron storage ring [14, 15] a THz scanning near-field imaging technology (SNIM) employing the time structure of the synchrotron radiation [16,17]. Here, conical near field probes together with a spectrometer [18] enable spectroscopic mapping of strongly absorbing materials, e.g. water containing objects with a spatial resolution well below the diffraction limit. However, the results were achieved using a strong source but at the expense of 4 orders of magnitude power losses using coaxial near-field probes as proposed by Keilmann [7]. The paper reports a development of improved near field probes based on the combination of self similar THz antennas embedded into a conical waveguide.



II. THEORETICAL BACKGROUND

A conical waveguide, as shown schematically in Fig. 1a, drastically attenuates the incident free-space THz radiation for radii shorter than the limiting radius at its exit. In this case most of the power is reflected at exit radii smaller than the wavelength. Conical waveguides can be analytically calculated using the vector potentials as given by a complete set of tesseral harmonics. In spherical coordinates the radial components of electric- A and magnetic F vector potentials of incident TM- and TE-Modes it can be written as:

$$A_r = \sum_m \sum_n (A_r)_{mn} \quad (1)$$

$$A_r = \sum_m \sum_n C_{mn} P_n^m(\cos \vartheta) \begin{Bmatrix} \sin m\varphi \\ \cos m\varphi \end{Bmatrix} \hat{H}_1(kr),$$

$$F_r = \sum_m \sum_n (F_r)_{mn} = \quad (2)$$

$$F_r = \sum_m \sum_n C_{mn} P_n^m(\cos \vartheta) \begin{Bmatrix} \sin m\varphi \\ \cos m\varphi \end{Bmatrix} \hat{H}_1(kr)$$

where

r, ϑ, φ = spherical coordinates,

C_{mn} = developing coefficients of an incident wave,

$\hat{H}_1(kr)$ = spherical hankel function of the first kind, and

P_n^m = associated Legendre functions of the first kind.

An incident plane wave can be developed in series of orthonormal eigenmodes having a normal propagation inward the cone up to the limiting radius. In this case most of the power is reflected at exit radii smaller than the wavelength. Hence, the required high spatial resolution of a SNIM forces its operation in a cut-off regime.

One option to avoid this drawback is the use of the TEM-Mode, which has no cut-off. Such probes were proposed first by Keilmann [7] employing a single bent wire in the centre of a conical waveguide (see Fig. 1b) in coaxial TEM-mode and a bended part in a non cut-off region. However, here the other modes are lost and a coaxial field distribution in the exit aperture of a conical waveguide is not the optimum for high resolution of a SNIM.

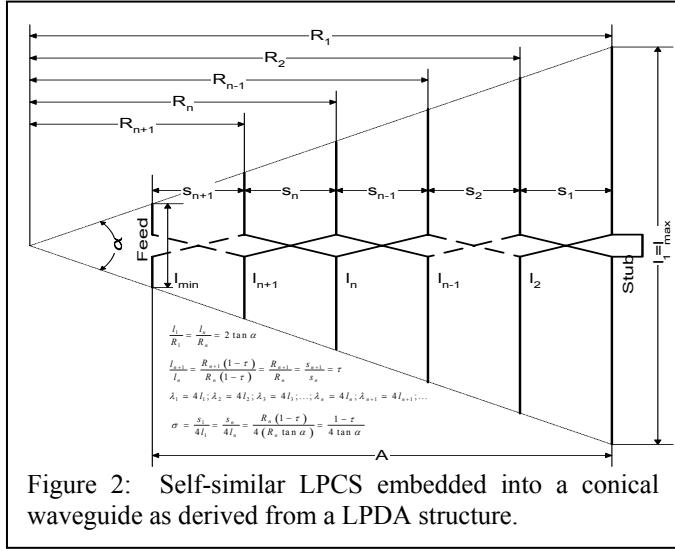


Figure 2: Self-similar LPCS embedded into a conical waveguide as derived from a LPDA structure.

A better solution might be the use of a two-wire structure in the centre of a conical waveguide (see Fig. 1c) also in TEM-mode feeding by a logarithmic periodic coupling structure (LPCS). Such logarithmic periodic structures are known from antenna theory. The LPCS is derived from a logarithmic periodic dipole antenna (LPDA) shown in Fig. 2, which was developed first by IsBell [19, 20] and realized later by Carrel [21]. The LPCS is a self-similar structure embedded in the cone without any frequency limit, because it has a transmission characteristic of constant input impedance over the entire frequency range. In a LPCS successive individual dipole antennas are connected alternately to a balanced transmission line called “feeder” [22]. The closely spaced elements are oppositely connected so that radiation flow into the direction of the shorter elements and the radiation perpendicular to the feeder tends to cancel. Radiated energy, at a given frequency, travels along the LPCS until it reaches a section of the structure where the electrical length of the elements and phase relationship are such as to produce strong coupling. As the frequency varies, the position of the resonant element is moved smoothly from one element to the next. The upper and lower frequency limit is then determined by lengths of the shortest and longest elements or in other words, these lengths have to be chosen to satisfy the bandwidth requirement.

The longest half-element must be roughly 1/4 wavelength at the lowest frequency of the bandwidth, while the shortest half-element must be about 1/4 wavelength of the highest frequency of the desired operation bandwidth [23]. The parameters τ , α and σ describe the geometry of the LPCS according to Fig. 2.

The relationships between α , τ , the element dipole lengths l_n , and distances R_n to the apex are determined by the geometry and can be written as:

$$\frac{l_1}{R_1} = \frac{l_n}{R_n} = 2 \tan \alpha \quad (3)$$

where

l_n = total length of the nth element,

R_n = distance from apex to the nth element, and

α = half-angle subtended by the ends of radiating elements.

In addition, the ratios of l_{n+1}/l_n , R_{n+1}/R_n and s_{n+1}/s_n are equal to τ , which is usually a number less than 1.0. That is

$$\frac{l_{n+1}}{l_n} = \frac{R_{n+1}(1-\tau)}{R_n(1-\tau)} = \frac{R_{n+1}}{R_n} = \frac{s_{n+1}}{s_n} = \tau \quad (4)$$

where s_n is the distance between the element n and the element (n+1). It is often convenient to think of the element spacing s_n in terms of wavelength. The free-space wavelength λ of a signal that resonates the first largest element, l_1 , is approximately four times l_1 , thus

$$\lambda_1 \approx 4l_1; \lambda_2 \approx 4l_2; \lambda_3 \approx 4l_3; \dots; \lambda_n \approx 4l_n; \lambda_{n+1} \approx 4l_{n+1}; \dots \quad (5)$$

For any value of n , the ratio $s_n/4l_n$ is a useful quantity. It is called spacing factor σ and can be expressed in terms of τ and α as follows:

$$\sigma = \frac{s_1}{4l_1} = \frac{s_n}{4l_n} = \frac{R_n(1-\tau)}{4(R_n \tan \alpha)} = \frac{1-\tau}{4 \tan \alpha} \quad (6)$$

The performance of an LPCS is a function of the parameters τ and α . In particular, the input impedance depends on τ and α . For example, if the value of τ is 0.95, then the unloaded feeder impedance is 104 Ω , and if α varies from 10° to 30°, the input impedance falls between the limits of 76 and 53 Ω . Here, the unloaded feeder impedance refers to the characteristic impedance of the central transmission line without all the elements. As the value of τ is decreased, the input impedance will increase up to the value of the unloaded feeder impedance. The reason is that fewer elements per feeder unit length are connected in parallel to the feeder. On the contrary, it is expected that for the higher values of τ the LPCS will be less dependent on frequency promising the possibility of an almost frequency independent design.

Using such structures in a conical waveguide leads to a self-similar frequency independent 3-wire TEM-waveguide with even and odd-modes. With a correct design, the even-mode is suppressed and only the odd-mode is propagated. This leads to a high field concentration on the tip of the cone between the two wires of the LPCS and also to a high spatial resolution of the corresponding SNIM. Fortunately, the incident plane waves may couple (without cone reflections)

into the LPCS, before and after being reflected by the exit aperture.

III. NUMERICAL COMPUTATIONS

For the design of such structures some numerical calculations have been performed using the code HFSS from Agilent Technologies. Fig. 3 shows the E-field vector at the tip of the cone within the LPCS at 100 GHz.

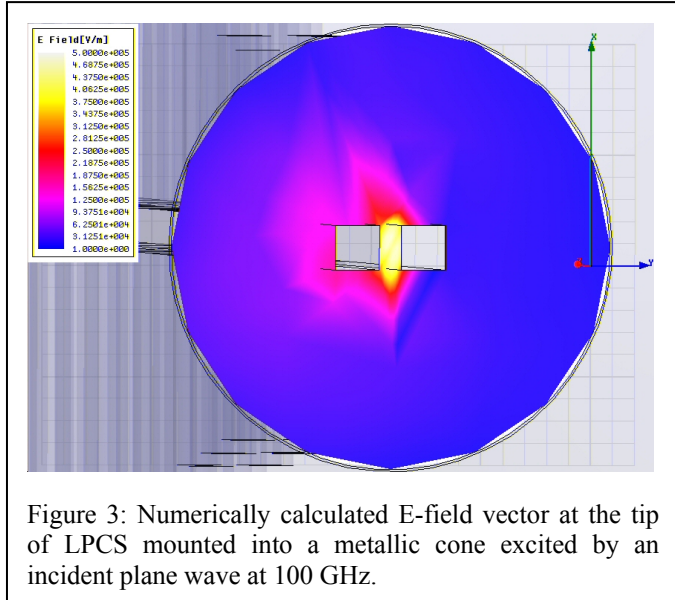


Figure 3: Numerically calculated E-field vector at the tip of LPCS mounted into a metallic cone excited by an incident plane wave at 100 GHz.

It is excited by a simulated incident plane wave. The highest field concentration is reached between the two wires of the coupling structure. Fig. 4 shows the E-field in the bulk of the cone for the same structure. Here, a high field concentration in the narrow part of the cone is obtained. Computations using moment methods [FEKO from EM Software & Systems] yield similar results. In general, the numerical simulations indicate much higher field strength at the tip of the cone compared to empty cones and cones using bended wires.

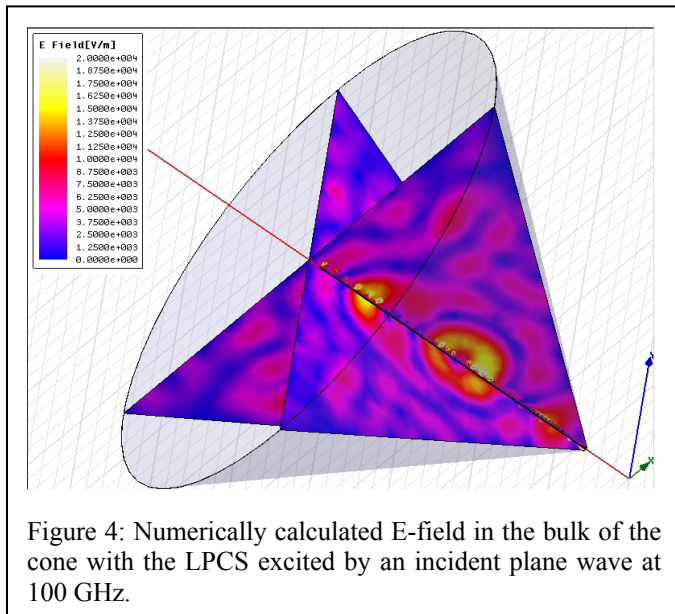


Figure 4: Numerically calculated E-field in the bulk of the cone with the LPCS excited by an incident plane wave at 100 GHz.

IV. MODEL MEASUREMENTS

Numerical calculations for the LPCS structure have been validated using a 100:1 scaled model for a conical THz-waveguide. With this model it was possible to cover the frequency range from 1 to 8.5 GHz equivalent to 0.1 to 0.85 THz. The effect of three different geometrical configurations are investigated by observing the electric field magnitudes at the tip of the cone.

The measurements are done with a planar nearfield scanner and an electric field probe (short monopole, about 0.1mm in length). The spatial resolution was chosen to 0.25mm in both axes. The distance in the scanner between the tip of the cone with/without the structures and the electric field probe was set to 0.5mm. A vector network analyzer with additional amplifier for higher dynamics was used to measure the transmission between a broadband double rigid horn on the input of the cone and the electric field probe.

The results are shown in Fig. 5 for a cone without any coupling structure. Here, it is shown that surface currents are flowing around the hole at the tip and that high insertion losses occur.

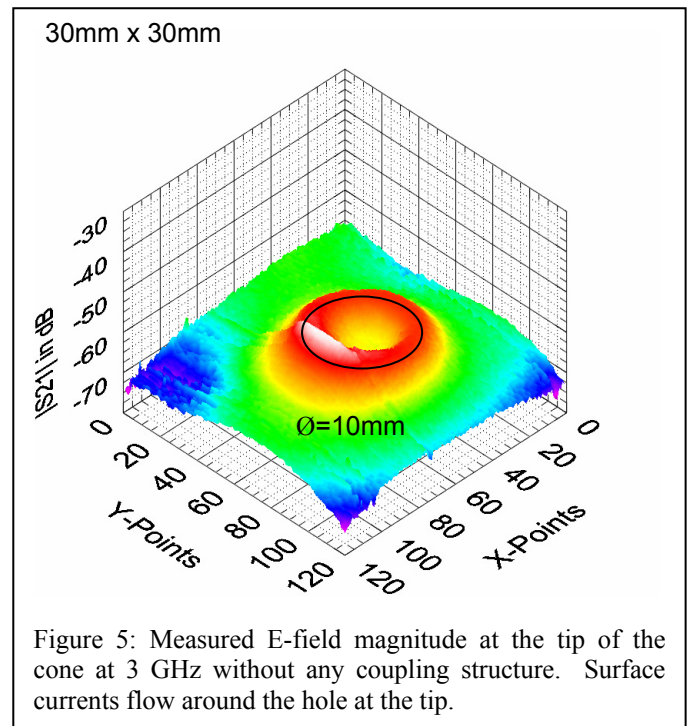
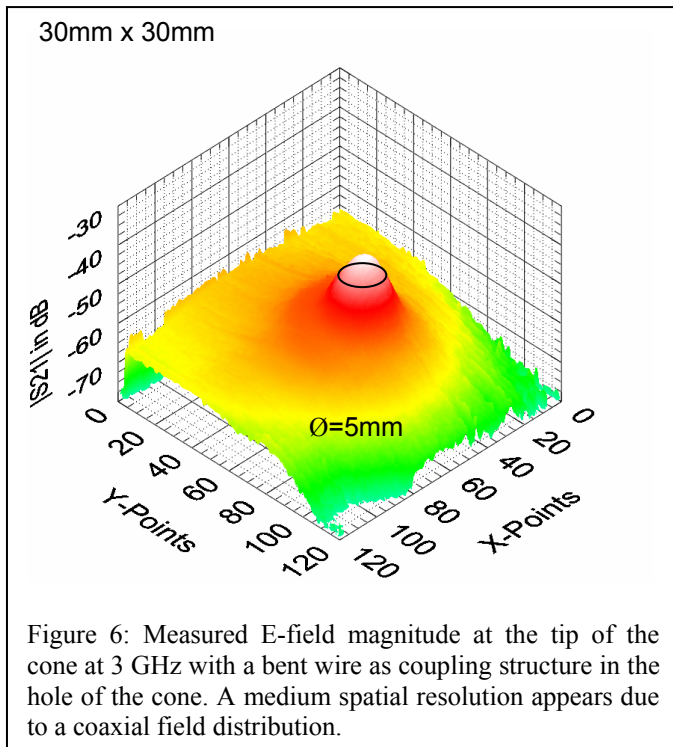
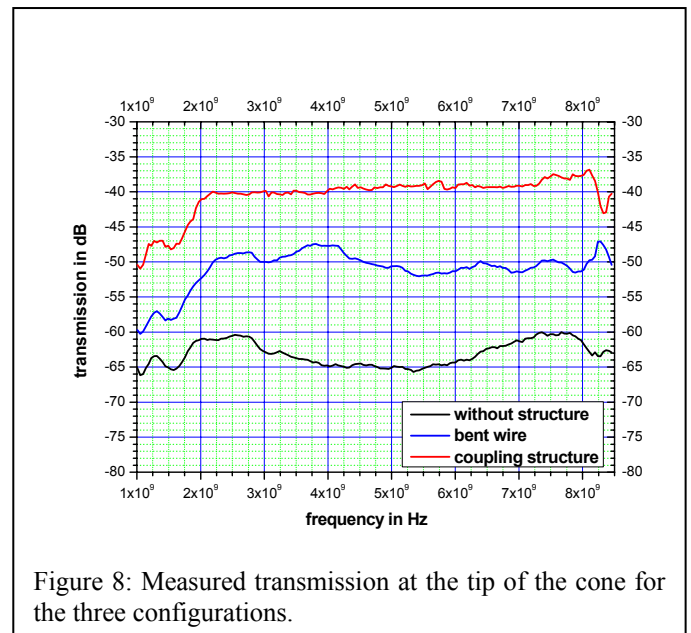
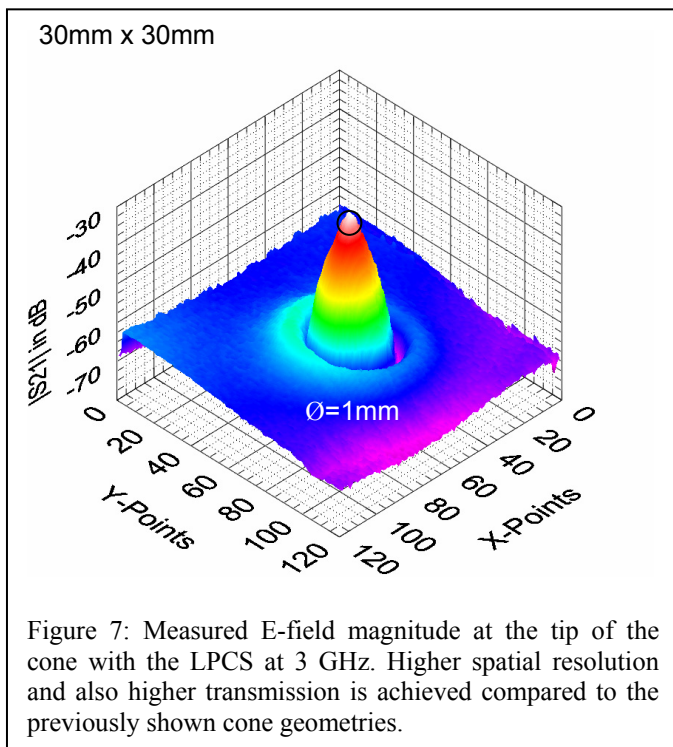


Figure 5: Measured E-field magnitude at the tip of the cone at 3 GHz without any coupling structure. Surface currents flow around the hole at the tip.

Fig. 6 shows the results for a cone with a bent wire in the configuration according to Keilmann [7]. This geometry has a better transmission than the conventional cone and a coaxial field distribution is observed.



Finally, in Fig. 7, the results for the cone with the LPCS are shown. This geometry yields a even better transmission compared to the other structures. The field confinement at the tip would allow a much higher spatial resolution at the SNIM.



For all three configurations, the frequency response was investigated and plotted in Fig. 8. The LPCS shows the highest transmission (10 dB better than the transmission for the cone with bended wire) and an almost flat-top frequency response.

V. TECHNICAL REALIZATION

Encouraged by the positive results of the numerical calculations and measurements of the scaled model, a LPCS structure for the THz range has been designed and produced by using micromechanics based on the LIGA-technology (German: “Lithographie, Galvanik und Abformung”).

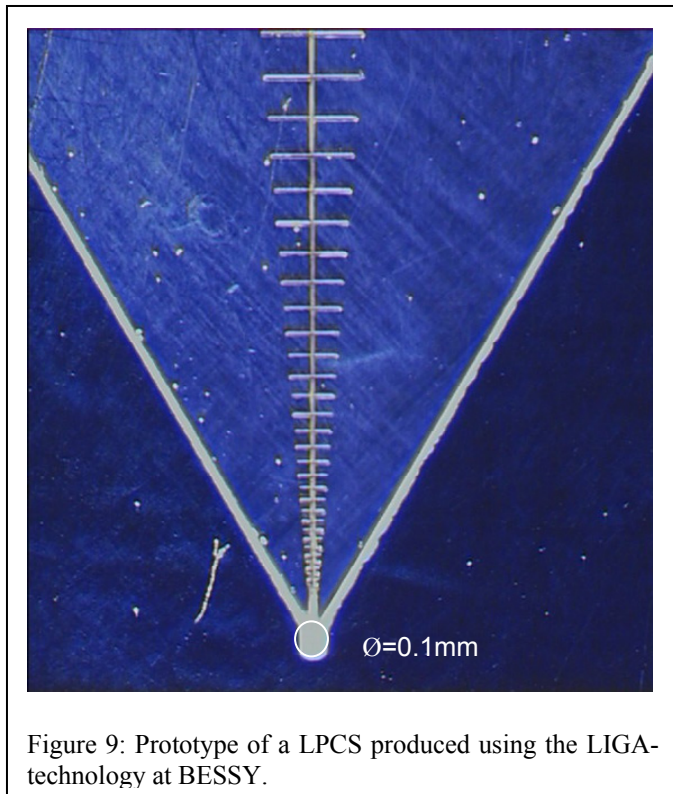
A microscope image of the tip of a prototype antenna structure for the range between 0.1 and 1 THz is depicted in Fig. 9. The two metallization layers of the antenna are 10 μm apart of each other (not visible in the photograph) and are buried in a 100- μm thick epoxy film which acts as a mechanical support for the antenna. The complete antenna structure is mounted in a metallic cone and was exposed to the BESSY THz source. First measurements demonstrate the expected high field intensity at the tip of the cone which can even destroy the tip in some cases (1 mW of input power results in up to 100 kV/m at the tip).

VI. OUTLOOK

SNIM and similar applications might benefit from the large transmission and the spectral properties of LPCS structures as waveguides for THz radiation. This has been shown by numerical studies together with measurements on scaled models. The concept proposed opens new perspectives to analyze samples spectroscopically with near-field probes in the THz region with sub-wavelength spatial resolution range. The LIGA technique could be an appropriate way for the technical realization of such probes.

VI. ACKNOWLEDGMENT

We are indebted to the support of D. Ponwitz, I. Rudolph (BESSY), and K. Wolf (TU Dresden).



VIII. REFERENCES

[1] B. Ferguson and X.-C. Zhang: "Materials for terahertz science and technology", *Nature Materials*, vol.1, pp.26-33, 2002, and references therein.

[2] D.M. Mittleman, R.H. Jacobsen, and M.C. Nuss: "T-Ray Imaging", *IEEE Journal of Selected Topics on Quantum Electronics*, vol.2, pp.679-692, 1996.

[3] D.M. Mittleman, M. Gupta, R. Neelami, R.B. Baraniuk, J.V. Rudd, and M. Koch: "Recent Advances in Terahertz Imaging", *Applied Physics*, vol. B 68, pp.1085-1095, 1999.

[4] T. Löffler, T. Bauer, K.J. Siebert, H.G. Roskos, A. Fitzgerald, and S. Czasch: "Terahertz dark-field imaging of biomedical tissue", *Optics Express*, vol.12, pp.616-621, 2001.

[5] B. Knoll and F. Keilmann: "Near-field probing of vibrational absorption for chemical microscopy", *Nature*, vol. 399, pp.134-137, 1999.

[6] H.-T. Chen, R. Kersting, and G.C. Cho: "Terahertz imaging with nanometer resolution" *Applied Physics Letters*, vol. 83, pp.3009-3001, 2003.

[7] F. Keilmann: "Scanning Tip for Optical Radiation", U.S. Patent No. 4,994,818, filed 1989, 1991.

[8] F. Keilmann: "Far-Infrared Microscopy", *Infrared Physics Technology*, vol.36, pp. 217, 1995.

[9] B. Knoll and F. Keilmann: "Electromagnetic fields in the cutoff regime of tapered metallic waveguides", *Optics Comm.*, vol. 162, pp.177-181, 1999.

[10] S. Hunsche, M. Koch, I. Brener, and M.C. Nuss: "THz near-field imaging", *Optics Communications*, vol.150, pp.22-26, 1998.

[11] Q. Chen, Z. Jiang, G.X. Xu, and X.C. Zhang: "Near-Field Terahertz Imaging with a Dynamic Aperture", *Optics Letters*, vol.25, pp.1122-1124, 2000.

[12] O. Mitrofanow, M. Lee, J.W.P. Hsu, I. Brener, R. Harel, J.F. Federici, J.D. Wynn, L.N. Pfeiffer, and K.W. West, *IEEE Journal of Selected Topics on Quantum Electronics*, vol.7, pp.600-607, 2001.

[13] B.T. Rosner and D.W. van der Weide: "High-frequency near-field microscopy" *Review of Scientific Instruments*, vol.73, pp.2505-2525, 2002, and references therein.

[14] M. Abo-Bakr, J. Feikes, K. Holldack, G. Wüstefeld, and H.-W. Hübers: "Steady-State Far-Infrared Coherent Synchrotron Radiation detected at BESSY II", *Physical Review Letters*, vol. 88, 254801, 2002.

[15] M. Abo-Bakr, J. Feikes, K. Holldack, P. Kuske, W.B. Peatman, U. Schade, G. Wüstefeld, and H.-W. Hübers: "Brilliant, Coherent Far-Infrared (THz) Synchrotron Radiation", *Physical Review Letters*, vol. 90, 094801, 2002.

[16] U. Schade, A. Röseler, E.H. Korte, F. Bartl, K.P. Hofmann, T. Noll, and W.B. Peatman: "New infrared spectroscopic beamline at BESSY II", *Review of Scientific Instruments*, vol. 73, pp.1568-1570, 2002.

[17] U. Schade, K. Holldack, P. Kuske, G. Wüstefeld, H.-W. Hübers: "THz near-field imaging employing synchrotron radiation", *Applied Physics Letters*, vol. 84, 1422-1424 2004.

[18] D.H. Martin and E. Puplett: "Polarised interferometric spectroscopy for the millimetre and submillimetre spectrum", *Infrared Physics*, vol. 10, pp.105-109, 1970.

[19] R.H. DuHamel and D.E. Isbell: "Broadband Logarithmically Periodic Antenna Structures", *IRE Convention Record*, part.1, pp.119-128, 1957.

[20] D.E. Isbell: "Log periodic Dipole Arrays", *IRE Transactions on Antennas and Propagation*, vol.8, pp.260-267, May 1960.

[21] R.L. Carrel: "Analysis and Design of the Log-Periodic Dipole Antenna", Ph.D.-Dissertation, Elec. Eng. Dept., University of Illinois, 1961, University Microfilms, Inc., Ann Arbor, MI.

[22] R.L. Carrel: "The Design of Log-Periodic Dipole Antennas", *IRE Convention Record*, part 1, pp.61-75, 1961.

[23] C. Balanis: "Antenna Theory, Analysis and Design", pp.553-566, 2nd ed., John Wiley and Sons, New York, 1997.

Minimising the Electromagnetic Exposure at Hot-Spot Areas using Hybrid (DVB-H/UMTS) Networks

Peter Unger, Moritz Schack, Thomas Kürner
Institut für Nachrichtentechnik (IfN)
Technische Universität Braunschweig
Braunschweig, Germany
Email: Unger@ifn.ing.tu-bs.de

Abstract— A hybrid mobile communication network as considered in this paper consists of a point-to-point network (UMTS) and a point-to-multipoint network (DVB-H). The benefit of combining these two networks is an optimised transfer of data by collecting several user requests for a single response via the broadcast network. Thus, capacity can be saved, UMTS cells can be unloaded and the mean response time of the system can be reduced. Besides these advantages, hybrid networks can be applied to decrease electromagnetic exposure at hot-spots. This problem will be analysed in this paper. Therefore, a scenario has been developed which includes a hot-spot area. Furthermore, this paper includes the definition of a criterion to estimate the benefit of reducing the electromagnetic exposure using a hybrid network. The results are shown in an example scenario.

I. INTRODUCTION

In this context, a hybrid mobile communication network consists of a point-to-point (unicast) system and a point-to-multipoint (broadcast) system. The benefits of both systems will be combined in order to optimise transfer of data. On the one hand bidirectional point-to-point channels are used for individual services. On the other hand, a unidirectional broadcast channel offers high data rates for the downlink. Requests of the same content can be combined to serve all users by only one transmission at the same time instead of individual transmissions. Thus, necessary capacity can be saved.

The herein described hybrid networks combine the mobile communication network UMTS (Universal Mobile Telecommunications System) and the broadcast system DVB-H (Digital Video Broadcasting - Handheld). DVB-H is a broadcast system based on DVB-T (Digital Video Broadcasting - Terrestrial). It is optimised for small devices such as mobile phones by using time slicing for less power consumption and an additional forward error correction (FEC) providing more robust signals [1], [2].

Besides reducing the necessary capacity, other advantages of hybrid networks are the reduction of the mean response time of the system and unloading the UMTS network by offering additional downlink capacity [3], [4].

In this paper it is investigated whether hybrid networks can be used to reduce electromagnetic exposure. Electromagnetic waves may have an influence on the human body, e.g. thermal influences on the human tissue [5]. The electromagnetic exposure of radio communications systems is seen critical by the

public. Thus, reducing the electromagnetic exposure of radio systems is an important issue.

A single UMTS network will be compared to a hybrid network, consisting of UMTS and DVB-H. Both network types are deployed in order to serve the same amount of user requests. Deploying a hybrid network consisting of UMTS and an additional DVB-H network can provide high data rates at the downlink. Especially at hot-spot areas, where many users are located at a close place, a broadcast transmitter could replace several Node-B's, which has an impact on the electromagnetic exposure.

This paper is organised as follows: In Section II the services, the reference UMTS network and the two different network types, the enhanced UMTS network and the hybrid network, are described. Section III specifies the criterion which is used to measure the amount of electromagnetic exposure. This criterion will be used in Section IV to compare the different networks.

II. SCENARIO

In order to investigate both network types on electromagnetic exposure, a scenario has been developed which also includes hot-spot areas. The scenario contains assumptions on user behaviour and geographical user distribution. Different service classes are described, which are offered to be transmitted by each type of network. Considering the user information, the UMTS reference network has been developed, including Node-B positions and transmitting power. Furthermore, the power level predictions are based on building data and topographical data.

For the scenario area, the city of Hannover was selected. The area has a size of $15\text{ km} \times 12\text{ km}$ and a resolution of $50\text{ m} \times 50\text{ m}$ per pixel. In order to show the benefit by reducing electromagnetic exposure in hot-spot areas, the football stadium of Hannover was selected, which is one of the FIFA football world championship arenas in Germany 2006. Especially during those events, thousands of spectators, inside or around the stadium, are expected to consume video content using their mobile terminals. Regarding this extreme amount of requested data, it is expected that the UMTS network will not be able to fulfil all user requests. Therefore, the UMTS network has to be enhanced by additional Node-B's, alternatively an additional DVB-H network can be used to strengthen the downlink.

A. Service Scenario

Two types of services are considered. On the one hand, typical services, such as voice telephony, will be transmitted solely by the UMTS network. On the other hand, high data rate download services, such as video, are considered to be transmitted either by the UMTS or by the hybrid network.

The typical UMTS services which can be requested by the users are based on the scenario of the IST-MOMENTUM project [6]. Assumptions on the user behaviour are given for each service, such as voice and video telephony, web-browsing, streaming multimedia, multimedia messaging service, e-mail, location based services and file download. The user behaviour, i.e. call attempt rates, depends on the location of the user. Thus, an operational environment map is used which specifies different usage classes, e.g. central business district, suburban or rural areas [6]. In addition, a population density map is necessary which specifies the geographical distribution and the density of the users.

Using these input data, maps are calculated providing the busy hour call attempts (BHCA) for each service. The BHCA values represent call attempt rates during the most active hour. The BHCA maps, indicating the geographical dependent user behaviour for each separate UMTS service, were used for designing the UMTS reference network.

The above mentioned eight service classes are typical UMTS services. In order to describe the football-video service, an additional class is included. Content of this service can be transferred either by the UMTS network in a point-to-point mode or by the DVB-H network in broadcast mode.

B. UMTS Reference Network

The UMTS reference network has been designed for fulfilling the user requests for the eight typical UMTS services. The design process is based on snapshots where users are randomly generated at the scenario area. Thus, a random value generator determining the active users has been developed. This generator requires the mean number of users for each position of the scenario. These values are generated using the BHCA maps and the mean holding time of each service.

The users of each snapshot are assigned to Node-B's. Therefore, potential Node-B locations were selected and for each one a signal level propagation was calculated. A propagation model for dense urban areas [7] was selected, which uses building data. For the UMTS network, a macro cell structure is assumed. The same configuration consisting of sectorisation, tilt and antenna type is applied for each Node-B.

In order to assign users to a serving Node-B, they are randomly selected from the snapshot. The Node-B is selected which is the best server for the user in terms of receiving power. A user will be assigned to the selected Node-B, if the uplink link budget restriction is satisfied. This means that the maximum uplink power of the terminal (21 dBm) is sufficient to reach the Node-B. Other criteria are the uplink and downlink load factor according to [8]. If these values meet a fixed threshold, the user will be assigned to the Node-B. Otherwise the next best server Node-B will be selected. If the user cannot be assigned to any Node-B, it will be marked as rejected. The number of rejected users is a measure for the quality of the UMTS network.

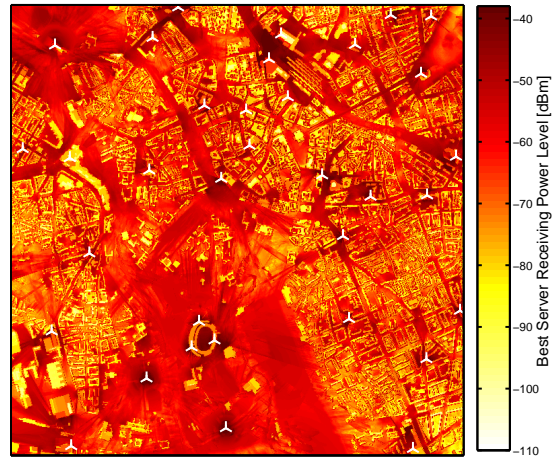


Fig. 1. UMTS reference network structure and best server receiving power level

At the beginning of the network design process more potential Node-B's were provided than probably necessary. Their positions were selected on roof tops. After the assignment process those Node-B's were removed which were not or very rarely used. The necessary UMTS transmitting power was adapted considering the necessary connections. Figure 1 shows the achieved UMTS reference network structure and the best server receiving level. About 100 snapshots were used for the assignment process. The fully occupied stadium is covered with three Node-B's.

C. Enhanced UMTS Network

The UMTS reference network was designed to serve the eight typical UMTS services. For the hot-spot area stadium a video service is assumed, offering highlights of the current and also other football matches, as well as news content. The video content is transferred by video streams with a data rate of 384 kbps and a resolution of 352×288 pixels according to CIF (common intermediate format) [9]. Adding the new video service, it is expected to produce a heavy traffic mix which cannot be handled by the UMTS reference network.

Figure 2 shows an assignment result of a representative snapshot including video users. Firstly it can be seen that a large number of users (about 65 of 389 total users) could not be assigned to a Node-B. Among these, about 30 voice users were rejected, caused by the random assignment procedure. Furthermore, many users at the stadium are connected to Node-B's far away. This indicates that the Node-B's inside the stadium are totally occupied. Furthermore, low signal quality may occur for these connections.

In order to serve the complete service mix, the capacity of the UMTS network has to be enhanced. This is done by including additional Node-B's. Simulations have shown that six new Node-B's with three sectors each are sufficient. In Figure 3 the enhanced UMTS network is shown. With the additional Node-B's it is possible to serve the users, also those who consume the video service.

D. Hybrid Network Architecture

Instead of enhancing the UMTS reference network by additional Node-B's, a DVB-H network could be deployed in order to form a hybrid network. DVB-H offers broadcast

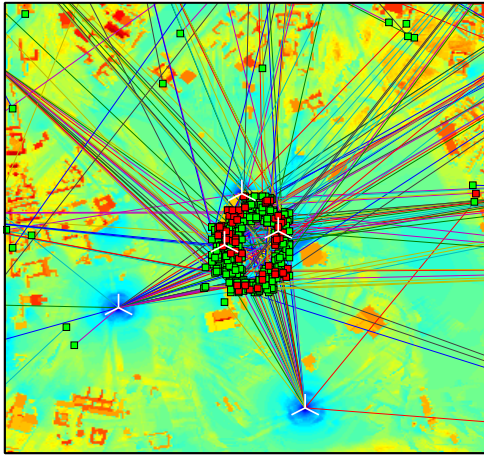


Fig. 2. Snapshot and user assignment to Node-B's at the UMTS reference network

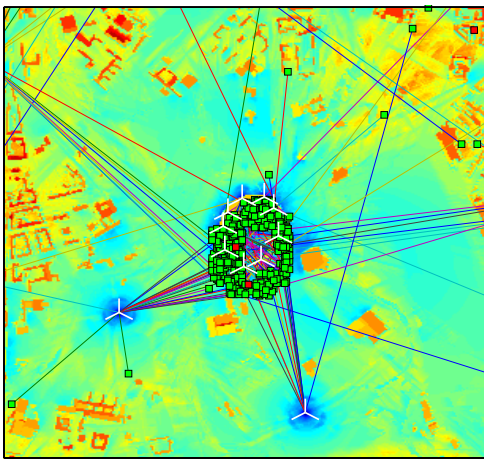


Fig. 3. Snapshot and user assignment to Node-B's at enhanced UMTS network; 6 additional Node-B's at the stadium

channels with high downlink data rates. Therefore, services requiring high data rates at the downlink, such as the video service, are suitable to be transmitted by the DVB-H network.

In a hybrid network, the video service can either be transmitted by the UMTS network or by the DVB-H network depending on the load balancing strategy. In order to optimise data transfer at the hybrid network, a load balancing algorithm will be applied [10]. This method analyses the popularity of content, user request rates and the load of the UMTS cells to decide the way of transmission. The popularity of content describes the frequency of user requests for the appropriate content. The more often a certain content is requested, the higher its popularity is. A possible distribution of popularity for video content is the Zipf distribution (Equation 1). In [11] it is shown that the Zipf distribution is suitable for the popularity distribution of video contents such as the football-video service.

$$P(i) = \frac{1}{\Omega i^\alpha} \text{ and } \Omega = \sum_{j=1}^C \frac{1}{j^\alpha}; 1 \leq i \leq C; i, C \in \mathbb{N}; \alpha \geq 0 \quad (1)$$

$P(i)$ gives the probability of the usage of channel i . The popularity function $P(i)$ depends on the number of offered

channels C and the shape parameter α . With α equal to zero, all channels have the same popularity. With an increasing α , the popularity of a small number of channels increases whereas the popularity of the other channels decreases.

For the video service it is assumed that nine different video streams are offered using a data rate of 384 kbps each. A Zipf shape value $\alpha = 1.1$ is assumed. This indicates a dominating stream of about 38.5% proportion of all user requests. This stream can be seen as a highlight video of the current match. The other streams have a fraction of 18%, 11.5%, 8.4%, 6.5%, 5.4%, 4.5%, 3.9% and 3.3% respectively.

The mean number of users of the video service at the stadium over all snapshots is 87 users. This leads to a distribution of about 34 users for the dominating stream and about 3 users for the stream with the lowest popularity. According to [10] it is assumed that all streams will be transmitted by the broadcast network due to sufficing popularity. Furthermore, the UMTS network is highly loaded, thus, the remaining data rate in each cell is limited.

In order to transmit nine different video streams having a data rate of 384 kbps each, a total capacity of about 3.5 Mbps is necessary. Therefore, one DVB-H cell having the DVB-H mode QPSK with code rate 1/2 and MPE-FEC 3/4 offering a data rate of 3.7 Mbps is sufficient.

Table I shows the assumed DVB-H configuration. The link budget includes the necessary carrier-to-noise ratio depending on the DVB-H mode, i.e. QPSK, and a fading margin. The minimum receiving power level results to $P_{min} = -74.95$ dBm which limits the coverage area.

Frequency	500 MHz
Bandwidth	8 MHz
Noise Floor Level	-105.2 dBm
Receiver Noise Figure	5 dB
Carrier-to-Noise	9.6 dB assuming the DVB-H mode 8K, QPSK, Viterbi code rate 1/2, MPE-FEC code rate 3/4
Receiver Antenna Gain	-9.65 dBi
Fading Margin	6 dB assuming a standard deviation of $\sigma = 6$ dB and, a coverage probability of 84%
Minimum Receiving Level	$P_{min} = -74.95$ dBm

TABLE I
PARAMETERS OF THE DVB-H NETWORK

A circular cell for covering the stadium is assumed using an isotropical antenna type. Due to the very limited area of the hot-spot, the size of the target area to be covered has a radius of 400 m. Regarding the propagation effects an ideal circular cell cannot be reached. The target is to cover the stadium also with indoor coverage and the near surrounding. It is assumed, that for the buildings close to the stadium indoor reception is not required. Due to the propagation effects a circular cell cannot be reached. Thus, the target area will be covered with a threshold of 95% of the total area size. The

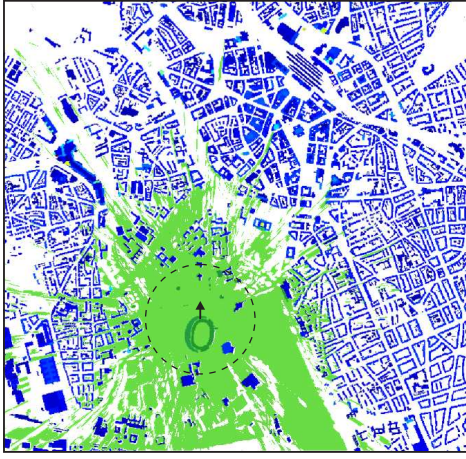


Fig. 4. Coverage Area of the DVB-H Cell

antenna height is set to 30 m at the north side of the stadium. Considering the minimum receiving level calculated in Table I, a transmitting power (EIRP) of 35 dBm is necessary. Figure 4 shows the coverage area of the hot-spot. The stadium with indoor reception and its surrounding are covered.

III. EXPOSURE ESTIMATION

In the section before, two network types were described, on the one hand a single UMTS network with the enhanced UMTS network structure described in Section II-C. On the other hand the hybrid network consisting of the UMTS reference network and one DVB-H transmitter covering the hot-spot area is considered. Both network types have to be compared in terms of the arising electromagnetic exposure.

To avoid too high exposure values, reference levels for the electromagnetic exposure are standardised. These thresholds are based on the general public exposure values in [5]. Table II specifies the reference levels for different frequency ranges.

Frequency range	Reference level of electromagnetic field strength $E_{L,f}$ [V/m]
10-400 MHz	28
400-2000 MHz	$1.375 \cdot \sqrt{f}$
2-300 GHz	61

TABLE II
REFERENCE LEVEL FOR GENERAL PUBLIC EXPOSURE [5]

The propagation model gives the predicted power maps as power level values. Thus, these values have to be transformed into the necessary electromagnetic field strength values. Equation 2 is used to transform the receiving power at the terminal depending on the frequency f and the antenna gain of the terminal G_e .

$$E[dB\mu V/m] = P_e[dBm] + 77.2 + 20\log f[MHz] - G_e[dBi] \quad (2)$$

In order to enable the comparison of the different network types, a criterion has to be applied which also considers the different transmitting frequencies of the hybrid network. The exposure limit at a certain position of the area is met

if the constraint of Equation 3 is satisfied [5, eq. 9]. The field strength value of each frequency part is related to the frequency dependent reference level specified in Table II. The sum of all ratios should not exceed the limit of 1.

$$\sum_{f=100kHz}^{1MHz} \left(\frac{E_f}{87/\sqrt{f}} \right)^2 + \sum_{f>1MHz}^{300GHz} \left(\frac{E_f}{E_{L,f}} \right)^2 \leq 1 \quad (3)$$

The networks considered in this work are UMTS at 2140 MHz and DVB-H at 500 MHz. As an assumption, these two frequencies are solely considered in order to estimate differences between the two network types in terms of electromagnetic exposure.

In Equation 4 the exposure ratio U is defined. The field strength value of a network is related to the reference level at the appropriate frequency. Considering the single UMTS network, the 500 MHz part does of course not exist.

$$U = \left(\frac{E_{2140MHz}}{E_{L,2140MHz}} \right)^2 + \left(\frac{E_{500MHz}}{E_{L,500MHz}} \right)^2 \quad (4)$$

The exposure ratio will be calculated for each point of the selected area of the scenario using Equation 4 resulting to an exposure ratio matrix. Two results are interesting for comparison, the maximum exposure ratio \hat{U} and the mean exposure ratio \bar{U} , which will be obtained from the exposure ratio matrix. The constraint of $\hat{U} \leq 1$ as the upper limit has to be met.

The benefit of the hybrid network is estimated with the gain value specified in Equation 5.

$$G = \frac{U_{UMTS}}{U_{hybrid}} \quad (5)$$

The exposure ratio value of the single UMTS network is compared to the exposure value of the hybrid network. Both cases, mean and maximum exposure ratio values, will be evaluated. A gain value of $G = 1$ indicates that a hybrid network does not bring a benefit in terms of reducing electromagnetic exposure. A gain value larger than 1 stands for the degree of reduction of electromagnetic exposure. A gain value smaller than one indicates that a hybrid network is not suitable in order to decrease electromagnetic exposure.

IV. SIMULATION RESULTS

The two network types, the enhanced UMTS network described in Section II-C and the hybrid network described in Section II-D, are compared in terms of electromagnetic exposure. The gain value defined in Equation 5 is used to estimate the benefit of the hybrid network in terms of decreasing electromagnetic exposure.

The calculation of the exposure ratio U , especially the mean value \bar{U} , is heavily dependent on the selected area. Due to the small size of the hot-spot and the small size of the coverage area, an area around the stadium of $1000\text{ m} \times 1000\text{ m}$ was selected.

Figure 5 shows the exposure ratio maps for the enhanced UMTS network. In Figure 6 the exposure ratio map of the hybrid network is depicted. It is obvious that the single UMTS network causes a higher exposure ratio, compared to the hybrid network, especially in immediate vicinity of the stadium.

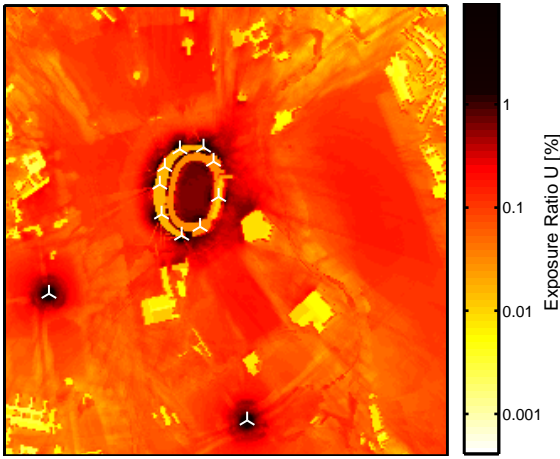


Fig. 5. Exposure ratio map of the enhanced UMTS network

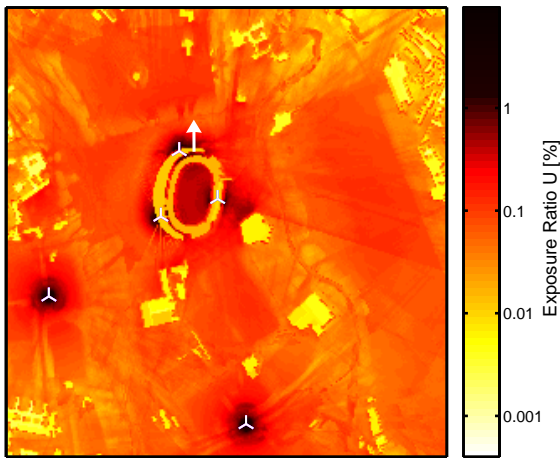


Fig. 6. Exposure ratio map of the hybrid (UMTS/DVB-H) network

In Table III the values for the exposure rate and the gain value are given. Using the mean exposure rate value \bar{U} , a gain of $G = 1.84$ is reached. The large saving of exposure is ascribed to the replacement of six Node-B's by only one DVB-H transmitter. The gain value using the maximum exposure ratio \hat{U} only reaches $G = 1.36$. This can be described by the close positioning of the DVB-H transmitter at the Node-B.

The simulations have shown that the exposure also depends on the UMTS network cell structure, i.e. on the used power of the common pilot channel (CPICH). For the reference UMTS network the same pilot power of 33 dBm is used. Changing the pilot power may cause problems during the planning process and particularly in operating UMTS networks, e.g. due to the decrease of the soft handover regions between cells. Nevertheless, the stadium can be seen as a zoned area, where lower pilot power levels could be applied without a significant influence of the surrounding cells. In Table III the results are shown, in case the pilot power for the Node-B's at the stadium in the enhanced UMTS network is reduced by half. It is assumed that the pilot power in the hybrid network is not changed. The exposure ratio of the single UMTS network is decreased. But the gain value for the mean exposure ratio of $G = 1.26$ is still larger than 1 and the hybrid network brings still a benefit in terms of saving exposure.

Pilot Power	Exposure Ratio	Enhanced UMTS Network	Hybrid Network	Gain G
33 dBm	\bar{U} [%]	$6.21 \cdot 10^{-4}$	$3.37 \cdot 10^{-4}$	1.84
	\hat{U} [%]	0.8349	0.6115	1.36
30 dBm	\bar{U} [%]	$4.24 \cdot 10^{-4}$	$3.37 \cdot 10^{-4}$	1.26
	\hat{U} [%]	0.6306	0.6115	1.03

TABLE III
RESULTS OF EXPOSURE

V. CONCLUSION

Reducing electromagnetic exposure of radio systems is an important issue. In this paper, it is shown that a hybrid network consisting of DVB-H and UMTS can be beneficial in terms of electromagnetic exposure especially at hot-spot areas. The additional high data rate downlink channel offered by the DVB-H network can be used for a more efficient transmission of video services. Thus, capacity can be saved compared to a single UMTS network. This benefit is used to reduce the electromagnetic exposure, because less Node-B's are necessary to serve the same amount of user requests. A gain value was defined, describing the benefit of the hybrid network compared to a single UMTS network. At the hot-spot stadium a gain value of $G = 1.84$ for reducing the mean exposure ratio was achieved.

ACKNOWLEDGMENT

This work has been funded by the Bundesministerium für Bildung und Forschung (BMBF) in the project *miniWattII*.

REFERENCES

- [1] U. Reimers, *Digital Video Broadcasting (DVB) - The International Standard for Digital Television*, 2nd ed., (Hrsg.), Ed. Springer: Berlin, Heidelberg, New York, 2004.
- [2] *Digital Video Broadcasting (DVB); Transmission System for Handheld Terminals (DVB-H)*, ETSI Std. EN 302 304 V1.1.1, November 2004.
- [3] C. Heuck and P. Unger, "Einflussfaktoren bei der Planung hybrider (DVB-H/UMTS)-Netze," in *ITG Fachbericht*, vol. 188, Dortmund, 2005, pp. 127–132.
- [4] P. Unger and T. Kürner, "Radio Network Planning of DVB-H/UMTS Hybrid Mobile Communication Networks," in *Proc. of 14th IST Mobile & Wireless Communication Summit*, Dresden, June 2005.
- [5] ICNIRP Guidelines, "Guidelines for limiting exposure to time-varying electric, magnetic and electromagnetic fields (up to 300 GHz)," *Health Physics*, vol. 74, no. 4, pp. 494–522, 1998.
- [6] L. Ferreira, L. M. Correia, D. Xavier, I. Vasconcelos, and E. R. Fledderus, "Final report on traffic estimation and services characterisation," IST-2000-28088 MOMENTUM, Tech. Rep. D1.4, 2003. [Online]. Available: <http://momentum.zib.de/paper/momentumd14.pdf>
- [7] T. Kürner and A. Meier, "Prediction of Outdoor and Outdoor-to-Indoor Coverage in Urban Areas at 1.8 GHz," *IEEE Journal on Selected Areas in Communications*, vol. 20, no. 3, pp. 496–506, April 2002.
- [8] H. Holma and A. Toskala, *WCDMA for UMTS - Radio Access For Third Generation Mobile Communications*, 3rd ed. John Wiley & Sons, 2005.
- [9] *Digital Video Broadcasting (DVB); Specification for the use of video and audio coding in DVB services delivered directly over IP*, ETSI Std. TS 102 005 V1.1.1, March 2005.
- [10] C. Heuck, "Analysis of the Performance of Hybrid (Broadcast/Mobile) Networks," in *Proc. of IEEE ISCE'04*, Reading, UK, September 2004.
- [11] J. Aaltonen, *Content Distribution Using Wireless Broadcast and Multicast Communication Networks*. Tampere University of Technology, 2003, Ph.D. thesis.

Application of Silicon Micromachining Techniques for the Manufacturing of New Passive THz-Components

Stephan Biber, Jan Schür, Lorenz-Peter Schmidt

University of Erlangen-Nuremberg, Institute for Microwave Technology, (LHFT)
Cauerstr. 9, 91058 Erlangen, Germany, Tel.: (+49)/9131/85-27223, Fax.: (+49)/9131/85-27212
stephan@lhft.de

Abstract—We present an overview on the application of silicon micromachining techniques to the fabrication of THz-components. Different machining techniques will be discussed with respect to their capability to generate complex 3-dimensional geometries and to meet the high mechanical tolerance requirements for THz-components. In order to demonstrate the potential of the technology, results for the application of micromachining techniques to the design of new THz-components will be discussed. Two different components such as a quasi-optical filter at 2.5 THz and a horn antenna at 600 GHz will be discussed exemplarily. We will emphasize the potential of silicon based micro-structures for the manufacturing of new devices.

I. INTRODUCTION

The development of new components such as quasi-optical devices or waveguide structures for THz-frequencies is mainly limited by the lack of suitable manufacturing techniques [1]. Wavelengths between 1mm and 50m place extremely high requirements against the manufacturing tolerances and make it difficult to design sophisticated components for THz-frequencies. On one hand conventional machining techniques based on milling, cutting and drilling suffer from comparatively poor tolerances and are limited by the minimum size of the machining tool. On the other hand the well developed structuring techniques used for micro-electronic and VLSI (very large scale integration) circuits, mainly based on photo-lithographical techniques, do not allow to generate 3D-structures with sizes up to several hundred microns as they are required in the THz-domain. The advent of silicon-based micromachining technologies driven by a strong economical demand for micro-electromechanical systems (MEMS) opens up new perspectives for the design of THz-circuits [2], [3]. The dimensions, shapes and aspect-ratios of the structures required for micromechanical sensors, microfluidic reactors and micro-optical systems are very similar to the geometries necessary to manufacture quasi-optical or waveguide components for frequencies between 0.3 and 5 THz. In section II of this paper a short introduction to the silicon micromachining technologies based on deep reactive ion etching (DRIE) and wet KOH-etching of silicon will be given. In section III we present two different exemplary components fabricated using these technologies in order to examine the new perspectives opened

up for THz circuit technology. The two different examples presented here are a quasi-optical bandpass filter based on a binary grating at 2.5 THz and an octagonal horn antenna for 600 GHz with waveguide interface.

II. SILICON MICROMACHINING TECHNOLOGIES

Silicon micromachining technologies have several advantages compared with conventional technologies. Firstly, the processes are mask based processes which allow to manufacture many similar devices simultaneously. This is not possible using traditional tool based technologies such as milling, drilling or electric discharge machining (EDM). Secondly the structures are defined by a photolithographic process which provides high repeatability and allows to define structures with an accuracy of approximately 1 μm . Several of these micromachining processes have also become increasingly interesting in the THz-community because of their potential to manufacture new components.

After photolithographically structuring a photoresist, the silicon areas which are not protected by the resist can be attacked using chemically dry or wet etching technologies. Anisotropic etching of silicon with KOH-solution generates complex geometrical structures due to the effect that the etching velocity strongly depends on the direction within the silicon crystal [4], [5]. KOH etches about 400 times faster along the $\langle 100 \rangle$ -direction than along the $\langle 111 \rangle$ -direction. Using silicon with different crystal orientation, this effect can be used to generate either oblique sidewalls with an angle of 54.7° for $\{100\}$ -wafers or vertical sidewalls for $\{110\}$. This is illustrated in Fig. 1. The geometric flexibility for generating structures using KOH-etching is strongly limited by the principal planes of the silicon crystal. Although it is possible to etch trenches in $\{110\}$ wafers using wet KOH-etching, it is not possible to generate intersecting trenches or trenches which are not parallel to each other. Therefore other processes, which are independent of the principal planes of the silicon crystal can be very useful. One of these processes is deep reactive ion etching (DRIE, "Bosch-process") of silicon [6]. Fig. 2 demonstrates how a DRIE-process can be used to

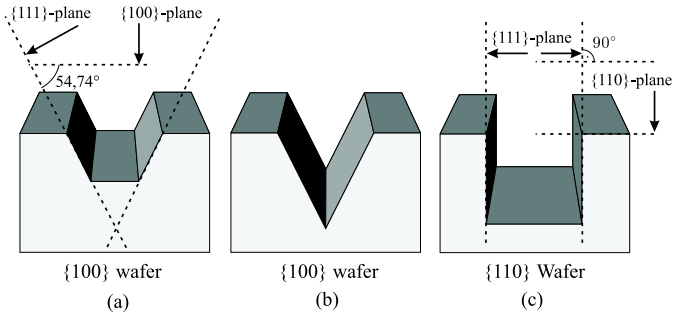


Fig. 1. (a-b) wet KOH-etching of $\{100\}$ wafers, (c) wet KOH-etching of $\{111\}$ wafers

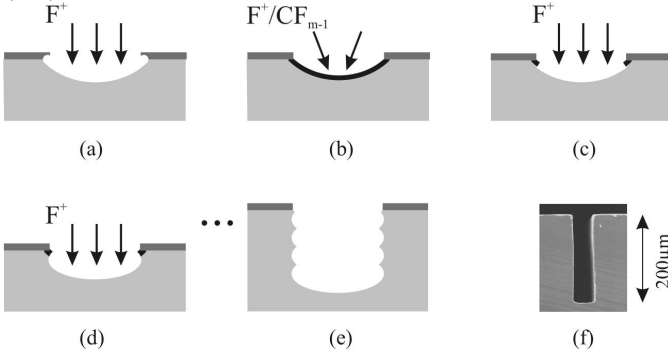


Fig. 2. Principle of DRIE-process. Fluorine radicals attack the silicon surface while a polymer layer, deposited in a subsequent process, protects the surface.

fabricate deep trenches with vertical sidewalls. consists of an etching and a passivation step. First, an etching step is applied to the patterned silicon substrate and the exposed silicon is etched in an almost isotropic manner (Fig. 2a). Second, the process switches to a polymerization step and a polymer layer is deposited on the exposed silicon surface (Fig. 2b). In the subsequent etching step, the polymer layer at the bottom of the structure is rapidly removed (Fig. 2c) by ion bombardment and the etching process continues to remove the exposed silicon (2d). Conversely, as shown in Fig. 2d, the polymer layer on the sidewall is consumed very slowly because of the strong spatial orientation of the ion bombardment, and therefore, protects the silicon on the sidewalls from being etched.

III. NEW PASSIVE THZ-COMPONENTS

With the technologies presented in section II, new quasi-optical and waveguide components for the THz-frequency domain can be machined. The presented binary grating was fabricated by deep reactive ion etching of silicon. The horn antenna was machined by DRIE- and KOH-etching of silicon. The example of the horn antenna demonstrates how complex geometries can be generated using a combination of different micromachining processes. These two examples were selected in order to demonstrate the potential of the micromachining processes for completely different circuit technologies and completely different component characteristics.

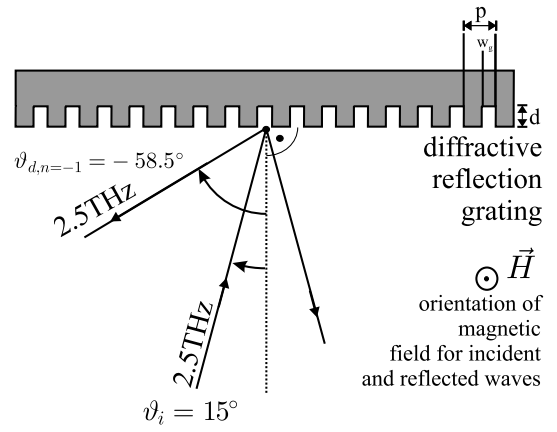


Fig. 3. Geometry of reflective binary grating as bandpass filter at 2.5 THz.

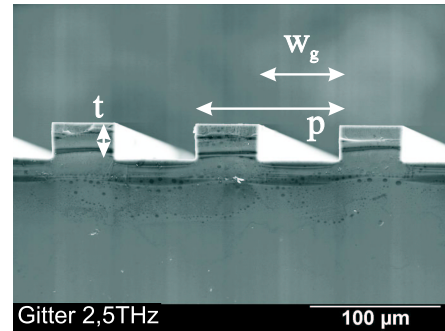


Fig. 4. SEM image of a cut through the grating machined by DRIE-etching of silicon.

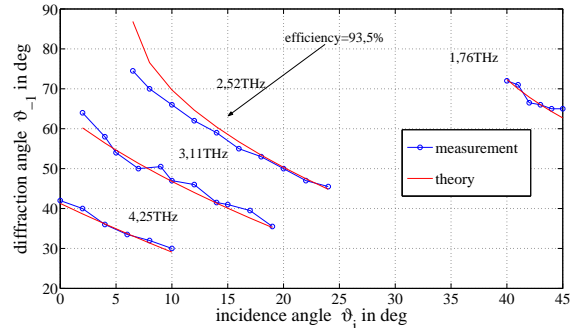


Fig. 5. Comparison of theory and measurement for the 2.5 THz grating

A. Binary Gratings as Quasi-optical Filters

In the optical domain, binary grating are widely used for spatial separation of different frequencies. The principle can also be applied to the submillimeter wave domain. We have machined a binary grating optimized for minimum passband insertion loss at 2.5 THz e.g. for harmonic separation in future frequency multipliers. The 2.5 THz beam, incident at an angle of $\vartheta_i=15^\circ$, is reflected into the -1st diffraction order at $\vartheta_m=-$

58.5° due to:

$$\sin(\vartheta_m) = \sin(\vartheta_i) - \frac{m\lambda_0}{p} \quad (1)$$

This was accomplished by machining a binary grating in silicon with a periodicity of $p = 107 \mu\text{m}$, a trench width $w_g = 56 \mu\text{m}$ and a trench depth of $t = 26 \mu\text{m}$. Fig. 3 shows a sketch of incident and the reflected beam. Fig. 4 shows a scanning electron microscope (SEM) image of a cut through the grating. In order to provide high electrical conductivity, the silicon grating was plated with gold. The overall size of the grating is 11x12 mm. A far infrared (FIR) laser, operating at 4 discrete frequency points was used to characterize the grating. It was found that the grating has an efficiency (which is the fraction of the power diffracted into the -1st diffraction order to the total incident power) of more than 93%. Fig. 5 shows a comparison between the theory (equation 1) and the measurements for the reflected beams at different incidence angles and frequencies. The good agreement between theory and measurement and the comparatively high efficiency demonstrate that this manufacturing technique was successfully applied to manufacture a quasioptical filter for spatial frequency separation in the submillimeter wave domain.

B. Octagonal Horn Antenna

While quasioptical circuit technology still dominates the frequency domain above 1 THz, waveguide components are becoming available for increasingly higher frequencies. As a transition between quasioptical circuits and waveguide circuits, horn antennas can be used. A critical parameter of these antennas is the coupling efficiency of the antenna with a fundamental mode Gaussian beam. Extending the findings of Hesler et al. [7], we present an approach how to manufacture a horn antenna with waveguide intersection purely based on silicon micromachining technologies.

The manufacturing process described in Fig. 6 shows the major steps for the production of the antenna and the necessary masking of the silicon structures. In step 1, a DRIE-process ("Bosch-process") is used to form one half of the waveguide and to form the antenna by opening the waveguide in the E -plane. The waveguides used for 600 GHz have dimensions of $a = 420 \mu\text{m}$ and $b = 210 \mu\text{m}$. Therefore an etching depth of $t_{DRIE} = a/2 = 210 \mu\text{m}$ is required. As such an antenna would be an E -sectoral horn antenna with a rather poor Gaussian coupling efficiency, an enhanced opening of the antenna aperture in the H -plane is required. This is accomplished in step 2 by using a KOH-etching process. The KOH-etching process is a wet etching process which allows strongly anisotropic etching of silicon crystals. With the 100-wafers used for this process, it is possible to use the 111-planes of the silicon crystal as etch-stop layers, because the etching rate in 111-direction is 400 times slower than it is in the 100-direction.

After the completion of the etching processes, the antennas are diced using a wafer-saw (Fig. 6c) and then coated with a

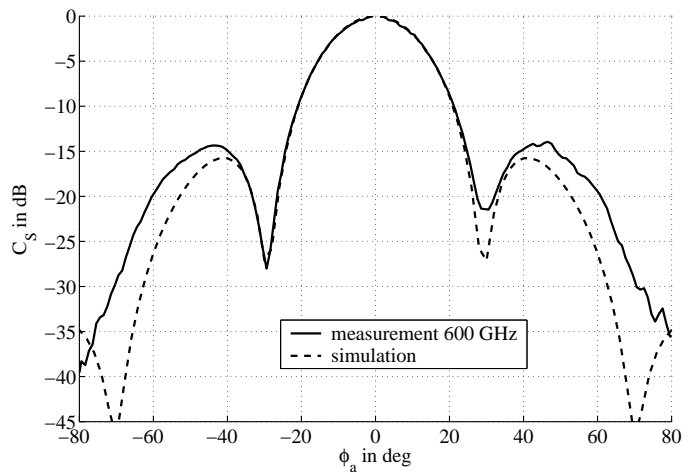


Fig. 7. Antenna pattern in the E -plane: Comparison of measurement results at 600 GHz with simulation results based on "Microwave Studio".

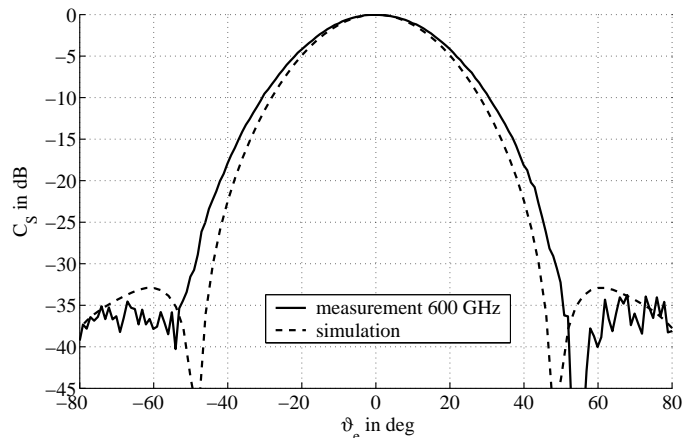


Fig. 8. Antenna pattern in the H -plane: Comparison of measurement results at 600 GHz with simulation results based on "Microwave Studio".

2 μm thick gold layer providing high electrical conductivity. In the final step 3 (Fig. 6d), the two split-block halves are assembled in a conventionally machined brass mount.

In order to characterize the antenna, which has a theoretically calculated coupling efficiency of 78%, the antenna pattern was measured in the E - and in the H -plane at a frequency of 600 GHz. Figs. 7 - 8 show these measurement results for the octagonal horn antenna. The agreement between theory and measurement is very good for the main beam in the E -plane. Although the measured main beam in the H -plane is slightly wider than the simulated main beam, a good agreement between theory and measurement was found. These findings demonstrate how complex geometries can be machined in silicon and how these structures can be applied to design and manufacture new THz-antennas.

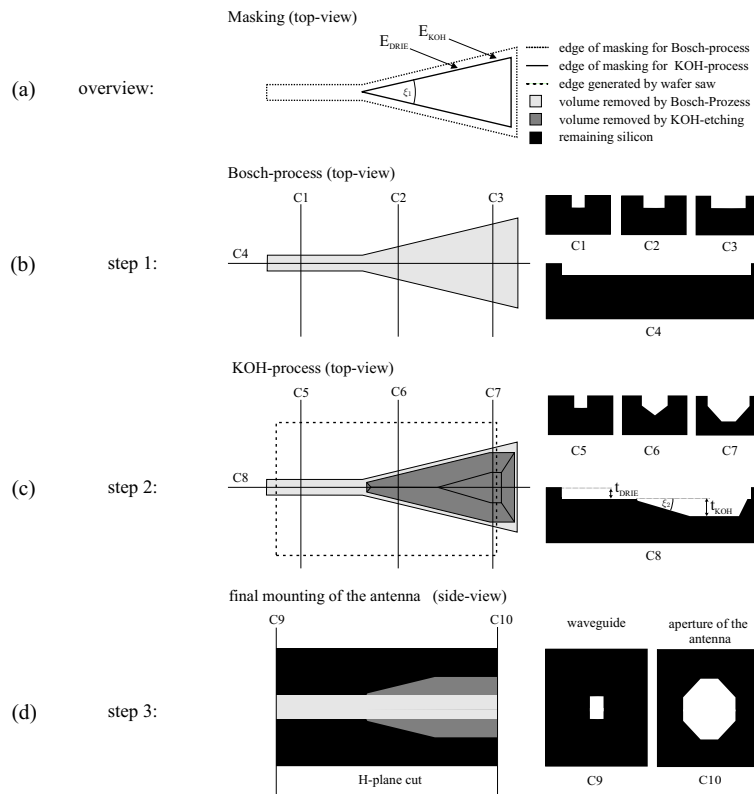


Fig. 6. Overview on the process. Left: top-view on the structures, right: respective cut-views (C1-C3, C5-C7, C9-C10) and (C4, C8).

IV. CONCLUSIONS AND OUTLOOK

Using two different examples for passive circuit components at THz-frequencies, it could be shown how silicon micromachining technologies can be used to solve the miniaturization problems. In the case of a binary grating as filter element, DRIE of silicon could be used to manufacture a reflective grating with an efficiency of 93% at a frequency of 2.5 THz. The manufacturing of significantly more complex geometries could be demonstrated exemplarily with an octagonal horn antenna. The antenna could be machined using a combination of DRIE and KOH etching. Its radiation pattern was verified experimentally and shows good agreement with the simulation.

With the tolerances of the silicon manufacturing technologies demonstrated above, new quasioptical devices up to approx. 5 THz and waveguide components and antennas up to approx. 3 THz can be manufactured. On wafers with 150 mm diameter, many components can be machined simultaneously. This allows not only cheap production of many components but - in the long run - also enables to efficiently manufacture new components such as antenna arrays or waveguide circuits for receiver and multiplier arrays. Complex waveguide circuitry, including couplers, filters etc. could be manufactured together with the feedhorns in the same, highly accurate, manufacturing process.

ACKNOWLEDGMENT

The authors would like to thank Axel Murk from the University of Bern for providing help with the submillimeter

wave measurement technology and for the numerous, fruitful discussions. Special thanks to Sven Berberich and Gudrun Rattmann from Fraunhofer Institute for Integrated Systems and Device Technology (IISB) in Erlangen for supporting the micromachining activities.

REFERENCES

- [1] S. Biber, J. Schür, A. Hofmann, and L.-P. Schmidt, "Design of new passive thz devices based on micromachining techniques," *Kharkov Symposium on Physics and Engineering of Microwaves, Millimeter and Submillimeter Waves, June 2004, Kharkov, Ukraine, 2004*.
- [2] C. Mann, "Fabrication technologies for terahertz waveguide," in *IEEE 6th international conference on terahertz electronics, Leeds*, pp. 46–49, 1998.
- [3] S. Biber, *Mikrostrukturierte Terahertz-Bauelemente auf Silizium-Basis*. Dissertation, University of Erlangen-Nuremberg, 2005.
- [4] E. Bassous, "Fabrication of novel three-dimensional microstructures by the anisotropic etching of (100) and (110) silicon," *IEEE Transactions on electron devices*, vol. 25, pp. 1178–1193, Oct. 1978.
- [5] M. Madou, *Fundamentals of Microfabrication - The Science of Miniaturization*, vol. ISBN 0-8493-0826-7. CRC Press, 2002.
- [6] F. Laermer and A. Schlip, "Method of anisotropically etching silicon," in *US Patent No. 5501893*.
- [7] J. L. Hesler, K. Hui, and T. Crowe, "Analysis of an octagonal micromachined horn antenna for submillimeter-wave applications," *IEEE Transactions on Antennas and Propagation*, vol. 49, pp. 997–1001, June 2001.

Dielectric Rod Waveguide Couplers as Harmonic Filters for Millimeter and Sub-Millimeter Wave Frequencies

A. Hofmann, M. Manglberger, S. Biber, J. Weinzierl, L.-P. Schmidt, H. Brand

University of Erlangen-Nuremberg (UEN), Institute for Microwave Engineering (Lehrstuhl für Hochfrequenztechnik, LHFT),
Cauerstr. 9, D-91058 Erlangen, Federal Republic of Germany
Tel. : ++49/(0)9131/85-27221
arnd@lhft.eei.uni-erlangen.de

Abstract—The paper describes the design and the realization of bandpass filters for suppression of harmonic frequencies based on coupled dielectric rod waveguides at 75 GHz, 300 GHz and 450 GHz [1]. The theoretical values determined by Marcattili’s method of approximation [2] were verified by broadband measurements on geometrically scaled coupler models at E-band frequencies. Afterwards, coupler filters were realized and experimentally characterized in the original frequency range at 300 GHz and 450 GHz. The filter setup was optimized with respect to low weight and compact dimensions for use on the mechanical field scanning unit of a modular vector field measurement system [3].

I. INTRODUCTION

A modular vector field measurement system (VFMS) for scanning spatially extended Gaussian beam fields at 150 GHz, 300 GHz and 450 GHz [3] was recently developed within the framework of a research project with contributions from the Technical Universities of Hamburg-Harburg and Darmstadt and from the University of Erlangen-Nuremberg called MEMSTIC (Multi Elements Multi Substrates Terahertz Integrated Circuits) [4]. The matter thereby is a novel quasi-optical circuitry for efficient power combining of multiple solid-state components at 150 GHz and its harmonics. These elements are arranged in two-dimensional arrays and solely connected by a spatially extended quasi-optical beam ([5],[6]). For controlling or optimizing the quasi-optical frequency multiplication, field measurements have to be done at the harmonics of interest. In this context, the presence of unwanted harmonics as well as the strong fundamental frequency has to be anticipated.

Consequently, bandpass filters at 300 GHz resp. 450 GHz to suppress the unwanted harmonics (in particular 450 GHz resp. 600 GHz) had to be developed and realized. Different concepts were evaluated. To integrate the harmonic filter on the mechanical field scanning unit of the vector field measurement system, the best suitable concept should fulfill the following requirements in equal measure:

- Low transmission losses in passband,
- high harmonic suppression in stopband (≥ 20 dB),

- required width of the passband $n \cdot (150 \text{ GHz} \pm 5) \text{ GHz}$, $n \in \{2,3\}$ (as a result of the maximum LO bandwidth),
- low weight of the filter setup as well as
- compact dimensions.

A combination of coupled dielectric rod waveguides (DWGs) and metal hollow waveguides was chosen as base for the harmonic filter. At frequencies lower than the passband, it reflects signals by the cutoff of the hollow waveguide. Moreover, the frequency-dependency of the dielectric coupler separates the higher harmonics. Though other investigated concepts like quasi-optical filters with a frequency selective surface on an (electrically) thick silicon substrate [7] also exhibit very good electrical properties, the coupler filter was preferred because of its low weight and the small filter setup. In addition, dielectric SMMW rod waveguides were used as main components of the VFMS anyway so the coupler filters do not cause any extra dielectric losses.

II. CALCULATION AND LAYOUT OF DIELECTRIC ROD WAVEGUIDE COUPLERS

A considerable part of the electromagnetic field is guided outside the (core) dielectric of the DWG which is also named "fiber" because of its tiny dimensions. Two parallel DWGs are therefore coupled, if the distance is low enough so that the electromagnetic wave is guided by both waveguides. This wave can formally be divided into two waves, namely the so-called even mode with the phase constant β_e and the so-called odd mode with the phase constant β_o . If β_e and β_o are different, a coupling length L_0 , the so-called zero-dB coupling length, exists as follows:

$$(\beta_e - \beta_o) \cdot L_0 = \pi. \quad (1)$$

This is illustrated by Fig. 1. The coupler is excited at port 1. After L_0 , there is a complete power transfer from one guide to the other because of destructive interference at guide 1 and constructive interference at guide 2.

As the power of the signal is concentrating more and more in

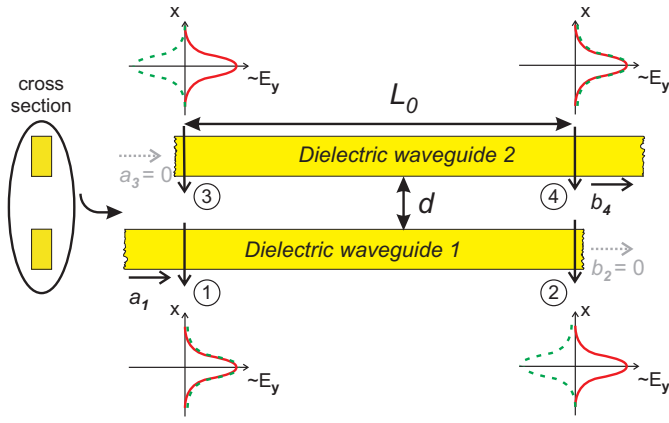


Fig. 1. Superposition of even and odd mode on coupled dielectric rod waveguides [8]; The distributions of the E-field (y-axis) are rotated by 90° for better presentability

the dielectric rod at increasing frequencies, L_0 is frequency-dependent. Its value increases strongly with the frequency.

Different parameters, like the axial propagation constant k_z (of a single DWG), have to be calculated numerically to determine the value of L_0 . We chose Marcattili's method of approximation [2] for this purpose as it is rather simple to implement (e.g. in MATLAB) at a sufficient accuracy.

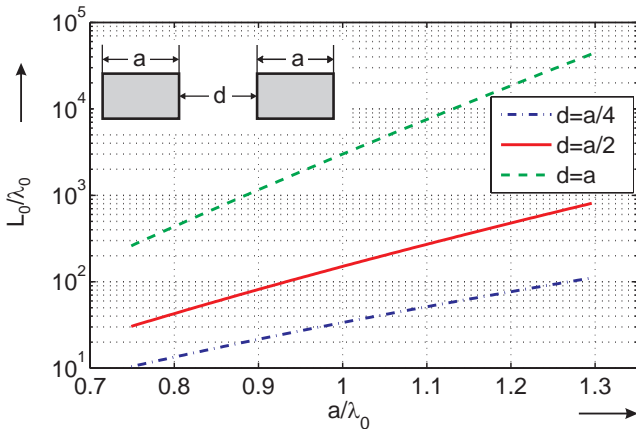


Fig. 2. L_0 in dependence on the width of the rod a for different distances d calculated by the method of Marcattili; L_0 and a are normalized to the wavelength λ_0

According to Fig. 1, the output power of the coupler at port 4, $P_4(l)$, can be specified as a function of the coupled waveguide length l as well as the input power $P_1(0)$ [9] :

$$P_4(l) = P_1(0) \cdot \sin^2 \left(\frac{\pi}{2} \cdot \frac{l}{L_0} \right). \quad (2)$$

This is exemplified in Fig. 3 by coupling signals with two different frequencies f_1 and f_2 ($f_1 < f_2$). The signal power alternates periodically between both guides. To achieve a coupling of 0 dB at f_1 , the belonging value of $L_0(f_1)$ is chosen as physical length of the coupler. At f_2 , only a small fraction of the signal is coupled from guide 1 to guide 2, as

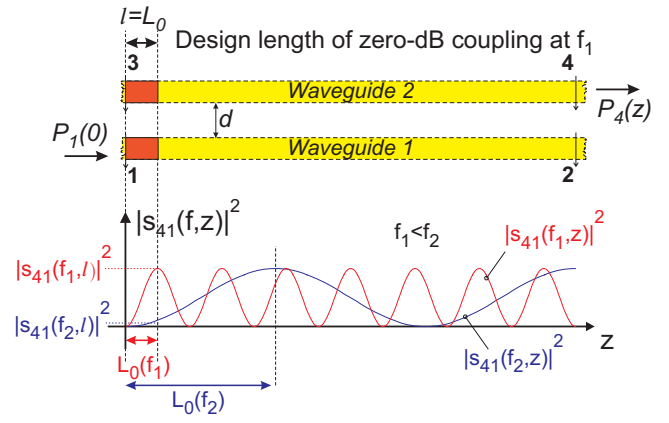


Fig. 3. Periodic frequency-dependent power transfer at coupled dielectric waveguides

$L_0(f_2) \gg L_0(f_1)$. The more f_1 and f_2 differ, the merrier is the filtering effect of the coupler.

By means of Eqn. (2), the theoretical insertion loss (without dielectric losses) was calculated for a filter based on a directional coupler with a passband at 150 GHz and harmonic suppression for $f \geq 300$ GHz. The appropriate dielectric fibers show the dimensions $a = 1.651$ mm and $b = 0.826$ mm. $L_0(f)$ was calculated for a distance between the fibers of $d = a/2$. The results are presented in Fig. 4. As L_0 is strictly increasing with the frequency, all higher harmonics are suppressed, contrary to filters based on resonant principles. Thereby, the stopband attenuation is also strictly increasing.

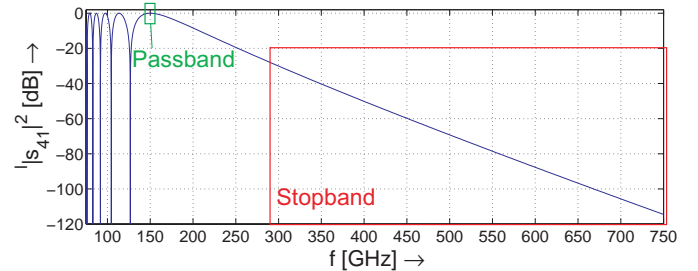


Fig. 4. Theoretical attenuation of a dielectric directional coupler according to Eqn. (2) for a 0 dB coupling at 150 GHz (without dielectric losses)

III. REALIZATION AND EXPERIMENTAL CHARACTERIZATION OF SCALED COUPLERS AT E-BAND FREQUENCIES

Beside the dimensioning of the couplers by theoretical calculations, an experimental optimization was performed at E-band frequencies (60–90 GHz).

The insertion loss was determined over frequency for different coupling lengths l at a fixed distance $d = a/2$ between the fibers, which was also used for the calculations before. The length with the lowest insertion loss was considered as "zero-dB coupling length". To extract the attenuation of the coupler, a continuous reference fiber was also measured in each case.

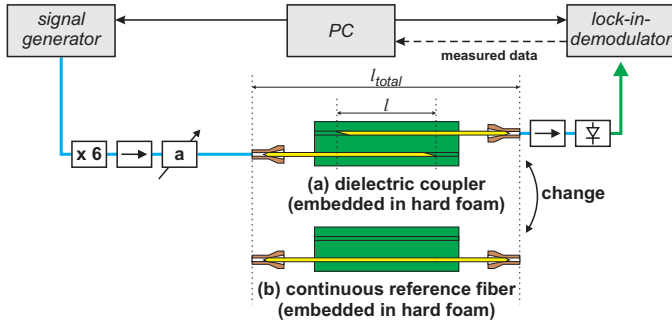


Fig. 5. Measurement setup of the scaled dielectric couplers at E-band frequencies (Fig. 5)

TABLE I
MEASURED AND CALCULATED ZERO-DB COUPLING LENGTH

f	L_0 calculated [mm]	L_0 measured (scaled) [mm]	ratio
300 GHz	64.9	59.4	1.09
450 GHz	37.1	34.9	1.06

Both the coupler and the reference fiber are embedded form-locking in hard foam (Styrodur[®] by BASF).

Former coupler configurations found in literature ([10]–[12]) separate the fibers outside the coupling zone by bends, which provides enough space to mount absorbers for attenuating unwanted harmonics remaining on the input fiber of the coupler. As the final filters are mounted directly on the field scanning unit, they are therefore exposed to mechanical stress. To avoid changes of the coupling length due to vibrations, our couplers are clamped by a cover also made from Styrodur. Consequently, bending the fibers is not possible. Instead of that the ends of the fibers were tapered and coated with glue, which acts as dielectric termination because of the high loss tangent of the glue (polar material). In addition, it is easier to fix the small fibers later at 300 GHz and 450 GHz in this way. Several test measurements proved that the glue does not cause any extra insertion loss despite the small distance between the coupled DWGs.

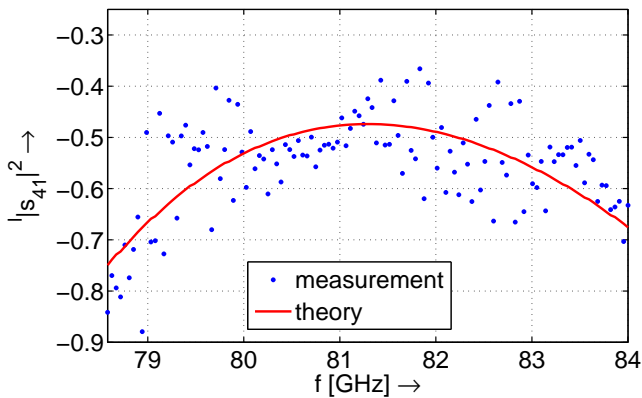


Fig. 6. Insertion loss (passband) of a scaled coupler for 450 ± 15 GHz at a measured center frequency of 81.3 GHz

The couplers were geometrically scaled to ensure an identical a/λ_0 (width of the dielectric fiber normalized to the wavelength), as the value of a/λ_0 is critical with respect to L_0 . The center frequency f_{scal} of the scaled passband (original frequency f_{orig}) can be determined by the widths a_{scaled} resp. a_{orig} of the belonging fibers as follows:

$$f_{scaled} = \frac{f_{orig} \cdot a_{scaled}}{a_{orig}}. \quad (3)$$

In Fig. 6, the insertion loss of a coupler with the passband at 450 GHz was measured at a scaled center frequency of 81.3 GHz ($450 \text{ GHz} \cdot 0.560 \text{ mm}/3.1 \text{ mm}$).

As the insertion loss of a scaled coupler at 300 GHz hardly differs from the results of the scaled coupler at 450 GHz, the results are not presented separately.

To prove the effectiveness of the filter at stopband frequencies, the E-band coupler has also been experimentally characterized at D-band frequencies (115–170 GHz).

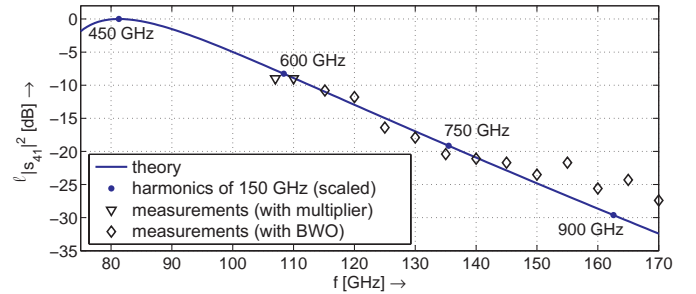


Fig. 7. Comparison between theoretical and measured stopband attenuation of the scaled coupler with a passband at 450 GHz

It can be seen from Fig. 7 that the stopband attenuation at 600 GHz of a single coupler at 450 GHz is only ≈ 7.5 dB because of the small frequency ratio of 4/3. To achieve a harmonic suppression of >20 dB, 3 couplers have to be cascaded. This is possible due to the low insertion loss and the broadband behavior of a single coupler (Fig. 6).

IV. REALIZATION AND EXPERIMENTAL CHARACTERIZATION OF HARMONIC FILTERS AT 300 GHz AND 450 GHz

The results of the theoretical calculations as well as the experimental characterization of the scaled coupler models can directly be transferred to the design and the realization of harmonic filters at 300 GHz resp. 450 GHz.

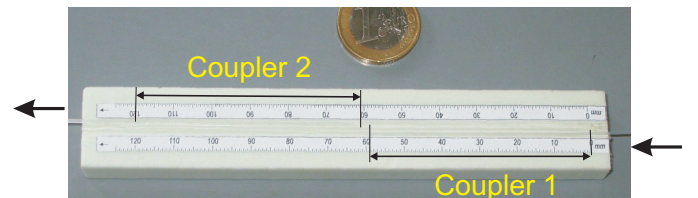


Fig. 8. Filter at 300 GHz consisting of 2 cascaded couplers embedded in Styrodur (cover not shown)

Fig. 8 shows a filter unit at 300 GHz consisting of 2 cascaded couplers embedded in Styrodur. The small grooves were milled on a conventional milling machine with a micro milling cutter. Tests with a microscope equipped with a precise length measuring system showed that the actual widths of the grooves only differ $\leq 10 \mu\text{m}$ from the required nominal width of $a=0.864 \mu\text{m}$ at 300 GHz resp. $a=0.560 \mu\text{m}$ at 450 GHz, which was easily compensable by fine-tuning the coupling length. An effect on the properties of the filter was practically not detectable.

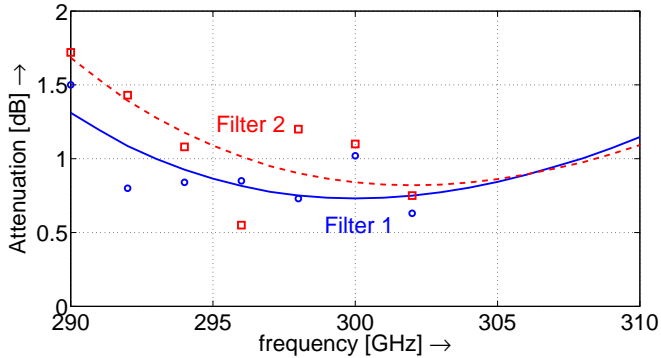


Fig. 9. Experimental characterization of the 2 harmonic filters at 300 GHz (2 cascaded couplers each) used with the VFMS (without dielectric losses)

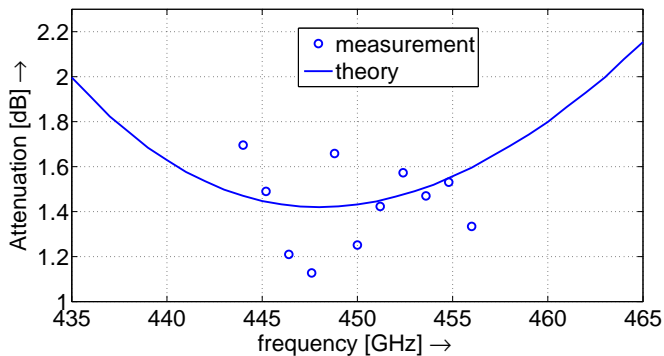


Fig. 10. Experimental characterization of a filter prototype at 450 GHz with 3 cascaded couplers (without dielectric losses)

TABLE II

TOTAL ATTENUATION OF THE CHARACTERIZED FILTERS AT 300 GHz AND 450 GHz INCLUDING DIELECTRIC LOSSES

Frequency [GHz]	Number of couplers	Passband attenuation [dB]
300	2	2.0 – 2.9
450	3	3.5 – 4.5

The measurement results at 300 GHz resp. 450 GHz are shown in Fig. 9 and Fig. 10. The maximum attenuation is < 2 dB at 300 GHz and < 2.5 dB compared to a continuous DWG of same length as the filter. The additional loss exhibits its maxima at both edges of the examined bandwidth and is < 1 dB. Furthermore, the realized filters at 300 GHz and

450 GHz show quite compact dimensions: 140 mm x 22 mm x 20 mm, and a very low weight of ≈ 30 g (filter without mount).

V. CONCLUSION

A combination of coupled dielectric rod waveguides and metal hollow waveguides was investigated as base for a band-pass filter for selecting desired harmonics of 150 GHz, namely 300 GHz or 450 GHz. The theoretical results determined by Marcatili's method of approximation were verified by broadband measurements on geometrically scaled coupler models at E-band frequencies. Afterwards, coupler filters were realized and experimentally characterized in the original frequency range at 300 GHz and 450 GHz. The filter setup was optimized with respect to low weight and compact dimensions for use on the mechanical field scanning unit of a modular vector field measurement system.

ACKNOWLEDGMENT

The authors would like to thank G. Bauer, L. Höpfel and J. Popp of the mechanical workshop of the UEN-LHFT for precisely fabricating the filter parts.

This work was supported by the German Research Society (DFG).

REFERENCES

- [1] A. Hofmann, E. Hörster, J. Weinzierl, L.-P. Schmidt, H. Brand, *Flexible Low-Loss Dielectric Waveguides for THz Frequencies with Transitions to Metal Waveguides*, Proceedings of 33rd EuMC, Munich, 2003, pp. 955–958.
- [2] E. A. J. Marcatili, *Dielectric Rectangular Waveguide and Directional Coupler for Integrated Optics*, The Bell System Technical Journal, vol. 48, Sept. 1969, pp. 2071–2103.
- [3] A. Hofmann, G. Seibert, M. Manglberger, A. Kalb, A. Göbel, J. Weinzierl, L.-P. Schmidt, H. Brand, *A Modular Vector Field Measurement System at 150 GHz, 300 GHz and 450 GHz*, Proceedings of the German Microwave Conference (GeMiC) 2005, Ulm, 2005, pp. 45–48.
- [4] H. Brand, J. Weinzierl, *MEMSTIC-Eine neue Schaltungstechnologie für den Submillimeterwellenlängenbereich*, Frequenz, vol. 54(3-4), 2000, pp. 106–111.
- [5] M. Shahabadi, K. Schünemann, *Millimeter-Wave Holographic Power Splitting/Combining*, IEEE Transactions on Microwave Theory and Techniques; vol. 45, no. 12; Dec. 1997, pp. 2316–2323.
- [6] M. Höft, *Spatial Power Divider/Combiner in D-Band*, IEEE Transactions on Microwave Theory and Techniques; vol. 52, no. 10; Oct. 2004, pp. 2379–2384.
- [7] S. Biber, O. Günther, M. Bozzi, L. Perregrini, B. M. Fischer, A. Hofmann, H. Jepsen, P. U. Helm, L.-P. Schmidt, *A Frequency Selective Surface for Harmonic Suppression in THz-Multipliers*, Proceedings of the German Microwave Conference (GeMiC) 2005, Ulm, 2005, pp. 132–135.
- [8] K. Herrmann, *Untersuchungen zum Submillimeterwellen-Empfang bei 600 GHz mit dem System Whisker-Antenne/Schottky-Diode*, PhD thesis LHFT-UEN, Erlangen, 1984.
- [9] E. Voges, *Directional Couplers with Rectangular Dielectric Waveguides*, AEÜ - Archiv für Elektronik und Übertragungstechnik, vol. 28, No. 11, Sep. 1974, pp.478–479.
- [10] J. A. Paul, Y.-W. Chang, *Millimeter-Wave Image-Guide Integrated Passive Devices*, IEEE Transactions on Microwave Theory and Techniques; vol. 26, no. 10; Oct. 1978, pp. 751–754.
- [11] K. Solbach, *The Calculation and the Measurement of the Coupling Properties of Dielectric Image Lines of Rectangular Cross Section*, IEEE Transactions on Microwave Theory and Techniques, vol. 27, no. 1; Jan. 1979, pp. 54–58.
- [12] S. Bhooshan, R. Mittra, *Multimode Waveguide Components for Millimeter-Wave Integrated Circuits*, AEÜ - Archiv für Elektronik und Übertragungstechnik, vol. 34, No. 1, Jan. 1980, pp.27–29.

A Survey Study on Some Symptoms and Sensations Occurred in Eyes Caused by Daily Talking Durations of Mobile Phones

H. H. BALIK^{1*}, K. BALIKCI², A. AKBAL³, I. C OZCAN⁴, D. TURGUT-BALIK⁵ and Z. GENÇ⁶

¹University of Firat, Dept. of Electrical and Electronics Eng. Elazig, Turkey, Tel:+904242410099,E-mail: hasanbalik@gmail.com

²University of Firat, Dept. of Informatics, Elazig, Turkey, Tel:+904242370000, Email: kbalikci@firat.edu.tr

³University of Firat,Dept. of Electrical and Electronics Eng. Elazig, Turkey, Tel:+904242370000,E-mail: ayhanakbal@gmail.com

⁴University of Firat, University Health Center, Elazig, Turkey, Tel:+904242370000,E-mail: icozcan@firat.edu.tr

⁵University of Firat, Dept. Biology, Elazig, Turkey, Tel:+904242370000,E-mail: dilekbalik@gmail.com

⁶University of Firat, Dept. of Informatics, Elazig, Turkey, Tel:+904242370000, Email: zulfugenc@hotmail.com

* Corresponding Author

Short Abstract— A survey study was conducted to investigate the possible effects of daily talking duration of mobile phone on eye related symptoms and sensations. These are obscuration of vision, redness on the eyes, vision disorders, crust round the eyes, inflammation in the eyes and water round the eyes. There is no effect on redness on the eyes and vision disorders, but some statistical evidences are found that mobile phone may cause obscuration of vision, crust round the eyes, inflammation in the eyes and water round the eyes.

Keywords-component; eye, mobile phones, daily talking duration, Biological Effects, Microwaves

I. INTRODUCTION

In the recent few years, the extensive use of mobile phones (MP) raises the question of possible health effects of the radio-frequency electromagnetic fields emitted by these phones. Mobile phones operate on wireless technology, with communication typically occurring via a 900-1800 MHz signal that is pulsed at 217 Hz. This signal carries essentially no power when the user is not talking or receiving, but when the user communicates the power of this pulsed electromagnetic field reaches a maximum of 250 mW (Croft *et al.*, 2002).

The effects of electromagnetic fields on biological systems have been extensively investigated over the last years (Gos *et al.*, 2000; Jech *et al.*, 2002; Braune *et al.*, 2002; Cook *et al.*, 2002). Particular attention has been given to the effects of microwave exposure on the central nervous system (Herman *et al.*, 1997; Croft *et al.*, 2002; Mause *et al.*, 2001; Beason *et al.*, 2002; Hossmann *et al.*, 2003) because of their use in close vicinity to the human brain. Unfortunately there are neither experimental nor survey studies concerning eye related symptoms caused by use of mobile phone found in the literature. In the literature only two survey studies carried out by the researchers about some other symptoms and sensations are found.

In the first survey study, some biological effects of mobile phones on people living or not in vicinity of mobile phone base station were tested in 530 people (Santini *et al.*, 2002 a). In the study, non specific health symptoms such as tiredness, headache, sleep disturbance, discomfort, dizziness, irritability, depression, lose of memory, etc. were detected depending on distance from base station and sex. It was suggested that minimal distance of people from mobile phone base stations should not be < 300 m in view of radioprotection.

One another survey study was conducted in 161 students and workers in a French engineering school on symptoms experienced during use of digital cellular phones (Santini *et al.*, 2002 b). According to the results, concentration difficulties, sleep disturbance, discomfort, warmth, and pricking of the ear during phone conversation as a function of calling duration per day and number of calls per day were experienced.

The main goal of this study in which a survey study, using questionnaire, was conducted in 695 people living in a city in Turkey, where these phones are extensively used, to detect the possible optical symptoms experienced by the users of mobile phones as well as by daily talking durations in order to light the way of further studies. The investigated eye symptoms are obscuration of vision, redness on the eyes, vision disorders, crust round the eyes, inflammation in the eyes and water round the eyes.

II. MATERIAL AND METHODS

A. Questionnaire

Questionnaire used in this study was composed of two sections. In the first section, general questions were asked to individuals to learn about their general health, use of mobile phone and physical environment to prevent miss leading positives. In the second section questions were asked to directly detect the effects of long term use of mobile phone on each individual's health.

In the survey, questions were asked to investigate the following symptoms and sensations; obscuration of vision,

redness on the eyes, vision disorders, crust round the eyes, inflammation in the eyes and water round the eyes.

If an individual gave positive answer to the questions about any above symptoms and sensations, some extra questions were also asked to detect the beginning of the symptoms and sensations. Otherwise the statistical results yielded would be meaningless, unless person has not the symptoms and sensations after he has started to use mobile phone.

B. Study Population

The study group was consist of 193 female and 503 male randomly selected from different ages, educations, earnings, locations and occupations in Elazig which is located in the east part of Turkey. Total number of attendant was 695. For simplicity, from now the person who has got a mobile phone and the person who has not got any mobile phone will be named as “mobile phone user” and “non-mobile phone user” respectively.

Among female, 157 women were mobile phone users whereas 36 were non-mobile phone users. 502 male attendants were consisting of 392 mobile phone users and 110 non-mobile phone users. These are summarized in Table 1.

Usage	Female	Male	Total
Mobile Phone Users	157 (81.3%)	392 (78.1%)	549 (79.0%)
Non-Mobile Phone Users	36 (18.7%)	110 (21.9%)	146 (21.0%)

Table 1: Number of people attended to the survey

As clearly seen in Table 1, although individuals were selected randomly around 80% of people were mobile phone users. This shows that mobile phone usage is very much common in the selected region and the results yielded from the survey could be valuable.

Since the aim of this survey is to investigate the possible eye symptoms and sensations experienced by daily talking durations, attendants were grouped according to daily total time of talking. Daily talking durations were divided into three sub-groups. These are 1 to 10 minutes, 10 to 20 minutes, 20 to 60 minutes respectively. Table 2 shows these intervals.

Daily Talking Duration	Female	Male	Total
1-10 min.	111 (71.2%)	306 (70.5%)	417 (70.7%)
10-20 min.	22 (14.1%)	97 (22.4%)	119 (20.2%)
20-60 min	23 (14.7%)	31 (7.1%)	54 (9.2%)

Table 2: Talking durations committed in a day

Table 2 showed that more than 70% of both female and male uses their mobile phone at least 10 min. every day.

C. Statistical Analysis

For this survey, an analysis of variance (ANOVA) were used and differences were considered significant at $P < 0.05$.

III. RESULTS

As mentioned in Section 2.A, some extra questions were also asked to detect the starting time of the symptoms and sensations. The answers were sorted and written in Table 3.

Symptoms and Sensations	Time	
	After Mobile Phone	Before Mobile Phone
Obscuration of vision	268 (68.3%)	122 (31.3%)
Redness on the eyes	74 (66.7%)	37 (33.3%)
Vision disorders	67 (57.8%)	49 (42.2%)
Crust round the eyes	24 (64.9%)	13 (35.1)
Inflammation in the eyes	76 (66.7%)	38 (33.3%)
Water round the eyes	67 (63.2%)	39 (36.8%)

Table 3: Starting time of the symptoms and sensations

When Table 3 were analyzed closely, majority of the mobile phone users reported that they had the symptoms and sensations after they had started using the cellular phone. With Table 3, statistical results found in this contribution should be taken into account.

Since analysis of variance (ANOVA) was used to analyze data, P -values of each symptom and sensation were given in Table 4. The first column of the table shows the considered symptoms and sensations. In the second column, P -values were calculated and written for mobile phone users and non-mobile phone users. For this column P -values of 4 out of 6 found to be meaningful. These symptoms and sensations are obscuration of vision, crust round the eyes, inflammation in the eyes and water round the eyes.

Symptoms and Sensations	Mobile Phone user & non-user	How long they use the phone
Obscuration of vision	0,000	0,000
Redness on the eyes	0,110	0,280
Vision disorders	0,149	0,445
Crust round the eyes	0,031	0,047
Inflammation in the eyes	0,034	0,203
Water round the eyes	0,031	0,164

Table 4: P -values (*: $p < 005$) for ANOVA

In the last column of Table 4, daily talking durations that individuals committed by the mobile phone were taken into account. For this case 2 out of 6 values of symptoms and

sensations which were obscuration of vision and crust round the eyes were found to be meaningful.

The main goal of this survey is to investigate the optical effects of mobile phone for total daily duration. As seen in Table 4, there are 6 eye related symptoms and sensations were investigated. Results were summarized including number of people attended to each case in Table 5 and their percentages were given in Table 6. The statistical results found here as follows;

Obscuration of Vision: According to the results given in Table 5 and 6, the use of mobile phone may cause obscuration of vision, because the percentages of having obscuration of vision were increased from 52.7% to %71.0. Moreover there was statistical evidence that the percentages were increased for long daily talking durations. Because the percentages of 1-10 min, of 10-20 min. and of 20-60 min. were 68.6%, 74.0% and 85.5% respectively.

Redness on the Eyes and Vision Disorders: As a result of Tables 3, 5 and 6, the use of mobile phone had no visible effects on any of the above symptoms and sensations.

Crust Round the Eyes : Our data showed an indication of causing crust round the eyes, this is why the percentages of having crust round the eyes were increased from 2.1% to 6.7% Moreover talking mobile phone for a long period in a day may increase the possibility of having crust round the eyes too. This was because the percentages increased from 5.8% to 9.1% when the survey attendants talk 10 min more in a day.

Inflammation in the Eyes: As a result of Table 5 and 6, the use of mobile phone may cause inflammation in the eyes. This is why the percentages of possibility of having increase inflammation in the eyes were increased from 13.0% to %20.8. But there were no statistical evidence that the percentages were increased for long talking duration. This was because total number of people, who users mobile phone, were almost equal to people who had were using mobile phone for 1-10 min. in a day. These percentages were 20.8% and 20.9% respectively.

Water Round the Eyes: According to data, the use of mobile phone may cause water round the eyes because the percentages were increased from 11.6% to %19.3. But there were no statistical evidence that for longer duration usage increases the possibility of having water round the eyes.

IV. DISCUSSION

As result of the survey, there were no evidence that the use of mobile phone may cause redness on the eyes and vision disorders. Unfortunately there are nothing available in the

literature for the above symptoms and sensations to compare with.

The use of mobile phone may cause obscuration of vision and crust round the eyes as results of our data. In addition talking with mobile phone for longer period in a day may increase possibility of having above symptoms and sensations. Again no published date was available in the literature for obscuration of vision and crust round the eyes as well.

Finally there were some evidence that the use of mobile phone may trigger inflammation in the eyes and water round the eyes. Likely no evidence that the more the mobile phone users talk the more they get the above two symptoms were available. No published journals concerning above two symptoms are available either.

REFERENCES

The template will number citations consecutively within brackets [1]. The sentence punctuation follows the bracket [2]. Refer simply to the reference number, as in [3]—do not use “Ref. [3]” or “reference [3]” except at the beginning of a sentence: “Reference [3] was the first . . .”

Number footnotes separately in superscripts. Place the actual footnote at the bottom of the column in which it was cited. Do not put footnotes in the reference list. Use letters for table footnotes.

Unless there are six authors or more give all authors' names; do not use “et al.”. Papers that have not been published, even if they have been submitted for publication, should be cited as “unpublished” [4]. Papers that have been accepted for publication should be cited as “in press” [5]. Capitalize only the first word in a paper title, except for proper nouns and element symbols.

For papers published in translation journals, please give the English citation first, followed by the original foreign-language citation [6].

- [1] G. Eason, B. Noble, and I. N. Sneddon, “On certain integrals of Lipschitz-Hankel type involving products of Bessel functions,” *Phil. Trans. Roy. Soc. London*, vol. A247, pp. 529–551, April 1955. (*references*)
- [2] J. Clerk Maxwell, *A Treatise on Electricity and Magnetism*, 3rd ed., vol. 2. Oxford: Clarendon, 1892, pp.68–73.
- [3] I. S. Jacobs and C. P. Bean, “Fine particles, thin films and exchange anisotropy,” in *Magnetism*, vol. III, G. T. Rado and H. Suhl, Eds. New York: Academic, 1963, pp. 271–350.
- [4] K. Elissa, “Title of paper if known,” unpublished.
- [5] R. Nicole, “Title of paper with only first word capitalized,” *J. Name Stand. Abbrev.*, in press.
- [6] Y. Yorozu, M. Hirano, K. Oka, and Y. Tagawa, “Electron spectroscopy studies on magneto-optical media and plastic substrate interface,” *IEEE Transl. J. Magn. Japan*, vol. 2, pp. 740–741, August 1987 [Digests 9th Annual Conf. Magnetics Japan, p. 301, 1982].
- [7] M. Young, *The Technical Writer's Handbook*. Mill Valley, CA: University Science, 1989.

Symptoms and Sensations	Non-Mobile Phone Users		Mobile Phone Users							
	Total		Durations						Total	
			1-10 min.		10-20 min.		20-60 min.			
	YES	NO	YES	NO	YES	NO	YES	NO	YES	NO
Obscuration of vision	77	69	286	131	57	20	47	8	390	159
Redness on the eyes	21	125	87	330	12	65	12	43	111	438
Vision disorders	23	123	91	326	14	63	11	44	116	433
Crust round the eyes	3	143	24	393	7	70	6	49	37	512
Inflammation in the eyes	19	127	87	330	15	62	12	43	114	435
Water round the eyes	17	129	78	339	16	61	12	43	106	443

Table 5: Distribution of people attended to the survey for symptoms and sensation

Symptoms and Sensations	Non-Mobile Phone Users		Mobile Phone Users							
	Total		Durations						Total	
			1-10 min.		10-20 min.		20-60 min.			
	YES	NO	YES	NO	YES	NO	YES	NO	YES	NO
Obscuration of vision	52,7	47,3	68,6	31,4	74,0	26,0	85,5	14,5	71,0	29,0
Redness on the eyes	14,4	85,6	20,9	79,1	15,6	84,4	21,8	78,2	20,2	79,8
Vision disorders	15,8	84,2	21,8	78,2	18,2	81,8	20,0	80,0	21,1	78,9
Crust round the eyes	2,1	97,9	5,8	94,2	9,1	90,9	10,9	89,1	6,7	93,3
Inflammation in the eyes	13,0	87,0	20,9	79,1	19,5	80,5	21,8	78,2	20,8	79,2
Water round the eyes	11,6	88,4	18,7	81,3	20,8	79,2	21,8	78,2	19,3	80,7

Table 6: Distribution of people attended to the survey for symptoms and sensations in percentages

Highly Efficient Slotted Waveguide Feeding Systems for 2.45 GHz Industrial Applicators

Sebastijan Stanculovic¹, Lambert Feher¹ and Manfred Thumm^{1,2}

¹Research Center Karlsruhe, Institute for Pulsed Power and Microwave Technology, IHM, P.O. Box 3640, D-76021 Karlsruhe, Germany, +497247823555, sebastijan.stanculovic@ihm.fzk.de

²University of Karlsruhe, Institute for Highfrequency Techniques and Electronics, IHE, Kaiserstrasse 12, D-76128 Karlsruhe, Germany

Short Abstract—Nonresonant slotted waveguides with two different polarizations have been designed as feeding systems for 2.45 GHz microwave applicators. Very good power coupling efficiency of manufactured slotted waveguide antennas was confirmed by measurements. Numerical calculations and preliminary near field measurements have proved a desired homogeneous radiation along the slotted waveguides.

Nonresonant slotted waveguides; feeding systems; microwave applicators; power efficiency; uniform radiation

I. INTRODUCTION

The strong requirements for highly efficient and low cost feeding systems, which transfer the microwave (MW) energy from the power source (magnetron) into the industrial microwave applicator, are defined as follows:

- total power transfer (minimized reflections inside the feeding system, $P_{\text{ref}} \approx 0$, see Fig. 1),
- support of an appropriate electromagnetic (EM) field distribution inside the microwave applicator (constant EM energy irradiation along the feed),
- very low level of cross coupling between the neighbouring feeding parts in multi-sources fed microwave applicators ($P_{\text{cc}} \approx 0$, see Fig. 1), and
- direct coupling of the microwave sources into the feeding systems (avoiding high cost microwave components, like tuners, isolators or circulators, as well as cooling devices).

Slotted waveguide (SW) radiators are a promising choice according the requirements, because they offer many parameters for the optimization of a MW heating system. By proper optimization of the slots in directly coupled rectangular aluminium waveguides, one can improve the power coupling efficiency of the microwave system, tune the desired EM field distribution inside the MW applicator and decrease the system costs for standard components (Fig. 1).

At the Research Center Karlsruhe (FZK), Germany, different types of slotted waveguides have been investigated, manufactured and measured at the ISM frequency 2.45 GHz, allocated for Industrial, Scientific and Medical applications[1].

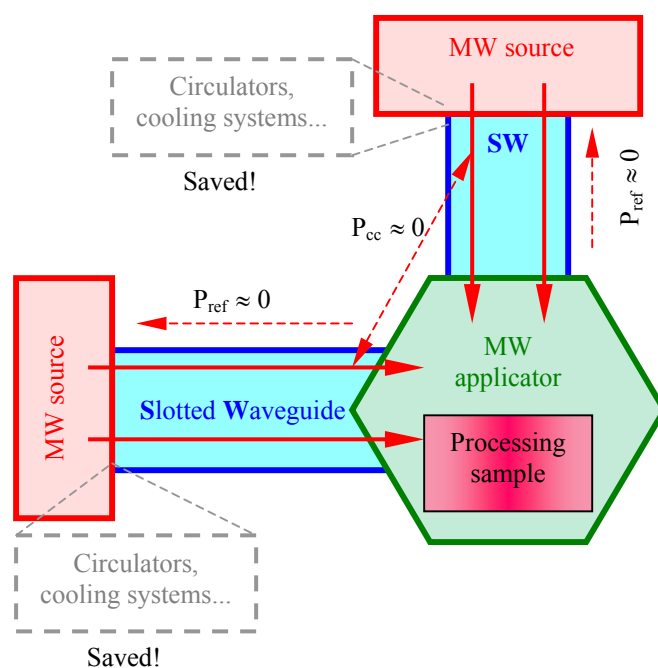


Figure 1. Schematic of microwave heating system with directly coupled highly efficient and low cost slotted waveguide feeds

They are used as feeding parts for an industrial microwave heating system named HEPHAISTOS (**H**igh **E**lectromagnetic **P**ower **H**eating **A**utoclaveless **I**njected **S**tructures **O**ven **S**ystem), that has been developed at FZK for automated processing of carbon fibre reinforced plastics [2,3].

In this paper new results for the design of nonresonant SW antennas with two different polarizations - vertical and horizontal in respect to the waveguide axis, are presented. First, the calculations of longitudinal and transversal slot parameters are explained in more details. For estimation of some important slot parameters, numerical calculations are done using the CST Microwave Studio software. EM fields in the slotted waveguides are also numerically obtained. A description and results of the experimental verification measurements are presented and discussed.

II. DESIGN OF NONRESONANT SLOTTED WAVEGUIDES

A. Vertically polarized slotted waveguides

To avoid a standing wave inside the waveguide (to minimize the reflections), nonresonant travelling wave SWs are chosen for the energy feeding parts, instead of resonant standing wave SWs, which are recommended in the literature for this application [4]. In a resonant SW some part of the MW energy is always captured in an oscillating standing wave inside the SW and can not be transferred into the MW applicator. Further, in resonant SWs the positions of the slots along the waveguide are already given by definition and this parameter can not be used in an optimization procedure of the antenna radiation pattern.

In the proposed nonresonant SWs the slots are equally spaced in a distance d (Fig. 2), which is shorter than the $\lambda_g/2$ resonant one ($\lambda_g = 0.174$ m is the wavelength in the waveguide at 2.45 GHz for given inner transversal dimensions of the WR340 standard).

The calculations of slot offsets from the central line of the broad SW wall were done using a linearization of the exponential attenuation function of the fundamental waveguide TE_{10} mode travelling in z direction along the SW. Further, a condition that all slots should radiate equally should be satisfied by the design, as well as the following input matching condition [4]:

$$g_{in} = 1, \quad (1)$$

where g_{in} is the input normalized conductance at the first slot in the equivalent circuit.

The calculated slot offsets are increasing from slot to slot in the direction of wave propagation (z direction) inside the waveguide. This is in agreement with the fact that an increasing slot conductance should compensate the attenuation of the travelling fundamental TE_{10} mode in the waveguide. So, they radiate constantly giving a homogeneous radiation along the SW. All longitudinal slot lengths are equal to $\lambda/2$ (resonant length), where $\lambda = 0.122$ m is the wavelength in the free space at 2.45 GHz. The slots are narrow with a constant width.

B. Horizontally polarized slotted waveguides

For the horizontally polarized slotted waveguide the input matching condition is:

$$r_{in} = 1, \quad (2)$$

where r_{in} is the input normalized resistance at the first transversal slot in the equivalent circuit. Calculated slot lengths are shorter than the $\lambda/2$ and they differ from slot to slot.

The desired uniform radiation is achieved using an optimization method, similar as for the diffraction gratings

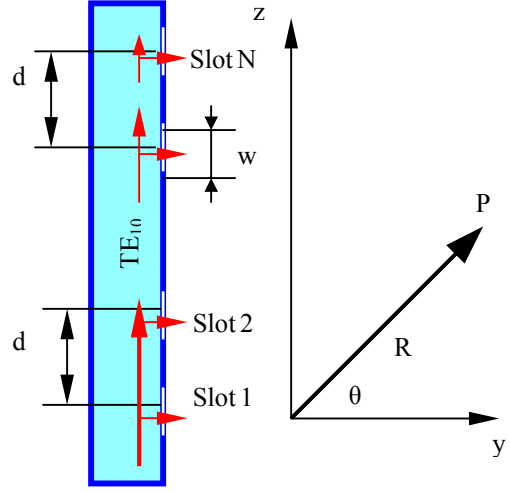


Figure 2. Calculation of the total E field in a far point P

in optics. The electric (E) field, irradiated from the i -th slot, in the far field point P can be determined as [5]:

$$E_{i,P} = \frac{1}{R} \int_{(i-1)d-\frac{w}{2}}^{(i-1)d+\frac{w}{2}} A_i \sin(\omega t - kR + kz \sin \theta - \beta z) dz, \quad (3)$$

where $i = 1, \dots, N$, then R is a distance from the center of the first slot to the point P, w is a slot width (small and constant), A_i is amplitude of the i -th slot E field, k is a phase constant in the free space and β is a phase constant in the waveguide for the TE_{10} fundamental mode. The total field in the point P is a sum of all radiated fields from the slots:

$$E_{tot,P} = \sum_{i=1}^N E_{i,P} \quad (4)$$

and it is a function of the angle θ between the y axis (normal to the slot plane) and the direction of R (see Fig. 2). By determination of an appropriate set of amplitudes A_i , a relatively uniform distribution for the total field and a desired radiation pattern of the SW antenna can be achieved in the full θ angle range. Determination of the slot field amplitudes A_i leads to the calculation of normalized slot resistances and to estimation of slot lengths.

Numerical simulations of the entire slotted waveguides radiating into the free space are performed using the CST Microwave Studio program. The S_{11} parameter (reflections) of both SW types and the EM fields are calculated. These results are used as an input for an additional experimental optimization procedure.

III. MEASUREMENTS

Experimental measurements for the verification of the design and the final optimization of the SW radiators have been

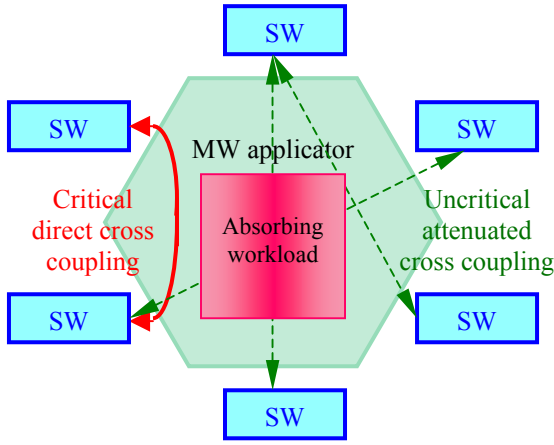


Figure 3. Cross coupling in the multi-sources fed MW applicator

performed using a Vector Network Analyzer (VNA), i.e. the manufactured SW antennas have been measured at a low power level.

The measurements have been performed for the case that SW antennas radiate into the free space and for the case that they radiate into the loaded HEPHAISTOS applicator. With the VNA the S_{11} parameter (reflections) inside the optimized SW is obtained.

Further, the critical direct cross coupling (S_{12} parameter) between neighbouring SW feeds with same polarization and with two different polarizations has been measured in the water loaded cavity (red in Fig. 3). The cross coupling between the not neighbouring SW feeds in the microwave applicator (green in Fig. 3) is at much lower uncritical levels in comparison to neighbouring slotted waveguides, because of the presence of the absorbing workload.

The near fields of the SW radiators have been measured, to verify the radiation homogeneity along the feeding element. In the free space at a distance of 1m from the slots plane, the E field was measured in 20 equidistant points along the line parallel to the waveguide axis.

IV. RESULTS

In Fig. 4. the numerically calculated distribution of the amplitude of the dominant E_x field component in the xz plane (parallel to the slots plane) at a distance of λ (free space wavelength) from the vertically polarized SW is presented. This near field calculation shows that the slots radiate relatively uniform and the vertically polarized SW feed should support a homogeneous EM distribution in the MW applicator.

For the SW radiator with horizontal polarization the amplitude distribution of the dominant E_z field component in the xz plane λ away from the slots is presented in Fig. 5. There is no critical large difference in the slot field amplitudes along the SW (z direction).

The numerically obtained 3-D far field patterns for the vertically and for the horizontally polarized SW antennas are

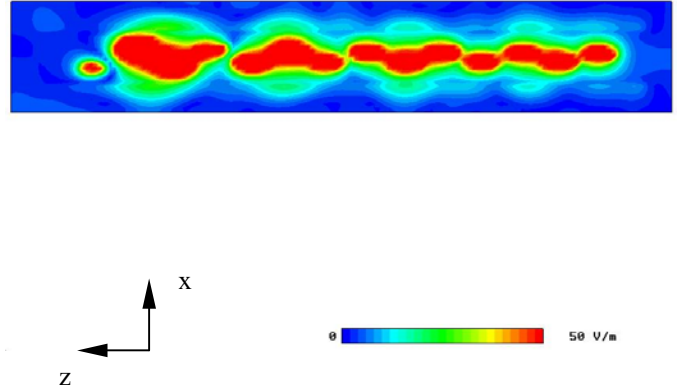


Figure 4. $|E_x|$ field distribution, λ away from the vertically polarized SW

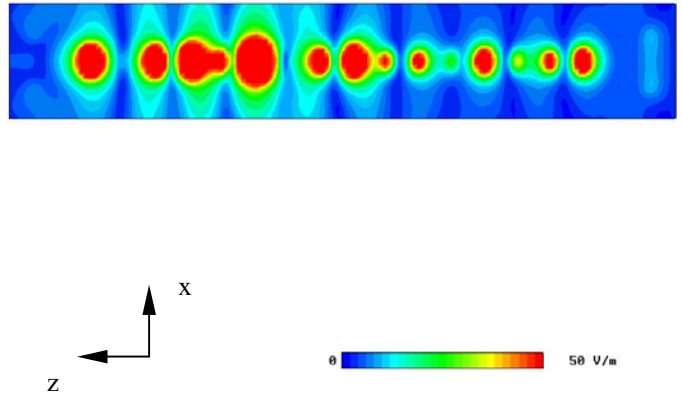


Figure 5. $|E_z|$ field distribution, λ away from the horizontally polarized SW

shown in Fig. 6 and Fig. 7, respectively. The SW axis is parallel to the z direction, the coordinate origin is at the middle point of the SWs and the slots plane is parallel to the xz plane. The relative good uniformity of the far field patterns can be seen in the zy plane for both SW types.

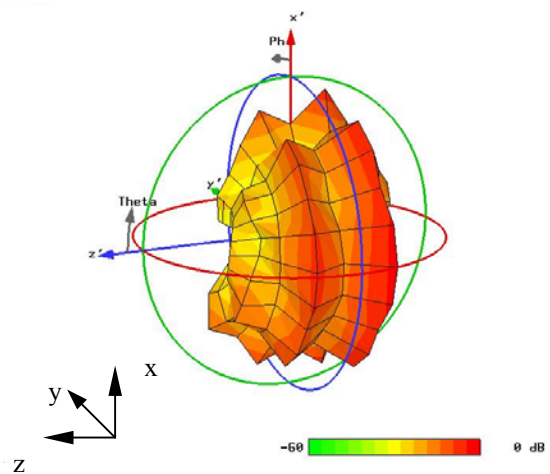


Figure 6. Far field pattern of the vertically polarized SW

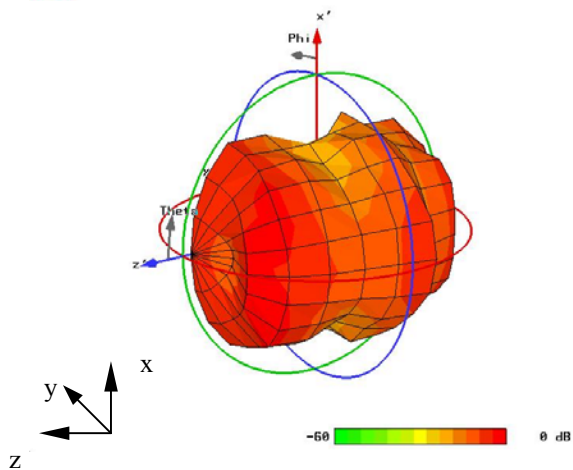


Figure 7. Far field pattern of the horizontally polarized SW

The free space measurements of reflections with the VNA have proved very low levels of reflected power at 2.45 GHz. $|S_{11}| = -28$ dB for vertically polarized and $|S_{11}| = -30$ dB for horizontally polarized SW have been measured.

The reflections inside the SW feeds were measured also for the case that the SW antennas radiate into the large HEPHAISTOS applicator loaded with water. Typical measured results of the $|S_{11}|$ parameters are presented in Fig. 8 (vertically polarized SW).

The frequency range of reflections below the 0.3 (-10 dB) level is marked by dashed lines and it fits well to the bandwidth of the magnetron sources.

With the VNA the S_{12} parameter was also measured, which defines the mutual coupling between two SW antennas in the MW heating system. With two different polarizations for neighbouring SW antennas, the critical coupling is decreased by almost 20 dB at 2.45 GHz, compared to the case that they are equally polarized (Fig. 9).

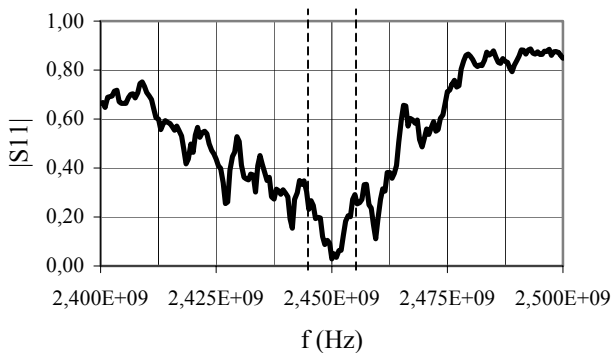


Figure 8. Typical measured reflections inside the vertically polarized SW radiating into the loaded HEPHAISTOS applicator

Preliminary results of the near field measurements show that the largest difference for the E field is about 10 dB along a line 1 m away from the SW and parallel to the SW axis, which is acceptable for supporting a high EM field homogeneity in the MW applicator.

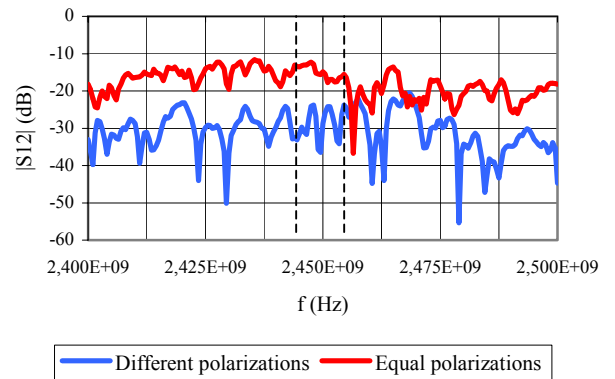


Figure 9. Measured mutual coupling of the SW antennas in the loaded HEPHAISTOS applicator

V. CONCLUSIONS AND OUTLOOK

Highly efficient nonresonant SW feeding systems with vertical and horizontal polarizations were calculated, optimized and measured. The design procedure, calculations of longitudinal and transversal slots in the SW wall and an optimization of SW antennas have been presented in more details.

Numerical calculations and experimental measurements have verified the very low levels of reflections inside the SW feeds, which can be directly coupled to the MW sources without isolators or circulators. In conclusion, the efficiency of the MW system is improved and, at the same time, the overall system costs are significantly decreased.

Using the idea of two different polarizations for neighbouring SW feeds, the critical cross coupling is reduced to a negligible level.

The relative uniform irradiation of SW antennas have been proved in numerical simulations and in preliminary near field measurements.

In the future verifications of the irradiated EM field distributions using near field calculations and measurements will be performed, as well as high power measurements and further tests on different sized industrial HEPHAISTOS systems.

REFERENCES

- [1] S. Stanculovic, L. Feher, and M. Thumm, "Design of nonresonant slotted waveguide feeds for 2.45 GHz industrial microwave heating systems," Proc. of 10th Int. Conf. on Microwave and High Frequency Heating, Modena, Italy, Sep 2005, pp 454-457.
- [2] Feher L, M. Thumm, "Microwave innovation for industrial composite fabrication-the HEPHAISTOS technology," IEEE Transactions on Plasma Science, Vol. 32, No. 1, February 2004, pp 73-79.
- [3] L. Feher, K. Drechsler, J. Filsinger and M. Thumm, "Development of the industrial 2.45 GHz HEPHAISTOS CA2 microwave processing system for composite fabrication," Proc. of 10th Int. Conf. on Microwave and High Frequency Heating, Modena, Italy, Sep 2005, pp 56-59.
- [4] Chow Ting Chan T. V. and H. C. Reader, Understanding Microwave Heating Cavities, Artech House Microwave Library, 2000, pp 225-239.
- [5] E.Hecht, Optik, Schaum Verlag, 1980, pp 175-176

Vehicle Occupant Monitoring with Capacitive Arrays

Martin Fritzsche¹, Christian Prestele¹, Tilo Schwarz¹, Sergiy Prutyanyy²

¹DaimlerChrysler AG, Research & Technology, Active Safety & Driver Assistance Lab, P.O. Box 2360, 89013 Ulm, Germany, Tel. ++49 (0)731 505 2114, martin.fritzsche@daimlerchrysler.com

²University of Stuttgart, Dep. of Electrical Engineering, Pfaffenwaldring 47, 70550 Stuttgart, Germany

Abstract—New generations of “smart airbags” with individually adapted safety characteristics require information about a passenger’s position and posture, to enable optimum protection at minimum injury risk. The technical solution discussed here is based on a 2D-capacitive electrode array, with the transmitting electrode integrated into the seat cover and the receiver array hidden behind the vehicle sky.

Keywords—2D capacitive array; safety; posture; regression

I. INTRODUCTION

In recent years airbags have made driving a lot safer and have significantly contributed to reduce fatal injuries in vehicle accidents. However, in extreme situations, e.g. in case a driver or a passenger is too close to the airbag unit at the instant of a crash, severe airbag-induced injuries may occur. New generations of intelligent airbags therefore require a distinct control of airbag inflation. Such a system would need to rely on the following information: What is the occupancy status of the passenger seat? If there is a person, what is his or her posture and weight? In compliance with the US federal standard FMVSS208 the categories that need to be discriminated are adults, children (age 3-6), rear facing infant seats and empty seats [1]. Ideally, one would further like to be able to separate between light weight and heavy adults.

Determining the *out-of-position* status (OOP) of a person can be treated as a subtask of *occupant classification* and represents the major focus of the work presented in this paper. The pursued aim is to define the posture of driver and passenger, to obtain their relevant distance to the airbag-unit. Hence, the following categories need to be discriminated, each of which has different consequences for airbag control: i) person-in-position, i.e. leaning back; ii) out-of-position, i.e. leaning forward; iii) critically out-of-position, i.e. leaning far forward.

To date, systems that address these occupation classification requirements are integrated into the seat pan or the seat structure and can be grouped into weight sensors; pressure sensitive mats; generating 2D profiles that are analyzed with pattern recognition techniques; capacitive systems measuring the electrical field strength between a seat and the vehicle body and combinations thereof. Optical systems currently under development – either mono, stereo or 3D-time-of-flight cameras [2, 3] – are usually located next to the roof console and are the only systems that have the potential to measure a person’s posture. In this paper we investigate the potential of

2D-capacitive arrays, as a low cost alternative to estimate head position and posture.

The paper is organised as follows: In section II we describe the operating principle and setup of the capacitive system, along with a system of string sensors that was used as a reference sensor, to generate ground truth head positions. Section III describes two different mathematical approaches to derive an estimate of 3D-head coordinates from measured data. Details of the data acquisition procedure and results obtained are given in Section IV. Conclusions and directions for further work are given in Section V.

II. SENSOR PRINCIPLE

A. Capacitive Sensor Setup

The capacitive system setup can be seen as that of a human body, put between the two plates of a capacitor, as illustrated in Fig. 1. With no occupant present, the capacitance C_{air} between the electrode and the array is very small. As a result, the signal received at the array is extremely low or non-existent. As capacitance between the transmitter and receiver increases, the received signal strength increases too. When an occupant is present in the seat, the capacitance between transmitter and receiver becomes much larger, since the medium between the transmitter and receiver has been changed to a human body (a conductor). The Figure below describes the occupied seat scenario.

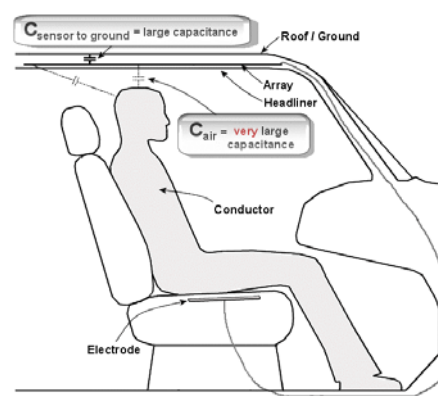


Figure 1. A person sits between the plates of a capacitor: the transmitter electrode is integrated into the seat surface, the 8x6 electrode receiver array is located in the vehicle sky (graphic courtesy to IMS).

The human body acts as a conductor for the transmitted signal. This effectively puts the source of the signal closer to the sensor array, and, since capacitance varies inversely with the square of the distance, the capacitance becomes much larger. Head position can be determined by detecting which element of the array has the strongest relative received signal. The detection range is defined by the electrode diameter and in our system given by around 25 cm.

The prototypic system, designed by IMS (Intelligent Mechatronic Systems, Canada [4]), consists of a 20x20 cm transmitter seat electrode, made of a conductive fabric, and a 8 x 6 electrode array located in the vehicle roof, orientated such that the long array axis points in the forward direction. Electrodes are made of copper foil and 9.65 cm squared in size. The operating frequency is 35 kHz, data is sampled with 50 Hz. Fig. 2 shows the laboratory system setup, with the transmitter on the seat and the electrode array above. The height of the plane of electrodes is chosen such that it matches the geometry of an S-class Mercedes.



Figure 2. Laboratory setup of the capacitive array system

B. Reference Sensor Setup

Robustness and accuracy of the capacitive approach to derive head coordinates can only be evaluated, if ground truth data is available. For this purpose we used a set of three string sensors, arranged such that the three strings span an area as large as possible. All strings are attached in the same point on a helmet-like device, worn by the test persons. The output voltages of the strings sensors are highly linear and can be

mapped directly to a length. With calibrated sensor positions, the three length measurements can be converted into a 3D position. Thus, every point within the observation space can be found from one of the two intersection points of three spheres – one sphere for every string.

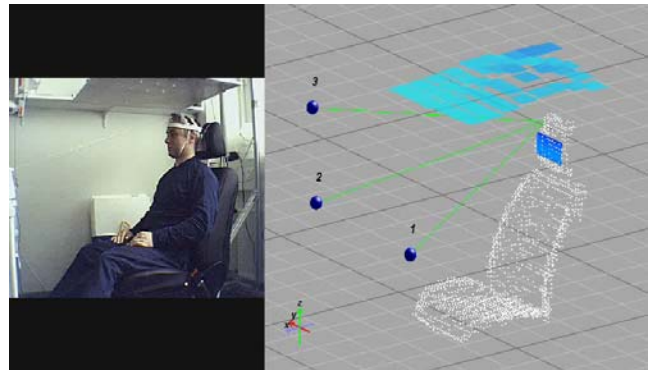


Figure 3. Left: Proband carries a helmet-like device, to which three string sensors are attached. From these three lengths the correct 3D position can be calculated for reference. Right: Capacitive values are maximum over the central head position. Blobs indicate string sensor positions.

For documentary purposes we complemented the setup with a web cam. All data are time stamped and recorded on a PC for offline synchronisation and processing. The left part of Fig. 3 shows a test person wearing a helmet, the blobs indicate string sensor positions. In the right part one can see how amplitudes increase towards the head centre.

III. ESTIMATION OF HEAD POSITION

A. Physical Models for 3D Position Estimation

Whereas horizontal head position can be directly obtained from the location of the electrode, where the maximum signal is recorded, the vertical distance to the array can only be derived indirectly. The simplest approach is to model amplitude profiles with the potential of a point charge, given by:

$$\psi \propto \frac{Q}{\sqrt{(z-z_0)^2 + (x-x_0)^2 + (y-y_0)^2}}, \quad (1)$$

where Q is the charge and x_0 , y_0 , z_0 denote head position. For every 8 x 6 data frame we use a non-linear *Least-Square* fit to approximate the measured surface. With regard to the determination of the horizontal position this allows to interpolate the exact maximum position with sub-cell accuracy. Our results show that the use of a rotationally symmetric model is well justified. However, the assumption of surface charges, induced in the skull, will come closer to reality. Consequently, we also investigated the model of a homogeneously charged disk, to model the measured potential, thus adding one more degree of freedom to the optimisation problem. But the results show that the accuracy of the height estimation does not improve significantly, compared to the point charge model. A drawback of the charged disk model is of course that it is computationally more expensive, as for every electrode location an elliptical integral needs to be calculated within the optimisation loop. This is further complicated by the fact that the induced charges will fluctuate when a person moves.

B. Regression Models for 3D Position Estimation

Quadratic regression methods are an alternative method, which allow to adapt a set of polynomial coefficients such that the output 3D coordinates match the reference position in the least-square sense. The forward (x) and lateral (y) position can be determined by simply using the column or row where the measured maximum occurs, respectively. In this manner two separate regression problems can be formulated, to estimate x and y coordinates.

To estimate the vertical (z) coordinate, we take a subset of the N (out of 48) largest amplitudes, which implies sorting the measured data for every time step. The sorting operation deliberately eliminates the spatial information of the horizontal maximum position and thus guarantees translation invariance. In our investigation $N=36$ produced favourable results.

An additional advantage of the regression approach is that implicitly a calibration operation is performed, thus taking into account that individual cells may have different sensitivity or dynamic range. Further to models that were motivated by either the underlying physics or standard quadratic regression techniques, we also investigated the use of neural networks or support vector machines. As these did not provide a significant improvement, we do not mention any further details within this paper.

IV. RECORDED DATA AND RESULTS

The results presented in this Section are currently based on recordings taken from 14 different persons, with heights ranging from 1.72 m to 2.04 m. Every test person was asked to perform roughly the same sequence of movements, moving back and forth and leaning left and right, with 20 s to 40 s duration. To adapt the regression coefficients, we applied the *leave-one-out* method, known from pattern recognition applications: In total, we performed 14 regression runs, where in every run 13 sequences were used to adapt the regression coefficients and the remaining sequence was used for testing. This permits to get an objective rating of the robustness of the method.

Figure 4 illustrates an exemplary result. One can clearly see the trajectory of a person leaning back and forth and left and right, followed by a movement along the boundary of the array.

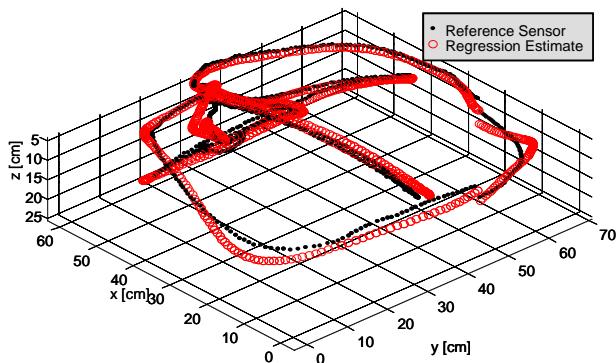


Figure 4. Example of calculated 3D head coordinates: Dots (black) indicate reference positions (ground truth), circles (red) are calculated based on a quadratic regression algorithm.

The rms-error for the horizontal position is around 2.4 cm and under 2 cm for the vertical direction. A distribution of the deviation from the reference position is depicted in Figure 5. In this case more than 80 % of the time head positions are calcu-

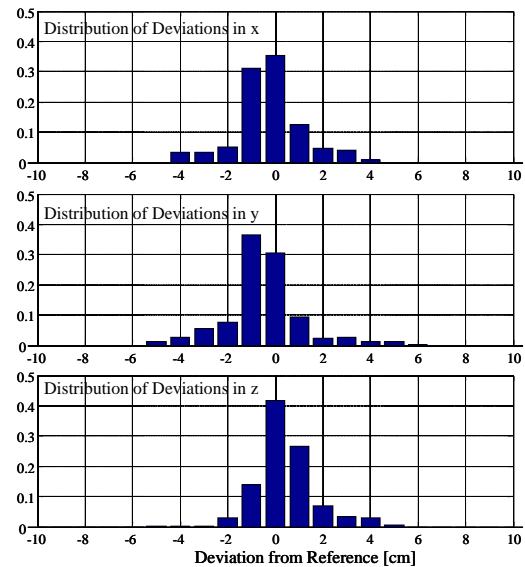


Figure 5. Distribution of deviations of the x -, y - and z -coordinates, calculated from the capacitive data, from the reference position.

lated correctly within a bound of ± 2 cm for the x -, y - and z -coordinate. As mean absolute deviation from the reference coordinates we obtained between 1.5 - 3 cm for x , between 1 - 2 cm for y and 1.5 - 3 cm for z , with standard deviations in the range of 2 - 3 cm for all coordinates.

For vehicles equipped with a sunroof the use of full 2D electrode arrays will not be an option. Consequently, we also investigated the quality of results if only a single column of electrodes is used. Obviously, a reliable estimation of the lateral and vertical head position is not feasible any more, but for airbag deployment control the forward head coordinate has the highest relevance. Fig. 6 shows where the 1D array would need to be located, extending from the rearmost position to the front, between the B-pillar and the sunroof. Fig. 7 compares the performance of the full array versus that of the outermost column. Although performance clearly deteriorates, still around 70% of the estimates are correct within ± 2 cm.



Figure 6. To determine forward position only, the 1D array needs to extend from the rear-most seat position forward, located between the B-pillar and the sunroof.

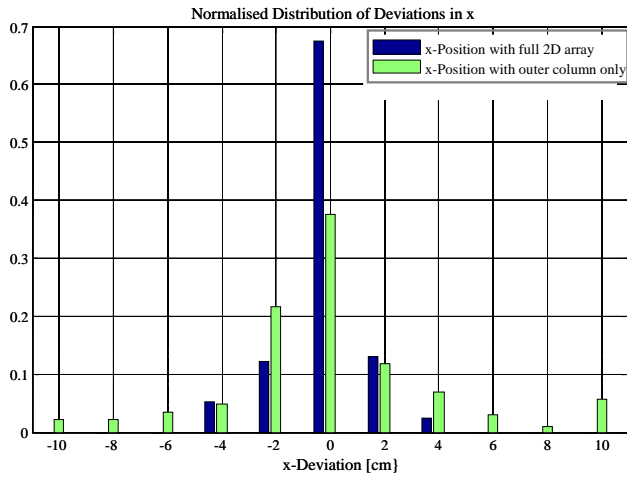


Figure 7. Comparison of 2D vs. 1D array performance for x-coordinate estimation.

V. SUMMARY AND CONCLUSION

We have demonstrated that the use of a 2D capacitive array allows to determine the head position of a vehicle occupant with an accuracy comparable to that of an optical stereo or time-of-flight camera. We could show that a simple regression approach delivers satisfactory accuracy, outperforming methods based on simple physical models, such as those of a point charge or homogeneously charged circular disks,

modelling the measured amplitudes profiles. We think that capacitive array systems thus have a potential to offer a low-cost solution to detect postures that may be critical for airbag deployment control. Further work will need not only to concentrate on extending the database available, but also on means to separate limbs from heads and to identify cases of misuse.

Beyond airbag control this device has of course potential for other applications, such as driver monitoring. Here the idea is to isolate characteristic pattern of movement that may be indicative of the driver state.

ACKNOWLEDGMENT

The work described in this paper has been partially funded by a European Research Programme (Project SENSATION), under contract No. 507231.

REFERENCES

- [1] National Highway and Safety Administration (NHTSA), People Saving People, Occupant Protection Program Update, Fall 1999. <http://www.nhtsa.dot.gov>
- [2] R. Schwarte et. al., New powerful sensory tool in automotive safety systems based on PMD-technology, Conf. Proc. Advanced Microsystems for Automotive Application, Berlin 2000, Springer-Verlag
- [3] M. Fritzsche, C. Prestele, G. Becker, M. Castillo-Franco, B. Mirbach, *Vehicle occupancy monitoring with optical range-sensors*. Intelligent Vehicles Symposium, May 13-18, 2004, Parma
- [4] Intelligent Mechatronic Systems, Canada, <http://www.intellimec.com>

Improved Patch Antenna Network Model

Klaus Solbach, Dinh Trung Tran

University Duisburg-Essen, Hochfrequenztechnik, Bismarckstr.81, 47048 Duisburg, Email: hft@uni-duisburg-essen.de

Abstract — Modeling of patch antennas using the conventional network model produces major discrepancies, in particular, if the patch height is relatively large. In an investigation of a patch antenna of variable height the antenna reflection coefficient was measured and an improved network model was fitted to the measured data. It turned out that in order to achieve the best fit, the conventional model has to be complemented by a series resistor in the feed section which is shown to represent radiation from the probe. Dependence of radiation resistance on patch height is such that the probe can be modeled as a Hertzian monopole over ground.

I. INTRODUCTION

Patch antennas have been used for decades as simple and inexpensive antenna elements fabricated on dielectric printed circuit boards. The understanding of the impedance and the radiation properties is well supported by a simple network model presented in many textbooks [1], [2] using a transmission line equivalent for the patch and representing the radiation by (slot radiator-) conductances terminating the transmission line. Probe coupling of the patch to a coaxial transmission line from behind the ground plane is successfully modeled by an inductor. As is well known, the impedance match bandwidth of patch antennas is too low for many applications and is limited mainly by the height of the patch over ground. However, when patch antennas of large height are investigated, it is found that the simple network model described above no longer works satisfactory: Both the radiation pattern degrades and the reflection coefficient plot deviates from the model prediction.

In an investigation aimed at analyzing the broadbanding technique of series resonant compensation of the probe inductance, the reflection coefficient of a patch antenna of variable height was measured and an extended network model was fitted to the measured data. The result gave new insight into the radiation mechanism and allows better design of wide bandwidth patch antennas.

II. CONVENTIONAL MODEL

The patch antenna under consideration is shown in Fig. 1: The patch is a solid plate of brass which is kept in place at variable height over the ground plane by a plastic screw in the center position of the patch. The patch is fed by a probe from an SMA coaxial plug mounted to the back of the ground plane; the probe is the center conductor of the coaxial transmission line. The reflection coefficient was measured for heights between 3% and

10% wavelength at resonance frequency around 1 GHz (h = 10mm, 18mm, 25mm and 30mm) as

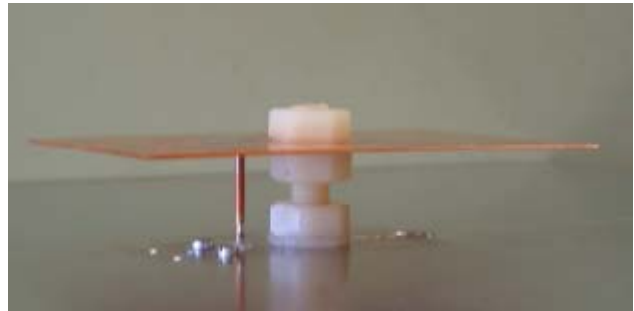


Fig.1. Experimental patch antenna

shown in Fig.2. It is seen that the resonance loop shift due to a series inductance progresses with increasing height and that the loop diameter decreases and the distance of the loop from the periphery of the smith chart ($r = 1$) increases at the same time.

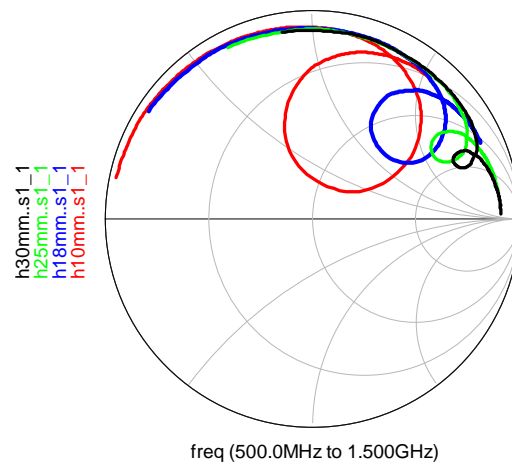


Fig.2: Measured reflection coefficient of patch antenna for patch height from 10mm to 30mm

The measurements were first fitted to a conventional network model as shown in Fig.3. It is seen from the schematic that the patch is represented by two sections of microstrip line (MLIN) and that the end effect is modelled by a microstrip gap (MGAP) to represent the end capacitance and a resistance to ground (ZIP) to represent the patch edge radiation. The terminal (Term) is connected via the inductor (L) to the interconnection of the two microstrip transmission line sections and a capacitor C_1 represents the stray electric field at the transition from the coaxial transmission line to the inductive probe.

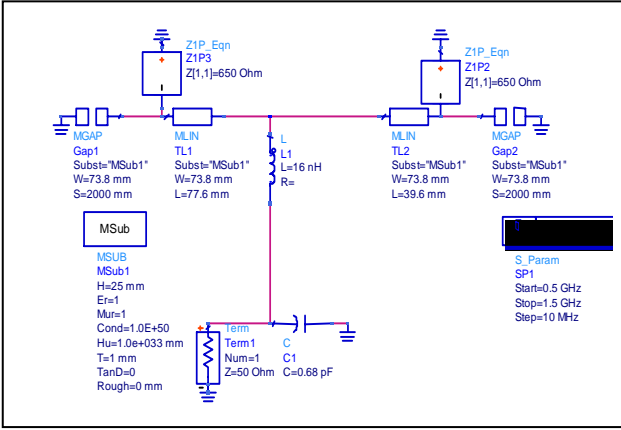


Fig.3(a): Schematic diagram representation of conventional patch antenna model

We can fit the network model to the measured data (with highest weight around resonance) by letting the simulation tool vary the capacitance, the length of the two sections of microstrip line and the edge radiation resistance. When we compare the reflection coefficients of the model and the measurement in Fig.3(b), we find that above resonance frequency the simulated reflection coefficient magnitude is too large (close to the Smith Chart outer circle) and at lower frequencies the reflection coefficient magnitude falls off contrary to the measurement.

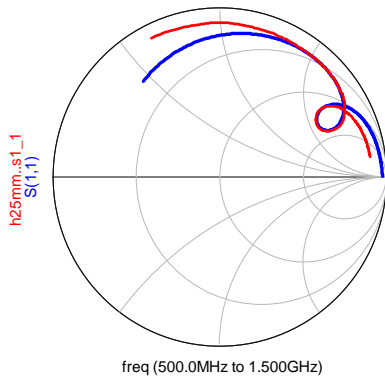


Fig.3(b): Simulated (blue line) reflection coefficient of patch antenna of 25mm height using conventional network model versus measured (red line)

III. IMPROVED MODEL

In order to improve the fit between network model and measured data, the network model was extended to include a resistor in series with the (probe-) inductor: The result was better match close to resonant frequency, but still strong deviations below and above resonance frequency. Very good fit even for frequencies further off

resonance was achieved by giving the series resistance and the patch edge slot radiation resistance (the inverse radiation conductance) quadratic frequency dependences. The network schematic and the resulting reflection coefficient versus frequency are shown in Fig.4:

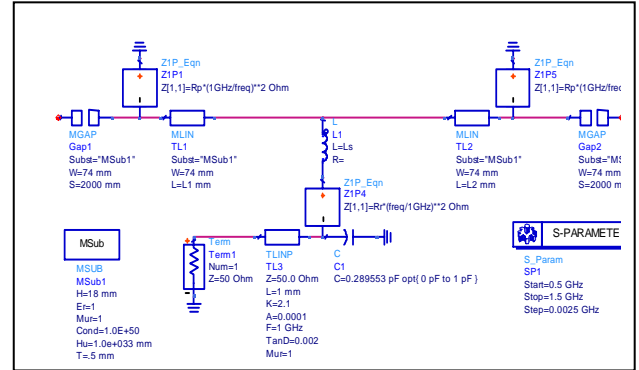


Fig.4(a): Schematic diagram representation of improved patch antenna model

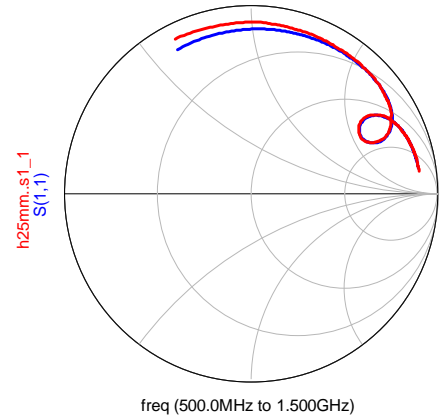


Fig.4(b): Simulated (blue line) reflection coefficient of patch antenna of 25mm height using improved network model versus measured (red line)

This exercise was done for all measurements (patch height varied) and equally close fit was achieved in all cases and produced results for the series resistance and inductance of the probe as a function of probe length.

IV. DISCUSSION OF MODEL PARAMETERS

Resistance values of the new series resistor as a function of patch height exhibit characteristic height dependence, see Fig. 5:

Due to the high resistance values and the close to quadratic dependence with patch height, the newly introduced series resistor probably does not represent conductor losses; at least we can conclude this from considering the probe resistance (resistance including skin effect would yield far below 1Ω) and a check on efficiency (a preliminary Wheeler-cap measurement exhibited about 95% efficiency).

A possible explanation could be radiation resistance of the probe: To check this assumption we model the probe

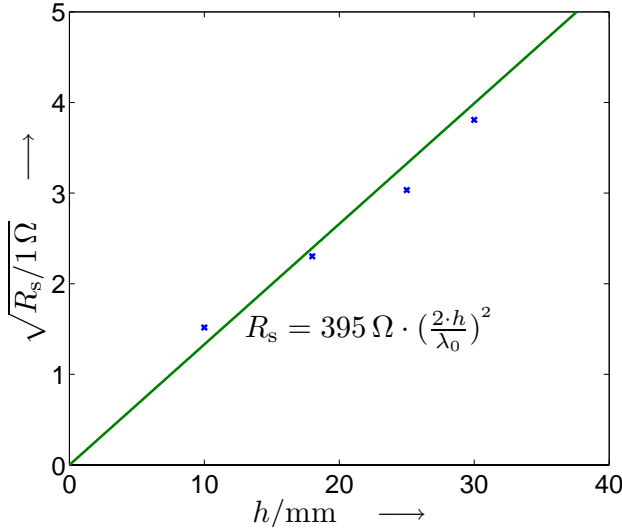


Fig.5: Resistance of series resistor as a function of patch height h ; red line for Hertzian monopole

as a Hertzian monopole over ground, with constant current distribution along its length, as shown in Fig.6.

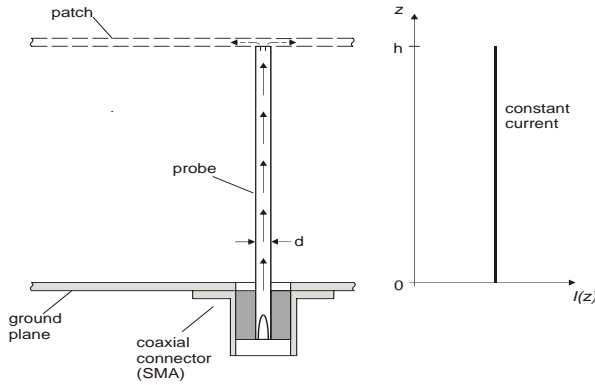


Fig.6: The patch antenna probe interpreted as a Hertzian dipole

The radiation resistance of a Hertzian dipole over conducting ground is calculated as half the resistance of a (double-length) Hertzian radiator in free space

$$R = \frac{1}{2} \cdot 790 \Omega \cdot \left(\frac{L}{\lambda} \right)^2 \quad (1)$$

where L is $2 \cdot h$.

E.g., with the patch height over ground $h=25$ mm ($h/\lambda \approx 0.08$) the radiation resistance R at 1 GHz becomes about 10Ω .

From Fig.5 we see a close agreement of the model series resistance points with our theoretical Hertzian monopole model, which supports our assumption concerning the nature of the resistive series component in the network equivalent.

A further support comes from the strong un-symmetry in the E-plane radiation pattern, Fig.7.

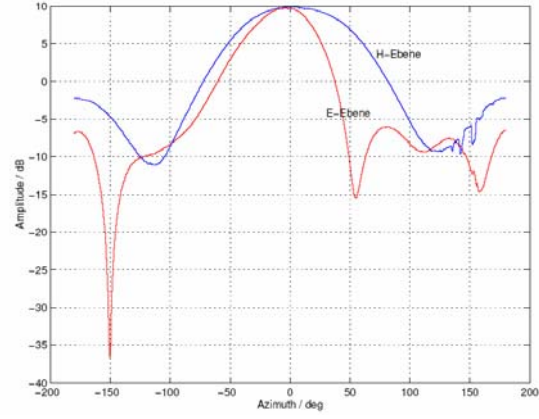


Fig.7: Measured patch radiation patterns

This degradation can be explained by superposition of fields from the patch edge slot radiators and the un-symmetrically positioned vertical probe while both have the same polarization in that plane; in H-plane the probe radiation is cross-polarized so that the co-polar pattern remains undisturbed.

On the other hand, the series inductance which models the probe exhibits a proportional increase with probe length (equal to patch height), as seen in Fig.8. The proportionality constant conforms closely to constant K_4 in the approximate formula for a straight wire in free space of 1.3mm diameter [3].

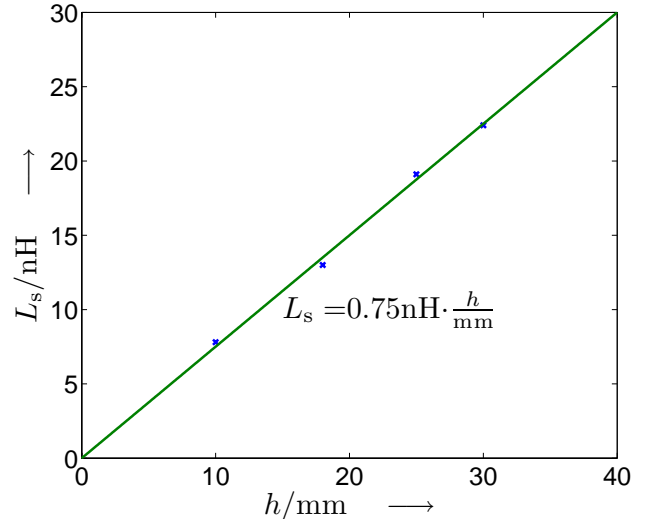


Fig.8: Inductance of probe as a function of patch height; red line for isolated conductor inductance

This behavior also supports the assumption of uniform current distribution along the probe length which is essential to the Hertzian monopole model of probe radiation.

Finally, improved tracking of the network model reflection coefficient and measured data for frequencies below and above the resonance range could only be achieved by giving the series resistance the frequency dependence due to (1) and in addition giving the patch edge slot radiation resistance (the inverse radiation

conductance) the inverse variation proportional to $(1/f)^2$ which we may assume in principle due to the single slot radiation conductance approximation for hemispherical radiation

$$G \approx \frac{1}{90\Omega} \cdot \left(\frac{w_{eff}}{\lambda} \right)^2 \quad (2)$$

where w_{eff} is the effective width of the slot radiator, equivalent to the effective width of the microstrip line.

Modeling the edge slot as an isolated slot neglects the mutual coupling effect. Mutual coupling, however, is accounted for at first order by the fitting procedure where the best fit radiation conductance is searched and found. Never-the-less, as seen from Fig.4(b), there still is a considerable deviation visible at low frequencies which requires that the radiation conductances in our model decay even more with frequency than predicted by eq.(2). The mechanism behind this decay is the phase relationship of the edge fields which follows from transmission line theory: At resonant frequency, the transmission line is half-wavelength so that the two edge voltages are at opposite polarization and the slot radiator fields therefore are in-phase; at very low frequencies, the two edge voltages are at equal phase which means the slot radiators are anti-phase, thus canceling radiation and leading to zero radiation conductance. Including a suitable transmission line factor in the variable expression for the edge slot radiation resistance of our network model thus produces better fit of model and measured data at the low-end frequency range, as seen in Fig.9:

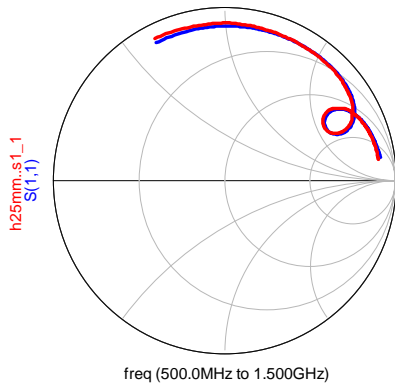


Fig.9: Simulated and measured reflection coefficient of patch antenna of 25mm height using series resistance, quadratic frequency dependence of radiation conductance and series resistance and additional transmission line factor

V. APPLICATION

The network model can be used to precisely predict the effect of compensation techniques used to match and broad - band the patch antenna input impedance. An example is shown in Fig.10(a), where we see the patch

antenna of 25mm height with a series capacitor to compensate the series inductance by series resonance.

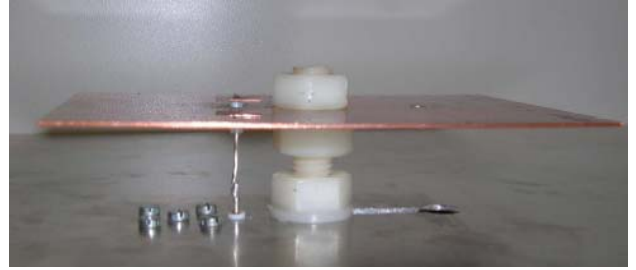


Fig.10(a): Patch antenna of 25mm height using series capacitor compensation

The measured reflection coefficient compares well with the simulation result using the network model of the patch antenna without modifications in the patch and probe structure and applying the best-fit capacitance ($C_s = 14.5\text{nF}$), as seen in Fig.10(b):

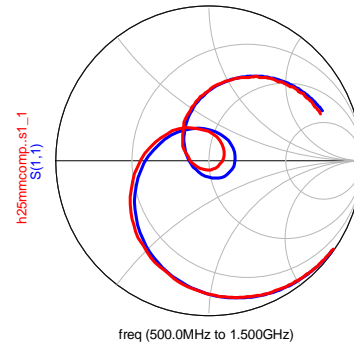


Fig.10(b): Simulated (blue) and measured (red) reflection coefficient of patch antenna of 25mm height using series capacitor compensation

III. CONCLUSION

Applying and extending the transmission line model of the patch antenna to include the frequency dependence of radiation resistances we have noticed that the probe has to be modeled as an inductor with a resistance in series. Based on the achieved high accuracy fitting of measured data and model simulations for patch antennas of variable height it was found that the series resistance conforms closely to the theoretical radiation resistance of a Hertzian monopole. Thus we conclude that the probe acts as an independent radiator of the top-loaded monopole type superimposing the ordinary patch radiation which also explains the un-symmetric E-plane radiation pattern of the patch antenna.

REFERENCES

- [1] G. Kumar, K.P. Ray, *Broadband Microstrip Antennas*, Artech House, Chapter 2
- [2] C.Balanis, *Antenna Theory*, chapter 14, John Wiley, 1997
- [3] H.Meinke, F.W.Gundlach, *Taschenbuch der Hochfrequenztechnik*, chapter 4, Springer, 1962

Influence of Metallic Primers on the Attenuation of CPW in the Millimeter- and Submillimeter Range

V. Müllerwiebus, K. Schünemann

Hamburg University of Technology, Microwave Engineering Department, Denickestr. 22, 21071 Hamburg, Germany, +494042878-2758, muellerwiebus@tu-harburg.de

Short Abstract—A metallic primer is often used between a conductor and a substrate to build up coplanar waveguides (CPW). These primers influence the attenuation of the CPW line and planar structures in general. The exact influence of metallic primers is described and a frequency-independent description to avoid uneligible primers is presented.

Keywords: primer; attenuation; CPW

I. INTRODUCTION

CPW lines are built by depositing a conductive layer on a dielectric substrate. The conductive layer is often regarded to be of electrically thick thickness. This approximation is sufficiently accurate, if the layer is thicker than $3d$, where d means skin depth. The conductor often does not cling to the chosen substrate, so that a primer has to be used in between. One possibility is to use another conductor as a *metallic* primer.

In the MEMSTIC-project [1], [2], CPW lines are built for the millimeter- and submillimeter wave region as shown in Fig. 1. The conductive layer is made of gold and the substrate of a $4\ \mu\text{m}$ thin dielectric membrane. This dielectric membrane is made of Hexamethyldisilazan (HMDS-N) and mounted on a mechanical carrier [2]. Titan is used as primer. (Optionally e.g. Wolfram would also be possible.) In the production process, $4\ \mu\text{m}$ thin HMDS-N is deposited on top of a silicon wafer. A thin layer of titan as primer to the thick layer of gold is sputtered above. These CPW lines achieve a simulated (using Agilent HFSS) effective relative permittivity of $\epsilon_{r,\text{eff}} \approx 1.25$. Dispersion is expected to not occur for frequencies below 500 GHz.

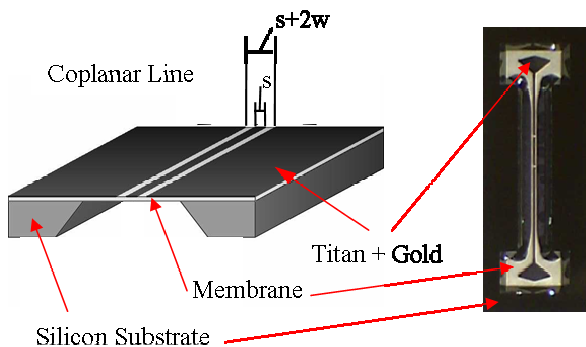


Figure 1. CPW lines on thin dielectric membrane, a schematic (left side) and a photo (right side).

Examples of measurements, especially for transitions of CPW to D-Band waveguides, can be found in [3].

II. ATTENUATION

Using these thin dielectric membranes as substrate results in low dielectric attenuation. The dielectric attenuation of CPW lines can be estimated as [4]:

$$\alpha_\epsilon [\text{dB/mm}] \approx 0.091 \cdot q_{\tan \delta_\epsilon} \cdot \tan \delta_\epsilon \cdot f \cdot \sqrt{\epsilon_{r,\text{eff}}}, \quad (1)$$

where the frequency f has to be inserted in GHz, $\tan \delta_\epsilon$ is the dielectric loss factor, and $q_{\tan \delta_\epsilon}$ is a filling factor due to dielectric losses. It is defined as

$$q_{\tan \delta_\epsilon} = \frac{\epsilon_r(\epsilon_{r,\text{eff}} - 1)}{\epsilon_{r,\text{eff}}(\epsilon_r - 1)}. \quad (2)$$

If the thickness t of the conductive layer fulfills $3d < t \ll s$ (s means stripe width and d skin depth), the attenuation due to the ohmic losses of the conductor layer is [4]

$$\alpha_\rho [\text{dB/mm}] \approx \frac{8.686 \cdot R_F \cdot \sqrt{\epsilon_{r,\text{eff}}}}{2 \cdot \eta_0 \cdot g \cdot K(k) \cdot K(k') \cdot (1 - k^2)} *$$

$$\left\{ \frac{1}{k} \left[\pi + \ln \left(\frac{4\pi w(1-k)}{t(1+k)} \right) \right] + \left[\pi + \ln \left(\frac{4\pi g(1-k)}{t(1+k)} \right) \right] \right\}, \quad (3)$$

where the wave impedance in free space is $\eta_0 = 120\pi\Omega$, $g = s + 2w$ with s stripe width and w gap width of the CPW line, t means conductor thickness, $k = s / (s + 2w)$, $k' = \sqrt{1 - k^2}$, and $K(k)$ is the complete elliptic integral of first order. R_F is the surface resistance, including the skin effect. Formula (3) shows that the attenuation due to ohmic losses is directly proportional to the surface resistance R_F , which is the only variable being affected by the existence of a metallic primer. Hence the influence of the primer on R_F shall be regarded in the following.

The ohmic attenuation due to ohmic losses is the dominant part of the total losses for CPW lines on dielectric membranes in the millimeter and submillimeter wave range. This can be deduced from formulas (1) and (3). Hence the influence of the metallic primer on this attenuation is not necessarily negligible

in the balance of the total losses and should be described and studied in detail.

The surface impedance of a single conductor layer is [5]

$$Z = \sqrt{\frac{\mu_0 \mu_r}{\epsilon_0 \epsilon_r}}, \quad \epsilon_r = \epsilon_r - j \left(\frac{\kappa}{\omega \epsilon_0} + \epsilon_r \tan \delta \right). \quad (4)$$

Good conductors are characterized by a dominating imaginary part of the relative permittivity. As shown in equation (4), this condition is approximately fulfilled, if the conductivity $\kappa \gg \epsilon_0 \omega$. In this case, $\epsilon_r \tan \delta$ is negligible, too. In the following considerations, only good conductors are regarded to be used as possible primers.

In the case of a good conductor and assuming $\mu_r \approx 1$, the surface impedance is calculated by (shown in formula (4), [6])

$$Z = \frac{1+j}{d \cdot \kappa} \quad \text{with skin depth } d = \sqrt{\frac{2}{\omega \cdot \kappa \cdot \mu_0}}. \quad (5)$$

The surface impedance of a layered conductor, made of an electrically thin layer (metal 1) of a primer and an electrically thick layer (covering metal 2) ($3d < l \ll s$) of gold as original conductor layer can be calculated as [5], [7]

$$Z_{\text{layered}} = Z_{\text{primer}} \frac{Z_{\text{Au}} \cosh(\gamma l) + Z_{\text{primer}} \sinh(\gamma l)}{Z_{\text{Au}} \sinh(\gamma l) + Z_{\text{primer}} \cosh(\gamma l)} \quad (6)$$

where l means thickness of metal 1 (or the primer in this case) and γ is calculated as:

$$\gamma = k_0 \sqrt{-\epsilon_r \mu_r}, \quad k_0 = \omega \sqrt{\epsilon_0 \mu_0}, \quad (7)$$

where ϵ_r is given in formula (4).

R_F equals the real part of the surface impedance Z . The influence of the dielectric HMDS-N-membrane on R_F is negligible.

The thickness l of the primer can be varied. In the manufacturing process of the used CPW lines, the height of the conductor layer made of gold has to be galvanically increased [2]. The thickness of the primer was set to $l = 300$ nm in the beginning [2]. This was due to that the wafer has to be biased at a single point during the galvanic step of the manufacturing process. The sputtered metallic cover of the wafer results in a feeding resistance of the galvanic procedure. This resistance has to be kept sufficiently low in order to enable an uniform galvanically grown structure.

The influence of metallic primers of various thickness at a frequency of $f = 150$ GHz is shown in Fig. 2 as a function of the conductivity of the primer layer (compared to a single electrically thick gold layer in the case of a vanishing primer with $l = 0$ nm). For comparison, the influence of an electrically thick layer of the primer without coating gold layer is shown in Fig. 3. R_F is directly proportional to the attenuation due to the ohmic losses of the CPW line. As is well known, the graph in Fig. 3 belonging to the pure and electrically thick primer layer is strictly monotonically decreasing, if it is regarded as function

of the primer conductivity. Fig. 2 shows that the surface resistance (and herewith the ohmic attenuation) always increases by adding a layer of a primer which has a lower conductivity than the covering gold layer. Additionally, the surface resistance (the ohmic attenuation) increases by adding thicker layers of a primer with fixed conductivity. These results are in good agreement with general expectations.

A point of intersection must appear in Figs. 2-5, at which the primer conductivity and that of the covering gold layer are equal ($\kappa_{\text{Primer}} = \kappa_{\text{Au}}$). On the other hand, the graphs converge to another intersection point, if primers of relatively low conductivities are considered. This can be explained by the electric field behaviour when penetrating into a metal. As is well known, the current density decreases in

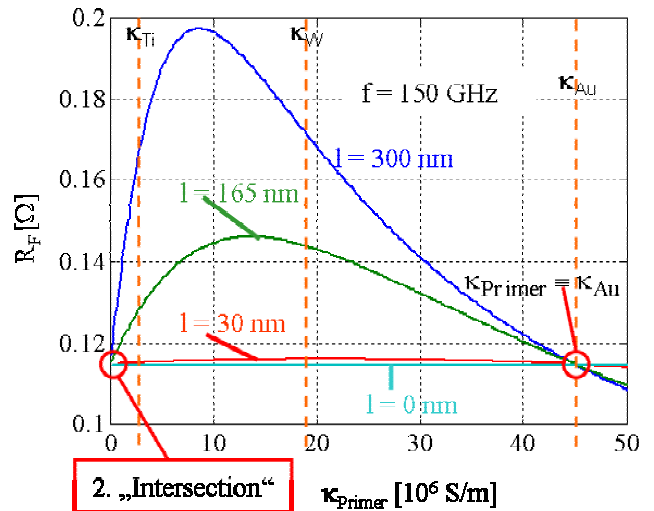


Figure 2. $R_F \propto \alpha_p$ as a function of primer conductivity and thickness at frequency $f = 150$ GHz.

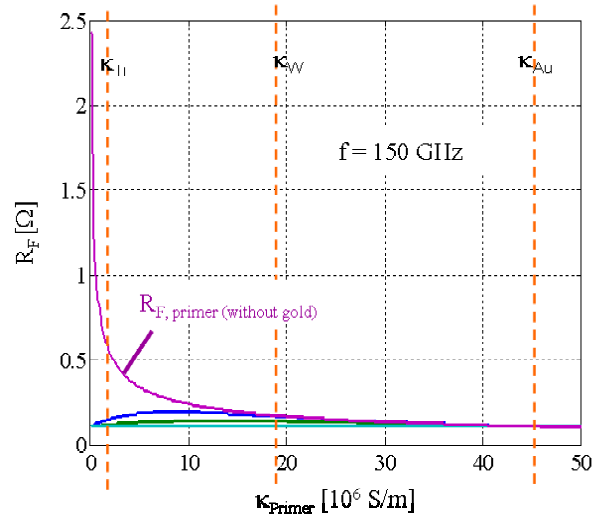


Figure 3. $R_F \propto \alpha_p$ as a function of primer conductivity at frequency $f = 150$ GHz compared to a single layer of an electrically thick primer material.

the metal in the direction perpendicular to the surface. At a distance of the skin depth d below the surface, the current decreases by the factor e^{-1} . As already described in formula (5), the skin depth d is inversely proportional to the conductivity of the regarded layer. A relatively low conductivity of the primer layer leads to a larger skin depth, which means that the electrical field is less influenced by the existence of this layer of fixed thickness. If the primer has a lower conductivity, the fixed thickness appears electrically thinner. Regarding a relatively low conductivity, the current density decreases less along the direction perpendicular to the metalsurface than in the case of a higher conductivity. At low primer conductivities, the current density at the intersection to the gold layer is similar to the current density at the top of the gold, if no primer layer were used at all. This leads to an intersection point at low conductivity values.

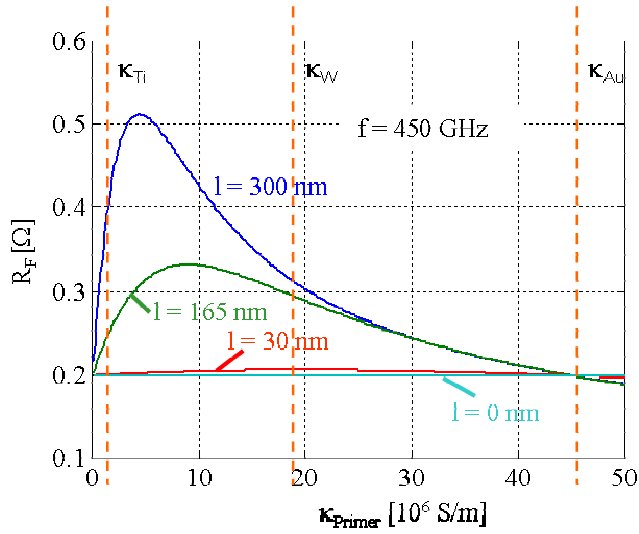


Figure 4. $R_F \propto \alpha_\rho$ as a function of primer conductivity and thickness at frequency $f = 450$ GHz.

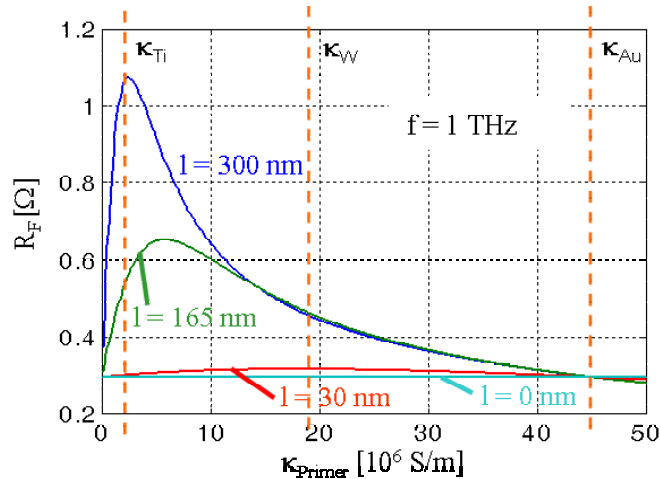


Figure 5. $R_F \propto \alpha_\rho$ as a function of primer conductivity and thickness at frequency $f = 1$ THz.

A similar effect of increasing the skin depth in resonant cavities with the help of certain layered material in order to avoid losses due to the skin effect has been mentioned in [8]. Another comparable effect is the existence of a minimum in the function of the resistance of a metal plate versus the thickness of this plate [9].

In between the two points of intersection, there exists a maximum, as is shown in Figs. 2-5. Fig. 4 depicts results at a frequency of $f = 450$ GHz. Regarding a frequency of $f = 1$ THz, the maximum of R_F increases as shown in Fig. 5. (The introduced CPW lines would suffer from dispersion at $f = 1$ THz and the requirements of formula (3) would not be fulfilled. Nevertheless, the effect may be regarded in general and in case of a usage of other substrates.) In conclusion, a metallic primer with medium conductivity can lead to a greater increase of the attenuation of CPW lines than a primer with lower conductivity. The primer has to be chosen carefully, depending on the desired thickness of the primer layer and on the frequency range.

Regarding CPW lines on $4\mu\text{m}$ thin dielectric HMDS-N-membranes, the effect of increasing the attenuation is not negligible in the desired frequency range for a primer thickness of $l = 300$ nm and titan as primer. By decreasing the thickness to $l = 30$ nm, however, the additional losses can almost be eliminated. Moreover, at this thickness, metallic primers of any conductivity can be used. Even at a frequency of $f = 1$ THz, the influence of the primer almost disappears, as shown in Fig. 5. The reduction of the thickness of the titan layer to $l = 30$ nm is possible during the manufacturing process. The application as a primer is not disturbed. To achieve a low feeding resistance to the galvanic manufacturing process, it is possible to add another structured layer on top of the first gold layer, which is completely removed after the galvanic manufacturing step.

III. DESIGN CONSIDERATIONS

The maxima in the surface resistance versus the conductivity curve have to be considered when selecting a primer. Depending on the desired frequency and the desired thickness of a primer, there exist regions of conductivity, which have to be avoided for the primer. Those primers would cause a non-negligible influence on R_F resulting especially in an increase of the attenuation of the CPW lines.

Regarding relatively thick primer layers, the influence of the maximum of R_F appears at a conductivity for which the skin depth has approximately the same value as the layer thickness, even though it does not converge against it. This is shown in Fig. 6. On the other hand, the maximum cannot appear at conductivities greater than half of the conductivity of the gold:

$$\kappa_{\text{Primer,Maximum}} \leq \kappa_{\text{Au}}/2. \quad (8)$$

This leads to the effect that the maximum in R_F appears at more and more smaller fractions of the skin depth, if relatively thin primer layers are regarded. It also means, that the maximum in R_F appears at relatively high primer conductivities, if very thin layers are regarded. This is shown in Fig. 6, too.

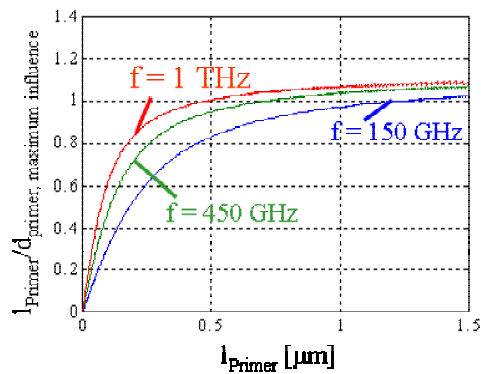


Figure 6. Points of maxima in R_F versus primer thickness.

The appearance and consequences of the maximum in R_F (which is proportional to the ohmic attenuation α_ρ) can be described independent of frequency f . This is shown in Fig. 7 and Fig. 8.

The conductivity of the primer which leads to a maximum in R_F is described as a function of the value of the thickness of the primer layer divided by the skin depth. As normalizing skin depth, that of the metal with conductivity taken at the location of the maximum, has been chosen. Then those primer conductivity values which have to be avoided can be found independent of frequency.

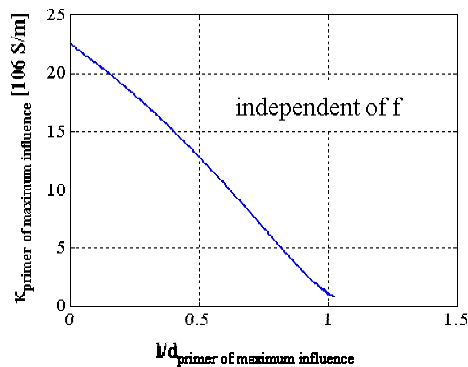


Figure 7. Primer conductivities of maximum in R_F can be described independent of frequency if the primer thickness is presented as a fraction of the skin depth.

Being able to use electrically thin layers of a primer (namely a small fraction of the skin depth), the maximum in R_F appears at higher values of the primer conductivity, but the effect can be neglected. If thicker layers of the primer cannot be avoided due to the manufacturing process, the maximum appears at lower values of the primer conductivity and the influence on the attenuation of the structures is significant. (see Figs. 7 and 8).

IV. CONCLUSIONS

Depending on the thickness of a required primer layer, metallic primers gain an influence on the attenuation of planar structures. To avoid this effect, the primer has to be highly

thinned or the conductivity of the primer has to be chosen carefully. A metallic primer with medium conductivity can lead to a greater increase of the attenuation of planar structures than a primer with lower conductivity. A description of the primers which have to be avoided and their detailed consequences have been formulated independent on frequency.

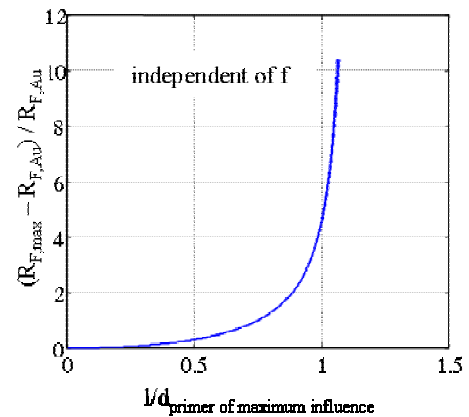


Figure 8. Influence of R_F maximum of a primer layer

ACKNOWLEDGMENT

The authors are indebted to the Deutsche Forschungsgemeinschaft for financial support as well as to K. Duwe, H. Feindt, and J. Müller from Department of Micro Systems Technology, Hamburg University of Technology, for assistance in manufacturing the micromachined structures as well as for advice and cooperation.

REFERENCES

- [1] M. Höft, „Ein Beitrag zur quasi-optischen Leistungsaddition mit periodischen Strukturen“, Mensch&BuchVerlag, 2003, Berlin, Germany
- [2] K. Duwe, „Planare Schaltungen für den Submillimeterwellenbereich auf dünnen HMDS-N-Membranen“, Shaker Verlag, 2004, Aachen, Germany
- [3] V. Müllerwiebus, „Experimental Characterisation and Behaviour to Misalignments of a D-Band-Transition from Rectangular to Coplanar Waveguide on Membrane“, Joint 29th International Conference on Infrared and Millimeter Waves and 12th International Conference on Terahertz Electronics, 2004, Karlsruhe, Germany, Conf. Digest, pp. 481-482
- [4] C. Schmelz, „Untersuchungen zum Verhalten von Millimeterwellen-Schaltungen in Flip-Chip-Technik auf koplanaren Leiterstrukturen“, Univ. der Bundeswehr, Diss., 2000, München, Germany
- [5] Ansoft Corporation, HFSS Online Help, Ansoft HFSS V10, USA
- [6] R.K.Hoffmann, „Integrierte Mikrowellenschaltungen“, Springer-Verlag, Berlin, Heidelberg, New York, Tokyo, 1983
- [7] M. Kasper, „Mikrosystementwurf, Entwurf und Simulation von Mikrosystemen“, Springer-Verlag, Berlin Heidelberg, Germany, 2000
- [8] Y. Gotoh, M. Kobayashi, K. Tanaka, „Thin-film multilayered electrode, high-frequency transmission line, high-frequency resonator, and high-frequency filter“, European Patent Specification, Bulletin 2005/37
- [9] Meinke, Gundlach, „Taschenbuch der Hochfrequenztechnik“, Springer-Verlag, Berlin Heidelberg, Germany, 1986

A K-band Biconical Antennas System for Wireless Wideband Communication Equipments

Vincenzo Stornelli¹, Mario Caramanico², Massimo Di Fabrizio² and Angelo Brigante²

¹Dept. of Electrical Engineering, University of L'Aquila, Italy; stornelli@ing.univaq.it

²R&D Dept. Thales Italia, Chieti Scalo, Italy; mario.caramanico@it.thalesgroup.com

Abstract— In this paper a biconical antennas system operating in a wideband TX/RX video and voice communications module is described. The antenna module is part of a K-band (38.3-38.6 GHz) equipment installed in a vehicle on the move composed by two different units: the IDU, indoor unit, is installed inside the vehicle and the ODU, outdoor unit, is installed on the top of the vehicle. The ODU is composed by the RF transceiver and the antennas system that is formed by two equal biconical antennas performing the transmitting (TX) and receiving (RX) functionality respectively. The fabricated antennas, characterized by reduced size and low weight, are fed through WR28 rectangular waveguide obtaining minimum insertion loss in connecting the antennas itself with the system.

Keywords — Broad Band Antennas, biconical antennas, wideband communication systems.

I. INTRODUCTION

The fast growing demand for microwave communication technologies, such as broadband wireless and space communication, point to point radio link, and a large variety of on the move network for data and voice exchange, is bringing up stringent requirements for high performance systems. In fact, the most critical requirements when treating with wireless communications equipment are range and power consumption being these two aspects interrelated. In these circumstances, enhanced performances are needed by the whole system and consequently there is a continuing demand for broader bandwidth and strict radiation pattern antennas, with reduced size and weight.

When the operational condition requires an omnidirectional link, the biconical one is an easy way to build up broad-band antennas with omnidirectional radiation pattern but, as the operation frequency increases, there is the need to avoid the classical coaxial feed in order to reduce the power loss between the antenna and the TX/RX circuit blocks.

In this paper a K-band biconical antenna is described. It is part of a system composed by two different units called ODU and IDU respectively and implements two equal antennas, fed through WR28 rectangular waveguide, performing respectively the TX and RX functionality.

II. SYSTEM OVERVIEW

In fig.1 the block diagram of the whole system is shown.

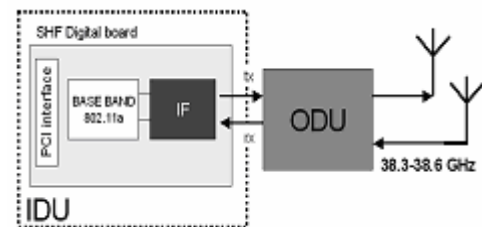


Figure 1: System overview

The ODU block diagram is shown in fig.2. The TX and RX chains of the ODU are connected with two different antennas avoiding any kind of switch. This is necessary when high sensitivity and long range are required from the transceiver. In fact, as the frequency increases up to about forty GHz, it is very difficult to realize signal switch with low insertion loss and high power handling, and consequently obtaining low system's noise figure. In fig.3 a view of the ODU is presented. As shown the two antennas are placed in different height positions in the way to achieve the best decoupling.

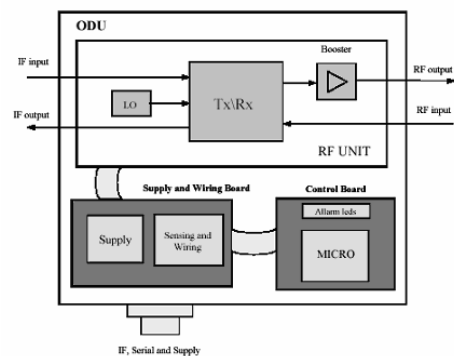


Figure 2: ODU block scheme



Figure 3: View of the ODU

III. ANTENNA DESIGN

As mentioned, when specifications require an omnidirectional link the biconical one is an easy way to build up a broadband antennas with uniform horizontal radiation pattern [1-4]. Moreover the biconical antenna allows an extremely flexible design of its characteristics at low cost. The biconical antenna consists of two opposite conical horns as shown in fig.4.

In traditional analysis of biconical antenna, only the dominant mode is excited. The dominant or fundamental mode of the biconical structure is the transverse ElectroMagnetic (TEM) mode which is the solution of Maxwell's equations (with biconical boundary conditions) and provides a field perpendicular to the radial direction. As mentioned a coaxial waveguide is typically used to excite the antenna with the TEM mode but, for our purpose (38.3-38.6 GHz operating frequency range), we choose a WR28 rectangular waveguide, realizing a rectangular to circular transducer [5-6], in order to reduce the guide insertion loss.

In fig.5 a front and bottom view of the designed structure are presented.

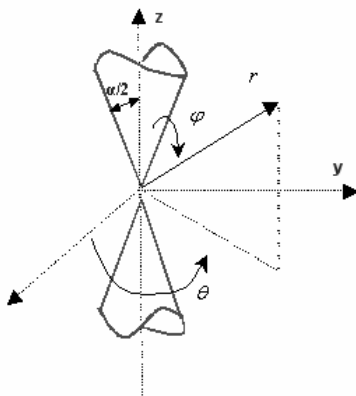


Figure 4: Ideal biconical antenna

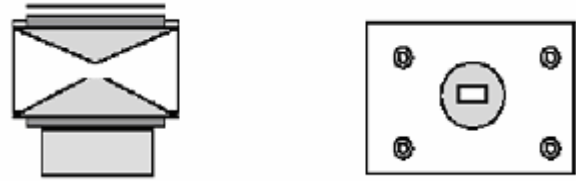


Figure 5: Front and top view of the designed antenna

The biconical antenna problem has been solved on a finite difference time domain grid in a cylindrical coordinate using Matlab [7-8]. Starting from the following expressions obtained by applying rotor operator to Maxwell equations in spherical coordinates:

$$\begin{aligned}
 (\nabla \times \vec{E})_t &= \frac{1}{r \sin \theta} \left[\frac{\partial}{\partial \theta} (E_\varphi \sin \theta) - \frac{\partial}{\partial \varphi} E_\theta \right] = -j\omega\mu_0 H_r \\
 (\nabla \times \vec{E})_\theta &= \frac{1}{r} \left[\frac{1}{\sin \theta} \frac{\partial}{\partial \varphi} E_r - \frac{\partial}{\partial r} (r E_\varphi) \right] = -j\omega\mu_0 H_\theta \\
 (\nabla \times \vec{E})_\varphi &= \frac{1}{r} \left[\frac{\partial}{\partial r} (r E_\theta) - \frac{\partial}{\partial \theta} E_r \right] = -j\omega\mu_0 H_\varphi
 \end{aligned} \tag{1}$$

due to the symmetry of the structure we have:

$$\begin{aligned}
 H_\varphi &= \frac{H_0}{\sin \theta} \frac{e^{-\beta r}}{r} \\
 E_\theta &= \eta_0 H_\varphi = \eta_0 \frac{H_0}{\sin \theta} \frac{e^{-\beta r}}{r}
 \end{aligned} \tag{2}$$

Of course, the structure shown in fig.4, with infinite cones dimension, is only an ideal one but non-idealities can be easily taken into account during the analysis. In particular great attention has been paid in considering corrective additional terms due to the insertion of the low dielectric constant material inserted between the cones in the way to support and insulate the antenna (and so the whole system) from the external environmental conditions.

Results:

In fig. 6, the photo of one antenna is shown. Fig. 7 shows the measured S_{11} , whereas in fig. 8 and fig. 9 the test bench of the measurements, carried out for the vertical and horizontal radiation pattern performed in anechoic chamber, is shown.



Figure 6: Biconical antennas sample

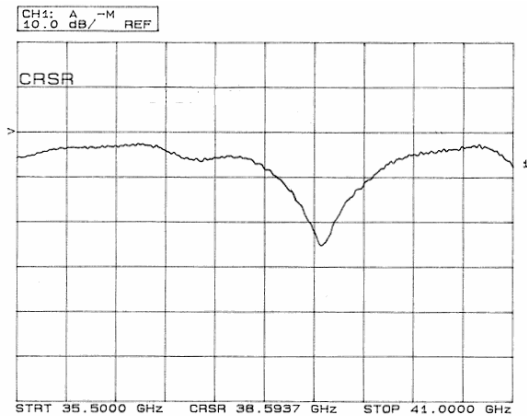


Figure 7: Measured S_{11}

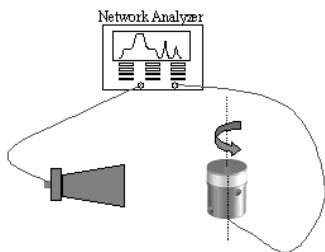


Figure 8: Test bench for the horizontal radiation pattern measurement

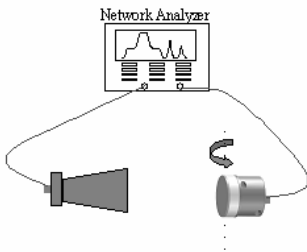


Figure 9: Test bench for the vertical radiation pattern measurement

Fig. 10 and fig. 11 show the measurement results for the vertical and horizontal radiation pattern respectively.

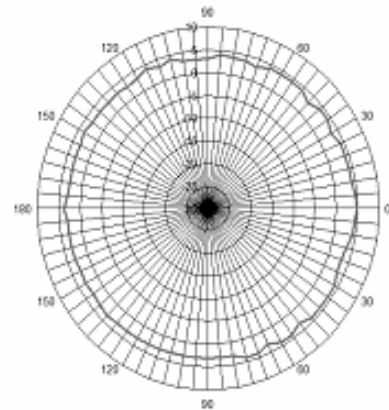


Figure 10: Measured horizontal radiation pattern

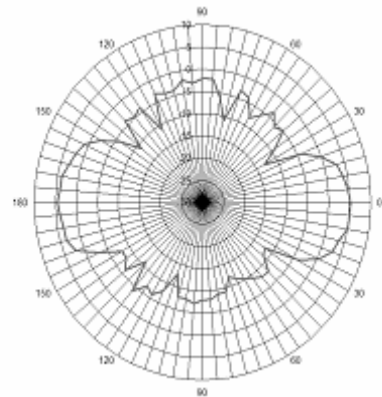


Figure 11: Measured vertical radiation pattern

IV. REALIZED ANTENNAS SYSTEM

As mentioned, the TX and RX antennas have been placed in different highness in order to achieve the best decoupling.

The RX antenna is the lower one (see fig. 3) in order to reduce the insertion loss between the antenna itself and the low noise amplifier placed inside the ODU.

Higher antenna's (TX antenna) performance are lightly modified by the RX antenna presence; its vertical and horizontal radiation pattern are almost unmodified concerning fig. 10 and fig. 11 results. As far as the RX antenna is concerned, it obviously suffers from a reduction of the radiated pattern gain in the direction of the higher one due to the presence of the waveguide that simultaneously feeds and supports the TX antenna itself. In fig. 12 the test bench for the

measurement of the horizontal radiation pattern of the two antennas placed on the ODU box is shown, whereas fig. 13 shows the new horizontal radiation pattern for the RX antenna.

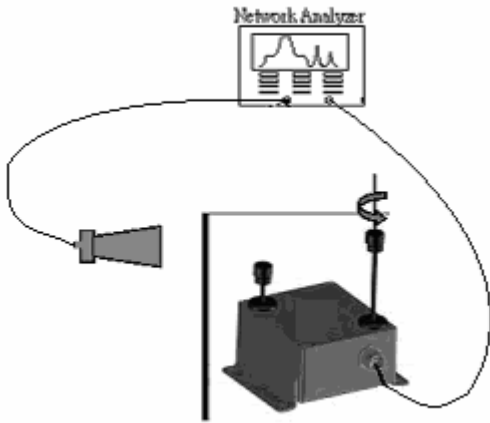


Figure 12: Test bench for the horizontal radiation pattern of

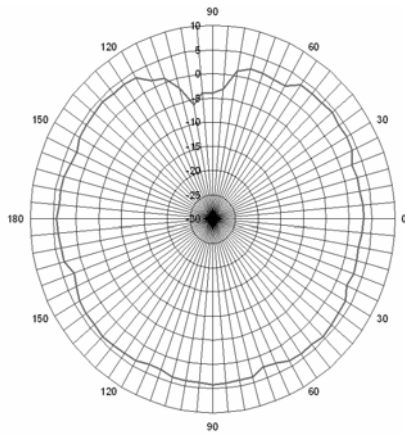


Figure 13: Measured horizontal radiation pattern for the RX antenna

V. CONCLUSION

In this paper, a biconical antennas system operating in a wideband TX/RX video and voice communications module has been presented. It is composed by two equal biconical antennas, operating in the 38.3-38.6 GHz frequency range, feeded through WR28 rectangular waveguide, performing respectively the TX and RX functionality. Measurement results, carried out in an anechoic chamber, have proven the excellent performance of the single antenna and the complete system.

ACKNOWLEDGMENT

This work has been carried out in Thales Italy Laboratory. The project is intended to provide a wireless network permitting data exchange, video and voice communications between mobile vehicles on the move.

REFERENCES

- [1] R. E. Collin. "Antennas and Radiowave Propagation". McGraw-Hill. 1985.
- [2] W. L. Stutzman and G. A. Thiele. "Antenna Theory and Design", Wiley, 1998.
- [3] S. A. Schelkunoif, "Advanced AntennaTheory." Wiley & Sons, Inc., New York, NY. 1952.
- [4] C. A. Balanis, "Antenna Theory." Harper & Row, Inc., New York, NY.1982.
- [5] B. N. Das, P. V. D. Somasekhar Rao, "Analysis of a Transition Between Rectangular and Circular Waveguides", IEEE Transactions on Microwave Theory And Techniques, vol. 39, no. 2, February 1991
- [6] P.H. Wolfert, "A wide-Band Rectangular-to-circular Mode Teansducer for Millimeter Waves", IEEE Transactions on Microwave Theory And Techniques, September 1963.
- [7] A. Tailove. "Computational Electrodynamics, The Finite-Difference Time Domain Method." Anech House. Inc.. Norwood, MA, 1995. pp. 203-225.
- [8] G.T. Roan, "Application of the FDTD Method to the Analysis of Biconical Antennas", Antennas and Propagation Society International Symposium, 1998. IEEE, Vol. 1, 21-26 June 1998 pp.:516 – 519.

A Fast Spectral Domain Approach for Analyzing Larger Structures Embedded in Multilayered Media

Thomas Vaupel¹, Thomas F. Eibert²

¹ FGAN-FHR, Neuenahrer Str. 20, 53343 Wachtberg, Germany, vaupel@fgan.de

² University of Stuttgart, Pfaffenwaldring 47, 70550 Stuttgart, eibert@ihf.uni-stuttgart.de

Abstract—This contribution presents a new kind of fast spectral domain method for the characterization of planar structures in multilayered media. It uses the well-known spectral domain Green’s function for multilayered media to construct a diagonalized translation operator on the Cartesian wavenumber plane. The bad convergence of the occurring spectral integrals is drastically improved by an adapted complex integration path deformation combined with enhanced Legendre-Filon and Laguerre quadrature techniques. Due to the use of diakoptic preconditioners, only a small number of iterations are required with the pertinent Krylov subspace solvers.

I. INTRODUCTION

A large class of structures like microstrip or combined slot/microstrip configurations can be modeled as so-called Planar-3D structures embedded within multilayered medias. The use of the method of moments (MoM) in combination with the Green’s function of the multilayered environment reduces the discretization effort to the strip and/or slot areas of the structure. However, due to the growing complexity of microwave circuits and antennas, the number of unknowns can easily become prohibitive, if standard MoM implementations are applied. To overcome the large computational effort of the standard MoM, different fast integral equation solvers for microstrip structures have been proposed. First implementations were based on a combination of the conjugate gradient method with the fast Fourier transform (CG-FFT) [1]. A further extension using the discrete complex-image technique for the characterization of the layered medium was presented in [2]. Other approaches make use of the adaptive integral method (AIM) for accelerating the matrix-vector products combined as well with the complex-image technique [3]. However, the numerical efficiency and accuracy of the complex-image technique strongly depends on the number of required complex images. Another approach employing a fast multipole method (FMM) can be found in [4] but is restricted to a thin grounded dielectric slab. In contrast to these methods, we present an approach completely based on the spectral domain Green’s function of the multilayered medium, which can be easily computed for arbitrary layer/metallization arrangements with the same numerical performance and accuracy.

II. FORMULATION

At first, the structure to be analyzed is decomposed into groups, which comprise typical components like couplers, patches, spiral inductors etc. (see Fig. 1).

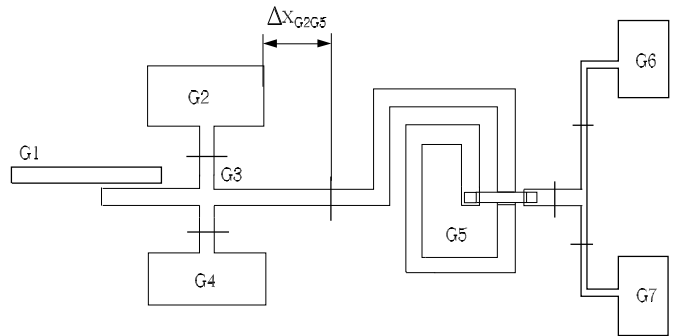


Fig. 1. Section of a typical microstrip structure with group decomposition and numbering.

If we concentrate on microstrip/stripline structures, we can use the surface impedance boundary condition on the metallizations

$$\vec{E}_s(x, y)|_{tan} = Z_F(x, y) \vec{J}_e(x, y) + \vec{E}_i(x, y)|_{tan}, \quad (1)$$

to formulate an integral equation for the surface currents in the spectral domain:

$$\frac{1}{4\pi^2} \int \int_{k_y, k_x} \overset{\leftrightarrow}{G}_J^E(k_x, k_y) \cdot \vec{J}_e(k_x, k_y) e^{jk_x x + jk_y y} dk_x dk_y |_{tan} = Z_F(x, y) \vec{J}_e(x, y) + \vec{E}_i(x, y)|_{tan}, \quad (2)$$

where $\overset{\leftrightarrow}{G}_J^E(k_x, k_y)$, $\vec{J}_e(k_x, k_y)$ and Z_F are the Fourier transforms of the Green’s function, the surface currents and the surface impedance, respectively.

The currents are discretized with subdomain basis functions by

$$\vec{J}_e(x, y) = \sum_{m=1}^N I_m \vec{f}_m(x, y). \quad (3)$$

Afterwards, the integral equation is solved using the Galerkin testing procedure, i.e. eq.(2) is multiplied with the basis functions itself and subsequent integration over these test

functions \vec{f}_n :

$$\int_x \int_y \vec{f}_n(x, y) \cdot \vec{E}_s(x, y) dx dy = \int_{k_y} \int_{k_x} [\vec{T}_{gg'}(k_x, k_y) \cdot \vec{F}_m(k_x, k_y)] \cdot \vec{F}_n^*(k_x, k_y) dk_x dk_y \quad (4)$$

introducing a spectral domain translation operator

$$\vec{T}_{gg'}(k_x, k_y) = \vec{G}_J \xrightarrow{E} (k_x, k_y) e^{jk_x(x_g - x_{g'})} e^{jk_y(y_g - y_{g'})} \quad (5)$$

and

$$\vec{F}_m(k_x, k_y) = \int_x \int_y \vec{f}_m(x, y) e^{jk_x(x_{g'} - x)} e^{jk_y(y_{g'} - y)} dx dy \quad (6)$$

the Fourier transform of the expansion function \vec{f}_m related to the group center $\vec{\rho}_{g'} = (x_{g'}, y_{g'})$ near this expansion function. Analogously $\vec{F}_n(k_x, k_y)$ is the Fourier transform of the test function \vec{f}_n related to the group center $\vec{\rho}_g = (x_g, y_g)$ near this test function.

The translation operator eq.(5) is used to construct a fast integral equation solver similar as in standard fast multipole methods (FMM).

However, if we carry out the spectral domain integrations eq.(4) using standard quadrature techniques with real wavenumbers k_x and k_y , significant convergence problems occur due to integrand singularities, a slow decay and an oscillatory behavior of the integrands.

To overcome these problems, we apply on one hand adaptive complex integration path deformations as depicted in Fig. 2, demonstrated here for the k_x wavenumber plane.

In the case, that $|\text{Re}\{k_y\}| < k_i$ (Fig. 2 a)), possible integrand singularities as poles due to guided waves and branchpoints are located near the real axis. They are circumvented by the sketched rectangular integration path in the first and third quadrant. This path is simultaneously used for the k_y -wavenumber. In the case $|\text{Re}\{k_y\}| > k_i$ (Fig. 2 b)), the integrand singularities are migrated on the imaginary axis, a circumvention is not necessary any more, thus an integration path remaining on the real axis for $|\text{Re}\{k_x\}| < k_i$ is used and as well for the k_y wavenumber.

The choice for the path $|k_x| \rightarrow \infty$ depends on the lateral separation between the source and the observation group. If the separation in x-direction is larger, i.e. $|x_{g'} - x_g| > |y_{g'} - y_g|$, the integration path for k_x is directed parallel to the imaginary axis in the third and fourth quadrant of the complex wavenumber plane, whereas for k_y the integration path is directed on the real axis for $|k_y| > k_i$ and vice versa for the case $|x_{g'} - x_g| < |y_{g'} - y_g|$. If the groups do not overlap (fulfilled for group interactions out of the near-zone), we get an exponential decay of the integrand $\sim e^{-k'_u \Delta u_{gg'}}$, ($k_u = k'_u + jk''_u$, $u = x$ or y), on the path sections parallel to the imaginary axis. $\Delta u_{gg'}$ denotes the lateral non-overlapping separation between the groups (see example in Fig.1 for group 2 and 5). If we want to use the same integration points for all group interactions,

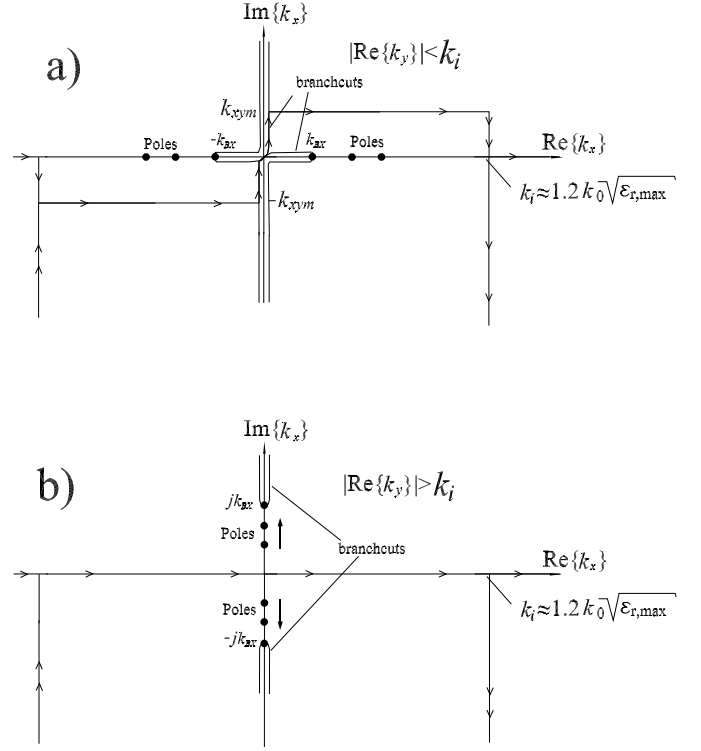


Fig. 2. Integration path deformation demonstrated for the k_x wavenumber plane.

a problem occurs due to the different exponential decay rates. If we choose the integration points with regard to a relatively small exponential decay, the integrand is not properly sampled in case of a fast exponential decay in context with group interactions with large lateral separations. To overcome this problem, we relate on the smallest group distance appearing in the group constellation. Group interactions with this group distance are then integrated with a corresponding Laguerre quadrature and integration points. If we have a group interaction with a faster exponential decay, we multiply the integrand with a corresponding increasing exponential to get the same decay as for the smallest group distance. To account for this multiplication, we compute extended Laguerre integration weights by a variational approach providing a small linear system of equations for the weights.

For the other wavenumber with the integration path on the real axis we have an oscillatory behavior depending on the group center distances $\sim e^{jk'_u |u_{g'} - u_g|}$. To compensate these oscillations, the integrand is multiplied with the pertinent exponential with opposite sign in the exponent $e^{-jk'_u |u_{g'} - u_g|}$. This compensative multiplication is then accounted for with adaptive integration weights provided by a Legendre-Filon quadrature we presented in [6]. The interactions between groups in the near-zone must be evaluated directly by computing the matrix entries of the standard MoM. In this context it is mentionable, that the outlined integration techniques can also be applied for the computation of the standard MoM matrix

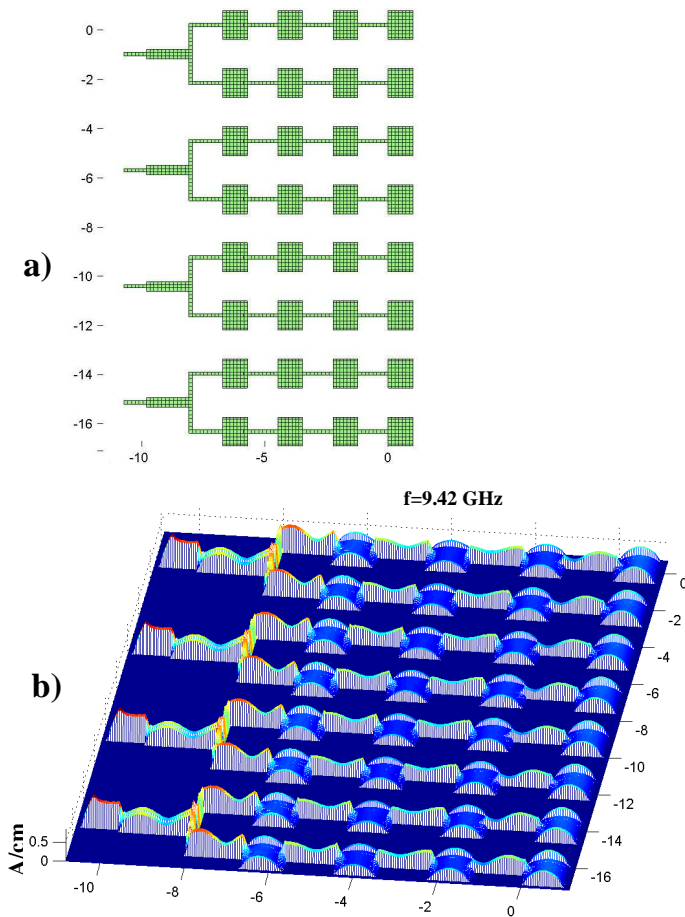


Fig. 3. Discretization and current distribution of a 32-element microstrip patch antenna array. Dimensions in cm.

entries with high accuracy, if the participated basis functions do not overlap.

The storage complexity of the described fast spectral domain approach amounts to $O(N)$, whereas the complexity for the evaluation of the matrix-vector products reaches $O(N^{1.5})$ with an optimized group size.

III. RESULTS

As first structure we consider a 32 element microstrip antenna array consisting of four subarrays with feeding network ($\epsilon_r = 2.2$, $h = 1.59$ mm). Fig. 3 a) shows the structure geometry and the discretization with 4200 unknowns. The structure was decomposed into 42 groups. Using our diakoptic preconditioning technique [7], only three iterations are necessary with a conjugate gradient solver for 1 percent residual error. If we use a generalized minimum residual solver (GMRES), only two iterations are required.

Together with the outlined fast spectral domain method for the computation of the matrix-vector products, less than 40 seconds are needed for the overall solution (3 GHz AMD PC). The current distribution of the array ($f=9.42$ GHz) is given in Fig. 3 b).

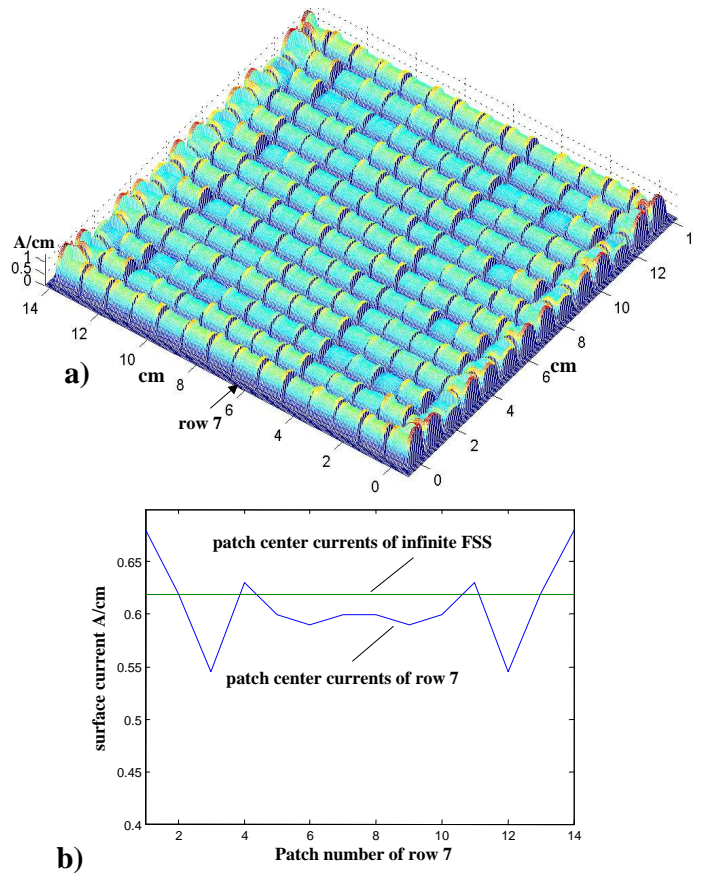


Fig. 4. Current distribution on a FSS-structure with 14×14 patches.

As second example we have analyzed a finite frequency selective surface (FSS) comprising 14×14 patches mounted on a dielectric slab with thickness 1.59 mm ($\epsilon_r = 2.2$). The patch dimensions are 9.6 mm, the periodicity in both directions is 10.4 mm. Fig. 4 a) shows the current distribution on the FSS resulting from an excitation with a plane wave (perpendicular incidence, 100 V/cm at 10 GHz, x-directed polarization) and a structure discretization with 11700 unknowns. Fig. 4 b) shows the center currents of the patches in row 7 compared with the solution of an FSS with infinite lateral extension, computed using the Floquet theorem [8]. We can observe a good agreement particularly for the center patches of the structure. Due to the strong couplings between the patches and the resonant behavior, 15 iterations are necessary using GMRES and an extended diakoptic preconditioning with an overall solution time of ≈ 50 min. This decreased performance is also due to a not yet optimized group size in this case.

IV. CONCLUSION

This contribution has introduced a new kind of fast spectral domain solver for the characterization of larger microwave structures embedded in arbitrary multilayered media. It reaches a storage complexity of $\approx O(N)$ and a complexity of $O(N^{1.5})$ for the matrix-vector product evaluation using an optimized group size. Together with diakoptic preconditioning

techniques, a fast convergence of the pertinent Krylov subspace solvers is achieved. Due to adaptive integration path deformations and enhanced integration techniques like higher-order Legendre-Filon and extended Laguerre quadrature rules, the discretization effort for the Cartesian wavenumber plane can be drastically reduced. The performance of the matrix-vector product evaluation can be still significantly improved by e.g. further optimized integration path deformations, the neglect of evanescent wave contributions and a multilevel approach.

REFERENCES

- [1] M. F. Catedra, J. G. Cuevas, L. Nuno, "A Scheme to Analyze Conducting Plates of Resonant Size Using the Conjugate-Gradient Method and the Fast Fourier Transform, *IEEE Trans. Antennas Propagat.*, Vol. 36, No. 12, pp. 1744–1752, Dec. 1988.
- [2] Y. Zhuang, K.-L. Wu, C. Wu, J. Litva, "A Combined Full-Wave CG-FFT Method for Rigorous Analysis of Large Microstrip Antenna Arrays," *IEEE Trans. Antennas Propagat.*, Vol. 44, No. 1, pp. 102–109, Jan. 1996.
- [3] F. Ling, C.-F. Wang, J.-M. Jin, "An Efficient Algorithm for Analyzing Large-Scale Microstrip Structures Using Adaptive Integral Method Combined with Discrete Complex-Image Method", *IEEE Trans. Microwave Theory Tech.*, Vol. 48, pp. 832-838, May 2000.
- [4] J.-S. Zhao, W. C. Chew, C.-C. Lu, E. Michielssen, J. Song., "Thin-Stratified Medium Fast-Multipole Algorithm for Solving Microstrip Structures", *IEEE Trans. Microwave Theory Tech.*, Vol. 46, No. 4, pp. 395–403, April 1998.
- [5] Vaupel, T., Hansen, V., Schäfer, F., "Radiation Efficiency Analysis of Submm-Wave Receivers Based on a Modified Spectral Domain Technique", *Radio Science*, Vol. 38, NO. 4, pp. 13-1–11, August 2003.
- [6] Vaupel, T., Eibert, T. F., Hansen, V., "Spectral domain analysis of large (M)MIC-structures using novel quadrature methods", *Int. Journal of Num. Modelling: Electronic Networks, Devices and Fields*, Jan./Febr. 2005, pp. 23–38.
- [7] Vaupel, T., Eibert, T. F., Hansen, V., "Diakoptic Basis Function Grouping Techniques Applied to the Method of Moment Solution of (M)MIC-Structures", *IEEE AP Symposium Digest 2003*, Columbus, Ohio, Vol. 2, pp. 1059–1062.
- [8] Aroudaki, H., Gemünd, H.-P., Kreysa, E., "Analysis of Low-Pass Filters Consisting of Multiple Stacked FSS's of Different Periodicities with Applications in the Submillimeter Radioastronomy", *IEEE Trans. Antennas Propagat.*, Vol. 43, No. 12, pp. 1486–1491, 1995.

Analysis of Modes in Rectangular-Waveguide Noncontacting Shorting Plunger

Vladimir BILIK, Jan BEZEK

Slovak University of Technology, Faculty of Electrical Engineering and Information Technology, Ilkovicova 3, 81219 Bratislava, Slovakia. Phone +421-2-60291455, E-mail: vladimir.bilik@stuba.sk.

Short Abstract—Modes propagating and resonating in a structure consisting of a section of R26 rectangular waveguide that houses a noncontacting brick-shaped shorting plunger have been analyzed with the assistance of an electromagnetic field solver. Effects of plunger waggle have also been investigated. Spurious resonances of modes trapped within the plunger-filled section deteriorate the short performance. The analysis serves as a preliminary work in an attempt to design a resonance-free noncontacting sliding short.

Keywords—noncontacting backshort; sliding short; waveguide components; industrial applications

I. INTRODUCTION

The sliding waveguide short is a useful and frequently utilized component in high-power industrial microwave installations. Contacting plungers have obvious disadvantages in wear and unreliable contact with the main waveguide, whereas the use of noncontacting shorts has been hindered by the existence of resonant dips in reflection coefficient within the operating frequency range. An overview of sliding shorts and problems associated with them can be found e.g. in [1]. The spurious resonances may be “stubborn” in the sense that they cannot be removed by for instance changing the plunger length or incorporating a standard microwave choke. The reflection dips are accompanied by peaks in transmission behind the shorting block, directing a substantial portion of the microwave power into a short-motion mechanism (which may lead to its damage) or into the environment (presenting health hazard). The resonances are caused by modes that can propagate within the plunger-filled waveguide section [2]. The excitation of the modes depends on the plunger offset and rotation from its ideally centered position (waggle). An experiment-based investigation for a specific, millimeter-wave case was undertaken in [2]. No effective software tools were available at the time to address the subject otherwise. The present analysis has been carried out in order to better understand the nature of these resonances and will serve as a starting point for the design of a high-power resonance-free waggle-tolerant noncontacting sliding short. The investigations have been fundamentally assisted by a full-wave electromagnetic field simulator (CST Microwave Studio [3]). The paper objectives are:

- To classify modes of electromagnetic waves that can exist in the plunger-filled waveguide.

- To discuss the modes that can propagate in 2 – 3 GHz band.
- To present their basic field distribution and give their cutoff frequencies as well as conversion coefficients from the TE_{10} mode in an empty waveguide.
- To investigate effects of plunger waggle.
- To analyze and discuss resonances that fall into 2 – 3 GHz band and draw some general conclusions.
- To discuss the behavior of a conventional microwave choke.

II. ANALYZED STRUCTURE

The analyzed structure (Fig. 1) consists of a brick-shaped perfectly conducting plunger of length L placed in a section of R26 waveguide (cross-sectional dimensions $a = 86.36$ mm, $b = 43.18$ mm). Ideally, the plunger sides are parallel with the waveguide walls and the plunger is cross-sectionally centered so that the gap between it and all guide walls is equally $s = 2$ mm.

A slightly modified structure with a semi-infinite plunger has been used for the analysis of propagating modes and their excitation by empty-guide TE_{10} : one plunger face has been extended up to the guide end, thus forming a section of TEM

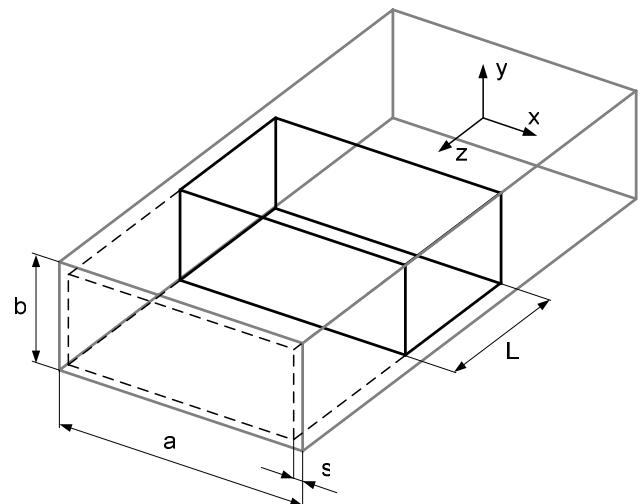


Figure 1. Analyzed structure.

transmission line with TEM output (dashed line in Fig. 1). To simulate wobble, the ideal plunger position was perturbed by x - and y -direction offsets of $x_0 = 0.5$ mm and $y_0 = 0.5$ mm, respectively, and a rotation around the guide z -axis by $\alpha_z = \pm 0.5^\circ$. All the combinations have been considered.

III. MODES IN PLUNGER-FILLED WAVEGUIDE

In direct analogy with a cylindrical coaxial transmission line [4] having the gap thickness s and the mean gap circumference $d = 2(a + b) - 4s$ equal to those of the plunger-filled waveguide, the modes existing in the waveguide can be under a small-gap assumption ($s \ll d$) categorized as follows:

- TEM mode;
- Low-frequency TE modes;
- High-frequency TE modes;
- TM modes.

A. TEM mode

The TEM mode has zero cutoff frequency: once excited, it can propagate in the structure.

B. Low-Frequency TE Modes

The low-frequency TE modes have the cutoff wavelengths given approximately by

$$\lambda_c \approx d/m, \quad m = 1, 2, \dots \quad (1)$$

The formula implies that a multiple (m) of free-space wavelengths must fit in the gap circumference at cutoff frequency f_c . The modes will be designated TE_{m0} . The second subscript (0) reflects the fact that the field varies slowly in radial direction (no oscillatory character with half-wavelength periodicity). Since d is comparable to the main guide dimensions a , b , several such modes can propagate in the frequency range of interest.

For each m there are actually two TE_{m0} modes: their field patterns appear “rotated” around the guide’s z -axis by $90/m$ degrees, and their cutoff frequencies are close to each other. This is again analogous to the higher-order modes in a coaxial line where two axially rotated but otherwise identical degenerate modes account for all possible polarizations. We will distinguish the members of such mode couple by additional letters a , b : TEa_{m0} and TEb_{m0} .

C. High-Frequency TE Modes and TM Modes

The high-frequency TE modes as well as (all) TM modes have cutoff wavelengths given approximately by

$$\lambda_c \approx 2s/n, \quad n = 1, 2, \dots \quad (2)$$

The modes are oscillatory in radial direction in that n free-space half-wavelengths fit in the gap thickness s at cutoff frequency. For millimeter-wide gaps this implies cutoff

frequencies in millimeter-wave range (hence the designation high-frequency modes). The modes are therefore insignificant in the studied context.

D. Basic Mode Properties

Accurate values of f_c as well as field patterns and conversion coefficients from the empty-guide TE_{10} mode have been obtained by the electromagnetic simulator. The results have revealed that besides TEM, up to four TE modes can propagate in the plunger-filled section. Their E-field patterns (except the obvious TEM) are illustrated in Fig. 2; a summary of their basic properties is given in Table I. The quantities marked *ideal* correspond to ideal plunger position, the quantities with subscripts *min* and *max* are limits for the plunger position perturbed (waggled) in the manner specified above. The cutoff frequencies vary by more than 50 MHz when the plunger is waggled. For TE_{20} modes, f_c are close to or within the ISM band (2.4 – 2.5 GHz), which is the source of the problems, as will be explained below.

TABLE I. PROPAGATING MODE PROPERTIES

Quantity	TEM	TEa ₁₀	TEb ₁₀	TEa ₂₀	TEb ₂₀
f_c (GHz) – ideal	0	1.198	1.206	2.396	2.411
$f_{c \text{ min}}$ (GHz)	0	1.138	1.190	2.340	2.395
$f_{c \text{ max}}$ (GHz)	0	1.203	1.263	2.402	2.452
Δf_c (MHz)	0	65	73	62	57
C (dB) – ideal	-	-6.3	-	-	-
C_{max} (dB)	-30.8	-6.0	-8.3	-16.2	-16.2

C is conversion coefficient from empty-guide TE_{10} mode at 2.45 GHz. In case of ideal plunger position, only TEa_{10} mode, whose field pattern conforms that of TE_{10} , is excited – strongly. (A consequence is that a potential choke should be designed for this mode rather than for the intuitively preferred TEM.) However, when perturbing the plunger position, mode symmetries evident in Fig. 2 will be lost, and more or even all of the modes will be excited. C_{max} is the maximum conversion coefficient in the frequency range 2 – 3 GHz for all the plunger offset and rotation combinations. Considering this, a choke design becomes ambiguous, if only due to differing

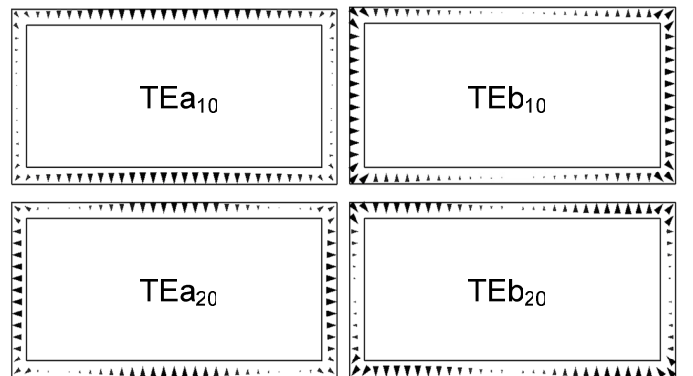


Figure 2. E-field of propagating TE modes in the plunger-filled guide.

wavelengths of the individual modes.

E. Surface Currents

Fig. 3 shows “snapshots” of longitudinal magnetic field components H_z of the propagating TE modes. Dark and white areas mark the locations of maximum field strength (with opposite polarities of H_z). With time, the patterns move along the waveguide axis. The importance of H_z lies in the fact that it is proportional to *transverse* surface currents. Suppressing these currents e.g. by longitudinal slots made at their maxima

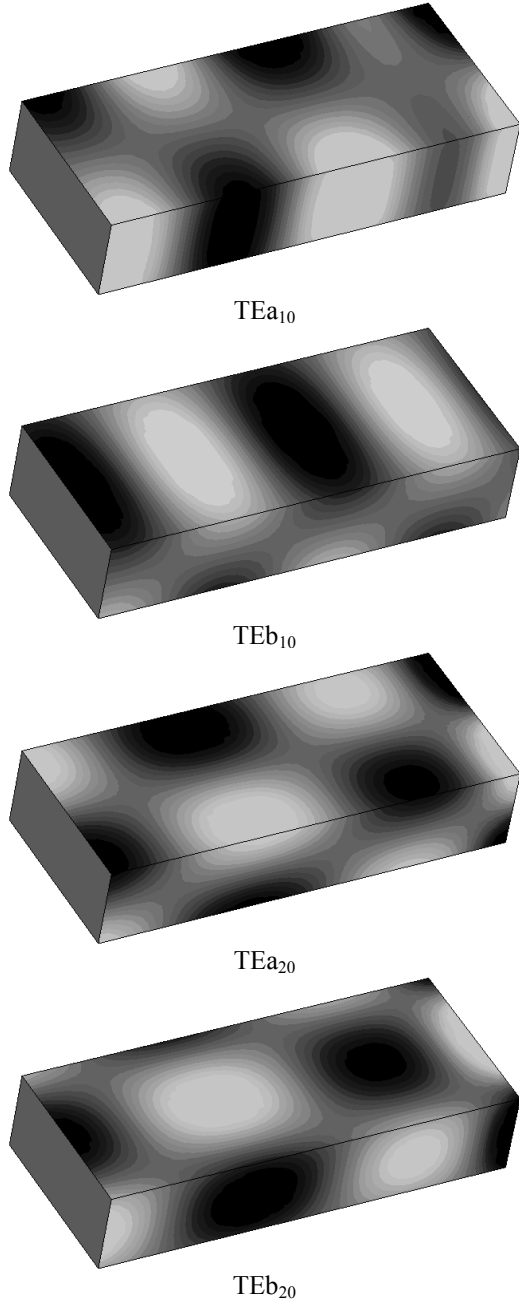


Figure 3. Longitudinal magnetic field component H_z .

can provide a method of how to suppress or influence the TE mode patterns without much affecting the TEM mode.

IV. PLUNGER RESONANCES

Modes of propagation trapped in the plunger-filled waveguide portion of Fig. 1 give rise to resonances that exhibit themselves as peaks/dips in the frequency response of transmission coefficient magnitude $|S_{21}|$. Except the modes independent of the plunger length L (those will be treated separately) the plunger-filled waveguide section can be approximately viewed as a transmission line almost open-ended at both sides, effectively longer than L by an amount ΔL due to fringing fields evanescent in the empty guide. In view of this, relation between a resonance frequency f_r and cutoff frequency f_c of an ideally positioned plunger can be approximated by

$$f_r^2 = f_c^2 + c^2 \left[\frac{p}{2(L + \Delta L)} \right]^2 \quad p = 1, 2, \dots \quad (3)$$

where c is light velocity and ΔL is the length correction factor. The subscript p will be added to the resonance mode designations (TEM_p , TEa_{m0p} , TEb_{m0p}).

In order to investigate the resonances, a plunger of length $L = 50$ mm has been simulated. Unlike the previous study of propagating modes, when the structure had to be (piecewise) homogeneous in z -direction, the plunger position could now be additionally perturbed by swaying it around the x - and y -axes (angles $\alpha_x = \pm 0.5^\circ$, $\alpha_y = \pm 0.5^\circ$ have been used in the computations).

Examples of $|S_{21}|$ for the plunger in the ideal position (thin curve) and the plunger offset by 0.5 mm simultaneously in x - and y -directions (thick curve) are shown in Fig. 4. (Rotating the plunger does not qualitatively affect the situation.)

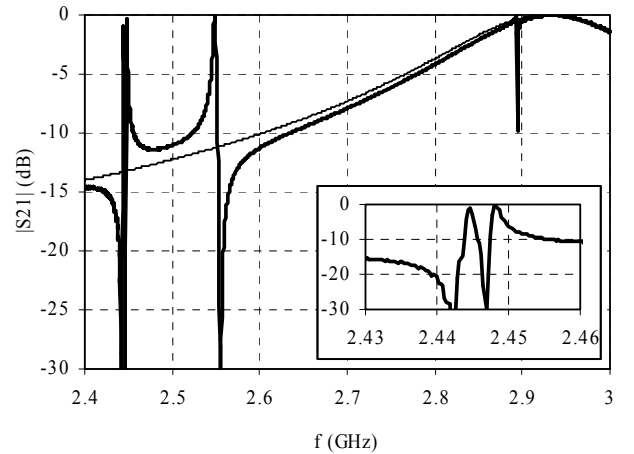


Figure 4. Transmission coefficient for ideal (thin curve) and perturbed (thick curve) plunger position.

A. Modes Dependent on Plunger Length

The case with the ideally positioned plunger exhibits only one, broad (due to the strong coupling) peak located at 2.925 GHz. It corresponds to the only excited mode, $TE_{a_{10}}$, resonating so that approximately one half of the standing wavelength is distributed along the plunger length ($p = 1$). The mode designation is therefore $TE_{a_{101}}$. Offsetting the plunger preserves this main peak but gives rise to four additional peaks of nearly total transmission. The one with the highest frequency (2.88 GHz) corresponds to the twin mode $TE_{b_{101}}$. (The peak is narrow because in this particular case the coupling to empty guide is weak – about -35 dB.)

The resonance located at 2.54 GHz is TEM with $p = 1$ (TEM_1).

Varying the plunger length necessarily varies the resonant frequency of each of the above three modes: by proper choice of L the peaks can be moved outside of the operating range.

B. Modes Independent of Plunger Length

The two closely spaced peaks located at 2.445 GHz and 2.448 GHz (see the inset in Fig. 4) correspond to resonance modes $TE_{a_{200}}$ and $TE_{b_{200}}$, respectively ($p=0$). In contrast to the previous cases, their field amplitude *does not* oscillate along the plunger length. The standing wave pattern can be imagined as set up from two opposite TEM waves, nearly uniform along z -direction, traveling circumferentially around the plunger, the plunger being terminated by imperfect magnetic walls at its ends. In case of perfect magnetic walls (ideal open circuits) the resonance frequencies would truly be independent of the plunger length L and (3) could be used with $p=0$. The reality is better approximated by

$$f_r^2 = f_c^2 + \left(\frac{c\delta}{2L}\right)^2 \quad (4)$$

where $\delta < 1$ is a correction factor accounting for the fringing-field effects. In our case, the equation is applicable for $L \geq 30$ mm. Since a typical value of δ is 0.01, the resonant frequencies depend only little on plunger length, nearly coinciding with the cutoff frequencies f_c .

Although derived for a specific case of R26 waveguide, these conclusions are valid quite generally. Incidentally and unfortunately, it is just the R26 waveguide for which these “obstinate” resonances fall exactly into the 2.45 GHz ISM band. Varying the gap thickness (the only parameter available) makes little sense due to its limited effect on f_c .

C. Microwave Choke

To attenuate an unwanted wave, a microwave choke can be embedded in the plunger as shown in Fig. 5. It is in principle a band-stop filter implemented as a series-connected short-ended transmission line section one quarter-wavelength long, transforming the terminating short to an open at its input. The “wavelength” here means the choke interior guide wavelength of the mode to be suppressed. Such choke can therefore suppress only one of the modes (more if their wavelengths are

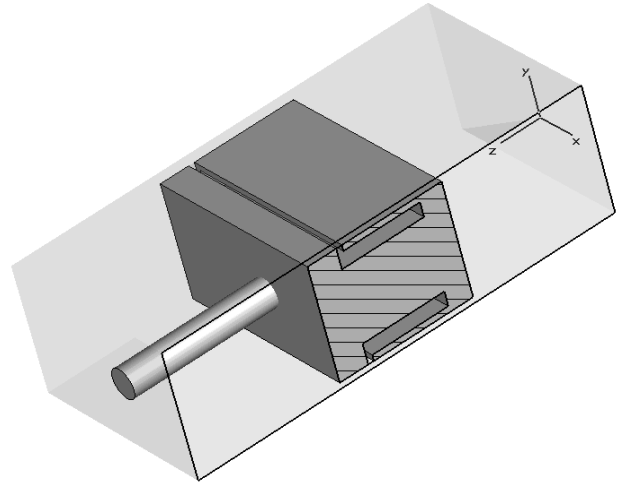


Figure 5. Shorting plunger incorporating a microwave choke.

close). This is nominally the case of a plunger in an ideal position, when only $TE_{a_{10}}$ is excited. When the tuner is waggled and up to five modes can be excited, the choke will also attenuate the twin $TE_{a_{10}}$ mode. It will not suppress the TEM but this mode’s resonance can be tuned out by properly choosing the plunger length L ; the remnant off-resonance TEM leakage in the operating band can be tolerable.

However, such choke will by no means suppress the $TE_{a_{20}}$ and $TE_{b_{20}}$ modes. It is because close to f_c the guide wavelength approaches infinity: any choke with a practical length transforms the terminating short to a short again, making thus the choke electrically nonexistent. These two modes, which could neither be tuned out by plunger length nor suppressed by a choke, constitute the main obstacle in designing a good noncontacting short. Ways to cope with the problem are yet to be found. A possible solution may lie in suppressing the TE modes by blocking their transverse surface currents by introducing longitudinal slots in the plunger surface, and tuning the choke for the only remaining TEM mode.

V. CONCLUSIONS

With the assistance of an electromagnetic field simulator, modes of propagation and resonances in an R26 waveguide loaded with a noncontacting rectangular shorting block have been analyzed, and some general conclusions have been drawn. Two resonances, designated $TE_{a_{200}}$ and $TE_{b_{200}}$, excited when the plunger is not strictly centered in the waveguide, have been found critical for the short performance. The resonances can neither be tuned out by changing the plunger length nor suppressed by a conventional choke because the resonant frequencies are practically fixed at cutoff frequencies of the corresponding modes of propagation, which for R26 waveguide incidentally fall into the 2.45 GHz ISM band. The analysis has helped to properly understand the nature of the problem and is believed to be a starting point to its solution.

REFERENCES

- [1] V. S. Möttönen, Receiver front-end circuits and components for millimetre and submillimetre wavelengths, PhD Thesis, Helsinki University of Technology, April 2005, ISBN 951-22-7615-1, pp. 20-23.
- [2] A. R. Kerr, "An adjustable short-circuit for millimeter waveguides," Electronics Division Internal Report No. 280, National Radio Astronomy Observatory, VA, USA, 1988.
- [3] Computer Simulation Technology, Darmstadt, Germany: CST Microwave Studio 2006. <http://www.cst.com>.
- [4] V. Tysl and V. Ruzicka, Theoretical foundations for microwave engineering, 1st ed., Prague: SNTL, 1989, ISBN 80-03-00141-2, pp. 111-121 [in Czech].

Modified M-Sequence UWB-Radar

J. Sachs¹, R. Herrmann¹, M. Kmec¹, P. Peyer^{1,2}

¹Technische Universität Ilmenau, Institut für Informationstechnik, Helmholtzplatz 2, 98693 Ilmenau
+49 3677 69 2623 juergen.sachs@tu-ilmenau.de

²MEODAT GmbH, Werner-von-Siemens-Straße 3, 98683 Ilmenau,
+49 3677 466 290 info@meodat.de

Short Abstract — This article demonstrates some improvements of a basic M-Sequence approach for ultra wideband (UWB) high resolution radar. These improvements consist of the enhancement of equivalent sampling rate and an improvement of the overall measurement bandwidth. The presented method permits the omission of RF anti-aliasing filters, which drastically increases the operational flexibility of the radar.

Keywords - ultra wideband; M-Sequence; sub-sampling; high resolution radar

I. INTRODUCTION

The goal of UWB radar is to provide the impulse response function (IRF) of a scenario under test. The quality of a measured IRF is mainly determined by the ability to separate closely located peaks and to avoid masking of smaller peaks due to noise or saturation effects caused by larger peaks. The first problem is a question of available bandwidth and the second one depends on the dynamic range of the receiver and transmitted power.

The classical UWB approach is based on impulse excitation, which implies that the whole transmission chain is burdened with high peak power shocks. Mainly analogue circuits tend to overload or saturate in such cases. Thus, the system performance degrades. In order to stress the electronics evenly, one is recommended to use continuous wideband signals. Typical examples of such signals are swept or stepped sine waves [1], [2], random noise [3], [4], [5], pseudo-noise (PN)-sequences, or others. However, this kind of target stimulation will not provide the IRF directly. It rather requires an appropriate impulse compression technique (i.e. Fourier Transform, correlation, or matched filtering), which is often the challenge for the different system concepts. After impulse compression, the even energy distribution of the signals is lost in order to form short impulses. Thus, the best one can do, is to carry out impulse compression in the digital domain. Digital dynamic range is only limited by the utilized number format, which usually can be selected freely.

A new UWB concept dealing with continuous wave excitation, a largely reduced analogue circuit part and a minimum of components was first introduced in 1999 [6]. It provides M-Sequence signals to stimulate the test objects. This original approach forms the basis for different extensions and improvements. At the current stage of development, the basic M-sequence modules can operate up to 7.5 GHz measurement bandwidth. Typical application covers the band from nearly DC to about 4 ... 5 GHz. A first modification was introduced

by adding an up-down conversion in order to shift the operational band to an arbitrary frequency band (e.g. 3 ... 10 GHz [7], [8] or 57 ... 63 GHz [9]). The goal of this article is to introduce a further modification, which greatly improves the operational flexibility and basically triples the useable bandwidth of the basic module.

After a short summary of the basic M-Sequence concept, the introduced modifications will be explained and their effect will be demonstrated. Finally, some measurement results from an experimental system will be shown.

II. BASIC M-SEQUENCE CONCEPT

Fig. 1 represents the basic configuration of an M-Sequence radar. For a detailed description of the working principle, the reader is referred to [10]. Here, only a short summary will be given: a single tone RF-clock pushes a shift register, which provides the stimulus signal, and a binary divider, which controls data acquisition. The shift register generates a PN-sequence defined by its internal feedback structure. An M-Sequence is a good choice in order to get a stimulus with a very short and clear auto-correlation function. Since PN-sequences are of periodic nature, data acquisition can be undertaken by means of a sub-sampling technique, which drastically reduces the technical requirements of the receiver electronics. An M-Sequence is composed of 2^m-1 chips and the binary divider takes care that after 2^m signal periods, one data sample has been taken from every chip of the sequence. This corresponds to an equivalent sampling rate of f_c , which results in a usable bandwidth from dc to $f_c/2$ according to the sampling theorem. The M-Sequence contains about 80% of its total energy within this band.

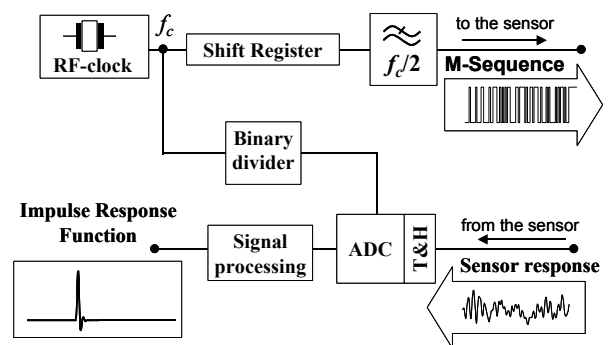


Figure 1. Basic M-Sequence concept using digital impulse compression.

Thus, from an energetic point of view, an increased equivalent sampling rate (i.e. higher receiver bandwidth) will only gain a small performance improvement since the captured noise power will dominate increasingly over the signal. Impulse compression after signal acquisition is undertaken either by Fast Hadamard Transform (i.e. a cross correlation referring to the ideal M-Sequence) or by Fast Fourier Transform. In this case a reference channel collects the actual transmitted waveform. The Fast Fourier Transform is more time consuming than the Fast Hadamard Transform, since the number of data points is not a power of 2. In the case

of the M-Sequence of the orders 6, 8, and 12, the performance degradation is, however, quite low [11].

The key features of the minimal configuration as shown in Fig.1 are excellent time stability and linearity of the time axis (note, the timing control exclusively deals with steep slopes and a stable single tone RF-oscillator) and all analogue signals exhibit low signal levels, which promotes an integration in a low-cost semi-conductor technology such as the SiGe-process.

By selecting the RF-clock rate, the bandwidth of the radar system can be matched to the actual needs, which already provides for great flexibility in its application. However, residual spectral power components of the M-Sequence are still to be found beyond $f_c/2$ making it necessary to use an anti-aliasing filter in order to satisfy the sampling theorem. In practice, this requires new filter designs every time the clock rate is changed and it will not be possible to arbitrarily change the RF-clock, i.e. in order to reduce interference and interception. In what follows, it will be shown how to avoid this inadequacy.

III. INCREASING THE EQUIVALENT SAMPLING RATE

In order to be able to waive the anti-aliasing filter, natural frequency limiting effects, namely the final bandwidth of the sampling circuit and the generated M-Sequence, need to guarantee satisfaction of the sampling theorem. However, their bandwidth is usually far beyond $f_c/2$, particularly if one recalls that the considered cutoff cannot be a 3dB-point, rather the signal must be damped down to the actual noise level, e.g. -60 dB ... -100 dB depending on the averaging number.

As a result, without an appropriate filter, the equivalent sampling rate must be largely increased. Or in others words,

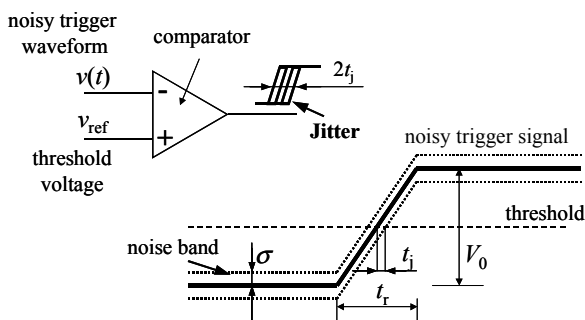


Figure 2. Generation of time instabilities, i.e. jitter or drift, by triggering with noisy ramps. Note, that variations of the trigger level result in the same effect as a perturbed waveform.

one has to take more than only one sample from each chip of the M-Sequence as in the basic system. For that purpose, either a controllable phase shifter can be inserted in the clock line before the binary divider or a steerable (pulse) delay circuit after the binary divider can be used to additionally retard the sampling clock. In both cases, the maximum variation of the additional delay is restricted to the length of one M-Sequence chip $\Delta t_{\max} = 1/f_c$. Since the number of necessary delay steps is also quite limited (usually less than 10), numerous circuit concepts can be employed, i.e. switched lines, stacked gate delays, “delay” ramp¹, phase shifters, IQ-modulators, or others.

It should be noted that by analogue methods such as phase shifters, IQ-modulators or a delay ramp, very small delay steps can be adjusted. In all these cases, an (sampling-) event is released, if the trigger waveform (sine wave or ramp) is crossing a threshold. Referring to Fig. 2, the uncertainty t_j of the trigger event is approximately given by:

$$t_j \approx \frac{\sigma}{c_v} \quad (1)$$

Herein, σ represents the rms-value of noise and c_v is the slew rate of the trigger waveform. This results in a *relative* reproducibility of trigger events depending on the *SNR*-value:

$$\frac{t_j}{t_r} \approx \frac{\sigma}{V_0} \approx \frac{1}{\sqrt{SNR}} \quad (2)$$

in the case of a linear ramp, and

$$\frac{t_j}{T_0} = t_j f_0 \approx \frac{\sigma}{2\pi V_0} \approx \frac{1}{\pi\sqrt{8SNR}} \quad (3)$$

for a sine wave of frequency $f_0 = 1/T_0$ and a zero threshold. Obviously, the absolute stability t_j of the delay time degrades, if the maximum control range (t_r or T_0) increases. Many classical UWB approaches suffer from this effect.

In the case considered here, the control range of the delay circuit only extends over one period of the RF-clock rate, which is usually well below 1 ns; typically it is in the order of 100 ps. Thus, the additionally introduced delay circuit will not affect the time stability of the M-Sequence system.

The data acquisition of the modified M-Sequence approach is organized in the following manner:

1. The complete period of the M-Sequence is gathered as usual, i.e. one sample per chip, while the delay circuit keeps its delay time constant. The procedure can be repeated in order to reduce noise by averaging.
2. The delay time is changed by a portion of the RF-clock period length and the measurement procedure of step 1. is repeated. Delay time variation is carried out until a whole RF-clock

¹ The “delay” ramp method can be used to retard a pulse flank. The flank to be delayed starts a voltage ramp releasing a new impulse by crossing a trigger threshold. The delay control can be made either by variation of the ramp slope or by shifting the threshold voltage.

period is covered by fine and equidistant delay steps.

3. The data samples must be reordered into their natural order.

The result is a data vector of increased length with increased noise for individual data samples. The increase of noise results from two effects. First, the number of averages per measurement point must be reduced in order to keep the overall measurement time constant. Second, large areas of the spectral band additionally captured by the new approach do only contain a small amount of signal energy. Thus, it is advisable to low-pass filter and down sample the data before other processing steps are undertaken. In contrast to the basic approach, low pass filtering can now be made in the digital domain. This gains the new flexibility to arbitrarily choose filter type and width of passband without changing any hardware. The resulting signal vector after this pre-processing will have a comparable length and *SNR* as would have been captured by the basic M-Sequence module.

IV. INCREASING THE STIMULUS BANDWIDTH

In the case that the Track & Hold circuit (T&H) has a large input bandwidth, the enlarged equivalent sampling rate can also be exploited to increase the measurement bandwidth of the system, if the stimulus can excite the spectral band beyond $f_c/2$ with additional signal power. A simple way to do this is by mixing the M-Sequence with its RF-clock (see [7], [8]), which shifts the spectral band to higher frequencies centered around f_c . However, the low frequency parts are lost. By appropriately adding the original M-Sequence to the up-converted one, this loss can be removed. Fig. 3 shows the corresponding block schematics of such an extended M-Sequence system. Fig. 4 contains a simulated spectrum and the resulting auto-correlation function of a continuous M-Sequence. It is compared to the basic M-Sequence approach. The auto-correlation functions were calculated from truncated spectra as they appear typically at the corresponding approach.

The modified sampling approach theoretically permits a nearly “continuous” representation of the autocorrelation

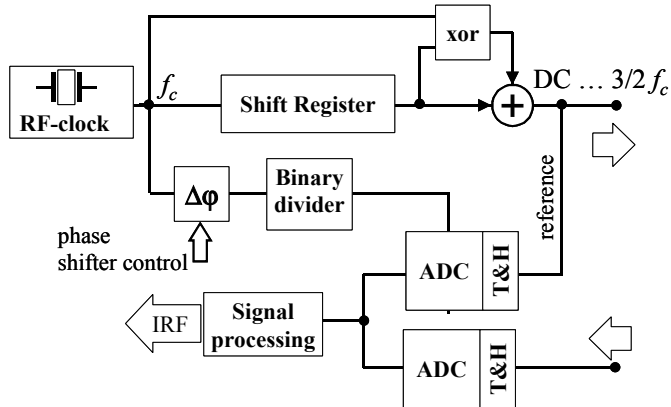


Figure 3. Block schematics of the extended M-Sequence. Note, that the phase shifter at the input of the binary divider can be replaced by a delay circuit which can also be placed at its output.

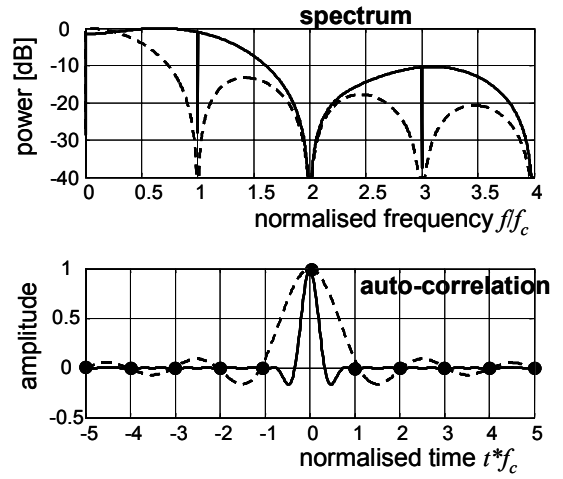


Figure 4. Idealized spectrum and (continuous) auto-correlation function of the basic M-Sequence- (dashed line) and extended M-Sequence-module (solid line). The auto-correlation function was calculated after truncation of the spectrum at $f_c/2$ (for the basic approach) and at $2f_c$ (for the extended approach), respectively.

function whereas the basic sampling method restricts the actual gathered data to the emphasized points.

Signal multiplication and addition can be made by a wideband mixer and a power divider. However, the better solution would be to use an XOR-gate and a difference amplifier instead, if an integrated circuit implementation is intended. As the estimation in Fig. 4 shows, the usable bandwidth can be extended from dc to $1.5f_c$ as long as the T&H-circuit can handle this bandwidth at its input.

It is wise to work with a reference channel, which acquires the actual time shape of the stimulus, since its structure is not as clear as in the case of the basic approach.

V. EXPERIMENTAL VERIFICATIONS

First trials were undertaken by using the available system components of the basic M-Sequence module [12] (still including the anti-aliasing filter), completed by a commercial double balanced mixer with about 4 GHz IF-bandwidth and a power divider for signal superposition. In order to avoid a spectral gap between the baseband and the modulated M-Sequence, the RF-clock f_c was chosen to be below 8 GHz due to the limited bandwidth of the mixer. For the experiments, a 7 GHz clock was used. Fig. 5 presents the spectrum of the generated waveform measured by a spectrum analyzer. The cutoff of the spectral energy at about 10.8 GHz is mainly due to mixer limitations and the retained low-pass filter.

The usable band up to about 11 GHz requires an equivalent sampling rate of at least 22 GHz in order to respect the sampling theorem. As mentioned above, the equivalent sampling rate provided by the binary divider is always f_c , i.e. 7 GHz in our case. Thus, the measurements needed to be repeated with 4 different phase values (e.g. 0° , 90° , 180° and 270°) to increase the equivalent sampling rate to 28 GHz. The actual rate of data acquisition (ADC-clock) used for the experiments was about 14 MHz.

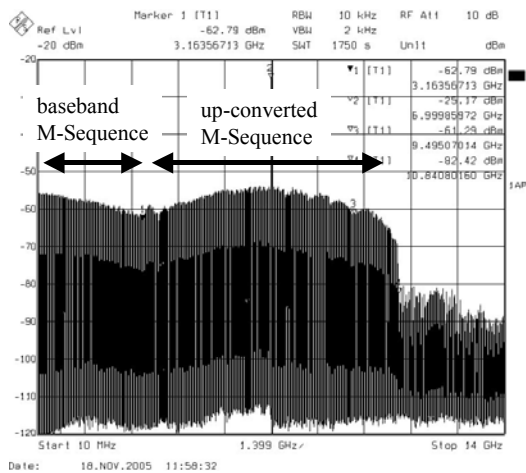


Figure 5. Spectrum of the generated signal.

Fig. 6 shows the measurement results. The spectrum calculated from the acquired data coincides well with the measurements of the spectrum analyzer. This indicates that the T&H-circuit does not yet limit the bandwidth of the system. The auto-correlation function shows a well pronounced sharp peak (FWHM-value of 71,4 ps) with two side lobes. They are still a bit disturbing, but they can be reduced by appropriate post-processing as well as better realizations of the mixing and superposition hardware.

VI. CONCLUSION

Some extensions of the basic ultra wideband M-Sequence radar principle were introduced. By adding a programmable phase shifter or a short delay line, the equivalent sampling rate of data acquisition can be increased. This enables broader operational bandwidths and helps to omit RF anti-aliasing filters. The bandwidth improvements were gained by shifting the spectrum of the M-Sequence to a higher band via mixing with the clock rate of the shift register and superimposing the resultant signal with the original M-Sequence.

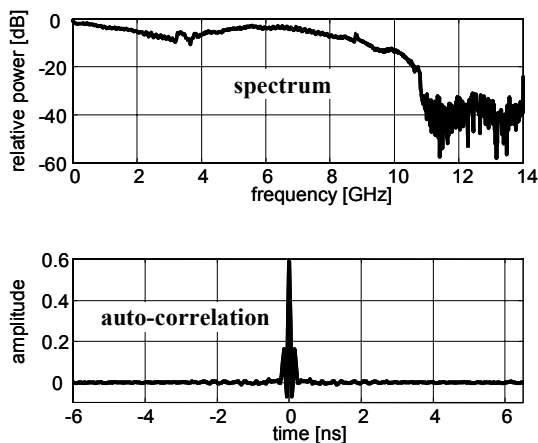


Figure 6. Spectrum and auto-correlation function determined from a data set acquired with an equivalent sampling rate of 28 GHz. The carrier frequency (due to the LO throughput of the mixer) as well as the DC components have been removed from the data.

It should be emphasized, that the approach gains a higher bandwidth by keeping the same semi-conductor technology. If the basic M-Sequence method is able to provide a sufficient bandwidth for a certain application (i.e. less than 7 GHz at the current stage), the presented methods permit to change to a less sophisticated RF technology. Especially power consumption can be reduced due to lower clock rates.

The renouncement of RF-anti-aliasing filters greatly increases the operational flexibility of the M-Sequence system, since an arbitrary clock rate can be selected without the need of any hardware changes.

ACKNOWLEDGMENT

This research was undertaken in the context of GPR-systems for salt-mine inspections, which required improved resolution. The authors wish to thank the German Ministry of Education and Research for the support of the project.

REFERENCES

- [1] F. Parrini, M. Pieraccini, C. Atzeni, A High-Speed Continuous Wave GPR, Proc. GPR 2004, p. 183-186, Delft, The Netherlands
- [2] E.S. Eide, Radar Imaging of Small Objects Closely Below the Earth Surface, PhD-thesis, Norwegian University of Science and Technology Trondheim, 2000
- [3] R.M. Narayanan, Y. Xu, P.D. Hoffmeyer, J.O. Curtis: Design and performance of a polarimetric random noise radar for detection of shallow buried targets. Proc. SPIE Vol. 2496, p20-30, Orlando, April 1995
- [4] S. R. J. Axelsson, Noise Radar using Random Phase and Frequency Modulation, IEEE Trans. Geosci. Remote Sensing, Vol. 42, No. 11, pp. 2370–2384, November 2004
- [5] R. Stephan, H. Loele: Ansätze zur technischen Realisierung einer Geschwindigkeitsmessung mit einem Breitbandradar. IEEE Workshop on Short Range Radars, 15-16 July 1999, Ilmenau, Germany
- [6] J. Sachs, P. Peyerl: A New Principle for Sensor-Array-Application. Proceedings of 16th IEEE Instrumentation and Measurement Technology Conference, IMTC/99, Venice, Italy, May 24-26, 1999, p. 1390-1395
- [7] J. Sachs, M. Kmec, R. Zetik, P. Peyerl, R. Rauschenbach: "MSCW-Radar – a Novel Ultra Wideband Radar Principle", IRS 2005 International Radar Symposium 2005, September 5 – 8, 2005, Berlin, Germany
- [8] M. Kmec, J. Sachs, P. Peyerl, P. Rauschenbach, R. Thomä, R. Zetik: "A novel Ultra-Wideband real-time MIMO Channel Sounder Architecture", XXVIIIth General Assembly of URSI, October 23 –29, 2005, New Delhi, India
- [9] S. Ranvier, M. Kmec, R. Herrmann, J. Kivinen, J. Koivunen, R.S. Thomä, P. Vainikainen: "mm-Wave wideband MiMo-Channel Sounding", XXVIIIth General Assembly of URSI, October 23 –29, 2005, New Delhi, India.
- [10] J. Sachs: M-sequence radar. In Ground Penetrating Radar 2nd edition, D.J. Daniels ed., IEE Radar, Sonar, Navigation and Avionics Series 15, pp. 225-237, 2004
- [11] J. Sachs, P. Peyerl, Ein neues Breitbandmessverfahren für das Basisband. IEEE Workshop on Short Range Radars, 15-16 July 1999, Ilmenau, Germany
- [12] J. Sachs, M. Kmec, R. Zetik, P. Peyerl, P. Rauschenbach: "Ultra Wideband Radar Assembly Kit", IGARS 2005 IEEE international Geoscience and Remote sensing Symposium, July 25 - 29, 2005, Seoul, Korea

Modeling HBT Low-Frequency Noise for Circuit Simulation

Matthias Rudolph¹, Friedrich Lenk¹, Sébastien Gribaldo², Olivier Llopis², Wolfgang Heinrich¹

¹ Ferdinand-Braun-Institut für Höchstfrequenztechnik (FBH),

Gustav-Kirchhoff-Str. 4, D-12489 Berlin, Germany (e-mail: rudolph@fbh-berlin.de)

²Laboratoire d'Analyse et d'Architecture des Systèmes du Centre National de la Recherche Scientifique (LAAS-CNRS), 31 077 Toulouse, France, and University Paul Sabatier, 31 077 Toulouse Cedex 4, France

Abstract— This paper addresses the question how to describe the low-frequency noise sources in a GaAs HBT large-signal model. Devices under test are two HBTs from the same process run, but epitaxially grown under slightly different conditions. Hence they show different low-frequency noise, but almost identical electrical performance otherwise. Residual phase-noise measurements are used to characterize noise upconversion. It is shown that in the large-signal case noise upconversion can only be simulated well if cyclostationary noise sources are considered. In contrast, low-frequency noise sources which are controlled by the DC current component only yield severely underestimated noise levels.

I. INTRODUCTION

Due to upconversion effects, low-frequency noise can play an important role also in microwave applications. Most prominent is the contribution to the phase noise of oscillators, where the low-frequency noise dominates the spectrum close to the carrier [1]. But also broad-band amplifiers are affected by upconverted base-band noise, or even the base-band noise itself.

However, it is still a field of intensive research how to formulate a large-signal model which is capable of predicting the noise upconversion effects, especially in case of GaAs HBTs. This paper addresses the low-frequency noise modeling considering both the small-signal and the large-signal regime.

In the small-signal case the question is how to implement low-frequency (LF) noise sources in a way that base-band noise is described well for all source impedances. It will be shown that a single noise source, on which standard BJT models rely on, is insufficient in the general case, although it might seem to be well suited if only a fixed source impedance is regarded.

In a second step, residual phase noise measurements are employed to investigate the optimum implementation of these LF sources for the large-signal case. The question is whether the sources are to be described as low-pass noise sources, i.e., excited by the DC current component only, or if they are cyclostationary sources, which means that they are excited by the instantaneous current. While standard models rely on the low-pass sources provided by the circuit simulator software, it was demonstrated in a recently published paper [2] that oscillator phase noise can only be described accurately with two cyclostationary sources. The present work shows that cyclostationary noise sources are also required when considering residual phase noise, which is measured operating the HBT in an almost linear amplifier mode.

In conclusion, this paper discusses the HBT model prerequisites for simulating low-frequency and oscillator phase noise with a harmonic balance simulator. It also addresses the mechanisms generating noise side-bands under large-signal operation in general.

II. HBT TECHNOLOGY AND MEASUREMENT CONDITIONS

The devices under test were fabricated in the 4'' In-GaP/GaAs HBT process line of the FBH [3]. HBTs with an emitter size of $3 \times 30 \mu\text{m}^2$ from two different wafers were measured. The sole difference between the wafers is that the emitter was grown in the MOVPE at a different temperature. Both were processed in the same batch, and no difference in the electrical behavior was observed. However, the low-frequency noise is different, as can be seen from Figs. 2, 3 showing the low-frequency collector short-circuit noise current measured as a function of collector DC current and source resistance.

Phase noise was investigated by means of residual phase noise measurements performed at LAAS-CNRS [4]. This measurement condition allows to determine the noise upconversion mechanisms in an open-loop configuration, i.e., when the transistor operates in amplifier mode. In our case, the full phase-noise spectrum is measured as a function of large-signal power at 3.5 GHz.

Along with this, simulations were performed using a commercial harmonic-balance circuit simulator and the FBH HBT model [5], comparing different descriptions for the low-frequency noise sources.

III. LOW-FREQUENCY NOISE MODEL AND SMALL-SIGNAL REGIME

Traditionally, bipolar large-signal models account for low-frequency noise generated at the base-emitter junction only. In the equivalent circuit, Fig. 1, the location of this noise source is denoted as “base-emitter noise source”. In case of the SPICE Gummel-Poon (SGP), VBIC and UCSD HBT [9] models, the noise depends on current and frequency according to

$$\langle |i_{nbf}|^2 \rangle = Kf \Delta f \frac{I_{be}^{Af}}{f^{Bf}} \quad (1)$$

with the parameters Kf , Af , and Bf , and the noise bandwidth Δf . In case of the SGP model, additionally the parameter Bfn is fixed to unity.

However, since recombination at the base-emitter junction is more pronounced in HBTs than in traditional silicon bipolar transistors, one commonly observes a Lorentz-spectrum.

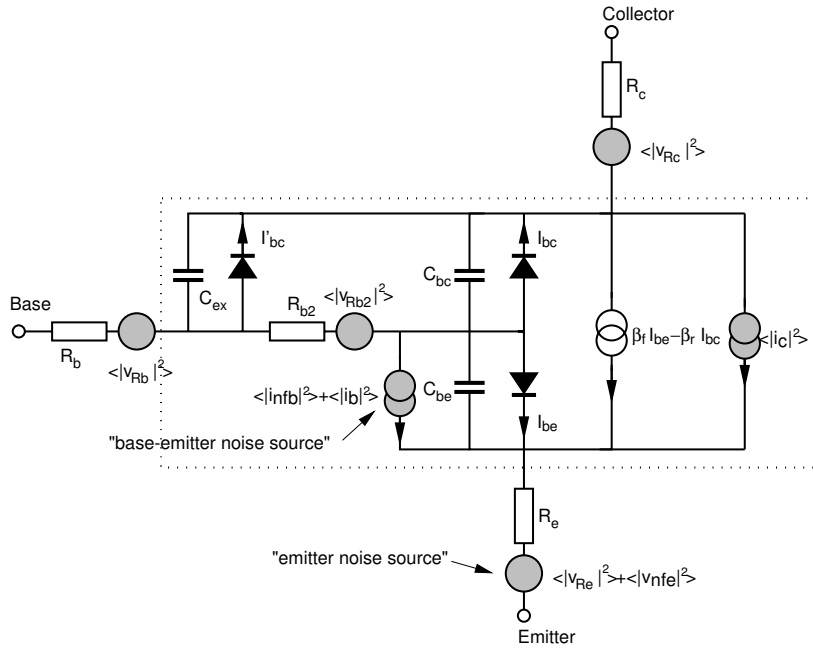


Fig. 1. Large-signal and noise HBT equivalent circuit, extrinsic inductances and capacitances not drawn for sake of simplicity. All resistances contribute thermal noise, $\langle |i_b|^2 \rangle$ and $\langle |i_c|^2 \rangle$ describe shot-noise. The sources at the base-emitter junction $\langle |i_{nfb}|^2 \rangle$ and at the emitter resistance $\langle |v_{nfe}|^2 \rangle$ contribute low-frequency noise.

In Fig. 3b, e.g., this Lorentz-type spectrum is responsible for the bump in the frequency dependence of the noise powers. The Agilent HBT [10] and FBH HBT [5] models, for example, account for this fact by introducing an additional term in the noise formula:

$$\langle |i_{nfb}|^2 \rangle = Kf \Delta f \frac{I_{be}^{Af}}{fBf} + Kb \Delta f \frac{I_{be}^{Ab}}{1 + (f/Fb)^2} \quad (2)$$

The corner frequency of the Lorentz spectrum can be defined by the parameter Fb , and its noise power and bias dependence are controlled through Kb , Ab . In case of the Agilent model, this noise source is split into two, in order to account for ideal and non-ideal base-emitter currents.

It has been shown that even this enhanced description is not sufficient to describe the low-frequency noise comprehensively [11]. In case that the base-emitter terminal is connected to a low-impedance source, such a model would predict very low collector noise currents. The reason is that the base and emitter resistances R_b , R_{b2} , and R_e are quite low in modern HBTs and, hence, the base-emitter noise source is almost shortened. This effect is shown in Figs. 2, 3. Measurements are compared to simulations using the FBH HBT model. The dotted lines in Figs. 2a, 3a refer to the case when accounting only for a base-emitter noise source, which results in deviations from measurements of beyond 10dB for a 10Ω source resistance. In contrast, the model performs well when connected to a high-impedance source (see Figs. 2b, 3b). This, of course, is not surprising since the parameters were extracted under this condition.

Obviously, at least a second source is necessary to describe the noise behavior in general. At this point, adding low-frequency noise sources seems to be ambiguous, since there are many possible locations to locate them: all parasitic resistances, and at the base-collector junction. From the practical point of view, it has to be stated that the number of low-frequency sources which can be distinguished reliably

from source-pull measurements does not exceed two [2], [11]. Additionally, due to Friis' formula, noise sources at the output, i.e., at the collector resistance and base-collector junction, will contribute less to the overall noise than the sources at the input which are amplified. Regarding the remaining possible locations, the emitter resistance noise is expected to exceed the noise generated in the base branch, since $I_e \gg I_b$. Additionally, comparison with measurements of epitaxial resistances has shown that the emitter noise source is quite close to the Hooge noise expected for the emitter layer.

One concludes that a the second low-frequency noise source should be located at the emitter resistance. In the FBH HBT model, the corresponding voltage source is defined by

$$\langle |v_{nfe}|^2 \rangle = Kfe \Delta f \frac{I_e^{Afe}}{fFfe} \quad (3)$$

with the parameters Kfe , Afe , and Ffe . The dashed lines in Figs. 2a, 3a show the improvement in simulation accuracy obtained by this arrangement. The noise simulated for the high-impedance source is not affected, since the emitter branch is almost connected to an open circuit then and, consequently, the voltage noise source does not drive any current.

IV. LARGE-SIGNAL REGIME

In the large-signal regime, the current exciting the low-frequency noise is no longer a constant DC current only, but it contains also harmonics with considerable amplitudes which cannot be neglected compared to the DC part. Hence, the question arises: Will the noise be determined by the DC current only, or will the instantaneous current drive the noise sources? The first alternative leaves the spectrum of the noise sources unchanged, independent of the large-signal RF signals. In the second case, the base-band noise is influenced by the large-signal current, which can be understood as

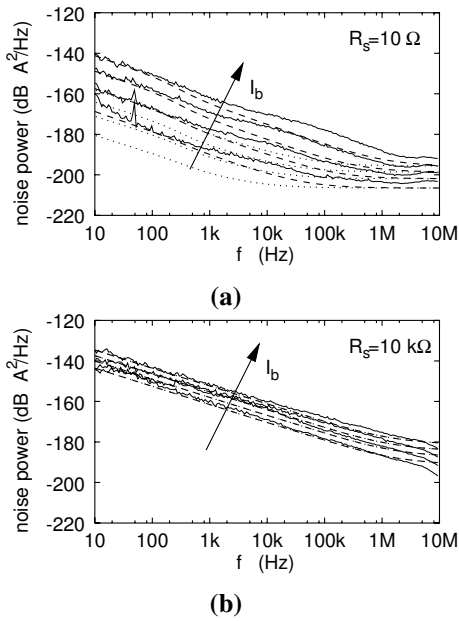


Fig. 2. Low-frequency noise of $3 \times 30 \mu\text{m}^2$ HBT, $V_{cc} = 3 \text{ V}$, $I_c = 2.5, 5, 10, 20 \text{ mA}$, Wafer A. Measurements (solid lines) compared to simulation with two noise sources (broken lines), and simulation neglecting emitter noise source (dotted lines). (a) 10Ω source resistance (b) $10 \text{ k}\Omega$ source resistance.

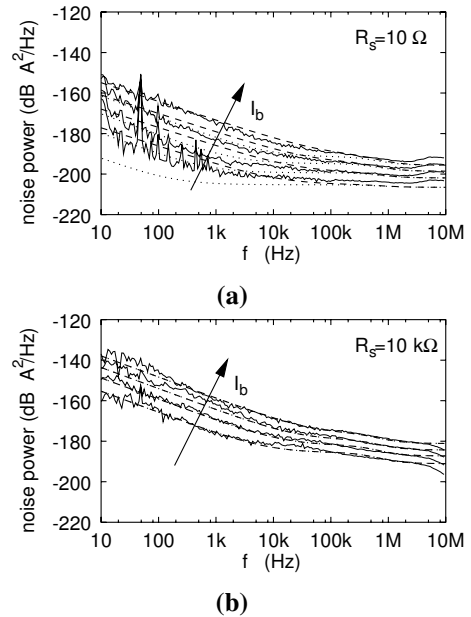


Fig. 3. Low-frequency noise of $3 \times 30 \mu\text{m}^2$ HBT, $V_{cc} = 3 \text{ V}$, $I_c = 2.5, 5, 10, 20 \text{ mA}$, wafer B. Measurements (solid lines) compared to simulation (broken lines), and simulation neglecting emitter noise source (dotted lines). (a) 10Ω source resistance (b) $10 \text{ k}\Omega$ source resistance.

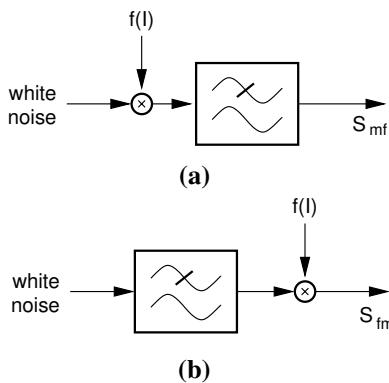


Fig. 4. Interpretation of current-dependent low-frequency noise as a mixing and filtering process of white noise, resulting either in low-pass noise (a), or in cyclostationary noise (b), after [6].

a mixing process. This means that noise side-bands are generated even without any mixing process external to the noise source, i.e., even in a linearly operating device.

Fig. 4 shows a circuit-oriented interpretation of the alternatives [6]. The low-frequency noise can be thought of as white noise, which is low-pass filtered and multiplied by a function of current. The question is: does the low-pass filtering follow or precede the mixing process? In the following, we will refer to the first type of source as “low-pass” noise source, and to the second one as “cyclostationary” source.

At first glance, it is not obvious why a noise source which shows a distinct low-pass behavior (e.g., $1/f$ noise) should be controlled by the instantaneous current. It would mean that the physical process causing the noise follows fast changes of the signal, and one would expect white noise from such a fast process and not the $1/f$ like frequency characteristics observed for LF noise. However, it has been pointed out that e.g. generation-recombination noise indeed is governed

by a white noise process. The low-pass characteristics are observed only when expressing it in terms of fluctuations in carrier number or current [7]. Physical simulation of various semiconductor structures has shown that, while the microscopic sources indeed show cyclostationary behavior, this could not be said *a priori* for the lumped noise sources of the corresponding equivalent-circuit based model [6].

The common circuit simulators use low-frequency noise sources following the “low-pass” concept. Accordingly, the built-in models rely on this formulation. It has recently been shown, on the other hand, that nonlinear noise modeling accuracy could be improved significantly by introducing cyclostationary sources. One example is the noise of resistive FET mixers [8], another one is the phase noise of HBT-based oscillators [2]. These noise models necessarily need to use a nonlinear subcircuit in order to obtain a cyclostationary noise source, as addressed e.g. in [8].

The present investigation relies on residual phase-noise measurements, i.e., on measuring the noise side-bands generated when the transistor is operated as an almost linear amplifier. It is the advantage of this set-up that the large-signal noise performance of the HBT alone is measured, while large-signal power, bias and source resistance can be controlled. Therefore, this measurement condition is able to provide a maximum of information compared to the measurement of circuits. Therefore, it is possible to investigate details such as the influence of a single source on HBT noise performance.

In the simulation, the FBH HBT model is used and the low-frequency noise sources are implemented in four different ways: as low-pass sources, as cyclostationary sources, and one as a low-pass source while the other one is cyclostationary.

Figs. 5, 6 present the results for an input power of -6 dBm . For both wafers, it can be stated that a model

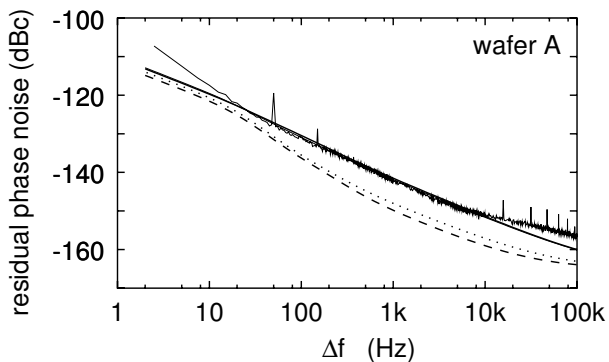


Fig. 5. Double side-band residual phase noise of $3 \times 30 \mu\text{m}^2$ HBT, input power $P_{in} = -6$ dBm at 3.5 GHz, $V_{cc} = 3$ V, $I_c = 30$ mA, wafer A. Measurement (thin solid line), compared to simulation: low-pass source (dashed line), cyclostationary sources: both sources and emitter source only (thick solid line), only base-emitter source cyclostationary (dotted lines).

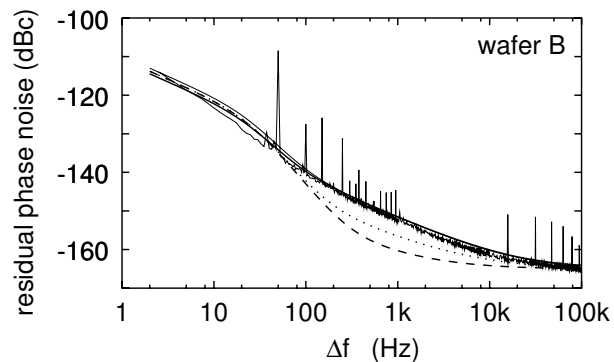


Fig. 6. Double side-band residual phase noise of $3 \times 30 \mu\text{m}^2$ HBT, input power $P_{in} = -6$ dBm at 3.5 GHz, $V_{cc} = 3$ V, $I_c = 30$ mA, wafer B. Measurement (thin solid line), compared to simulation: low-pass source (dashed line), cyclostationary sources: both sources and base-emitter source only (thick solid line), only emitter source cyclostationary (dotted lines).

based on low-pass sources is not capable of reproducing the simulation data, since it underestimates the phase noise power significantly, partly by more than 10 dB (dashed lines in the figures). On the other hand, if both sources are assumed to be cyclostationary, the model yields an almost perfect fit (thick solid lines). It is, however, interesting to note that both wafers have one dominating noise source. In case of wafer A, it is the emitter noise source, but for wafer B it is the base-emitter noise source. If only this source is modeled cyclostationary, the result is indistinguishable from the result obtained with two cyclostationary sources (thick solid lines). Vice versa, if this dominant source is described by a low-pass source, while the other one is cyclostationary, only little improvement over the low-pass case is achieved (dotted lines).

The observation that the low-pass formulation yields residual phase noise levels considerably below the measured ones has a further consequence for understanding the origins of phase noise. It means that upconversion of baseband noise due to the device nonlinearities does *not* significantly contribute to phase noise (at least beyond an offset frequency of 100 Hz) and that the large-signal current causes noise sidebands even if the HBT is still in linear operation. Moreover, one concludes that oscillator phase noise can be optimized only to a certain extent by reducing the low-frequency part of the noise sources, e.g. when selecting special baseband terminations in order to suppress upconversion in the nonlinearly operating device.

V. CONCLUSION

This paper addresses the implementation of low-frequency noise sources in GaAs HBT large-signal models. The following conclusions can be drawn:

- In linear operation, two noise sources are required in order to be able to describe the low-frequency noise for all source impedances. If only a base-emitter source is used as it is the case in traditional bipolar models, the noise power level will be underestimated if the HBT is connected to a low-impedance source.
- In nonlinear operation, both low-frequency sources have to be described by cyclostationary sources in order to describe noise upconversion effects properly. The common simulator software packages, on the other

hand, provide only low-pass sources. Thus, relying on the built-in models yields grossly underestimated noise power levels. It has been shown that, depending on the actual device, either of the two sources can dominate phase noise generation. Therefore, in a general model it is necessary to have both noise sources described as cyclostationary sources.

These findings explain why noise simulations relying on common bipolar and HBT models provided by harmonic-balance circuit simulators are generally not capable of describing GaAs HBT phase noise with the expected accuracy. The results are also important for understanding the noise generation processes in GaAs HBT oscillators.

REFERENCES

- [1] D. Leeson, "A simple model of feedback oscillator noise spectrum," *Proc. IEEE*, vol. 54, pp. 329 – 330, Feb. 1966.
- [2] J.-Ch. Nallatamby, M. Prigent, M. Camiade, A. Sion, C. Gourdon, J.J. Obregon, "An Advanced Low-Frequency Noise Model of GaInP/GaAs HBT for Accurate Prediction of Phase Noise in Oscillators," *IEEE Trans. Microwave Theory Tech.*, vol. 53, pp. 1601 – 1612, May 2005.
- [3] J. Hilsenbeck, F. Lenk, W. Heinrich, J. Würfl, "Low Phase Noise MMIC VCOs for Ka-Band Applications with Improved GaInP/GaAs-HBT Technology," *IEEE GaAs IC Symp. Dig.*, 2003, pp. 223 – 226.
- [4] G. Cibiel, L. Escotte, O. Llopis, "A Study of the Correlation Between High-Frequency Noise and Phase Noise in Low-Noise Silicon-Based Transistors," *IEEE Trans. Microwave Theory Tech.*, vol. 52, pp. 183 – 190, Jan. 2004.
- [5] M. Rudolph, "FBH HBT Model," 2005. [Online]. Available: <http://www.fbh-berlin.de/modeling.html>
- [6] F. Bonani, S. Donati Guerrieri, G. Ghione, "Noise Source Modeling for Cyclostationary Noise Analysis in Large-Signal Device Operation," *IEEE Trans. Electron Devices*, vol. 49, pp. 1640 – 1647, Sept. 2002.
- [7] C.M. Van Vliet, "Macroscopic and Microscopic Methods for Noise in Devices," *IEEE Trans. Electron Devices*, vol. 41, pp. 1902 – 1915, Nov. 1994.
- [8] M. Margraf, G. Böck, "Analysis and Modeling of Low-Frequency Noise in Resistive FET Mixers," *IEEE Trans. Microwave Theory Tech.*, vol. 52, pp. 1709 – 1718, July 2004.
- [9] "HBT Model Equations — rev 9.001a 3/2000," 2000. [Online]. Available: <http://hbt.ucsd.edu/>
- [10] Agilent Technologies, "AgilentHBT_Model (Agilent Heterojunction Bipolar Transistor Model)," in *Nonlinear Devices Manual for Advanced Design System*, 2004, pp. 2–4 – 2–42.
- [11] P. Heymann, M. Rudolph, R. Doerner, F. Lenk, "Modeling of low-frequency noise in GaInP/GaAs hetero-bipolar transistors," in *IEEE MTT-S Int. Microwave Symp. Dig.*, 2001, pp. 1967 – 1970.

Experimental Study of Time-Domain to Frequency-Domain Correlation for GaAs-HBT Based TWAs for 20 Gbps and 40 Gbps

C. Meliani and M. Rudolph

Ferdinand-Braun-Institut für Hochofrequenztechnik (FBH), 12489 Berlin / Germany
Email: meliani@fbh-berlin.de

Short Abstract—The capabilities of the GaAs HBT technology in terms of maximum bit rates and output amplitudes for TWAs are studied investigating the correlation between cut-off frequency, gain shape and ripple, and eye diagrams. Particularly, it turns out that, if the bit-rate frequency (e.g., 40 GHz for 40 Gbps) exceeds the cut-off frequency, the Bessel gain characteristic proves to be superior to the conventional Chebyshev type. As an example, 40 Gbps TWA is realized with an f_c around 25 GHz achieving 4 Vpp output amplitude at a maximum gain of 12 dB.

Keywords—TWA, HBT, GaAs, eye diagram, high bit-rate transmission

I. INTRODUCTION

Recently, several ultra high-speed amplifiers have been realized using high-performance technologies such as InP HEMTs or HBTs [1], or GaAs pHEMTs [2]. But such high-end processes are expensive and, therefore, the target today is to explore the high-bit rate capabilities of technologies with lower cost. Thus, presently the SiGe-HBT technology is the prime candidate for the 40 Gbps range [3]. Despite their high cut-off frequencies, however, the Si technologies still suffer from frequency limitations when driving large currents, restricting them to low output-voltage swings.

A particular issue in developing such high-speed traveling-wave amplifiers (TWAs) is to have an understanding of how the basic transistor properties translate into TWA performance and how these TWA frequency-domain characteristics translate into time-domain performance. The questions are

- whether one can derive a quantitative relationship between the transit frequency f_T and the maximum frequency of oscillation f_{max} of a transistor on the one hand and bandwidth and gain characteristics of the TWA on the other hand and, moreover,
- whether gain and cut-off frequency can be used as indicators for the time domain behavior of the circuit.

For more details on the first question see [4]. In this paper, we focus on the second question, i.e., understanding the correlation between the frequency-domain and time-domain characteristics. It is well known that an NRZ signal can be amplified employing a cut-off frequency around 70% of the bit rate. What is to be discussed is the quality of the signal, i.e., the

opening of the resulting eye diagram. In the course of our study we also found examples where the shape of the gain curve was much more important than the cut-off frequency itself, either because the group delay was not flat enough or because of limitations in gain and maximum available current. Moreover, in some cases the Chebyshev gain characteristic was better than the Bessel type, the conventional one for the case when f_c exceeds the targeted bit rate.

The paper is organized as follows: Sec. II describes the process and modeling tools including the large and small signal model of the transistor. Sec. III then presents briefly the small-signal description of the TWA and the options in terms of design parameters we have chosen. Finally, Sec. IV provides the measurement results and discusses the correlation between the frequency domain and time domain.

II. TECHNOLOGY AND TRANSISTOR MODEL

The HBT MMICs are fabricated on the FBH 4" process line. The epitaxial layers are grown by Metalorganic Vapor-Phase Epitaxy (MOVPE). Very high f_{max} values (beyond 170 GHz at $V_{CE}=3$ V) are achieved as compared to more industry-standard f_T values (36 GHz at $V_{CE}=3$ V). See Fig. 1 for details of the f_T and f_{max} behavior.

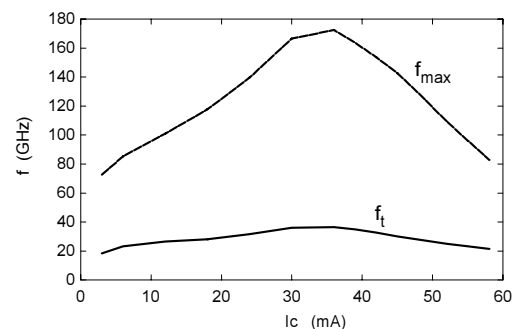


Fig. 1. Extracted values of f_T and f_{max} against collector current for a $3 \times 30 \mu\text{m}^2$ HBT at $V_{CE}=3$ V.

A customized CAD library containing both passive and active devices is used for circuit simulation. Key part is the FBH large-signal HBT model [5]. It includes partition of intrinsic and extrinsic base-collector diode, non-ideal base currents,

self-heating, base-emitter and base-collector break-down, current-dependence of base-collector capacitance $C_{bc,intr}$, and collector transit time τ_c (i.e., velocity modulation and Kirk effect, which are responsible for the f_T and f_{max} peaking to be seen in Fig. 1).

III. TWA DESIGN METHODOLOGY

A. Small-Signal Problem

A TWA is formed by the parallel connection of amplifying cells via inductors. The input and output capacitances and inductances of the active devices together with the connecting lines form equivalent transmission lines with, in principle, 50 ohms characteristic impedance. Thus, an HBT-based TWA can be represented by the equivalent circuit in Fig. 2.

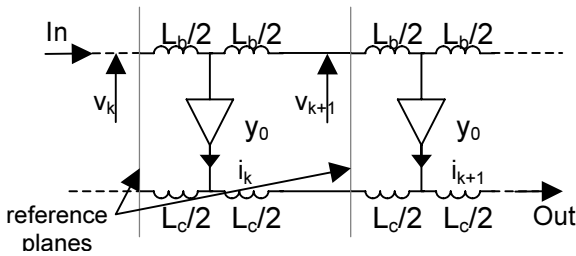


Fig. 2. Distributed amplifier representation.

In principle, the collector (output) line is terminated by a 50 ohms load as is the base (input) line, in order to absorb backward waves and to feed either the base or the collector.

B. Circuit Design

We use transistors with $3 \times 30 \mu m^2$ emitter area in order to optimize the output voltage amplitude as well to maintain high cut-off frequency properties. To have common basic parameters for the amplifiers to be compared, we decided to design 5 stage TWA examples, which is a good trade-off between frequency limits and output current [4]. The classical problem of the gain-frequency slope is mainly solved by the unit-cell design. On the one hand, this is achieved by optimizing numerically the value of the emitter feedback resistor. On the other hand, the decoupling of the second cascode base represents a key condition for high-frequency operation. We finally end up with some intermediate values.

When using large transistors, only relatively low cut-off frequencies around 25 GHz are possible. In this configuration, the maximum possible flat gain is around 10 dB. We designed Chebyshev-like amplifiers where flat gain was the most important parameter as well as other ones where cut-off frequency was the main target. Additionally, Bessel-like amplifiers with more gain (>13 dB) were designed.

IV. EXPERIMENTAL RESULTS AND DISCUSSION

Three TWA versions were designed, realized and measured. S11 and S22 are well matched for all three cases. We will focus our study on S21 and the eye diagram. Fig. 3 presents the gain curves of the three different TWAs.

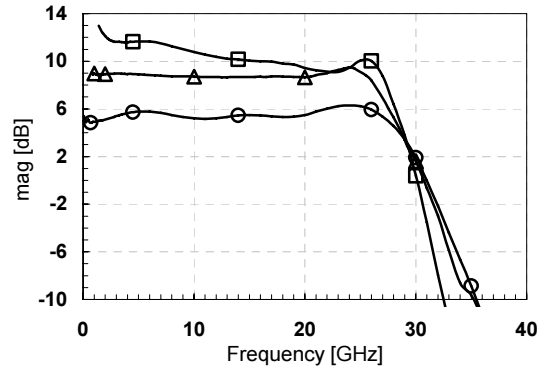


Fig. 3. S21 as a function of frequency for the three different amplifiers, (□): Bessel-like, (Δ) Chebyshev-like I (current capabilities and flat gain), (○) Chebyshev-like II (high cutoff-frequency).

A. (Δ) Chebyshev-like I

This amplifier was designed with emphasis on current (i.e., using large transistors) and on having a very flat-gain with the highest possible cut-off frequency. On-wafer measurements show 9 dB broadband gain with less than 1 dB in-band ripple. F_c reaches 27 GHz. DC consumption of the circuit is about 1400 mW at 100 mA DC current. Input and output matching is better than 5 dB within the bandwidth. The large-signal behavior was tested with a $2^{31}-1$ PRBS NRZ bit pattern.

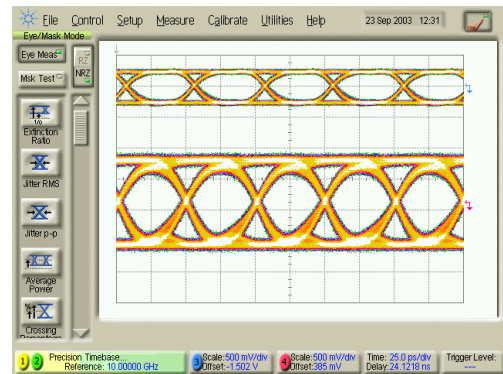


Fig. 4. 20 Gbps input (top) and output (bottom) eye diagrams for the Chebyshev type I amplifier at 500 mVpp. (500 mVpp/Div)

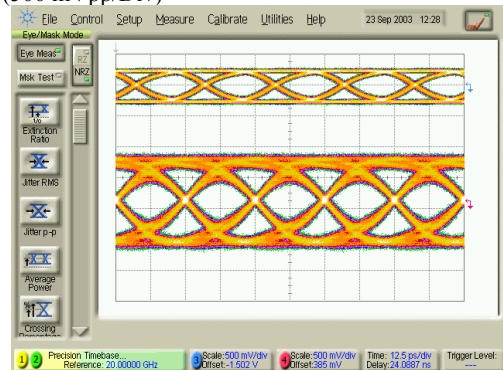


Fig. 5. Data of Fig. 4 for 40 Gbps.

Figs. 4 and 5 show the measured input and output accumulated eye diagrams with 500 mVpp input at 20 Gbps and 40 Gbps, respectively. The circuit delivers an output signal amplitude of 1.4 Vpp. For the 40 Gbps one can see that the signal is somehow rounded but it is interesting to notice that the eyes are still open despite the low f_c for this bit rate.

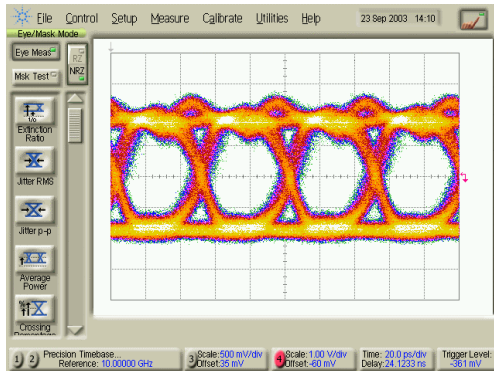


Fig. 6. 20 Gbps output-signal eye diagrams for input voltage of 1.7 V_{pp}.

In order to explore the large-signal behavior, an input signal of 1.7 V_{pp} at 20 Gbps was applied to the amplifier. Fig. 6 presents the eye diagram of the corresponding output signal with a 4 Vpp amplitude. Large signal gain is 7.5 dB. One can already notice some saturation effects in addition to noise on the high level, which means that the amplifier is operated at its limits.

B. (o) Chebyshev-like II

This amplifier version was designed optimizing primarily the cut-off frequency. On-wafer measurements show 5 dB broadband gain with a 2.5 dB in-band ripple. The -3dB cut-off-frequency reaches 30 GHz. Input and output matching are better than 5 dB within the bandwidth. This amplifier can be compared directly with the former one (type I, see Subsection A). It shows a higher cut-off frequency than type I, which comes at the cost of a slightly higher ripple.

Figs. 7 and 8 present the corresponding output eye diagrams at 20 Gbps and 40 Gbps.

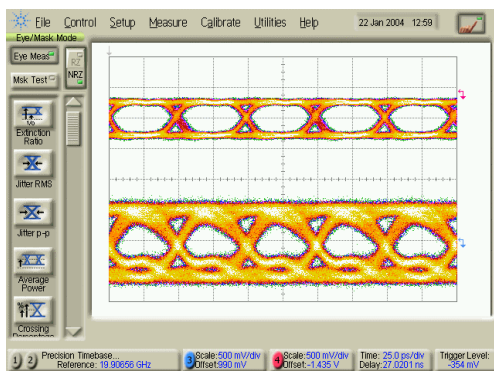


Fig. 7. 20 Gbps input (top) and output (bottom) eye diagrams for the Chebyshev type II amplifier at 500 mVpp. (500 mVpp/Div).

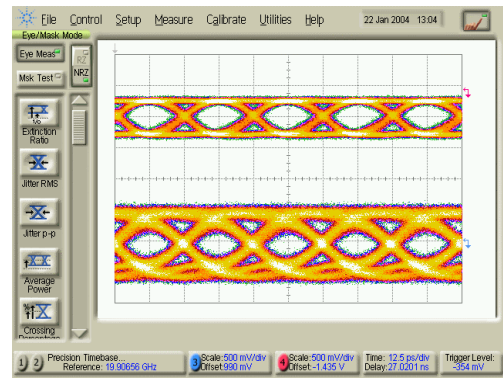


Fig. 8. Data of Fig. 8 for 40 Gbps.

One clearly observes that the signal is more degraded than that of the precedent amplifier (i.e., type I). This result highlights the importance of gain flatness. The problem for this circuit is that it has not have enough bandwidth margin so that the signal could be amplified correctly despite the gain ripple.

The maximum possible output amplitude reaches about 4 Vpp. Fig. 9 illustrates the results. The waveform quality was absolutely not useful.

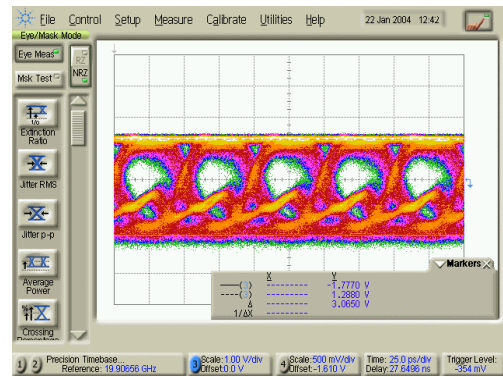


Fig. 9. 20 Gbps output signal eye diagrams for increased input voltage (maximum voltage amplitude), 1 Vpp/Div; other data as in Fig. 7.

C. (□) Bessel-like

This circuit was designed by maximizing the gain. With this approach, the solution is to start with a Bessel-like gain shape and to optimize it in a way to achieve the correct signal waveform despite of the frequency limitations. On-wafer small-signal measurements show 12 dB broadband gain with a smooth continuous decrease up to a 3 dB cut-off-frequency of 24 GHz. Input and output matching are better than -5 dB within the bandwidth.

Fig. 10 shows the corresponding eye diagram at 20 Gbps. Because of the higher ripple than in the case of the very flat first amplifier, we notice a ripple on the eye diagram even for the 20 Gbps case.

Figs. 11 and 12 provide measured input and output accumulated eye diagrams at 40 Gbps for two different input amplitudes. The circuit delivers an output signal amplitude of 2

2 Vpp and 4 Vpp with a well-opened eye diagram, at a large-signal gain of approximately 12 dB in both cases.

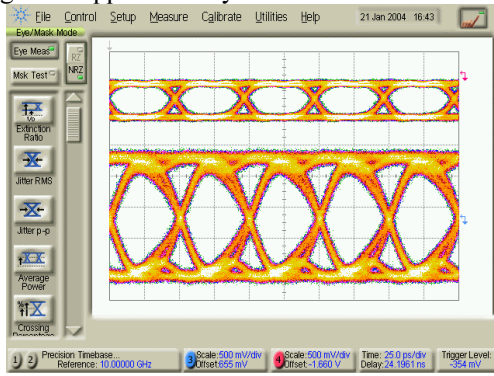


Fig. 10. Eye diagram for the Bessel-like amplifier version: 2 Vpp output at 20 Gbps (bottom) for a 0.5 Vpp input signal (top). (0.5 V/Div).

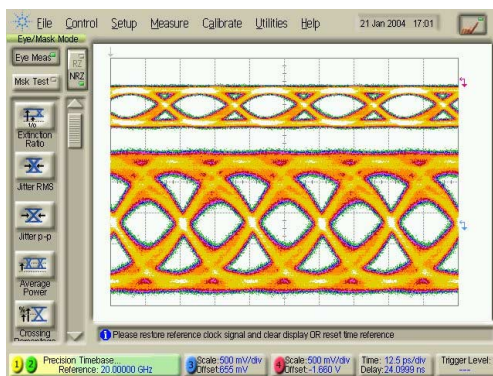


Fig. 11. Results of Fig. 10 for 40 Gbps.

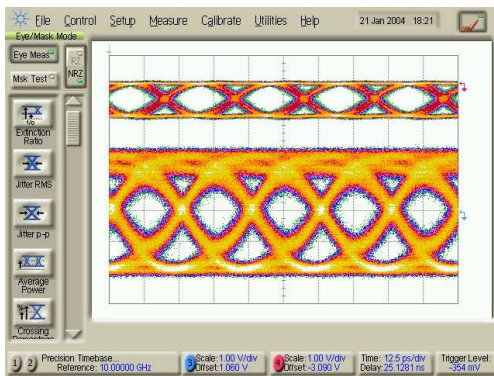


Fig. 12. Data of Fig. 11 for maximum output: 4 Vpp output 40 Gbps eye diagram (bottom) for a 1 Vpp input signal (top). (1 V/Div).

The performance of the Bessel-type amplifier design at 40 Gbps is much better than that of the first amplifier (Chebyshev type I), despite the fact that the type I approach had better eye diagrams at 20 Gbps. This is due to the fact that the improvement of the waveform at 40 Gbps is not due to any enlargement of the bandwidth but due to the modification of the

group delay behavior around the cut-off frequency and above. It is well known that such Bessel-like curves smooth the group delay also above the cut-off frequency, which improves the signal at 40 Gbps. On the other hand, we had to accept a slight degradation at 20 Gbps in our case because we could achieve the desired high-speed group-delay characteristics only by tolerating a gain ripple within the bandwidth.

V. CONCLUSIONS

Three different types of TWAs were designed and fabricated, with the aim to investigate the correlation between time and frequency domain. Special about this investigation is that the amplifiers were realized with a transit-frequency close to or lower than the bit-rate frequency (i.e., an f_c around 27 GHz for 20 Gbps and 40 Gbps). The two first TWA design concepts are based on a Chebyshev-like gain curve, the third one uses a Bessel-like shape. The circuits were measured in the small and large signal regime. Cut-off frequencies of 27 GHz, 30 GHz, and 24GHz are achieved, at small signal gains of 9 dB, 5 dB, and 12 dB, respectively.

The comparison between the two Chebyshev amplifiers shows that, for such low cut-off frequencies compared to the bit-rate value, gain flatness is the key issue. A ripple of more than 1 dB degrades the signal waveform considerably. In terms of waveform, the first amplifier, the design of which focuses on gain flatness, clearly outperforms the second one, which exhibits a gain ripple of more than 2.5 dB, despite a higher cut-off frequency of 30 GHz

The Bessel-like TWA design exhibits a lower cut-off frequency than the first type (Chebyshev I) but yields both a better waveform at 40 Gbps and a higher output amplitude (4 Vpp). This is achieved at the expense of a slight degradation of the eye diagram at 20 Gbps. This seems to be the best compromise for high output amplitude applications when using an HBT technology with transit frequencies close to bit rate.

REFERENCES

- [1] S. Masuda, T. Hirose, T. Takahashi, M. Nishi, S. Yokokawa, S. Iijima, K. Ono, N. Hara, K. Joshin, "An over 110-GHz InP HEMT flip-chip distributed baseband amplifier with inverted microstrip line structure for optical transmission systems", in Proc. IEEE Gallium Arsenide Integrated Circuit Symposium, Monterey, CA, Oct. 2002, pp. 99 – 102.
- [2] M. Häfele, C. Schwörer, K. Beilenhoff, and H. Schumacher, "A GaAs PHEMT distributed amplifier with low group delay time variation for 40 Gbit/s optical systems", in Proc. European Microwave Conference – Munich, Germany, Oct. 2003, pp. 1091– 1094.
- [3] O. Wohlgenuth, P. Paschke, and Y. Baeyens, "SiGe broadband amplifiers with up to 80 GHz bandwidth for optical applications at 43 Gbit/s and beyond", European Microwave Conference – Munich, Germany, Oct. 2003, pp. 1087– 1090.
- [4] C. Meliani, M. Rudolph, and W. Heinrich, « A 40 Gbps GaAs-HBT Distributed Amplifier with an Over-1T Cut-Off Frequency: Analytical and Experimental Study », in Proc. IMS 2005, Long Beach, CA.
- [5] M. Rudolph, R. Doerner, K. Beilenhoff, P. Heymann, "Unified Model for Collector Charge in Heterojunction Bipolar Transistors" IEEE Trans. Microwave Theory Tech., vol. 50, pp. 1747 – 1751, Jul. 20

Active Microwave Filters based on the Combined Dynamic Negatrons

Filinyuk N.A.¹, Kuzemko A.M.¹, Lischinskaya L.B.¹, Salech M.M. Jourban¹, Vojtsehovska E.V.¹

¹Vinnitca National Technical University, Vinnitca, Khmelnytsky shosse 95, 21021, Ukraine, +38 0432 580075, filinyuk@vstu.vinnitca.ua

Abstract—Representation of the FET as generalized imittance converters is considered, that has allowed constructing new elements on its basis. Schemes of analogues of inductive elements (with low-Q inductor and inductor-less) based on the common-drain scheme are developed. Schemes are developed for active microwave filters, suitable for development as a hybrid or integrated microcircuits.

I. INTRODUCTION

Continuous process of complication of radio-electronic systems and their use on microwave frequency has put before implementors of the equipment two problems of vital importance: increase of dependability and reduction of overall dimensions at preservation of high electric parameters. At the decision of these problems the most significant difficulties have arisen at a stage of creation of frequency-selective filters in an integrated-circuit form. Frequency discrimination of filters depends on Q-factor of their elements. With increase of frequency Q-factor of reactive elements decreases, that conducts to deterioration of discrimination. Q-factor of inductors especially strongly decreases; for its increase it is necessary to increase the sizes, but it complicates miniaturization of LC-filters. To overcome these difficulties it is possible by creation of the digital filters which characterized by high stability and accuracy, simplicity of adjustment and an opportunity of use as adaptive systems, or analog active filters, for example based on gyrators, amplifiers with the limited transmission gain, operating amplifiers and others. The range of application of such filters is limited by frequencies on which it is possible to neglect frequency dependence of current gain of the transistor (up to hundreds megahertz). In a microwave band high-selective miniature filters are manufactured on the micro-strip lines, spiral resonators and ferro-electric elements. Each of these filter's groups possesses the specific advantages. But all these filters have two important limitations:

- Decrease of Q-factor with reduction geometrical size
- Presence of signal losses in a pass-band.

Hence, for miniaturization of microwave-range filters expediently use of methods and construction tools of filters, which electric parameters (Q-factor) would not depend on the elements geometrical sizes. To such requirements the active filters based on negatrons are correspond. Now they are manufactured on two basic schemes. In the first scheme the passive filter joins the semiconductor element with negative dynamic resistance. It allows raising Q-factor of filter tank,

due to indemnification losses. As such devices uses tunnel and avalanche transit time diodes. A limitation of Esaki diodes is their small saturation level that narrows a dynamic band of the filter. Avalanche transit time diodes possess the raised level of noise.

The schemes using generalized imittance converters (GIC) based on the transistors [1], [2] concern to the second group of microwave active filter.

At creation of microwave active filter dependence of a current transmission gain of the transistor and influence of feedback in the transistor uses. It allows using in a wide frequency band the transistor as GIC for synthesis high-Q reactive and negative active dynamic resistance. In comparison with passive microwave filters active filters possess greater Q-factor, the best size characteristics and the expanded functionality. The important advantage of these filters is the opportunity of their realization not only as hybrid microcircuits, but also kind of monolithic microcircuits based on GaAs-structures with Shottki's gate.

The purpose of this work is use of field-effect transistor for synthesis of high-Q analogues of the inductor and active microwave filters based on it.

II. MIROWAVE ACTIVE FILTERS MODELLING AND RESEARCH

To research FET as GIC we must use small-signal equivalent circuit of field effect transistor. The common direct extraction procedure of small-signal equivalent circuit parameter should lead to frequency-independent values. With increasing frequency, however, often a decreasing real part of the output admittance Y_{ds} is obtained and may become negative. The effect can be explained by stationary Gunn domain. It is nucleating at the drain side of the gate when the maximum electric field exceeds the threshold value for the negative differential mobility in GaAs. Authors in [3] suggest an extended equivalent circuit with negative resistance in the output part. This modification improves model accuracy over the entire range of operation conditions.

Using this small-signal equivalent circuit (Fig. 1) was modeling dependence invariant stability factor over frequency of a signal for common source, common drain and common gate schemes has been lead. The analysis of results has shown, that the widest area of potential unstable stability have common drain and common gate schemes. This defines expediency of

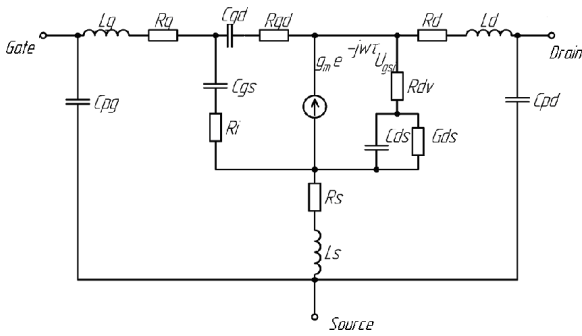


Fig. 1. Small-signal FET equivalent circuit

use these schemes as GIC at creation of microwave active filters possess. The common-drain circuit is the immittance converter. This means that inclusion on the scheme's input terminal of the inductor (Fig. 2(a)) allow realize on an scheme's

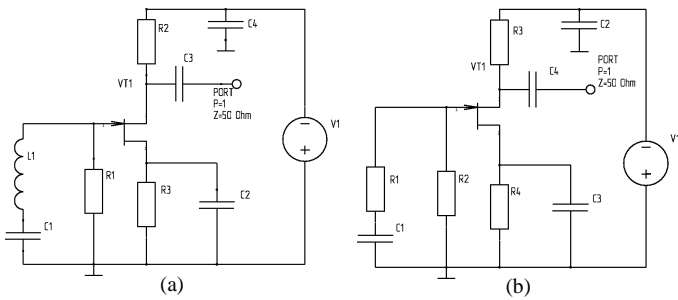


Fig. 2. Shema of active microwave inductor with low-Q coil (a) and with inductor-less active inductor (b)

output inductive resistance with negative active component. At inclusion on the scheme's input terminal resistor (Fig. 2(b)), on output of the scheme we receive inductive element with positive ohmic resistance. Q-factor of such inductor will be $Q \approx 1$. Cascade interconnection of two common-drain field-effect transistors with inclusion on an input terminal of the resistor (Fig. 5), will allow to realize on the output of the scheme inductor-less high-Q analogue of the inductor. Use of such scheme allows realizing active microwave filters without inductors. The analysis of modeling results shows, that common drain scheme with the inductor on an input terminal allows to realize the inductive element with negative output impedance up to -400 Ohm on frequency 12 Ghz (see Fig. 3). Common drain scheme with the ohmic resistance included on an input terminal allows to realize analogue low-Q ($Q \approx 1$) inductivity with resistance $R \approx X = 200$ Ohm on the frequency 5 Ghz (see Fig. 4).

Cascade inclusion of these two schemes allow to realize transistor analogue of the high-Q inductor-less element that allows to manufacture it as monolithic microcircuit. This sheme allow realized in a frequency band 10–16 Ghz possesses inductive $X = 500$ Ohm and negative $R = -120$ Ohm differential resistance (see Fig. 6).

Using this schemes of inductor were development active band-pass and stop-band microwave filters, suitable to manu-

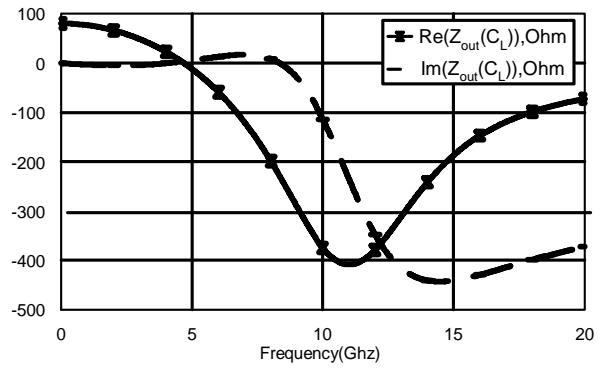


Fig. 3. Output impedance of active inductor with low-Q coil

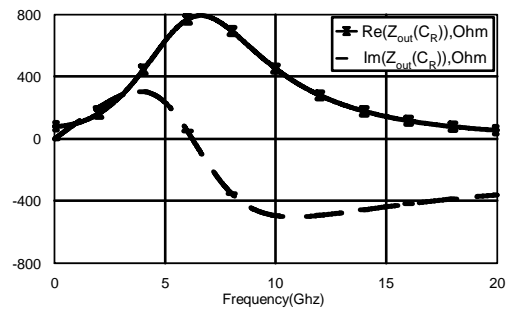


Fig. 4. Output impedance of low-Q inductor-less active inductor

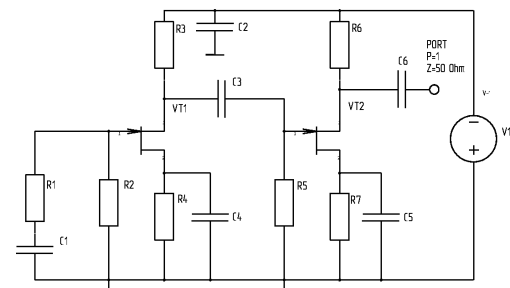


Fig. 5. High-Q inductor-less active inductor

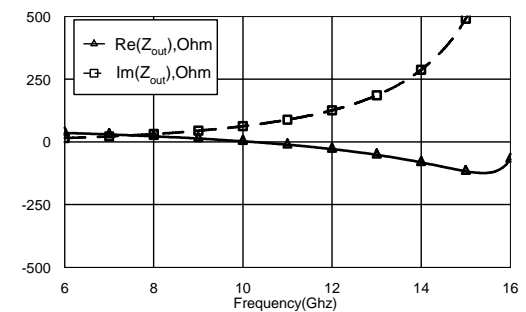


Fig. 6. Output impedance of high-Q inductor-less active inductor

facture as a hybrid or the monolithic microcircuit.

Example in which the principle of transformation low-Q inductors in active high-Q inductor is realized was band-pass and stop-band filters schemes (Fig. 7, 8, 9, 10). In these filters as the inductive element using microstrip inductor with Q-factor less than 10 units. Results of modelling (see Fig. 11, 12, 13, 14) using such low-Q inductor with GIC allow to realize high signal rejection outside passband (-40 dB and -60 dB accordingly for band-pass filter) and a small signal amplification in a passband ($+3$ dB) on the frequency $f = 10$ GHz. For single-resonator stop-band filter signal rejection was -42 dB, for two-resonator -73 dB. These filters are designed for realization as a hybrid microcircuit.

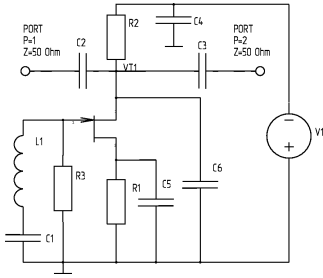


Fig. 7. One-pole bandpass active filter with low-Q inductor

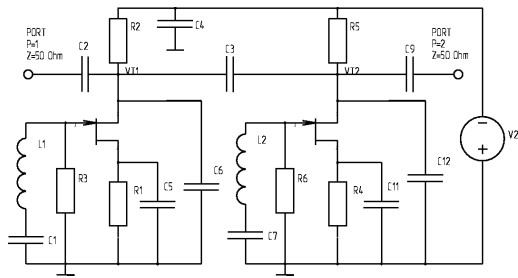


Fig. 8. Two-pole bandpass active filter with low-Q inductor

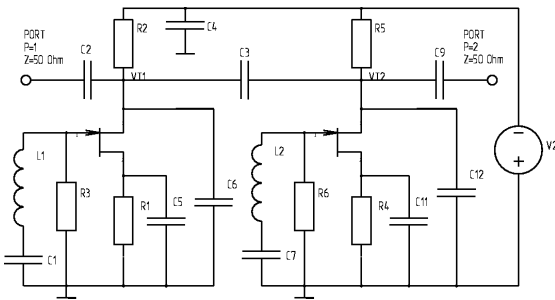


Fig. 9. One-pole bandstop active filter with low-Q inductor

Use of the inductor-less active inductor (see Fig. 5) allows to construct active bandpass (Fig. 15, 16) and bandstop filter (Fig. 17, 18) with following parameters: for single-resonator band-pass filter (Fig. 19) signal attenuation outside a passband -30 dB; for two-resonator band-pass filter (Fig. 20) signal attenuation outside a passband -60 dB; for single-resonator stop-band filter signal signal attenuation -24 dB; for two-resonator stop-band filter (Fig. 21) -47 dB. The analysis

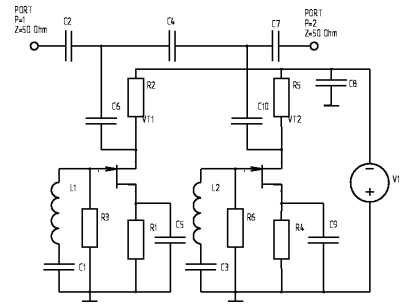


Fig. 10. Two-pole bandstop active filter with low-Q inductor

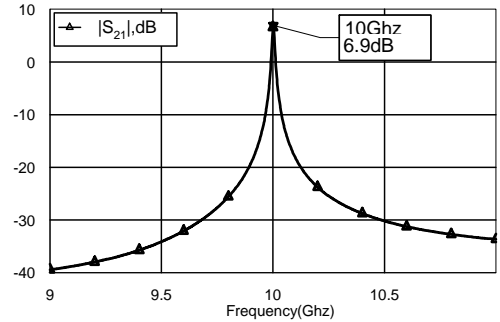


Fig. 11. Simulation results of one-pole bandpass active filter with low-Q inductor

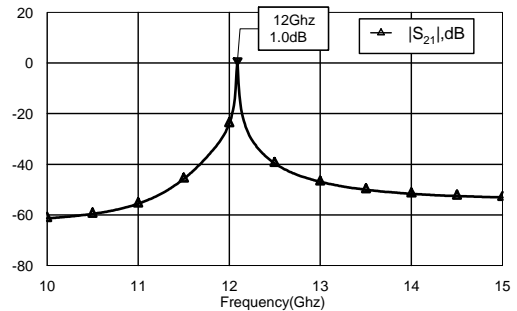


Fig. 12. Simulation results of two-pole bandpass active filter with low-Q inductor

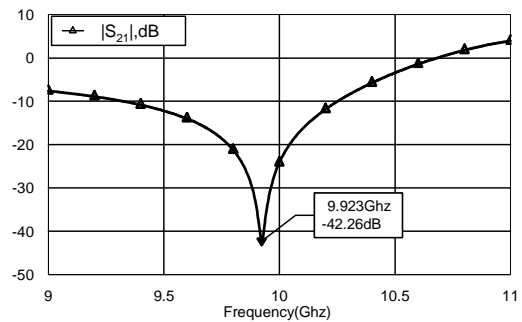


Fig. 13. Simulation results of one-pole bandstop active filter with low-Q inductor

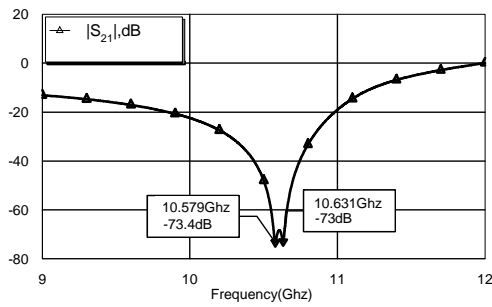


Fig. 14. Simulation results of two-pole bandstop active filter with low-Q inductor

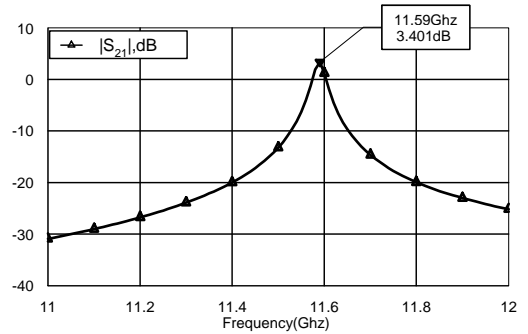


Fig. 19. Simulation results of one-pole bandpass inductor-less active filter

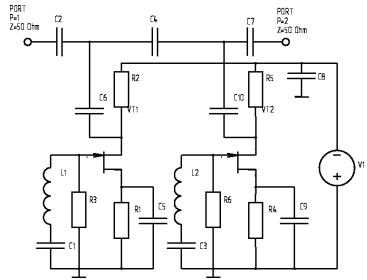


Fig. 15. One-pole bandpass inductor-less active filter

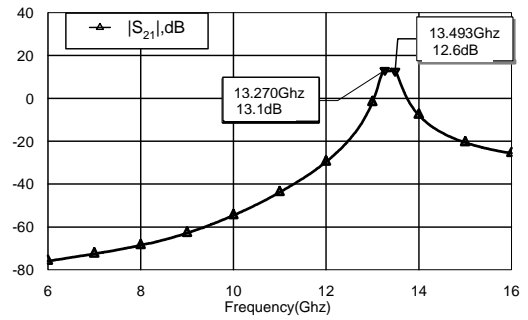


Fig. 20. Simulation results of two-pole bandpass inductor-less active filter

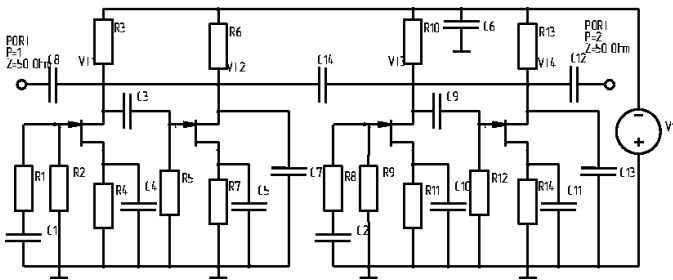


Fig. 16. Two-pole bandpass inductor-less active filter

of results enables to approve about perspectivity of developing inductor-less active inductors analogues and an opportunity of realization on it of active microwave filters as hybrid, and monolithic microcircuits of a large-scale integration.

III. DUAL-GATE FET ACTIVE FILTER

Using dual-gate FET allow realize two-resonator active filter on the single chip. This allow to get better temperature stability, decrease consumed power and size. This filter consist of two equivalent circuit: common drain circuit with included on an input terminal inductor element and common source circuit with included inductor between gate and drain. As a dual-gate FET can be represent as connection of two single-gate FET with couple first FET drain and second FET source. There is a manufactured dual-gate FET with addition noise-suppressing terminal, connected to the point of couple first

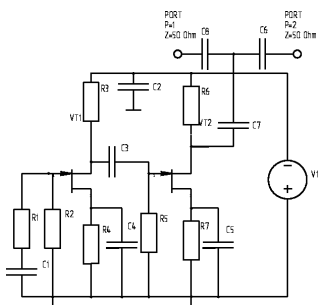


Fig. 17. One-pole bandstop inductor-less active filter

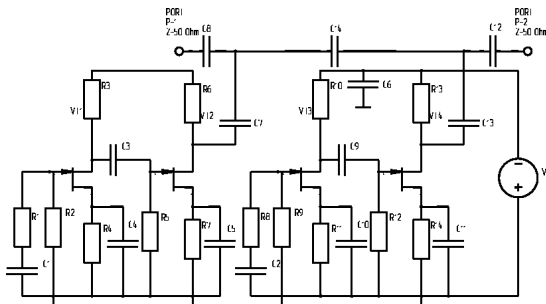


Fig. 18. Two-pole bandstop inductor-less active filter

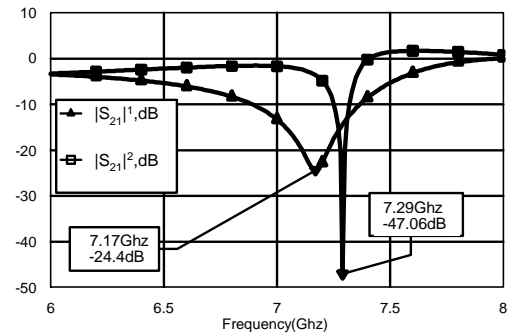


Fig. 21. Simulation results of one-pole and two-pole bandstop inductor-less active filter

FET drain and second FET source. Schematic and result of simulation of such filter are shown on Fig. 22 and Fig. 23. The analysis of results shown that such filter can reduce

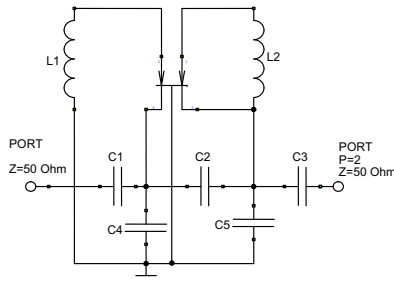


Fig. 22. Two-pole bandpass dual-gate inductor-less active filter (without bias circuit)

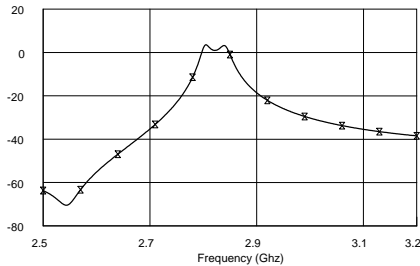


Fig. 23. Simulation results of two-pole bandpass dual-gate inductor-less active filter

geometrical size of hybrid IC.

IV. CONCLUSION

Experimental researches of schemes of FET inclusion by criterion of stability have allowed choosing the common-drain circuit as base scheme GIC for active microwave filters, as the most high-frequency and possessing properties of the immittance converter.

Modelling of output impedance for the common-drain circuit with included on an input terminal inductor element and ohmic resistance has enabled to realize high-Q ($Q \gg 1$) and low-Q ($Q \approx 1$) inductor analogues. Result of synthesis of these schemes became analogue of high-Q active inductivity without inductive elements.

Carried out research of the generalized immittance converter based on the field-effect transistor has allowed to realize based on the common-drain GIC schemes of band-pass and stop-band active microwave filters suitable for manufacture as a hybrid or monolithic microcircuits. As a result of modelling following parameters are received:

- For filters with inductive elements - for single-resonator band-pass filter signal attenuation outside a passband -40 dB; for two-resonator band-pass filter signal attenuation outside a passband -60 dB; for single-resonator

stop-band filter signal attenuation was -42 dB, for two-resonator stop-band filter -73 dB;

- For inductor-less filters - for single-resonator band-pass filter signal attenuation outside a passband -30 dB; for two-resonator band-pass filter signal attenuation outside a passband -60 dB; for single-resonator stop-band filter signal signal attenuation -24 dB; for two-resonator stop-band filter — -47 dB.

For two-pole band-pass dual-gate FET active filter signal attenuation outside a passband -60 dB, and a small signal amplification in a passband ($+3$ dB) on the frequency $f = 2.8$ Ghz.

REFERENCES

- [1] A. D.K. and H. R.Y.C., "Active filter for UHF and microwave frequencies," *IEEE Trans.*, vol. MCC-17, no. 9, pp. 662-670, 1969.
- [2] Filinyuk. N.A., *Active microwave filter on the transistors.* Moskow.: Radio and Communications, 1987.
- [3] F. Lenk, R. Doerner, and P. Heymann, "Negative resistance in GaAs-MESFET nonlinear modeling," *INMMC 4th Int. Workshop on Integrated Non-linear Microwave and Millimeterwave Circuits, Gerhard-Mercator University Duisburg*, vol. 47, pp. 77 – 82, October 9-11 1996.

FDTD Analysis of a Microwave/mm-wave FET Based on the Fully Distributed Model

A.Taeb, A.Abdipour, A.Mohammadi

Amirkabir University of Technology, E.E. Department, Microwave/mm-wave & Wireless Communication Research Lab.
Hafez Avenue, Tehran, 15914, Iran, (+98)-21-64543394
E-mail: aidin59@aut.ac.ir, abdpour@aut.ac.ir

Abstract-In this paper, the time domain response of a FET is obtained by means of the fully distributed model. The research novelty is the use of the Finite-Difference Time-Domain (FDTD) technique to solve the derived equations. By applying the procedure to a pi-gate GaAs MESFET, the S matrix is computed from time domain results over a frequency range of 10-28 GHz.

Keyword- distributed model; MESFET; Finite-Difference Time-Domain; differential equation; scattering parameter .

I. INTRODUCTION

Accurate and perfect analysis of a transistor is the main step in overall analysis of the microwave circuits containing them. Recent developments in mm-wave applications of FETs demand more attention on modeling problem for their future application. The performance of a three coupled active line structure acting as a typical transistor can be investigated by using different methods. Several models capable of describing the operation of a transistor such as the lumped and semi-distributed models have appeared in the literature [1], [2] and [3]. It is obvious that each model applies to a certain range of frequency. At high frequencies, where the dimension of the transistor becomes comparable to the wavelength, advanced methods accounting for wave propagation along the gate-width direction are needed. The most generalized and accurate approach is the Full-wave method. Unfortunately this method is time-consuming and causes an additional complexity in the solving process.

The analysis of the transistor at high frequencies leads us to develop the semi-distributed model. The distributed model is a modified version of the sliced model (semi-distributed model) obtained by increasing the number of segments to infinite. In the semi-distributed model, a general response is achieved by cascading the limited segments that consist of elements in which scaling method is used [4]. On the other hand, in the distributed model obtained from quasi TEM assumption, the KVL and KCL are applied to the equivalent circuit. The selection of the best model is a tradeoff between procedure complexity and response accuracy. Using the distributed model in comparison with sliced model will have an ability to increase frequency range. Also in this technique loading effects as an external parameter could be investigated.

This Paper can be summarized as follows: first we extract the differential equation system obtained by applying the transmission line theory to the distributed model.

Then, the FDTD technique is applied to the obtained equations. Our discussion focuses on the utilization of the FDTD technique to solve dependent equations explaining the nature characteristic of the transistor. Subsequently, the waveform in each point of the electrodes is computed as a time domain response.

Our procedure applies to a submicrometer-gate GaAs NE710 transistor and the results are compared with ADS outputs (sliced method).

II. THE DISTRIBUTED MODEL AND ITS ELEMENTS

A typical millimeter-wave FET is shown in Fig. 1. The proposed device consists of three coupled electrodes fabricated on a thin layer of GaAs, supported by a semi insulating GaAs substrate. In the proposed model each unit segment is divided into two parts, active and passive, whose elements are per unit length. The passive part describes the behavior of the transistor as a three passive coupled line and the interaction between them. The active part relates to the standard performance of a FET, which in this paper is modeled by a linear circuit. Fig. 2 shows the two parts of one segment of the three coupled microstrip line.

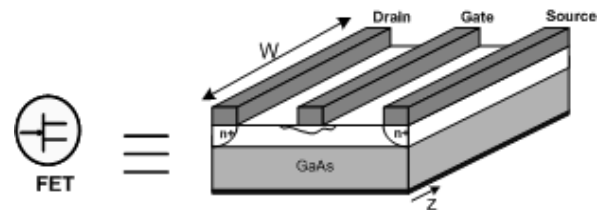


Figure 1. 3D structure of FET used in millimeter wave frequency.

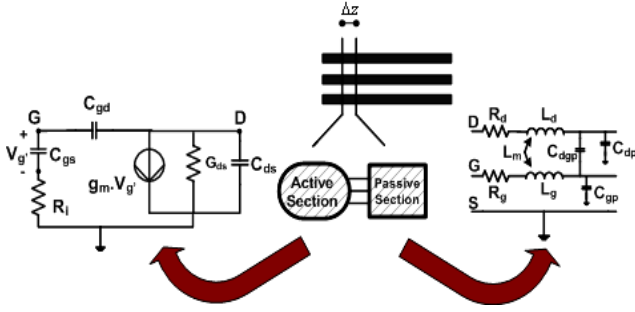


Figure 2. The different parts of a segment in the distributed model (with linear model for the active part)

III. THE FDTD FORMULATION

This new look to transistor modeling leads us to a set of differential equations interpreting the operation of a FET. On the other hand, using the transmission line theory and expanding it to our topology, the current-voltage differential equations that describe the model of Fig. 2 could be written as follows:

$$\frac{dI_d}{dz} + (C_{gd} + C_{gdp} + C_{ds} + C_{dp}) \frac{dV_d}{dt} - (C_{gd} + C_{gdp}) \frac{dV_g}{dt} + g_m V_g' + G_{ds} V_d = 0 \quad (1)$$

$$\frac{dI_g}{dz} + (C_{gd} + C_{gdp} + C_{gp}) \frac{dV_g}{dt} - (C_{gd} + C_{gdp}) \frac{dV_d}{dt} + C_{gs} \frac{dV_g'}{dt} = 0 \quad (2)$$

$$\frac{dV_d}{dz} + R_d I_d + L_d \frac{dI_d}{dt} + L_m \frac{dI_g}{dt} = 0 \quad (3)$$

$$\frac{dV_g}{dz} + R_g I_g + L_g \frac{dI_g}{dt} + L_m \frac{dI_d}{dt} = 0 \quad (4)$$

The above equations are obtained with regard to the effect of parasitic elements. Now a proper technique should be selected to solve the differential equations. One of the best numerical methods which can be chosen is FDTD technique. The FDTD technique seeks to approximate the derivatives in obtained equations with regard to discrete solution points defined by the spatial and temporal cells. Extending the problem to nonlinear distributed modeling in the future research and raising the accuracy of response are the main reasons for this selection. The primary idea of using FDTD technique is taken from [5].

Discretizing the derived equations using explicit time-space centered finite-difference scheme (Fig. 3) gives follow equations:

$$\frac{dI_i^{n+1/2} - dI_i^{n-1/2}}{\Delta z} + (C_{gd} + C_{gdp} + C_{ds} + C_{dp}) \frac{dV_i^{n+1} - dV_i^n}{\Delta t} - (C_{gd} + C_{gdp}) \frac{dV_i^{n+1} - dV_i^n}{\Delta t} + g_m \frac{dV_i^{n+1} + dV_i^n}{2} + G_{ds} \frac{dV_i^{n+1} + dV_i^n}{2} = 0 \quad (5)$$

$$\frac{dI_i^{n+1/2} - dI_i^{n-1/2}}{\Delta z} + (C_{gd} + C_{gdp} + C_{gp}) \frac{dV_i^{n+1} - dV_i^n}{\Delta t} - (C_{gd} + C_{gdp}) \frac{dV_i^{n+1} - dV_i^n}{\Delta t} + C_{gs} \frac{dV_i^{n+1} - dV_i^n}{\Delta t} = 0 \quad (6)$$

$$- (C_{gd} + C_{gdp}) \frac{dV_i^{n+1} - dV_i^n}{\Delta t} + C_{gs} \frac{dV_i^{n+1} - dV_i^n}{\Delta t} = 0$$

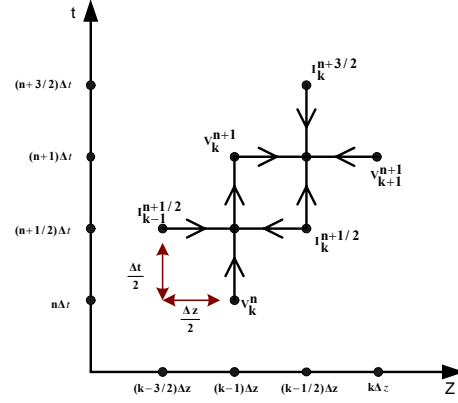


Figure 3. Definition of the voltage and current solution points and times in the FDTD discretization of the equations for each electrode

$$\frac{dV_{i+1}^{n+1} - dV_i^{n+1}}{\Delta z} + R_d \frac{dI_i^{n+3/2} + dI_i^{n+1/2}}{2} + L_d \frac{dI_i^{n+3/2} - dI_i^{n+1/2}}{\Delta t} + L_m \frac{dI_i^{n+3/2} - dI_i^{n+1/2}}{\Delta t} = 0 \quad (7)$$

$$\frac{dV_{i+1}^{n+1} - dV_i^{n+1}}{\Delta z} + R_g \frac{dI_i^{n+3/2} + dI_i^{n+1/2}}{2} + L_g \frac{dI_i^{n+3/2} - dI_i^{n+1/2}}{\Delta t} + L_m \frac{dI_i^{n+3/2} - dI_i^{n+1/2}}{\Delta t} = 0 \quad (8)$$

Where we denote

$$V_i^n \equiv V((i-1)\Delta z, n\Delta t) \quad \text{for the gate electrode} \quad (9)$$

$$I_i^n \equiv I((i-1/2)\Delta z, n\Delta t) \quad \text{for the gate electrode} \quad (10)$$

The equations system consisting of (5) and (6) is used to find the unknown parameters related to the gate and drain electrodes, V_i^{n+1} and V_i^{n+1} . But it is clear that there is another unknown parameter, the gate-source capacitance voltage $(V_i^{n+1})'$, which should be considered. The effect of this unknown parameter can be explained by an extra equation:

$$R_i C_{gs} \frac{(V_i^{n+1})' - (V_i^n)'}{\Delta t} + \frac{(V_i^{n+1})' + (V_i^n)'}{2} = \frac{V_i^{n+1} + V_i^n}{2} \quad (11)$$

It should be outlined that various conditions exist in terminals and these boundary conditions must be applied to discretized equations. The achieved auxiliary equations can explain not only the nodes which are known as the input and output of the transistor but also the loading effects at the beginning and at the end of the electrodes. So it can be said that the final result related to many conditions such as load location and node excitation.

By incorporating the terminal conditions we can reach to the recursive equation system of whose solving gives time domain response of different discretized nodes. In this trend, an innovative method which uses the time domain results to obtain scattering matrix is utilized.

IV. RESULTS

In this work we consider a Pi-gate MESFET transistor suitable for low-noise applications. The schematic of the proposed transistor including parasitic elements is shown in Fig. 4. The end of each electrode is supposed to be open. This configuration can be specified by an 2×2 S matrix (with the source is grounded at all points).

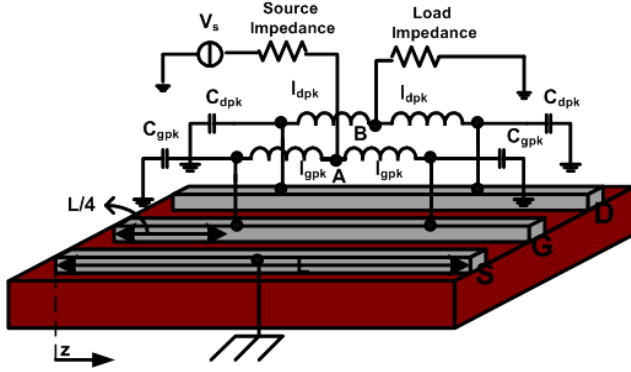


Figure 4. The schematic of a pi-gate FET including parasitic elements.

TABLE I. NUMERICAL VALUES OF DISTRIBUTED MODEL ELEMENTS
 $V_{ds} = 3 \text{ V}, I_{ds} = 10 \text{ mA}$

The distributed model elements	Numerical Values (per unit length)
C_{gs}	.771 nF/m
C_{ds}	.0178 nF/m
C_{gd}	.1178 nF/m
g_m	146.42 S/m
R_i	.002 ohm/m
L_d	780 nH/m.
L_g	161 nH/m
L_m	360 nH/m
C_{gp}	29.6 pF/m
C_{dp}	148 pF/m
C_{gdp}	29 pF/m
R_d	900 ohm/m
R_g	34300 ohm/m
C_{gpk}	.036 pF/m
C_{dpk}	.0296 pF/m
L_{gpk}	.766 nH/m
L_{dpk}	.868 nH/m

The transistor has a $0.3 \times 280 \mu\text{m}$ gate which is biased at $V_{ds} = 3 \text{ V}$ and $I_{ds} = 10 \text{ mA}$. The inductances and capacitances shown in Fig. 4 indicate the effects of bounding. The element values used in the distributed model are shown in Table. I. Fig. 5 shows the waveform of node 'B' obtained from distributed model at 25 GHz . The results are compared with ADS simulation in which slicing model is used. And also, the distributed model can be useful to derive the voltage and current waveforms in each point of the electrodes. Using the Fourier transform the voltage gain described by $\frac{V_d(z)}{V_A}$ is plotted in Fig. 6.

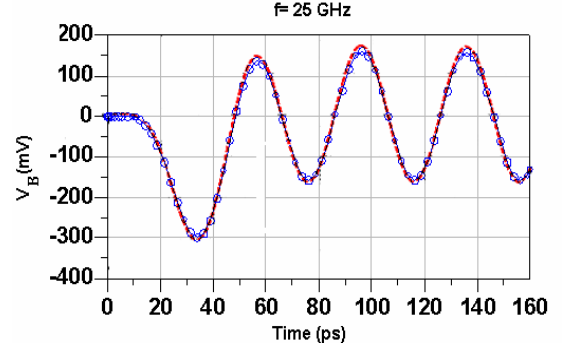


Figure 5. waveform of node 'B' compared with the ADS result (sliced model). The line marked by the circle is the ADS outcome.

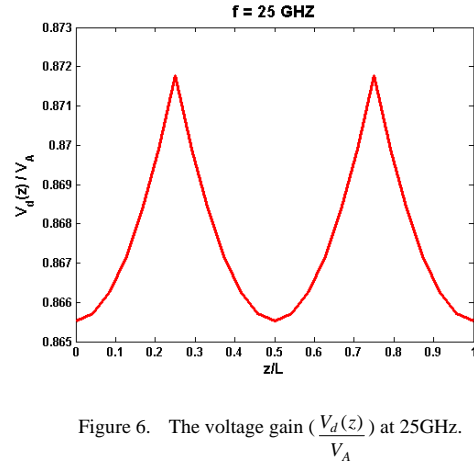


Figure 6. The voltage gain ($\frac{V_d(z)}{V_A}$) at 25GHz.

The Pi-gate structure can be known as a two-port network as shown in Fig. 7. Finally the S parameters of the transistor in 10-28 GHz band which are obtained from MATLAB simulation are plotted in Fig. 8. These outcomes are compared with results derived from ADS. Our results were also compared with the experimental data presented in [1] and a very good agreement has been achieved.

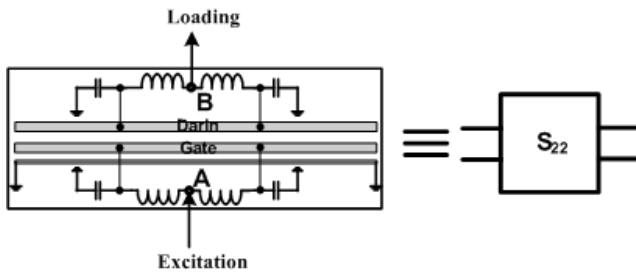


Figure 7. The equivalent network for obtaining the scattering parameter.

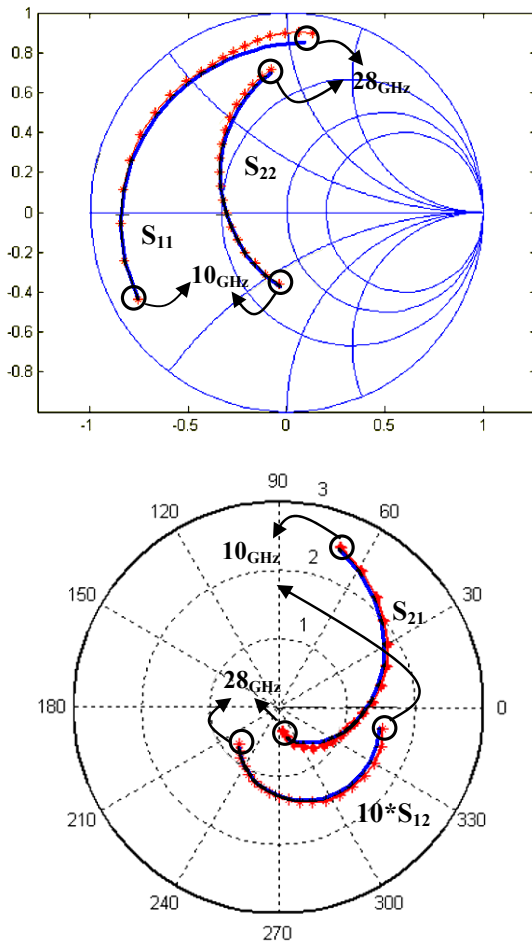


Figure 8. Comparison between scattering parameters obtained from distributed model and ADS results (sliced model) over a frequency range of 10-28 GHz. The lines marked by the asterisk are the distributed model results.

V. CONCLUSION

An accurate and new method for transient analysis of microwave/mm-wave transistor using the FDTD technique has been described. In this way, the fully distributed model for investigation of the wave propagation along the electrodes is introduced. Using this modeling method, scattering parameter of the three active coupled transmission lines as a transistor was obtained.

This approach can be applied to any MESFET or HEMT at millimeter-wave frequency. Also operating at the nonlinear region can be easily proposed in the model. Finally, using this method the optimization of the device geometry for improving its performance is possible.

REFERENCES

- [1] A.Abdipour, and A.Pacaud, "Complete sliced model of microwave FET's and Comparison with lumped model and experimental results", IEEE Trans. Microwave Theory Tech., Vol. 44,NO. 1, pp. 4-9, Jan. 1996.
- [2] M.Waliullah, S.M.El-Ghazaly, and S.Goodnick, "Large-signal circuit-based time domain analysis of high frequency devices including distributed effects", in IEEE MTT-S Dig., pp. 2145-2148, 2002
- [3] S.J.Nash, A.Plazker, and W.Struble, "Distributed small signal model for multi-fingered GaAs PHEMET/MESFET devices", in IEEE Symp. Microwave Millimeter-Wave Monolithic Circuit, pp. 219-222, 1996.
- [4] G.Moradi, A.Abdipour, A.Ghorbani, and F.Farzaneh, "Signal and noise analysis in sliced model of a FET mixer", in 2nd Int. Conf. Microwave & Millimeter-Wave Tech., pp. 5-8, 2002
- [5] J.A.Roden, C.R.Paul, W.T.Smith, and S.D.Gedney, "Finite-difference,time-domain analysis of lossy transmission lines", IEEE Electromag. Compat, vol. 38, NO. 1, pp. 15-24, Feb. 1996.
- [6] A.Taeb, A.Abdipour and A.Mohammadi, "FDTD analysis of lossy coupled transmission lines loaded by nonlinear devices", Asia Pacific Microwave Conference, (APMC'05), China, Vol. 5, pp. 3105-3108, Dec. 2005.
- [7] E.Ongareau, R.G.Bosisio, M.Aubourg and J.Obregon and M.Gayral "A non-linear and distributed modeling procedure of FETs", Int. Journal Numerical Modeling, Vol. 6,pp. 237-251, 1993 .
- [8] N.O.Sadiku, *Numerical techniques in electromagnetics*, CRC Press LLC, Second Edition, 2001.

Measurement and Modelling of a High Power Amplifier for the Integration in MIMO-OFDM System Simulations

C. Kuhnert, A. Ossowska, and W. Wiesbeck

Institut für Höchstfrequenztechnik und Elektronik (IHE)
Universität Karlsruhe (TH), D-76128 Karlsruhe, Germany
Phone: +49 721 608 3178, E-Mail: christiane.kuhnert@ihe.uka.de

Abstract— Future mobile communication systems will be based on a combination of MIMO and OFDM. For the design of MIMO techniques system simulations are an important tool, if they accurately predict behaviour in reality. For the realistic inclusion of high power amplifier (HPA) behaviour, this paper describes a measurement procedure as well as the adaptation to behavioural modeling. The amplifier model is then applied to a comprehensive MIMO OFDM system simulation. The effect of saturation and nonlinearity of the HPA on bit error performance of a MIMO OFDM system is investigated. It is shown that due to the sensitivity of OFDM to clipping the design of the HPA is critical, however the requirements can be relaxed by combining OFDM with MIMO.

I. INTRODUCTION

Mobile communication systems with multiple antennas at both link ends are a promising candidate for future consumer based mobile communication systems [1]. Orthogonal frequency division multiplexing (OFDM) has been adopted by several standards such as IEEE 802.11a. OFDM in combination with multiple input multiple output (MIMO) schemes has gained much popularity in mainstream fourth generation mobile communication research [2]. It is currently investigated by several groups developing communication protocols. Algorithms are developed and performance is evaluated by system simulations.

The sensitivity of MIMO-OFDM systems to physical impairments is of great interest [3], [4]. Generic and comprehensive simulation models are developed in a modular fashion to help a system designer predict the effect of component behaviour on the performance of MIMO-OFDM communication systems in terms of bit error rates [5]. In [6] the impact of RF impairments such as IQ-imbalance and DC-offset have been investigated in terms of a WCDMA communication system for High Speed Downlink Packet Access. The impact of front-end non-idealities has only been shown at the receiver. The communication system has been realized as a single input single output system, thus, the results do not represent a MIMO communication system.

In this paper the high power amplifier (HPA) at the transmitter is investigated. In section II the measurement procedure as well as the adaptation to behavioural modeling is described.

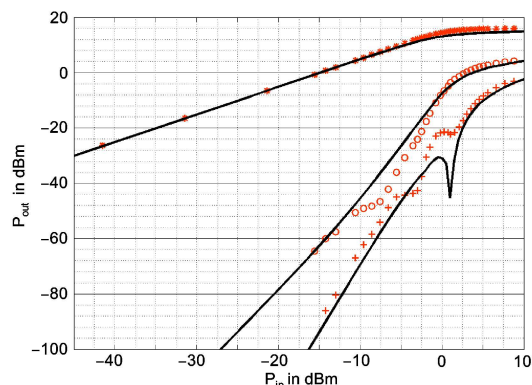


Fig. 1. Measurement results for the fundamental(*), third-order harmonics(o) and fifth-order harmonics(+). The solid lines show the fit to a polynomial model.

Section III deals with the integration of the HPA model in a MIMO-OFDM system simulator, followed by simulation results, see section IV. Finally, a conclusion is drawn.

II. AMPLIFIER MEASUREMENT AND BEHAVIOURAL MODEL

For the realistic inclusion of high power amplifier behaviour measurements have been carried out at an RF frequency of 2.14 GHz. An amplifier from Hittite (HMC375) was chosen as an example, however the procedure is general and any amplifier component available can be applied.

Three characteristics have been measured: The fundamental input-output relation at 2.14 GHz, the third order harmonics and the fifth order harmonics using a two-tone test with a spacing of 1 MHz between the tones. The measurement results are presented in Fig. 1.

For the inclusion in a MIMO-OFDM simulator, an analytical description is required. A 9th order polynomial model has been chosen:

$$y = a_1x + a_3x^3 + a_5x^5 + a_7x^7 + a_9x^9 \quad (1)$$

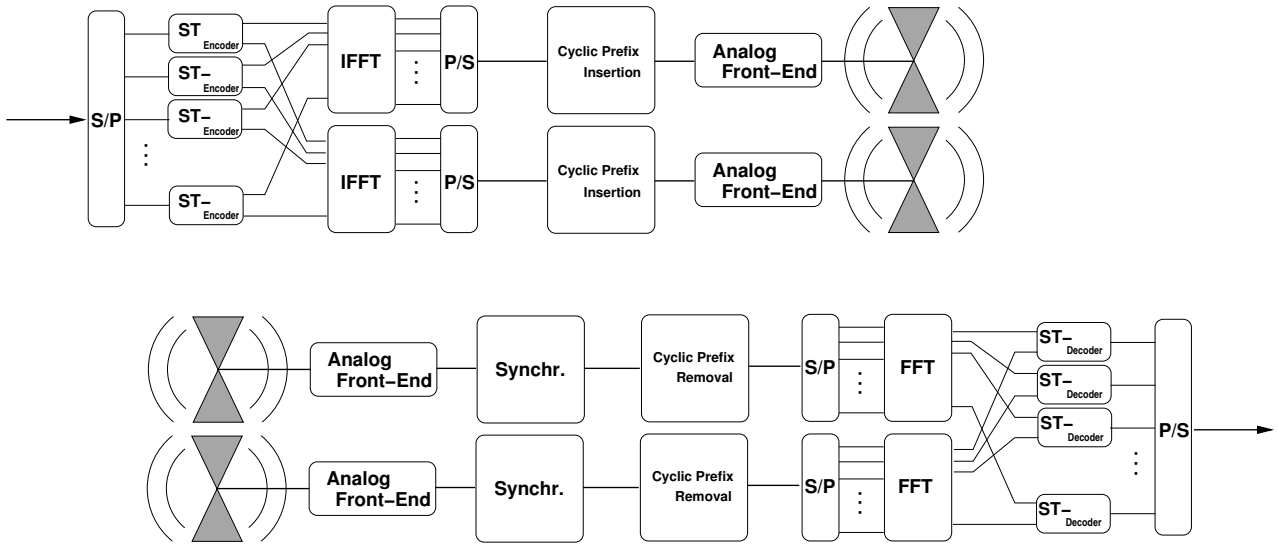


Fig. 2. Block diagram of the MIMO-OFDM system. A 2×2 system is shown as example.

The coefficients of this model are calculated from following amplifier properties:

- forward transmission gain S_{21}
- output power level at 1 dB compression point P_{-1dB}
- output power level at saturation P_{sat}
- gain compression at saturation G_c
- third-order intercept point IP_3

From the measurement results these parameters have been figured out as follows:

Parameter	Value
S_{21}	14.85 dB
P_{-1dB}	17 dBm
P_{sat}	19 dBm
G_c	5 dB
IP_3	31.75 dBm

The resulting characteristics are shown in Fig. 1. The agreement of measured values and polynomial model is obvious.

III. INTEGRATION IN MIMO-OFDM SIMULATOR

A high-level block diagram of the MIMO-OFDM system is shown in Figure 2. Random bits are delivered to a MIMO-OFDM modulator, which basically consists of a QPSK modulator, a Space-Time Coder which distributes the OFDM symbols onto the transmit antennas according to the scheme given in [7] followed by OFDM modulation (IFFT and cyclic prefix insertion).

There is an analog front-end (AFE) for each transmit antenna. For the investigations of non-ideal components in the transmit AFE, the component under investigation is described by a behavioural model. In this case, the behavioural model of the high power amplifier derived in section II is applied. Additive White Gaussian Noise is injected at each receive antenna. Each receive antenna is connected to an AFE.

The MIMO-OFDM demodulator consists of a synchronization block for each antenna, where time and frequency synchronization is carried out by maximum likelihood (ML) estimation [8]. After OFDM demodulation (cyclic prefix removal and FFT) the channels between each pair of transmit and receive antenna are estimated based on pilot subcarriers. The channels for other subcarriers are obtained by linearly interpolating the estimated channels. The Space-Time decoder combines the received signals in order to obtain the transmitted OFDM symbols. The QPSK symbol stream is then converted to a bit stream by ML detection. Finally, the bit error rate is obtained.

A generic model of a MIMO-OFDM system has been implemented in HP-ADS, a commercial software tool. ADS allows for a simultaneous co-simulation of analog and digital parts of a communication system.

IV. PERFORMANCE RESULTS

A. Simulation Parameters

For providing example results, two systems are compared: SISO 1×1 with one transmit and one receive antenna, and MIMO 2×2 with two transmit and two receive antennas. The parameters are given in the following table:

Parameter	Value
RF frequency	2.14 GHz
subcarrier spacing	2.68 kHz
number of subcarriers	1705
number of pilots	176
guard time	23 μ s
guard to symbol ratio	1/16

B. Simulation Results

Performance is analyzed in this paper in terms of bit error rate. The bit error rate (BER) is the ratio of the number

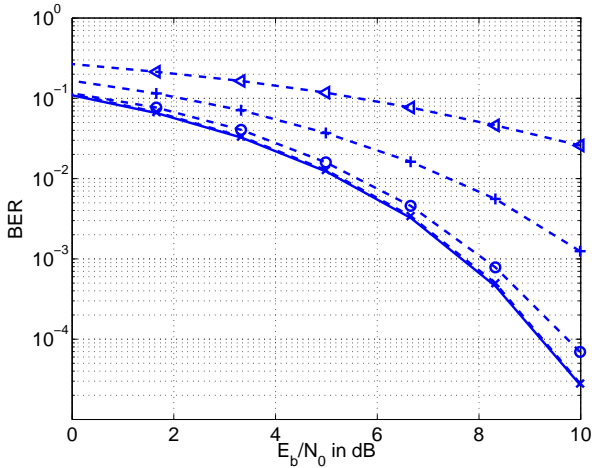


Fig. 3. Bit error rate (BER) for a SISO system for a transmit power of -20 dBm (\times), 0 dBm (\circ), 5 dBm ($+$), 10 dBm (\triangleleft), if the transmit high-power amplifier is nonlinear. As reference, the curve with a perfectly linear transmit high-power amplifier is provided as solid line.

of erroneous bits to the total number of bits. It depends on the signal to noise ratio, which is expressed in a normalized form (normalization with respect to bitrate and bandwidth) as E_b/N_0 , where E_b is the bit energy and N_0 is the noise spectral density.

The BER can be calculated analytically for additive white Gaussian noise (AWGN) channels [9]. For QPSK modulation, the relationship between E_b/N_0 and BER is

$$\text{BER} = \frac{1}{2} \text{erfc} \left(\sqrt{\frac{E_b}{N_0}} \right) \quad (2)$$

where $\text{erfc}(\cdot)$ is the complementary Gaussian error function.

The simulation results are shown in Fig. 3 for the SISO case and in Fig. 4 for the MIMO case. As reference, the curves with ideal components are provided. The reference curves of the ideal systems perfectly match the well-known theoretical bit error probability curves for QPSK.

In OFDM systems the peak to average power ratio is a problem because the transmit high power amplifier may be driven into saturation. The transmit power determines the operating point of the transmit HPA. In the MIMO case, the total transmit power is equally distributed on the two transmit antennas.

In Fig. 3 and 4 bit error performance is shown for the SISO and the MIMO case with four different values for the total transmit power, namely -20 dBm, 0 dBm, 5 dBm, and 10 dBm. The simulation results show, that the systems are nearly not affected if the amplifiers operate at least 5 dB below the input 1 dB compression point. The space time coding system with two transmit antennas relax the requirements by 3 dB compared to a system with only a single transmit antenna and the same total transmit power.

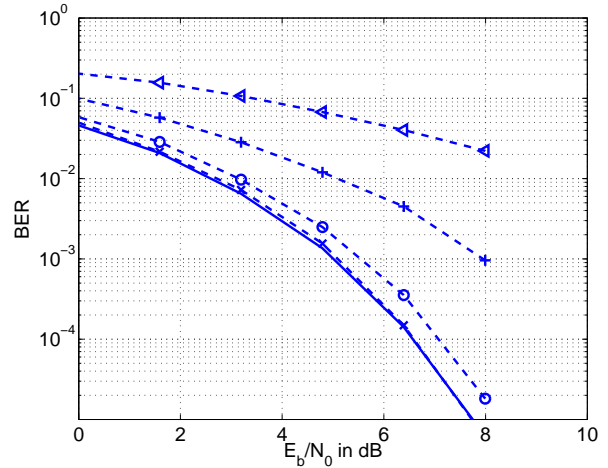


Fig. 4. Bit error rate (BER) for a 2×2 MIMO system for total transmit power of -20 dBm (\times), 0 dBm (\circ), 5 dBm ($+$), 10 dBm (\triangleleft), if the transmit high-power amplifiers are nonlinear. As reference, the curve with perfectly linear transmit high-power amplifiers is provided as solid line.

V. CONCLUSION

A method for the inclusion of measured HPA characteristics in system-level simulations of MIMO-OFDM communication systems has been presented.

OFDM goes along with a high peak-to-average power ratio, hence it is very sensitive to clipping. The design of the HPA is critical. The requirements can be relaxed by combining OFDM with MIMO, because the total transmit power remains fixed, i.e. each transmit antenna is supplied with less power.

ACKNOWLEDGMENT

The first author would like to thank Deutsche Telekom Stiftung for supporting her research activities.

REFERENCES

- [1] A. J. Paulraj, D. A. Gore, R. U. Nabar, and H. Bölcskei, "An Overview of MIMO Communications - A Key to Gigabit Wireless," *Proceedings of the IEEE*, vol. 92, no. 2, pp. 198–218, Feb. 2004.
- [2] G. L. Stüber, J. R. Barry, S. W. McLaughlin, Y. Li, *et al.*, "Broadband MIMO-OFDM Wireless Communications," *Proceedings of the IEEE*, vol. 92, no. 2, pp. 271–294, Feb. 2004.
- [3] J. Liu, F. Petre, A. Bourdoux, *et al.*, "Impact and Design Specifications of Analog Front-ends in MIMO-OFDM Downlink Transmission," in *Proc. ITG Workshop Smart Antennas*, Duisburg, Germany, Mar. 2005.
- [4] C. Degen, O. Koch, W. Keusgen, and B. Rembold, "Evaluation of MIMO Systems with Respect to Front-End Imperfections," in *Proc. 11th European Wireless*, Nicosia, Cyprus, Apr. 2005.
- [5] C. Kuhnert, S. Schulteis, C. Waldschmidt, and W. Wiesbeck, "Front-end requirements for MIMO communication systems," *Proceedings of the European Microwave Association*, vol. 1, no. 2, pp. 140–148, June 2005.
- [6] B. Lindorff, P. Malm, and O. Wintzell, "Impact of RF impairments on HSDPA Performance," *IEEE Int. Conference on Communications*, pp. 3265–3269, June 2004.
- [7] S. M. Alamouti, "A simple transmit diversity technique for wireless communications," *IEEE Journal on Sel. Areas in Comm.*, vol. 16, no. 8, pp. 1451–1458, Oct. 1998.
- [8] J.-J. van de Beek, M. Sandell, and P. O. Börjesson, "ML Estimation of Time and Frequency Offset in OFDM Systems," *IEEE Transactions on Signal Processing*, vol. 45, pp. 1800–1805, July 1997.
- [9] J. G. Proakis, *Digital Communications*, 4th ed. McGraw-Hill, 2001.

Detection, Localisation and Tracking of Foreign Objects Using UWB-Pulses

A. Gülck, O. Schimmer, R. Knöchel

Microwave Laboratory, Faculty of Engineering, University of Kiel, Kaiserstr.2, 24143 Kiel, Germany, + 49 431 880-6151

Abstract — This paper addresses the problem of non-contacting localisation of moving foreign bodies. For this purpose, an ultra-wideband interrogating signal is utilised, which interacts with potentially appearing foreign bodies in an otherwise homogeneous environment. The variation of the measurement signal due to influences of an interfering body is processed in order to determine the presence and the exact position within the observed area.

I. INTRODUCTION

The determination of presence and position of foreign objects in material streams or of material parameters is often required in e.g. modern industrial processes. Due to their unique properties microwaves are well suited to serve that purpose. The frequently used FMCW- and carrier frequency pulse-radars have the advantage of being largely independent of environmental influences and are capable of penetrating materials but are prone to distortions due to multipath effects and multiple reflections in near range applications.

Such interferences and parasitic echoes can be largely suppressed by using short pulses with ultra wide bandwidth (UWB) at low repetition frequency. The low frequency spectral components of UWB baseband pulses guarantee very good material penetration and deep interaction with the investigated material and possible foreign bodies. The capability of UWB signals for highly accurate determination of the position of dielectric obstacles was shown in [1]. In that work, the application of artificial neural networks was proposed for extracting the information from the received (Rx) signal of an ultra-wideband antenna array. Although the applied signal-processing method yields very good results, the effort for the determination of the artificial neural network during the training procedure is relatively high.

In this paper, a new signal processing approach is presented, which tries to reduce the analysis effort and facilitates direct physical interpretation of the measurement signals. Furthermore non-optimised short linear antennas are investigated for the reception of the signal instead of ultra-wideband antennas, which were used previously and which suffer from large geometrical dimensions.

II. MEASUREMENT SETUP

Fig. 1 shows the measurement system. The transmitter (Tx) consists of a pulse generator which generates a quasi Gaussian

monocycle using the technology, proposed in [2]. The pulse has a duration of approximately $t_p = 400$ ps and a peak-to-peak voltage of $U_{pp} = 6$ V (Fig. 2). The corresponding spectrum covers a frequency range from 700 MHz to 3.5 GHz, which is emitted via a UWB double-ridged waveguide horn-antenna. A foreign body, represented by a dielectric cube made of ceramic filled plastic material with permittivities of 4 and 9 and an edge length of 2.5 cm, is located between the horn and the receiving antenna array which is built up with short coaxial monopoles, having the advantage of being low cost and easily producible. Although the antennas are not optimised for the reception of UWB signals, the received pulse shape remains satisfactorily recognisable. The positions of the unknown foreign bodies are varied within the x/z-plane, whilst the y-position remains constant. The received signals of the antenna array, having the shapes of differentiated Gaussian monocycles, are recorded and digitised successively in a sampling oscilloscope. The small linear receiving antenna array can be arranged with shorter distances between the elements, leading to a high spatial resolution.

First measurements with 6 receiving antennas and a spacing of 3 cm in a line array were carried out. The transmitting horn antenna was placed in a distance of 50 cm above. To simulate the movement of a material under test, the cubes were directed in steps of 10 mm through the setup.

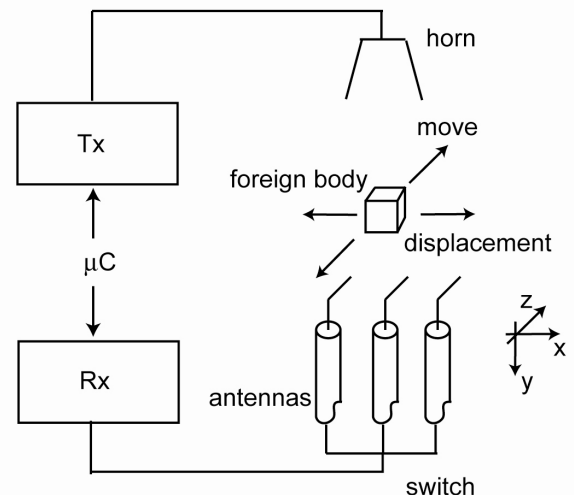


Figure 1. Measurement setup with foreign body and linear antennas.

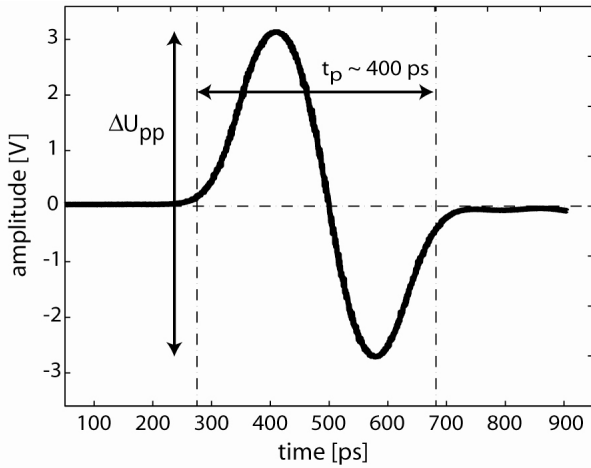


Figure 2. Transmitted pulse.

III. SIGNAL-PROCESSING

In a previous paper [1], the application of artificial neural networks for the extraction of the desired information from measurement data was proposed. If the problem has only a few degrees of freedom, variables like permittivity or position can thus be identified correctly. Unfortunately, this approach requires a considerable calibration effort and is specific only for a clearly defined problem. In a number of cases, it can be too complex and time-consuming to train the network for all kinds of variations, which can occur in the measurement setup.

In this paper a new analysis method is suggested to reduce the complexity of the data-processing. The method works without training prior to the relevant measurements. The results of the new procedure can be interpreted physically after pre-processing the raw data. This is sufficient for the identification and localisation of moving foreign bodies and largely independent from the shape of it.

The various linear antennas in the line array initially show slightly different behavior with respect to the amplitudes of the received pulses. Therefore, the amplitudes of the signals are normalised to the peak-to-peak voltage V_{pp} , as it is shown for one particular antenna in Fig. 3a. The normalisation factor for each antenna can be extracted from undisturbed signal portions. Hence there is no need for further calibration measurements. Next, as a second and most important step, the derivative is taken with respect to the z -direction as shown in Fig. 3b what produces a moving average. Thus, reference measurements are not necessary. In other signal processing approaches, a background signal as a reference is commonly subtracted from the actually measured signal. This procedure reduces perturbations due to omnipresent multiple reflections and clutter signals, which otherwise would spoil the reception signals. The disadvantage of that background subtraction approach, however, is the susceptibility against a drift of the system which is mainly caused by temperature changes of certain subsystems. The presented new approach does not have that shortcoming.

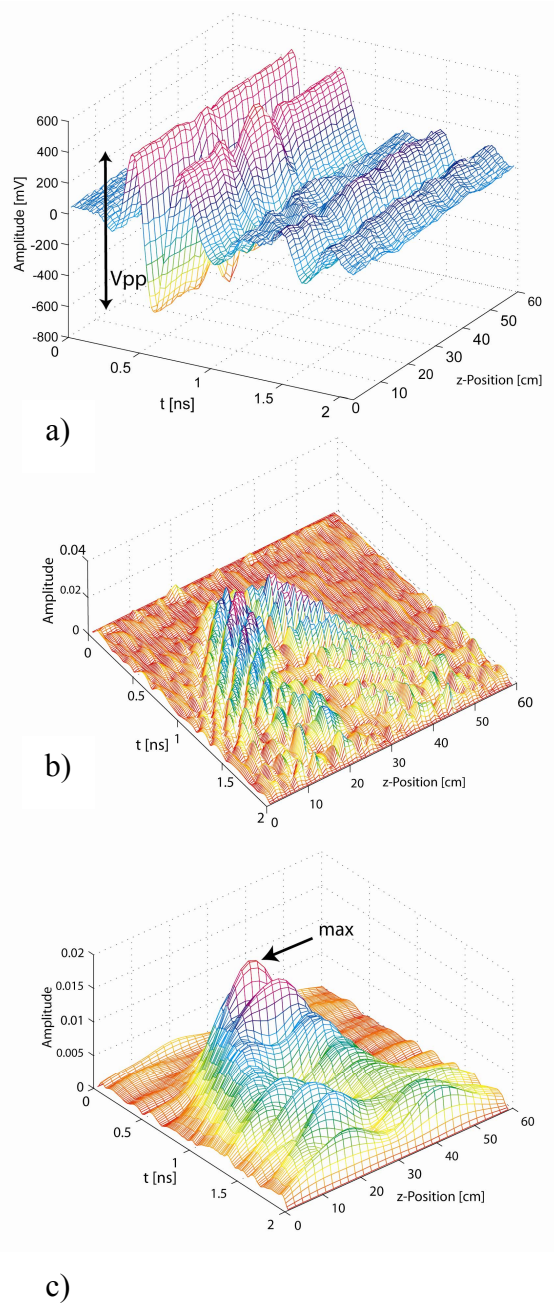


Figure 3. Amount of data during signal-processing from one antenna. (a) Raw data, (b) differentiated and norm, (c) smoothed.

The analysis is based on signal changes caused by potentially appearing foreign objects. It is somewhat similar to “moving target indication” (MTI), well known from conventional radar. By taking the smoothed absolute values of the differentiated signals, the maximum of the data surface indicates the presence and z -position of a foreign body. This is shown in Fig. 3c. The evaluation is based on this particular point.

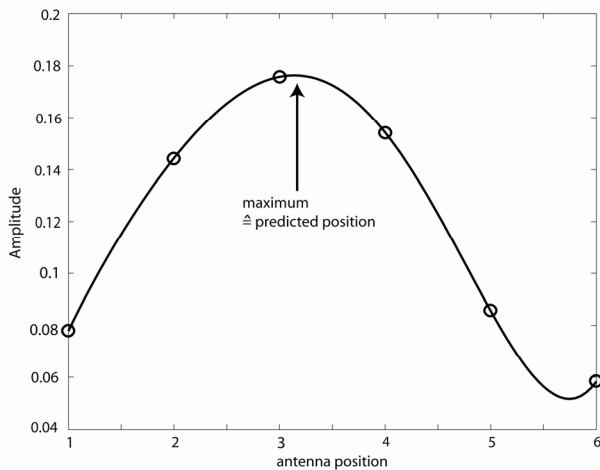


Figure 4. Interpolated maximum values of the 6 antennas in the x-direction.

The x-position of an object is indicated by that antenna of the receiving array, which shows the largest variation of the measurement signal (Fig. 4). For an increased resolution, the values of all six antennas can be interpolated, thus yielding interim values. The maximum of this interpolated curve indicates the position of the object across the array transversal dimension x.

IV. RESULTS

Measurements have been carried out which show that the described analysis is effective and fast. A foreign body of cubic shape having a permittivity value of 9 was investigated at several positions between the antennas. The displacement of the target was varied in transversal direction of the array (x-axis) and in longitudinal direction (z-direction), where the transportation of the material is supposed to take place. The results in Fig. 5 show the predicted positions plotted against the true positions. The root mean square error in x-direction ($RMSE_x$) is approximately 6.6 mm and for the z-direction ($RMSE_z$) 7.2 mm. The array of simply designed non-optimised linear antennas does not corrupt the localisation accuracy, but, on the contrary, admits a large improvement of spatial resolution, in contrast to previously used ultra wideband antennas.

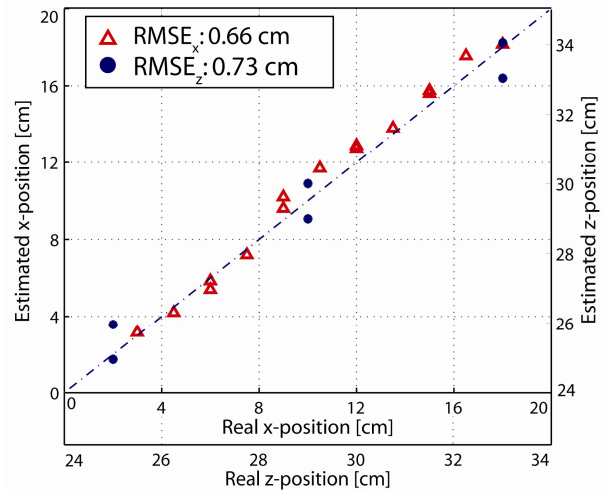


Figure 5. Predicted position of the foreign body. x-direction (triangles) and z-direction (dots)

V. CONCLUSIONS

The presented method for the localisation of foreign bodies describes a new approach for the simplified and efficient data-processing.

The received ultra-wideband pulses are reduced in their complexity and filtered. The system does not require training or a priori knowledge of possible incidents. Therefore the data-processing works without the huge calibration effort that results from the use of artificial neural networks. It does not even require a reference measurement. The mathematical methods are simply applied and require no excessive hardware. It is possible to separate between disturbed and undisturbed observation areas and to locate a possible foreign body quite accurate. A non-optimised linear antenna array is employed which however yields good results. An increased accuracy seems to be possible by using etched antennas instead of coaxial ones, because of well defined shapes and reduced distances.

REFERENCES

- [1] A. Gülck, T. Lehmann, R. Knöchel, "Characterisation of dielectric obstacles using ultra-wideband techniques", Proc. 35th EuMW, EuRAD 2005, Paris, pp. 259–262, October 2005.
- [2] O. Schimmer, A. Gülck, F. Daschner, J. Piotrowski, R. Knöchel, "Non-contacting determination of moisture content in bulk materials using sub-nanosecond UWB-pulses", IEEE Trans. Microwave Theory and Techniques, 53, No. 6, pp. 2107–2113, 2005

MW Disinfestations of Pallets

Bruno Bisceglia, sj¹, Roberto De Leo², Nicola Diaferia³

¹University of Salerno, Department of Electrical and Information Engineering, Via Ponte Don Melillo 1, 84084 Fisciano (SA), Italy +39 328 7041900, bbisceglia@unisa.it

¹University of Sannio at Benevento, Engineering Faculty, Corso Garibaldi 107, 82100 Benevento, Italy, bbisceglia@unisa.it

²Università Politecnica delle Marche, Dipartimento di Elettromagnetismo e Bioingegneria, Via Brecce Bianche 12, 60131 Ancona, Italy, r.deleo@univpm.it

³Emitech srl, Viale delle Palme, 70033 Corato (BA), Italy, diaferia.n@emitech.it

Abstract—Wood packaging represents a pathway for the introduction and spread of pests. In March 2002, the Food and Agriculture Organization (F.A.O.) issued some regulations describing globally approved phytosanitary measures that significantly reduce the risk provoked by most of pests. The main purpose of this work is to describe the disinfecting system of pallets through the microwaves treatment.

I. INTRODUCTION

The mentioned F.A.O. report describes the globally approved measures that reduce the risk of pest spread which should be adopted by all Members to avoid the hazard provoked by most of quarantine pests in international trade. The guidelines established in the document refer to the packaging material of raw wood (mostly coniferous wood) which could act as a pathway for the spread of pests, representing a threat to living trees. They include pallets, stowage materials, crates, boxes, loading platforms, cages, pallet collars, skids in use in most of the international deliveries. Paragraph 3 of the document is entitled: *Measures applied for wood packaging* and reviews both approved and pending approval measures. In this work some of the approved measures are dealt with.

II. TREATMENTS

A. Heat treatment (HT)

Wood packaging material should be heated in conformity with a specific time/temperature program which assures a wood core temperature of 56° C for a minimum of 30 minutes.

B. Methyl bromide fumigation (MB)

Wood packaging material should be fumigated with methyl bromide according to specific treatment protocols which, anyway, foresee a minimum temperature of 10° C and a minimum exposure time of 16 hours. At present, the thermal treatment through microwaves irradiation is not included among the globally approved measures which reduce the risk of spread of pests infesting the wood packaging material.

III. PRELIMINARY EXPERIMENTATION

Pinus pinaster, *Quercus robur* and *Populus plants* have been found infested in the subcortical zone and in the woody tissues. As for the nematode parasites of the *Bursaphelenchus* species

the tests have been carried out through observation on larvae and adults taking into account that in this group, unlike the cyst nematode, eggs are less resistant so the killing of larvae and adults can be considered a sign of the materials disinfection. As for the *Xylophagous coleoptera*, which have been studied and included in the group of phytosanitary interest, the observations were mainly focused on larvae because this stage represents the longest one in their development and also the stage which is more easily and frequently transported by packaging material. On the contrary, the egg of these insects is not a resistant stage.

IV. MW EXPOSURE

The disinfecting treatment was effectuated using 2 prototypes of shielded reverberating chamber in the Emitech laboratory; these were projected and realized by Emitech itself. Tests were carried out using nine standard pallets inside a shielded microwave reverberating chamber with a device generating 48 kW. Treatment time and consumption of energy were also considered. During the tests the following parameters were constantly monitored:

1) *Temperature on the pallets' surface*: It was monitored by means of an infrared thermo-camera, Flir Thermacam (SC 2000), interfaced with a computer that elaborates the temperature trend as a graphic.

2) *Inner temperature of each pallet*: Nine thermal resistances (Pt 100) made of mineral oxide and with a diameter of 2,5 mm were used. The thermal measure points were placed in the central part of each block in the pallet, inside which we executed a core sampling (diameter: 3 mm; depth: 4 cm).

3) *Electrical consumption of the system*: It was measured by means of a multimeter (HT GSC 57), equipped with amperometric clamps.

4) *MW Treatment*: The material treated with microwaves consists of nine standard pallets piled and placed inside the reverberating chamber. Each pallet has the following dimensions: 800 cm x 1200 cm; weight: 18 Kg. The weight of the whole pile is 162 Kg. The results obtained are showed in the following figure:

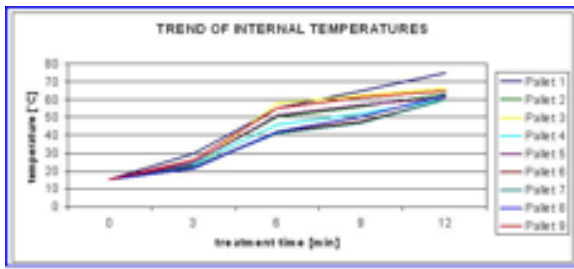


Fig. 1. Inner pallet temperature

V. MW DISINFESTATIONS SYSTEMS

A. Disinfesting tunnel

This particular solution, suitable for large industrial establishments producing pallets, allows the in line treatment. The tunnel can be installed at the end of the pallet production chain and just before the automatic stacking system. The system is provided with a device for the internal transfer of pallets, of that kind which is also used in the production of pallets. Thanks to this, the production line is not modified, but only extended in the final part.

The tunnel is a modular microwave shielded structure composed of electrically well connected, shielded elements in order to assure the highest efficiency of the system. Each part has one or more microwave power generators, a system of stirrers and a system of aspiration and humidity evacuation. The dimensions in section have been studied in order to optimize the process of the electromagnetic reverberation and to allow the treatment of standard pallets.

The homogeneity of the electromagnetic shield is always guaranteed and the irradiation process can be continuative, avoiding the down periods which are due to the loading/unloading of the treatment chamber.

This system typology allows to adapt the duration of the disinfestations/desiccation treatment to the time of production (180-360 pallets per hour). If necessary, the system can be multiplied with more treatment lines in case of very fast production lines (more than 360 pallets per hour).

The system is equipped with sensors for the thermo-hygrometric control of the material before and after treatment in order to assure a better calibration of the thermal microwaves process (also realized by means of a feedback on the microwaves generator) and an actual control of the irradiated material thermo-hygrometric conditions.

B. Static chamber for disinfestations

This particular solution is appropriate for small and middle-sized companies and for wood packaging repairers.

This system permits a flexible disinfesting treatment, since it is adaptable to the present productive requirements and to processing speed, allowing a just in time treatment.

The treatment system is a microwave reverberating and shielded chamber realized inside an ISO STANDARD 20' container. The system is equipped with several microwave

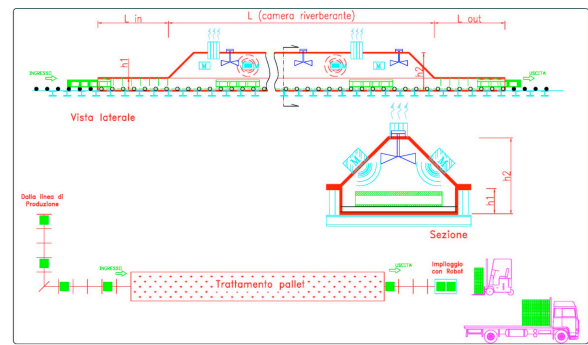


Fig. 2. Layout of riverberating tunnel for pallet disinfestations

power generators, their number depends on the needs of the loading.

The position of the stirrers and of the spouts for the microwaves irradiation is properly studied in order to optimize the irradiation uniformity and homogeneity in the treated material and, consequently, to optimize the heating process induced by microwaves.

This system configuration allows to treat piles of processed material (pallets), large volumetries of semi-processed material (planks, heels etc.) or raw wood, trunks, in a very short time.

The system can be integrated adding to the treatment chamber two chambers of smaller dimensions; the pre-chamber has an automated and shielded entry, the post-chamber has a similar exit.

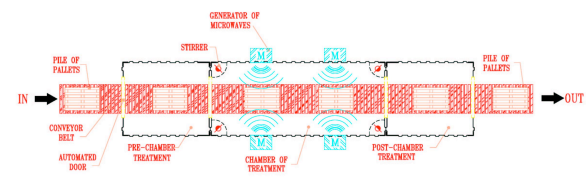


Fig. 3. Layout of riverberating tunnel for disinfestations of a stack of pallets

VI. CONSIDERATIONS

The tests performed showed a high efficiency of microwaves treatments in reverberating chambers towards phytoparasitic nematodes. As for *Bursaphelenchus mucronatus*, very rare specimens were found alive using a power of 3 kW and 4.5 kW, instead all nematodes were killed with a power of 9 kW and a 360'' exposure.

Referring to the *Bursaphelenchus* species, associated with the oak that was recorded for the first time in Italy during the collection of material for the treatments in the reverberating chambers, a 360'' exposure at 6 kW was sufficient to assure a **100% mortality**.

A **100% mortality** of the *Coleoptera Cerambycids*, in particular of the most noxious *Monochamus galloprovincialis*, was reached using only 3 kW of power for 360''.

In the case of the *Coleoptera Buprestidae* the efficaciousness was even more successful during the treatments of

coniferous wood. An exposure of 180'' only at a 3 kW power assured a **100% mortality**.

A power of 4.5 kW and a 360'' exposure were enough to exert a total control of material containing *Coleoptera Curculionidae* larvae.

For the last group taken into consideration, included among the *Scolytidae* of the conifers and broad-leaves, a 240'' exposure at 6 kW and 9 kW of power, respectively, permitted to reach a **100% mortality**.

ACKNOWLEDGMENT

The authors would like to thank Luzie Zaza for the accuracy used in the translation and in the revision of the English text.

REFERENCES

- [1] L. Ambrogioni, S. Caroppo, *Morphology and morphometrics of italian populations of bursaphelenchus species*, Nematol. Medit, 26: 97-116, 1998.
- [2] L. Ambrogioni, L. Marinari, A. Palmisano, *Description of Bursaphelenchus tusciae sp. n. from Pinus pinea in Italy*, Nematol. Medit, 26: 243-254, 1998.
- [3] D. Andreuccetti, M. Bini, A. Ignesti, A. Gambetta, R. Olmi, *Microwave Destruction of Woodworms*, Journal of Microwave Power and Electromagnetic Energy, Vol. 29, No. 3, 1994.
- [4] D. Andreuccetti, M. Bini, A. Ignesti, A. Gambetta, R. Olmi, *Feasibility of Microwave Disinfestation of Wood*, Proc. of 26th Annual Meeting IRG/WP, Helsingor (Denmark), doc. no. IRG/WP/95-40051, June 1995.
- [5] D. Andreuccetti, M. Bini, A. Ignesti, R. Olmi, A. Gambetta, R. Vanni, *A microwave device for woodworm disinfestations*, Proc. of the International Conference on Microwave and High Frequency Heating, St John's College, Cambridge (UK), September 1995.
- [6] H.J. Banks, *Stored Grain Research Laboratory*, CSIRO Entomology, Canberra, ACT 2601, Prospects for heat disinfestation.

Design and Performance of an UWB Antenna for a Mono-static Microwave Radar System

Amnoiy Ruengwaree, Abhijit Ghose, and Günter Kompa

University of Kassel, Department of High Frequency Engineering,
 Wilhelmshoer Alee 73, D-34121 Kassel, Germany,
 Tel: +49-561-804-6528, Fax: -6529, E-mail: amnoiy@hfm.e-technik.uni-kassel.de

Abstract — In this research work, design and performance of an ultra wideband (UWB) microwave antenna is described. The antenna is backed by a reflector and fed through the image ground plane. Intersection of two circular areas of different radius of curvature makes up the antenna element. Antenna element is made of Aluminum. Bandwidth is determined by the radius of curvature of lower circular section of the antenna element. The UWB antenna is suitable for detection of ultra-short electric pulses as given by the measured VSWR from 0.1 GHz to 20 GHz (Percent bandwidth of 198%). The UWB antenna is used in a mono-static radar system. Analysis and performance details are described for the resistive duplexer. Measurement results are presented for the far-field radiation of the antenna using ultra-short pulses. Average error in distance measurement using the mono-static system was measured to be 1.59% at a distance of 1 meter.

Keywords — mono pulse radar; position measurement; pulse radar; radar detection; UWB antenna.

I. INTRODUCTION

UWB antenna is used for receiving and transmitting sub-nanosecond electromagnetic pulses in a pulsed microwave radar system. This is known as pulse-echo radar [1]. The distance of the object is calculated from the received signal by using time-of-flight principle [2]. A bi-static configuration of the UWB microwave radar, with spatial separation of the transmitter and receiver antenna elements, can be found in [3]. In a bi-static system two antennas are used, one as transmitter and other as receiving antenna. In the present work, mono-static configuration is used, as shown in Fig. 1, where single antenna element is used for transmitting and receiving the pulses. In case of mono-static configuration, prior knowledge of the object angle to the antenna plane is not necessary for determining distance of the object, this is suitable for determination of buried objects inside another material. Mono-static configuration is reduced in size, and suitable for antenna array.

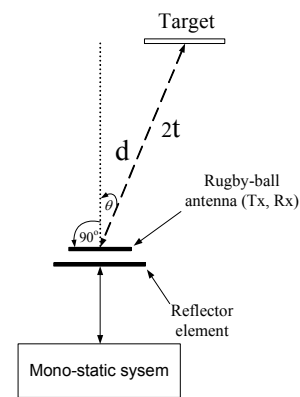


Figure 1. Mono-static microwave radar configuration.

II. MONO-STATIC UWB MICROWAVE RADAR SYSTEM

In Fig. 2, the system blocks of the mono-static microwave radar system is described. Antenna is connected through the broadband duplexer.

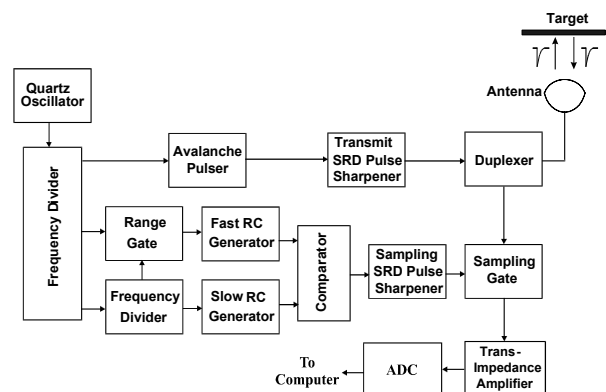


Figure 2. Block diagram of the mono-static UWB microwave radar system.

Basic clock signal is provided by the stabilized 20 MHz quartz oscillator, which feeds a frequency divider circuit. A CMOS IC which has selectable output from 20 kHz to 10 MHz sets the pulse repetition frequency of the radar. Frequency divider output is amplified by an avalanche pulse. Step recovery diode (SRD) is used for shaping the transmitted pulses (FWHM: 140 ps, Rise time: 100 ps) with maximum pulse amplitude of 7 V. A broadband duplexer is used for separating the transmitted and received pulses. Outputs from two RC charging circuits are compared, and comparator output is followed by a second SRD based pulse sharpener, output of which is used for sampling of the received pulses. Diode (Schottky) bridge is used for the sampling of the received pulses. Received signal is sampled with the sampling aperture of 50 ps. Extended-time sampling is used to down-convert the received picosecond pulses into the millisecond range. Received pulses are fed directly into a high-gain trans-impedance amplifier. Target range information from the received signals are extracted using a computer.

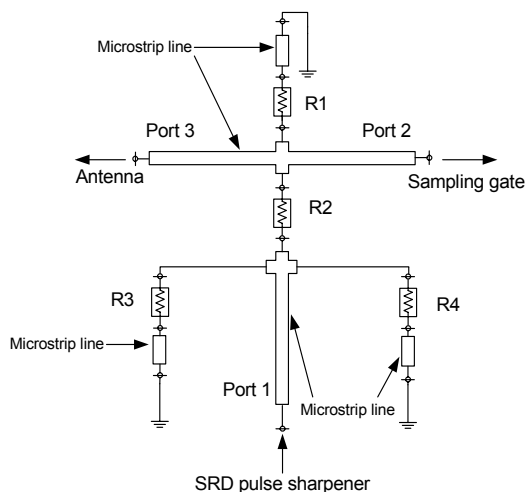


Figure 3. The schematic of the resistive duplexer.

A. Broad-band Resistive Duplexer

The resistive duplexer (Fig. 3) is designed on the basis of bridge-reflectometer concept [4]. The three port divider contains lossy components to improve simultaneous matching of all ports. The divider consists of symmetrical resistive films deposited on ceramic substrate. The circuit was realized on planar microstrip transmission line. Measurement and simulation results of the reflection and transmission coefficients of the divider are shown in Fig. 4 and Fig. 5, respectively. Optimization of the circuit has been performed using electromagnetic field simulator. Transmission coefficient is shown in Fig. 5. Measured

transmission is decreased beyond 10 GHz due to parasitic effects at the microstrip to coaxial transitions [5].

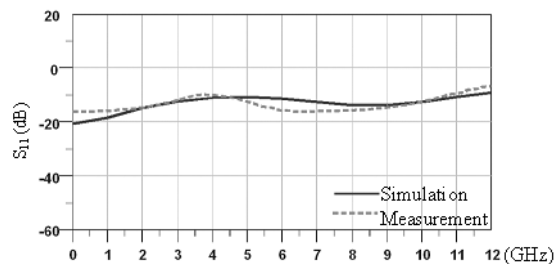


Figure 4. The eigen reflection coefficients of the signal divider at port 1.

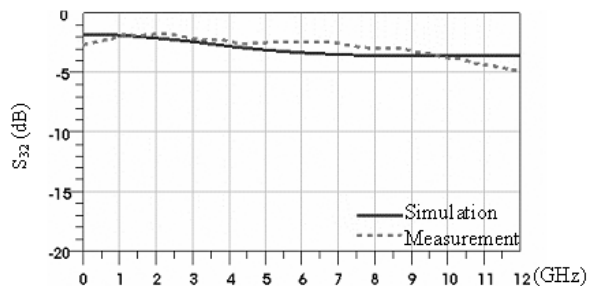


Figure 5. The transmission coefficients of the signal divider.

B. A novel rugby-ball antenna for pulse radiation

Wideband matching of the antenna is needed for radiating electrical pulses of sub-nanosecond region. Also simple and cost-effective fabrication of the antenna is desired.

For wideband applications a bow-tie antenna was proposed in [6]. Problems with the bow-tie configuration is that additional loading (capacitive or resistive) is needed to reduce unwanted reflections from the drive point. Planar ‘trapezoidal’ antenna was proposed in [3]. Planar Trapezoidal antenna is useful only for bandwidth of 1 GHz to 5 GHz. In another attempt, ‘Planar Inverted Cone Antenna (PICA)’ was proposed in [7] for radiating ultra wideband signals. In the present approach, antenna element consists of intersecting areas of two circles of different radius of curvature. The antenna is termed as Rugby-ball antenna for the similarity of its shape with Rugby-ball [8]. The advantage of the new antenna is improved impedance bandwidth and VSWR performance in the frequency range from 0.1 GHz to 20 GHz compared to the previous UWB antennas. It is seen in Fig. 6 that the lower circular contour of the antenna has smaller diameter compared to the upper part of the antenna.

The UWB antenna was simulated using a 3D electromagnetic field simulator. In Fig. 6, The diagram of the shape of the antenna and surface mesh elements are shown. Aluminium plate of thickness 2 mm is used to fabricate the antenna element, reflector and ground plane.

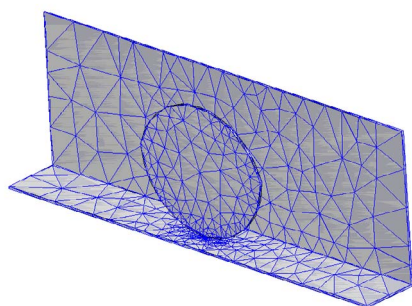


Figure 6. Antenna shape and surface mesh elements.

The placement of feed point have significant effect on the antenna impedance. The height between ground plane and antenna element was chosen such that it optimises the input matching of the antenna. The VSWR was further optimised using the 3D electromagnetic field simulation to obtain VSWR, impedance, and percent bandwidth. The reference plane for the measurements was set at the SMA connector feed point which is just underneath the image ground plane. The measurements were carried out using a vector network analyzer (HP8510). Simulation and measured VSWR of the antenna from 0.1 GHz to 20 GHz as shown in Fig. 7.

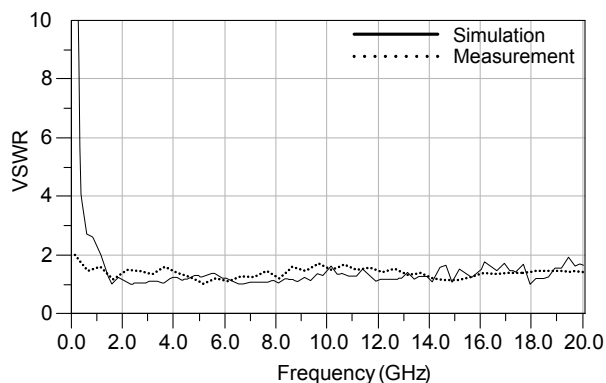


Figure 7. Simulated and measured VSWR of antenna.

The broadside far-field pulse radiation of the Rugby-ball antenna were measured and are shown in Fig. 8. Amplitude of radiated pulses were measured with different angles of θ in broadside direction [8]. Electric field were

measured for different elevation angles of θ as shown in Fig. 8.

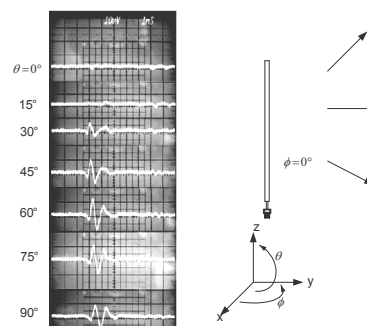


Figure 8. Measurement results for the broadside far-field radiation of the antenna.

From broadside radiation of antenna, it can be seen that maximum peak pulse amplitude is attained at an angle of θ equal to 60° (Fig. 8). Radiation decreases gradually towards zero degree.

III. EXPERIMENTAL RESULTS OF THE UWB RADAR

Fig. 9 shows the measured reference and reflected pulse from the target. A metallic target was used as object in the mono-static radar system. First pulse is the reference pulse and the second is the reflected pulse from the target. Distance between antenna and target is determined by time-of-flight principle.

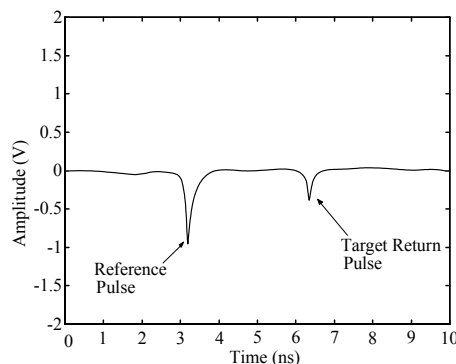


Figure 9. Measured reference and reflected pulse of the UWB mono-static microwave radar using the Rugby-ball antenna.

In Fig. 10, measured distance error of the object is plotted in case of mono-static configuration. Measurements were performed equipped with the UWB antenna. Average difference is shown together with

maximum and minimum difference of 10 measurements. Average error is found to be 1.59 % for mono-static system.

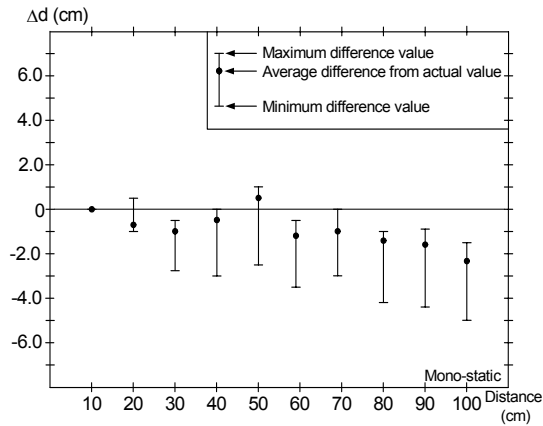


Figure 10. Measurement result of UWB mono-static microwave radar system using the UWB antenna.

IV. CONCLUSION

Design details of a new UWB antenna and a wideband diplexer is presented for a mono-static pulsed microwave radar. Low VSWR performance is achieved for the frequency bandwidth from 0.1 GHz to 20 GHz by optimizing the upper and lower radius of curvature of the antenna element, which is suitable for transmission of UWB pulses. Extended-time-sampling method was used in the receiver of the radar system, which reduces the hardware cost of the system, as the signal processing is performed in the low frequency region. Using the mono-static pulsed microwave radar system, low (1.59%) average error in near range (1m) distance measurement is achieved.

REFERENCE

- [1] J. E. Mast, "Microwave pulse-echo radar imaging for the non-destructive evaluation of civil structures," University of Illinois at Urbana-Champaign, Illinois, U.S.A., 1993.
- [2] S.A. Hovanesian, Introduction to Sensor Systems, Norwood : Artech House, 1988, pp. 55-68.
- [3] A. Duzdar "Design and modeling of an UWB antenna for a pulsed microwave radar sensor," H.F.T., University of Kassel, Kassel, Germany, July 2001.
- [4] F. van Raay and G. Kompas, "A new active balun reflectometer concept for DC to microwave VNA applications," Proc. 28th European Microwave Conf., Amsterdam, The Netherlands, Oct. 1998, pp. 108-113.
- [5] G. Kompas, Practical Microstrip Design and Applications, Norwood : Artech House, 2005.
- [6] K. L. Shlager, G. S. Smith, and J. G. Maloney, "Optimization of bow-tie antennas for pulse addition," IEEE Trans. Antennas Propagat., vol. 42, no. 7, pp. 975-982, Jul. 1994.

- [7] Seong-Youp Suh "A comprehensive investigation of new planarwideband antennas," Virginia Polytechnic Institute and State University, Virginia, U.S.A., 2002.
- [8] A. Ruengwaree, R. Yuwono, and G. Kompas, "A novel rugby-ball antenna for pulse radiation," Proc. 35th European Microwave Conf., Paris, France, Oct. 2005, pp. 455-458.

A 2.14 GHz inverse class F Si-LDMOS power amplifier with voltage second harmonic peaking

W. Gerhard, R. Knöchel

University of Kiel, Microwave Laboratory, Kaiserstrasse 2, D-24143 Kiel, Germany, + 49 / 431-880-6167, wg@tf.uni-kiel.de

Short Abstract—A simplified inverse class F power amplifier (PA) with a voltage second harmonic peaking and third harmonic short operating at 2.14GHz for WCDMA base station applications has been developed. The load network is based on transmission line harmonic traps and provides high impedance at the second and low impedance at the third harmonic to the PA. The PA uses a packaged Silicon LDMOS transistor and provides an output power of 13.8W and a drain efficiency of 66%. Due to the high gain of 13.4dB an excellent power added efficiency (PAE) of 64% is obtained. The 6dB back off PAE is 35%. To the author's knowledge, the highest obtained output power and PAE for a packaged Si-LDMOS transistor based on this architecture at this frequency is presented.

Keywords – *rf power amplifier, LDMOS, inverse class F, efficiency, WCDMA.*

I. INTRODUCTION

The growing demand for efficient and linear power amplifiers (PA) in today's digitally modulated wireless communications systems (e.g. WCDMA, WLAN) urgently requires research and development of suitable PA architectures. State of the art class AB PAs, which are used in such systems, make a compromise between obtained efficiency and linearity. These PA's are often combined with digital predistortion to achieve the linearity requirements. PAs based on the concept of harmonic tuning such as class F and inverse class F amplifiers [1] can achieve a substantially higher efficiency as class B or class AB amplifiers. An increase of the peak efficiency leads also to an increase of the important back off efficiency of these amplifiers. Although, due to the nonlinear transistor trans-conductance, the nature of these amplifiers is nonlinear in the vicinity of the pinch-off voltage, a digital predistortion scheme to achieve the linearity requirements is still possible but complicated. Harmonically tuned PAs can also be combined with other efficiency and linearity improvement techniques such as envelope elimination and restoration (EER), envelope tracking (ET), LINC and Doherty [2-4]. Even switching PAs operating in class D or class E using Si-LDMOS are reported, but are not suitable to obtain high output power and high efficiency beyond 2GHz. Table I shows the performance of PAs reported in the literature in terms of output power and efficiency. In [9] a PA with a PAE of 60% at 1.78GHz is presented. The load network utilizes a quarter wavelength transmission line and an additional series tuned lumped tank circuit. Four harmonics were taken into account. Now, this paper will present a simplified load network topology based on a packaged single Si-LDMOS transistor having transmission line harmonic traps, without any transforming lumped components. Inverse class F amplifiers offer the practical

advantage of ease of realization of the required open condition for the 2. harmonic instead of an open condition for the 3. harmonic, which is required for regular class F amplifiers. Due to the package parasitics, in particular the series inductance, the generation of a perfect short circuit at the intrinsic transistor terminals is not possible. In contrast, an open circuit can be implemented as a parallel resonance which includes the output drain-source capacitance. In the proposed network only the first three harmonics are taken into consideration, whereas only the 2. drain-source voltage harmonic is peaked and added to the fundamental voltage. An improved efficiency in comparison to a class B design (59%) and a good agreement between the simulated (70%) and measured PAE (66%) could be achieved.

TABLE I

Performance values for PA's using single Si-LDMOS

PA class	Freq, GHz	Output Power, W	Efficiency, %
D [5] (Ericsson PTF 10135)	1.0	13	Drain: 60 PAE: 58
E [6] (Freescale MRF-282)	1.0	6.2	Drain: 69 PAE: 64
E/F [7]	0.8	30	Drain: 64
F [8]	0.5	20	Drain: 76.6
Inv. F [9] (Freescale MRF-282)	1.78	13	Drain: 60 PAE: 54
this paper, Inv. F (Philips XLF4G21-15)	2.14	13.8	Drain: 66 PAE: 64

II. PA ARCHITECTURE

A. Theory and Practise of Harmonic Tuning

The output network for a single ended class B amplifier provides a short circuit for all higher harmonics and can be regarded as a special case of harmonic tuning. In class F and inverse class F designs, respectively, the even and odd harmonic voltage or current components are peaked by applying a short or an open circuit to the PA's output. If an infinite number of harmonics is theoretically taken into account, the waveforms are put into the shape of a half sinusoid (even harm.) and a square wave (odd harm.) for the voltage or current, respectively. Fig. 1 shows the respective waveforms which result in an efficiency of 100%. To that respect class F and inverse class F designs are dual. In the case of inverse class F PAs the voltage at the transistor takes the form of a half

sinusoid and the current is a square wave. In practice, however, only a few harmonics can be controlled. If only 3 harmonics would be taken into consideration (up to 3 fo) class F

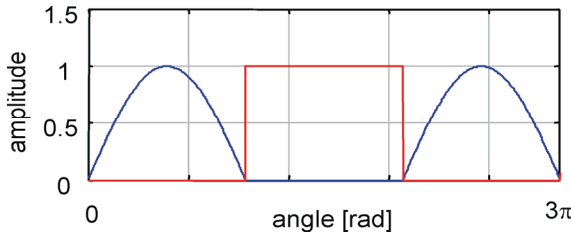


Fig. 1. Square wave (odd harmonics) and half sinusoid (even harmonics) for ideal class F / inverse class F PA.

theoretically would achieve a slightly higher efficiency of 88.4% as inverse class F, which would deliver 84.9%. Table II lists the achievable efficiencies and impedance conditions for various classes of operation. It is assumed that higher

TABLE II

Efficiencies for different harmonic tuning, Load-Pull Sim.

PA class	2 fo	3 fo	higher ∞	eff. / % Theory	eff. / % Simul.
B, ideal	short	short	short	78.5	59
F, 3 fo	short	open	short	88.4	75
Inv. F, 3 fo	open	short	short	84.9	73

harmonics are short-circuited (e.g. by the drain-source capacitance). Due to the package parasitics (series inductance) a perfect 2. harmonic short can usually not be realized at the intrinsic transistor, if the drain-source capacitance is small enough and does not provide a short-circuit (or low impedance) by itself. The output transistor characteristics, especially the ohmic region (knee voltage) as well as the transistor and package parasitics are causing strong limitations in the design

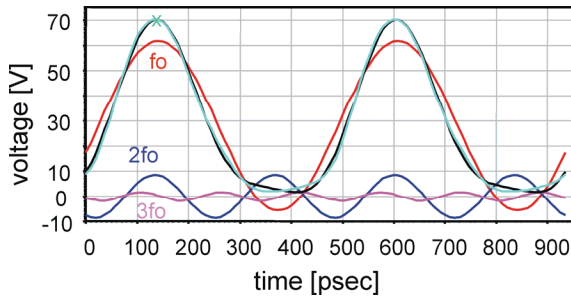


Fig. 2. Simulated drain voltage and harmonics. Drain voltage denoted as (x).

of harmonic impedance terminations. Thus reduced efficiencies in practical realizations result. Furthermore in practice it is always simpler to control the 2. instead of the 3. harmonic impedance. Therefore an inverse class F design, based on a packaged transistor, showing only 2. harmonic

voltage peaking with a 3. harmonic short-circuiting is offering some practical advantages. However, an increased drain-voltage swing results and has to be taken into consideration. Fig. 2 plots the simulated drain voltage (green, marked as “x”, 5 harmonics included in simulation) and the first three voltage-harmonics. The shaping of the drain voltage as a sinusoidal wave can be seen. If only the 2. harmonic is peaked and added to the fundamental voltage component, the black curve in Fig. 2 results (partly covered by the green curve). Thus it is indicated that just 2. harmonic peaking is sufficient for improving the efficiency. Taking higher harmonics into account does no longer improve the results, because the drain-source capacitance (5pF) will ultimately short-circuit all higher harmonics. In Table II the simulated drain efficiencies for different classes of operations are displayed. They are obtained through load pull simulations of the used LDMOS transistor without the package. It can be seen, that an inverse class F design could potentially improve the efficiency by about 14% in comparison to a class B design.

B. Back-off Efficiency

The back-off efficiency, which is an important figure of merit in the characterization of a PA can be calculated for an ideal class B amplifier as:

$$\eta = \frac{\pi}{4} \cdot \frac{V_{output}}{V_{PEP}}$$

The efficiency as function of the power back off is plotted in Fig. 3. It can be deduced, that the efficiency drops down by 50% at a power back-off of 6dB (39.5%). The efficiency back-off response of such an ideal class B PA will be used for comparison with the inverse class F design.

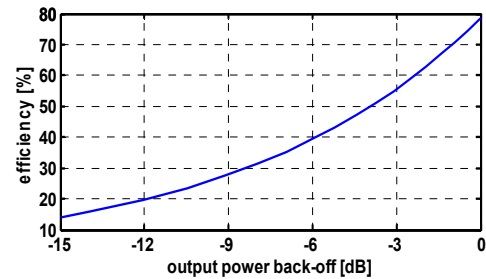


Fig. 3. Efficiency of an ideal class B amplifier vs. power back off.

C. PA-Design

The transistor used in this design is a 15W Silicon LDMOS (XLF4G21-15) from Philips Semiconductors, Nijmegen, The Netherlands. Using load pull simulations the optimum load impedance was found for an DC drain voltage of 28V. The gate was set to the pinch-off voltage of 2.6V. The output network shows harmonic traps and is designed to provide an open at the 2. harmonic and a low impedance at the 3. harmonic at the intrinsic drain port. The drain-source capacitance as well as the package parasitics are taken into account. Furthermore the matching circuit transforms the 50ohm load to a 35ohm load as

seen from the transistor. Details of the load network are shown in Fig. 4. The simulated drain current and voltage waveforms indicating the inverse class F operation are displayed in Fig. 5. All circuits were using RO4003 20mil substrate. The simulated

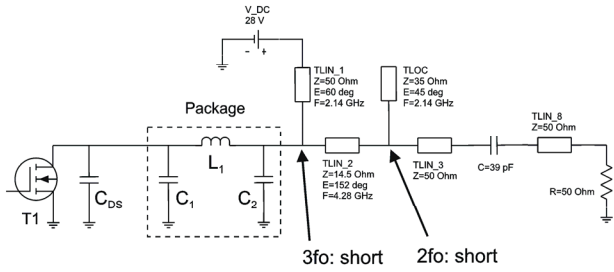


Fig. 4. Schematic of the inverse class F PA architecture.

drain efficiency of the overall design is only slightly reduced from 73% (unpacked chip die) to 70% with an output power of 16.9W (42.3dBm) at 2.14GHz and a driving power of 28dBm. In Fig. 6 the practical implementation of the PA can be seen.

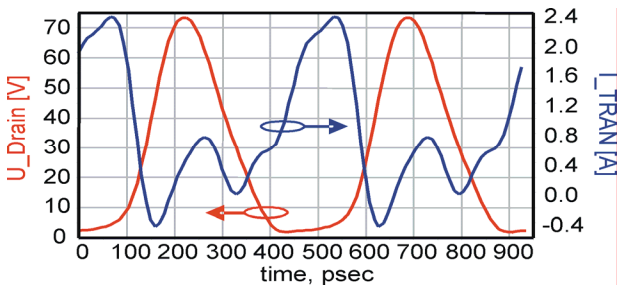


Fig. 5. Simulated drain current and voltage waveforms at the intrinsic transistor at 2.14GHz. Drain eff.: 70%, Pout: 16.9W (42.3dBm).

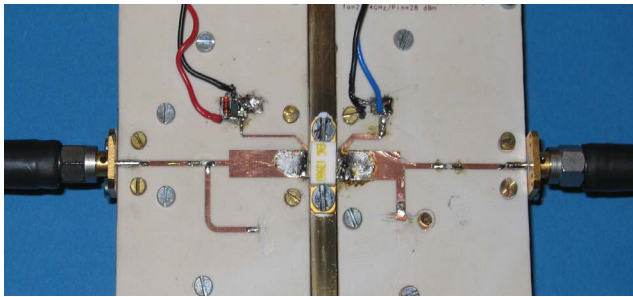


Fig. 6. Implementation of the inverse class F PA.

III. MEASUREMENT RESULTS AND DISCUSSION

A. Inverse class F PA characterisation

Fig. 7 shows the measured output power as a function of the input power. The obtained maximum output power was 13.8W (41.4dB). It is 0.9dB less than expected by the simulation result. The corresponding large signal gain is thus 13.4dB. The behavior and the comparison of the simulated and measured

drain efficiency as well as power added efficiency (PAE) as a function of the output back off power is shown in Fig. 8. A good agreement between simulation and practical results can be observed. At peak power the measured drain efficiency is 66% (70% simulated) and the PAE is 64% (68% simulated).

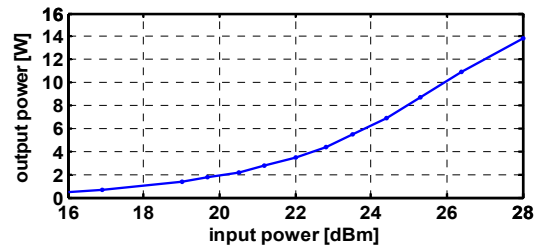


Fig. 7. Measured output power vs. input power.

Because the gain is quite high, the degradation to the PAE is only small. At 6dB output power back off the PA shows a PAE of 35%, which compares very well to the theoretical back off efficiency of a class B PA (50% reduced efficiency at -6dB).

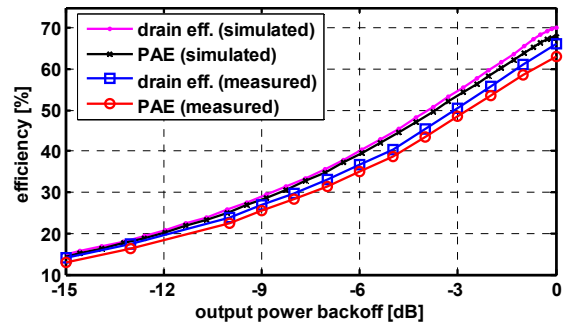


Fig. 8. Simulated and measured drain efficiency and power added efficiency (PAE) vs. output back off power.

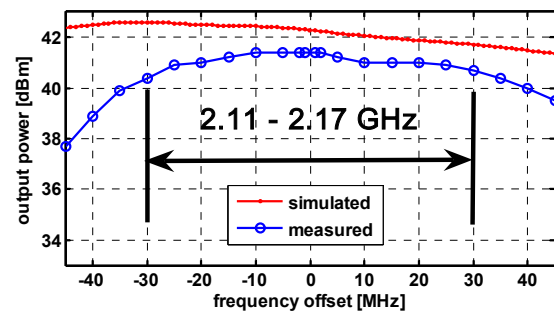


Fig. 9. Simulated and measured output power vs. frequency offset (fc: 2.14GHz).

The input matching, being -15dB at the peak power, is also working well. To evaluate the frequency response of this PA a frequency sweep was carried out. The output power response is shown in Fig. 9. Unfortunately the driving PA and the whole complex measurement set-up do not provide a large bandwidth. The driving output power decreases at frequency

offsets beyond about ± 25 MHz. Thus the measurement results include the bandwidth limitation of the driving PA. However within the WCDMA (UMTS) base station downlink bandwidth the power variation is less than 1 dB. The frequency dependence of the simulated and measured drain efficiency as well as power added efficiency is plotted in Fig. 10. Within the UMTS 60 MHz bandwidth the measured drain efficiency remains higher than 60%.

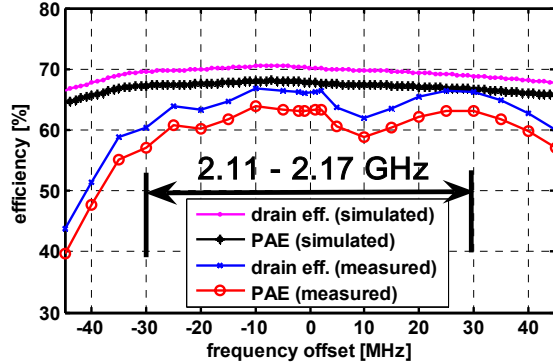


Fig. 10. Simulated and measured drain efficiency and power added efficiency (PAE) vs. frequency offset (f_c : 2.14 GHz).

B. Characterisation of distortions

Finally distortions of the PA have to be determined in terms of AM/AM and AM/PM conversions. Fig. 11 and Fig. 12 plot the corresponding normalized AM/AM- and AM/PM-curves, respectively, for different frequency offsets. It can be deduced

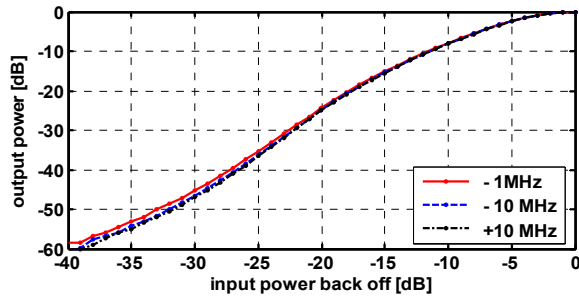


Fig. 11. Measured AM/AM conversion for various frequencies.

that the complex transfer characteristics of the PA do not change much with frequency variation. The AM/AM curve shows the power compression at peak power and at low levels of back off power as the typical nonlinear behavior due to the nonlinear transistor transconductance (pinch off). Strong AM/PM distortion characteristics with a phase change of about 30 degrees can be observed over an output power range of 60 dB (input power: 40 dB). From these curves (AM/AM and AM/PM are monotonic functions) a digital predistortion function could be derived and theoretically, a perfect pre-distortion could be achieved for the PA, arriving at a linear transfer function and a corresponding PAE of 35% at 6 dB output power back off. However the PA's behavior is strongly nonlinear and a

predistortion is more complicated in comparison to a "more linear" class AB power amplifier.

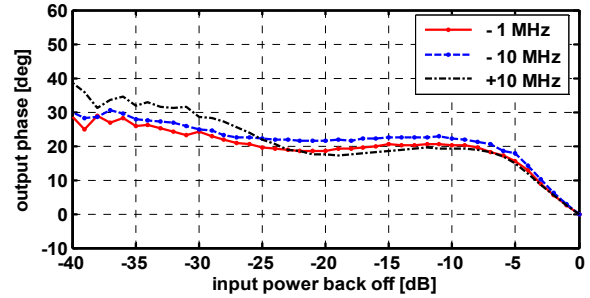


Fig. 12. Measured AM/PM distortion for various frequencies.

IV. CONCLUSIONS

A new design of a PA based on a simplified inverse class F architecture at 2.14 GHz using a packaged Si-LDMOS transistor is presented. A transmission line load network with harmonic traps, taking only 3 harmonics into consideration, is utilized. The maximum output power was measured as 13.8 W. Excellent performance values of the power added efficiency of 66% at peak and 35% at 6 dB back-off power could be obtained. Over the UMTS-bandwidth of 60 MHz the drain efficiency remains higher than 60% and the power variation is less than 1 dB. To investigate the possibilities of a digital predistortion the AM/AM and AM/PM conversion functions are investigated. The realization of the predistortion circuit is subject of further research.

ACKNOWLEDGMENT

The authors wish to acknowledge support by Philips Semiconductors, Nijmegen, The Netherlands.

REFERENCES

- [1] A.V. Grebennikov, *RF and Microwave Power Amplifier Design*, McGraw-Hill, 2005.
- [2] H.L. Krauss, C.W. Bostian, F.H. Raab, *Solid State Radio Engineering*, J. Wiley & Sons Inc., 1980.
- [3] S.C. Cripps, *Advanced Techniques in RF Power Amplification Design*, Artech House, 2002.
- [4] P.B. Kenington, *High-Linearity RF Amplifier Design*, Artech House, 2000.
- [5] A. Long, J. Yao, S.I. Long, "A 13 W Current Mode Class D High Efficiency 1 GHz Power Amplifier," *45th Midwest Symposium on Circuits and Systems*, vol. 1, 4-7, pp. 1-33-36, August 2002.
- [6] A. Adahl, H. Zirath, "An 1 GHz Class E LDMOS Power Amplifier," *11th GAAS Symposium*, Munich, 6-10. Oct. 2003.
- [7] W.N. Edelstein, C. Andricos, A. Moussessian, F. Wang, D.B. Rutledge, "High-efficiency L-band transmit/receive module for synthetic aperture radar," *IEEE Radar Conf.*, pp. 238-243, May 2003.
- [8] A. Grebennikov, "Circuit design technique for high efficiency class F amplifiers," *IEEE MTT-S Int. Microwave Symp. Dig.*, vol. 2, pp. 771-774, June 2000.
- [9] F. Lepine, A. Adahl, H. Zirath, "L-Band LDMOS power amplifiers based on an inverse class-F architecture," *IEEE Trans. on MTT*, vol. 53, No. 6, pp. 2007-2012, June 2005.

A proximity fed circularly polarized microstrip patch antenna with a cross slot in the ground plane

Kshitiz Agarwal^(a), G.P. Rao^(a), M.V. Kartikeyan^(a), M.K. Thumm^(b,c)

(a) Department of Electronics & Computer Engineering, Indian Institute of Technology Roorkee
Roorkee 247 667, Uttaranchal, India

(b) Forschungszentrum Karlsruhe, Institut für Hochleistungsimpuls- und Mikrowellentechnik (IHM)
P.O. Box 3640, D-76021 Karlsruhe, Germany

(c) Universität Karlsruhe, IHE, Kaiserstr. 12, D-76128 Karlsruhe, Germany

Abstract

In this work, we present a circularly polarized microstrip patch antenna. In this antenna a quasi-square patch is fed by proximity coupling. The ground plane of the antenna has a cross slot to improve the coupling level to the patch. The simulated results show that it has a 3-dB axial ratio bandwidth of 3% from 2.362 GHz to 2.436 GHz. The antenna also shows a gain greater than 7.86 dBi over all of its usable bandwidth. The back lobe of the antenna is at least 19 dB down with respect to the front lobe at the center frequency of 2.4 GHz.

Introduction

Circular polarization is required in applications like satellite communications where the depolarization due to propagation effects preclude the use of linearly polarized antennas. To achieve circular polarization, a two-point feed can be used, where the feed points are spatially 90° apart, and are fed with equal amplitude signals in phase quadrature. The required power-dividing circuit takes up additional real estate, and increases the insertion loss (thus decreasing the antenna efficiency). This added complexity can be avoided by adopting a single-point feed system. In this antenna a single-point feed system is implemented using a quasi-square patch fed by proximity coupling with the feed line placed parallel to the diagonal length of the patch. Due to the quasi-square nature of the patch, two orthogonal modes are generated at two close frequencies. If the coupling to the two modes is same and the distance between the two frequencies of these modes is adjusted such that at the center of these frequencies the phase difference between the two modes is 90° then circular polarization results at this center frequency. The axial ratio deteriorates as we move away from this frequency. The disadvantage of the single-point-fed microstrip configurations is that they usually produce narrow CP bandwidths.

Proximity coupling offers the advantage of low cross polarization levels. But, at the same time this technique suffers from inherently low coupling levels and difficulties in impedance matching. Due to this, relatively low bandwidths are achieved using this feed. This problem can be solved up to a good extent by using a slot in the ground plane. The slot in the ground plane helps to couple more energy to the patch. The size of the slot can be used for impedance matching. And with this wider bandwidths can be achieved. It has been shown in [1] that impedance bandwidth as high as 21% can be achieved using this kind of configuration.

Adding a slot helps in improving the coupling level and the bandwidth of the antenna, but at the same time this also adds to the back radiation due to the slot as the slot radiates bidirectionally. Therefore care should be taken while designing the antenna regarding the size of the slot. It should be kept just large enough to get an impedance match. And because the slot in the ground plane and the feed line below it, both contribute to the back radiation, an aperture coupled microstrip patch antenna has a higher back radiation as compared to a proximity coupled patch antenna. This is also shown in [1]. A similar configuration for dual polarization is presented in [2].

Antenna Configuration

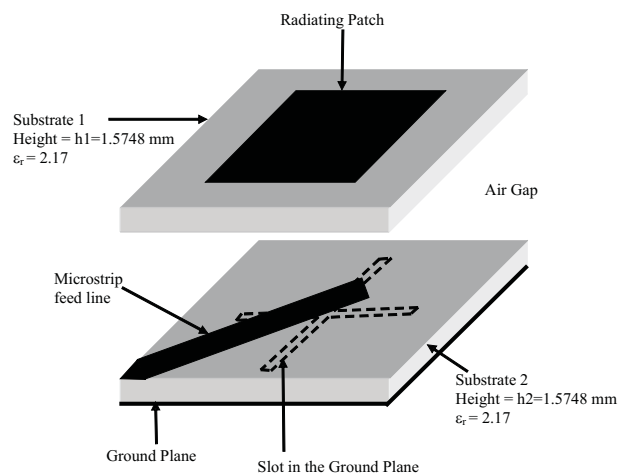


Figure 1: A three dimensional view of the antenna configuration.

The configuration of the proposed antenna is as shown in Figure 1 and Figure 2. The configuration consists of two substrates, a top substrate called the antenna substrate and a bottom substrate called the feed substrate separated by an air gap. Both the substrates are made of same dielectric material Arlon 880B0625517.001 with a dielectric constant, $\epsilon_{r1} = \epsilon_{r2} = 2.17$ and with a height, $h_1 = h_2 = 1.5748\text{mm}$. An air gap of $h_3 = 3\text{mm}$ is used between the two substrates. On the top of the feed substrate a microstrip feed line is designed so as to have a characteristic impedance of 50Ω . The feed line runs parallel to the diagonal length of the radiating patch with a length $l_f = 38.12\text{mm}$ extending into the patch. The bottom of the feed substrate has a metallic ground plane with a cross slot

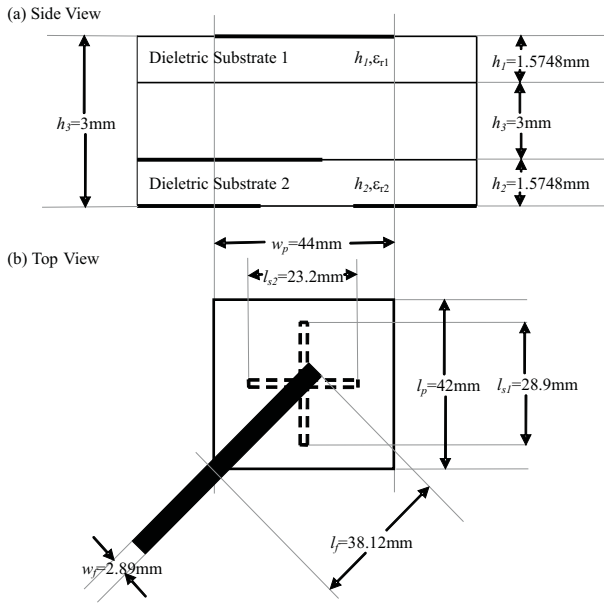


Figure 2: Configuration of the antenna.

etched in at its center. The dimensions of the slot are given by $l_{s1} = 28.9\text{mm}$ and $l_{s2} = 23.2\text{mm}$ in the two orthogonal directions. The width of each arm of the slot is 1mm. The antenna substrate has a metallic patch over it and the other side of this substrate is etched completely. The size of the patch is given by dimensions $l_p = 42\text{mm}$ and $w_p = 44\text{mm}$.

Results and Discussions

As can be seen in Figure 3 the antenna has an axial ratio less than 3dB from 2.362 GHz to 2.436 GHz. This accounts for 3% 3dB axial ratio bandwidth at a center frequency of 2.4 GHz. The value of the axial ratio at the center frequency is 0.31 dB. The axial ratio deteriorates as we move away from the center frequency. The

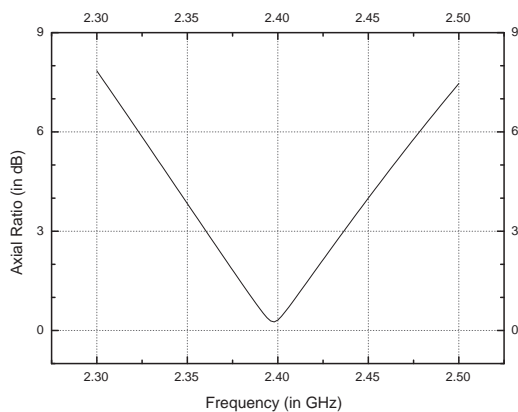


Figure 3: Axial Ratio of the antenna configuration.

antenna shows good impedance match for all the axial ratio bandwidth of the antenna as shown in Figure 4. The return loss is greater than 22dB for all of this

bandwidth. Also it can be noted here as in Figure 5 that there are two resonances, one at 2.332 GHz and the other at 2.475 GHz. The two resonances correspond to the two dimensions of the resonating patch and are mutually orthogonal to each other. The frequency of these resonances can be adjusted by directly adjusting the patch dimensions.

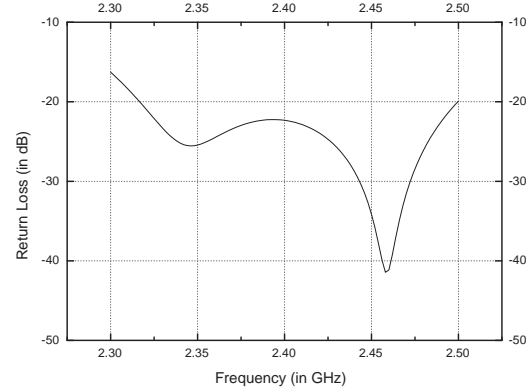


Figure 4: Return loss of the antenna configuration.

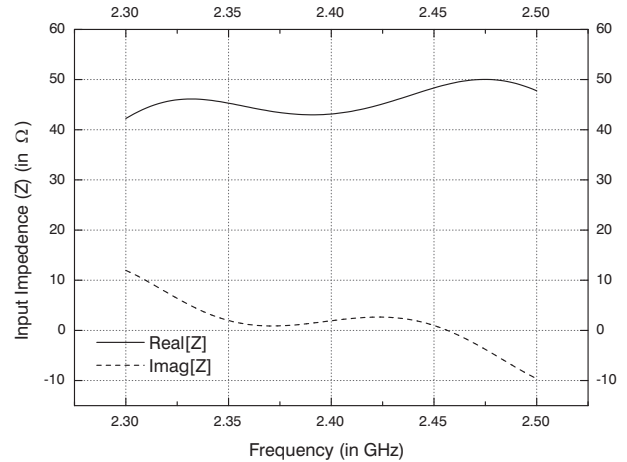


Figure 5: Input impedance of the antenna configuration.

Figure 6 shows that the gain of the antenna is fairly constant around 8 dBi and is greater than 7.86 dBi over all the bandwidth of the antenna. To further enhance the gain of the antenna, placing a dielectric substrate over the radiating patch can be tried. Arrays of this antenna element can also be implemented to improve the gain of the structure. Figure 7 shows that both the antenna efficiency and the radiation efficiency is greater than 95% in all the bandwidth of the antenna. This is a measure of the low power being reflected from the antenna at the feed port and the low losses occurring in the antenna.

Finally, Fig. 8 and Fig. 9 show the radiation pattern of the antenna in two orthogonal planes perpendicular to the plane of the antenna. The $\varphi = 0^\circ$ plane represents the plane containing the dimension w_p of the radiating patch and the broadside direction. Similarly the $\varphi =$

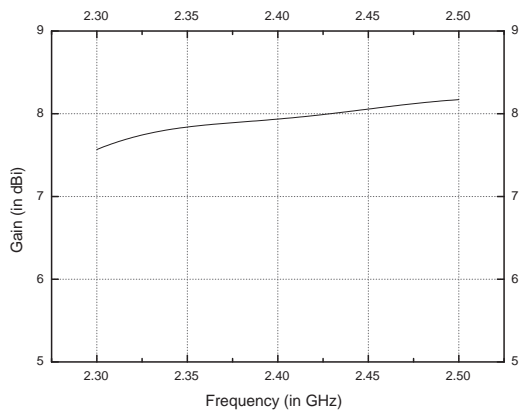


Figure 6: Gain of the antenna configuration.

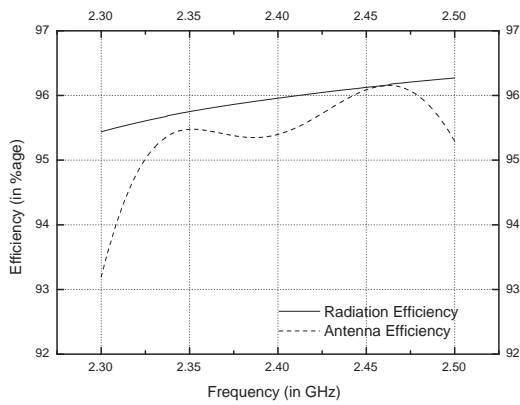


Figure 7: Efficiency of the antenna configuration.

90° plane represents the plane containing the dimension l_p of the radiating patch and the broadside direction. The patterns show a front lobe to back lobe ratio of at least 19dB at the center frequency. The antenna has a 3 dB axial ratio beamwidth of 76° in $\phi = 0^\circ$ plane and 79° in $\phi = 90^\circ$ plane at the same frequency.

Conclusion

A single feed circularly polarized antenna has been simulated with good simulation results. The antenna has a good 3-dB axial ratio bandwidth of 3% with good front lobe to back lobe ratio of more than 19dB. The configuration has a very good impedance match (return loss > 22 dB) and good gain characteristics (> 7.86 dBi in broadside direction at center frequency) over all the usable part of the bandwidth of the antenna. Arrays can be implemented with this antenna as its elements for enhancement in gain. Also the simulated antenna does not have a high profile.

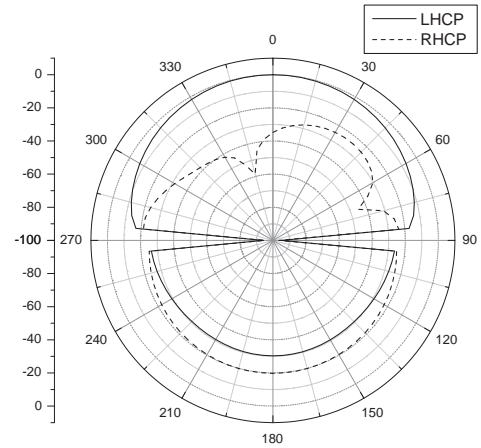


Figure 8: Normalized radiation pattern of the antenna in $\phi = 0^\circ$ plane at 2.4 GHz. (Units in dB)

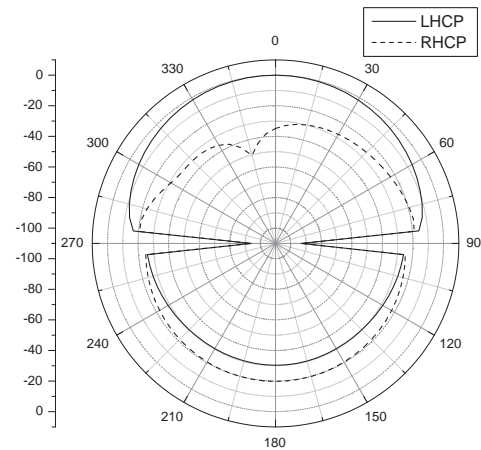


Figure 9: Normalized radiation pattern of the antenna in $\phi = 90^\circ$ plane at 2.4 GHz. (Units in dB)

References

- [1] S.Y.Ke, "Broadband proximity coupled microstrip antennas with an H-shaped slot in the ground plane," Antennas and Propagation Society International Symposium, IEEE, vol. 2, pp. 530-533, June 2002.
- [2] S.Gao and A.Sambell, "Dual-Polarised Broad-band Microstrip Antennas Fed by Proximity Coupling," IEEE Transactions on Antennas and Propagation, vol. 53, no. 1, pp. 526-530, January 2005.

WIDEBAND SINGLE PATCH E-SHAPED COMPACT MICROSTRIP ANTENNA FOR HIGH SPEED WIRELESS LOCAL AREA NETWORKS

G. Purnachandra Rao¹, Kshitiz Agarwal¹, M. V. Kartikeyan¹, M.K.Thumm^{2,3}

¹Department of Electronics & Computer Engineering
Indian Institute of Technology, Roorkee 247 667, Uttaranchal, India

²Forschungszentrum Karlsruhe,IHM,Postfach 3640, D76021 Karlsruhe, Germany

³Universitat Karlsruhe, IHE, D76128 Karlsruhe, Germany

Abstract— This paper presents a single wideband E-shaped compact microstrip antenna for high speed WLANs operating in the 5 – 6 GHz range. By using only single patch a high impedance bandwidth is achieved. The simulated impedance bandwidth (VSWR<2) is 25.9%, and measured bandwidth is approximately equal to 24.85%. This prototype antenna has a gain of 8.5 dB. The back radiation lobe is also > 20 dB. This antenna is fed by a co-axial probe feeding. In this paper, the effects of different parameter of antenna are also studied.

Index Terms — E-shape microstrip antenna, wideband, wire less local area networks, dual parallel slots.

I. INTRODUCTION

MICROSTRIP patch antennas are widely used because of their several advantages [1] such as light weight, low volume, low fabrication cost, and capability of dual and triple frequency operations. However microstrip antennas suffer from a number of disadvantages. Narrow bandwidth is a serious limitation of these microstrip patch antennas. Different techniques are used to overcome this narrow bandwidth limitation. These techniques include increasing the thickness of the dielectric substrate, decreasing dielectric constant [1], and using parasitic patches [2]. These techniques have limitations like, excitation of surface waves and increase in antenna size. In wireless local area networks the antenna used is in PCMCIA format where a small size, low volume antenna is required. A rectangular patch with a U slot [3] embedded in it has been found to be a broadband antenna, and a single E-shaped patch with a height of 15 mm provide bandwidth up to 30%.

In this paper, we present a wideband single E-shaped microstrip patch antenna with compact size that provides a bandwidth (VSWR < 2)

approximately equal to 26%. This bandwidth covers both the high speed WLAN frequency bands (5.15 - 5.35 GHz and 5.725 - 5.80 GHz). It is to be noted that the antenna height is less than 5mm, so this antenna can be conveniently used for WLAN adapter cards in PCMCIA format.

II.E-SHAPED MICROSTRIP PATCH ANTENNA

When two parallel slots are incorporated into the rectangular microstrip patch antenna, it becomes an E-shaped microstrip patch antenna. The E-shaped microstrip patch antenna is simpler in construction. The geometry is shown in Fig.1.

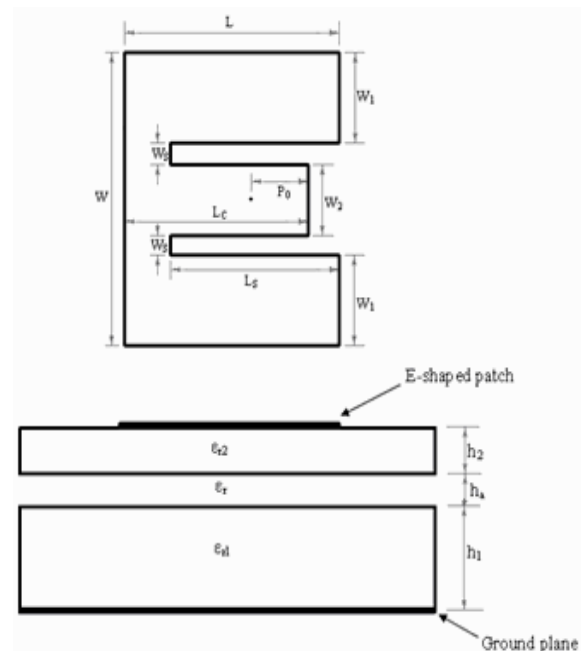


Figure 1: Geometry of the E-shaped microstrip patch antenna

The E-shaped microstrip patch antenna has width (W), two outer patch strips of length L and width W_1 , one central patch strip of length L_C and width W_2 . Two slots of length L_S and width W_S are introduced symmetrically with respect to the probe position. The patch is fed at position P_0 by a coaxial probe. Two dielectric substrate materials are used for fabrication of antenna element. An air gap of 1mm is taken between the two substrates.

The upper substrate was chosen with high dielectric constant for compact size. The lower substrate is foam dielectric material to provide ground plane. An air gap was used as the thickness of foam material is fixed, and it helps in optimization for wide bandwidth.

III. DESIGN OF SINGLE PATCH E-SHAPED MICROSTRIP ANTENNA

First the rectangular microstrip patch antenna was designed and then two parallel slots were incorporated into the patch. The parameters for the design of rectangular microstrip antenna are:

1. Frequency of operation (f_0): The high-speed computer wireless local area networks operate at two frequency bands (5.15 - 5.35 GHz and 5.725 - 5.850 GHz_Z). The resonant frequency selected for rectangular patch is centre frequency of upper band (5.8 GHz_Z). With the introduction of two slots the E-shaped microstrip antenna will cover the lower band.

2. Selection of the substrates: Two substrates are used for the fabrication of antenna. Lower foam substrate has dielectric constant $\epsilon_{r1}=1.25$ and thickness $h_1=2.6924$ mm. An air gap of 1.0 mm has been used between the two substrates. The foam substrate and air gap are used for large band width. Upper substrate has dielectric constant $\epsilon_{r2}=6.15$ and thickness $h_2=1.27$ mm.

The microstrip antennas are used with WLAN adaptor cards in the PCMCIA (also known as PC) format. These cards have standard thickness of 5 mm. So we have limited the overall height (4.9624 mm) of the antenna less than 5 mm. For the design of the microstrip antenna IE3D electromagnetic simulator is used. The dimensions of the optimized antenna element are given in Table 1.

IV. PARAMETRIC ANALYSIS

The following section shows the effect various parameters. With the increase in L_S whole VSWR curve shifts towards lower frequencies. There is

more change in resonant frequency of higher mode, as relative change in current path length for higher mode is greater than lower mode current path. This is shown in Fig. 2. The width W_S significantly effects the matching to the input port while it marginally effects the resonant frequencies of the two modes as shown in Fig. 3.

Table 1: Dimension of optimized antenna parameters

Frequency (f)	5 – 6 GHz
Width of the E-shaped patch (W)	20 mm
Length of the outer patch strip (L)	14 mm
Width of the outer patch strip (W_1)	6.25 mm
Length of the central patch strip (L_C)	10.25 mm
Width of the central patch strip (W_2)	5.5 mm
Length of the slot (L_S)	10.5 mm
Width of the slot (W_S)	1 mm
Probe position (P_0)	2.25 mm
Total height (h)	4.9624 mm

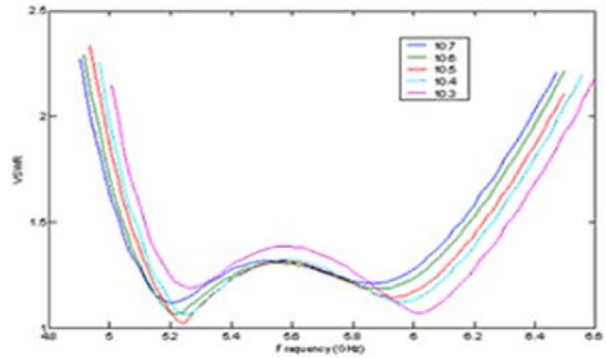


Figure 2: Effect of slot length (L_S)

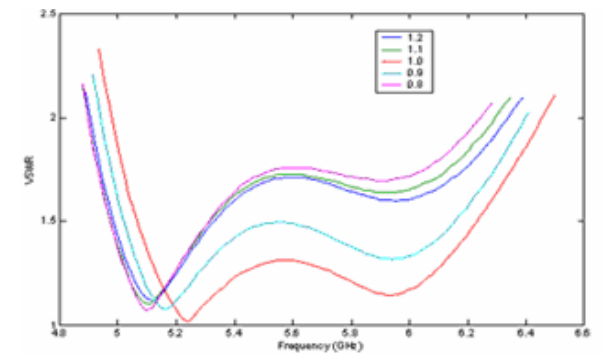


Figure 3: Effect of slot width (W_S)

The slot position P_s used to optimize the matching of both the modes is shown in Fig. 4.

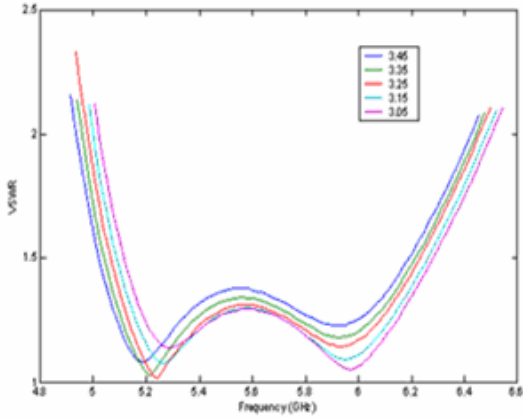


Figure 4: Effect of slot position (P_s)

The resonant frequency of higher mode decreases with increase in L_c while there is no significant change in resonant frequency of the lower mode. This is shown in Fig. 5.

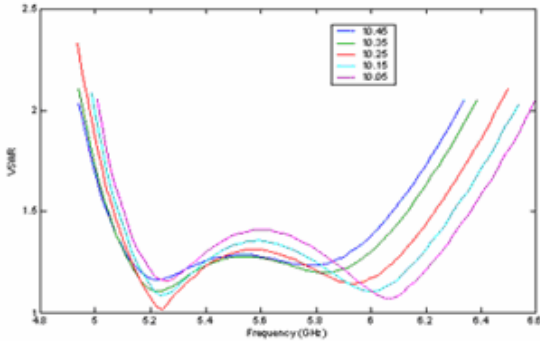


Figure 5: Effect of central patch strip length (L_c)

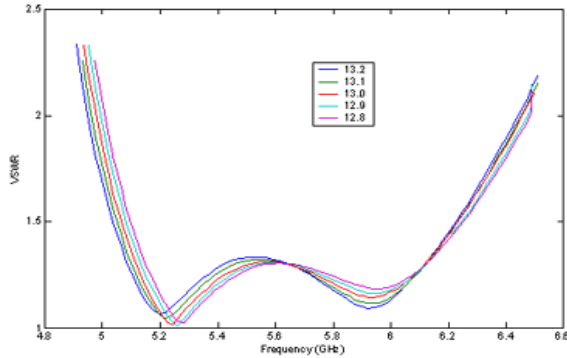


Figure 6: Effect of outer patch strip length (L)

The resonant frequency of lower mode decreases with increase in L while there is no significant change in resonant frequency of the higher mode and this is shown in Fig. 6.

V. RESULTS

The simulated 2:1 VSWR bandwidth is 25.9 % covering the (4.976 – 6.458 GHz) frequency band as shown in Fig. 7. The measured 2:1 VSWR bandwidth is 24.85 % covering (5.557 – 7.134 GHz) frequency band is also shown in Fig. 8. The shift in the frequency band is due to decrease in height of the upper substrate with high dielectric constant in the fabrication process. The decrease in height of upper dielectric substrate is approximately equal to 0.4 mm, which results in this shift of frequency band. The radiation pattern is measured in anechoic chamber. There are back lobes in the measured radiation patterns due to finite size of ground plane. The front to back ratios (FBR) is quite low and is equal to 25.95 dB.

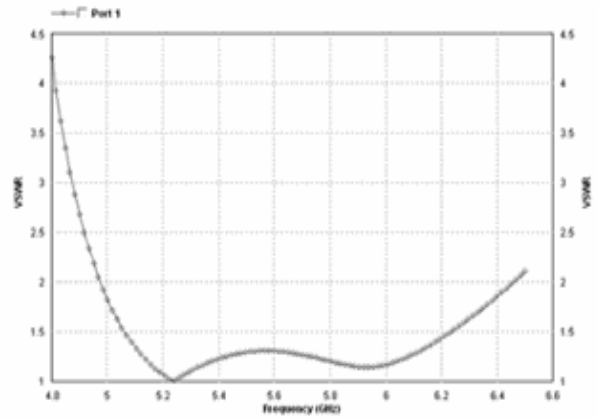


Figure 7: simulated impedance (VSWR < 2) bandwidth of wideband E-shaped microstrip patch antenna.

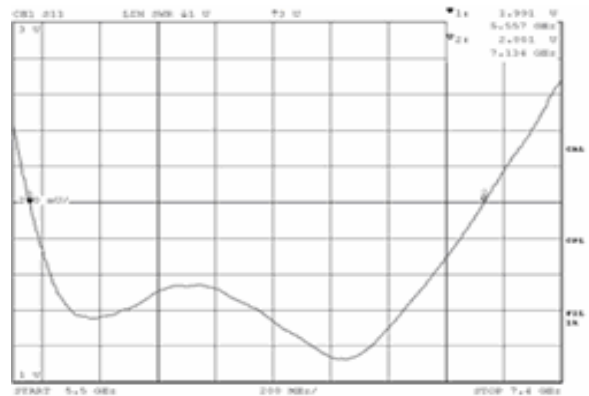


Figure 8: measured impedance bandwidth (VSWR < 2) of E-shaped microstrip patch antenna

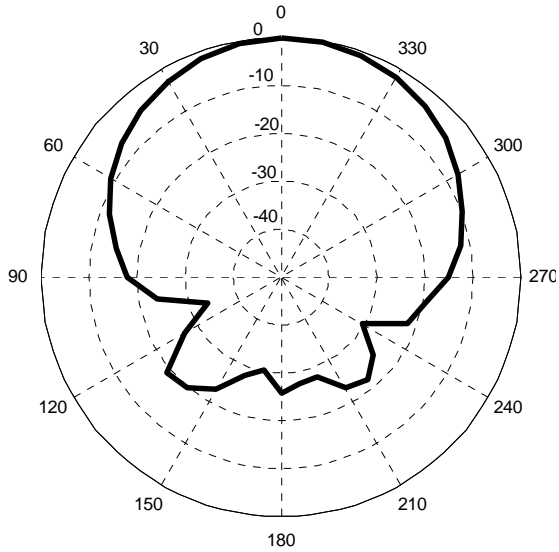


Figure 9: measured radiation pattern of E-shaped patch antenna

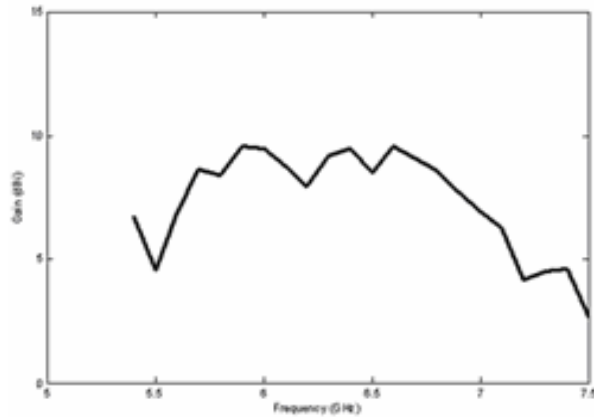


Figure 10: measured gain of E-shaped microstrip patch antenna.

REFERENCES

- [1] Ramesh Garg, Prakash Bartia, Inder Bhal and Apsiak Ittipiboon, “*Microstrip Antenna Design Hand Book*,” Artech House, Norwood, MA, 2001.
- [2] D.M.Pozzar “*Microstrip Antenna Coupled to Microstripline*,” *Electron Lett.*, vol. 21, no.2, pp. 49-50, January 1995.
- [3] T.Huynh and K.F.Lee, “*Single-layer single patch wideband microstrip antenna*,” *Electron Lett.*, vol.31, no.16, pp. 1310– 1312, August 1995.
- [4] Fan Yang, Xui-Xia Zhang, Xioning Ye, and Yahya Rahmat-Sami, “*Wideband E-shaped Patch Antenna for Wireless Communications*,” *IEEE Transactions on Antennas and Propagation*, vol. 49, no.7, July 2001.
- [5] Constanantine A Balanis, “*Antenna Theory Analysis and Design*,” John Wiley & Sons, New York, 1997.

VI. CONCLUSIONS

From the simulated and measured results, we can say that the E-shaped patch antenna geometry provides wide bandwidth with single patch. The measured and simulated bandwidths are matched (approximately 26%). This antenna has good front to back radiation (FBR) ratio, and is equal to 26dB. Without changing the permittivity and height of the substrates, the effect of various parameters of E-shaped patch antenna are studied.

Studies on a 250 GHz, 50 W, CW Second Harmonic Gyrotron for Spectroscopy

M.V. Kartikeyan^(a), E. Borie^(b), M.K. Thumm^(b,c)

(a) Department of Electronics & Computer Engineering, Indian Institute of Technology Roorkee
Roorkee 247 667, Uttaranchal, India

(b) Forschungszentrum Karlsruhe, Institut für Hochleistungsimpuls- und Mikrowellentechnik (IHM)
P.O. Box 3640, D-76021 Karlsruhe, Germany

(c) Universität Karlsruhe, IHE, Kaiserstr. 12, D-76128 Karlsruhe, Germany

Abstract

The objective of this work is to investigate the design feasibility of a 250 GHz, 100 Watt, CW, second harmonic gyrotron. Mode competition has been studied with regard to operation at the second harmonic, since competition with first harmonic modes is an important limitation. Starting currents are calculated for the candidate modes with their respective second harmonic and first harmonic competitors. Another aspect considered in the mode selection was the preferable output system. Cavity design and interaction computations will be carried out for power and efficiencies.

Introduction

Gyrotrons and their variations, popularly known as gyro-devices, are microwave and millimetric wave sources that provide very high powers ranging from long pulse to continuous wave (CW) for various technological, scientific and industrial applications. From their conception (monotron-version) in the late fifties until their successful development for various applications, these devices have come a long way technologically and made an irreversible impact on both users and developers. The possible applications of high power millimeter and sub-millimeter waves from gyrotrons and their variants (gyro-devices) span a wide range of technologies. The plasma physics community has already taken advantage of the recent advances of gyrotrons in the areas of RF plasma production, heating, non-inductive current drive, plasma stabilization and active plasma diagnostics for magnetic confinement thermonuclear fusion research, such as lower hybrid current drive (LHCD) (8 GHz), electron cyclotron resonance heating (ECRH) (28–170 GHz), electron cyclotron current drive (ECCD), collective Thomson scattering (CTS) and heat-wave propagation experiments. Other important applications of gyrotrons are electron cyclotron resonance (ECR) discharges for the generation of multi-charged ions and soft X-rays, as well as industrial materials processing and plasma chemistry. Submillimeter wave gyrotrons are employed in high frequency, broadband electron paramagnetic resonance (EPR) spectroscopy. Additional future applications await the development of novel high power gyro-amplifiers and devices for high resolution radar ranging and imaging in atmospheric and planetary science as well as deep space and specialized satellite communications, RF drivers for next generation high gradient linear

accelerators (supercolliders), high resolution Doppler radar, nonlinear spectroscopy, materials processing and plasma chemistry [1, 2].

A series of gyrotrons operating at submillimetric wavelengths at the second harmonic have successfully been developed and some relevant studies have been reported elsewhere [3–7]. A gyrotron operating at the second harmonic has the advantage that one can obtain the radiation at the given frequency with only half the magnetic field required. One of the major obstacles to the use of high frequency (> 10 GHz) microwaves for scientific and technological applications is the fact that suitable, inexpensive, easy-to-use sources are not readily available. Some experiments have been performed with low power (≈ 50 – 100 W) microwaves at frequencies around 250–460 GHz and the results are encouraging [10, 11]. In our earlier studies, we considered the possibility of a moderate power (25–50 kW) gyrotron operating at the ISM (industrial, scientific, medical) frequency of 24.1 GHz. In addition, we have a very good experience with the design of second harmonic gyrotrons at 24 and 42 GHz respectively for industrial and plasma heating applications [8, 9].

In this work, a design concept for a second harmonic operation of a 250 GHz, 100 W CW gyrotron for spectroscopic applications (*enhanced nuclear magnetic resonance via dynamic nuclear polarization experiments*) has been presented. The design parameters and goals are given in Table 1. Mode competition and mode

Table 1: Design parameters.

Frequency	250	GHz
Output power	≈ 100	Watts (CW)
Diffraction Q	$\approx 30,000$ – $35,000$	
Beam current (I_b)	50–70	mA
Beam voltage (U_b)	15–20	kV
Magnetic field at interaction	≈ 4.60 – 4.80	T
Velocity ratio (α)	≈ 1.40 – 1.50	
Total output efficiency	≈ 20	%
Estimated wall losses	< 2.0	kW/cm^2
Overall losses	< 8	%

selection are carefully studied; the cavity design and interaction computations will be carried out later.

Mode Selection and Starting Currents

For the mode selection, two important rules are observed to choose a suitable mode. The first one is the mode which supports a dimpled-wall quasi-optical mode converter with $\Delta m = 3$ perturbation for

azimuthal focussing. For this, one should have a mode with $m/\chi_{m,p} \approx 0.5$ or $360^\circ/\varphi \approx 3.0$ (see Table 2). We have scanned these values for all the candidate modes, as listed in Table 2; the numbers indicate that the $\text{TE}_{6,2}$ mode proves to be a good choice. It is to be noted that the sign \pm after the mode indices indicates corotating ($-$) and counter-rotating ($+$) modes, with respect to the gyrating electrons.

Table 2: Azimuthal index, radial index, mode eigenvalue, and $m_2/2 (= 360^\circ/\varphi)$ for the probable candidate modes

m	p	$\chi_{m,p}$	$m/\chi_{m,p}$	$\varphi(^{\circ})$	$m_2/2(= 360^\circ/\varphi)$
6	2	11.734936	0.51	118.67	3.03
6	3	15.268181	0.39	134.09	2.68
6	5	21.931715	0.27	74.33	4.84
7	3	16.529366	0.42	130.33	2.76
8	3	17.774012	0.45	126.51	2.84
9	3	19.004593	0.47	123.93	2.90

In the second stage, starting currents are computed for all the candidate modes considering (i) second harmonic neighbors, (ii) fundamental competitors, and (iii) modes supporting similar beam radius. For this, the cavity radius and optimum beam radius for the probable candidate modes if the gyrotron is to operate at 250.00 GHz are given in Table 3.

Table 3: Azimuthal index, radial index, mode eigenvalue, cavity radius and beam radius for probable candidate modes

m	p	$\chi_{m,p}$	R_0 (mm)	R_b (mm)
6	2	11.734936	2.24	1.01
6	3	15.268181	2.92	1.01
6	5	21.931715	4.19	1.02
7	3	16.529366	3.16	1.23
8	3	17.774012	3.39	1.43
9	3	19.004593	3.63	1.64

The given frequency corresponds to a wavelength of 1.2 mm. For operation in the $\text{TE}_{m,q}$ mode, the cavity radius is related to λ by $R_0 = \frac{x_{m,q}\lambda}{2\pi}$ where x_{mq} is the q 'th root of $J'_m(x)$. For operation at the first harmonic ($s=1$) the optimum beam radius is given by $R_e = \frac{x_{m\pm 1,i}R_0}{x_{m,q}} = \frac{x_{m\pm 1,i}\lambda}{2\pi}$ ($i=1$ or 2). In general, the co-rotating mode (with the lower sign) is chosen, since this provides better coupling of the electron beam to the RF-field. Following standard mode selection procedures taking into account the design constraints [1], the $\text{TE}_{6,2}$, and $\text{TE}_{6,3}$ modes are considered for further consideration since these modes seem to be promising to suit the design requirements and goals.

Simulation results

The starting current plots for all the modes considered are shown in Figs. 1–2. In these calculations, the candidate modes, their neighboring satellite modes, and the first harmonic competitors with similar beam radius are considered. The calculations were performed assuming two different beam radii, one is the optimized beam radius and another a slightly higher one.

For the $\text{TE}_{6,2}$ mode, the major nearby second harmonic competitors are $\text{TE}_{1,4}$, $\text{TE}_{3,3}$ and $\text{TE}_{10,1}$. The main first harmonic competitors are $\text{TE}_{5,1}$, $\text{TE}_{2,2}$. The azimuthal neighbors are not very near the

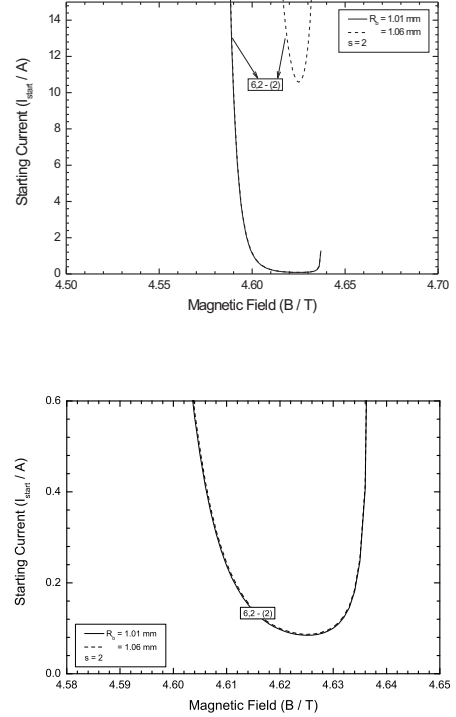


Figure 1: Starting current I_{start} as a function of magnetic field B for various modes with beam radius (R_b) optimized for the $\text{TE}_{6,2}^{(2)}$ mode. The sign \pm after the mode indices indicates corotating ($-$) and counter-rotating ($+$) modes, respectively. Here, the accelerating voltage $U_0 = 20$ kV, beam velocity ratio $\alpha = 1.5$, cavity radius $R_0 = 2.24$ mm, and beam radius $R_b = 1.01/1.06$ mm. The bottom figure is the same with a different scale.

candidate mode. In the starting current calculations, none of these possible competing modes was likely to interfere with the candidate mode (see Fig. 1).

For the $\text{TE}_{6,3}$ mode, the only significant nearby second harmonic competitors is the $\text{TE}_{9,2}$ mode. The major first harmonic competitor is the $\text{TE}_{6,1}$. From the starting current plots (see Fig. 2), it is obvious that one can operate stably with the $\text{TE}_{6,3}$ mode as its first harmonic competitor, the $\text{TE}_{6,1}$ mode, is sufficiently far away on the lower side of the frequency spectrum.

Outlook

This work has just been started few months ago. We are, at present, investigating the following feasibility studies:

- Cold cavity design (conventional type).
- Magnetron injection gun.
- Interaction computations.

An investigation of these design tasks is in progress.

References

- [1] M. V. Kartikeyan, E. Borie, M. K. Thumm, “Gyrotrons—High Power Microwave and Millimeter Wave Technology,” Springer-Verlag: Berlin, Germany, 2004.

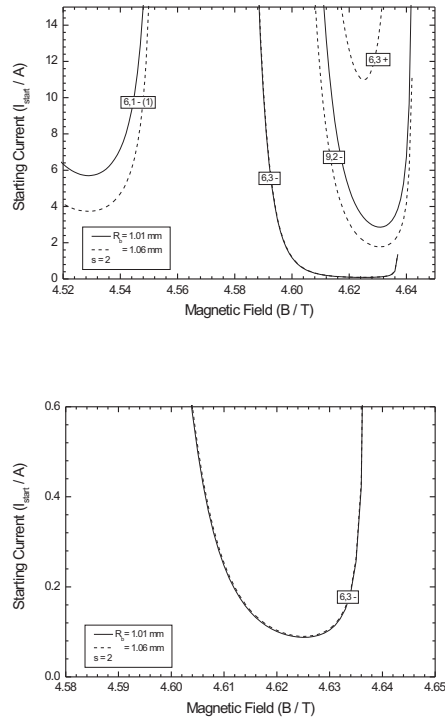


Figure 2: Starting current I_{start} as a function of magnetic field B for various modes with beam radius (R_b) optimized for the $TE_{6,3}^{(2)}$ mode. The sign \pm after the mode indices indicates corotating ($-$) and counter-rotating ($+$) modes, respectively. Here, the accelerating voltage $U_0 = 20$ kV, beam velocity ratio $\alpha = 1.5$, cavity radius $R_0 = 2.92$ mm, and beam radius $R_b = 1.01/1.06$ mm. The bottom figure is the same with a different scale.

at the second harmonic,” *Int. J. Infrared Millimeter Waves*, 21, pp. 1917–1943, 2000.

- [9] M. V. Kartikeyan, E. Borie, O. Drumm, S. Illy, B. Piosczyk, M. Thumm, “*Design of a 42-GHz 200-kW gyrotron operating at the second harmonic,*” *IEEE Trans. MTT*, vol. 52, no. 2, pp. 686–692, February 2004.
- [10] P.P. Woskov, V.S. Bajaj, M.K. Hornstein, R.J. Temkin, R.G. Griffin, “*Corrugated Waveguide and Directional Coupler for CW 250-GHz Gyrotron DNP Experiments,*” *IEEE Trans. Microwave Theory and Techniques*, vol. 53, no. 6, pp. 1863–1869, June 2005.
- [11] M.K. Hornstein, V.S. Bajaj, R.G. Griffin, K.E. Kreischer, I. Mastovsky, M.A. Shapiro, J.R. Sirigiri, R.J. Temkin, “*Second harmonic operation at 460 GHz and broadband continuous frequency tuning of a gyrotron oscillator,*” *IEEE Trans. Electron Devices*, vol. 52, no. 5, pp. 798–807, May 2005.

- [2] M. Thumm, “*State-of-the-art of high power gyro-devices and free electron masers update 2004,*” Scientific Report FZKA 7097, Forschungszentrum Karlsruhe, Germany, February 2005.
- [3] T. Idehara, T. Tatsukawa, I. Ogawa, T. Mori, H. Tanabe, S. Wada, G. F. Brand, M. H. Brennan, “*Development of a second cyclotron harmonic gyrotron operating at submillimeter wavelengths,*” *Phys. Fluids B*, vol. 4, pp. 267–273, 1992.
- [4] T. Idehara, Y. Shimizu, “*Mode cooperation in a submillimeter wave gyrotron,*” *Phys. Plasmas*, vol. 1, pp. 3145–3147, 1994.
- [5] G. F. Brand, T. Idehara, T. Tatsukawa, and I. Ogawa, “*Mode competition in a high harmonic gyrotron,*” *Int. J. Electron.*, vol. 72, pp.745-758, 1992.
- [6] P.-K. Liu, E. Borie, “*Mode competition and self-consistent simulation of a second harmonic gyrotron oscillator,*” *Int. J. Infrared Millimeter Waves*, vol. 21, pp. 855–882, 2000.
- [7] E. Borie, “*Study for second harmonic gyrotrons in the submillimeter region,*” *Int. J. of Infrared and Millimeter Waves*, vol. 15, pp. 311–336, 1994.
- [8] P.-K. Liu, E. Borie, M.V. Kartikeyan, “*Design of a 24 GHz, 25-50 kW technology gyrotron operating*

An 84 GHz, 500 kW, CW Gyrotron

M.V. Kartikeyan^(a), E. Borie^(b), B. Piosczyk^(b), M.K. Thumm^(b,c)

(a) Department of Electronics & Computer Engineering, Indian Institute of Technology Roorkee
Roorkee 247 667, Uttaranchal, India

(b) Forschungszentrum Karlsruhe, Institut für Hochleistungsimpuls- und Mikrowellentechnik (IHM)
P.O. Box 3640, D-76021 Karlsruhe, Germany

(c) Universität Karlsruhe, IHE, Kaiserstr. 12, D-76128 Karlsruhe, Germany

Abstract

The design studies of an 84 GHz, 500 kW, CW gyrotron for ECRH in an experimental Tokamak are presented in this paper. Mode competition and mode selection procedures are carefully investigated by considering various candidate modes and the TE_{10,4} mode is chosen as the operating mode. A suitable cold cavity was designed and interaction computations (both self-consistent and time-dependent) were carried out. The results show that an output power of well over 500 kW, CW and efficiency around 40% can be reached without a depressed collector.

Introduction

Gyrotrons are capable of providing hundreds of kilowatts of power at millimetric and sub-millimetric wavelengths. They are mainly used for plasma heating. Other applications include high power communications, industrial heating and material processing. For the past two decades, gyrotrons are considered as the most promising sources for electron cyclotron resonance heating (ECRH) of plasmas for thermonuclear fusion experiments in tokamaks and stellarators because of the distinct advantage that they provide power levels of more than 1 MW at frequencies 30–170 GHz with long pulse to CW range of output, which is the basic requirement for plasma heating [1, 2]. The work presented in this paper is a technological extension of our earlier conceptual design of a device operating at both the fundamental and second of the cyclotron harmonics [3, 4] at 42 GHz. Gyrotrons operating at 84 GHz are designed and developed by GYCOM (Russia) and CPI (USA) [5–10] respectively for plasma heating applications. Although this technology is now quite mature, it will be useful to carry out the basic design aspects which will lead to the conceptual design and later the design translation to an actual device. In this work, the design feasibility of an 84 GHz, 500 kW gyrotron operating in the TE_{10,4} mode preferably with radial output coupling is presented. This device will serve as a heating source for a small experimental Steady State Tokamak which requires a high power microwave source at 84 GHz, preferably in the form of a Gaussian beam. The design parameters and goals are given in Table I.

Mode Selection and Simulation Results

The given frequency corresponds to a wavelength of 3.57 mm. Following standard mode selection procedures taking into account the design constraints [1], the TE_{10,4} mode is chosen as the most promising

Table 1: Design Parameters and Goals for a TE_{10,4} gyrotron.

Frequency	84	GHz
Output power	500 kW	CW
Diffraction Q (Q_D)	≈ 1000	
Beam current (I_b)	15 – 20	A
Accelerating voltage (U_b)	65 – 70	kV
Magnetic field (interaction)	≈ 3.2 – 3.3	T
Compression ratio	≈ 14.0	
Beam radius (interaction)	6.09	mm
Velocity ratio (α)	1.35–1.45	
Total output efficiency	≈ 40	%
Estimated wall losses	< 1.0	kW/cm ²
Overall losses	< 8	%

candidate for the operating mode. It gives a cavity radius (R_0) around 13.52 mm. Other possibilities are the operation with TE_{12,5}, TE_{15,n}, ($n = 2, 3, 4$) modes as reported earlier [2]. After a careful inspection of the mode spectrum for candidate modes, three modes, namely, TE_{10,4}, TE_{12,5} and TE_{15,4} appear to be particularly interesting. As far as the wall loading is concerned, all these modes tend to operate well within the limitation of 1 kW/cm² for ideal copper and one can produce a suitable transverse output coupling scheme effectively. However, as a matter of earlier experience [1], TE_{10,4} mode is chosen as the operating mode. In addition, the TE_{10,4} mode operating at 84 GHz can also be used as a complementary dual regime mode to TE_{6,2} mode operating at 42 GHz, since these two modes form a similar caustic radius with nearly equal cavity radius and can be used for the dual mode regime operation at 84 and 42 GHz respectively.

Cold cavity design and self-consistent calculations for power and efficiency are carried out for a range of external parameters, namely: beam energy, beam velocity ratio, beam current and applied magnetic field. Computations are carried out for three cavity mid-section lengths $L_2 = 22.0 / 23.0 / 24.00$ mm that gives the $Q_D = 810 / 896 / 986$ respectively.

Resonator geometry and cold-cavity field profile for the above cavity dimensions give a $Q_D \approx 895$ and are shown in Fig. 1. The results of the cavity design based on self-consistent and time-dependent computations are shown in Figs. 2–3.

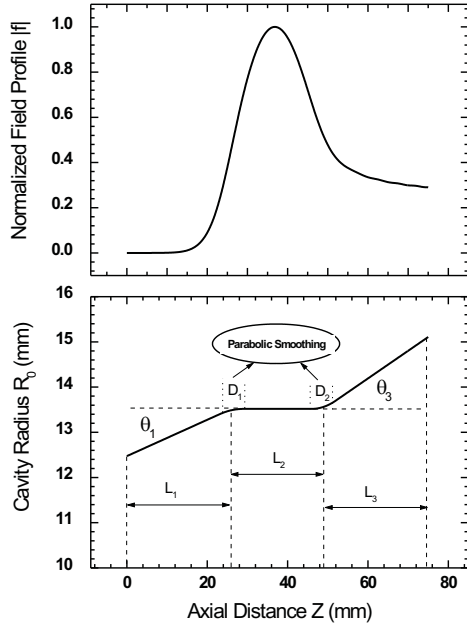


Figure 1: Resonator geometry and cavity field profile for a cavity with $Q_D = 895$.

Outlook

This work has been started a while ago and the feasibility leading to conceptualization is in the final stage. In addition, the following design studies are in progress:

- Magnetron injection gun.
- RF window design.
- Quasi-optical mode converter.

An investigation of these design tasks is in progress.

References

- [1] M. V. Kartikeyan, E. Borie, M. K. Thumm, "Gyrotrons—High Power Microwave and Millimeter Wave Technology," Springer-Verlag: Berlin, Germany, 2003.
- [2] M. Thumm, "State-of-the-art of high power gyro-devices and free electron masers update 2004," Scientific Report FZKA 7097, Forschungszentrum Karlsruhe, Germany, February 2005.
- [3] M. V. Kartikeyan et al., "Conceptual design of a 42 GHz, 200 kW gyrotron operating in the $TE_{5,2}$ mode," Int. J. Electronics, vol. 87, pp. 709-723, 2000.
- [4] M. V. Kartikeyan, E. Borie, O. Drumm, S. Illy, B. Piosczyk, M. Thumm, "Design of a 42-GHz 200-kW gyrotron operating at the second harmonic," IEEE Trans. MTT, vol. 52, no. 2, pp. 686-692, February 2004.

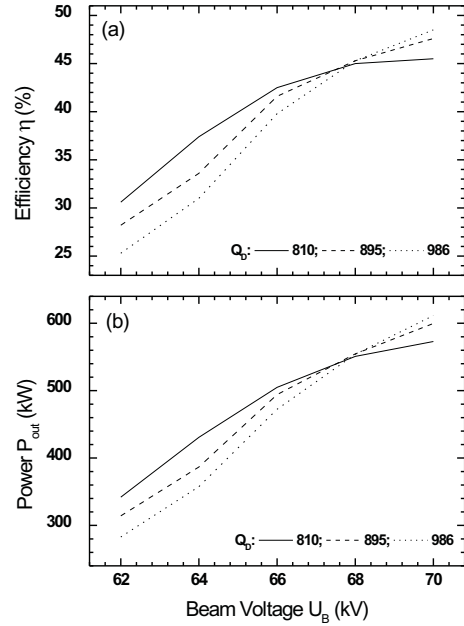


Figure 2: Output power and efficiency as a function of beam voltage (U_B) for various values of Q_D . Here, $I_B = 18$ A, $B = 3.25$ T and $\alpha = 1.40$.

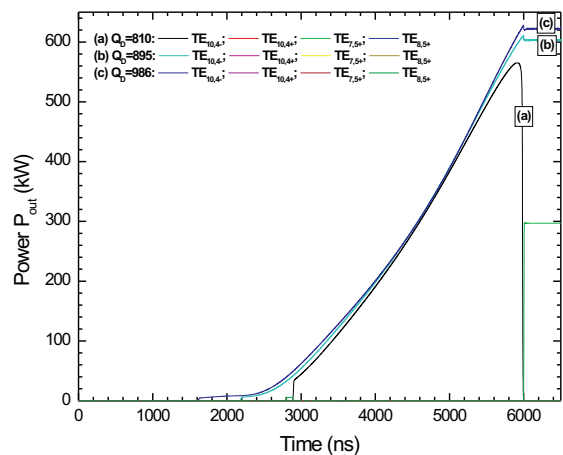


Figure 3: SELFT simulation results for a $TE_{10,4}$ gyrotron considering the probable competing modes. Here, $U_B = 30-70$ kV, α varies accordingly, $I_B = 18$ A and $B = 3.25$ T.

- [5] Zapevalov, V.E., Kalynov, Yu.K., Lygin, V.K., Malygin, O.V., Malygin, S.A., Moiseev, M.A., Manuilov, V.N., Khizhnjak, V.I., Solujanova, E.A., Tai, E.M., "Low frequency gyrotrons for fusion," 13th Joint Workshop on Electron Cyclotron Emission and Electron Cyclotron Resonance Heating, Nizhny Novgorod, Russia, May 17–20, 2004.
- [6] Belousov, et, al., "The test results of the 84 GHz/200 kW/CW gyrotron," 13th Joint Workshop on Electron Cyclotron Emission and Electron Cyclotron Resonance Heating, Nizhny Novgorod, Russia, May 17–20, 2004.
- [7] Litvak, A.G., Agapova, M.V., Denisov, G.G., Kurbatov, V.I., Tai, E.M., Malygin, S.A., Myasnikov, V.E., Ilyin, V.I., Usachev, S., Zapevalov, V.E., "New results in development of MW output power gyrotrons for fusion systems," Proc. 27th Int. Conf. on Infrared and Millimeter Waves, San Diego, USA, 295–296, 2002.
- [8] Bykov, Yu., Ereemeev, A., Glyavin, M., Kholoptsev, V., Luchinin, A., Plotnikov, I., Denisov, G., Bogdashev, A., Kalynova, G., Semenov, V., Zharova, N., "24–84-GHz gyrotron systems for technological microwave applications," IEEE Transactions on Plasma Science, vol. 32, no. 1, pp. 67–72, February 2004.
- [9] Chu, T.S., Blank, M., Borchard, P., Cahalan, P., Cauffman, S., Felch, K., Jory, H., "Operation of a 500 kW, 84 GHz, long pulse gyrotron with collector potential depression," Proc. 27th Int. Conf. on Infrared and Millimeter Waves, San Diego, USA, 5-6, 2002
- [10] Blank, M., Borchard, P., Cahalan, P., Cauffman, S., Chu, T.S., Felch, K., Jory, H., "Development and demonstration of gyrotron oscillators and amplifiers at CPI," Proc. 5th Int. Workshop on Strong Microwaves in Plasmas, Nizhny Novgorod, ed. A.G. Litvak, Inst. of Applied Physics, Russian Academy of Sciences, Nizhny Novgorod, 2003, Vol. 1, pp. 7-15.

Periodical Protrusions for UWB Slot Antennas

Jiunn-Nan Hwang¹, Werner Sörgel², and Werner Wiesbeck²

¹ Department of Communication Engineering, National Chiao Tung University, 1001 Tahsueh Rd., Hsinchu 300, Taiwan, +886-3-571-2121 ext. 545613, emigma.cm91g@nctu.edu.tw

²University of Karlsruhe (TH), Institut für Höchstfrequenztechnik und Elektronik, Kaiserstr. 12, 76131 Karlsruhe, Germany, +49 721 608 2522, Werner.Wiesbeck@ihe.uni-karlsruhe.de

Short Abstract— In this paper, the periodical T-type protrusions are applied on the UWB slot antennas. The planar diamond shaped antenna with periodical protrusions is studied. It is found that the bandwidth performance can be improved by designing the size of periodical protrusions properly. The simulated S_{11} and electric far-field characteristics in frequency and in time domain are demonstrated.

Keywords- UWB slot antennas, diamond shaped antenna,

I. INTRODUCTION

Spectrum is presently one of the most valuable goods worldwide as the demand is permanently increasing and it can be traded only locally. Since the United States Federal Communications Commission (FCC) has opened the spectrum from 3.1 GHz to 10.6 GHz, i.e. a bandwidth of 7.5 GHz, for unlicensed use with up to -41.25 dBm/MHz EIRP numerous applications in communications and sensor areas are showing up. Like all wireless devices these have an antenna as integral part of the air interface. For small, handheld terminals slot antennas, which may be directly integrated with the housing of the device are an interesting choice. The slot antenna has generated many interests for broadband application [1-4]. In this work, the design process for improved performance of a modified diamond shaped antenna, which has been firstly presented in [1], is shown in the following.

II. SIMULATION RESULTS

First, the propagation characteristics of periodical T-type protrusions are analyzed. Fig. 1 shows the slot line with T-type protrusions. The slot width between signal and ground planes is 1.5mm. The length of b is 0.2mm. The dispersion diagram of the slot line with T-type protrusions is studied, as shown in Fig. 2. The propagation constant is increased with the addition of T-type protrusions and the resonant frequency can be shifted toward lower frequency band.

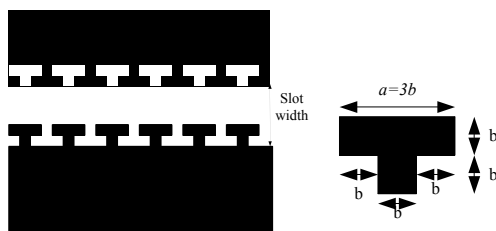


Fig. 1 Slot line with T-type protrusion.

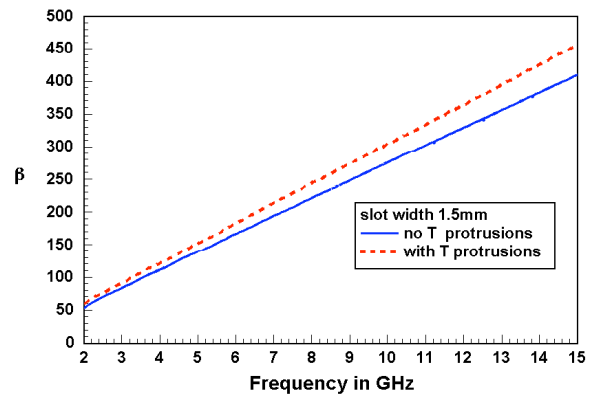


Fig. 2 Dispersion diagram for slot with periodical protrusion.

We have designed the diamond shaped antenna (DSA) for broadband application, as shown in Fig. 3. This antenna is similar to volcano smoke antenna (VSA) but has a simpler structure. The thickness and dielectric constant of the DUROID[®] substrate are $d = 1.57$ mm and $\epsilon_r = 2.2$, respectively. The dimensions in xy plane are 35 mm \times 35 mm. The DSA can have better bandwidth performance after choosing the size of inner conductor and slot width properly. The simulated S_{11} is performed by the commercial software CST Microwave Studio. As shown in Fig. 4, the matching bandwidth (S_{11} below -10 dB) of this antenna is extended from 2.37 GHz to 8.84 GHz.

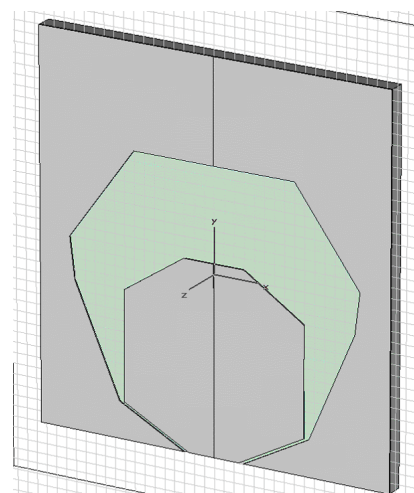


Fig. 3 Designed diamond shaped antenna (DSA).

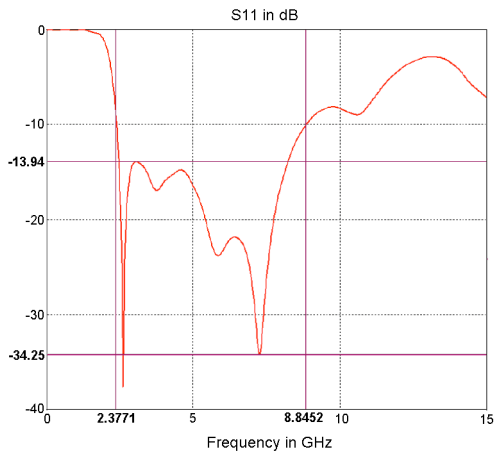


Fig. 4 Simulated S_{11} of the designed DSA.

The diamond shaped antenna with periodical protrusions is studied with two designs of the protrusion dimension $b = 0.35$ mm and $b = 0.4$ mm. Fig. 5 shows the DSA with T-type protrusions $b = 0.35$ mm. Simulation result is shown in Fig. 5. Compared to the DSA without protrusions, it is found that the S_{11} around 9 GHz is reduced and shifted toward lower frequency. A better bandwidth performance extended from 2.32 GHz to 10.11 GHz can be obtained.

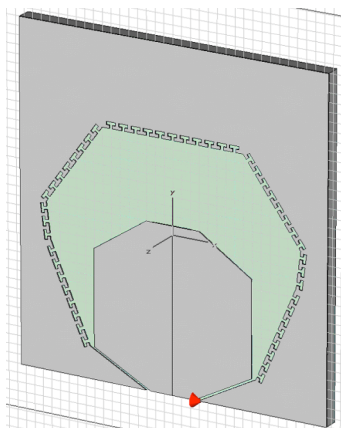


Fig. 5 The designed DSA with T-type protrusions.



Fig. 6 Simulated S_{11} of DSA with T-type protrusions $b = 0.35$ mm.

The DSA with protrusions $b = 0.4$ mm are analyzed. As shown in Fig. 7, although the peak S_{11} around 9 GHz is reduced, it can be seen that S_{11} around 3 GHz is increased. The bandwidth with this design ranges from 3.43 GHz to 10.07 GHz. To obtain a better bandwidth performance, the dimensions of the periodical protrusions should be designed properly.

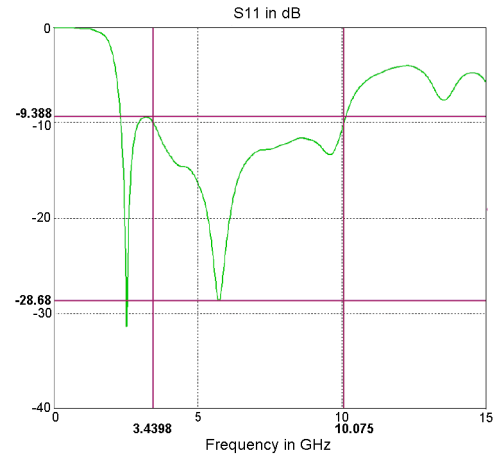


Fig. 7 Simulated S_{11} of DSA with T-type protrusions $b = 0.4$ mm.

The diamond shaped antenna is fed by a 50Ω connector soldered to a CPW transmission line. As shown in Fig. 9, the feeding network is considered into simulation. For 50Ω CPW transmission line, the center conductor width and gap width are 5 mm and 0.5 mm, respectively. The size of the DSA with feeding network in xy plane is $35 \text{ mm} \times 42 \text{ mm}$. The feeding network should be designed carefully to minimize the influence on the bandwidth performance of DSA.

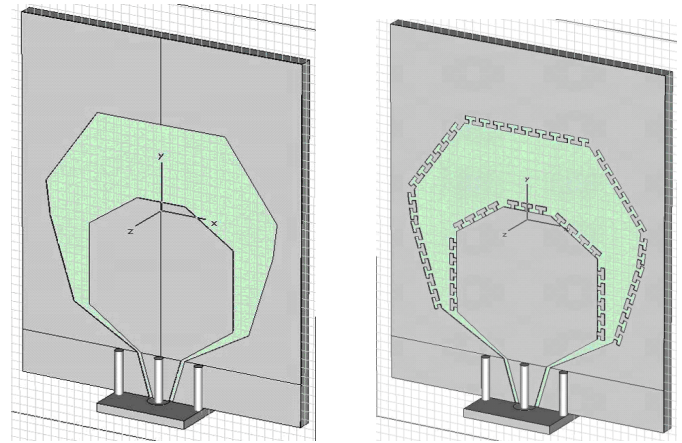


Fig. 8 DSA with feeding network.

In the following the bandwidth performance of the DSA with feeding network is studied. As shown in Fig. 9, the bandwidth ranges from 2.35 GHz to 8.25 GHz. With the use of periodical T-type protrusions $b = 0.45$ mm, the S_{11} around 9 GHz is reduced and a broader bandwidth ranges from 2.22 GHz to 9.89 GHz can be achieved.

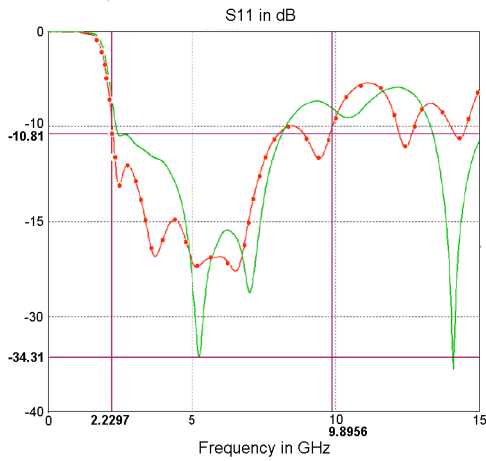


Fig. 9 Comparison of S_{11} with feeding network transition (solid line: without T protrusions dot marked line: with T protrusions).

Fig. 13 and Fig. 14 show the electrical far field of the antenna without and with T protrusions, respectively. The simulated results are similar to each other. The periodical protrusions will not affect the electrical far field significantly with the given excitation of a Gaussian pulse with a width at half maximum FWHM = 50 ps, which was used for simulation and interpretation of the frequency domain measurement.

III. MEASUREMENT RESULTS

The antenna with and without T-protrusions has been measured regarding the input reflection coefficient S_{11} , the far field patterns at discrete frequencies and the impulse transmission.

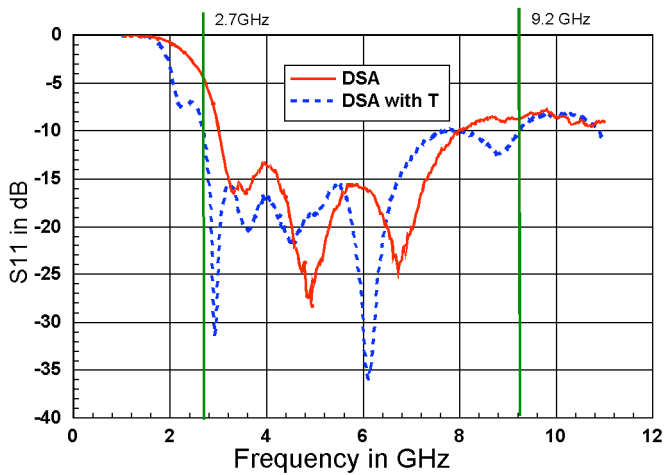


Fig. 10. Measurement results of S_{11} in dB.

As shown in Fig. 10, the designed DSA with T-type protrusions shifted the resonant frequencies toward the lower frequency band, as expected from simulation. The impedance bandwidth increases and ranges from 2.7 GHz to 9.2 GHz.

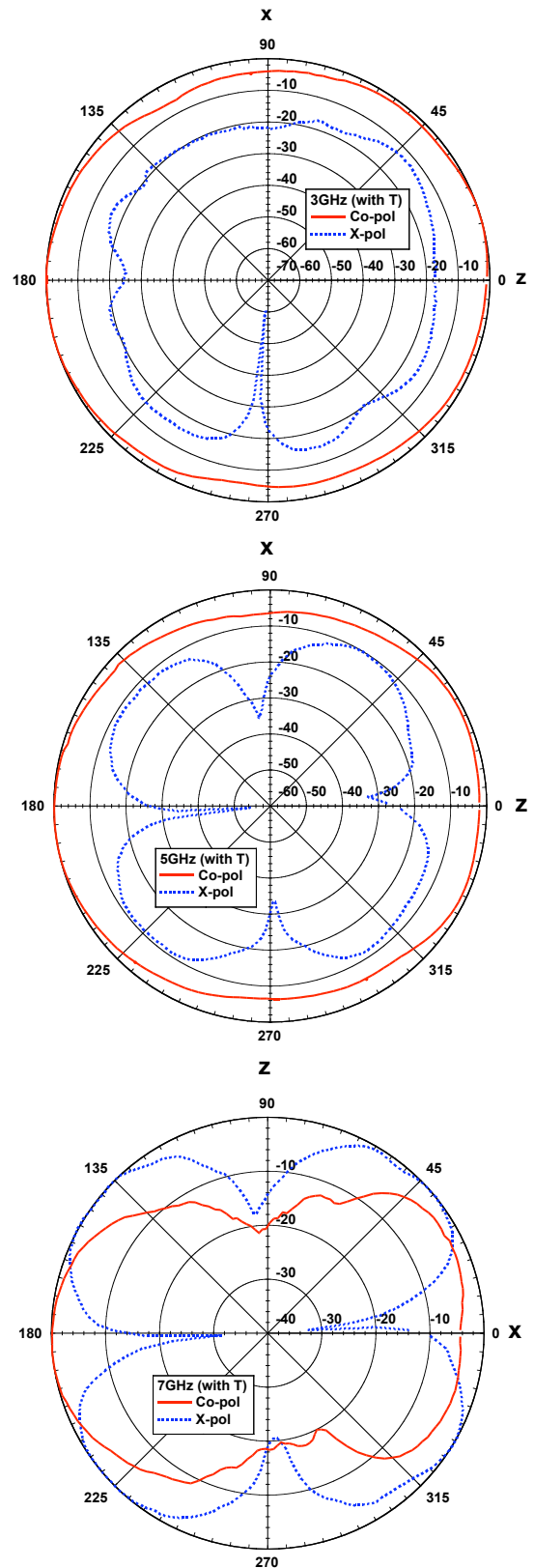


Fig. 11. Measured far field patterns for 3, 5 and 7 GHz in azimuth (H-plane) with T-protrusions

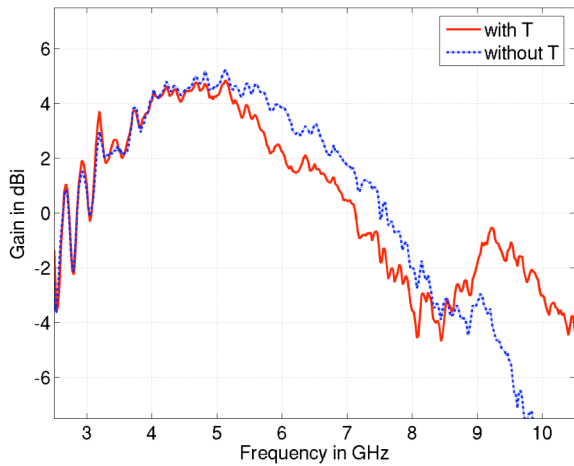


Fig. 12. Measured gain in boresight direction for both antenna types.

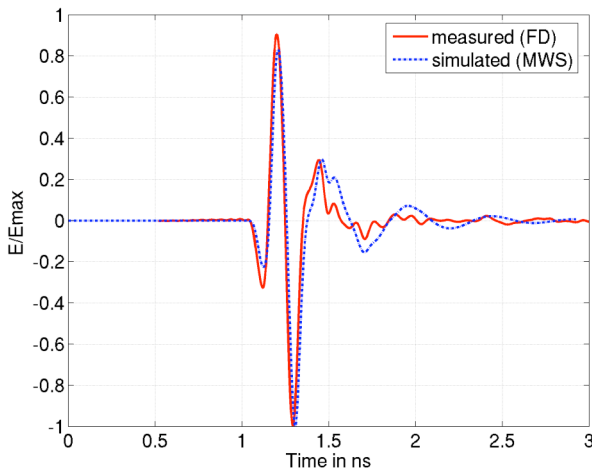


Fig. 13. Measured and simulated electric far field (without T protrusion) copolarized in boresight direction, Gaussian mono pulse excitation with FWHM 50 ps.

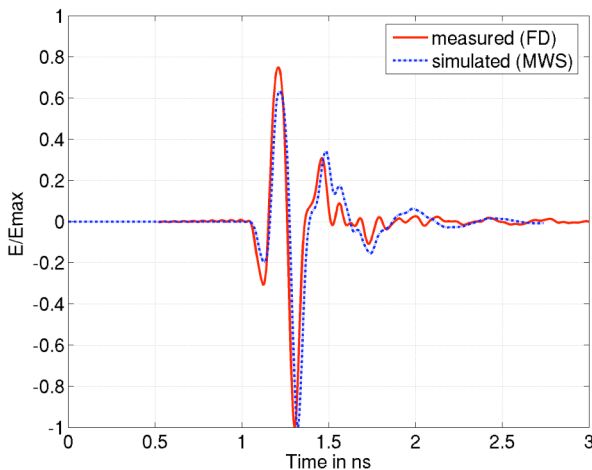


Fig. 14. Measured and simulated electric far field (with T protrusion) copolarized in boresight direction, Gaussian mono pulse excitation with FWHM 50 ps.

In Fig. 11 the radiation pattern in azimuth (H-plane, co-polarization) are presented for the antenna with T-type protrusions. The x-direction ($\psi = 0^\circ$) refers to the boresight direction of the antenna (normal to the metallization). The antenna exhibits very good omnidirectionality in the lower frequencies. At 7 GHz the pattern is more directive, due to the excitation of a higher order current mode. For the antenna without T-type protrusion this effect is shifted a little bit to higher frequencies. However, the antenna with T-type protrusions is able to operate up to 10 GHz as can be seen from the gain plot for the boresight direction in Fig. 12.

The transient transmission characteristics are measured in frequency domain with a network analyzer according [5,6]. The impulse response of the antenna exhibits a FWHM of 150 ps, which is sufficient for short pulses in the UWB communications frequency range. The electric far field in 3 m distance to the antenna is compared to the numerical simulations. One observes that the ringing in the measurement is lower than in the simulation, see Fig. 13 and Fig 14. This is mainly due to the higher losses in the measurement, since the calculations have been performed with perfect electric conducting metallization and loss free dielectrics. The T-type structures broaden the first peak of the response a little bit.

IV. CONCLUSIONS

The planar diamond shaped antenna exhibits very good ultra wideband properties combined with a co-planar or a coaxial feed. The influence of the feed on the matching has been characterized numerically. T-type protrusion are employed with success to improve the over all input reflection properties and the radiation at high frequencies by enabling slow waves propagating in the slot. The planar single layer slot structure promises easy integration in handheld UWB devices, which is one important scope for further investigations.

REFERENCES

- [1] J-Y. Tham, B. L. Ooi, M. S. Leong, "Novel Design of Broadband Volcano-Smoke Antenna", *IEEE-APS Int. Symp. Dig.*, CD-ROM, Washington, July 2005
- [2] L. Paulsen, J. B. West, W. F. Perger, and J. Kraus, "Recent investigating on volcano smoke antenna", *IEEE-APS Int. Symp. Dig.*, Columbus, Ohio, pp. 845-848, June 2005
- [3] J. Yeo, Y. Lee, and R. Mittra, "Wideband slot antennas for wireless communications", *IEE Proc.-Microw. Antennas Propag.*, vol. 151, pp. 351-355, Aug. 2004
- [4] J-Y. Tham, B. L. Ooi, M. S. Leong, "Diamond-shaped broadband slot antenna, Antenna Technology", *IEEE International Workshop on Small Antennas and Novel Metamaterials, 2005. IWAT 2005*, pp. 431-433, March 2005
- [5] Werner Sörgel, Werner Wiesbeck, "Influence of the Antennas on the Ultra Wideband Transmission", *EURASIP Journal on Applied Signal Processing*, special issue UWB - State of the Art, March 2005
- [6] W. Soergel, F. Pivit, W. Wiesbeck, "Comparison of Frequency Domain and Time Domain Measurement Procedures for Ultra Wideband Antennas", *Proceedings Antenna and Measurement Techniques Association, 25th Annual Meeting and Symposium*, pp. 72-76, Irvine, California, Oct. 2003

A Low Power, Variable Gain Common-Gate LNA

Thomas Stücker, Niels Christoffers, Rainer Kokozinski, Stephan Kolnsberg, and Bedrich J. Hosticka

Fraunhofer Institute for Microelectronic Circuits and Systems (IMS)
 Finkenstr. 61, D-47057 Duisburg, Germany
 Email: thomas.stuecke@ims.fraunhofer.de
 Telephone: (+49) 203-3783-258, Fax: (+49) 203-3783-153

Abstract—In this paper a novel variable gain common-gate LNA is presented, which features adaptive gain dependent bias current. The CG-LNA is designed in a $0.25 \mu\text{m}$ CMOS technology and consumes only $831 \mu\text{A}$ in maximum gain mode. The current consumption can be reduced further by factor 7 in the minimum gain mode.

I. INTRODUCTION

There are different requirements upon low noise amplifiers (LNAs), e.g. low noise, high linearity, high gain and the lowest possible current consumption. Based on the system simulation [1] it can be shown that the linearity and noise figure requirements are much more relaxed for wireless sensor network receivers (IEEE 802.15.4 - ZigBee [2]) than for other communication systems, e.g. UMTS, GSM or GPS. Hence, battery lifetime of up to two years becomes feasible for a IEEE 802.15.4 receiver, whereas for GSM or UMTS it is difficult to achieve larger battery lifetime than one week.

As known from literature, there are two basic topologies for LNAs: common-source (CS) and common-gate (CG) configurations [3], [4]. The noise figure (NF) of the CS-LNA is bias-dependent, since it is a function of the bias-dependent f_T . The noise figure of the CG-LNA is bias independent in a first order approximation. Thus, the noise factor (F) of CS-LNA is a linear function of the ratio carrier frequency f_0 to transit frequency, while it is constant with respect to it for the CG-LNA [5]. For large values of this ratio, the CG-LNA outperforms the CS-LNA in terms of noise figure. However, for small bias currents, the f_T becomes low and, hence, the ratio $\frac{f_0}{f_T}$ becomes large. Therefore, the CG-LNA is more suitable for relaxed noise figure requirements but tough demands for low current consumption as shown in [6].

The basic CG-LNA architecture is depicted in Fig. 1. The operating point is adjusted using the bias current source at the source terminal and the supply voltage at the gate terminal of the MOSFET. The inductor at the drain terminal resonates with the parasitic capacitors of the MOSFET and the inductor itself and the input capacitor of the following circuit (mixer) at the desired carrier frequency. The resulting equivalent resistor $R_{P,Load}$ of the resonance circuit can be determined for this frequency.

In a first order approximation, the voltage gain becomes

$$G_V = \left| \frac{v_{out}}{v_{in}} \right| \approx g_{ms} \cdot R_{P,Load} \quad (1)$$

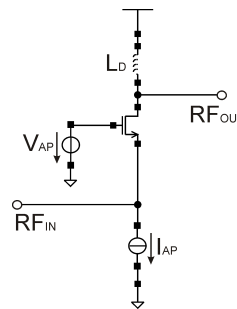


Fig. 1. Principle CG-LNA architecture.

and the input impedance is approximately equal to

$$Z_{in} \approx \frac{1}{g_{ms}}, \quad (2)$$

where g_{ms} denotes the drain-source transconductance of the MOSFET as proposed in [7]. To suppress reflection at the input, the input impedance of the LNA must match the output impedance of the preceding stage, e.g. 50Ω [3], [4].

The input signal of a LNA covers typically a large dynamic range. For the IEEE 802.15.4 receiver the sensitivity is specified as $P_{IN}|_{min} = -92 \text{ dBm}$ and the maximum input signal as $P_{IN}|_{max} = -20 \text{ dBm}$ [2]. To avoid saturation effects of subsequent stages, the gain of the LNA should be reduced for large input signals. A new concept of gain adjustment is presented in the paper.

This paper is structured as follows: Section II discusses the feasibility of adjusting the gain. The adaptive gain adjustment for the CG-LNA is explained in Section III and simulation results are presented in Section IV. Finally, conclusions are drawn in Section V.

II. GAIN ADJUSTMENT OF LNAs

A. Basic Concepts

There are two options to reduce the gain for large input signals. According to (1) the first option is to reduce the resistor $R_{P,Load}$ by shunting the inductor at the drain of the MOSFET by a additional resistor R_x as shown in Fig. 2. This is the typical way to reduce the gain. The input impedance (2) does not vary, if the impedance at the drain changes. The current remains constant, since the MOSFET is biased from a constant current source. Thereby, the energy is wasted,

just if a large input signal is received. The input signal of a receiver is not continuously at the receiver sensitivity in practice. Therefore, this gain adjustment option is not a adequate solution for receivers operating in low power wireless sensor networks.

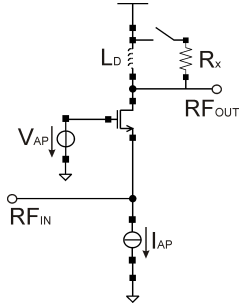


Fig. 2. Gain adjusting by shunting the drain inductor.

The second way to reduce the gain according to (1) is a reduction of the source transconductance $g_{m,s}$. This is done by reducing the bias current of the MOSFET as shown in Fig. 3, but unfortunately the input impedance of the MOSFET (2) also changes. To ensure a constant 50Ω input impedance, a shunt resistor is added at the input. The input impedance of the LNA is then

$$Z_{in} \approx \frac{1}{g_{m,s} + \frac{1}{R_x}}, \quad (3)$$

where $\frac{1}{g_{m,s}}$ is the input impedance of the MOSFET and R_x is the shunt resistor.

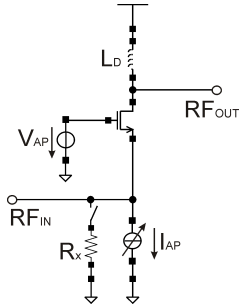


Fig. 3. Gain adjusting by adequate bias current and resistive input shunting.

Resistive termination at the input of a LNA is discussed as very unfavorable option for LNA design in [4]. On the other hand, the resistor is only added, if the input signal is very large and hence above the noise floor.

B. SNR Performance

According to the previous subsection, the LNA varies the as function of the gain. Therefore, it is necessary to show that the signal to noise ratio (SNR) performance does not deteriorate in the low gain mode. For this purpose the ratio of SNR at the output must be calculated for the different gain modes. Starting with the most common definition of noise factor (F)

$$F = \frac{SNR|_{IN}}{SNR|_{OUT}} \quad (4)$$

in agreement with [3], [4], [8]. Then, the SNR output ratio Δ is

$$\Delta = \frac{SNR_2|_{OUT}}{SNR_1|_{OUT}} = \frac{SNR_2|_{IN}}{SNR_1|_{IN}} \cdot \frac{F_1}{F_2} = \frac{P_2}{P_1|_{IN}} \cdot \frac{F_1}{F_2}, \quad (5)$$

where the index 1 denote the high gain mode, 2 the low gain mode, and P the input signal power, respectively. It can be also expressed in dB as

$$\Delta_{dB} = \Delta_{P_{IN,dB}} - \Delta_{NF} \quad (6)$$

and it is a measure of performance improvement in spite of the higher noise of the LNA in low gain mode.

III. REALIZATION OF THE ADAPTIVE GAIN FOR CG-LNA

The adaptive gain CG-LNA was designed in a $0.25 \mu\text{m}$ CMOS technology for a use in an IEEE 802.15.4 receiver, suitable for a carrier frequency of 868.3 MHz (ISM band). The schematic is depicted in Fig. 4. External components such as off-chip inductors or external matching networks are dispensable.

The CG-LNA core comprises the MOSFETs M1 - M3 as presented in [6] and is biased in moderate inversion exploiting the higher current efficiency in this operation region. This is a good compromise for low power RF-systems [9].

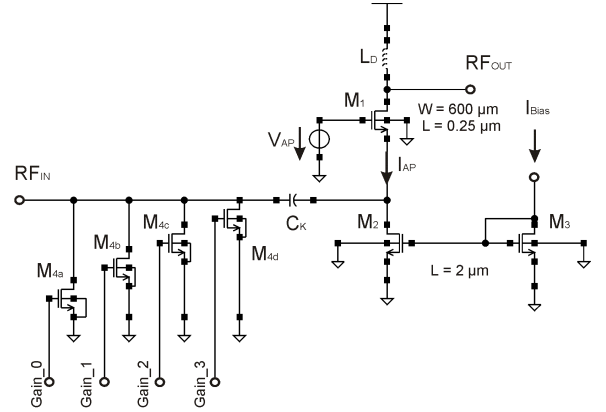


Fig. 4. Realization variable gain CG-LNA.

The resistor at the input can be realized using a MOSFET in triode region, which works as an imperfect switch with a relatively high ON-resistance. The maximum equivalent input voltage at input matching is very low ($u_{in}|_{max} = 31.6 \text{ mV}$), even for large input signals of $P_{IN}|_{max} = -20 \text{ dBm}$. Thus, the MOSFET resistor does not change its resistance and, hence, does not degrade the linearity performance.

An adjustable resistor was implemented using four MOSFETs (M4a - M4d), which are controlled by the logic using a gain control word. Thereby, it becomes possible to select various gain settings digitally. Since four MOSFETs provide sixteen gain stages, the gain step size is approximately 1 dB. The appropriate bias currents are supplied via the current mirror M2 and M3.

The LNA is designed as follows: First, the CG-LNA is designed for maximum gain in accordance with the specification. Then, the gain in linear or logarithmic scale is computed. After that, the bias current for each gain step is determined. From simulation the input impedance is determined and the shunt resistor calculated. From that, the corresponding shunt MOSFET is inserted. In an empirical way, the finger length and width are determined.

The parasitic capacitance was minimized by taking appropriate measures in the layout of M4. M4a to M4d use a different number of fingers equal length and width ($L = 0.25 \mu\text{m}$, $W = 1 \mu\text{m}$). The multipliers are 1,3,7 and 12.

IV. SIMULATION RESULTS

A. Gain, Noise Figure, and IIP3

The circuit simulation is performed using Cadence and are based on the BSIM 3.3 MOSFET model. The pad parasitics are modeled as well as the bondwire inductors and accounted for in the simulation.

The inductor was modeled by its π -equivalent circuit with ten elements as described in [10]. The parameter of the inductor model can be determined either by separate EM-simulation of the coil or by measurement of the inductor, followed by a parameter fitting.

The simulated voltage gain at the different stages is depicted in Fig. 5. The maximum voltage gain (gain word 0000) is marked by squares and it amounts to is 4.41 which is equivalent to 12.89 dB on logarithmic scale. It steps 1-dB-wise down to -2.61 dB at minimum gain (gain word 1111). The frequency of maximum gain varies only slightly towards lower frequencies at low gain stages, but is still close to the carrier frequency $f_0 = 868.3$ MHz.

The current consumption is already very low in maximum gain mode ($831 \mu\text{A}$), but it can be reduced further if a lower gain stage is chosen. In the minimum gain mode is the current consumption only $118 \mu\text{A}$, which means a reduction by factor 7.

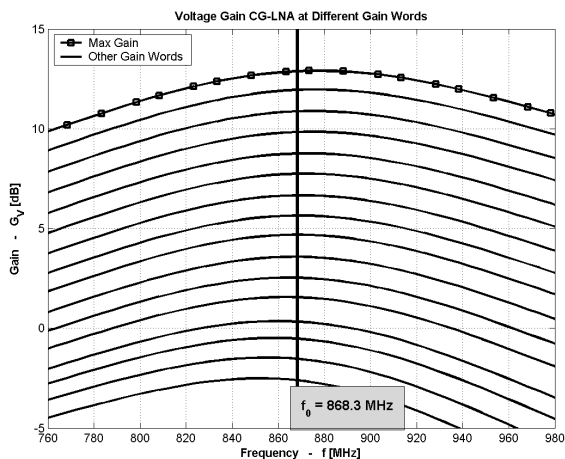


Fig. 5. Simulation result: voltage gain CG-LNA.

Fig. 6 shows simulated noise figure. The circuit simulation shows a noise figure of 4.5 dB which is equivalent to a noise factor of 2.8 at maximum gain (marked by squares). The maximum noise figure of 18.3 dB is achieved at minimum gain (gain word 1111).

It is very important to note that these simulations results include the noise contributed from the load of the LNA. A common way in the literature e.g. [3], [4] is to neglect this part, but it is valid theoretically only, if the load and thus the gain approaches infinity. Since the LNA needs a finite load impedance to achieve a voltage gain, NF calculations must consider it [6].

The BSIM 3.3 model used in these simulations does not allow for several parasitic effects raising the noise. Considering this, a worst case NF of about 5 dB is expected [6]. According to the system simulation [1], this is sufficient to meet the IEEE 802.15.4 requirements. Therefore, the here presented curves must be corrected only a little bit.

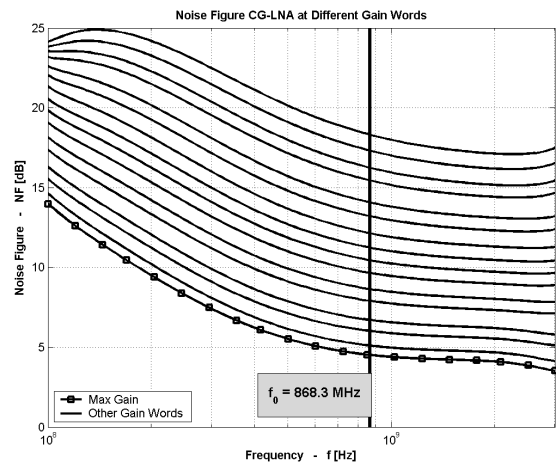


Fig. 6. Simulation result: noise figure (NF) CG-LNA.

The simulated input reflection coefficient S_{11} is depicted in Fig. 7. In the maximum gain mode (marked by squares) is $S_{11} = -15.51$ dB and in minimum gain mode $S_{11} = -18.08$ dB. The maximum reflection coefficient is -14.94 dB (gain word 0001) and the minimum reflection is -22.9 dB (gain word 1011). The remaining reflection coefficient is due to the parasitic effects of the gate source capacitance, the bondwire and pads. Consequently, the input impedance is close to 50Ω at all gain stages.

Fig. 8 depicts the simulation result of the linearity. The solid lines represent the fundamental and the dotted lines the 3rd order intermodulation product (IM3). For sake of legibility, only the curves for maximum gain (gain word 0000), minimum gain (gain word 1111) and as an arbitrary example the gain word 1000 are shown. The first data point of the IM3 curve for the gain word 1111 can be considered as a numerical error.

The IIP3 is the abscissa at the intersection of the extrapolated fundamental and IM3 curve. The IIP3 is -6.37 dBm, -7.41 dBm and -7.24 dBm for the gain word 0000, 1111 and

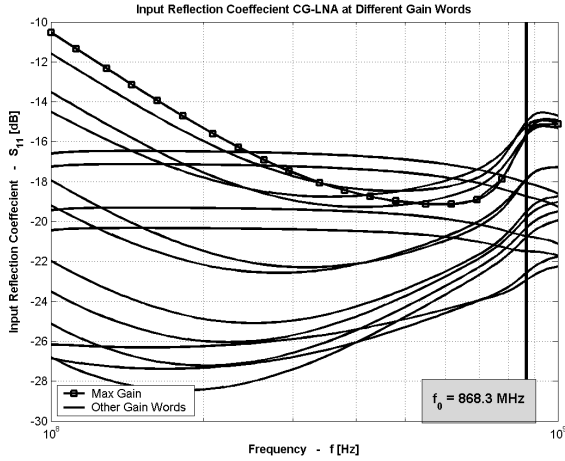


Fig. 7. Simulation result: input reflection coefficient S_{11} CG-LNA.

1000 respectively.

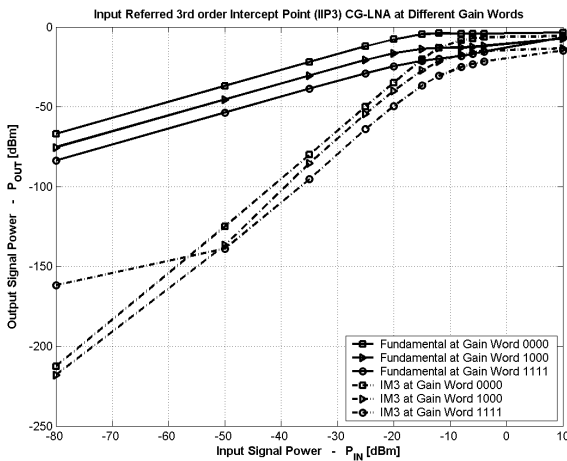


Fig. 8. Simulation result: Linearity (IIP3) CG-LNA.

B. SNR Performance

To show that the SNR performance does not deteriorate in the low gain mode, the SNR output ratio Δ is calculated as described in section II. The minimum input signal power is taken as the reference $P_1|_{IN} = -92 \text{ dBm}$. For the gain word 1000, the minimum input signal is $P_2|_{IN} = -56 \text{ dBm}$. The noise figure changes from $NF_1 = 4.51 \text{ dB}$ to $NF_2 = 11.23 \text{ dB}$. From this follows $\Delta_{dB} = 36 \text{ dB} - 6.72 \text{ dB} = 29.28 \text{ dB}$. An equivalent calculation can be done for the other gain stages. From these results it can be seen clearly, that SNR performance does not deteriorate in the low gain mode, even though the noise of the LNA in this mode is higher. The simulation results for three different gain words are summarized in Table I.

TABLE I
SIMULATION RESULTS.

G-Word	$I_{AP} [\mu A]$	G [dB]	S_{11} [dB]	NF [dB]	Δ [dB]
0000	830.95	12.89	-15.51	4.51	NaN
1000	281.76	4.69	-20.27	11.23	+29.28
1111	117.58	-2.61	-18.08	18.30	+53.71

V. CONCLUSION

In this paper a new adaptive gain CG-LNA is presented as well as the corresponding design strategy. It was shown that it is possible to reduce the bias current for the low gain stages and shunting a resistor to the input to ensure impedance matching. Thereby, it becomes possible to save energy if large signals are received. Furthermore it was shown, that SNR performance does not deteriorate in the low gain mode, even in spite of the higher noise of the LNA in this mode.

The designed CG-LNA is used in our IEEE 802.15.4 (ZigBee) receiver, which is at the moment in production at our $0.25 \mu\text{m}$ CMOS technology. Measurement results will be presented after the fab-out.

REFERENCES

- [1] T. Stücker, N. Christoffers, R. Kokozinski, and S. Kolnsberg, "BER Optimization for Micro Power Receivers Using Quick and Accurate System Simulation," in *Proc. of the 14th IST Mobile and Wireless Communications Summit*, 2005.
- [2] "IEEE Std 802.15.4 -2003, IEEE Standard for Information technology - Telecommunications and information exchange between systems - Local and metropolitan area networks - Specific requirements - Part 15.4: Wireless Medium Access Control (MAC) and Physical Layer (PHY) Specifications for Low-Rate Wireless Personal Area Networks (WPANs)," available in the internet: www.zigbee.org.
- [3] T. Lee, *The Design of CMOS Radio-Frequency Integrated Circuits*, 2nd ed. Cambridge, New York, Melbourne, Madrid, Cape Town: Cambridge University Press, 2004.
- [4] B. Razavi, *RF Microelectronics*, 1st ed. Cambridge, New York, Melbourne, Madrid, Cape Town: Cambridge University Press, 1998.
- [5] D. Allstot, X. Li, and S. Shekhar, "Design considerations for CMOS low-noise amplifiers," in *IEEE Radio Frequency Integrated Circuits (RFIC) Symposium, Digest of Papers*, 2004, pp. 97-100.
- [6] T. Stücker, N. Christoffers, R. Kokozinski, S. Kolnsberg, and B. Hosticka, "LNA für Low Power, Low Data Rate PAN Anwendungen," in *Kleinheubacher Tagung, Miltenberg*, 2005.
- [7] C. Enz, F. Kruppenacher, and E. Vittoz, "An analytical MOS transistor model valid in all regions of operation and dedicated to low-voltage and low-current applications," *Analog Integrated Circuits Signal Processing*, vol. 8, pp. 83-114, 1995.
- [8] D. Pozar, *Microwave and RF Design of Wireless Systems*, 1st ed. New York: John Wiley and Sons, 2001.
- [9] C. Enz and Y. Cheng, "MOS transistor modeling for RF IC design," *IEEE J. Solid-State Circuits*, vol. 35, no. 2, pp. 186-201, 2000.
- [10] J. Long, "Passive Components and RF IC Design," Advanced Engineering Course on RF IC Design, at the EPFL, Lausanne 4.- 8.October 2004.

Compact Planar Filters for Wireless Communication Systems

M. G. Banciu¹, N. Militaru², A. Ioachim¹, G. Lojewski²

¹National Institute of Materials Physics, Microwave Group, Atomistilor 105 bis, Bucharest-Magurele, Postcode 077125, Romania, Phone +40-21-4930047 ext 123, E-mail gbanciu@infim.ro

²“Politehnica” University of Bucharest, Faculty of Electronics, Telecommunications and Information Technology, Iuliu Maniu 1-3, Bucharest, Romania, Phone +40-21-4024831, E-mail george.lojewski@munde.pub.ro

Abstract—Investigations on compact planar devices are presented in this paper. The proposed patch dual mode filter occupies about 16% of the surface area of a conventional square patch. The six-pole filter with compact cross-coupled resonators provides an improved rejection band.

Keywords—microstrip devices; dual-mode filters; cross-coupled filters

I. INTRODUCTION

The rapid evolution of the mobile communications requires small-size and cost-effective devices with improved parameters. New compact planar resonators and filters manufactured by using a simple technology are presented in this paper. Moreover, the discussed devices are cost-effective and offer an easy integration with other devices in planar RF and microwave circuits.

Experimental models of new types of band-pass filters presented in this paper were designed in microstrip technology on a 0.635 mm height Rogers substrate with a 10.8 dielectric constant. However, no via holes are required for filter manufacturing and the design principles remain the same for various substrates such as ceramic or single-crystal substrates. Furthermore, the new designs can be easily applied to the devices using superconductors of high critical temperature (HTS) in order to achieve high quality factors for planar resonators.

II. DUAL MODE FILTERS

Since the pioneering paper by Wolff [1], the microstrip dual mode resonators and filters evolved continuously. A significant role in this evolution was played by the developments in HTS thin films devices. The high Q -factor resulted in low in-band insertion losses of the narrow-band dual mode filters [2].

Each dual mode resonator contributes with two-poles to the band-pass filter or multiplexer, and low-cost compact devices with narrow pass-band can be designed. In order to reveal the coupling effects between the orthogonal modes of a planar dual mode filter, a simple transmission-line model for a closed meander loop dual-mode filter as the one shown in Fig. 1 was investigated.

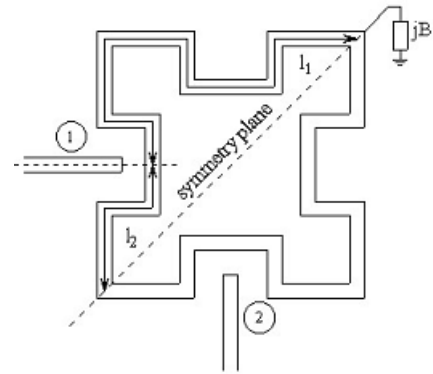


Figure 1. Model of a dual-mode filter.

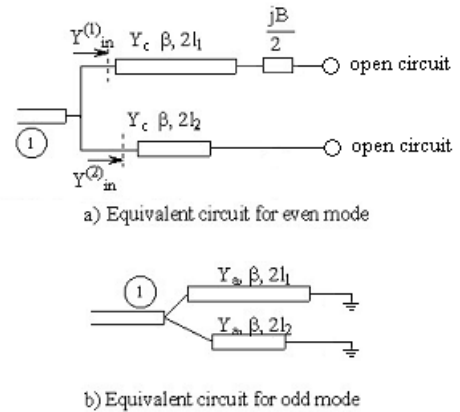


Figure 2. Equivalent circuit of the dual-mode resonator shown in Fig. 1. (The ground of the transmission lines is not shown.)

The effect of the symmetrically positioned perturbation is represented by a reactance jB . The external couplings and the corner discontinuities were neglected. Assuming additionally that there are no dispersion effects, i.e. the electromagnetic waves propagate with a speed v_{eff} , which does not depend on frequency, the frequency of the fundamental resonance mode is

$$f_0 = \frac{v_{eff}}{2(l_1 + l_2)}, \quad (1)$$

where the lengths l_1 and l_2 are defined in Fig. 1.

Two resonance modes are possible in this structure. The perturbation does not modify the odd mode, therefore the frequency f^o remains the same as in the unperturbed case $f^o = f_0$. For the even mode, the resonance condition imposes $Y_{in} = Y_{in}^{(1)} + Y_{in}^{(2)} = 0$ and the resonant frequency of the even mode is

$$f^e = f_0 \left(1 - \frac{1}{\pi} \tan^{-1} \left(\frac{b}{2} \right) \right), \quad (2)$$

where b is the perturbation susceptance B , normalized to the characteristic admittance Y_c of the line. The coupling coefficient of the two modes, defined as the ratio between the frequency shift $\Delta f = |f^e - f^o|$ and the central frequency $f_c = (f^e + f^o) / 2$, becomes

$$k = \frac{\frac{1}{2\pi} \left| \tan^{-1} \left(\frac{b}{2} \right) \right|}{1 - \frac{1}{2\pi} \tan^{-1} \left(\frac{b}{2} \right)}. \quad (3)$$

The conventional square patch dual mode resonator offers a simple design and a good power handling capability, which is very essential for HTS devices. However, its large size can be an important drawback. In order to overcome this drawback, a new type of patch dual mode filter is proposed in this paper.

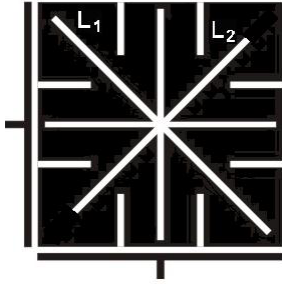


Figure 3. Proposed dual mode filter (not to scale).

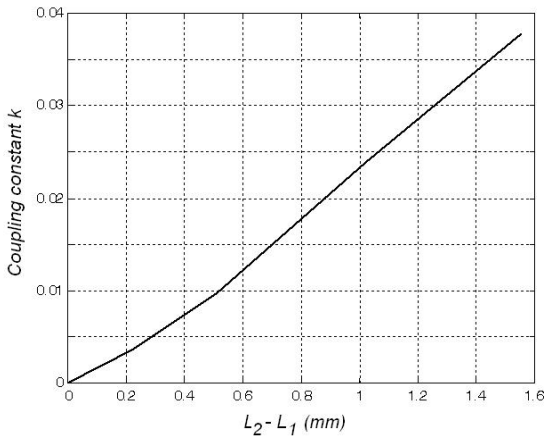


Figure 4. Coupling constant k versus the $\Delta L = L_2 - L_1$..

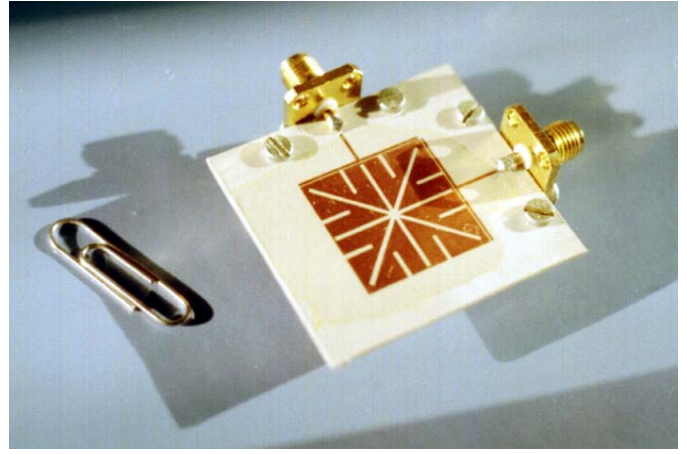


Figure 5. Picture of the proposed dual mode filter.

In order to reduce the size of the patch dual mode filter, several slots and cuts were performed, as shown in Fig. 3. The resonance frequency can be tuned by modifying the lengths L_1 and L_2 of the diagonal slots. The perturbation stays in a slight difference $\Delta L = L_2 - L_1$, in these slot lengths. The coupling coefficient between the dual modes was investigated, as a function of ΔL . The results are presented in Fig. 4.

In Fig. 5 is shown a two-pole dual mode filter, designed for a 900 MHz central frequency. It has a square-shape with the edge of 20.5 mm, what means that it occupies only about 16% of the surface area of a conventional square patch dual mode resonator designed on the same substrate for the same frequency band. Conversely, a conventional square patch dual mode filter of the same size as the proposed filter exhibits a pass-band centered at a frequency about 2.4 times higher than the central frequency of the proposed filter, as shown in Fig. 6.

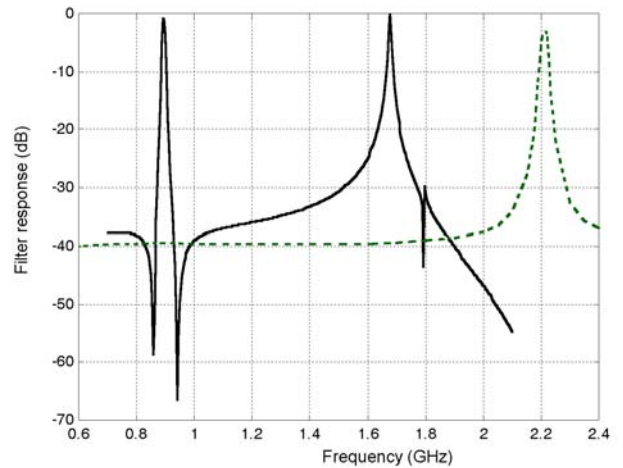


Figure 6. Simulated response of the proposed dual mode filter (continuous line) compared to the response of a conventional patch dual mode filter (dashed line).

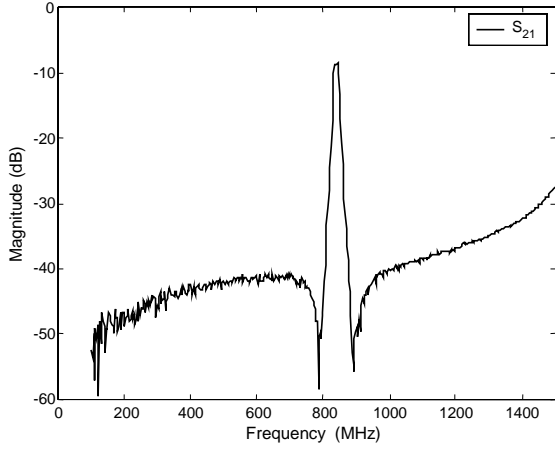


Figure 7. Measured response of the proposed dual-mode filter.

Preliminary investigations on the proposed dual-mode filter lead to a response shown in Fig. 7. The central slots performed in the patch result in a steep response with two attenuation poles on each side of the pass-band. Such attenuation poles do not occur for a conventional square patch dual mode filter. The difference between the two types of response can be seen in Fig. 6.

The in-band insertion loss is proportional to the inverse of the filter bandwidth and to the inverse of the unloaded quality factor Q of the resonator. Therefore, in order to achieve narrowband filters with low in-band insertion loss, high- Q resonators are required. A possible solution to this problem is given by the high temperature superconductors (HTS) technology.

III. CROSS-COUPLED FILTERS WITH NEW COMPACT RESONATORS

By cross-coupling single-mode resonators, an easy tailoring of the filter response can be accomplished [3]. Moreover, the stepped-impedance resonators (SIR) can exhibit a total length less than the conventional half-wavelength resonators, for a compact design. The length of a SIR decreases with the increase of the admittance ratio S [4].

A further size-reduction can be achieved by using new types of resonators, which were developed from the folded stepped-impedance resonators [5]. The addition of non-uniform stubs to a folded stepped-impedance resonator reduces significantly the resonance frequency.

For the beginning let us assume a pair of uniform stubs of length l_3 , added to a stepped-impedance resonator at a distance l_1 from the end of SIR. For this new resonator, the dependence of the first two resonant frequencies, i.e. of the fundamental mode f_0 and of the first higher mode f_1 , while the resonator length is kept constant to the length of a conventional half-wavelength resonator ($\lambda_{0\text{init}}/2$), was investigated. The frequency of the fundamental mode f_0 decreases with the stub length l_3 . However, the ratio f_1/f_0 does not depend monotonically on l_3 and exhibits a maximum at $l_3 = l_1 = \lambda_{0\text{init}}/8$, as shown in Fig. 8.

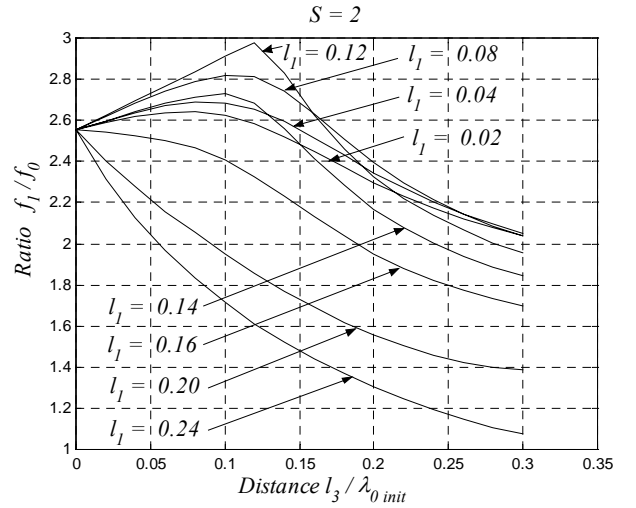


Figure 8. Dependence of the f_1/f_0 ratio on the stub length l_3 and stub position l_1 for an admittance ratio $S = 2$. (The distance l_1 is normalised to $\lambda_{0\text{init}}$).

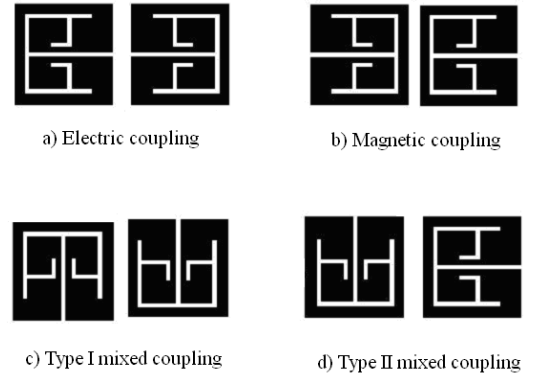


Figure 9. Couplings between compact resonators.

By using this design technique, square microstrip resonators occupying only 32% of the surface area of a folded half-wavelength resonator were achieved. The resonators were designed by using an in-house developed FDTD method, and all the discontinuity effects were included in the design. The coupling coefficients versus coupling gaps were also investigated by FDTD, for several types of couplings shown in Fig. 9. Furthermore, curves of the external quality factor, Q_{ext} , versus feed-line position were drawn. Finally, a six-pole cross-coupled filter was then designed by using the following coupling matrix

$$\mathbf{M}_6 = \begin{bmatrix} 0 & 0.0342 & 0 & 0 & 0 & 0 \\ 0.0342 & 0 & 0.01917 & 0 & -0.0078 & 0 \\ 0 & 0.01917 & 0 & 0.0245 & 0 & 0 \\ 0 & 0 & 0.0245 & 0 & 0.01917 & 0 \\ 0 & -0.0078 & 0 & 0.01917 & 0 & 0.0342 \\ 0 & 0 & 0 & 0 & 0.0342 & 0 \end{bmatrix} \quad (4).$$

The corresponding values of the external quality factor of the terminal resonators are $Q_e = 19.69$.

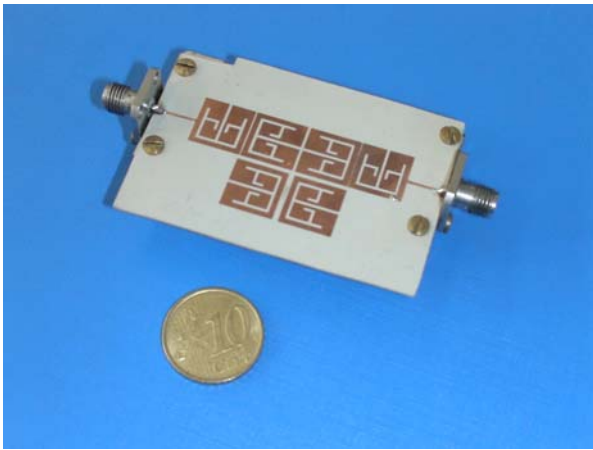


Figure 10. Picture of the six-pole cross-coupled filter.

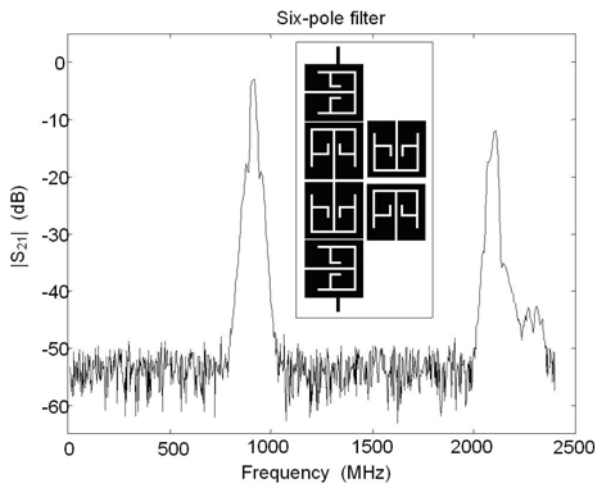


Figure 11. Measured response of the six-pole cross-coupled filter.

The cross-coupled six-pole band-pass filter, which was designed for the 900 MHz bandwidth of the GSM / GPRS, is shown in Fig. 10. The frequency response on a wide-band range is given in Fig. 11. An out-of-band rejection better than the dynamic range of the network analyzer of 55 dB was achieved on a very wide band. The designed procedure offered in this case a much easier control of the attenuation poles on each side of the pass-band than in the case of the dual-mode filter.

IV. CONCLUSIONS

The proposed devices are cost-effective, easy to fabricate and to integrate in planar RF and microwave circuits. No extra lumped components or via-holes are required. The presented designs are fully compatible with substrates of high dielectric constant ceramics [6, 7]. The design procedure can be applied also to high temperature superconductors (HTS) devices in order to achieve high unloaded quality factors, for narrowband devices with a very low in-band insertion loss.

The further research will include investigations on the possibilities of obtaining stronger capacitive couplings with the external circuit, by performing slots in the ground plane just underneath of the coupling gaps.

REFERENCES

- [1] I. Wolff, "Microstrip bandpass filter using degenerate modes of a microstrip ring resonator", *Electronics Letter*, vol. 8, no. 12, pp. 302-303, 1972.
- [2] H. Huber, M. Manzel, H. Bruchlos, F. Thrum, M. Klinger, A. Abramowicz, "TBCCO-microstrip filters based on dual-mode ring resonators", *Proceedings of the Applied Superconductivity*, 30 June- 3 July, The Netherlands, 1997, Inst. Phys. Conf. Ser. 158, p. 347, 1997.
- [3] M.G. Banciu, G. Lojewski, A. Ioachim, N. Militaru, "Compact cross-coupled filters for UMTS applications", *Proceedings of the International Symposium on Signals, Circuits and Systems, ISSCS 2005*, Iassy Romania, vol. II., pp.725-728, 2005.
- [4] M. Sagawa, M. Makimoto, S. Yamashita, "Geometrical structures and fundamental characteristics of microwave stepped-impedance resonators", *IEEE Transactions on Microwave Theory and Techniques*, vol. MTT-45, pp. 1078-1085, 1997.
- [5] M. G. Banciu, R. Ramer, A. Ioachim, "Microstrip filters using new compact resonators", *Electronics Letters*, vol. 38, pp. 228-229, 2002.
- [6] A. Ioachim, M. I. Toacsan, M. G. Banciu, L. Nedelcu, G. Stoica, G. Annino, M. Cassettari, M. Martinelli, R. Ramer, "ZST type material for dielectric resonators and substrates for hybrid integrated circuits", *Journal of Optoelectronics and Advanced Materials*, vol. 5, no. 5, pp. 1395-1398, 2003.
- [7] A. Ioachim, M. I. Toacsan, M. G. Banciu, L. Nedelcu, H. V. Alexandru, C. Berbecaru, D. Ghetu, G. Stoica, "BNT ceramics synthesis and characterization", *Materials Science and Engineering B*, vol. 109, pp. 183-187, 2004.

A Novel 2-GHz Tunable Differential Three-Branch Channelized Bandpass Filter Integrated on Silicon

S. Darfeuille¹, R. Gómez-García², B. Barelud¹, L. Billonnet¹, B. Jarry¹, H. Marie³, P. Gamand³

¹ XLIM, UMR CNRS 6172, Université de Limoges, 123 Avenue Albert Thomas, 87060 Limoges cedex, FRANCE

² Dpto. SSR, ETSI Telecomunicación, Universidad Politécnica de Madrid, 28040 Madrid, SPAIN

³ Innovation centre RF, Philips Semiconductors, 2 rue de la girafe, 14079 Caen cedex, FRANCE

Abstract—In this paper, we present a tunable integrated three-branch channelized bandpass filter implemented on Silicon. Typical designs of channelized filters in hybrid technology require the use of distributed power splitters/combiners and transmission-line elements not suitable for Silicon integration. As an alternative, we propose here a new arrangement based on an original active power divider and elementary recursive stages for the filter branches. This circuit, with a chip size smaller than 3 mm^2 , is fully tunable within the 2-2.2 GHz range. Its filtering response exhibits a 3-dB bandwidth of approximately 90 MHz and a power transmission gain of 12 dB. Furthermore, very good out-of-band rejection performance is achieved through the generation of adjacent power transmission zeros. The chip has been implemented using Philips QUBIC4 Si BiCMOS process [1].

I. INTRODUCTION

The telecommunication market has grown exponentially over the last few years. Until now, the most widely adopted solution for RF front-ends design supporting communication and radar applications has consisted of using off-chip passive filters. These circuits are expensive and space consuming. Moreover, they cannot easily be tuned. Consequently, multi-standard equipment using such filters must include as many units as desired standards.

An alternative to counteract the aforementioned limitations is the use of active filters, joining in the same module the bandpass filtering and low-noise amplifying functions. This leads to more compact and lower cost circuit realizations. Furthermore, these filters are generally frequency tunable and can be integrated in a single chip with other functions such as mixers. Thus, the design of flexible transceiver architectures dedicated to multi-function systems can be enormously simplified in terms of space and circuit complexity.

In this article, we propose an original MMIC tunable three-branch channelized bandpass filter integrated on Silicon. The circuit uses an active divider and simple first-order reconfigurable recursive stages for the filter branches. Note that, since all the circuits presented in this paper are of the differential type, the results reported here are expressed using the mixed-mode S-parameters formulation (i.e. common mode and differential mode) [2]. Thus, the differential power transmission gain will be referred to as S_{dd21} .

II. THEORETICAL BACKGROUND

Microwave channelized filters were firstly introduced in 1996 [3]. This class of filters allows to derive a large variety

of highly-selective filtering responses (i.e. lowpass, highpass, passband or stopband) from the composition of low-order transfer functions. Indeed, thanks to the generation of transmission zeros, very sharp passband-to-stopband transitions and high out-of-band power rejection levels can be achieved. Channelized filters have been generally built with no more than two [4] or three [5] channels. The selectivity achievable with the three-branch topology is higher than that of the two-branch solution. However, this is done at the expense of complicating the design process of the whole filter. Furthermore, the overall filtering response becomes very sensitive to the partial responses of branches, non-tunable in hybrid technology [3]-[5]. This drawback makes the three-branch topology specially suitable for MMIC applications, where transfer functions of each channel can be adjusted as required by means of control elements.

A conventional functional block diagram of three-branch channelized bandpass filter, such as that proposed in [5] for hybrid technology, is detailed in Fig. 1.

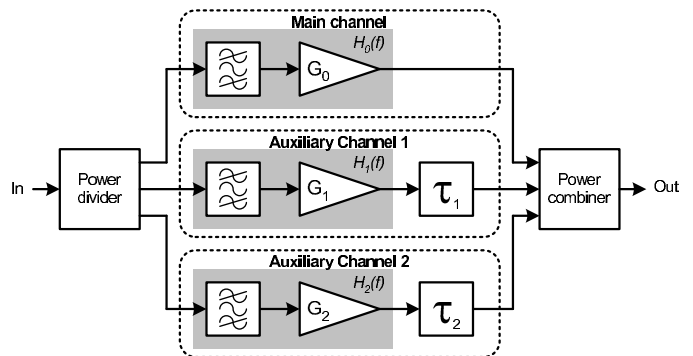


Fig. 1. Functional block diagram of a 3-branch channelized bandpass filter

As shown, this filter is composed of a power divider and combiner at the input and output respectively, and three channels composed of a passive low-order passband filter, an amplifier stage and a delay element for auxiliary channels. The passive filter determines the filtering profile for each channel. The amplifier provides gain and reverse isolation. The delay element, typically built using a transmission-line segment, achieves appropriate phase conditions by producing destructive interferences between the output signals to be combined at the edges of the intended channelized-filter passband.

Note that, from a theoretical perspective, the presence of the delay sections leads to extra frequency-dependant phase terms $e^{-j\varphi_1(f)}$ and $e^{-j\varphi_2(f)}$ in the overall transfer function $H(f)$ as detailed in (1), where $H_i(f)$ denotes the transfer function of the single i -th channel. This is an intrinsic property of mixed channelized-transversal topologies or, in a broader sense, to a generalized channelized filter arrangement with non-constant phase differences between the output signals of channels.

$$H(f) = H_0(f) + H_1(f) \cdot e^{-j\varphi_1(f)} + H_2(f) \cdot e^{-j\varphi_2(f)} \quad (1)$$

III. MMIC IMPLEMENTATION

In Silicon MMIC technology, it is not possible to integrate distributed power splitters/combiners and transmissions lines due to the big physical dimensions of such components. Moreover, the low resistivity of the Silicon substrate leads to very lossy elements. Thus, a conventional lumped-element passive filter solution is not suitable to implement the low-order bandpass filter stages of the channelized module branches.

Here, the design of a MMIC tunable three-branch channelized bandpass filter with constant phase differences between the output signals of channels is approached. As previously explained, this is the best solution for achieving an overall filtering response with maximized out-of-band rejection levels. In the proposed configuration, this phase difference is provided by an active power divider, which also splits the input signal into three output signal components, placed at the input of the global filter. The phase opposition leads to the generation of destructive interferences between the output signals once processed by channels, thus producing, by setting appropriate values of gain in each channel, two adjacent transmission zeros in the overall response.

In the channels, the set shaped by the passive bandpass filters and the amplifiers is replaced by simple first-order tunable recursive filters. The tunability of these active blocks allows to precisely adjust the gains, bandwidths and centre frequencies of the channels responses for obtaining the intended overall filtering profile.

Furthermore, the use of identical filters in the branches with adequate output matching makes the output power combiner unneeded. Thus, the different channel outputs are directly reconnected. Finally, in order to simplify the design of the divider, the choice has been made to use single outputs instead of differential ones. Nevertheless, the total structure presents differential input and output, with differential-type divider and recursive filters. The simplified functional block diagram of the described overall filter is shown in Fig. 2. Deeper insight into each basic block is made below.

A. Active divider

The primary role of the divider is to split the input signal into three signals, not necessarily of equal amplitude since an eventual imbalance can be corrected later with the tunable recursive filters. Its secondary task is to provide a frequency-independent 180° phase shift between the signal component of the main channel and the signals injected to the auxiliary channels. The proposed solution is presented in Fig. 3.

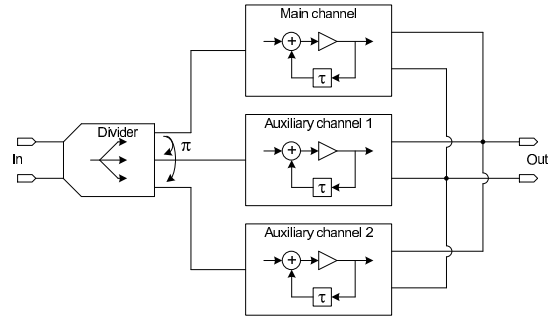


Fig. 2. Block diagram of the proposed channelized filter

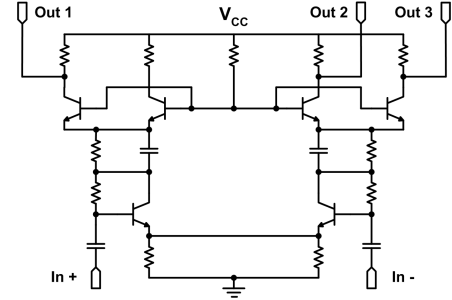


Fig. 3. Electrical scheme of the proposed active divider

As shown, it consists of a standard cascode differential amplifier where the cascode stage (i.e. the base-coupled transistor pair) is doubled in order to provide four potential outputs (even if, in the current case, no more than three of them are used). Moreover, as the structure provides a good inherent common-mode rejection, only differential signals will be present at the output. This means that the signal of output 1 is necessarily in phase opposition regarding the signals of outputs 2 and 3. The differential power transmission gain parameters for the three outputs obtained with a differential input signal are presented in Fig.4. In this graph, $|S_{sd21}|$ refers to the gain taken between the differential input (d) and the first single output (s) of Fig. 3. $|S_{sd31}|$ and $|S_{sd41}|$ denote the gains at the second and third outputs, respectively. As can be seen, the gains at the second and third outputs are perfectly equal, and only 0.3 dB higher than the gain achieved at the first output.

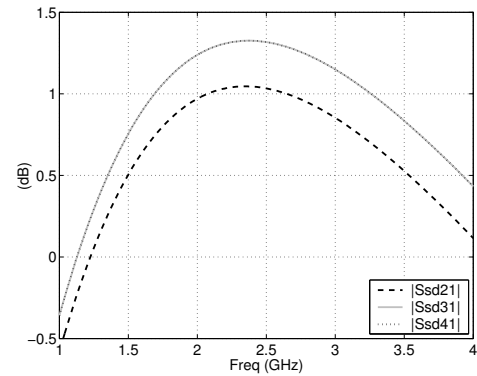


Fig. 4. Divider differential-input to single-output gain

B. First-order recursive filters

The chosen recursive filter topology is derived from the recursive filter schemes presented in [6] and [7]. As shown in Fig. 5, it is based on the use of an active adder, a passive delay cell and an output buffer.

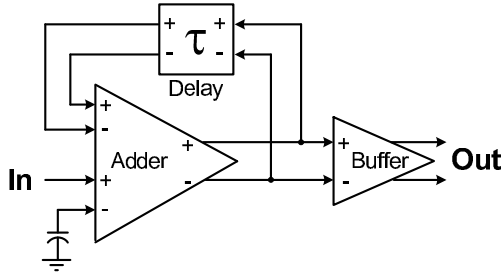


Fig. 5. Functional block diagram of the proposed recursive filter

The adder is built with two differential amplifiers sharing their load resistors in order to provide a common output. The direct input amplifier is arranged in a differential cascode configuration with a fixed gain. One physical port is grounded in order to present only a single input. The feedback input amplifier is a simple emitter-coupled transistor pair with gain control by means of a current mirror source. This current source allows to adjust the feedback loop gain, thus ensuring electrical stability. It also gives control on the selectivity of the filter response.

The passive delay section is built with lumped inductors and capacitors, and can be controlled thanks to varactor diodes. This feature makes the filters frequency-tunable.

Finally, the output buffer is a variable-gain low-noise amplifier (LNA), which also allows to set the global gain of the structure. The buffer's output is matched to a 150- Ω impedance in order to obtain the standard 50- Ω output matching for the overall filter.

Some typical power transmission responses of this filter for different tuned centre frequencies are drawn in Fig.6.

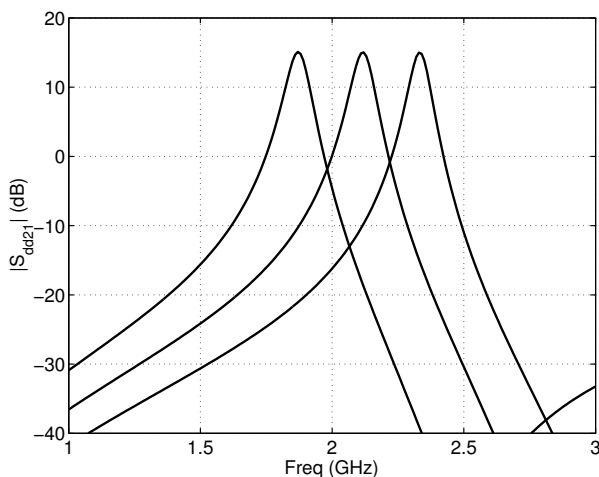


Fig. 6. Power transmission responses of the recursive filter for different tuned centre frequencies

C. Overall channelized filter

The chip layout of the designed channelized filter is presented in Fig. 7. Its dimensions are 2.03x1.40 mm². However, nearly 25 percent of this surface is not used. The effective surface is then about 2.15 mm².

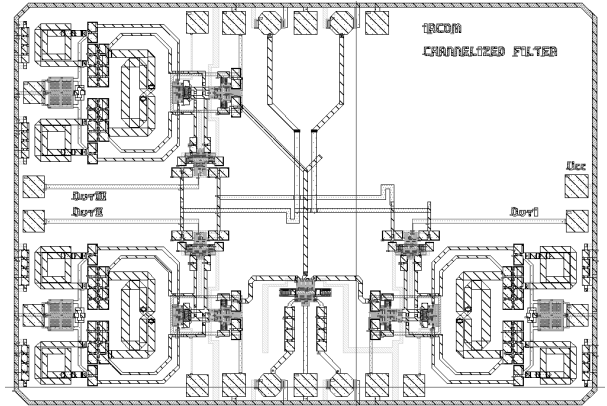


Fig. 7. Filter layout

IV. SIMULATION RESULTS

Thanks to the different adjustment points on the unitary filters, a great variety of bandpass filtering profiles can be obtained through the proposed MMIC channelized structure. In Fig. 8, the power transmission response of the designed three-branch channelized filter with two transmission zeros around a fixed centre frequency is drawn. The corresponding responses of the three single branches are also provided in Fig. 9.

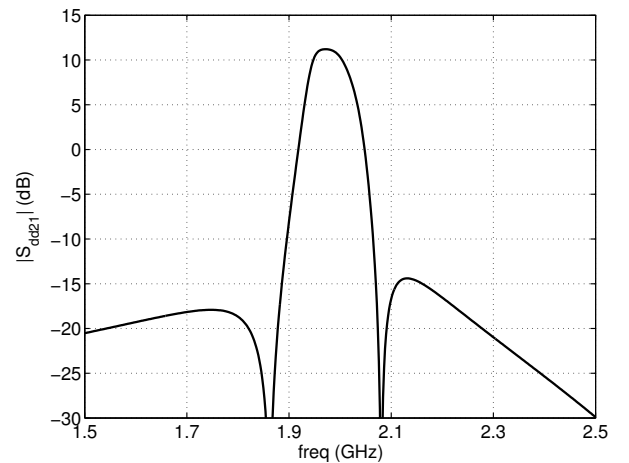


Fig. 8. Channelized filter's Power transmission response (two transmission zeros)

As shown, the overall power transmission gain is 12 dB and the 3-dB bandwidth is about 85 MHz. The out-of-band rejection is higher than 26 dB for frequencies whose separation from the 1.97-GHz centre frequency is more than 100 MHz. $|S_{dd11}|$ is lower than -10 dB up to 2.1 GHz and $|S_{dd22}|$ is below -15 dB up to more than 2.5 GHz.

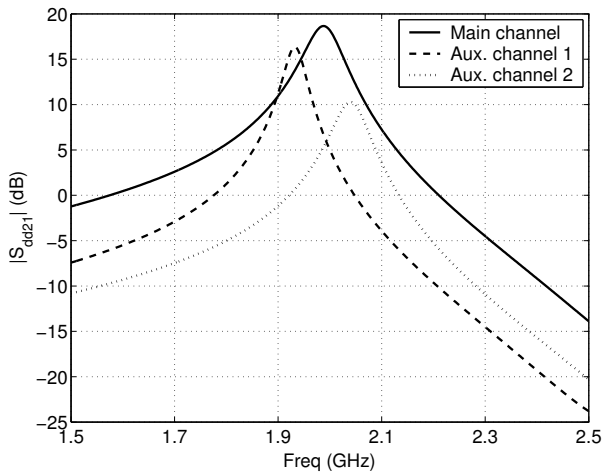


Fig. 9. Power transmission responses of the branches (two transmission zeros)

The power consumption of the whole circuit is less than 28 mA for a supply voltage of 2.7 V.

The centre frequency tuning performance of the designed filter is represented in Fig. 10. As demonstrated, a centre-frequency tuning range of 1.95-2.2 GHz is achieved. Note also that although the general shape of the filter response is preserved, both the instantaneous bandwidth and the power transmission gain are varied as different centre frequencies are tuned.

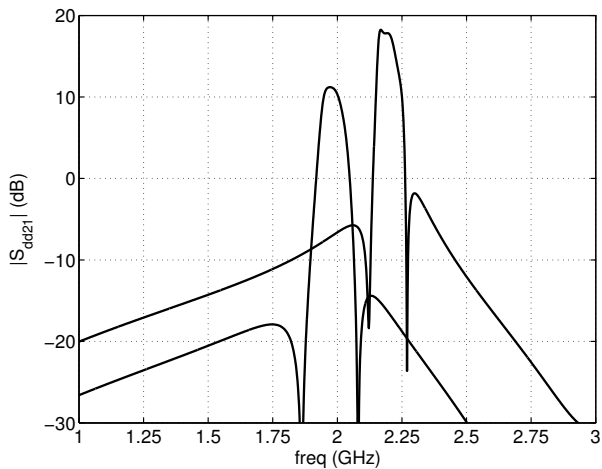


Fig. 10. Centre-frequency tuning performance of the channelized filter

Filtering responses with a single transmission zero, and hence with different selectivity performances above and below the centre frequency, can also be obtained. This is proven in Fig. 11. The interest of such responses is that, without significantly affecting the rejection capabilities in the upper band, an in-band flatness higher than that of the transfer function with two transmission zeros is achieved. Furthermore, this transmission zero can be shifted as desired from the lower to the upper band by acting on the tuning voltages of the filter control elements.

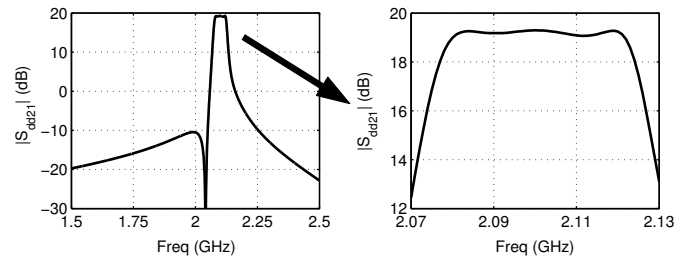


Fig. 11. Channelized filter's power transmission response (one transmission zero)

In any case, the common-mode gain of this channelized filter is smaller than -20 dB at the centre frequency. Therefore, it can be considered as negligible.

V. CONCLUSION

In this paper, a novel tunable three-branch channelized bandpass filter integrated on Silicon has been presented. To our knowledge, this is the first MMIC channelized filter reported to date. It is based on an original active divider circuit and elementary stages of recursive filters for the three branches. Simulations have proven the viability of the proposed filter topology, with a power transmission gain varying from 12 to 20 dB within the 1.95-2.2 GHz centre-frequency tuning range. The 3-dB bandwidth is comprised between 80 and 100 MHz, and the out-of-band rejection level is close to 30 dB for frequencies allocated 100-MHz far away from the tuned centre frequency.

ACKNOWLEDGMENT

The authors wish to acknowledge the Philips Semiconductors R&D Department team in Caen for their assistance during the conception of the chip.

REFERENCES

- [1] D. Szymd, R. Brock, N. Bell, S. Harker, G. Patrizi, J. Fraser and R. Dondero, "QUBIC4 : a Silicon RF-BiCMOS Technology for Wireless Communication ICs", *Proceedings of the 2001 bipolar/BiCMOS Circuits and Technology Meeting*, pp. 60-63
- [2] D. Bockelman and W. Eisenstadt, "Combined Differential and Common-Mode Scattering Parameters: Theory and Simulation", *IEEE Trans. Microwave Theory Tech.*, vol. 43, no. 7, July 1995, pp. 1530-1539.
- [3] C. Rauscher, "Microwave channelized Active Filters - A New Modular Approach to Achieving Compactness and High Selectivity", *IEEE Trans. Microwave Theory Tech.*, vol. 44, no. 1, pp. 122-132, Jan. 1996
- [4] R. Gómez-García, J.I. Alonso, C. Briso-Rodríguez, "On the Design of High-Linear and Low-Noise Two-Branch channelized Active Bandpass Filters", *IEEE Trans. Circ. Sys. II*, vol. 50, no. 10, pp. 695-704, Oct. 2003
- [5] R. Gómez-García, J.I. Alonso, "A Design Technique for Three Branch channelized Bandpass Filters", *33rd European Microwave Conference*, Munich, 7-9 Oct. 2003, vol. 1, pp. 215-218
- [6] S. Darfeuille, Z. Sassi, B. Barelaud, L. Billonnet, B. Jarry, H. Marie, N.T. Luan Le, P. Gamand, "A Fully-Differential 2 GHz Tunable Recursive Bandpass Filter on Silicon", *2005 German Microwave Conference*, GeMIC 2005, Ulm, April 5-7 2005
- [7] S. Andersson, P. Caputa and C. Svensson, "A Tuned, Inductorless, Recursive Filter LNA in CMOS", *Proc. of the ESSCIRC 2002 conference*, Florence, Italy, 24-26 Sept. 2002, pp. 351-354

Broadband Millimeter-wave FMCW Radar for Imaging of Humans

A. Dallinger*, S. Schelkshorn, J. Detlefsen

Technische Universität München, Lehrstuhl für Hochfrequenztechnik,
 Fachgebiet Hochfrequente Felder und Schaltungen, Arcisstr. 21, 80333 München, Germany

*alexander.dallinger@tum.de

Abstract— We present design and realization of a broadband FMCW Radar working in the Millimeter-Wave (MMW) region. The usable frequency range lies between 91 GHz and 102 GHz. We use a homodyne radar setup. Thus only one MMW source is necessary which is used for TX and LO generation simultaneously. The complex RX radar signal is calculated by a Hilbert transform in order to avoid a broadband MMW IQ mixer.

A free space calibration procedure is used to obtain a flat amplitude response and a fixed phase center. Static non-linearities of the transmitted chirp signal are compensated by predistortion of the VCO's tuning voltage characteristic. A microwave coaxial delay line combined with a time domain resampling method corrects dynamic non-linearities.

The ultra wide bandwidth of 11 GHz is necessary for the purpose of a high resolution imaging task. Due to the fact that MMWs propagate easily through common clothing it is feasible to image objects like concealed weapons worn beneath the cloth. Imaging of humans in the MMW region is one possibility to enhance the capabilities of nowadays security checkpoints, e. g. at airports.

I. INTRODUCTION

High resolution imaging heavily depends on broadband imaging sensors no matter whether one applies passive or active systems, direct imaging or synthetic aperture focusing methods. The resolution along at least one image axis, in most cases the range or propagation delay axis, is directly proportional to bandwidth and does not depend on the actual frequency domain. The selection of the frequency domain can be based on considerations with respect to the available technology and can be further chosen according to the desired propagation characteristics of the electromagnetic waves.

The MMW region (30 GHz . . . 300 GHz) and the THz region (300 GHz . . . 10 THz) provide fairly well conditions for short range, high resolution and ultrawideband imaging applications. Above ca. 300 GHz the use of spectroscopic information is possible.

For security applications dealing with the imaging of concealed objects, which are metallic materials, ceramic materials or explosives, the spectroscopic properties of the THz region could be a major advantage. The technology of THz sensors yet is not suitable for environments outside the laboratory and also is still very expensive [1], which is not the case for the MMW region. This fact makes the MMW region a good candidate. But it should be kept in mind that it cannot provide the spectroscopic information which could be used

to identify certain materials unambiguously. Today one can also find fully developed devices and systems up to 200 GHz including all components needed for a broadband radar, e. g. sources, mixers, LNAs, power amplifiers and antennas.

The imaging of concealed objects, which in our case are mainly dielectric objects, requires the sensor to have high sensitivity and dynamic range even though a short range application with ranges below approx. 3 m is intended.

The system is supposed to operate in an indoor environment which requires a source in order to illuminate the person under surveillance no matter whether an active or passive sensor (radiometer) is applied.

In order to implement a measurement system for the MMW range we developed and realized an ultrawideband FMCW radar which provides the bandwidth and dynamic range needed for high resolution images.

II. SYSTEM CONCEPT

A. Homodyne Radar Setup

Figure 1 illustrates the schematic of the MMW FMCW Radar. Basically a homodyne radar setup has been chosen. The

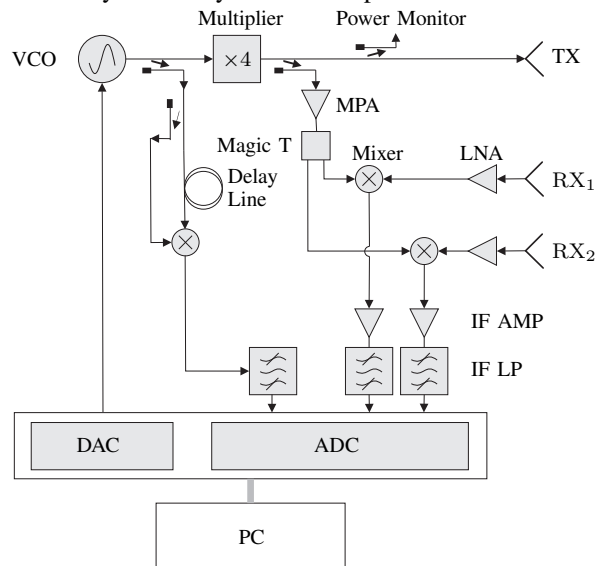


Fig. 1: Schematic of the homodyne MMW FMCW Radar: 1 TX channel and two RX channels

radar consists of a sweeping source connected to a frequency

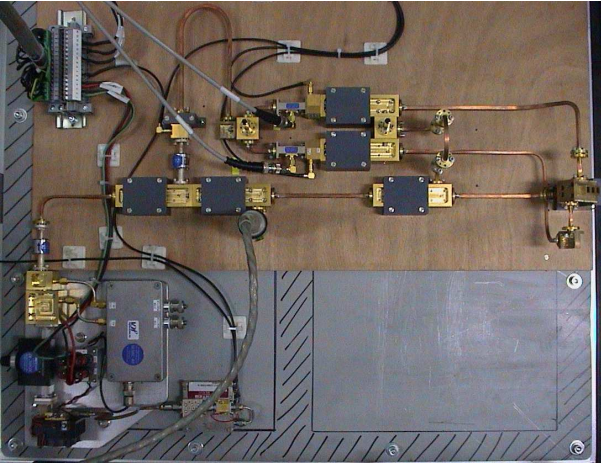


Fig. 2: Photo of the radar front end

multiplier which is used for transmitting and LO generation simultaneously. Hence only one MMW source is needed which is by far the most expensive component of the setup. A photo of the radar front end is shown in figure 2. The transmitted signal (TX) is linearly frequency modulated. The frequency swept signals returned from the object are delayed copies of the transmitted signal. The delay is given by the round trip propagation time to the object and back.

The received signal (RX) is down-converted to baseband. This results in an instantaneous difference in frequency between the transmitted and received signal. The baseband signal is the so called beat frequency f_b which is linearly proportional to the range r to the object. The range resolution $\Delta r = c_0/2B$ is only depending on the usable system bandwidth B .

1) *TX Signal:* The TX and LO signal is generated by a voltage controlled oscillator (VCO) operating between 22.5 GHz and 25.5 GHz. It drives a frequency multiplier which has a multiplication factor of four. The usable output frequency range of the multiplier stage lies within 90.5 GHz and 102 GHz providing approx. 20 dBm output power. Most of this power is needed for the LOs. The pumping power at the mixers LO port is required to be within 10 dBm to 13 dBm. In order to reduce the power ripple of the multiplier at the LO input port of the mixer a broadband medium power amplifier (MPA) operating in saturation at approximately 17 dBm output power is used.

2) *TX/RX Antenna:* The TX signal is transmitted by a linearly polarized horn antenna. For TX and RX separate antennas are used in order to avoid the effects of the return loss. Another reason for separation is that we consider to have two similar built receiver channels. These two channels either can be used for interferometric imaging approaches or for measurements with two orthogonal polarizations. Figure 3 shows a photo of the antenna which is milled out of a single brass block.

3) *RX Signal:* The RX signal is amplified by a low noise amplifier (4.5 dB noise figure, 20 dB gain) before downconverting to baseband. The baseband signal is a low frequency

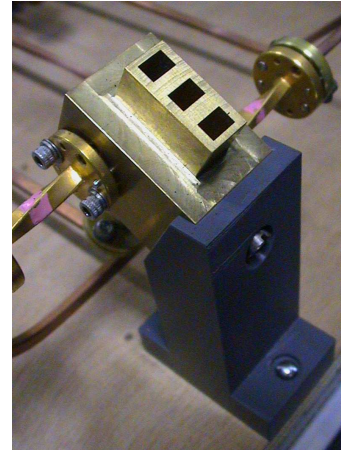


Fig. 3: Milled horn antenna block consisting of three antennas: 1 TX, 2 RX

low pass signal (0 Hz to 300 kHz). The upper frequency limit is only depending on the maximum expected range. For distances up to three meters we use 16 bit AD conversion equipment with a maximum sampling rate of about 1.5 MS/sec.

4) *Data Acquisition:* Because the FMCW radar transmits and receives simultaneously, signal generation and data acquisition have to be synchronized. In order to drive the VCO we use a 16 bit DA converter which is synchronized by a common clock to the AD conversion of the received signal and the further data processing.

B. Hilbert Transform Receiver

The realization of broadband quadrature mixers in W-Band is nontrivial because a broadband 90° phase shifter with sufficient accuracy cannot be realized easily. Also the calibration process and the removal of DC offsets on the I and Q channels require considerable computational efforts.

The homodyne measurement system acquires a real valued beat frequency signal which is band limited and assumed to have a causal impulse response. It is considered to represent the real part $u_{s,Re}(t)$ of the complex analytical signal, $u_s(t) = u_{s,Re}(t) + ju_{s,Im}(t)$. It is desirable to compute the analytical signal in order to obtain phase information which is necessary for coherent imaging and radar purposes.

The relationship between the real and imaginary components of $u_s(t)$ can be derived by applying the causality principle and can be calculated by the Hilbert transform. The Hilbert transform can either be realized in time domain by using a correlation filter or in frequency domain by means of a multiplication with the spectral response of the Hilbert operator which is $\mathcal{H}(f) = -j\text{sgn}(f)$ [2]. The analytical signal is obtained by

$$u_{s,\mathcal{H}}(t) = \mathcal{F}_f^{-1}\{\mathcal{F}_t\{u_{s,Re}(t)\} \cdot \mathcal{H}(f)\}. \quad (1)$$

\mathcal{F} stands for the Fourier Transform.

The impulse response of a Hilbert transformer has an infinite extent with respect to time. A physical measurement system can only measure a time limited portion of the signal. That

means we measure the time windowed (rectangular window) real part of the analytical signal and thus the Hilbert transform only can provide an approximate solution for the imaginary part. The errors introduced by using the Hilbert transform can be reduced by using an appropriate window function before applying the Fourier transform [3] in equation 1.

III. CALIBRATION

Similar to a network analyzer calibration the amplitude and phase response of the radar system have to be calibrated in order to obtain a flat amplitude response and to establish a fixed phase center. Due to the radar functionality of the homodyne measurement system the calibration has to be done in free space. Hence one has to use a reference calibration object like a corner reflector with a known and precise free space reflection coefficient S_{11} , e. g. a trihedral. By measuring the response of the reference object $u_{\mathcal{H},s,\text{ref}}(t)$ and the response of the empty room $u_{\mathcal{H},s,\text{emp}}(t)$ a calibration procedure for the measured data $u_{\mathcal{H},s,m}(t)$ can be implemented by [4]

$$u_{s,\text{cal},m}(t) = \frac{u_{\mathcal{H},s,m}(t) - u_{\mathcal{H},s,\text{emp}}(t)}{u_{\mathcal{H},s,\text{ref}}(t) - u_{\mathcal{H},s,\text{emp}}(t)} \cdot S_{11,\text{ref}} \quad (2)$$

IV. LINEARIZATION

The FMCW radar performance heavily depends on the linearity of the transmitted linear frequency modulated signal. Especially the range resolution is affected, which gets worse with increasing range. Frequency sweep non-linearities are often the limiting factor in FMCW radar range resolution [5].

A. Predistortion

As seen in figure 1 the chirped TX signal is generated by the VCO. The frequency output is controlled by the tuning voltage which is supplied by the DA conversion equipment. The frequency vs. tuning voltage characteristic can be measured in a static setup, e. g. by means of a spectrum analyzer or frequency counter. This data can be used to generate a predistorted tuning voltage ramp for the VCO. One has to note that this method cannot correct for dynamic non-linearities.

B. Resampling Method

Dynamic non-linearities are efficiently compensated for by a software resampling method [6]. If the transmitter generates an ideal linear chirp a static target causes a linear phase behavior of the beat frequency signal. The phase is proportional to the targets distance R with respect to the sensor, that is $\varphi_b = 2\pi \frac{B}{T} \tau$, ($\tau = 2R/c_0$). Any non-linearities in the chirp will cause non-linearities in the beat frequency phase. These phase errors can be equalized by resampling the measured signal in the way, that sampling is not performed at fixed time intervals Δt , but at fixed beat frequency signal phase increments $\Delta\varphi_b$. A certain upsampling of the data is necessary to enable a convenient computation of a new time/sampling axis.

This method may be realized by using a delay line with a known length l_d and propagation velocity. The delay line produces an isolated target signature at distance $l_d/2$. Assuming

that the frequency sweep is linear during a small time span Δt_i the instantaneous frequency of the beat signal equals

$$f_{b,i} = \frac{\Delta f_i}{\Delta t_i} \tau = \frac{1}{2\pi} \frac{\Delta\varphi_{b,i}}{\Delta t_i}, \quad (3)$$

where Δf_i is the frequency increment. Hence the actual transmitted bandwidth B can be calculated by

$$B = \sum_{i=1}^{N_s-1} \frac{\Delta\varphi_{b,i}}{2\pi l_d/c_0}, \quad (4)$$

which is important because the range axis is related to the bandwidth.

In order to avoid attenuation and dispersion effects of rectangular waveguides the delay line is realized by a coaxial cable for the microwave signal, i. e. before multiplying the VCOs output signal.

Figure 4 shows the result obtained by this method. We use a delay line of length $l_d = 4.6$ m. Its propagation velocity is 77% of the free space velocity. After downconversion the beat frequency signal is Hilbert transformed in order to obtain the phase information. The non-linear phase behavior of the beat frequency is shown in 4a and the unfocused range profile in 4b. The range profile of the resampled beat frequency signal can be seen in figure 4c. The resampling indices are stored in a file and are used for linearization of the radars beat frequency signals.

V. RESULTS

All following results have been obtained with the parameter settings documented in table I:

frequency range	$f_{\min} \dots f_{\max}$	91 GHz .. 102 GHz
bandwidth	B	11 GHz
sweep time	T	1.25 ms
RX AD sampling rate	$f_{\text{RX},s}$	1 MHz
RX $\text{samples}_{\text{sweep}}$	$N_{\text{RX},s}$	1250
VCO DA sampling rate	$f_{\text{VCO},s}$	1 MHz
VCO linearization method	predist. & delay line	
VCO $\text{samples}_{\text{sweep}}$	$N_{\text{VCO},s}$	1250
range resolution	Δr	13.64 mm
unambiguous range	r_{amb}	17.05 m
maximum beat frequency (limited by low pass filter)	$f_{b,\max}$	300 kHz
maximum range	$r_{\max} = \frac{r_{\text{amb}}}{2}$	8.53 m

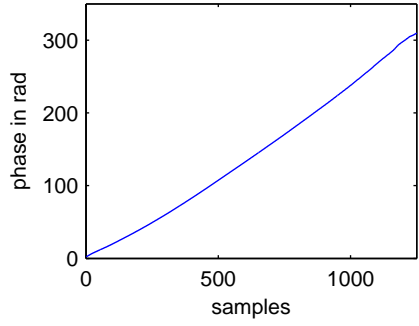
TABLE I: Parameter settings used for operation

A. Linearization Using Predistortion and Resampling

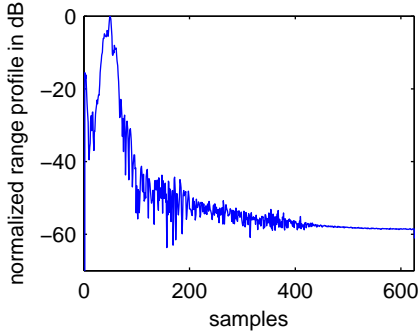
By using the predistortion and resampling method as explained above an effective linearity of about 0.1% was achieved.

B. Performance of the Calibrated Data

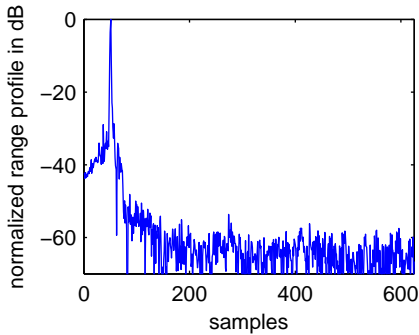
Fig. 5 shows the calibrated data of a trihedral which was also used as the reference calibration object when positioned with a small spacial offset. The peak's 3dB resolution width for the trihedral's position at about 0.75 m is very close to



(a) unwrapped non-linear beat frequency phase



(b) range profile before resampling

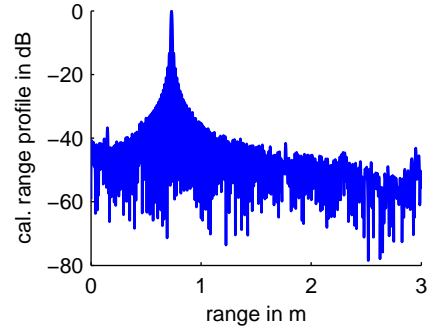


(c) linearized range profile

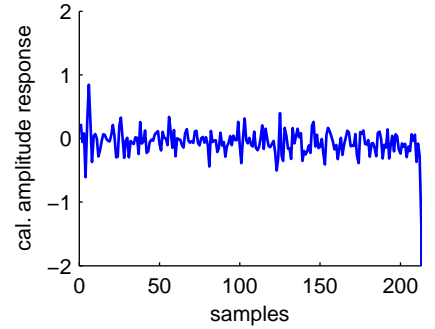
Fig. 4: Linearization by resampling method by means of a coaxial delay line with length $l_d = 4.6$ m and propagation velocity $c_d = 0.77c_0$

the theoretical expectation of approx. 14 mm. The dynamic range is dependent on the sidelobe levels of the peak. In the case of a rectangular window it was about 60 dB measured from the peak down to the lowest sidelobe level at a distance of ca. 3 m. It can be further increased by using a suitable windowing function (e. g. a Kaiser–Bessel window), i. e. the dynamic range yet is not limited by noise within the range of reasonable window functions. The non-symmetric behavior of the sidelobe spectrum results from the errors produced by the Hilbert transform when applied on non-causal signals. These errors may be further reduced by using a window function before calculating the Hilbert transform [3].

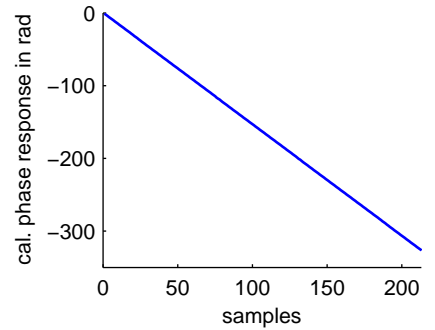
The calibrated amplitude response of the calibration reference has a ripple of ± 1 dB as shown in figure 5b.



(a) range profile



(b) amplitude response



(c) phase response

Fig. 5: Linearized and calibrated data of a trihedral at about 0.75 m distance to the antenna at range zero, range gated at ca. 3 m

VI. CONCLUSIONS

We have developed an ultrawideband, homodyne MMW FMCW Radar with more than 10 GHz bandwidth and approx. 16 dBm TX power. It is designed for short range imaging applications with ranges up to 3 m. The complex radar signal required for calibration is obtained by applying a Hilbert transform. The radar is showing a dynamic range better than 60 dB which is expected to be sufficient for this type of application. Predistortion and a resampling method are implemented in order to correct for static and dynamic non-linearities, respectively.

REFERENCES

- [1] J. F. Federici, B. Schulkin, F. Huang, D. Gary, R. Barat, F. Oliveira, and D. Zimdars, "Thz imaging and sensing for security applications and explosives, weapons and drugs," *Semiconductor Science and Technology*, vol. 20, no. 7, p. S266, 2005.
- [2] J. G. Proakis and D. G. Manolakis, *Digital Signal Processing*, 3rd ed., ser. Principles, Algorithms, and Applications. New Jersey: Prentice Hall, 1996.
- [3] D. Lipka, "A modified hilbert transform for homodyne system analysis," *AE*, vol. 42, no. 3, pp. 190–192, 1988.
- [4] F. C. Smith, B. Chambers, and J. C. Bennett, "Calibration techniques for free space reflection coefficient measurements," *Science, Measurement and Technology, IEE Proceedings-*, vol. 139, no. 5, pp. 247–253, 1992.
- [5] S. O. Piper, "Homodyne fmcw radar range resolution effects with sinusoidal nonlinearities in the frequency sweep," 1995, pp. 563–567.
- [6] M. Vossiek, T. v. Kerssenbrock, and P. Heide, "Signal processing methods for millimetrewave fmcw radar with high distance and doppler resolution," in *27th European Microwave Conference*, Jerusalem, 1997, pp. 1127–1132.

Factor and Principle Component Analysis for Automatic Landmine Detection Based on Ground Penetrating Radar

Fawzy Abujarad and Abbas S. Omar

University of Magdeburg, Chair of Microwave and Communications Engineering,
P.O. Box, Magdeburg D-39016, Germany ,
Tel.+493916720079, fjarad@iesk.et.uni-magdeburg.de
Tel.+493916718499 a.omar@ieee.org

Abstract— Statistical signal processing for clutter reduction in stepped-frequency ground penetrating radar (SF-GPR) data is presented for detecting buried Anti-personnel (AP) landmines. Two algorithms are proposed to separate the target and clutter based on factor analysis (FA) and principle component analysis (PCA). The two algorithms have been experimentally evaluated and compared using non-metallic AP landmines. The experimental data were collected by using an SF-GPR operating on the frequency band from 1 GHz to 20 GHz.

I. INTRODUCTION

According to United Nations estimates, over 100 million anti-personnel mines are scattered across the world, killing about 20 000 civilians yearly. Of course, mines were detectable because of their metal content. Recently, new advanced materials that may last for many years have made it possible to produce varieties of mines. These new materials are practically undetectable with the classical metal detector methods. The Ground Penetrating Radar (GPR) is an active device that, in many cases, performs better than the classical metal detector for low-metal-content AP mines.

Therefore, the main part of our work focuses on the processing of data produced by this particular sensor. The detection of non-metallic (NM) and minimum-metal (MM) antipersonnel land mines (APLs) with GPR is difficult to carry out. The difficulty of mine detection is attributed to the extreme clutter environment within the first 5 cm of the soil surface. The major problem here is how to distinguish between the scattered signal from the mines and the background interference. In a blind source separation BSS formulation one is presented with multivariable data measured by m sensors. These data may arise from n source signals that are mixed together by some linear transformation and corrupted by noise. However the sources are not observable and nothing is known about their properties, or about the properties of the mixing process and the noise. In the absence of this information one has to proceed blindly to recover the source signals from their observed noisy mixtures [1].

Despite its signal processing appearance, BSS is an issue of statistical modeling of data. In this context, one wishes to

describe the m observed variables that are generally correlated in terms of a smaller set of n unobserved variables. The simplest such description is given by a probabilistic linear model,

$$x_i = \sum_{j=1}^n a_{ij}s_j + e_i$$

$i = 1, \dots, m$, or in the matrix notation

$$\mathbf{x}(k) = A\mathbf{s}(k) + \mathbf{E}(k)$$

Where $\mathbf{x}(k) = [x_1(k), x_2(k), \dots, x_m(k)]^T$ is a vector of sensor signals (observed variables), $\mathbf{s}(k) = [s_1(k), s_2(k), \dots, s_n(k)]^T$ is a vector of sources, $\mathbf{E}(k) = [e_1(k), e_2(k), \dots, e_m(k)]^T$ is a vector of additive noise, and A is an unknown full rank $m \times n$ mixing matrix [2].

In general the statisticians task is to estimate a_{ij} and s_j . For this purpose two well-known models, namely, the Factor Analysis and the Principal Components Analysis will be used. They differ only in how the noise (e) is dealt with.

The Factor analysis is a statistical method for reducing data, which is based on the correlations between individual variables. It represents in fact a linear Gaussian model and is therefore related to many other models including probabilistic principal component analysis (pPCA), the noisy independent component analysis (ICA), and Kalman filter models etc [3]. The general idea in factor analysis is to model the correlations amongst a large set of observed variables in terms of a few underlying factors, where the observed variables are subject to additive Gaussian noise. The principal component analysis (PCA) on the other hand is one of the most popular techniques for signal processing, data compressing, data visualization, image analysis and pattern recognition. PCA has proven to be an exceedingly popular technique for dimensionality reduction and is discussed at length in most texts on multivariate analysis. As FA and PCA are second-order statistical methods, only covariances between the observed variables are used in the estimation. Both methods have similar goals; namely to express data sets in terms of linear combinations of a small set

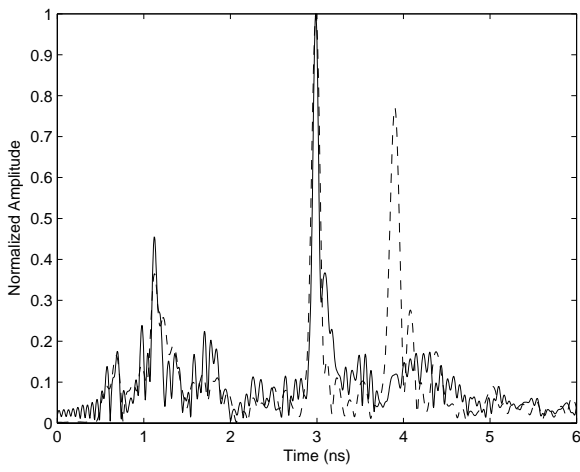


Fig. 1. A scans in the presence (dashed) and absence (solid) of a mine

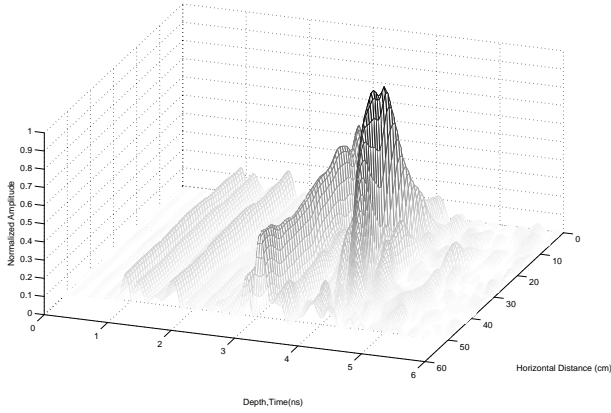


Fig. 2. B-Scan of one non-metallic Anti-personnel landmines (PMN) at location 3.9ns

of factors that are assumed to be uncorrelated and gaussianly distributed. However, there exists a crucial difference between the two methods. PCA is in fact a data reduction rather than a factor-analysis method. It became popular decades ago when computers were slow and expensive to use. It was a quicker, cheaper alternative to real factor analysis. It is computed without regard to any underlying structure caused by latent variables; components are calculated using all of the variance of the manifest variables. The aim of the factor analysis on the other hand is to reveal any latent variables that cause the manifest variables to covary. During factor extraction the shared variance of a variable is partitioned from its unique variance and error variance to reveal the underlying factor structure so that only shared variance appears in the solution.

II. GPR MEASUREMENTS

The data have been acquired with a bistatic-stepped frequency GPR system at IESK, Magdeburg University, Germany. The system consists of a network analyzer (Rohde & Schwarz), which is controlled by a PC (type Pentium 4)

and two ultra-wideband (UWB) transmitting and receiving antennas [4]. A wooden box with dimensions $1.1 \times 1.1 \times 1.1$ m whose internal sides are covered by absorption material and is filled by sand of 0.5 m height has been used. The transmitting and receiving antennas are mounted on a 2D scanning system and were placed above the ground surface at height 30 cm. The measurement grid covers the area bounded by $x = 27 \rightarrow 76$ cm and $y = 39 \rightarrow 89$ cm with a distance between the measurements of 1 cm in both x and y directions. The measurements form a two dimensional matrix, referred to as a B-scan. The column vector of the B-scan matrix (image) is called an A-scan and it represents the data, at each individual point on the basic surface of the soil. The receiving antenna is used to collect this A-scan data. An example of A-scans in the presence and absence of a landmine are displayed in Fig. 1. The radar system operates in the frequency range of 1 GHz to 20 GHz and the number of samples is 1600 for each A-scan. A reflected sheet material has been put between the two antennas to decreasing the cross-talk.

III. FACTOR ANALYSIS

The different methods of factor analysis first extract a set of factors from the data set. These factors are almost orthogonal and are ordered according to the proportion of the variance of the original data that these factors explain. In general, only a (small) subset of factors is kept for further consideration and the remaining factors are considered as either irrelevant or nonexistent (i.e., they are assumed to reflect measurement error or noise) [5]. The mathematical model of FA in relation to the data matrix is

$$X = FA^T + E \quad (1)$$

Where X is the data matrix, with dimensions $N \times p$, F is the matrix of factor scores (latent variables) with dimensions $N \times k$, A is the matrix of factor loading with dimensions $p \times k$, and E is a matrix of residuals or error terms. Here k is a scalar denoting the number of factors to be used and is generally much smaller than p . The scalar notation for the n th row and i th column of the data matrix reads

$$x_{ni} = \sum_{j=1}^k f_{nj}a_{ij} + e_{ni}$$

If x^T represents a row vector of X , then

$$x^T = f^T A^T + e^T,$$

where f^T and e^T are row vectors of F and E respectively. The transpose of the above equation reads

$$\mathbf{x} = A\mathbf{f} + \mathbf{e} \quad (2)$$

Equation (2) is the fundamental model equation for many forms of factor analysis. In this model, it is assumed that the underlying distribution of f is $\mathcal{N}(0; \mathbf{I})$ and e follows $\mathcal{N}(0; \Psi)$, where $\Psi = \text{diag}(\psi_1, \psi_2, \dots, \psi_p)$. Since it is assumed that the e'_i s are uncorrelated and the x'_i s are conditionally uncorrelated given \mathbf{f} . Another way of approaching the factor model is from

the consideration of the covariance matrix. The factor model in terms of variances and covariances reads [5]

$$\begin{aligned} \frac{1}{N} X^T X &= A \left[\frac{1}{N} F^T F \right] A^T + A \left[\frac{1}{N} F^T E \right] \\ &+ \left[\frac{1}{N} E^T F \right] A^T + \frac{1}{N} E^T E \end{aligned}$$

and

$$\Sigma = A\Phi A^T + \Psi$$

where Σ is the $p \times p$ population covariance matrix of the observed variables, Φ is the $k \times k$ covariance matrix of the factors and Ψ is the $p \times p$ residual covariance matrix.

Let us now assume that the factors are uncorrelated, that is, $\Phi = \mathbf{I}$, and the p -dimensional e is distributed according to $\mathcal{N}(0; \Psi)$, where Ψ is diagonal. The diagonality of Ψ is in fact one of the key assumptions of factor analysis. It means that the observed variables are conditionally independent (given the factors). According to this model, the distribution of x has zero mean and covariance Σ .

The goal of the factor analysis is to find A and Ψ that best model the covariance structure of \mathbf{x} . Several algorithms have been proposed in the literature for computing the matrices A and Ψ . For example the squared multiple correlation coefficient (SMC) model assumed that [5]

$$\hat{\Psi} = (\text{diag} C_x^{-1})^{-1}$$

where $C_x = X^T X / N$. More efficient methods of estimating A and Ψ are the generalized least squares (GLS), which minimizes

$$\text{tr} (C_x^{-1} \Sigma - I)^2,$$

where tr is the trace operator and the maximum likelihood method (ML). In this work, the factor loadings matrix A and Ψ have been computed by using the Expectation-Maximization (EM) algorithm. An EM algorithm for a maximum likelihood estimation of FA has been proposed in [6] and reviewed in [7] and [8]. The log likelihood can be written

$$\begin{aligned} \ell(A, \Psi) &= \log \left[\prod_{i=1}^N (2\pi)^{-p/2} |\Sigma|^{-1/2} \exp \left\{ -\frac{1}{2} x_i^T \Sigma^{-1} x_i \right\} \right] \\ &= c - \frac{N}{2} \log |\Sigma| - \frac{N}{2} \text{tr} (C_x \Sigma^{-1}) \end{aligned}$$

where c is a constant which is independent of the other parameters. The EM algorithm maximizes ℓ by iterating through two steps: In the so called E-step, $E[s|x]$ and $E[ss^T|x]$ are computed using current A and Ψ . A and Ψ are then updated using the newly computed $E[s|x]$ and $E[ss^T|x]$ in the so called M-step (for the details see, [3] and [8])

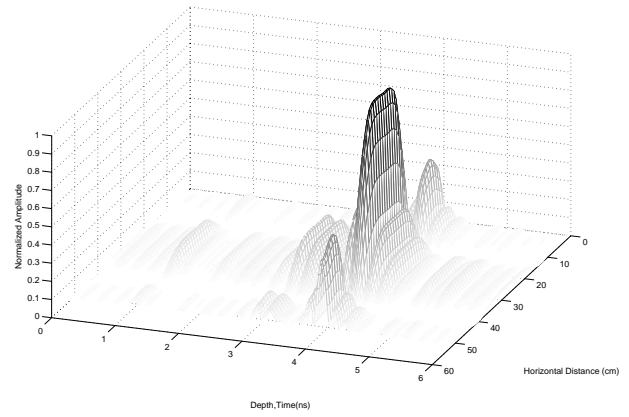


Fig. 3. The data after applying the factor analysis

IV. PRINCIPAL COMPONENT ANALYSIS

A central problem in signal processing is to find a suitable representation of the data, using a suitable transformation. In most cases, the representation is sought as a linear transform of the observed variables.

$$Y = A^T X,$$

where X and Y are $m \times n$ matrices related by linear transformation A . The purpose of principal component analysis is to derive a relatively small number of decorrelated linear combination (principal component) of a set of random zero-mean variables while retaining as much of the information from the original variables as possible [2]. The basic idea in PCA is to find the rows of the $Y_1^T, Y_2^T, \dots, Y_m^T$. PCA assumes that A is an orthonormal matrix ($A_i^T \cdot A_j = \delta_{ij}$) such that the covariance matrix of Y (C_y) is diagonalized. In practice, the computation of A can be simply accomplished using the covariance matrix. Let X is the observed data after normalization to unity norm and subtracting the grand mean. The covariance matrix (C_x) reads then

$$C_x = \frac{1}{n} \sum_{i=1}^n X_i X_i^T = \frac{1}{n} X X^T$$

The eigenvector and eigenvalue matrices of (C_x) Φ and Λ , respectively, are computed as:

$$C_x \Phi = \Phi \Lambda,$$

where $\Lambda = \text{diag}(\lambda_1, \lambda_2, \dots, \lambda_n)$, and $\lambda_1, \lambda_2, \dots, \lambda_n$ are the eigenvalues. If one assumes that eigenvalues are sorted in a decreasing order, $\lambda_1 \geq \lambda_2 \geq \dots \geq \lambda_n$, then the n leading eigenvectors matrix A is given by

$$A = [\Phi_1, \Phi_2, \dots, \Phi_n]$$

In the application of landmine detection using GPR signals, the PCA can be used to detect landmines and reduce the noise. This is done by selecting some components that mainly carry mine information, say A_k which the rest represent the clutter.

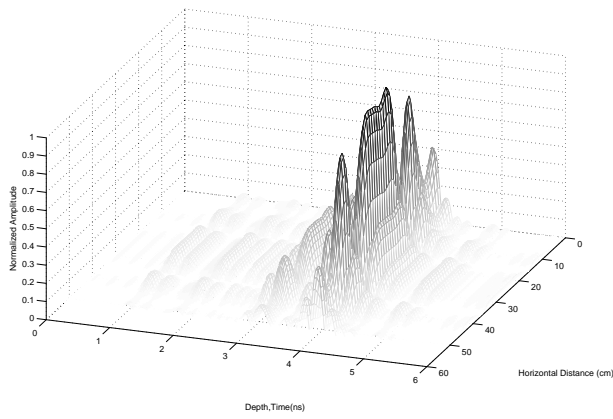


Fig. 4. The data after applying the principal component analysis

The reconstructed clutter-free signal space can be extracted from the original GPR entire signal space according to

$$S = A_k^T X$$

We select the matrix A to be a matrix whose rows A_k are the eigenvectors of XX^T (the principal components of X). Computing PCA of a data set X entails (1) subtracting the mean of each measurement type and (2) computing the eigenvectors of XX^T [9].

V. RECEIVER OPERATING CHARACTERISTIC (ROC)

As a performance measure of the reduction of clutter the area under the ROC curve is used. In general, the ROC curve shows the performance of a particular detector or classifier. However, in this paper the ROC curve is considered a measure on the clutter reduction, i.e., the signal-to-clutter ratio. The ROC curve is shown in Fig. 5, and the area under the ROC curves is calculated (0.64 for raw data, 0.72 for factor analysis and 0.67 for principle component). The ROC curve is thus looked at as a measure on how good the selected landmine signals are separated from the clutter, rather than a measure in general on classification or detection.

VI. CONCLUSION

The present work deals with the problem of detecting buried landmine using ground penetrating radar. In this paper, two different signal processing techniques for reducing clutter in GPR data have been presented. There are the factor analysis (FA) and principle component analysis (PCA). From Figs. 3,4 and the ROC curve (Fig.5), the FA showed significant improvement over PC. In all measurements, and in both techniques, the reflection from the surface has been removed or has been at least reduced.

REFERENCES

[1] H. Attias, *Independent factor analysis*, Neural Computation, vol. 11, no. 4, pp. 803-851, 1999.

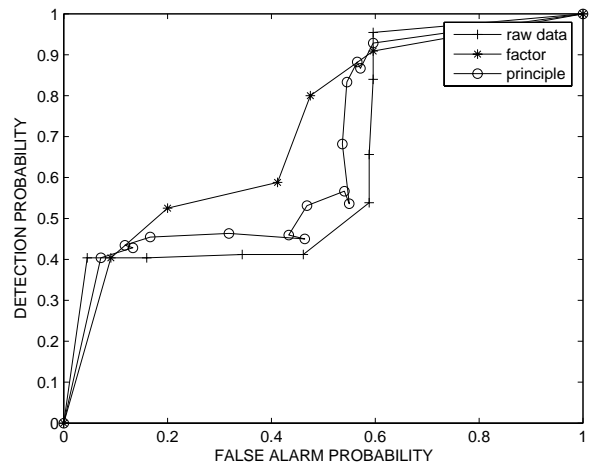


Fig. 5. ROC curves, Three ROC curves, the first curve is raw data, which is from real data (Fig. 1). The second curve is ROC after PC, and the third is ROC after applied FA.

[2] Andrzej Cichocki, Shun-ichi Amari, *Adaptive Blind Signal and Image Processing: Learning Algorithms and Applications*, John Wiley & Sons, Inc., New York, NY, 2002.

[3] F. B. Nielsen, *Variational Approach to Factor Analysis and Related Models*, master thesis, Technical University of Denmark, DTU, 2004.

[4] V. I. Koshelev, Y. I. Buyanov, Y. A. Andreev, V. V. Plisko and K. N. Sukhushin, 2001. *Ultrawideband radiators of high-power pulses*. Proc. IEEE Pulsed Power Plasma Science Conf., 2001, v. 2, p. 1661-1664.

[5] R. Reymont and K. G. Jreskog, *Applied Factor Analysis in the Natural Sciences* NY: Cambridge University Press 1993.

[6] D. Rubin and D. Thayer, *Em algorithms for ML factor analysis*, Psychometrika, 47(1):69-76, 1982.

[7] Z. Ghahramani and G. Hinton, *The em algorithm for mixtures of factor analyzers*, Technical Report CRG-TR-96-1, University of Toronto, 1997.

[8] L. Saul and M. Rahim, *Maximum likelihood and minimum classification error factor analysis for automatic speech recognition*, IEEE Transactions on Speech and Audio Processing, 8(2):115-125, 1999.

[9] J. Shlens *A Tutorial on Principal Component Analysis: Derivation, Discussion and Singular Value Decomposition*, 2001. www.sn1.salk.edu/shlens/pub/notes/pca.pdf

Compact Setup for an Homogeneous Plane-Wave Exposure for *In-Vivo* Experiments

S. Tejero, S. Schelkshorn, J. Detlefsen

Technische Universität München, Institute for Highfrequency Engineering
80290 München, Germany
+49 89 28923395, simon.tejero@tum.de

Abstract—This article describes a compact concept for the homogeneous electromagnetic exposure of a high number of living rats. The setup is intended for a controlled, long-term and continuous exposition (20 Months, 24 h/day) with standard GSM and UMTS signals, at 900 MHz and 1966 MHz, respectively. A minimum of 100 rats per setup can be exposed simultaneously. The continuous, long-term and *in-vivo* nature of the exposure imposes air-conditioning and access to the cages for the daily animal care. The animals will be exposed to a linear polarized plane wave. Of course, the local variations of the exposure dose must be kept as small as possible. These conditions are fulfilled by the exposure system presented here, which is based on a mass-production parabolic reflector. Although the setup is designed for GSM and UMTS bands, the concept can be applied to any other frequency as well.

Measurements show a total variation of the exposure dose due to setup-conditioned causes of max. 30%. Simulations show variations in the order of 50% due to the free-movement and change of attitude of the animals.

I. INTRODUCTION

Together with the great expansion of mobile communications in the last years, the public concern about possible negative effects of these systems on human beings has grown. Several groups are investigating on possible effects on RF exposed living creatures. In order to be able to compare experiments carried out anywhere, it is of capital importance to expose the animals under reproducible and standard conditions. The plane-wave RF exposure condition has been chosen as it is the most used and a well defined exposure condition for RF experiments at mobile communication bands [1], [2]. Three chambers are required: GSM-, UMTS- and sham-exposure, with high isolation between them. A minimum of 100 rats per setup should be exposed simultaneously to provide sufficient statistical support for the biological experiments. Other requirements are imposed by the continuous, long-term and *in vivo* nature of the exposure: the chambers must be air-conditioned and the access to the cages must be assured for the daily animal care. The animals will be exposed to a linear polarized plane wave. Of course, the local variations of the exposure dose must be kept as small as possible. These conditions are fulfilled by the exposure system presented here. Although the setup is designed for GSM and UMTS bands, the concept can be applied to any other frequency as well.

TABLE I
EXPOSURE SETUP REQUISITES

Controlled linear polarized plane wave exposure
Identical construction of three setups: GSM at 900 MHz, UMTS at 1966 MHz and sham
Appropriate conditions for animal well-being and animal care
Exposition of a high number of animals (> 100) simultaneously
Low-cost setup with standard components

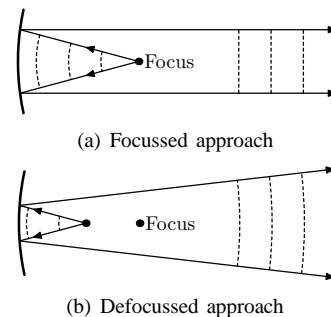


Fig. 1. Waves reflected by a parabolic reflector

II. EXPOSURE CONCEPT

The setup presented in this document is in analogy to the “compact range” concept (e. g. [3]), which is used in antenna measurement facilities to obtain a plane wave at relative short ranges. A parabolic reflector is used to convert a spherical wavefront emanating from the focus of the paraboloid into a plane wave. The reduced error requirements for exposition in comparison to antenna measurements allow us to use a standard reflector instead of a high-precision one. The selected reflector has a diameter of 320 cm and a focal distance of 112 cm and is a low-cost mass-product.

Due to the low focal distance-to-diameter ratio, it is rather difficult to achieve a uniform illumination across the reflector’s surface when illuminating from the focus. The required beamwidth for the primary feed would be 142°. In this approach, this problem is overcome by moving the exposure zone away from the focal plane and axially defocussing the feed by placing it closer to the reflector.

As shown in fig. 1 in the defocussed approach, the reflected wave shows spherical wavefronts with a slight curvature—it can be considered as quasi-plane wave within the volume

of a cage—and also an increase of the usable volume of the reflected beam. The defocussing together with the placement of the exposure zone far enough from the reflector are used to reduce the primary source’s beamwidth requirements. This is of benefit also for the minimization of the diffraction effects caused by the reflector rims, which are illuminated with less intensity. In addition, if the exposure zone is moved away from the primary feed, the influence of its backward radiated and its near field becomes smaller, as it decreases with the square of the distance.

As primary feed an open waveguide operating in the fundamental mode TE_{10} has been used due to its wide beamwidth and its relative simplicity. The waveguide is fed by a monopole and, to reduce the backward radiated field, a conducting plane surrounds the aperture. The dimensions of the aperture are $20 \times 10\text{cm}^2$ for the GSM setup and $9.5 \times 5\text{cm}^2$ for the UMTS one.

The optimum defocussing distance has been selected based on simulations. The electric field in a cylindrical exposure volume, with space for 40 cages, was obtained for different defocussing distances d_z . The distance which led to minimum relative deviation of $|\vec{E}|$ was chosen, $d_z = -48\text{ cm}$ for the GSM setup and $d_z = -60\text{ cm}$ for the UMTS setup.

Figure 2 shows the final exposure setup. It is placed in a metallic shielded chamber to avoid external influences and to decouple the different exposed groups. The inner walls are covered with absorber material to avoid uncontrolled reflection of the waves propagating in the chamber. The animals are inside polysulfone cages with a size of $(H \times W \times L)$ $24 \times 28.5 \times 42.5\text{ cm}^3$. The cages are placed on wooden slats with the cage frontal looking towards the reflector.

III. EXPOSURE FIELD CHARACTERIZATION

Three exposure chambers have been built. Due to the closed metallic construction a high electromagnetic shielding over 100 dB is achieved.

For the exposure setup assessment, the electromagnetic field in the exposure volume has been simulated and also a measurement campaign to validate the simulations and to characterize the influence of the neighbor animals was carried out.

A. Field simulation

The exposure setup model shown in fig. 3 has been simulated using the *Method of Moments* (MoM).

Simulations show that the plane wave condition has been fulfilled with a phase deviation from the plane wave in the volume of a cage of max. 12° . The standard deviation of the power density \mathcal{P} within the whole exposure volume—with room for 40 cages—is 14.9% for the GSM setup and 15.5% for the UMTS one.

Field simulations have also been used to assess the scattering effects due to the cages and wooden shelves. In a volume of a cage the maximum absolute value deviation from the mean was 25% and the standard deviation from the mean power 10%.

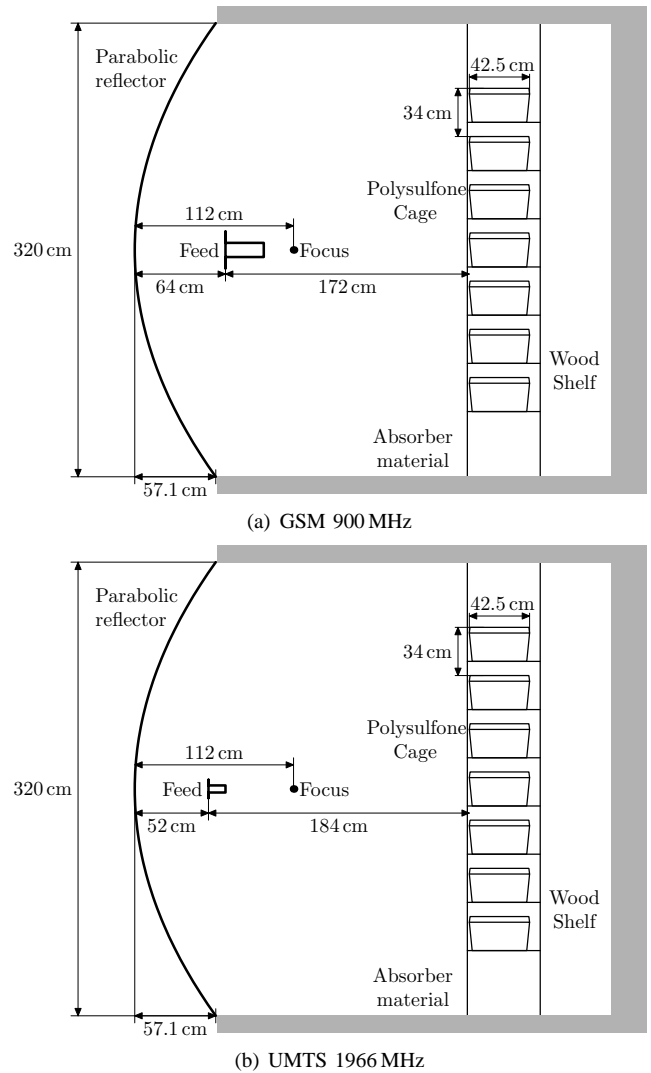


Fig. 2. Exposure setups

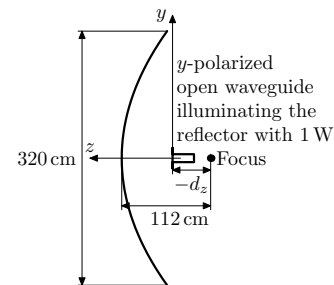


Fig. 3. Simulation model of the setup. The final defocussing distances are: $d_z = -48\text{ cm}$ for GSM and $d_z = -60\text{ cm}$ for UMTS

TABLE II

POWER DENSITY MEASUREMENTS WITHOUT ANIMALS IN THE CHAMBER
NORMALIZED TO $P_{\text{feed}} = 1$ W. RESULTS ARE GIVEN FOR THE BEST
40 CAGE POSITIONS

Parameter	GSM Setup	UMTS Setup
Frequency	900 MHz	1966 MHz
$ \vec{E} $ mean value	7.8 V/m	8.2 V/m
\mathcal{P} standard deviation	14%	27%

B. Field distribution measurement

For the field measurement campaign open waveguides operating in the fundamental mode TE_{10} have been used to measure the local field intensity. The dimensions of the apertures were $20 \times 10 \text{ cm}^2$ for the 900 MHz antenna and $8.6 \times 4.3 \text{ cm}^2$ for the 1966 MHz one. The receiving apertures of course have an integration effect with respect to the local field distribution. The dimensions were chosen to be comparable to the size of the animals and thus the measured results are expected to be in accordance with the total animal exposure. Two different measurements were carried out: without animals in the chamber to characterize the power density coming from the reflector and with animals in cages surrounding the measuring antenna to characterize the power density coming from the neighbor rats.

For the measurement without animals the antennas were placed at each possible cage position in the wooden shelf, with its aperture aligned to the front of the shelf and pointing to the reflector. The standard deviation of the measured power density for the best 40 cage positions—those with higher exposure levels—was 14% for the GSM setup and 27% for the UMTS setup.

For the measurements with animals, full populated cages were placed surrounding the antenna. Three different measurements were carried out: with the antenna pointing to the reflector, to the cage at his left side and to the one at his right side. Long-term measurements were carried out. Mean values for measurements with and without animals for the “front” antenna orientation are coincident. The total standard deviation in the exposure dose due to the presence of the animals has been calculated as

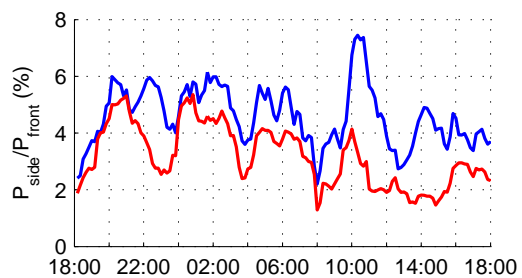
$$\sqrt{\sigma_{\text{front}}^2 + \sigma_{\text{left}}^2 + \sigma_{\text{right}}^2} \quad (1)$$

and resulted in 7% for GSM and 4% for UMTS.

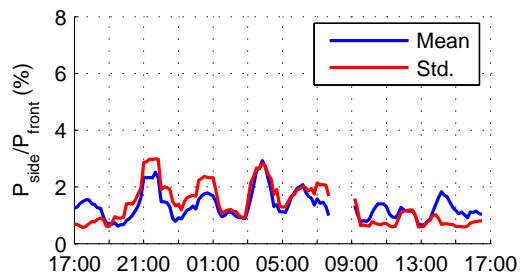
IV. SAR SIMULATION

The standard exposure measure is the *Specific Absorption Rate* (SAR). The exposure rate on the rats should be 0.4 W/kg *Whole Body SAR* (WB-SAR), i.e. the SAR averaged over the whole body. The relation between the measured power density and the WB-SAR in the rats is obtained by means of simulations using the *Finite Integrations Technique* (FIT).

Based on three voxel models of Sprague-Dawley rats—model identical to Wistar rats for SAR simulation purposes—several rat scenarios with different arrangement of the animals



(a) GSM setup



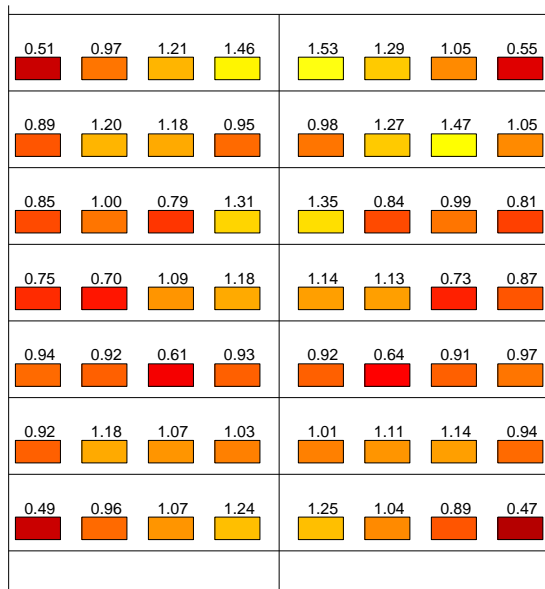
(b) UMTS setup

Fig. 5. Measured power density with full populated cages surrounding the measured position. Antennas pointing to a cage at their side. Statistics obtained with data acquired within 1 hour measured every 1 s. Results normalized to the mean value of the “front” measurement, i.e. measurements with the antenna pointing to the reflector.

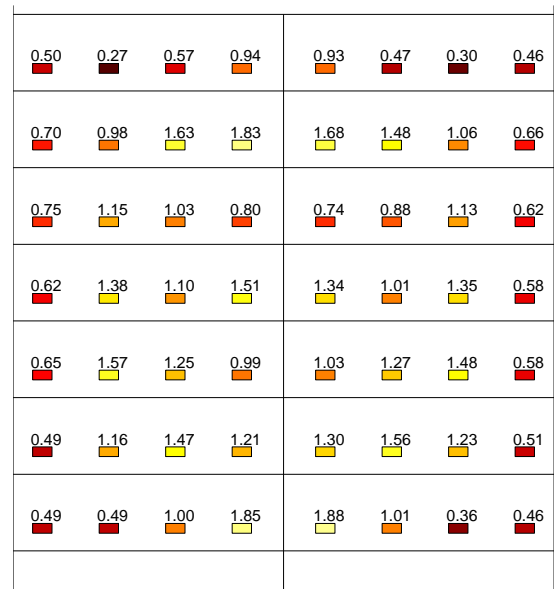
have been created: one male rat (370 g), one female rat (275 g), one baby rat (15 g), four scenarios with three female rats, two scenarios with two male rats and two scenarios with one female rat and eight baby rats. Each scenario has been simulated with a plane wave coming from the three main axes at 900 MHz and 1966 MHz, i.e. six times. The WB-SAR results have been analyzed and are summarized in table III. It can be noted that the variation in the WB-SAR under ideal exposure conditions is 45%. The variation in scenarios with only one adult animal is 50% and 26% for 900 MHz and 1966 MHz, respectively. It can be concluded, that the main factor of WB-SAR variation in the rats is due to the free movement of the animals in the exposed cage, which is an indispensable requirement for continuous, long-term, *in-vivo* experiments.

V. SUMMARY AND CONCLUSIONS

The exposure concept based on a defocussed parabolic reflector results in a low-cost and energy efficient exposure setup. A high number of rats (40 cages) can be exposed simultaneously with quasi-plane wave condition and high homogeneity. The conditions for the animal well-being and care are fulfilled, i.e. the concept is applicable for long-term *in-vivo* exposition. The use of a mass production reflector reduces the cost considerably. Shielding measurements show a high isolation from external fields and between the exposed groups. Possible variations in the exposure dose have been



(a) GSM setup



(b) UMTS setup

Fig. 4. Measured power density normalized to the global mean value at each cage position in the wooden shelf

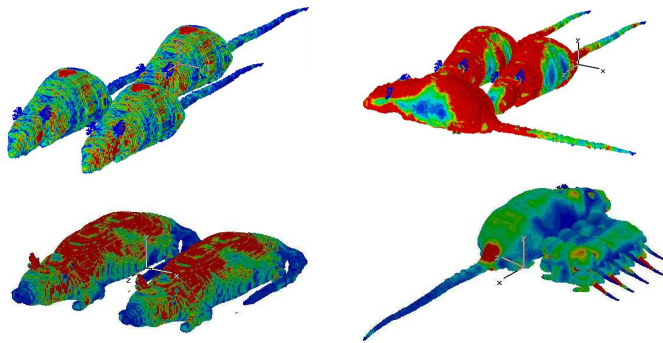


Fig. 6. Example of simulated multi-rat scenarios

TABLE III

WB-SAR SIMULATION RESULTS. STATISTICS OF THE FOUR THREE-FEMALE AND TWO TWO-MALE RAT SCENARIOS (48 CASES PER FREQUENCY)

Parameter	900 MHz	1966 MHz
WB-SAR Mean value for $ \vec{E} = 1 \text{ V/m}$	$3.82 \cdot 10^{-5} \text{ W/Kg}$	$3.68 \cdot 10^{-5} \text{ W/Kg}$
Standard deviation	41%	45%
Required $ \vec{E} $ for WB - SAR = 0.4 W/Kg	102 V/m	104 V/m
Required input Power [†] for WB - SAR = 0.4 W/Kg	172 W	161 W
SAR efficiency	$0.0023 \text{ W} \cdot \text{Kg}^{-1} / \text{W}$	$0.0025 \text{ W} \cdot \text{Kg}^{-1} / \text{W}$

[†]Ratio input power P_{in} to mean $|\vec{E}|$ from table IITABLE IV
VARIATION OF THE WB-SAR

Origin	GSM Band	UMTS Band
Cage position in the chamber	14%	27%
Animals in the neighborhood	7%	4%
Size and change in attitude of the animals in the cage	> 42%	> 45%

characterized by means of measurements and simulations. The power density coming from the reflector and scattered at the neighbor cages have been measured separately. Several simulations have been carried out to characterize the WB-SAR in different multi-rat scenarios. The standard deviation of the WB-SAR in the rats is mainly due to the changes in size, attitude of the rats and by their free movement in the exposed cage, which is an indispensable requirement for continuous, long-term, *in-vivo* experiments.

ACKNOWLEDGMENT

The authors thank the Bundesamt für Strahlenschutz (BFS) for supporting this work.

REFERENCES

- [1] V. W. Hansen, A. K. Bitz, and J. R. Streckert, "RF exposure of biological systems in radial waveguides," *IEEE Transactions on Electromagnetic Compatibility*, vol. 41, no. 4, pp. 487–493, November 1999.
- [2] Q. Balzano, C.-K. Chou, R. Cicchetti, A. Faraone, and R. Y.-S. Tay, "An efficient RF exposure system with precise whole-body average SAR determination for *in vivo* animal studies at 900 mhz," *IEEE Transactions on Microwave Theory and Techniques*, vol. 48, no. 11, pp. 2040–2049, November 2000.
- [3] C. A. Balanis, *Antenna Theory Analysis and Design*, 2nd ed. New York: John Wiley & Sons, 1997.

Development on Ku-Band Feed Chains for Satellite Antennas

Christian Hartwanger¹, Ralf Gehring¹, UnPyo Hong¹, Helmut Wolf¹

¹EADS Astrium GmbH, D-81663 Munich (Germany), Email: christian.hartwanger@astrium.eads.net

Short Abstract—The payload of next generation multimedia telecommunication satellites demands on an increased number of communication channels and improved EIRP and G/T performance. Especially in Ku-band, the request for combined BSS/FSS Transmit / Receive antennas grows. The feed system is considered to be the key component of an antenna. EADS Astrium responds to the needs of the market regarding feed systems with two major developments under ESA contract.

Keywords: *Ku-band; Feed Chain; OMT; Horn; High Power; Wide Band;*

I. INTRODUCTION

The payload of next generation multimedia telecommunication satellites demands on an increased number of communication channels and improved EIRP and G/T performance. Especially in Ku-band the request for a combined BSS (Broadcast Satellite Services) / FSS (Fixed Satellite Services) Tx (Transmit) / Rx (Receive) feed chain grows. Therewith, the Tx and Rx functions for the FSS and BSS services could be combined in a single dual polarized antenna. Thus the mass and space required for the individual top floor Rx antenna can be saved and allows for the accommodation of additional antennas and services.

Consequently the overall frequency band, the numbers of channels and the RF power per channel to be operated by the antennas will considerably increase. Therefore the requirements on the linearity have to be further improved, compared to state of the art systems, in order to avoid the generation of Passive Intermodulation Products (PIMP). For an effective re-use of the frequency bands it is obvious to use both polarizations for the individual channels with an excellent polarization decoupling. These major requirements are mainly influenced by the feed systems of the antennas. A thorough and mature design of the feed systems is a key factor for a successful antenna design. EADS Astrium responds to the needs of the market regarding feed systems with two major developments under ESA contract.

Benefiting from past feed product developments and extensive heritage, an innovative High Power Ku-band Feed Chain (HPFC) [1] was developed and qualified for space applications. Based on those results, an enhancement regarding the band width of the feed chain is currently under development (concluded 2006).

This article summarizes the performance of the High Power Ku-band Feed Chain Engineering Qualification Model (EQM)

and the RF performance of the Wide Ku-band Feed Chain Bread Board Model (BBM).

The main foci for the development of the High Power Feed Chain were:

- Significantly higher multipacting threshold,
- Combined Tx/Rx operation with reduced PIM risk,
- Improved thermal performance,
- Remain excellent RF performance, compared to state of the art feed chains.

While the High Power Ku-band Feed Chain covers the frequency band from 10.7GHz to 14.5GHz (FSS Tx/Rx and BSS Tx), the main focus of the wide band feed chain development is the extension to the frequencies 17.2GHz – 18.4GHz (BSS Rx). The success of this enormous enhancement could not be presumed, hence, the development was split into two phases. During the current finalized first phase the feasibility of a wide Ku-band feed chain has been demonstrated based on BBM measurements. For phase two a detailed design update will be performed and an EQM will be manufactured and fully RF qualified.

Both feed chains consist of:

- A conical horn;
- A circular to square wave guide transition;
- An Orthomode Transducer (OMT).

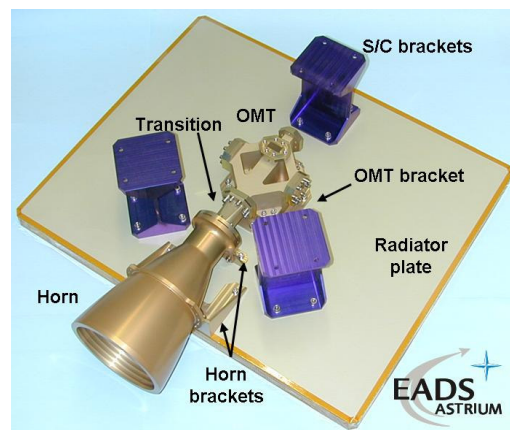


Figure 1. EQM High Power Feed Chain assembly.

See for example the yellow chromated EQM of the High Power Feed Chain in Fig. 1. The feed chain is mounted on an aluminium honeycomb structure, which radiates the temperature resulting in cause of power dissipation. Via three titanium brackets, the plate is mounted on a space craft.

A typical application for both feed chains as source in a Gregorian satellite antenna is illustrated in Fig. 2. Just as well, the feed chains can be utilized in a single offset reflector antenna.

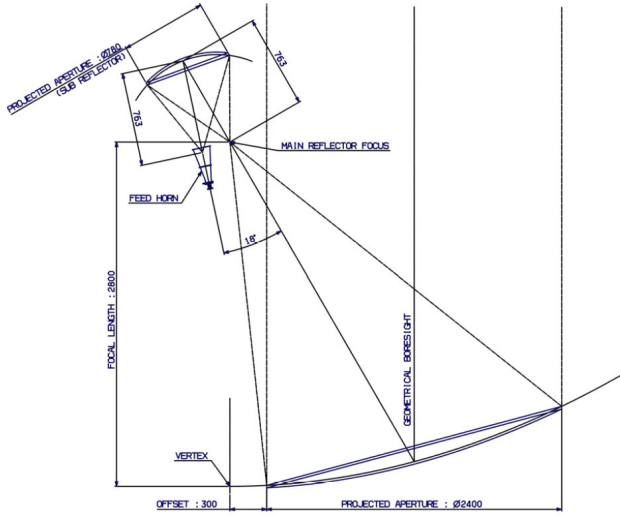


Figure 2. Typical antenna geometry for the feed chain.

II. HIGH POWER KU-BAND FEED CHAIN

A. General RF- Specifications of the High Power Ku-Band Feed Chain

The specifications are derived from the requirements of past and planned Ku-band missions to ensure that the needs for future applications will be covered. The relevant RF specifications are summarized in Table I.

TABLE I. RF-SPECIFICATION OF HIGH POWER KU-BAND FEED CHAIN

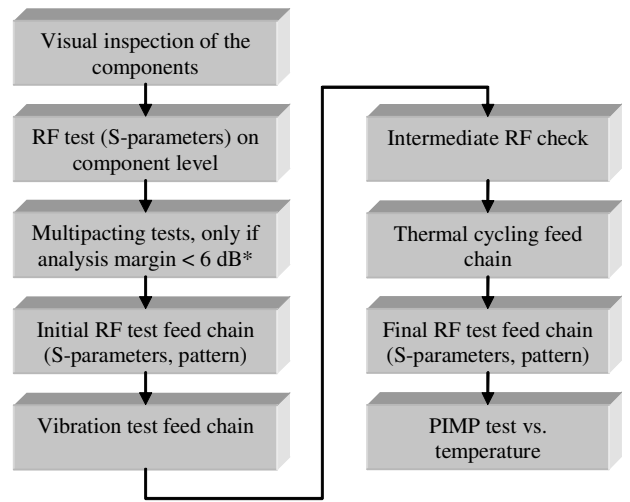
Item	Specification
Operating frequency	10.70-13.20 GHz (Transmit) 13.70-14.50 GHz (Receive)
Polarisation	Dual linear
Power handling	24x110 Watt carriers per polarisation
3rd order PIMP	< -135 dBm with 2x110W carriers over Temperature (-135° C to +135° C)
Return loss	< -23 dB
Maximum Cross-polar Peak	< -43 dB
Insertion loss	< 0.12 dB

The mechanical requirements are derived from an internal EADS Astrium document describing the Design, Interface, Construction and Test Requirements for Antennas on Eurostar 3000 Spacecraft.

Based on the requirements from previous commercial Ku-band projects the temperature range for qualification of the Ku-band feed chain shall be -150° C to +146° C.

B. EQM Qualification Tests

To qualify the High Power Feed Chain to EQM-status, a special test philosophy is necessary. The test flow is shown in Fig. 3.



* Due to the high number of channels it is permitted to use the "20 gap crossing rule"

Figure 3. Test flow for qualification tests.

After an initial visual inspection of the feed chain, the S-parameters are measured on component level. When the components are integrated to the feed chain, a multipaction test has to be done, if the analysis margin is lower the 6dB. An initial RF test is performed to verify the feed design and to have a data base to which the results can be compared after the environmental tests. The intermediate RF check is an S-parameter measurement to be sure that the hardware did not change during vibration test. After the thermal cycling test, a final RF measurement is made and the results are compared to the initial test. The EQM qualification ends with a thermal PIMP test. This proceeding guarentees a proper workmanship.

C. EQM Qualification Test Results of High Power Ku-Band Feed Chain

According to the test flow (Fig. 3), all tests have been performed for the High Power Ku-band Feed Chain.

Fig. 4 shows the measured return loss of the feed chain for both polarizations. The specification of -23dB is fulfilled with margin.

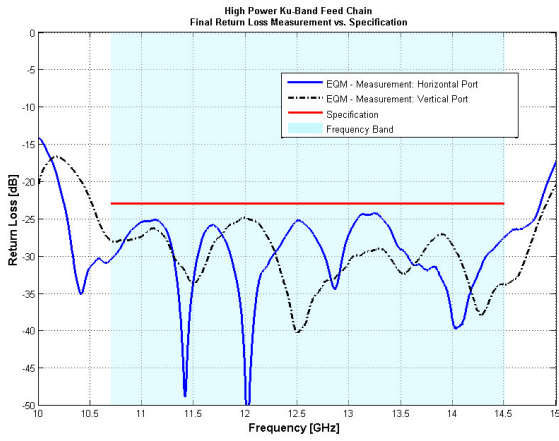


Figure 4. EQM feed chain – Final measured return loss of the horizontal and vertical port.

A picture of the HPFC installed in the feed chamber for pattern measurement is shown in Fig. 5.

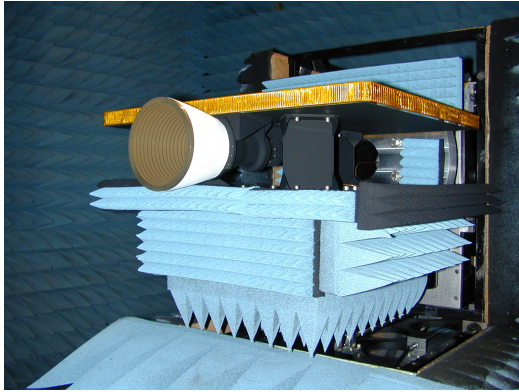


Figure 5. EQM feed chain in feed chamber.

A result of the pattern measurement is illustrated in Fig. 6. As well as the measured co polar pattern, the measured cross polar coincides with the predicted values.

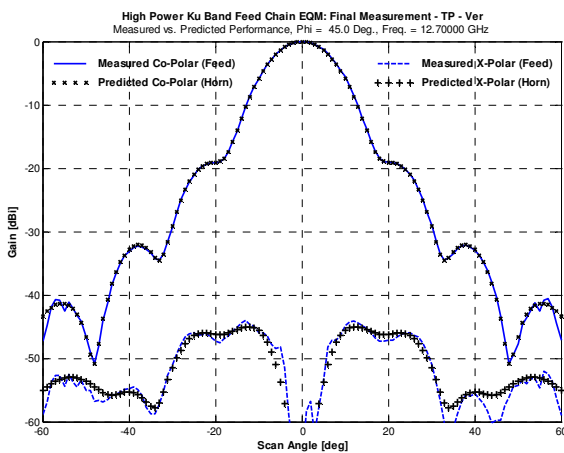


Figure 6. Pattern Measurement at 12.7GHz (Vertical port).

The structural analyses of the feed chain assembly were done using NASTRAN and the pre- and post processor PATRAN. Static and dynamic analyses were performed to verify the overall strength and integrity. The test predictions based on a sine response analysis with 1g input up to 2000Hz were carried out for several accelerometer positions and for the main interface loads.

Fig. 7 shows an example for the results of stress and strength analysis for the horn and the OMT.

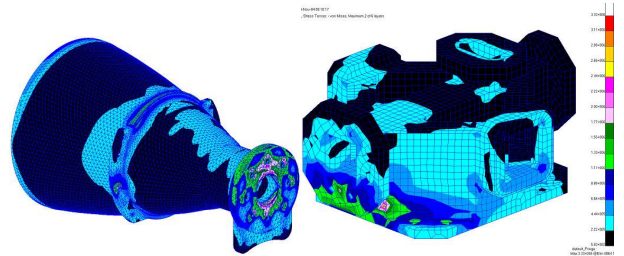


Figure 7. Stress plot with maximum stress at the horn (left) and the Orthomode Transducer (right)

A picture of the HPFC on the shaker for vibration test is shown in Fig. 8.

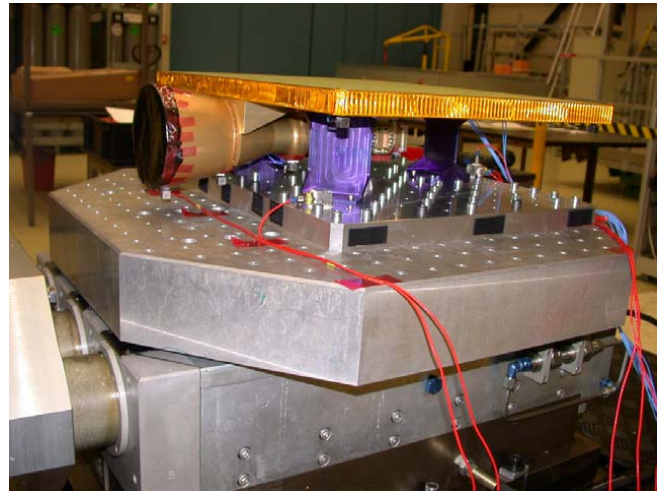


Figure 8. EQM feed chain on shaker for vibration test.

In Table II the analysed worst case multipacting performance for the yellow chromated horn and the OMT is summarized. The MP margins are calculated in comparison to the standard wave guide R 120.

TABLE II. MP ANALYSIS RESULTS FOR THE HIGH POWER FEED CHAIN FOR 2 X 24 CARRIERS, 110 W PER CARRIER.

	Margin N^2P -rule [dB]	Margin P_{20} [dB]
WG R 120	-0.8	13.0
OMT	-2.4	10.8
Horn	3.4	17.2

Because the margin of the analyzed multipaction threshold is larger 6dB, a multipaction test was not required.

A thermal PIM test has been performed over a thermal cycle between +135°C and -135 °C. Two 120 Watt carriers at 11.0 GHz and 12.5 GHz respectively were applied to the feed. A sketch of the set up is shown in Fig. 9. The PIMP was measured at 14.00GHz. Temperature was controlled by thermocouples attached to the OMT, transition and horn. A PIM level of -120 dBm could be demonstrated based on a limited available test setup performance of -123 dBm.

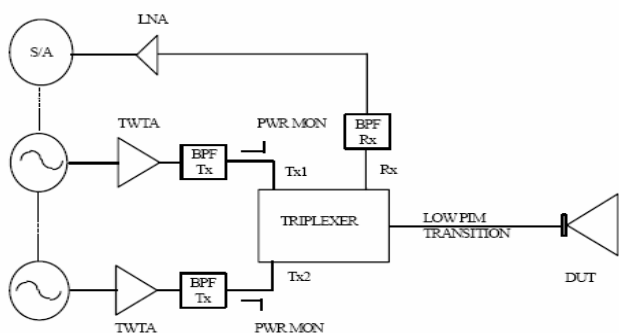


Figure 9. PIM test configuration

The losses of the OMT including transition were measured to be less than 0.07dB. Together with a conservative assessment of the horn losses of 0.04dB, the requirement for the feed chain is fulfilled.

All tests were performed successfully which leads to an EQM qualification of the High Power Ku-Band feed chain.

III. WIDE KU-BAND FEED CHAIN

As a consequent enhancement of the High Power Ku-band Feed Chain, a Wide Ku-band Feed Chain is currently under development in EADS Astrium. In order to verify the design and to demonstrate the feasibility of such a component, a Bread Board Model was manufactured.

A. General RF-Specifications of the Wide Ku-Band Feed Chain

The specifications for the Wide Ku-band Feed Chain are given in TABLE III. As well as the specifications for the HPFC, they are based on customer requests.

The thermal and mechanical requirements and the principle thermal and structural design of the Wide Band Feed Chain are similar to the High Power Feed Chain. Therefore, an RF qualification of the Wide Ku-band Feed Chain is sufficient.

TABLE III. RF-SPECIFICATION OF WIDE KU-BAND FEED CHAIN

Item	Specification
Service frequency bands (BSS/FSS)	10.70-14.50 GHz 17.20-18.40 GHz
Polarisation	Dual linear
Power handling	20x110 Watt carriers per polarisation
3rd order PIMP	< -135 dBm with 2x110W carriers over Temperature (-135° C to +135° C)
Return loss	< -21 dB
Maximum Cross-polar	< -40 dB
Insertion loss	< 0.18 dB

B. Rf-Performance of BBm Wide Ku-Band Feed Chain

Due to the wide frequency band (10.7GHz - 18.4GHz), two RF interfaces (R 120 and R 140) were used for the scattering parameter measurements in order to achieve minimum measurement errors.

Fig 10. shows the result of the return loss measurement of the BBM Wide Band Feed Chain for the vertical polarization. The result for horizontal port also fulfills the requirement.

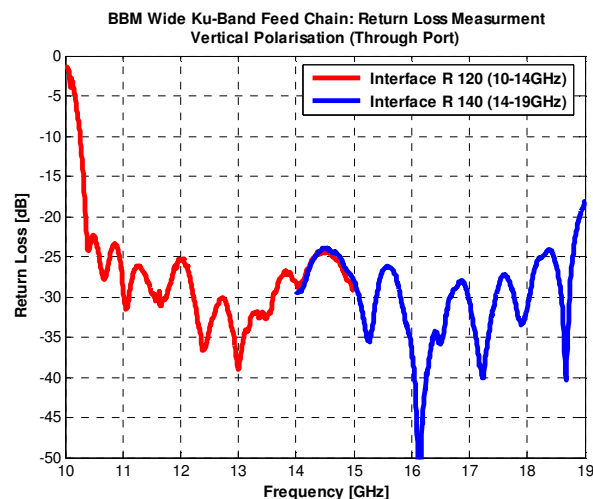


Figure 10. Wide Band BBM Feed Chain – Return loss: vertical polarization.

In Fig. 11, the measured isolation is recorded, which satisfies the requirement of 50dB with margin. A typical co and cross polar pattern cut is shown in Fig. 12. The pattern coincides with the prediction.

The multipaction analysis shows a worst case result of 8dB margin with respect to the 20 gap crossing rule. Hence, no multipaction test had to be performed. Compared to the High Power feed chain, only a slightly degradation of 2 dB can be observed.

The measured data demonstrate the feasibility of a dual polarized high performance feed chain covering the entire FSS/BSS frequency band from 10.7GHz to 18.4GHz.

IV. CONCLUSION

Two feed chains for Ku-Band have been presented.

A High Power Feed Chain for applications in Ku-band Satellite Communication Systems was developed and qualified to EQM-status at EADS Astrium GmbH. The RF design of this feed chain was optimized for high RF power applications, i.e. high multipaction threshold (closed to standard waveguide), low losses (less than 0.12 dB) and high linearity (3rd order PIM < -120 dBm, based on an available PIM setup validation of about -123 dBm), while maintaining excellent radiation characteristics. All scattering parameter requirements (return loss > 24 dB, port to port isolation > 58 dB) are fulfilled. The mechanical and thermal design of the feed chain allow for applications in single or dual offset reflector systems, accommodated either at the Earth faced panel or the side panels of a GEO positioned satellite.

Based on the design and results of the High Power Feed Chain, a design for a Wide Ku-Band Feed Chain was optimized and a BBM was built. The BBM was RF tested in order to demonstrate the feasibility of a wide band feed chain. The results are promising and therefore, following an update of the initial design, an EQM will be manufactured and RF qualified during 2006.

V. ACKNOWLEDGMENT

The above described hardware has been developed under ESTEC Contracts. EADS Astrium is grateful to ESA / ESTEC, especially to Arturo Martín Polegre and Luca Salghetti Drioli for the support of the development and qualification activities.

- [1] R. Gehring, C. Hartwanger, U. Hong, M. Schneider, H. Wolf, "Ku-Band High Power Feed Chain", Proc. 28th ESA Antenna Workshop on Space Antenna Systems and Technologies, ESTEC, Noordwijk, The Netherlands, 2005

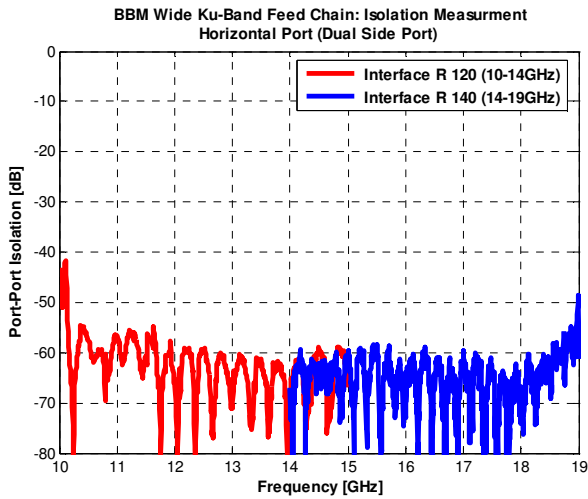


Figure 11. Wide Band BBM Feed Chain – Isolation measurement.

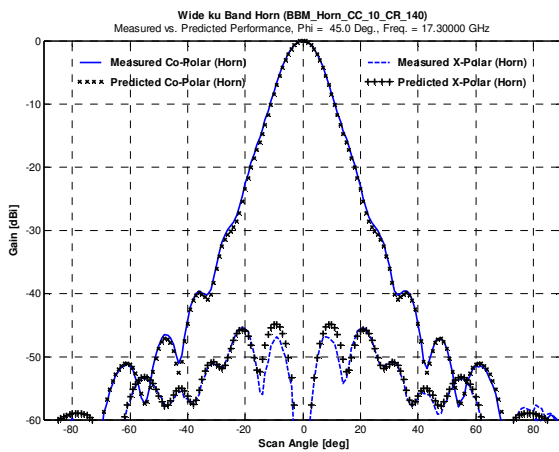


Figure 12. Wide Band BBM Feed Chain – Pattern measurement at 17.3GHz.

Spatial Resolution of Millimeter Wave Imaging at 75-100 GHz and 600 GHz

Hue Phat Tran, Frank Gumbmann, Jochen Weinzierl, Lorenz-Peter Schmidt

University of Erlangen-Nuremberg, Institute for Microwave Technology, (LHFT)
Cauerstr.9, 91058 Erlangen, Germany, Phone:(+49) 9131 8527236, Fax:(+49) 9131 8527212
phat@lhft.eei.uni-erlangen.de

Abstract—This paper presents results of two different imaging techniques using free space millimeter wave measurement setups at 75-100 GHz and 600 GHz. On the one hand focused transmission and reflection measurements at 75-100 GHz and on the other hand focused transmission measurements at 600 GHz have been investigated. In order to focus the beam of two conical horn antennas, dielectric lenses for the frequency range 75-100 GHz and elliptical metallic mirrors at 600 GHz have been used. The influence of wavelength and bandwidth on the spatial resolution of the millimeter wave image have been examined. For the evaluation of the image quality a suitable polyethylene step wedge has been chosen. The first part of the paper deals with focused measurements at 75-100 GHz using a vector network analyzer, in the second part the results of the scalar measurements at 600 GHz will be discussed.

I. INTRODUCTION

In recent years considerable progress in applying millimeter waves for non-destructive testing applications has been made. Due to the advantages regarding a good penetration of the electromagnetic waves into dielectric materials, the importance of microwave and millimeter wave non-destructive testing is rapidly growing.

There are various different methods for the measurement of material properties [1], [2]. They can be classified into two main groups:

- free space methods,
- waveguide methods employing coaxial lines, hollow waveguides and cavity resonators.

For imaging applications only free space methods are of interest. Free space methods can be divided in transmission and reflection setups. There are two possibilities of focusing: It can be accomplished in terms of hardware components (e.g. dielectric lenses, elliptical mirrors) or without specific focusing elements but in combination with signal processing algorithms like SAR (Synthetic Aperture Radar). This paper presents measurement results which have been achieved only by hardware focusing. In order to compare the capabilities of the measurement setups at different frequencies, the goal was to realize a minimum footprint of the Gaussian beam on the device under test (DUT) in each frequency range. Focusing elements like a combination of conical horn antennas and dielectric lenses as well as a combination of conical horn antennas and elliptical mirrors have been designed. The lenses were fabricated of high density polyethylene (HDPE) with low

dielectric losses. Due to the increasing loss of HDPE with increasing frequency, the performance of dielectric lenses in a measurement setup at 600 GHz degrades ($\tan\delta = 3.1 \cdot 10^{-4} - 6.3 \cdot 10^{-4}$ @ 160–970 GHz [3]). However they are well suited for the measurement setup at 75–100 GHz, especially because of the simple adjustment. Other disadvantages of a horn-lens combination are internal reflection losses between the horn antenna and the dielectric lens and additionally frequency dependent spherical aberrations. In contrast to dielectric lenses, elliptical mirrors show lower losses, but have to operate off axis. Therefore, distortion effects such as cross polarisation or higher order modes always appear. A detailed knowledge of all these effects has to be considered in the design of a free space measurement system [4], [5]. Additionally, the minimum achievable beam width, according to the Gaussian beam theory, depends on the wavelength and affects the spatial resolution of focused free space methods. A second difficulty when using focused measurement setups, is the finite depth of focus, which is again frequency dependent. Thereby the far-field divergence angle depends on the beam waist w_0 in the focal plane.

The goal of the investigation was to determine the influence of relevant parameters like wavelength, bandwidth, scalar or coherent measurement on the spatial resolution of a millimeter wave image. In addition it is to be clarified to what extent the described distortion effects affect the measurement results.

II. MEASUREMENT OBJECT

In order to determine and to compare the spatial resolution of the setups an adequate measurement object is needed. It is also interesting to examine the influence of the material properties and the geometry of the DUT on the received signal. In order to compare the results of the different measurement methods we used a step wedge made of polyethylene (PE) with several different step heights and hole diameters (Fig. 1). PE is a low loss dielectric material, which is often used for quasioptical components in the millimeter wave region [6]. Due to this property of the material, the determination of the step height is challenging because of the low attenuation contrast between the different steps. For this reason the PE step wedge can be used both for transmission and reflection measurements.

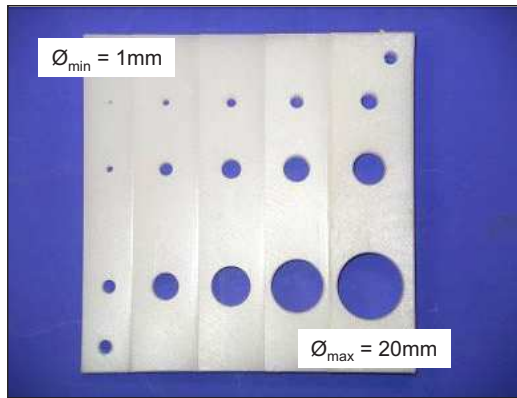


Fig. 1. PE step wedge with several different hole diameters; Height of steps: 6, 7, 8, 9, 10 mm

III. MEASUREMENT SETUP AT 75 – 100 GHz

Fig. 2 and 6 illustrate the principles of the quasi optical transmission and reflection measurement setups at 75 – 100 GHz. In both cases, the focus of the Gaussian beam was adjusted on the surface of the thickest step (right step in Fig. 1). In these measurement setups a pair of focusing horn-lens combinations is used, which are fed by means of flexible, dielectric rod waveguides [7] to a vector network analyzer (VNA). With the HP 8510XF VNA an accurate broadband and complex characterization in magnitude and phase can be accomplished. The horn-lens combination consists of a conical horn antenna and a spherical dielectric lens, which are mounted in a holder. The horn-lens combination focuses the electromagnetic plane wave at a focal distance of 5 cm. For precise measurements, we had to consider two distortion effects caused by multiple reflections: On the one hand at the transition between the dielectric rod and rectangular hollow waveguide and on the other hand at the transition between the conical horn antenna and the dielectric lens. Therefore an appropriate calibration technique had to be chosen. In the case of a reflection measurement a thru-calibration on a metal plate, which replaces the measurement object at the reference plane, has to be carried out. The transmission measurements were calibrated by placing the horn-lens antennas at a distance twice the focal distance of the lenses. The measured complex transmission coefficient S_{21} can be used to calculate the complex permittivity of the material [8], [9], [10].

A. Transmission Measurement

The focused transmission measurement setup is shown in Fig. 2. The transmitter and receiver antennas are facing each other at a distance of 10 cm. The measurement object is moved by a 2-axis stepper motor controlled fixture perpendicularly to the propagation direction of the gaussian beam. The waist radius of the beam in the focal plane is $w_0 = 3.34$ mm at 94 GHz. It is important to place the measurement object in the focal plane because the waist of the gaussian beam expands rapidly depending on the far-field divergence angle.

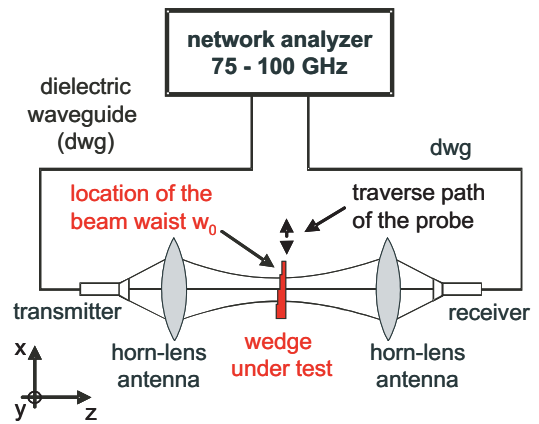


Fig. 2. Transmission measurement setup at 75 – 100 GHz

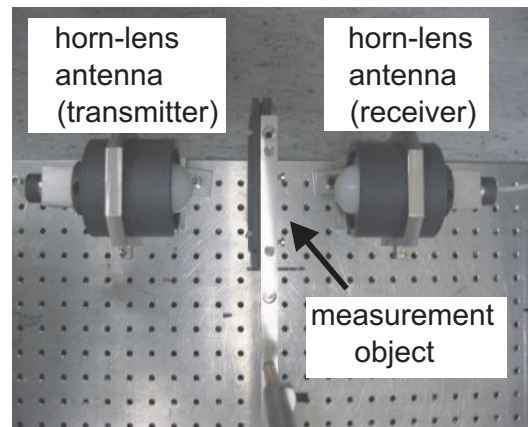


Fig. 3. Realization of the transmission measurement setup at 75 – 100 GHz

Fig. 4 shows the average of the measured magnitude over 201 frequencies. Averaging over several frequencies has the advantage of eliminating the influence of standing waves between the horn-lens antennas and the measurement object. The effect of noise in the image can be reduced as well. In addition the resulting millimeter wave image gets smoother. As expected, there is only a low attenuation contrast between each step of the PE wedge. Therefore the steps and drill holes are only visible because of diffraction at the edges. It is also observable that the diffraction effects increase and the spatial resolution decreases at every step from the right to the left in Fig. 4. This is because of an expanding beam waist outside the focal plane whereas the right step was placed within this plane. A spatial resolution of $\delta_{x,y} \geq 3$ mm is achievable with this measurement setup.

A coherent measurement setup allows to determine the phase of the received signal. In Fig. 5 the signal phase at 87.5 GHz is plotted. Regarding the phase information, the steps can clearly be separated because of different signal delay times at different step heights. The phase information at a single frequency is ambiguous because the signal delays may be caused by different step heights or changing material properties.

As a benefit of the broadband measurement technique it

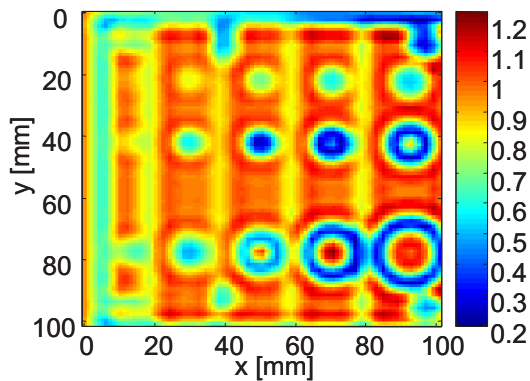


Fig. 4. Average of the magnitude [lin.] of the transmission coefficient over 201 frequency points (75 – 100 GHz)

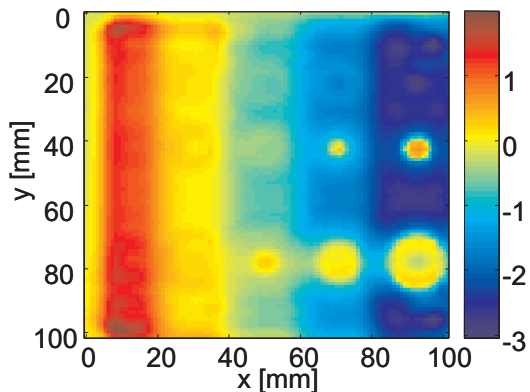


Fig. 5. Phase [rad] of the transmission coefficient at 87.5 GHz

is possible to apply several signal processing tools to the complex (magnitude and phase) measurement data. With these tools it is possible to evaluate the signal delays of the received measurement signals and an range and depth profile of the measurement object can be determined.

In section V a new approach based on such signal processing methods will be presented.

B. Reflection Measurement

Fig. 6 and 7 show the setup of the reflection measurements at 75 – 100 GHz.

Due to the fact that the footprints of the transmitter and receiver horn-lens antennas have to be focused at the same location, the antennas had to be tilted about 30 degrees towards the measurement object. This results in an elliptical spot and a bigger illumination area in its focal plane in the horizontal axis. This leads to more distinct diffraction effects at edges and finally results in a lower spatial resolution.

The steps and drill holes are also visible in Fig. 8 because of diffraction at the step edges. On the contrary to Fig. 4 these effects are more distinct because of the elliptical spot in the measurement plane.

This decreased the horizontal spatial resolution to $\delta_x \geq 8$ mm.

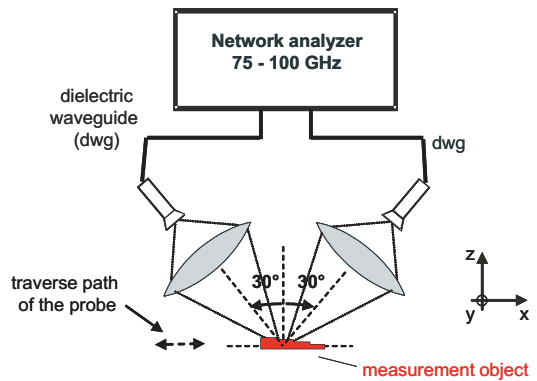


Fig. 6. Reflection measurement setup at 75 – 100 GHz

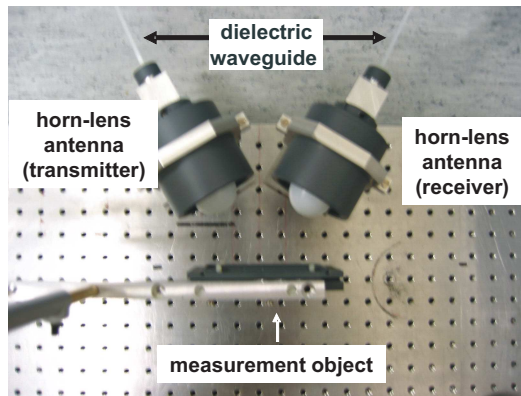


Fig. 7. Realization of the reflection measurement setup at 75 – 100 GHz

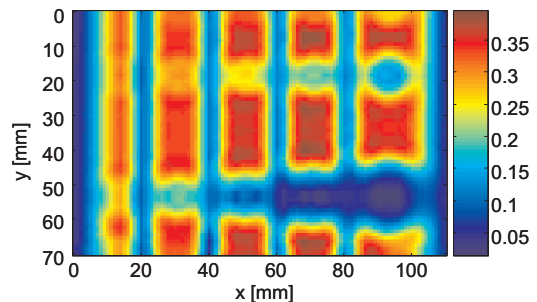


Fig. 8. Average of the magnitude [lin.] of the reflection coefficient over 201 frequency points (75 – 100 GHz)

IV. MEASUREMENT SETUP AT 600 GHz

Fig. 9 and 10 show the setup for the measurements at 600 GHz. The system consists of a heterodyne receiver with scalar signal detection.

A BWO (A) was used as local oscillator, the Gaussian beam was emitted by a conical horn antenna and split-up in a reference and a measurement path (B) by a polarization selective wire grid. Elliptical mirrors ($S_1 - S_3$) were used to focus and to redirect the gaussian beam. The receivers of the reference and measurement path were subharmonic mixers with corner cube antennas (C), (D). The beam was focused between mirror S_2 and S_3 to a waist radius $w_0 = 0.46$ mm.

In this plane the measurement object was moved through the focus perpendicular to the propagation direction of the gaussian beam.

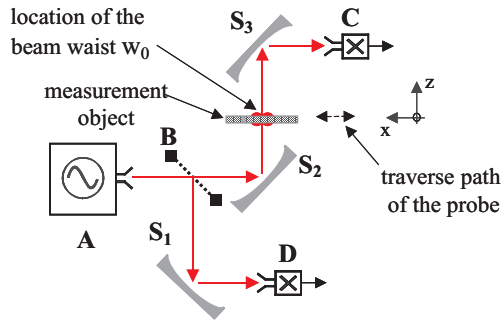


Fig. 9. Transmission measurement setup at 600 GHz

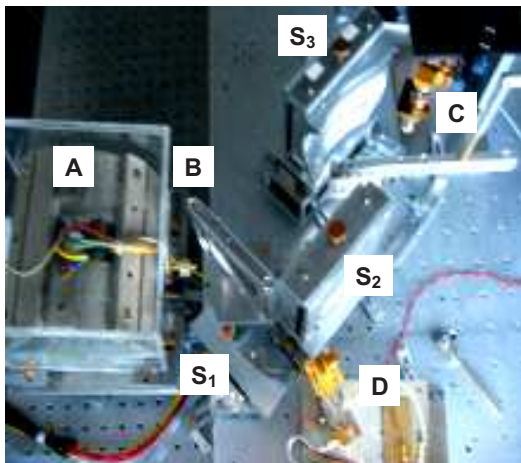


Fig. 10. Realization of the transmission measurement setup at 600 GHz

Fig. 11 shows the magnitude of the received measurement signal at 600 GHz. Because of a very small waist radius of $w_0 = 0.46$ mm in the focal plane, only a small area is illuminated at each measurement point. This results in little diffraction at edges. So the steps and drill holes are clearly visible. A spatial resolution of $\delta_{x,y} \geq 1$ mm is achievable with this focused transmission measurement setup. With regard to the transmission measurements setup at 75 – 100 GHz there are two reasons for a finer spatial resolution with the 600 GHz setup, verified by our measurements. On the one hand it is possible to realize smaller beam waists w_0 at higher frequencies, which results in a better differentiation of nearby measurement objects. On the other hand the value of the material parameter is averaged in a smaller region of the beam footprint, which means minor diffraction effects. In contrast to the commercial vector network analyzer at 75 – 100 GHz there are only scalar and single frequency measurements realizable with this setup. Therefore the phase information could not directly be retrieved and therefore signal processing algorithms to determine the step heights are not applicable. Furthermore, a drift of the local oscillator created noise in the detected signal

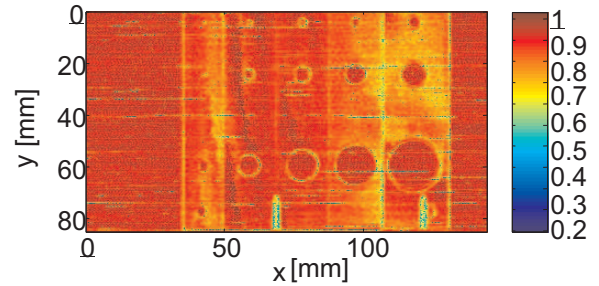


Fig. 11. Magnitude [lin.] of the transmission coefficient at 600 GHz

(Fig. 11).

V. ADVANCED BROADBAND SIGNAL PROCESSING

As mentioned above it is possible to apply several signal processing tools to broadband measurements to determine the time delays of the received signals. Further on, the knowledge of the time delays gives information about the thickness or variations of the material properties of the measurement object.

A common approach in processing broadband measurement data is the application of the Inverse Fast Fourier Transform (IFFT). This approach suffers from limited range resolution caused by the limited signal bandwidth. The achievable range resolution Δr with IFFT processing is determined by equation (1) [11].

$$\Delta r = \frac{c_0}{2\Delta f} \quad (1)$$

Regarding our signal bandwidth of $\Delta f = 25$ GHz, a minimum range resolution of $\Delta r \simeq 6$ mm is achievable. It is obvious that the steps of the PE step wedge with a step height difference of 1 mm can not be resolved by the IFFT processing.

To overcome these limitations it is possible to apply model based spectral estimation techniques [12]. The main advantage of these methods is the a priori assumption of a signal model. This leads to a better separation of nearby signal components and thereby to a better range resolution.

We tested several autoregressive (AR) spectral estimation and eigenvalue-based spectral estimation algorithms with simulated and measurement data. These tests demonstrated that the Matrix Pencil Method (MPM) [12] and the ESPRIT (Estimation of Signal Parameters via Rotational Invariance Technique) [13] provide the best results for this application. The following results were processed with the MPM.

Fig.12 shows the time delay of the received signals after the application of the MPM on each pixel. In contrast to the IFFT processing all steps can be resolved. The delay profile in Fig.13 b) shows that each step with a height of 1 mm can be resolved with this model based spectral estimation technique. In comparison to the conventional IFFT processing the range resolution can be improved by a factor of 6 when

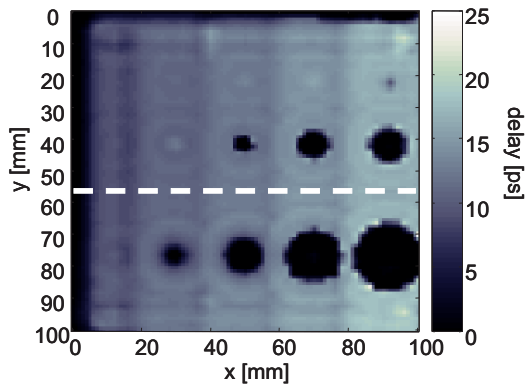


Fig. 12. Time delay [ps] for each data pixel (the dashed line marks the vertical position of slice in Fig.13 b))

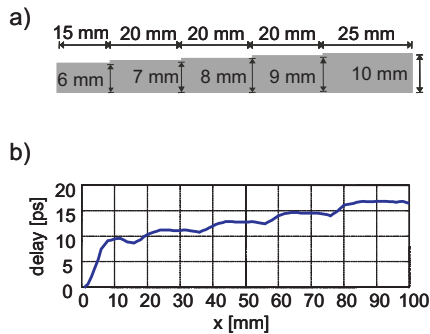


Fig. 13. a) Scheme of the step wedge profile, b) Signal delay profile at the marked position (dashed line) in Fig.12 of the step wedge

applying the MPM.

If the geometric or material properties of the measurement object are known, one of these parameters can be reconstructed from the knowledge of the signal delays and therefore it is possible to detect defects within the material.

VI. CONCLUSION

We have investigated two focusing millimeter wave imaging setups at 75-100 GHz and 600 GHz and compared their potential with regard to the spatial resolution. Obviously, it can be observed, that the spatial resolution increases with decreasing wavelength. The depth of focus effect did not become apparent in the case of the transmission measurements at 75-100 GHz and 600 GHz because of the small step height differences, whereas, in the case of the reflection measurements, the image quality is distorted due to the elliptical footprint which is caused by the tilted antennas. Diffraction effects in the reflection measurement are more evident. The additional broadband phase information of the coherent measurement results at 75-100 GHz can be used to achieve additional range information, because signal processing algorithms can only be applied if phase information is available. We demonstrated the performance of the spectral estimation technique Matrix Pencil Method (MPM), where time delays and step heights of the different steps can be determined more accurate. A honorable

improvement of the minimum range resolution towards $\Delta r \simeq 1$ mm can be achieved. The broadband measurement results can also be used for reducing the multiple reflection effects between the horn-lens combination and the measurement object. In addition the permittivity profile can be reconstructed with inverse scattering methods.

ACKNOWLEDGEMENT

The authors would like to thank the mechanical workshop of the LHFT for the precise fabrication of all components of the setups such as conical horn antennas, wire grids, dielectric waveguides, dielectric lenses and elliptical mirrors.

REFERENCES

- [1] M. N. Afsar, J. R. Birch, R. N. Clarke, *The Measurement of the Properties of Materials*, Proceedings of the IEEE, Vol. 74, No. 1, January 1986, pp. 183-199
- [2] J. R. Birch, et al., *An Intercomparison of Measurement Techniques for the Determination of the Dielectric Properties of Solids at Near Millimetre Wavelengths*, IEEE Transactions on Microwave Theory and Techniques, Vol. 42, No. 6, June 1994, pp.956-965
- [3] J. W. Lamb, *Miscellaneous Data on Materials for Millimetre and Submillimetre Optics*, International Journal of Infrared and Millimeter Waves, Vol. 17, No. 12, 1996, pp.1997-2034
- [4] P. F. Goldsmith, *Quasioptical Systems: Gaussian Beam Quasioptical Propagation and Applications*, IEEE Press, New York, 1998
- [5] H. Kogelnik, T. Li, *Laser Beams and Resonators*, Proceedings of the IEEE, Vol. 54, No. 10, October 1966, pp. 1312-1329
- [6] M. N. Afsar, *Dielectric Measurements of common Polymers at Millimetre Wavelength Range*, IEEE MTT-S Digest, 1985, pp. 439-442
- [7] J. Weinzierl, Ch. Fluhrer, H. Brand, *Dielectric Waveguides at Submillimetre Wavelengths*, Proceedings of 6th International Conference on THz electronics, Leeds, U.K., 1998, pp. 166-169
- [8] D. K. Ghodgaonkar, V. V. Varadan, V. K. Varadan, *Free-space Measurement of complex permittivity and complex permeability of magnetic materials at Microwave Frequencies*, IEEE Transactions on Instrumentation and Measurement, Vol. 39, No. 2, April 1990, pp. 387-393
- [9] J. Musil, F. Zacek, *Microwave Measurements of Complex Permittivity by Free Space Methods and their Applications*, Elsevier Science Publishers, 1986.
- [10] R. M. A. Azzam, N. M. Bashara, *Ellipsometry and Polarized Light*, Elsevier B.V., 1987.
- [11] D. R. Wehner, *High Resolution Radar*, Artech House, 1987.
- [12] T. K. Sarkar, O. Pereira, *Using the Matrix Pencil Method to Estimate the Parameters of a sum of Complex Exponentials*, IEEE Transactions on Antennas and Propagation Magazine, Vol. 37, No. 1, February 1995, pp. 48-55
- [13] R. Roy, T. Kailath, *ESPRIT-Estimation of Signal Parameters Via Rotational Invariance Techniques*, IEEE Transactions on Acoustics, Speech, and Signal Processing, Vol. 37, No. 7, July 1989, pp. 984-995

Load Variation Tolerant Balanced Amplifier with Two Elements LC-Coupler

Irfan Ibrahim, Norbert Peters, and Holger Heuermann

Department of High Frequency Technologies, University of Applied Science Aachen,
Eupener Str. 70, 52066 Aachen, Germany, E-mail: heuermann@fh-aachen.de, Tel.: +49/241-60092108

Abstract—This paper presents the architecture of a new balanced amplifier with two elements LC-coupler tolerant to load variations at input and output. At first this paper presents an overview of four existing solutions to implement a load variation tolerant front-end. Later the detail description of new proposed amplifier architecture are given. In order to verify the performance of new proposed design ADS simulations are made both for an existing design and the new design. The simulations result show a very good input and output matching, gain flatness, PAE, and ACPR performance of the proposed amplifier design under various load mismatch conditions. The proposed design has linear output power up to 27 dBm and ACPR value better than -50 dBc over the linear region. With less part count, cost, complexity, and losses the new balanced amplifier with LC-coupler can be the choice for UMTS, WLAN, and other mobile radio communication devices.

Index Terms—Isolator, balanced antenna, balanced amplifier, load invariance, LC-coupler, power added efficiency, adjacent channel power ratio.

I. INTRODUCTION

In mobile communication modules for standards like UMTS, WCDMA, UWB, etc., one of the great emphases is the strict linearity requirements of RF power amplifiers. The high linearity is required to insure low error vector magnitude (EVM) for complex modulation modes like 64QAM and minimum interference between different mobile communication devices [1].

The linearity of an amplifier is dependent upon different design parameters. Such as an amplifier class, bias point, and load match. The optimum load match conditions are usually determined by the time consuming load pull measurement method, [2]. Based on these measurements result a particular load condition is selected for an amplifier to give highest linear output power and lowest inter modulation distortion level. Therefore the linearity of RF amplifier is greatly effect by the degree of matching between the amplifier and the load impedance. The load impedance in wireless mobile communication devices changes with the changes in surrounding environment. This drifts the amplifier load from its optimum load value. It will effect the matching of an antenna (load) with RF amplifier resulting in the loss of amplifier linearity. It will cause the re-growth of spectral components and will degrade the adjacent channel power ratio (ACPR) performance. These conditions give a challenge to design an amplifier which is tolerant to load variations. This is one of the important areas of research for power amplifier designers. Different solutions are proposed to overcome this problem. However, at the same time these solutions have increased the amplifier cost, complexity, and expensive integrated chip area.

The following section will present some of the existing techniques applied to achieve amplifiers tolerant to load vari-

ations. The techniques described here includes the use of isolators, balanced antenna, [3], and amplifiers with phase shift approach, [4]. In the next section the detail description of new proposed load variation tolerant balanced amplifier with LC-coupler is presented. It also includes the ADS simulation results of an existing solution and new proposed design. The ADS results include amplifier performance parameters like input and output matching, power added efficiency (PAE), gain, linearity, and adjacent channel power ratio (ACPR) under the various load mismatch conditions. The results showed that the new proposed design has high degree of tolerance to load variations. It has comparable efficiency and ACPR performance to existing designs but with less part count, complexity, and cost.

II. EXISTING SOLUTIONS

This section gives an overview of some of the existing solutions to overcome amplifier linearity problems due to load mis-match. These solutions include amplifiers with isolators, balanced antenna and phase shift approach (PSA) to cancel out the reflections due to antenna mis-match. It will also develop the background necessary to understand and evaluate the concept of new balanced amplifier with LC-coupler presented in this paper.

A. Amplifier with Isolator

In mobile communication devices antenna mis-match can produce reflections that travels toward the amplifier and result in standing wave pattern. One classical way to prevent standing wave pattern due to reflections is by the use of isolators, [5], shown in Fig. 1.

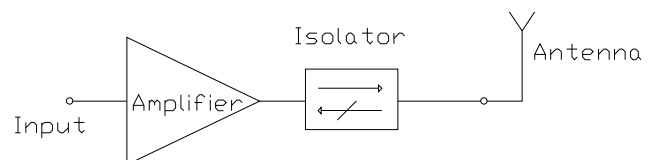


Fig. 1. The classical way to realize load variation tolerant amplifier

Although isolators provide better isolation but at the same time they are suffered by the number of disadvantages. Which includes large integration space required by the isolators, high component cost, and difficulty of realizing the isolator with different technologies. The insertion loss of isolators will also introduce losses in RF path and will decrease the power added efficiency of an amplifier. This effect will reduce the battery operating time in hand held devices.

B. Amplifier with Balanced Antenna

Another quite new concept to overcome the impedance mismatch at power amplifier output due to antenna mis-match is presented in [3]. It uses a balanced antenna [6] including two elements LC-coupler, shown in Fig. 2. The 90° LC-coupler [7] consists of one inductor and one capacitor. The phase variation from port 1 to port 2 is -45° and from port 1 to port 4 is $+45^\circ$. The power amplifier is attached to port 1 and port 3 is terminated in 50Ω matched load. Port 2 and port 4 are connected to two similar symmetrical antennas, placed closed to each other. The impedances Z_1 and Z_2 are given by

$$Z_1 \cdot Z_2 = Z_o^2 \quad (1)$$

and

$$|Z_1| = |Z_o| = \left| \frac{1}{j\omega C} \right|, \quad (2)$$

$$|Z_2| = |Z_o| = |j\omega L|. \quad (3)$$

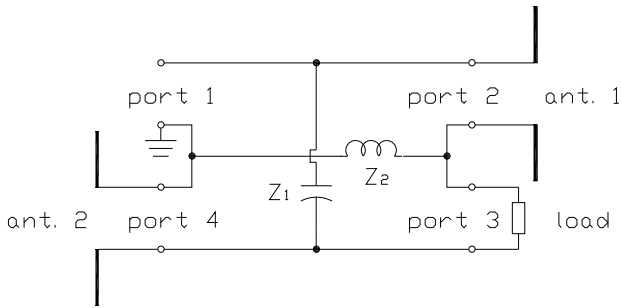


Fig. 2. Balanced antenna with 90° LC-coupler

The mis-match at antennas due to environmental changes will affect the two antennas in same order. The wave traveling from port 1 to port 2 and reflected back due to mis-match at antenna will suffer total phase change of -90° . In the same manner wave reflected from port 4 to port 1 will suffer total phase change of $+90^\circ$. Now the two reflected waves are 180° out of phase and will cancel each other at port 1, preventing the standing wave pattern due load mis-match. The reflected power will dissipate in 50Ω matched load connected to port 3.

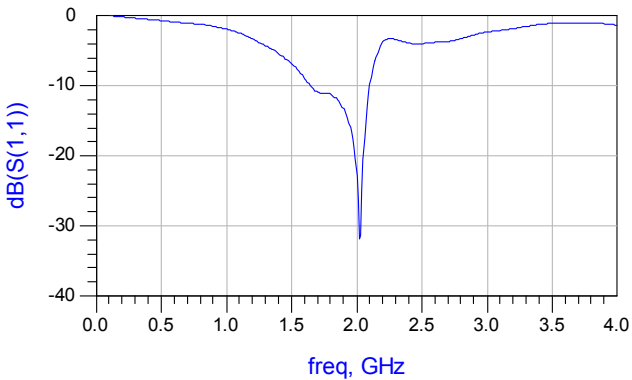


Fig. 3. The magnitude of reflection response of balanced antenna with metal reflector in the direct vicinity over frequency

Fig. 3 shows the reflection S_{11} response of balanced antenna under high load mis-match conditions which is usually the

case when hand held communication devices come close to metal surfaces. The value of $S(1,1)$ is better than -15 dB with the bandwidth of 200 MHz when a metal plate is placed in the direct vicinity of balanced antennas. The drawback of this technique is, that balanced antennas are not commercially available for communication platforms. However balanced antennas approach gives good load variation tolerance and can be a choice in the future developments of communication devices.

C. Amplifier with Phase Shift Approach (PSA)

One approach to avoid ACPR degradation due to amplifier non-linearity caused by load mis-match is presented [4]. In this technique two amplification paths are used with phase shifting and matching networks at the input and output section, as shown in Fig. 4.

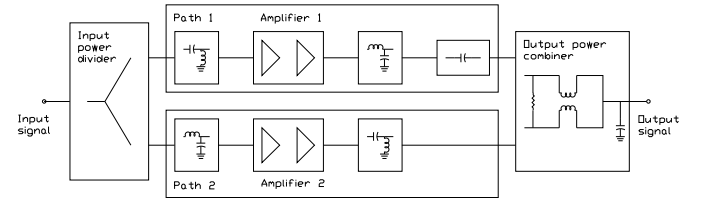


Fig. 4. Amplifier with phase shift approach

Under the load mis-match conditions a matching network at the output stage of each amplifier behaves complementary to each other. In case of impedance mis-match one path of the amplifier presents high impedance to the output of amplifier and second path presents the low impedance to the output of second amplifier. Therefore increasing the ACPR performance of amplifier in one branch and decreasing in the other branch. The resultant ACPR performance under the mis-match condition lies between the ACPR performances of individual amplifiers. This gives an overall improved ACPR performance under various antenna mis-match conditions.

In Fig. 4 the reflected wave due to antenna mis-match is divided equally into two paths and travels toward the amplifiers. The wave in each path is reflected again by the amplifier output and causes the standing wave pattern. However the wave traveling from antenna to amplifier output and back undergoes through the phase change of 90° in one path and -90° in other path. The two waves are now 180° out of phase and are canceled by each other at output of power combiner. And also due to 180° phase difference the reflected energy is dissipated in the resistor of the power combiner.

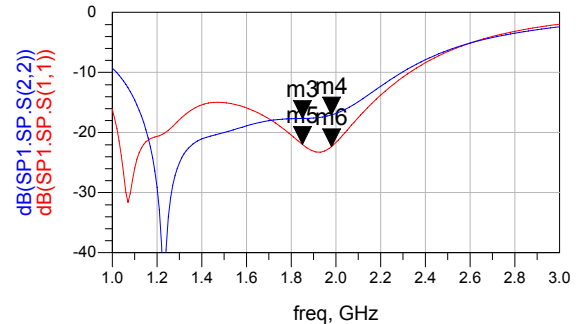


Fig. 5. The input reflection $S(1,1)$ and output reflection $S(2,2)$ response of PSA

The ADS simulations are performed by using the TriQuint library for the PSA amplifier. The matching response of PSA amplifier is shown in Fig. 5. It shows the input and output matching is better than -17 dBm. Fig. 6 shows PSA has in-band transmission gain of 29 dB with gain flatness of ± 0.4 dB.



Fig. 6. The transmission coefficient $S(2,1)$ of phase shift approach (PSA) amplifier

Fig. 7 shows reverse isolation response of PSA amplifier. It has an in-band reverse isolation value better than -60 dB.

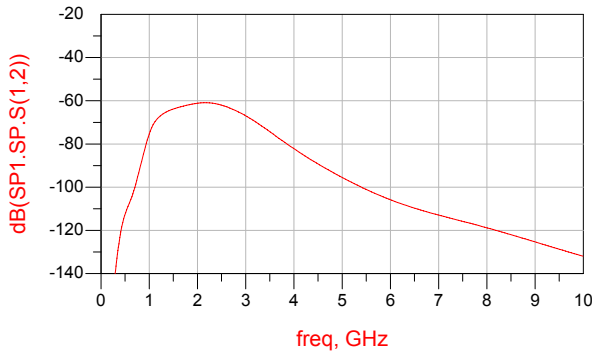


Fig. 7. Reverse transmission coefficient $S(1,2)$ (isolation) of PSA amplifier

Fig. 8 shows the stability factor (k) of PSA amplifier. The stability factor k is higher than 19.

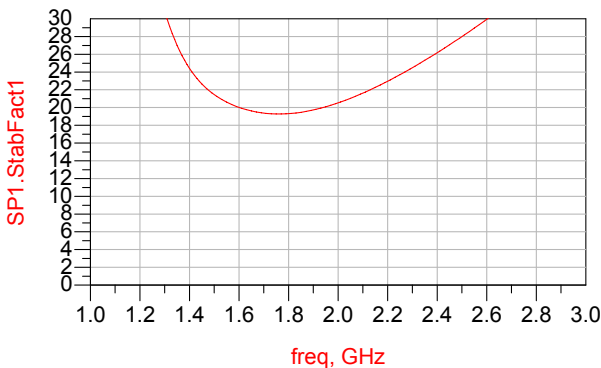


Fig. 8. The stability factor (k) of PSA over frequency

The drawback of PSA approach is the excessive use of inductors and capacitors in the input and output phase shift circuits. Also inductors are required for the implementations of input power splitter and output power combiner circuits. This will use expansive chip area, and is expensive.

D. Adaptive Matching Network

Adaptive matching network [8] is another new concept to overcome load mis-match conditions. The larger benefit of this technique is that, any primitive antenna can be used to achieve a good match for any desired frequency band while using the same mis-antenna. The mis-match caused due to environmental changes, e.g. in the vicinity of large metallic objects will be dynamically compensated by the matching network, shown in Fig. 9. The figure shows a π -matching network with variable element values. The adaptive matching network can be realized in the form of step matching network.

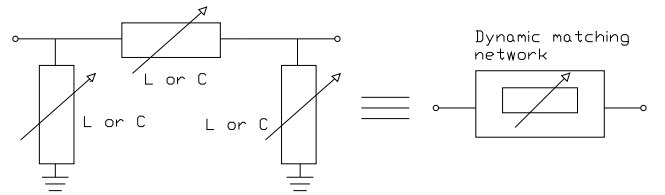


Fig. 9. The dynamic L- or C-matching network

Fig. 10 shows a possible complete front-end solution implemented with adaptive matching network. It uses directional coupler to separate the reflected wave from incident wave. The magnitude of the reflected wave is measured with the detector attached to the coupled arm of the directional coupler. The magnitude information of the reflected wave is processed by the logic control unit. Which alters the value of variable elements in the adaptive matching network in such a way to reduce the magnitude of reflected waves. In this way it is then possible to achieve good load match conditions under changing environmental conditions. The drawback of this technique is the use of lot of hardware for additional matching control loop.

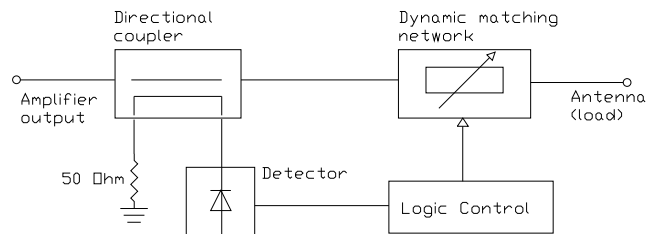


Fig. 10. Adaptive matching network

III. BALANCED AMPLIFIER WITH LC-COUPLER

This section presents the operational principle and simulation results of proposed balanced amplifier (BA) with two elements LC-coupler.

A. Operating Principle

The concept of the new balanced amplifier is illustrated in Fig. 11 [9]. The realization of a balanced amplifier with two elements LC-coupler is shown in Fig. 12. The power is feed to the amplifier through the unbalanced port 1 of LC-coupler (input). The differential inputs of amplifiers PA1 and PA2 are connected to the differential grounded-unsymmetrical port 2 and port 4 of LC-coupler, respectively. The port 3 of LC-coupler is matched to 50Ω . The output of amplifiers PA1 and PA2 are connected to differential grounded-unsymmetrical

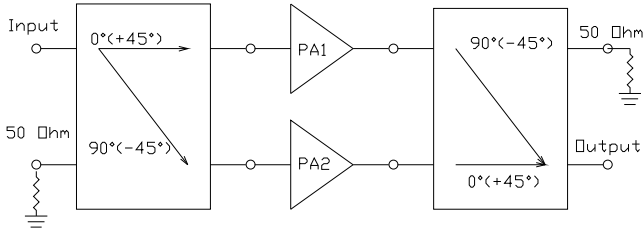


Fig. 11. The concept of balanced amplifier with LC-coupler

port 2' and port 4' of LC-coupler. Port 3' is matched to 50 Ω and port 1' gives the unbalanced amplified output. In the actual design cross mode blockers [13] are added at the input and output section of balanced amplifier.

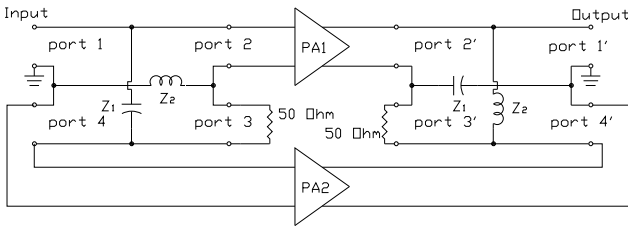


Fig. 12. Balanced amplifier with LC-coupler

The power applied to the input port 1 of balanced amplifier configuration Fig. 12 is divided equally into two paths. The LC-coupler will introduce a phase difference of 90° between the power at port 2 and port 3 so that the phase of the wave at the input of amplifier PA1 is lag by 45° and at the input of amplifier PA2 is lead by 45° with respect to the phase of applied signal. From the output of amplifier PA1 to the output port 1' the phase change is +45° and -45° from the output of amplifier PA2 to output port 1'. This will cancel the effect of phase change introduced in the input section of the balanced amplifier. Hence the waves reaching to port 1' from each amplifier are in phase and will add constructively. Under the matched conditions total power delivered to the load is equal to the sum of the output power from each amplifier, [10].

In case of mis-match present at the output port 1', reflections will occur traveling toward the differential amplifiers. The wave traveling from the output of PA1 to output port 1' and reflected back will undergo the total phase change of 90°. In the similar manner total phase change of -90° will occur for the wave traveling from the output of amplifier PA2 to output port 1' and reflected back to PA2. The two reflected waves are now 180° out of phase and will superimpose destructively at the output of differential amplifiers. Due to 180° phase difference between the reflected waves, current will flow in 50 Ω matched load connected to port 3', dissipating the reflected power. This principle provides isolation to amplifiers from the reflected waves and makes the balanced amplifier configuration tolerant to load variations. The concept well known from the classical balanced amplifier theory [11]. The performance of proposed design is presented in next section.

B. Simulation Results

The proposed design of new balanced amplifier is simulated in Advance Design System (ADS) using the TriQuint Semiconductor design library.

Fig. 13 shows the amplifier input and output matching response. At 1900 MHz the input matching $S(1,1)$ is better than -15 dB and output matching $S(2,2)$ is better than -29 dB. Fig. 14 shows the transmission $S(2,1)$ response of BA over the frequency sweep. The plot shows that balanced amplifier has in-band transmission $S(2,1)$ gain of 28 dB. The plot also shows the in-band gain has flatness of ± 0.2 dB at 1900 MHz.

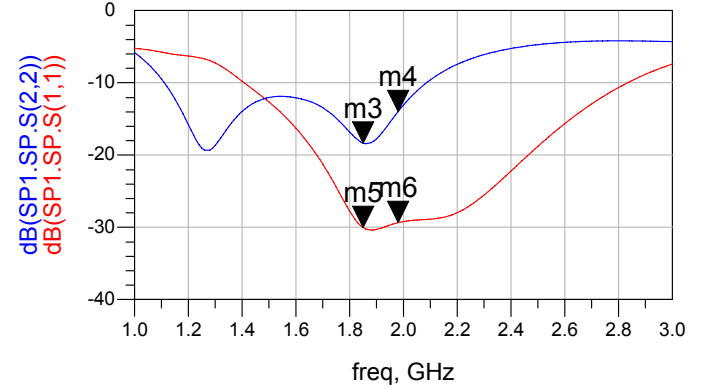


Fig. 13. The input and output matching response of balanced amplifier (BA)

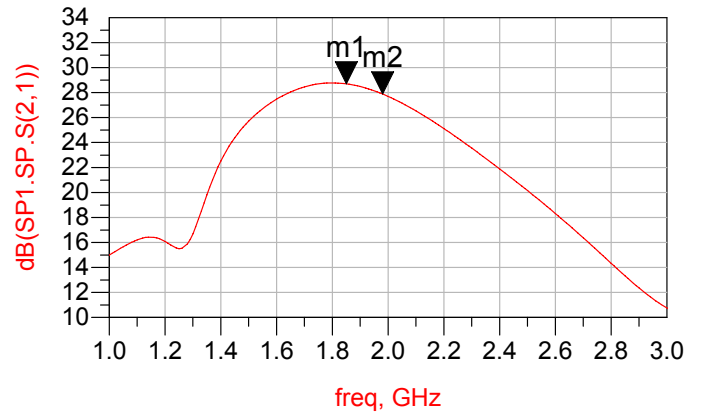


Fig. 14. The $S(2,1)$ response of BA over the frequency variation

Fig. 15 shows the plot of BA stability factor (k) over a wide frequency band of 5 GHz.

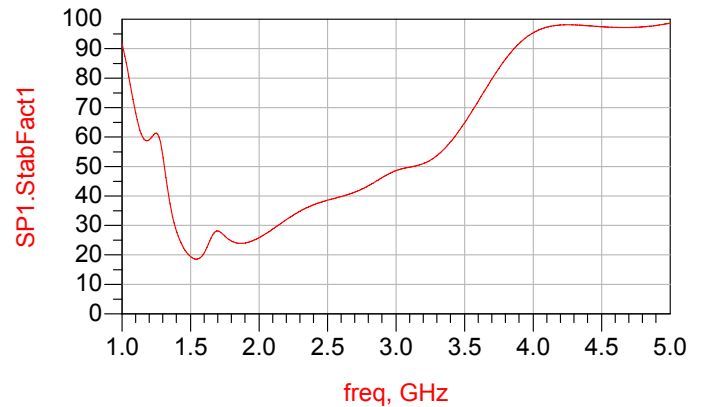


Fig. 15. The stability plot of balanced amplifier

Fig. 16 shows the linearity response of the proposed balanced amplifier and phase shift approach amplifier (PSA). The

balanced amplifier has higher output power and compression starts at 27 dBm output power. The PSA has lower output power and similar compression point. The overall response of two architectures is close to each other.

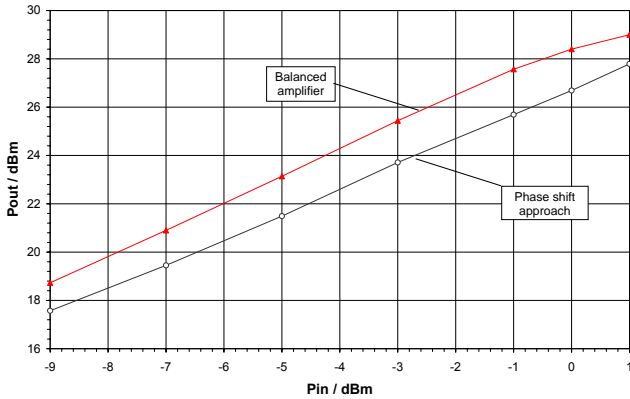


Fig. 16. The linearity response of balanced amplifier and phase shift approach amplifier

Fig. 17 shows the ACPR performance of balanced amplifier. It showed the BA has ACPR value of -49 dBc at the linear output power range of 27 dBm. The value is suitable for the EDGE application and communication devices requiring amplifiers with high output power and low adjacent channel interference.

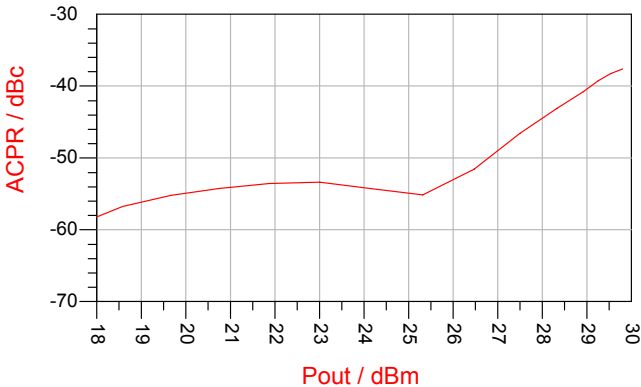


Fig. 17. The ACPR of balanced amplifier over the output power

Fig. 18 shows the ACPR performance of two architectures under the mis-match conditions. It shows under the perfect VSWR value of 1 the ACPR of both amplifiers is around -54 dBc. Now due to the load variation tolerant property the performance of ACPR does not fall rapidly with increasing VSWR values. This is an important requirement for power amplifiers in hand held devices to behave well under mis-match conditions.

Usually the amplifier design requires good linearity and low harmonics up to VSWR of 4:1, [12]. The plot shows that ACPR value of BA is below -43 dBc for VSWR 4:1. This plot also shows the comparison of ACPR values of BA and PSA amplifiers. At higher VSWR 5:1 the ACPR response of BA is around 5 dBc better as compared to PSA amplifier.

Fig. 19 shows the efficiency of balanced amplifier and PSA amplifier. The plot shows the two approaches have nearly the same efficiency of 33% at maximum linear output power.

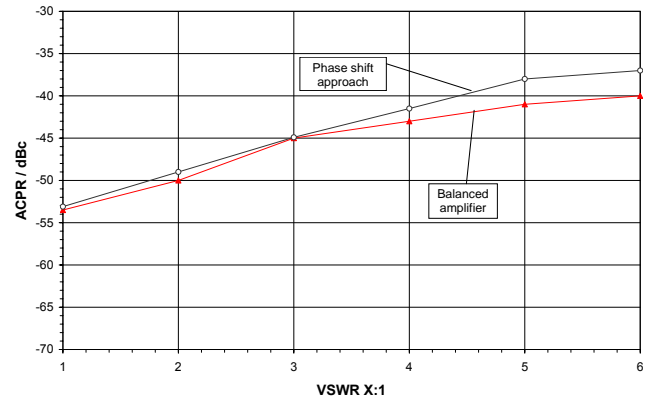


Fig. 18. The ACPR performance of BA and PSA amplifier over VSWR at an output power of 26 dBm

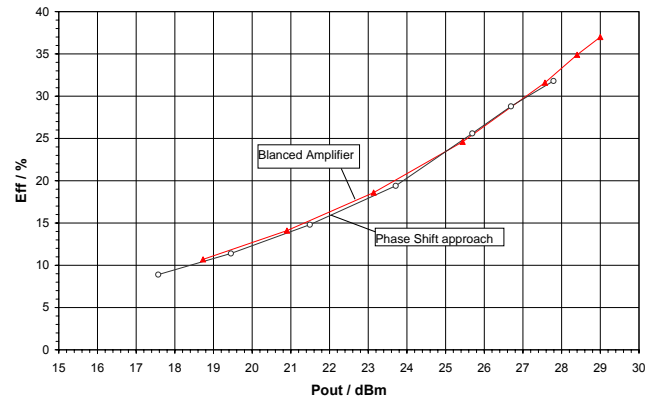


Fig. 19. The efficiency of BA and PSA amplifier over an output power of 28 dBm

IV. CONCLUSION

A new concept of load variation tolerant balanced amplifier with two elements LC-coupler has been presented. The paper started with an overview of existing amplifiers with load variation tolerant techniques. The performances of existing techniques were examined with ADS simulation. The main features and drawbacks of these techniques were also described. After that the concept of the new balanced amplifier has been presented. The design has been simulated in ADS, using the TriQuint Semiconductor design library. In order to verify the performance of new design the results of important amplifier design parameters like input matching, output matching, stability factor, linearity response, efficiency, ACPR over the input power, and ACPR over the varying VSWR were also included. These results showed the proposed design has a stability factor higher than 25, output linearity of 27 dBm and ACPR value better than -50 dBc at maximum output linear power. Further the load variation tolerant feature of balanced amplifier was tested over the VSWR 5:1. All said parameters were also compared with other load variation tolerant amplifier designs. The proposed design has similar performance to other designs but with much reduced architecture complexity and cost which makes it preferable choice for high integrated circuit solutions of the mobile RF communication devices.

REFERENCES

- [1] P. B. Keningtons, "Distortion in amplifiers," High-Linearity RF Power Amplifier Design. Boston, London: Artech-House, 1999, chapter 1, pp. 1-17

- [2] S. C. Cripps, "Linear Power Amplifier Design," RF Power Amplifiers for Wireless Communications. Boston, England: Artech-House, 1999, chapter 2, pp. 17-36.
- [3] N. Peters, T. Schmitz, A. Sadeghfam, H. Heuermann, "Concept of Balanced Antennas with Load-Invariant Base Impedence Using a Two Element LC-Coupler," Proceeding European Microwave Conference, Jun. 2005, pp. 117-112.
- [4] S. W. Chang, H. J. Finlay, N. Cheng, B. Park, "Load Variation Tolerant Radio Frequency (RF) Amplifier," Patent # US 2004/0185916 A1, Sept. 23, 2004.
- [5] David M. Pozar, "Theory and Design of Ferrimagnetic Components," Microwave Engineering, 2nd ed., John Wiley & Sons, Inc., 1998, chapter 9, pp. 523-530.
- [6] H. Heuermann, "Antennenarchitektur und Koppler," Patent # D 0 2004 054 442.5, Nov. 16, 2004.
- [7] H. Heuermann, Hochfrequenztechnik, Lineare Komponenten hochintegrorierter Schaltungen, Vieweg-Verlag, ISBN 3-528-03980-9, Aug. 2005.
- [8] A. Sadeghfam, H. Heuermann, "Anpassnetzwerk," Patent # D 10205058875.1, Dec. 9, 2005.
- [9] N. Peters, Entwicklung eines neuartigen integrierten linearen balancierten UMTS-Verstärkers in HBT-Technologie, Diplomarbeit, FH-Aachen, Germany Jun. 2005, Kapitel 1.
- [10] David M. Pozar, "Design of Microwave Amplifiers and Oscillators," Microwave Engineering, 2nd ed., John Wiley & Sons, Inc., 1998, chapter 11, pp. 632-631.
- [11] G. Gonzalez, "Noise, Broadband, and High-Power Design Methods," Microwave Transistor Amplifiers Analysis and Design, 2nd ed, Prentice Hall, Inc., 1997, chapter 4, pp. 323-333.
- [12] Peter Wright, "The shrinking RF front-end," Proceeding European Microwave Conference, Jun. 2005, pp. 95-103.
- [13] H. Erkens, H. Heuermann, "Blocking Structures for Mixed-Mode Systems," Proc. 34th European Microwave Conf., Amsterdam, Netherland, Oct. 2004, pp. 297-300.

Characterization of 35 GHz Tunable Reflectarray Unit-Cells Using Highly Anisotropic Liquid Crystal

Radu Marin, Alexander Mössinger, Jens Freese, and Rolf Jakoby.
 Technische Universität Darmstadt, Institut für Hochfrequenztechnik
 Merckstraße 25, 64283 Darmstadt, Germany
 Email: {marin, moessinger}@hf.tu-darmstadt.de

Abstract—This paper presents the study, realization, and measurement of different tunable unit-cells for reconfigurable reflectarrays at 35 GHz. The emphasis of the work lies in the use of nematic Liquid Crystal, a material with electrically tunable dielectric properties. Unit cells have been optimized with respect to the trade-off between maximum attainable phase range and losses. The realised structures have been tested in a waveguide simulator and phase ranges up to 290° could be demonstrated.

I. INTRODUCTION

Microstrip reflectarray antennas have benefitted from increased attention from the part of the antenna community in the recent past [1]–[3], since they combine some of the advantages of reflectors and of array antennas. The main advantage of reflectarrays is the reflectorlike spatial power distribution by means of a feed antenna, thus replacing the lossy power distribution network. The phase of the reflected wave can be adjusted element-wise, thus enabling the possibility of beam-scanning. Low profile, low weight and easy fabrication are additional features which make microstrip reflectarrays appealing.

There have been various attempts to make reflectarrays with steerable beam, using different approaches to control the unit cells. In [4], [5] the use of varactor diodes is proposed. An approach making use of MEMS is presented in [6]. In [7], we proposed an alternative approach, based on the dielectric properties of Liquid Crystal (LC), a material that changes permittivity when DC voltage is properly applied. In this paper, the design and measurement of different cell topologies with improved characteristics is presented.

The next section of the paper presents the two concepts proposed for the LC-unit cell, section III describes the realization of the different unit-cells and of the measurement set-up, and the measured results are finally presented in section IV.

II. CONCEPT OF TUNABLE UNIT-CELL BASED ON NEMATIC LCS

Properties of nematic LCs as phase shifting material at microwave frequencies have been studied lately [8]. Under an applied DC-voltage the molecular arrangement of LC changes, causing a change in LC permittivity. We make use of this property, in order to obtain the necessary phase shift at each unit cell of the reflectarray.

In this section we propose two concepts for tunable unit-cells for reflectarrays, based on nematic LCs. The first concept is

based on modifying the resonance frequency of a microstrip patch by changing the permittivity of the LC. In order to achieve this, a cavity has to be formed under the patch and filled with LC, as shown in Fig. 1. A single patch as well as stacked patches could be used, with no additional layer, since they can be printed on both sides of the substrate.

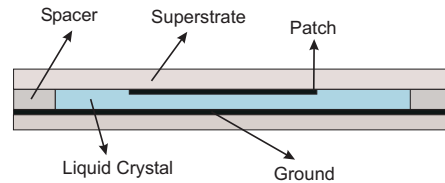


Fig. 1: Configuration of the LC-loaded unit-cell employing microstrip patch element.

The second concept consists of a delay line coupled to the microstrip patch by means of an aperture in the ground plane. The phase of the reflected wave can be controlled by filling LC under the line, as in Fig. 2. By varying the permittivity of the LC, the electric length of the line changes, and thus the phase of the reflected wave can be adjusted, since it holds:

$$\Delta\varphi = \Delta(\beta \cdot \ell) = \frac{2\pi \cdot \ell}{\lambda} \cdot \Delta(\sqrt{\epsilon_r}) \quad (1)$$

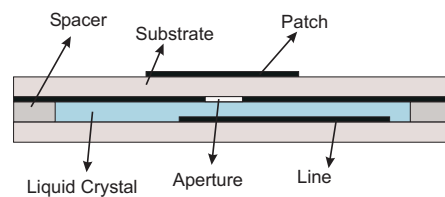


Fig. 2: Configuration of the LC-loaded unit-cell with aperture coupled line.

Both concepts have advantages as well as drawbacks. The first concept, employing a single patch (or stacked patches) is simpler and thus easier to realise, whereas the dimensions of the components at 35 GHz make it harder to etch the line and the aperture accurately and to align them to the desired position. On the other hand, with a single/stacked patch cell, theoretically a maximal phase range of 360° can

be achieved (practically even less), while with an aperture coupled line a theoretically unlimited phase range can be reached, in accordance with Eq.1. It is obvious from Eq. 1 that the physical length of the microstrip line can be increased, thus increasing the tunable phase range. In reality, one will nevertheless eventually come across physical limitations due to the finite space available for the line belonging to one unit cell.

In both cases, the LC-cavity must be very thin ($\leq 150\mu\text{m}$), in order to allow the prearrangement of the LC-molecules parallel to the ground and microstrip patch (or microstrip line respectively), with the aid of a polyimide film (A reduced thickness of the LC layer also helps improving the otherwise low response times of the LC). The prealignment of the LC molecules parallel to the surface due to the polyimide film causes a $\epsilon_{eff\perp}$. A DC-voltage applied between the lower microstrip patch (microstrip line) and the ground plane will cause the molecules to rearrange, until reaching a saturation voltage, when they are completely aligned with the static electric field. In this state the LC molecules are almost parallel to the RF-field and the permittivity is denoted as $\epsilon_{eff\parallel}$.

In order to test the both concepts, simulations were made with values of ϵ_r between $\epsilon_{eff\perp}=2.6$ and $\epsilon_{eff\parallel}=3.4$, which are situated in the attainable measured range reported in [9]. These values refer to a LC provided by Merck.

The simulations were aimed at improving the ratio between attainable phase range and return loss, since there is a trade-off between the two. A steeper slope of the phase curve means wider tunable range, but also more losses, because of the sharper resonance. The most promising results, two cells with stacked patches, one cell with a single patch and one cell using aperture coupled line were manufactured and measured in a waveguide simulator.

III. REALIZATION OF THE UNIT CELLS AND OF THE MEASUREMENT SETUP

As known from the theory, in the waveguide simulator it is possible to emulate the plane wave impinging on a infinite array, but not at normal incidence. The field distribution propagating in the waveguide in the main TE_{10} -mode is similar to the field distribution of two plane waves who make an angle of $\theta_i = \arcsin(\lambda_0/\lambda_c)$ with the plane containing the unit cells (λ_0 : free-space wavelength, λ_c : cut-off wavelength). For the particular structure that we investigated this angle amounts to about 37° , and since the phase response of the unit cell is dependent of the incidence angle, we expect slight differences between simulation and measurement results. However it has been shown ([10]) that this differences are not very severe, and thus the setup can be seen as adequate for the purpose of testing the functionality of a LC-unit-cell.

As mentioned in the previous section, we decided to manufacture and test different structures, who showed promising results in the simulations. One of the structure had a simple patch etched on one side of the substrate (**Structure 1**), two of them employed stacked patches (**Structure 2** and **Structure 3**), finally, **Structure 4** designates the cell using

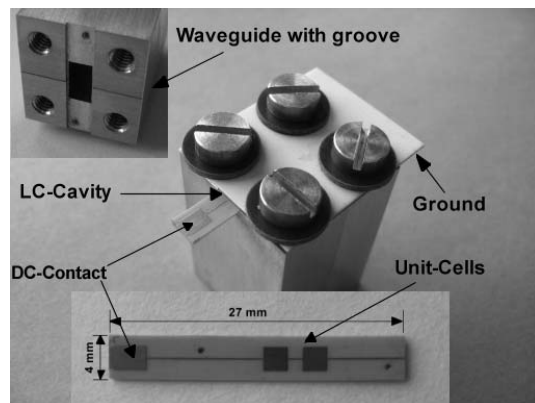


Fig. 3: Setup for measuring the unit cells in a waveguide simulator.

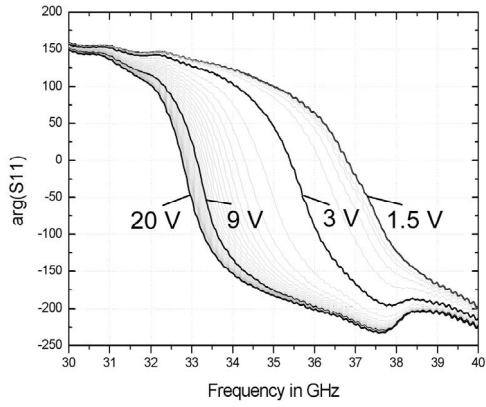
the aperture coupled line as phase shifter.

For the structures 1 to 3 TMM3 with a thickness of 0.5 mm was used as substrate. The two patches on the LC-side are connected through a thin line, which is then prolonged over the edge of the metal-block in order to ensure a proper soldering point for the DC-Voltage lead. This line has very little influence on the measurement, since, due to the polarization of the E-field, it is placed in a quasi zero-field point. The same technique is used to connect the two aperture coupled lines to the DC-Voltage, as can be seen in Fig 3 and Fig 6.

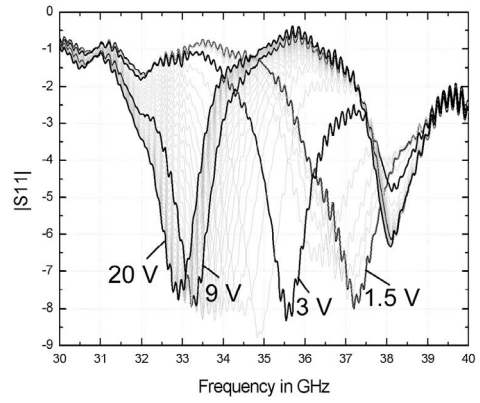
For structure 4 we employed RTDuroid 5880 with 0.5 mm thickness as substrate: on one side were printed the patches, on the other side the apertures in the ground plane. The lines were printed on TMM3, 0.5 mm thick. RTDuroid 5880, 0.127 mm thick was used as spacer for all structures. On both sides of the LC-cavity a 300 nm thick polyimide film was spinned, having the role to prealign the LC molecules.

IV. MEASUREMENT RESULTS

The applied control voltage was swept during the measurements between 0 V and 20 V. The measured frequency dependent phase and magnitude of the reflection coefficient are shown exemplarily for Structure 1 (simple patch) in Fig. 4. In Fig. 5, the phase and magnitude of the reflection coefficient are shown in dependence of the control voltage at a chosen frequency (we chose in each case the frequency where the maximum phase range was obtained). **Structure 1** (single patch) showed a phase range of about 270° between 34 GHz and 36 GHz, while return loss had values between -0.5 dB and -8 dB depending on the frequency and on the control volage. With **Structure 2** (stacked patches) the phase could be controlled in a range of roughly 250° , with somewhat higher return loss, between -4 dB and -11 dB. **Structure 3** (stacked patches) exhibited phase range of 270° to 290° between 31 GHz to 32.5 GHz, while the return loss was again between 0.5 dB and -8 to -9 dB. **Structure 4** (aperture coupled line) showed the poorest performance of all, with around 240°

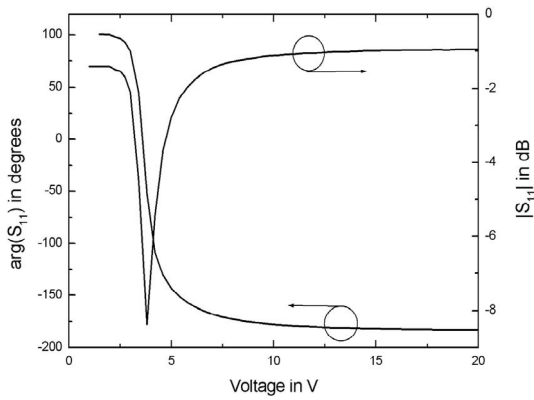


(a) Phase - $\arg(S_{11})$

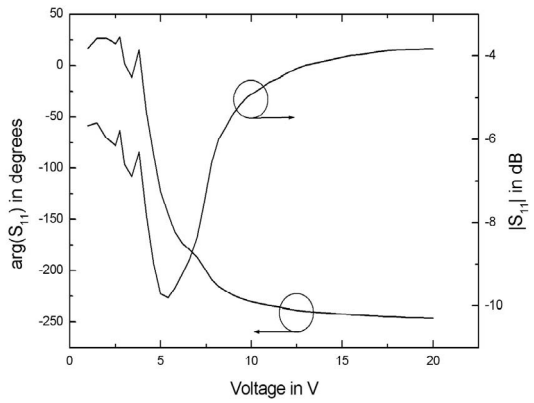


(b) Magnitude - $|S_{11}|$

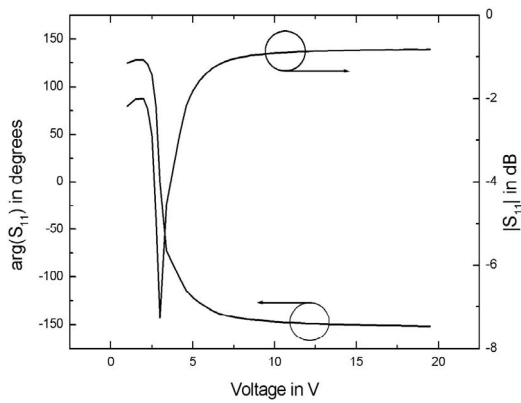
Fig. 4: Frequency dependent variation of the reflection coefficient, shown exemplarily for **Structure 1**



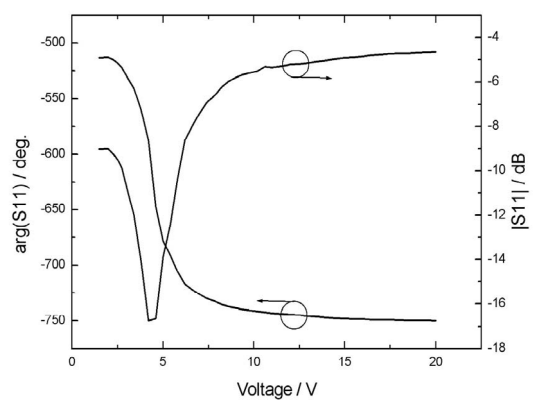
(a) **Structure 1** - at 35 GHz



(b) **Structure 2** - at 33 GHz



(c) **Structure 3** - at 31 GHz



(d) **Structure 4** - at 36 GHz

Fig. 5: Phase and magnitude of the reflection coefficient for the four mesured unit-cell structures in dependence of the control voltage - at the frequency of maximum phase range.

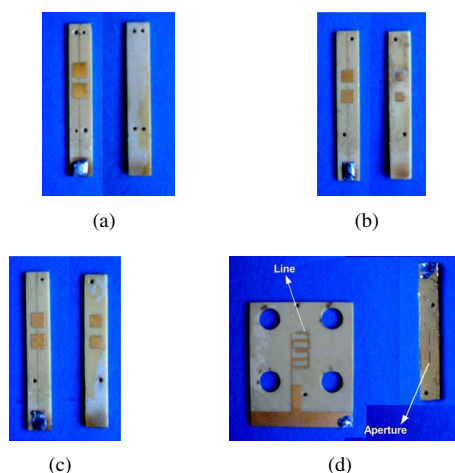


Fig. 6: (a) Structure 1 - patch, (b) Structure 2 and (c) Structure 3 - stacked patches, (d) Structure 4-aperture coupled line.

phase range and return loss between -5 dB and -15 dB. **Structures 1** and **3** showed almost similar performance, so one can assume those two structures to be most suitable candidates for the realisation of an electronically reconfigurable reflectarray. Even though the peak losses are high (around -8 dB), in a reflectarray they would be between -1 dB and -8 dB, depending on the phase distribution on the aperture. The measured results of **Structure 4** exhibit much higher loss than expected and a somewhat narrower phase range, which can be due to manufacturing and alignment tolerances. **Structure 2**, though having a somewhat reduced phase range, of only 250° and higher losses, compared to the structures 1 and 3, exhibits a rather broad frequency range where it can be used (31.5 GHz to 34 GHz) without noticeable performance degradation. This fact encourages the assumption that not only narrow-band unit-cells are possible, as expected from a highly resonant structure.

V. CONCLUSION AND OUTLOOK

Several structures to be used as tunable unit-cells in a LC-based electronically reconfigurable reflectarray have been proposed, realised and measured in a waveguide simulator. The results show a usable phase range of up to 290°, with control voltage between 0 V and 20 V. However, additional structures which may exhibit lower losses are currently under investigation.

Simulations based on the measured unit cell results (phase range and losses) resulted in usable patterns. As shown in Fig. 7, the simulated pattern of a 15x15 reflectarray using structure 3 as unit cell, has a 4 dB lower gain than the pattern of a fixed beam reflectarray using microstrip patches of variable sizes on RTDuroid. The gain difference is expected, since the 4 dB represent the averaged losses of the structure. The realisation of a small reconfigurable LC-reflectarray demonstrator is currently in progress.

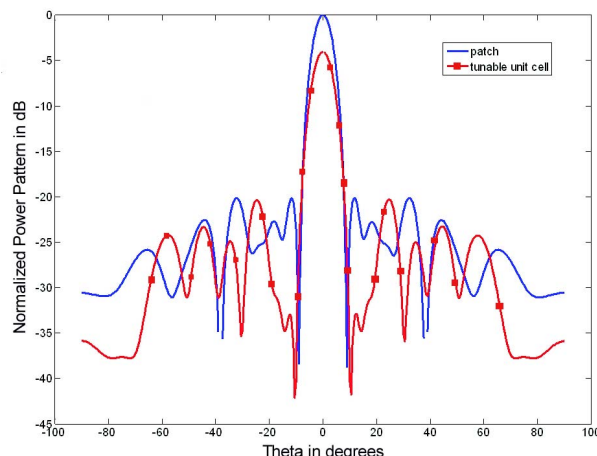


Fig. 7: Simulated patterns of the reflectarrays using microstrip patches and Structure 3 as unit cell respectively (patterns normalized with respect to the array with microstrip patches).

ACKNOWLEDGEMENT

Thanks are due to Merck KGaA for providing the Liquid Crystal mixture and to CST GmbH for providing the *CST Microwave Studio* package for simulations.

REFERENCES

- [1] David M. Pozar, Stephen E. Targonski and H. D. Syrigos: *Design of Millimeter Wave Microstrip Reflectarrays*. IEEE Transactions on Antennas and Propagation, vol. 45, Feb. 1997.
- [2] John Huang and Ronald J. Pogorzelski: *A Ka-Band Microstrip Reflectarray with Elements Having Variable Rotation Angles*. IEEE Transactions on Antennas and Propagation, Vol. 46, No. 5, May 1998
- [3] Jose A. Encinar: *Design of Two-Layer Printed Reflectarrays Using Patches of Variable Size*. IEEE Transactions on Antennas and Propagation, Vol. 49, No. 10, Oct. 2001.
- [4] Hum, S.V., Okoniewski, M. and Davies, R.J.: *Realizing an electronically tunable reflectarray using varactor diode-tuned elements*. IEEE Microwave and Wireless Components Letters, vol. 15, June 2005.
- [5] Boccia, L., Venneri, F., Amendola, G. and Di Massa, G.: *Experimental investigation of a varactor loaded reflectarray antenna*. IEEE Microwave Symposium Digest, 2002 IEEE MTT-S International Vol. 1, 2-7 June 2002.
- [6] Legay, H., Pinte, B., Charrier, M., Ziaei, A., Girard, E. and Gillard, R.: *A steerable reflectarray antenna with MEMS controls*. IEEE International Symposium on Phased Array Systems and Technology, 14-17 Oct. 2003 Page(s):494 - 499.
- [7] Marin, R., Mössinger, A., Freese, J., Müller, S. and Jakoby, R.: *Basic Investigations of 35 GHz Reflectarrays and Tunable Unit-Cells for Beamsteering Applications*. Proceedings of the 8th European Microwave Week, Page(s): 291 - 294, Paris, Oct. 2005.
- [8] Stefan Müller, Patrick Scheele, Carsten Weil, Michael Wittek, Christian Hock and Rolf Jakoby: *Tunable Passive Phase Shifter for Microwave Applications Using Highly Anisotropic Liquid Crystals*. Microwave Symposium Digest, 2004 IEEE MTT-S International, Vol. 2, June 6-11, 2004.
- [9] Andreas Penirschke, Stefan Müller, Patrick Scheele, Carsten Weil, Michael Wittek, Christian Hock, and Rolf Jakoby: *Cavity Perturbation Method for Characterization of Liquid Crystals up to 35 GHz*. Proceedings of the 34th European Microwave Conference, Page(s): 545 - 548, Amsterdam, Oct. 2004
- [10] Targonski, S.D. and Pozar, D.M.: *Analysis and Design of a Microstrip Reflectarray Using Patches Of Variable Size*. Antennas and Propagation Symposium Digest, Vol. 3, Page(s):1820 - 1823, 20-24 June 1994

A Wideband Amplifier with 2.4 mm Connectors Operating up to 48 GHz

M. Häfele^{*‡}, C. Schick^{*}, F. Hernandez-Guillen^{*}, A. Trasser^{*}, P. Abele^{*†}, and H. Schumacher^{*}

^{*}Dept. of Electron Devices and Circuits, University of Ulm, D-89069 Ulm, Germany

[†]Now with United Monolithic Semiconductors (UMS) GmbH, D-89081 Ulm, Germany

[‡]Now with DaimlerChrysler AG, Research and Technology, D-89013 Ulm, Germany

Phone: +49 731 5052026, e-mail: Martin.Haefele@DaimlerChrysler.com

Abstract—In this paper, we report about an assembly technology for a wideband distributed amplifier (DA). The amplifier MMIC is fabricated in a commercially available GaAs pHEMT process with 150 nm gate length. The amplifier is connected to a 50 Ω microstrip-line on an external rf-laminate with 2.4 mm connectors attached to the input and output. A via-hole process was developed for the Teflon based substrate material. All elements are assembled on top of this substrate. To provide bias decoupling down to the kHz-range, an external surface mount device (SMD) resistor and capacitor are attached to the artificial drain line termination of the DA. This enables the amplifier to operate in non-return to zero (NRZ) optical communication systems.

The packaged amplifier exhibits a gain of 11.2 dB near dc. The midband gain equals to 8.9 dB \pm 1.5 dB between 2 GHz and 48.5 GHz.

Index Terms—Distributed amplifiers, traveling wave amplifiers, optoelectronic devices, high-speed integrated circuits, packaging

I. INTRODUCTION

For the assembly technology, an important technical problem that must be overcome is how to cope with parasitic effects [1]. As the bandwidth becomes wider and the frequency becomes higher, the effects of circuit patterns or structure increase significantly [1]. In particular, chip mounting is most crucial, where the wavelength of the electrical signal approaches the physical size of the mounting elements such as the package cavity, input/output leads, and bonding wires [1].

For achieving an excellent bandwidth performance [2] a DA topology is utilized for the MMIC. The idea of a DA is to use several small active devices in parallel instead of one large transistor and to separate its parasitic capacitances by high impedance transmission lines. The resulting small signal structure at the input and output is designed to behave like a 50 Ω artificial transmission line and therefore shows both small input and output reflection as well as flat gain over a large bandwidth. With this circuit topology, one can simultaneously have the high frequency characteristics of one unit-cell together with gain and output power performance of all unit-cells in parallel. This concept is often used for high speed broadband amplifiers with moderate gain.

II. CIRCUIT DESIGN OF THE MMIC

The circuit design of the MMIC is described in detail in [3]. The used topology is a distributed amplifier with four cascode unit-cells based on a pseudomorphic GaAs pHEMT low noise

process with 150 nm gate length from United Monolithic Semiconductors (UMS). A circuit schematic is shown in Fig. 1.

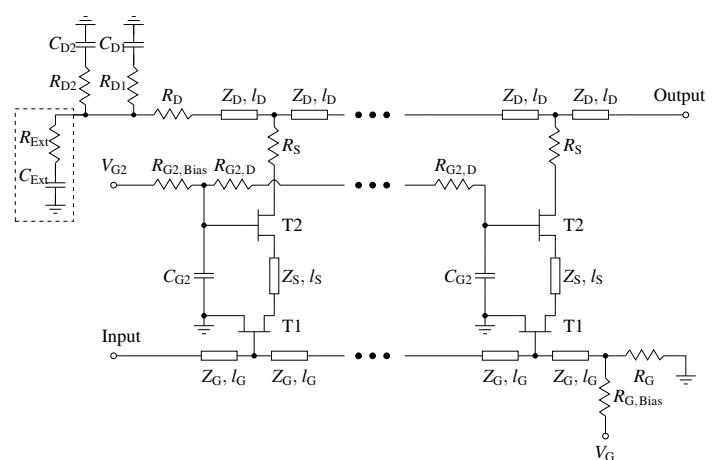


Fig. 1. Schematic of the MMIC. On the top left is the drain bias decoupling shown.

Despite the gate line, also at the artificial drain line a 50 Ω termination is needed for the reverse traveling wave. To have no dc-current flowing through the resistor R_D , serial blocking capacitors are needed. High frequency components of the wideband signal are already grounded on chip. To enable a flat frequency response down to very low frequencies, additionally an external SMD capacitor with a high capacitance of 100 nF has to be attached to the chip.

The transmission lines at the input and output are kept as short as possible. By this, the bond-wire inductance is embedded into the circuit design and compensates for the parasitic capacitance of the first and last transistor unit-cell. The circuit design was optimized for a bond-wire inductance of 0.1 nH.

The circuit performance up to 50 GHz is shown in detail in [3]. Measurements up to 110 GHz were carried out at two different bias points. For a bandwidth exceeding 60 GHz, a drain biasing of 3.0 V is applied via the internal bias-Tee of the measurement setup. Additionally a second gate voltage of $V_{G2} = 2.0$ V is used. The small signal measurements for this bias point are depicted in Fig. 2.

The measured gain close to dc equals 10.5 dB with a gain ripple of ± 1.0 dB between 10 MHz and 60 GHz. The -3 dB bandwidth equals 62.2 GHz. Up to 50 GHz, input reflections are smaller than -12 dB. Output reflections are lower than

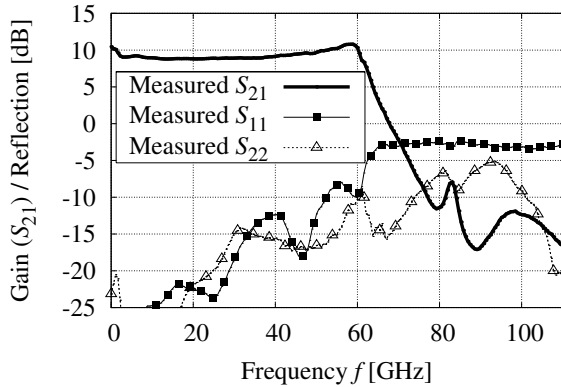


Fig. 2. On-wafer small-signal parameters, measured up to 110 GHz. For a drain biasing of $3V_{pp}$ the amplifier is biased for maximum bandwidth. For this bias point the gain close to dc equals 10.5 dB with a -3 dB bandwidth of 62.2 GHz.

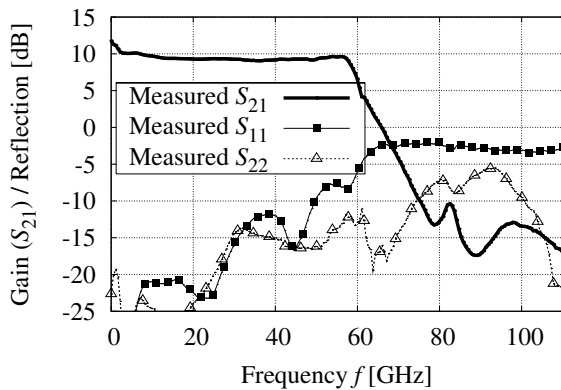


Fig. 3. On-wafer small-signal parameters, measured up to 110 GHz. A drain biasing of 5.0 V is applied for a flat frequency response. Between 2 GHz and 57.2 GHz the gain variation is within ± 0.6 dB. The gain at dc equals 11.8 dB.

-14 dB up to 50 GHz and less than -5 dB over the whole measurement band.

Alternatively the amplifier can be biased for higher gain with a very flat frequency response. In this case, the drain biasing equals to 5.0 V with a second gate voltage of 3.7 V. Small signal measurements at this bias-point are shown in Fig. 3.

Close to dc the gain equals 11.8 dB. The gain variation between 10 MHz and 57.8 GHz is ± 1.4 dB. The increased gain at low frequencies is due to the fact, that an additional external resistor with 10Ω is used in series to the external SMD capacitor. This resistor is needed to prevent a resonance between the on-chip capacitor-network and the parasitic inductance of the bond-wire which is needed to connect an external SMD capacitor to the artificial drain line. The external SMD capacitor is needed to have good bias decoupling down to frequencies in the kHz-range, especially if the amplifier is intended for applications in optical communication networks with NRZ signal encoding.

Between 2 GHz and 57.2 GHz the gain ripple is within

± 0.6 dB. For the bandwidth from 10 GHz up to the cut-off frequency of 57.2 GHz, the gain variation is even smaller and equals ± 0.3 dB. Input reflections are better than -9.6 dB up to 50 GHz. The output reflections are better than -10 dB up to 74 GHz and less than -5 dB over the whole 110 GHz measurement band.

For this amplifier, a demonstrator with 2.4 mm connectors is assembled, which is described in the following.

III. ASSEMBLY TECHNOLOGY

A. Substrate Material

At frequencies exceeding 20 GHz, the requirements for the substrate material are critical. The generation of unwanted rf-modes has to be prevented and substrate losses have to be small. Typically two types of substrates are used at the high frequency end. One is an Al_2O_3 based substrate. Losses for this substrate material are very small (typically $\tan \delta = 0.0002$ at 10 GHz). However, one disadvantage is that the material is very hard. Therefore it is critical to apply a via-hole process to it. In comparison, a Teflon based substrate is very soft and is perfectly suited for test-structures, since it can be easily cut and transmission lines can be trimmed to the desired length even after fabrication. Additionally a via-hole process is possible but critical, since processing is not easy. An other advantage is the very low dielectric constant ϵ_r of the substrate. Since the width of the microstrip line is wider for lower values of ϵ_r , etching of 50Ω microstrip lines can be done with a standard printed-circuit-board process.

Due to the above described advantages, a Teflon based rf-laminate was chosen as substrate material. Despite substrate materials for low frequencies, Rogers Corp. provides a Teflon based substrate (RT/Duroid 5880) which is typically intended for military applications. For the substrate height, a thickness of $127 \mu m$ was chosen to approximately fit the $100 \mu m$ height of the fabricated GaAs MMIC. This gives the possibility for short bond-wires if both, the amplifier and the substrate are fixed next to each other on a metal block. The copper cladding for this substrate equals to $17 \mu m$ and the dielectric constant is $\epsilon_r = 2.20$. The loss tangent $\tan \delta$ is very low and equals 0.0004 at 1 MHz and 0.0009 at 10 GHz. For this type of substrate, a via-hole process is developed using reactive ion etching and a gold galvanic process. The via-holes are already drilled by the standard printed-circuit-board process. To achieve stickiness of the gold vaporization at the via-hole walls, a reactive ion etching process was used providing some roughness to the substrate. The substrate is etched three times with five seconds and additional three minutes break to avoid too much heating of the substrate. Afterwards, gold vaporization is used to achieve conductivity of the via holes. This gold layer is very thin which results in a low conductivity of the via-holes. Thus, an additional gold galvanic process is applied to the substrate. The gold galvanic process is uncritical and a thick (approximately $1 \mu m$) gold layer is deposited to achieve a good conductivity of the via-holes.

B. Connector

As connector, an edge mount jack from the Rosenberger RPC 2.4 mm series is used. The Rosenberger connector 09K243-40ME3 provides easy assembly to the metal brass and

a very low insertion loss of $< 0.2 \text{ dB} \times \sqrt{f/\text{GHz}}$. The voltage standing wave ratio (VSWR) is below 1.5 up to 40 GHz.

C. Assembly

Typically there exist three ways for assembling an amplifier to an external rf-laminate. One possibility is to use flip-chip technology, with the amplifier placed up-side-down on top of an rf-substrate. In this case, grid ball bonds are used to have a smaller and well controlled parasitic inductance compared to bond-wires. This is especially useful in terms of high frequency operation. However, arranging of the amplifier to the pads on the substrate is critical. Especially, the ground-signal-ground pad spacing is only $70 \mu\text{m}$ for the already fabricated amplifier, which would additionally make the fabrication of the transmission lines critical. Additionally, there are other main road blocks for flip-chip technology. A lack of experience and proven design data requires additional efforts for production environment [4]. Furthermore, using flip-chip technology implies a basic change in design strategy and an additional bump fabrication step to the process flow on the wafer level at the foundry side [4]. Due to the above reasons, flip-chip technology is not utilized for this amplifier.

Another possibility is to mount both, the transmission line and the amplifier to a metal block. The transmission lines and the amplifier can thereby be fixed by a silver filled epoxy glue. The amplifier's input and output signal-lines are connected to the microstrip line of the rf-laminate by bond-wires.

This is a very elegant way to connect the amplifier and the substrate if both have approximately the same height. By this, the bond-wire length can be kept relatively short, reducing the parasitic inductance. This assembly technique is especially useful if a rigid substrate material like AlO_3 based materials is taken. In this case, the amplifier and the substrate can be fixed close to each other easily.

If the substrate material is suited for a via-hole process, then the amplifier can also be attached on top of the substrate. The via-holes of the rf-laminate provide a good ground to the backside of the MMIC. This makes the assembly-process easy, because all passive structures can be easily glued on the same piece of substrate. The above described assembly method is utilized for the amplifier described here and is depicted in Fig. 4.

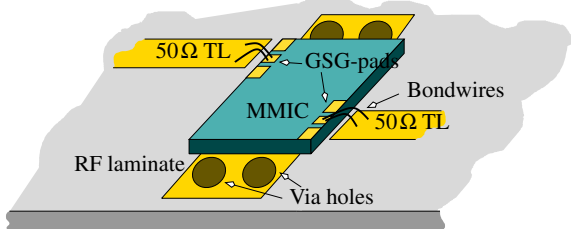


Fig. 4. MMIC mounted on top of an rf-laminate. Via-holes of the rf-laminate provide a good ground to the backside-metalization of the MMIC.

A micrography of the assembled amplifier is shown in Fig. 5.

On the top right, one can see a detailed view of the amplifier MMIC. Two bond-wires in parallel are used for connecting the

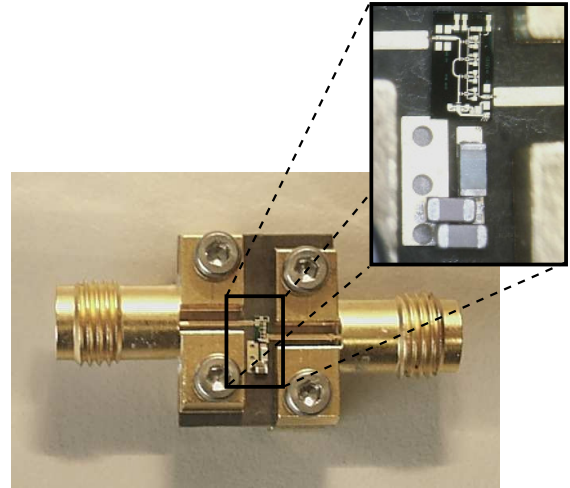


Fig. 5. Picture of the fabricated low noise amplifier with Rosenberger connectors attached. The picture on the left side shows a complete view of the amplifier, on the right side a zoomed in view shows more details of the assembled chip.

amplifier's input and output to the 50Ω transmission lines. Underneath the amplifier are several via-holes to provide a good ground and heat-sink to the amplifier.

Close to the on-chip drain line termination of the amplifier is a pad provided for connecting bond-wires to a substrate with external SMD components. From this pad, three bond-wires are connected to a pad with a 10Ω resistor. In series to the resistor, two capacitors in parallel are mounted to a pad with via holes to ground.

The size of the assembled amplifier is $1.2 \times 1.5 \times 1.1 \text{ cm}^3$ for the metal block or $3.1 \times 1.5 \times 2.7 \text{ cm}^3$ for the metal block with the 2.4 mm connectors.

IV. MEASUREMENT RESULTS FOR THE ASSEMBLED AMPLIFIER

Measurements of the small signal parameters of the amplifier are carried out with a single supply which provides a drain voltage of 3.0 V and a current of 55 mA, resulting in a total power consumption of 165 mW. The drain biasing is applied via the internal bias-Tee of the used vector network analyzer. Alternatively the drain biasing can be applied via the reverse drain line termination, see [3]. This would provide the advantage that no external bias-Tee is needed, but at the expense of an increased power consumption. The gate of the common source transistors is grounded via the 50Ω resistor of the artificial gate line termination. No additional gate biasing is used for both, the common source and the common gate transistor. Applying biasing to the gates could slightly improve gain flatness and overall gain performance, but at the expense of increased assembly effort and therefore cost. The small signal measurements of the assembled amplifier are shown in Fig. 6.

Near dc, the gain equals to 11.3 dB due to an external resistor of 10Ω used for decoupling of the on-chip capacitances and the bond-wire inductance. This resistor was not included into original simulations and therefore results in a slightly increased gain at low frequencies. However, this problem can be easily overcome with a modified chip design as is shown

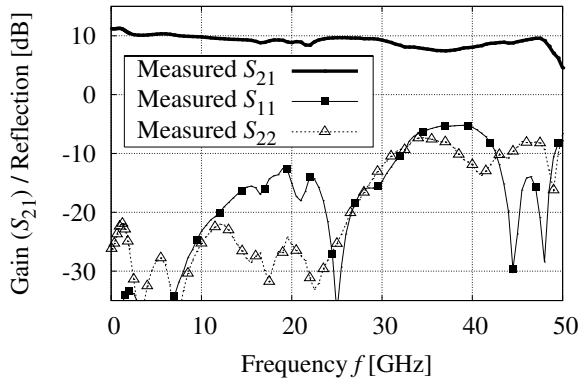


Fig. 6. Measured small-signal performance of the mounted low-noise amplifier biased with a drain voltage of 3 V. At 2.0 GHz the gain equals to 10.4 dB with a -3 dB bandwidth of 48.5 GHz. Due to the external bias decoupling, the gain increases to 11.3 dB close to dc.

for example in [5]. Input and output reflections are better than -12 dB up to 30 GHz. Over the whole measurement bandwidth of 50 GHz reflections are still less than -5 dB.

V. SUMMARY

In this paper we presented new measurement results up to 110 GHz for an earlier published amplifier [3]. A drain biasing of 3 V results in a gain of $10.5 \text{ dB} \pm 1.0 \text{ dB}$ up to 60 GHz and a -3 dB bandwidth in excess of 62 GHz. This amplifier is then mounted on top of a Teflon based rf-laminate (Ro5880) with 50Ω transmission lines at the input and output of the amplifier. A via-hole process was developed for the rf-laminate to enable easy attachment of the amplifier and SMD components needed for off-chip drain bias decoupling. Rosenberger 09K243-40ME3 connectors are used to enable attachment to 2.4 mm connectors. The assembled amplifier shows a gain of 10.4 dB at 2 GHz with a -3 dB cut-off frequency of 48.5 GHz. A bandwidth extension to lower frequencies is possible by a redesign of the on-chip termination network of the MMIC. Input and output reflections are better than -12 dB up to 30 GHz.

VI. ACKNOWLEDGMENTS

The authors would like to thank the "Fraunhofer Institute for Reliability and Microintegration IZM" for performing small-signal measurements of the amplifier MMIC up to 110 GHz.

REFERENCES

- [1] T. Shibata, S. Kimura, H. Kimura, Y. Imai, Y. Umeda, and Y. Akazawa, "A Design Technique for a 60 GHz-Bandwidth Distributed Baseband Amplifier IC Module," *IEEE Journal of Solid-State Circuits*, vol. 29, no. 12, pp. 1537–1544, Dec. 1994.
- [2] K. Takahata, Y. Muramoto, H. Fukano, K. Kato, A. Kozen, S. Kimura, Y. Imai, Y. Miyamoto, O. Nakajima, and Y. Matsuoka, "Ultrafast Monolithic Receiver OEIC Composed of Multimode Waveguide p-i-n Photodiode and HEMT Distributed Amplifier," *IEEE Journal of Selected Topics in Quantum Electronics*, vol. 6, no. 1, pp. 31–37, Feb. 2000.
- [3] M. Häfele, K. Beilenhoff, and H. Schumacher, "A GaAs PHEMT Distributed Amplifier with Low Group Delay Time Variation for 40 GBit/s Optical Systems," in *Proc. 33th European Microwave Conf.*, Munich, Germany, Oct. 2003, pp. 1091–1094.
- [4] W. Heinrich, "The Flip-Chip Approach for Millimeter-Wave Packaging," *IEEE Microwave Magazine*, vol. 6, no. 3, pp. 36–45, Sep. 2005.

- [5] M. Häfele, A. Trasser, K. Beilenhoff, and H. Schumacher, "A GaAs Distributed Amplifier with an Output Voltage of $8.5 V_{pp}$ for 40 Gb/s Modulators," in *Proc. 13th Gallium Arsenide and other Compound Semiconductors Application Symposium*, Paris, France, Oct. 2005, pp. 345–348.

Cavity Perturbation Method for Temperature Controlled Characterization of Liquid Crystals at 38 GHz

A. Penirschke¹, S. Mueller¹, F. Goelden¹, A. Lapanik², V. Lapanik³, V. Bezborodov³, W. Haase² and R. Jakoby¹

¹Technische Universität Darmstadt, Institut für Hochfrequenztechnik, Merckstr. 25, 64283 Darmstadt, Germany

²Technische Universität Darmstadt, Institut für Physikalische Chemie, Petersenstrasse 20, 64287 Darmstadt, Germany

³Belarusian State University, Institute of Applied Physics, Minsk 220064, Belarus

Abstract—Liquid Crystals (LCs) are very promising agile materials for tunable microwave components. Hence, precise microwave measurements are required to characterize these materials.

In this paper measurement results of five novel Nematic Liquid Crystals (NLCs) are presented. The measurements were done using a cavity perturbation method with an aperture coupled rectangular cavity at 38 GHz between -5°C and 135°C . The complex permittivities of these samples are extracted and tunability as well as material quality factor - a ratio between tunability and highest material losses - of the LCs are measured using an external magnetostatic field in order to orient the LC-molecules parallel and perpendicular to the RF-field in the cavity. The results show that all NLCs exceed the quasi-standard LC K15 concerning microwave tunability, material quality factor and nematic temperature range.

I. INTRODUCTION

Liquid Crystals (LCs) are promising materials for frequency agile components like tunable filters, phase shifters, reflectarrays etc. at microwave frequencies, especially above 10 GHz [1] - [4]. The exact knowledge of the LC material parameters is necessary for the realization of such components. The cavity perturbation method is well suited for the precise characterization of the complex permittivity and the complex permeability of material samples [5]. Measurement results of five NLC mixtures at 38 GHz in a temperature range from -5°C up to 135°C exhibits a large nematic phase from room temperature at least up to 135°C .

Measurement errors such as mispositioning of the probe in the resonator, systematic errors due to finite frequency and quality factor resolution of the RF measurements or inaccurate temperature measurements leads to uncertainties in the extraction of the complex permittivity and permeability. An estimation of the influence of these errors in the extracted parameters is carried out in this paper.

II. PROPERTIES OF LIQUID CRYSTALS

LCs exhibit one or more mesophases between solid (crystalline) and liquid (isotropic) phase. The mesophases can be separated by orientational and positional far range order into nematic, smectic, and cholesteric.

In the following, only LCs with a nematic mesophase (NLCs) are investigated. NLCs exhibit a far range orientational order. The orientation of such LCs can be realized by the following external influences:

- 1) electrostatic fields,
- 2) magnetostatic fields,
- 3) surface interactions with specific prepared materials like mechanically rubbed polyimide films.

A defined director N points in the same direction as the NLC molecules. Using the Maxwell relations, a dielectric tunability can be defined by the different microwave permittivities parallel and perpendicular to the director N compared to the RF-field:

$$\tau_\varepsilon = \frac{\varepsilon_{r,\parallel} - \varepsilon_{r,\perp}}{\varepsilon_{r,\parallel}} \quad (1)$$

Besides a large tunability also low insertion losses are required at RF-frequencies. Therefore a quality factor η_ε can be defined by the ratio of the tunability and the maximum loss factor $\tan\delta_{\varepsilon,max}$:

$$\eta_\varepsilon = \frac{\tau_\varepsilon}{\tan\delta_{\varepsilon,max}} \quad (2)$$

III. RESONATOR SETUP

The cavity perturbation method is widely used in the field of precise material characterization of low-loss materials at high frequencies [6], [7].

In this paper a rectangular resonator operating at the TE_{102} -Mode is used for characterization of the complex permittivity of a small perturber located at the maximum electric field inside the cavity. In a previous paper [5] we found, that the dielectric anisotropy of NLCs dominates the diamagnetic anisotropy distinctly, so that only the dielectric properties are investigated here.

In the center of the cavity the magnetic field reaches a maximum value while the electric field becomes zero. At a quarter of the resonator length the electric field is maximum while the magnetic field becomes zero. To measure a perturber at these positions, two insertion holes are drilled in the cavity walls in order to place a PTFE-tube in the maximum electric and magnetic fields of the cavity. Only the hole at the maximum electric field is necessary to extract the complex permittivity.

For a z-oriented waveguide resonator with perfect conduct-

ing walls, the following field equations are valid:

$$\begin{aligned} \underline{E}_X &= \underline{E}_Z = \underline{H}_Y = 0 \\ \underline{E}_Y &= G \frac{\pi}{a} \sin\left(\frac{\pi}{a}x\right) \sin\left(\frac{2\pi}{c}z\right) \end{aligned} \quad (3)$$

$$\underline{H}_X = \frac{k_z}{\omega\mu} G \frac{\pi}{a} \sin\left(\frac{\pi}{a}x\right) \cos\left(\frac{2\pi}{c}z\right) \quad (4)$$

$$\underline{H}_Z = -G \frac{k^2 - k_z^2}{j\omega\mu} \cos\left(\frac{\pi}{a}x\right) \sin\left(\frac{2\pi}{c}z\right) \quad (5)$$

Two assumptions are necessary to find closed form solutions for complex $\underline{\varepsilon}_r$:

- 1) The perturbation is small so that the energy in the cavity remains the same as without perturbation,
- 2) The E- and H-fields outside the perturber remain unchanged by its presence.

At the electrical field maximum, the electrical flux density \vec{D} has only a component in y-direction [5]. \underline{D}_y is described by

$$\underline{D}_y = \underline{\varepsilon}_{r,y} \underline{E}_y \quad (6)$$

An external magnetostatic field orients the NLC molecules in parallel to the RF-field distribution. The x-directed magnetostatic field orients the molecules perpendicular to the RF-field and therefore $\underline{\varepsilon}_{r,y} = \underline{\varepsilon}_{r\perp}$ can be analyzed, whereas $\underline{\varepsilon}_{r,y} = \underline{\varepsilon}_{r\parallel}$ can be extracted with an y-directed magnetostatic field.

Using [6] and [7], a complex resonance peak is described by

$$\begin{aligned} \frac{\omega_{LC} - \omega_0}{\omega_0} &\approx \frac{f_{r,LC} - f_{r,0}}{f_{r,LC}} + j \frac{1}{2} \left(\frac{1}{Q_{LC}} - \frac{1}{Q_0} \right) \\ &= \frac{1 - \underline{\varepsilon}_r}{2} \frac{\iiint_{V_1} \underline{E}_0 \underline{E}_{LC}}{\underbrace{\iiint_V |\underline{E}_0|^2}_C} \end{aligned} \quad (7)$$

where $f_{r,LC}, Q_{LC}$ are the resonance frequency and the Q-factor of the perturbed cavity and $f_{r,0}, Q_0$ are the parameters for the unperturbed cavity. V_1 is the volume perturber and V is the complete resonator volume. These parameters can be obtained from the absolute value of the transmission $|S_{21}(f)|$ assuming that the resonator is weakly coupled. Within the

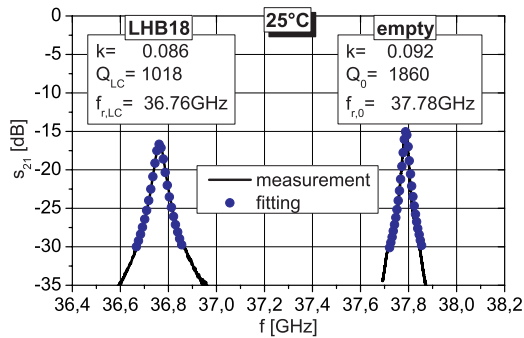


Fig. 1. Parameter extraction using Lorenz fitting by means of the example of LHB18 at 25° C.

–3dB bandwidth around the resonance maximum the curve progression matches the Lorentz-Function [10]

$$|S_{21}(f)|^2 = \frac{4 \cdot k^2}{(1 + 2k)^2 + Q^2 \cdot \left(\frac{f}{f_r} - \frac{f_r}{f} \right)^2}, \quad (8)$$

where f_r is the resonance frequency and k is the coupling factor of the RF-signal into and out of the resonator. Using a standard curve fitting algorithm, the parameters of the Lorentz-Function can be adjusted so that the Lorentz-Function fits the resonance peak. As shown in Fig. 1, the fitting algorithm is very suitable for an extraction of coupling factor, quality factor and resonance frequency.

The constant C in equation (7) only depends on the position of the perturber in the cavity and its geometry and can be calculated a priori.

$\underline{\varepsilon}_r$ can be calculated with the following equation:

$$\underline{\varepsilon}_r = 1 - \frac{2}{C} \frac{f_{r,LC} - f_{r,0}}{f_{r,LC}} + j \frac{1}{2} \left(\frac{1}{Q_{LC}} - \frac{1}{Q_0} \right) \quad (9)$$

A. 38 GHz Resonator Design

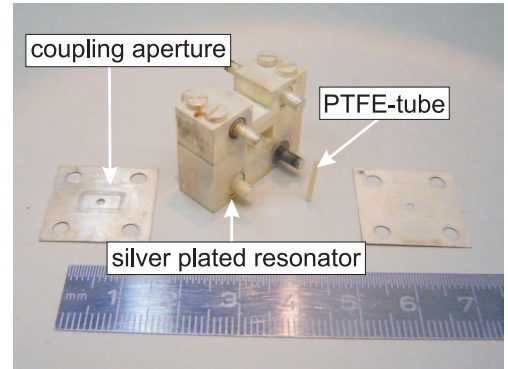


Fig. 2. Aperture coupled rectangular waveguide resonator at 38 GHz.

The rectangular resonator at 38 GHz, as shown in Fig. 2, consists of a silver plated standard Ka-band waveguide with the length of 9.45 mm, shorted at both ends. The coupling is realized by two identical cylindrical apertures at the ends of the resonator section. The perturber consists of a PTFE-tube with an inner radius of 0.4 mm and a wall thickness of 0.05 mm, filled with air or LC, respectively. In order to insert the probe at the maximum electric field, the insertion whole at one quarter of the resonator length is used. The unperturbed Q-factor is $Q_{empty} \approx 1900$ at 38.24 GHz.

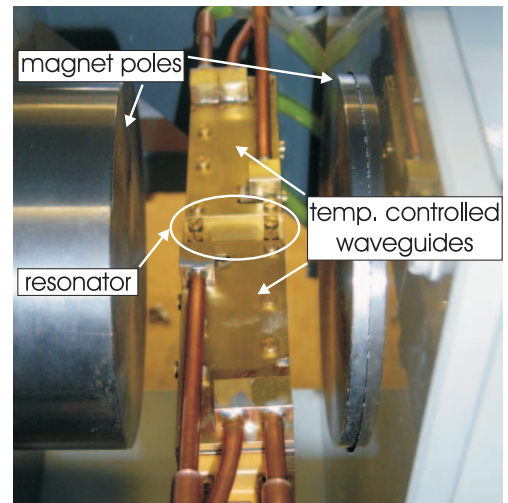


Fig. 3. Measurement setup at 38 GHz.

The temperature is adjusted by two temperature controlled waveguides at both ends of the resonator, as shown in Fig.

3. The temperature is increased from -5°C up to 135°C . A temperature sensor detects the temperature of the resonator.

B. Error Estimation

The insertion holes of the resonator affect the electric as well as the magnetic fields in the cavity. The diameter of both insertion holes is less than $1/10$ of the waveguide width and the length of the drilled hole is about $1/2$ of the cavity height. Estin and Bussey [9] showed that in this case the influence of the hole is not significantly large and therefore, it is neglected here.

With this setup a direct temperature measurement of the NLC is not possible. The PTFE-tube isolates the NLC from the metallic resonator. The temperature of the NLC in the tube differs by $\pm 1.5^\circ\text{C}$ compared to the resonator temperature. The nonlinearity of the temperature sensor is below $\pm 0.5^\circ\text{C}$ in the investigated temperature range. Therefore, a maximum temperature deviation of $\pm 2^\circ\text{C}$ between the detected temperature of the cavity and the real temperature of the LC is assumed.

A magnetic field is used to orient the LCs into two orthogonal directions. The LCs are aligned to the desired direction by a magnetic field strength of $B = 0.35\text{ T}$, which is more than 150% of the minimum field strength needed in this case and therefore misalignment errors are neglected.

The uncertainty of $\underline{\varepsilon}_r$ caused by the finite frequency resolution can be estimated by the total differential:

$$\begin{aligned} \Delta \underline{\varepsilon}_r = & \left| \frac{\partial \underline{\varepsilon}_r}{\partial f_{r,0}} \right| \cdot \Delta f_{r,0} + \left| \frac{\partial \underline{\varepsilon}_r}{\partial f_{r,LC}} \right| \cdot \Delta f_{r,LC} \\ & + \left| \frac{\partial \underline{\varepsilon}_r}{\partial Q_0} \right| \cdot \Delta Q_0 + \left| \frac{\partial \underline{\varepsilon}_r}{\partial Q_{LC}} \right| \cdot \Delta Q_{LC} \end{aligned} \quad (10)$$

Inserting equation (9) into (10) results in:

$$\Delta \varepsilon_r = \frac{2}{C f_{r,LC}} \left(\Delta f_{r,0} + \frac{f_{r,0}}{f_{r,LC}} \Delta f_{r,LC} \right) \quad (11)$$

$$\Delta \tan \delta = \frac{C f_{r,LC}}{4} \cdot \frac{\left(\frac{\Delta Q_0}{Q_0^2} + \frac{\Delta Q_{LC}}{Q_{LC}^2} \right)}{\left(\Delta f_{r,0} + \frac{f_{r,0}}{f_{r,LC}} \Delta f_{r,LC} \right)} \quad (12)$$

With a frequency step size of 2 MHz and an extraction inaccuracy of ± 5 for the loaded Q factor, maximum absolute systematic errors of $\Delta \varepsilon_r \leq 0.0076$ and $\Delta \tan \delta \leq 0.0027$ are possible. The relative measurement uncertainty of ε_r is less than 0.4% for an absolute permittivity of $\varepsilon_r = 2$ and the relative error for $\tan \delta$ is more than 27% for $\tan \delta = 0.01$.

IV. MEASUREMENT RESULTS

The temperature dependency of the NLCs is measured versus rising temperature in steps of 3°C around the phase transition from crystal to nematic and in steps of $10 \dots 20^\circ\text{C}$ in the nematic phase.

In Fig. 4, the measured parallel and perpendicular permittivity ($\varepsilon_{r,\parallel} / \varepsilon_{r,\perp}$) as well as the parallel and perpendicular ($\tan \delta_{\parallel} / \tan \delta_{\perp}$) dielectric losses are presented.

Compared to the "quasi-standard"-NLC K15 Fig. 4(a), all mixtures exhibits a much broader anisotropic temperature phase from about 15°C up to at least 135°C . The transition from crystal to nematic phase of LHB17 only (Fig. 4(e)) is below -5°C , which leads to an anisotropic phase with a span of more than 140°C . The behaviour of LHB17 below 5°C could be explained by the supercooling effect of NLC mixtures, which will be further investigated.

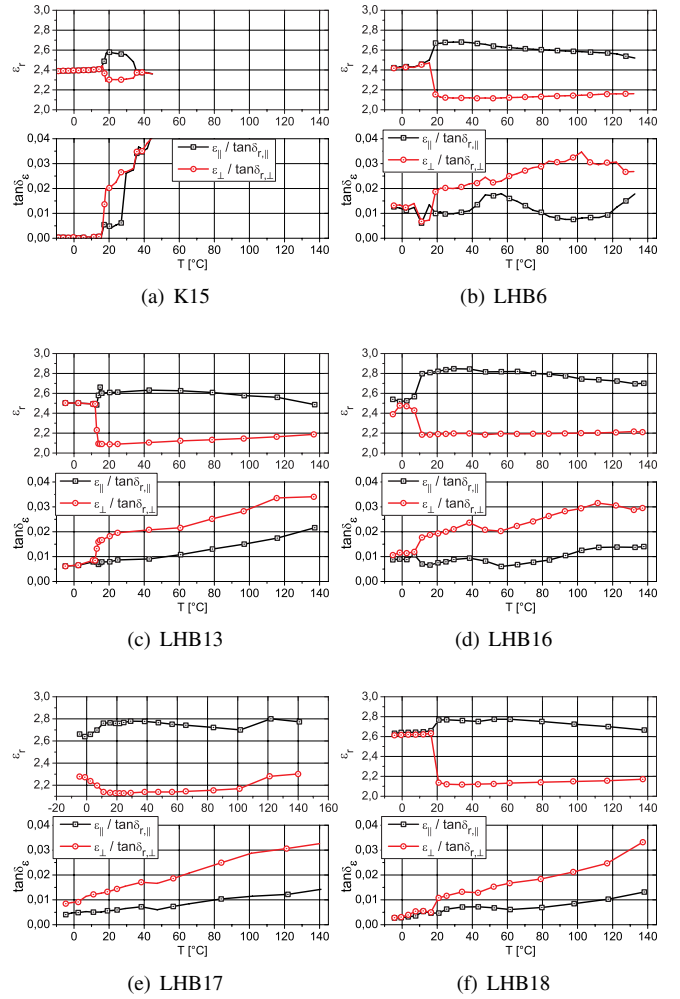


Fig. 4. Measured parallel and perpendicular permittivity ($\varepsilon_{r,\parallel} / \varepsilon_{r,\perp}$) as well as the parallel and perpendicular ($\tan \delta_{\parallel} / \tan \delta_{\perp}$) dielectric losses versus temperature.

For all NLCs, the dielectric losses parallel and perpendicular increase by rising temperature, whereas in the nematic phase the perpendicular losses $\tan \delta_{\perp}$ exceeds the parallel losses $\tan \delta_{\parallel}$. An abrupt rise of the perpendicular losses from crystal to nematic phase occurs. The parallel dielectric losses remain almost constant within this phase transition.

According to equation (1) and (2), the tunability τ_{ε} and the material quality factor η_{ε} are calculated from the measurement data and presented in Fig. 5.

All mixtures exhibit a tunability τ_{ε} of more than twice the tunability of K15. Nevertheless, the mixtures can be separated into two groups with different tunability in the whole nematic phase. The tunability of LHB16, LHB17, and LHB18 (group A) is 3...4% higher than for LHB6 and LHB13 (group B). The maximum achieved tunability is 23.5% for LHB18. The tunability decreases by rising temperature, which can be explained by a decrease of the far range orientational order of NLCs. Obviously, LHB17 exhibits a tunability of approximately 15% between 5°C and room temperature.

The highest material quality factor is 21 for LHB18 at 20°C , due to the lowest perpendicular losses of 0.01. For LHB17, the maximum material quality factor of 18.5 occurs already at 11°C . The NLCs LHB6, LHB13, and LHB16

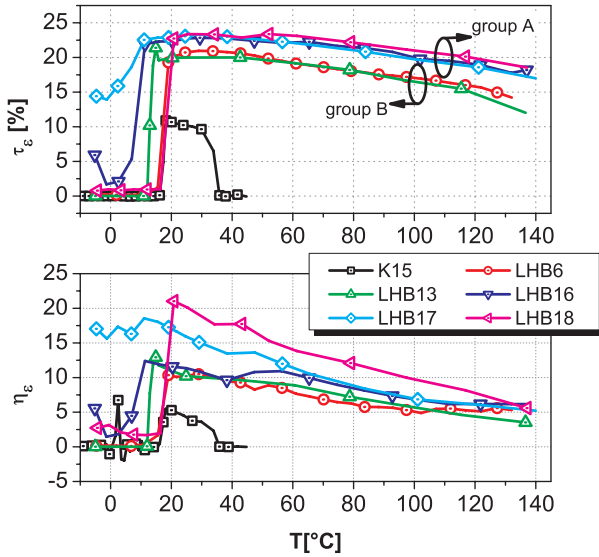


Fig. 5. Tunability τ and material quality factor η versus temperature (see equations (1) and (2)).

show almost identical behaviour versus temperature with a maximum material quality factor of about 12. As shown in Fig. 5, all NLCs are best suitable for an operation around room temperature concerning tunability as well as material quality factor.

In Tab. I, the parameters permittivity and losses (parallel and perpendicular) as well as tunability and material quality factor at 0° C, 25° C, and 100° C are presented.

TABLE I
MEASURED MATERIAL PARAMETERS OF NLCs AT 0° C, 25° C, AND 100° C, ALL VALID AT 38 GHz.

	$T = 0^\circ \text{C}$					
	ϵ_{\parallel}	$\tan \delta_{\parallel}$	ϵ_{\perp}	$\tan \delta_{\perp}$	τ	η
K15	2.39	0.001	2.39	0.001	0%	0
LHB6	2.42	0.012	2.42	0.013	0%	0
LHB13	2.50	0.007	2.50	0.007	0%	0
LHB16	2.52	0.009	2.48	0.012	1.6%	2.3
LHB17	2.64	0.005	2.27	0.009	14%	15.6
LHB18	2.64	0.003	2.62	0.003	0.8%	2.5

	$T = 25^\circ \text{C}$					
	ϵ_{\parallel}	$\tan \delta_{\parallel}$	ϵ_{\perp}	$\tan \delta_{\perp}$	τ	η
K15	2.57	0.005	2.30	0.022	10.5%	4.77
LHB6	2.68	0.010	2.12	0.020	20.9%	10.4
LHB13	2.61	0.009	2.09	0.020	19.9%	10.0
LHB16	2.84	0.008	2.19	0.020	22.9%	11.4
LHB17	2.77	0.006	2.13	0.014	23.1%	16.5
LHB18	2.77	0.006	2.12	0.012	23.5%	19.6

	$T = 100^\circ \text{C}$					
	ϵ_{\parallel}	$\tan \delta_{\parallel}$	ϵ_{\perp}	$\tan \delta_{\perp}$	τ	η
K15	-	-	-	-	-	-
LHB6	2.58	0.008	2.15	0.035	16.7%	4.8
LHB13	2.58	0.015	2.15	0.028	16.7%	6.0
LHB16	2.74	0.013	2.20	0.029	19.7%	6.8
LHB17	2.70	0.011	2.17	0.029	19.6%	6.8
LHB18	2.72	0.008	2.15	0.021	21.0%	10.0

At 0° C, except LHB17, nearly no anisotropy occurs, because of the presence of the crystalline phase. Nevertheless, the losses of K15 in the crystalline phase is in the range of low loss standard substrates such as *RT-Duroid* or *LCP* from Rogers Corp. At room temperature (25° C), the highest tunability of LHB18 of 23.5% occurs. Even at high temperatures like 100° C, the mixtures still exhibit a tunability and a material quality factor above 16.7% and 4.8, respectively.

V. CONCLUSION AND OUTLOOK

Several liquid crystals are characterized by using a cavity perturbation method at 38 GHz between -5° C and 135° C. The complex permittivity is presented for K15 and five novel NLC-mixtures. Using horizontal and vertical magnetostatic fields, the molecules are oriented in order to characterize the dielectric tunability of the NLCs.

All NLC mixtures exceed the quasi-standard NLC K15 concerning temperature range of the nematic phase, tunability, and material quality factor. LHB18 exhibits the highest material quality factor of 21 and LHB17 exhibits the broadest anisotropic temperature range between at least -5° C and 135° C. Concerning the tunability, 3 NLCs (LHB16, LHB17, and LHB18) show nearly identical properties with a maximum tunability of up to 23.5%. Altogether, none NLC fulfills all possible requirements. Therefore, the choice of a LC depends on the specific requirements of an application.

It could be shown, that a careful design of NLC mixtures can increase the quality factor η_e by at least a factor of 3.75 compared to K15. Beyond optical applications, such highly anisotropic mixtures with additional low losses could open up totally new fields of microwave and millimeter wave applications like phase shifters [1], [2] or reflectarrays [4].

REFERENCES

- [1] C. Weil, St. Müller, P. Scheele, P. Best, G. Lüssem, and R. Jakoby, "Highly anisotropic liquid-crystal mixtures for tuneable microwave devices", in *electronics letters*, vol. 39, No. 24, November 2003, pp. 1732-1734
- [2] St. Müller, P. Scheele, C. Weil, M. Wittek, C.Hock, and R. Jakoby, "Tunable Passive Phase Shifter for Microwave Applications using Highly Anisotropic Liquid Crystals", in *IEEE IMS*, Fort Worth, June 2004, pp. 1153-1156.
- [3] St. Müller, C. Weil, P. Scheele, Y. Kryvoschupka, and R. Jakoby, "Novel Liquid Crystals for Tunable Microwave Components", in *IEEE IMS2004*, Workshop WMC
- [4] R. Marin, A. Mössinger, J. Freese, S. Müller, and R. Jakoby, Basic, "Investigations of 35GHz Reflectarrays and Tunable Unit-Cells for Beamsteering Applications", in *Proc. 35th European Microwave Conf.*, October 2005, pp.2015-2018
- [5] A. Penirschke, St. Müller, P. Scheele, C. Weil, M. Wittek, C.Hock, and R. Jakoby, "Cavity Perturbation Method for Characterization of Liquid Crystals up to 35 GHz", in *IEEE Microwave Conference*, Munich, October 2004, pp. 545-548.
- [6] R. G. Carter, "Accuracy of Microwave Cavity Perturbation Measurements", in *IEEE Trans. on Microwave Theory and Techniques*, Vol. 49, No. 5, May 2001, pp. 918-923.
- [7] L. Chen, C. K. Ong, B. T. G. Tan "Amendment of Cavity Perturbation Method for Permittivity Measurement of Extremely Low-Loss Dielectrics", in *IEEE Trans. on Instrumentation and Measurements*, Vol. 48, No. 6, December 1999, pp. 1031-1037.
- [8] H. Kawabata, H. Tanpo, Y. Kobayashi "A rigorous analysis of a TM₀₁₀ mode cylindrical cavity to measure accurate complex permittivity of liquid", in *IEEE Microwave Conference*, Vol.2, October 2003, pp 759-762.
- [9] A.J. Estlin, H.E. Bussey "Errors in Dielectric Measurements Due to a Sample Insertion hole in a Cavity", in *IRE Transactions on microwave Theory and Techniques*, Vol.8, No 6, November 1960, pp 650-653.
- [10] M. Sucher, and J. Fox, "Handbook of Microwave Measurements Volume II", in *Polytechnic Press*, 1963

Evaluation of Potting Possibilities for RF Circuits up to 24 GHz

Magnus O. Olbrich, Wolfgang Kiermeier, Erwin Biebl

Technische Universitaet Muenchen , Fachgebiet Hoechstfrequenztechnik, Arcisstr. 21, 80333 Muenchen, Germany, +498928923930, olbrich@tum.de

Electrical parameters of potting materials are usually specified by the manufacturer only up to some MHz. We have determined the real part of relative permittivity and loss tangent of a potting compound at discrete frequencies up to 24 GHz by use of ring resonators. The results are validated by the design and measurement of a bandpass filter at 11 GHz. For designing this test circuit the gained potting material parameters were already included in the simulation.

Keywords-component; potting; encapsulation;

I. INTRODUCTION

Encapsulants and potting compounds provide environmental protection against moisture or mechanical stress and electrical isolation for electronic components. Their use is widely spread for dc and low frequency ac circuits, but not yet for rf circuits due to their influence on the rf circuit characteristics.

However also for rf circuits potting would be interesting from a mechanical and moisture protection point of view. The manufacturers of potting materials specify the rf relevant material properties usually only up to some MHz. The very ideal potting material characteristics would be the same as from air. Therewith a circuit can be designed and measured with air, and afterwards be produced and potted without any change. A potting material with the same characteristics as the substrate would result in a different kind of line. E.g. a microstrip line could be transferred into a stripline. Therefore the circuit has to be potted also for measurement. But this would only be a mentionable effort for very low lots of the final product. For a mass market product this additional effort is negligible and good line characteristics, e.g. real TEM propagation without dispersion instead of quasi TEM mode would be achieved.

References [1] and [2] discuss microstrip characteristics with a dielectric overlay in general. This work evaluates the possibilities of potting planar rf circuits up to 24 GHz in terms of additional attenuation and inclusion of the gained material parameters into the simulation.

II. BASICS

Whereas for dc potting parameters like heat conductivity or dielectric strength play the most important role, for higher frequencies additional parameters have to be taken into account. As for the substrate material the permittivity of the

dielectric ϵ in its complex form becomes relevant the same holds true for the potting material.

The difference for the relative permittivity lies in the susceptibility of electromagnetic fields. Potting compounds are adhesives or resins. For understanding rf characteristics the molecule structure has to be considered. In general two different molecular structures exist. Nonpolar ones like polyethylene have symmetric molecule structures and therefore are only susceptible for electromagnetic fields by the displacement of the electron cloud compared to the core. Whereas polar ones like polyvinyl chloride (PVC) show a dipole moment to electromagnetic field by their asymmetric structure. These two configurations are shown exemplarily in Fig. 1. For rf applications only nonpolar materials are suitable due to their much lesser losses.

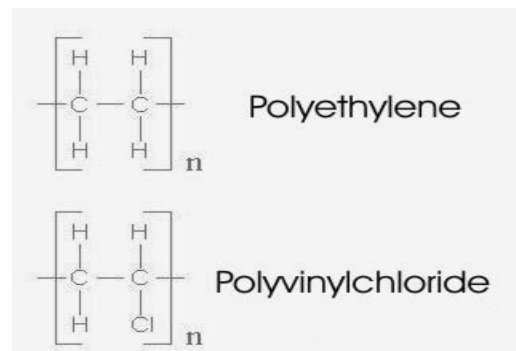


Figure 1. Example of nonpolar and polar molecules.

Especially at high frequencies dielectric constants are often determined by use of resonators. For rf design the relative permittivity in its complex form has to be known. We specify the real part of the relative permittivity ϵ_r' and the $\tan\delta$, because these parameters are given to the simulation tool and are equipollent to the complex form.

From the various forms of resonators the ring resonator in a microstrip line technology was chosen. Compared to simple straight open ended designs, ring resonators have the best quality factor. This is because of the elimination of open end fringing and thereby sharp defined resonant length. Furthermore, a considerably large contact area to the potting resin is realized this way. The ring itself as well as the feeding

lines were designed for a line impedance of 50 Ohms at the respective designated frequency. Coupling was realized at both sides as shown in Fig. 2 using 0.15 mm wide gaps. This causes some distortion in the results due to the influence of the potting material not only on the ring but also on the coupling. However the test design measurements showed that this effect is negligible, because the 2D analysis simulation is not only applied to the resonator itself, but in fact to the whole circuit including the coupling section. This can easily be achieved by a simulation with a complete upper hemisphere consisting of the respective potting material.

The final dielectric constants cannot be derived directly from the comparison of empty and potted circuit measurements because of the unknown asymmetric electric field distribution over and below the microstrip. Therefore the measured resonator center frequencies and quality factors have to be transferred into a 2D EM simulation program, varying the simulation dielectric values of the overlay to achieve coincidence of measured and simulated parameters.

Preliminary tests and simulations showed that thin layers of potting compounds were sufficient for satisfactory precision. No further frequency shift or damping occurred above a height of approximately 5 mm. Thus all measurements were taken using 10 mm high layers to certainly eliminate thickness influence.

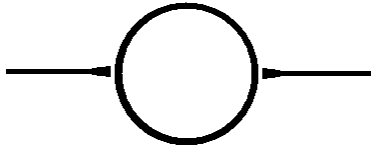


Figure 2. Ring resonator with side coupling.

III. CIRCUITS

The frequency range was evaluated by certain discrete values to keep the effort manageable. Resonator circuits were designed and fabricated for 2.4 GHz, 5.8 GHz, 12 GHz and 24 GHz, because these frequencies represent the needs of most technical applications. To keep the size of the circuit small for 2.4 GHz the substrate CER-10 with a high permittivity of 9.5 was used. For the other circuits TLP-5-0100 substrate with a permittivity of 2.2 was utilized. The high permittivity substrate would shrink these circuits to a size that brings the fabrication accuracy to its limits. Moreover, and especially important for the higher frequencies, the TLP substrate has lower losses.

Different mounting and supports were used to comply the diverse demands of the frequency bands. Exemplarily the circuit used for 12 GHz, and also for 24 GHz by exciting the first harmonic, is shown in Fig. 3. A small paper tube on top of resonator and coupling serves as a resin container and prevents the mounting from being glued. At 2.4 GHz and 5.8 GHz standard SMA printed-circuit-connectors in conjunction with a metal resin-container were applied, see Fig. 4.



Figure 3. Mounting of the 12GHz & 24 GHz resonator.

IV. MEASUREMENTS

One of the evaluated potting materials (amongst some epoxy and polyurethane resins) was the KC-Produkte SH 33650 that is originally intended to cushion vibrations and to firm up the mechanical strength. It is a copolymer of polyethylene and polyvinyl acetate (EVA) that was specified by KC at 50 Hz ($\epsilon_r' = 2.1$; $\tan\delta < 0.001$). In contrast to the more traditional 2-component based potting systems it has to be applied to the circuit by heating it up to 120 °C where it becomes liquid.



Figure 4. Potted resonator for 5.8 GHz.

Fig. 4 shows the potted 5.8 GHz resonator that was measured by a network vector analyzer. In this work $|S_{21}|$ was measured and used for the following analysis. The potting compound changes the resonators centre frequency and the quality factor compared to a measurement before the potting. The gained parameters for the different frequencies are given in table I. It is obvious that they are comparable to those of usual microwave substrates.

TABLE I. MEASURED PARAMETERS FOR KC SH 33650

Frequency	2.4 GHz	5.8 GHz	12 GHz	24 GHz
ϵ_r'	2.25	2.27	2.27	2.15
$\tan\delta$	0.001	0.007	0.01	0.01

A further series of measurements shall demonstrate the comparably poor rf performance of a fast curing 2-component epoxy resin, that is extensively used for more traditional low frequency potting applications, namely the R+G “5 minute epoxy”. The values for its relative permittivity and loss tangent can be found in table II (measured 15 min after potting) and table III (measured 1 day after potting). The much worse values of the uncured / partially cured epoxy are due to ionic components in the resin.

TABLE II. MEASURED PARAMETERS FOR EPOXY RESIN, 15 MIN CURED

Frequency	2.4 GHz	5.8 GHz	12 GHz	24 GHz
ϵ_r'	3.75	3.55	3.25	2.90
$\tan\delta$	0.09	0.09	0.08	0.1

TABLE III. MEASURED PARAMETERS FOR EPOXY RESIN, 1 DAY CURED

Frequency	2.4 GHz	5.8 GHz	12 GHz	24 GHz
ϵ_r'	3.5	3.4	3.0	2.8
$\tan\delta$	0.03	0.07	0.06	0.08

V. TEST CIRCUIT

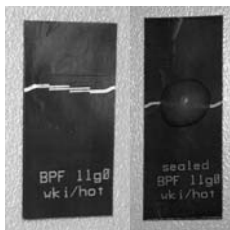


Figure 5. Original (left) and potted 11 GHz bandpass.

To prove the applicability of the gained material parameters a test circuit was designed. A coupled line bandpass filter with a center frequency of 11 GHz was used. The gained KC material parameters were applied to the simulation tool ADS and the circuit design included the potting layer from its very beginning. The original and the potted circuit are shown in Fig. 5. The left circuit represents the original given bandpass filter designed for traditional operation in air, while the right circuit shows the redesigned potted filter with identical center frequency and quality factor. The circuit showed the

parameters $f_c=11.00$ GHz, $A=-1.22$ dB and $Q=11.3$ in the simulation. The measurement results correspond very good the predicted simulation results. The measured parameters are $f_c=11.00$ GHz, $A=-1.92$ dB and $Q=12$. The marginal higher attenuation A also exists in the measurement without potting and is originated by the measurement test set. Fig. 6 shows the simulated S_{21} in magnitude and Fig. 7 the measured S_{21} magnitude of the potted 11 GHz bandpass filter.

Figure 6. Simulation of the potted 11 GHz bandpass.

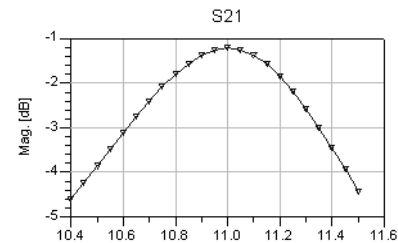
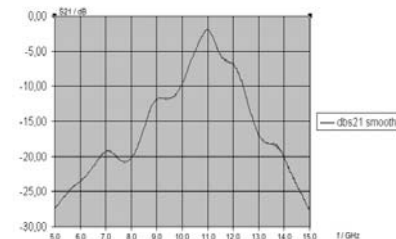


Figure 7. Measurement results of the 11 GHz bandpass.



VI. CONCLUSION

By use of ring resonators the relevant electrical parameters of several potting compounds for rf application were determined at certain frequencies up to 24 GHz. These parameters are the real part of the relative permittivity and the loss tangent. To validate the gained parameters a coupled line bandpass filter at 11 GHz was designed including the potting compound parameters already in the simulation. The measurement results of this test circuit corresponds very good with its simulation.

REFERENCES

- [1] I. J. Bahl and S. Stuchly, “Analysis of a microstrip covered with a lossy dielectric,” *IEEE Trans. on MTT*, vol. 28, no. 2, pp. 104–109, February 1980.
- [2] K. K. Joshi, R. D. Pollard and V. Postoyalko, “Microstrip with dielectric overlay: variational analysis and validation,” *IEE Proc. Microw. Antennas Propag.*, vol. 141, no. 2, pp. 138–140, April 1994.

Low-order Models for Spatial Diversity Systems Including Real Antenna Characteristics

Oliver Klemp, Gunnar Armbrecht and Hermann Eul
Institut für Hochfrequenztechnik und Funksysteme
Universität Hannover
Appelstr. 9A, 30167 Hannover, Germany
Email: klemp@hft.uni-hannover.de

Abstract—In order to provide highly reliable transmission links in mobile communications, wireless systems offering multiple branches for antenna diversity are recommended due to the property of mitigating fading effects in multipath environments. An accurate prediction of the performance of those diversity systems requires a complete description of antenna radiation behavior for the exact modeling of the interactions between real antenna configurations and suitable multipath channel scenarios. Closed-form solutions that account for real antenna radiation patterns and mutual coupling can be achieved applying a spherical eigenmode (SME) expansion of antenna radiation fields. Combining this field decomposition with a stochastic description of the communication channel, the presented analysis establishes an analytical framework for the calculation of antenna envelope correlation, mean effective gain and diversity performance that speeds up the computation of link budgets especially for large antenna arrays at the receiver.

I. INTRODUCTION

Diversity concepts as in [1], [2], [3] incorporating independent antenna branches at the receiver are well known techniques in order to enhance the signal-to-noise ratio in fading environments without increasing signal power. Different diversity techniques like spatial-, polarization- and pattern diversity have been considered [4]. Provided uncorrelated fading processes at each branch of the receiver, diversity antenna configurations may effectively mitigate signal fading. The optimum of diversity performance can be achieved with identical input powers and uncorrelated envelopes at each branch of the diversity antenna. Therefore the output voltages have to be superimposed in a suitable diversity combination network as in [1], where different methods of diversity combining may be applied. Using standard diversity combination techniques, the combined output signal yields an improvement in signal-to-noise performance due to diversity gain. With respect to the fact that the signal powers at the feeding bridges of the individual antenna elements are given by the interaction of the entire port-related antenna radiation patterns and the spatial distribution of impinging waves at the receiver array due to multipath propagation [5], antenna radiation behavior plays an integral role in terms of diversity performance of the antenna array. Therefore mutual coupling and the array topology may have a significant impact on antenna correlation and diversity performance. Realistic models of reduced order that account for the overall radiation behavior have to be taken into account for an accurate prediction of diversity performance.

The spherical mode expansion is a well known technique for an analytical approach of a various number of applications in the fields of electromagnetic scattering and radiation [6], [7]. The technique is well suited for the application in diversity antenna configurations [8] because it enables the investigation of closed-form solutions for the overall diversity performance. In order to qualify the spherical eigenmode decomposition for diversity performance computations, antenna arrays of co-axial oriented, $\lambda/2$ -resonant linear dipole elements are regarded in this research in Section III. Based on a stochastic formulation to account for the multipath properties of the considered channel scenario as in [9], the presented analysis provides an analytical framework for low-order modeling of multi-element antenna configurations for diversity reception. In Section IV the presented analysis is adopted to the computation of the most relevant performance figures such as antenna correlation, mean effective gain and diversity performance for arrays of $\lambda/2$ dipole antennas at the receiver.

II. STOCHASTIC MODEL FOR ANTENNA DIVERSITY

This paper deals with a simple model of the diversity receiver including the influences of real antenna radiation patterns as given in Fig. 1. The n regarded diversity branches are given by the signal envelopes $r_1(t)$ through $r_n(t)$ that are related to the receive envelopes of a multi-element array configuration. $\tilde{C}_1(\vartheta, \varphi)$ through $\tilde{C}_n(\vartheta, \varphi)$ denote corresponding antenna radiation patterns, respectively. Subsequent diversity combining yields the output envelope $\tilde{r}(t)$. For signal-to-noise (SNR) analysis of the diversity system, additive white Gaussian noise $n_i(t)$ is introduced at each diversity branch i . Branch weights α_i are used according to [1], [10] in order to perform a maximum ratio combining (MRC). It is assumed that correlation exclusively arises at the antenna and can be computed from the radiation patterns of the diversity antenna [9]. The resulting signal correlation matrix \mathbf{R}^{RX} is then used for a transformation of uncorrelated complex Gaussian radio signals into correlated Rayleigh envelope processes according to [11]. Therefore, the generated complex Gaussian sequences

$$\mathbf{w} = \begin{bmatrix} w_1 \\ \vdots \\ w_n \end{bmatrix} = \begin{bmatrix} w_{\Re,1} + j w_{\Im,1} \\ \vdots \\ w_{\Re,n} + j w_{\Im,n} \end{bmatrix} \quad (1)$$

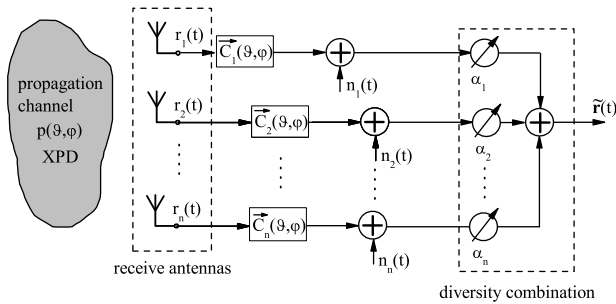


Fig. 1. Model of diversity receiver applying co-located antenna elements and maximum ratio diversity combination.

are transformed involving the lower triangular matrix \mathbf{L}^{RX} that results from the Cholesky factorization of the antenna correlation matrix \mathbf{R}^{RX} with $\mathbf{R}^{\text{RX}} = \mathbf{L}^{\text{RX}}\mathbf{L}^{\text{RX}H}$. Those complex correlated Gaussian processes are given as follows:

$$\mathbf{x} = \begin{bmatrix} x_1 \\ \vdots \\ x_n \end{bmatrix} = \mathbf{L}^{\text{RX}} \begin{bmatrix} w_{\Re,1} + j w_{\Im,1} \\ \vdots \\ w_{\Re,n} + j w_{\Im,n} \end{bmatrix}. \quad (2)$$

Respective Rayleigh envelopes of the i th diversity branch are derived from $r_i = |x_i|$. The correlation matrix \mathbf{R}^{RX} of the receive antenna array is given by the correlation coefficients $\rho_{i,j}$ between antenna elements i and j as follows:

$$\rho_{i,j} = \frac{R_{i,j}}{\sqrt{\sigma_i^2 \sigma_j^2}}. \quad (3)$$

In (3), $R_{i,j}$ and $\{\sigma_i^2, \sigma_j^2\}$ denote antenna covariance- and variances. For the diversity analysis of the considered multi-element antenna configurations, Monte-Carlo simulations are carried out, involving $N_w = 10000$ realizations of uncorrelated Rayleigh fading coefficients \mathbf{w} .

III. ANALYTICAL APPROACH FOR ANTENNA PARAMETERS

The diversity performance of a multi-element receive antenna configuration in a multipath communication environment is affected by the properties of mutual coupling between the individual antenna elements. Mutual coupling causes amplitude- and phase distortions of the antenna radiation patterns that lead to a change of the mean effective gain and the correlation properties between the distinct diversity branches in contrast to isolated antenna elements. For that reason it is important to include the effects of real antenna equipment and electromagnetic coupling within reliability studies of multi-element antenna arrays for diversity reception. The spherical mode expansion (SME) of antenna radiation patterns may account for those effects and enables an analytical formulation for the interactions between antenna radiation behavior and multipath environment. The latter analysis therefore provides a simplification of complex design terminology for diversity communication systems in the interface plane between antenna radiation characteristics and multipath channel. This section deals with a spherical mode expansion of antenna radiation patterns $\tilde{C}_i(\vartheta, \varphi)$ for antenna element i that is applied in

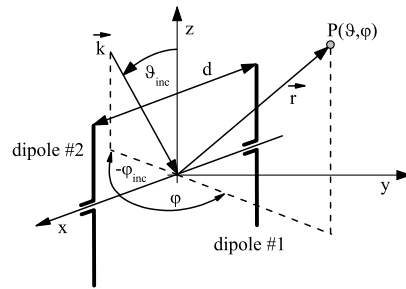


Fig. 2. Configuration of two vertical $\lambda/2$ -resonant linear dipole antennas.

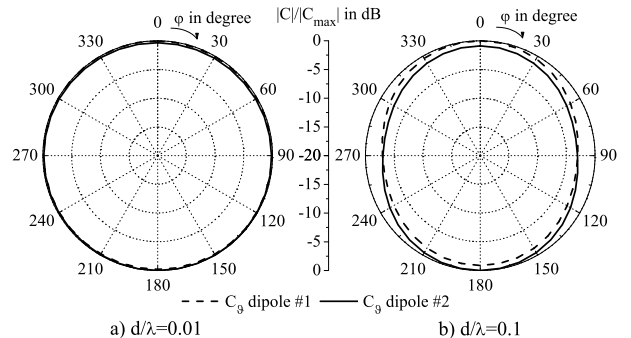


Fig. 3. Antenna radiation patterns for $\lambda/2$ -resonant linear dipole antennas with normalized spacings a) $d/\lambda = 0.01$ and b) $d/\lambda = 0.1$.

Section III-A for the computation of antenna correlation. In Section III-B the SME analysis is adopted to antenna gain patterns $\tilde{G}_i(\vartheta, \varphi)$ for mean effective gain analysis in a multipath channel scenario.

Referring to [5], the spatial properties of the radio channel are given by means of a two-dimensional probability density $p_{\vartheta, \varphi}(\vartheta, \varphi)$ that accounts for the angle-of-arrival (AoA) distribution at the receiver in dependence of the coordinates ϑ and φ . For simplicity, the spatial distributions are assumed to be identical for the orthogonal polarization states C_ϑ and C_φ of the radiation pattern. The accomplished diversity analysis is based on antenna arrays at the receive-side as depicted in Fig. 2. The arrays consist of two vertically oriented, $\lambda/2$ -resonant, linear dipole elements with an interelement spacing d . The AoA-behavior can be represented in terms of plane waves with a wave vector \vec{k} impinging at a direction ϑ_{inc} and φ_{inc} at the receiver. A variation of the normalized interelement spacing d/λ will be carried out in this paper in order to address the specific performance figures of diversity combining. Antenna spacing d/λ plays a significant role for diversity antenna configurations due to the fact that it mainly affects interelement correlation and determines the geometrical size of the antenna front-end.

Fig. 3 depicts normalized co-polar, horizontal ($\vartheta = 90^\circ$) radiation patterns $C_{\vartheta, i}(\vartheta = 90^\circ, \varphi)$ of the two dipole antennas for variable spacings d/λ as derived by a conventional full-wave simulator based on the finite-element-method (FEM). Basically, as can be seen from Fig. 3 b), mutual coupling causes pattern distortions that yield a modified spatial selectivity of the related antenna radiation patterns.

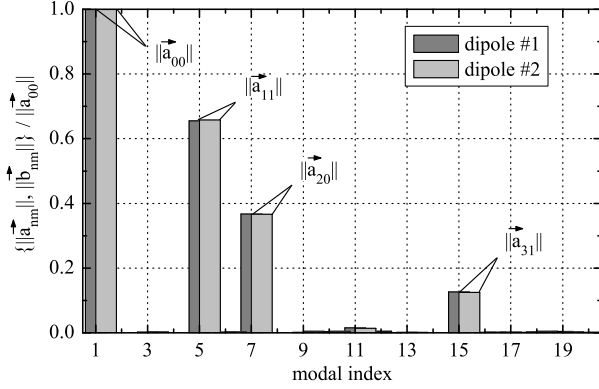


Fig. 4. Mode decomposition ($N = 3$) for $\lambda/2$ -resonant linear dipole antennas with normalized spacing $d/\lambda = 0.1$.

In order to derive an analytical description for antenna radiation patterns $\vec{C}_i(\vartheta, \varphi)$ of antenna element i , a spherical eigenmode expansion as given in [6], [7] can be accomplished:

$$\vec{C}_i(\vartheta, \varphi) = \sum_{n_i=0}^{\infty} \sum_{m_i=0}^{n_i} \left\{ \vec{a}_{n_i m_i} Y_{n_i m_i}^e(\vartheta, \varphi) + \vec{b}_{n_i m_i} Y_{n_i m_i}^o(\vartheta, \varphi) \right\}. \quad (4)$$

In (4), $\vec{a}_{n_i m_i}$ and $\vec{b}_{n_i m_i}$ denote the vector expansion coefficients of the field approach that provide specific weights according to any individual antenna radiation pattern. The normalized eigensolutions of the field expansion may be reformulated in terms of normalized spherical harmonics $Y_{nm}^e(\vartheta, \varphi)$, $Y_{nm}^o(\vartheta, \varphi)$ according to [6]. For a numerical investigation, the upper infinite summation bound of (4) has to be replaced by a finite value N . Based on the method of numerical point matching [12], [8], the individual weights $\vec{a}_{n_i m_i}$ and $\vec{b}_{n_i m_i}$ can be computed from a given radiation pattern $\vec{C}_i(\vartheta, \varphi)$ that was derived by FEM analysis in this research. E. g. an expansion degree of $N = 3$ yields a complete description of antenna radiation patterns in terms of 20 complex valued vector expansion coefficients. Sampling the same antenna radiation pattern on the far-field sphere providing an angular resolution of 5° as for this research requires a number of 2701 complex valued vector coefficients in comparison. Fig. 4 depicts the normalized spherical mode coefficients for the dipole antennas with a normalized interelement spacing of $d/\lambda = 0.1$ and $N = 3$. The normalization is performed with respect to the absolute value of the expansion coefficient of degree $n = 0$ and order $m = 0$, \vec{a}_{00} which yields normalized weights $\|\vec{a}_{nm}\| / \|\vec{a}_{00}\|$ in terms of expansion coefficients related to even spherical harmonics $Y_{nm}^e(\vartheta, \varphi)$ and $\|\vec{b}_{nm}\| / \|\vec{a}_{00}\|$ for expansion coefficients of odd spherical harmonics $Y_{nm}^o(\vartheta, \varphi)$. The modal index indicates the alternating sequence of modes \vec{a}_{nm} and \vec{b}_{nm} in the field approach. The normalized absolute values of the modal contributions are equal for both dipole elements. This is due to the symmetry properties of the related antenna radiation patterns with respect to the y -axis as well as the spherical harmonics $Y_{nm}^e(\vartheta, \varphi)$ and $Y_{nm}^o(\vartheta, \varphi)$, [6].

As can be seen from the decaying behavior of modal contributions with increasing degree n and order m of the harmonics, it becomes feasible to limit the number of modes by a finite value N in order to derive a complete description of antenna radiation fields that is easy to handle with respect to its reduced complexity.

A. Antenna Correlation

Using the complete vector antenna far-field representation given by its components $C_\vartheta(\vartheta, \varphi)$ and $C_\varphi(\vartheta, \varphi)$ for antenna element i and j , as well as the normalized two-dimensional probability distribution $p_{\vartheta, \varphi}(\vartheta, \varphi)$, antenna covariance $R_{i,j}$ may be computed in accordance with [9] and [5] as shown in (5). Accounting for polarization conversion by the multipath channel we refer to a cross-polarization discrimination $\text{XPD} = 1$ which is the worst case for linear-polarized antenna elements for space diversity applications. The latter is due to the fact that half of the power at the receive array, impressed by a vertical transmit antenna, is converted to the horizontal plane.

$$R_{i,j} = K_0 \int_{\varphi=0}^{2\pi} \int_{\vartheta=0}^{\pi} [C_{\vartheta,i}(\vartheta, \varphi) C_{\vartheta,j}^*(\vartheta, \varphi) + \text{XPD} C_{\varphi,i}(\vartheta, \varphi) C_{\varphi,j}^*(\vartheta, \varphi)] e^{j\vec{k}\vec{r}_{ij}} p_{\vartheta, \varphi}(\vartheta, \varphi) \sin \vartheta d\vartheta d\varphi. \quad (5)$$

In (5), \vec{r}_{ij} denotes the spatial separation between antenna elements i and j , K_0 is a proportionality constant and \vec{k} is the wave vector. Following [8], antenna radiation patterns in (5) can be replaced by a spherical mode expansion of finite degree N yielding a separation between antenna- and channel related quantities. By replacing the indices $j = i$ in (5) a closed form representation of antenna variances σ_i^2 (see (3)) is derived in addition.

B. Mean Effective Gain

In order to derive an optimum of diversity gain, the input powers at the distinct diversity branches have to be equal. A measure to determine the input power is given in terms of the mean effective gain G_{MEG} of the respective antenna element in the considered multipath channel scenario given by the two-dimensional probability density $p_{\vartheta, \varphi}(\vartheta, \varphi)$. According to [9] the mean effective gain $G_{\text{MEG},i}$ is related to the complex antenna gain pattern $\vec{G}_i(\vartheta, \varphi)$ as follows:

$$G_{\text{MEG},i} = \int_{\varphi=0}^{2\pi} \int_{\vartheta=0}^{\pi} \left[\frac{1}{1 + \text{XPD}} G_{\vartheta,i}(\vartheta, \varphi) + \frac{\text{XPD}}{1 + \text{XPD}} G_{\varphi,i}(\vartheta, \varphi) \right] p_{\vartheta, \varphi}(\vartheta, \varphi) \sin \vartheta d\vartheta d\varphi. \quad (6)$$

In (6), $G_{\vartheta,i}(\vartheta, \varphi)$ and $G_{\varphi,i}(\vartheta, \varphi)$ represent the components of the polarization variant antenna gain pattern $\vec{G}_i(\vartheta, \varphi)$ for antenna element i . They are related to the components $C_{\vartheta,i}(\vartheta, \varphi)$ and $C_{\varphi,i}(\vartheta, \varphi)$ of the antenna radiation patterns and scaled by the respective antenna efficiency and the available power at the feeding bridge.

Replacing the gain patterns by an SME-based analytical field approach in analogy to (4) for antenna radiation patterns, a

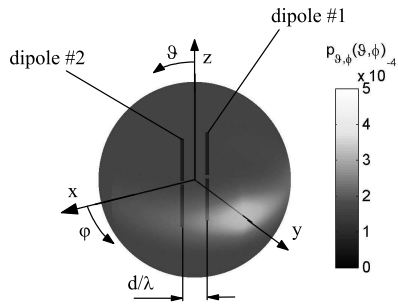


Fig. 5. Probability density plot of $p_{\vartheta, \varphi}(\vartheta, \varphi)$.

modal characterization of antenna gain patterns in terms of spherical harmonics can be obtained:

$$\vec{G}_i(\vartheta, \varphi) = \sum_{n_i=0}^{\infty} \sum_{m_i=0}^{n_i} \left\{ \vec{a}_{n_i m_i}^G Y_{n_i m_i}^e(\vartheta, \varphi) + \vec{b}_{n_i m_i}^G Y_{n_i m_i}^o(\vartheta, \varphi) \right\}. \quad (7)$$

In (7), $\vec{a}_{n_i m_i}^G$ and $\vec{b}_{n_i m_i}^G$ represent the vector expansion coefficients for antenna gain patterns, respectively. The computation of vector expansion coefficients for antenna gain patterns is again based on a point-matching procedure involving computed antenna gain patterns as derived by the finite-element-method (see Section III and [8]).

IV. SIMULATION RESULTS

For the computation of antenna correlation, mean effective gain and diversity performance by means of a spherical mode expansion, the considered channel scenario $p_{\vartheta, \varphi}(\vartheta, \varphi)$ is given by a Laplacian density in azimuth and a Gaussian density in elevation according to [13]. The AoA situation can be completely characterized by its mean values $m_{\vartheta} = 90^\circ$ and $m_{\varphi} = 90^\circ$ in elevation and azimuth and the corresponding angular spreads $\sigma_{\vartheta} = 10^\circ$ and $\sigma_{\varphi} = 60^\circ$. The spatial distribution of the probability density for incoming waves at the receiver is depicted in Fig. 5. Reference results are derived from simulated antenna radiation patterns using the FEM. The antenna elements are matched to transmission line impedances of 50Ω and the related field quantities are sampled on an equiangular grid as described in Section III. The series expansion of the respective radiation fields is limited by a finite degree N . Fig. 6 depicts the results of power correlation $\rho_p \simeq |\rho_{1,2}|^2$ between antenna elements #1 and #2 for variable interelement spacings d/λ . For small spacings, $d/\lambda \leq 0.1$, power correlation remains reasonably high. Increasing the normalized dipole separation yields a sufficient decorrelation due to space diversity effects. SME-based results for antenna power correlation including field expansion degrees $N = 0, 1, 3$ and 5 are also included in Fig. 6. For field expansion degrees $N = 0, 1$ FEM-based reference values for antenna correlation cannot be approximated very well. This is due to the fact that the SME-based results for low field expansion degrees cannot accurately recreate the complete and to some extent distorted radiation pattern due to the small number of eigenmodes within the field approach.

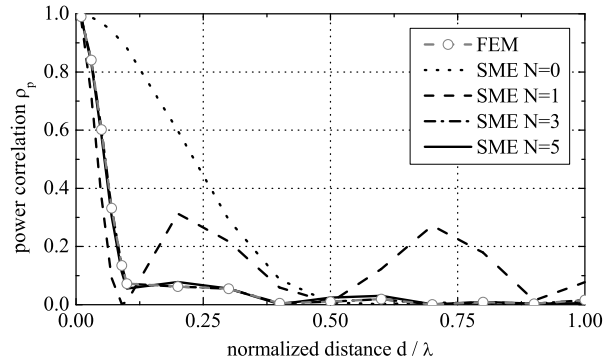


Fig. 6. Power correlation ρ_p between two $\lambda/2$ -resonant linear dipole antennas for normalized spacings d/λ within the regarded channel scenario.

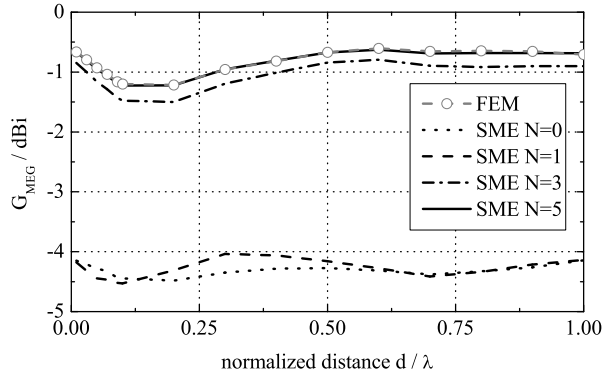


Fig. 7. Mean effective gain of antenna element #1 for variable normalized spacings d/λ .

However, increasing the order of the spherical mode expansion to $N = 3, 5$ yields a very good fit between FEM- and SME-based computations of antenna correlation. Due to the fact that the AoA distribution is assumed to be symmetrical with respect to the array topology as can be seen from Fig. 5, the mean effective gains of antenna elements #1 and #2 are identical. Therefore, in Fig. 7 only the results for antenna element #1 are plotted versus the normalized spacing d/λ . In an interval of normalized spacings $0.1 \leq d/\lambda \leq 0.2$, G_{MEG} mainly degrades due to mutual coupling between the antenna elements. The provoked pattern distortion leads to a reduction of the antenna's spatial selectivity in the directions with a high probability for impinging waves. Reference results again are in a very good agreement with the results as derived by spherical mode expansion ($N = 3, 5$). The cumulative distribution functions (CDFs) that account for the diversity performance of the two-element dipole configuration are given in Fig. 8 a) for a normalized interelement spacing $d/\lambda = 0.01$ and in Fig. 8 b) for $d/\lambda = 0.1$. The CDFs are normalized with respect to the time average of the stronger diversity branch [10]. As a result from the high values of antenna power correlation ρ_p at a small interelement spacing of $d/\lambda = 0.01$, the diversity gain remains low: Following FEM-based reference results, diversity combining of the two branch envelopes yields a diversity gain of $G_{10\%} = 3.2$ dB at an outage level of 10%. Referring to Fig. 8 b), maximum ratio diversity combining yields an enhanced diversity gain of $G_{10\%} = 6.5$ dB (as indicated by FEM computations) for a normalized spacing of $d/\lambda = 0.1$

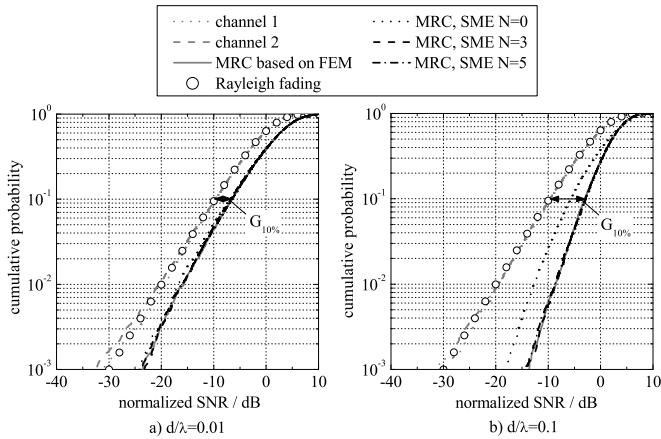


Fig. 8. CDFs of diversity performance of two $\lambda/2$ -resonant linear dipole antennas with normalized distances a) $d/\lambda = 0.01$ and b) $d/\lambda = 0.1$.

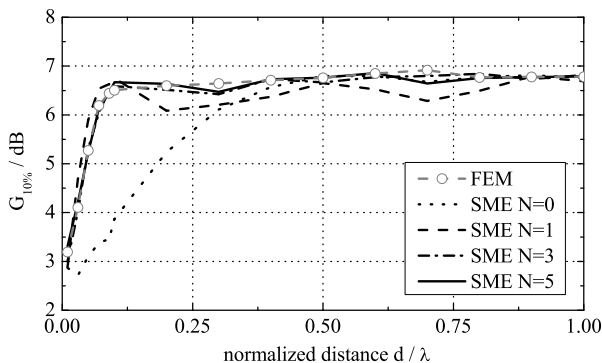


Fig. 9. Diversity gain $G_{10\%}$ for configuration of $\lambda/2$ -resonant linear dipole antennas with variable normalized spacings d/λ .

due to the reduced spatial correlation between the two diversity branches. For an outage probability of 10%, Fig. 9 shows the respective diversity gains $G_{10\%}$ for variable normalized interelement distances d/λ . At a reduced interelement spacing $d/\lambda \leq 0.1$, diversity performance of the antenna configuration mainly degrades due to the high amount of power correlation between the respective diversity branches. With an increase of the normalized antenna spacing, starting at $d/\lambda \simeq 0.1$, a diversity gain of approximately $G_{10\%} = 6.6$ dB can be retained at an outage level of 10% within the considered channel scenario $p_{\vartheta, \varphi}(\vartheta, \varphi)$. Referring to Figs. 8 and 9, results based on SME computations are in a very good agreement with the FEM-based reference results if a reasonable amount of modes was used in the SME field approach. Following Fig. 9, low field expansion degrees of $N = 0, 1$ cause impairments in comparison to the given reference results. Additionally, referring to Fig. 8 a), the CDF for the combined output for $N = 0$ does not provide a sufficient approximation of the FEM-based reference CDF of the combiner output. However, with an increase of the field expansion degree to $N = 3, 5$, reference results can be approximated very well. Diversity gains for a 10%-outage probability are also summarized in Table IV for normalized interelement distances $d/\lambda = 0.01, 0.1$ and 0.5 depending on the computational technique that was used. The spherical mode expansion yields a very good approximation of the diversity gains as indicated by the FEM-based reference results especially for field expansion degrees $N = 3, 5$.

TABLE I
DIVERSITY GAINS $G_{10\%}$ IN dB FOR 10%-OUTAGE PROBABILITIES AND DIFFERENT NORMALIZED INTERELEMENT SPACINGS d/λ .

d/λ	reference, FEM	N=0	N=1	N=3	N=5
0.01	3.2	2.9	2.9	3.0	3.3
0.1	6.5	3.9	6.8	6.6	6.7
0.5	6.8	6.8	6.7	6.7	6.8

V. CONCLUSION

This paper presents an analytical approach for the computation of performance figures of multielement antenna configurations for diversity reception. Therefore the analysis was based on an orthonormal field expansion for antenna radiation- and gain patterns using spherical harmonics. Applying a stochastic formulation for the channel properties at the receive antenna array, closed-form solutions for antenna diversity performance were derived that establish a framework for the low-order analysis of diversity communication systems including real antenna characteristics. The analysis was applied to the investigation of the diversity performance for array configurations consisting of two linear dipole antennas at the receiver. For limited degrees N of the modal field expansion, very good convergence was found for all performance figures in comparison to conventional computational techniques based on the finite-element-method. Especially for large antenna arrays the presented analysis provides an accurate low-order modeling of antenna diversity performance including real antenna radiation behavior.

REFERENCES

- [1] W. C. Jakes, *Microwave Mobile Communications*. New York: IEEE Press, Inc., 1974.
- [2] R. G. Vaughan and J. B. Andersen, "Antenna diversity in mobile communications," *IEEE Trans. Veh. Technol.*, vol. 36, pp. 149–172, 1987.
- [3] T. S. Rappaport, *Wireless Communications Principles and Practice, 2nd Edition*. Upper Saddle River, NJ: Prentice Hall PTR, Inc., 2002.
- [4] C. B. Dietrich, K. Dietze, J. R. Nealy, and W. L. Stutzman, "Spatial, polarization, and pattern diversity for wireless handheld terminals," *IEEE Trans. Antennas Propagat.*, vol. 49, pp. 1271–1281, 2001.
- [5] K. Fujimoto and J. R. James, *Mobile Antenna Systems Handbook, 2nd Edition*. Boston, London: Artech House, Inc. Antennas and Propagation Library, 2000.
- [6] J. A. Stratton, *Electromagnetic Theory*. New York: McGraw Hill, 1941.
- [7] D. H. Werner and R. Mittra, *Frontiers in Electromagnetics*. New York: IEEE Press Series on Microwave Technology and RF, 2000.
- [8] O. Klemp and H. Eul, "Radiation pattern analysis of antenna systems for MIMO and diversity configurations," *Advances in Radio Science*, vol. 3, pp. 157–165, 2005.
- [9] T. Taga, "Analysis for mean effective gain of mobile antennas in land mobile radio environments," *IEEE Trans. Veh. Technol.*, vol. 39, pp. 117–131, 1990.
- [10] K. Dietze, C. B. Dietrich, and W. L. Stutzman, "Analysis of a two-branch maximal ratio and selection diversity system with unequal SNRs and correlated inputs for a rayleigh fading channel," *IEEE Transactions on Wireless Communications*, vol. 1, pp. 274–281, 2002.
- [11] S. Sorooshyari and D. G. Daut, "Generation of correlated rayleigh fading envelopes for accurate performance analysis of diversity systems," *14th IEEE 2003 International Symposium on Personal, Indoor and Mobile Radio Communications*, vol. 1, pp. 1800–1804, 2003.
- [12] C. Hafner, *The Generalized Multipole Technique for Computational Electromagnetics*. Boston, London: Artech House, Inc., 1990.
- [13] T. Svantesson, "Correlation and channel capacity of MIMO systems employing multimode antennas," *IEEE Trans. Veh. Technol.*, vol. 51, pp. 1304–1312, 2002.

Systematic Measurements for Testing the Influence of an Internal Noise Source on the Phase Noise of an Oscillator

Michael H.W. Hoffmann, Holger Weiß

University of Ulm, Dept. of Microwave Techniques, Albert-Einstein-Allee 41, 89069 Ulm, Germany, +49 (731) 5026352
Michael.Hoffmann@ieee.org

Short Abstract — Based on a novel theory of phase noise of resonator oscillators, the influence of an internal noise source on the phase noise behavior of a differential-amplifier oscillator is measured for different feedback parameters and compared to simulation using modern CAD software. The results will constitute the basis for a further development of the novel theory.

Keywords - phase noise; oscillators; feedback; spectrum; noise

I. INTRODUCTION

Generation of sinusoidal signals with low phase noise is and will remain an important objective for a large number of applications. There are many publications available dealing with the analysis of the spectral purity of signals produced by certain types of oscillators [1]. There exist also publications on the systematic and non-linear theory of sinusoidal oscillations [2]-[4]. These publications are highly instructive for those having a thorough background in very special fields of mathematics, as for instance the theory of non-linear differential equations and of the evaluation of nonlinearly processed stochastic processes. Due to their high specialization, though, they are not easily readable for the practitioner, and it is often not easy to see the link between the spectral properties of diverse noise sources in the oscillator circuitry and the phase-noise that is finally produced. In a recent paper [5] of one of the authors, a theory of oscillators has been developed that is based on standard mathematics of modern engineering curricula. In order to test the theory, systematic measurements have been performed. This paper will demonstrate first steps towards the validation of the theory.

To that aim, an oscillator circuit with a relatively simple non-linearity has been developed, where additional noise sources might be included on purpose. With these, measurements have been performed to cast a new light on the following questions:

- Can the phase noise be minimized by variation of feedback parameters?
- How do the feedback parameters influence the phase noise spectrum?
- How does the external noise source influence the phase noise spectrum?
- How good do measured results agree with standard CAD simulation?

II. THE OSCILLATOR AND THE NOISE SOURCE

The oscillator was designed using a differential amplifier, which provides a relatively simple nonlinearity in the non-saturated case. In saturated operation, it provides another, more complex non-linearity, which makes possible a comparison of results for different non-linearities. In order to study the influence of feedback parameters on the phase noise and the nonlinear behavior, the oscillator circuit has been designed such that the feedback parameters might be adjusted. Additionally, two controllable current sources have been included, the control voltage of which might be a noise-source.

A. The differential oscillator

The differential oscillator topology is shown in Fig.1. Two dual-type NPN BFE520 transistors are forming a differential amplifier. The collector resistance R_{coll} allows an adjustment for the loop gain of the oscillator. The collector voltage U_{coll} is decoupled via a bypass-capacitor to a subsequent emitter-follower stage. The LC-resonance circuit is placed in the feedback branch between the emitter follower and the differential amplifier. The current sources I_{src1} and I_{src2} are simple current mirrors to provide a constant current of 5mA thru the differential amplifier and the emitter-follower. The

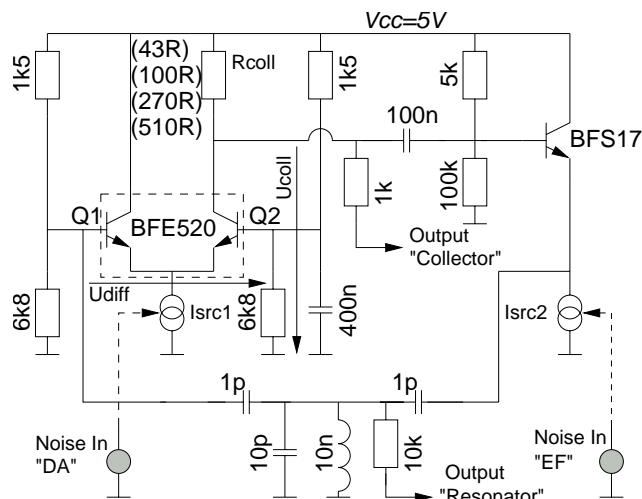


Figure 1. Differential amplifier topology with LC-resonator.

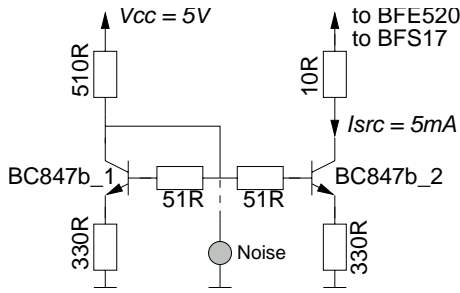


Figure 2. Current sources I_{src1}, I_{src2} with voltage noise source

topology of the current sources is shown in Fig.2. The external noise source is connected to the base resistors of the current source transistors and the noise voltage is transformed into a noise current in the collector of BC847b_2. Fig.3 shows the nonlinear DC transfer function of the differential amplifier for different values of R_{coll} . Up to a resistance value of 330Ω , transistors Q1 and Q2 are working in their active forward region. For larger values of R_{coll} , Q2 is working in the saturated region, where both the base-emitter and the base-collector diode are forward biased. The circuit is assembled in SMD technology on a 0.5mm FR4 substrate material. For the passive components a 0603/0805 package size is used. The active devices are simulated using standard Gummel-Poon models as implemented in ADS2004A. The $1/f$ -noise model parameters are not included in the model and therefore not simulated.

B. The external noise source

The noise source is shown in Fig. 4. It provides a constant, white noise spectral density over a frequency range from DC to 20MHz with an adjustable output voltage. The noise voltage is generated by a Zener-diode. It is coupled to an active 8th-order Butterworth filter as shown in Fig. 5. The spectral noise voltage density at the output of the filter can be adjusted in a dynamic range from $-20 \text{ dB}\mu\text{V}/\sqrt{\text{Hz}}$ to $+28 \text{ dB}\mu\text{V}/\sqrt{\text{Hz}}$. The noise source is capable to drive loads down to 50Ω . Typical noise spectra are shown in Fig.6. They are compared to the noise-floor of the measurement equipment.

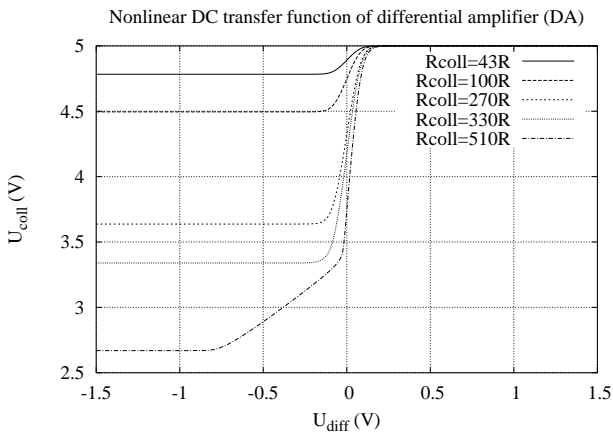


Figure 3. Simulated DC voltage transfer function with different values for R_{coll}

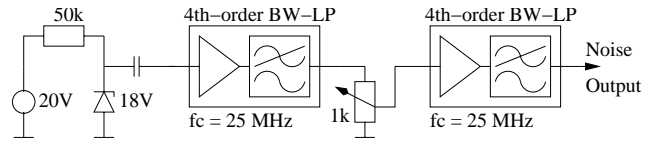


Figure 4. Noise source topology with zener diode

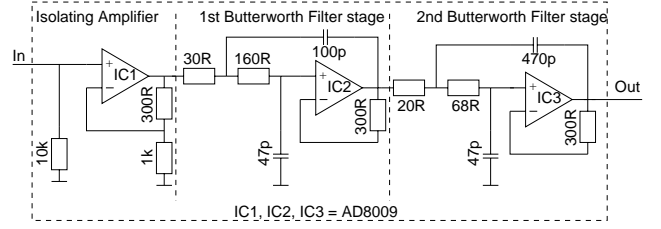


Figure 5. 4th order active low-pass butterworth filter circuit topology

III. MEASUREMENT AND SIMULATION RESULTS

For the measurements, a HP8565EC spectrum analyzer and a MITEQ AU-1261 low-noise preamplifier were used. The phase noise was measured with the phase noise utility, implemented in the HP8565EC. For the $\pm 5\text{V}$ supply for both the noise source and the oscillator, two HPE3610A DC power supplies were used.

A. Measurements without external noise source

The large signal simulation and measurement results without external noise source for $R_{coll}=100\Omega$, are compared in Tab.1. The simulated oscillation frequency is 40MHz above the

TABLE I. SIMULATION AND MEASUREMENT RESULTS WITHOUT EXTERNAL NOISE SOURCE

Results for $R_{coll}=100\Omega$	HB Simulation	TRAN Simulation	Measurement Results
DC current $I_{src1/2}$ (mA)		5.11	5.1
Frequency f_0 (MHz)	463.8	463.4	423
Power $P_{coll@50\Omega}$ (dBm)	-30.1	-31.9	-33.3
PHN@10kHz (dBc/Hz)	-99.7	not sim. ^a	-100

a. Large signal phase noise simulation for transient simulation not available in ADS2004.

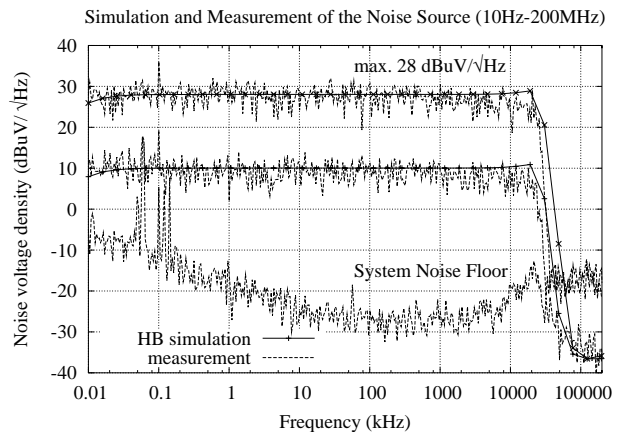


Figure 6. Low frequency noise source voltage density spectrum for different noise densities adjusted.

measured frequency, which is an accuracy of about 10%. For the collector power and the phase noise, the differences between simulation and measurement are very small. The power at the collector was measured without the preamplifier stage, directly with the 50Ω input of the spectrum analyzer. In Fig. 7 the simulated and measured results for the SSB (single side band) phase noise are shown. The phase noise measured with $R_{\text{coll}}=100\Omega$ is -100dBc/Hz at 10kHz offset. The lowest relative phase noise was measured with $R_{\text{coll}}=270\Omega$ for -103dBc/Hz at 10kHz offset. This measurement is not included in the diagram. As long as the transistor Q2 operates in its active forward region, the slope of the phase noise spectrum is -20dB/dec . If the transistor Q2 operates in its saturated region ($R_{\text{coll}}=510\Omega$), the slope increases to -30dB/dec for offset frequencies below 20kHz. The simulated results are in the same range as the measured results. However, in the simulation, the minimum phase noise is obtained for $R_{\text{coll}}=510\Omega$, and could even be minimized for higher values for R_{coll} . This could not be observed by measurement. The simulated slope with $R_{\text{coll}}=43\Omega$, decreases for offset frequencies below 10kHz to -10dB/dec . This might be due to the missing $1/f$ -noise parameters in the transistor model. The 50kHz spurious responses in the phase noise spectrum are produced by the DC power supply. They occur only in the phase noise spectrum for $R_{\text{coll}}=510\Omega$. The measured phase noise spectra at the collector output and at the resonator output are identical.

B. Measurements with external noise source

The measurement and characterization procedure of the oscillator with the external noise source was as follows. For each of the four collector resistor values $R_{\text{coll}}=43/100/270/510\Omega$, the “right-sided” SSB phase noise spectrum from 500Hz–50MHz offset frequency and the carrier spectrum in a 100MHz bandwidth were measured, both at the collector output and at the resonator output, for external noise voltage densities of $10\text{dB}\mu\text{V}/\sqrt{\text{Hz}}$ and $25\text{dB}\mu\text{V}/\sqrt{\text{Hz}}$, with noise input at the differential amplifier current source I_{SRC1} (noise in “DA”) and at the emitter follower current source I_{SRC2} (noise in “EF”). This procedure results in 64 measured spectra which cannot be presented completely in this paper. Therefore, some

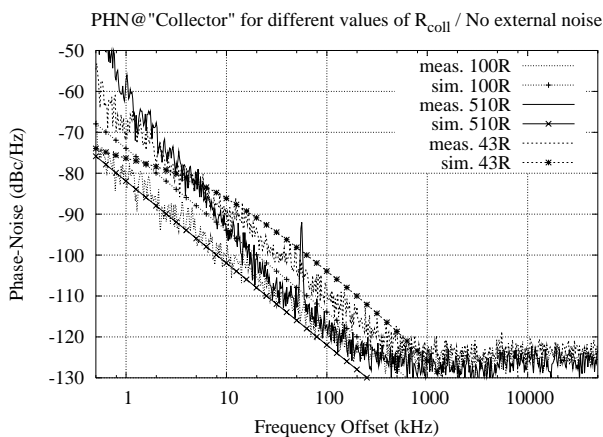


Figure 7. Phase noise without external noise for $R_{\text{coll}}=43/100/510\Omega$

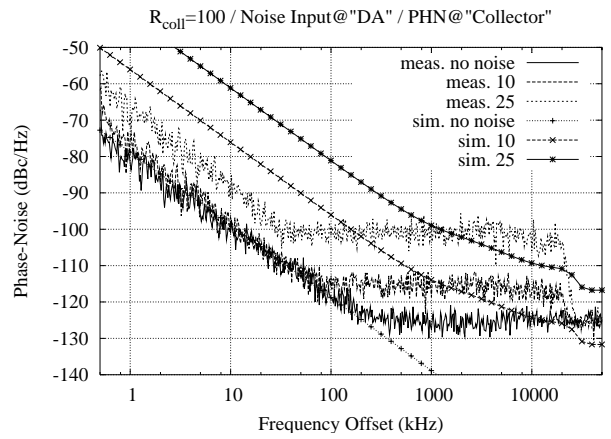


Figure 8. Simulated and measured phase noise spectrum for different noise voltage densities. Collector resistance $R_{\text{coll}}=100\Omega$.

selected and representative measurements will be discussed. The complete set of measurements might be found in [6].

The simulated and measured phase noise spectra at the collector, with external noise input at “DA”, are shown for $R_{\text{coll}}=100/510\Omega$ in Fig. 8 and Fig. 9 respectively. The limited bandwidth of the noise source might be observed at 25MHz frequency offset. As it was expected, with increasing noise voltage density the phase noise is also increasing. For $R_{\text{coll}}=510\Omega$, the -30dB/dec slope is changed into -20dB/dec . The simulated phase noise is in the range of the measured phase noise only for $R_{\text{coll}}=270/510\Omega$. For $R_{\text{coll}}=43/100\Omega$ the simulated phase noise quantity and shape differs substantially from measurement.

A comparison of measured noise spectra at the collector with different resistor values, for an input voltage noise density of $25\text{dB}\mu\text{V}/\sqrt{\text{Hz}}$ at “DA” is shown in Fig. 10. The influence of the external noise source on the phase noise is worst for $R_{\text{coll}}=43\Omega$ and best for $R_{\text{coll}}=100\Omega$. For $R_{\text{coll}}=100/510\Omega$, two regions in the phase noise spectra can be distinguished clearly: A -20dB/dec region close to the carrier and a constant (white) noise region up to 25MHz offset frequency. The corner frequency between those two regions depends on the value for

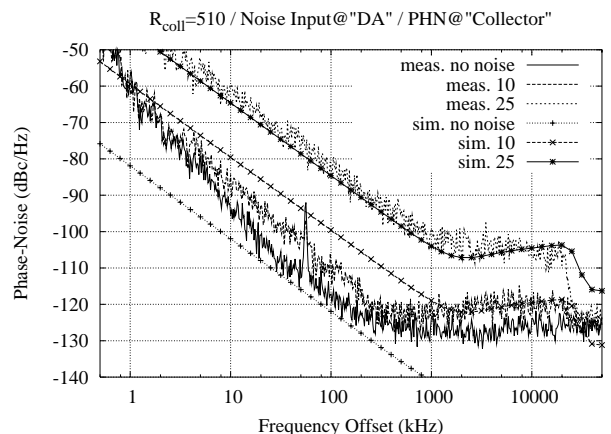


Figure 9. Simulated and measured phase noise spectrum for different noise voltage densities. Collector resistance $R_{\text{coll}}=510\Omega$.

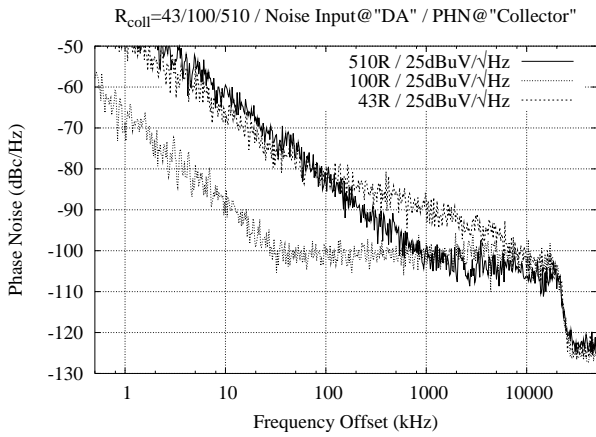


Figure 10. Measured phase noise for $R_{\text{coll}}=43/100/510\Omega$ with a noise voltage density $25\text{dBuV}/\sqrt{\text{Hz}}$ at noise input "DA".

R_{coll} . It is important to mention, that the LC-resonance circuit is not changed and is the same for all measurements. A comparison for an input voltage noise density of $25\text{dB}\mu\text{V}/\sqrt{\text{Hz}}$ at "EF" is shown in Fig. 11. The influence of the external noise source on the phase noise is worst for $R_{\text{coll}}=510\Omega$ and best for $R_{\text{coll}}=100\Omega$. The measured phase noise for $R_{\text{coll}}=100\Omega$ below 20kHz offset frequency is identically to the measurement results for noise input at "DA". A white noise region, as in Fig. 10 with band limitation to 25MHz , could not be observed. As can be seen in Fig. 12 the high-to-low and low-to-high transition between the maximum and minimum voltage, is slow for $R_{\text{coll}}=43\Omega$ and faster for $R_{\text{coll}}=100\Omega$ and $R_{\text{coll}}=510\Omega$. For $R_{\text{coll}}=100\Omega$ the high state has a flat shape, without peaks or overshoots, as it is for $R_{\text{coll}}=510\Omega$. According to [3], this indicates a low sensitivity of the oscillator steady state signal, against impulse distortions. In this experiment, the value $R_{\text{coll}}=100\Omega$ is the best choice for minimum influence of the external noise source. It was also found that for offset frequencies from 500Hz - 1MHz the measured phase noise shape and quantity is the same at the resonator and the collector output. For larger offset frequencies (1MHz - 50MHz) the measured phase noise at the resonator is smaller than at the

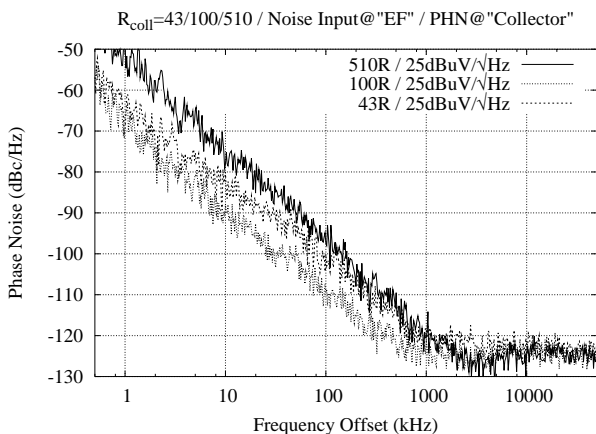


Figure 11. Measured phase noise for $R_{\text{coll}}=43/100/510\Omega$ with a noise voltage density $25\text{dBuV}/\sqrt{\text{Hz}}$ at noise input "EF".

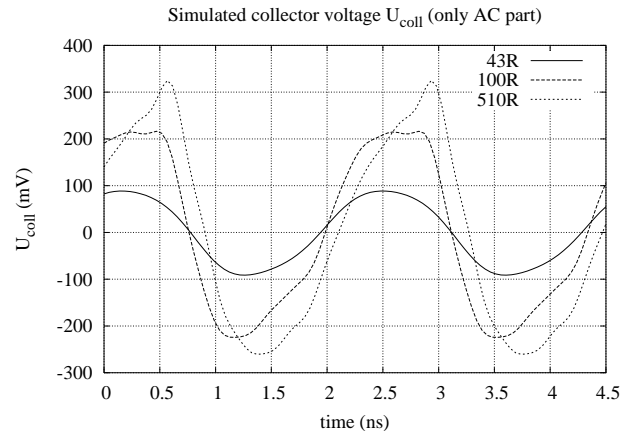


Figure 12. Collector voltage time domain signal U_{coll} obtained from HB simulation.

collector. This behaviour might be seen in the measured carrier spectra from Fig. 13 and Fig. 14.

The simulated and measured carrier spectra at the collector output and at the resonator output are shown in Fig. 13 and Fig. 14 respectively. The carrier spectra were measured without external noise and for a noise density of $10\text{dB}\mu\text{V}/\sqrt{\text{Hz}}$ and $25\text{dB}\mu\text{V}/\sqrt{\text{Hz}}$. The spectra for $R_{\text{coll}}=270\Omega$ are chosen, because some effects might be seen more clearly with this resistance. The effects are more or less present for all other resistance values. The LC-resonator values in the simulation were changed, in order to achieve the same oscillation frequency, as in the measured spectra. This simplifies the comparison between simulated and measured spectra. The differences between the simulated power, spectrum and phase noise for the different LC-resonator values are neglectable small. The spectra are simulated using the harmonic balance mixer noise simulation. The spectrum at the collector output (Fig. 13) shows a virtually white noise power spectrum for offset frequencies up to $\pm 20\text{MHz}$, whereas the spectrum at the resonator in Fig. 14 is a filtered version of the collector spectra. The shape of the simulated spectra correspond to the measurements, but the quantity and the noise floor do not fit

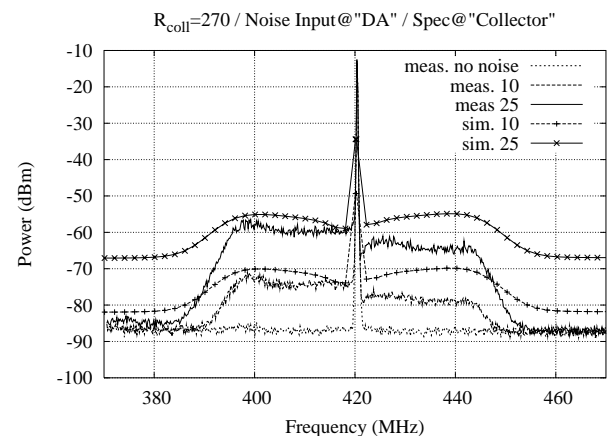


Figure 13. Simulated and measured spectrum at the "collector output" in a 100MHz frequency band around the carrier.

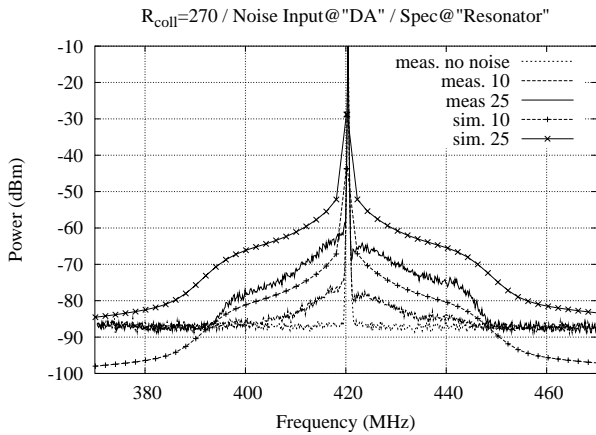


Figure 14. Simulated and measured spectrum at the “resonator output” in a 100MHz frequency band around the carrier.

very well to the measurements, especially not for the resonator output. Another finding is the asymmetric spectra around the carrier. The “left-sided” power spectra is 5dB higher than the “right-sided” spectra. Close to the carrier, there is a “kink” in the “right-sided” spectra. The simulated spectra are symmetric around the carrier. Therefore different quantities and spectra for phase noise might be measured, if either the “right-sided” or the “left-sided” spectrum is defined as SSB phase noise.

C. Colpitts Oscillator for comparison purposes

A Colpitts oscillator (Fig. 15) was designed for comparison purposes of the phase noise spectra. The transistor in the Colpitts oscillator is typically driven into saturation, when the oscillator is in a steady state. As can be seen in Fig. 16, the slope changes from -20dB/dec to -30dB/dec for offset frequencies below 10kHz, whereas the slope for the non-saturated differential oscillator is about -20dB/dec .

IV. CONCLUSION

In this experiment a low frequency external noise source was used to measure the noise upconversion in an oscillator under different feedback parameters. It was shown, that for small offset frequencies (500Hz-1MHz) the phase noise is the same at the resonator and at the collector, but for larger offset frequencies (1MHz-50MHz) the phase noise spectrum at the resonator is a filtered version of the collector spectrum. The spectrum of the low frequency noise source is not symmetrically upconverted around the carrier. An optimum resistance value with $R_{\text{coll}}=100\Omega$ was found, for which the noise source influence is minimized.

As long as the transistors operate in the active forward region, the slope is -20dB/dec . Furthermore it was shown that an -30dB/dec slope region appears close to the carrier, in the phase noise spectrum, if one of the transistors is operating in the saturated region.

Thus, valuable conclusions might be found. One of them is that now evidence is given that white noise at certain points in the oscillator circuitry produces a phase-noise spectrum in a range near the carrier, and with -20dB/dec , if the used

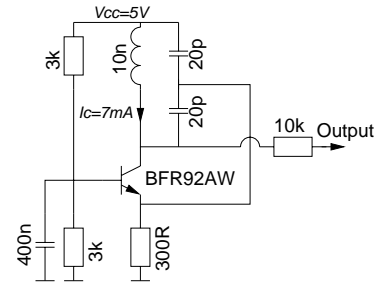


Figure 15. Colpitts oscillator ($f_0=437\text{ MHz}$) designed for phase noise comparison purposes (typically operating in saturated region).

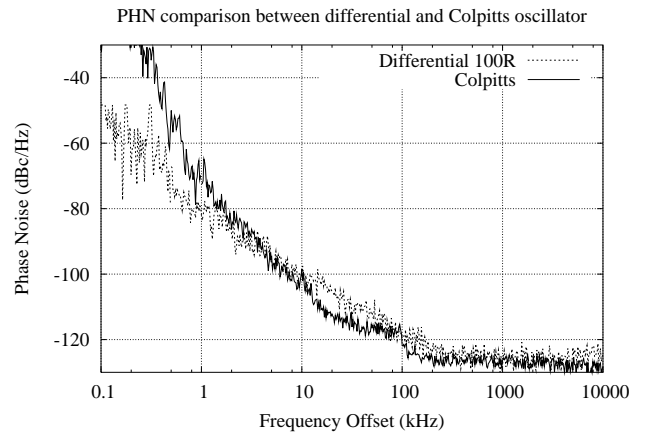


Figure 16. Measured phase noise spectrum for the Colpitts oscillator and the differential oscillator with $R_{\text{coll}}=100\Omega$

nonlinearity is having an odd characteristic. It produces also a part of the spectrum that is white. If the nonlinearity changes symmetry such that also even parts of the characteristic are important, then a part of the phase noise spectrum close to the carrier, is produced that decreases with -30dB/dec . Therefore, there is evidence that in the used differential-amplifier-oscillator, the most important mechanism for phase noise is the upconversion of noise in the input circuitry of the amplifier by virtue of its nonlinear transfer characteristic, as it was assumed in [5].

REFERENCES

- [1] E. E. Hegazi, J. Rael and A. A. Abidi, *The Designer's Guide to High-Purity Oscillators*. Springer, Berlin, Heidelberg, New York, 2005.
- [2] F. X. Kärtner, *Untersuchung des Rauschverhaltens von Oszillatoren*. PhD thesis, Technical University of München, 1988.
- [3] A. Hajimiri and T. H. Lee, "A general theory of phase noise in electrical oscillators," *IEEE Journal of Solid-State Circuits* 33, pp. 179 - 194, 1998.
- [4] A. Demir, A. Mehrotra, J. Roychowdhury: "Phase Noise in Oscillators: A Unifying Theory and Numerical Methods for Characterization," *IEEE Trans. Circuits and Systems I* 47, pp. 655-674 May 2000
- [5] M.H.W. Hoffmann, "A novel method for determining the phase-noise behaviour of resonator-oscillators," *Proc. of SPIE conference on Noise and Fluctuations*, Austin, Texas, May 2005
- [6] H. Weiß, *Comparison between Theory, Simulation and Measurement of the Nonlinear Behaviour and the Phase Noise of an Oscillator*, Master Thesis, University of Ulm, 2006

Design of a 10GSps 5 bit flash A/D converter

Pietro Monsurrò¹, Prof. Andreas Thiede², Prof. Alessandro Trifiletti¹

¹University of Rome “La Sapienza”, Rome, Italy

²University of Paderborn, Paderborn, Germany

Abstract—In this paper we describe the design of a very fast (10GSps) Flash A/D converter for optical applications. This A/D converter can be employed for the digital equalization of Polarization Mode Dispersion (PMD) in optical receivers. The converter has been designed using IHP Microelectronics SG25H1 technology, which is a BiCMOS Si-Ge:C process with 200GHz f_T NPN HBTs and 0.25 μ m CMOS devices. Simulations show very good performances in terms of THD.

Keywords: Flash, optical, PMD, Track and Hold, NRZ, high-speed, A/D converters.

I. INTRODUCTION

This paper describes the design of an analog-to-digital converter to be employed for digital equalization of ISI (Inter-Symbol Interference), as caused mainly by PMD (Polarization Mode Dispersion) in optical receivers.

PMD appears when optical fibers are not ideally circular, thus having different group delays in the two orthogonal polarisation modes. This causes a pulse transmitted in the optical fiber to be distorted, because different components of the same pulse will arrive at different instants of time.

PMD causes the eye diagram to be closed and increases the Bit Error Rate of the system. It has been proposed [4] to reduce the impact of PMD on optical systems' performance through digital equalization. This technique needs a very fast A/D conversion of the signal with sufficient accuracy in order to work properly. In this kind of application also jitter is an important factor, because of its effect on the eye diagram.

Specifications in Tab. I have been derived considering a 10GSps SDH or SONET communication system as target application.

TABLE I. SPECIFICATIONS

Sampling Frequency	f_S	10	GSps
Input Bandwidth	BW	5	GHz
Nominal Resolution	N_{BIT}	5	bits
Signal-to-Noise-Ratio	SNR	>32	dB
Total Harmonic Distortion	THD	>20	dB
Supply Voltage	V_{DD}	2.5	V
Clock Jitter	τ_J	<1	ps

An A/D converter with similar performances has been reported in [1]. Our goal is to obtain similar performances in

mature Silicon based BiCMOS technology, with lower supply voltage and current consumption, while at the same time investigating an innovative architecture for the converter.

The ADC has been designed using IHP Microelectronics Si-Ge:C BiCMOS technology. It has NPN HBTs with 200GHz f_T and CMOS 0.25 μ m devices. HBT devices have a breakdown voltage of 1.9V, which is lower than the supply voltage (2.5V)

II. ARCHITECTURE OF THE FLASH CONVERTER

In this section we describe the architecture of the A/D converter, and the design of the main blocks: the track and hold (T/H), the reference ladder and the comparators.

A. Overview of the architecture

Fig. 1 shows the architecture of the flash converter.

The input is initially sampled and held by a T/H stage. The held signal is fed into a driver stage, which is a buffer that drives four parallel resistive reference ladders. The outputs of the ladders provide the difference between the input voltage and the thresholds. In fact, a bank of 31 zero-crossing comparators evaluates the sign of these outputs. Finally, these outputs are encoded by the ECL logic in order to have a 5 bit output. The T/H is driven by a clock buffer with optimized jitter performance; after the T/H, jitter is no longer a concern. The digital part of the integrated circuit is driven by a larger clock buffer, with variable delay and high swing. The delay can be externally controlled in order to optimally synchronize transition times in the data path. High swing clock is required because triple-tail logical cells (described in [5]) are employed instead of conventional Gilbert-type cells.

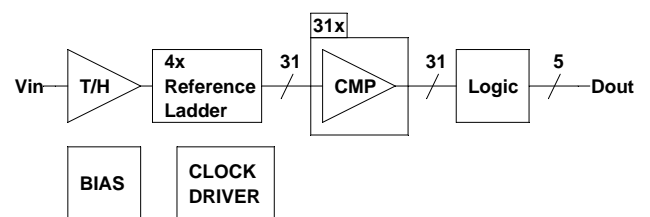


Figure 1. FLASH architecture

This architecture has been chosen because it makes the design of comparators easier, and only zero-crossing detectors are needed, thus enabling lower complexity, lower power consumption and higher sensitivity.

The converter has been designed with low voltage supply, thus introducing severe design constraints. These limitations are evident considering the difficulty of implementing Gilbert-

type ECL latches, or the necessity to use voltage followers and differential pairs alternatively (It is not possible to have two cascaded V_{BE} voltage drops).

B. The Track and Hold (T/H) stage

The T/H stage has an open loop architecture because of the very high operating speed. It is a resistively-degenerated fully-differential pair with passive load, that drives Switched Emitter Followers (SEF). Fig. 2 shows its schematic. Degeneration increases input swing and permits to control gain, which is roughly equal to the ratio between the load and degeneration resistors. Cascoded transistors have been used to avoid breakdown of the devices.

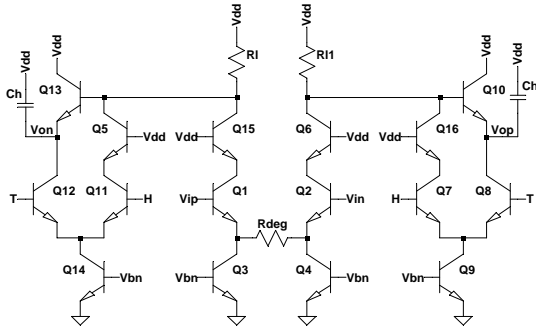


Figure 2. T/H schematic

The main specifications of the T/H are listed in Tab. II.

TABLE II. SPECIFICATIONS OF THE T/H

Sampling Frequency	f_s	10	GSps
Input Bandwidth	BW	5	GHz
Signal-to-Noise-Ratio	SNR	>38	dB
Total Harmonic Distortion	THD	>26	dB
Nominal Gain	A_V	0	dB
Clock Jitter	τ_J	<1	ps
Input Voltage Swing	D_{IN}	0.8	$V_{PP,diff}$

Specifications are tighter than those of the entire A/D converter to have design margins.

C. The resistive reference ladder

In this design we have used a particular topology for the reference ladder, which has been proposed in the literature [2]. Fig. 3 shows the simplified schematic.

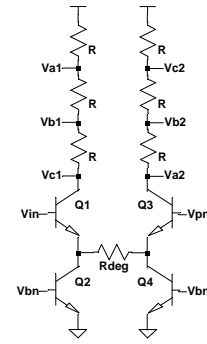


Figure 3. Resistive Reference Ladder (simplified)

The input signal is turned into a current and processed by a resistive ladder. By choosing the resistor ratios correctly it is possible to have zero-crossing at the outputs for particular values of the input. The conversion gain is set by controlling the current of the stage, thus a precise replica biasing is necessary to control the reference voltage.

The main advantage of this stage is that comparators do not need to have two inputs (the input and the reference), because only a zero-crossing is needed. In this way a simpler topology for the comparator is possible, thus saving current and improving sensitivity. As the comparator bank is the main responsible for power dissipation, this feature is promising for low power converters.

Besides, the data path does not have long lines (whose delays and parasitic capacitances may be a concern for the design). The only long lines are present at the outputs of the reference ladder, which contain only zero-crossing information. Besides, relative delays are not a concern because of the input T/H.

The main defect of this architecture is the difficulty in controlling the conversion gain, because it needs a precise biasing.

D. The comparators

Comparators are very simple because they are just zero-crossing detectors.

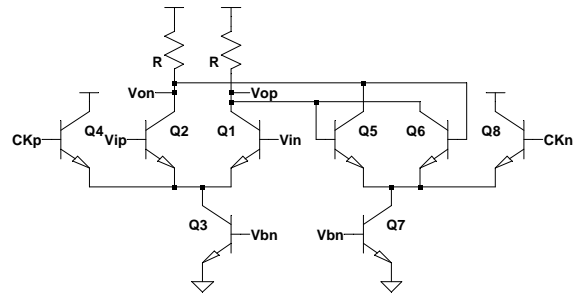


Figure 4. Latch schematic (simplified)

The whole comparator is made by a single stage pre-amplifier, which is a differential pair without degeneration and passive load, and two master/slave latches. The schematic of a single latch is presented in Fig. 4.

The input amplifier is used to improve sensitivity, but it needs additional power dissipation (while bandwidth is very high). Sensitivity is very good and it seems that it is possible to get rid of it, thus reducing power dissipation even more.

The two latches form a master-slave (M/S) flip-flop. The M/S architecture has been used to reduce the probability of meta-stability errors. The triple-tail architecture of the latches is necessary because of the low voltage supply. The clock shall have high swing (higher than the signal), to steer the bias current and turn on or off the input differential pair.

The swing of the digital signals is $0.8V_{pp}$ (differential). This is obtained by using two differential resistors with a voltage drop of $0.2V$ and one common-mode resistor connected to the output. An RC low-pass is used to filter out digital swing noise on the supply voltage.

III. SIMULATING THE A/D CONVERTER

The main blocks have been first simulated separately and, then, the parts have been simulated together, with the exception of the logic. Preliminary simulations of the entire A/D show that the choice of simulating the parts separately is efficient in reducing design time, while giving reliable information about expected performances. The layout of several blocks (the T/H and the comparator's latches) has been completed, and simulations do not show any impact on performances.

A. Simulations of the T/H

The test bench of the T/H contains the T/H, an input voltage follower with 50Ω matching resistors, a loading amplifier at the output, and the clock buffer (with input buffer and matching resistors). The output of the T/H is connected to a driver stage (which drives the subsequent reference ladders), in order to take into account the effect of base currents and linear and non-linear load capacitors. The clock path is similar.

The T/H has been simulated at $16GSps$ instead of $10GSps$. Simulations have been performed considering layout parasitics of the T/H.

Transient simulations with low-frequency maximum-swing input signals show a good linearity, despite the straightforward architecture of the transconductor. At higher input frequency linearity is reduced, but it is well within specifications. Simulated noise ($1.9mV$ at $120^\circ C$) is low, and it is expected that performances of the ADC will not be SNR-limited.

Fig. 5 shows the transient at low-frequency input ($16GHz/64$) input. Fig. 6 shows the output transient at high frequency input ($16GHz/64+8GHz$). In order to compute the FFT (Fast Fourier Transform) in the second case a 2:1 down-sampling has been performed to down-convert the output signal at $16GHz/64$.

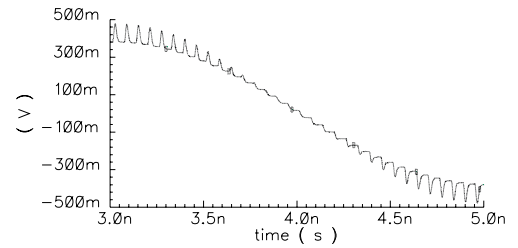


Figure 5. T/H output with low frequency input

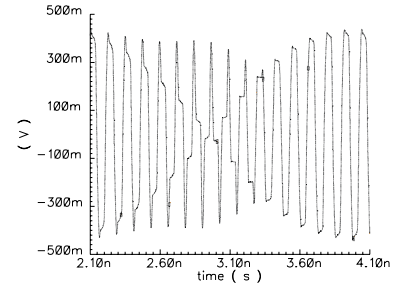


Figure 6. T/H output with high frequency input

TABLE III. SIMULATED RESULTS FOR THE T/H

Current consumption			
Input Buffer	4.0	mA	
Clock Buffer	5.9	mA	
Track And Hold	7.9	mA	
Driver Amplifier	15.5	mA	
Total	37.3	mA	
Distortions and Noise			
Low Frequency	HD ₃	39	dB
	HD ₅	50	dB
High Frequency	HD ₃	31	dB
	HD ₅	44	dB
Noise	SNR	-46	dB

B. Simulations of the comparators

The comparator has been simulated with the digital clock buffer and the input voltage follower. The input is a square wave at $8GHz$, with $4mV_{pp}$ differential swing, the clock is a sinusoid at $16GHz$. Frequency overhead has been considered to take into account the effect of parasitic capacitances, besides, the latches have been simulated with layout parasitics. The output voltage swing is $0.8V_{pp}$ (differential). The comparator latches correctly throughout PVT variations.

Monte Carlo simulations show that the comparators latch always in the same way when $4mV_{pp}$ are at the input, but not when the input is $2mV_{pp}$.

Both these simulations show that the comparators have a resolution higher than 7 bits.

TABLE IV. SIMULATED RESULTS FOR THE COMPARATOR

Current consumption		
Pre-Amplifier	3.9	mA
Master/Slave Flip-Flop	11.7	mA
Total	15.6	mA
Offset	<4	mV _{PP,DIFF}

C. Simulations of the A/D converter

The parts of the A/D converter have been simulated together, with the exception of the logic. The output is encoded without error correction by behavioral circuits in order to have a sinusoid. Distortion is evaluated on this sinusoid.

Fig. 7 shows the output sinusoid and Fig. 8 shows the output spectrum, in the case of high frequency input.

TABLE V. SIMULATED RESULTS FOR THE T/H

Current consumption			
Analog part	150	mA	
Comparators	480	mA	
Digital (estimated)	200	mA	
Total (estimated)	830	mA	
Distortions			
Low Frequency	HD ₃	37	dB
	HD ₅	35	dB
	Higher Order Harmonics	>41	dB
High Frequency	HD ₃	32	dB
	HD ₅	35	dB
	Higher Order Harmonics	>44	dB

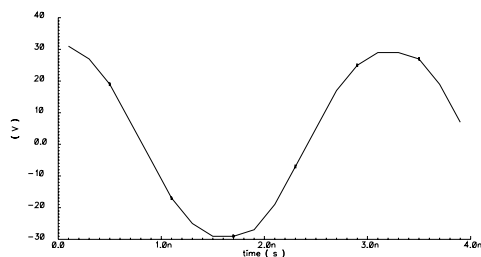


Figure 7. Sub-sampled A/D output with high frequency input.

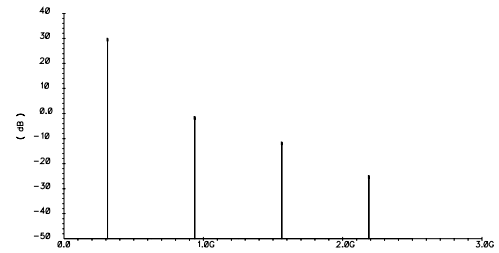


Figure 8. Sub-sampled A/D output spectrum with high frequency input

D. Layout and post-layout simulations

Layout of the converter is not complete. The T/H and the comparator have been simulated with layout parasitics, and performances of the converter were not affected. Anyway, simulations have been performed at higher sampling frequency to take into account the reduced speed due to parasitic capacitances. Both the T/H and the comparator have been simulated at 16GSps for this purpose. A 10GSps T/H has been shown in this technology in [3], so that we expect to obtain the required performances after proper layout design.

IV. CONCLUSIONS

A low-voltage high-speed Flash ADC is being designed. Simulations show that the technology makes the fulfilling of specifications possible. The architecture of the A/D is non-conventional, and it has some advantages, especially in terms of power consumption (even though some additional optimization is required). Low-voltage operation imposes lots of constraints in the design, both in the analog and in the digital circuitry. Power dissipation seems low, even though the digital part has not been considered, yet, thanks to the low supply voltage and the simple structure of the comparators.

ACKNOWLEDGMENT

The authors thanks go to Prof. Kraemer of IHP Microelectronics Frankfurt Oder, Germany, for providing access to the design kits.

REFERENCES

- [1] J. Lee, P. Roux, U.V. Koc, T. Link, Y. Baeyens, Y.K. Chen, "A 5-b 10-GSample/s A/D Converter for 10-Gb/s Optical Receivers"; IEEE Journal of Solid-State Circuits, vol. 39, no. 10, October 2004;
- [2] R. Petschacher, B. Zojer, B. Astegher, H. Jessner, A. Lechner, "A 10-b 75-MSPS Subranging A/D Converter with Integrated Sample and Hold"; IEEE Journal of Solid-State Circuits, vol. 25, no. 6, December 1990;
- [3] Y. Borokhovych, H. Gustat, B. Tillack, B. Heinemann, Y. Lu, W. M. L. Kuo, X. Li, R. Krithivasan, J. D. Cressler, "A Low-Power, 10Gs/s Track-and-Hold Amplifier in SiGe BiCMOS Technology", European Solid-State Circuits Conference. ESSCIRC, September 2005.
- [4] F. Buchali, H. Bülow, "Adaptive PMD Compensation by Electrical and Optical Techniques", Journal of Lightwave Technology, vol. 22, no. 4, April 2004.
- [5] B. Razavi, Y. Ota, R. G. Swartz, "Design Techniques for Low-Voltage High-speed Digital Bipolar Circuits", IEEE Journal of Solid-State Circuits, vol. 29, no. 3, March 1994.

Integration of inverted F-antennas in small mobile devices with respect to diversity and MIMO systems

S. Schulteis¹, C. Kuhnert¹, J. Pontes¹, and W. Wiesbeck¹

¹ Institut für Höchstfrequenztechnik und Elektronik (IHE)
Universität Karlsruhe (TH), Germany
Tel: +49-721-608-7676, Fax: +49-721-691-865
E-mail: Stephan.Schulteis@ihe.uka.de

Abstract—For multimedia applications three antennas are placed inside the housing of a personal digital assistant (PDA) with respect to MIMO and diversity. One planar and two newly designed buckled inverted F antennas are used. As diversity performance indicator the correlation coefficient is applied. MIMO capacity is calculated with a MIMO system model including accurate antenna modeling and a double-directional multipath indoor channel model. Both analysis are carried out under consideration of the influence of a user. It will be shown, that for new, efficient diversity and MIMO systems, antenna design and placement must take into account the complete system including the user.

I. INTRODUCTION

New upcoming data and multimedia devices require high and reliable data rates. The need of efficient communication systems with high reliability of connectivity can be fulfilled with the use of diversity and multiple input multiple output (MIMO) techniques.

Development of small antennas for the integration into small mobile devices plays a significant role for implementation of diversity and MIMO systems. In [1] and [2] the inverted F antenna is miniaturized for the application in MIMO systems. Compact and efficient arrays can be designed by the use of polarization diversity [3].

For coverage of both wireless local area network (WLAN) spectrums at 2.45 GHz and at 5.2 GHz dual band antennas are required. Additionally, placement and design of antennas should consider not only housing but also the adjacent body parts of the user. In this paper a housing of a personal digital assistant (PDA) is taken to integrate three dual band W-LAN antennas. For this, the antennas are miniaturized with respect to bandwidth and impedance. It is commonly known that size reduction decreases the antenna bandwidth whereas the impedance also diminishes, see [4] and [5].

In section II the design and the integration of balanced dual band, miniaturized IFA antennas into the housing of a PDA is shown. Simulations concerning antenna parameters like input impedance, pattern and gain are carried out. For MIMO purposes coupling of antennas is analyzed. Measurement results regarding the integration of three antennas into a PDA housing are presented in section III. Constitutive to previous sections a model for the investigation of user's influence is presented in section IV. The diversity performance parameters are explained and analyzed for the PDA model equipped with three antennas under consideration of users influence, section

V. MIMO capacity is investigated in section VI. Finally a conclusion is drawn.

II. INTEGRATION OF ANTENNAS INTO A PDA

The integration of three miniaturized antennas into a small housing of a PDA is very challenging. For integration three balanced inverted F antennas are used. The shape of a balanced inverted F-antenna is shown in figure 1.

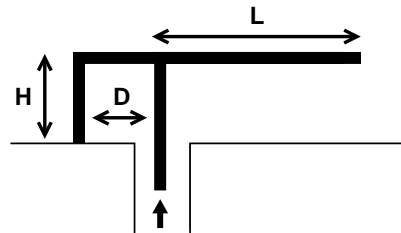


Fig. 1. Parameter of a balanced, non-miniaturized inverted F antenna.

The length L and the height H determine the resonant frequency according to equation (1).

$$T = L + H \approx \lambda_{res}/4 \quad (1)$$

The input impedance can be adjusted with the stub length D . A detailed description of the influence of all parameters can be found in [2]. The benefits of balanced antennas compared to unbalanced antennas are a reduced sensitivity to objects in the near surrounding of the antenna [6] and a doubled input impedance. Additionally the antenna design is independent of groundplane size thus the antenna design does not depend on the design of the PCB.

For integration of three antennas into a small housing like a PDA housing the antennas have to be as small as possible. Therefore inverted F antennas are miniaturized by capacitive and inductive loading, see figures 2 and 3.

For inductive loading the parameters are the width of the meander structure b_m , the gap between the meander lines x_m and the width of the meander line itself d_m . As can be seen in figure 3 for capacitive loading a capacitance is integrated with width u_c of and height v_c . A detailed description of the influence of these parameters can be found in [?]. Each antenna is connected to a 50Ω coaxial cable by a feeding network. The dual band operation can be achieved by a parasitic element in addition to the inverted F antenna shape,

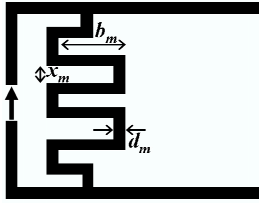


Fig. 2. Simulation model for inductively loaded inverted F antenna.

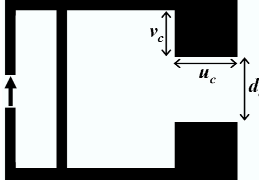


Fig. 3. Simulation model for capacitively loaded inverted F antenna.

see [?]. For an increase of bandwidth the parasitic element and the antenna structure are placed on different sides of the substrate. In addition the antenna structure is shifted by $q = 0.0082 \lambda_{2.45}$ and $p = 0.0525 \cdot \lambda_{2.45}$ for a resonant wavelength λ_{res} at 2.45 GHz as can be seen in figure 4.

For decoupling the antennas must be spaced as far away from each other as possible and polarization diversity should be exploited.

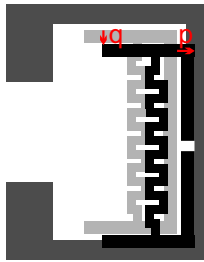


Fig. 4. Asymmetric positioning of parasitic element for an increased bandwidth.

Space in PDA's housing is limited thus a decoupling of antennas due to spacing is not possible. Further on, an antenna as shown in figure 4 cannot be integrated vertically in the housing, because the height is too small. As solution to these limitations the antenna is buckled in the middle of the height of the antenna, see figure 5.

According to the buckled shape of one antenna type, the polarization and pattern is different for the two types of inverted F antennas.

For the placement of antennas in a PDA housing some considerations concerning user's influence should be made. It is expected that the user covers the lower part of the housing in most cases. In fewer cases the user's hand covers the upper part of the housing. Hence it is beneficial to place the antennas in that way that in most cases only one antenna is covered.

Figure 6(a) shows the simulation model of the PDA, which is developed under previous considerations, with three antennas integrated.

One possibility is shown here, the two buckled inverted F

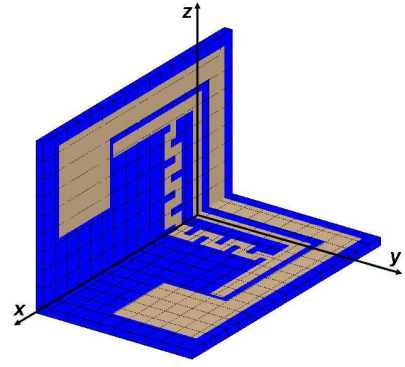


Fig. 5. Simulation models for buckled miniaturized dual band inverted F antennas.

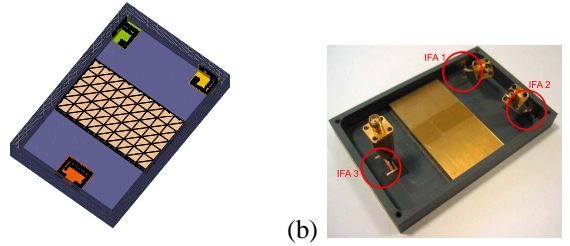


Fig. 6. Simulation model and model for measurements of three inverted F antennas integrated into a PDA's housing.

antennas are placed at the top in the right and left corner. The third antenna, a planar inverted F antenna is placed at the bottom.

The model of the PDA (8 cm x 12 cm x 1.5 cm) consists of a metallic block, representing the battery and the display of the device, and a PVC housing with a wall thickness of 4 mm. The permittivity of the PVC material equals $\epsilon_r = 3$, the loss factor $\tan \delta = 1 \cdot 10^{-4}$. For simulations the housing is closed by a top cover.

All simulations were carried out with FEKO, see [7], a standard EM code based on method of moments. FEKO was applied for calculating the pattern of the coupled antenna system as well as mutual coupling and self impedances of the antennas.

III. ANTENNA MEASUREMENTS

In order to verify the simulations measurements have been carried out at both frequencies 2.45 GHz and 5.2 GHz. Gain and pattern measurements were carried out in an anechoic chamber. The patterns can be found in figure 7. The gain for the inverted F antennas integrated into the PDA housing can be found in table I.

The antenna patterns differ clearly in horizontal and vertical polarization, which is a good premise for pattern diversity. If antenna patterns are too similar, correlation would degrade diversity performance.

Coupling and S-parameters were measured with a network analyzer. The reflection coefficient of the i^{th} antenna is denoted as S_{ii} . As an example the reflection coefficient of the first antenna is shown in figure 8. The antenna is suitable for both frequencies.

TABLE I
MEASURED GAIN FOR INTEGRATED ANTENNA STRUCTURES IN THE PDA'S HOUSING WITHOUT USER'S INFLUENCE, SEE FIGURE 6(B) AT 2.45 GHz AND 5.2 GHz.

	@2.45 GHz	@5.2 GHz
IFA1	0.8 dBi	1.2 dBi
IFA2	0.8 dBi	1.2 dBi
IFA3	5.5 dBi	1.2 dBi

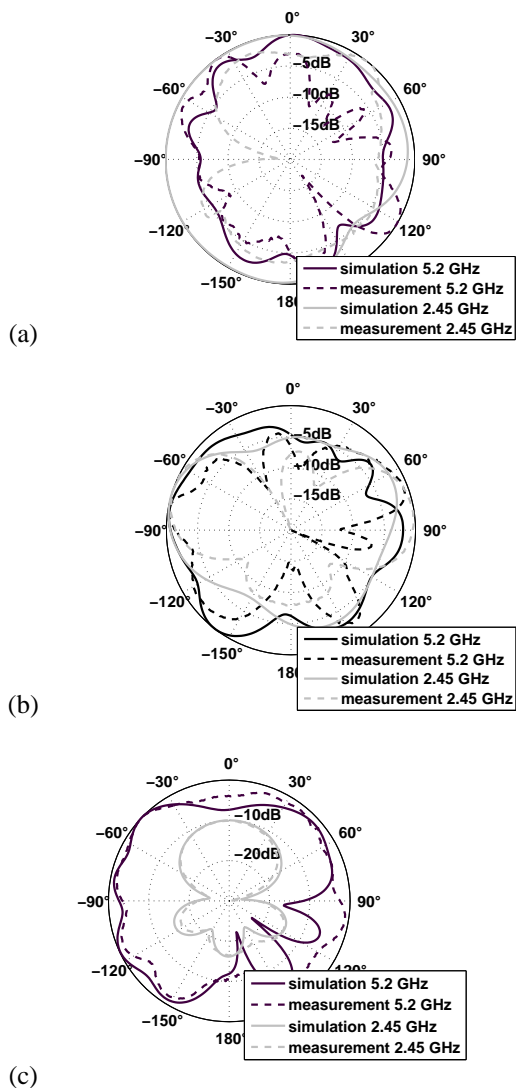


Fig. 7. Simulated and measured azimuth pattern for horizontal polarization of the (a) IFA 1, (b) IFA 2, and (c) IFA3.

Figure 9 shows the measurement and simulation results for coupling coefficients of different pairs of antennas integrated in the PDA. It can be seen, that simulations and measurements predict a coupling of less than -18 dB in the frequency band between 2 GHz and 6 GHz.

The gain and pattern simulations and measurements demonstrate that the antennas are suitable for MIMO and diversity systems at both WLAN frequency bands.

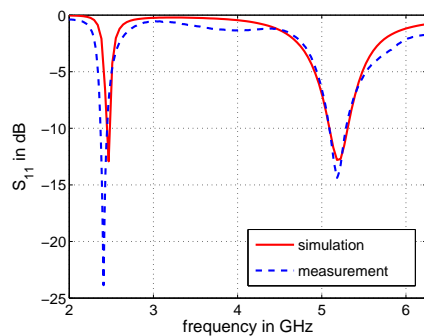


Fig. 8. Simulation and measurement results for the reflection coefficient of the integrated antenna, denoted with number one, see figure 6(b).

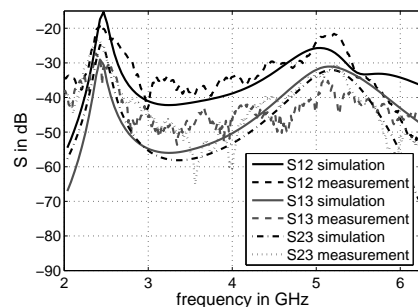


Fig. 9. Simulated and measured coupling coefficient between the ports of integrated dualband inverted F antennas.

IV. INVESTIGATION OF USER'S INFLUENCE

For investigation of diversity systems and MIMO capacity the influence of user's hand is not negligible. Therefore a hand model is included. Two different hand positions are analyzed. One where the user holds the PDA at the top and the second and most significant one, where the user places his hand at the bottom of the PDA, see figure 10.

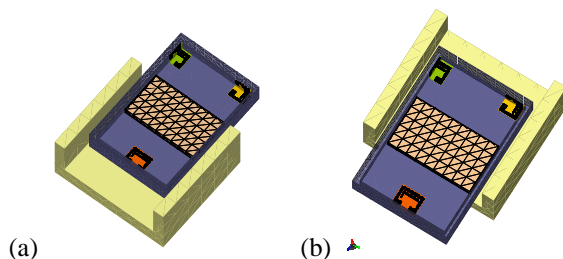


Fig. 10. Simulation model of PDA and the investigated hand position on bottom 10(a), covering one antenna, and with hand on top 10(b), covering two antennas.

The shape of the hand is like a U profile. The hand model has an extension of 10 cm by 10 cm on bottom. The height below the PDA is 1.5 cm and the height of the side plates equals 4.9 cm. The width of side plates is 1 cm and the gap between the hand and the PDA housing on bottom is 0.9 cm and between the side plates and the PDA it is 0.5 cm. For bottom position, the part of the PDA which is not covered

by the hand has a length of 4.4 cm. For top position it has a length is 3.5 cm.

Power is absorbed in the hand, hence power transfer in the communication system is possibly affected.

V. DIVERSITY PERFORMANCE

The received signal level correlation coefficient can be used to investigate antenna array's quality for diversity applications [8], [9]. However, correlation of signals is only given for two signals. In the case of more than two antennas, a figure of merit must be found, which should not only concentrate on correlation properties but also on received signal strength from the antennas.

For investigation of correlation properties of antenna arrays the power correlation coefficient $\rho_{e,v_i v_j}$ for all possible pairs of antennas has to be computed according to [8]. $v_{i,\xi_{i\alpha}}$ denotes the received voltage of antenna i , if the antenna is not loaded. α denotes the polarization, for example $\alpha = h$ for horizontal and $\alpha = v$ for vertical polarization.

$$\begin{aligned} \rho_{e,v_i v_j} &\approx |\rho_{v,v_i,\xi_{ih} v_j,\xi_{ih}} + \rho_{v,v_i,\xi_{iv} v_j,\xi_{iv}}|^2 \\ &\leq |\rho_{v,v_i,\xi_{ih} v_j,\xi_{ih}}|^2 + |\rho_{v,v_i,\xi_{iv} v_j,\xi_{iv}}|^2 \end{aligned} \quad (2)$$

For this equation the cross polarized power correlation for the antennas is neglected. The power correlation coefficients of all antennas are placed in a power correlation matrix ρ_{NN} .

$$\rho_{NN} = \begin{pmatrix} \rho_{e,v_1 v_1}(\Delta\vec{x}) & \cdots & \rho_{e,v_1 v_N}(\Delta\vec{x}) \\ \vdots & \ddots & \vdots \\ \rho_{e,v_N v_1}(\Delta\vec{x}) & \cdots & \rho_{e,v_N v_N}(\Delta\vec{x}) \end{pmatrix} \quad (3)$$

N denotes the maximum number of antennas used in the array. The main diagonal elements $\rho_{e,v_1 v_1}(\Delta\vec{x})$ are equal to one. The matrix elements are all less than 1 and due to equation (2) larger than or equal to zero. Due to the fact that the matrix is symmetric the eigenvalues λ_n , with $n \in \{1 \dots N\}$, are real numbers. The maximum eigenvalue can be used as a basic parameter for investigation of antenna array power correlation. It is referred to as correlation factor.

Figure 11 shows the correlation factor for the previously described positions of user's hand. Impinging power is uniformly distributed in azimuth and Gaussian distributed, with expectation value of 90° and standard deviation of 60° , in elevation.

Correlation properties are influenced by the user's hand. However, the correlation factor is less than 0.1, which is remarkable. Sophisticated antenna placement exploits spatial, pattern and polarization diversity, leading to decorrelated signals.

VI. MIMO PERFORMANCE

For determination of MIMO performance simulations are carried out with a MIMO system model, see section VI-A. As figure of merit the transmission gain and the spectral efficiency are applied.

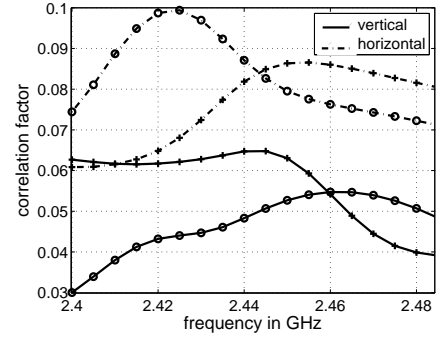


Fig. 11. Power correlation factor for typical indoor channel distributed impinging power with users hand on top (+) and users hand on bottom (o).

A. MIMO System Model

For evaluation of MIMO performance of this antenna design, a system model of a complete transmission link is applied [10].

The model of the whole MIMO transmission link allows for a very accurate antenna modeling, including all mutual coupling effects, and a precise analysis of the power transmission gain and therewith the efficiency of the arrays. The basic idea is to model the whole MIMO transmission link to be composed of single network units, which are the transmitter, the transmit array S^{TxA} , the propagation channel S^C , the receive array S^{RxA} and the receiver. It is essential to take the transmitter and receiver as load networks, connected to the antenna arrays into account to model the matching of the antennas and the mutual coupling effects correctly. The antenna arrays S^{TxA} and S^{RxA} are modeled by scattering parameters, too. The basic idea of the scattering parameter representation of an antenna array is that each single antenna is a two port device with an excitation port and a directional far field port. For the following investigations the base station consists of three dipoles arranged as triangle. As channel model an indoor stochastic double-directional multipath indoor channel model given in [11] is used. 2000 realizations of the channel have been generated for random positions of the transmitter Tx and the receiver Rx .

B. Power transmission gain

Since PDAs are battery-driven, the efficiency of the antennas is an important topic. Mutual coupling among closely spaced antennas does not only influence the signal flow and the correlation properties, it can also strongly reduce the efficiency of an array in terms of power. The system model, given in [10], allows for considering the power transmission gain of the whole MIMO link, including the antennas. The power transmission gain is the ratio of the power received at the signal drain to the power fed into the transmit antennas. The latter is not equal to the power which is radiated from the transmit antennas, if the efficiency of the transmit array is not 100%.

By comparing the power transmission gain of MIMO systems with different arrays in the same channel, conclusions on the performance of the arrays in terms of power can be drawn.

Figure 12 shows the cumulative distribution function of the power transmission gain for different hand positions at the PDA. For comparison, a single input single output (SISO) system with a single dipole element at transmit and receive is shown.

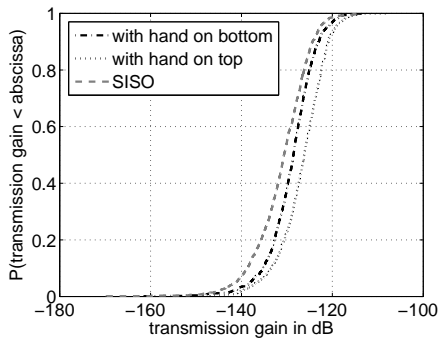


Fig. 12. Simulation result of MIMO power transmission gain for the indoor channel and different hand positions compared to SISO case at 2.45 GHz

It seems to be surprising, that if the hand is on top the power transmission gain is lower than if the hand is on bottom. This phenomenon can be explained by the gain of the antennas. The planar inverted F antenna on bottom has a gain of 5.5 dBi @ 2.45 GHz in comparison to the buckled antennas, 0.8 dBi @ 2.45 GHz, which are covered if the user's hand is on top.

C. Spectral efficiency

Spectral efficiency calculations are carried out taking all coupling effects and the user's hand into account. In order to assess a MIMO transmission system by the spectral efficiency usually a fixed SNR and a channel matrix, which is normalized by the Frobenius norm, is used. With this normalization, the influence of the correlation properties of the channel matrix on the spectral efficiency becomes visible, but any interrelation between the SNR and the correlation properties of H is neglected. If H is not normalized, that means the path loss and the gain of the single antenna elements are included in H , the spectral efficiency is

$$C = \log_2\left(\det\left(I + \frac{P_T}{\sigma^2 m} H H^\dagger\right)\right) \quad (4)$$

P_T is the transmit power, which is equally distributed among the m transmit antennas if no channel state information is available at the transmitter. σ^2 is the noise power. This formula allows for a comparison of different MIMO systems, including the influence of the transmission gain and therewith of the SNR.

The transmit power remains fixed, i.e. no normalization in terms of power is performed. As a result the cumulative distribution function (cdf) for the MIMO spectral efficiency at 2.45 GHz is shown in figure 13. The spectral efficiency is relatively large with respect to the limited space available for the antennas in a PDA and with respect to the dual-band operation.

Hold in mind, that if the hand is on top, the two buckled inverted F antennas are covered. In this case the power transmission gain is lower than if only the planar inverted F

antenna is covered. Despite degradation of power transmission gain if one antenna is covered the spectral efficiency for user's hand on bottom is enlarged in comparison to user's hand on top. This is because if only one antenna is covered the residual two antennas on top can be used for MIMO. However, even if the user's hand is placed on top and both buckled antennas are covered, the spectral efficiency is higher than for SISO case.

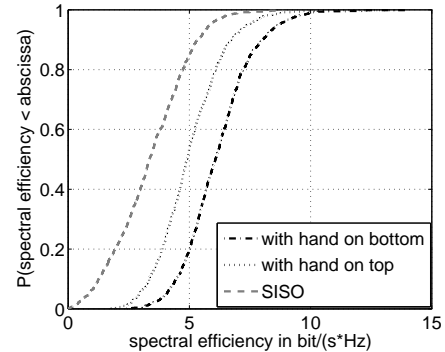


Fig. 13. Simulation result of MIMO spectral efficiency for different hand positioning on PDA at 2.45 GHz

VII. CONCLUSION

A sophisticated dual-band antenna design and its integration into a PDA has been presented. The antenna design and placement has been carried out taking MIMO and diversity aspects into account. The results show that this antenna configuration is appropriate for MIMO in both WLAN frequency bands. The influence of user's hand is not negligible, especially the absorption of power in the human tissue, if some antenna elements are covered by the hand.

REFERENCES

- [1] S. Schulteis, C. Waldschmidt, C. Kuhnert, and W. Wiesbeck. Design of a miniaturized dual band inverted f antenna. *IEEE Antennas and Propagation Society International Symposium*, 3:3123–3126, June 2004.
- [2] S. Schulteis, C. Waldschmidt, W. Soergel, and W. Wiesbeck. A small planar inverted f antenna with capacitive and inductive loading. *IEEE Antennas and Propagation Society International Symposium*, 4:4148–4151, June 2004.
- [3] C. Waldschmidt, C. Kuhnert, S. Schulteis, and W. Wiesbeck. Compact mimo-arrays based on polarization diversity. *IEEE Antennas and Propagation Society International Symposium*, 2:499–502, June 2003.
- [4] R. C. Hansen. Fundamental Limitations in Antennas. *Proceedings of the IEEE*, 69(2):170–182, February 1981.
- [5] J. S. McLean. The Radiative Properties of Electrically-Small Antennas. *IEEE International Symposium on Electromagnetic Compatibility*, pages 320–324, August 1994.
- [6] A.T. Arkkio. Effect of Ground Plane Size on the Free-Space Performance of a Mobile Handset PIFA Antenna. *Proceedings International IEE Conference on Antennas and Propagation*, pages 316–319, April 2003. Conf. Publ. No. 491.
- [7] <http://www.feko.info>.
- [8] K. Fujimoto, A. Henderson, K. Hirasawa, and J.R. James. *Small Antennas*. Research Studies Press LTD., 1993.
- [9] William C. Jakes, editor. *Microwave Mobile Communications*. Wiley, New York, 1974.
- [10] C. Waldschmidt, S. Schulteis, and W. Wiesbeck. Complete RF system model for the analysis of compact MIMO arrays. *IEEE Trans. on Veh. Techn.*, 53(3):579–586, May 2004.
- [11] T. Zwick, C. Fischer, and W. Wiesbeck. A stochastic multipath channel model including path directions for indoor environments. *IEEE Journal on Sel. Areas in Comm.*, 20:1178–1192, 2002.

Parts of the work are outcome of the ACE network of excellence.

Using Metamaterial structures with frequency agile basestations

Gunther Dehm-Andone, Grzegorz Adamiuk, Georg Fischer, *Member, IEEE*

Abstract—The requirement for basestations that are more and more flexible and multiband capable leads to the need for multiband RF functional blocks and tunable filters. By presenting several examples like a coupler, a duplex filter and a balun it is shown that metamaterial structures can be of great advantage for frequency agile RF systems as they can be designed for multiband capability. Also electronic tuning of highly selective duplex filters becomes feasible through tunable Metamaterial structures leading to software defined duplex filters.

Index Terms— Metamaterial, tunable circuits and devices, tunable filters, tuning, transmission line theory, transmission line circuits, microwave filters, microwave circuits, micro strip circuits, micro strip couplers,

I. INTRODUCTION

BASED on research by Veselago [9] published in 1968, Pendry *et al.* developed the first practical application of his theoretical results on metamaterials, a metallic structure with negative permittivity [10] and with negative permeability [11]. C. Caloz *et al.*, Iyer and Eleftheriades followed with a transmission line approach on metamaterials [12],[13] and further theoretical expansions on CLRH structures [14]-[16]. The Caloz / Itoh research group also applied these results in [3],[5]-[7] for dualband components. In this paper application examples for three band and tunable metamaterials are provided, given by the need for having a single RF signal path with frequency agile basestations.

II. FREQUENCY AGILE RF SYSTEMS

f/ MHz	Duplex gap/ MHz	GSM GPRS EDGE GERAN	CDMA CDMA2000 3G1X EVDO/DV	UMTS FDD TDD HSDPA
450	2.4	X	X	
480	2.8	X	X	
850	20	X	X	X
900	10	X		X
1800	20	X		
1900	20	X	X	X
2100	130		X	X
2600	70		X	X

Table 1: Frequency bands used with mobile communication

Increasing attention in the mobile communication sector directs not only to multi standard Software Defined Radio but

also to frequency agile multiband radio platforms (table 1) that reduce costs with the manufacturer due to logistical savings and offer tremendous flexibility for the user.

Until now mainly techniques for switching between a number of predefined bands have been implemented with the RF system of basestations [17]. However this approach has its merits given that the number of frequency bands opened for mobile communication is constantly increasing due to de-regulation and a further band cannot be added once a system is deployed.

Consequently a step up at the architectural level from reconfiguration between predefined settings to full tune ability is required. The specific challenge however is that the mobile communication bands by now already span nearly 3 octaves e.g. from 450 to 2600 MHz. It shows up that Metamaterial (MTM) structures can be very beneficial in this context if they can be designed as multiband capable or being tunable.

Fig. 1 illustrates where MTM structures can be used with the RF system of a frequency agile basestation. At some locations static structures are sufficient, at other locations the MTM structures need to be tuned by either MEMS (Micro Electromechanical systems) [18] or ferroelectric varactors like e.g. BST (Barium Strontium Titanate) components.

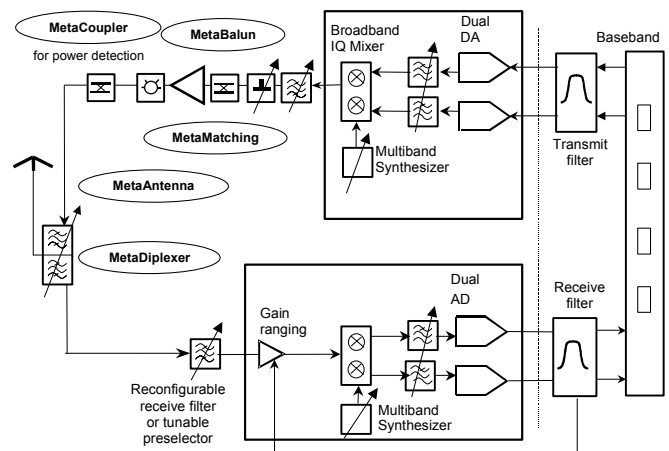


Fig. 1: Frequency Agile RF system approach

The specific challenge however with tunable MTM structures carrying RF signals of high power is the current and voltage handling capability of the tuning elements.

III. APPLICATION EXAMPLES

With the following subsections results on the simulation, and optimization of various application examples of MTM structures either static or tunable from above RF system approach are presented. These are a multiband coupler, a tunable duplex filter and a multiband Rat-Race-Balun.

The focus on the work reported here is not the accuracy of predicting the behavior of MTM structures, so the minimization of differences between simulation and measurement but the understanding of what functions at system level are enabled by MTM.

A. COUPLER EXAMPLE

1) Motivation

By the advent of new wide bandgap RF power transistor technologies like SiC-MESFET and GaN-HEMT it becomes possible to realize reconfigurable or tunable amplifiers that can operate in multiple bands [19]. In order to supervise those amplifiers, especially the in- and output power, multiband power detectors become necessary. Implementing multiple couplers for different frequency sub ranges would be very inefficient as unused couplers would contribute additional losses and by that reduce the gain and effective usable efficiency of the amplifier. It is therefore desirable to have a single coupler that can operate in multiple bands. Standard couplers even if they follow a broadband design approach are insufficient as wide bandgap amplifiers can easily span 3 octaves.

2) Comparison between standard MSL couplers and metamaterial coupler

Directional couplers with coupled lines for example use the coupling field of micro strip lines to couple the signal from one line to the near other line over a length of $\lambda/4$. So the operating frequency range is very limited. On top a coupling factor over 10dB is hardly to achieve and only the harmonic frequency bands are also coupled. The factor between those bands is restricted to integer multiples. At other Pi- or Pi/2-hybrids there are the same problems. In the most common case branch line coupling with a line connection of different impedance is used. Here the two arriving waves at the according ports result in constructive or destructive superposition.

Therefore their phase difference and the impedances of the lines have to be optimized for the frequency band. But it is necessary for the application to have a small and stable coupling at multiple and broad bands which are separated with a non-integer multiple. [6] showed a way to realize it for two bands. In this paper it will be shown for three bands.

3) Design approach

The design approach towards a 11dB-coupler followed here is based on a right-handed Pi/2-hybrid with a thin connection to the coupled port. Figure 2 shows a single band coupler with right-handed behaviour.

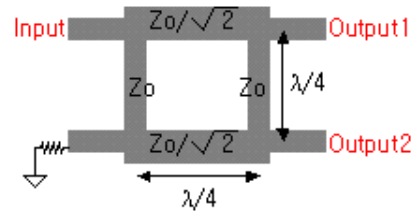


Fig. 2: RH branch line coupler

Inserting a line section with left-handed (LH) behaviour in all four lines (fig. 3) results in a multiband coupler.

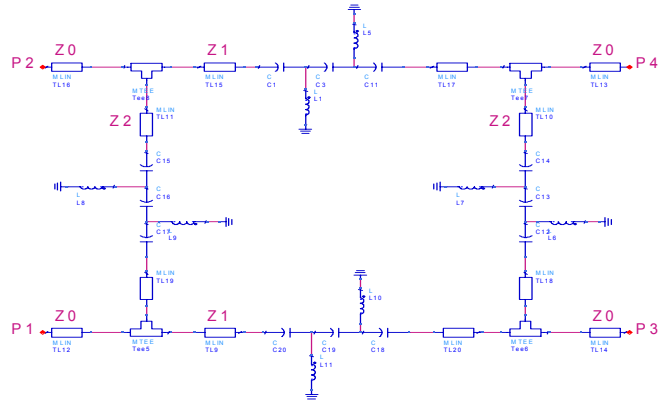


Fig. 3: layout of coupler with LH sections

When looking at the phase shifts of the four lines the difference can be observed. The following fig. 4 points out the difference of the phase at the transmission output w/o LH section. Because of the low application frequency between 400 and 2200 MHz and the small dimensions compared to the guided wavelength the phase difference shown is not very big.

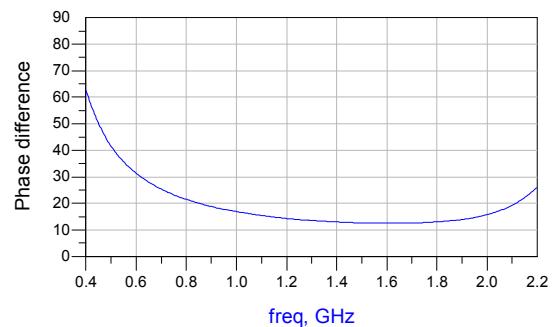


Fig. 4: Phase difference w/o LH section of coupler transmission path

Of course the right phase is not enough for good performance. The requirements for all frequency bands were defined as following:

- $S_{11}, S_{22} < -10$ dB (Reflection)
- $S_{21} > -1$ dB (Transmission)
- -12 dB $< S_{31} < -11$ dB (Coupling)

The next few graphs show the simulated performance of the "metacoupler" with component S-parameter files, which means the parasitics of the concentrated elements are fully reflected in the design.

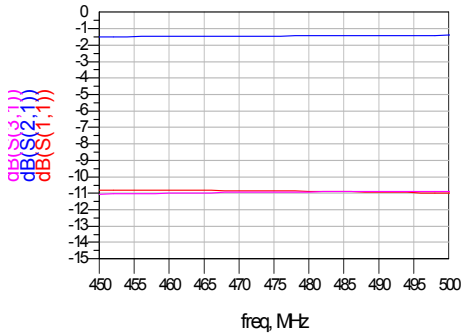


Fig. 5: S-parameters of coupler at low frequency band

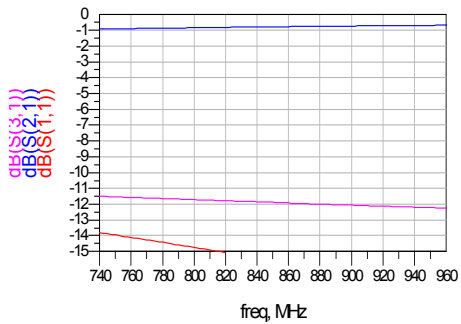


Fig. 6: S-parameters of coupler at middle frequency band

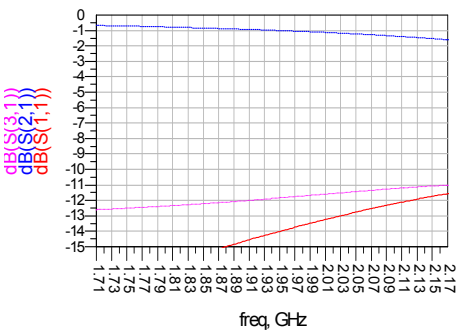


Fig. 7: S-parameters of coupler at high frequency band

Figs 5, 6 and 7 prove that the requirements can be fulfilled even when parasitic effects with the discrete components used in the left-handed section are considered.

For a good current handling up to 1.8 A high current inductivities from Coilcraft were used. Like [5] the LH part was realized as a compact package of SMD components for reducing dispersion effects. Tolerance didn't have effect neither in the simulation nor in the measurement because of the averaging effect provided by using multiple discrete components in series or parallel. Furthermore the structure in

itself is not very resonant, so that frequency shifts don't significantly change behaviour at system level.

4) Realization

Fig. 8 shows the practical realization of the 3-band metamaterial coupler.



Fig. 8: 3-band metamaterial coupler realization

The Measured performance showed good agreement for the low band but deviations in mid and high band. The reason for the deviation was identified to be in the ground via and the LH line sections. These vias can easily result in additional inductances of 1 nH, which haven't been considered in the design.

B. FILTER EXAMPLE

1) Motivation

For a frequency agile basestation it is required that not only the radio and the PA are frequency agile, but also the duplex filter and the antenna to facilitate a remote alteration of the operating frequency band.

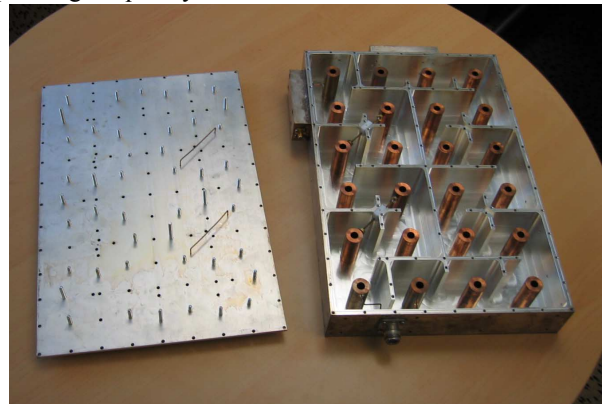


Fig. 9: Typical Duplex-Filter with a UMTS basestation (open)

Fig. 9 shows a standard UMTS duplexer by today. It has the size of 24cm x 36cm x 5cm. Lambda quarter coaxial resonators offering Q-factors up to 5000 are used. In order to

achieve the required selectivity 14 resonators are required at TX side and 10 at RX side. These duplexers not only are large in form factor and of heavy weight, but also expensive in manufacturing. During manufacturing the duplexers are aligned for the exact filter function by tuning the screws at the top cover.

There do exist techniques for tuning coaxial resonators e.g. by moving dielectric or additional metal plates into the cavities. However these techniques only allow for marginal tuning of a few percent and are far away from octave tuning. These tuning mechanisms can therefore only be used to do block tuning inside a band. A further problem with those tuning techniques is that the tuning by a dielectric degrades the Q-factor and by that selectivity is lost.

It would therefore be desirable to have a duplexer that can be tuned over a wider range, say at least an octave and that comes at smaller form factor and lower costs offering about the same selectivity even under the constraint of lossy tuning elements.

A unified duplexer, whose filter function could be tuned an octave or more would provide dramatic logistical savings as the number of duplexer variants by today goes much beyond the number of band specific radio and PA variants as a separate duplex filter is needed for every sub block of a frequency band.

2) Theory on CLRH metamaterials in filter applications

As described in [2], [3], [4] and [8], the equivalent network unit cell for one-dimensional metamaterial with capacitors and inductors was modeled in the circuit simulator of Agilent ADS including also their losses by inserting resistors. The analyzed CLRH structure is shown in figure 10.

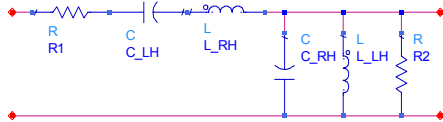


Fig. 10 CLRH unit cell incl. losses

For a filter effect these cells have to be repeated periodically. From the performance of a single unit cell and the required total performance the number of unit cells is obtained. Especially the loss model is important here, which will be described later.

The first goal for a duplexer based on metamaterial was to have a pass band loss of less than 1dB (like a standard CDMA duplexer). To achieve these small losses a very good matching of the structure is required. Thus also the characteristic impedance has to be optimized. As expected the impedance is a function of the frequency or omega as Eq. (1) points out.

$$Z_{characteristic} = \sqrt{\frac{L_{RH} + \frac{R_1}{j * \omega} - \frac{1}{\omega^2 * C_{LH}}}{C_{RH} + \frac{1}{R_2 * j * \omega} - \frac{1}{\omega^2 * L_{LH}}}}$$

Eq. 1: Characteristic Impedance of CLRH structure

Another stringent requirement on filters is always the group delay variation and the phase response. To calculate the phase velocity and afterwards both required value plots we need the phase “constant” beta. Equivalent to [3] beta was calculated with the resulting equation (2).

$$\beta = N * \text{Im} \left\{ \sqrt{\frac{C_{RH} + \frac{L_{RH}}{L_{LH}} + \frac{R_1}{R_2} - \omega^2 * L_{RH} * C_{RH} - \frac{1}{\omega^2 * L_{LH} * C_{LH}}}{j * \left(\omega * \left(R_1 * C_{RH} + \frac{L_{RH}}{R_2} - \frac{R_1}{\omega^2 * L_{LH}} - \frac{1}{\omega^2 * R_2 * C_{LH}} \right) \right)}} \right\}$$

Eq. 2: phase constant β for N unit cells

Also the resonance frequencies of the serial (Eq. 3) and parallel part (Eq. 4) are very important parameters of the structure because they define the edges of the band gap.

$$f_{serial} = \frac{1}{2\pi \sqrt{L_{RH} C_{LH}}}$$

Eq. 3: Serial resonance frequency of unit cell

$$f_{parallel} = \frac{1}{2\pi \sqrt{L_{LH} C_{RH}}}$$

Eq. 4: Parallel resonance frequency of unit cell

Figures 11 and 12 show the transmission and beta graph of a typical not optimized CLRH structure with 10 unit cells. The peaks in the first graph are results of the resonances in the structure at $\beta = \pm n * \pi / N$ (N = number of cells, n = resonance index).

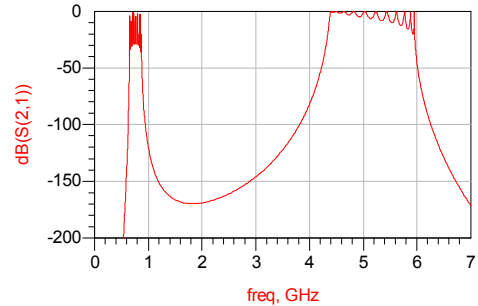


Fig. 11: transmission of CLRH structure

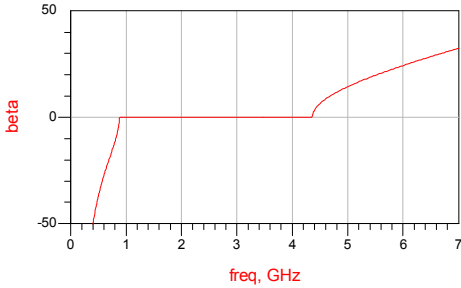


Fig. 12: beta over frequency

Beta is equal zero at the edges of the band gap. Near $\beta=0$ at the edges the attenuation is also near zero and therefore perfect for applications. But the band gap itself is not usable because no wave propagation is possible here. Outside and near the band gap if beta is near 0 almost no voltage is laying on the serial resistor and almost no losses appear. At the parallel resistor the voltage can be ignored because this value can be realized very high. So the filter impact at band gap edge is very high through the steep rising edge at low frequency distance. Additionally a high one-sided Q is feasible and it is not susceptible to the serial losses! To proof this effect we simulated a sweep of the resistor values, the phase differences between the unit cells and also the absolute phase values over the frequency. The figs. 13 and 14 show the phase equality at 4.1 GHz.

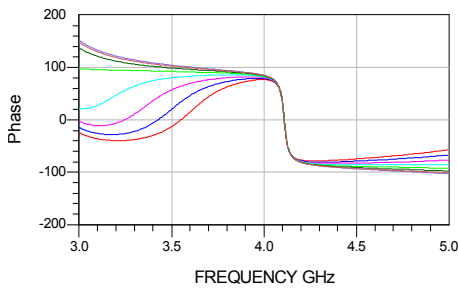


Fig. 13 absolute phase simulated between unit cells

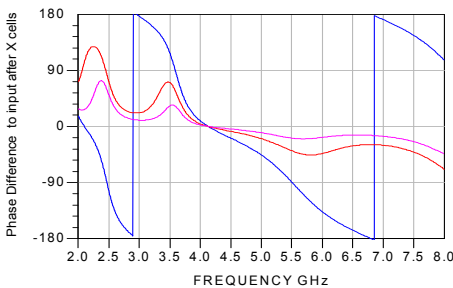


Fig. 14 phase difference between unit cells

The fact that the phase difference is positive left of the zero order resonance ($\beta=0$) also indicates the presence of left-handed behavior.

Figure 15 shows the influence of the series resistor value at each cell when sweeping from 0.1 ohm to 10 ohms.

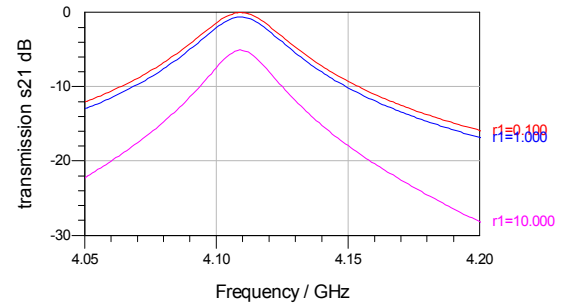
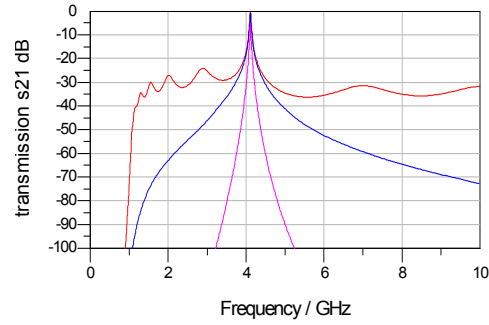


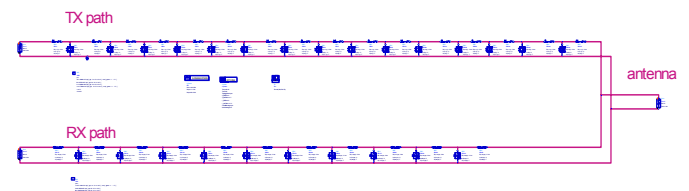
Fig. 15 Influence R-sweep (a) 10GHz span (b) 200MHz span

As can be seen with fig. 15 the Q factor stays stable with increasing loss at the 0th order resonance frequency. The losses only show up as a pass band loss, but not as degraded selectivity. This allows introducing tuning elements in the structure. These always contain losses, but the losses can be tolerated as they only show up as pass band loss and not as a degraded selectivity, which would be the case on classical resonator technology.

3) Duplex filter design

In basestations transmit and receive paths have to be separated by a duplexer which has to handle high power up to 160 W peak and at the same time the sensitivity of the receive path should not be degraded. In the context of a distributed filter approach [19] the TX path of the filter has to have higher attenuation (~ 110 dB/ 10 MHz away from channel) than the RX path (~ 70 dB/ 10 MHz) but only one-sided high Q is needed. Together with the tuning/ switching of parameters for single channel filtering metamaterials are applicable without the need for using the whole metamaterial transmission band (ripples through resonances not disturbing).

Fig. 16 shows TX (high pass band) and RX (low pass band) of the duplexer 3 port device. Here 15 unit cells for TX and 10 unit cells for RX are selected.



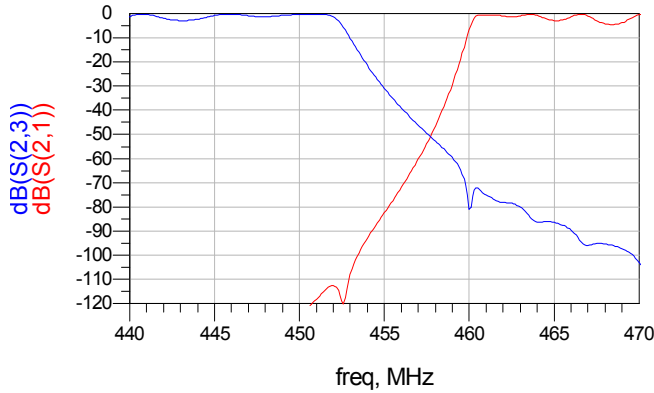


Fig. 16: duplexer transmissions:
 RX: 450.4 - 451.65 MHz, TX: 460.4 – 461.65 MHz
 a) topology, b) Performance

Using a 50 ohm system forces us also to match the duplexer structure to 50 ohm. Unfortunately at exactly $\beta=0$, so at the band edge, the characteristic impedance is either near 0 ohm or infinite depending on whether f_{ser} or f_{par} defines the edge. For the necessary 50 ohms it turned out to be favorable to choose the f_{ser} -edge. For the duplexers TX path f_{ser} had to be greater f_{par} and for the RX path vice versa.

Component tolerances don't influence the transmission performance but the filter edge frequency. Tuning the capacities can solve this problem, for example by using varicap diodes or BST- or RF-MEMS-varactors and switching of certain metamaterial elements.

The further object of research therefore are technologies for high current and voltage carrying capacity and realization aspects with minimal parasitics.

4) Realization aspects

During first realization steps it was found that the models for the SMD components provided by the manufacturers are not sufficient enough and therefore the SMD components were characterized on the target substrate by means of a calibration PCB to get a better understanding of parasitic influences.

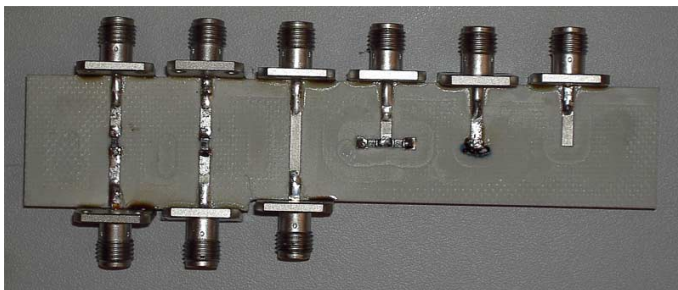


Fig. 17: Calibration board for SMD device characterization

Mesured S-parameters of the SMD components were then used to design a first structure with 5 unit cells (fig. 18).

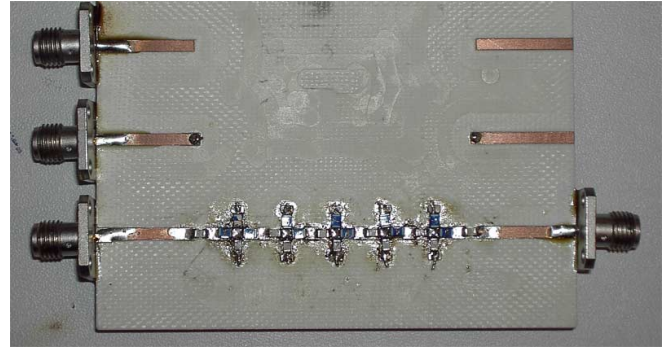


Fig. 18: filter structure with 5 unit cells and calibration lines

From the simulation and measurements it was found that although the zero order resonance is robust against losses in the serial path ($R1$ in fig. 10), it is not robust against losses in the parallel path ($R2$ in fig 10). High selectivity and large filter steepness was only achieved with a high number of unit cells resulting in an unacceptable high pass band loss of more than 1 dB.

Therefore future research will concentrate on using distributed elements in micro strip technology, realizing the capacitors and inductances in micro strip configurations. Also a better predictability is expected, as mechanical tolerances are easier to control than the electrical tolerances of SMD components.

Next steps will also be to include tuning elements like varactors in the metamaterial structures for alteration of the serial and parallel resonance frequencies creating tunable metamaterial structures, which will allow for tuning the filter functions. Through varactors combined with a D/A converter for driving them a digital access to the analog filter function will become feasible leading to *software defined duplex filters* perfectly complementing *software defined radio* technology.

C. RAT-RACE-BALUN

1) Motivation

For the frequency agile RF System a highly efficient Class-S-Amplifier is considered with comprises a differential output of 12.5 ohm. Because of the 50-ohm-duplexer and the 50-ohm-antenna system that are single-ended a triband balun with impedance transformation from 12.5 balanced to 50 ohm unbalanced was needed to match them together. Most variants of baluns are only single-band. [5] showed a dualband metamaterial balun for a 50 ohm system. In this paper a triband balun will be proposed which can handle also the impedance matching at the same time.

2) Theory on Rat-Race-Hybrids and application requirements

Compared to classical right-handed (RH) couplers also RH-baluns functions with superposition of electromagnetic waves that travel on two ways and meet at output or input. A phase difference of multiples of 90 degrees ($n \cdot \lambda/4$) between the four

balun ports provides a balun function when using the right ports. Figure 19 shows such a RH micro strip line rat race. If the input ports and the output port are used like in figure 19 then the ring hybrid has the function of a balun.

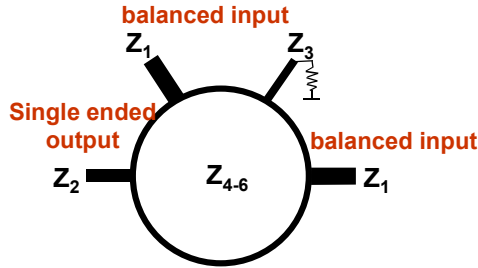


Fig. 19 MSL RH rat race

The balanced input is not only mapped onto a single-ended asymmetric output but performs an impedance transformation from 12.5 ohms to 50 ohms at three bands with the use of six left-handed line sections at all physical 60 degree bends.

3) Optimization

A hybrid optimization was needed to achieve the required performance in all three bands between 450 MHz and 2200 MHz of:

- $S_{11}, S_{22} < -9$ dB (Reflection)
- $S_{21} > -1$ dB (Transmission)
- Realizability / Physical requirements (lengths, widths)
- High impedance and high reflection for even mode
- Impedance matching

A search room with 26 parameters did not allow simple gradient search, which would result in a local optimum and not result in a passing of the odd mode signals and blocking of the even mode signals. Therefore each of the 6 line sections was optimized individually for its required phase and impedance response and then this was used as a starting point for the overall optimization.

4) Design

The optimization also had to be made under certain layout constraints as the ring with the rat race has to be closed (Fig. 17).

A practical realization hasn't been performed yet, but from the simulations the principal functionality has been proven under consideration of imperfections of the SMD components.

Given the deviation found with the metamaterial coupler by not paying attention to the via inductance a redesign of the metamaterial balun will be made considering the via inductance before going into realization and characterization.

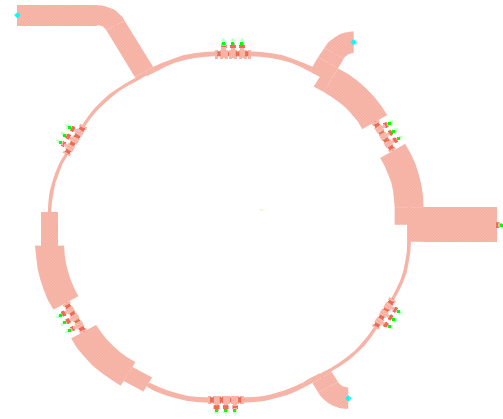


Fig. 17 Layout of three band Rat Race Balun with LH line sections

IV. CONCLUSION

It was shown by various examples taken from a frequency agile RF system design approach, that Metamaterial structures are very beneficial in terms of providing the required multiband capability. Furthermore in the context of tunable duplex filters it was shown that the presence of zero order resonances with CRLH structures allows for the introduction of lossy tuning elements without degrading the filters selectivity.

As zero order resonances are only robust against losses in the serial path but not the parallel path future work will concentrate on replacing concentrated SMD components with distributed micro strip ones.

V. ACKNOWLEDGMENT

The author, G. Dehm-Andone, would like to thank Horst Schenkel and Peter Gunreben, both Bell Labs Europe, for their help with simulation tools and analysis of results.

The author, G. Adamiuk, thanks to Prof. Dr.-Ing. Dr. h.c. W. Wiesbeck for the creation of the opportunity to gain the excellent professional experience during his internship at Bell Labs Europe. He would like to thank also the Bell Labs Nuernberg Team, especially H. Schenkel and P. Gunreben for their support during the research.

The author, G. Fischer, would like to thank the German Ministry of research and education (BMBF) for funding part of this work under grant 01BU387 ErGaN (Reconfigurable GaN based Amplifiers) and MARIO 01BU571 (Metamaterial based flexible duplex filters). Further, he wants to thank the European commission for financial support in the area of MEMS-based reconfigurable RF circuits and multiband measurement couplers with frequency agile amplifiers within the European IST program FP6 Network of Excellence Top Amplifier Research Group in a European Team (TARGET).

VI. REFERENCES

- [1] P. Gunreben, F. Obernosterer, "Impact of the CDMA2000 Duplex Filter on UMTS/HSDPA signal processing", Bell-Labs Europe, Nuremberg, Germany, v. 0.2, April 6, 2005
- [2] C. Korthals, "Untersuchung der Wellenausbreitung in planaren, periodischen Leitungsstrukturen im Mikrowellenbereich", University Erlangen-Nuremberg, Nov. 17, 2004
- [3] A. Lai, T. Itoh, "Composite Right/Left-Handed Transmission Line Metamaterials", IEEE Microwave Magazine, pp.34-50, Sept. 2004
- [4] T. Itoh, "Novel Electromagnetic Materials: Transmission Line Approach and Microwave Applications", Microwave Electronics Lab
- [5] I-H. Lin, M. DeVincentis, C. Caloz, T. Itoh, "Arbitrary Dual-Band Components Using Composite Right/Left-Handed Transmission Lines", IEEE Transactions on Microwave Theory and Technique, Vol. 52, No. 4, April 2004
- [6] C. Caloz, A. Sanada, T. Itoh, "A novel Composite Right-/Left-Handed Coupled-Line Directional Coupler With Arbitrary Coupling Level and Broad Bandwidth", IEEE Transactions on Microwave Theory and Techniques, Vol. 52, No.3, March 2004
- [7] H. Okabe, C. Caloz, T. Itoh, "A Compact Enhanced-Bandwidth Hybrid Ring Using an Artificial Lumped-Element Left-Handed Transmission-Line Section", IEEE Transactions on Microwave Theory and Technique, Vol. 52, No.3, March 2004
- [8] C. Caloz, T. Itoh, "Transmission Line Approach of Left-Handed(LH) Materials and Microstrip Implementation of an Artificial LH Transmission Line", IEEE Transactions on Microwave Theory and Techniques, Vol. 52, No.5, May 2004
- [9] V. G. Veselago, "The electrodynamics of substances with simultaneously negative values of ϵ and μ ", Sov. Phys.-Usp., vol. 10, pp. 509-514, Jan.-Feb. 1968
- [10] J. B. Pendry, A. J. Holden, W. J. Stewart and I. Youngs, "Extremely low frequency plasmons in metallic microstructures", Phys. Rev. Lett., vol. 76, no. 25, pp. 4773-4776, Jun. 1996
- [11] J. B. Pendry, A. J. Holden, D. J. Robbins, and W.J. Stewart, "Magnetism from conductors and enhanced nonlinear phenomena", IEEE Trans. Theory Tech., vol. 47, no. 11, pp. 2075-2084, Nov. 1999
- [12] D. R. Smith, W. J. Padilla, D. C. Vier, S. C. Nemat-Nasser, and S. Schultz, "Composite medium with simultaneously negative permeability and permittivity", Phys. Rev. Lett., vol. 84, no. 18, pp. 4184-4187, May 2000
- [13] D. R. Smith and N. Kroll, "Negative refractive index in left-handed materials", Phys. Rev. Lett., vol. 85, no. 14, pp. 2933-2936, Oct. 2000
- [14] R. A. Shelby, D. R. Smith, and S. Schultz, "Experimental verification of a negative index refraction", Science, vol. 292, pp. 77-79, April 2001
- [15] C. Caloz, H. Okabe, T. Iwai, and T. Itoh, "Transmission line approach of left-handed (LH) materials", in USNC/URSI Nat. Radio Science Meeting, vol. 1, Jun. 2002, p. 39
- [16] A. K. Iyer and G. V. Eleftheriades, "Negative refractive index metamaterials supporting 2-D waves", in IEEE MTT-S Int. Microwave Symp. Dig., vol. 2, Jun. 2002, pp. 1067-1070
- [17] G. Fischer, W. Eckl, G. Kaminski, "RF-MEMS and SiC/GaN as Enabling Technologies for a Reconfigurable Multi-Band/Multi-Standard Radio", Bell Labs Technical Journal, Vol. 7, No. 3, 2002
- [18] P. Gammel, G. Fischer, J. Bouchaud, "RF MEMS and NEMS Technology, Devices, and Applications, Bell Labs Technical Journal, Vol. 10, No. 3, 2005
- [19] G. Fischer, *Architectural benefits of wide bandgap RF power transistors for frequency agile basestation systems*, IEEE MTT, 6th annual Wireless and Microwave Technology Conference, Clearwater, Florida, April 2004
- [20] C. Caloz, T. Itoh, *Electromagnetic Metamaterials*, IEEE press, Wiley, Hoboken NJ, 2006



G. Dehm-Andone was born in 1980 and studies since 2000 electrical, electronic and communication engineering at University of Erlangen-Nuremberg with special focus on RF, microwave and communications.

He worked as research assistant at Fraunhofer Institute for Integrated Circuits in Tennenlohe/Erlangen from 2002 until 2004. During this time he worked on low power microcontroller applications and adaptive antenna arrays receivers. In 2005 he had an internship at Lucent

Technologies Bell Labs Europe in Nuremberg. Here the present focus of research lies on metamaterial theory, application and realization. His professional interest is in antennas, RF circuits and metamaterial applications.



G. Adamiuk was born in Olsztyn, Poland in 1982. He began his studies in 2001 at the Technical University of Gdansk, Poland. After two years of study he received a scholarship at the Technical University of Karlsruhe, Germany where he studies within the framework of double degree programme.

In 2004 he focused his professional interest at the high frequency technology by choosing the Institut fuer Hoehstfrequenztechnik und Elektronik in Karlsruhe as

his further path of education. From 2004 to 2005 he was with this institute as a helper of the head of the institute. The part of the work that he authored was developed during his internship in Lucent Technologies Bell Labs Europe in Nuernberg, Germany. At the moment of publication he is preparing his diploma thesis at the University of Karlsruhe.



G. Fischer (M'01) was born in 1965 and studied electrical engineering at University of Aachen from 1986 till 1992 with special focus on communications and microwave. From 1993 to 1996 he was a research assistant at University of Paderborn, from where he received his Ph. D in 1997. During this time he worked on a receiving system comprising an adaptive antenna array at 12 GHz for mobile satellite reception.

End of 1996 he joined the department of basestation forward looking at Lucent Technologies in Germany. He became a physical layer expert and as such acted as a chairman in ETSI during the physical layer standardization of the GSM-EDGE system. His professional interest is in basestation RF technology and physical layer techniques for coverage and capacity enhancement of wireless networks.

Dr. Fischer is also a member of VDE/ITG. In 2000 he got promoted a Lucent DMTS (Distinguished Member of Technical Staff) and in 2001 a Lucent CMTS (Consulting Member of Technical Staff). End of 2003 he moved to the Bell Labs Europe organization of Lucent. Since 2001 he is holding lectures at University of Erlangen on basestation RF technology with specific focus on receiver and transmitter architectures.

PHASE SENSITIVITY TO SOIL MOISTURE IN CONTROLLED ANECHOIC CHAMBER: MEASUREMENTS AND FIRST RESULTS

K. Ben Khadhra ⁽¹⁾, M. Nolan ⁽²⁾, T. Börner ⁽¹⁾, D. Hounam ⁽¹⁾, M. Chandra ⁽³⁾

¹ German Aerospace Center (DLR) - Microwaves and Radar Institute, Oberpfaffenhofen,

D-82234 Wessling, Germany (Email: kais.benkhadhra@dlr.de, Tel: 0049-8153-2386, Fax: 0049-8153-1449)

² Institute of Northern Engineering, 455 Duckering Bldg, University of Alaska Fairbanks Fairbanks, AK 99775-5860

³ TU Chemnitz, Elektrotechnik und Informationstechnik, Reichenhainer Strasse 70, D-09107 Chemnitz, Germany

Abstract — in this work, we will present new Bistatic X-band (9.6 GHz) laboratory measurements, which have been carried out in the Bistatic Measurement Facility at the DLR Oberpfaffenhofen, Microwaves and Radar Institute in Germany. The Bistatic facility enables us to have full polarimetric data with different Bistatic angles and different soil moistures controlled by a TDR (Time Domain Reflectivity) system. After calibration of the measuring system using a large metal plate, the sensitivity of phase and reflectivity with regard to moisture variation and therefore the penetration depth was evaluated. Current results demonstrate a non-linear relationship between the signal phase and the soil moisture, as expected, confirming the possibility of using DInSAR to measure variations in soil moisture.

Keywords: *bistatic measurement; signal phase; soil moisture; penetration depth; interferometry; anechoic chamber*

I. INTRODUCTION

To date many radar methods and models have been reported for the estimation of soil moisture, such as the Oh-model or the Dubois model. Those models, which use only the magnitude of the backscattered signal, show results with 5 to 10% accuracy. In the last two decades SAR Interferometry (InSAR) and differential InSAR (DInSAR), which uses the phase of the backscattered signal, has been shown to be a useful tool for the creation of Digital Elevation Models (DEMs), and temporal changes due to earthquakes, subsidence, and other ground motions. Matt Nolan [1-3] also suggested the possibility to use DInSAR penetration depth as a proxy to estimate the soil moisture. The principal is based on the relationship between the penetration depth and the permittivity, which varies as a function of soil moisture.

II. THEORY

The penetration depth (eq. 1) [4] is defined as the distance over which the field amplitude decreases by a factor of 1/e. It

could be a reliable proxy to assess the soil moisture. The moisture variation (penetration depth variation) causes a change in path length and yields a change in phase, the so-called signal phase (eq. 2).

$$\delta_p = \frac{\lambda \sqrt{\epsilon'}}{2\pi} \quad (1)$$

$$\phi_{sig} = \delta 2k = \delta \frac{4\pi}{\lambda} \quad (2)$$

The Hallikainen model [5,6] relates the dielectric constant to the frequency, the volumetric moisture content and the percentage of sand and clay contained in the soil. It has been used to prove the relationship between the soil moisture and the penetration depth.

$$\epsilon_c = (a_0 + a_1 S + a_2 C) + (b_0 + b_1 S + b_2 C) m_v + (c_0 + c_1 S + c_2 C) m_v^2 \quad (3)$$

ϵ_c is the complex dielectric constant, S is the percentage of sand, C is the percentage of clay, m_v is the volumetric moisture content, and the coefficients a_i , b_i and c_i depend on the frequency.

Because of the nonlinear relationship between soil moisture and penetration depth (fig. 1), a measurement of a change in penetration depth cannot be directly converted to a change in soil moisture unless one of the soil moisture values is known a priori or if some linearizing assumptions can be made.

For example, a measured displacement of 5 mm could ambiguously mean a change in soil moisture from 1% to 2% or from 10% to 17%.

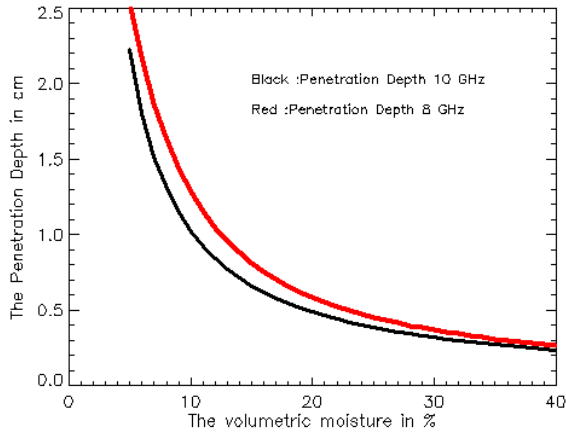


Figure 1. The penetration depth versus volumetric soil moisture

However, if the initial soil moisture value is known, and assuming that a phase change is fully attributable to a change in penetration, the initial value can be converted to a penetration depth using the equations presented previously.

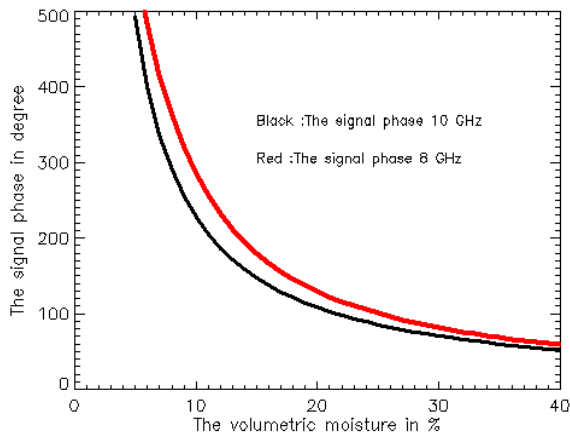


Figure 2. The signal phase versus volumetric soil moisture

III. BISTATIC MEASUREMENT FACILITY

The X-band Bistatic Measurement Facility (Microwaves and Radar Institute, DLR Oberpfaffenhofen, Germany) has been used to measure a full polarimetric data set for quasi-bistatic angles from 24° to 140° with controlled conditions in an anechoic chamber (fig. 3). The transmitting and receiving horn antennas are moving in the plane of incidence, where the azimuth angle of the transmitter is 0° and the azimuth angle of the receiver is 180° . The transmitter and the receiver can move from 12° to 70° similarly (specular case) or separately to measure the incoherent term.

The chosen target was a flat soil with different moisture levels controlled by a TDR system. An average of four soil moisture measurements has been used for each target. The soil sedimentation shows that the soil contains 100% (pure) sand and no clay contributions. Therefore the swelling effect of soil caused by clay can be completely neglected.



Figure 3. The bistatic measurement facility at DLR

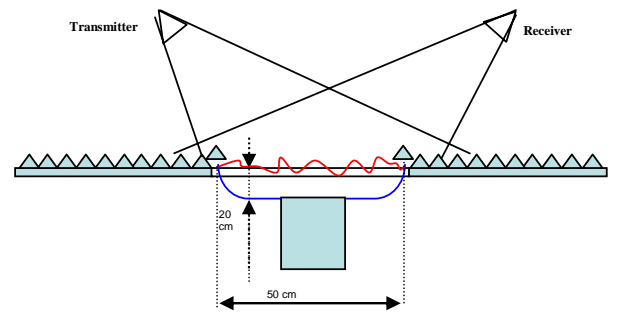


Figure 4. Bistatic geometry of the facility

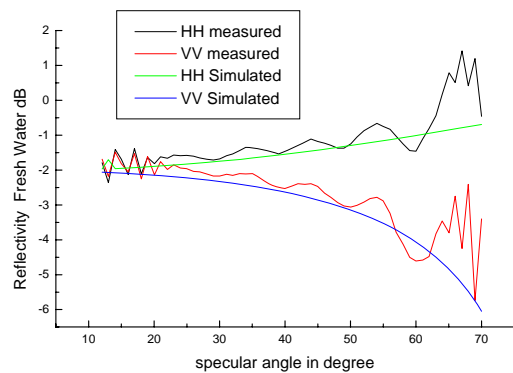


Figure 5. The Reflectivity of fresh water

The Isolated Antenna Calibration Technique (IACT) [7] has been used to calibrate the measured data. A large metal plate has been used as calibration target. The validation of the calibration has been achieved by comparing the simulated and measured reflectivity of fresh water (fig. 5).

IV. MEASUREMENTS AND RESULTS

Specular measurements with different soil moistures have been carried out to prove the signal variation with the soil moisture, as the penetration depth is related to the magnitude of the signal. The variation of reflectivity with soil moisture is shown in fig. 6; the incidence angle was 20°.

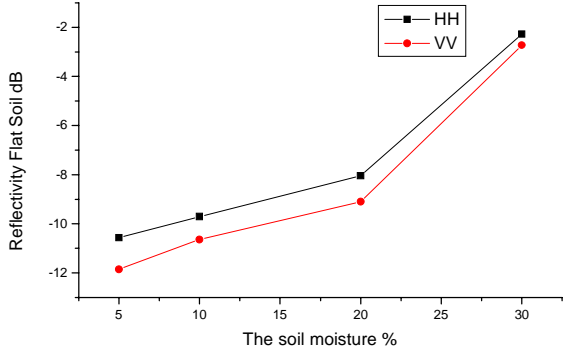


Figure 6. The Reflectivity of flat soil versus the soil moisture

The reflectivity of flat soil increases as the soil moisture increases for both polarizations H and V . Apparently the penetration depth depends on soil moisture. Fig. 7 shows that the signal phase is also changing with soil moisture (for the same geometry and the same soil roughness).

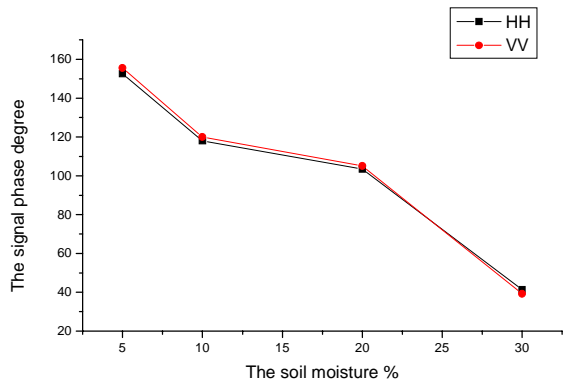


Figure 7. The signal phase versus the soil moisture

The simulation of the signal phase using the Fresnel reflection coefficient yields a variation of about 1 degree for a

soil moistures varying from 5% to 40% (fig. 8). This means that the measured variation of the signal phase of up to 100° cannot be explained by the pure dielectric effect covered by the Fresnel equations!

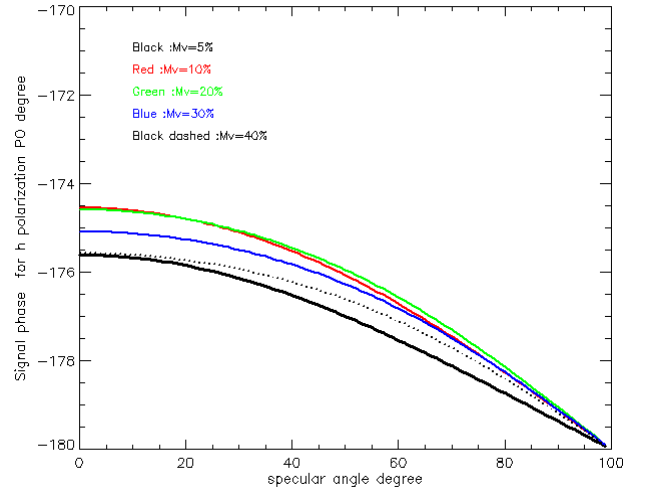


Figure 8. The Reflectivity of flat soil versus the soil moisture

V. INTERFEROMETRIC ANALYSIS

The assessment and interpretation of the signal phase for the different soil moistures using the complex interferometric coherence seems to be reasonable. The coherence Γ is defined as:

$$\Gamma = \frac{\langle S_i S_r^* \rangle}{\sqrt{\langle |S_i|^2 \rangle \langle |S_r|^2 \rangle}} \quad (4)$$

where S_r is the reference signal of a surface with soil moisture $m_{v,1}$. S_i with $i \in \{2,3,\dots\}$ is the complex amplitude of the signal for the surfaces with soil moistures $m_{v,i}$. $\langle \dots \rangle$ denotes ensemble averaging. As expected, due to the coherent nature of the surface (flat soil), the magnitude of the interferometric coherence for two relatively wet surfaces is almost 1. However, the main purpose of this experiment was the analysis of the signal phase measured for different soil moistures at the same geometry and roughness. Therefore only the argument of the complex coherence, i.e. the phase shift due to the soil moisture variation, will be taken into account. From fig. 9 we can see that this phase shift can be a good proxy to assess the soil moisture variation. Due to the absence of clay in our soil (no swelling effects) the phase shift can be directly related to the penetration depth of the electromagnetic wave into the soil.

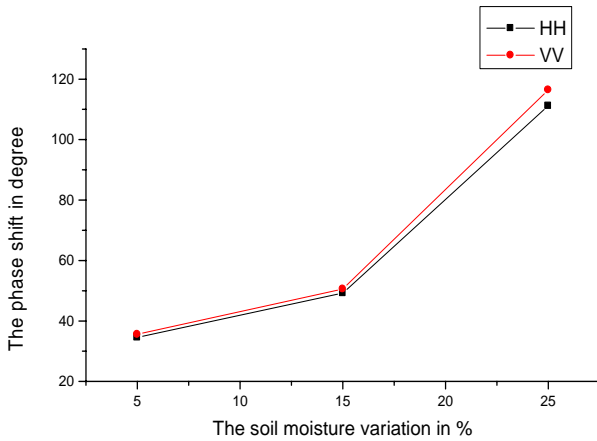


Figure 9. The interferometric phase versus the soil moisture variation

VI. CONCLUSION AND DISCUSSION

The variation of the reflectivity with regard to soil moisture could be a reliable tool to understand the relationship between the penetration depth and the soil moisture. As expected it can be seen from the measurements that the penetration depth decreases with increasing reflectivity.

The dependence of signal phase on soil moisture demonstrates that the path of the electromagnetic wave through the soil is strongly related to its dielectric properties.

The nonlinearity of the signal phase variation to the soil moisture variation can be clearly seen, but the biggest changes in phase are occurring at the higher ranges of soil moisture which is contrary to theory. It could be a problem of correct phase unwrapping (i.e. cycle slips), but maybe also due to inaccuracies in the measurements.

The effects of surface roughness with respect to varying bistatic angles and polarisation will be subject to future studies. The clear aim is to find ways of independently estimate soil moisture and surface roughness.

ACKNOWLEDGEMENTS

The authors should like to thank Dr. Erich Kemptner and Stefan Thurner from the "Signatures" group for their outstanding support with the laboratory measurements and equipment.

REFERENCES

- [1] M. Nolan, D.R. Fatland, and L. Hinzman, "DInSAR Measurements of Soil Moisture," *IEEE Trans. Geosci. Remote Sensing*, vol. 41, no. 12, December 2003.
- [2] M. Nolan, and D.R. Fatland, "New DEMs May Stimulate Significant Advancements in Remote Sensing of Soil Moisture," *EOS Trans. AGU*, vol. 84, no. 25, pp. 233-240, 24 June 2003.
- [3] M. Nolan, and D.R. Fatland, "Penetration Depth as a DInSAR Observable and Proxy for Soil Moisture," *IEEE Trans. Geosci. Remote Sensing*, vol. 41, no. 3, pp. 532-537, March 2003.

- [4] F.T. Ulaby, R.K. Moore, and A.K. Fung, *Microwave Remote Sensing*. Reading, MA: Addison-Wesley, 1982, vol. 2, Fundamentals and Radiometry.
- [5] M.T. Hallikainen, F.T. Ulaby, M.C. Dobson, and M.A. El-Rayes, "Microwave dielectric behaviour of wet soil - Part I: Empirical models and experimental observations," *IEEE Trans. Geosci. Remote Sensing*, vol. GE-23, pp. 25-34, Jan. 1985.
- [6] M.C. Dobson, F.T. Ulaby, M.T. Hallikainen, and M.A. El-Rayes, "Microwave dielectric behaviour of wet soil - Part II: dielectric mixing models," *IEEE Trans. Geosci. Remote Sensing*, vol. GE-23, pp. 35-46, Jan. 1985.
- [7] K. Sarabandi, F.T. Ulaby, and M.A. Tassoudji, "Calibration of polarimetric radar systems with good polarization isolation," *IEEE Trans. Geosci. Remote Sensing*, vol. 28, no. 1, pp. 70-75, Jan. 1990.

Design of an Airborne Dual-Polarized Triple Stacked Patch Antenna for Broadband SAR Applications in P-Band

M. Limbach, B. Gabler, R. Scheiber, R. Horn

Deutsches Zentrum für Luft- und Raumfahrt e.V. (DLR)
82234 Oberpfaffenhofen, Germany
Tel: +49 8153 28 30 60, E-Mail: markus.limbach@dlr.de

Conference topic: Antennas

Short Abstract— The development of a P-band antenna for airborne SAR application is presented. Wide band operation, static electrical antenna beam pointing and small size were key parameters of this antenna array design. First results are shown.

Keywords- wide band; airborne SAR; patch array antenna; dual polarization; low cross-pol-level;

I. INTRODUCTION

Considerable interest has developed recently in wide bandwidth, fully polarimetric, fine resolution synthetic aperture radar (SAR) systems, operating at VHF/UHF bands. The combination of low frequency and high bandwidth creates a variety of applications. These systems appear to be extremely useful for the detection of targets concealed by foliage and/or camouflage, detection of buried objects, forestry applications and archeological and geological exploration.

In 1994 DLR's well-known airborne experimental synthetic aperture radar system, named E-SAR, was upgraded by a first P-band subsystem. Up to now a moderate bandwidth of 50 MHz restricted this frequency band to medium resolution radar applications. Severe RFI problems at the original centre frequency of 450 MHz asked for extensive filtering methods for obtaining an acceptable image quality.

Driven by these constraints, a new fully polarized fine resolution P-band subsystem was developed at DLR's Microwaves and Radar Institute. The configuration of the P-band equipment, as well as the design of key hardware components, like front-end, high power amplifier and the new dual polarized patch array antenna is described. A bandwidth of more than 28% is achieved at a lower centre frequency, corresponding to a range resolution better than 2.1m. Measurements of system gain, cross polarization suppression, system sensitivity and some antenna parameters are shown.

II. ANTENNA

The small size of the aircraft, a Dornier Do 228-212, gives one of the major restrictions for antenna design in the meter wavelength domain.

Common methods to enhance the bandwidth of microstrip antenna elements are established e.g.: aperture-coupling [1], stacked-patch configuration [2], matching network [3] and the proper choice of substrates [4]. In this case all these options are used together to increase bandwidth, because of the requirement of mounting the antenna at the small aircraft.

The optimal width of the antenna would be about 200cm. On the other side the width of the cabin of the airplane is only 150cm. On that account the antenna has to consist of dielectric material of $\epsilon_r \gg 1$ to scale down the antennas overall dimensions at least to the cabin's size.

High cross-polarization isolation is a major requirement for the use of the new P-band antenna in polarimetric SAR applications. Additional information of the targets can be obtained by analyzing their behavior in changing polarization angle during reflection process. Antennas cross polarization isolation should be better than 25dB. For a properly designed microstrip element the level of cross polarization level is usually 20dB below the co polarization level [5]. Therefore a suited group configuration has to give better cross polarization isolation than a single element and at the same time proper side lobe suppression [6].

For full polarimetric measurements the beam shape in both polarizations should be equitable and point in the same direction, in the case of P-band antenna $\Theta_0 = 42^\circ$ off boreside. The array consists of 16 elements in a 4 x 4 configuration. Centre frequency is 350MHz.

The distance, d , between two elements in the array has to be smaller 50cm, see (1), to prevent grating lobes. The antenna will be mounted under the fuselage of a Dornier Do 228 and the suppression of received signals from opposite swath has to be as good as possible.

$$\frac{d}{\lambda} < \frac{1}{1 + \sin|\theta_{0\max}|} \quad (1)$$

Cause of the overall dimensions the antenna array is mechanically divided into four subgroups. Otherwise the substrate materials were not available. The materials used were FR 4 glass fiber and "Roofmate", a Styrofoam. Styrofoam boards consist of extruded polystyrene foam. The extrusion process produces a uniform structure of small closed cells. It is

highly resistant to water absorption. The boards are very resistant to the passage of water vapour and are unaffected by repeated freeze/thaw cycles. By its characteristic it will not change its size if air pressure varies.

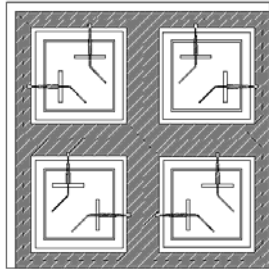


Figure 1. Rear side of one field with 4 radiating elements and feeding lines.

The array consists of 16 elements, each with three stacked microstrip patch resonators. They are aperture coupled to a microstrip line with an impedance matching line section. The amplitude taper and phase shift for each element is formed by a network of discrete power dividers and coaxial lines of different length.

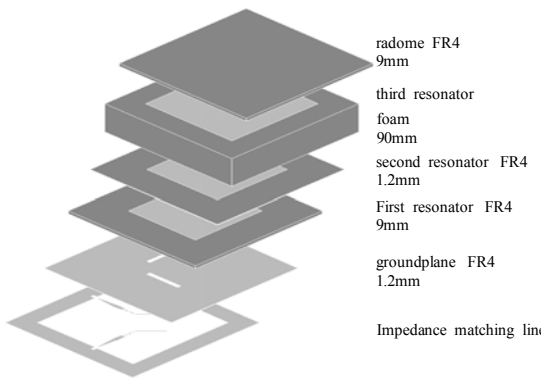


Figure 2. Structure of the substrates of one antenna element.

In Figure 2 the internal structure of one single antenna element is shown. Five dielectric layers form a 10.92cm thick composite. Three quadratic copper areas with increasing edge length inside form the resonators. The coupling apertures in the ground plane are of rectangular shape and located under the first patch to excite dual linear polarization. Measurements of input reflection are shown in Figure 3.

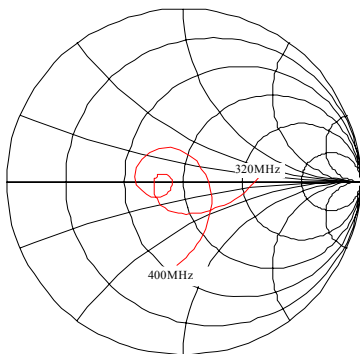


Figure 3. Reflection of a single element in the environment of the full array.

	length	width
resonator 3	239mm	239mm
resonator 2	194mm	194mm
resonator 1	185mm	185mm
slot	85mm	9mm

Table 1 Resonator and slot dimensions

Four elements are put together to a subgroup on one composite. With an element spacing of 35cm the group measures 70cm squared. Four subgroups are mounted on an aluminium frame and represent the complete radiating part of the antenna. This frame is used to assemble the subgroups and connect them to the aircraft's fuselage. It also assures that the distance between the microstrip matching lines as well as the coupling slots and the metallic bottom of the cabin is about 1/4 of a wavelength. The second part of the antenna, the network, in particular a plate carrying the power dividers for both polarizations, is attached to this frame.

The side looking property, a requirement for SAR application, is excited by the coaxial cable network. 125° degree phase shift from row to row results in a 42° degree off-nadir shift of the main beam of the antenna. Together with the arrangement of the feeding positions of the single antenna elements with respect to each other, good cross-polarization isolation is achieved [6].

		flight direction				
		direction of view				
→	↑					
+	*	+	+	*	+	330°
*	*			*	*	phase
						offset
						220°
						phase
						offset
						110°
						phase
						offset
						0°
						phase
						offset

* reference phase
+ reference phase +180° degree

Table 2 Port plan with phase offset and port distribution for each element. Rear view.

The port distribution described in the paper: "Cross-Polarization and Sidelobe Suppression in Dual Linear Polarization Antenna Arrays" [6], as configuration "E" provides good results, even for this small group. The influence of phase shift over the antenna group was not investigated in this paper. To prevent proper cross-polarization isolation two antennas are excited from opposite edges, with respect to the network the signals merge in with another 180° degree phase shift, so the cross portion is nullified.

Because of the small element spacing, the coupling between adjacent elements within the array is very strong, so standard amplitude taper routines become not successful. During far-field measurements the power dividing network was optimized. Far field measurements show good results of the antenna for both polarizations. Voltage standing wave ratio is better 1.6 over the whole frequency range of 100MHz, corresponding to 28% bandwidth. Antenna gain is 10dBi, cross

polarization level on average is -24dB. In Figure 4 an exemplary far-field diagram at 350MHz is plotted.

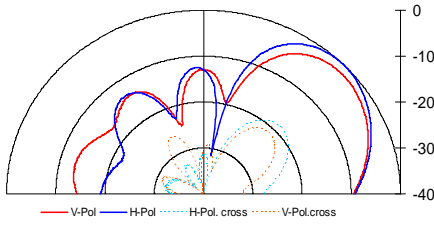


Figure 4. Far field diagram for h- and v- polarisation at 350MHz.



Figure 5. Antenna mounted on DLR's Dornier DO 228-212.

The antenna is protected against mechanical stress of wind, rain and ice with the help of a wind deflector. It is made of glass fiber and covers the antenna at their side walls. Figure 5 shows the antenna together with its wind deflector mounted under the Do 228-212.

III. FRONT-END DESIGN

A new front-end configuration was necessary caused by the new centre frequency and the extra in bandwidth.

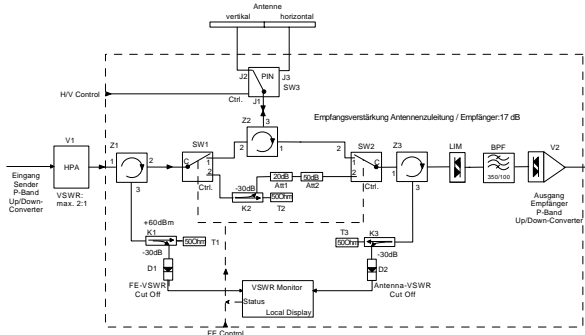


Figure 6. P-band front-end design

Some interesting features are integrated into the P-band front-end. First of all there is a VSWR monitoring unit which is able to shut down the high power transmitter amplifier immediately if the reflected power is higher than a certain threshold. An internal loopback for testing and calibrating the transmit / receive path is also integrated. By switching off the antenna a complete characterization of the P-band subsystem for calibration or test is possible. Polarization switch and transmit / receive controller are integrated. The overall receiver gain is 87dB at a noise figure of 2.9, isolation between the channels for H and V polarization is better than 75dB.

IV. FIRST SAR-IMAGE

After the process of airworthiness certification the new hardware inside and outside the airplane was tested in flight. During this flight SAR-data were recorded and the first results are presented here.

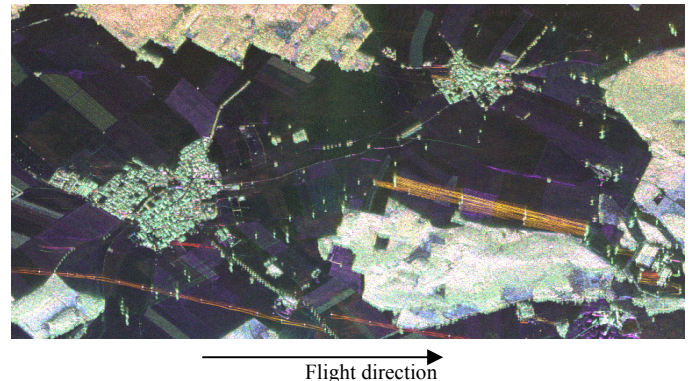


Figure 7. Colour composite SAR image (red : HH ; green : HV ; blue : VV). Oberbrunn, Germany.

The raw data was processed in a 4 look mode and thus the image shows a resolution of 2.1 x 4.0 meters (range x azimuth). It is a small sector of a SAR image of one of our calibration sites near Oberpfaffenhofen, Germany, shown in Figure 7. It's a colored composite of the backscatter intensities in H-, V- and the cross-polarization channel. The image shows forested areas as well as farmland and two small villages. High-voltage power lines, aligned in flight direction, are visible in HH polarization. The raw data was processed without any filtering in frequency domain and shows an enhancement in image quality in relation to the former P-band subsystem. In a single look image resolution in azimuth is 1.8m. In range direction 2.1m is reached.

V. CONCLUSION

The performance of the P-band subsystem as a part of the E-SAR system is increased in relation to the former subsystem design. Improvement in bandwidth together with a lower centre frequency yields a better image quality with higher range resolution and less RFI disturbances.

REFERENCES

- [1] D. M. Pozar, "A Microstrip Antenna Aperture-Coupled to a Microstrip Line" *Electron. Lett.*, vol.21, pp 49-50, 1985
- [2] C. H. Chen, et. al., "Broadband Two-Layer Microstrip Antenna" *IEEE Trans. Antennas Propaga.*, vol.38, no.8, pp 1176-1185, Aug. 1990
- [3] H. F. Pues and A. R. van de Capelle, "An Impedance-Matching Technique for Increasing the Bandwidth of Microstrip Antennas" *IEEE Trans. Antennas Propaga.*, vol. AP-37, no.11, pp 1345-1354, Nov. 1989
- [4] K. R. Carver and J. W. Mink, "Microstrip Antenna Technology" *IEEE Trans. Antennas Propaga.*, vol. AP-29, no.1, pp 2-24, Jan. 1981
- [5] D. M. Pozar and B. Kaufman, "Design Considerations for Low Sidelobe Microstrip Arrays" *IEEE Trans. Antennas Propaga. Symp. Digest.*, pp 251-254, 1984
- [6] K. Woelders and J. Granholm, "Cross-Polarization and Sidelobe Suppression in Dual Linear Polarization Antenna Arrays" *IEEE Trans. Antennas Propaga.*, vol.45, no.12, pp 1727-1740, Dec. 1997

Determination of Dielectric Material Parameters using a Flexible Waveguide Setup

Thorsten Kayser, Mario Pauli, and Werner Wiesbeck
 Universität Karlsruhe (TH), Institut für Höchstfrequenztechnik und Elektronik
 Kaiserstraße 12, 76131 Karlsruhe, Germany
 Email: thorsten.kayser@ihe.uka.de
 Tel. +49 721 608 7677, Fax: +49 721 691865

Abstract—This paper presents a method for the determination of the complex permittivity of materials from measured scattering parameters. The setup consists of a waveguide applicator for housing in the material sample. The considered frequency range is 2 – 3 GHz. The complex scattering parameters are measured by a vector network analyzer. The material samples can be either liquid, granular or solid. Depending on the sample state the waveguide layout can be changed to accommodate the samples requirements. The setup has been successfully used to perform measurements of soils and solvents over temperature as well as measurements of anisotropic materials.

I. INTRODUCTION

The determination of dielectric material parameters is significant for field calculations in all microwave applications. Such applications occur for example in the area of microwave heating. To acquire the complex permittivity of the material under test (MUT) an adequate sample of the material is placed inside a waveguide setup. The complex scattering parameters S_{11} and S_{21} are measured with a network analyzer (NWA). In the following two different waveguide setups are presented. The five layered structure contains two dielectric walls with a section for the material sample (MUT) in-between. Materials can be liquid and granular. For solid materials the two dielectric walls are dispensable and therefore omitted.

II. WAVEGUIDE SETUP

The configuration of the five layered structure is shown in Fig. 1. A waveguide with a cross section of 86.36 mm×43.18 mm is used which conforms the IEC 153-R26 standard. This waveguide covers the frequency range from 2 to 3 GHz. The sections are labeled with the numbers 1 to 5. Sections 1 and 5 are filled with air. The purpose of these sections is to attenuate higher order modes eventually generated by imperfect homogeneity in the sections with higher permittivity. Therefore, they must have a minimum length of

$$l_{\min} = \frac{5}{2\pi} \left[\frac{1}{a^2} - \left(\frac{f_{\max}}{c_0} \right)^2 \right]^{-\frac{1}{2}} \quad (1)$$

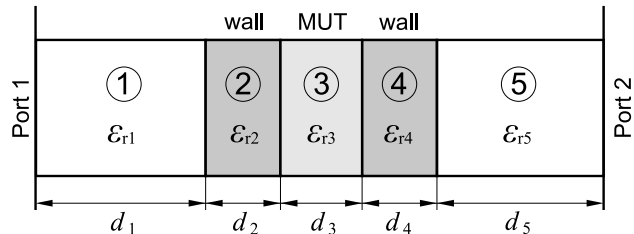


Fig. 1. Waveguide with 5 dielectric sections

that corresponds to five times the attenuation constant of the H_{20} -Mode. The broad-side dimension of the waveguide is denoted by a . So all modes higher than the basic H_{10} -mode are attenuated by at least -43 dB. For the setup with $f_{\max} = 3$ GHz the minimum length l_{\min} is 14 cm. The sections 2 and 4 are dielectric walls. The purpose of these is to build a container for the measured material sample (MUT in section 3) in case the material is liquid or granular. For solid material samples the walls should be omitted to avoid air gaps between walls and sample. This can be achieved by setting $\epsilon_{r,2} = \epsilon_{r,1}$ and $\epsilon_{r,4} = \epsilon_{r,5}$. For practical purposes the layout should be symmetric, i. e. section 1 and 5 as well as section 2 and 4 have the same geometric and electric parameters, respectively. However, the describing equation system, only little simplifies by assuming this condition. Hence, the general approach is discussed in this paper. The scattering parameters are determined with respect to the reference planes labeled as Port 1 and Port 2. For the measurement the location of the reference planes are defined by performing a TRL calibration.

III. ANALYTICAL DESCRIPTION

In the first step the S-parameters S_{11} and S_{21} are derived as a function of the permittivity of the MUT (Section 3 in Fig. 1). The magnetic permeability is assumed to $\mu_r = 1$, i. e. only non-magnetic materials are considered.

For each section n a propagating H_{10} mode with the complex amplitudes E_n and H_n for the E-field and transversal H-field is assumed, respectively. The fields are split in a forward (denoted by superscript f) and a

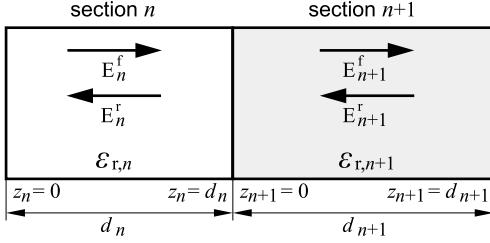


Fig. 2. Direction of wave propagation and associated fields

backward propagating wave (denoted by superscript r):

$$E_n(z_n) = E_n^f e^{-\gamma_n z_n} + E_n^r e^{\gamma_n z_n} \quad (2)$$

$$H_n(z_n) = H_n^f e^{-\gamma_n z_n} + H_n^r e^{\gamma_n z_n} \quad (3)$$

$$\gamma_n = \sqrt{\left(\frac{\pi}{a}\right)^2 - \left(\frac{2\pi f}{c_0}\right)^2} \varepsilon_n \quad (4)$$

γ_n is the propagation constant of the medium in section n . Forward propagation is defined in positive z -direction, which is from left to right (cf. Fig. 2). The transversal H-field can be expressed in terms of the E-Field using the wave impedance

$$Z_{F,n} = \frac{j2\pi f \mu_0}{\gamma_n} \quad (5)$$

This results in

$$H_n(z_n) = \frac{E_n^f e^{-\gamma_n z_n} - E_n^r e^{\gamma_n z_n}}{Z_{F,n}} \quad (6)$$

At the interface between two sections n and $n+1$ the tangential components of the E-field and the H-field have to be continuous. The continuity applies to each mode separately, because the different possible modes are linearly independent. For the H_{10} -mode follows from equations (2) and (6)

$$E_n^f e^{-\gamma_n d_n} + E_n^r e^{\gamma_n d_n} = E_{n+1}^f + E_{n+1}^r \quad (7)$$

$$\frac{E_n^f e^{-\gamma_n d_n} - E_n^r e^{\gamma_n d_n}}{Z_{F,n}} = \frac{E_{n+1}^f - E_{n+1}^r}{Z_{F,n+1}} \quad (8)$$

for $n = 1, \dots, 4$. E_5^r can be set to zero because there is no reflection at port 2. This yields to a linear equation system of eight equations for the eight unknowns $E_1^r, E_2^f, \dots, E_5^f$, which can be solved if the incident amplitude E_1^f and the permittivities ε_r, n are known. From this solution the S-parameters can be calculated to

$$S_{11} = \frac{E_1^r}{E_1^f}, \quad S_{21} = \frac{E_5^f e^{-\gamma_5 d_5}}{E_1^f} \sqrt{\frac{\gamma_5}{\gamma_1}} \quad (9)$$

Usually, the sections 1 and 5 are filled with air, so that $\varepsilon_{r,1} = \varepsilon_{r,5}$. Under this condition the square root in (9) is 1. For fixed dimensions d_1, \dots, d_5 and known permittivities of the wall materials in section 2 and 4, the S-parameters in (9) are a function of the permittivity $\varepsilon_{r,3}$ in section 3.

IV. INVERSE PROBLEM

As shown in the previous section it is possible to calculate the scattering parameters S_{11} and S_{21} analytically for known permittivity $\varepsilon_{r,3}$ of the MUT. For the determination of material parameters, the inverse problem has to be solved, i.e. for a given set of measured S-parameters S_{11}^{meas} and S_{21}^{meas} a $\varepsilon_{r,3}$ has to be found that solves

$$S_{11}(\varepsilon_{r,3}) = S_{11}^{\text{meas}} \quad (10)$$

$$S_{21}(\varepsilon_{r,3}) = S_{21}^{\text{meas}} \quad (11)$$

simultaneously. This system is overdetermined because two independent complex equations have to be solved with only one complex unknown. Due to the fact that S_{11}^{meas} and S_{21}^{meas} contain errors of measurement the system of the equations (10) and (11) generally cannot be solved exactly. Instead the problem is redrafted as follows: The goal is to find a $\varepsilon_{r,3}$ that minimizes the squared norm

$$n(\varepsilon_{r,3}) := |S_{11}(\varepsilon_{r,3}) - S_{11}^{\text{meas}}|^2 + |S_{21}(\varepsilon_{r,3}) - S_{21}^{\text{meas}}|^2 \quad (12)$$

If an exact solution $\varepsilon_{r,3}$ can be found $n(\varepsilon_{r,3})$ becomes zero. Of course, it is also possible to consider only one of the equations (10) and (11), which means to determine $\varepsilon_{r,3}$ out of only one complex equation using either S_{11}^{meas} or S_{21}^{meas} . The reason for using (12) is simply practical. For a MUT with low permittivity S_{11}^{meas} would be very low, thus it cannot be measured reliably with a network analyzer that is limited in dynamic range. The same holds to S_{21}^{meas} for a MUT with a very high permittivity. As a good compromise both scattering parameters are used in an equal fashion. The squared norm as defined in (12) implicitly gives more weight to the S-parameter with higher magnitude.

A. Solution of the Inverse Problem

The problem that has to be solved is to find a value for $\varepsilon_{r,3}$ such that $n(\varepsilon_{r,3})$ as defined in (12) achieves a global minimum. For this purpose, it is convenient to consider $n(\varepsilon_{r,3})$ as a function of two real variables $\varepsilon'_{r,3}$ and $\varepsilon''_{r,3}$ defined by

$$n(\varepsilon'_{r,3}, \varepsilon''_{r,3}) := n(\varepsilon'_{r,3} - j\varepsilon''_{r,3}) \quad (13)$$

Standard optimization algorithms are usually designed for finding a local minimum by iterative improvement of an initial guess. The so obtained minimum is generally not the global one. To find the global minimum a different approach has to be used. First of all it is required to define an interval $I \subset \mathbb{R}^2$ that includes the possible solution $(\varepsilon'_{r,3}, \varepsilon''_{r,3})$. This interval can be chosen relatively large, so that only little knowledge about the MUT is necessary. A good choice for most materials would be

$$I = [1, 100] \times [0, 60] \quad (14)$$

The interval I is meshed by an equidistant grid. At each grid point (13) is evaluated. The pair $(\varepsilon'_{r,3}, \varepsilon''_{r,3})$ for which the minimum value of $n(\varepsilon'_{r,3}, \varepsilon''_{r,3})$ is obtained is used as

initial value for a succeeding optimization procedure. For this final optimization the two dimensional quasi-Newton method has proven to work fine. It finds the minimum usually in less than ten iterations. The so obtained local minimum is less than all values found by the grid search. If there is no further local minimum between the grid points with a lower value, the so obtained minimum is global. To meet this condition a sufficient mesh density is needed. Practical experience has shown that for the interval (14) a distance of 1 in both directions works very well. This means a total of 6100 grid points have to be evaluated which takes less than ten seconds on a Pentium 4 computer with 3 GHz. Of course, if there is a certain knowledge of the range of permittivity for the MUT the interval size and the number of grid points can be reduced to save computation time.

In a slight variation the grid can be pre-optimized. This means a gradient search is performed originating from each grid point that stops after a fixed number of iterations. Usually two iterations are enough. The so obtained points $n(\varepsilon'_{r,3}, \varepsilon''_{r,3})$ form an irregular grid which is evaluated as in the case before. The pre-optimized grid can be less dense than the unmodified grid. But for the linesearches performed during the gradient optimization additional evaluations of (13) are necessary. The number of these additional evaluations for each grid point is nearly the same as the number of grid points that can be saved per grid point.

For measurements over frequency the grid evaluation only has to be done for the first frequency. The corresponding calculated permittivity serves immediately as initial value for the quasi-Newton optimization at the next frequency point. Of course, this assumes that there is no dramatic change in permittivity between two adjacent frequency points, which is usually the case.

B. Calibration

Calibration in this context means to determine the permittivities of the walls in section 2 and 4 which are initially not exactly known. This problem can be solved easily. If both walls consist of the same material, their permittivity can be obtained by measurements using a known material as MUT. The best choice is to use air with $\varepsilon_{r,3} = 1$. The permittivity of the walls $\varepsilon_{r,2} = \varepsilon_{r,4}$ is calculated from the measured S_{11}^{meas} and S_{22}^{meas} in the same manner as described for $\varepsilon_{r,3}$ in this section.

V. MEASUREMENTS

For the measurements the waveguide is connected with the two ports of a network analyzer via two coaxial to waveguide adapters as shown in Fig. 3. The NWA is calibrated using a TRL calibration, with three standards: reflection, transmission line of known length and direct connection (through). This also eliminates the influence of the waveguide to coaxial adapters, thus the NWA shows

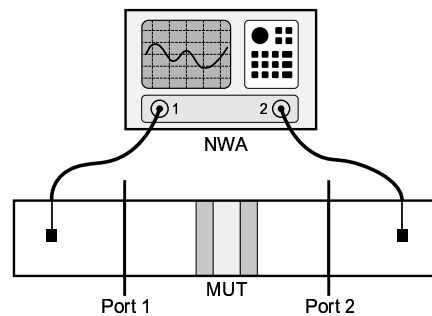


Fig. 3. Measurement setup with NWA

directly the measured S-parameters of the waveguide structure, with the reference planes at port 1 and port 2. From these S-parameters the permittivity of the MUT can be calculated with the algorithm described in the previous section.

For inserting the material sample in the waveguide one side wall must be opened. The waveguide should be designed such that the opening is at the narrow side. A possible air gap emerges basically between the MUT and the cover. If this cover is placed at the narrow side, the influence on the measured S-parameters is much lower as if it is at the broad side. This is illustrated in the next section. With this setup several materials including soil, solvents, fuels and wood have been measured. The results can be found in [1].

VI. ERROR ESTIMATION

The measured S-parameters generally contain errors. Possible reasons are the limited accuracy of the network analyzer, inaccurate calibration, deficiencies in sample preparation, undesirable air gaps between the MUT and the waveguide walls, etc. These errors lead to a wrong determination of the permittivity.

The influence of the S-parameters on the permittivity can be estimated by

$$\frac{d\varepsilon_{r,3}/\varepsilon_{r,3}}{dS_{11}/S_{11}} = \frac{S_{11}}{\varepsilon_{r,3}} \left(\frac{dS_{11}}{d\varepsilon_{r,3}} \right)^{-1} \quad (15)$$

$$\frac{d\varepsilon_{r,3}/\varepsilon_{r,3}}{dS_{21}/S_{21}} = \frac{S_{21}}{\varepsilon_{r,3}} \left(\frac{dS_{21}}{d\varepsilon_{r,3}} \right)^{-1} \quad (16)$$

which give the relative error of $\varepsilon_{r,3}$ over the relative variation of one single S-parameter. In Fig. 4 the relative error is shown for the applicator described in the previous section.

A common cause of errors is the presence of undesirable air gaps between the MUT and the walls of the waveguide. Such an air gap emerges for example if the material under test does not completely fill the cavity. In this case the air gap occurs between MUT and the side walls of the waveguide.

Fig. 5 shows the relative error of the measured S-parameters as function of the width of the air gap. The

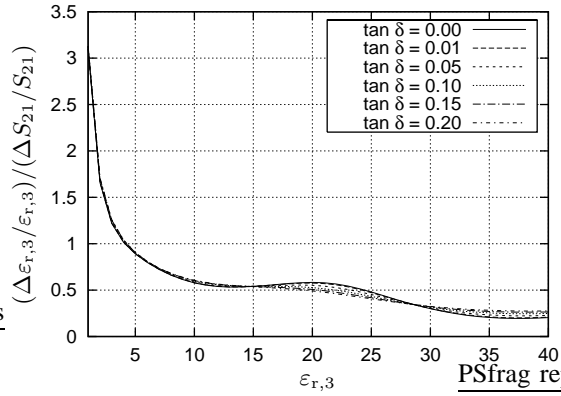
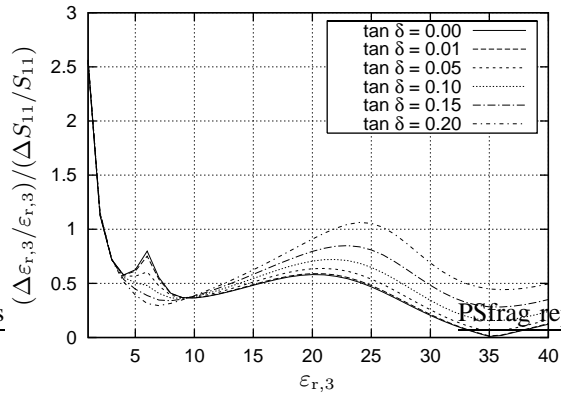
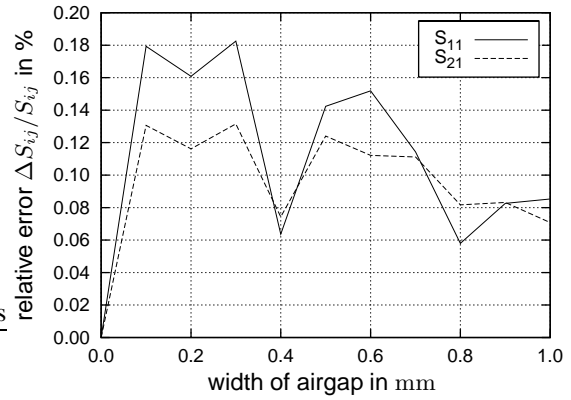


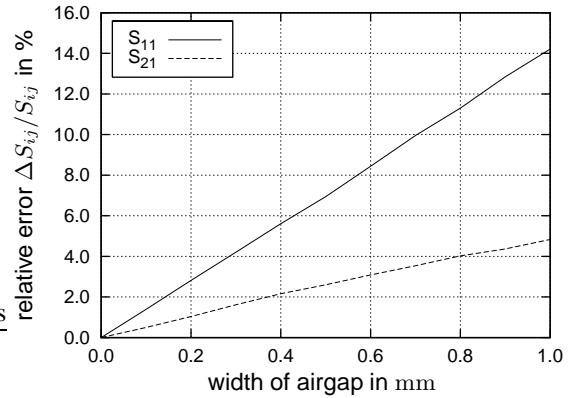
Fig. 4. Relative error dependent on the permittivity of the MUT over the relative change in the S-parameters.

orientation of the electric field with respect to the air gap has a high influence on the measured scattering parameters. In Fig. 5(a) the air gap is placed at the narrow side of the waveguide. The electrical field vector is tangential to the air gap. It can be seen that the resulting error in the measured S-parameters is less than 0.2% for air gaps up to 1 mm. This small error is due to the continuity of the tangential E-field, so there is no step in the electrical field distribution. Furthermore, the E-field vanishes at the narrow side of the waveguide hence the E-field is nearly zero inside the gap.

Fig. 5(b) shows the case of an air gap between the MUT and the broad side of the waveguide. This means the electrical field is orthogonal to the air gap. The resulting error is nearly 100 times higher as in the previous case and is nearly proportional to the width of the air gap. Due to the orthogonal orientation of the E-field there is a discontinuity in the field distribution because the E-field is attenuated by a factor of $1/\epsilon_{r,3}$ inside the MUT. The influence of the error of the measured S-Parameters on the calculated material parameters can be estimated using (15) and (16).



(a) E-field tangential to gap (at narrow side of waveguide)



(b) E-field orthogonal to gap (at broad side of waveguide)

Fig. 5. Relative error of the S-parameters in dependence of the width of the airgap between MUT and waveguide wall. The permittivity of the MUT is $\epsilon_{r,3} = 4 - 0.35j$.

VII. CONCLUSION

A waveguide setup for the determination of dielectric material parameters in the frequency range from 2 to 3 GHz is presented. This configuration is highly suited for liquid, granular and solid materials. The permittivity is computed from the measured S-parameters with a robust algorithm. The main reason for measurement errors are possible air gaps between the material samples and the waveguide walls. It has been shown that the influence of the air gaps can be minimized if the applicator is designed, such that the electrical field is tangential to the air gap.

REFERENCES

- [1] M. Pauli, T. Kayser, and W. Wiesbeck, "Material Parameter Measurement of Soils and Liquids with a Waveguide Setup", *Proceedings of the ISEMA 2005, 6th International Conference on Electromagnetic Wave Interaction with Water and Moist Substances*, pp. 182 – 189, Weimar, Germany, May/June 2005

Exposure Reduction in GSM Networks by Cell Splitting

Michael A. Baldauf, Sandra Knörzer, Werner Sörgel, and Werner Wiesbeck
Institut für Höchsthfrequenztechnik und Elektronik (IHE)
Universität Karlsruhe (TH), Germany
Phone: +49 721 608 6261, Fax: +49 721 691 865
E-mail: Michael.Baldauf@ihe.uka.de

Abstract—Spectrum for mobile communications is limited. With increasing number of customers the resources have to be used more efficient. Therefore, there is a trend to implement a higher density of base stations. Since the exposures of wireless techniques are more and more under consideration the question arises how denser network structures will change the exposure. It is shown that increasing the number of base stations will not generally raise the exposure but can rather help to lower it significantly.

Index Terms—exposure, network planning, cell splitting

I. INTRODUCTION

WITH the increasing number of users the precious resources in a mobile radio network have to be deployed more efficient. Reusing the available channels in spatially separated areas increases the efficiency. This leads to a higher density of access points i.e. a larger number of base stations is required to cover the same area. Although the exposure at places where people usually stay is well below the limit values, part of the people claims that there is still an evidence for a risk. The fear is the more and the closer the base stations are the higher is the potential risk.

It is well known that decreasing the cell range leads to lower a transmit power per base station. Furthermore, the total network power can be lowered [1]. This yields a reduction of emissions. But decreasing the cell size will in general also lead to lower antenna heights resulting in smaller separations between persons and radiating antennas. Therefore, the question arises what effect the emission reduction in combination with modified antenna heights has on the exposure.

Absorption of the electromagnetic fields in the frequency ranges used in mobile communications results in a temperature increase in the human body. A measure of the absorbed energy is the specific absorption rate which is proportional to the square of the electric field in the body. Therefore, the power density, which is in the far field of a source and outside any media proportional to the square of the electric field, is a measure of the exposure.

II. RADIO NETWORK PLANNING

In order to satisfy their customers a mobile radio network has to cover all area where users can be with a good quality. This can be achieved by providing a required signal to noise ratio (SNR). Noise is due to the noise generated in the

receiving device and the interference caused by other signals lying within the bandwidth of the receiver. In a system where no relevant interference occurs radio planning can be based simply on a calculation of signal levels.

Conventional cell planning is done considering the following main constraints:

- assure desired quality
- allocate needed resources
- minimize costs

The emerging exposure within and beyond the coverage area is usually not considered in conventional cell planning since the resultant field values are well below the limit values.

III. THE MODEL

The main elements in the presented model are:

- network layout
- wave propagation model
- base station's technical data and configuration
- mobile station's technical data and configuration
- additional propagation losses
- user distribution

These items and their modeling will be described in detail in the following sections.

As GSM is the most popular system the calculations are presented for this system. Interference can be neglected as long as the spacings of the carrier frequencies used in nearby cells are large.

A. Network Layout

A homogenous area is subdivided into hexagonal cells (cf. Fig. 1). Two rings of hexagons are added around a center hexagon to take the impact of surrounding cells into account. Base stations are placed in the center of the hexagons. All cells are identical concerning the number of active users and technical configurations of the terminals. The exposure is determined for the center cell. Simulations have shown that adding further two rings around the center cell will increase the exposure only by some tenth of a dB, which is negligible. Therefore, it is sufficient to limit the number of neighboring hexagons around a considered center hexagon to two rings.

In the middle of Fig. 1 the definition of the cell radius and the orientation of the considered sector antennas are shown. On the right hand side the notation of the angles in the spherical coordinate system is depicted.

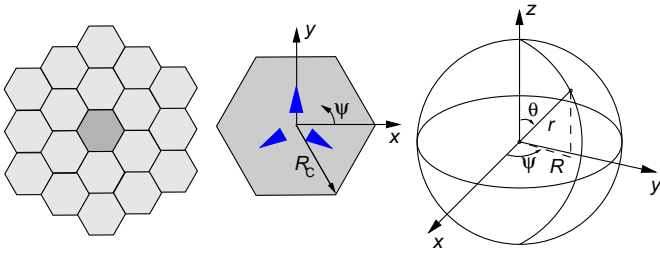


Fig. 1. Left: Considered network layout. A center hexagon is surrounded by two rings of hexagons. Middle: Definition of the cell radius and orientation of the sector antennas. Right: Convention for angles in a spherical coordinate system.

B. Wave Propagation Model

A very popular model to describe the path loss in mobile communications, which is also quite simple, is the COST-Hata model [2]. The model is COST-231's extension of Hata's model [3] for frequencies in the range from 1.5 GHz to 2 GHz. The COST-Hata model gives the path loss L between a transmitter and receiver depending on the antenna heights of the base station h_{BS} and mobile station h_{MS} , the distance R between both and their operating frequency f . The model is completely empirical since it is based solely on measurements.

According to the COST-Hata model the path loss L in an urban area is given by [2]:

$$\begin{aligned}
 L_{\text{urban}}^{\text{dB}} = & 46.3 + 33.9 \log\left(\frac{f}{\text{MHz}}\right) - 13.82 \log\left(\frac{h_{BS}}{\text{m}}\right) \\
 & - \left(1.1 \log\left(\frac{f}{\text{MHz}}\right) - 0.7\right) \frac{h_{MS}}{\text{m}} \\
 & - \left(1.56 \log\left(\frac{f}{\text{MHz}}\right) - 0.8\right) \\
 & + \left(44.9 - 6.55 \log\left(\frac{h_{BS}}{\text{m}}\right)\right) \log\left(\frac{R}{\text{km}}\right) + C_m
 \end{aligned} \quad (1)$$

The logarithm is to the base 10. For metropolitan centers the path loss L_{urban} is increased by $C_m = 3$ dB. In the following $C_m = 0$ dB, which holds for medium sized cities and suburban centers with medium tree density [2]. As frequency $f = 2$ GHz is considered. No difference is made between uplink and downlink frequency since the frequency difference would produce only negligible deviation in signal attenuation compared to the range of the overall attenuation.

In an open area the path loss L is smaller due to the very limited impact of obstacles, which might have an influence on the wave propagation. Therefore, a correction term has to be added to (1) when considering an open area [3]:

$$\begin{aligned}
 \Delta L_{\text{open}}^{\text{dB}} = & -4.78 \left(\log\left(\frac{f}{\text{MHz}}\right)\right)^2 \\
 & + 18.33 \log\left(\frac{f}{\text{MHz}}\right) - 40.94
 \end{aligned} \quad (2)$$

At 2 GHz (2) computes to -32.5 dB and is, thus, very different from (1), which holds for an urban area.

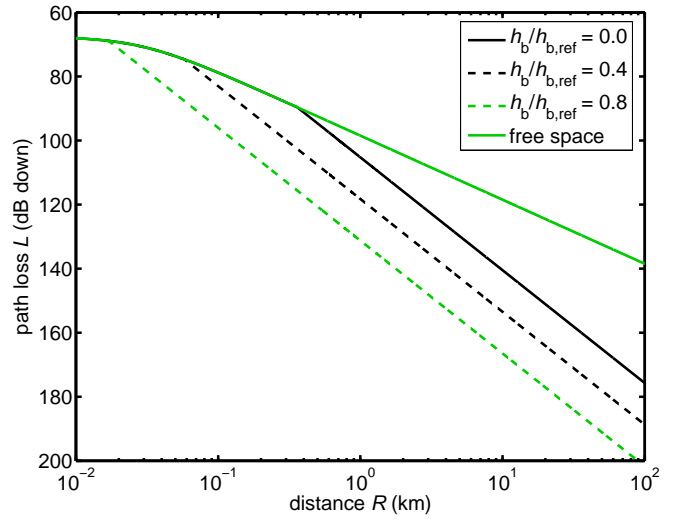


Fig. 2. Dependence of the path loss L /dB on the horizontal distance R . Shown are the path losses assuming free space propagation (bright solid line), the COST-Hata model with $h_b/h_{b,\text{ref}} = 0$ (dark solid line), $h_b/h_{b,\text{ref}} = 0.4$ (dark dashed line), and $h_b/h_{b,\text{ref}} = 0.8$ (bright dashed line). Parameters: $f = 2$ GHz, $h_{BS} = 30$ m, $h_{MS} = 1.5$ m.

In order to assess the influence of building heights easily the path loss for a built up area is calculated here by

$$\frac{L}{\text{dB}} = \frac{L_{\text{urban}}}{\text{dB}} + \frac{\Delta L_{\text{open}}}{\text{dB}} \left(1 - \left(\frac{h_b}{h_{b,\text{ref}}}\right)\right). \quad (3)$$

$h_b/h_{b,\text{ref}}$ is an empirical correction factor which resembles the degree of the building development. h_b can be thought to be the average building height and $h_{b,\text{ref}}$ a reference building height for which the path loss L is given by (1).

The path loss according to the COST-Hata model is shown in Fig. 2 for different building developments $h_b/h_{b,\text{ref}}$. For distances where the path loss according to the COST-Hata model would yield values smaller than the free space value the path loss is set to the free space value (bright solid line). The path loss according to the free space model decreases by 20 dB per decade. The clear bending for small distances suggesting a smaller decrease is due to the fact that for small separations the direct line of sight distance is much larger than the horizontal distance R , which measured in the (x, y) -plane. This horizontal distance is used as abscissa in Fig. 2.

C. Base Station

The base station serves as an air interface of the mobile radio network. The equipment and configuration are chosen in order to provide mobile services to customers within a limited area. In the following the most important parameters, which have an influence on the exposure, are explained.

1) *Antenna Height:* Whereas for large cells it is practicable to build antennas on high towers for smaller cell sizes only lower mounted antennas seem to be feasible. Therefore, changing the cell size will modify also the antenna height. Assuming an antenna height that will increase with increasing cell size takes this dependency into account. The simulation results presented here assume at a cell radius of $R_C = 500$ m

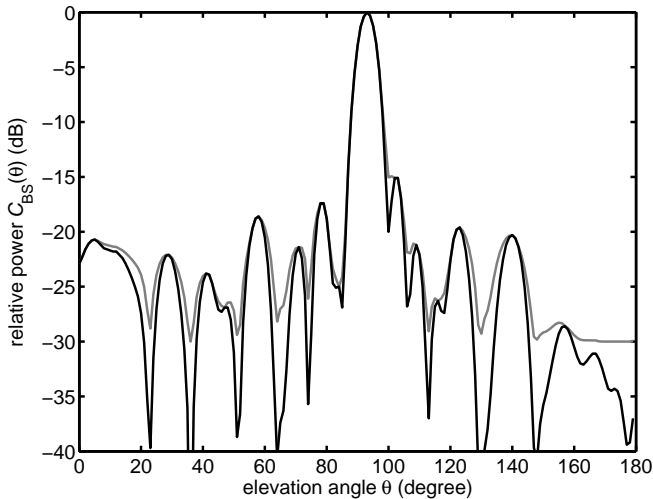


Fig. 3. Elevation pattern of Kathrein's antenna type 742212 ($G_{BS} \approx 18$ dBi) with 3° electrical downtilt. Shown is the pattern $C_{BS}(\theta)$ /dB for one polarization of the X-polarized antenna. Dark color: unmodified manufacturer data; bright color: smoothed and limited pattern data. Half power beamwidth in elevation $\theta_{3dB} \approx 7^\circ$, half power beamwidth in azimuth $\psi_{3dB} \approx 65^\circ$.

an antenna height of $h_{BS} = 10$ m increasing linearly to $h_{BS} = 60$ m at a cell radius of $R_C = 10$ km.

Regarding solely macro cells the antenna height is assumed to be always above the height of buildings close to the base station.

2) *Antenna Type and Downtilt*: A typical base station antenna type with a gain of $G_{BS} \approx 18$ dBi is chosen. The pattern data is available as text file on a CD [4].

Due to the impact of reflections the elevation pattern is smoothed (cf. Fig. 3). The usually smooth azimuth pattern remains unchanged. The three dimensional pattern $C_{BS}(\theta, \psi)$ is calculated by multiplying the azimuth and elevation pattern

$$C_{BS}(\theta, \psi) = C_{BS}(\theta) C_{BS}(\psi), \quad (4)$$

which is commonly done when no three dimensional data is available.

The considered sector antennas are slightly tilted down. The downtilt angle is chosen in such a manner that the direction where the antenna has its half power beamwidth above the main beam direction is directed at the height of the mobile station's antenna at the cell radius R_C .

A three sector configuration with main beam directions of $\psi = \{90^\circ, 210^\circ, 330^\circ\}$, is chosen for Kathrein's 742212 (cf. Fig. 1).

3) *Transmit Power*: The calculated minimum path loss from all possible locations of the mobile stations to any base station determines the power which is necessary to transmit the mandatory broadcast control channel (BCCH) in every sector independent of the number of active users in the cell.

For time slots which are not transmitted on the BCCH carrier an optional power control is possible. According to the specifications [5] a maximum power reduction of 30 dB compared to the transmit power of the BCCH carrier is allowed in time slots serving users at positions where the smaller path losses allow a reduction of transmit power.

4) *Channel Configuration*: Each active user in a cell occupies one time slot for speech transmission. Within the BCCH carrier one time slot contains cell specific information which is necessary for mobile terminals to find a cell. The remaining timeslots of the BCCH carrier can be filled with users. If not all time slots are needed for users or signalling information they are transmitted anyway containing dummy bursts.

The simulations are done assuming that the BCCH carrier should be kept clear of user data and all signalling is handled by this carrier.

5) *Sensitivity*: The sensitivity level as minimum received power of the base station is assumed to be $P_{R,BS,min} = -104$ dBm [5] independent of the cell size.

D. Mobile Station

The mobile station's antenna height is chosen to be 1.5 m above the ground. As antenna an isotropic radiator is regarded. The sensitivity level is assumed to be $P_{R,MS,min} = -102$ dBm [5].

Only speech calls are considered where one time slot is used by an active user. The transmit power in a time slot can be adjusted from 0 dBm up to 30 dBm in dependence on the path loss. The average transmit power is one eighth of the power per time slot. Discontinuous transmission (DTX), which would lead to a lower average power, is not considered.

E. Additional Damping

Choosing the transmit powers to be minimum received power plus the path loss will yield just the minimum received power at the other end. In order to assure good quality further losses have to be considered. To allow a connection a 3 dB loss due to the user and 7 dB due to signal fading are taken into account. There is a high probability that these losses occur. For this reason the signal levels and, therefore, the transmit powers need to be at least 10 dB higher than what is predicted from the path loss model.

To further increase signal quality and to take into account that part of the active users might be situated in buildings further 10 dB are added to the transmit powers of the base and mobile station. For the calculation of the coverage this quality improvement is not considered.

F. User Distribution

Mobiles are assumed to be equally distributed. Three cases are considered:

- network without load — no active user
- very low loaded network — 1 active user per km^2
- medium loaded network — 100 active users per km^2

IV. RESULTS

To evaluate the influence of a change of the cell size on the exposure the power density at the height of the mobile station $h_{MS} = 1.5$ m is calculated for the modelled center hexagon (cf. Fig. 1). The statistical relevant values considered here are the average and median value of the power density. All calculations are performed with Matlab.

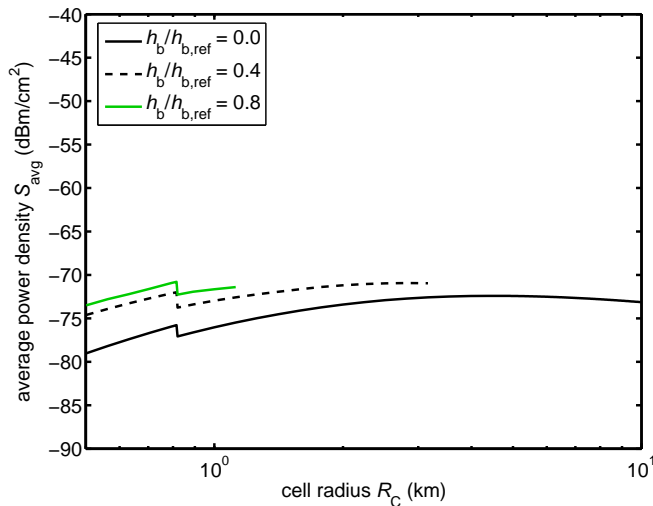


Fig. 4. Average value of the power density S_{avg} in dependence on the cell radius R_C for different building developments assuming a network with no active users.

Fig. 4 shows the run of the average power density S_{avg} in dependence on the cell radius R_C assuming a mobile network without users. Due to the higher path loss for higher building developments $h_b/h_{b,\text{ref}}$ the maximum achievable cell radius gets smaller.

The average power densities for larger building developments are higher. The (not shown) transmit powers are by some 12 dB larger when increasing $h_b/h_{b,\text{ref}}$ from 0 to 0.4. This is due to the increase of the path loss when increasing the building development (cf. Fig. 2). For all building developments decreasing the cell size generally yields slightly smaller values of S_{avg} . The slight but abrupt increase around a cell radius of $R_C = 800$ m is due to an integer change of the downtilt angle from 3° to 4° .

Fig. 5 shows that increasing the number of users in a cell will increase the average power density S_{avg} , since a higher transmit power is needed to serve the customers. Decreasing the cell size shows that the curves get closer together, which is due to the dominant contribution of the compulsory BCCH carrier to the transmit power in smaller cells containing fewer active users.

Since the resources are limited the case of 100 active users per square kilometer typically can't be realized with a cell size of 10 km. Depending on the number of available frequencies and reuse factor of them the cell size might be smaller e.g. around 1 km.

The median power density S_{med} differs from the average power density S_{avg} but the general results are the same (cf. Fig. 6). There is almost no change of S_{med} when there are no users in the cell. Increasing the number of active users shows clearly a lower exposure for smaller cell sizes.

V. CONCLUSION

It is shown that decreasing the cell sizes in mobile cellular networks can help to lower the exposure. This is mainly due to the reduction of the number of active users in smaller cells.

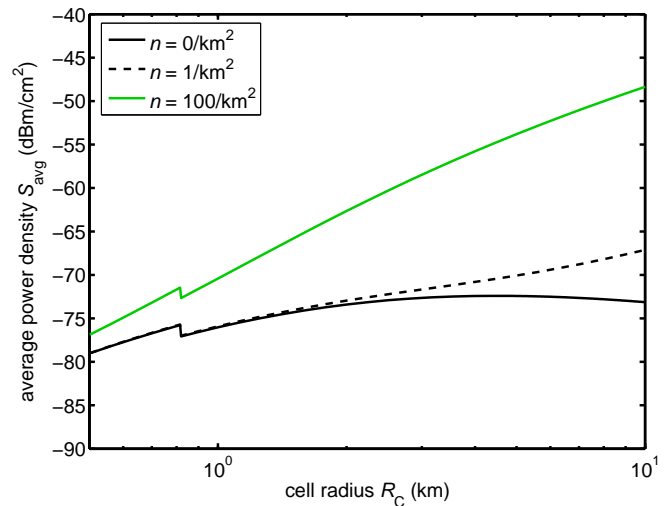


Fig. 5. Average value of the power density S_{avg} in dependence on the cell radius R_C for different numbers of active user densities. $h_b/h_{b,\text{ref}} = 0$.

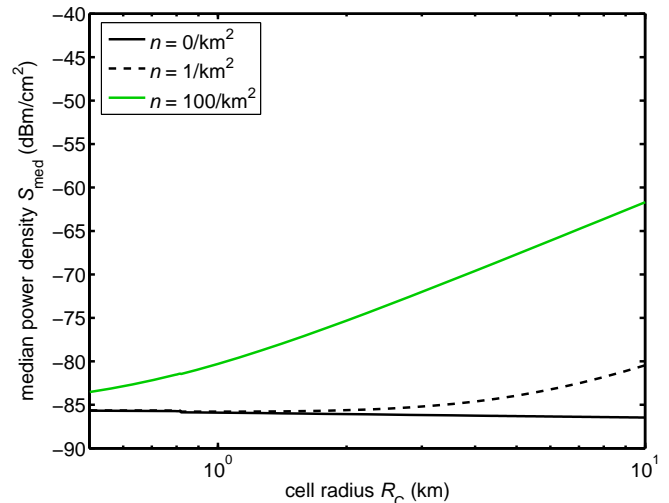


Fig. 6. Median value of the power density S_{med} in dependence on the cell radius R_C for different numbers of active user densities. $h_b/h_{b,\text{ref}} = 0$.

Building up more base stations in areas where no users are will not change the exposure significantly. Concerning the exposure there is no reason to limit the number of base stations.

REFERENCES

- [1] M. A. Baldauf, A. Herschlein, W. Sörgel, W. Wiesbeck, "Safety distances in mobile communications," in *Proceedings of 2nd International Workshop on Biological Effects of Electromagnetic Fields*, Rhodes, Oct. 2002, pp. 148–156.
- [2] COST 231, "Digital mobile radio towards future generation systems," European Commission, Directorate General XIII, EUR 18957, Tech. Rep., 1999.
- [3] M. Hata, "Empirical formula for propagation loss in land mobile services," *IEEE Trans. Veh. Technol.*, vol. 29, pp. 317–325, 1980.
- [4] KATHREIN-Werke KG. [Online]. Available: <http://www.kathrein.com/>
- [5] 3rd Generation Partnership Project, Technical Specification Group GSM/EDGE Radio Access Network, "Radio transmission and reception (Release 1999)," Technical Specification, 3GPP TS 05.05, 2003.

A novel antenna design for soil decontamination with microwaves

M. Pauli¹, T. Kayser¹, and W. Wiesbeck¹

¹Universität Karlsruhe, Institut für Höchstfrequenztechnik und Elektronik,
Kaiserstrasse 12, 76131 Karlsruhe, Germany
Phone: +49 721 608 6259, E-Mail:mario.pauli@ihe.uka.de

Abstract—This paper deals with the investigation of different antenna types suited for high power microwave applications at a frequency of 2.45 GHz. The antennas presented here are intended to be deployed in a microwave assisted soil decontamination process. For this purpose, an antenna has to fulfill several requirements. The radiation pattern has to be omnidirectional in the azimuthal plane and the radiated power should be uniformly distributed over the complete antenna length. This is necessary to achieve a homogeneous heating of the surrounding soil. For these reasons, a coaxial antenna design was chosen. The antenna matching strongly depends on the complex permittivity of the surrounding soils. Since the dielectric properties of the soil change with moisture content and temperature the antennas must provide a sufficient matching over a wide range of permittivity. Two possible antenna designs are presented with simulated values for the matching and the field distribution in the soil and the antenna, respectively. A comparison between simulated and measured values is given for verification. Subsequently, the temperature distribution inside the soil is measured in a laboratory setup.

I. INTRODUCTION

In different situations such as traffic accidents involving tankers, or idle industrial sites, soil contaminations can occur. In most cases the soils are polluted with halogenated hydrocarbons, mineral oils, fuels, aromatic hydrocarbons or heavy metals. These contaminations are dangerous for humans, animals and the environment. In Germany, an exact determination of the contaminated areas with respect to quantity and size is impossible. According to information issued by the German Government there exist more than 10500 contaminated sites and over 230000 sites that are suspected to be contaminated [1]. To minimize the risk of exposure to humans, remediation of contaminated areas is necessary. It is also of extreme importance for the conservation of the environment and for ecological recovery. For soil remediation several technologies exist. These can be divided into two groups: in-situ and ex-situ technologies. Ex-situ methods, where the contaminated soil is excavated, are most common. They are extremely invasive and create additional possible dangers, e.g. releasing toxic gases during the excavation process.

Therefore, a new in-situ technology for remediation of soils contaminated with volatile organic compounds is being investigated and presented in this paper. In-situ means that there is no need to excavate the soil and the remediation

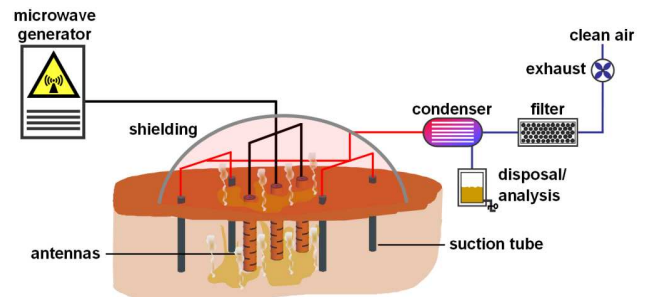


Fig. 1. System for soil decontamination with high power microwaves

process takes place in the contaminated area. A schematic of the decontamination system can be seen in Figure 1.

The microwaves are generated using a magnetron with an operating frequency of 2.45 GHz. The microwave energy is coupled into the soil by the use of slotted coaxial antennas. Due to the losses of the surrounding soil and the contaminants, the soil is heated and the contaminants evaporate. The so generated gases are exhausted by in-ground suction tubes near the antennas and by a suction socket on the surface. This socket also serves as an electromagnetic shielding of the whole system.

After extraction, the gases are condensed and collected for disposal and analysis, respectively. Subsequently, the gases are filtered by active carbon filters and leave the system as clean air.

In this paper, the focus is on the design of antennas suited for this application. The operational frequency is 2.45 GHz and the antennas must handle a power of several kW. Furthermore, the antenna has to fulfill several requirements: the electromagnetic energy has to be radiated omnidirectionally in the azimuthal plane and also uniformly over the length of the antenna. To avoid soil and humidity inside the antenna either a thin radome or a dielectric filling is used.

For the use in deeper soil regions a coaxial antenna offers some advantages. Due to the design of the antenna it can easily be inserted into the ground. The microwave energy couples through slots in the outer sheath of the antenna nearly omnidirectionally into the surrounding soil and the radiation is uniform along the antenna. Since the antenna has a modular design, a good matching can be achieved over a wide range of soil types and moisture contents.

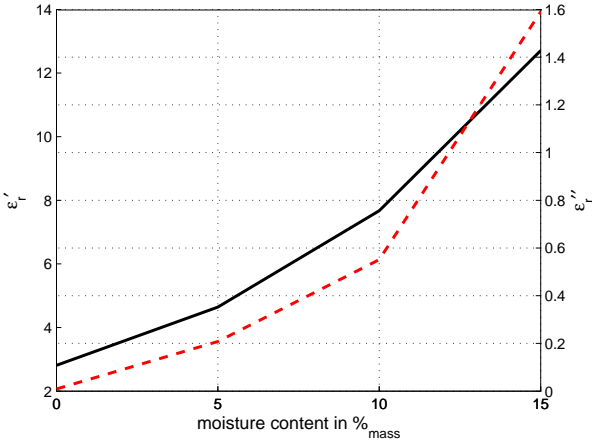


Fig. 2. Permittivity (—) and losses (- -) of sand as a function of gravimetric moisture content

II. COMPLEX PERMITTIVITY OF SOILS

The complex permittivity of the soil plays an important role in the antenna design. For this reason, it is necessary to know the complex permittivity of the soil. However, the dielectric properties do not only depend on the type of the soil but also on the moisture content, the frequency, the temperature and the salinity [2]. Different soil samples have been investigated and the complex permittivity has been determined as a function of gravimetric moisture content and temperature. The complex permittivity $\epsilon_r = \epsilon_r' - j\epsilon_r''$ for sand with different gravimetric moisture contents is shown in Figure 2. The solid line shows the real part of the complex permittivity while the dashed line corresponds to the imaginary part, indicating the losses of the material.

It can be seen that the real part of the permittivity increases with higher moisture content and ranges from $\epsilon_r' = 2.8$ to $\epsilon_r' = 12.7$. The imaginary part also increases with the moisture content and varies between $\epsilon_r'' = 0.01$ and $\epsilon_r'' = 1.6$. This means that loss factor lies between $\tan \delta = 3.5 \times 10^{-3}$ and $\tan \delta = 0.126$. Additionally, several other soil samples have been measured and the dielectric properties showed to be approximately in the same range. A comparison of the measured data with literature [3] shows a good agreement. More measurement results can be found in [4]. A detailed description of the measurement setup and the reconstruction algorithm is given in [5].

III. COAXIAL ANTENNA DESIGNS

For contaminations in deeper regions of the ground, it is necessary that the antenna can be inserted sufficiently deep. Via these antennas the microwave energy is symmetrically radiated around the antenna and uniformly along the slotted length. In this way, the contaminants within the soil are uniformly heated around the antenna and can be evaporated. These requirements are fulfilled by a leaky coaxial antenna. During the heating process the moisture content in the soil decreases, leading to lower values of the permittivity, as can be seen in Figure 2. By a modular construction of the antenna,

a good matching can be achieved over a wide range of permittivity. The coaxial antenna is shorted at one end with a metal plate whereas the inner conductor is screwed onto the shorting plate. In this way, the inner conductor can easily be replaced by another one with a different diameter to allow for a good matching under varying soil conditions. Furthermore, the antenna can be filled with a dielectric material which can additionally improve the matching at different environmental conditions.

Position, size and design of the slots have an influence on the antenna efficiency and on the field distribution around the antenna. The maximum field around the antenna is achieved when the slots are placed in the maxima of the surface currents and in the maxima of the magnetic field inside the antenna, respectively. These slots are placed around the outer conductor in 10 periodic levels, each with 2 horizontal slots. The distance between two slot levels is $\lambda/2$ and each level is rotated 90° with respect to each other. The dimensions of the antenna are a tradeoff between small antenna size, high power capability and the prevention of higher order modes.

Since an omnidirectional radiation pattern is desired it is necessary to have a symmetric field distribution inside the antenna. For this, the principal mode or TEM-mode (transverse electromagnetic mode) of the coaxial antenna is required. In order to suppress higher modes inside the coaxial antenna that can interact with the basic TEM-mode, the dimensions of outer (r_o) and inner (r_i) conductor are limited to [6], [7]

$$r_o - r_i \leq \frac{\lambda_0}{2 \cdot \sqrt{\epsilon_r'}} \quad (1)$$

with the free space wavelength $\lambda_0 = c_0/f = 122.5$ mm.

IV. AIR-FILLED COAXIAL ANTENNA

In case of an air filled coaxial antenna the maximum power P_{\max} that can be transmitted only depends on the highest allowable field strength. In the case of dry air the breakdown field strength is in the range of 3 kV/mm, depending on pressure, temperature and humidity [8].

According to

$$P_{\max} = \frac{E_{\max}^2}{120\Omega} r_i^2 \ln \frac{r_o}{r_i} \quad (2)$$

the theoretical maximum power that can be transmitted is in this case more than $P_{\max} = 2.5$ MW. However, it has to be taken into account, that the breakdown field strength drops rapidly with increasing humidity. For safety reasons the field strength should not be beyond 10 % of the breakdown field strength, i.e. 300 V/mm. This reduces the maximum power to 1/100. In the laboratory setup, a maximum power of 2 kW is used.

A. Antenna Design

A schematic of the antenna including all relevant dimensions is shown in Figure 3. Assuming the same number of slots, the antenna length has no influence on the antenna characteristics. In this way the antenna can be easily adapted to different depths. On one side the antenna is shortened and

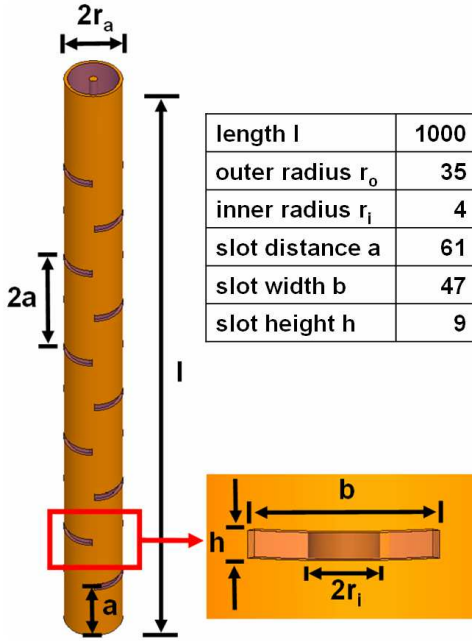


Fig. 3. Schematic of coaxial antenna with dimensions in mm

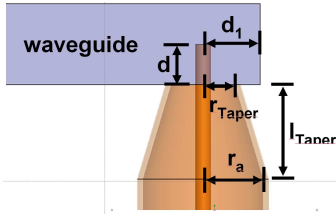


Fig. 4. Waveguide to coaxial transition

the first slot is placed at a distance of $\lambda/2$ from the shorting plate. The inner and outer conductors of the antenna consist of aluminum.

The antenna is directly coupled to the output of the microwave generator. A standard rectangular S-band waveguide with cross-section dimensions of $a = 86.36$ mm and $b = 43.18$ mm forms the output of the generator. In this waveguide an H_{10} mode propagates. With the feeding system this mode is transformed into the TEM-wave required for the coaxial antenna. The outer conductor of the antenna is directly tapered on the rectangular waveguide, as can be seen in Figure 4. Here, the smaller radius of the transition is $r_{\text{taper}} = 17$ mm, the taper length is $l_{\text{taper}} = 32$ mm, and the outer radius of the taper corresponds to the radius of the coaxial antenna. The inset depth of the inner conductor into the waveguide is $d = 22$ mm and the distance to the shorted end of the waveguide is $d_i = 30.5$ mm.

In Figure 5 a picture of the antenna and the coaxial-to-waveguide transition is shown. The spike on the one side simply has a practical purpose as it allows an easier insertion of the antenna into the soil.



Fig. 5. Coaxial antenna with feeding

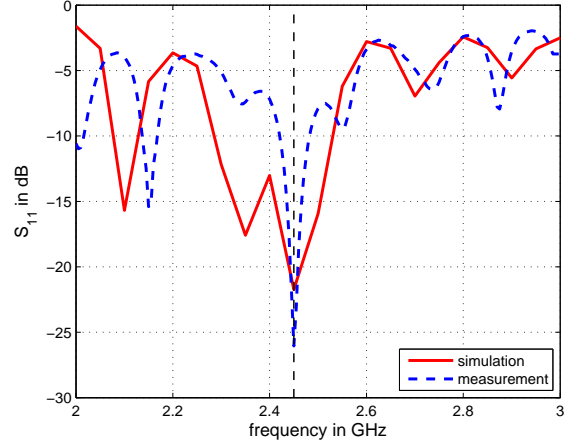


Fig. 6. Comparison between simulated (—) and measured (---) S_{11} -parameter

B. Antenna Matching and Field Distribution

In this section simulated results of the matching of the coaxial antenna inserted in sand are presented and compared to measured results of the reflection factor. The complex permittivity of the sand used is $\epsilon_r = 2.8 - j0.084$. This corresponds to a dry sand. Simulations are performed with Ansoft *HFSS* (High Frequency Structure Simulator). In simulations the antenna is placed inside a soil cylinder, resulting in a rotationally symmetric model. The cross-section of the model can be seen in Figure 7. To save computing time, only a quarter of the model is simulated. In the case of soils with low losses it is possible that not all energy is dissipated in the soil volume. To avoid reflected energy at the soil boundary, the boundary conditions of the outer soil surface are set to radiation boundary. Thus, the soil can be treated as an infinite volume.

For the measurements the antenna is inserted into sand with a known permittivity and connected to an Agilent E8357A vector network analyzer (VNA). The reflection coefficient S_{11} is measured. Simulations and measurements are performed in a frequency range from 2–3 GHz. Simulated and measured values for S_{11} agree well as can be seen in Figure 6. In both cases S_{11} is smaller than -20 dB at 2.45 GHz.

Additionally, the field distribution inside the antenna and the surrounding environment is investigated in simulations. The soil around the antenna has a depth of $d = 1$ m and an outer radius of $r_{\text{soil}} = 0.1$ m. In the simulations the input power of the antenna is set to 1 W. Figure 7 shows the electric and magnetic field configuration in the soil as a cross-sectional plot. The fields between the inner and outer conductor are shown, and it can be seen that the slots are placed in the maxima of the magnetic field strength to obtain high radiation.

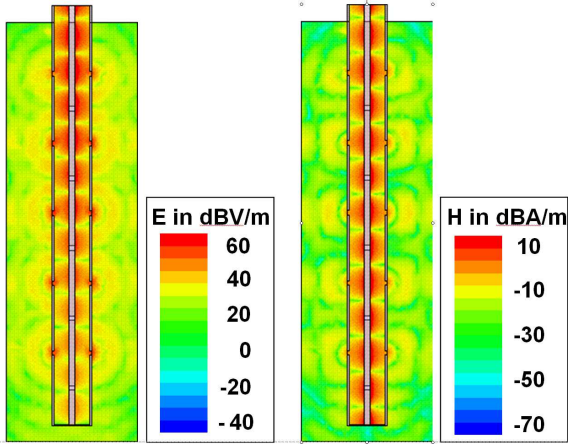


Fig. 7. Electric (left) and magnetic (right) field distribution inside the soil

Inside the soil the power is coupled out uniformly along the antenna.

V. PTFE-FILLED COAXIAL ANTENNA

In a next step the coaxial antenna is filled with Polytetrafluoroethylene (PTFE, Teflon) as a dielectric. PTFE offers well-suited dielectric properties: The specific resistance is nearly independent of temperature and is in the range of $10^{18} \Omega\text{cm}$. The permittivity is $\epsilon'_r = 2.1$ and is frequency independent between 50 Hz and 10 GHz. Additionally, the dielectric properties are constant in a temperature range from -50°C to over 200°C . The loss factor is $\tan \delta = 0.001$ and the break down field strength lies between 50–80 kV/mm.

The maximum power that can be transmitted by the antenna is in this case not limited by the maximum field strength but by the losses inside the PTFE. According to (2) the maximum power is more than 690 MW, but the dielectric losses inside the material limit the maximum power to

$$P_{\max} = (T_{\max} - T_0) \cdot \frac{4\pi\sqrt{\epsilon'_r}\sigma_c}{\omega\epsilon_0\epsilon''_r \ln(r_o/r_i)} \quad (3)$$

With the dielectric properties of PTFE, a thermal conductivity σ_c of 0.3 W/Km and a maximum temperature at the inner and outer conductor of 200°C and 150°C , respectively, this results in a maximum power capability of more than 4.3 MW for a diameter of the inner conductor of 6 mm, and more than 11.7 MW for an inner conductor of 24 mm diameter.

A. Antenna Design

The antenna design is similar to the design of the air-filled coaxial antenna. Due to the dielectric filling the wavelength is shortened by a factor of $\sqrt{\epsilon'_r}$ and consequently the slot distance is decreased. The antenna dimensions can be found in Table I. The diameter of the inner conductor is set to 6 mm if the soil permittivity is below $\epsilon'_r = 5$ and to 24 mm for higher permittivities.

TABLE I
DIMENSIONS OF PTFE-FILLED ANTENNA

length in mm	1000
outer diameter in mm	60
inner diameter in mm	6
$\epsilon'_r = 2-5$	
inner diameter in mm	24
$\epsilon'_r = 5-10$	
wall thickness in mm	3
slot width in mm	40.1
slot height in mm	6
slot distance in mm	42.25

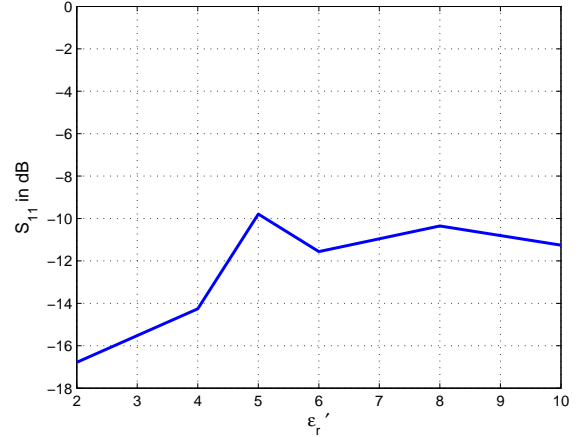


Fig. 8. Matching of the PTFE-filled antenna as function of soil permittivity

B. Antenna Efficiency

Since the difference between the dielectric constant of PTFE and the surrounding soil is lower than in the case of air as dielectric the matching of the antenna improves. As can be seen in Figure 8 the reflection coefficient is better than -10 dB in a permittivity range from $\epsilon'_r = 2$ to $\epsilon'_r = 10$. The loss factor in this case is set to $\tan \delta = 0.01$ and has only little influence on the antenna matching.

From $\epsilon'_r = 2$ to $\epsilon'_r = 5$ the inner conductor has a diameter of 6 mm and for higher permittivities the diameter increases to 24 mm. The power that is dissipated into heat in the PTFE equals approximately 34 mW. This corresponds to a reflection factor of better than -10 dB, and to a minimum antenna efficiency of 90 %.

VI. TEMPERATURE MEASUREMENT

Since it is difficult to measure the electric field inside the soil directly, the temperature distribution is investigated. The temperature gives an indirect measure for the electric field. Hence, as a first approximation a homogeneous temperature implies a homogeneous field distribution. This is especially true for short time periods since in this case thermal conduction can be neglected. The dissipated energy inside a lossy material can be calculated by

$$dP = 2\pi f \epsilon_0 \epsilon''_r |E|^2 dV \quad (4)$$



Fig. 9. Laboratory measurement setup

Equation (4) shows that the dissipated power and therefore the temperature is a function of the electrical field inside the soil. The measurement setup and results of the temperature measurements are presented in the following section.

A. Measurement Setup

Thermal measurements are performed with the laboratory measurement setup consisting of a magnetron with an output power of $P = 2$ kW and a tub filled with approximately 0.250 m^3 of sand. To avoid electromagnetic leakage the tub and its cover are shielded inside with copper foil. The laboratory setup is shown in Figure 9.

B. Measurement Results

The following results in Figure 10 show the temperature after a heating time of 60 min with a power of 2 kW. At a distance from the antenna of 5 cm and 10 cm, respectively, the temperature is nearly constant at depths from 15 cm to 45 cm. This indicates a homogeneous electric field. In the upper regions the temperatures decrease due to thermal radiation losses and in depths beyond 45 cm there are no slots in the antenna to radiate. The dash-dotted line represents a distance from the antenna of 20 cm. In this case, the temperature is homogeneous over the depth. It has to be mentioned that the moisture content in this measurement was relatively high. Therefore, the penetration depth of the microwaves is limited and the heating shown here is based primarily on heat conduction.

VII. CONCLUSION

In this work a novel antenna design for soil decontamination with microwaves was introduced. It has been shown that the antenna radiates omnidirectionally azimuthally and couples the energy uniformly over its whole length into the surrounding soil. In this way, the antenna is capable for remediation of deeper soil layers. Due to the modular design of the antenna

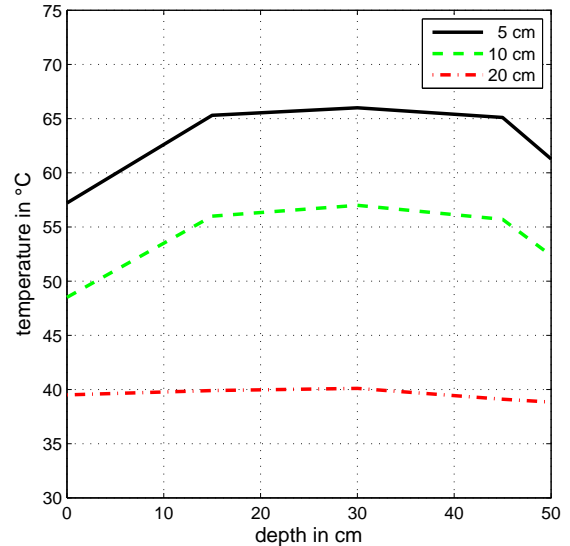


Fig. 10. Temperature over soil depth in different distances from the antenna

with a replaceable inner conductor and the possibility to insert a dielectric, a good matching can be achieved over a wide range of soil conditions. A simulation result is shown with PTFE as dielectric. The matching was showed to be better than 10 dB for a soil permittivity range from $\epsilon'_r = 2$ to $\epsilon'_r = 10$. The simulation results of the air-filled antenna have been verified with measured values of the reflection coefficient. The uniform coupling along the antenna was shown by measuring the temperature at different depths in the laboratory setup. A homogeneous heating could be achieved in radial direction as well as in different depths.

ACKNOWLEDGMENT

The authors would like to thank the Helmholtz Association for the support of this work and Rolf Gerber for the soil samples. Rolf Gerber is with the Institut für Bodenkunde und Bodenerhaltung at the Justus-Liebig Universität Giessen.

REFERENCES

- [1] U. Martensen, http://www.bundestag.de/bic/hib/2004/2004_244/02, October 2004.
- [2] A. C. Metaxas and R. J. Meredith, *Industrial Microwave Heating*, Peter Peregrinus Ltd., London, 1993.
- [3] A. R. von Hippel, *Dielectric Materials and Applications*, Artech House, Boston, 1995.
- [4] M. Pauli, T. Kayser, and W. Wiesbeck, "Material Parameter Measurement of Soils and Liquids with a Waveguide Setup", *Proceedings of the ISEMA 2005, 6th International Conference on Electromagnetic Wave Interaction with Water and Moist Substances*, pp. 182 - 189, Weimar, Germany, May/June 2005.
- [5] T. Kayser, M. Pauli, and W. Wiesbeck, "Determination of Dielectric Material Parameters using a flexible Waveguide Setup", *Proceedings of the GeMiC 2006, German Microwave Conference*, Karlsruhe, Germany, March 2006.
- [6] M. Kummer, *Grundlagen der Mikrowellentechnik*, VEB Verlag Technik, Berlin, 1986.
- [7] N. Marcuvitz, *Waveguide Handbook*, Mc Graw-Hill Book Company, New York, 1986.
- [8] P. A. Tipler, *Physik*, Spektrum Akademischer Verlag, Heidelberg, 1998.

Evaluation and Optimization of CDMA System Performance in Macrocell Environments based on Antenna Radiation Pattern

J. A. Pontes¹, S. Schulteis¹, M. A. Baldauf¹, and W. Wiesbeck¹

¹Institut für Höchstfrequenztechnik und Elektronik (IHE)
Universität Karlsruhe (TH), Germany
Tel: +49-721-608-8276, Fax: +49-721-691-865
E-mail: Juan.Pontes@ihe.uka.de

Short Abstract— In this paper an ideal model for antenna optimization is presented and validated. The model consists of a simplified scenario and a set of evaluation criteria taking into consideration CDMA cellular network problems such as coverage, handover and interference. It is shown that even under assumption of a simplified model, practical results very near to those obtained with dynamic simulators are possible, therefore offering a possible approach into solving the backward antenna problem and optimizing the radiation pattern of base station antennas.

Keywords-component; Base Station Antennas; CDMA; UMTS.

I. INTRODUCTION

Despite the great interest in the improvement of cellular networks and systems there are still some components, like the base station antennas, that remain non-optimized. This is regardless of the fact that a lot of work has been done in improving the different issues and configuration schemes within a cellular network. Yet the main part of this previous work deals only with specific problems on a system level, like power allocation, or when related to the antennas, it considers configuration problems such as downtilt or ideal beamwidth. To our knowledge the computation of new radiation patterns has, with certain exceptions [1], not been considered. And in case of [1], it has been done only dynamically in the form of a smart antenna. As a result an essential component of all cellular systems remains non-optimized, namely the base station antenna.

In order to optimize base station antennas the backward problem between system behavior and the antenna gain pattern has to be known. However, knowing how to change the antenna pattern in order to obtain a better system performance is in most cases not possible with conventional dynamic and static simulators because of the complexity of all the variables involved in a cellular system. Therefore a simplified model which allows the formulation of a backward problem for antenna design and, at the same time, accurately represents cellular networks problems like coverage, interference and handover has to be prepared. With this model an ideal antenna

can be computed, and based on it a real antenna of N elements can be synthesized.

In this paper such an ideal model will be presented and validated. For this purpose, in section II, a simplified analytical model, i.e. our simulation environment, will be presented. With it a set of evaluation criteria for antenna evaluation will be specified, in section III. In section IV two different commercial antennas will be evaluated under different configurations. The results will then be compared with those already published in [2].

II. SIMPLIFIED SIMULATION ENVIRONMENT

Performance of cellular systems is measured in terms of required transmit power, coverage, QoS and interference. This is done with the help of dynamic and static simulators, which simulate the whole environment including topography, users and provided services in order to give an estimate of the system behavior. Desired is, however, a set of criteria that directly relate system performance with base station antenna. For this purpose a three-dimensional simulator has been designed, to evaluate only the antennas performance. With this simulator the received power at different user heights is calculated and based on it a set of criteria are met to assure coverage and reduce interference under different conditions of downtilt and base station height. The simplified scenario as implemented in Matlab[®] is depicted in Fig. 1.

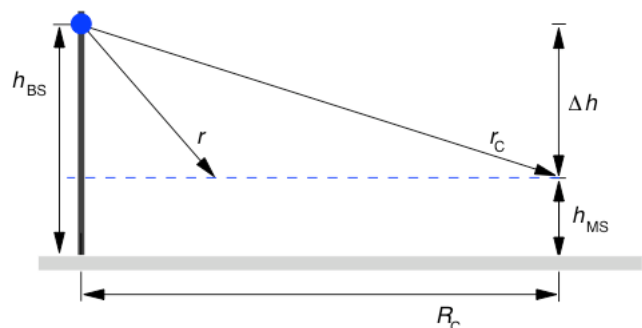


Figure 1. Scenario for simplified simulation environment

This scenario is constituted by a base station at height h_{BS} , which surmounts the mobile station height h_{MS} by Δh and is equipped with a set of antennas serving a circular coverage area, i.e. cell radius R_C . Each antenna covers a circular segment or cell and no power control algorithms are implemented, i.e. only the propagation problem is considered. As a result, very simple considerations can be made towards which antenna will provide the best coverage. This has been done in the past for ground mapping radars and aircraft beacons, but only under consideration of free propagation models and only for the illumination area. In cellular systems, on the other hand, special consideration has to be given to the area beyond coverage, namely neighbor cells. This can be easily done with our simulator since it is possible to determine received power at different heights, ranges and under different system conditions (antenna downtilt, downtilt type, antenna type, base station height, etc.). Additionally, because in this work only CDMA Networks that operate at 1.8 GHz are considered, the COST-Hata model for urban areas has been selected for propagation computations.

III. EVALUATION CRITERIA

The most important issue to be considered is coverage. Any model for cellular system evaluation or design must consider a sufficient coverage. Within the frame of this work a minimum of 90% of cell coverage is expected, where the minimum transmit power needed to reach this minimum coverage constitutes the first optimization criterion, i.e. the coverage criterion. The minimum received power in the cell P_D is set to -80 dBm and the cell is defined as a circle segment of radius R_C and angular aperture of 120° and 60° for the cases of six sectored and three sectored sites respectively.

Once coverage is assured interference has to be minimized while still allowing a certain handover margin. This can be evaluated based on how much power is radiated beyond the cell radius. In this work, the amount of power radiated outside the cell will be compared with the power radiated within the cell. For handover, the power to be exceeded is that of P_D minus a handover margin. In consequence, the area percentage outside the cell exceeding this received power conforms the second evaluation criterion or handover criterion. On the other hand, the area percentage in which the received power is higher as P_D minus an interference margin constitutes the third criterion or interference criterion. In each case the handover and interference margins are set to 4 dB and 8 dB respectively. With the specification of these parameters a set of criteria as shown in table I, is complete, with which it is possible to see how the antenna influences the system without consideration of topography or traffic.

TABLE I. EVALUATION CRITERIA

Criteria	Region	Size	Desired Received Power Level
Coverage	$< R_C$	90 percentile of cell	P_D dBm
Handover	$> R_C$	15 percentile of cell	$P_D - 4$ dB
Interference	$> R_C$	50 percentile of cell	$P_D - 8$ dB

As example of how an antenna can be benchmarked based on these parameters, Fig. 1 to 4 show the results obtained through simulation, once a fixed coverage of -80 dBm in 90% of the coverage region has been fulfilled through power increase or decrease. Fig. 1 shows the radiation on ground for an antenna with 7° electrical downtilt and 33 dBm pilot power, i.e. transmit power, Fig. 2 the areas with power levels higher as P_D dBm, $P_D - 4$ dB and $P_D - 8$ dB, and Fig. 3 and 4 a benchmark in form of cell percentage with received power higher than the abscissa value for both the cell and the area outside of it, which for the cell case is equivalent to the complementary cumulative distribution function. With these results it is now possible to use the necessary transmit power for sufficient coverage as coverage criterion and to read the handover and interference criteria out of Fig. 4, which in this case are 50% and 120%. Furthermore, when a system parameter is varied in a way that a minimum for one of these criteria is reached then an optimum configuration for this criterion is said to have been found. To validate this approach some results based on commercial antennas are analyzed in the next section.

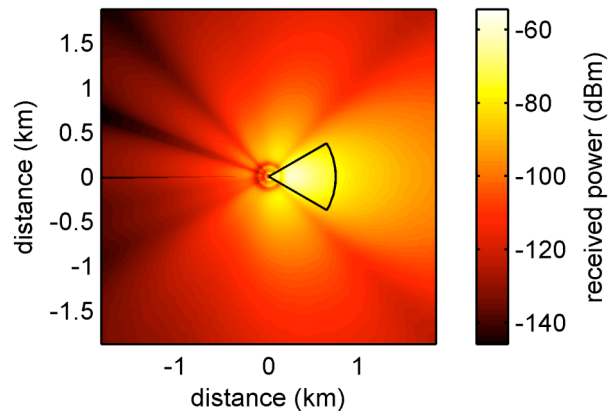


Figure 2. Radiation seen at mobile height with Δh of 45m, R_C of 750m and 742 351 Kathrein antenna with 7° electrical downtilt.

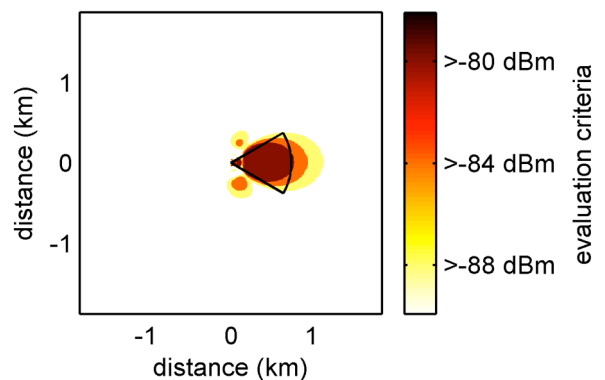


Figure 3. Zones in which received power at mobile height is higher than -80 dBm, -84 dBm and -88 dBm, with same conditions as in Fig. 2.

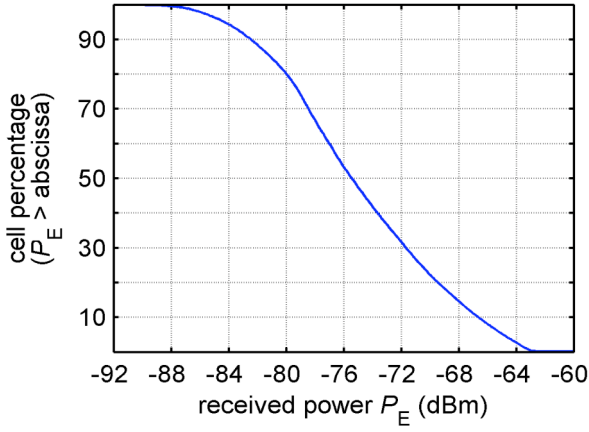


Figure 4. Zones in which received power at mobile height is higher than -80 dBm, -84 dBm and -88 dBm, with same conditions as in Fig. 2.

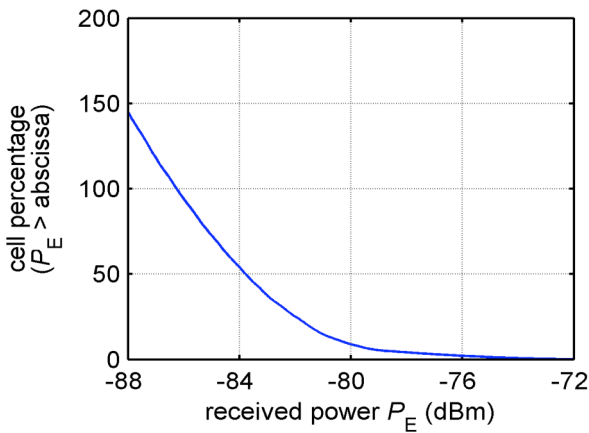


Figure 5. Zones in which received power at mobile height is higher than -80 dBm, -84 dBm and -88 dBm, with same conditions as in Fig. 2.

IV. EVALUATION OF COMMERCIAL ANTENNAS

Based on this approach two commercial antennas are evaluated for eight different configurations, in which downtilt angle is the parameter to be optimized. The corresponding horizontal and vertical beamwidths along with gain and antenna model are all listed in Table II [3]. In all cases concerning these two antennas only radiation patterns supplied by the fabricant are used. The evaluation itself consists on measuring the downtilt angle at which the best performance for each criterion is achieved.

In Table III all downtilt angles required for optimum coverage under consideration of 8 different configurations are presented. In the different configurations antenna height, cell radius and tilt type is varied. In the case of mechanical downtilt only the 0° pattern is tilted, while for electrical downtilt the given patterns at steps of 1 degree are used. It is seen that not each criterion has the same optimum angle. For all measured configurations the handover and other cell interference criteria required a larger downtilt angle as the one needed for optimum coverage. To validate these results a comparison with the optimum downtilt angles presented in [2] was done. An overall

TABLE II. COMMERCIAL ANTENNAS USED FOR SIMULATION

Type No.	Beamwidth ($^\circ$)		Gain (dBi)
	Horizontal	Vertical	
Kathrein 742 211	65	12	15.5
Kathrein 742 351	33	6	21

agreement with a maximal difference of 2° for both mechanical and electrical downtilt in all configurations is found when compared with the coverage criterion.

TABLE III. OPTIMUM DOWNTILT ANGLES FOR COVERAGE

Antenna No.	Tilt Type	Radius (m)	Ant. Height (m)	Optimum Downtilt ($^\circ$)
742 351	Mech.	500	25	4
		750	25	2
		750	45	5
	Elec.	500	25	4
		750	25	2
		750	45	5
742 211	Mech.	500	25	5
	Elec.	500	25	4

As it can be seen from Fig. 3 and the results from Table III depending on how each optimization criterion is fulfilled, it is possible to predict the impact of the antenna on the system concerning coverage, handover and interference. Furthermore optimum radiation patterns can be designed to obtain the desired performance for a certain configuration without the need of complicated system simulators. For example if an antenna is optimized to have only 15% of the received power outside the cell higher than -84 dBm and 50% higher than -88 dBm interference will be reduced without worsening handover, thus improving the current antennas performance.

V. CONCLUSIONS

It has been shown that an adequate antenna performance evaluation can be done based on three simple evaluation criteria without the use of topography or traffic. As result of this, antenna design can be improved and tuned to comply with system requirements like coverage or interference without the use of complicated simulation scenarios. Furthermore, results validating this approach have been presented.

REFERENCES

- [1] P. Nahi, C. Parini, L. Du, et al., "Cell Shaping using Pattern Synthesis for a distributed Load Balancing Scheme in Cellular Networks", IEEE Wireless Communications and Networking, Vol. 1, 2003, pp. 93-97.
- [2] J. Niemelä, T. Isotalo and J. Lempiäinen, "Optimum Antenna Downtilt Angles for Macrocellular WCDMA Network", EURASIP Journal on Wireless Communications and Networking, No. 5, 2005, pp. 816-827.
- [3] Kathrein, Technical Information and new products. Available: <http://www.kathrein.de/> (Aug. 2004).

PROSPECTS of ELECTROMAGNETIC MATERIALS PROCESSING by USE of cm-, mm- and μm -WAVES

M. Willert-Porada

University of Bayreuth, Faculty of Applied Natural Sciences, Chair of Materials Processing, Universitätsstr. 30, D-95447, Germany, 49-921-55-7201, Monika.Willert-Porada@uni-bayreuth.de

Short Abstract—The paper presents examples of industrial and scientific work in the area of high frequency electromagnetic materials processing. Underlying fundamentals of material-microwave and material-laser radiation interaction are summarized with particular emphasis on the penetration depth, energy density and atmospheric plasma contribution upon different processes. Finally, as a new approach, combined application of different frequencies is described, e.g., direct microwave heating combined with microwave atmospheric plasma and laser + microwave application for sintering, coating, and structuring of surfaces.

Keywords-materials; microwaves; laser radiation; atmospheric plasma; coating; sintering; surface modification.

I. INTRODUCTION

Utilization of high frequency radiation, from 10^{15} Hertz to 10^9 Hertz for materials processing, from the Ultraviolet (UV), Visible (VIS), Infrared (IR) down to the Microwave (MW) range of the electromagnetic spectrum, as shown in Figure 1, is currently a fast expanding area of technology. Unfortunately, this is not fully recognized as an unified approach by the community of experts in “Electromagnetic Material Processing”, abbreviated as EMMP, due to the severe fragmentation among the relevant scientific and industrial branches involved.

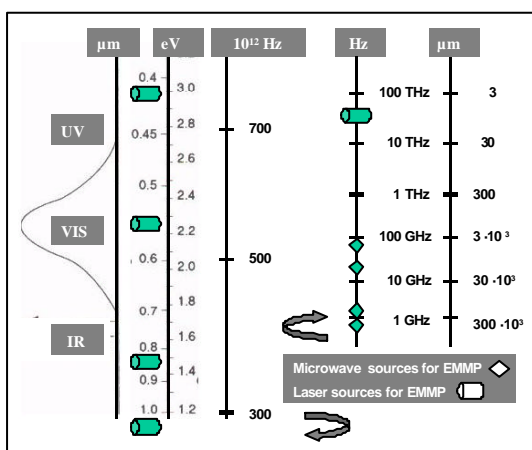


Figure 1. Range of frequencies used for electromagnetic materials processing

Welding, cutting, drilling, melting, sintering, curing, coating, cladding, ablation (PLA, Pulsed Laser Ablation) are some of the general processing methods to be named, with numerous examples from different classes of materials, such as metals, ceramics, polymers and composites. To the authors knowledge, with exception of the first interdisciplinary book on dielectrics [1], only few modern “Electroheat”-textbooks (I am not going to list all, in order to avoid problems of incompleteness) implemented chapters on high frequency electromagnetic radiation processing, like e.g., [2-4], most probably because of the vast number of original papers published over the past 15-20 years. Currently, an internet based scientific and technical search engine shows a large difference in R&D activity for laser, IR and microwave processing of materials: on laser processing >4500 papers appear for the period 2006-2000, whereas for microwave processing less than 1000 papers are shown for the period 2006-1990, and a search for “IR-processing” yields ~3500 hits, from all possible application area’s [5].

In order to stimulate the discussion, the following paper will therefore address some of the common features of “high frequency electromagnetic processing of materials”, coining the term EMMP for it, and highlight future prospects for materials processing by μm - (UV and IR), mm- and cm-waves (MW), using examples of processes currently investigated at the Chair of Materials Processing in Bayreuth.

II. RADIATION SOURCES FOR ELECTROMAGNETIC MATERIAL PROCESSING

The driving forces for the development of EMMP are: maturity of micrometer-, millimeter- and centimeter-wave sources and increased fundamental knowledge about the interaction of solids and gasses with high frequency radiation. The transfer from research into application is motivated by the need of increased throughput of industrial production, cost reduction by automation and manpower savings, and by increased quality demand for commodity products. Some examples of contemporary radiation sources used for materials processing are given in Table 1 and in Table 2. These powerful, coherent radiation sources can be employed either for direct heating of solid materials or for indirect energy deposition.

TABLE I. WAVELENGTH, ELECTRICAL EFFICIENCY, POWER AND APPLICATION OF COMMON LASER-SOURCES FOR MATERIALS PROCESSING

Laser-Source	λ [μm]	h [%]	P [kW]	Examples of Application [6,7]
Excimer laser	0,193 – 0,325	< 1	10^5 pulsed	PLA, Microstructuring
Ar or He/Ne	0.488 – 0.632	0.1-1.0	10^2 pulsed	Curing, Cleaning
Diode laser	0.810 – 0.940	0.1 – 4.0	10^2 pulsed	Different (e.g., Ablation, Hardening, Curing)
Nd-YAG	1.064	5.0	10^2 pulsed	Melting, Welding, Hardening, Sintering
CO ₂	10.6	5.0-10.0	10^2 cont.	Cutting, Welding, Drilling

TABLE II. WAVELENGTH, ELECTRICAL EFFICIENCY, POWER AND APPLICATION OF COMMON MILLIMETER AND CENTIMETER-WAVELENGTH SOURCES FOR MATERIALS PROCESSING

Microwave-Source	λ [μm]	h [%]	P_{CW} [kW]	Examples of Application [8]
Gyrotion < 100 GHz	$\sim 3\text{-}30\cdot 10^3$	30-40	10-40	Sintering, Welding, Plasma
Magnetron < 10 GHz	$\sim 100\text{-}1000\cdot 10^3$	~ 65	1-100	Sintering, melting, Drying, Curing, Plasma
Klystron < 10 GHz	$\sim 30\text{-}1000\cdot 10^3$	~ 75	~ 100	Sintering, Curing, Drying, Plasma

III. PROCESS DEVELOPMENT BASED ON DIRECT HEATING

The direct energy deposition by dissipation of high frequency radiation in the solid is governed by the choice of the wavelength and the material properties, as shown in Figure 2 for metals and radiation with wavelengths from μm to cm. The indirect energy deposition occurs via a gas plasma powered by the laser or microwave source or, e.g., via UV-radiation emitted from the plasma itself [7].

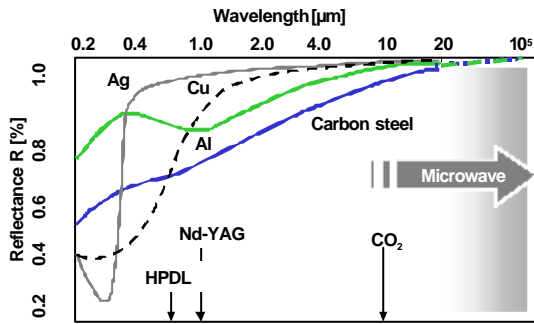


Figure 2. Reflectance of different metals towards laser and microwave radiation at low temperature. HPDL: high power diode laser.

Metals are the major class of materials processed by lasers, although the reflectance is high and it decreases only for lasers with a wavelength < 5 μm . It is the extremely high power density and short interaction time, which governs the majority of laser applications in materials processing, combined with indirect heating [6,7]. Compared with μm -wave length, mm- and cm-wavelength radiation offers higher penetration not only for metals but for semiconductors and insulators as well, as

shown schematically in Figure 3 for one frequency only, 2.45 GHz [9].

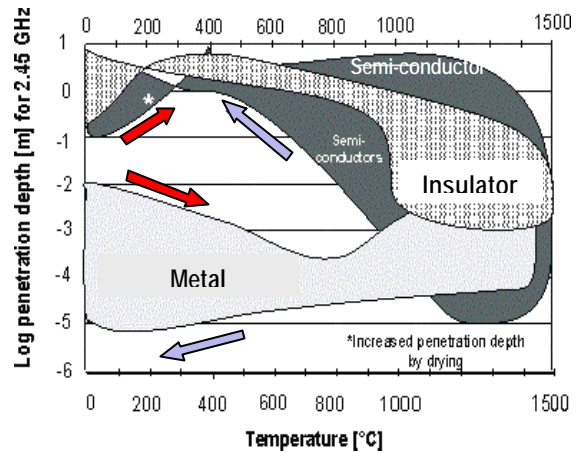


Figure 3. Hysteresis of penetration depth upon microwave processing (full arrows indicate heating, empty arrow cooling) of different classes of materials, after [9].

However, the majority of the early work on microwave processing of materials was devoted to dielectric ceramics [9-12]. Only recently broader recognition has grown, that semiconducting and metallic materials can be processed by microwave radiation as well [13-16]. As shown in Figure 4, the choice of wavelength – laser or microwave - should be based on more parameters, than the penetration depth only. Rapid Prototyping techniques on one hand and high throughput production of sintered parts offer a good example for the advantage and disadvantage of laser versus microwave processing and vice versa. Selective Laser Sintering, SLS and numerous variants, e.g., Direct Laser Forming, DLF [17] will find applications as well as microwave sintering of ceramics, cemented carbides and metals and microwave melting and casting [13,15,18].

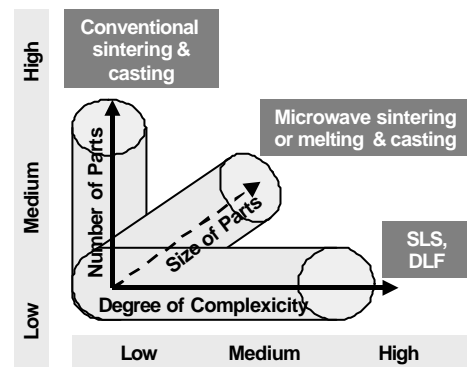


Figure 4. Process selection chart for EMMP

IV. PROCESS DEVELOPMENT BASED ON INDIRECT HIGH FREQUENCY ENERGY DEPOSITION

In bulk solids only few parameters govern the penetration depth δ of monochromatic, high frequency electromagnetic

radiation into a material: the complex conductivity σ^* , the magnetic susceptibility μ_r as material properties, and the frequency f of the externally applied radiation. The well defined penetration depth of high frequency electromagnetic radiation into a metal or semiconductor is a pre-requisite for the controlled energy deposition in a surface near area, leading to fast melting and evaporation of the material. Fast melting or evaporation occurs because heat generation by dissipation of the mm- and μ m-wave radiation exceeds significantly the capability of the material to transport heat into the remaining volume by conduction or convection. In addition, a very high power density exists also in the surface near gas phase, due to reflection of the radiation from the material. As a consequence, ionisation and plasma ignition might occur as secondary effect.

As soon as a plasma, which absorbs the electromagnetic energy, is formed, it screens the processed material off from the laser or microwave radiation. Depending upon the electron and ion temperature, UV-radiation might be emitted from the plasma and re-absorbed by the material. Particularly upon laser processing of metals high energy photons might be generated, which contribute to heating, evaporation and further ionisation of the material. The absorption coefficient of the electron gas in metals is much higher for UV-radiation than for IR-radiation. Metal heating can therefore become very efficient due to the secondary effect of plasma generation [19].

There are some subtle differences with respect to secondary effects, when laser and microwave processing of materials is compared. Upon microwave processing the strong dependence of dielectric properties on temperature might become a dominating effect. As shown in Figure 3, a “hysteresis” of penetration depth of the microwave radiation has to be taken into account, when heating of a material occurs by microwave absorption. Therefore, although at low temperature dissipation of microwaves might occur in the volume of the material, upon temperature increase the depth of penetration can be significantly reduced and the power density per volume therefore strongly increased, leading to plasma formation. In case of metals, efficient heating might still go on, e.g., due to UV-emission from plasma, not due to the “screened off” microwave radiation. For other materials the electronic conductivity as well as ionic conductivity can dominate the process at such “combined” millimeter and micrometer wave exposure.

Direct energy dissipation from the microwave radiation into the material depends only on the local electric field strength, E_{local} , as shown in Eq. (1), and on the electric (conductivity σ)/dielectric (complex dielectric constant ϵ) properties of the material processed.

$$P_{abs} = \text{Re}(\sigma^*) \cdot E_{local}^2 = (\sigma + i\omega \epsilon_0 \epsilon''_r) \cdot E_{local}^2 \quad (1)$$

$$E_{eff} = E_0 / \sqrt{1 + \frac{\omega^2}{v_{eff}^2}} \quad \gamma = \left[\frac{E_{eff}}{n_0} \right] \geq \gamma_{critical} \quad (2)$$

If the effective electrical field strength, E_{eff} depending upon the frequency ω of the electromagnetic radiation and the collision frequency of electrons, v_{eff} exceeds a threshold value γ , governed by the concentration of neutral species n_0 , than

dielectric break down of the gas atmosphere occurs, as shown in Eq. (2). The only material property, which contributes to this process is the vapor pressure of easy ionisable atoms or molecules, escaping from the processed material.

The role of the temperature dependence of loss behavior is usually defined for an “ideally isotropic and monolithic” material. When local electrical field strength and evaporation due to heating is taken into account, then the real structure of the materials plays an important role in high frequency electromagnetic processing of materials. Upon microwave sintering of metals and in high temperature processing of ceramics (~2000°C) the numerous interfaces are contributing to energy deposition by different heating mechanisms, including plasma discharge, corresponding with a whole range of different electrical conductivity values. The role of plasma upon microwave processing of materials is described in detail in [20]. An industrially interesting example of “combined processing” are functionally graded cutting tools, where coating or surface treatment is intentionally combined with sintering by a controlled combination of direct microwave heating with a superimposed microwave plasma treatment.

V. NEW PROCESSES USING COMBINED DIRECT AND INDIRECT HEATING BY HIGH FREQUENCY RADIATION

The contribution of additional mm- and μ m-waves (generated by the interaction of the processed material with the “monochromatic” laser or microwave radiation as a “secondary” effect) to ignition of plasma and to its sustained presence is not understood in detail yet for such processes like e.g., Selective Laser Sintering, SLS [21,22] and Laser Assisted Microwave Processing, LAMP [23-25]. Such processes work at ambient pressure, in many different reactive or inert atmospheres.

From laboratory scale experiments some empirical findings are available. For SLS an empirical formula for a plasma formation threshold, I_{plasma} , upon laser processing is given by Eq. (3), utilising the pulse duration τ , the pulse repetition rate ν and the average pulse power P_0 as a measure for the peak power (valid for 0.248 – 10.6 μ m and pulse duration from 10 ns to 1 ms [22]).

$$I_{Plasma} = 4 \times \frac{10^4}{\sqrt{\tau}} \quad \nu_{Plasma} = \frac{P_0}{\tau_P \cdot \pi \cdot r_B^2} \cdot \frac{1}{I_{Plasma}} \quad (3)$$

Such a plasma might be destructive because of the recoil pressure generated as the plasma escapes from the surface. With respect to low surface roughness and stress free surface layers therefore processes like LAMP could become attractive. With respect to the pressure exerted at the solid surface a comparison could be drawn between “pure” laser (Nd:YAG) processing and LAMP, utilizing a Nd-YAG-Laser for surface preheating and a 2.45 GHz, 1 atm Ar-plasma for coating a oxide ceramic surface of composition A with another ceramic of composition B [23]. As can be seen from Table 3, the “ignition” temperature T_{crit} depends clearly on a certain concentration of ionisable atoms in the gas layer above the ceramic surface. From model experiments on different oxides a simple relation between material and process parameters has been developed, which allows the prediction of a critical

surface temperature as a threshold for the ignition of a surface plasma, as shown in Table 3. The important feature is the metal concentration of the vapor phase, which is sufficient to reduce the break down strength of the surface-near gas phase. Experimental evidence was found, that a partial pressure of 10^{-8} bar metal atoms is needed.

TABLE III. PARTIAL PRESSURE OF DIFFERENT METALS IN NEUTRAL AND OXIDIZING ATMOSPHERE.

Metal	neutral	at 0,2 bar O ₂	T _{crit} [°C]
	p(Me) [bar]	p(Me) [bar]	
Ni (NiO)	$3,15 \cdot 10^{-8}$	$8,82 \cdot 10^{-12}$	1200
Zn (ZnO)	$4,48 \cdot 10^{-8}$	$1,50 \cdot 10^{-11}$	850
Mg (MgO)	$3,25 \cdot 10^{-8}$	$9,28 \cdot 10^{-12}$	1450
Sn (SnO ₂)*	$4,58 \cdot 10^{-8}$	$1,05 \cdot 10^{-14}$	1210

After plasma ignition, microwave power is increased to a level which sustains the plasma and the focussed laser beam is used to guide the surface attached plasma ball over the surface [23,24]. The ion pressure p_{ion} of the near surface gas discharge is calculated according to Eq. (4) [26].

$$p_{ion} = 2m_{ion} n_{ion} v_2 \quad (4)$$

m , mass of the ion; n , ion density; v ion velocity (calc. from temperature)

A value of 0.003 – 0.009 Pa is obtained, in comparison to the equivalent photon pressure of a laser beam depositing a comparable amount of photons to account for the energy absorbed by the solid. The “laser only” processing would exert a 10x higher photon pressure of 0.060 Pa. In order to achieve high surface quality, LAMP could therefore be superior over pure laser processing. Furthermore, the electric efficiency of a 2.45 GHz microwave source is much higher than for an Nd-YAG laser (p_{max} 90 W). Combined laser and microwave heating was used for the formation of an eutectic ZrO₂-NiO ceramic, utilized as anode material in solid oxide fuel cells [25]. Radiant heating is not sufficient to develop locally an eutectic melt – temperatures exceeding 1800 °C at high Q-activity are needed and, in addition, extensive mass and charge transport. Upon conventional heating no eutectic microstructure formation was observed.

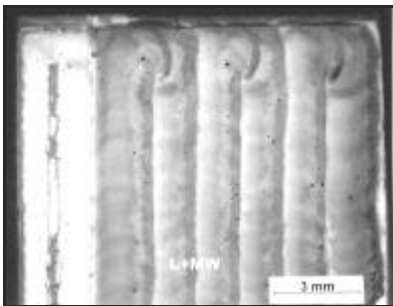


Figure 5. Glazed (Silicate containing melt) plasma sprayed thermal barrier coating layer; left – microwave only; right LAMP.

An optical microscope picture of a LAMP-glazed plasma sprayed thermal barrier coating is shown in Figure 5.

For processing of finely divided materials, like fibres or particles, laser application is not efficient. Opposite to this, microwave radiation combined with a microwave plasma can easily be used for coating or surface etching of particles or short fibers in a fluidised bed reactor. AlN-coated carbon fibers are shown in Figure 6. The dual stage Plasma-CVD-reactor, described in [27] for TiN-coating of carbon fibres and re-distribution of Co-metal in WC-Co-granules was used. Without circulating the fluidised fibres, homogeneous thick AlN-coating from AlR₃ in Ar/H₂ was obtained at atmospheric pressure [28].

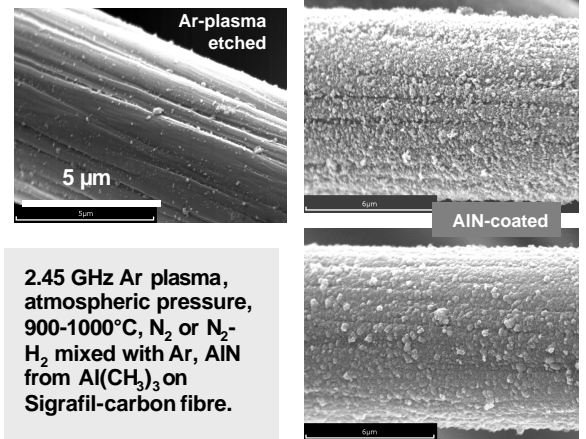


Figure 6. Plasma enhanced coating of microwave (2.45 GHz) heated carbon fibres in a Dual Stage Fluidized Bed Reactor

VI. CONCLUSION

The potential of high frequency electromagnetic radiation with cm-, mm- and µm-wavelength for further development of different efficient industrial material processing technologies is very high, based on the numerous up- and down-conversion paths for such radiation upon interaction with different classes of materials. The defined penetration depth of laser and microwave radiation into metals, ceramics, polymers and composites enables the control of the thermal field inside the material, over a large range of dimensions, from bulk down to surface treatment and individual particle coating. Indirect energy transfer, mainly connected with atmospheric plasma, can be applied concomitantly with direct heating. Based on the high power density of “monochromatic” radiation sources, simultaneous application of few distinguished wave lengths together with polychromatic radiation could contribute to significant reduction of energy consumption for materials processing and improved product quality.

LAMP: the combined application of laser heating for reduction of the break down voltage close to the surface of a material heated by microwaves is an example of utilizing a “secondary microwave effect” for controlled microwave plasma surface treatment at ambient pressure. Without the laser assistance, scanning of a cavity microwave plasma over the surface of a material is impossible. As compared to “pure laser” or to other microwave plasma devices, like e.g., plasma

torches a unique combination of low photon and almost no gas impact of the surface is achieved by means of LAMP.

DZ-FBR: For smooth and simple particle and fiber coating operations, a Dual Zone Fluidized Bed Reactor, which utilizes direct microwave heating and microwave plasma assisted CVD has been developed.

For further progress in the area of EMMP, a thorough analysis of "processing maps" could be helpful, as already existing in laser processing, e.g., for high-power diode laser material processing or laser welding [19,29].

ACKNOWLEDGMENT

Financial support of the Bavarian Ministry for Science, Research and Arts, through the program "New materials", X/1-27/52c(16)-10b/25428 is gratefully acknowledged.

REFERENCES

- [1] Von Hippel, A., "Dielectric Materials and Applications"; "Dielectrics and Waves", both MIT, Cambridge, Maryland, 1954
- [2] Davies, E.J., Conduction and Induction Heating, Peter Peregrinus, (IEE), Stevanage, 1990.
- [3] Metaxas, A.C., "Foundations of electroheat: a unified approach", John Wiley & Sons Ltd, 1996
- [4] Mühlbauer, A., (Ed.), Industrielle Elektrowärmetechnik, Vulkan-Verlag, Essen, 1992
- [5] <http://www.sciencedirect.com>, February 28th, 2006.
- [6] Crafer, R.C. and Oakley, P.J. (Eds.), Laser Processing in manufacturing, Capman and Hall, London, 1993.
- [7] J.C. Miller, R.F. Haglund (Eds.), Laser Ablation: mechanisms and Applications, Springer-Verlag Berlin Heidelberg New York, 1991.
- [8] Detailed technical papers in "Advances in Microwave and Radio Frequency Processing", M. Willert-Porada (Ed.), Springer-Verlag Berlin Heidelberg New York 2006, ISBN-13 978-3-540-43252-4
- [9] Willert-Porada, M., W. Bartusch, G. Dhupia, G. Müller, A. Nagel, G. Wötting, Material and Technology Development for Microwave Sintering of High Performance Ceramics, in "Ceramics-Processing, Reliability, Tribology and Wear", Ed. G. Müller, Wiley-VCH, p. 87-93 Euromat Vol. 12 (2000)
- [10] Wroe, F.C.R., Rowley, A.T., (1995), Microwave enhanced sintering of ceramics, in Ceram. Trans. 59, 69-76
- [11] Müller, H., Mehringer, R., (1999) Microwave processing of ceramics at 28 GHz frequency, cfi, Berichte der Deutschen Keramischen Gesellschaft, 1999
- [12] Gerdes, T., M. Willert-Porada, (1999), Technology Development for Microwave Sintering of Silicon Nitride Components in a Hot-Wall Applicator, 9th Cimtec World Ceramic Congress, Ceramics: Getting into 2000's - Part C, Ed. P. Vincenzini, Techna Srl, 1999, 379-388, and lit. cited there
- [13] Sato M., S. Takayama, T. Ochiai, A. Kagohashi, (2003), Development of microwave kilns for industries in Japan, 9th International Conference on Microwave and High Frequency Heating, Loughborough, September 2003
- [14] Kolaska, Rödiger, Willert-Porada, Gerdes, „Verbundwerkstoff und Verfahren zu seiner Herstellung (Mikrowellensintern)“, Ger. Pat. Appl. P 43 40 652.1, (1993), DE 43 40 652 A1, PCT/DE95/00548
- [15] M. Willert-Porada, T.Gerdes, H. Kolaska, K. Rödiger, Einsatz von Mikrowellen zum Sintern pulvermetallurgischer Produkte, Pulvermetallurgie in Wissenschaft und Praxis, Bd. 11, Hrsg. H. Kolaska, DGM Informationsges. mbH (1995), S. 177-210.
- [16] R. Roy, DK. Agrawal, S. Gedevarishvili, J. Cheng, Full sintering of powdered-metal bodies in a microwave field, Nature, Vol. 399, S. 668-670 (1999)
- [17] Simchi, A., Pohl, H., Effects of laser sintering processing parameters on the microstructure and densification of iron powder, mater. Eng. A359, 119-128 (2003).
- [18] Ripley, E.B., Eggelston, P.A., White, T.L. Direct microwave coupling to metals at elevated temperatures, Proceedings of the 3rd World Congress on Microwave and Radio Frequency Processing, Sydney, Australia, Folz, D.C., Booske, J.H., Clark, D.E. and Gerling, J.F., (Eds.), p. 241-246 (2002).
- [19] Li, Lin, The advances and characteristics of high-power diode laser materials processing, (2000), Optics and Lasers in Engineering, Vol. 34, 231-253
- [20] T. Gerdes, R. Tap, M. Willert-Porada, The role of plasma upon microwave sintering processes, Novel materials Processing (MAPEES'04), S. Miyake (Ed.), Elsevier Ltd., Trans. Tech. Publ., p. 139-142 (2005).
- [21] Fischer, P., Karapatis, N., A model for the interaction of near infrared pulses with metal powders in selective laser sintering, Appl. Phys., 2002, A74, 467-74
- [22] Fischer, P., Romano, V., Weber, H.P., Karapatis, N.P., Boillat, E., and Glardon, R., Sintering of commercially pure titanium powder with a Nd:YAG laser source, Acta Materialica, 51, 1651-1662 (2003)
- [23] Gerk, Ch., M. Willert-Porada, Laser assisted microwave processing as a new tool in ceramic processing, Ceram. Trans., Vol. 111, 451-458 (2001); Gerk, C., M. Willert-Porada, DE 199 51 143 A1 (1999) Offenlegungsschrift 2001
- [24] Gerk, C., (2001), Herstellung keramischer Eutektika durch simultanen Laser- und Mikrowelleneinsatz, VDI Fortschritt-Berichte Reihe 5 Nr. 619
- [25] Gerk, Ch. Willert-Porada, M., New Composite Ceramic Powders for SOFC Anodes from a Eutectic Ceramic Melt Process, Proc. of the 10th Intl. IUPAC Conference, High Temperature Materials Chemistry (2000)
- [26] Schmoll, R., (1995), Plasma-Wand Wechselwirkung strukturierter Materie, PhD Thesis, Ruhr Universität Bochum, 1995.
- [27] R. Tap, M. Willert-Porada, Dual Zone PE-CVD Circulating Fluidized Bed Reactor, IEEE Transactions on Plasma Science, IEEE Transactions on Plasma Science, Vol. 32 [5], 2085-2092 (2004)
- [28] Z. Pajkic, unpublished results 2006.
- [29] Bayraktar, E., Kaplan, D., Parametric approach model for determining welding conditions: New type of welding limit diagrams (WLD), J. Mater. Proc. Technol., 170 477-486 (2005).

RF MEMS market

Jérémie Bouchaud¹, Bernardo Knoblich², Henning Wicht³

¹Wicht Technologie Consulting, Frauenplatz 5, 80331 Munich, Germany, +49 89 2070260 20, jeremie.bouchaud@wtc-consult.de

²Wicht Technologie Consulting, Frauenplatz 5, 80331 Munich, Germany, +49 89 2070260 40, bernardo.knoblich@wtc-consult.de

³Wicht Technologie Consulting, Frauenplatz 5, 80331 Munich, Germany, +49 89 2070260 10, henning.wicht@wtc-consult.de

Short Abstract— RF MEMS components first appeared in 2002 in the form of Bulk Acoustic Wave (BAW) resonators for mobile phone applications. In the meantime, other RF MEMS products have become commercially available, including switches, inductors and micro-mechanical resonators. Although currently, the RF MEMS market is limited, RF MEMS components are expected to satisfy future requirements for telecommunications systems in terms of improved performance, ease of reconfiguration and miniaturisation. This paper presents the status of the RF MEMS industry, an overview of applications and the markets for the 2004–2009 time periods.

Keywords—component; Switches, tunable filters, bulk acoustic wave devices, cavity resonator filters, timing circuits

I. INTRODUCTION

Radio Frequency (RF) systems for telecommunications will offer one of the next major opportunities for Microsystems Technologies. Although currently, the RF MEMS market is limited, RF MEMS components are expected to satisfy future requirements for telecommunications systems in terms of improved performance, ease of reconfiguration and miniaturisation. In essence, the market for RF applications is expected to be the next major breakthrough for MEMS technology, following the earlier successes of Inkjet Heads, DLP chips from Texas Instruments, Pressure and Inertial sensors.

Examples of devices are micro-switches, tunable capacitors, micro-machined inductors, micro-machined antennas, micro-transmission lines and resonators including micro-mechanical resonators, BAW (Bulk Acoustic Wave) resonators and cavity resonators.

In addition to their potential for integration and miniaturization, RF MEMS offer lower power consumption, lower losses, higher linearity, and higher Q factors than conventional communications components. RF MEMS also enable new architectures for the next generations of telecommunication systems, easily and rapidly reconfigurable and operating over a wide frequency range. WTC has investigated the status of the industry and the potential for 6 types of RF MEMS components in 10 potential applications from cell phones to military applications [1]. The objective of this study was to identify their advantages and drawbacks including implementation prospects, given performance, reliability, supply and price issues, as well as highlight technical and other significant aspects.

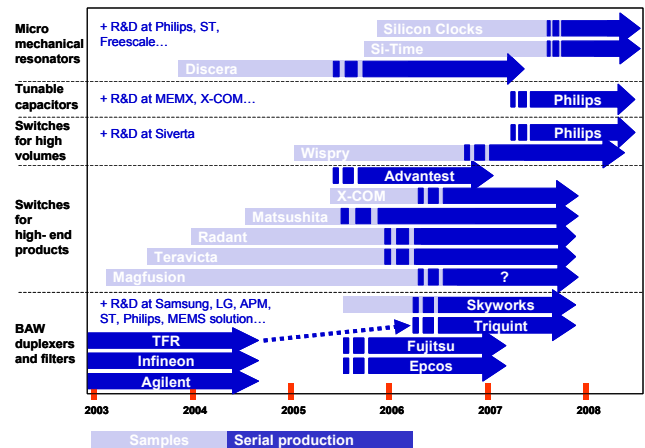


Figure 1. Commercialisation status of RF MEMS products

II. THE COMMERCIAL STATUS OF RF MEMS IN 2005

The commercial status of RF MEMS is featured in Figure 1.

Bulk Acoustic Wave (BAW) devices, including FBARs and SMRs, are currently the most mature components and represent the major part of the RF MEMS market today. Serial production has started in 2002. Agilent dominates the market followed by Infineon. As of end 2005, several other companies are close to commercializing BAWs, including EPCOS and Fujitsu. It is worth noting two RFIC companies, Skyworks and Triquint, who recently acquired the BAW technology from Agere and TFR, respectively.

MEMS switches attracted the most attention among RF MEMS products. However, even after considerable efforts of academic and industrial research over the last decade, only a handful of companies have started or are close to commercialising MEMS switches. The "hype curve of new technologies" can be perfectly fitted to the RF MEMS switch technology curve shown in Figure 2. Switches reached their peak visibility - also called the "Peak of inflated expectations" - in 2003, when the first samples were announced. The impossibility of processing the demands for samples and some confusion concerning announced specifications, frustrated potential users, as a result MEMS switches entered the phase called "Trough of Disillusionment". As of End 2005, MEMS switches emerged shining into the "Slope of Enlightenment", an indicator that the

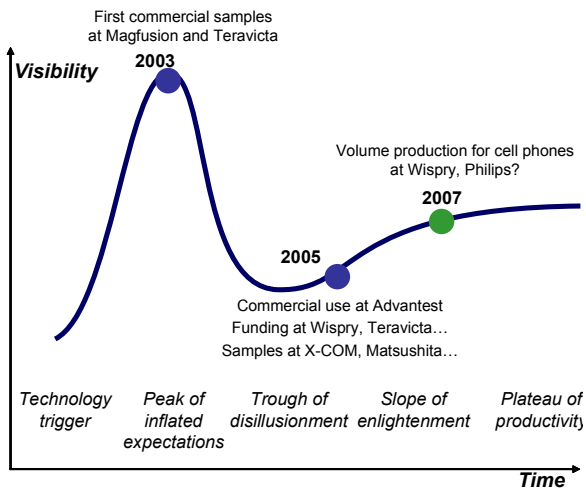


Figure 2. The RF MEMS switch hype curve

industry and technology is maturing. The last level, "the so-called Plateau of Productivity", is expected to be conquered after 2007, by which time several companies will have reached serial production.

Tunable capacitors are technologically close to switches, however have not received the same level of attention and few companies are working on commercialisation. Nevertheless, in the second quarter of 2005 it had entered the "industrialisation phase" for cell phone applications. Serial production should commence in 2007 or 2008.

Recent progress on micro-mechanical resonators has been significant and specifically involves temperature stability and packaging. Samples have been provided in 2004, expected to enter the serial production by the summer 2005. Micro-mechanical resonators are very promising as a replacement for conventional off-chip quartz reference oscillators. However, the technology is new and it is not yet clear whether micro-mechanical resonators will deploy as rapidly as BAW or if this device will first enter a "Trough of Disillusionment", as switches did.

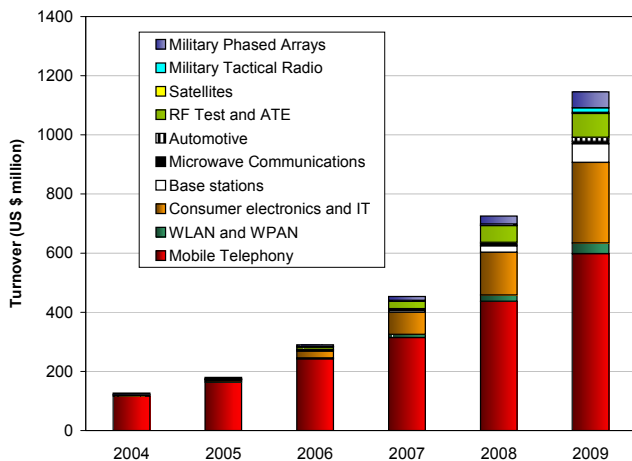


Figure 3. Total turnover forecasts for the RF MEMS market by applications, 2004-2009

III. RF MEMS MARKET POTENTIAL THROUGH 2009

The market for RF MEMS components was US\$ 126 million in 2004, confirming the WTC forecast from 2002. It is expected to grow rapidly in the next few years to over US\$ 1.1 billion in 2009. In addition, the market will accelerate quickly in the period 2007 through 2009 as full-scale production starts for the majority of RF MEMS components. The turnover forecasts for the RF MEMS market by application are shown in Figure 4.

The major part of the market in 2004 was for BAW devices, which include duplexers and filters for mobile phones. This product amounted to US\$ 116 million. In 2009, mobile telephony BAWs will continue to dominate and will constitute around US\$ 470 million or 40% of the total market.

MEMS switches and micro-mechanical resonators will also offer interesting opportunities in both volume and high-end markets as issues with reliability, packaging and CMOS integration are solved. The main development effort is no longer on the RF MEMS component side but now requires designers to develop novel architectures that fully leverage the potential of RF MEMS.

Also worthy of mention is that micro-mechanical resonators start to replace bulky off-chip quartz oscillators used as timing devices in consumer electronics and IT peripherals. These MEMS resonator-based clock devices will account for more than 20% of the RF MEMS market in 2009. Switches are expected to penetrate cell phone applications from 2007 onwards, mainly for band and mode switching functions. Other lucrative markets for switches include Automated Test Equipment and RF Test, an opportunity that will total US\$ 80 million, while defence applications for switches are expected to exceed US\$ 70 million in 2009.

IV. CONCLUSION

In conclusion, RF MEMS is taking its rightful place as one of the emerging MEMS products with the highest potential. Along with established markets for inkjet heads, Digital Micro Mirrors and pressure sensors, RF MEMS technology represents one of the few MEMS markets that will exceed the US\$ billion mark. After mobile phones, great opportunities exist for spin-off applications in consumer and IT sectors. Outside of mass markets, RF Instrumentation and Automated Test Equipment as well as military applications offer the best prospects, especially for MEMS switches. The next biggest opportunities for components - after bulk acoustic wave duplexers and filters - belong to switches and micro mechanical resonators.

REFERENCES

- [1] J. Bouchaud, "RF MEMS Market II 2005-2009, analysis, forecasts and Technology Review", October 2005.
- [2] A. Ghahary. Fully integrated dc-dc converters. Power Electronics Technology, pages 24-27, August 2004.
- [3] R. Jones and M. Chapman. Rf mems in mobile phones. RFDESIGN, pages 20-26, September 2005.
- [4] N. Hoivik et Al. Rf mems switches using copper-based cmos interconnect manufacturing technology. Solid-State Sensor, Actuator and Microsystems, June 2004.

Tunable Transmission Lines on Silicon Based upon Periodic Photonic Bandgap Structures

Samir El Rai¹, Ralf Tempel¹, and Dieter Jäger²

¹ATMEL Duisburg GmbH, Bismarckstr. 120, 47057 Duisburg, Germany

²Universität Duisburg-Essen, Zentrum für Halbleitertechnik und Optoelektronik (ZHO), Lotharstr. 55, 47057 Duisburg, Germany

Abstract—Differential transmission lines (DTL) can be synthesized as a chain of identical 2-Port unit cells UC. These DTL are interesting to use for either matching circuits or realizing small resonators serving in filters or oscillators. In this paper, we introduce new DTLs – by using the proposed cell structure – with characteristic impedances beyond that of classical TLs and, even more important, longer electrical length at much smaller size. Moreover the electrical length can be tuned by means of varactors. These results, for the first time, provides a real alternative for DTL applications in MMIC design below 10GHz.

Index Terms—Differential transmission lines, Periodic structures, Photonic bandgap structures, Silicon.

I. INTRODUCTION

In standard silicon Microwave Monolithic Integrated Circuits (MMICs) differential transmission lines (DTLs) are commonly used for transferring symmetrical signals from one position to another. The functionality of DTLs is based upon transmission lines (TLs) in ODD-mode. Moreover, small-sized lines are foreseen to be of high interest for resonant circuit applications like in filters and oscillators.

This paper describes for first time how to design DTLs in MMICs by acceptable area consumption. The proposed DTLs show much higher area efficiency than standard ones due to using higher specific inductances (by spirals) and higher specific capacitances (by MIMs). Also it will be shown that DTLs can exhibit very high impedance in connection with low insertion losses even on standard silicon substrates. Last but not least it will be shown that impedance and electrical length of the proposed structures can be changed very easily in a wide range by tuning the spirals and / or MIMs or varactors.

II. TRANSMISSION LINES

The electrical length of relevant DTLs is in-between $\lambda/8$ and 2λ . But the dimensions of classical DTLs exceed available space on MMICs in microwave applications. Furthermore they show high insertion loss even at higher characteristic impedance. Fig 1a depicts symbol while 1b shows equivalent circuit diagram of short DTL.

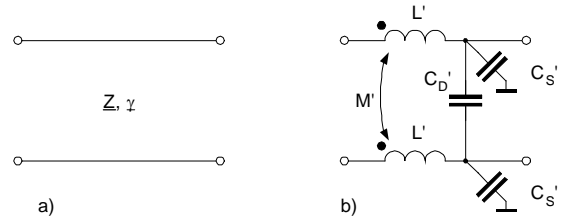


Figure 1. a) General TL symbol, b) Equivalent circuit diagram of a electrical short DTL.

III. PERIODIC STRUCTURE

Now lets try to decrease the size of classical TLs toward a size, which permits an application in MMIC design. Papers about PBG structures have been published in the literature for some years. A good overview – named here: left-handed metamaterials – can be found in [1]. Many applications have been described during the last five years; most of the recently presented PBG structures use combinations of lumped-element inductors and capacitors on one-dimensional (1-D) or two-dimensional (2-D) high-pass TL configurations [2-4].

But up to now there wasn't any description that introduced PBG structures onto Silicon. In that paper PBG structures on Silicon have been investigated to shrink classical TL in size and to extend its limited characteristic impedance.

But how to scale down a TL? Z_{TL} remains constant while γ will increase when both L' and C' increasing by the same factor according to (1) and (2). This can be done by using elements with high specific inductance (spirals) / capacitance (MIMs). The elements L' , C' , and M' of standard lines in the equivalent circuit diagram can be replaced by lumped elements L , C , and M now with relatively good approximation. Theoretically it's equivalent to an improvement of effective relative permittivity ($\epsilon_{r,eff}$) and effective magnetic permeability ($\mu_{r,eff}$). The resulting TL still demonstrates classical homogeneous behavior in a wide frequency range.

By active usage of magnetic coupling between line sections laying face-to-face the characteristic impedance can be increased above values that can't be achieved with classical line shapes. At the same time higher die size efficiency has been achieved too. More than that die size efficiency can be increased additionally by applying MIM capacitors or diodes to that TLs. Choosing suitable L and C values the TL char-

acteristics can be optimized and / or matched to certain impedances.

The DTL impedance can be described as

$$\underline{Z}_{DD} = \sqrt{\frac{2 * L - M}{C_s/2 + C_D}} \quad (1)$$

$$\underline{\gamma}_{DD} = \omega \sqrt{(2 * L - M) * (C_s/2 + C_D)} \quad (2)$$

Keep in mind for later discussion that the differential capacitance C_D has significant influence in opposite to C_s , the parasitic capacitance to substrate, on characteristic impedance and propagation constant. Also creating a negative mutual coupling factor will increase inductivity.

Moreover connecting several identical or similar TL sections (cells) together results in a new TL, which will be named periodic structure (PS) now. Differently to a classical TL the new PS consists of an integer number of n multiplied by one unit cell (UC) element. That includes only discrete electrical TL length can be adjusted. Synthesizing a new TL electrical length of one cell has to be adjusted accurately. Fig. 2 illustrates that relationship. It should be pointed out here that this method supposes electromagnetic walls as terminations of each cell. Special care has been needed coupling different cells directly.

As long as electrical length of one considered cell remains short the continuous behavior of the PS will be described pretty well by concentrated elements of L and C . That results in their characteristic impedance \underline{Z}_{TL} and propagation constant $\underline{\gamma}$.

IV. PS DESIGN

In that chapter the electrical and geometrical characteristics of a cell will be discussed. The calculation of the differential 2-port S-parameter (part of mixed-mode S-parameter) from the single ended 4-port S-parameter have been shown in [8-9]. As results either of measurements or simulations S-parameter can be derived. In a first step the S-parameter matrix has been transformed into A- (or chain) parameter matrix:

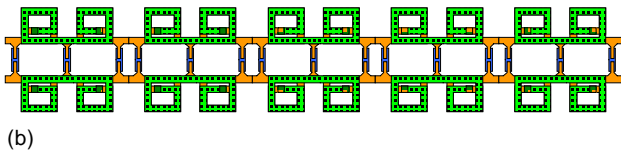
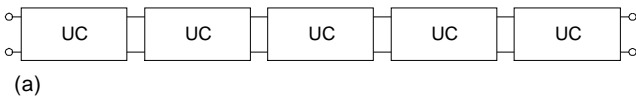


Figure 2. TL established by several series connected UC forming a PS: a) Schematic, b) Layout.

$$\begin{bmatrix} \underline{S}_{DD11} & \underline{S}_{DD12} \\ \underline{S}_{DD21} & \underline{S}_{DD22} \end{bmatrix} \Rightarrow \begin{bmatrix} \underline{A}_{DD11} & \underline{A}_{DD12} \\ \underline{A}_{DD21} & \underline{A}_{DD22} \end{bmatrix} \quad (3)$$

$$\begin{bmatrix} \underline{A}_{DD11} & \underline{A}_{DD12} \\ \underline{A}_{DD21} & \underline{A}_{DD22} \end{bmatrix} = \begin{bmatrix} \cosh(\underline{\gamma}_{UC}) & \underline{Z}_{UC} * \sinh(\underline{\gamma}_{UC}) \\ \frac{1}{\underline{Z}_{UC}} * \sinh(\underline{\gamma}_{UC}) & \cosh(\underline{\gamma}_{UC}) \end{bmatrix} \quad (4)$$

with: $\underline{\gamma} * 1 \Rightarrow \underline{\gamma}_{UC}$ (5)

That results in the characteristic impedance \underline{Z}_{UC} and the propagation constant $\underline{\gamma}$. $\underline{\gamma} * 1$ describes the propagation characteristic of a classical TL. Because the length isn't as usable as characteristic line parameter in a cell anymore, $\underline{\gamma}_{UC}$ will be defined as propagation characteristic of a cell.

Characteristic impedance as well as propagation constant can be derived from A-Matrix:

$$\underline{Z}_{DD} = \sqrt{\frac{\underline{A}_{DD12}}{\underline{A}_{DD21}}} \quad (6)$$

$$\underline{\gamma}_{DD,UC} = \text{arccosh}(\underline{A}_{DD11}) \quad (7)$$

The cell (and so the PS) will be defined by means of characteristic impedance and electrical length. So a competition of new PS (based on UC) vs classical TL is possible by using the Quality (Q)-factor for cell now:

$$Q_{DD} = \frac{\text{Im}(\underline{\gamma}_{DD,UC})}{2 * \text{Re}(\underline{\gamma}_{DD,UC})} \quad (8)$$

The imaginary part of $\underline{\gamma}_{DD,UC}$ specifies the value of the electrical length or – in other words – how much phase shift can be achieved at a given frequency while the real part of $\underline{\gamma}_{UC}$ represents the loss of one cell.

V. SIMULATION & MANUFACTURE

Because of the complex interacting of both electric and magnetic fields the calculation of one cell is very extensively. Therefore a 3D-EM field simulator has been used - the EMPIRE simulator [5] bases on the powerful finite differences time domain method. Co-simulations have been carried out by means of HFSS [6].

For both simulation and manufacture ATMEL's advanced SiGe BiCMOS technology [7] has been used. In standard option it's a three-metal layer process with additional inductor layer based on a 19- Ω cm substrate.

VI. DESIGN & RESULTS

In this chapter several different cells will be discussed. As described before nearly arbitrary cases exist to combine L and C elements. Moreover TLs can be formed now with new characteristics, which couldn't be achieved with classical TLs. Fig. 3 depicts some cell examples. Fig. 3a shows the classical Cell. Fig. 3b depicts the series inductor shunted by a capacitor, which decreases the impedance at higher frequencies. Fig. 3c shows the opposite: the parallel capacitor is bridged by an inductor, which shorted the line at low frequencies; while Fig. 3d combines the characteristics of both figures 3b and 3c.

The following cell examples have been derived from 3a.

A. Cells with spirals

Inductors form the first cell mainly. To improve die size efficiency two metal layers have been used building stacked inductors. Fig. 4 depicts such structure, metallization have been achieved by M3 and M4. The size of one PS is $184\mu\text{m}$ by $145\mu\text{m}$. The structure has been established similar to a classical TL that means symmetrically along the propagation direction. Fig. 5 - 7 show simulation and measurement results (three dies) of the differential characteristic impedance $Z_{PS,DD}$, Phase, and Q-Factor. The real part of $Z_{PS,DD}$ is around 250Ω @ 10GHz. Q is increasing with frequency up to cut-off (not shown here); electrical length behaves linear vs. frequency. A free-space TL length exceeds the corresponding cell length by a factor of 3.

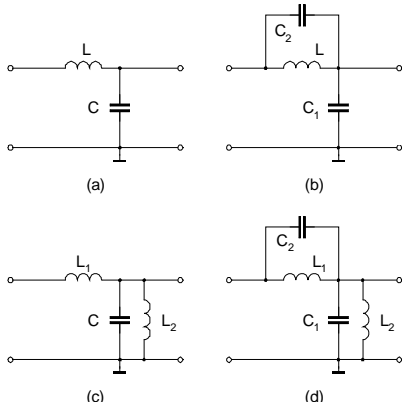


Figure 3. Examples for UC with new characteristics.

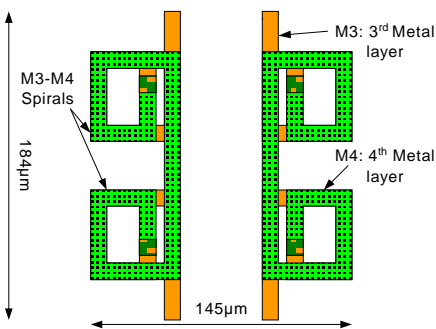


Figure 4. UC of PS 1 - Using stacked inductors consist of M3 and M4 metal layers.

B. Cells with spirals and MIMs

PS 2 has been build by adding MIMs as capacitive elements to the PS1. Fig. 8 illustrates that structure. The necessary characteristic impedance can be achieved by using a suitable capacitance value of used MIM or Diode. The differential characteristic impedance is 86Ω @ 10GHz while phase and Q-Factor are 42° and 5.5 respectively. A free-space TL length exceeds the corresponding cell length by a factor of 7.

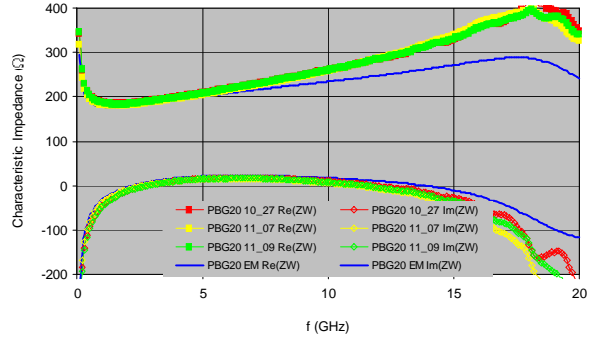


Figure 5. Characteristic impedance for PS 1 vs. frequency.

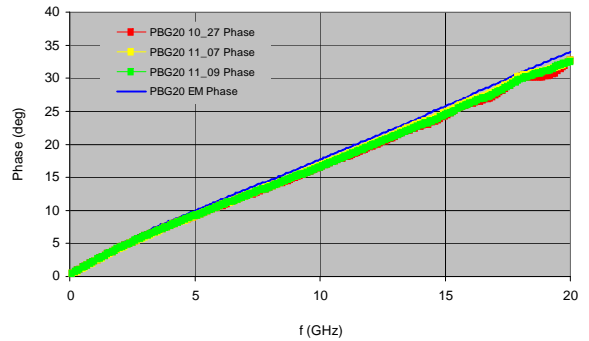


Figure 6. Phase for PS 1 vs. frequency.

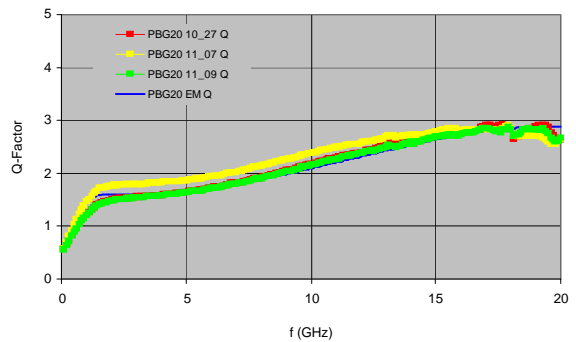


Figure 7. Q-factor for PS 1 vs. frequency.

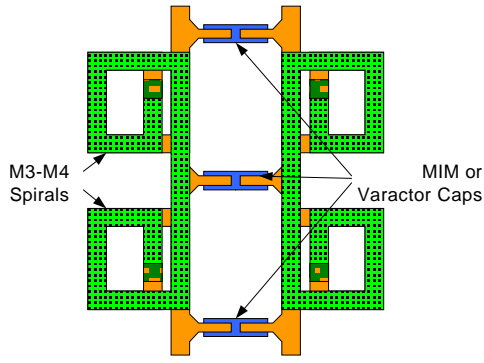


Figure 8. UC of PS 2 / 3 - Using inductors and MIM / Varactors capacitors for adjusting phase shift.

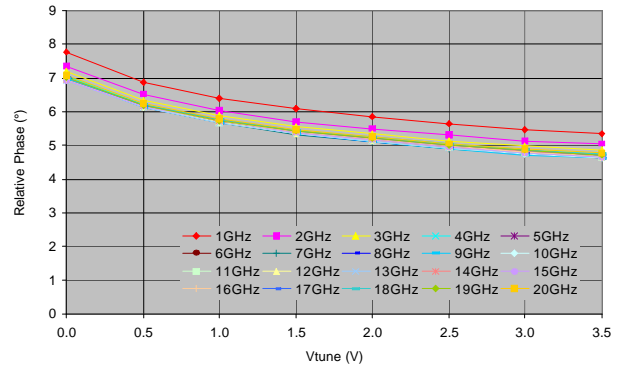


Figure 10. Q-factor for PS 3 vs. frequency.

C. Cells with spirals and varactors

Replacing the MIMs by diodes or varactors the characteristic impedance and / or phase shifting can be tuned now, simply by changing a DC voltage. This has been done in PS 3. The real part of the $Z_{PS,DD}$ is around 100Ω ; only slightly depending from adjusted tuning voltage.

Figure 9 depicts the relative phase shifting values per GHz for a UC. PS 3 can be adjusted by varactor voltage between 4.6 and 7.0° means 46° to 70° @ 10GHz respectively. The corresponding Q-Factor is between 4.5 and 5.1.

A free-space TL length exceeds the corresponding cell length by a factor in-between 7 and 12. The corresponding Q-Factor is between 4.5 and 5.1. A free-space TL length exceeds the corresponding cell length by a factor in-between 7 and 12.

While varactors can be used for continuous change of impedance, switched capacitors can be used for stepping the impedance in certain steps. Due to higher cap ratios the absolute impedance variation can be improved drastically.

VII. MEASUREMENTS

On-wafer measurements have been performed by means of 4-port Network Analyzer N5230A in conjunction with symmetrical RF coplanar probe tips in GSSG configuration.

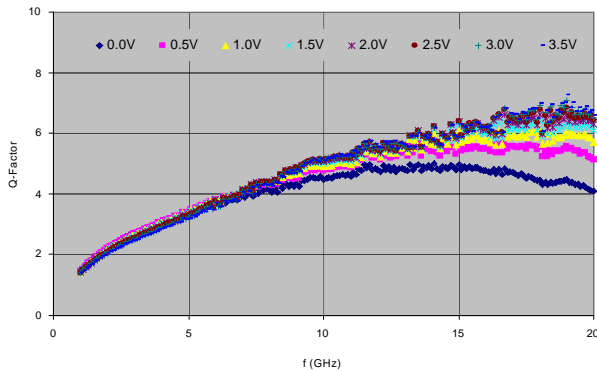


Figure 9. Relative (/ GHz) phase shift vs. tuning voltage for one UC of PS 3.

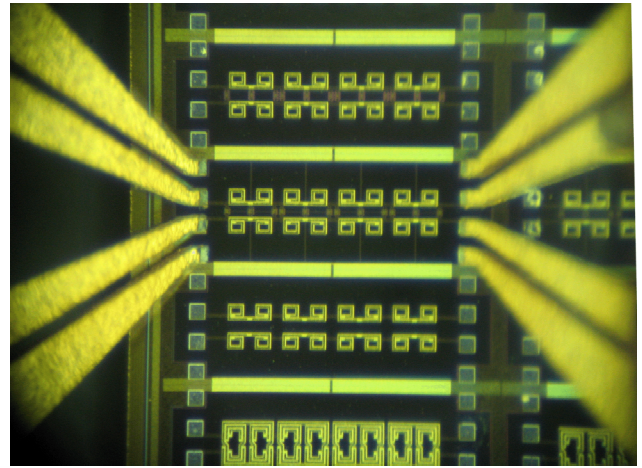


Figure 11. PS 3 connected to the two RF (left and right) probes.

Fig. 11 depicts the PS 3 DTL connected by two RF probes left, and right; the DC probe are above and not shown here.

Fig. 12 depicts the DTL PS 1-3. The DTLs exhibit a total length of four UC with dimension of $736\mu\text{m} \times 145\mu\text{m}$. The RF measurement pads possess an area of $50\mu\text{m} \times 50\mu\text{m}$ with $100\mu\text{m}$ pitch.

VIII. CONCLUSION

DTL can be synthesized by identical or different cells. These new DTLs can be used not only for matching one circuit to another; also small resonators can be established serving in filters or oscillators. These new PS – by using the proposed cells – allows characteristic impedances beyond that of classical TL and in addition at much smaller size. It is the first time that PS structures form a real alternative for applications in silicon MMIC design below 10GHz.

The measurement results – obtained by on-wafer measurements – fit very well to the simulation ones.

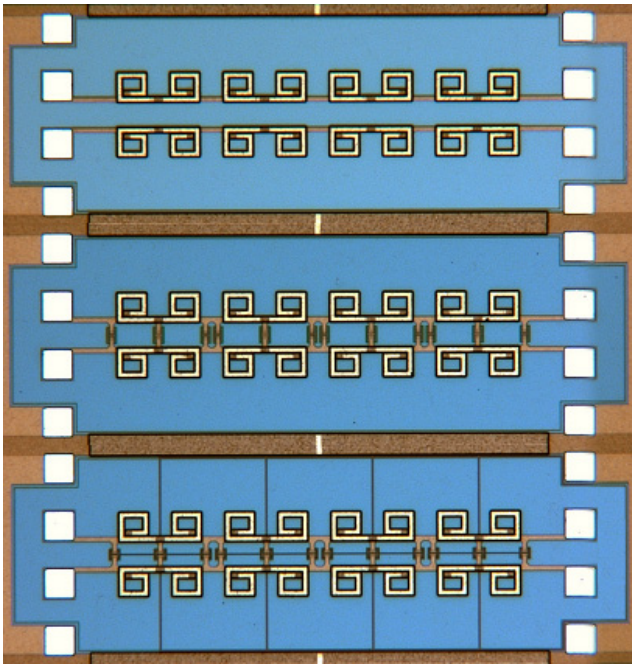


Figure 12. PBG DTL realized by inductors (top), by inductors and MIM capacitors (middle), and by Inductors and varactors (bottom).

REFERENCES

- [1] A. Lai, C. Caloz, and T. Itoh, "Composite Right / Left-Handed Transmission Line Metamaterials," *IEEE Microw. Magazine*, pp. 34-50, September 2004.
- [2] S.-G. Mao, S.-L. Chen, and C.-W. Huang, "Effective Electromagnetic Parameters of Novel Distributed Left-Handed Microstrip Lines", *IEEE Trans. Microwave Theory Tech.*, vol. 53, no. 4, pp. 1515-1520, April 2005.
- [3] F. Falcone, F. Martin, J. Bonache, R. Marques, T. Lopetegui, and M. Sorolla, "Left-Handed Coplanar Waveguide Band Pass Filters Based on Bi-layer Split Ring Resonators", *IEEE Microw. and Wireless Components Letters.*, vol. 14, no. 1, pp. 10-12, Jan. 2004.
- [4] A. Sanada, C. Caloz, and T. Itoh, "Characteristics of the Composite Right/Left-Handed Transmission Lines", *IEEE Microw. and Wireless Components Letters.*, vol. 14, no. 2, pp. 68-70, February 2004.
- [5] 3D-FDTD Simulator EMPIRE version 4.1, IMST GmbH, Kamp-Lintfort, Germany, 2004.
- [6] 3D-FEM Simulator HFSS version 9.0, Ansoft Corp., Pittsburgh, USA.
- [7] AT46000 Rev 0.7 SiGe BiCMOS Technology, ATMEL Corp., Colorado Springs, CO, USA, 2004.
- [8] A. Ferrero and M. Pirola, "Generalized Mixed-Mode S-Parameters," *IEEE Transactions on MTT*, vol. 54, no. 1, pp. 458 – 463, Jan. 2006, Digital Object Identifier 10.1109/TMTT.2005.860497
- [9] H. Shi, W.T.Beyene, J. Feng,, B. Chia, and X. Yuan, "Properties of Mixed-Mode Parameters of Cascaded Balanced Networks and Their Applications in Modeling of Differential Interconnects," *IEEE Transactions on MTT*, vol. 54, no. 1, pp. 360 – 372, Jan. 2006, Digital Object Identifier 10.1109/TMTT.2005.861654

Spatial Time Domain Reflectometry for Monitoring Transient Soil Moisture Profiles – Applications of the Soil Moisture Group, Univ. of Karlsruhe

R. Becker^{1,2}, S. Schlaeger^{1,3}, C. Hübner^{1,4}, A. Scheuermann^{1,5}, W. Schädel^{1,6}

¹University of Karlsruhe, Soil Moisture Group, 76128 Karlsruhe, info@smg.uni-karlsruhe.de

²IMKO, Mikromodultechnik GmbH, Im Stöck 2, 76275 Ettlingen, r.becker@imko.de

³SCHLAEGER - mathematical solutions & engineering, Herrenstr. 13, 76133 Karlsruhe, info@stefan-schlaeger.de

⁴University of applied sciences, Department of electrical engineering, 68163 Mannheim, c.huebner@fh-mannheim.de

⁵University of Karlsruhe, Institute of rock mechanics and soil mechanics, 76128 Karlsruhe, alexander.scheuermann@ibf.uka.de

⁶University of Karlsruhe, Institute for water and river basin management, 76128 Karlsruhe, wolfram.schaedel@iwg.uka.de

Short Abstract— Monitoring of transient soil moisture profiles yields valuable insight into soil hydraulic processes. A recently developed reconstruction algorithm allows to derive water content profiles along extended moisture probes from Time Domain Reflectometry (TDR) signals in time domain. The algorithm is based on inverse modeling of parameter distributions along a numerical transmission-line. The method named Spatial TDR will be explained and practical applications presented, aiming at monitoring spatial and temporal evolution of soil moisture.

Time domain reflectometry, water content profile, inverse problem, spatial TDR

I. INTRODUCTION

The spatial distribution of soil moisture and its evolution in time is a valuable information for many investigations in hydrology, agriculture, and soil science. However the monitoring of a sufficient number of soil moisture profiles can be expensive, laborious, and invasive, especially if the profiles are determined point-wise by a large amount of single probes buried in soil. A recently developed reconstruction algorithm [1,2] allows to compute complete soil water content profiles along single moisture probes from time domain reflectometer (TDR) samples in a short time. This method leads to a reduction of probes accompanied by a higher spatial resolution of moisture profiles at the same time. The whole technology of soil moisture profile retrieval has been named Spatial TDR [3]. This method is being developed and applied by the Soil moisture Group (SMG), an interdisciplinary research group at the Univ. of Karlsruhe. In this article we first introduce the basic concept of STDR with emphasis on its algorithmic core and the initial probe calibration by way of a coated 3-rod-probe. Then we assess the theoretical accuracy of the yielded moisture profiles by means of electromagnetic (EM) field simulations of the TDR process. To check the method under field conditions we realized a laboratory experiment in order to compare the reconstructed water content profiles with results from oven drying method in a real soil [3]. Finally two examples of practical STDR applications are demonstrated, a

flood warning system [4] and a dike monitoring system [5], two ongoing research projects of the SMG.

II. METHODS

A. The Inverse Problem

A TDR instrument located at x_0 emits a voltage step pulse $V_I^{(m)}(t, x_0)$ via a feeding cable into a waveguide (moisture probe) buried in soil. When the propagating EM wave hits the junction between cable and probe it is generally split due to impedance discontinuity. Part is reflected and traveling back, part is transmitted into the waveguide, interacting with the surrounding soil. When the pulse reaches the probe end it is reflected again. Hence $V_I^{(m)}(t, x_0)$ (input, measured) excites the system under test (SUT) probe/soil which reacts with voltage waves whose superposition $V_O^{(m)}(t, x_0)$ (output, measured) is sampled by the TDR instrument. The elapsed time between first and second main reflection is the pulse travel time forth and back the moisture probe. This travel time can be transformed into average soil moisture by appropriate calibration functions and/or mixing rules. This is generally what common TDR signal evaluation does.

But the TDR signal contains more information. The reflectogram, especially the part between first and second main reflection at the probe's beginning and end is a finger print of the dielectric profile along the waveguide, which is mainly ruled by the water content. Unfortunately the moisture distribution cannot be calculated directly from the TDR signal but has to be estimated indirectly. The basic idea of STDR is to transform the sampled output signal $V_O^{(m)}(t, x_0)$ into the soil moisture profile $\theta(x)$ along the probe by means of inverse modeling. The essence of the approach is to simulate the propagation of the TDR signal along the waveguide in time domain by employing a numerical model (forward problem) based on the telegraph equation.

This simplified model assumes that the relevant properties of the transmission-line can be described by bulk electronic parts like resistors, inductors, and capacitors (Fig. 1). Among the conditions for this electronic circuit model to hold the most important are: wave modes other than the transversal-electromagnetic (TEM) mode may be neglected, and frequency dependence of transmission-line properties may be neglected. The first condition requires a well-behaving waveguide with little distortion on the signal propagation, the second is only met, if the losses in the SUT are not too large.

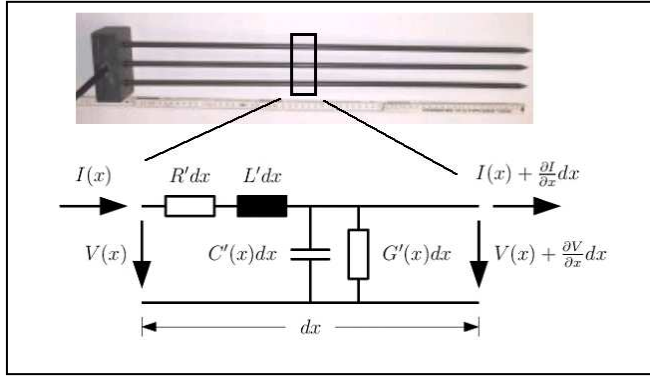


Figure 1. The simplified moisture probe model consisting of bulk electronic parts. Above: coated 3-rod-probe as an example for a moisture probe (TDR waveguide); below: equivalent circuit of the transmission line.

Reference [1] derived the following wave equation from the circuit model for describing the propagation of a voltage pulse $V(x,t)$ along the buried waveguide:

$$\left(L'(x)C'(x)\frac{\partial^2}{\partial t^2} + L'(x)G'(x)\frac{\partial}{\partial t} + \frac{\partial L'(x)/\partial x}{L'(x)}\frac{\partial}{\partial x} - \frac{\partial^2}{\partial x^2} \right) V(x,t) = 0 \quad (1)$$

Capacitance $C'(x)$ and effective conductance $G'(x)$ are influenced by the soil water content distribution $\theta(x)$ along the waveguide. Inductance $L'(x)$ is a function of the transmission-line only and piecewise constant for coaxial cable and moisture probe. The spatial derivative of $L'(x)$ in (1) describes the change of inductance between coaxial cable and probe. Resistance R' along the waveguide has been neglected. All parameters are given per unit length.

Strictly spoken the equivalent circuit of Fig. 1 is not totally correct, because the conductor G' should be enclosed by two capacitors due to the rod coating. Therefore G' is not the real ionic conductance of the soil but a kind of correcting parameter in the determination of C' . According to former results we assume that this simplification does not have a large influence on the results.

Eqn. (1) is solved numerically with appropriate initial and boundary conditions to simulate a TDR measurement

$V_O^{(s)}(t, x_0 | C', G')$ for given $C'(x)$ and $G'(x)$. The result of the simulation is compared to the TDR measurement. An optimization algorithm described in [1,2] is used to modify the electrical parameters $C'(x)$ and $G'(x)$ along the simulated moisture probe until the simulated TDR reflectogram $V_O^{(s)}(t, x_0)$ matches the measurement $V_O^{(m)}(t, x_0)$ sufficiently well. The final parameter distributions resulting from the simulation are the best estimate of the electric properties along the real probe in soil.

B. From Capacitance to Dielectric Permittivity

To derive the volumetric water content profile $\theta(x)$ the dielectric permittivity profile $\epsilon(x)$ of the soil/water/air mixture has to be extracted from the capacitance profile $C'(x)$ first. For the simple moisture probe it is possible to find a convenient parametric form for $C'(\epsilon)$:

$$1/C'(\epsilon) = 1/(\epsilon \cdot C_1') + 1/C_2' \quad (2)$$

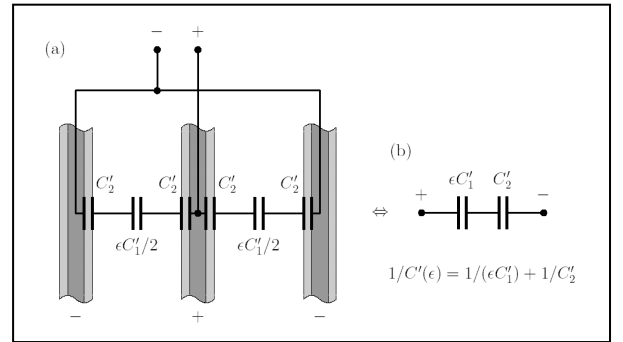


Figure 2. Capacitance C' of a 3-rod-probe as a function of the soil's dielectric permittivity ϵ . (a) segment of three parallel rods encompassed by soil; light gray: PVC coating; dark gray: metallic core; (b) equivalent circuit. C_1' , C_2' : constant capacitance parameters determined by the probe's geometry and material.

C. From Dielectric Permittivity to Water Content

The second step performs the transition from dielectric permittivity to water content. An empirical relationship between ϵ and θ often used in TDR applications was found by [7]. We use a more simple but less general empirical formula, which we derived from laboratory experiments with a loamy sand:

$$\theta(\epsilon) = 30.1 \cdot \epsilon^{0.31} - 41.1 \text{ (%Vol)}. \quad (3)$$

D. Probe Parameters

The rods of the 3-rod-probe under investigation consist of stainless steel cores of 6 mm diameter with a 1 mm thick PVC coating. The rods are 30 mm apart. They are screwed into the probe head which connects them to a 50 Ohms coaxial cable.

According to (1) and (2) it is necessary to determine the three parameters C_1' , C_2' , and L' for the rod probe. This can be done empirically by measuring TDR pulse propagation velocities $v_i = v(\varepsilon_i)$ for two different media with dielectric permittivities ε_1 , and ε_2 , respectively. The pulse propagation velocity along the coated probe rods is:

$$v(\varepsilon) = 1/\sqrt{L' \cdot C'(\varepsilon)} \quad (4)$$

The pulse velocity is determined empirically by measuring the time span between the first two main reflections in the TDR reflectogram. Combining (4) for the two materials one yields:

$$\begin{aligned} C_1' &= (\varepsilon_2 - \varepsilon_1)/(\varepsilon_2 \varepsilon_1 (v_1^2 - v_2^2) \cdot L') \text{ and} \\ C_2' &= (\varepsilon_2 - \varepsilon_1)/((\varepsilon_2 v_2^2 - \varepsilon_1 v_1^2) \cdot L') \end{aligned} \quad (5)$$

The rod impedance Z can be used to get L' :

$$Z(\varepsilon) = \sqrt{L'/C'(\varepsilon)} \quad (6)$$

The impedance mismatch between coaxial cable and probe rods leads to a partial reflection of the incident excitation pulse. The amplitude of incident and reflected signal are denoted by A_I and A_R , respectively. Then the reflection coefficient yields:

$$r(\varepsilon) = A_I / A_R = (Z(\varepsilon) - Z_0)/(Z(\varepsilon) + Z_0) \quad (7)$$

which can be determined experimentally from TDR measurements. The combination of the last equations yields:

$$L' = (1 + r(\varepsilon))/(1 - r(\varepsilon)) \cdot Z_0 / v(\varepsilon) \quad (8)$$

Eqns. (5) and (8) are sufficient to determine the parameters for the coated 3-rod-probe from TDR reflectograms.

E. Empirical Relationship between Capacitance and Effective Conductance

The wave equation (1) needs two parameter distributions $C'(x)$ and $G'(x)$. These parameter distributions could be found simultaneously by inverse modeling, if two independent TDR measurements were available for the same moisture probe, which is possible only with special probes (double sided). In case of single sided probes it is reasonable to assume a relationship between $C'(x)$ and $G'(x)$, since both parameters are linked by soil moisture: higher water content leads to higher dielectric permittivity and higher conductivity. The following relationship is proposed:

$$G'(C') = \begin{cases} G'_\infty \cdot (1 - \exp(-(C' - C'_0)/C_d)), & \text{if } C' \geq C'_0, \\ 0, & \text{if } 0 \leq C' \leq C'_0. \end{cases} \quad (9)$$

With this relationship a given capacitance profile can be transformed into an effective conductance profile. Both parameter distributions are inserted into (1).

F. Electrodynamics Simulation of the TDR Measuring Process with Microwave Studio

To test the Spatial TDR method together with the 3-rod-probe several TDR reflectograms are simulated with Microwave Studio (MWS), an EM simulation tool based on the full wave solution of Maxwell's equations. In the numerical model the 3-rod-probe is embedded in a three layered material, whose dielectric permittivity and ionic conductance can be modified ideally. A voltage step pulse of 1 Volt amplitude and 1 GHz bandwidth is fed into the probe. The simulated TDR reflectograms are used for three purposes: 1. determination of the probe parameters according to (5) and (8), 2. determination of the empirical C' - G' -relationship (9), and 3. generation of test reflectograms to assess the quality of the Spatial TDR algorithm.

III. RESULTS

To assess the quality of the algorithm which determines the water content profile from a TDR reflectogram by inverse parameter estimation, the MWS is fed with three soil layers of different moisture. Tab. I shows the applied soil parameters.

TABLE I. MATERIAL PARAMETERS USED IN MICROWAVE STUDIO

Table Head	Moisture state		
	θ (%vol)	ε (-)	σ mS/m
'dry'	0.5	2.9	0
'moist'	8	4.9	14
'wet'	13	6.8	23

Dielectric permittivity ε and ionic conductivity σ of a soil for different volumetric water contents θ . The parameters were derived from loamy sand in laboratory experiments. For the sake of simplicity the moisture states are named 'dry', 'wet', and 'moist', respectively.

Each simulated reflectogram together with the excitation pulse was fed into the Spatial TDR algorithm and a reconstruction process was conducted to retrieve the soil moisture profiles, which should match the predefined as close as possible.

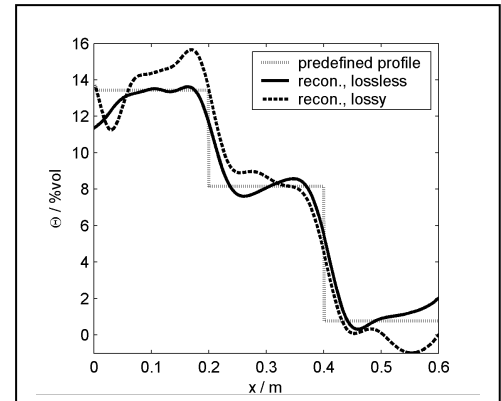


Figure 3. Moisture profile, sequence wet/moist/dry, predefined in the MWS model, and reconstructed by means of the Spatial TDR algorithm.

The predefined and reconstructed soil moisture profile for the sequence wet/moist/dry is shown in Fig. 3. Two cases were realized: one with and the other without consideration of ionic conductivity σ (lossy and lossless case). Fig. 4 displays the corresponding TDR reflectograms simulated with MWS and reconstructed by the Spatial TDR algorithm.

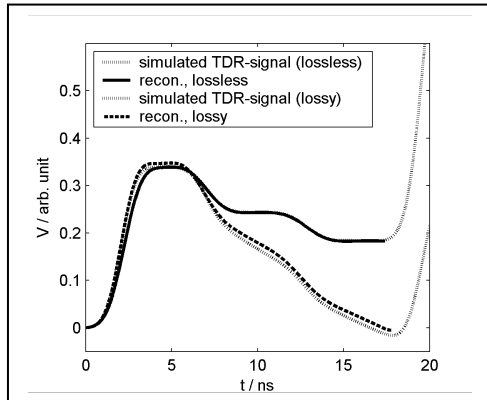


Figure 4. TDR reflectograms simulated by MWS and the corresponding signal approximations resulting from the reconstruction algorithm. Material sequence wet/moist/dry. Energy losses due to ionic conductance lead to a strong falling trend of the TDR signals.

To test Spatial TDR in laboratory a box with three chambers of 0.2m length each was prepared in accordance to the MWS numerical model and filled with soil of predefined moisture (s. Tab. I). A 3-rod-probe of 0.6m length (s. Fig. 1) was installed such that it crossed all chambers. TDR measurements were performed with a Tektronix metallic cable tester 1502B. With each material sequence four soil samples of known volume were taken from each chamber. Their volumetric water content was determined by oven drying. Fig. 5 shows the result for the material sequence dry/moist/wet.

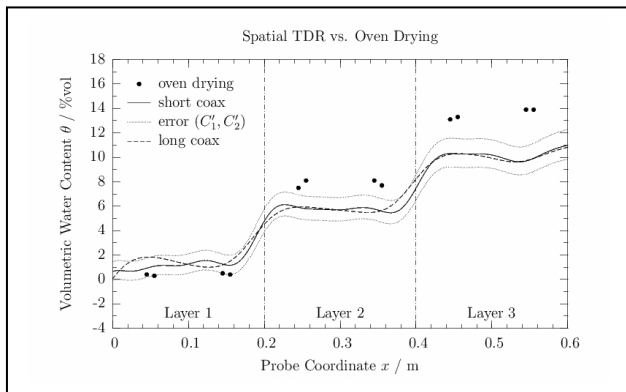


Figure 5. Spatial TDR application to a real soil moisture profile. Material sequence dry/moist/wet. Reconstruction results compared to volumetric water content of soil samples determined by oven drying. Differences up to 3%vol are due to imperfect calibration of the real 3-rod-probe.

The overall accuracy of Spatial TDR with coated rod probe is sufficient for many applications in soil science. A lysimeter experiment with 1 m³ loamy sand showed that the method is capable of tracking transient soil moisture profiles under irrigation with high spatial and temporal resolution [3].

IV. APPLICATIONS

A. Measuring of water content for flood warning

The high variability of the rainfall-runoff process can be partly explained by the catchments state which is linked to soil moisture (cf. [8]). Not only the mean moisture content is crucial but also its distribution (cf. [6]). At the Goldersbach catchment near Tübingen 46 twin rod probes were installed in order to measure the extension of a saturation zone. A brook divides the measurement site, which is dominated by podzolic soils. The measurements of water content were reconstructed spatially along the 60 cm long twin rod probes in a distribution of 2 mm and interpolated into a quasi three-dimensional soil moisture space. Fig. 6 shows the soil moisture distributions as a cut in the depth of 15 cm for dry and wet conditions. As a result of the measurements most of the soil moisture dynamic was found on the top 30 cm of the soil horizon.

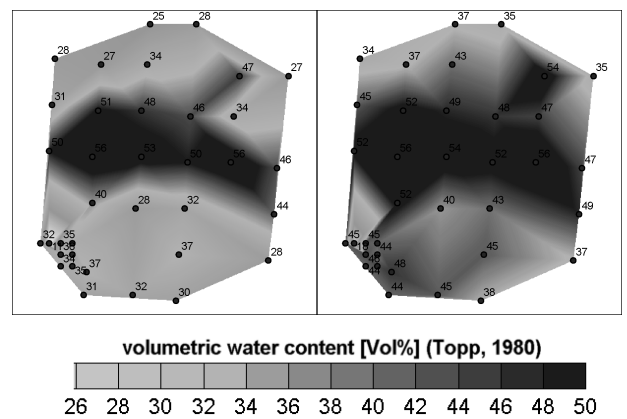


Figure 6. Horizontal cut of the three dimensional soil moisture space in the depth of 15 cm, for dry conditions (left) and wet conditions (right) as volumetric soil moisture

B. Measuring of water content on a full-scale Dike model

In order to investigate transient hydraulic processes in river dikes during a flood, a full-scale dike model at the Federal Waterways and Research Institute was equipped vertically with 12 sensor cables between 0.7 m and 3.0 m in length. Both sides of the sensor cables were connected to the TDR device. The model was built up homogeneously with uniform sand (grain size 0.2 to 2 mm) and it is based on a waterproof sealing of plastic. As a result of this construction, the water infiltrating into the dike will flow to a drain at the toe of the land side slope and directed to a measuring device (cf. Fig. 7).

In the course of the investigation mentioned above, flood simulation tests and sprinkling tests were carried out on the dike model (cf. [4] and [5]). Fig. 8 shows the steady state of seepage condition during a flood simulation test in December 2000. The measurements of water content were reconstructed spatially along the sensor cable (cf. [1,2]) and interpolated as distribution of saturation in the considered cross section (assumed porosity of 37 %). The dots represent the position of the sensor cables together with the saturation at these points. On the water side the water level in the basin is shown, and the

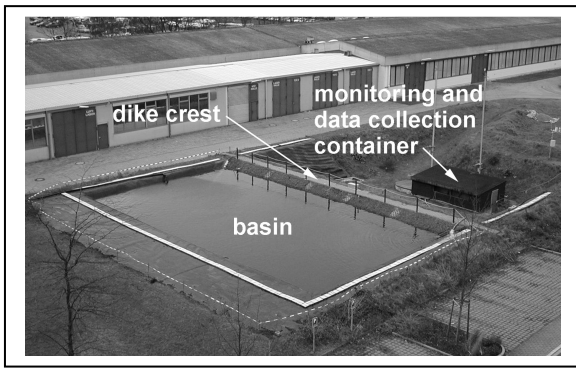


Figure 7. Full-scale dike model at the Federal Waterways and Research Institute (BAW) in Karlsruhe during a flood simulation test in December 2000 (steady state of seepage condition).

position of the phreatic line within the body of the dike is given, as estimated from the pore water pressure measurements in the base of the dike. It can be seen that the measurements of the water content correspond very well with the position of the phreatic line. During the flood simulation tests on the dike model it was discovered that the percolation area below the phreatic line does not become fully saturated. Up to 15 % of the pore space remained filled with air. This observation was verified by independent measurements during the steady state condition.

With this system it is possible to record the distribution of water content in a cross section within 5 minutes. This way, measurements of the water content with a spatial resolution of

3 cm are possible. The profiles of saturation can be determined with an average uncertainty of $\pm 4\%$ compared to other independent field measurements.

REFERENCES

- [1] S. Schlaeger, Inversion von TDR-Messungen zur Rekonstruktion räumlich verteilter bodenphysikalischer Parameter, Ph.D. thesis, Institute of Soil Mechanics and Rock Mechanics, Univ. of Karlsruhe, 2002.
- [2] S. Schlaeger, A fast TDR-inversion technique for the reconstruction of spatial soil moisture content, Hydrology and Earth System Sciences, vol. 9, pp.481-492, 2005.
- [3] R. Becker, Spatial Time Domain Reflectometry for Monitoring Transient Moisture Profiles, Ph.D. thesis, Institute for Water Resources, Hydraulic and Rural Engineering, Univ. of Karlsruhe, 2004.
- [4] A. Scheuermann, S. Schlaeger, C. Huebner, A. Brandelik, and J. Brauns, "Monitoring of the spatial soil water distribution on a full-scale dike model," Proceeding of the Fourth International Conference on Electromagnetic Wave Interaction with Water and Moist Substances, edited by K. Kupfer, 343-350, Weimar, 2001.
- [5] A. Scheuermann, Instationäre Durchfeuchtung quasi-homogener Erddeiche, Ph.D. thesis, Institute of Soil Mechanics and Rock Mechanics, Univ. of Karlsruhe, 2005.
- [6] W. Schädel, „Schritte zur Verbesserung der Hochwasserwarnung mittels Online-Bodenfeuchtemessungen“, Ph.D. thesis, Institute of Water and River Basin Management, Univ. of Karlsruhe, 2006.
- [7] G.C. Topp, J.L. Davis, and A.P. Annan, Electromagnetic determination of soil water content: Measurement in coaxial transmission lines, Water Resources Research, vol. 16(3), pp. 574-582, 1980
- [8] G. Peschke, "Hydrological processes of storm runoff generation". PIK Report, 48, 75-87, Potsdam, 1998.

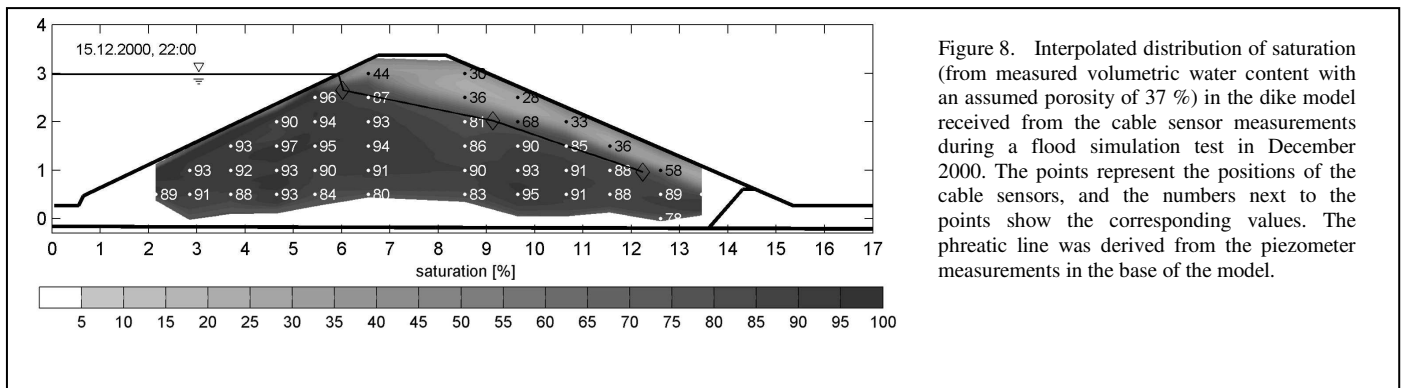


Figure 8. Interpolated distribution of saturation (from measured volumetric water content with an assumed porosity of 37 %) in the dike model received from the cable sensor measurements during a flood simulation test in December 2000. The points represent the positions of the cable sensors, and the numbers next to the points show the corresponding values. The phreatic line was derived from the piezometer measurements in the base of the model.

Optimisation of the microwave assisted SHS of intermetallics in single mode applicators

C. Leonelli, G. Poli, P. Veronesi

University of Modena and Reggio Emilia, Department of Materials and Environmental Engineering, Via Vignolesse 905, 41100 Modena, Italy, Tel. +39 059 2056207, E-mail: paolov@unimore.it

Short Abstract—Microwave assisted Self propagating High temperature Synthesis (SHS) of NiAl intermetallic in single mode applicator has been optimized by means of electromagnetic field numerical simulation and Design of Experiments techniques. The optimized synthesis conditions have been applied to the reactive sintering of NiAl on titanium substrates, evidencing the formation of a hard dendritic layer, belonging to the Ni-Al-Ti system. The dendritic layer could not be directly formed using conventional (resistance) heating.

Keywords: microwave assisted SHS, intermetallic, NiAl, titanium

I. INTRODUCTION

A relatively economic route for the production of intermetallics in bulk form is Combustion Synthesis (CS) or Reaction Synthesis (RS), a process used for decades to obtain ceramics and their composites, benefiting of the widely acknowledged energy and economic savings [1-5]. Reaction synthesis (combustion synthesis) is a process which uses the exothermic reaction of reactants, properly ignited to spontaneously transform into products. Depending on the mode of ignition, the process can be subdivided into *Self-propagating High temperature Synthesis* (SHS) in which a reactant compact is typically ignited at one end, and thermal explosion, in which the whole volume of the compact is heated to the ignition temperature. Both methods of ignition have been used in the past in the fabrication of nickel aluminides, and recently the use of microwaves to ignite CS has been reported for the Ni₃Al intermetallic [6]. The direct microwave absorption, within the skin depth, of the metal powders, can not completely explain the microwave-matter interaction. In case of metallic powder compacts immersed in relatively high intensity electromagnetic field, other phenomena can occur, leading to a more pronounced and deeper heating of the conductive material, like arcing and plasma formation [7,8]. Moreover, the oxide layer which can be present on the metallic powders can give a further heating contribution by dielectric heating [9]. One of the main drawbacks in using microwaves to ignite the CS lies in its intrinsically low reproducibility. Many factors affect the way a load can be heated in a microwave applicator, and small compositional inhomogeneities (variations of electric, magnetic or dielectric properties), or non-controllable electromagnetic field distributions contribute in perturbing the heat generation. Aim of the present work is the optimisation of the Microwave Assisted Combustion Synthesis (μ wACS) of intermetallics in a single mode applicator, in order to achieve the highest yields, energy efficiency and process

reproducibility. An application of the method to the synthesis of NiAl and to the reactive sintering of NiAl compacts on Ti substrates is presented as well

II. NUMERICAL SIMULATION TO OPTIMISE THE SYNTHESIS CONDITIONS

The software Concerto 4.0 (Vector Fields, U.K.) has been used to numerically simulate the heating behavior of a metallic powder compact in a microwave single mode applicator, based on the WR340 waveguide geometry. The aim of the modeling step, preliminary to the experimental activity, is to determine the most suitable refractory support to be used during Microwave Assisted Combustion Synthesis. As a matter of fact, the refractory deeply influences the heating behavior and the energy efficiency of the whole process, since it can absorb or reflect microwaves, as well as modify the electromagnetic field distribution around the sample. The model is composed of a rectangular metallic enclosure (microwave applicator) containing a 70 mm diameter disc upon which lies a 30 mm diameter silicon carbide disc and an optional third graphite disc, 20 mm of diameter. The SiC disc, acting as an auxiliary absorber, is used to increase the temperature of the load, placed on top, in order to improve its microwave coupling efficiency. This setup has demonstrated, in a previous work [10] that the presence of an auxiliary absorber helps improving the reproducibility of the results, while a direct microwave absorption by the metallic powder compact is more prone to arcing and lack of homogeneity. The material of which the base disc is constituted has been varied from a total reflective behavior (metal), to a lossy (SiC) or to a transparent (Al₂O₃) one. The length of the applicator can be varied as well, to simulate the presence of a movable plunger, while the remaining dimensions (86 x 43 mm) are fixed. On one side of the applicator is positioned a port excited sinusoidally in the fundamental TE₁₀ mode, simulating the magnetron, operating at 500W power, 2.45 GHz frequency. Four different configurations have been tested, namely a metallic, a low-loss, a lossy disc, and a low loss disc having a third graphite disc on top. The presence of a different support material (base disc) will affect the heating behaviour of a load positioned on the top of the SiC element, as shown in fig. 1. This difference can be quantitatively evaluated integrating the calculated SAR values over the second disc volume, as depicted in fig.2. The best conversion of microwave power into heat occurs in case of alumina as a refractory support. The presence of a thin graphite disc on the top of the SiC disc slightly worsen the efficiency, while the presence of a lossy material lowers the power

available to heat the SiC disc of more than one order of magnitude, while the metallic support lowers the electric field intensity in the SiC disc, as well as drastically changing the impedance matching of the system.

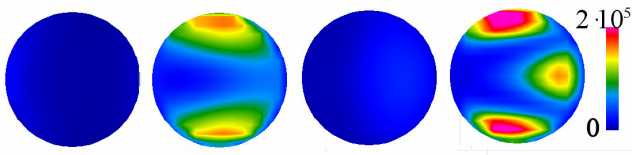


Figure 1. SAR envelope (W/kg) of the SiC disc layer nearest to the reacting Ni-Al powders, placed on (from left to right): a metallic disc, a low-loss disc, a lossy disc, and a low loss disc having the third graphite disc on top

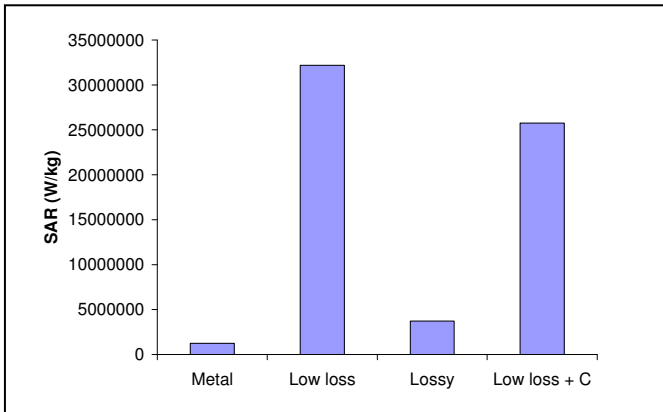


Figure 2. SAR in the SiC disc volume as a function of the base disc material and of the presence of the optional third graphite disc

III. EXPERIMENTAL

A. NiAl synthesis

The software Design Expert v.6 was used to reduce the number of experiments needed to gather information regarding the optimization of the SHS of NiAl. Independent variables were: microwave forward power (500, 1500 W), sample mass (3, 5 g), sample forming pressure (50, 150 MPa), atmosphere (Ar, air) and support material (SiC, graphite). Dependent variables were ignition temperature, ignition time and a calculated merit factor proportional to the amount of NiAl obtained. A two level factorial fractional ($1/2$) design was chosen, leading to 16 experimental conditions, repeated for two blocks. Ni carbonyl powders (99% pure, 5-7 μm in diameter) and Al gas atomized powders (99.8% pure, 10-50 μm in diameter) were mixed in a Al_2O_3 ceramic jar for 30 minutes under vacuum in a 1:1 atomic ratio. Successively, to compact the powder mixtures, an uniaxial pressure of 50 or 150 MPa, in a cylindrical metal mould, was applied; the diameter of the compacted samples was 20 mm. A microwave TE10n single mode applicator operating at 2.45 GHz was used to start the SHS. Forward and reflected power were monitored by means of a directional coupler, while a 3-stub tuner and a movable short circuit were used for impedance matching purposes during the whole test runs. A 3 kW magnetron, water cooled, was used to feed the applicator, interposing a 3-port circulator

to protect the generator from the reflected power. The magnetron forward power was set to constant power (500 or 1500 W) for all the runs. Reacted samples were subjected to optical microscopy and Scanning Electron Microscopy (SEM) to evidence the microstructure evolution, while phase analysis was performed by means of X-Ray Diffraction analysis (XRD). EDS (Energy Dispersive x-ray microanalyzer Spectroscopy), attached to the SEM, was used to confirm the absence of potentially deleterious unhomogenous regions, presenting a Ni/Al ratio different from 1. A merit factor was defined as the ratio between the NiAl XRD main peak intensity and the sum of the NiAl and Al_2O_3 main peak, the latter if present.

B. Reactive sintering of NiAl compacts on Ti substrates

The optimized synthesis conditions previously determined for the SHS of NiAl intermetallics were applied to reactive sintered Ni-Al (1:1 atomic ratio) powder compacts on Ti and Ti6Al4V discs. The high temperature involved in the synthesis can be higher than the titanium melting point, thus leading to the rapid formation of ternary Ni-Al-Ti intermetallic compounds. In order to compare microwave assisted SHS with conventional SHS methods, reactive sintering tests have been performed in a resistance heating furnace, maintaining unaltered the experimental conditions (atmosphere and system geometry) and applying similar heating rates to the reacting powders, when possible.

IV. RESULTS AND DISCUSSION

Microwave assisted SHS of NiAl intermetallic was successful in all the experimental conditions considered, despite some pronounced differences in the final products aspect and composition. The variation of the synthesis conditions allowed to investigate the influence of the main variables, as depicted in fig. 3.

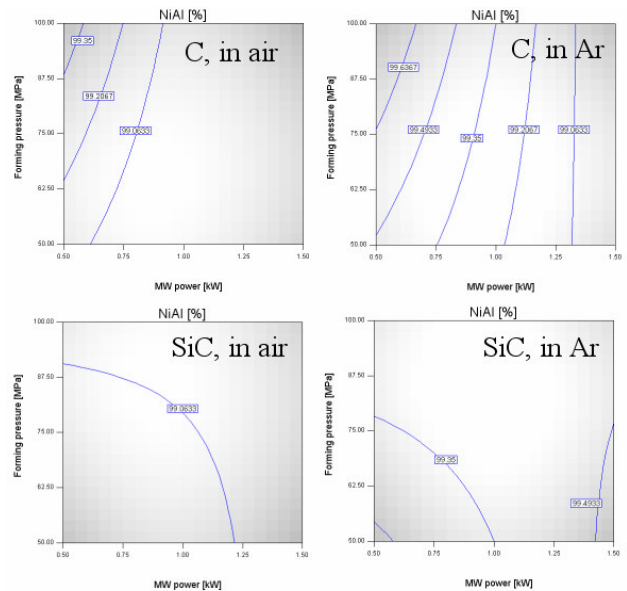


Figure 3. NiAl yields as a function of the synthesis conditions: forming pressure, microwave power, substrate material (C or SiC) and atmosphere

From the experimental results, it can be inferred that:

- Ar flux increases the NiAl yield, as well as reaction time. This can be explained considering the prevention from the oxidation offered by the Ar flux, but also its cooling effect at the sample's surface.
- the use of SiC, without any further conductive layer, leads to the highest reproducibility of results and the higher NiAl yield. The SiC, as a matter of fact, is governing the early stages of heating and constitutes a somewhat fixed load which is able to partially compensate the sample's properties variation. Moreover, the higher temperature surrounding the sample improves the propagation of the reaction from the ignition points.
- a lower forming pressure increases the microwave coupling and thus reduces the synthesis time. This phenomenon can be ascribed to a slightly higher microwave penetration in a partially dense compact, and a lower thermal conductivity of the sample, which, thus, dissipates less heat to the environment

Integrating the forward and reflected power curves as a function of time, and dividing by the NiAl mass obtained, it has been possible to quantify the specific energy consumption. Fig.4 summarizes the calculation results, evidencing that the specific energy consumption is lower in case of use of the SiC alone and without Ar flux, leading to an average 3.1 Wh/g of synthesised NiAl. Despite the presence of an auxiliary absorber, the lower reflected power, as well as the improved synthesis conditions, allow the obtainment of the highest energy efficiency.

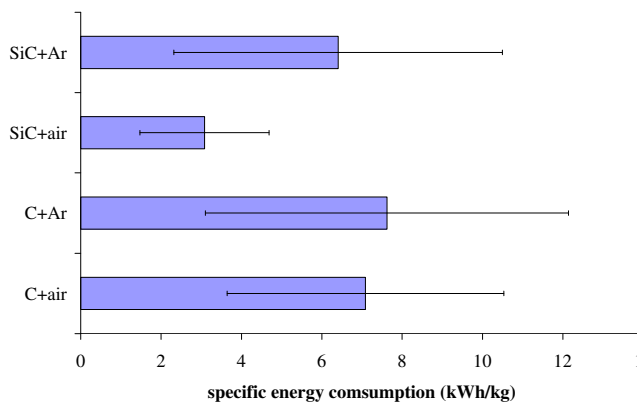


Figure 4. Average specific energy consumption for the microwave assisted NiAl synthesis as a function of the substrate material and of the atmosphere.

When the optimized experimental conditions (in terms of NiAl yield, i.e. using SiC and Ar flux) are applied to the microwave assisted synthesis of the intermetallic on a reactive layer, like titanium and its alloys, there is the formation of a dendritic layer, whose composition belongs to the Ni-Al-Ti system [11]. This dendritic layer is not observed after conventional SHS performed in the same conditions. The dendritic layer is not homogenous, compare spectra 1 and 2 in

fig. 5, and its titanium content progressively decreases moving from the substrate to the region where the NiAl powders compacts were placed. A NiAl free zone, obtained avoiding to completely cover the titanium substrate with the reacting powders, allowed to determine that there is no diffusion of titanium, the ternary dendritic region being formed exclusively by liquid NiAl diffusion in the titanium. This issue can explain the different microstructure observed when performing the SHS on titanium by microwaves rather than conventionally.

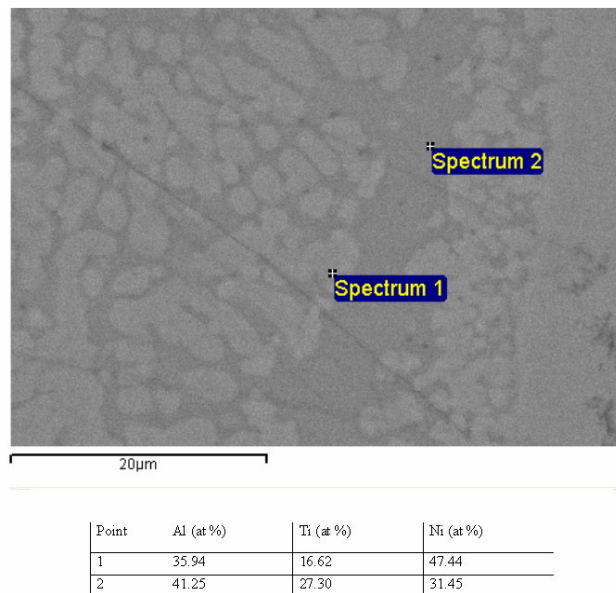


Figure 5. SEM Micrograph and EDS analysis of two regions belonging to the dendritic layer between the titanium substrate and the synthesized NiAl intermetallic

In conventional SHS, the temperature of the furnace is raised up to the temperature needed to ignite the reaction. As soon as the reaction starts, the high temperature due to the exothermic reaction tend to invert the heat flow, so that the newly formed intermetallic transmits heat to the surrounding environment. During microwave treatments, instead, energy can still be conveyed to the newly formed NiAl during and after the synthesis, and heat can still be generated inside the liquid NiAl phase, thus partially compensating the heat losses towards the cooler surroundings. This phenomenon could help slowing the solidification of the newly formed NiAl (and its compounds presenting different stoichiometry [12]) maintaining it in the liquid state for longer time, thus favoring its diffusion and reaction with the titanium substrate. From an application point of view, this peculiar aspect of microwave assisted SHS leading to reactive sintering of the starting Ni and Al powders presents numerous advantages, like the possibility of joining titanium parts with minimum overall heating of the parts (only the joining region is heated directly), or cladding titanium with layers presenting interesting mechanical properties. Fig. 6 shows the results of a scratch test, at 1N constant load, conducted on the interface regions among the titanium substrate, the dendritic layer, and the synthesized NiAl. The dendritic layer present a lower friction coefficient

(yellow curve), as well as higher hardness, deducible from the residual depth curve (green) and from fig 7. In addition it can be observed that the dendritic region is completely crack-free, and presents some crack-stopping capabilities, as evidenced in fig.7, where a crack from the NiAl region is not able to completely propagate through the dendritic layer.

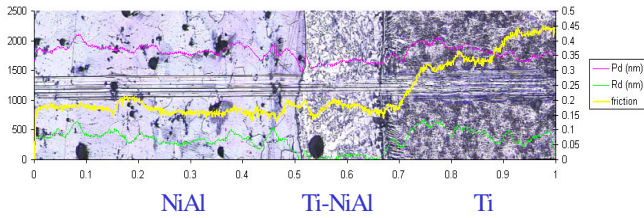


Figure 6. Scratch test (1N) on the dendritic interface: Pd= penetration depth of the indenter during the scratch test; Rd= residual depth of penetration after the test; friction= friction coefficient.

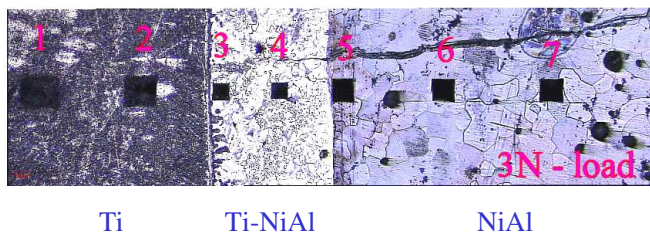


Figure 7. Vickers microhardness indentations on the titanium substrate, on the dendritic layer and on the NiAl intermetallic

V. CONCLUSIONS

Coupling the numerical simulation of the SHS of metallic powder compacts with a proper Design of Experiments can help reducing both the modeling and the experimental time required to optimise the process. An application of this approach to the synthesis of NiAl is presented, aimed at achieving the highest process reproducibility, yield and efficiency. Once the best synthesis conditions have been determined, the reactive sintering of NiAl on titanium substrate has been performed, both conventionally and by microwave heating. In the first case, no adhesion was observed between the substrate and the newly formed NiAl, while in the second case a pronounced dendritic layer, of composition belonging to the Ni-Al-Ti system, was formed. Its formation can be ascribed to the possibility offered by microwaves of conveying energy to the molten NiAl during synthesis and cooling, thus slowing its solidification and favoring its reaction with the titanium substrate. The dendritic layer present interesting mechanical properties, like low friction and high hardness, as well as crack-stopping capabilities.

ACKNOWLEDGMENT

The authors would like to thank Eng. Ramona Sola for performing the NiAl SHS experiments, and Eng. Monia Bernabei for her help in providing the titanium substrates and performing the reactive sintering treatments.

REFERENCES

- [1] H.C. Yi, J.J. Moore, "Self-propagating high-temperature (combustion) synthesis (SHS) of powder-compacted materials", *J. Mater. Sci.*, vol. 25 n.2, pp. 1159–1168, February 1990.
- [2] Z.A. Munir, U. Anselmi-Tamburini, "Self-propagating exothermic reactions: The synthesis of high-temperature materials by combustion", *Materials Science Reports*, Vol. 3, pp. 277-365, 1989
- [3] D.C. Dunand, "Reactive synthesis of aluminide intermetallics", *Mater. Manuf. Process.*, vol. 10, n.3, pp. 373–403, 1995.
- [4] J.J. Moore, H.J. Feng, "Combustion synthesis of advanced materials: Part I. Reaction parameters and Part II: Classification, applications and modelling", *Prog. Mater. Sci.*, vol. 39, pp. 243–316, 1995.
- [5] C.R. Bowen, B. Derby, "Self-propagating high temperature synthesis of ceramic materials", *Br. Cer. Trans.*, vol. 96, n.1, pp. 25–31, 1997.
- [6] S. Gedevisanishvili, D. Agrawal, R. Roy, " Microwave Combustion Synthesis and Sintering of Intermetallics and Alloys" *J. Mater. Sci. Letts*. Vol. 18, n.9, pp. 665–668, April 1999.
- [7] P. Veronesi, C. Leonelli, E. Bassoli, A. Gatto, L. Iuliano, " Microwave assisted sintering of SLS green metal parts", *Proc. of Sintering 2003 - Penn State (USA) - CD-ROM*.
- [8] M. Willert-Porada, T. Gerdes, J. Grosse-Berg, H.-S. Park, " The role of plasma in microwave systems for materials processing ", *Plasma Science, ICOPS 2003*, p. 125 , 2003.
- [9] Yu.V. Bykov, K.I. Rybakov, V.E. Semenov, " High-temperature microwave processing of materials", *J. of Physics D: Applied Physics*, vol. 34, pp. R55 – R75, April 2001.
- [10] P. Veronesi, S. Ferrari, G.Poli, " Microwave sintering of spherical powders deriving from industrial machining" (in Italian), *Metal. Ita.*, vol. 1/2006, pp.17-20, January 2006.
- [11] A. Casagrande, G.P. Cammarota, C. Leonelli, G. Poli, P. Veronesi, "Microwave assisted reactive sintering of intermetallic coatings on titanium", *proceedings of PM2005*, in press.
- [12] J.C. Oliveira, A. Manaia, J.P. Dias, A. Cavaleiro, D. Teer, S. Taylor, "Structure and mechanical properties of Ti–Al films deposited by magnetron sputtering", *Surface and Coatings Technology*, Vol. 200, Iss. 1-4, pp. 395-398, 2005.